پرتال جامع مهندسی عمران به پشتوانه تیمی مجرب از دانشجویان تحصیلات تکمیلی مهندسی عمران دانشگاه شیراز جهت ارائه خدمات به دانشجویان و مهندسین محترم عمران با ایده هایی نو و رویکردی متفاوت راه اندازی شده است.

جهت ورود به بخش های مختلف وب سایت بر روی عنوان مورد نظر خود کلیک نمایید

AN INTRODUCTION TO GEOTECHNICAL ENGINEERING

SECOND EDITION

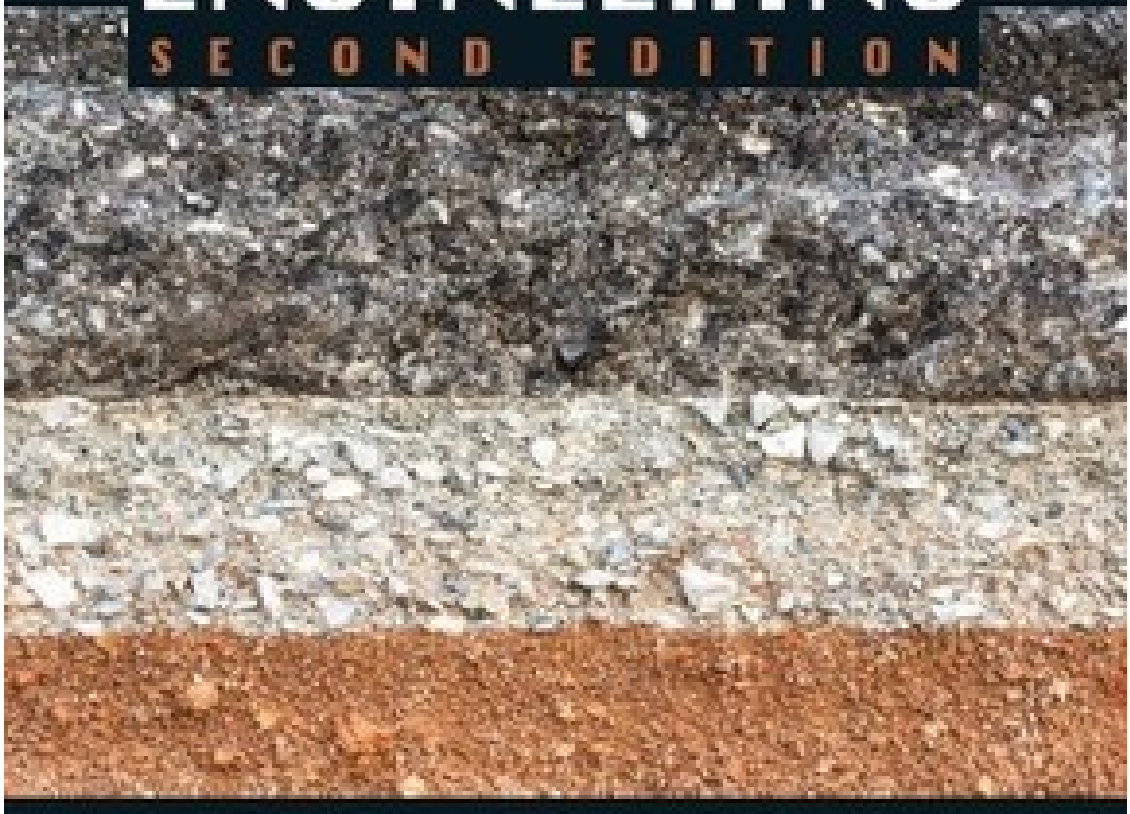

Robert D. Holtz • William D. Kovacs
Thomas C. Sheahan

ALWAYS LEARNING

PEARSON

AN INTRODUCTION TO GEOTECHNICAL ENGINEERING

Second Edition

Robert D. Holtz, Ph.D., P.E., D.GE
University of Washington

William D. Kovacs, Ph.D., P.E., D.GE
University of Rhode Island

Thomas C. Sheahan, Sc.D., P.E.
Northeastern University

PEARSON

Upper Saddle River Boston Columbus San Francisco New York
Indianapolis London Toronto Sydney Singapore Tokyo Montreal
Dubai Madrid Hong Kong Mexico City Munich Paris Amsterdam Cape Town

Preface

It has been thirty years since the publication of the first edition of *An Introduction to Geotechnical Engineering.* During those years, the practice of geotechnical engineering has greatly changed, but the fundamentals of soil mechanics and soil properties have remained essentially the same. Engineering education also has changed during that time, mostly for the better. On the other hand, reduced graduation requirements and the increased use of computations instead of the laboratory experience have often resulted in a tendency toward reduced rigor and over-simplification of some undergraduate education and textbooks.

We still believe that there is a need for more detailed and modern coverage of the engineering properties of geo-materials than is found in most undergraduate texts. This applies to students who concentrate in geotechnical engineering as well as the general civil engineering undergraduate student. Our students will be involved in increasingly more complex projects, especially those in transportation, structural, construction and environmental engineering. Those projects will increasingly involve environmental, economic and political constraints that will demand innovative solutions to civil engineering problems. Modern analytical techniques using digital computers have had a revolutionary effect on engineering design practice. However, the validity of the results from these computational procedures (which typically include striking graphical output) is highly dependent on the quality of the geotechnical engineering design parameters as well as the geology and site conditions.

Like the first edition, this edition is intended for use in the first of a two-course sequence in geotechnical engineering usually taught to third- and fourth-year undergraduate civil engineering students. We assume the students have a working knowledge of undergraduate mechanics, especially statics and mechanics of materials, including fluids. In the first course we introduce the "language" of geotechnical engineering—that is, the classification and engineering properties of soils and rocks. Once the student has a working knowledge of the behavior of geo-materials, he/she can begin to predict soil behavior and, in the second course, carry out the design of simple foundations and earth structures.

We have tried to make the text easily readable by the average undergraduate. To this end, *An Introduction to Geotechnical Engineering* is written at a rather elementary level, although the material covered may at times be quite sophisticated and complex. Involved derivations are relegated to appendices, where they are available to the interested student.

The emphasis throughout is on the practical, and admittedly empirical, knowledge of soil and rock behavior required by geotechnical engineers for the design and construction of foundations, embankments, and underground structures. Most of the material in the text is descriptive, since most of the engineering design applications are usually left to the second course in foundation engineering. Consequently, in order to strengthen this connection between the fundamental and applied, we have tried to indicate wherever possible the engineering significance of the property being discussed, why the property is needed, how it is determined or measured, and, to some extent, how it is actually used in specific design applications. We illustrate some simple geotechnical designs—for example, determining the

flow, uplift pressures, and exit gradients in 2-D seepage problems, and estimating the settlement of shallow foundations on sands and saturated clays.

One thing that has not changed in thirty years is that units remain a problem with U.S. geotechnical engineers. In line with the rest of the world, the American Society of Civil Engineers, and the American Society for Testing and Materials, we have used the S.I. System of Units in the text. Most students are conversant in both the U.S. customary (or British) engineering units and S.I., but readers unfamiliar with S.I. may find Appendix A helpful. We have examples and problems in both systems, and we have been careful to use the correct definition of density (mass/unit volume) in phase relationships as well as in geostatic and hydrostatic pressure computations.

We consider the laboratory component of the first course to be an essential part of the neophyte engineer's experience with soils as a unique engineering material. How else is the young engineer to begin to develop a "feel" for soils and soil behavior, so essential for the successful practice of geotechnical engineering? An emphasis on laboratory and field testing is found throughout the text. The organization and development of the material in the text is traditional and generally follows the order of the laboratory portion of our first courses. The early chapters introduce the discipline of geotechnical engineering, phase relationships, index and classification properties of soils and rocks, geology, landforms, and the origin of geo-materials, clay minerals, soil and rock structures, and rock classification. Chapter 3, "Geology, Landforms, and the Origin of Geo-Materials," has been added to this edition because these topics are so critical to understanding the properties and subsequent behavior of geo-materials under various loading conditions. These chapters provide the background and terminology for the remainder of the text.

Following a very practical discussion of compaction in Chapter 5, Chapters 6 and 7 describe how water influences and affects soil behavior. Topics presented in Chapter 6 include groundwater and vadose water, capillarity, shrinkage, swelling, and collapsing soils, frost action, and effective stress. Chapter 7 discusses permeability, seepage, and seepage control.

The last six chapters deal with the compressibility and shear strength of soils and rocks. The treatment of these topics is quite modern and has been updated considerably. We now have stress distribution and settlement analyses, including immediate settlement, in a new Chapter 10 to separate these practical procedures from the more basic time-rate and compressibility behavior of natural and compacted soils and rock masses described in Chapters 8 and 9. In these latter chapters we have included new material on Janbu's tangent modulus method, in situ determination of compressibility of soil and rock, Burland's intrinsic compressibility of soils, and finite difference solution to the Terzaghi consolidation equation. We have extended the Schmertmann method for prediction of field compression curves to overconsolidated soils, and we have updated Mesri's work on secondary compression.

We received much criticism about the length of Chapter 11 on shear strength in the first edition, so now shear strength properties of soils and rocks are discussed in three new chapters. New Chapter 11 on the Mohr circle, failure theories, and strength testing of soil and rocks has new material on the obliquity relations and in situ tests for shear strength. Chapter 12 is an introduction to shear strength of soils and rock and is primarily suitable for undergraduate students. More advanced topics in shear strength of soils and rocks are discussed in Chapter 13, which graduate students and practicing geotechnical engineers should find useful. New material in Chapter 12 includes multistage testing, in situ tests for the shear strength of sands and the strength of compacted clays, rocks, and transitional materials. We now have the stress-path method in Chapter 13, which also includes sections on critical-state soil mechanics and an introduction to constitutive models. We then discuss some advanced topics on the shear strength of sands that start with the fundamental basis of their drained, undrained, and plane-strain strengths. The residual shear strength of sands and clays provides a transition into the stress-deformation and shear strength of clays, where we discuss failure definitions, Hvorslev strength parameters, stress history, the Jürgenson–Rutledge hypothesis, consolidation methods to overcome sample disturbance, anisotropy, plane-strain strength, and strain-rate effects. We end Chapter 13 with sections on the strength of unsaturated soils, properties of soils under dynamic loading, and failure theories for rock.

Even though it is primarily for the beginning student in geotechnical engineering, advanced students in other disciplines and engineers desiring a refresher in engineering properties may find the book helpful. Because of the many fully worked example problems, the book is almost "self-teaching." This aspect of the text also potentially frees the instructor in a formal course from the necessity of working example problems during lectures. It allows the instructor to concentrate on explaining basic principles and illustrating specific engineering applications of the points in question. From the first edition, we know that many practicing geotechnical engineers will find this book useful as a refresher and for the typical values given for classification and engineering properties for a wide variety of soils; we have found such a compendium very useful in our own engineering practice.

The solutions manual and test manual as well as PowerPoint figures of all images and tables from this book can be downloaded electronically from our Instructor's Resource Center located at www.pearsonhighered.com. The material available through the Instructor Resource Center is provided solely for the use of instructors in teaching their courses and assessing student learning. All requests for instructor access are verified against our customer database and/or through contacting the requestor's institution. Contact your local sales representative for additional assistance or support.

ACKNOWLEDGMENTS

To acknowledge all who have contributed to this book is a formidable task. We have tried whenever possible to indicate by references or quotations, concepts and ideas originating in the literature or with our former teachers, especially Profs. B. B. Broms, A. Casagrande, R. J. Krizek, C.C. Ladd, J. K. Mitchell, J. O. Osterberg, and H. B. Seed. Others have made helpful suggestions or reviewed portions of the text, resulting in improvements to the final product. These include Roy Borden, David Chang, Herbert Einstein, Milt Harr, Vic Kaliakin, Jerry Leonards, Bill Likos, Harry Stewart, Dayakar Penumadu, Siva Sivakugan, and Tom Zimmie, and countless others who have made comments about the first edition over the years. The comments of Dick Galster, Teresa Taylor, and Hank Waldron significantly improved early drafts of Chapter 3.

We are grateful to our Production Project Manager, Clare Romeo, for the patience, diligence and humor she exhibited in the face of many challenges, and for her help in ensuring the quality of the final product. We also acknowledge those who assisted in the development of the 2nd edition through contributions of figures, reports, and administrative assistance. Figures and other resources were graciously supplied by John Burland, Don DeGroot, and Paul Mayne, among others from the 1st edition. At Northeastern, Joan Omoruyi, Ed Stevens, and Brett McKiernan provided research and administrative assistance.

Thank you to the reviewers of this edition: Kamal Tawfiq, Florida State University; Monica Prezzi, Purdue University; Jay DeNatale, California Polytechnic State University; Robert Mokwa, Montana State University; Balasingam Muhunthan, Washington State University; Trevor Smith, Portland State University; Tom Zimmie, Rensselaer Polytechnic Institute; Scott Ashford, University of California–San Diego; Robert D'Andrea, Worcester Polytechnic Institute; Samuel Clemence, Syracuse University; Dave Elton, Auburn University; and Khaled Sobhan, Florida Atlantic University.

On a personal note, we wish to thank our respective spouses, Cricket, Eileen and Maryrose, who endured from a few to several years of delays, sporadic periods of stress, and many evenings and weekends that should have been spent with their husbands instead of sharing their marriages with this book.

R. D. HOLTZ
SEATTLE, WASHINGTON

W. D. KOVACS
KINGSTON, RHODE ISLAND

T. C. SHEAHAN
BOSTON, MASSACHUSETTS

CHAPTER 1

Introduction to Geotechnical Engineering

1.1 GEOTECHNICAL ENGINEERING

Geotechnical engineering is concerned with the application of civil engineering technology to some aspect of the earth, usually the natural materials found on or near the earth's surface. Civil engineers call these materials *soil* and *rock*. *Soil*, in an engineering sense, is the relatively loose agglomerate of mineral and organic materials and sediments found above the bedrock. Soils can be relatively easily broken down into their constituent mineral or organic particles. *Rock*, on the other hand, has very strong internal cohesive and molecular forces which hold its constituent mineral grains together. This is true for massive bedrock as well as for a piece of gravel found in a clay soil. The dividing line between soil and rock is arbitrary, and many natural materials encountered in engineering practice cannot be easily classified. They may be either a "very soft rock" or a "very hard soil."

Other scientific disciplines have different meanings for the terms soil and rock. In geology, for example, *rock* means all the materials found in the earth's crust, including what most of us would call soil. Soils to a geologist are just decomposed and disintegrated rocks found in the very thin upper part of the crust and usually capable of supporting plant life. Similarly, pedology (soil science) and agronomy are concerned with only the very uppermost layers of soil—that is, those materials important to agriculture and forestry. Geotechnical engineers can learn much from both geology and pedology. Geotechnical engineering has considerable overlap with these fields, especially with engineering geology and geological engineering. But beginning students should remember that these fields may have different terminology, approaches, and objectives than geotechnical engineering.

Geotechnical engineering has several different aspects or emphases. *Soil mechanics* is concerned with the engineering mechanics and properties of soil, whereas *rock mechanics* is concerned with the engineering mechanics and properties of rock—usually, but not limited to, the bedrock. Soil mechanics applies to soils the basic principles of mechanics including kinematics, dynamics, fluid mechanics, and the mechanics of materials. In other words, soil—rather than water, steel, or concrete, for example—is the engineering material whose properties and behavior we must understand in order to build with it or upon it. A similar statement could also be made for rock mechanics. However, because in significant ways soil masses behave differently from rock masses, in practice there is not much overlap between

the two disciplines. This divergence is unfortunate from the viewpoint of the practicing civil engineer. Inconveniently, the world does not consist only of soft or loose soils and hard rock, but rather, most geo-materials fall somewhere between those extremes. In your professional practice you will have to learn to deal with a wide range of material properties and behaviors.

Foundation engineering applies engineering geology, soil mechanics, rock mechanics, and structural engineering to the design and construction of foundations for civil engineering and other structures. The foundation engineer must be able to predict the performance or response of the foundation soil or rock to the loads the structure imposes. Examples include foundations for industrial, commercial, and residential buildings, bridges, towers, and retaining walls, as well as foundations for oil and other kinds of tanks and offshore structures. Ships must have a drydock during construction or repairs, and the drydock must have a foundation. During construction and launch, rockets and appurtenant structures must be safely supported. Related geotechnical engineering problems the foundation engineer faces are the stability of natural and excavated slopes, the stability of permanent and temporary earth-retaining structures, problems of construction, control of water movement and water pressures, and even the maintenance and rehabilitation of old buildings. Not only must the foundation safely support static structural and construction loads, but it must also adequately resist dynamic loads due to wind, blasting, earthquakes, and the like.

If you think about it, we cannot design or construct *any* civil engineering structure, whether built on the earth or extraterrestrial, without ultimately considering the foundation soils and rocks. The performance, economy, and safety of any civil engineering structure ultimately are affected or even controlled by its foundation.

Earth materials are often used as a construction material because they are the cheapest possible building material. However, their engineering properties such as strength and compressibility are often naturally poor, and measures must be taken to densify, strengthen, or otherwise stabilize and reinforce soils so that they will perform satisfactorily. Highway and railway embankments, airfields, earth and rock dams, levees, and aqueducts are examples of earth structures, and the geotechnical engineer is responsible for their design and construction. Dam safety and rehabilitation of old dams are important aspects of this phase of geotechnical engineering. A related consideration, especially for highway and airfield engineers, is the design of the surface layer on the earth structure—the pavement. Here the overlap between the transportation and geotechnical disciplines is apparent.

Rock engineering, analogous to foundation engineering for soils, is concerned with rock as a foundation and construction material. Because most of the earth's surface is covered with soil (or water), rock engineering usually occurs underground (tunnels, underground power houses, petroleum storage rooms, mines, yours, and so on). But some rock engineering problems occur at the surface, such as in the case of building and dam foundations carried to bedrock, deep excavations to bedrock, stability of rock slopes, and the like.

In recent years, geotechnical engineers have become increasingly involved in the solution of environmental problems involving soil and rock. This developing interdisciplinary field is called *geoenvironmental engineering* or *environmental geotechnics*. Especially challenging are problems of polluted groundwater, proper disposal and containment of municipal and industrial wastes, design and construction of nuclear waste repositories, and remediation of hazardous waste repositories (aka dumps) and other contaminated sites. Although all these problems have a major geotechnical engineering component, they are interdisciplinary in nature, and their solutions require that geotechnical engineers work together with environmental and chemical engineers, environmental and public health specialists, geohydrologists, and regulatory agency personnel.

In presenting some of the typical problems facing the geotechnical engineer, we wanted you to see, first, how broad the field is and, second, how important it is to the design and construction of civil engineering structures, as well as to the basic health and safety of society. In a very real sense, geotechnical engineering combines the basic physical and mathematical sciences, geology, and pedology, with

environmental, hydraulic, structural, transportation, construction, and mining engineering. It truly is an exciting and challenging field.

1.2 THE UNIQUE NATURE OF SOIL AND ROCK MATERIALS

We mentioned earlier that soil—from a civil engineering point of view—is the relatively loose agglomeration of mineral and organic materials found above the bedrock. In a broader sense, of course, even shallow bedrock is of interest to geotechnical engineers, as illustrated by examples given above.

The nature and behavior of soil and rock are discussed in greater detail throughout this text. For now, we want just to set the stage for what you are about to study. We assume you understand that rock refers to any hard solid aggregate or mass of mineral matter found in the earth's crust. You also already have a layperson's idea about soil. At least you know in general what *sand* and *gravel* are, and perhaps you even have an idea about fine-grained soils such as *silts* and *clays*. These terms have quite precise engineering definitions, as we shall later see, but for now the general concept that soils are particles will suffice.

Soils are particles of what? Well, usually particles of mineral matter or, more simply, broken-up pieces of rock that result from weathering and other geologic processes (described in Chapter 3) acting on massive rock deposits and layers. If we talk for the moment about the size of the particles, gravels are small pieces of rock and typically contain several minerals, whereas sands are even smaller pieces, and each grain usually consists of only a single mineral. If you cannot *see* each individual grain of a soil, then the soil is either a silt or a clay or a mixture of each. In fact, natural soils generally are a mixture of several different particle sizes and may even contain organic matter. Some soils, such as *peat*, may be almost entirely organic. Furthermore, because soils are a particulate material, they have voids, and the voids are usually filled with water and air. The physical and chemical interaction of the water and air in the voids with the particles of soil, as well as the interaction of the particles themselves, makes soil's behavior complicated and leads to some of its unique properties.

Because of the nature of soil and rock materials and the complexity of the geological environment, geotechnical engineering is highly empirical. It is perhaps much more of an "art" than the other disciplines within civil engineering. Soils and rocks are often highly variable, even within a distance of a few millimeters. In other words, soils and rocks are *heterogeneous* rather than *homogeneous* materials. That is, their material or engineering properties may vary widely from point to point within a soil or rock mass. Furthermore, these materials in general are *nonlinear*; their stress-strain curves are not straight lines. To further complicate things (as well as make them interesting!), soils especially are nonconservative materials. That is, they have a fantastic memory—they remember almost everything that ever happened to them, and this fact strongly affects their engineering behavior. Instead of being *isotropic*, soils and rocks are typically *anisotropic*, which means that their material or engineering properties are not the same in all directions.

Most of our theories about the mechanical behavior of engineering materials assume that they are homogeneous and isotropic and obey linear stress-strain laws. Common engineering materials such as steel and concrete do not deviate too significantly from these ideals, so we can use, with discretion, simple linear theories to predict the response of these materials to engineering loads. With soils and rock, we are not so fortunate. We may assume a linear stress-strain response, but then we must apply large empirical correction or "safety" factors to our designs to account for the real materials' behavior. Furthermore, the behavior of soil and rock materials in situ is often controlled by joints (just don't inhale), fractures, weak layers and zones, and other "defects" in the material, which our laboratory tests and simplified methods of analysis often do not or are unable to take into account. That is why the practice of geotechnical engineering is more an "art" than a science. Successful practice depends on the good judgment and experience of the designer, constructor, or consultant.

Put another way, the successful geotechnical engineer must develop a "feel" for soil and rock behavior before a safe and economic foundation or tunnel design can be made, an earth structure can be safely built, or an environmentally sound waste containment and disposal system or a site remediation plan can be developed.

In summary, because of their nonlinear, nonconservative, and anisotropic mechanical behavior, plus the variability and heterogeneity of natural deposits due to the capriciousness of nature, soils and rocks are indeed complex engineering and construction materials. Helping you find some order in this potential chaos is our primary objective in this book.

1.3 SCOPE OF THIS BOOK

In this introductory text, rather than attempt an all-inclusive approach to geotechnical engineering, we put primary emphasis on the *classification and engineering behavior of soil and rock materials*. The reason is that successful practice of geotechnical engineering requires a thorough knowledge and understanding of the engineering properties and behavior of soils and rocks in situ—that is, when they are subjected to engineering loads and environmental conditions. Therefore the beginning student must first develop an appreciation for the engineering properties of geo-materials as distinct from other common civil engineering materials before learning how to analyze and design foundations, earthworks, tunnels, and the like.

Actually, this first part is the hard part. Most engineering students (and engineers) are very good at analysis and performing design calculations. But these are worthless if an incorrect picture of the site geology has been assumed or the wrong engineering properties assumed for the design.

As much of the practice of geotechnical engineering depends on the site geology, landforms, and the nature of the soil and rock deposits at a site, we have included an optional Chapter 3 on geology and landforms—just in case you haven't had a basic course in geology. If you have had such a course, you can skip this chapter. If you haven't, you are strongly encouraged to take a physical geology or an engineering geology course in connection with your studies of geotechnical engineering.

In the early chapters, we introduce some of the basic definitions, index properties, and classification schemes for geo-materials which are used throughout the book. *Classification* of soils and rocks is important because it is the "language" engineers use to communicate certain general knowledge about the engineering behavior of the materials at a particular site.

The rest of the book is concerned with the *engineering properties* of soils and rocks—properties that are necessary for the design of foundations, earth and underground structures, and geoenvironmental systems. We describe how water affects soil and rock behavior, including hydraulic conductivity and seepage characteristics. Then we get into compressibility, the important engineering property we need to understand in order to predict the settlement of structures constructed on soil and rock masses. Finally, we describe some elementary strength characteristics of both soils and rocks. Strength is very important for the stability of, for example, foundations, retaining walls, slopes, tunnels, and waste containment systems.

Keep in mind that this is an elementary text that emphasizes the fundamentals, but with an eye toward the practical applications that you as a civil engineer are likely to encounter. Having studied this text, you will be well prepared for follow-up courses in foundations and earthwork engineering, environmental geotechnics, rock mechanics, and engineering geology. You should have a fairly good idea of what to look for at a site and how to obtain the soil and rock properties required for most designs. If you are able to accurately classify the materials, you will know the probable range of values for a given soil or rock property. Finally, we hope you will learn enough about soils and rocks to be aware of your own limitations, and to avoid costly and dangerous mistakes in those aspects of your professional career that involve soils and rocks as engineering materials.

1.4 HISTORICAL DEVELOPMENT OF GEOTECHNICAL ENGINEERING

As long as people have been building things, they have used soils and rocks as a foundation or construction material. The ancient Egyptians, Babylonians, Chinese, and Indians knew about constructing dikes and levees out of the soils found in river flood plains. Ancient temples and monuments built all around the world involved soil and rock in some way. The Aztecs constructed temples and cities on the very poor soils in the Valley of Mexico long before the Spaniards arrived in the so-called New World. European architects and builders during the Middle Ages learned about the problems of settlements of cathedrals and large buildings. The most noteworthy example is, of course, the Leaning Tower of Pisa. Vikings in Scandinavia used timber piles to support houses and wharf structures on their soft clays. The "design" of foundations and other constructions involving soil and rock was by rule of thumb, and very little theory as such was developed until the mid-1700s.

Coulomb is the most famous engineering name of that era. He investigated the problems of earth pressures against retaining walls, and some of his calculation procedures are still in use today. The most common theory for the shear strength of soils is named after him (Coulomb, 1776). During the next century, the French engineers Collin and Darcy and the Scotsman Rankine made important discoveries. Collin (1846) was the first engineer to systematically examine failures in clay slopes as well as the measurement of the shear strength of clays. Darcy (1856) established his law for the flow of water through sands. Rankine (1857) developed a method for estimating the earth pressure against retaining walls. In England, Gregory (1844) utilized horizontal sub drains and compacted earth-fill buttresses to stabilize railroad cut slopes.

By the turn of the century, important developments in the field were occurring in Scandinavia, primarily in Sweden. Atterberg (1911) defined consistency limits for clays that are still in use today. During the period 1914–1922, in connection with investigations of failures in harbors and railroads, the Geotechnical Commission of the Swedish State Railways (Statens Järnvägers Geotekniska Kommission, 1922) developed many important concepts and apparatuses in geotechnical engineering. They developed methods for calculating the stability of slopes as well as subsurface investigation techniques such as weight sounding and piston and other types of samplers. They understood important concepts such as sensitivity of clays and consolidation, which is the squeezing of water out of the pores of the clay. At that time, clays were thought to be absolutely impervious, but the Swedes made field measurements to show they weren't. The Commission was the first to use the word *geotechnical* (Swedish: *geotekniska*) in today's sense: the combination of geology and civil engineering technology.

Even with these early developments in Sweden, the true father of soil mechanics is an Austrian, Prof. Karl Terzaghi. He published the first modern textbook on soil mechanics in 1925, and in fact the name "soil mechanics" is a translation of the German word *Erdbaumechanik*, which was part of the title of that book (Terzaghi, 1925a). Terzaghi was an outstanding and very creative engineer. He wrote several other important books (for example, Terzaghi, 1943; Terzaghi and Peck, 1967; and Terzaghi, Peck, and Mesri, 1996) and over 250 technical papers and articles. His name will appear often in this book. He was a professor at Robert College in Istanbul, at Technische Hochschule in Vienna, at M.I.T., and at Harvard University from 1938 until his retirement in 1956. He continued to be active as a consultant until his death in 1963 at the age of 80. An excellent reference about his life and engineering career is that of Goodman (1999) and is well worth reading.

Another important figure is Prof. Arthur Casagrande, who was at Harvard University from 1932 until 1969. You will see his name often in this book, because he made many important contributions to the art and science of soil mechanics and foundation engineering. Since the 1950s the field has grown substantially, and many people have been responsible for its rapid advancement. Important contributors to the field include Taylor, Peck, Tschebotarioff, Skempton, Bjerrum, Seed, Ladd, and Leonards.

Both Terzaghi and Casagrande began the teaching of soil mechanics and engineering geology in North America. Before the Second World War, the subject was offered only at a very few universities, mostly as a graduate course. After the war, it became common for at least one course in the subject to be required in most civil engineering curricula. In recent years graduate programs in geotechnical engineering have been implemented at many universities. Finally, there has been a real information explosion in the number of conferences, technical journals, and textbooks published on this subject during the past three decades.

Important recent developments you should know about include soil dynamics and geotechnical earthquake engineering, the use of computers for the solution of complex engineering problems, deformation-based analyses and designs, the introduction of probability and statistics into geotechnical engineering analysis and design, and geo-environmental engineering and technology.

1.5 SUGGESTED APPROACH TO THE STUDY OF GEOTECHNICAL ENGINEERING

Because of the nature of soil and rock materials, both laboratory and field testing are very important in geotechnical engineering. Student engineers can begin to develop a feel for soil and rock behavior in the laboratory by performing the standard tests for classification and engineering properties on many different types of soils and rocks. In this way the novice can begin building up a "mental data bank" of how certain soils and rocks actually look, how they might behave with varying amounts of water in them and under different types of engineering loads, and the range of probable numerical values for the different tests. This is sort of a self-calibration process, so that when you are faced with a new soil deposit or rock type, you will in advance have some idea as to the engineering problems you will encounter at that site. You can also begin to judge, at least qualitatively, the validity of laboratory and field test results for the materials at that site.

Also important is a knowledge of geology. Geology is, of course, the "geo" part of geotechnical engineering, and you should get as much exposure to it as you can during your academic career. After a basic course in physical geology, courses in geomorphology and engineering geology are recommended. Geomorphology is concerned with landforms, which are important to geotechnical engineers because the soils and rocks at a site (and therefore the engineering problems) are strongly related to the particular landform. Engineering geology is concerned with the applications of geology to primarily civil engineering and has considerable interaction and overlap with geotechnical engineering.

The theoretical and analytical aspects of geotechnical engineering design also require a sound knowledge of engineering mechanics, including strength of materials and fluid mechanics. It also helps if you are familiar to some extent with basic structural analysis, reinforced concrete and steel design, hydraulic engineering and hydrology, surveying and engineering measurements, basic environmental engineering, and civil engineering construction—in other words, just about all the courses in a typical undergraduate civil engineering curriculum.

1.6 NOTES ON SYMBOLS AND UNITS

At the beginning of each chapter, we list the pertinent symbols introduced in the chapter. As with most disciplines, a standard notation is not universal in geotechnical engineering, so we have tried to adopt the symbols most commonly used. For example, the American Society for Testing and Materials (ASTM, 2010) has a list of Standard Definitions of Terms and Symbols Relating to Soil and Rock Mechanics, Designation D 653, which was prepared jointly some years ago with the American Society of Civil Engineers (ASCE) and the International Society of Rock Mechanics (ISRM). The International Society for Soil Mechanics and Foundation Engineering (ISSMFE, 1977) published an extensive list of symbols. Although we sometimes deviate from these recommendations because of our personal preference, we have generally tried to follow them.

Units used in geotechnical engineering can be politely called a mess, and, less politely, several worse things. There has developed in practice, at least in the United States, a jumbled mixture of cgs-metric, Imperial or British Engineering units, and hybrid European metric units. With the introduction of the universal and consistent system of units, "Le Système International d'Unités" (SI) in the United States and Canada, the profession has a wonderful opportunity to bring some coherence to units in geotechnical engineering practice. However, since British Engineering units are still rather commonly used in the United States, American students need to be familiar with the typical values in both sets of units. To assist you with unit conversion where necessary, we have included a brief explanation of SI units as applied to geotechnical engineering in Appendix A.

1.7 SOME COMMENTS ON HOW TO STUDY IN GENERAL

It takes a while to learn how to study most effectively. You are probably using the study habits that you got by with in grade school and high school. As you progress professionally, things are going to get much harder, starting in your third year of university or college, when you take mostly preprofessional courses.

We have all used the following methods to do homework assignments. (1) Just read the assignment to satisfy the moral obligation to do so. (2) Go further by underlining or highlighting passages to emphasize the main points. Consider what you are doing physically: the information goes through the eyes, down your neck and arm into the writing fingers, completely bypassing the brain! Both (1) and (2) are pretty much a waste of time unless you have a photographic memory. If we are really going to learn anything, most of us need to study a third way: (3) Read a few pages and then *close* the book. Write down in your *own words* what the main concepts are; a "bullet" format is OK. In order to do this, you must have the material in the *brain* to begin with. If you can't write down anything about the pages you have just read, go back and read again, perhaps fewer pages this time. Repeat. Close the book and write in your own words the main points. Yes, this will take more time than "studying" using methods (1) and (2), but you will not be wasting your time.

A useful argument for doing it the recommended way is that you will have already started preparing for the exams, because now you *know* the material. The rest of the time, you are brushing up or *reviewing* the material, so you won't need to cram.

One big problem is that there may not be enough time in the week to use method (3) when you are taking three or four other courses. However, follow it as much as you can. You have invested a lot in your education. Don't waste time with methods (1) and (2).

Don't ask us to tell you how long it took for *us* to learn the correct way to study (it's too embarrassing).

Our suggested approach will help you prepare for the Fundamentals of Engineering (FE or EIT) exam and later the PE or PEng (professional engineer's exam). We *strongly* encourage you to take (and pass) the FE exam before you graduate and receive your engineering degree.

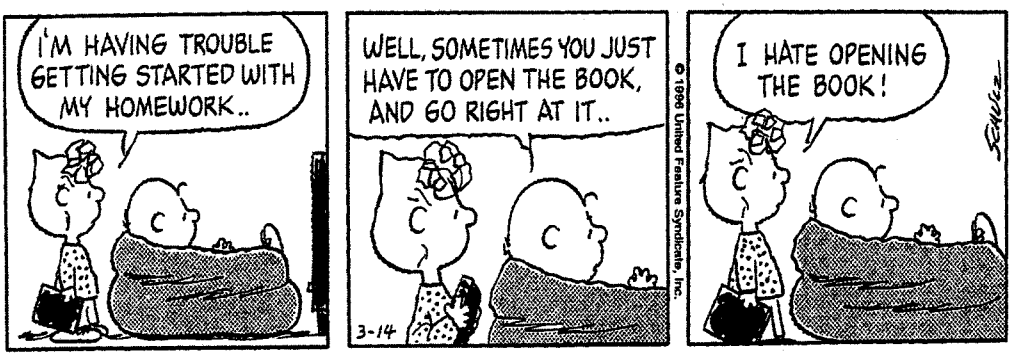

PROBLEMS

1.1 Interview a faculty member (other than your instructor) or a practicing engineer in Geotechnical Engineering. Ask him or her how they became involved with this specialty and what education is necessary these days to practice. (You will be surprised how much help you will receive, because we all like to talk about our "life's work"!) Ask about the importance of taking the FE examination and obtaining the PE (or P.Eng.) license and their influence on one's salary and promotion.

1.2 Get on the WWW and, using a search engine, type in the following letters: USUCGER. Report on the meaning of the letters; list the various *links* that you find in terms of subject matter or key words. Comment on the number of cross links found. Finally, select a web page and explore it; prepare a short summary of your findings in grammatically correct sentences (the hardest part of the question!).

1.3 Contact the Board of Registration for Professional Engineers in your state or province and find out the requirements for becoming a registered professional engineer. Start planning to take the FE examination when it is given in your area next year.

CHAPTER 2

Index and Classification Properties of Soils

2.1 INTRODUCTION

In this chapter we introduce the basic terms and definitions used by geotechnical engineers to index and classify soils. The following notation is used in this chapter.

Symbol	Dimension	Unit	Definition
C_c	–	–	Coefficient of curvature - Eq. (2.36)
C_u	–	–	Coefficient of uniformity - Eq. (2.35)
D_{10}	L	mm	Diameter for 10% finer by weight
D_{30}	L	mm	Diameter for 30% finer by weight
D_{60}	L	mm	Diameter for 60% finer by weight
e	–	(decimal)	Void ratio - Eq. (2.1)
F_B	MLT^{-2}	N	Buoyant force
G	–	–	Specific gravity - Eq. (2.24)
G_m	–	–	Bulk specific gravity - Eq. (2.25)
G_s	–	–	Specific gravity of solids - Eq. (2.26)
G_w	–	–	Specific gravity of water - Eq. (2.27)
g	LT^{-2}	g's	Acceleration of gravity
LI or I_L	–	–	Liquidity index - Eq. (2.40)
LL or w_L	–	–	Liquid limit - Eq. (2.38)
M'	M	kg	Submerged (net) mass (Sec. 2.3.1)
M_t	M	kg	Total mass
M_s	M	kg	Mass of solids
M_w	M	kg	Mass of water
N	–	blows	Blow count in liquid limit test - Eq. (2.38)
n	–	(%)	Porosity - Eq. (2.2)

(Continued)

Symbol	Dimension	Unit	Definition
Pc	—	—	Phnarg coefficient
PI or I_P	—	—	Plasticity index - Eq. (2.39)
PL or w_P	—	—	Plastic limit - Eq. (2.37)
S	—	(%)	Degree of saturation - Eq. (2.4)
SL or w_S	—	(%)	Shrinkage limit
V_a	L^3	m^3	Volume of air
V_s	L^3	m^3	Volume of solids
V_t	L^3	m^3	Total volume
V_v	L^3	m^3	Volume of voids
V_w	L^3	M^3	Volume of water
W	M	kg	Weight (Sec. 2.3.1)
W'	M	kg	Submerged (net) weight (Sec. 2.3.1)
w	—	(%)	Water content - Eq. (2.5)
γ_d	$ML^{-2}T^{-2}$	kN/m^3	Dry unit weight - Eq. (2.28)
γ_m or γ_t or γ	$ML^{-2}T^{-2}$	kN/m^3	Moist or total unit weight - Eqs. (2.20), (2.30)
γ_s	$ML^{-2}T^{-2}$	kN/m^3	Solids unit weight - Eq. (2.22)
γ_{sat}	$ML^{-2}T^{-2}$	kN/m^3	Saturated unit weight - Eq. (2.33)
γ_w	$ML^{-2}T^{-2}$	kN/m^3	Water unit weight - Eq. (2.23)
γ'	$ML^{-2}T^{-2}$	kN/m^3	Buoyant unit weight - Eq. (2.34)
ρ	M/L^3	kg/m^3	Total, wet, or moist density - Eq. (2.6)
ρ'	M/L^3	kg/m^3	Buoyant density - Eq. (2.11)
ρ_d	M/L^3	kg/m^3	Dry density - Eq. (2.9)
ρ_s	M/L^3	kg/m^3	Density of solids - Eq. (2.7)
ρ_{sat}	M/L^3	kg/m^3	Saturated density - Eq. (2.10)
ρ_w	M/L^3	kg/m^3	Density of water - Eq. (2.8)

In this list, L = length, M = mass, and T = time. When densities of soils and water are expressed in kg/m^3, the numbers are rather large. For instance, the density of water ρ_w is 1000 kg/m^3. Since 1000 kg = 1 Mg, to make the numbers more manageable, we will often use Mg/m^3 for densities. If you are unfamiliar with SI metric units and their conversion factors, it would be a good idea to read Appendix A before proceeding with the rest of this chapter.

For each of the ρ notations, there is a corresponding γ notation, which denotes unit weight, rather than density. This γ notation should be used when units of force (F) are used (for example, lb or kN) instead of units of mass. This is described further in Sec. 2.3.2.

2.2 BASIC DEFINITIONS AND PHASE RELATIONS FOR SOILS

In general, any mass of soil consists of solid particles with voids in between. The solids are small grains of different minerals, whereas the voids can be filled with either water or other fluid (for example, a contaminant) or with air (or other gas), or filled partly with some of each (Fig. 2.1). Also, as noted in the introduction, while we can have units of either mass or weight, we will assume that our problems are in mass units.

So, the total volume V_t of the soil mass consists of the volume of soil solids V_s and the volume of voids V_v. The volume of voids is in general made up of the volume of water V_w and the volume of air V_a.

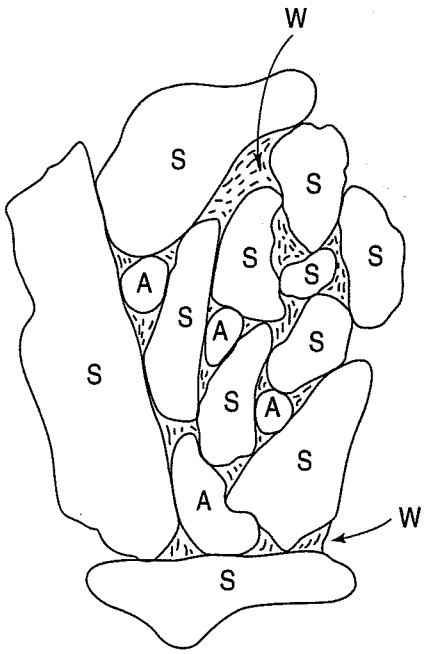

FIGURE 2.1 Soil skeleton containing solid particles (S) and voids with air (A) and water (W).

A *phase diagram* (Fig. 2.2) shows the three phases separately. It's as if we could "melt down" all the solids into a single layer at the bottom, then have the water sit on top of that, and finally have the air in a single layer at the top. The phase diagram helps us solve problems involving soil phase relationships. On the left side we usually indicate the volumes of the three phases; on the right side we show the corresponding masses. Even though the diagram is two dimensional, it is understood that the volume shown is in units of L^3, such as cm^3 or ft^3. Also, since we're not chemists or physicists, we assume that the mass of air is zero.

In engineering practice, we usually measure the total volume V_t, the mass of water M_w, and the mass of dry solids M_s. Then we calculate the rest of the values and the mass-volume relationships that we need. Most of these relationships are independent of sample size, and they are often dimensionless. They are very simple and easy to remember, especially if you draw the phase diagram.

Three volumetric ratios that are very useful in geotechnical engineering can be determined directly from the phase diagram (Fig. 2.2).

1. The *void ratio*[1] e is defined as

$$e = \frac{V_v}{V_s} \tag{2.1}$$

where V_v = volume of the voids, and

V_s = volume of the solids.

The void ratio e is normally expressed as a *decimal* rather than a *percentage*. The maximum possible range of e is between 0 and ∞. However, typical values of void ratios for sands may range from 0.4 to about 1.0; typical values for clays vary from 0.3 to 1.5 and even higher for some organic soils.

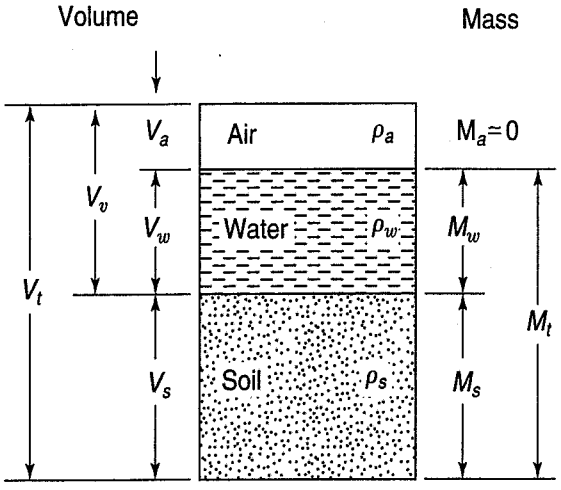

FIGURE 2.2 Volumetric and mass relationships for a soil shown in a phase diagram.

[1]Readers with British backgrounds will note that the correct terminology is *voids ratio*.

2. The *porosity n* is defined as

$$n = \frac{V_v}{V_t} \times 100(\%) \tag{2.2}$$

where V_v = volume of voids, and

V_t = total volume of soil sample.

Porosity is traditionally expressed as a *percentage*. The maximum range of n is between 0 and 100%.

From Fig. 2.2 and Eqs. (2.1) and (2.2), it can be shown that

$$n = \frac{e}{1 + e} \tag{2.3a}$$

and

$$e = \frac{n}{1 - n} \tag{2.3b}$$

3. The *degree of saturation S* is defined as

$$S = \frac{V_w}{V_v} \times 100(\%) \tag{2.4}$$

The degree of saturation tells us what *percentage* of the total void space contains water. If the soil is completely dry, then $S = 0\%$, and if the pores are completely full of water, then the soil is fully saturated and $S = 100\%$.

Now let us look at the other side, the mass side, of the phase diagram in Fig. 2.2. First, we define a mass ratio that is probably the single most important thing we need to know about a soil. It is also the only strictly mass-based parameter that we'll define for phase relationships. We want to know how much water is present in the voids relative to the amount of solids in the soil, so we define a ratio called the *water content w* as

$$w = \frac{M_w}{M_s} \times 100(\%) \tag{2.5}$$

where M_w = mass of water, and

M_s = mass of soil solids.

The ratio of the amount of water present in a soil volume to the amount of soil grains is based on the *dry mass* of the soil and not on the total mass. The water content, which is usually expressed as a *percentage*, can range from zero (dry soil) to several hundred percent. The natural water content for most soils is well under 100%, although in some marine and organic soils it can range up to 500% or higher.

The water content is easily determined in the laboratory. The standard procedure is detailed in ASTM (2010) standard D 2216. A representative sample of soil is selected and its total or wet mass is determined. Then it is dried to constant mass in a convection oven at 110°C. Normally a constant mass is obtained after the sample is left in the oven overnight. The mass of the drying dish must,

of course, be subtracted from both the wet and dry masses. Then the water content is calculated according to Eq. (2.5). Example 2.1 illustrates how the calculations for water content are actually done in practice.

Example 2.1

Given:

A specimen of wet soil in a drying dish has a mass of 462 g. After drying in an oven at 110°C overnight, the sample and dish have a mass of 364 g. The mass of the dish alone is 39 g.

Required:

Determine the water content of the soil.

Solution: Set up the following calculation scheme; fill in the "given" or measured quantities **a**, **b**, and **d**, and make the calculations as indicated for **c**, **e**, and **f**.

a. Mass of total (wet) sample + dish = 462 g
b. Mass of dry sample + dish = 364 g
c. Mass of water (**a** − **b**) = 98 g
d. Mass of dish = 39 g
e. Mass of dry soil (**b** − **d**) = 325 g
f. Water content (**c**/**e**) × 100% = 30.2%

In the laboratory, masses are usually determined in grams (g) on an ordinary balance. The required sensitivity of the balance depends on the size of the specimen, and ASTM D 2216 gives some recommendations.

The water content may also be determined using an ordinary microwave oven. ASTM (2010) standard D 4643 explains the procedure. To avoid overheating the soil specimen, microwave energy is applied for only brief intervals and repeated until the mass becomes nearly constant. A heat sink, such as a glass beaker filled with water, helps to prevent overheating of the soil by absorbing microwave energy after water has been removed from the soil pores. Otherwise, the water content is determined exactly as indicated above. Note that the microwave water content is not a replacement for the oven dry (D 2216) water content but is used when the water content is needed quickly. Other methods sometimes used in the field for water content determination are described in Chapter 5, Sec. 5.7.

It is easy to be confused by the concepts of *mass* and *weight*. From physics, you know that the mass of an object is a measure of how much matter the object contains, while the weight of an object is determined by the gravitational force that causes its downward acceleration. Recall that weight W equals mass m times g, the acceleration due to gravity, or $W = mg$. As noted in Appendix A, when we weigh something in the laboratory, we really are determining its mass—either by comparing two masses on a balance or by using a device calibrated against objects of known mass. It is basically an English-language problem; we really should say "we massed it" when we determine the mass of an

object in the laboratory. Another very useful concept in geotechnical engineering is *density*. You know from physics that density is mass per unit volume, so its units are kg/m^3. (See Appendix A for the corresponding units in the cgs and British engineering systems.) The density is the ratio that connects the volumetric side of the phase diagram with the mass side. Several densities are commonly used in geotechnical engineering practice. First, we define the total, wet, or moist density ρ; the density of the particles, solid density ρ_s; and the density of water ρ_w. Or, in terms of the basic masses and volumes of Fig. 2.2:

$$\rho = \frac{M_t}{V_t} = \frac{M_s + M_w}{V_t} \tag{2.6}$$

$$\rho_s = \frac{M_s}{V_s} \tag{2.7}$$

$$\rho_w = \frac{M_w}{V_w} \tag{2.8}$$

In natural soils, the magnitude of the total density ρ will depend on how much water happens to be in the voids as well as the density of the mineral grains themselves. Thus, ρ can range from slightly above 1000 kg/m^3 to as high as 2400 kg/m^3 (1.0 to 2.4 Mg/m^3).

Typical values of ρ_s for most soils range from 2500 to 2800 kg/m^3 (2.5 to 2.8 Mg/m^3). Most sands have ρ_s ranging between 2.6 and 2.7 Mg/m^3. For example, a common mineral in sands is quartz; its ρ_s = 2.65 Mg/m^3. Most clay soils have a value of ρ_s between 2.65 and 2.80 Mg/m^3, depending on the predominant mineral in the soil, whereas organic soils may have a ρ_s as low as 2.5 Mg/m^3. Consequently, for most phase problems, unless a specific value of ρ_s is given, it is usually close enough for geotechnical work to *assume* a ρ_s of 2.65 or 2.70 Mg/m^3. The density of water varies slightly, depending on the temperature. At 4°C, when water is at its densest, ρ_w exactly equals 1000 kg/m^3 (1 g/cm^3), and this density is sometimes designated by the symbol ρ_o. For ordinary engineering work, it is sufficiently accurate to take $\rho_w \approx \rho_o$ = 1000 kg/m^3 = 1 Mg/m^3.

Three other densities very useful in soils engineering are the *dry density* ρ_d, the *saturated density* ρ_{sat}, and the *submerged* or *buoyant density* ρ' or ρ_b.

$$\rho_d = \frac{M_s}{V_t} \tag{2.9}$$

$$\rho_{sat} = \frac{M_s + M_w}{V_t} (V_a = 0, S = 100\%) \tag{2.10}$$

$$\rho' = \rho_{sat} - \rho_w \tag{2.11}$$

Among other uses, the dry density ρ_d is a common basis for judging a soil's degree of compaction after we have applied some mechanical energy to it, for example by using a roller or vibratory plate (Chapter 5). The saturated density ρ_{sat}, as the name implies, is the total density of the soil when 100% of its pores are filled with water; in this special case, $\rho = \rho_{sat}$. The concept of submerged or buoyant density ρ' is often difficult for students to understand, so it is discussed later after we have done a few example problems. However, you may be familiar with this concept from studying aggregates, where a "basket" of aggregate is weighed while it is submerged under water. Typical values of ρ_d, ρ_{sat}, and ρ' for several soil types are shown in Table 2.1.

From the basic definitions provided in this section, other useful relationships can be derived, as we show in the examples in the next section.

TABLE 2.1 Some Typical Values for Different Densities of Some Common Soil Materials

	Density (Mg/m^3)		
Soil Type	ρ_{sat}	ρ_d	ρ'
Sands and gravels	1.9–2.4	1.5–2.3	0.9–1.4
Silts and clays	1.4–2.1	0.6–1.8	0.4–1.1
Glacial tills	2.1–2.4	1.7–2.3	1.1–1.4
Crushed rock	1.9–2.2	1.5–2.0	0.9–1.2
Peats	1.0–1.1	0.1–0.3	0.0–0.1
Organic silts and clays	1.3–1.8	0.5–1.5	0.3–0.8

Modified after Hansbo (1975).

2.3 SOLUTION OF PHASE PROBLEMS

Phase problems are very important in soils engineering. In this section, with the help of some numerical examples, we illustrate how most phase problems are solved. As in many disciplines, practice helps; the more problems you solve, the simpler they are and the more proficient you become. Also, with practice you soon memorize most of the important definitions and relationships, so you save time by not having to look them up.

Probably the single most important thing you can do in solving phase problems is to *draw a phase diagram*. This is especially true for the beginner. Don't spend time searching for the right formula to plug into. Instead, always draw a phase diagram and show both the given values and the unknowns of the problem. For some problems, simply doing this leads almost immediately to the solution; at least the correct approach to the problem is usually indicated. Also, you should note that there often are alternative approaches to the solution of the same problem, as illustrated in Example 2.2. The following steps are recommended to solve these problems:

1. List the information you know (from the problem narrative).
2. Draw phase diagram, fill in the knowns and the unknowns.
3. Try to avoid big formulas.
4. If no masses or volumes are given, you can assume either one volume or one mass.
5. Fill in one side of the diagram until you get stuck or completely solve it, then "cross over" to the other side using one of the ρ's or G_s.
6. Write out equations in symbol form. Then place the numerical value along with its **units** in the same order, and solve.
7. Check units and reasonableness of your answer.

Example 2.2

Given:

$\rho = 2.70\ Mg/m^3$ (total density)

$w = 10\%$ (water content)

$\rho_s = 2.70\ Mg/m^3$ (assumed)

Required:

Compute ρ_d (dry density), e (void ratio), n (porosity), S (degree of saturation), and ρ_{sat} (saturated density).

Solution: Draw the phase diagram (Fig. Ex. 2.2a). Assume that $V_t = 1\ m^3$.

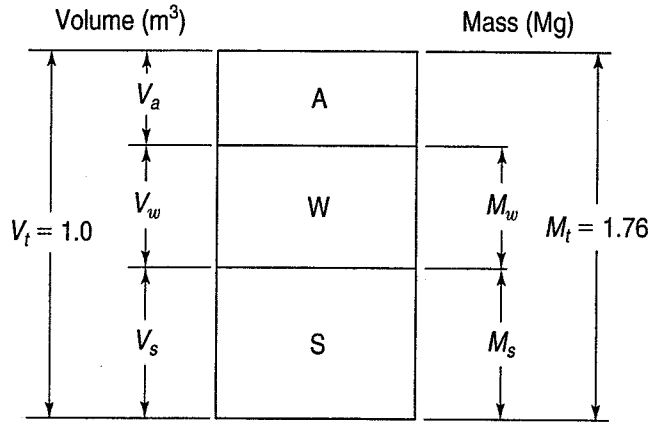

FIGURE Ex. 2.2a

From the definition of water content [Eq. (2.5)] and total density [Eq. (2.6)] we can solve for M_s and M_w. Note that in the computations water content is expressed as a decimal.

$$w = 0.10 = \frac{M_w\ \text{Mg}}{M_s\ \text{Mg}}$$

$$\rho = 1.76\ \text{Mg/m}^3 = \frac{M_t}{V_t} = \frac{(M_w + M_s)\ \text{Mg}}{1.0\ \text{m}^3}$$

Substituting $M_w = 0.10M_s$, we get

$$1.76\ \text{Mg/m}^3 = \frac{(0.10M_s + M_s)\ \text{Mg}}{1.0\ \text{m}^3}$$

$$M_s = 1.60\ \text{Mg and } M_w = 0.16\ \text{Mg}$$

These values are now placed on the mass side of the phase diagram (Fig. Ex. 2.2b), and the rest of the desired properties are calculated.

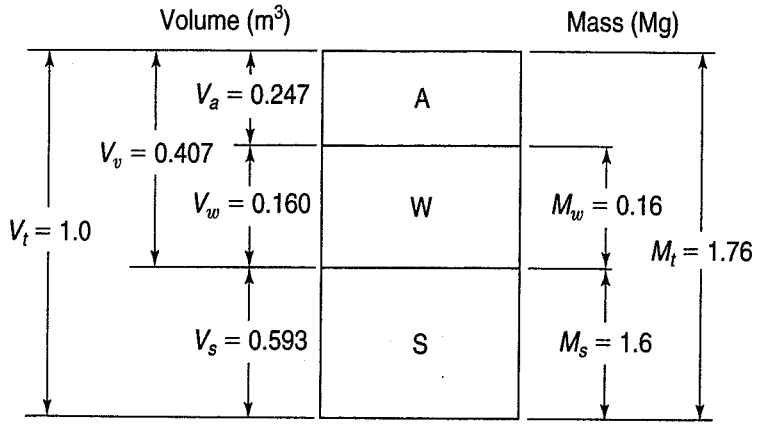

FIGURE Ex. 2.2b

From the definition of ρ_w [Eq. (2.8)] we can solve for V_w.

$$\rho_w = \frac{M_w}{V_w}$$

or

$$V_w = \frac{M_w}{\rho_w} = \frac{0.16\ \text{Mg}}{1\ \text{Mg/m}^3} = 0.160\ \text{m}^3$$

Place this numerical value on the phase diagram (Fig. Ex. 2.2b).

To calculate V_s, we must assume a value of the density of the solids ρ_s. Here assume $\rho_s = 2.70\ \text{Mg/m}^3$. From the definition of ρ_s [Eq. (2.7)] we can solve for V_s directly, or

$$V_s = \frac{M_s}{\rho_s} = \frac{1.6\ \text{Mg}}{2.70\ \text{Mg/m}^3} = 0.593\ \text{m}^3$$

Since $V_t = V_a + V_w + V_s$, we can solve for V_a, since we know the other terms.

$$V_a = V_t - V_w - V_s = 1.0 - 0.593 - 0.160 = 0.247\ \text{m}^3$$

Once the phase diagram has been filled in, solving the rest of the problem involves just plugging the respective numbers into the appropriate definition equations. We recommend that, when you make the computations, you write out the equations in symbol form and then insert the numbers in the same order as written in the equation. Also, it is a good idea to have the units accompany the calculations.

Solving for the remainder of the required items is easy.

From Eq. (2.9),

$$\rho_d = \frac{M_s}{V_t} = \frac{1.6\ \text{Mg}}{1\ \text{m}^3} = 1.6\ \text{Mg/m}^3$$

From Eq. (2.1),

$$e = \frac{V_v}{V_s} = \frac{V_a + V_w}{V_s} = \frac{(0.247 + 0.160)\ \text{m}^3}{0.593\ \text{m}^3} = 0.686$$

From Eq. (2.2),

$$n = \frac{V_v}{V_t} = \frac{V_a + V_w}{V_t}100 = \frac{(0.247 + 0.160)\ \text{m}^3}{1.0\ \text{m}^3}100 = 40.7\%$$

From Eq. (2.4),

$$S = \frac{V_w}{V_v} = \frac{V_w}{V_a + V_w}100 = \frac{0.16\ \text{m}^3}{(0.247 + 0.160)\ \text{m}^3}100 = 39.3\%$$

At the saturated density ρ_{sat} all the voids are filled with water—that is, $S = 100\%$ [Eq. (2.10)]. Therefore, if the volume of air V_a were filled with water, it would weigh $0.247\ \text{m}^3 \times 1\ \text{Mg/m}^3$ or 0.247 Mg. Then

$$\rho_{\text{sat}} = \frac{M_w + M_s}{V_t} = \frac{(0.247\ \text{Mg} + 0.16\ \text{Mg}) + 1.6\ \text{Mg}}{1\ \text{m}^3} = 2.01\ \text{Mg/m}^3$$

Another, and perhaps even easier, way to solve this example problem is to assume V_s is a unit volume, 1 m^3. Then, by definition, $M_s = \rho_s = 2.7$ (when ρ_s is assumed equal to 2.70 Mg/m^3). The completed phase diagram is shown in Fig. Ex. 2.2c.

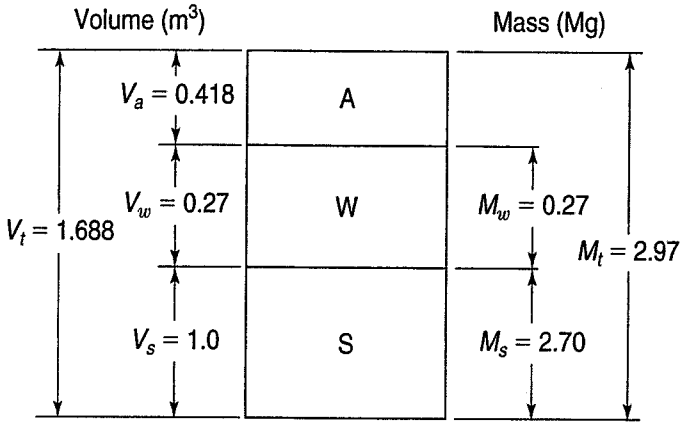

FIGURE Ex. 2.2c

Since $w = M_w/M_s = 0.10$, $M_w = 0.27$ Mg and $M_t = M_w + M_s = 2.97$ Mg. Also $V_w = M_w$ numerically, since $\rho_w = 1$ Mg/m^3; that is, 0.27 Mg of water occupies a volume of 0.27 m^3. Before we can proceed, two unknowns remain to be solved: V_a and V_t. To obtain these values, we must use the given information that $\rho = 1.76$ Mg/m^3. From the definition of total density [Eq. (2.6)],

$$\rho = 1.76 \text{ Mg/m}^3 = \frac{M_t}{V_t} = \frac{2.97 \text{ Mg}}{V_t}$$

Solving for V_t,

$$V_t = \frac{M_t}{\rho} = \frac{2.97 \text{ Mg}}{1.76 \text{ Mg/m}^3} = 1.688 \text{ m}^3$$

Therefore

$$V_a = V_t - V_w - V_s = 1.688 - 0.27 - 1.0 = 0.418 \text{ m}^3$$

You can use Fig. Ex. 2.2c to verify that the remainder of the solution is identical to the one using the data of Fig. Ex. 2.2b. This example illustrates that there often are alternative approaches to the solution of the phase problems.

Example 2.3

Given:

Equations (2.3a) and (b) relating the void ratio e and the porosity n.

Required:

Express the porosity n in terms of the void ratio e [Eq. (2.3a)] and the void ratio in terms of the porosity [Eq. (2.3b)].

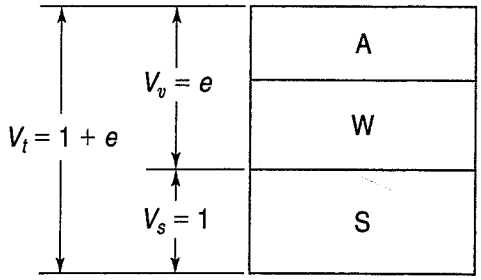

FIGURE Ex. 2.3a

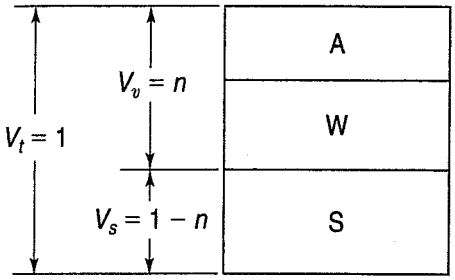

FIGURE Ex. 2.3b

Solution: Draw a phase diagram (Fig. Ex. 2.3a).

For this problem, assume $V_s = 1$ (units arbitrary). From Eq. (2.1), $V_v = e$, since $V_s = 1$. Therefore $V_t = 1 + e$. From Eq. (2.2), the definition of n is V_v/V_t, or

$$n = \frac{e}{1 + e} \tag{2.3a}$$

Equation (2.3b) can be derived algebraically or from the phase diagram (Fig. Ex. 2.3b). For this case, assume $V_t = 1$.

From Eq. (2.2), $V_v = n$, since $V_t = 1$. Therefore $V_s = 1 - n$. From Eq. (2.1), the definition of $e = V_v/V_s$. So

$$e = \frac{n}{1 - n} \tag{2.3b}$$

Example 2.4

Given:

$e = 0.62$, $w = 15\%$, $\rho_s = 2.65\ \text{Mg/m}^3$.

Required:

a. ρ_d
b. ρ
c. w for $S = 100\%$
d. ρ_{sat} for $S = 100\%$

Solution: Draw phase diagram (Fig. Ex. 2.4).

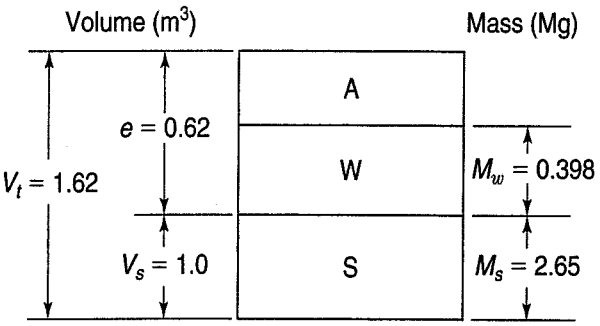

FIGURE Ex. 2.4

a. Since no volumes are specified, assume $V_s = 1\ \text{m}^3$. Just as in Example 2.3, this makes the $V_v = e = 0.62\ \text{m}^3$ and $V_t = 1 + e = 1.62\ \text{m}^3$. From Eq. (2.9),

$$\rho_d = \frac{M_s}{V_t}$$

and $M_s = \rho_s V_s$ [from Eq. (2.7)]. So

$$\rho_d = \frac{\rho_s V_s}{V_t} = \frac{\rho_s}{1 + e}, \qquad \text{since } V_s = 1 \text{ m}^3 \text{ in Fig. Ex. 2.4}$$

$$= \frac{2.65 \text{ Mg}}{(1 + 0.62) \text{ m}^3} = 1.636 \text{ Mg/m}^3$$

Note: The relationship

$$\rho_d = \frac{\rho_s}{1 + e} \tag{2.12}$$

is often very useful in phase problems.

b. Now for ρ:

$$\rho = \frac{M_t}{V_t} = \frac{(M_s + M_w) \text{ Mg}}{V_t \text{ m}^3}$$

We know that

$$M_w = wM_s \text{ [from Eq. (2.5)] and } M_s = \rho_s V_s$$

$$\rho = \frac{\rho_s V_s + w\rho_s V_s}{V_t} = \frac{\rho_s(1 + w)}{1 + e}, \qquad \text{since } V_s = 1 \text{ m}^3$$

Plug in the numbers.

$$\rho = \frac{2.65 \text{ Mg } (1 + 0.15)}{(1 + 0.62) \text{ m}^3} = 1.88 \text{ Mg/m}^3$$

The following relationship is often useful to know.

$$\rho = \frac{\rho_s(1 + w)}{(1 + e)} \tag{2.13}$$

Check:

$$\rho_d = \frac{\rho}{1 + w}$$

$$= \frac{1.88}{1.15} = 1.63 \text{ Mg/m}^3 \tag{2.14}$$

You should verify that $\rho_d = \rho/(1 + w)$, which is another very useful relationship to remember.

c. Water content for $S = 100\%$:

From Eq. (2.4), we know that $V_w = V_v = 0.62 \text{ m}^3$. From Eq. (2.8), $M_w = V_w\rho_w = 0.62 \text{ m}^3 \times (1 \text{ Mg/m}^3) = 0.62 \text{ Mg}$. Therefore w for $S = 100\%$ must be

$$w_{(s=100\%)} = \frac{M_w}{M_s} = \frac{0.62}{2.65} = 0.234 \text{ or } 23.4\%$$

d. ρ_{sat}:

From Eq. (2.10), we know $\rho_{sat} = (M_s + M_w)/V_t$, or

$$\rho_{sat} = \frac{(2.65 + 0.62)\ \text{Mg}}{1.62\ \text{m}^3} = 2.019 \text{ or } 2.02\ \text{Mg/m}^3$$

Check, by Eq. (2.13):

$$\rho_{sat} = \frac{\rho_s(1 + w)}{1 + e} = \frac{2.65(1 + 0.234)}{1.62} = 2.02\ \text{Mg/m}^3$$

Example 2.5

Given:

The definitions of the degree of saturation S, void ratio e, water content w, and the solid density ρ_s [Eqs. (2.4), (2.1), (2.5), and (2.7), respectively].

Required:

Derive a relationship between S, e, w, and ρ_s.

Solution: Look at the phase diagram with $V_s = 1$ (Fig. Ex. 2.5).

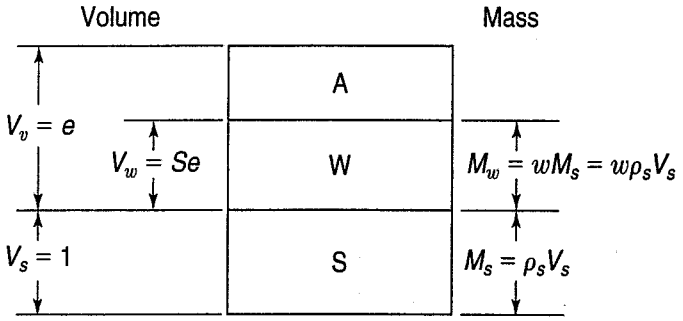

FIGURE Ex. 2.5

From Eq. (2.4) and Fig. Ex. 2.5, we know that $V_w = SV_v = Se$. From the definitions of water content [Eq. (2.5)] and ρ_s [Eq. (2.7)], we can place the equivalents for M_s and M_w on the phase diagram. Since from Eq. (2.8), $M_w = \rho_w V_w$, we now can write the following equation:

$$M_w = \rho_w V_w = wM_s = w\rho_s V_s$$

or

$$\rho_w Se = w\rho_s V_s$$

Since $V_s = 1\ \text{m}^3$,

$$\rho_w Se = w\rho_s \tag{2.15}$$

Equation (2.15) is among the most useful of all equations for phase problems. You can also verify its validity from the fundamental definitions of ρ_w, S, e, w, and ρ_s.

Note that, using Eq. (2.15), we can write Eq. (2.13) another way:

$$\rho = \frac{\rho_s\left(1 + \dfrac{\rho_w Se}{\rho_s}\right)}{1 + e} = \frac{\rho_s + \rho_w Se}{1 + e} \tag{2.16}$$

When $S = 100\%$, Eq. (2.16) becomes

$$\rho_{sat} = \frac{\rho_s + \rho_w e}{1 + e} \tag{2.17}$$

Example 2.6

Given:

A soil contaminated with gasoline (specific gravity = 0.9) with the following characteristics: $\rho_s = 2.65$ Mg/m^3, $w = 25\%$, volume of the gasoline is 20% of the volume of the water, and 85% of the void space is filled with gasoline and water (after T. F. Wolff).

Required:

a. Complete the phase diagram in Fig. Ex. 2.6a.

b. Find the void ratio and porosity of the specimen.

c. Find the total and dry density of the specimen.

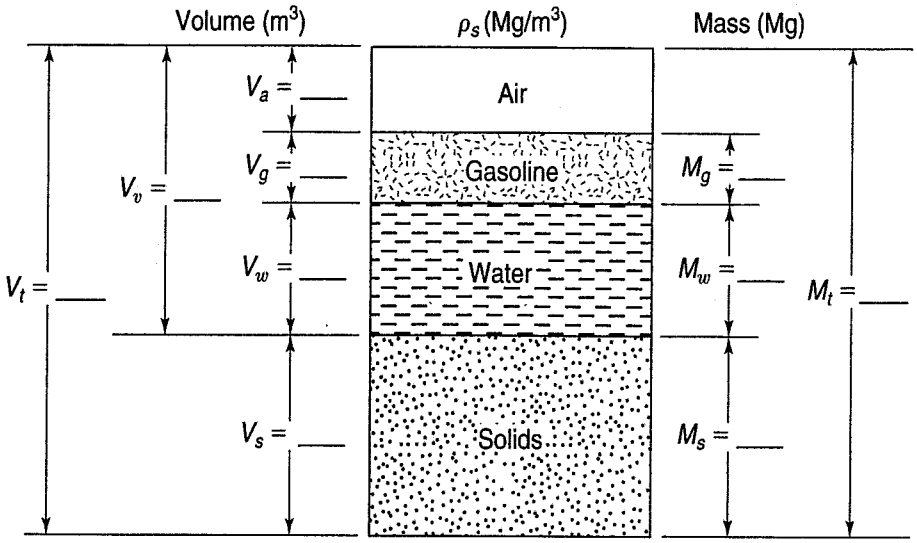

FIGURE Ex. 2.6a

Solution:

a. As we did with Examples 2.3 and 2.4, assume $V_s = 1$ m^3. Then, using the basic definitions for water content, density, and degree of saturation, fill in the blanks as shown in Fig. Ex. 2.6b.

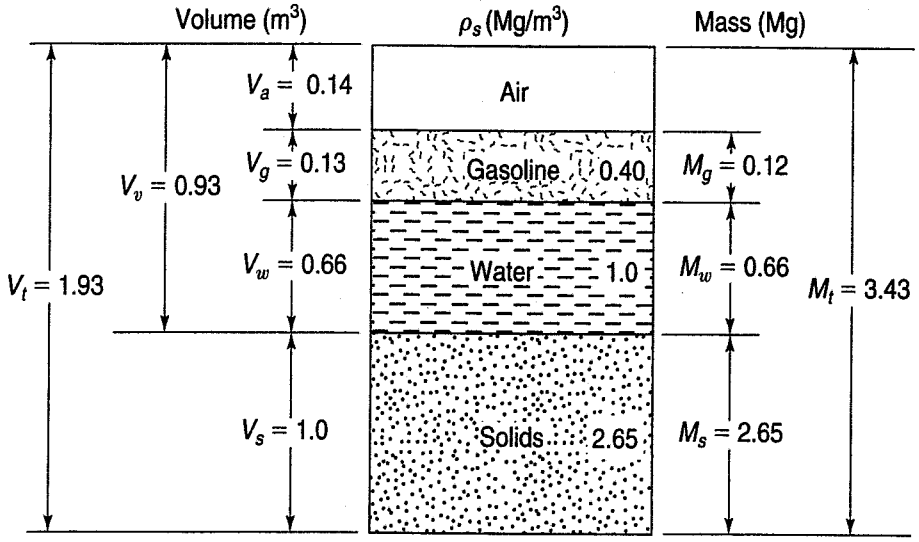

FIGURE Ex. 2.6b

b. Again, use the basic definitions of e and n. We find that $e = 0.93$ and $n = 48.2\%$.

c. For both ρ_t and ρ_d, simply take the values for M_t (3.43 Mg) and M_s (2.65 Mg) and divide each by 1.93 m^3 to obtain $\rho_t = 1.78$ Mg/m^3 and $\rho_d = 1.37$ Mg/m^3. Note that using Eqs. (2.13) and (2.14) will give you erroneous results.

Here are the details: Calculate the mass of water by noting that $M_w = wM_s = 0.25 \times 2.65$ Mg of solids. (We assumed that $V_s = 1$ m^3, remember?) So, $M_w = 0.66$ Mg. Add that to the phase diagram. Also, the volume of water is $M_w/\rho_w = 0.66$ Mg divided by 1 Mg/m^3, or $V_s = 0.66$ m^3. Then the volume of gasoline = 20% of $V_w = 0.2 \times 0.66$ m^3 = 0.13 m^3. Because the specific gravity (Sec. 2.3.2) of gasoline is 0.9, its density is $0.9 \times \rho_w$. So the mass of the gasoline $M_g = 0.9 \times \rho_w \times V_g$ = 0.9 Mg/m^3 × 0.13 m^3 = 0.12 Mg. Add these items to the phase diagram (Fig. Ex. 2.6b).

Because 85% of the voids are filled with water and gasoline, the total amount of voids is $(V_w + V_g)/0.85 = (0.66 + 0.13)/0.85 = 0.93$ m^3. Subtracting $V_w + V_g$ from V_t, we find that $V_a = 0.14$ m^3. Now all the "holes" on the phase diagram are filled. The rest is a piece of cold apple pie (parts **b** and **c**).

$$e = \frac{V_v}{V_s} = \frac{0.93\ \text{m}^3}{1.00\ \text{m}^3} = 0.93$$

$$n = \frac{V_v}{V_t} = \frac{0.93}{1.93} \times 100 = 48.2\%$$

$$\rho_t = \frac{M_t}{V_t} = \frac{3.43\ \text{Mg}}{1.93\ \text{m}^3} = 1.78\frac{\text{Mg}}{\text{m}^3}$$

$$\rho_d = \frac{M_s}{V_t} = \frac{2.65\ \text{Mg}}{1.93\ \text{m}^3} = 1.37\frac{\text{Mg}}{\text{m}^3}$$

In summary, for the easy solution of phase problems, you don't have to memorize lots of complicated formulas. Most of the formulas you need can easily be derived from the phase diagram, as illustrated in the preceding examples. Just remember the following simple rules:

1. Draw a phase diagram.
2. Remember the basic definitions of w, e, ρ_s, S, and so on.

3. Assume either $V_s = 1$ or $V_t = 1$, if no masses or volumes are given.
4. Write out equations in symbol form. Then, place the numerical value along with its **units** in the same order, and solve.
5. Check units and reasonableness of your answer.

2.3.1 Submerged or Buoyant Density

In Eq. (2.11), we simply defined the submerged or buoyant density as $\rho' = \rho_{sat} - \rho_w$, without any explanation other than giving some typical values of ρ' in Table 2.1. Strictly speaking, the total ρ should be used instead of ρ_{sat} in Eq. (2.11), but in most cases submerged soils are also completely saturated, or at least that is a reasonable assumption.

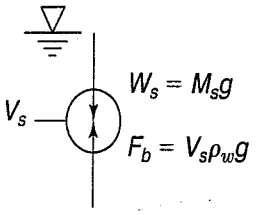

FIGURE 2.3a Free-body diagram of a submerged soil particle.

So when a soil is submerged, the total density as expressed by Eqs. (2.13) and (2.16) is partially balanced by the buoyant effect of the water. You will recall from Archimedes' principle that the buoyancy effect is equal to the weight of water displaced by the solid particles in the soil mass. This is shown in Fig. 2.3(a), where the submerged (net) weight is

$$W' = W_s - F_b$$

In terms of masses,

$$W' = M_s g - V_s \rho_w g = M' g$$

Thus, the submerged (net) mass

$$M' = M_s - V_s \rho_w$$

We obtain densities by dividing by the total volume V_t:

$$\frac{M'}{V_T} = \rho' = \frac{M_s}{V_T} - \frac{V_s}{V_T}\rho_w$$

Because $\rho_s = M_s/V_s$ [and using Eq. (2.12)], we obtain

$$\begin{aligned} \rho' &= \frac{M_s}{V_T} - \frac{M_s}{V_T}\frac{\rho_w}{\rho_s} = \rho_d\left(1 - \frac{\rho_w}{\rho_s}\right) \\ &= \frac{\rho_s}{1+e}\left(\frac{\rho_s - \rho_w}{\rho_s}\right) \\ &= \frac{\rho_s - \rho_w}{1+e} \end{aligned} \tag{2.18}$$

There are several other ways to get Eq. (2.18). One way is to use Eq. (2.13).

$$\rho' = \frac{\rho_s(1+w)}{1+e} - \rho_w$$

Using Eq. (2.15), $\rho_s w = \rho_w e (S = 100\%)$,

$$\begin{aligned} \rho' &= \frac{\rho_s + \rho_w e - \rho_w - \rho_w e}{1+e} \\ \rho' &= \frac{\rho_s - \rho_w}{1+e} \end{aligned} \tag{2.19}$$

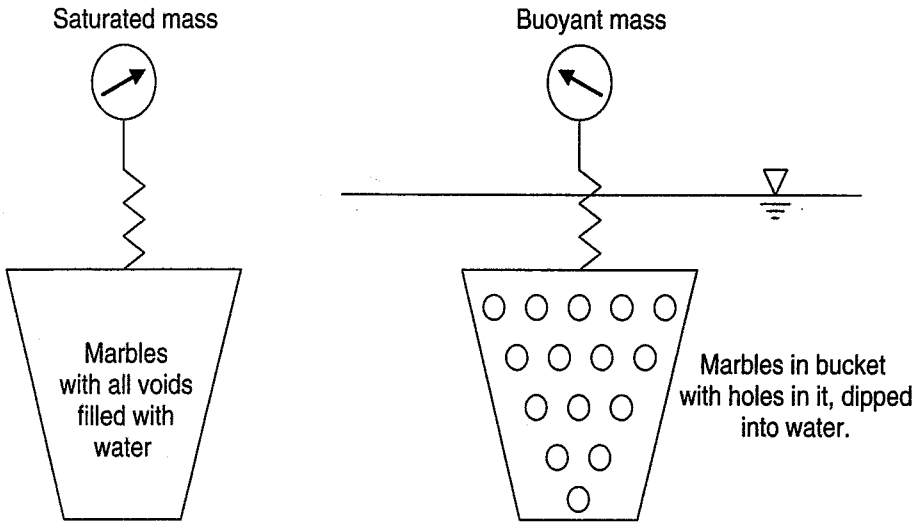

FIGURE 2.3b Schematic showing the relevant change in mass due to buoyancy.

Note carefully the different meanings of the densities described above. The *saturated density* is the total soil and water density when $S = 100\%$, while the *submerged density* is really a buoyant or an effective density. Note, too, that the difference between the saturated and submerged densities is exactly the density of water [Eq. (2.11)].

Some physical examples will help you understand the concept of submerged or buoyant density. First, consider a bucket full of marbles; the relevant density is, of course, the dry density. Then fill the bucket with water, and the relevant density is ρ_{sat}. If the marbles are now placed in a bucket that has numerous holes in it so that water can move freely into and out of the bucket submerged in a tank of water, then the correct density of the marbles is the submerged or buoyant density ρ' [Fig. 2.3(b)]. If we remove the bucket from the tank but keep it completely saturated, then the appropriate density is again ρ_{sat}.

A second, more realistic example is the case of *rapid drawdown*, which occurs when the water level in a reservoir, canal, or river is quickly lowered. The result is that the density of the soils in the adjacent dam or slope increases from submerged or buoyant to saturated. This is a critical case for the stability of the dam or slope, because the gravitational forces acting on the embankment approximately double in magnitude. Therefore the factor of safety against slope instability is approximately cut in half. See Table 2.1 for typical values of ρ_{sat} and ρ'.

Example 2.7

Given:

A silty clay soil with $\rho_s = 2700\ \text{kg/m}^3$, $S = 100\%$, and water content $w = 46\%$.

Required:

Compute the void ratio, the saturated density, and the buoyant or submerged density in kg/m^3.

Solution: Place the given information on a phase diagram (Fig. Ex. 2.7).

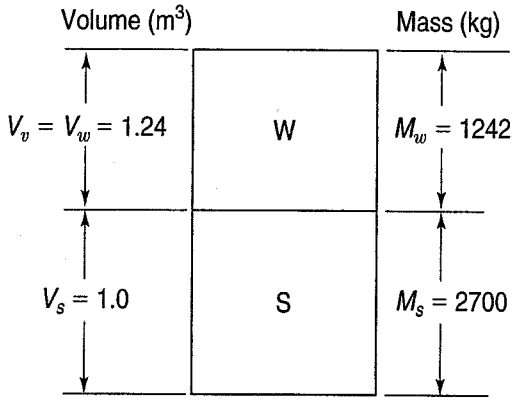

FIGURE Ex. 2.7

Assume $V_s = 1\ \text{m}^3$; therefore $M_s = V_s\rho_s = 2700\ \text{kg}$. From Eq. (2.15a), we can solve for e directly:

$$e = \frac{w\rho_s}{\rho_w S} = \frac{0.46 \times 2700\ \text{kg/m}^3}{1000\ \text{kg/m}^3 \times 1.0} = 1.242$$

But e also equals V_v, since $V_s = 1.0$; likewise $M_w = 1242\ \text{kg}$, since M_w is numerically equal to V_w, because $\rho_w = 1000\ \text{kg/m}^3$. Now that all the unknowns have been found, we may readily calculate the saturated density [Eq. (2.10)]:

$$\rho_{\text{sat}} = \frac{M_t}{V_t} = \frac{M_w + M_s}{1 + e} = \frac{(1242 + 2700)\ \text{kg}}{(1 + 1.24)\ \text{m}^3} = 1758\ \text{kg/m}^3$$

We could also use Eq. (2.17) directly:

$$\rho_{\text{sat}} = \frac{\rho_s + \rho_w e}{1 + e} = \frac{[2700 + 1000(1.242)]\ \text{kg}}{(1 + 1.242)\ \text{m}^3} = 1758\ \text{kg/m}^3$$

The buoyant density ρ' from Eq. (2.11) is:

$$\rho' = \rho_{\text{sat}} - \rho_w = 1758\ \text{kg/m}^3 - 1000\ \text{kg/m}^3 = 758\ \text{kg/m}^3$$

In this example, ρ' is less than the density of water. Go back and look at Table 2.1 for typical values of ρ'. The submerged or buoyant density of soil will be very important later on in our discussion of consolidation, settlement, and strength properties of soils.

2.3.2 Unit Weight and Specific Gravity

In geotechnical practice it is often convenient to use *unit weight* rather than density in engineering calculations. Unit weight γ is simply weight per unit volume; thus its SI units are N/m^3, because the Newton (N) is the SI unit of force, and in British units it is typically expressed in lb/ft^3, sometimes abbreviated pcf. Recall that the weight of an object is due to the force exerted by the earth's gravitational field, or $W = mg$, where g is the acceleration due to gravity. Then to get unit weight γ we simply divide the weight by the unit volume V, or:

$$\gamma = \frac{W}{V} = \frac{m}{V}g = \rho g \tag{2.20}$$

As noted in Appendix A, the value of g varies slightly with latitude and elevation, but for ordinary engineering purposes we usually assume it is a constant (standard $g = 9.807\ \text{m/s}^2$) for most places on the Earth.

The unit weights analogous to the densities described earlier [Eqs. (2.6), (2.7), and (2.8)] are the total, wet, or moist unit weight γ, the unit weight of solids γ_s, and the unit weight of water γ_w. In terms of the basic weights and volumes, they are

$$\gamma = \frac{W_t}{V_t} \tag{2.21}$$

$$\gamma_s = \frac{W_s}{V_s} \tag{2.22}$$

$$\gamma_w = \frac{W_w}{V_w} \tag{2.23}$$

To convert between density and unit weight, use Eq. (2.20) and $g = 9.81\ \text{m/s}^2$. If you round off g to $10\ \text{m/s}^2$, the error is only 2%.

Example 2.8

Given:

The densities ρ_s, ρ_{sat}, and ρ' in Example 2.7.

Required:

Compute the equivalent unit weights, using

a. SI units,

b. British engineering units.

Solution:

a. SI units:

From Example 2.7:

$$\rho_s = 2700\ \text{kg/m}^3 = 2.7\ \text{Mg/m}^3$$
$$\rho_{sat} = 1758\ \text{kg/m}^3 = 1.76\ \text{Mg/m}^3$$
$$\rho' = 758\ \text{kg/m}^3 = 0.76\ \text{Mg/m}^3$$

From Eq. (2.20), $\gamma = \rho g$, we obtain:

$$\gamma_s = 2.7\ \text{Mg/m}^3 \times 9.81\ \text{m/s}^2 = 26.5\ \text{kN/m}^3 \text{ (Note: } 1\ \text{kg} \times \text{m/s}^2 = 1\ \text{N)}$$
$$\gamma_{sat} = 1.76\ \text{Mg/m}^3 \times 9.81\ \text{m/s}^2 = 17.2\ \text{kN/m}^3$$
$$\gamma' = 0.76\ \text{Mg/m}^3 \times 9.81\ \text{m/s}^2 = 7.4\ \text{kN/m}^3$$

If you use the rounded-off value of $g = 10\ \text{m/s}^2$, the values of γ_s, γ_{sat}, and γ' are, respectively, 27, 17.6, and $7.6\ \text{kN/m}^3$. As mentioned, the difference is only about 2% and normally negligible.

b. British engineering units:

To convert the unit weight from kN/m^3 to lbf/ft^3 (pcf), merely multiply the value in kN/m^3 by 6.366. Or

$$\gamma_s = 26.5 \text{ kN/m}^3 = 168.7 \text{ pcf}$$
$$\gamma_{sat} = 17.2 \text{ kN/m}^3 = 109.5 \text{ pcf}$$
$$\gamma' = 7.4 \text{ kN/m}^3 = 47.1 \text{ pcf}$$

Note that the product of 6.366 and g (9.807) equals 62.43 or 62.4 lbf/ft^3, the unit weight of water in British engineering units. (If the rounded-off value of 10 m/s^2 is used, the conversion factor is slightly more or 63.7.) So to convert directly from density in Mg/m^3 to unit weight in lbf/ft^3, just multiply by 62.4!

If you need some practice converting between density and unit weight and between the various systems of units, review the examples in Appendix A.

In summary, to convert density in Mg/m^3 to unit weight in kN/m^3, multiply by 9.81 or 10. To convert density in Mg/m^3 to unit weight in lbf/ft^3 (pcf), multiply by 62.4. To help you get a feel for the magnitude of unit weights in both SI and British engineering units, we have converted the typical densities in Table 2.1 to unit weights in Table 2.2 in terms of kN/m^3 and pcf.

You may recall from physics that the *specific gravity* G of a substance is the ratio of its unit weight γ to the unit weight of water, usually pure water at 4°C (symbol: γ_o), or

$$G = \frac{\gamma}{\gamma_o} \tag{2.24}$$

Although several different specific gravities can be defined, only the bulk specific gravity G_m, the specific gravity of solids G_s, and the specific gravity of water G_w are of interest in geotechnical engineering. These are defined as

$$G_m = \frac{\gamma}{\gamma_o} \tag{2.25}$$

TABLE 2.2 Some Typical Values for Different Unit Weights of Common Soil Materials in Units of kN/m^3 and pcf

	Unit Weight					
	γ_{sat}		γ_d		γ'	
Soil Type	kN/m^3	pcf	kN/m^3	pcf	kN/m^3	pcf
Sands and gravels	19–24	119–150	15–23	94–144	9–14	62–81
Silts and clays	14–21	87–131	6–18	37–112	4–11	25–69
Glacial tills	21–24	131–150	17–23	106–144	11–14	69–87
Crushed rock	19–22	119–137	15–20	94–125	9–12	56–75
Peats	10–11	60–69	1–3	6–19	0–1	0–6
Organic silts and clays	13–18	81–112	5–15	31–94	3–8	19–50

Note: Values are rounded to the nearest 1 kN/m^3 and 1 pcf.

$$G_s = \frac{\gamma_s}{\gamma_o} \tag{2.26}$$

$$G_w = \frac{\gamma_w}{\gamma_o} \tag{2.27}$$

Because the density and therefore the unit weight of water are a maximum at 4°C, the specific gravity of water is exactly 1.0000 at that temperature. Because the value of G_w ranges between 0.9999 at 0°C and 0.9922 at 40°C, it is sufficiently accurate for most geotechnical work to assume $G_w = 1.00$ and $\gamma_w \approx \gamma_o$ = constant. Note that specific gravity is a dimensionless quantity and its numerical values are similar to what we used for densities in Mg/m^3. For example, the specific gravity of solid quartz (that is, if we could create a piece that had no void space) is 2.65, and typical values for most soils range from 2.60 to 2.80. Organic soils will have lower specific gravities, while heavy metallic minerals may occasionally have higher values.

If you need to determine the specific gravity of a soil, use ASTM (2010) standard D 854.

Example 2.9

Given:

A sample of soil has a bulk specific gravity of 1.91 and a specific gravity of solids of 2.69, and a water content of 29% (after Taylor, 1948).

Required:

Determine the void ratio, porosity, degree of saturation, and the dry density of the sample in **a.** British engineering units and **b.** SI units.

Solution: As before, when the size of the sample is not given, assume any convenient weight or volume. For the SI case, let's assume the total volume $V = 1$ ft^3, and for part **b**, assume $V = 1$ m^3. Draw the phase diagram for each case.

a. British engineering units:

From Eqs. (2.25) and (2.21), $G_m = W_t/V_t\gamma_w$; so $W_t = G_m V_t \gamma_w = (1.91)(1\,\text{ft}^3)(62.4\,\text{lbf/ft}^3) = 119$ lbf. From the definition of water content, we know that $W_s + 0.29W_s = 119$ lbf. Therefore, $W_s = 92$ lbf and $W_w = 27$ lbf.

From Eqs. (2.26) and (2.22), $V_s = W_s/G_s\gamma_w$; so 92 lbf/(2.69)(62.4 lbf/ft^3) = 0.55 ft^3. From Eqs. (2.27) and (2.23), $V_w = W_s/G_w\gamma_w$; so 27 lbf/(1.0)(62.4 lbf/ft^3) = 0.43 ft^3. Figure Ex. 2.9a is the completed phase diagram for part **a** of this example.

Therefore, the answers are $e = 0.82$; $n = 45\%$; $S = 96\%$; and $\gamma_d = 92$ pcf.

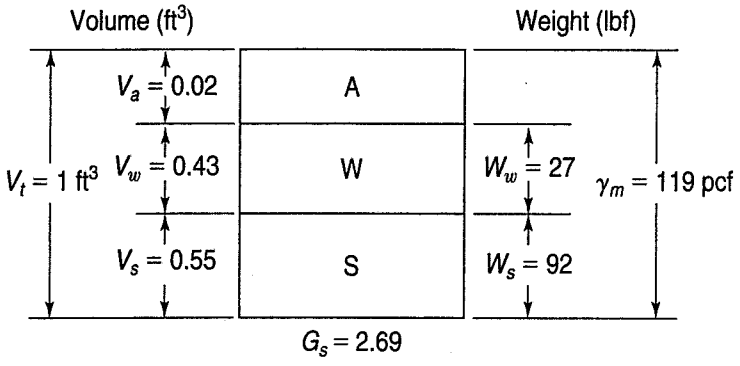

FIGURE Ex. 2.9a

b. S.I. units:

The solution for part **b** is basically the same as for part **a**, except you use $V_t = 1\ m^3$ and $\gamma_w = 10.0\ kN/m^3$. The answers for e, n, and S are identical, and $\rho_d = 1.48\ Mg/m^3$. See Fig. Ex. 2.9b for the completed phase diagram.

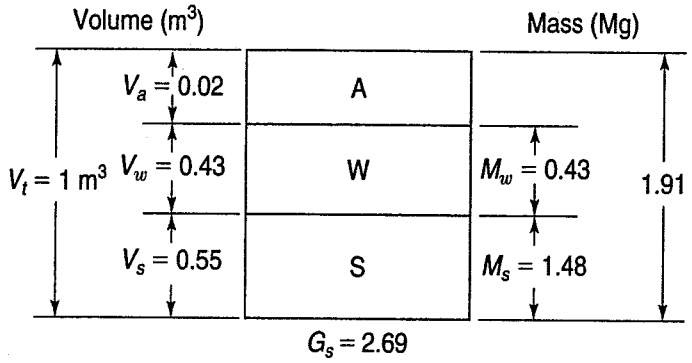

FIGURE Ex. 2.9b

Example 2.10

Given:

Equations (2.12), (2.15), and (2.16).

Required:

Develop the corresponding relationship for these equations in terms of unit weights and specific gravity of solids.

Solution: Use Eq. (2.20) ($\gamma = \rho g$) and the appropriate definitions for specific gravity of solids and water.

From Eq. (2.12):

$$\rho_d = \frac{\rho_s}{1 + e}$$

Substituting,

$$\frac{\gamma_d}{g} = \frac{\frac{\gamma_s}{g}}{1 + e}$$

or

$$\gamma_d = \frac{\gamma_s}{1 + e} = G_s\gamma_w/(1 + e) \tag{2.28}$$

From Eq. (2.15):

$$\rho_w Se = w\rho_s$$

$$\frac{\gamma_w}{g}Se = w\frac{\gamma_s}{g} = w\frac{G_s\gamma_w}{g}$$

Therefore,

$$Se = wG_s \tag{2.29}$$

For Eq. (2.16),

$$\rho = \frac{\rho_s + \rho_w Se}{1 + e}$$

$$\frac{\gamma}{g} = \frac{\frac{\gamma_s}{g} + \frac{\gamma_w}{g} Se}{1 + e}$$

Therefore,

$$\gamma = \frac{G_s + Se}{1 + e}\gamma_w \tag{2.30}$$

Using procedures similar to those shown in Example 2.10, you can readily develop the corresponding relationships for Eqs. (2.13), (2.14), (2.17), and (2.18) in terms of unit weights and specific gravity of solids. The corresponding equations, Eqs. (2.31) through (2.34), are given in Table 2.3, as are those developed in the above example.

TABLE 2.3 Corresponding Equations Showing Density and Unity Weight Relationships

Equation	Density	Equation	Unit Weight
(2.13)	$\rho = \frac{\rho_s(1 + w)}{1 + e}$	(2.31)	$\gamma = \frac{G_s(1 + w)}{1 + e}\gamma_w$
(2.14)	$\rho_d = \frac{\rho}{1 + w}$	(2.32)	$\gamma_d = \frac{\gamma}{1 + w}$
(2.12)	$\rho_d = \frac{\rho_s}{1 + e}$	(2.28)	$\gamma_d = \frac{\gamma_s}{1 + e}$
(2.17)	$\rho_{sat} = \frac{\rho_s + \rho_w e}{1 + e}$	(2.33)	$\gamma_{sat} = \frac{G_s + e}{1 + e}\gamma_w$
(2.18)	$\rho' = \frac{\rho_s - \rho_w}{1 + e}$	(2.34)	$\gamma' = \frac{G_s - 1}{1 + e}\gamma_w$

2.4 SOIL TEXTURE

So far we haven't said much about what makes up the "solids" part of the soil mass. In Chapter 1 we gave the usual definition of soil from an engineering point of view: the relatively loose agglomeration of mineral and organic materials found above the bedrock. We briefly described how weathering and other geologic processes act on the rocks at or near the earth's surface to form soil. Thus the solid part of the soil mass consists primarily of particles of mineral and organic matter in various sizes and amounts.

The *texture* of a soil is its appearance or "feel," and it depends on the relative sizes and shapes of the particles as well as the range or distribution of those sizes. Thus coarse-grained soils such as *sands* or *gravels* obviously appear coarse textured, while a fine-textured soil is composed mainly of very small mineral grains invisible to the naked eye. *Silts* and *clay* soils are good examples of fine-textured soils.

The texture of soils, especially of coarse-grained soils, has some relation to their engineering behavior. In fact, soil texture has been the basis for certain soil classification schemes, although these are more common in agronomy than in geotechnical engineering. Still, textural classification terms (gravels, sands, silts, and clays) are useful in a general sense in geotechnical practice. A convenient dividing line is the smallest grain that is visible to the naked eye. Soils with particles larger than this size (about 0.075 mm) are called coarse grained, while soils finer than the size are (obviously) called fine grained. Sands and gravels are coarse grained while silts and clays are fine grained.

For fine-grained soils, the presence of water greatly affects their engineering response—much more so than grain size or texture alone. Water affects the interaction between the mineral grains, and this may affect their *plasticity* (roughly defined as the soil's ability to be molded) and their *cohesiveness* (its ability to stick together). While sands are nonplastic and noncohesive (cohesionless), clays are both plastic and cohesive. Silts fall between clays and sands: they are fine grained yet nonplastic and cohesionless. These relationships as well as some general engineering characteristics are presented in Table 2.4.

Note that the term *clay* refers both to specific minerals called *clay minerals* (discussed in Chapter 4) and to soils which contain clay minerals. The behavior of some soils is strongly affected by the presence of clay minerals. In geotechnical engineering, for simplicity, such soils are usually called *clays*, but we really mean *soils that contain enough clay minerals to affect their engineering behavior.*

It is a good idea to get some practice identifying soils according to texture and other general characteristics, such as plasticity and cohesiveness. This process is best done in the laboratory, and in fact ASTM standard D 2488 provides an excellent guide for describing and identifying soils visually and manually. Visual-manual description of soil is also mentioned when we discuss soil classification later in this chapter.

TABLE 2.4 Textural and Other Characteristics of Soils

	Soil Name		
	Gravels, Sands	Silts	Clays
Grain size	Coarse grained Can see individual grains by eye	Fine grained Cannot see individual grains	Fine grained Cannot see individual grains
Characteristics	Cohesionless Nonplastic Granular	Cohesionless Nonplastic Granular	Cohesive Plastic —
Effect of water on engineering behavior	Relatively unimportant (exception: loose, saturated granular materials and dynamic loadings)	Important	Very important
Effect of grain-size distribution on engineering behavior	Important	Relatively unimportant	Relatively unimportant

2.5 GRAIN SIZE AND GRAIN SIZE DISTRIBUTION

As suggested in the preceding section, the size of the soil particle, especially for granular soils, has some effect on engineering behavior. Thus, for classification purposes, we are often interested in the particle or grain sizes present in a particular soil as well as the distribution of those sizes.

The range of possible particle sizes in soils is enormous. Soils can range from boulders or cobbles several centimetres in diameter down to ultrafine-grained colloidal materials. (Particles in colloidal materials are so small that their interactions are governed by electrostatic rather than gravitational forces.) The maximum possible range is on the order of 10^8, so usually we plot grain size distributions versus the *logarithm* of average grain diameter. We often use such scales in engineering and other disciplines to expand the small-scale data and compress the larger-scale data. Figure 2.4 indicates the divisions between the various textural sizes according to three common engineering classification schemes. Traditionally in the United States the units for the various sizes depend on the grain size. For materials greater than about 5 mm (about ¼ in.) units of inches are still commonly used in the United States, although millimetres are becoming more common. Grain sizes between 5 mm and 0.074 mm are classified according to U.S. Standard sieve number, which of course can be directly related to a specific grain size, as shown in Fig. 2.4. Soils finer than the No. 200 sieve (openings of 0.075 mm) are usually dimensioned in millimeters or, for the very fine-grained colloidal particles, in micrometers.

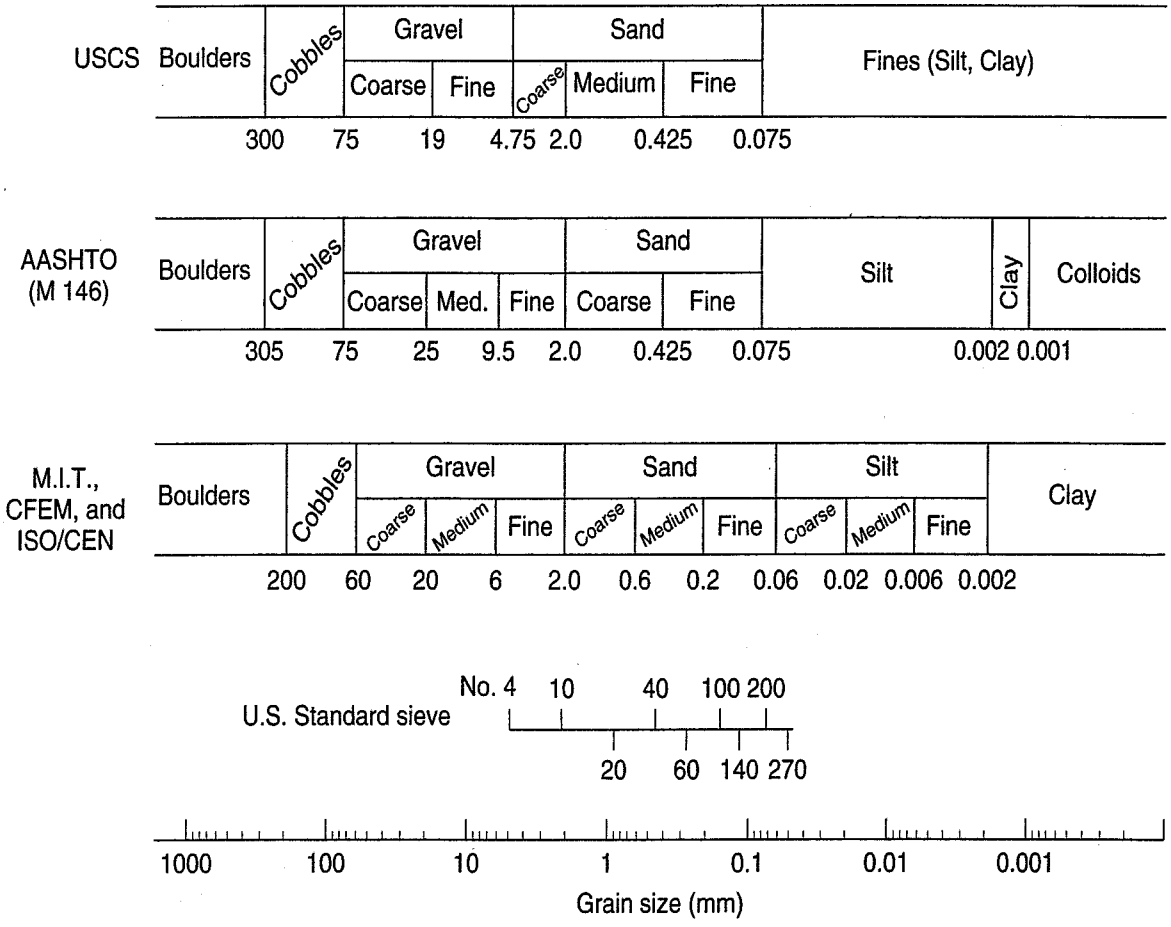

USCS = Unified Soil Classification System (U.S. Bureau of Reclamation, 1974; U.S. Army Engineer WES, 1960); ASTM D 2487

AASHTO = American Association for State Highway and Transportation Officials (1998)

M.I.T, C.F.E.M., ISO/CEN = Massachusetts Institute of Technology (Taylor, 1948); Canadian Foundation Engineering Manual (2006); International Standardisation Organisation and Comité Européen de Normalisation.

FIGURE 2.4 Grain size ranges according to several engineering soil classification systems (modified after Al-Hussaini, 1977).

How is the particle-size distribution obtained? The process is called *particle-size analysis*, or sometimes the *mechanical analysis* or the *gradation test.* For coarse-grained soils a *sieve analysis* is performed, in which a specimen of dry soil is shaken mechanically for several minutes through a series of woven-wire square-mesh sieves with successively smaller openings. Since the total mass of the specimen is known, the percentage retained on or passing each size sieve can be determined by weighing the amount of soil retained on each sieve after shaking. Detailed procedures for this test are specified by ASTM (2010) standard C 136 and D 422. The corresponding AASHTO (2007) test standards are T 27 and T 88.

The U.S. Standard sieve numbers commonly employed for the particle-size analysis of soils are shown in Table 2.5. Since soil particles are rarely perfect spheres, when we speak of particle diameters, we really mean an *equivalent* particle diameter as determined by the sieve analysis.

Note that as the standard sieve numbers increase, the openings become smaller. This is sometimes a source of confusion. Specifications should refer to the actual size of the sieve openings rather than the sieve numbers. For example, refer to the 425 μm sieve instead of the U.S. No. 40 sieve. Then there is no ambiguity about what sizes you mean.

It turns out that the sieve analysis is impractical for sieve openings less than about 0.05 to 0.075 mm (No. 200 U.S. Standard sieve). Thus for the fine-grained soils (silts, and clays) the *hydrometer analysis* can be used. The basis for this test is Stokes' law for falling spheres in a viscous fluid. This law relates the terminal velocity of the grains in suspension, their density, and the density of the fluid. We can thus calculate the grain diameter from the distance and time of fall. The hydrometer also determines the specific gravity (or density) of the suspension, and this lets us calculate the percentage of particles of a certain equivalent particle diameter at a given time. As with the sieve analysis, the percentage of the specimen still in suspension (or already out of suspension) can therefore readily be

TABLE 2.5 U.S. Standard Sieve Sizes and the Corresponding Open Dimension (ASTM 2010)

U.S. Standard Sieve No.	Sieve Opening (mm)
3-in.[a]	75 mm
2-in.	50 mm
1.5-in.[a]	37.5 mm
1-in.	25.0 mm
0.75-in.[a]	19.0 mm
0.375-in.[a]	9.5 mm
4[a]	4.75 mm
8[a]	2.35 mm
10	2.00 mm
16[a]	1.18 mm
20	850 μm
30[a]	600 μm
40	425 μm
50[a]	300 μm
60	250 μm
100[a]	150 μm
140	106 μm
200[a]	75 μm

[a]Use these sieves to provide a uniform spacing on the grain-size distribution curve.

determined. Detailed procedures for the hydrometer test are given by ASTM (2010) standard D 422, and AASHTO (2009) Standard Method T 88. The U.S. Department of the Interior (1990) and U.S. Army Corps of Engineers (1986) also have similar standardized procedures for this test.

The proportional distribution of different grain sizes can be shown as either a histogram or, more commonly, on a cumulative frequency diagram. For each grain "diameter" (represented by a particular sieve size), the proportion of the sample captured on that sieve is plotted. The grain diameters are plotted on a logarithmic scale (x-axis), whereas the percentage by mass (or weight) of the total specimen passing (finer than) is shown on a regular arithmetic scale (y-axis). Figure 2.5 shows some grain size distributions plotted both as histograms and as cumulative frequency diagrams. You will recognize that the histogram in Fig. 2.5(a) has a shape very similar to a normal distribution; in this case it would of course be a *log normal* distribution. The cumulative frequency diagram, commonly called a *gradation curve*, shows that this soil has a fairly good representation of particle sizes over a rather wide range. Each data point on the gradation curve indicates what proportion of the total sample passes through that particular sieve size; in other words, if only that sieve were used to sort the sample, it gives the percentage that would pass through it.

The gradation curve of Fig. 2.5(a) would be considered a *well-graded* soil. Figure 2.5(b) is a skewed distribution, and its gradation curve is less well graded. A *poorly graded* soil is one in which there is either an excess or a deficiency of certain sizes. The bimodal distribution shown in Fig. 2.5(c) results in a *gap-graded* or *skip-graded* distribution; in this particular soil, the proportion of grain sizes about 1–3 mm is relatively low, and the soil is also poorly graded. In general, the steeper the curve over a particular range of particle sizes, the more particles there are in that range. Conversely, the flatter the curve over a particular range, the fewer particles there are in that range.

Figure 2.6 shows grain size distributions for three typical soils. Note that this figure could just as well be plotted with the smaller grain sizes going toward the right, and this is a very common way of showing gradation curves. Another small point is that we show the y-axes of Figs. 2.5 and 2.6 as "percent passing or finer than"; they could just as easily be plotted as "percent retained or coarser than," the difference being that

$$\%\ \text{passing or finer than} = 100 - (\%\ \text{retained or coarser than})$$

Very often, practitioners will refer to the percent passing a particular sieve as the "minus No. [sieve number]" percentage. For example, in Fig. 2.6, for the well-graded curve, the minus No. 10 portion is 40%.

We could, of course, obtain the usual statistical parameters (mean, median, standard deviation, skewness, kurtosis, etc.) for the grain size distributions, but this is more commonly done in sedimentary petrology than in soil mechanics and geotechnical engineering. Of course the *range* of particle diameters found in the sample is of interest. Besides that, we use certain grain diameters D which correspond to an equivalent "percent passing" on the grain size distribution curve. For example, D_{10} is the grain size that corresponds to 10% of the sample passing by weight. In other words, 10% of the particles are smaller than the diameter D_{10}. This parameter locates the grain size distribution curve (GSD) along the grain size axis, and it is sometimes called the *effective size*. The *coefficient of uniformity* C_u is a crude shape parameter, defined as

$$C_u = \frac{D_{60}}{D_{10}} \tag{2.35}$$

where D_{60} = grain diameter (in mm) corresponding to 60% passing, and

D_{10} = grain diameter (in mm) corresponding to 10% passing, by weight (or mass).

Actually, the uniformity coefficient is misnamed, since the smaller the number, the more *uniform* the gradation—so it is really a coefficient of "disuniformity." For example, a $C_u = 1$ would be a soil

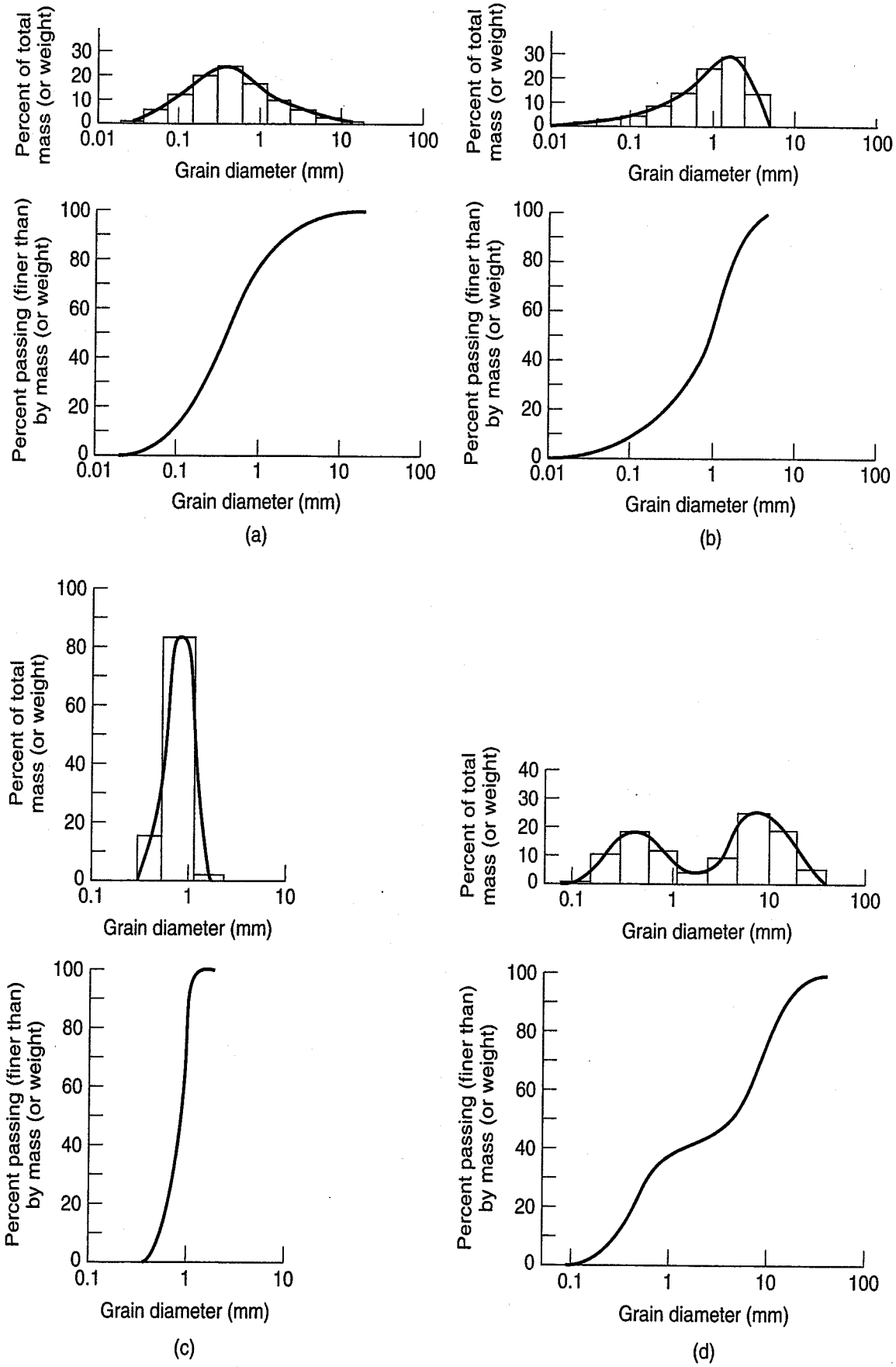

FIGURE 2.5 Histograms and cumulative grain-size distributions: (a) log normal; (b) skewed; (c) uniform; (d) gap graded.

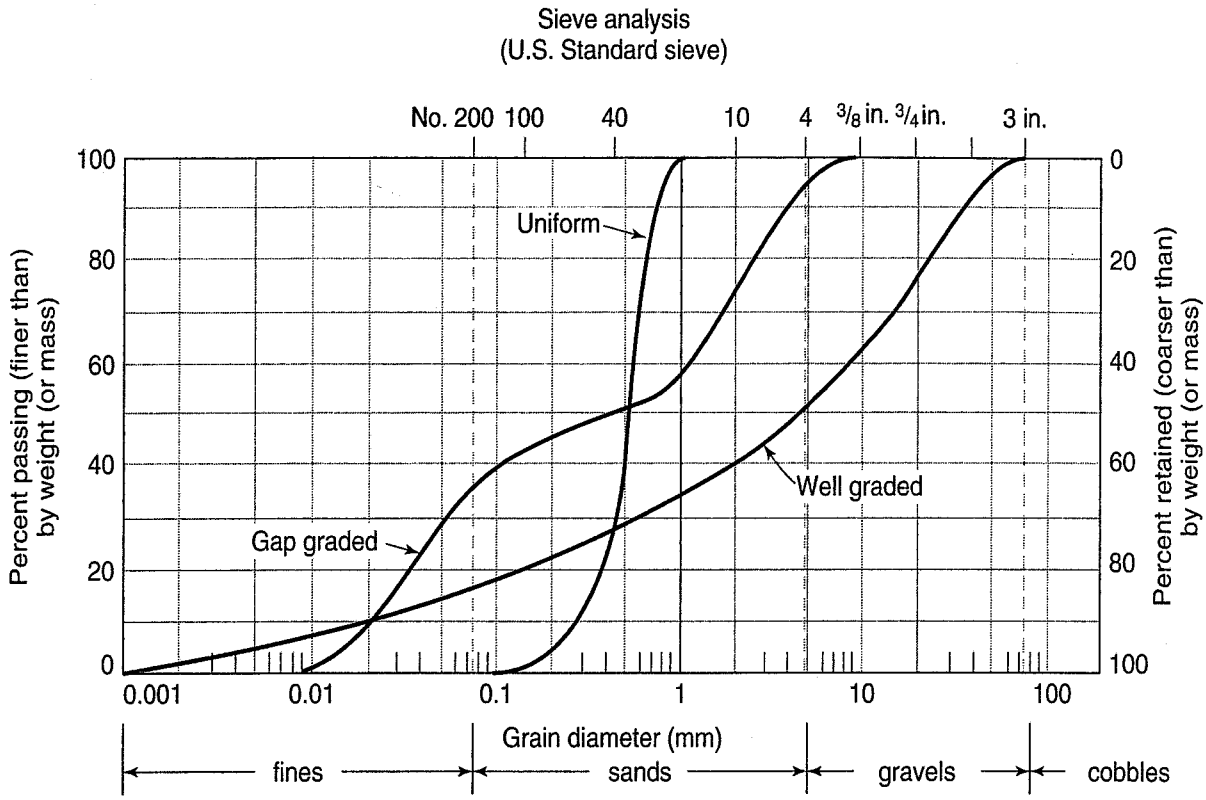

FIGURE 2.6 Typical grain size distributions.

with only one grain size. Very poorly graded soils, such as beach sands, have a C_u of 2 or 3, whereas very well graded soils may have a C_u of 15 or greater. Occasionally the C_u can range up to 1000 or so. As an example, the clay core material for Oroville Dam in California has a C_u of between 400 and 500; the sizes range from large boulders down to very fine-grained clay particles.

Another shape parameter sometimes used for soil classification is the *coefficient of curvature*, defined as

$$C_c = \frac{D_{30}^2}{D_{10}D_{60}} \tag{2.36}$$

where D_{30} = grain diameter (in mm) corresponding to 30% passing by weight (or mass). The other terms were defined previously.

A soil with a coefficient of curvature between 1 and 3 is considered to be well graded as long as the C_u is also greater than 4 for gravels and 6 for sands.

Example 2.11

Given:

The grain size distributions shown in Fig. 2. 6.

Required:

Determine D_{10}, C_u, and C_c for each distribution.

Solution: For Eqs. (2.35) and (2.36), we need D_{10}, D_{30}, and D_{60} for each gradation curve in Fig. 2.6.

a. Well-graded soil:

Simply pick off the diameters corresponding to 10%, 30%, and 60% passing.

$$D_{10} = 0.02 \text{ mm}, \quad D_{30} = 0.6 \text{ mm}, \quad D_{60} = 9 \text{ mm}$$

From Eq. (2.35),

$$C_u = \frac{D_{60}}{D_{10}} = \frac{9}{0.02} = 450$$

From Eq. (2.36),

$$C_c = \frac{D_{30}^2}{D_{10}D_{60}} = \frac{0.6^2}{(0.02)9} = 2$$

Since $C_u > 15$ and C_c is between 1 and 3, this soil is indeed well graded.

b. Gap-graded soil:

Use the same procedure as in part **a**.

$$D_{10} = 0.022 \text{ mm}, \quad D_{30} = 0.052 \text{ mm}, \quad D_{60} = 1.2 \text{ mm}$$

From Eq. (2.35),

$$C_u = \frac{D_{60}}{D_{10}} = \frac{1.2}{0.022} = 55$$

From Eq. (2.36),

$$C_c = \frac{D_{30}^2}{D_{10}D_{60}} = \frac{0.052^2}{0.22(1.2)} = 0.0102$$

Even though by the uniformity coefficient criterion this soil is well graded, it fails the coefficient of curvature criterion. Therefore it is indeed poorly graded.

c. Uniform soil:

Use the same procedure as in part **a**.

$$D_{10} = 0.3 \text{ mm}, \quad D_{30} = 0.43 \text{ mm}, \quad D_{60} = 0.55 \text{ mm}$$

From Eq. (2.35),

$$C_u = \frac{D_{60}}{D_{10}} = \frac{0.55}{0.3} = 1.8$$

From Eq. (2.36),

$$C_c = \frac{D_{30}^2}{D_{10}D_{60}} = \frac{0.43^2}{(0.3)0.55} = 1.12$$

This soil is still poorly graded, even though the C_c is slightly greater than unity; the C_u is very small.

2.6 PARTICLE SHAPE

The shape of the individual particles is at least as important as the grain size distribution in affecting the engineering response of granular soils. It is possible to quantify shape according to rules developed by sedimentary petrologists, but for geotechnical engineering purposes such refinements are rarely warranted. Only a qualitative shape determination is usually made as part of the visual identification of soils. Coarse-grained soils are commonly classified according to the shapes shown in Fig. 2.7.

A distinction can also be made between particles that are *bulky* and those with other shapes—for example, flat, elongated, needlelike, or flaky. ASTM (2010) standard D 2488, gives some criteria for describing the shape of nonbulky particles. Mica flakes are an obvious example of flaky-shaped particles, while particles of Ottawa sand have a bulky shape. Cylinders of these soils behave very differently when compressed by a piston. The bulky grained sand compresses hardly at all, even when in a very loose state, but the mica flakes will compress, even under small pressures, up to about one-half of their original volume. When we discuss the shear strength of sands, you will learn that grain shape is very significant in determining the frictional characteristics of granular soils.

2.7 ATTERBERG LIMITS

We mentioned in Table 2.4 that the presence of water in the voids of a fine-grained soil can markedly affect its engineering behavior. Not only is it important to know how much water is present in, for example, a natural soil deposit (the water content), but we need to be able to compare or scale this water content against some standard of engineering behavior. Another important distinguishing characteristic of fine-grained soils is plasticity. In fact, plasticity is the most conspicuous physical characteristic of clayey soils (Casagrande, 1932b). As noted in Table 2.4, plasticity could be used to distinguish between plastic and nonplastic soils—that is, between clays and silts. Plasticity could also be used to classify clays by their degree of plasticity. Finally, plasticity depends on the water content of a clay soil.

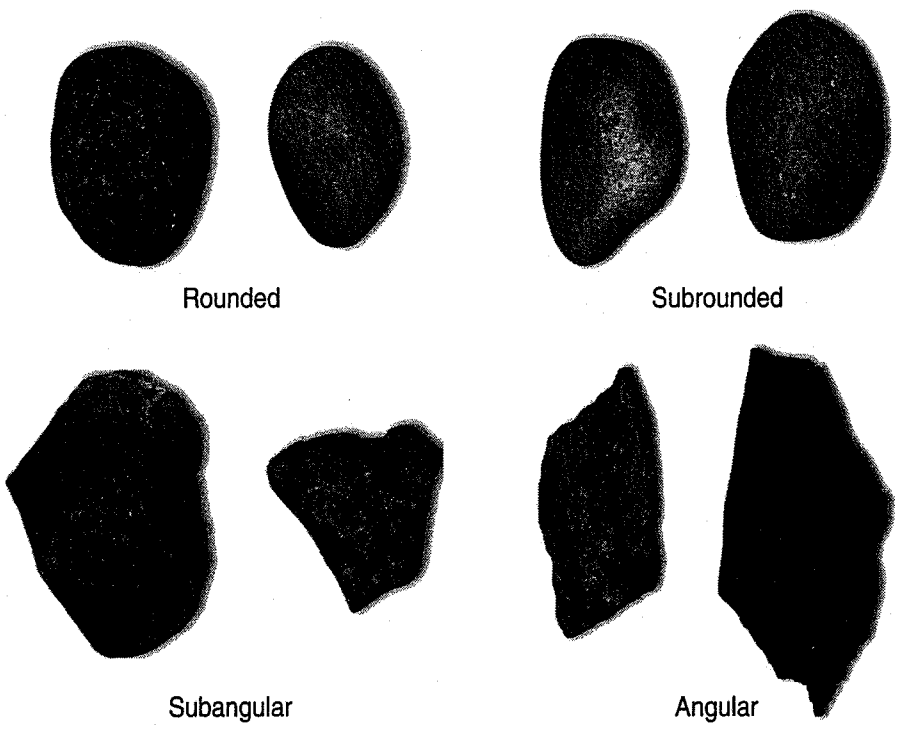

FIGURE 2.7 Typical shapes of coarse-grained bulky particles (photograph by M. Surendra).

And this brings us to the Atterberg limits—the threshold *water contents* at which certain types of engineering behavior can be expected. These water content boundaries are unique for each soil, but the referenced soil behavior is the same. If we know the soils' water content at a site relative to their Atterberg limits, then we already know a great deal about their engineering behavior. Along with the natural water content, the Atterberg limits are the most important items in the description of fine-grained soils. They are used in classification of such soils, and they are useful because they correlate with the engineering properties and engineering behavior of fine-grained soils.

The Atterberg limits were developed in the early 1900s by a Swedish soil scientist, Albert Atterberg (1911; 1916). His extensive research on the consistency properties of remolded fine-grained soils is the basis of our current understanding of how water influences the plasticity of these soils. Atterberg defined several limits of fine-grained soil behavior and developed simple manual tests to define them. They were:

1. Upper limit of viscous flow.
2. Lower limit of viscous flow.
3. Liquid limit—lower limit of viscous flow.
4. Sticky limit[2]—clay loses its adhesion to a metal blade.
5. Cohesion limit[3]—grains cease to cohere to each other.
6. Plastic limit—lower limit of the plastic state.
7. Shrinkage limit—lower limit of volume change.

After much experimentation, Atterberg realized that at least two parameters were required to define plasticity of clays—the upper and lower limits of plasticity. He also defined the *plasticity index*, which is the range of water content where the soil is plastic, and he was the first to suggest that it could be used for soil classification. Later on, in the late 1920s, K. Terzaghi and A. Casagrande (1932b), working for the U.S. Bureau of Public Roads, standardized the Atterberg limits so that they could be readily used for soil classification purposes. In present geotechnical engineering practice we usually use the liquid limit (LL or w_L), the plastic limit (PL or w_P), and sometimes the shrinkage limit (SL or w_S). The sticky and the cohesion limits are more useful in ceramics and agriculture.

Since the Atterberg limits are *water contents* where the soil behavior changes, we can show these limits on a water content continuum, as in Fig. 2.8. Also shown is the behavior state for a given range of water content. As the water content increases, the state of the soil changes from a brittle solid to a plastic solid and then to a viscous liquid. We can also show on the same water content continuum the generalized material response (stress-strain curves) corresponding to those states.

You may recall the curves shown in Fig. 2.9 from fluid mechanics, where the shear velocity gradient is plotted versus the shear stress. When this relationship is linear, the liquid is called Newtonian, and the slope of the line is, of course, the viscosity. If the viscosity is not a constant, then the material is a real or non-Newtonian liquid. Recall, too, that a liquid is defined as a material that cannot support a static shear stress; so, as shown in Fig. 2.9, when $v = 0, \tau = 0$ for both liquids. Depending on the water content, it is possible for soils to have a response represented by all these curves except the ideal Newtonian liquid. Note, too, how different this response is from the stress-strain behavior of other engineering materials such as steel, concrete, or wood.

Atterberg's original consistency limit tests were rather arbitrary and not easily reproducible, especially by inexperienced operators. As mentioned, Casagrande (1932b, 1958) worked to standardize the tests, and he developed the liquid limit device (Fig. 2.10) so that the test became more operator

[2] *Klebrigkeitsgrenze.*
[3] *Zusammenhaftbarkeitsgrenze.*

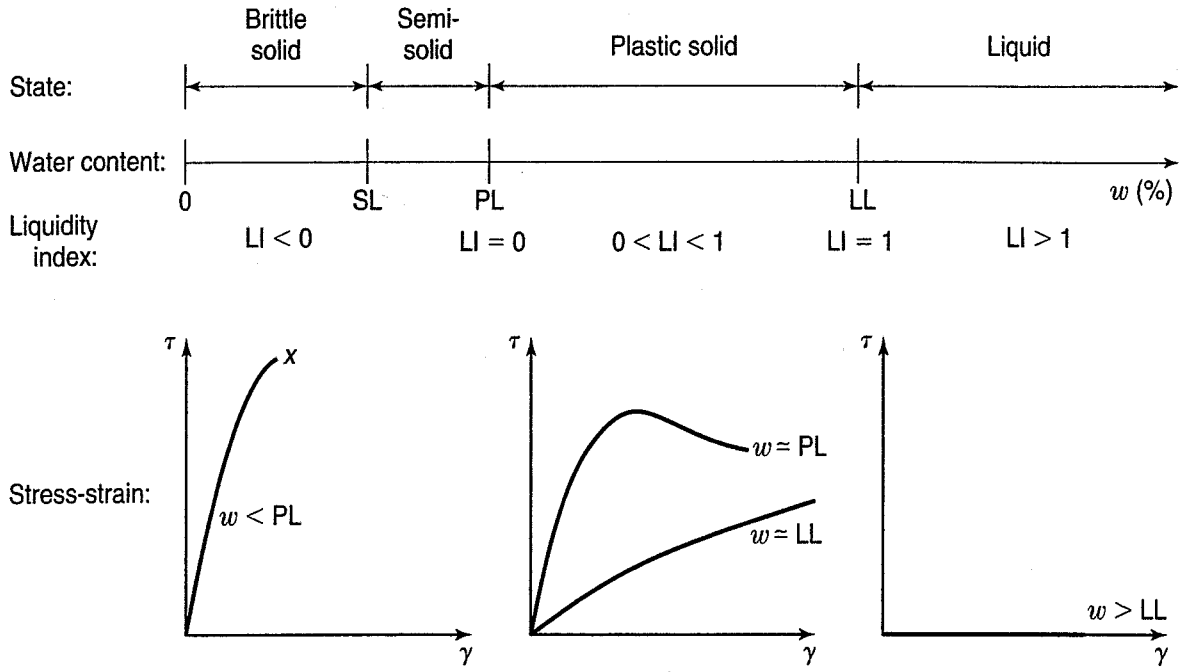

FIGURE 2.8 Water content continuum showing the various states of a soil as well as their generalized stress-strain response.

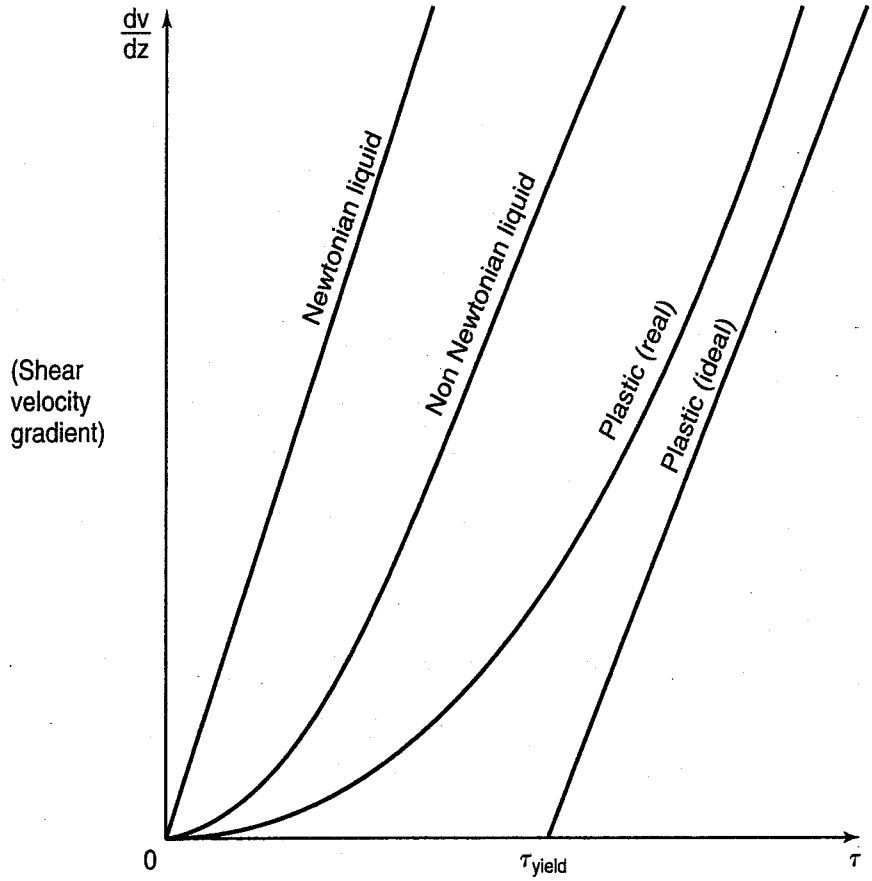

FIGURE 2.9 Behavior of several materials, including soils, over a range of water contents.

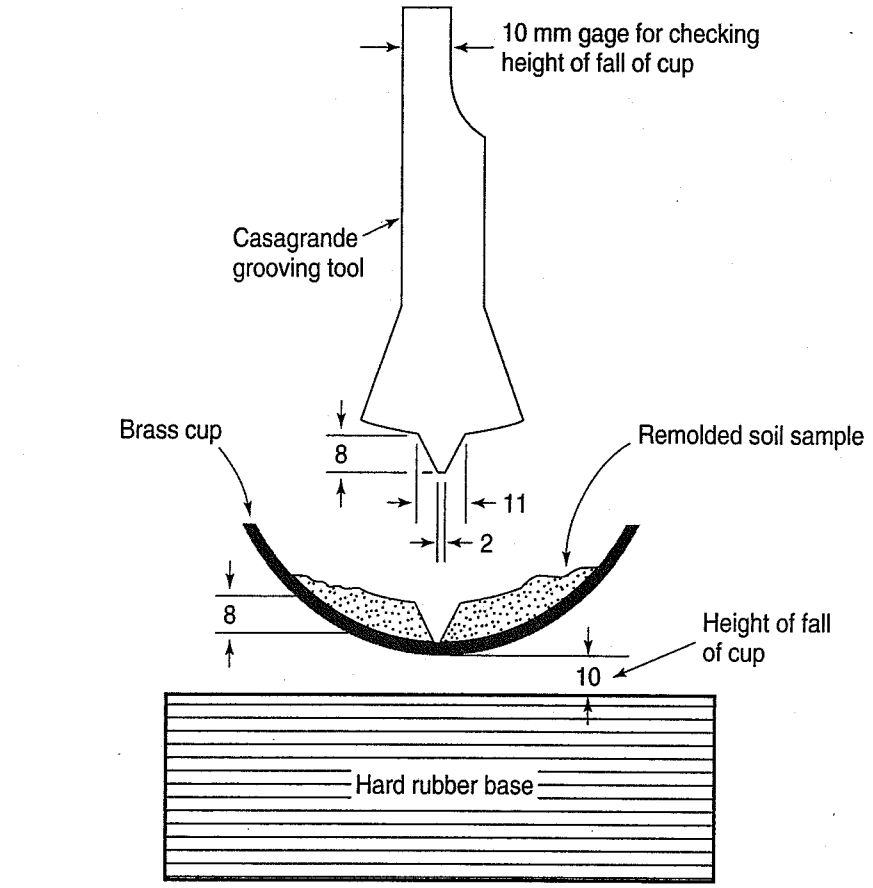

(a)

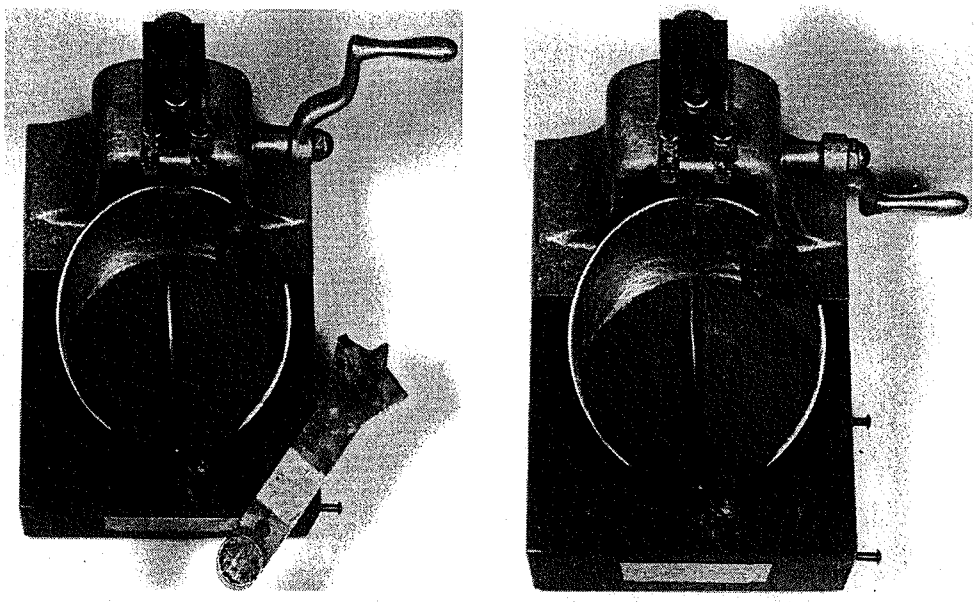

(b) (c)

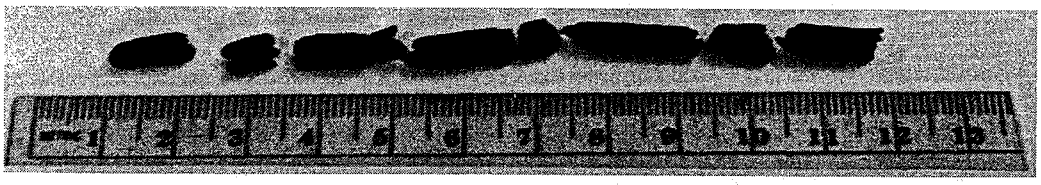

(d)

FIGURE 2.10 (a) Schematic diagram of the Casagrande liquid-limit device and grooving tool; dimensions in millimetres. (b) Cut groove prior to turning the crank. (c) After turning the crank to apply sufficient blows of the cup to close the groove 13 mm. (d) Plastic-limit threads. [Parts (a) through (c) after Hansbo (1975); photographs by M. Surendra.]

independent. He defined the LL as that water content at which a standard groove cut in the remolded soil sample by a grooving tool [Figs. 2.10(a), (b)] will close over a distance of 13 mm ($^1/_2$ in.) at 25 blows of the LL cup falling 10 mm on a hard rubber plastic base [Fig. 2.10(c)]. In practice, it is difficult to mix the soil so that the groove closure occurs at exactly 25 blows, so we generally mix and test the soil at 5 to 6 different water contents, each resulting in the $^1/_2$-in. groove closing at blow counts higher and lower than 25. Casagrande found that if you plot the water contents versus the logarithm of the number of blows, you get a slightly curved relationship called the *flow curve*. Where the flow curve crosses 25 blows, that water content is defined as the liquid limit.

The plastic-limit test is a bit more arbitrary, and it requires some practice to get consistent and reproducible results. The PL is defined as the water content at which a thread of soil *just crumbles* when it is carefully rolled out to a diameter of 3 mm ($^1/_8$ in.). It should break up into segments about 3 to 10 mm ($^1/_8$ to $^3/_8$ in.) long. If the threads can be rolled to a smaller diameter, then the soil is too wet (i.e., above the PL). If it crumbles before you reach 3 mm ($^1/_8$ in.) diameter, then the soil is too dry and you are below the PL. Properly rolled-out PL threads should look like those shown in Fig. 2.10(d).

Detailed descriptions of specimen preparation, LL-device calibration, grooving-tool specifications, and conducting of both the LL and PL tests are given in ASTM (2010) standard D 4318, U.S. Dept. of the Interior (1990), and U.S. Army Corps of Engineers (1986).

The tests should be conducted on material passing the No. 40 425 μm sieve that has not previously been air or oven dried. Although we are technically characterizing the fine-grained materials passing the No. 200 (0.075 mm) sieve, the difficulty in separating especially highly plastic materials on that sieve is such that we use the No. 40 sieve, because it is the finest practical sieve size. Even though these tests appear simple, some practice is required to get accurate and consistent results. Inadequate mixing and nonuniform water content are the most common reasons for unreliable LL results. They cause scatter in the data points used to plot the flow curve, and this makes the LL determination ambiguous. The problems with the PL test are due mostly to operator and weighing errors, and it is especially difficult for beginning students to achieve reliable PL results. As a measure of PL validity, the following criterion is recommended:

$$PL = PL_{avg} \pm 0.05PL_{avg} \tag{2.37}$$

where PL_{avg} is the average of all the PL test attempts.

For example, if the average of all your PL tests is 20.0, then all valid attempts must be between 19 and 21. Any water content determinations outside that range must be discarded and excluded from the average. An even more stringent criterion is 0.02 of the PL_{avg}, which means that for this example, all PLs must lie with the range of 19.6 and 20.4 to be valid. Such a result can ordinarily be achieved only by very experienced technicians. Note that ASTM (2010) D 4318 has a statistically based approach to the precision of the PL test results that appears to give approximately the same result as Eq. (2.37) for soils with PL's about 20. Also included as in option in ASTM (2010) standard D 4318 is a recently developed mechanical PL rolling device that should make it easier to get repeatable PL results.

A word about grooving tools: the dimensions shown in Fig. 2.10 are specified so that the shape of the groove can be accurately controlled. Another tool that you sometimes see in the lab has a pyramidal cross section and is curved like a short hook. This is the AASHTO grooving tool (AASHTO, 2010, standard T 89). The problem with it is that the height of the groove is not controlled, which can lead to erroneous results. We recommend that you always use the Casagrande-ASTM tool and that you occasionally check its dimensions to see that it meets specifications.

2.7.1 Cone Liquid Limit

In recent years, the fall-cone test developed in Sweden to determine the liquid limit (Hansbo, 1957) has gained in popularity. It seems to give more consistent results than the Casagrande device, especially for

certain clays with interparticle cementations in their natural state, and it is somewhat simpler to use. Karlsson (1977) presents an excellent discussion of the reliability of both procedures.

A 60-g metal cone with an apex angle of 60° is suspended in a device and positioned so that the cone tip just barely touches the surface of a remolded soil specimen; then the cone is released and its penetration into the soft soil measured. The test is repeated at different water contents, and the cone LL is defined as the water content at which the cone penetration is exactly 10 mm. The cone liquid limit is also the standard procedure in the United Kingdom (BS 1377: Part 2, 1990), although they use an 80-g cone with a 30° apex. From a plot (very similar to the flow curve) of cone penetration versus water content, the cone LL is defined as the water content at 20 mm penetration. According to Hansbo (1994), the British and Swedish procedures give very similar results.

So, how well do the cone LL and the Casagrande (percussion) LL compare? Karlsson (1977) and Head (2006) report that they agree very well up to LL values of about 100; above 100, the cone LL tends to give lower values than the Casagrande LL. When reporting LL results, it is a good idea to distinguish between the cone LL and the Casagrande LL.

2.7.2 One-Point Liquid Limit Test

When using the Casagrande device, we can use the approximately linear flow curve to help us obtain a fairly good estimate of the LL from the one-point liquid limit test. All we have to do is to prepare a LL test specimen at a water content so that the groove closes at a blow count N between 20 and 30, obtain the water content w_N, and use the relationship

$$\text{LL} = w_N\left(\frac{N}{25}\right)^a \tag{2.38}$$

The exponent a is an empirical "constant" that ranges from 0.115 to 0.13, and has an average value of 0.121 (Waterways Experiment Station, 1949; Lambe, 1951; Corps of Engineers, 1986; U.S. Dept. of Interior, 1990; ASTM, 2010). Equation (2.38) was developed from a regression analysis of log w vs. log N determined on 767 different soils by the U.S. Army Corps of Engineers at the Waterways Experiment Station (T. F. Wolff, Personal Communication, 1986). Note that there are similar one-point test procedures for the cone LL (Karlsson, 1977; Head, 2006).

Example 2.12

Given:

Liquid-limit data in the table below (after U.S. Dept. of the Interior, 1990).

	Trial No.			
	1	2	3	4
No. of blows	16	21	29	34
w (%)	23.3	22.5	21.8	21.5

Required:

a. From the data in the table above, plot the flow curve and determine the LL of the soil.

b. Determine the flow index (defined as the slope of the flow curve).

c. Compute the LL using Eq. (2.38) and compare results.

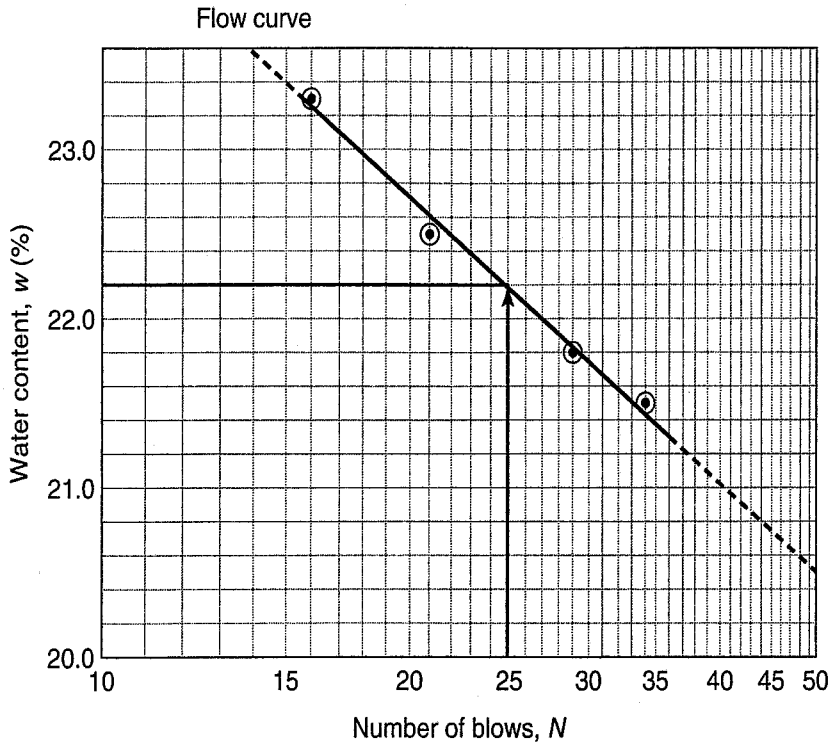

FIGURE Ex. 2.12 Water content versus log number of blows.

Solution:

a. Plot the water content versus the log of the number of blows, as shown in Fig. Ex. 2.12. From the curve, find the water content at 25 blows to be 22.2%.

b. To determine the flow index, find the slope of the flow curve. If the graph extends over one log cycle, the easiest approach is to take the variation in water content over one log cycle of blows, or from 10 to 100 blows. However, in the case of Fig. Ex. 2.12, just extend the flow curve to the limits of the graph (shown dashed) and obtain the following points: at water content = 23.6%, the blow count = 13.8. At the other end of the line, where the number of blows is 50, the water content = 20.55%. Therefore the slope is:

$$\text{slope} = \frac{\Delta w}{\log\dfrac{(N_2)}{(N_1)}} = \frac{23.6 - 20.55}{\log\dfrac{50}{13.8}} = \frac{3.05}{0.56} = 5.45$$

So, the flow index is 5.45. Note that it is generally between 2 and 20.

c. Use Eq. (2.38) to calculate the one-point LL. If we follow ASTM, we should use the data for blow counts between 20 and 30, or only for Trials 2 and 3. For Trial 2 we have:

$$\text{LL} = w_n\left(\frac{N}{25}\right)^{0.12} = 22.5\left(\frac{21}{25}\right)^{0.12} = 22.0\%$$

For Trial 3:

$$\text{LL} = 21.8\left(\frac{29}{25}\right)^{0.12} = 22.2\%$$

Note that the one-point LL test is not as accurate as taking the LL directly from the flow curve, but for most soils the differences are small.

2.7.3 Additional Comments on the Atterberg Limits

The range of liquid limits can be from zero to 1000, but most soils have LL's less than 100. The plastic limit can range from zero to 100 or more, with most being less than 40. Even though the Atterberg limits are really water contents, they are also boundaries between different engineering behaviors, and Casagrande (1948) recommends that the values be reported *without* the percent sign. As we show later in this chapter, they are *numbers* to be used to classify fine-grained soils, and they provide an *index* of soil behavior. You will, however, see the limits reported both ways and using both symbols: LL and PL, and w_L and w_P with a percent sign. (As you may have already deduced, civil engineers never have been models of consistency when it comes to units and symbols.)

The other Atterberg limit sometimes used in geotechnical engineering practice, the shrinkage limit, is discussed in Chapter 6 and can be important for certain regions where soils experience seasonal swelling-shrinkage cycles.

We mentioned earlier that Atterberg also defined an index called the *plasticity index* to describe the range of water content over which a soil behaves plastically, or is moldable. The plasticity index, PI or I_p, therefore is numerically equal to the difference between the LL and the PL, or

$$\text{PI} = \text{LL} - \text{PL} \tag{2.39}$$

The PI is useful for the engineering classification of fine-grained soils, and many engineering properties have been found to empirically correlate with the PI.

When we first started the discussion on the Atterberg limits, we said that we wanted to be able to compare or scale our water content with some defined limits or boundaries or engineering response. In this way, we would know if our sample was likely to behave as a plastic, a brittle solid, or even possibly a liquid. The index for scaling the natural water content of a soil is the *liquidity index*, LI or I_L, defined as

$$\text{LI} = \frac{w_n - \text{PL}}{\text{PI}} \tag{2.40}$$

where w_n is the natural water content of the soil in question. If the LI is less than zero, then, from the water content continuum of Fig. 2.8, you know that the soil will behave in a brittle or friable way if sheared. If the LI is between zero and one, then the soil will behave plastically, or in a moldable way. If LI is greater than one, the soil will be essentially a very viscous liquid when sheared. Such soils can be extremely sensitive to breakdown of the soil structure. As long as they are not disturbed in any way, they can be relatively strong, but if for some reason they are sheared and the structure of the soil breaks down, then they literally can flow like a liquid. There are deposits of very *sensitive* (or "quick") *clays* in Eastern Canada and Scandinavia. Figure 2.11 shows a sample of Leda clay from Ottawa, Ontario, in both the undisturbed and remolded states at the same water content. The undisturbed sample can carry a vertical stress of more than 100 kPa; when thoroughly remolded, it behaves like a liquid. Such clays, and even those with much less sensitivity, can cause significant design and construction problems, since they lose much of their shear strength when excavated or loaded beyond their yield stress.

We emphasize at this point that the limits are conducted on thoroughly *remolded* soils. When we discuss the structure of clays in Chapter 4, we will see that the natural structure of a soil very strongly governs its engineering behavior. So, why do the Atterberg limits work? Like many properties in geotechnical engineering, they work empirically. That is, they correlate with engineering properties and behavior, because *both the Atterberg limits and the engineering properties are affected by the same things*. Among these "things" are the clay minerals, the ions in the pore water, and the geologic history of the soil deposit. These factors are discussed in detail in Chapter 4. For now, just accept that these very simple, arbitrary, and empirical Atterberg limits are most useful in classifying soils for engineering purposes and that they correlate quite well with the engineering behavior of soils.

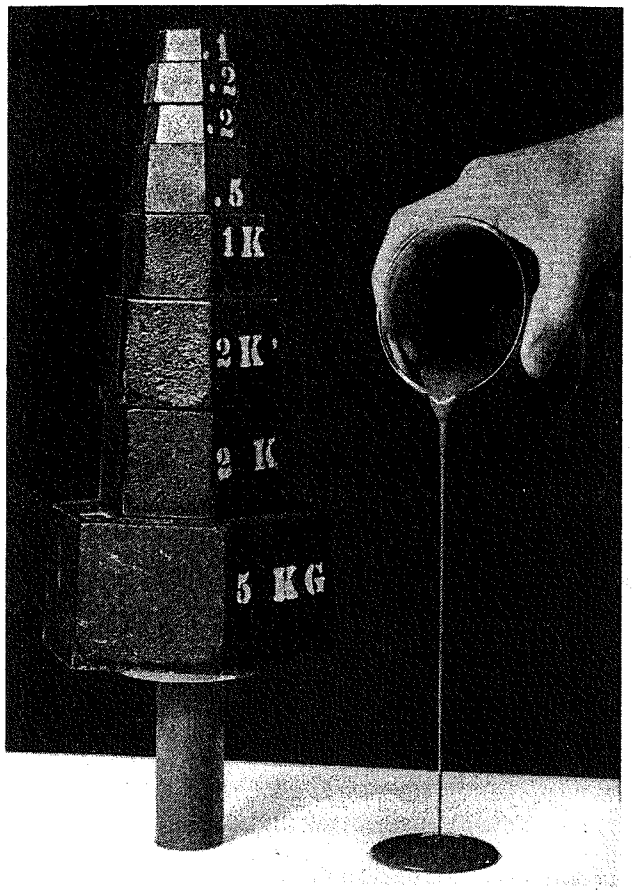

FIGURE 2.11 (left) Undisturbed and (right) thoroughly remolded sample of Leda clay from Ottawa, Ontario (photograph courtesy of the Division of Building Research, National Research Council of Canada, hand by D. C. MacMillan).

2.8 INTRODUCTION TO SOIL CLASSIFICATION

From our previous discussion on soil texture and grain size distributions, you should have a general idea about how soils are classified. For example, in Sec. 2.4 we described sands and gravels as coarse-grained soils, whereas silts and clays were fine grained. In Sec. 2.5, we showed the specific size ranges for these soils on a grain size scale (Fig. 2.4) according to the standards of USCS, AASHTO, etc. Usually, however, general terms such as sand or clay include such a wide range of engineering characteristics that additional subdivisions or modifiers are required to make the terms more useful in engineering practice. These terms are collected into *soil classification systems*, usually with some specific engineering purpose in mind.

A soil classification system represents, in effect, a language of communication between engineers. It provides a systematic method of categorizing soils according to their probable engineering behavior, allowing engineers access to the accumulated experience of other engineers. A classification system does not eliminate the need for detailed soils investigations or more sophisticated testing for engineering properties. However, engineering properties have been found to correlate quite well with the index and classification properties of a given soil deposit. Thus, by knowing the soil classification, the engineer already has a fairly good general idea of the suitability of the soil for a particular application and its behavior during construction, under structural loads, and so on.

Figure 2.12 illustrates the role of a soil classification system in geotechnical engineering practice.

During the past 75 years or so, many soil classification systems have been proposed. As Casagrande (1948) pointed out, most systems used in civil engineering had their roots in agricultural soil science. This is why the first systems used by civil engineers classified soil by grain size or soil texture. Atterberg (1905) apparently was the first to suggest that something other than grain size could be used for soil classification. To this end, in 1911 he developed his consistency limits for the behavior of fine-grained soils (Sec. 2.7), although at that time for agricultural purposes. In the 1920s, the U.S. Bureau of

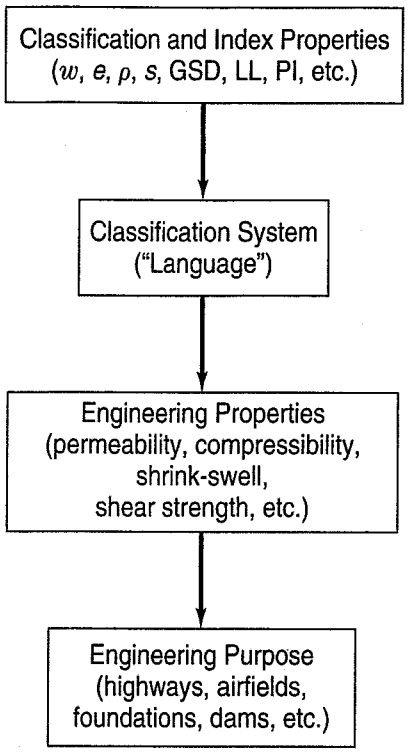

FIGURE 2.12 Role of classification systems in geotechnical engineering.

Public Roads started classifying fine-grained highway subgrade soils using the Atterberg limits and other simple tests. Casagrande (1948) describes several other systems that have been used in highway engineering, airfield construction, agriculture, geology, and soil science.

Today in North America, only the Unified Soil Classification System (USCS) and the American Association of State Highway and Transportation Officials (AASHTO) system are commonly used in civil engineering practice. The USCS is by far the more common of the two, and it is used by engineering agencies of the U.S. Government (e.g., U.S. Army Corps of Engineers, U.S. Bureau of Reclamation, Federal Aviation Administration) and virtually all geotechnical consulting firms and soil testing laboratories in the United States and Canada. The USCS is also the best-known and most widely used engineering soil classification system in the world.

The only other classification system used in North America is the AASHTO system, developed primarily for evaluating subgrade soils under highway pavements. It is still used for that purpose by state departments of transportation. Once you become familiar with the details, both the USCS and AASHTO systems are easy to use in engineering practice.

2.9 UNIFIED SOIL CLASSIFICATION SYSTEM (USCS)

Because of difficulties experienced with other classification systems for the design and construction of military airfields during World War II, Professor A. Casagrande developed the Airfield Classification (AC) System for the U.S. Army Corps of Engineers (Casagrande, 1948). In 1952, the AC system was modified by the U.S. Department of the Interior and the U.S. Army Corps of Engineers in consultation with Professor Casagrande to make it also applicable to dams, foundations, and other construction. This expanded system is known as the Unified Soil Classification System or the USCS (U.S. Army Engineer Waterways Experiment Station, 1960). The basic concept of the USCS is that coarse-grained soils can be classified according to their grain sizes and grain size distributions, whereas the engineering behavior of fine-grained soils is related primarily to their plasticity. In the USCS, therefore, only the results of a sieve analysis and the Atterberg limits are necessary to completely classify a soil. This also means that a hydrometer test, which can be relatively time consuming and subject to operator error, is not necessary to classify soils.

ASTM (2010) standard D 2487, U.S. Department of the Interior (1990), Designation USBR 5000, and the U.S. Army Corps of Engineers (1960) are the best references on the USCS. They define the soil terms used in the system, tell you how to sample the soil and prepare specimens for classification, and then give you a step-by-step procedure for classifying soils. The ASTM and USBR procedures may be summarized as follows.

First, the system defines the various soil components according to their grain sizes and other characteristics (Table 2.6). These are strict engineering definitions. The fine-grained soils—*silt*, *clay*, *organic silt* and *organic clay*, and *peat*—are defined not according to grain size but according to certain visual and manual characteristics. These definitions are given below when we describe the classification of fine-grained soils.

TABLE 2.6 USCS Definitions of Particle Size, Size Ranges, and Symbols

Soil Fraction or Component	Symbol	Size Range
Boulders	None	Greater than 300 mm
Cobbles	None	75 mm to 300 mm
(1) Coarse-grained soils:		
Gravel	G	75 mm to No. 4 sieve (4.75 mm)
Coarse		75 mm to 19 mm
Fine		19 mm to No. 4 sieve (4.75 mm)
Sand	S	No. 4 (4.75 mm) to No. 200 (0.075 mm)
Coarse		No. 4 (4.75 mm) to No. 10 (2.0 mm)
Medium		No. 10 (2.0 mm) to No. 40 (0.425 mm)
Fine		No. 40 (0.425 mm) to No. 200 (0.075 mm)
(2) Fine-grained soils:		
Fines		Less than No. 200 sieve (0.075 mm)
Silt	M	(No specific grain size—use Atterberg limits)
Clay	C	(No specific grain size—use Atterberg limits)
(3) Organic Soils:	O	(No specific grain size)
(4) Peat:	Pt	(No specific grain size)

Gradation Symbols	*Liquid Limit Symbols*
Well-graded, W	High LL, H
Poorly-graded, P	Low LL, L

The basic features of the USCS are shown in Table 2.7. Take a few minutes to look through the table and its footnotes, and you will notice a number of important characteristics about this system. First, as shown in Column (1), there are three major soil divisions: (1) *coarse-grained soils*, (2) *fine-grained soils*, and (3) *highly organic soils*. These are further subdivided into 15 basic soil groups [see Column (5)] and group names [Column (6)]. Note that the classification of a particular soil depends only on its grain-size distribution and Atterberg limits, and for a complete and unambiguous classification both the group name and group symbol [Column (5)] should be given.

Classification is performed on the material passing the 75 mm sieve. Larger particles are called *cobbles* (equivalent diameter 75 to 300 mm) and *boulders* (larger than 300 mm).

If more than 50% of the soil is coarser than the No. 200 sieve (or less than half passes the No. 200 or is finer than 0.075 mm), the soil is coarse grained. The coarse-grained soils are subdivided [Column (2)] into *gravels* (symbol G) and *sands* (symbol S). This is perhaps the trickiest part of the USCS—deciding whether a soil is a gravel or sand. One must examine the coarse fraction. Gravels are those soils having more than 50% of the coarse fraction (particles larger than 4.75 mm diameter) retained on the No. 4 sieve, while sands are those having 50% or more of the coarse fraction passing the No. 4 sieve. Beyond this level of classification, one needs to look at the percent passing the No. 200 sieve, and this is divided into three categories:

- *Less than 5%:* Determine the C_u [Eq. (2.35)] and C_c [Eq. (2.36)]. If the C_c is between 1 and 3, and the C_u is greater than 4 for gravel and 6 for sand, then the soil is well graded. The symbol would be either GW or SW. If the gradation requirements are not met, then the soil is poorly graded and the symbol would be GP or SP.

TABLE 2.7 Unified Soil Classification System

Criteria for Assigning Group Symbols and Group Names Using Laboratory Tests[a]				Soil Classification	
				Group Symbol	Group Name[b]
(1)	(2)	(3)	(4)	(5)	(6)
COARSE-GRAINED SOILS More than 50% retained on No. 200 sieve	GRAVELS More than 50% of coarse fraction retained on No. 4 sieve	CLEAN GRAVELS Less than 5% fines[c]	$C_u \geq 4$ and $1 \leq C_c \leq 3$	GW	Well-graded gravel[f]
			$C_u < 4$ and/or $1 > C_c > 3$	GP	Poorly graded gravel[f]
		GRAVELS WITH FINES More than 12% fines[c]	Fines classify as ML or MH	GM	Silty gravel[f,g,h]
			Fines classify as CL or CH	GC	Clayey gravel[f,g,h]
	SANDS 50% or more of coarse fraction passes No. 4 sieve	CLEAN SANDS Less than 5% fines[d]	$C_u \geq 6$ and $1 \leq C_c \leq 3$	SW	Well-graded sand[i]
			$C_u < 6$ and/or $1 > C_c > 3$	SP	Poorly graded sand[i]
		SANDS WITH FINES More than 12% fines[d]	Fines classify as ML or MH	SM	Silty sand[g,h,i]
			Fines classify as CL or CH	SC	Clayey sand[g,h,i]
FINE-GRAINED SOILS 50% or more passes No. 200 sieve	SILTS AND CLAYS Liquid limit less than 50	Inorganic	PI > 7 and plots on or above "A"-line[j]	CL	Lean clay[k,l,m]
			PI < 4 and plots below "A"-line[j]	ML	Silt[k,l,m]
		Organic	$\frac{LL_{oven\text{-}dried}}{LL_{natural}} < 0.75$	OL	Organic clay[k,l,m,n] Organic silt[k,l,m,o]
	SILTS AND CLAYS Liquid limit 50 or more	Inorganic	PI plots on or above "A"-line	CH	Fat clay[k,l,m]
			PI plots below "A"-line	MH	Elastic silt[k,l,m]
		Organic	$\frac{LL_{oven\text{-}dried}}{LL_{natural}} < 0.75$	OH	Organic clay[k,l,m,p] Organic silt[k,l,m,q]
Highly organic soils		Primarily organic matter, dark in color, having organic odor		Pt	Peat

[a]Based on the material passing the 3 in. (75 mm) sieve.
[b]If field sample contained cobbes and/or boulders, add "with cobbles and/or boulders" to group name.
[c]Gravels with 5% to 12% fines require dual symbols:
GW-GM well-graded gravel with silt.
GW-GC well-graded gravel with clay.
GP-GM poorly graded gravel with silt.
GP-GC poorly graded gravel with clay.
[d]Sands with 5% to 12% fines require dual symbols:
SW-SM well-graded sand with silt.
SW-SC well-graded sand with clay.
SP-SM poorly graded sand with silt.
SP-SC poorly graded sand with clay.
[e]$C_u = D_{60}/D_{10}$ [Eq. (2.35)];
$C_c = (D_{30})^2/D_{10} \times D_{60}$ [Eq. (2.36)].
[f]If soil contains ≥ 15% sand, add "with sand" to group name.
[g]If fines classify as CL-ML, use dual symbol GC-GM, SC-SM.
[h]If fines are organic, add "with organic fines" to group name.
[i]If soil contains ≥ 15% gravel, add "with gravel" to group name.
[j]If the liquid limit and plasticity index plot in the hatched area on plasticity chart, soil is a CL-ML, silty clay.
[k]If soil contains 15% to 19% plus No. 200, add "with sand" or "with gravel," whichever is predominant.
[l]If soil contains ≥ 30% plus No. 200, predominantly sand, add "sandy" to group name.
[m]If soil contains ≥ 30% plus No. 200, predominantly gravel, add "gravelly" to group name.
[n]PI ≥ 4 and plots on or above "A" line.
[o]PI < 4 or plots below "A" line.
[p]PI plots on or above "A" line.
[q]PI plots below "A" line.

After U.S. Dept. of the Interior (1990).

- *Between 5% and 12%:* Again, C_u and C_c need to be evaluated, but now there are sufficient fines to also run Atterberg limits on the minus No. 40 material. The soil is classified as either W or P based on the C_u and C_c, and the fines are classified using the plasticity chart (Fig. 2.13). A dual symbol is then assigned, with each part of the symbol starting with either G or S. These dual symbols are:

  GW-GC GP-GC
  GW-GM GP-GM
  SW-SC SP-SC
  SW-SM SP-SM

  Notice that the L and H from the plasticity chart don't make it into the classification, but they can be included in the verbal description of the soil.
- *Greater than 12%:* The Atterberg limits are performed on the minus No. 40 material, and the primary symbol is modified by C or M, as follows:

  GC, GM, SC, SM

In all of the cases cited above for coarse-grained soils, O can be substituted for C or M if the fines are determined to be primarily organic in nature.

The fine-grained soils, *silts and clays*, are those having 50% or more passing the No. 200 or 0.075 mm sieve, and they are classified according to their Atterberg limits and whether they contain a significant amount of organic matter. Based on Casagrande's plasticity chart (Fig. 2.13), a distinction is made between soils with LL less than or greater than 50 (symbols L and H), and between inorganic soils above or below the "A-line." The A-line generally separates clayey from silty soils (symbols C and M).[4]

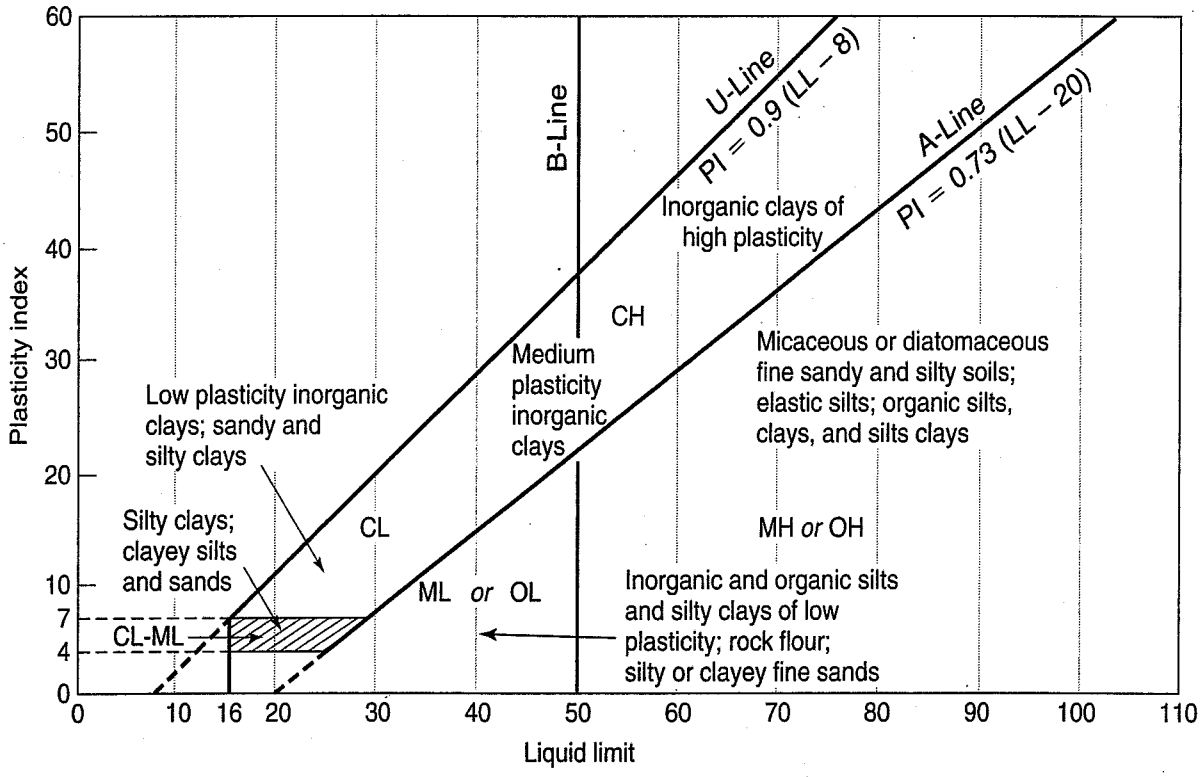

FIGURE 2.13 Several representative soil types shown on Casagrande's plasticity chart (developed from Casagrande, 1948, and Howard, 1984).

[4]The symbol M is from the Swedish terms *mo* (= very fine sand) and *mjäla* (= silt).

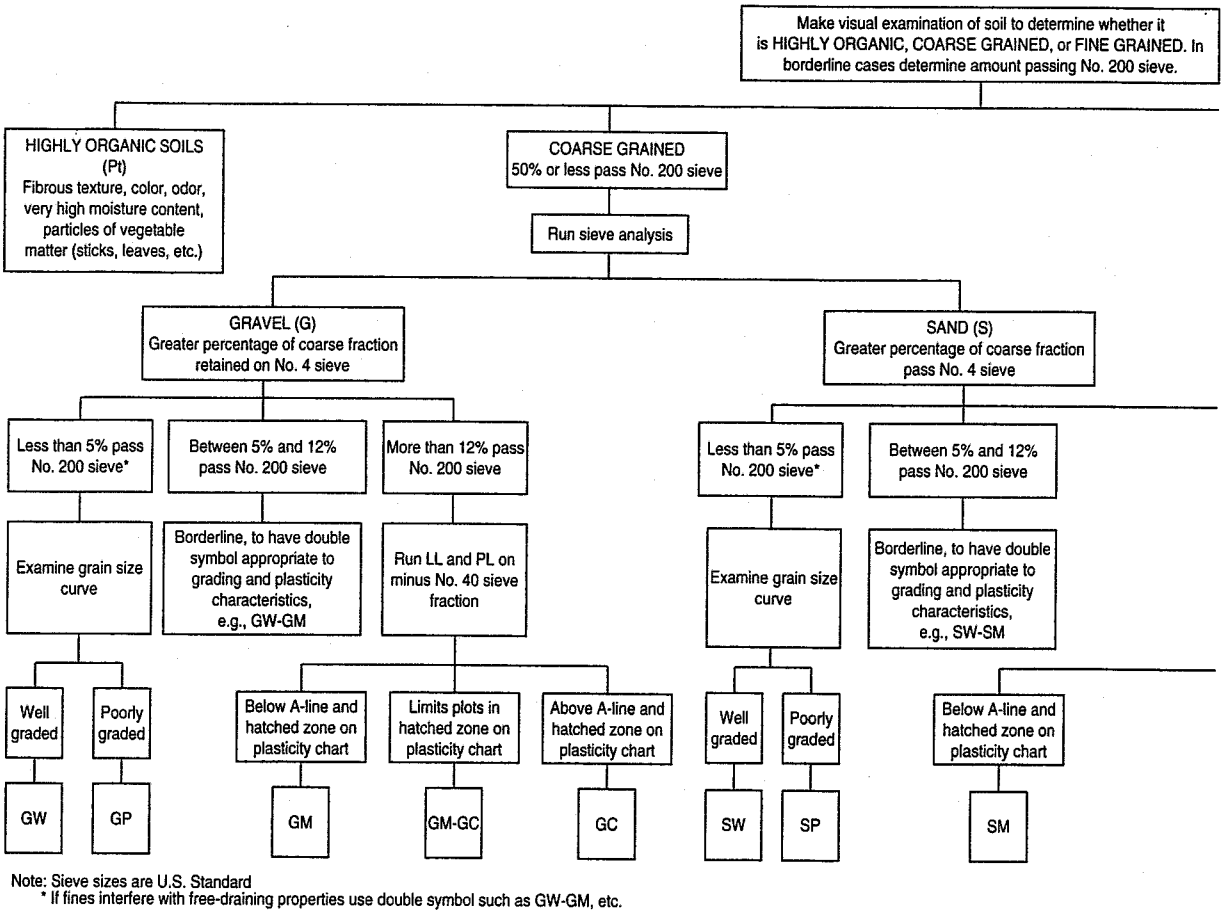

Note: Sieve sizes are U.S. Standard
* If fines interfere with free-draining properties use double symbol such as GW-GM, etc.

FIGURE 2.14 Auxiliary laboratory identification procedure (after USAEWES, 1960).

The U-line is an upper-limit line. Casagrande developed his chart by plotting Atterberg limit results from various soils from around the world, and he found that no soils plotted above this line (A. Casagrande, personal communication, 1966). If you plot results above this line, you've made either soil history or an error (you can figure the odds). Note that the U-line is vertical at LL = 16, because LL's below 16 are not very reliable, since the soil is sliding on the LL cup rather than flowing or shearing through the soil itself. Howard (1984) reports that of over 1000 LL tests performed by the USBR, only four had LL = 17, one had LL = 16, and none had LL below 16.

Silts and clays that contain sufficient organic matter to influence their properties are classified as *organic*. It has been found that the LL of organic clays and silts decreases after oven drying, so this is a simple indicator of the presence of significant organic matter. If the ratio of the oven-dried LL to the LL not dried is less than 0.75, then the soil is considered to be organic and has the symbols OL or OH.

The third major group is highly organic soils. These consist primarily of organic matter, are dark brown to black in color, and have an organic odor. They are given the group symbol Pt and the group name of *peat*. Peats are composed of vegetable matter and plant debris in various stages of decomposition, and thus they often have a fibrous to amorphous texture as well as the dark color and organic odor mentioned above. See ASTM standard D 4427 for a system for classifying peat.

Both the ASTM D 2487 and USBR 5000 procedures give flow charts for coarse-grained, fine-grained, and organic soils to help you conveniently assign the appropriate name and "group name" to a soil. In addition, we have always found the step-by-step procedure in Fig. 2.14 useful, because it shows a process of elimination of all the possibilities until only the correct classification remains. Figure 2.14 should always be used together with Table 2.7.

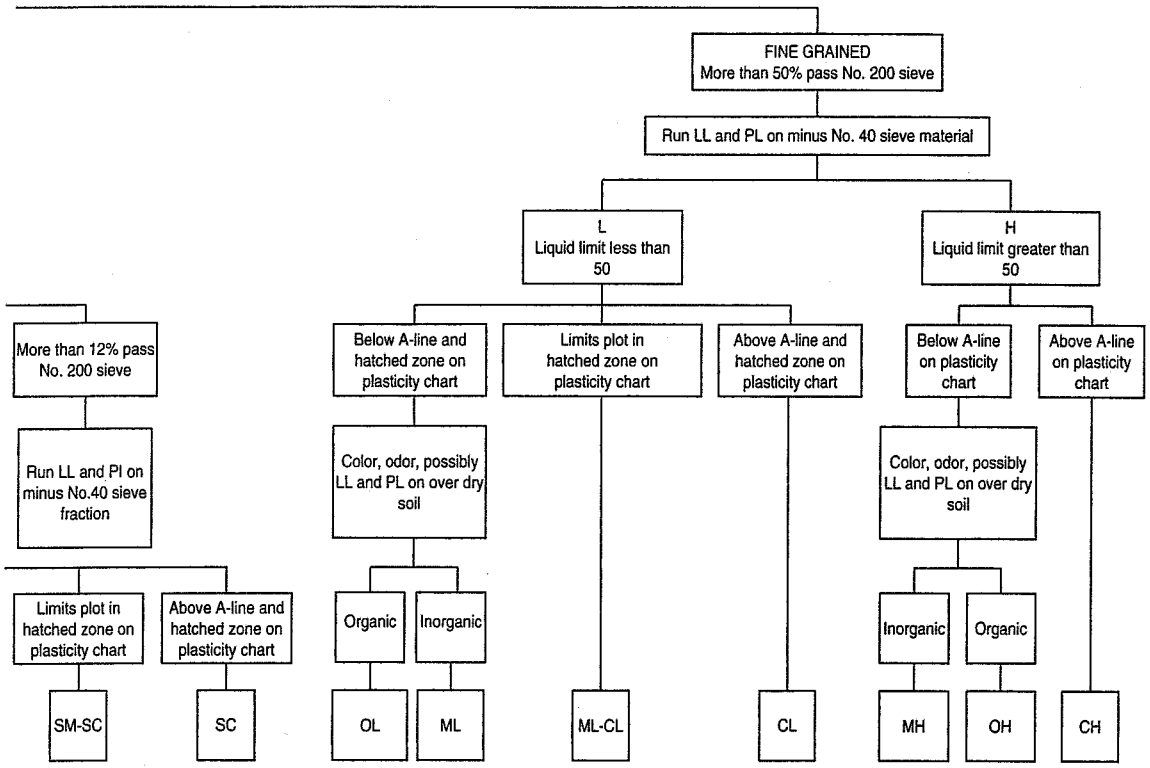

FIGURE 2.14 Continued.

Example 2.13

Given:

Sieve analysis and plasticity data for the following three soils.

Sieve Size	Soil 1, % Finer	Soil 2, % Finer	Soil 3, % Finer
No. 4	99	97	100
No. 10	92	90	100
No. 40	86	40	100
No. 100	78	8	99
No. 200	60	5	97
LL	20	—	124
PL	15	—	47
PI	5	NP[a]	77

[a]Nonplastic.

Required:

Classify the three soils according to the Unified Soil Classification System and provide a group name.

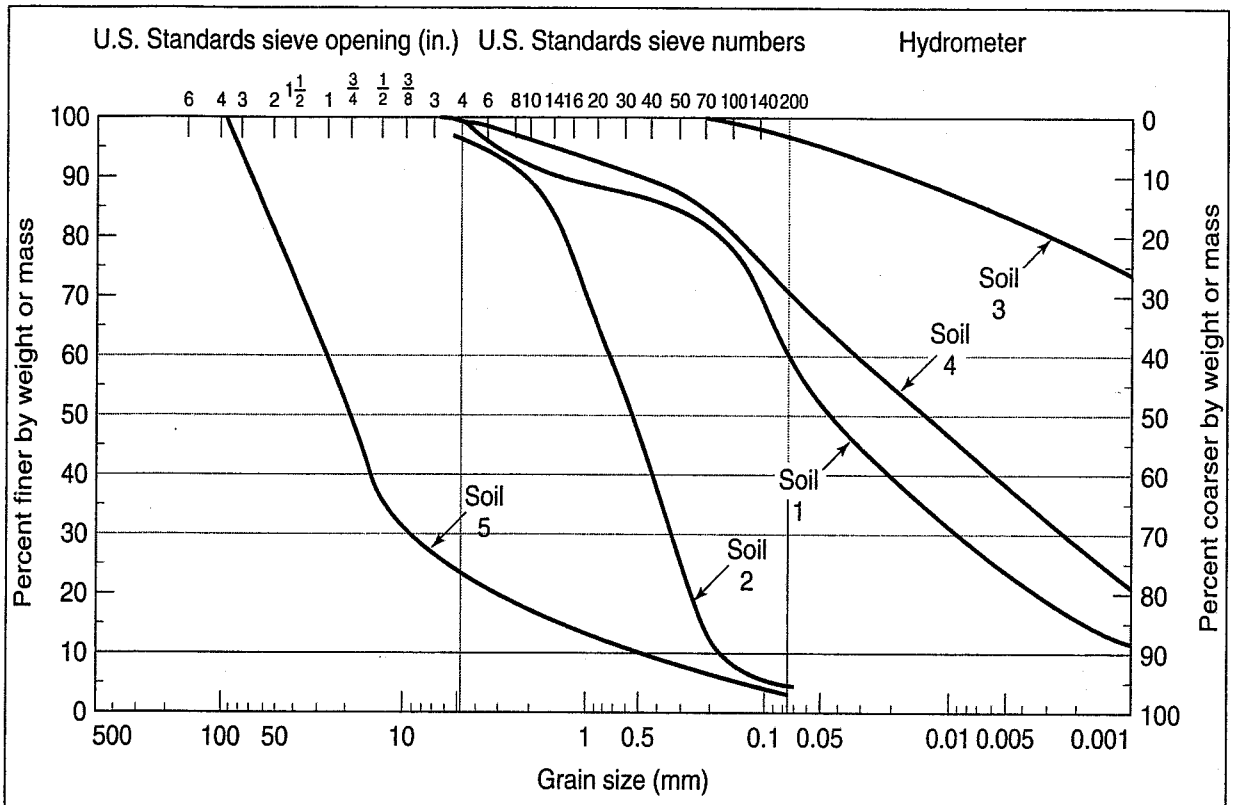

Sample No.	Elev. or depth	Classification	Nat w%	LL	PL	PI
1				20	15	5
2						NP
3				124	47	77
4				49	24	25
5						NP

Gradation Curves

Project Ex. 2.13

Area

Boring no.

Date

FIGURE Ex. 2.13

Solution: Use Table 2.7 and Fig. 2.14.

1. Plot the grain-size distribution curves for the three soils (shown in Fig. Ex. 2.13).
2. For soil 1, we see from the curve that more than 50% passes the No. 200 sieve (60%); thus the soil is fine grained and the Atterberg limits are required to further classify it. With LL = 20 and PI = 5, the soil plots in the hatched zone on the plasticity chart (Fig. 2.13), so it is a CL-ML. Continue now by using Table 2.7 to obtain the group name. With > 30% passing the No. 200 sieve, looking at the grain size curve, the % sand ≥ % gravel, and with < 15% gravel, footnote *l* in Table 2.7 indicates that "sandy" should be added, so that the soil's group name is "Sandy Silty Clay."
3. Soil 2 is immediately seen to be coarse grained, since only 5% passes the No. 200 sieve. Since 97% passes the No. 4 sieve, the soil is a sand rather than a gravel. Next, note the amount of material passing the No. 200 sieve (5%). From Fig. 2.14, the soil is "borderline" and therefore

has a dual symbol such as SP-SM or SW-SM, depending on the values of C_u and C_c. From the grain-size distribution curve, Fig. Ex. 2.13, we find that $D_{60} = 0.71$ mm, $D_{30} = 0.34$ mm, and $D_{10} = 0.18$ mm. The coefficient of uniformity C_u is

$$C_u = \frac{D_{60}}{D_{10}} = \frac{0.71}{0.18} = 3.9 < 6$$

and the coefficient of curvature C_c is

$$C_c = \frac{(D_{30})^2}{D_{10} \times D_{60}} = \frac{(0.34)^2}{0.18 \times 0.71} = 0.91$$

For a soil to be considered well graded, it must meet the criteria shown in Column (4) of Table 2.7; it does not, so the soil is considered poorly graded and its classification is SP-SM. (The soil is SM because the fines are nonplastic and probably silty.)

For the group name, from footnote *d* in Table 2.7, a soil with symbol SP-SM is "poorly graded sand with silt." [Because this soil is almost borderline with < 5% fines, one could also end up with a group name of poorly graded sand (SP). Even a small percentage of fines changes the engineering properties quite a bit.]

4. A quick glance at soil 3's characteristics indicates that it is fine grained (97% passes the No. 200 sieve). Since the LL is greater than 100, we cannot directly use the plasticity chart (Fig. 2.13). We use instead the equation for the A-line on Fig. 2.13 to determine whether the soil is a CH or MH.

$$\text{PI} = 0.73(\text{LL} - 20) = 0.73(124 - 20) = 75.9$$

Since the PI is 78 for soil 3, it lies *above* the A-line, and thus the soil is classified as a CH.

From Table 2.7, at the CH group symbol, with 97% passing, only 3% is retained on that sieve, and none of the footnotes *k*, *l*, or *m* apply, so the group name is "Fat Clay."

Commentary on this example and engineering practice: The only way—repeat, ONLY way—that the correct classification symbol, let alone group name, may be found is by having both the Atterberg limits AND the grain size analysis. Otherwise it is an educated *guess*—unless you have lots of experience with the visual-manual classification procedure.

2.9.1 Visual-Manual Classification of Soils

Although the letter symbols and group names in the USCS are convenient, they do not completely describe a soil or soil deposit. For this reason, descriptive terms should also be used for a complete soil classification. Burmister (1948) is credited with introducing the concept of systematically describing soils, and the U.S. Army Corps of Engineers (1960), Howard (1977), ASTM D 2488, various government agencies, and consulting firms have developed variations of basic descriptive categories. These are called *visual-manual* procedures because they use only observations and manual manipulation to describe and identify soils. No sieves or Atterberg limits are used—just your eyes and fingers.

Characteristics such as color, odor, moisture condition, and homogeneity of the deposit should be observed and included in the sample description. A typical set of soil colors includes the following: gray, brown, mottled yellow and brown, yellowish, reddish brown, gray brown, and other combinations of the basic colors. The word "mixed" is used if the material is fill comprised of various soil components from different sources. Odor is important, since it can be used to assess the presence of organics and contaminants; in fact, caution should be used when one is handling and "sniffing" soil that is believed

to be severely contaminated. The moisture condition description can be as simple as dry (dusty), moist (damp) or wet (free water).

For cohesionless, predominantly coarse-grained soils, such items as grain shape, mineralogical content, degree of weathering, in situ density, and the presence or absence of fines should be noted and included. Adjectives such as rounded, angular, and subangular are commonly used to describe grain shape (see Fig. 2.7). The in situ density is normally obtained using the standard penetration test or a cone penetrometer, but a cruder version of this test is to use a No. 4 ($^1/_2$-in. diameter) piece of reinforcing steel: very loose soil can be penetrated with the bar pushed by hand, while to penetrate very dense soil even a few millimetres may require a sledge hammer. Terms such as *very loose*, *loose*, *medium*, *dense*, and *very dense* are used to describe in situ density.

For fine-grained soils, consistency, remolded consistency, and some measure of plasticity should be noted in the sample description. *Consistency* in the natural state corresponds in some respects to the in situ density in coarse-grained soils, and is usually evaluated by noting the ease with which the deposit can be penetrated. Such terms as *very soft*, *soft*, *medium*, *stiff* (or *firm*), *very stiff*, and *hard* are employed to describe consistency. Table 2.8 describes four methods for field testing of soils, and their relationship to particular fine-grained soil types and plasticity.

You can probably see that the visual-manual classification of soils is much more subjective than USCS classification, which means that descriptive classification will be more dependent on the person doing it. Therefore, getting a consistent descriptive classification for a given soil requires considerable experience. However, the method mentioned above, as well as the tests described in Table 2.8, provide a starting point for this part of soil classification.

When we discussed texture of soils in Sec. 2.4 and at the beginning of this section, we suggested that you get some practice identifying soils according to texture and other characteristics. Excellent guides for doing this are given by ASTM (2010) standard D 2488 and U.S. Dept. of the Interior (1990) Procedure USBR 5005. Although they are similar to the USCS and use the same group names and symbols, these procedures rely only on visual examination and simple manual tests—and not on laboratory tests for grain size distribution and Atterberg limits—to describe and identify soils. They also have flow charts to help you get the correct group name and visual-manual classification. We encourage you to obtain a copy of one of these procedures and use it as a guide in learning to visually and manually classify different soils. The procedures are very simple, and with a little practice on a variety of soils, especially under the guidance of an experienced soil classifier, you can become quite good at it. (See Chapters 3 and 4 for rock classification.)

Table 2.9 is a checklist of the items that should be included in a visual-manual soil description. Of course, not all these items will be required for all soils; you just use those that are applicable for your particular soil sample. Also be sure to include all pertinent information on the origin or source of the sample, the project or job name and number, bore hole or test pit number, sample number, and any other appropriate identification marks and information.

Years ago, we prepared a set of ten samples of moist soils along with a small container of the same soils air dried. About 25 very experienced soils engineers were invited to classify the samples according to the Unified Soil Classification System and provide a name for each soil (without knowing the Atterberg limits or grain size). (This test occurred long before ASTM had group names in their standards.) There probably was about 400 years of total geotechnical experience in the room.

Each participant was given a clipboard and pencil and was free to poke, feel, and even taste (if they wanted) the soil in order to classify it. Everyone was under the gun, especially the more senior people. The result was entirely unanticipated. The average grade, as compared with the laboratory-determined USCS classification of these ten soils, was only 3 out of 10! Most of the engineers were consistently off (horizontal translation) regarding the "fineness" of a soil sample. They were calling silts, clays and sands, silts. In other words, they perceived the soils to be finer than they actually were. *Conclusion:* It takes practice and continual self-calibration to become an effective and accurate

TABLE 2.8 Field Identification Procedures for Fine-Grained Soils or Fractions[a]

Property Tested	Test Procedures and Results Interpretation
Dilatancy (reaction to shaking)	• Prepare a pat of moist soil with a volume of about 5 cm^3. • Add enough water to make the soil soft but not sticky. • Place the pat in the open palm of one hand and shake vigorously against the other hand several times. • A positive reaction consists of water appearing on the surface of the pat, which becomes filmy and glossy. Then, when the sample is squeezed between the fingers, the water and gloss disappear, the pat stiffens, and it finally cracks or crumbles. **Results Interpretation:** Very fine, clean sands give the quickest and most dramatic reaction, while a plastic clay gives no reaction. Inorganic silts show a moderately quick reaction.
Dry Strength (crushing properties)	• Mold a pat of soil to the consistency of putty, adding water if necessary. • Allow the pat to dry completely by oven, sun, or air, then test its strength by breaking and crumbling between the fingers. • The dry strength increases with increasing plasticity. **Results Interpretation:** High dry strength is characteristic of a CH clay. A typical inorganic silt has only very slight dry strength. Silty fine sands and silts have about the same dry strength, but the fine sand feels gritty after breaking, while a typical silt feels smoother and more like flour.
Toughness (consistency near the plastic limit)	• Mold a specimen of soil about the size of a 12 mm cube (like a sugar cube) to the consistency of putty, adding water or slightly drying if necessary. • Roll out the specimen by hand on a smooth surface or between the palms into a thread about 3 mm in diameter. Fold and refold the thread repeatedly—moisture is lost; the specimen stiffens, finally loses it plasticity, and crumbles when the plastic limit is reached. • After the thread crumbles, the pieces should be lumped together and a slight kneading action continued until the lump crumbles. • The tougher the thread near the plastic limit and the stiffer the lump when it finally crumbles, the more potent the clay fraction in the soil. **Results Interpretation:** Weakness of the thread at the plastic limit and quick loss of coherence of the lump below the plastic limit indicate either inorganic clay of low plasticity or materials such as kaolin-type clays and organic clays that occur below the A-line. High-organic clays have a very weak and spongy feel at the plastic limit.
Plasticity (estimate of natural plasticity)	• Mold a specimen of soil at its natural water content into a lump. • Roll out the specimen by hand on a smooth surface or between the palms into the smallest thread possible without causing excessive cracking or crumbling. • The smaller the thread that can be rolled out, the more plastic the soil. **Results Interpretation:**

Degree of plasticity	Soil type	Smallest Diameter of Thread
Nonplastic	SILT	None
Slight	Clayey SILT	6 mm
Low	SILT and CLAY	3 mm
Medium	CLAY and SILT	1.6 mm
High	Silty CLAY	0.8 mm
Very High	CLAY	0.4 mm

Note: Soil type in caps is the predominant soil type.

[a]All tests are for soil or soil fractions minus No. 40 sieve size.

After U.S. Army Engineer Waterways Experiment Station (1960), Howard (1977), and von Rosenvinge (2006).

TABLE 2.9 Checklist for Description of Soils (U.S. Dept. of the Interior, 1990)

1. Group name
2. Group symbol
3. Percent of cobbles and/or boulders (by volume)
4. Percent of gravel, sand and/or fines (by dry mass)
5. Particle-size range: Gravel—fine, coarse; Sand—fine, medium, coarse
6. Particle angularity: angular, subangular, subrounded, rounded
7. Particle shape (if appropriate): flat, elongated, flat and elongated
8. Maximum particle size or dimension
9. Hardness of coarse sand and larger particles
10. Plasticity of fines: nonplastic, low, medium, high
11. Dry strength: none, low, medium, high, very high
12. Dilatancy: none, slow, rapid
13. Toughness: low, medium, high
14. Color (in moist condition)
15. Odor (mention only if organic or unusual)
16. Moisture: dry, moist, wet
17. Reaction with HCl: none, weak, strong

For intact samples:

18. Consistency (fine-grained soils only): very soft, soft, firm, hard, very hard
19. Structure: stratified, laminated, fissured, slickensided, lensed, homogeneous
20. Cementation: weak, moderate, strong
21. Local name
22. Geologic interpretation

Additional comments:

Presence of roots or root holes
Presence of mica, gypsum, etc.
Surface coatings on coarse-grained particles
Caving or sloughing of auger hole or trench sides
Difficulty in auguring or excavation

classifier. Follow ASTM D 2488 and USBR 5005 and get some experience! And calibrate yourself frequently with a variety of soils with known Atterberg limits and grain size curves.

2.9.2 What Else Can We Get from the LL-PI Chart?

Besides being useful for the classification of fine-grained soils (e.g., Fig. 2.13), we can get several other things from Casagrande's LL-PI chart. For example, representative fine-grained soil types are shown in Fig. 2.15. These names also should correlate with the group names in Column (6) of Table 2.7. Figure 2.16 from Casagrande (1948) shows the Atterberg limits for a number of typical soils from around the world, while the inset at the upper left of the figure shows data primarily from the United States.

You can see from these figures that several different soil types tend to plot in approximately the same area on the LL-PI chart, which means that they tend to have about the *same engineering behavior*. This is basically why the Casagrande chart is so useful in the engineering classification of soils. For example, Casagrande (1948) observed the behavior of soils at the same liquid limit with plasticity index increasing, as compared with their behavior at the same plasticity index but with increasing liquid limit. The results are shown in Table 2.10.

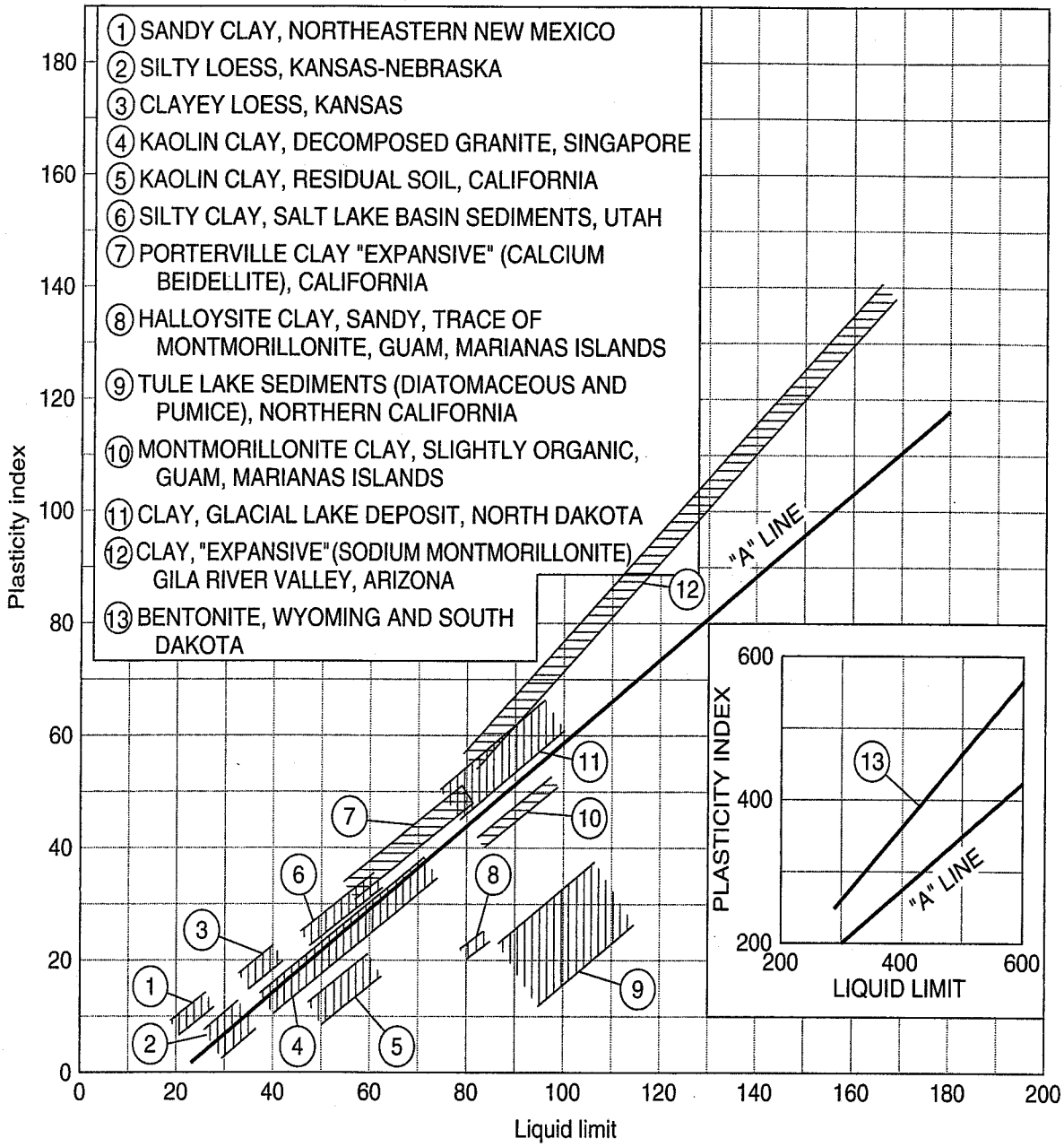

FIGURE 2.15 Relation between the liquid limit (LL) and the plasticity index (PI) for various soils (U.S. Dept. of the Interior, 1990).

TABLE 2.10 Relation Between Position on the LL-PI Chart and Physical Properties

Characteristic	Soils at Equal LL with Increasing PI	Soils at Equal PI with Increasing LL
Dry strength	Increases	Decreases
Toughness near PL	Increases	Decreases
Permeability	Decreases	Increases
Compressibility	About the same	Increases
Rate of volume change	Decreases	—

After Casagrande (1948).

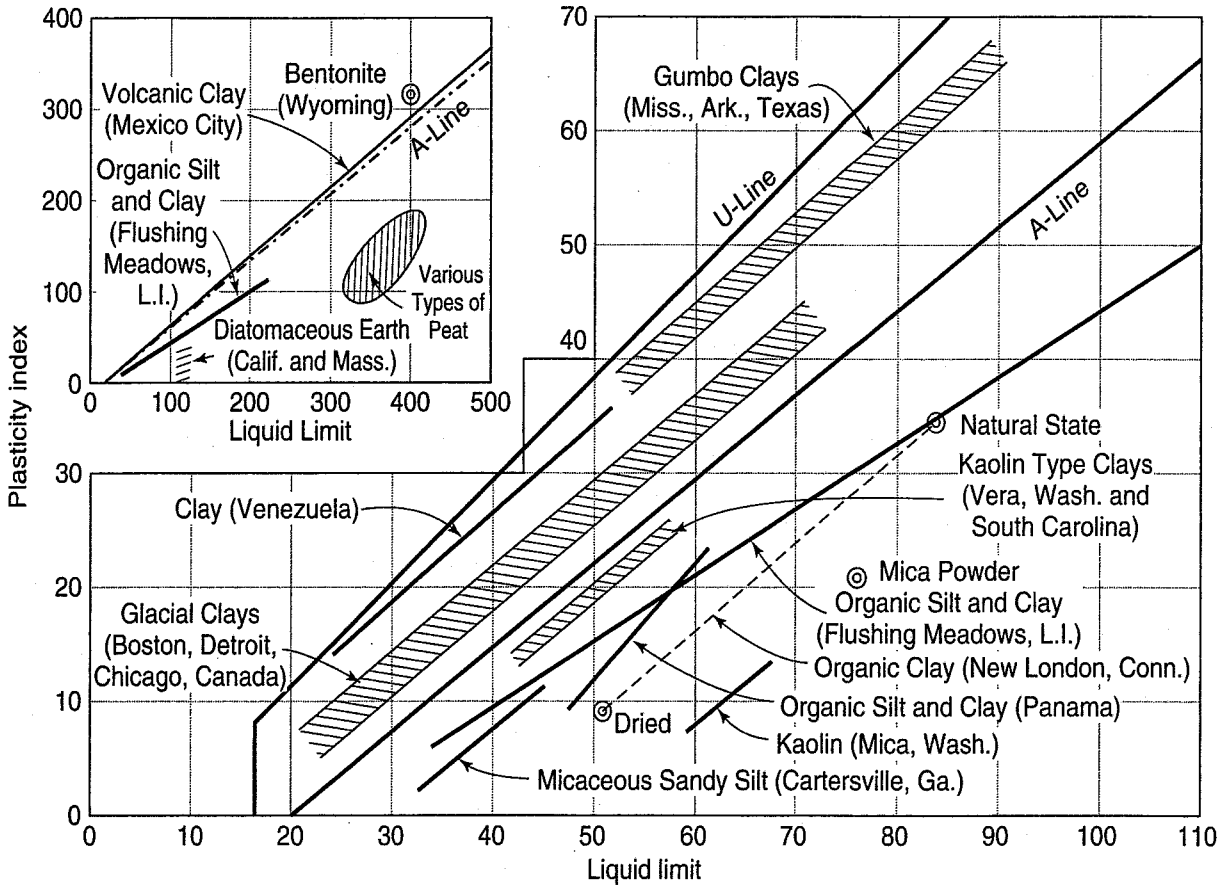

FIGURE 2.16 Relationship between liquid limit and plasticity index for typical soils (Casagrande, 1948).

Toughness near the PL and dry strength are very useful visual classification properties, as shown in the preceding section (see Table 2.8). The other three characteristics are engineering properties, and they are discussed in great detail later in this book. For now, just rely on your general knowledge and ingenuity to figure out what those three words mean.

We shall see in Chapter 4 that Casagrande's plasticity chart can be used to identify qualitatively the predominant clay minerals in a soil (Fig. 4.14), along with correlation with the *activity*.

2.9.3 Limitations of the USCS

As noted by Galster (1999), the USCS does have some limitations. For one thing, it does not consider the geologic origin or source of the materials being classified. As will be noted in Chapter 3, the nature of the soils and their engineering properties are often strongly influenced by their geologic origin. Thus, when you are classifying a soil deposit, it would be prudent to mention the geologic origin of the materials you are working with, in addition to the USCS group name and symbol. (This is item 22 in Table 2.9.)

Another difficulty with the USCS is that it says very little about materials larger than gravels, such as cobbles and boulders. Furthermore, the angularity of cobbles and boulders is not mentioned, although, as we will later see, particle shape strongly influences the strength of granular materials.

Although the USCS is meant for classifying naturally occurring mineral and organo-mineral soils, Howard (1984) mentions that it is often used to classify materials such as shale, siltstone, claystone, sandstone, crushed rock, slag, cinders, and shells, which do not occur naturally as soils. If these materials are crushed or otherwise broken down by construction activity, it is still OK to classify them as soils according to the USCS (see ASTM D 2488 and USBR 5005). However, be sure to indicate that the materials did not naturally occur in this state.

2.10 AASHTO SOIL CLASSIFICATION SYSTEM

In the late 1920s the U.S. Bureau of Public Roads (now the Federal Highway Administration, FHWA) conducted extensive research on the use of soils in local or secondary road construction, the so-called "farm-to-market" roads. That research led to the development of the Public Roads Classification System (Hogentogler and Terzaghi, 1929), based on the stability characteristics of soils used as a road surface or with only a thin tar or asphalt pavement. The PR system was modified several times for subgrades under thicker pavements. The latest revision was in 1942, and this is essentially the present AASHTO (2004) system. Its details are given in AASHTO Designation M 145 and ASTM (2010) standard D 3282. Although AASHTO states that the system "should be useful in determining the relative quality of the soil material for use in embankments, subgrades, subbases, and bases," you should keep in mind its original purpose. (See Casagrande, 1948, for some comments on this point.)

The AASHTO system classifies soils into seven groups, A-1 through A-7, and it includes several subgroups. Soils within each group are evaluated according to the *group index*, which is calculated by an empirical formula. The only tests required are the sieve analysis and the Atterberg limits.

There are several significant differences between the USCS and AASHTO soil classification systems, which is not surprising, considering the differences in their history and purpose. Al-Hussaini (1977) and Liu (1970) compare the two systems in terms of the probable corresponding soil groups.

PROBLEMS

Phase relationships

2.1 From memory, draw a phase diagram (like Fig. 2.2, but *don't* look first!). The "phases" have a Volume side and Mass side. Label all the parts.

2.2 From memory, write out the definitions for water content, void ratio, dry density, wet or moist density, and saturated density. If you just look them up and copy them, you will satisfy the moral obligation to do the homework but you will not *learn* them.

2.3 Assuming a value of $\rho_s = 2.7$ Mg/m^3, take the range of saturated density in Table 2.1 for the six soil types and calculate/estimate the range in void ratios that one might expect for these soils. Doing so will give you an idea of what to expect in the future. Remember this range. Matlab or a spreadsheet would be nice!

2.4 Prepare a spreadsheet plot of dry density in Mg/m^3 as the ordinate versus water content in percent as the abscissa. Assume $\rho_s = 2.65$ Mg/m^3 and vary the degree of saturation, S, from 100% to 40% in 10% increments. A maximum of 50% water content should be adequate (except for very soft clays, to be defined shortly). [*Note:* Such a graph is very useful to check problems that you do in this chapter, as there is a unique relationship between dry density, water content, and the degree of saturation for any given density of solids. Void ratio, wet density, and so on are then readily computed. Similar graphs for density of other solids may be easily computed and plotted.] Show all your equations as comments on your sheet for future reference.

2.5 Prepare a graph like that in Problem 2.4, only use dry density units of kN/m^3 and pounds per cubic feet.

2.6 Prepare a graph like that in Problem 2.4, only for $S = 100\%$, and vary the density of solids from 2.60 to 2.80 Mg/m^3. You decide the size of the increments you need to "satisfactorily" evaluate the relationship as ρ_s varies. Prepare a concluding statement of your observations.

2.7 The dry density of a compacted sand is 1.87 Mg/m^3 and the density of the solids is 2.67 Mg/m^3. What is the water content of the material when saturated? Phase diagram!

2.8 A soil that is completely saturated has a total density of 2045 kg/m^3 and a water content of 24%. What is the density of the solids? What is the dry density of the soil? Phase diagram!

2.9 What is the water content of a fully saturated soil with a dry density of 1.72 Mg/m^3? Assume $\rho_s = 2.72$ Mg/m^3.

2.10 A dry quartz sand has a density of 1.68 Mg/m^3. Determine its density when the degree of saturation is 75%. The density of solids for quartz is 2.65 Mg/m^3.

2.11 The dry density of a soil is 1.60 Mg/m^3 and the solids have a density of 2.65 Mg/m^3. Assuming the soil is saturated, find (a) water content, (b) void ratio, and (c) total density.

2.12 A natural deposit of soil is found to have a water content of 20% and to be 90% saturated. What is the void ratio of this soil?

2.13 A chunk of soil has a wet weight of 62 lb and a volume of 0.56 ft^3. When dried in an oven, the soil weighs 50 lb. If the specific gravity of solids $G_s = 2.64$, determine the water content, wet unit weight, dry unit weight, and void ratio of the soil.

2.14 In the lab, a container of saturated soil had a mass of 113.27 g before it was placed in the oven and 100.06 g after the soil had dried. The container alone had a mass of 49.31 g. The specific gravity of solids is 2.80. Determine the void ratio and water content of the original soil sample.

2.15 The natural water content of a sample taken from a soil deposit was found to be 12.0%. It has been calculated that the maximum density for the soil will be obtained when the water content reaches 22.0%. Compute how many grams of water must be added to each 1000 g of soil (in its natural state) in order to increase the water content to 22.0%.

2.16 A cubic meter of dry quartz sand ($G_s = 2.65$) with a porosity of 60% is immersed in an oil bath having a density of 0.92 g/cm^3. If the sand contains 0.27 m^3 of entrapped air, how much force is required to prevent it from sinking? Assume that a weightless, permeable membrane surrounds the specimen. (Prof. C. C. Ladd.)

2.17 A soil sample taken from a borrow pit has a natural void ratio of 1.15. The soil will be used for a highway project where a total of 100,000 m^3 of soil is needed in its compacted state; its compacted void ratio is 0.73. How much volume has to be excavated from the borrow pit to meet the job requirements?

2.18 A sample of moist soil was found to have the following characteristics:

Total volume: 0.01456 m^3
Total mass: 25.74 kg
Mass after oven drying: 22.10 kg
Specific gravity of solids: 2.69

Find the density, unit weight, void ratio, porosity, and degree of saturation for the moist soil.

2.19 A gray silty clay (CL) is sampled from a depth of 12.5 feet. The "moist" soil was extruded from a 6-inch-high brass liner with an inside diameter of 2.83 inches and weighed 777 grams.

(a) Calculate the wet unit weight in pounds per cubic feet.
(b) A small chunk of the original sample had a wet weight of 140.9 grams and weighed 85.2 grams after drying. Compute the water content, using the correct number of significant figures.
(c) Compute the dry density in Mg/m^3 and the dry unit weight in kN/m^3.

2.20 A cylindrical soil specimen is tested in the laboratory. The following properties were obtained:

Sample diameter	3 inches
Sample length	6 inches
Wt. before drying in oven	2.95 lb
Wt. after drying in oven	2.54 lb
Oven temperature	110°C
Drying time	24 hours
Specific gravity of solids	2.65

What is the degree of saturation of this specimen?

2.21 A sample of saturated silt is 10 cm in diameter and 2.5 cm thick. Its void ratio in this state is 1.35, and the specific gravity of solids is 2.70. The sample is compressed to a 2-cm thickness without a change in diameter.

(a) Find the density of the silt sample, in g/cm^3, prior to being compressed.
(b) Find the void ratio after compression and the change in water content that occurred from initial to final state.

2.22 A sample of sand has the following properties: total mass $M_t = 160$ g; total volume $V_t = 80$ cm^3; water content $w = 20\%$; specific gravity of solids $G_s = 2.70$. How much would the sample volume have to change to get 100% saturation, assuming the sample mass M_t stayed the same?

2.23 Draw a phase diagram and begin to fill in the blanks: A soil specimen has total volume of 80,000 mm^3 and weighs 145 g. The dry weight of the specimen is 128 g, and the density of the soil solids is 2.68 Mg/m^3. Find the (a) water content, (b) void ratio, (c) porosity, (d) degree of saturation, (e) wet density, and (f) dry density. Give the answers to parts (e) and (f) in both SI and British engineering units.

2.24 A sample of soil plus container weighs 397.6 g when the initial water content is 6.3%. The container weighs 258.7 g. How much water needs to be added to the original specimen if the water content is to be increased by 3.4%? (After U.S. Dept. of Interior, 1990.)

2.25 A water-content test was made on a sample of clayey silt. The weight of the wet soil plus container was 18.46 g, and the weight of the dry soil plus container was 15.03 g. Weight of the empty container was 7.63 g. Calculate the water content of the sample.

2.26 A soil sample is dried in a microwave oven to determine its water content. From the data below, evaluate the water content and draw conclusions. The oven-dried water content is 23.7%. The mass of the dish is 146.30 grams. (After U.S. Dept. of Interior, 1990.)

Time in Oven, min	Total Oven Time, min	Mass of Soil + Dish, grams
0	0	231.62
3	3	217.75
1	4[a]	216.22
1	5	215.72
1	6	215.48
1	7	215.32
1	8	215.22
1	9	215.19
1	10	215.19

[a]This total time of 4 minutes is from 3 minutes before and one more minute, giving a mass of soil + dish = 216.22 grams, and so on.

2.27 The mass of a sample of silty clay soil plus container is 18.43 g and the weight of the dry soil plus container is 13.67 g. The container weighs 8.84 g. Compute the water content of the sample.

2.28 A specimen of fully saturated clay soil that weighs 1389 g in its natural state weighs 982 g after drying. What is the natural water content of the soil?

2.29 The volume of water in a sample of saturated soil is 0.24 m^3. The volume of solids V_s is 0.25 m^3. Given that the density of soil solids ρ_s is 2600 kg/m^3, find the water content.

2.30 For the soil sample of Problem 2.29, compute (a) the void ratio and (b) the porosity.

2.31 For the soil sample of Problem 2.29, compute (a) the total or wet density and (b) the dry density. Give your answers in Mg/m^3, kg/m^3, and lbf/ft^3.

2.32 A 592-cm^3 volume of moist sand weighs 1090 g. Its dry weight is 920 g and the density of solids is 2680 kg/m^3. Compute the void ratio, porosity, water content, degree of saturation, and total density in kg/m^3.

2.33 The saturated density γ_{sat} of a soil is 137 lbf/ft^3. Find the buoyant density of this soil in both lbf/ft^3 and kg/m^3.

2.34 A sand is composed of solid constituents having a density of 2.68 Mg/m^3. The void ratio is 0.58. Compute the density of the sand when dry and when saturated and compare it with the density when submerged.

2.35 A sample of natural glacial till was taken from below the groundwater table. The water content was found to be 52%. Estimate the wet density, dry density, buoyant density, porosity, and void ratio. Clearly state any necessary assumptions.

2.36 A 1-m^3 sample of moist soil weighs 2000 kg. The water content is 10%. Assume ρ_s is 2.70 Mg/m^3. With this information, fill in all blanks in the phase diagram of Fig. P2.36.

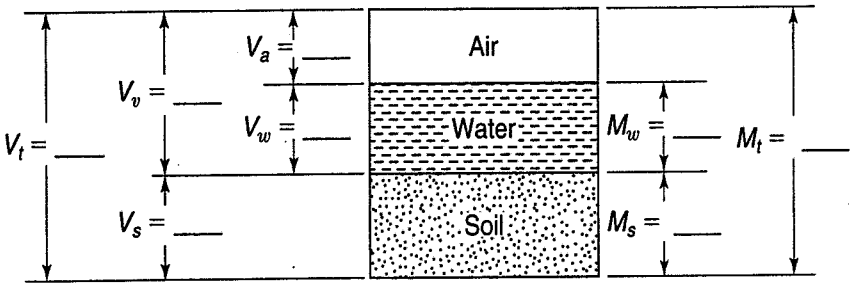

FIGURE P2.36

2.37 For the information given in Problem 2.36, calculate (a) the void ratio, (b) the porosity, and (c) the dry density.

2.38 The void ratio of clay soil is 0.6 and the degree of saturation is 75%. Assuming the density of the solids is 2710 kg/m^3, compute (a) the water content and (b) dry and wet densities in both SI and British thermal units.

2.39 A specimen of saturated glacial clay has a water content of 38%. On the assumption that $\rho_s = 2.70$ Mg/m^3, compute the void ratio, porosity, and saturated density.

2.40 The values of minimum e and maximum e for a pure silica sand were found to be 0.50 and 0.70, respectively. What is the corresponding range in the saturated density in kg/m^3?

2.41 Calculate the maximum possible porosity and void ratio for a collection of (a) tennis balls (assume they are 64.14 mm in diameter) and (b) tiny ball bearings 0.3 mm in diameter.

2.42 A plastic-limit test has the following results:

Wet weight + container	= 23.12 g
Dry weight + container	= 20.84 g
Container weight	= 1.46 g

Compute the PL of the soil. Can the plastic limit be evaluated by a one-point method?

2.43 During a plastic-limit test, the following data was obtained for one of the samples:

Wet weight + container	= 23.13 g
Dry weight + container	= 19.12 g
Weight of container	= 1.50 g

What is the PL of the soil?

2.44 The degree of saturation of a cohesive soil is 100%. The clay when wet weighs 1489 g and after drying weighs only 876 g. Find the water content of the soil. Draw a phase diagram and properly label it.

2.45 For the soil in the previous problem, compute the void ratio and the porosity. Does your answer compare with what you would expect for a saturated cohesive soil?

2.46 For the soil in the previous two problems, compute (a) the total or wet density and (b) the dry density. Provide your answers in units of Mg/m^3, kN/m^3, and lbf/ft^3.

2.47 A soil specimen had a buoyant density of 73 pounds per cubic foot. Calculate its wet density in kg/m^3.

2.48 Verify from first principles that:

(a) $\rho = \rho_s\left(\dfrac{1+w}{1+e}\right) = \dfrac{\rho_s + \rho_w Se}{1+e}$

(b) $\rho = \rho_d(1+w)$

(c) $w\dfrac{\rho_s}{\rho_w} = Se$

(d) $e = \dfrac{n}{1-n}$

(e) $n = \dfrac{e}{1+e}$

2.49 Derive an expression for ρ_s in terms of the porosity n and the water content w for (a) a fully saturated soil and (b) a partially saturated soil.

2.50 Derive an expression for (a) dry density, (b) void ratio, and (c) degree of saturation in terms of ρ, ρ_s, ρ_w, and w.

2.51 Develop a formula for (a) the wet density and (b) the buoyant density in terms of the water content, the density of the soil solids, and the density of water.

2.52 From Archimedes' principle show that Eq. (2.11), $\rho' = \rho_{sat} - \rho_w$, is the same as $(\rho_s - \rho_w)/(1+e)$.

2.53 The "chunk density" method is often used to determine the unit weight (and other necessary information) of a specimen of irregular shape, especially of friable samples. The specimen at its natural water content is (1) weighed, (2) painted with a thin coat of wax or paraffin (to prevent water from entering the pores), (3) weighed again ($W_t + W_{wax}$), and (4) weighed in water (to get the volume of the sample + wax coating—remember Archimedes?). Finally, the natural water content of the specimen is determined. A specimen of cemented silty sand is treated in this way to obtain the "chunk density." From the information given below, determine the (a) wet density, (b) dry density, (c) void ratio, and (d) degree of saturation of the sample.

Given:

Weight of specimen at natural water content in air	= 181.8 g
Weight of specimen + wax coating in air	= 215.9
Weight of specimen + wax in water	= 58.9
Natural water content	= 2.5%
Soil solid density, ρ_s	= 2650 kg/m^3
Wax solid density, ρ_{wax}	= 940 kg/m^3

Phase diagram!!

2.54 A sensitive volcanic clay soil was tested in the laboratory and found to have the following properties:

(a) ρ = 1.28 Mg/m^3
(b) e = 9.0
(c) S = 95%
(d) ρ_s = 2.75 Mg/m^3
(e) w = 311%

In rechecking the above values, one was found to be inconsistent with the rest. Find the inconsistent value and report it correctly. Show all your computations and phase diagrams.

2.55 A cylinder contains 510 cm^3 of loose dry sand which weighs 740 g. Under a static load of 200 kPa the volume is reduced 1%, and then by vibration it is reduced 10% of the original volume. Assume the solid density of the sand grains is 2.65 Mg/m^3. Compute the void ratio, porosity, dry density, and total density corresponding to each of the following cases:

(a) Loose sand.
(b) Sand under static load.
(c) Vibrated and loaded sand.

Soil Classification

2.56 On five-cycle semilogarithmic paper, plot the grain-size distribution curves from the following mechanical analysis data on six soils, A through F. For each soil determine the effective size as well as the uniformity coefficient and the coefficient of curvature. Determine also the percentages of gravel, sand silt, and clay according to (a) ASTM, (b) AASHTO, (c) USCS, and (d) the British Standard.

U.S. Standard Sieve No. or Particle Size	Percent Passing by Weight					
	Soil A	Soil B	Soil C	Soil D	Soil E	Soil F
75 mm (3 in.)	100		100			
38 (1-1/2)	70		–			
19 (3/4)	49	100	91			
9.5 (3/8)	36	–	87			
No. 4	27	88	81		100	
No. 10	20	82	70	100	89	
No. 20	–	80	–	99	–	
No. 40	8	78	49	91	63	
No. 60	–	74	–	37	–	
No. 100	5	–	–	9	–	
No. 140	–	65	35	4	60	
No. 200	4	55	32	–	57	100
40 μm	3	31	27		41	99
20 μm	2	19	22		35	92
10 μm	1	13	18		20	82
5 μm	< 1	10	14		8	71
2 μm	–	–	11		–	52
1 μm	–	2	10		–	39

Note: Missing data is indicated by a dash in the column.

2.57 **(a)** Explain briefly why it is preferable, in plotting GSD curves, to plot the grain diameter on a logarithmic rather than an arithmetic scale.

(b) Are the shapes of GSD curves comparable (for example, do they have the same C_u and C_c) when plotted arithmetically? Explain.

2.58 The soils in Problem 2.56 have the following Atterberg limits and natural water contents. Determine the PI and LI for each soil and comment on their general activity.

Property	Soil A	Soil B	Soil C	Soil D	Soil E	Soil F
w_n, %	27	14	14	11	8	72
LL	13	35	35	–	28	60
PL	8	29	18	NP	NP	28

2.59 Comment on the validity of the results of Atterberg limits on soils G and H.

	Soil G	Soil H
LL	55	38
PL	20	42
SL	25	–

2.60 The following data were obtained from a liquid-limit test on a silty clay.

No. of Blows	Water Content, %
35	41.1
29	41.8
21	43.5
15	44.9

Two plastic-limit determinations had water contents of 23.1% and 23.6%. Determine the LL, PI, the flow index, and the toughness index. The flow index is the slope of the water content versus log of number of blows in the liquid-limit test, and the toughness index is the PI divided by the flow index.

2.61 Classify the following soils according to the USCS:

(a) A sample of well-graded gravel with sand has 73% fine to coarse subangular gravel, 25% fine to coarse subangular sand, and 2% fines. The maximum size of the particles is 75 mm. The coefficient of curvature is 2.7, while the uniformity coefficient is 12.4.

(b) A dark brown, wet, organic-odor soil has 100% passing the No. 200 sieve. The liquid limit is 32% (not dried, and is 21% when oven dried!) and the plastic index is 21% (not dried).

(c) This sand has 61% predominately fine sand, 23% silty fines, and 16% fine subrounded gravel size. The maximum size is 20 mm. The liquid limit is 33% and the plastic limit is 27%.

(d) This material has 74% fine to coarse subangular reddish sand and 26% organic and silty dark brown fines. The liquid limit (not dried) is 37% while it is 26% when oven dried. The plastic index (not dried) is 6.

(e) Although this soil has only 6% nonplastic silty fines, it has everything else! It has gravel content of 78% fine to coarse subrounded to subangular gravel, and 16% fine to coarse subrounded to subangular sand. The maximum size of the subrounded boulders is 500 mm. The uniformity coefficient is 40, while the coefficient of curvature is only 0.8. (After U.S. Dept. of the Interior, 1990.)

2.62 You know what is coming. Classify the five soils in the preceding question according to the AASHTO method of soil classification. You can find procedures for doing this in the references given in Section 2.10 or on the Web.

2.63 The results of a sieve test below give the percentage passing through the sieve.

(a) Using a spreadsheet, plot the particle-size distribution.

(b) Calculate the uniformity coefficient.

(c) Calculate the coefficient of curvature.

Sieve	Percent Finer by Weight
1/2"	71
No. 4	37
No. 10	32
No. 20	23
No. 40	11
No. 60	7
No. 100	4

2.64 For the data given below, classify the soils according to the USCS. For each soil, give both the letter symbol and the narrative description.

(a) 65% material retained on No. 4 sieve, 32% retained on No. 200 sieve. $C_u = 3$, $C_c = 1$.

(b) 100% material passed No. 4 sieve, 90% passed No. 200 sieve. LL = 23, PL = 17.

(c) 70% material retained on No. 4 sieve, 27% retained on No. 200 sieve. $C_u = 5$, $C_c = 1.5$.

2.65 A sample of soil was tested in the laboratory and the following grain-size analysis results were obtained.

Sieve No.	Sieve Opening (mm)	Percent Coarser by Weight
4	4.75	36
10	2.00	52
20	0.85	64
40	0.425	69
60	0.25	71
100	0.15	77
200	0.075	91
Pan	—	100

LL = 26, PL = 23, 30% is coarser than the 1/2-inch sieve. Classify this soil according to the USCS, providing the group symbol for it.

2.66 A minus No. 40 material had a liquidity index of 0.73, a natural water content of 44.5%, and a plasticity index of 24.7. Classify this soil according to the USCS, providing the group symbol for it. You do *not* need to graph this data; use linear interpolation if you need specific values not given.

2.67 A sample of soil was tested in the laboratory and the following grain-size analysis results were obtained:

Sieve No.	Sieve Opening (mm)	Percent Coarser by Weight
4	4.75	37
10	2.00	52
20	0.85	64
40	0.425	69
60	0.25	71
100	0.15	77
200	0.075	90
Pan	—	100

LL = 60, PL = 26. Classify this soil according to the USCS, providing the group symbol for it.

2.68 A sample of soil was tested in the laboratory and the following grain-size analysis results were obtained:

Sieve No.	Sieve Opening (mm)	Percent Finer by Weight
4	4.75	100
10	2.00	100

(Continued)

Sieve No.	Sieve Opening (mm)	Percent Finer by Weight
20	0.85	100
40	0.425	94
60	0.25	82
100	0.15	66
200	0.075	45
Pan	—	0

Atterberg limits on minus No. 40 material were: LL = 36, PL = 14.

Determine the USCS classification symbol for this soil.

2.69 Laboratory testing was performed on two soil samples (A and B) and the data is summarized in the table.

Sieve No. and/or Opening Size	Sample A Percent Passing	Sample B Percent Passing
3 in. (76.2 mm)	100	
1.5 in. (38.1 mm)	98	
0.75 in. (19.1 mm)	96	
4 (4.75 mm)	77	100
10 (2.00 mm)	Not used	96
20 (0.85 mm)	55	94
40 (0.425 mm)	Not used	73
100 (0.150 mm)	30	Not used
200 (0.075 mm)	18	55
Liquid limit	32	52
Plastic limit	25	32

Determine the USCS classification for samples A and B.
Use log interpolation as necessary.

2.70 A sample of soil was tested in the laboratory and the following grain-size analysis results were obtained:

Sieve No.	Sieve Opening (mm)	Percent Coarser by Weight
4	4.75	0
10	2.00	5.1
20	0.85	10.0
40	0.425	40.7
60	0.25	70.2
100	0.15	84.8
200	0.075	90.5
Pan	—	100

Atterberg limits on minus No. 40 material: LL = 62, PL = 20. Determine the USCS letter symbol (e.g., GP) for this soil.

2.71 A sample of a brown sandy clay was obtained to determine its Atterberg limits and then classify its soil type according to the Unified Soil Classification System. For one of the PL determinations, the wet weight + dish = 11.53 g and the dry weight + dish = 10.49 g. The dish only weighed 4.15 g. Compute the plastic limit. Another plastic limit was 16.9%. Three determinations of the liquid limit were made. For 17 blows, the water content was 49.8%; for 26 blows, the water content was 47.5%; and for 36 blows, the water content was 46.3%. Evaluate the soil type, indicate the information on a plasticity chart, and give the Unified Soil Classification symbol.

CHAPTER 3

Geology, Landforms, and the Origin of Geomaterials

3.1 IMPORTANCE OF GEOLOGY TO GEOTECHNICAL ENGINEERING

Geotechnical engineering is the branch of civil engineering that applies civil engineering technology to some aspect of the earth. Knowledge of geology is very important to the successful practice of geotechnical engineering, and is helpful in several other areas of civil engineering as well. So in this chapter we introduce you to relevant and important aspects of geology. We believe that students should know something about the origin and nature of geologic materials before beginning to study geotechnical engineering. As pointed out by Heim (1990), geotechnical engineers and geologists are "truly handicapped" in their professional activities if they do not know the origin of the deposits they are working with.

Although this chapter provides some of the basics, it is not a substitute for formal courses in physical geology, geomorphology, and engineering geology, and you are encouraged to take as many of these courses as your schedule permits. If you have already had one or more courses in geology, this chapter will be useful as a review. Finally, at the end of the chapter we describe some books, articles, and websites that you can go to for additional information.

3.1.1 Geology

Basically, *geology* is the science of the earth. It is primarily a descriptive science that is concerned with the history, form, composition, structure, and natural processes acting on or in our planet. It is an extremely broad field that includes the study of rocks (petrology) and minerals (mineralogy), structural geology and geophysics, geochemistry and environmental geology, historical geology and paleontology (study of fossils), economic geology, geomorphology and hydrogeology. Geologic processes such as volcanism, glaciation, sedimentation, as well as the material deposits associated with these processes, also are a part of geology. The branches of geology most relevant to civil engineering are physical geology, geomorphology, and hydrogeology. Petrology is important in construction materials engineering, and some aspects of structural geology apply to rock mechanics, rock engineering, and earthquake engineering. In addition to hydrogeology, geochemistry and environmental geology are

important aspects of geoenvironmental engineering. Although engineering geology is sometimes considered another branch of geology, we consider it to be an interdisciplinary field between geology and civil engineering that is very closely related to geotechnical engineering practice.

3.1.2 Geomorphology

Geomorphology is that branch of geology concerned with the form or shape of the earth's solid surface. Geomorphology involves the study of specific landforms: their origin, the geologic processes involved in their formation, and their composition.

Why study landforms? Well, if we can identify the particular landform(s) at our site, then we know how it was formed and the geologic processes involved, what soils and rocks probably exist at the site, and something about their likely engineering properties. This information helps us anticipate engineering problems that may occur at that site. This is essentially how geomorphology is applied in geotechnical practice. The basic equation for geotechnical engineers then is:

$$\text{geology} \Rightarrow \text{specific landform} \Rightarrow \text{soils/rocks} \Rightarrow \text{engineering information and potential problems at a site} \tag{3.1}$$

In general, any landform is a function of:

1. the original rocks or soils (composition and structural relationship),
2. the processes acting on those rocks and soils (for example water transport), and
3. the timeframe over which these processes act.

In this chapter we discuss these factors, the landforms produced, and typical rocks and soils commonly found in these landforms. We also mention important engineering characteristics and problems often associated with the landforms.

3.1.3 Engineering Geology

Engineering geology is an interdisciplinary field between engineering and geology, closely related in professional practice to geotechnical engineering. Engineering geologists obtain the geologic information and data necessary to describe the pertinent geologic features and processes, the structure and characteristics of rocks and other deposits at a site or project, and they interpret this information for use by civil (geotechnical, materials, or construction) engineers. Engineering geologists have a major role in the planning, design, and construction of large civil engineering projects. As Galster (1992) noted, engineering geology provides:

> a complete and accurate geologic description of a site and relevant areas, determining of the adequacy of geologic conditions for the intended project, and making available appropriate advice to the engineer/designer throughout the design, construction, and operational period of the project.

In recent years engineering geologists have become increasingly active in the environmental aspects of geotechnical engineering (also known as *geoenvironmental engineering*). A good example is the important role that geologic conditions play in determining groundwater movement and the design of facilities such as landfills.

As a civil engineer, you should recognize the limitations of your own education and experience, especially with regard to geology, and when appropriate, be prepared to call upon the services of a professional engineering geologist.

3.2 THE EARTH, MINERALS, ROCKS, AND ROCK STRUCTURE

3.2.1 The Earth

The planet Earth consists of a dense molten core, surrounded by a less dense, quasi-solid to ductile *mantle* and a relatively thin (25–75 km thick) least-dense *crust*. The earth's *lithosphere*, a composite layer of the crust and outermost part of the mantle, consists of several large, solid, relatively brittle rocky plates that slowly move around on the mantle, propelled by convection cells that circulate the earth's internal heat. These plates contain the relatively light continental lithosphere, heavier oceanic lithosphere, or a combination of both. Most of the volcanic and mountain-building activity on the earth's surface occurs where these large lithospheric plates meet, collide, or move alongside or under one another. Plate intersections also seem to be the primary loci of recorded seismic (earthquake) activity. The study of the plates and their movements, an important aspect of modern geology and geophysics, is called *plate tectonics*.

In civil engineering practice we are concerned mostly with the rocks, soils, and human-made materials found on or near the surface of the Earth's crust. Only in the case of *earthquake engineering* is the deeper realm of plate tectonics and geophysics of interest. (Earthquake engineering is concerned with the design, performance, and operation of civil engineering structures and other facilities that may be subjected to earthquakes during their service lives.)

3.2.2 Minerals

A *mineral* is a naturally occurring inorganic solid with a specific chemical composition and having its atoms arranged in a systematic internal structure. Mineralogists have identified more than 3,000 different types of minerals found in soils and rocks, but probably fewer than 20 are important for civil engineering purposes. The four major rock-forming mineral groups are silicates, carbonates, oxides and "other," mostly salt minerals (sulfates and chlorides). The most important minerals under each group are:

1. *Silicates*: Quartz (and chert), feldspar (orthoclase and plagioclase), mica (biotite and muscovite), chlorite, amphibole (hornblende), pyroxene, olivine, serpentine, talc, and the clay minerals.
2. *Carbonates*: Calcite, dolomite.
3. *Oxides*: Limonite, hematite.
4. *Others*: Gypsum, anhydrite, halite (NaCl), pyrite (fool's gold), and graphite (carbon).

Identification of these and other less common minerals is based on their visual appearance, hardness, and certain characteristics of the crystals in the mineral. Tables and charts in Goodman (1989), FHWA (1991), Goodman (1993), and West (1995) as well as in basic geology texts provide a simple but systematic approach to mineral identification. According to T. Taylor (personal communication, 1999), a list of minerals you definitely should not know would include the following: amblygonite, atacamite, boulangerite, brochanthite, cerargyrite, chloanthite, corbomite, crocoite, dumortierite, erythrite, ferberite, hausmannite, jarosite, phnarghite, pyrargyite, pyrochloremicrolite, smaltite, smithosonite, tennantite, torbernite, tyuyamunite, vivianite, witherite, xenotime, and zincite.

Only a small number of minerals are responsible for most engineering problems. For example, some minerals are soluble (e.g., calcite, dolomite, gypsum, anhydrite, and halite), while others release sulfuric acid when they weather (e.g., pyrite). Some minerals have low friction coefficients (e.g., clay minerals, talc, chlorite, serpentine, micas, and graphite). Potentially swelling minerals include anhydrite and the clay minerals montmorillonite and vermiculite (described in Chapter 4). You probably know from your study of concrete that several minerals that may be part of the aggregate composition (e.g., chert, gypsum, mica, and some volcanic rocks) react adversely with Portland cement in concrete.

3.2.3 Rocks

Rock is any naturally occurring aggregation or mass of one or more minerals found in the earth's crust. Petrologists (geologists who specialize in rocks) usually classify rocks, according to their genesis or origin, into three main groups: *igneous*, *sedimentary*, and *metamorphic*. Igneous rocks are formed from molten mineral material that has cooled and solidified either deep in the earth (*plutonic*) or in volcanic eruptions at or near the earth's surface. Sedimentary rocks are formed from the accumulation and aggregation of particles derived from preexisting rocks and ranging in size from the coarsest rubble down to the finest colloidal sized particles. They may also come from crystalline precipitates and biologic deposits in oceans and lakes, and from buried plant and animal remains. Metamorphic rocks result from the alteration of the structure and/or chemical composition of rocks of any type by heat, pressure, or chemical reactions. Goodman (1989), FHWA (1991), Goodman (1993), and West (1995), among others, provide tables and charts to help you with rock identification and classification.

The following rock classification scheme (Galster, 1992) appears to be a practical one for civil engineers. A few examples are given after each rock type.

I. Igneous rocks
- **A.** Volcanic rocks
  1. Volcanoclasitics: volcanic ejecta, tuff, breccia, pumice
  2. Lavas: basalt, andesite, rhyolite, feldsite, and trachite
  3. Volcanic intrusives: diabase, pahoehoe, aa
- **B.** Plutonic and other coarsely crystalline rocks: granite, granodiorite, diorite, quartz diorite, syenite, gabbro

II. Sedimentary rocks
- **A.** Precipitates: chert, limestone, dolomite, rock salt, gypsum, anhydrite
- **B.** Clastics: sandstone, shale, siltstone, claystone, conglomerate, sedimentary breccia, argillite
- **C.** Biological sediments: coal, coral reef limestone, chalk, diatomite

III. Metamorphic rocks
- **A.** Nonfoliated:
  1. Quartzite, hornfels, amphibolite, marble
  2. Numerous volcanic and sedimentary rocks with meta as a prefix
- **B.** Foliated:
  1. Schist, phyllite, slate, amphibolite, serpentinite
  2. Bedded metamorphics (argillite, gneiss, metasandstone, quartzite)

A few more definitions are in order. *Clastic* texture refers to rocks made up of broken fragments of preexisting rocks and assorted minerals bound or cemented together by another mineral or chemical. Thus *volcanoclastics* are clastic rocks of volcanic origin, while sedimentary clastic rocks are transported, sedimented, and then transformed into clastic sedimentary rocks by chemical cementation, pressure, and/or temperature. *Lava* is a general name for molten rock from volcanoes deposited on the surface, while plutonic rock refers to those volcanic rocks that are intruded into pre-existing materials below the surface of the earth.

Crystalline texture means that the rocks are mostly composed of mineral crystals that have developed in the rock itself. Because of rapid cooling at the surface, lava rocks generally contain minerals with very small crystals, too small to be seen without a microscope. On the other hand, plutonic rocks have cooled very slowly at depth and thus are coarsely crystalline, because their mineral crystals are relatively large.

Precipitates are those sedimentary rocks that resulted from chemical precipitation in either a marine or fresh water environment. Clastics have already been defined. Biological sediments and rocks obviously have an organic origin. *Foliated* metamorphic rocks are banded or laminated (in contrast with the stratification and bedding planes of sedimentary rocks); they result from the flattening of the constituent mineral grains due to the extreme temperatures and pressures that cause metamorphism. Nonfoliated metamorphic rocks are those that did not develop foliation as a result of their metamorphism.

There are many examples of engineering problems associated with specific rock types. For example, dams have failed and reservoirs have leaked when they were constructed on soluble rocks such as carbonates and gypsum, and such deposits can also result in sinkholes, particularly when chemically aggressive groundwater is present (e.g., from mining wastes or tailings). Shales can swell or soften when exposed to water or even air and become weak and compressible. Swelling rocks cause serious problems in tunnel construction when the materials are de-stressed during excavation. Foliated and bedded rocks often have planes of weakness that can cause landslides and stability problems in excavations. Kiersch and James (1991) describe a number of spectacular failures of civil engineering structures directly related to these and other geologic conditions, as well as human activity. These failures, many of them deadly, illustrate how important it is for civil engineers to recognize potentially dangerous geologic conditions as early as possible in the design and construction process.

3.2.4 Rock Structure

When rock masses are subjected to different stress conditions such as compression, tension, and shear, they can fold, shift, and rupture, even under conditions of high confining pressure and temperature. These processes result in features such as joints, folds, and faults, all of which strongly influence the engineering behavior of the rock mass.

Joints are regularly occurring and relatively planar fracture surfaces in the rock mass, with spacings ranging from a few millimetres to several metres, along which little or no movement has occurred. Joints occur because of tensile or shear strains in the rock mass, and they are extremely important in rock mechanics and rock engineering. Even if the intact rock between the joints is very strong and impermeable, the joints usually make a rock mass weaker and more permeable. See Goodman (1989) and West (1995) for details as to how rock joints are observed, measured, and tested for strength and frictional characteristics. Wyllie (1996 and 1999) describes how rock joints are treated and strengthened in the field. When beds and strata, especially of sedimentary rocks, are subjected to bending without rupture, the deformation of the beds creates a number of structures, such as different kinds of *folds*, *domes*, *basins*, and *arches*. Some of these structures are very large and may cover hundreds of square kilometres of the earth's surface. Fold structures are shown in Fig. 3.1.

A *fault* occurs when the rock mass ruptures and movement or shearing displacement takes place along the rupture surface. Several types of faults have been identified, depending on how movement takes place, and these are shown in Fig. 3.2. A series of closely spaced, approximately parallel faults is called a *shear* or *fault zone*.

The spatial orientation of geologic features such as rock layers, joints, folds, and faults is described by the terms dip and strike, as illustrated in Fig. 3.3 for a tilted stratum. The dip or dip angle of a geologic feature is the acute angle between the feature and some reference plane, usually the horizontal. The strike is the azimuth or direction of the feature in the horizontal plane. Note that the dip and strike are at right angles to each other.

Rock structures produce a number of interesting landforms. Some of the more significant ones will be discussed in Sec. 3.3.9.

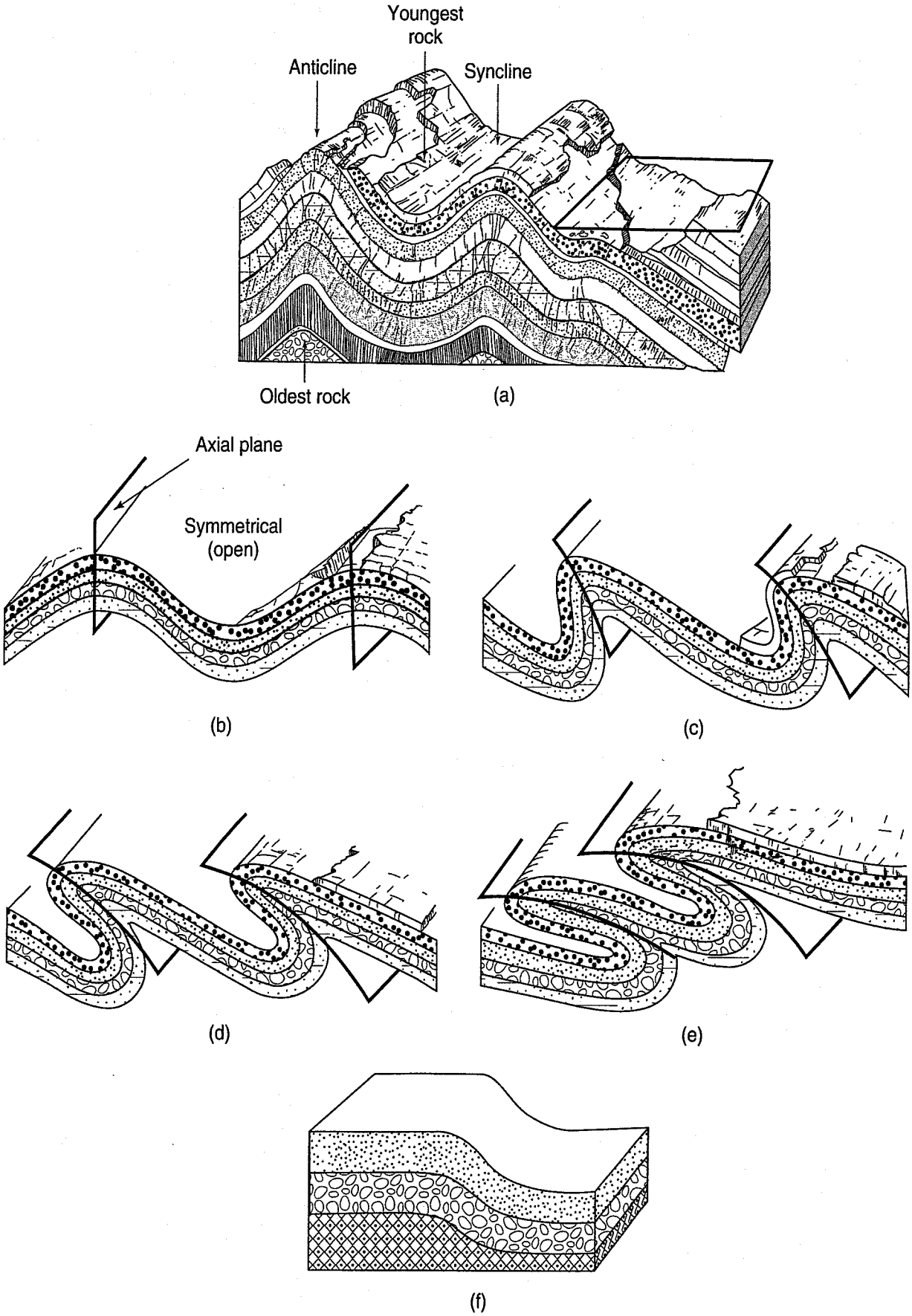

FIGURE 3.1 Fold structures: (a) anticline and syncline; (b) symmetrical anticline; (c) asymmetrical anticline; (d) overturned anticline; (e) recumbent anticline; (f) monocline (after Chernicoff and Venkatakrishnan, 1995, and Emmons et al., 1955).

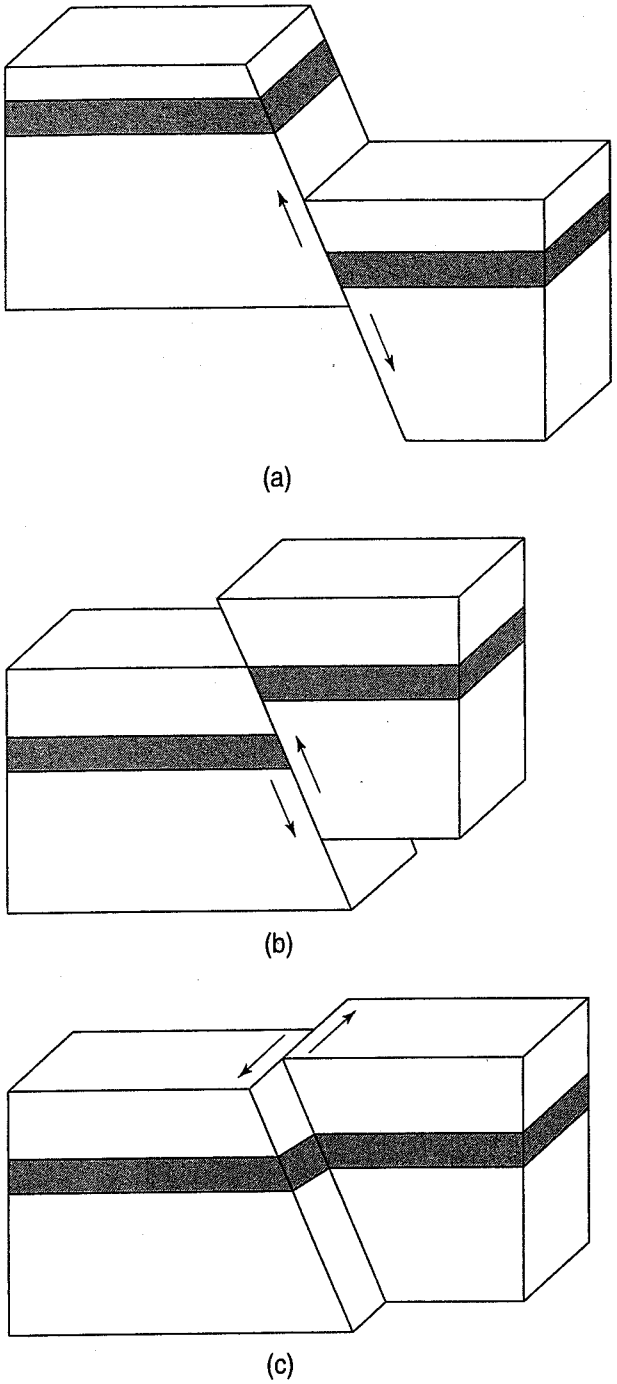

FIGURE 3.2 Faults: (a) normal; (b) reverse or thrust; (c) strike-slip (after Z.Z. Zipczeck, 1956).

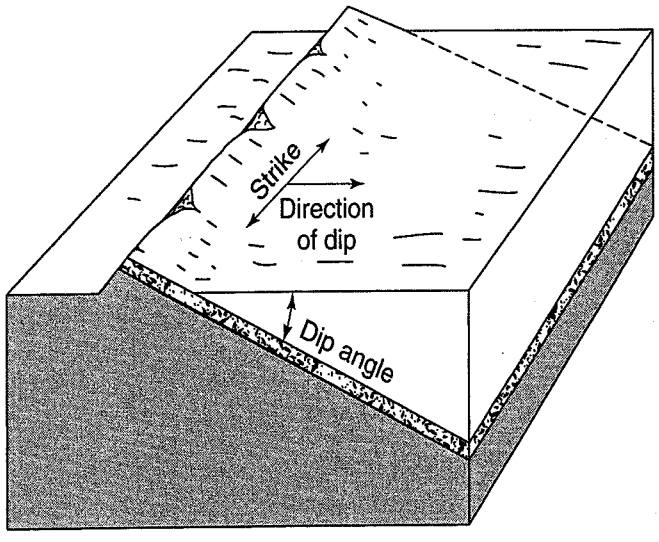

FIGURE 3.3 Strike and slip defined (after Emmons et al., 1955).

3.3 GEOLOGIC PROCESSES AND LANDFORMS

Earlier we mentioned that geomorphology deals with landforms: their origin, the geologic processes involved in their formation, and their composition. Because specific landforms indicate the geologic processes that produced them, it is important to be able to recognize the different landforms and their commonly associated earthen materials and potential design and construction problems.

The three factors controlling the formation of a particular landform are the (1) earth materials (their composition and structural relationship), (2) geologic processes acting on the earth materials, and (3) time over which these processes act.

Geologic time, to most humans, is almost incomprehensibly long. Still, it has aspects we need to understand. Some geologic processes are very long acting while others can take place in a relatively short period—for example, during a construction project. Both contemporary and ancient processes and their resulting landforms can significantly influence engineering projects. To civil engineers, the relative age of a deposit or landform is ordinarily more important than absolute age, although absolute age may be important in understanding contemporary processes. Table 3.1 will help you appreciate the geologic time scale.

In this section we describe a particular geologic process, the landforms produced, typical soils and rocks involved, and some of the engineering concerns associated with each landform.

3.3.1 Geologic Processes and the Origin of Earthen Materials

Geologic processes can be described according to the origin of their activity, that is, (1) on the earth's surface, (2) below the earth's surface, and (3) in rare cases, extraterrestrially.

Geologic processes originating on the earth's surface include weathering, gravity, surface water, ice (glaciers), wind, volcanic activity, the action of organisms (plants and animals, including human beings), and combinations of these processes. Surficial geologic processes can also be classified according to the results of the process, whether aggregational (depositional or building up) or degradational (erosional or tearing down). Most processes are both degradational and aggregational at the same time, if not at the same geographic location. Rivers and glaciers, for example, can be eroding at one place and depositing at another, all within the same river or glacier system. Volcanoes can be both degradational and aggregational in the same event. In the Mount St. Helen's (Washington) eruption of May 1980, about 400 m of the top of the volcano was blown away (definitely degradational!) while large volumes of volcanic ash varying in thickness from a few metres down to a mild dusting were deposited.

Subsurface geologic processes of interest to geotechnical engineers include groundwater, tectonic, and plutonic processes. These are described toward the end of the chapter.

Extraterrestrial objects (meteors) striking the earth's surface can leave craters that are locally important but not ordinarily of engineering concern.

Table 3.2, adapted from Galster (1992), lists the origin of different surficial sediments and materials together with the particular geologic process that produced them.

Identification of the origin is important, because knowing the origin of a particular soil deposit helps you estimate its distribution, variation, and even some of its potential uses and limitations as a foundation or construction material. One special example is aeolian or wind-deposited materials. Because the particles had to be small enough and sufficiently lacking in cohesion to be windborne, these are generally silty materials that are loosely deposited—not very good to put foundation on, and prone to erosion.

3.3.2 Weathering

Weathering is the alteration of the composition or structure of rocks at or near the earth's surface by physical, chemical, or biological processes. *Physical weathering* causes mechanical disintegration of rocks by changes in temperature (freezing and thawing), the action of agents such as glaciers, wave

TABLE 3.1 Geologic Time for Civil Engineers (after Chernicoff and Venkatakrishnan, 1995; T. Taylor, personal communication, 1995)

Eon	Era	Period	Epoch	Duration (yr before present × 10^6)	Age of Boundary (yr before present × 10^6)	Translation for Engineers
Phanerozoic	Cenozoic	Quaternary	Holocene	0.015		*Very* young
			Pleistocene	1.6	1.6	Young
		Tertiary	Pliocene	3.7		
			Miocene	18.4		
			Oligocene	12.9		Not so young
			Eocene	21.2		
			Paleocene	8.6	66.4	
	Mesozoic	Cretaceous		78		
		Jurassic		64		Old
		Triassic		37	245	
	Paleozoic	Permian		41		
		Pennsylvanian		34		
		Mississippian		40		
		Devonian		48		Older
		Silurian		30		
		Ordovician		67		
		Cambrian		65	570	
Precambrian	Proterozoic			1930		
	Archean			1300		*Very* old
	Hadean			800	~4600	

action, and wind. Biological activity includes the actions of plants and animals, and it can be physical and/or chemical.

Chemical weathering causes decomposition of rocks by chemical action—oxidation, reduction, hydrolysis, carbonization, and the action of organic acids. In general, chemical weathering dominates in temperate and tropical climates, whereas physical weathering tends to be more important in arctic climates and at higher elevations in temperate zones.

The products of weathering are all types of soils, sometimes called residuum. Physical weathering tends to produce coarser-grained soils, ranging from boulders and cobbles to gravel, sands, and silts (these grain sizes are defined exactly in Chapter 2). Chemical weathering produces various types

TABLE 3.2 Surficial Geologic Processes and Materials Produced

Surface Process	Description	Material Produced [soil name, if any]
Weathering	Material weathered in place	Residual [residuum]
Gravity	Gravity deposition; slope wash	Colluvial [colluvium]
Surface water	Fluvial (stream) deposition	Alluvial [alluvium]
Marine and coastal	Marine and coastal deposition	Marine and coastal
Lacustrine	Deposition in lakes	Lacustrine
Ice	Deposition associated with glacial ice and frozen ground	Glacial
Wind	Deposition by wind	Eolian
Volcanic	Deposition by volcanism	Volcanic
—	Human activities	Artificial fill

After Galster (1992).

of clay minerals. For example, the hydrolysis of feldspar and mica (biotite) minerals in granitic rocks produces the clay mineral kaolinite, an important constituent of fine-grained soils. Other types of clay minerals are produced from different rock minerals under different chemical, climatic, and drainage conditions. Clay minerals and other products of weathering are discussed in detail in Chapter 4.

Karst and Karstic Features—Sometimes specific landforms result from weathering. The best-known and most important example is the development of *karst* topography and karstic features on soluble bedrock, as shown in Fig. 3.4.

The name "karst" comes from a particular limestone plateau located on the Dalmatian coast of Croatia and extending into Slovenia and Italy along the Adriatic Sea. Because limestone and other carbonate rocks are so common throughout the world, karstic features and topography are very important geotechnically where such rocks occur.

Rainwater is slightly acidic because it dissolves carbon dioxide from the atmosphere, yielding carbonic acid, and it may become even more acidic from air pollution and organic-enriched soils on the ground. Extreme levels of groundwater acidity can result from mining operations and the wastes (or tailings) produced. Carbonate rocks are attacked by this acidic groundwater and slowly dissolve,

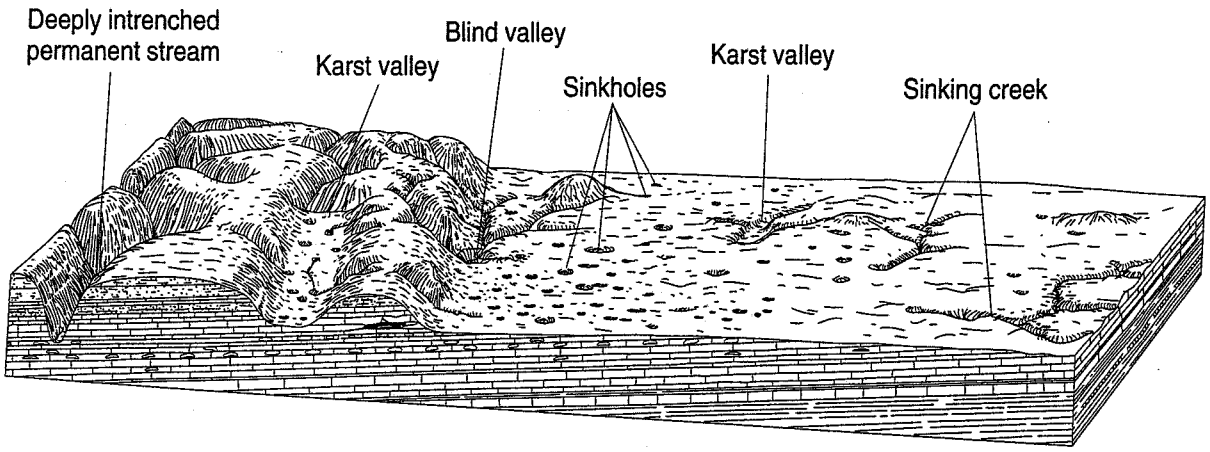

FIGURE 3.4 Typical karstic landscape features (Thornbury, 1954).

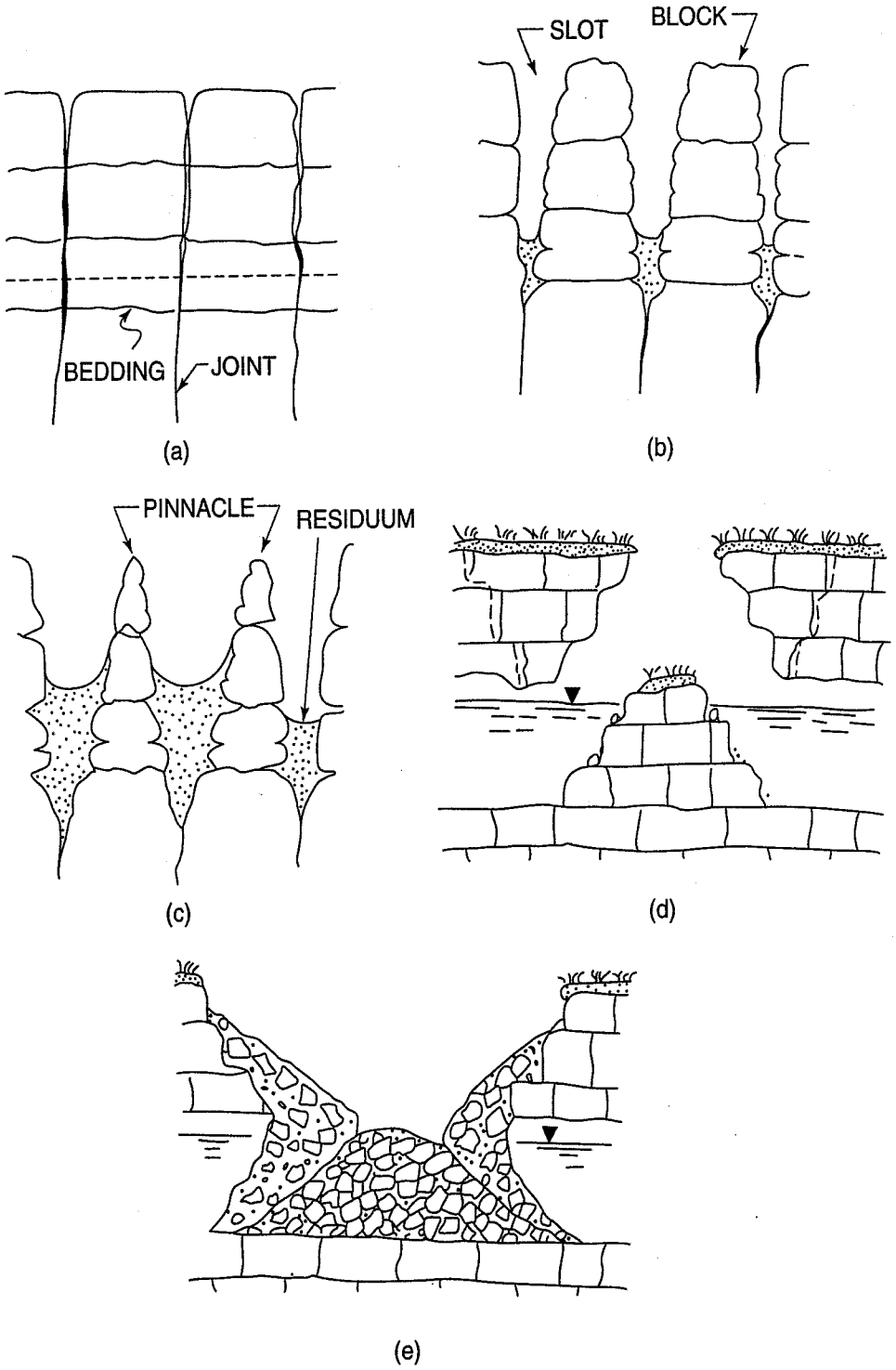

FIGURE 3.5 Development of solution cavities and karstic features, starting with (a) solution cracks, leading to (b) slots and blocks, and eventually (c) pinnacles and residuum. Formation of a collapse sinkhole in a shallow cavern; (d) initial collapse with rock overhang, and subsequent (e) rim collapse and debris mound (Sowers, 1996).

leaving solution cavities, subterranean caves and caverns, enlarged vertical joints (often filled with silty clay soil), and a highly irregular bedrock surface (Fig. 3.5) resulting from ground collapse. Sometimes large blocks of more resistant limestone are completely isolated from adjacent bedrock and may even be underlain by clay or other weaker materials. Shallow caves and domes often collapse, leaving surface depressions called sinkholes (Figs. 3.4 and 3.5) that may be filled with clay or even

water. Large collapsing sinkholes in built-up areas can be very destructive to surface structures and facilities. The design and construction of foundations on karstic bedrock present serious challenges to geotechnical engineers (Sowers, 1996). Reservoirs in karstic country often experience severe leakage.

The most important karstic regions in North America are in central Florida and in the large area of southern Indiana, west-central Kentucky, and north-central Tennessee. A number of other areas in the United States and Canada have deposits of soluble rocks with solution features such as caves and caverns.

Residual and Tropical Soils—Soils that result from the in-place weathering of rock or other earthen materials, and are not subsequently transported, are known as *residual* soils. They can develop from just about any bedrock type. A progressive and gradual weakening and decomposition takes place from the ground surface down to the unweathered material (Fig. 3.6). There is often no definite boundary between rock and soil, either vertically or horizontally, because weathering generally follows the joints and bedding planes in the rock. The degree of disintegration and the thickness of the zone of residual soil depends on the type of bedrock (local "parent" material), climate, drainage conditions, and topography. Goodman (1993) and Wesley and Irfan (1997) discuss the difficult problem of classifying weathered rock and residual soils profiles for engineering purposes.

As noted by Lyons Associates (1971) and Mitchell and Soga (2005), because of high temperatures and high rainfall in tropical regions, intense chemical weathering and decomposition of the parent bedrock occurs along with rather complex chemical alteration of the minerals in the bedrock. Chemical processes of hydration, hydrolysis, solution, and carbonation result in the alteration of minerals in the rock, and new minerals, mostly clay minerals (Chapter 4) are formed due to water, oxygen, carbon dioxide, and organic acids derived from decaying vegetation. The process is known as "laterization." The resulting soils, called *laterites* (Latin: *later* = brick), are red, because of a high concentration of aluminum and iron oxides (because the silicates have been weathered away).

Weathering profiles [Fig. 3.6(a)] can be very deep in the tropics, often tens of metres deep. The upper clayey zone can be a metre or two thick, then underlain by a silty or sandy zone, which in turn transitions into a highly irregular weathered zone and finally into sound rock. The thickness of these zones varies greatly, even at a specific site, and this variability in thickness and soil properties creates difficult problems for foundation design and construction.

Saprolites are also weathered residual soils, usually rich in clays, that result from the chemical decomposition of bedrock, forming primarily in humid temperate or subtropical climates. Sometimes saprolites retain the original (relict) texture and structure of the parent rock, especially when they form on gneiss and schist bedrock [Fig. 3.6(c)].

Another residual soil, which is locally important in the desert southwest as well as in higher elevations of the Sierra Nevadas and other western mountain ranges, is *decomposed granite* (also known as DG). It forms largely due to chemical weathering of granitic bedrock in situ, and it leads to highly variable and irregular soil and bedrock profiles. Most DG is primarily granular (sands and fine gravel) in size, but it may contain relict boulders.

Possible engineering problems in areas of deeply weathered rock and residual soils are summarized by Jennings and Brink (1978) and by Blight (1997). These problems often lead to unstable slopes, including landslides and debris flows (described in the next section), reservoirs that leak, especially on DG, and difficulties with foundation exploration, construction, and performance. For example, in making excavations at sites in deeply weathered rock, what is rock and what is soil for quantity payment purposes may result in costly disagreements between the owner and contractor. Deep foundations for heavy structures such as bridges can be very problematic due to variable lengths, end bearing conditions, and installation. Residual soils also are often difficult to compact when used for road bases. They may appear to be sandy and free draining when excavated, but when compaction energy is applied, the granules break down, and the result is a fine-grained, almost clayey material that is difficult to compact and is not free draining. Furthermore, the presence of mica in both saprolite and DG may result in lower compacted densities (Chapter 5) and more compressibility than desirable.

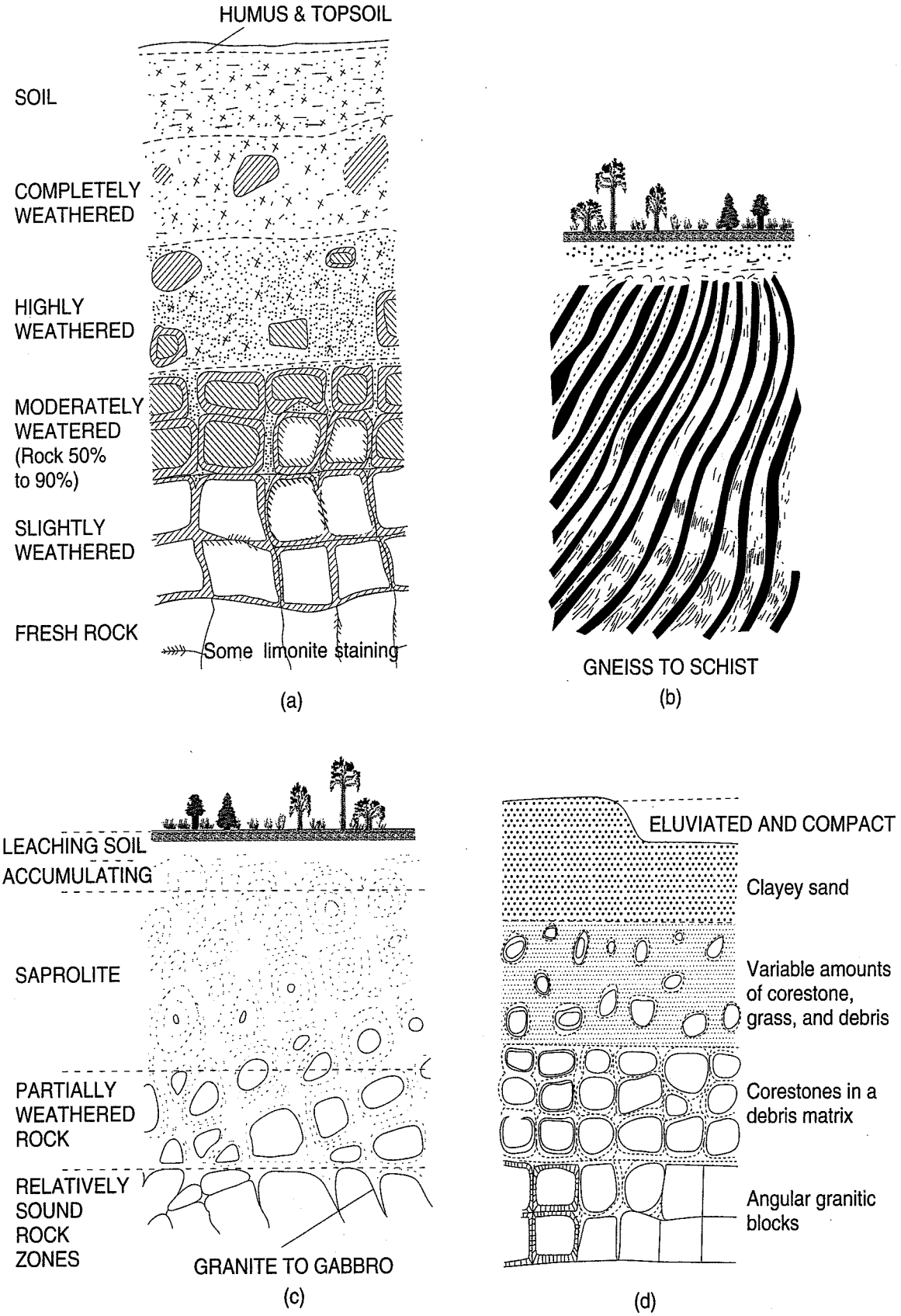

FIGURE 3.6 Typical residual soil profiles: (a) tropical residual soils (Blight, 1997, after Little, 1969); (b) humid temperate regions on igneous bedrock (Sowers and Richardson, 1983); (c) humid temperate regions on metamorphic bedrock (Sowers and Richardson, 1983); and (d) decomposed granite (Mitchell and Soga, 2005).

Because of extensive erosion by glaciation (Sec. 3.3.7) in Canada and the northern United States, residual soils in North America are mainly found south of the continental ice limit: in the central and southern Great Plains states, the southeastern states in the Appalachian Mountains, Hawaii, the Colorado Plateau in the "four-corners" area of the southwest United States, and the coastal areas of California, Oregon, Washington, and British Columbia. Additional information on the engineering problems of residual soils can be found in the proceedings of the ASCE Specialty Conference on Engineering and Construction in Tropical and Residual Soils held in Honolulu in 1982, Blight (1997), and Edelen (1999).

3.3.3 Gravity Processes

Mass movement (or mass wasting) is a geologic term for a variety of processes that result in the movement of rock and soil masses down a slope under the influence of gravity. The generic term for this is *landslide*. Downslope movements include falls, flows, spreads, soil creep, solifluction, and talus. Ground collapse is also briefly discussed in this section, because the geological process is gravitational. Although there are a number of possible ways to identify and classify downslope movements, we follow Cruden and Varnes (1996), who classify landslides according to (1) type of movement and (2) type of material. Possible landslide movements are fall, topple, slide, spread, and flow (shown in Fig. 3.7), or possibly combinations of these.

Slide materials can be rock, debris, or earth (soil). Rock refers to a rock mass that was intact and in its natural place before sliding; earth consists of predominately sands, silts, and clays; and debris contains a significant amount of coarse materials (gravel and larger). So, for example, a landslide might be a rock fall, a debris flow or an earth slide. Additional terms may be added to these names to further describe landslides.

Table 3.3 is a glossary for forming landslide names. It gives adjectives to describe the state, distribution, and style of the landslide, followed by descriptions of the rate of movement, water content, material type, and slide type. The table also gives some indication of the damage the landslide can cause. Cruden and Varnes (1996) provide detailed definitions and illustrations of the terms in Table 3.3, so we will give just a few examples of some of the more common landslide types.

Because the term "mud" does not have a precise engineering definition (it is a mixture of earth and water) and should be avoided in technical discussions, mudslide or mudflow is often used by nonengineers to describe several different types of landslides. These slides can involve rock, earth, or debris, be moist or wet, and be complex or composite in style. Some mudslides are simply earth slides, while others may be retrogressive, composite rock slides or advancing slow, moist earth slides. Mudflows are, for example, often active, advancing, complex, rapid to moderate, very wet debris flows or earth slides. Thus, to avoid confusion, it is important to be able to describe a landslide precisely.

Spreads can occur on rather gentle slopes, and after movement starts, they may progress or retrogress very rapidly. Spreads are common on water-bearing thin seams of sands and silts overlain by relatively competent rock, homogeneous clays, or constructed earth fills. Spreads may result from liquefaction (Chapters 7 and 13) of the sand and silt seams, triggered by earthquakes, blasting, or pile driving in the vicinity.

A number of important *flows* have also been identified. These include *debris flows*, *lehars* [debris flows from volcanoes (Indonesian, from *laharisa*, meaning hot mud)] and *debris avalanches* (extremely rapid, active, advancing debris flows). *Rock glaciers*—accumulations of broken rock, some finer-grained materials, and ice that slowly creep downslope in mountainous areas—are "very slow, wet debris flows." *Solifluction* is the slow downslope flowage or "creep" of saturated surficial soil layers. In the new terminology, solifluction is "very slow, wet earth flow." Because the term *creep* is ambiguous, it should be replaced by the appropriate rate modifiers (very slow or extremely slow) in Table 3.3.

Since the earthen materials have been disturbed, landslide landforms have an irregular surface, usually with one or more ridges where slide material has bunched together. Because of the sudden

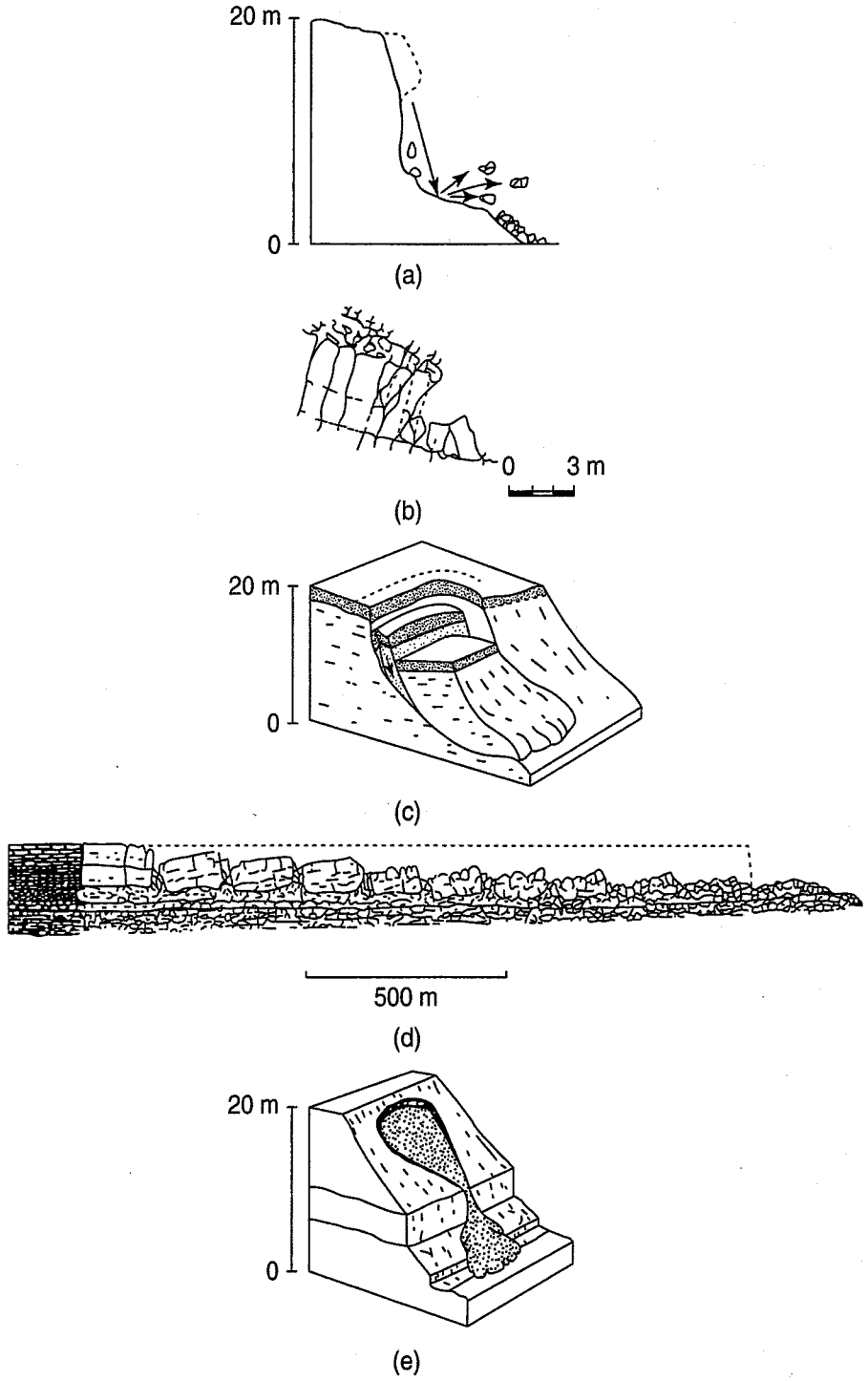

FIGURE 3.7 Types of landslides: (a) fall; (b) topple; (c) slide; (d) spread; and (e) flow (after Cruden and Varnes, 1996).

material movement, there is often an abnormal surface drainage pattern. Usually there is a *scarp* [the steep slope at the top of the slide—see Fig. 3.7(c) and (e)] that indicates the uppermost and widest lateral extent of the slide area. The size of landslides varies from a few square metres to square kilometres. Engineering problems associated with landslides include variable groundwater conditions and highly variable and often poor foundation conditions. Probably the most difficult problem is determining the potential for additional movement and sliding, either of the landslide material itself or of intact materials in the vicinity. Slopes experiencing solifluction may contain trees with bent

TABLE 3.3 Glossary for Forming Names of Landslides and Rates of Landslide Movements

State of Activity	Distribution of Activity	Style of Activity	Rate of Movement	Velocity	Water Content	Material	Type	Example
Active	Advancing	Complex	Extremely rapid	>5 m/s	Dry	Rock	Fall	Major catastrophe
Reactivated	Retrogressive	Composite	Very rapid	>3 m/min	Moist	Earth	Topple	Some lives lost
Suspended	Widening	Multiple	Rapid	>1.8 m/hr	Wet	Debris	Slide	Evacuation possible; structures destroyed
Inactive	Enlarging	Successive	Moderate	>13 m/mo	Very wet		Spread	Maintenance possible
(Dormant)	Confined	Single	Slow	>1.6 m/yr	Sloshing		Flow	Remedial construction possible
(Abandoned)	Diminishing		Very slow	>16 mm/yr				Some permanent structures undamaged
(Stabilized)	Moving							Imperceptible without instruments
(Relict)			Extremely slow	<16 mm/yr				

Modified after Cruden and Varnes (1996).

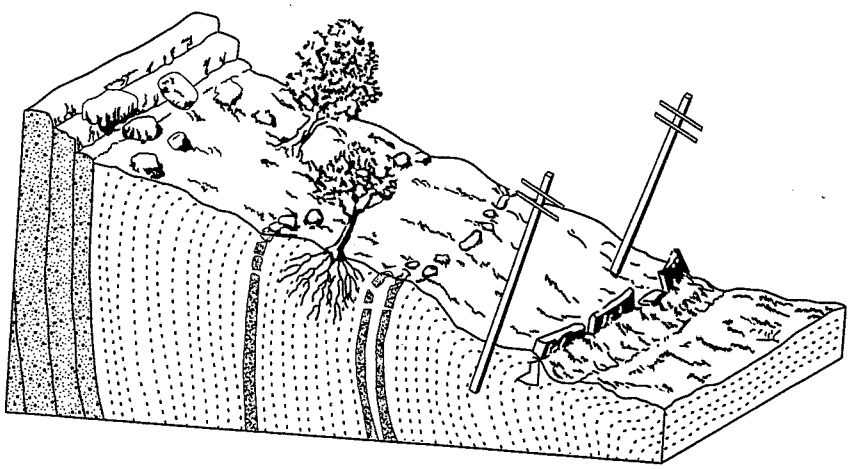

FIGURE 3.8 Schematic illustrating a slope experiencing solifluction (after Lambert, 1988).

trunks or leaning power poles, a sure indication that downslope movement is slow and continuous and that the slope is not very stable (Fig. 3.8).

Another gravity-induced landform, quite common on mountain slopes, is a talus slope. *Talus* is the accumulation of rock fragments (ranging in size from boulders through gravel) derived from and lying at the base of a cliff or a very steep rock slope. Talus results from the physical weathering (alternate freezing and thawing) of an exposed rock face. Talus slopes form at 30–50 degrees and they may extend upslope tens to hundreds of metres. Talus slopes are called *active* if they continuously creep and *inactive* if they have become stabilized, generally by vegetation. In constructing facilities near or through talus slopes, it is important to know whether the slope is still active or not, and whether an excavation into or construction on the slope will cause instability and undesirable movements. Engineering information required for talus stabilization includes the sizes of the rock particles in the slope, whether there are finer materials in the rock voids, and the groundwater conditions in the slope.

The loose and often incoherent soil and rock materials deposited down slope due to the action of gravity are called *colluvium*. Colluvium includes all landslide debris, no matter the type of slope movement, including creep. Note that the materials in talus are an example of colluvium.

Ground collapse, another gravitational process, depends on loss of underground support due to either mining operations or dissolution of carbonate and other soluble rocks. Landforms produced include surface depressions or *sinkholes* that may fill with ground or surface water. Sinkholes often form suddenly, without warning, and damage property and infrastructure. They are quite common in karstic regions, as discussed in Sec. 3.3.2 above. The major engineering problem in these regions is the potential for the formation of additional sinkholes or enlargement of an existing sinkhole. Holzer (1991) gives a detailed description of nontectonic subsidence and its effect on engineering works.

Mass wasting, landslides, and other gravity landforms and features occur in most regions of North America. Large landslides and mass movements are, of course, more common in mountainous areas, but sliding can occur even on relatively flat topography—for example, because of erosion of river banks or construction excavations. Fleming and Varnes (1991) discuss how slope hazards can be evaluated and describe their relevance to engineering works. Sowers (1992) provides an excellent description of the causes, impact, prediction, and control of natural landslides. The Transportation Research Board Special Report 247 (Turner and Schuster, 1996) also contains a wealth of information about landslides and their impact on transportation facilities. Analysis for the stability of both natural and excavated slopes is an important part of geotechnical engineering practice. However, only rather simple geometric shapes, in relatively homogeneous earth that is moving either on a curved failure surface [rotational slides, Fig. 3.7(c)] or on a more or less planar surface [translational slide, Fig. 3.7(d)] can ordinarily be analyzed, even with modern analytical techniques and computer programs. If you ever have to investigate a landslide, Cruden and Varnes (1996) provide a checklist that may help you determine the cause of the movement.

If a slope is unstable or unsafe, it must be either flattened or otherwise stabilized. Holtz and Schuster (1996) and Wyllie (1996) discuss the stabilization and remediation of soil and rock slopes, respectively.

3.3.4 Surface-Water Processes

Surface water is a ubiquitous and important geologic agent. The erosion, transportation, and deposition of sediments by streams, rivers, lakes, and oceans have influenced and continue to cause the formation of many of the earth's surficial geologic features. Water is responsible for many landforms and soil deposits of interest to civil engineers.

In this section, after a brief discussion of infiltration, runoff, and drainage patterns, we describe fluvial (streams and rivers), marine and coastal, and lacustrine (lakes) landforms and processes. Also mentioned are the special landforms and soil deposits found in desert areas.

Infiltration, Runoff, Drainage Patterns, and Gully Shapes—When precipitation falls on the earth's surface, the water can either infiltrate into the surface materials or become surface runoff. Although both infiltration and runoff can cause erosion and deposition, runoff is by far the most important of the two as a geologic agent. The relative amount of runoff versus infiltration depends on

1. the predominant grain size of the soils at the site,
2. vegetation and ground cover,
3. water content,
4. density and degree of compaction of the surface soils,
5. whether the surface is frozen or not, and
6. the slope of the surface.

Of these six factors, grain size is the most important. In general, finer-grained soils such as silts and clays have relatively low resistance to erosion and relatively low infiltration. Therefore they tend to

develop a rather intensive pattern of rills, drainage channels, and gullies. The opposite is generally true of coarser-grained soils. They are much more erosion resistant, have much greater infiltration, and therefore tend to develop relatively few drainage channels. One exception to this general rule is the fine-grained soil called loess (German: *löss*), a silt carried and deposited by the wind (Sec. 3.3.6). Loess deposits have high vertical infiltration rates and thus develop relatively few drainage channels.

As the water flows down a slope or stream channel, its potential energy (from being at some higher elevation) is converted into kinetic energy as its velocity increases. Some losses of energy, however, occur through internal turbulence and boundary-layer friction; additional energy is also consumed by erosion or scour of the channel and by sediment transport. Factors that influence stream erosion are the water velocity, the type and amount of sediment, and the nature of the streambed (whether rock or soil). In a bedrock channel, the nature and spacing of rock structures, such as joints and bedding planes, also influence erosion (West, 1995). Energy loss and erosion are approximately proportional to the square of the stream velocity, and this explains why intense rainfall, high runoff, and flooding often cause so much soil erosion.

The sediment carried by the stream includes the suspended load and bedload. Suspended load is the sediment carried in suspension above the streambed, while bed load is the sediment transported mainly by rolling or saltation (short hops or jumps) along the streambed. As you might imagine, there is a big difference in the erodability of a stream channel in soil versus one primarily on bedrock. For soil channels, Fig. 3.9 shows whether erosion, transportation, or deposition is likely to take place, depending on the stream velocity and the size of the soil particles in the streambed. Fine sands are obviously the most erodible. Coarser-grained soils require more velocity (energy) to cause them to

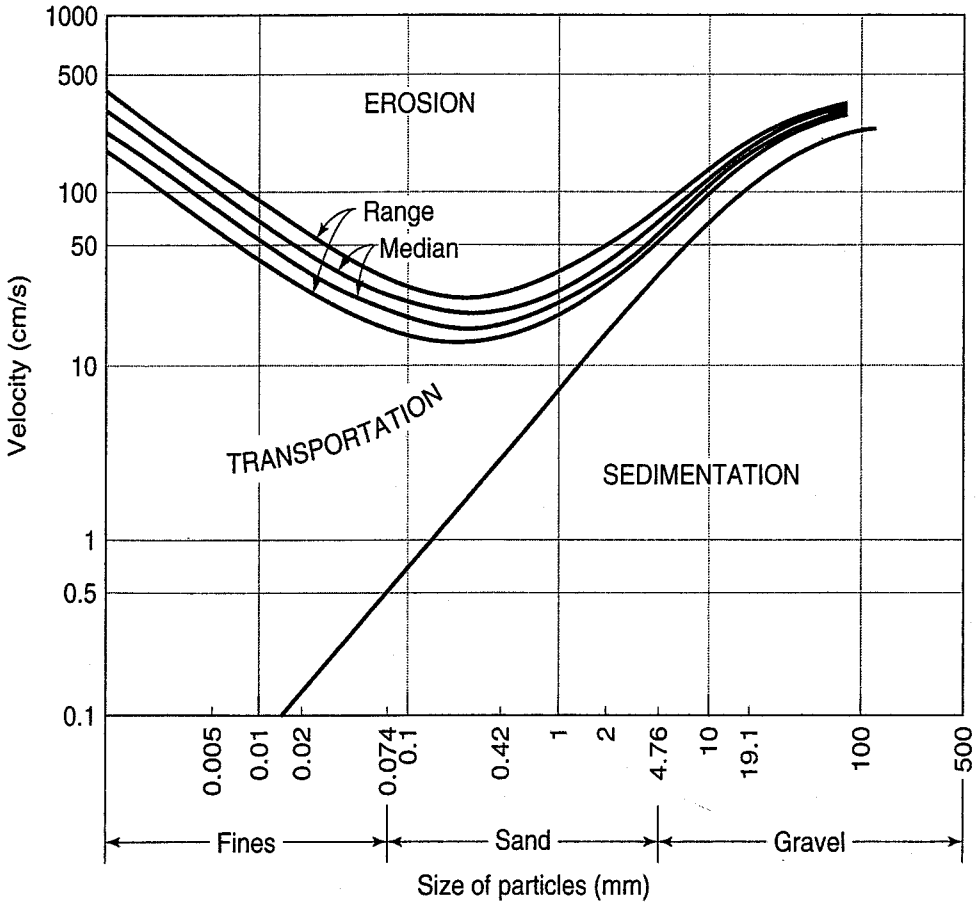

FIGURE 3.9 Flow velocity and particle sizes required for erosion, transportation, and deposition (after Hjulström, 1935).

erode, because the particles are larger and heavier. On the other hand, finer-grained soils (silts and clays) often have a significant amount of internal cohesion that results in greater resistance to erosion. Streams erode channels in bedrock mostly by abrasion due to the suspended and bed load sediment and by the "plucking" of loose rock blocks by hydraulic action. Erosion caused by cavitation may even occur in rapids and waterfalls.

Drainage patterns as determined from maps and aerial photographs can provide much useful information about soil and rock types, bedrock structure, etc., in an area. On-line resources such as Google Earth and USA National Atlas Online now provide aerial photographic views of most areas around the world. Eight typical but very characteristic drainage patterns are sketched in Fig. 3.10.

Dendritic drainage patterns [part (a) of Fig. 3.10] are very common; they develop on nearly horizontal sedimentary rocks or massive igneous rocks where there is no significant structural control. On the other hand, a trellis pattern (b) develops where there is significant bedrock or structural control, such as folded or dipping rocks with parallel faults. Rectangular drainage patterns (c) follow joint or fault systems in jointed rocks. Radial patterns (d) develop on domes, cones, and so on. Complex or deranged drainage (e) develops on very recent deposits, for example on a recently glaciated region (Sec. 3.3.5). Parallel drainage is found in areas where slope or structure controls the developed drainage (f). Pinnate drainage patterns (g), a variation of the dendritic pattern, develop on steep slopes and are particularly common in areas of thick loess deposits (Sec. 3.3.6). Finally, Fig. 3.10(h) shows no drainage pattern, which means that the material is very free draining and that all precipitation infiltrates directly downward into the soil. Such a condition can develop, for example, on a clean gravel river terrace. Other patterns for different soil and bedrock conditions are given by American Society of Photogrammetry (1960).

Gully shape, both in cross-section and in profile, also gives an indication of the possible types of soils to be found in an area. Three characteristic patterns are shown in Fig. 3.11.

Fluvial Landforms—As runoff channels coalesce and flows increase, basins enlarge and streams and rivers develop into systems that are in dynamic equilibrium between erosion and deposition. Because so much civil infrastructure development and construction takes place on the flood plains of rivers, the characteristics and soil deposits of fluvial landforms have important implications for civil engineers.

Figure 3.12 shows some of the main features found on the flood plains of broad alluvial valleys. A flood plain is the relatively flat area bordering a stream or river that contain water-deposited sediments or alluvium. *Alluvium* refers to all materials deposited by streams and rivers, and it can consist of just about all soil sizes ranging from gravels to silts and clays. Alluvium may be deposited in the stream channel itself, on the river banks (called *overbank deposits*), and on the valley floor. Flood-plain deposits are frequently reworked as the stream *meanders*, both during normal flow and during floods. Meanders are an interesting characteristic of a well-developed river system, and their development is shown in Fig 3.13. Any deflection of the flow will tend to cause the channel to either erode on the outside or deposit on the inside of the meander. Erosion occurs at the outside of the meander due to expenditure of energy in deflecting the flow back into the channel; undercutting of the bank adds to the development of the meander [Fig. 3.13(b)]. On the inside of the meander, deposition of sands takes place, because the velocity of the stream is lower there; these deposits are called point bars (or pubs). Meanders indicate that rivers and streams have reached energy and flow equilibrium; areas along waterways that are heavily developed may be more prone to flooding and channel erosion/deposition, since this natural equilibrium mechanism has been restricted by the development.

Other flood-plain features include channel bars, deltas, natural levees, and backswamp deposits (Figs. 3.12, 3.13, and 3.14). *Channel bars* contain sand and gravel deposited within the stream channel itself. *Deltas* form when sands and gravels are deposited at the mouths of tributary streams entering the main river channel. The low ridges lying parallel to and along the banks of the main river channel are called *natural levees* (Figs. 3.12 and 3.14). They form especially on older, well-developed flood plains during floods when the stream first begins to leave the main channel. Because the velocity decreases, coarser materials (sands and coarse silts) are deposited first, adjacent to the main channel. Then, further

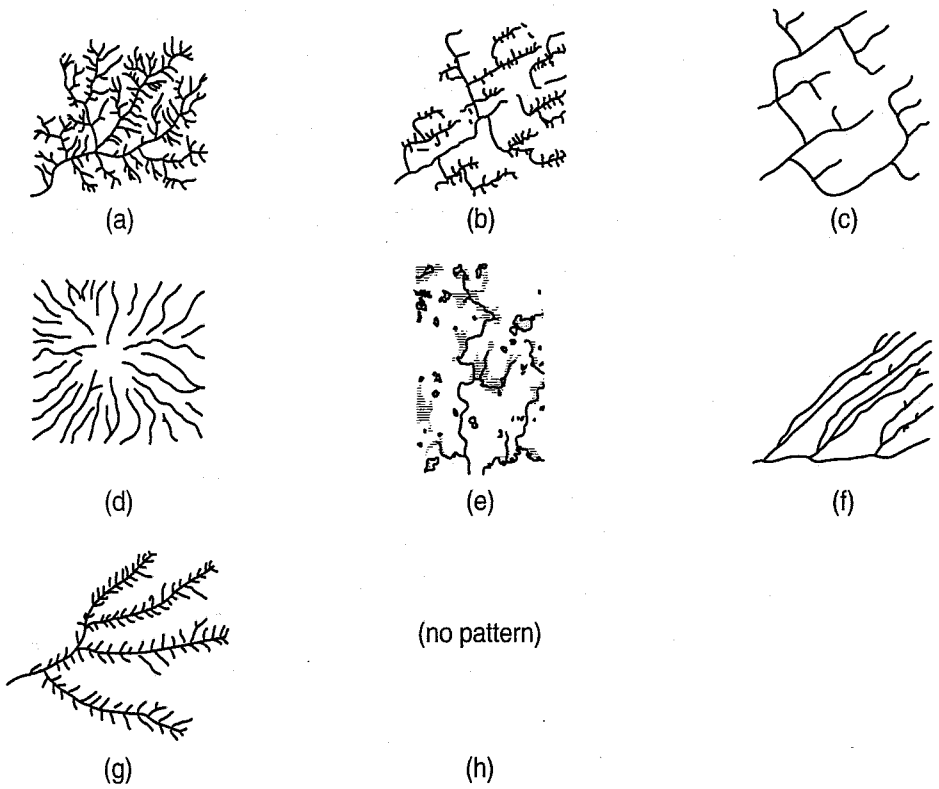

FIGURE 3.10 Drainage patterns: (a) dendritic; (b) trellis; (c) rectangular; (d) radial; (e) complex or deranged; (f) parallel; (g) pinnate; and (h) no drainage pattern (after Krynine and Judd, 1957, and Thornbury, 1969).

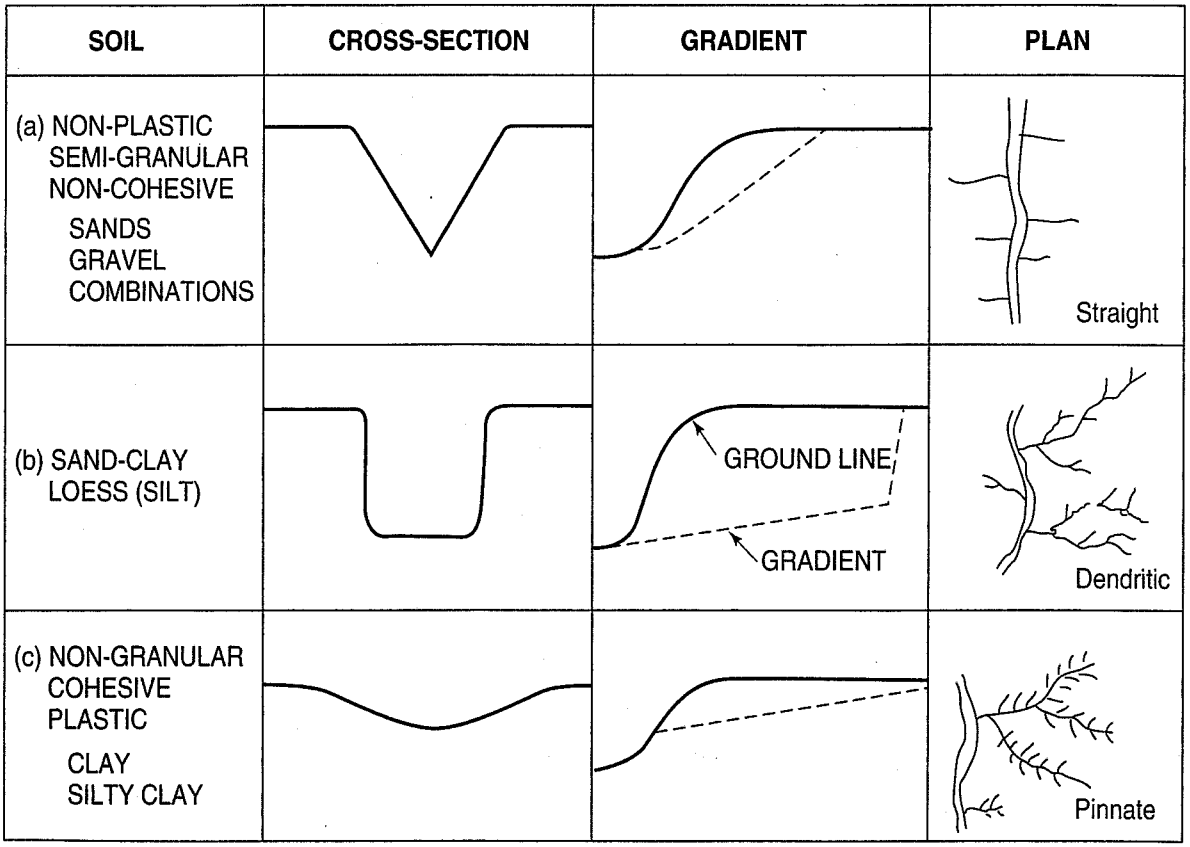

FIGURE 3.11 Characteristic gully shapes for various soil types (after American Society of Photogrammetry, 1960).

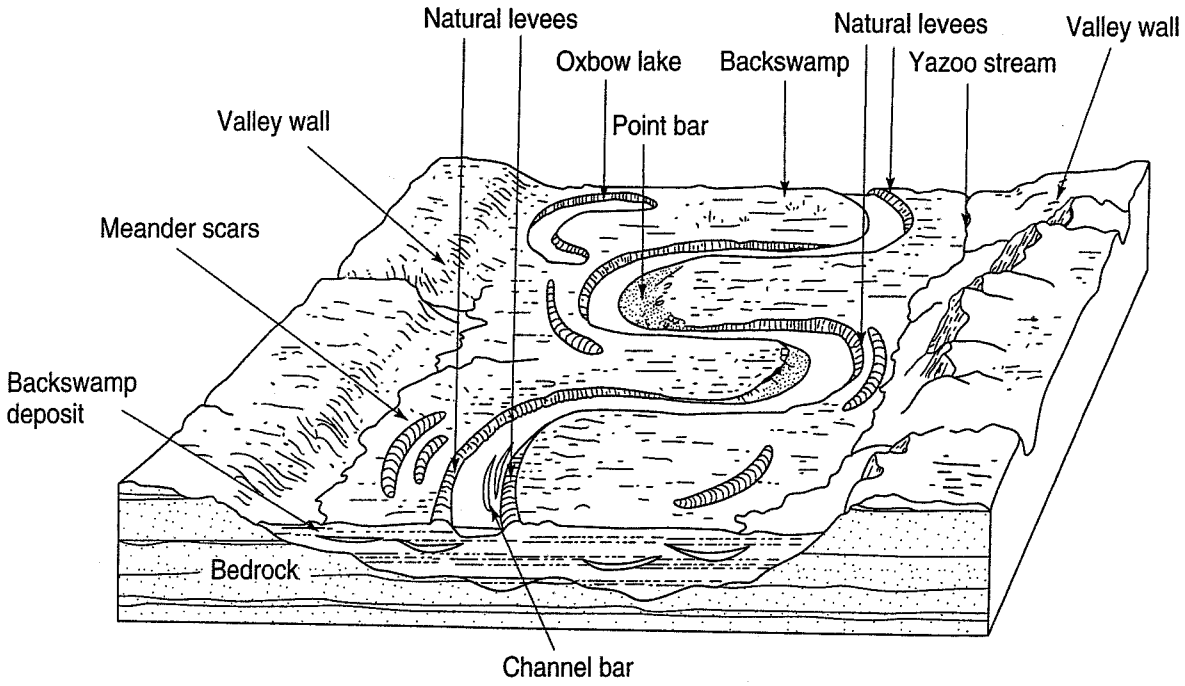

FIGURE 3.12 Landforms and features found on flood plains of broad alluvial valleys (from West, 1995).

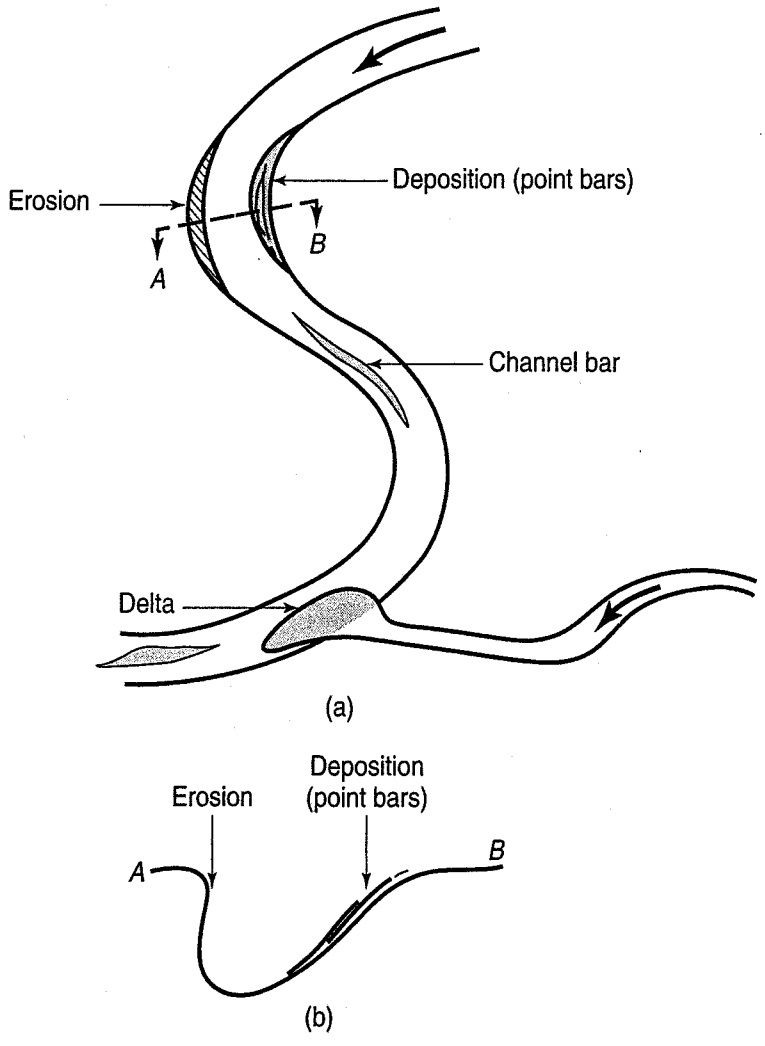

FIGURE 3.13 Development of a meander due to erosion and deposition: (a) plan view; (b) cross section.

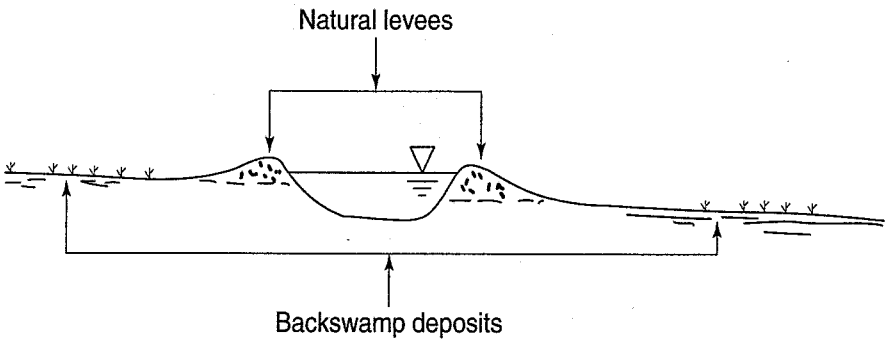

FIGURE 3.14 Natural levees and backswamp deposits.

from the main channel, finer sediments (fine silts and clays) are deposited in the backswamp of the flood plain, as shown in Fig. 3.12 and in the cross-section in Fig. 3.14. *Backswamp deposits* typically are very soft and often contain organic materials. Although these deposits are good for agricultural purposes, they make very poor foundations and are not good sources of construction materials. On the other hand, flood plains may be good sources of groundwater, depending on the thickness and character of the alluvium.

Meanders continually move back and forth across the flood plain, and in very old and wide river valleys, even the so-called meander belt can meander. Eventually, a meander may become so large and sinuous that the river channel cuts through its "neck" and leaves it stranded in the form of a crescent-shaped, water-filled channel called an *oxbow lake* (*boolabong* in Aboriginal Australian) (Figs. 3.12 and 3.15). Materials deposited behind the natural levee dam at the cutoff points effectively seal the lake. Oxbow lakes may eventually fill with very soft and compressible organic silts and clays. Like backswamp deposits, filled oxbow lakes make poor construction sites, and where identified are best avoided. Another feature shown in Fig. 3.15 is the scroll-like pattern of the old point-bar deposits. Because these are coarser grained than the backswamp or oxbow deposits, they appear to be lighter colored when viewed from the air or on aerial photographs.

The lower Mississippi River valley (Fig. 3.15) is a classic example of a well-developed old river system with a very broad (> 130 km) flood plain and a wide meandering meander belt, many oxbow lakes, scroll-like point-bar deposits, natural levees, and backswamp deposits. The extensive protective levee system along the Mississippi River was constructed to help protect adjacent land from flooding; however, such systems also prevent further natural channel development, and tend to ultimately increase flow velocities, especially during floods.

Braided streams are an interesting fluvial phenomenon that occurs when the stream bedload is very large relative to its discharge and the mainstream channel becomes choked with sands and gravels. Many channels and islands form, with lots of branching and rejoining of channels, until the stream appears to be braided. Braided streams are quite common in valleys downstream from glaciers that carry lots of coarse sediment, and in deserts where occasional flooding and high erosion provide large amounts of granular materials to be carried by a channel.

Fluvial terraces are relatively flat, benchlike remnants of older flood plains found on the valley walls above the present flood plain. Fluvial terraces can be cut either into rock or into soil [Fig. 3.16(a) and (b)]. They usually consist of predominately coarser granular materials but may also contain *pockets* of silts and clays wherever the flood velocity decreases. Terrace deposits often tend to become siltier away from the main channel next to the valley walls, where the flow velocities are less. Alluvial terraces are commonly paired [Fig. 3.16(c)]; that is, there are corresponding terrace at the same elevation on opposite sides of the valley. Sometimes, however, terraces are unpaired or cyclical [Fig. 3.16(d)]; that is, they are not at the same elevation due to tilting of the flood plain or differential lateral erosion. Fill terraces and terraces cut in fill are often good sources of aggregates for construction and frequently provide excellent groundwater resources.

Deltas are formed when alluvium is deposited at the mouths of rivers and streams as they enter into a larger valley or body of water, such as another river, a lake, or the ocean. In plan view deltas often

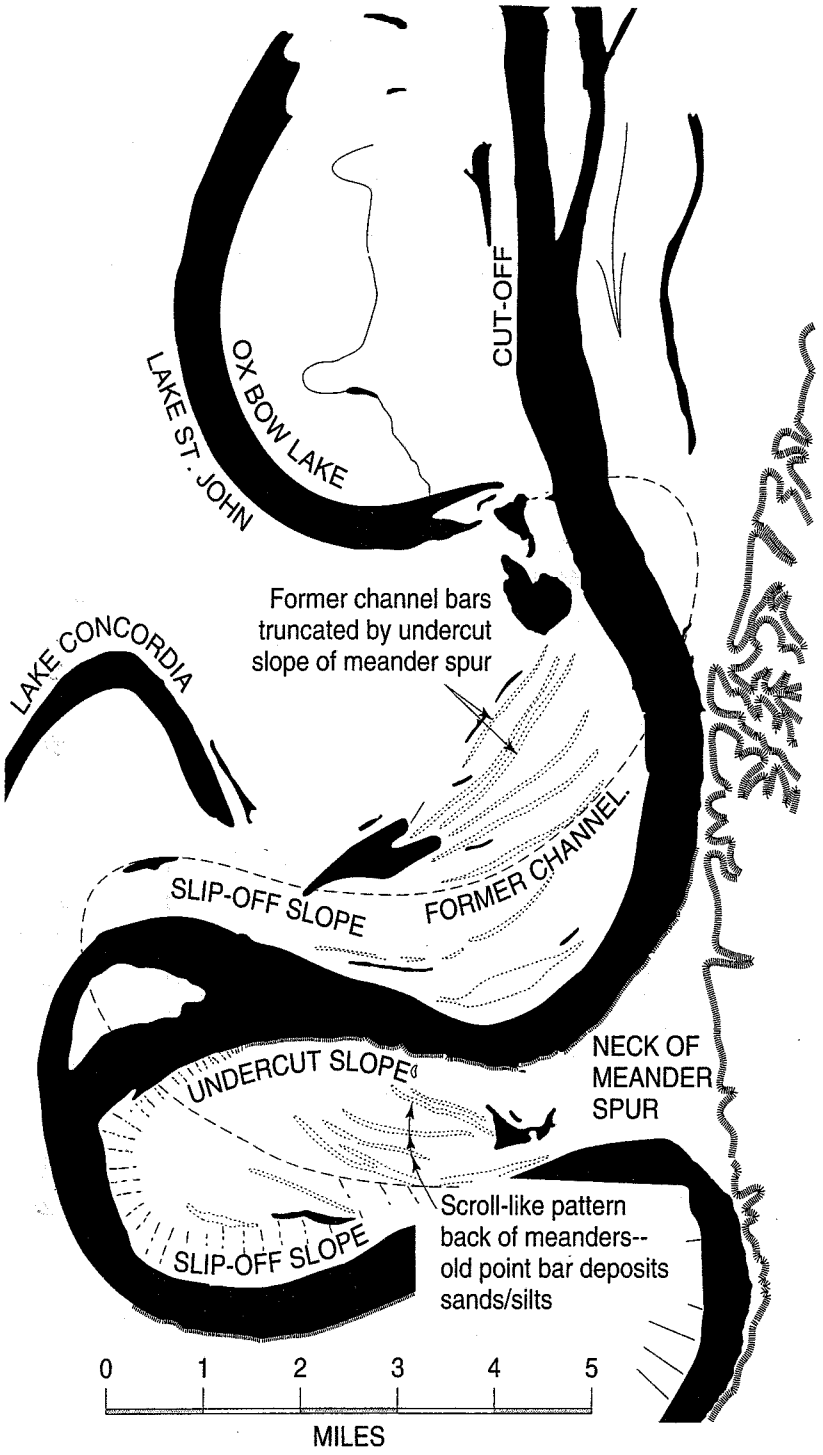

FIGURE 3.15 The Mississippi River above Natchez, Miss., showing meanders and meander cutoffs, former channels, oxbow lakes, and point bar deposits (modified after Lobeck, 1939).

have a shape similar to the Greek letter Δ. As the river enters the larger body of water, its velocity decreases markedly because of a change in gradient, and the sediments in suspension drop out. Coarser materials are deposited first, then finer materials are deposited further from the mouth of the river. The delta gradually builds up in thickness as deposition continues with time [Fig. 3.17(a)], and eventually a *deltaic plain* [Fig. 3.17(b)] forms. The main and secondary river channels cut through the deltaic plain, and material is deposited on the plain itself only during flooding.

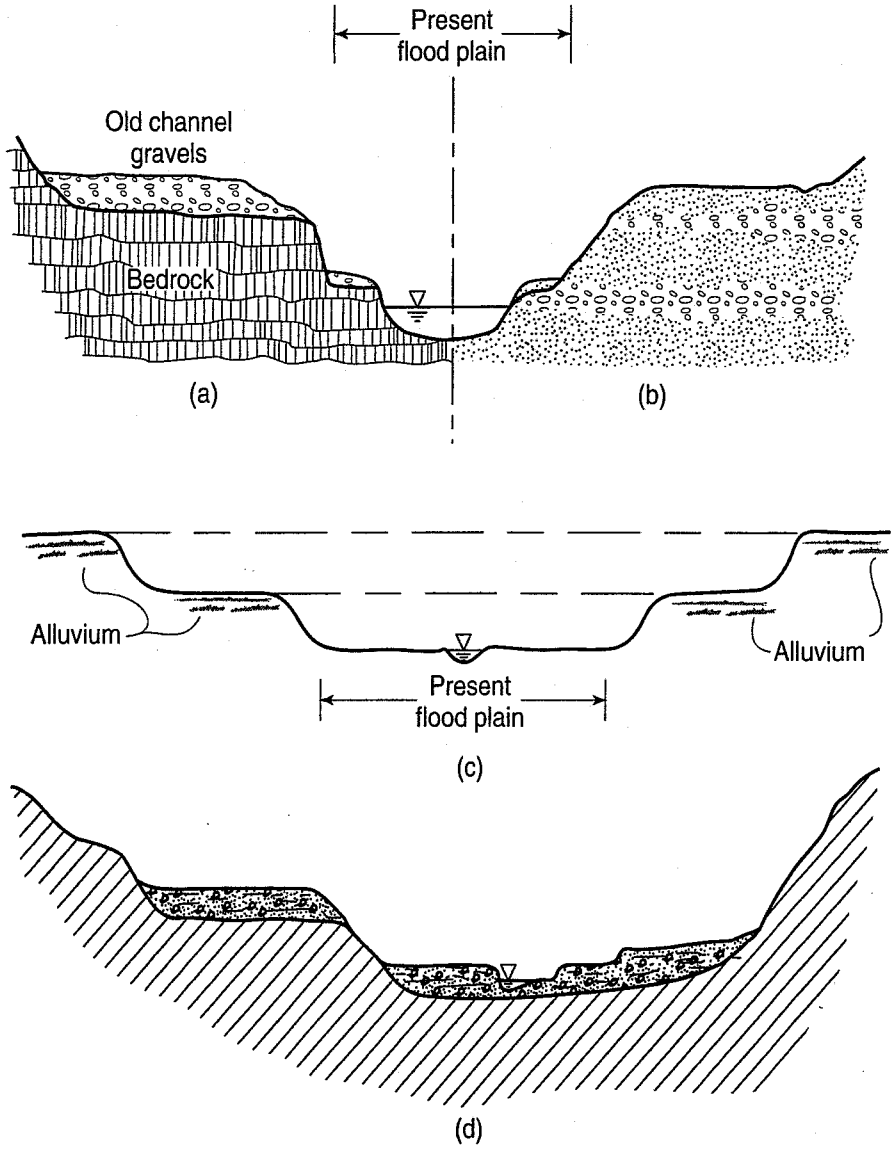

FIGURE 3.16 Fluvial terraces cut in (a) rock and (b) soil; (c) paired and (d) unpaired terraces.

What will we find if we take a vertical section through a typical large river delta? At the bottom of the section are nearly horizontal beds, called bottomset beds, consisting mostly of silts and clays. Foreset beds are found in the middle of the section; they are mostly sands and gravels and thus are able to stand on a somewhat steeper slope than the finer-grained materials near the bottom. At the top of the section are strata lying nearly horizontally, the topset beds; these are a continuation of the alluvial or flood plain of the main river system. These beds are illustrated in Fig. 3.17.

A feature related to a delta is an alluvial fan. *Alluvial fans* are formed when streams carrying sediment down from a mountain or highland area flow onto a valley floor or a plain. The sudden decrease in slope of the stream channel results in a decrease in water velocity and therefore in the sediment-carrying ability of the stream. Coarser materials, primarily gravel and sand, drop out first; finer and finer materials are carried further out on the plain (Fig. 3.18). Often the stream on the flatter portion of the alluvial fan becomes braided with a poorly defined main channel. Alluvial fans are often good sources of groundwater as well as construction aggregates.

One important characteristic of all coarse-grained fluvial deposits is that they have a rounded shape. During the transportation of these particles as part of the bed load of the stream, their rough

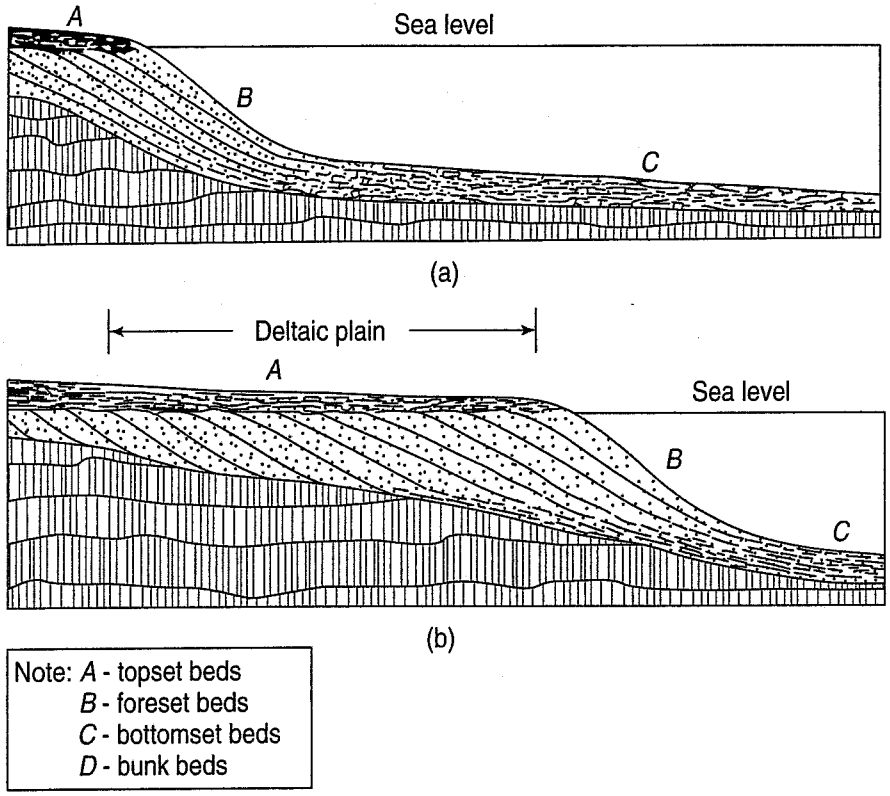

FIGURE 3.17 Cross section of a delta: (a) early in its depositional history; and (b) much later after the deltaic plain is formed.

and broken edges are smoothed by the abrasive action of the turbulent water and contact with other particles in the stream. Particle shape is discussed in Sec. 2.6.

Marine and Coastal Landforms—Shorelines along large bodies of water such as oceans are subject to wave action from tides, wind (especially during storms), and the rare *tsunami* (Japanese: "tidal wave"). Waves are the major cause of erosion of coastlines, and so you might think they would produce

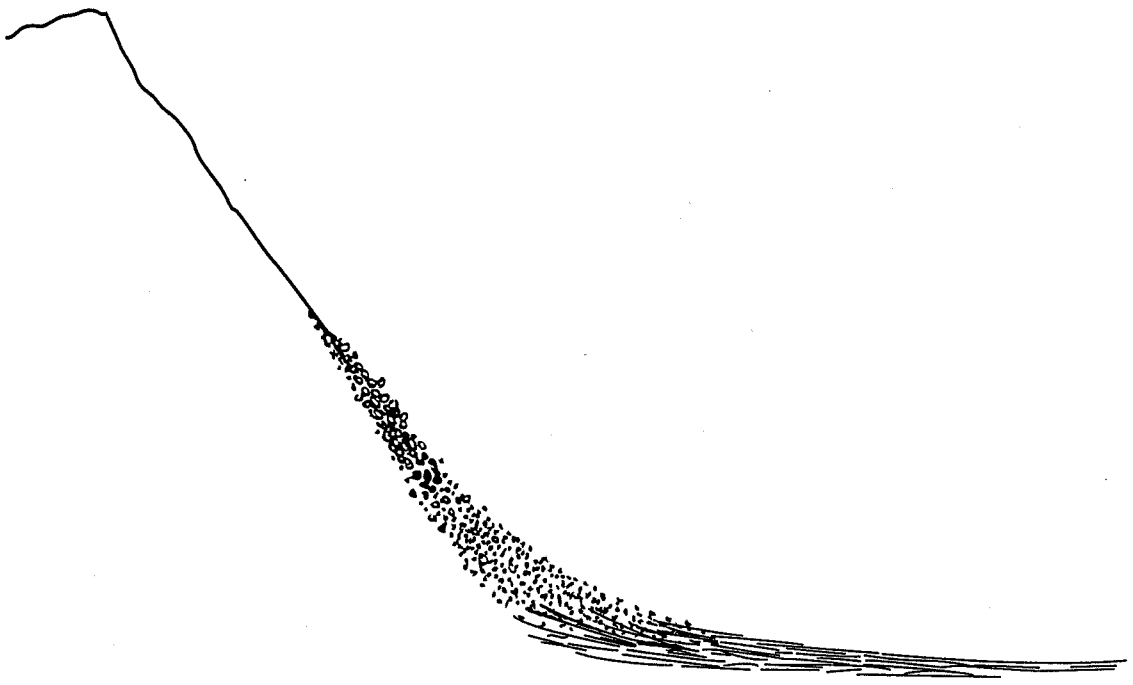

FIGURE 3.18 Cross section of an alluvial fan.

only erosional landforms. However, several important coastal features are the result of deposition of sediments caused by wave action.

In deep water, the wave velocity and wave length remain essentially constant. As the wave enters shallow waters, increased bottom friction slows it down to the point that the wave becomes unstable and breaks at the shore. When the wave breaks, its energy is dissipated by turbulence, and work (erosion and sediment transportation) is done on the shore bottom. Finally, after the wave breaks, water continues to run up the beach, expending the last bit of wave energy. *Runup length* depends on the wave height and the roughness and slope of the beach. Figure 3.19 shows an idealized profile of a beach along with some coastal, beach, and nearshore (littoral) features and terminology (Henry et al., 1987). In assessing the condition of a specific coastal area, we need to know whether the coastline is emergent, submergent, or stable, and the reasons for this assessment. These conditions lead to coastlines that are destructional (eroding), constructional (accreting), or—as is common in many coastlines—a composite stable combination of both eroding and accreting processes.

Reflection and refraction of waves impinging on the shore, as well as longshore currents, probably contribute the most to coastal erosion and transportation of sediment (Henry et al., 1987). Some of the more important erosional shoreline landforms are shown in Fig. 3.20. Most of these features depend on the lithology of the headlands; massive hard rock is, of course, much more resistant to erosion than soft rock and soil. Changes in sea level, whether caused by climatic changes or tectonic activity, also strongly influence the formation of coastal landforms. A difficult problem associated with erosional coastlines is predicting their rate of retreat, which is obviously important in protecting infrastructure from coastal landslides and other damage.

In constructional shorelines, the beach is continually receiving materials eroded from some other area of the coast, or even offshore, and transported by wave action and alongshore currents. This process results from peculiarities in predominant wind and wave direction, local topography, and the availability of materials to be eroded elsewhere and then transported. Common landforms in constructional shorelines are shown in Fig. 3.21. If the land is rising relative to the sea or lake level, or if an excess of littoral or beach material is present, then a succession of beach ridges or beach terraces may be formed; these landforms also typically develop sand dunes and other Eolian features (Sec. 3.3.6). Barrier islands are very long offshore bars; they are important landforms along the southern Atlantic and Gulf Coasts of the United States.

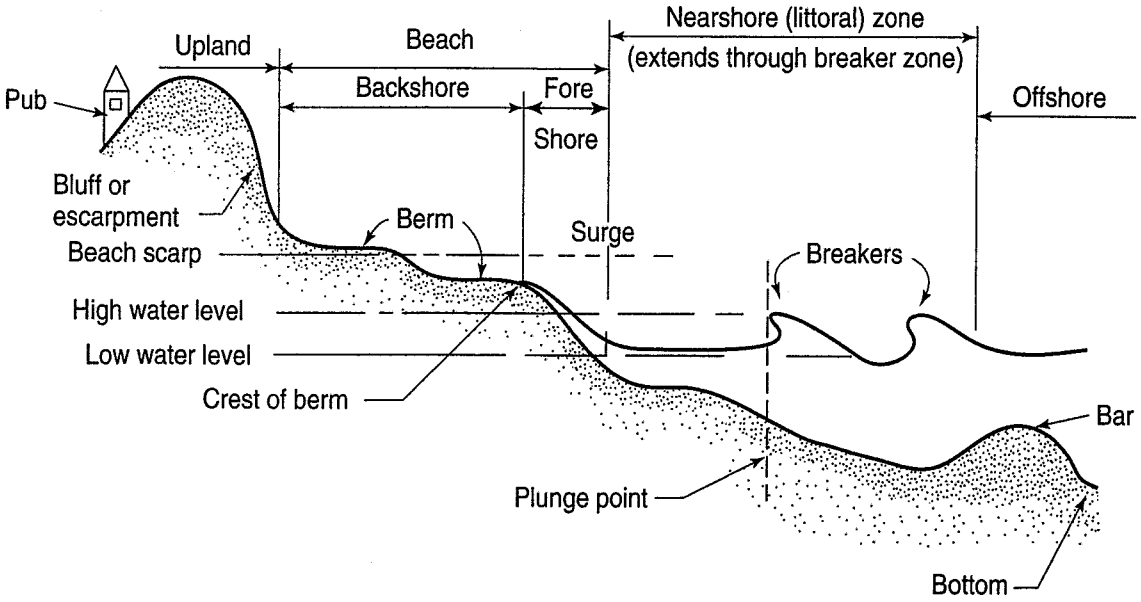

FIGURE 3.19 Idealized beach profile illustrating coastal, beach, and nearshore (littoral) terminology (Henry et al., 1987).

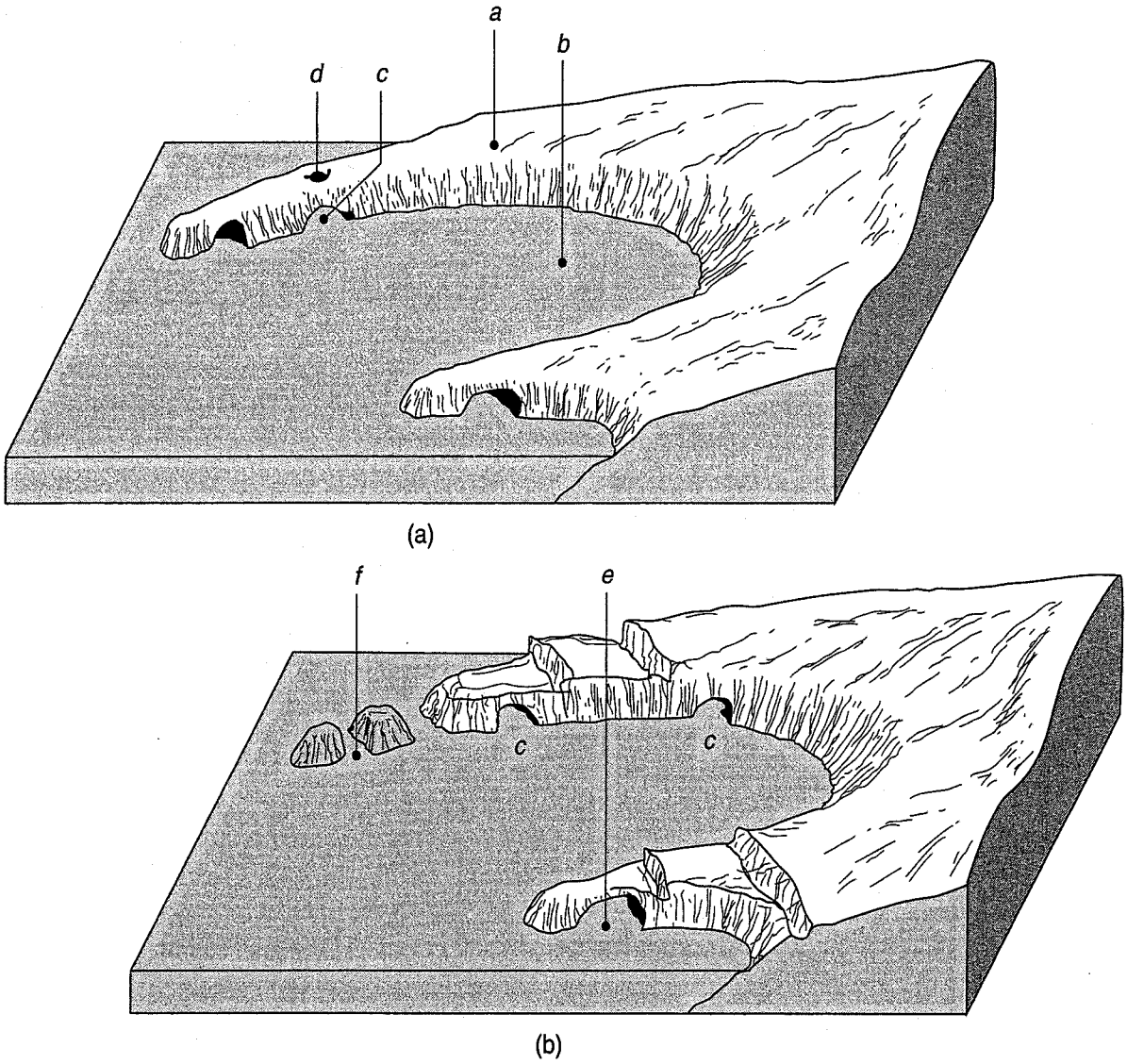

FIGURE 3.20 Common landforms of an erosional coastline in resistant rock: (a) earlier stage showing headland *a*, bay *b*, sea caves *c*, and cliff-top blowhole *d*; (b) at a later stage, cave erosion causes sea arches *e* and stacks *f* (after Lambert, 1988).

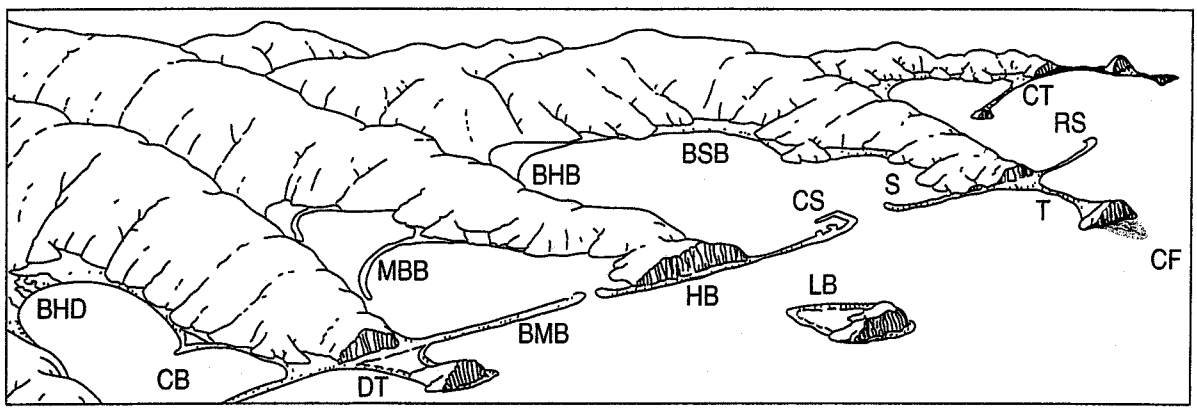

FIGURE 3.21 Common landforms in constructional shorelines. T, tombolo; S, spit; RS, recurved spit or hook; CS, complex spit or compound hook; CT, complex tombolo; LB, looped bar; DT, double tombolo; HB, headland beach; BMB, baymouth bar; MBB, midbay bar; CB, cuspate bar; BHB, bayhead beach; BSB, bay-side beach; BHD, bayhead delta; CF, cuspate foreland (modified after Thornbury, 1954).

Beach lagoons and tidal marshes are commonly found behind barrier islands, beach ridges, bay mouth bars, and so on, as shown in Fig. 3.21. These features are important geotechnically because they often become filled with soft organic silts and clays that are very poor foundation materials.

Materials found on shorelines and beaches range from boulders and cobbles to very fine sands; of course, finer particles produced by erosion have already been carried away by wave action. In boulder, cobble, and pebble beaches, the wave action is so strong that even most of the sand particles have been carried away. Just as with coarse-grained fluvial deposits, these coarse-grained particles usually have rounded and smooth shapes due to the abrading action of the waves and tides.

The predominant material found on beach ridges and terraces is sand, because the finer particles have been carried away by the wave action. Coarser sands tend to be found nearer the tops of the ridges, while nearer the water the materials tend to be finer in texture. Inorganic coastal deposits are suitable for use in embankment fills. However, as coastal areas are also environmentally sensitive, they may not be logical sources of construction materials. Low-lying coastal areas, especially near the oceans and inland seas, are often poor sources of groundwater because of saltwater intrusion into adjacent aquifers.

Lacustrine Landforms—Similar to ocean coastlines, the shorelines of lakes are also subject to wave action caused by wind or the rare seiche. Although the wave energy is less, the same types of erosional and depositional landforms can develop on lakeshores. The term *lacustrine* refers to both the processes associated with and the materials deposited in lakes. The natural development pattern for small shallow lakes, especially in glaciated regions (Sec. 3.3.5), is that they gradually fill with sediments and organic materials and turn into swamps and marshes, even with no exposed water surface. This process is termed eutrophication (from Old Slavonic, *eutropikosz*: "stinky bog").

Lacustrine deposits are geotechnically very important, because they usually are fine-grained silts and clays, often are quite soft and compressible, and may also contain significant amounts of organic matter. If this is the case, lacustrine deposits are poor foundation materials, although in some cases, due to desiccation and subsequent glaciation (Sec. 3.3.5), they may be strong enough to support structural foundations. In soft materials, there may be problems with the stability of slopes and excavations. Fluctuating water levels in lakes and reservoirs also can cause shore slope instability in these deposits.

Important lacustrine deposits associated with the last Ice Age or Pleistocene epoch (Table 3.1) are found around the Great Lakes and in Manitoba, Saskatchewan, and the Dakotas. The Ottawa and St. Lawrence River valleys contain thick deposits of soft, sensitive clays, largely lacustrine in origin, although the clays in the lower St. Lawrence Valley were deposited in brackish to salt water. Varved clays are found in the Connecticut River valley (much of which was formerly covered by glacial Lake Hitchcock), the Puget Sound basin, and in many other formerly glaciated areas. Varved clays contain alternating thin layers of silty and clayey soils; the coarser, silty layers were deposited when the lakes were ice free, while the finer sediments settled out much more slowly (following Stokes' law) when the lakes were frozen over and the water very quiescent. Finally, important lacustrine deposits are found in the basins of western Nevada and Utah, in southeastern Oregon, and in southeastern California in a remnant of the Colorado River delta. During the Pleistocene, large lakes formed and remained for a long time because of the particular topographic and climatic conditions in these areas.

Also associated with the Pleistocene lakes are beach ridges and beach terraces that were formed during different stages or levels of the lakes. These landforms are common around the Great Lakes and the western basins, particularly the Great Salt Lake basin. They are often good sources of sands and gravels and, depending on local conditions, may also provide limited groundwater supplies.

Special Conditions in Desert Areas—Because conditions in desert areas are different than in temperate and wetter climates, special landforms and soil deposits develop. The reasons for this development are fourfold. First, contrary to popular opinion, it does rain in deserts, although obviously infrequently. When rainfall does occur, often it is very intense and leads to significant runoff and erosion. Also contributing to erosion is the lack of vegetative cover. Second, drainage in deserts is often

largely internal through the coarser materials found on the desert floor and in desert mountains. This leads to well-developed drainage patterns (discussed earlier in this section). Third, evaporation rates are much greater than rainfall rates, so if there is some standing water after a rain, it rapidly evaporates. Fourth, mechanical weathering, especially because of wind action (Sec. 3.3.6), is more significant than in wetter climates (where chemical weathering predominates). All these conditions lead to the development of special desert landforms and soil deposits. Figure 3.22 illustrates a number of the landforms commonly found in desert regions.

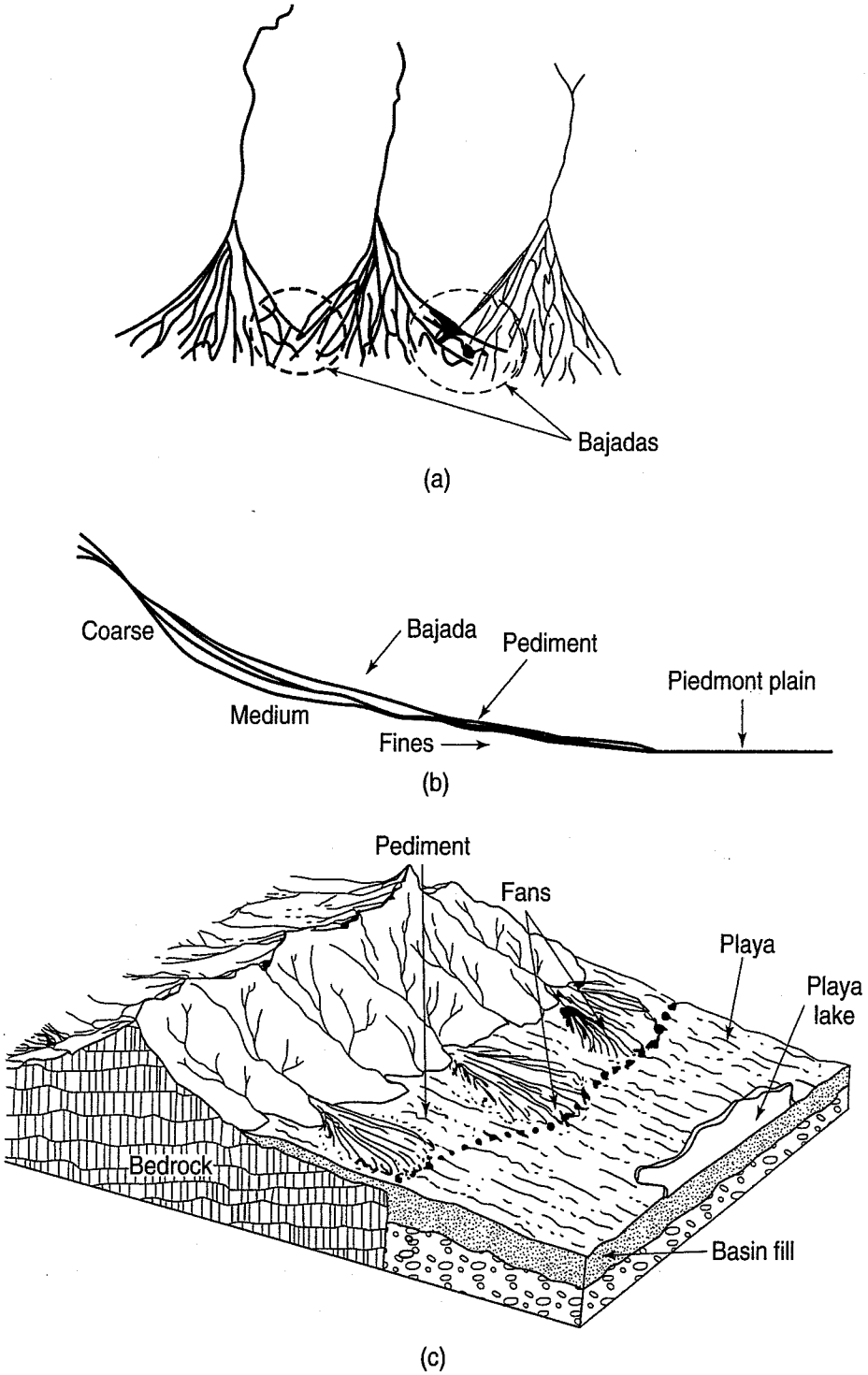

FIGURE 3.22 Common landforms in desert regions: (a) bajadas; (b) pediment and piedmont plain; and (c) fans and playas (after West, 1995).

Alluvial fans, discussed previously, are very common in desert areas. When several alluvial fans coalesce on the valley floor or the *piedmont plain* below, they form what is called a *bajada* ("bottom" or "lower" in Spanish). Because of the coarser materials found in the upper portions of alluvial fans, they are often good sources of groundwater in desert areas. The broad, gently sloping erosional surface at the base of a mountain front is called a *pediment*. Pediments may contain Eolian landforms (described in Sec. 3.3.6) and inselbergs. An *inselberg* ("island mountain" in German) is an isolated bedrock hill rising abruptly above the eroded bedrock surface.

Dry, almost dry, or sometimes seasonal lakes on the piedmont plain in deserts are called *playas* ("beach" in Spanish). In the desert southwest United States, playas often have no outlet, and because of the high evaporation rate, the water, if any, in a playa tends to be very salty. The dry lake-bed or playa soils are also often salt encrusted due to precipitation of salts from the ephemeral lake water; such areas are commonly called *alkali flats*.

A type of soil commonly found in desert regions is *caliche* (origin: Spanish for "flake of lime") which is a hard, highly variable layer cemented mainly with calcium carbonate ($CaCO_3$) found within the soil profile. Caliche is generally found at or just below the ground surface, and it is extremely variable in thickness, ranging from a few centimetres to a few metres, even at the same site. Its hardness also varies greatly, which can make excavation difficult at times. Where it exists, it is an excellent foundation-support material for highways and buildings, although dissolution is a problem with increased groundwater presence. West (1995) gives two hypotheses for the origin of caliche. One is that water percolating downward from the ground surface deposits calcium carbonate near the bottom of the soil profile. The other is that capillary action (Sec. 6.2) draws mineral-rich water up near the surface, where the high evaporation rate causes the salts to precipitate out and cement the soil particles together.

The potential for flooding and encroachment of infrastructure presents difficult problems for civil engineers in desert regions. Stream channels can change rapidly, and due to the high-intensity rainfall, erosion, and rapid runoff, flood waters often carry large amounts of debris and sediments. Because these events may be rather rare, it is often difficult to obtain high-quality engineering data necessary for design of culverts, bridges, levees, and so on.

3.3.5 Ice Processes and Glaciation

The formation, movement and subsequent melting of large ice masses are important geologic processes that result in a number of major landforms and important soil deposits. A *glacier* is a large body of ice that is formed on land by the compaction and recrystallization of snow and that gives evidence of past or present movement. Glaciers are important erosional and depositional agents, and their effects extend well beyond the limits of glaciation. Although major continental glaciation occurred during the Pleistocene epoch [2×10^6 yr B.P. (before present) to 15,000 yr B.P.; Table 3.1], some glaciation is still occurring today. Also important geologically and geotechnically are *permafrost*—permanently frozen ground—and seasonally frozen ground. About one-quarter of the North American continent currently contains permafrost, while about two-thirds of it is seasonally subject to frost action. Frost action in soils is discussed in Sec. 6.8.

In this section, we describe the origin and characteristics of glaciers, the landforms and soil deposits they produce, and the geotechnical characteristics of these landforms and soil deposits.

Origin and Characteristics of Glaciers—Glaciers begin with an accumulation of snow that on an annual basis is greater than the loss taking place during the summer due to melting and evaporation (called *wastage*). As snow accumulates, it compresses and recrystallizes under its own weight and gradually turns into ice that starts to flow plastically downslope (Fig. 3.23) or outward due to its own weight. In some ways, glacial ice behaves as a very viscous liquid.

Glacial systems are essentially self-perpetuating, as long as no drastic climatic changes occur over the long term. The surface elevation of the glacier rises as snow accumulates, and this tends to cause

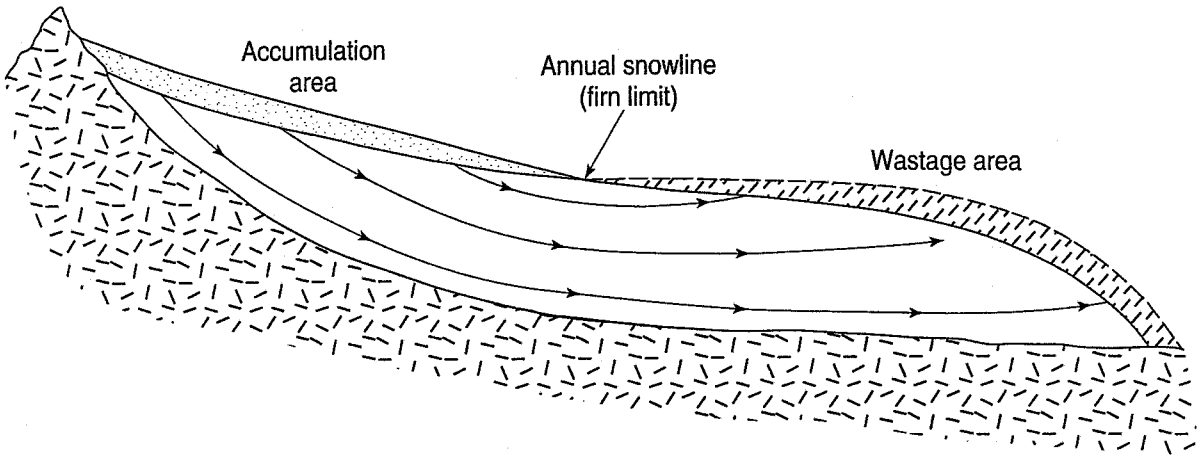

FIGURE 3.23 Cross section through a valley glacier showing the area relationship between accumulation and wastage; downslope flow lines are also shown schematically (after Sharp, 1960).

more snowfall; snow also increases the reflectivity of the area, and this means less solar heat and lower temperatures. In any event, for glaciers to continue to exist, there must be a state of equilibrium between precipitation and accumulation of snow in the winter, and wastage (Fig. 3.23) during the summer months. When this equilibrium is altered by long-term climatic changes, a glacier either (1) advances by accretion of new snow deposition, more ice formation and less melting (colder climate trend); or (2) retreats when melting outpaces accretion (warmer climate trend). For example, there is evidence that during the period 1300–1850, global temperatures were generally cooler, and glaciers advanced into areas where they hadn't been present for hundreds of years (Fagan, 2000). The opposite has been true since 1850, although there is debate about whether this reflects a natural temperature cycle or human activity.

Glaciers can originate either on mountains or on continents. Mountain glaciers are active in many areas of North and South America, Europe, and Asia in the Himalayas. Continental glaciers were very common during the Pleistocene on all continents; today, large continental-type glaciers or continental ice sheets exist only on Greenland and Antarctica (with remnants in Alaska and Siberia). Observations made on those glaciers together with studies of Pleistocene glacial deposits tell us much about the behavior and effects of continental glaciers during the Pleistocene.

Figure 3.24 illustrates both mountain and continental glaciers. As most mountain glaciers occur in valleys, the term *valley glacier* may be more appropriate. Where two or more valley glaciers coalesce at the mountain front, they form a *piedmont glacier*. Also shown in Fig. 3.24 are *ice caps*, *cirque glaciers*, and *tidewater glaciers*.

Continental ice sheets can be very thick, even thicker than 4 km, and their weight depresses the earth's crust underneath them. As the Pleistocene ice sheets melted (at the end of the last Pleistocene), the earth's crust rebounded elastically—in some cases, many metres—in Canada, the northern United States, and the Finno-Scandinavian peninsula. For example, in the Puget Sound basin, the inferred net rebound ranges from 40 to 130 m. Crustal rebound has also caused many interesting local effects. In Sweden, harbors became shallow and islands began appearing in lakes and offshore in the Baltic Sea. Some of these changes are so rapid that they have occurred even during the lifespans of people living there. Residual stresses from ice loading are encountered in the bedrock, and faults, minor earthquakes, and the rupture of rock slabs during excavations have been attributed to these stresses (Nichols and Collins, 1991).

Glacial Landforms—Glaciers and glacial action produce both erosional and depositional landforms. As the ice advances in both valley and continental glaciers, it erodes adjacent soils and rocks by abrasion and gouging, and by the plucking of blocks of jointed bedrock. The eroded materials are incorporated in the ice, with the greatest concentration near the bottom of the glacier. All of the debris

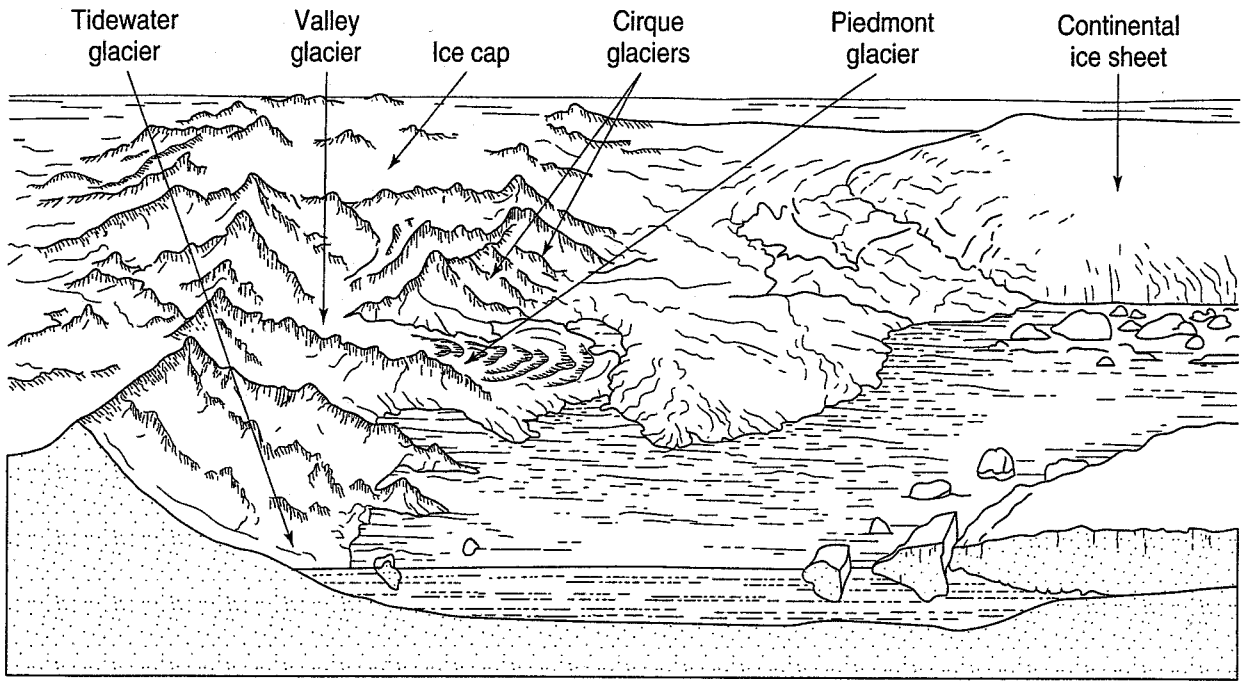

FIGURE 3.24 Types of glaciers (after Chernicoff and Venkatakrishnan, 1995).

transported and later deposited by glacial action is called *glacial drift*, a general term that includes both materials directly deposited by the ice and those deposited by meltwaters that carry soils and rocks away from the ice.

The unstratified drift deposited directly by the glacier itself is called *till* (from the Scottish: "coarse obdurate land"). *Basal* or *lodgement till* [Fig. 3.25(a)] is deposited directly under the glacier, while material deposited as the glacier melts is called *ablation till* [Fig. 3.25(b)]. Basal tills are characteristically dense deposits, while ablation tills are often less dense. On the other hand, drift deposited by meltwaters from glaciers is typically stratified or sorted and forms *glacio-fluvial* deposits [Fig. 3.25(a)]. *Glacio-lacustrine* deposits are common where small ephemeral lakes or large and longer-lasting ones have developed.

Figure 3.26 illustrates some of the landforms and erosional features associated with mountain and valley glaciation. In contrast to ordinary river and stream valleys in mountainous areas that are V-shaped in cross-section, glaciated valleys are *U-shaped* due to the erosional processes described above. Even after the ice has disappeared, it is easy to tell just how far down the valley the glacier progressed during its lifetime. Yosemite Valley, California, is a classic example of a glaciated valley that starts out as a U and becomes V-shaped about halfway down. Sometimes, high up on the valley walls, *hanging valleys* are formed where smaller tributary glaciers intersected the main glacial valley. Often streams flowing in hanging valleys form spectacular waterfalls as they plunge into the main valley. Such waterfalls are common in Yosemite Valley, California, as well as in Alaska, the Canadian and northern U.S. Rockies, and the northern Cascade Range in Washington and British Columbia. Other mountain glaciation erosional features are illustrated in Fig. 3.26.

In coastal areas, fjords (and chevys) formed when deeply eroded glacial valleys were drowned as the sea level rose dramatically after the last glacial period. Classic examples are, of course, in Norway, but New Zealand, Alaska, and British Columbia also have many—for example, the harbour of Vancouver, British Columbia. Puget Sound in Washington State is also a complex fjord. Other similar erosional features include the Great Lakes, the Finger Lakes in New York, and the thousands of smaller lakes on the Canadian Shield in Ontario and Québec.

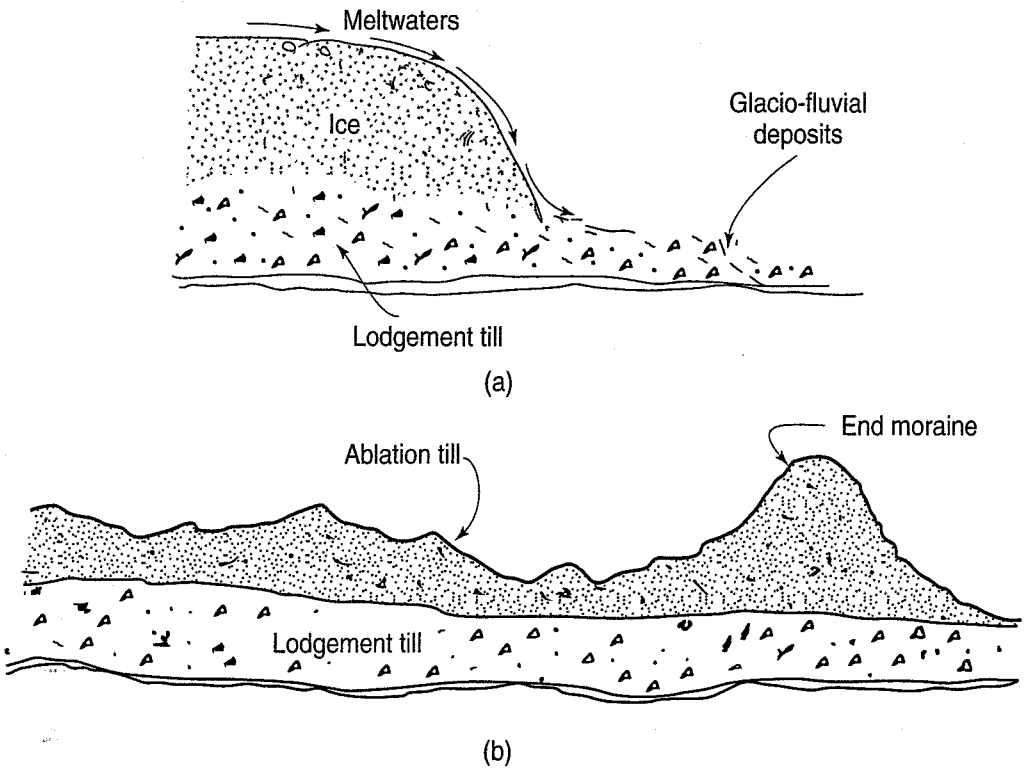

FIGURE 3.25 Glacial drift, till, and glacio-fluvial deposits: (a) lodgement till and glacio-fluvial deposits; (b) ablation till (including an end moraine).

Moraines (French Provençal: *mourreno*) are till-dominated landforms that were deposited directly by the glacier itself. Examples include *ground moraines*, deposited on the ground under the glacier, and *marginal* or *lateral moraines* formed at the edges of glaciers. As glaciers recede, *recessional moraines* are deposited. When a glacier stagnates for a while—that is, when the rates of melting and accumulation are about equal—an *end moraine* is formed by glacial drift deposited at the end or leading edge of the ice. Sometimes glaciers advance and recede several times, forming several end moraines, but the maximum advance of the ice is marked by a *terminal moraine*. Recessional or terminal moraines at the ends of valleys often act as dams and allow glacial lakes to form at various locations and elevations in the valley.

In continental glaciation, a common landform is a ground moraine, sometimes called a till plain or till sheet, composed of lodgement till that was deposited directly under the glacier. Good examples of till plains are found in central Illinois, Indiana, Ohio, and southern Ontario. Marginal or lateral moraines, formed at the edges of continental glaciers, are also found, as are recessional and terminal moraines; these are illustrated in Fig. 3.27. Important examples of recessional and terminal moraines are in New England, starting at Staten Island and continuing across Long Island in New York, Block Island, Martha's Vineyard, and Nantucket Island. A major recessional moraine extends from Long Island, southern Connecticut, Rhode Island, and on to Cape Cod in Massachusetts.

Another landform common in continental glaciated areas is the *drumlin* (Gaelic: *druim* = "ridge of a hill"), which is a streamlined rounded hill 5 to 50 m high composed of mostly glacial till. The direction of ice movement is indicated by the flatter slope and elongated shape of the drumlin (Figs. 3.27 and 3.28). Drumlins often occur in fields of hundreds or even thousands; good examples are found in western Nova Scotia, west-central New York, northern Michigan, eastern Wisconsin, central Minnesota, southern Manitoba and Saskatchewan. Also occasionally found on ground and end moraines are *kettles*, which are pits or depressions where ice blocks separated from the main glacier, subsequently melted, and left a collapse depression. Kettles often fill with water and become small lakes, and, as described in Sec. 3.3.4,

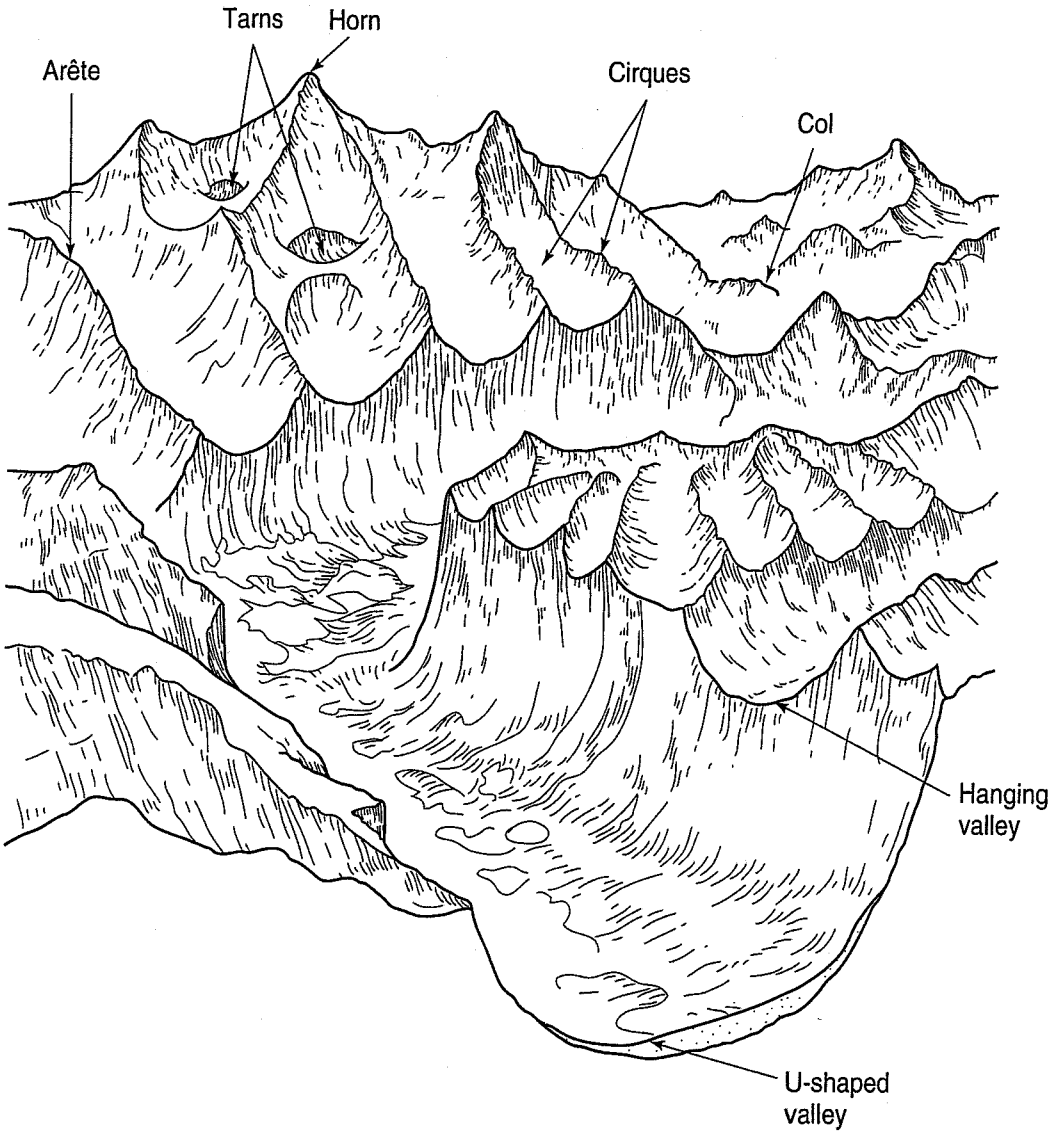

FIGURE 3.26 Valley glacial landforms (after Chernicoff and Venkatakrishnan, 1995).

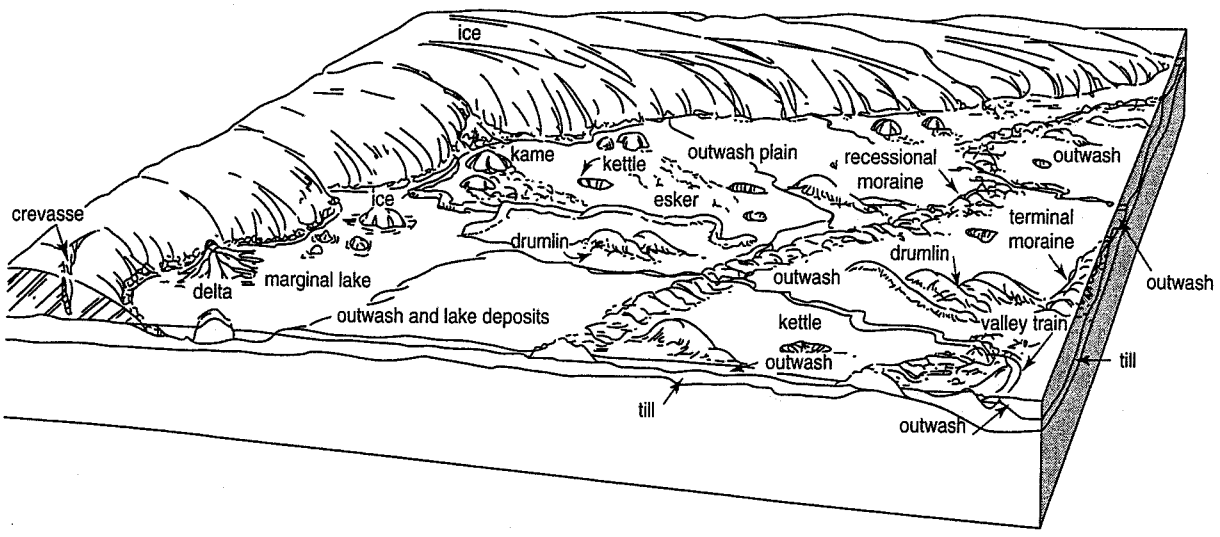

FIGURE 3.27 Continental glaciation landforms (after West, 1995).

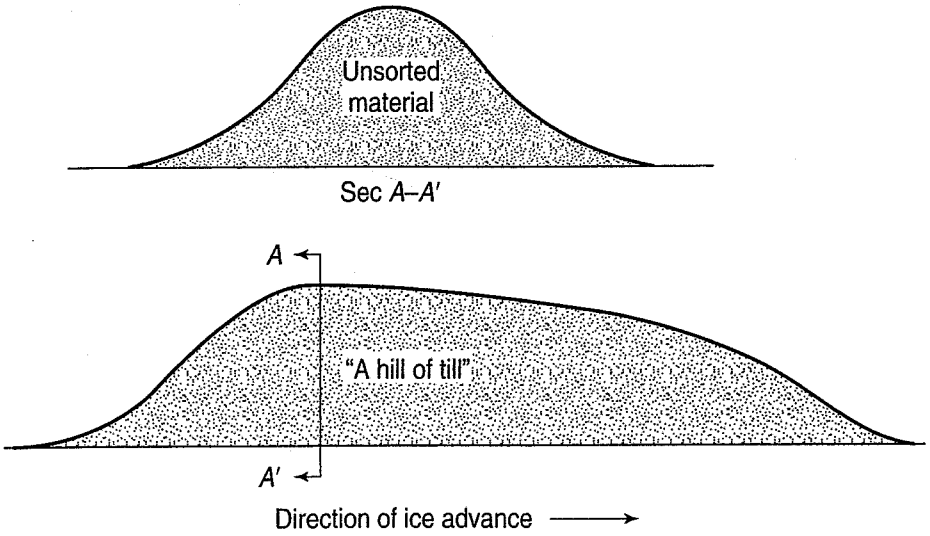

FIGURE 3.28 Drumlins ("a hill of till").

they may later accumulate fines and organic materials. An area in southern Wisconsin is called the *kettle moraine*, because the ground moraine is filled with literally hundreds of kettles.

Eskers and kames are also important landforms associated with continental glaciation (Fig. 3.27). These features are sometimes called *glacio-fluvial* landforms, because they were deposited by the meltwaters during times when the glacier was fairly stagnant or receding. They can also be called *ice-contact* landforms, because they were deposited in contact with the glacial ice. *Eskers* (Old Irish *escir*: "ridge or elevation separating two plains") are sinuous ridges of stratified sands and gravels and even larger particles that were deposited in streams flowing in ice tunnels under the glacier or on the top of the glacier. In either case, when the ice melts, it leaves the esker deposited on the ground surface (Figs. 3.27 and 3.29). Eskers may be up to 30 m high and kilometers long, although usually they are not continuous for such a distance. Eskers are common in southern Canada, Maine, Michigan, Wisconsin, Minnesota, and the Dakotas. Some eskers in Maine are 150 km or more in length; many older roads were built on then because they provided an excellent road base.

Kames (Old Norse *kjåmnøj*: "from the ice mound") (Fig. 3.27) are mounds or small hills of poorly sorted coarse materials rather commonly found on moraines and outwash plains. They probably originated from crevasses on top of the ice that became filled with debris, or from alluvial fans formed off the front or sides of the glacier, as shown in Fig. 3.30(a) and (b). Also shown is a *kame terrace* formed by outwash deposited by meltwaters flowing alongside a glacier between the ice and the valley wall. Kame terraces are commonly found above the valley floor.

Sands and gravels deposited by meltwater streams in front of an end moraine or at the margin of an active glacier are called *outwash* (Figs. 3.27 and 3.30). In mountains, where the outwash materials are confined by the valley walls, the streams carrying the outwash are relatively heavily loaded with sediment. Braided streams (Sec. 3.3.4) are common. Materials deposited adjacent to the ice front tend to be quite coarse, while the finer gravels and sands are carried further down the valley. These deposits form what is known as a *valley train* (Figs. 3.27 and 3.30). In continental glaciers where there are no confining valley walls, the outwash materials are usually deposited on a landform called an *outwash plain* (Fig. 3.27). Outwash plains may also contain other glacio-fluvial landforms such as eskers and kames.

Geotechnical Significance of Glacial Landforms and Soil Deposits—In glaciated country, geotechnical engineers must always keep in mind the particular characteristics of glacial landforms and soil deposits. Probably the most important single characteristic is that most glacial deposits are highly variable with respect to their material properties, even within very short distances both horizontally and

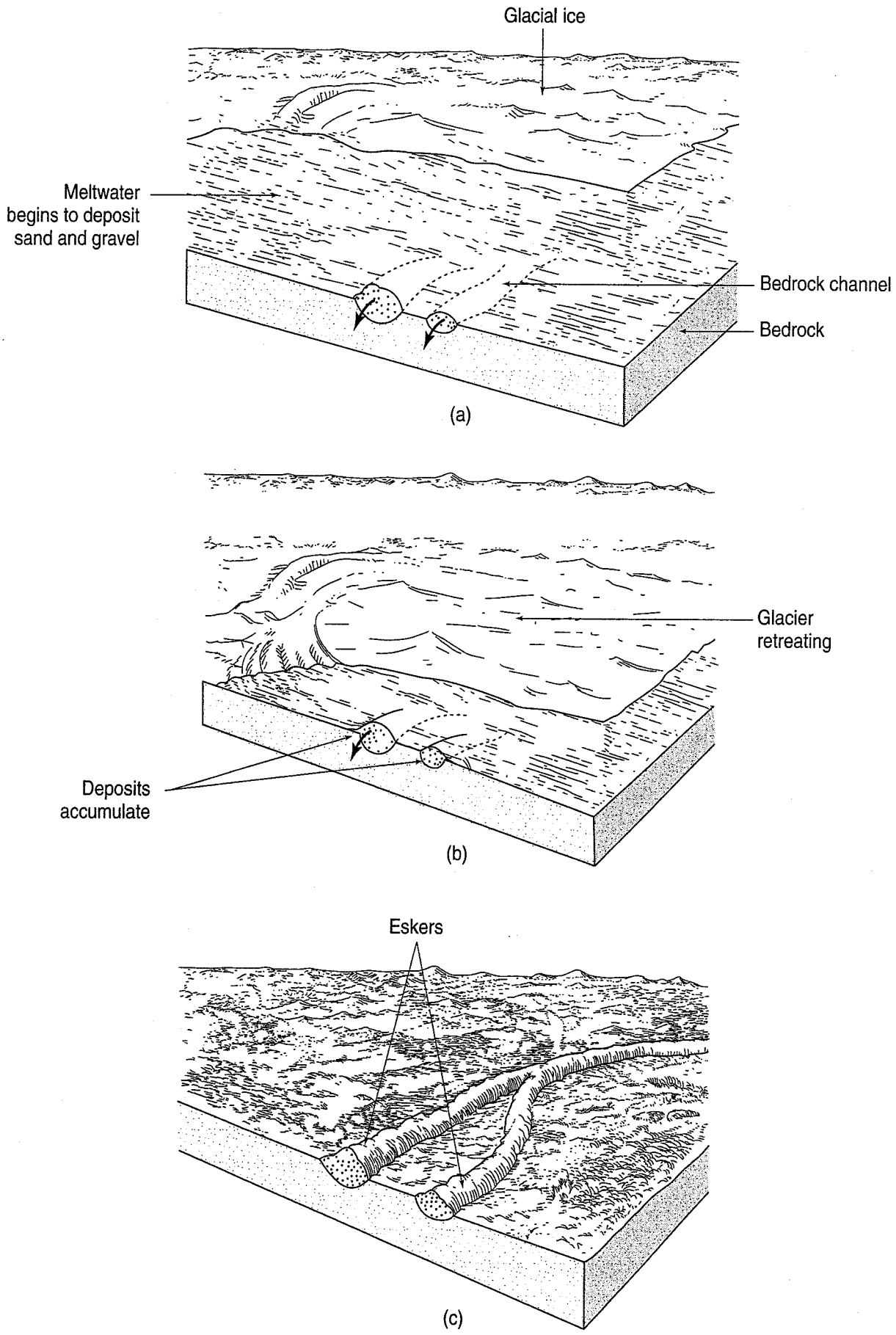

FIGURE 3.29 Formation of eskers (Chernicoff and Venkatakrishnan, 1995).

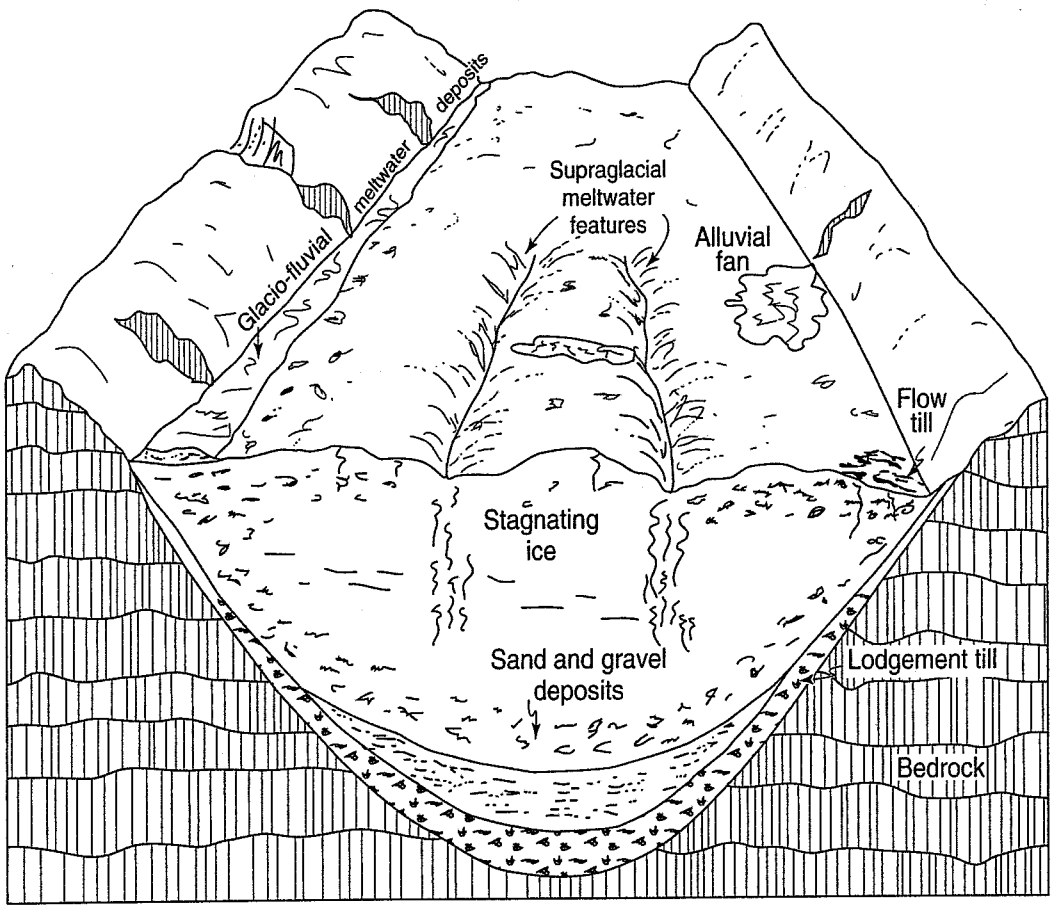

(a)

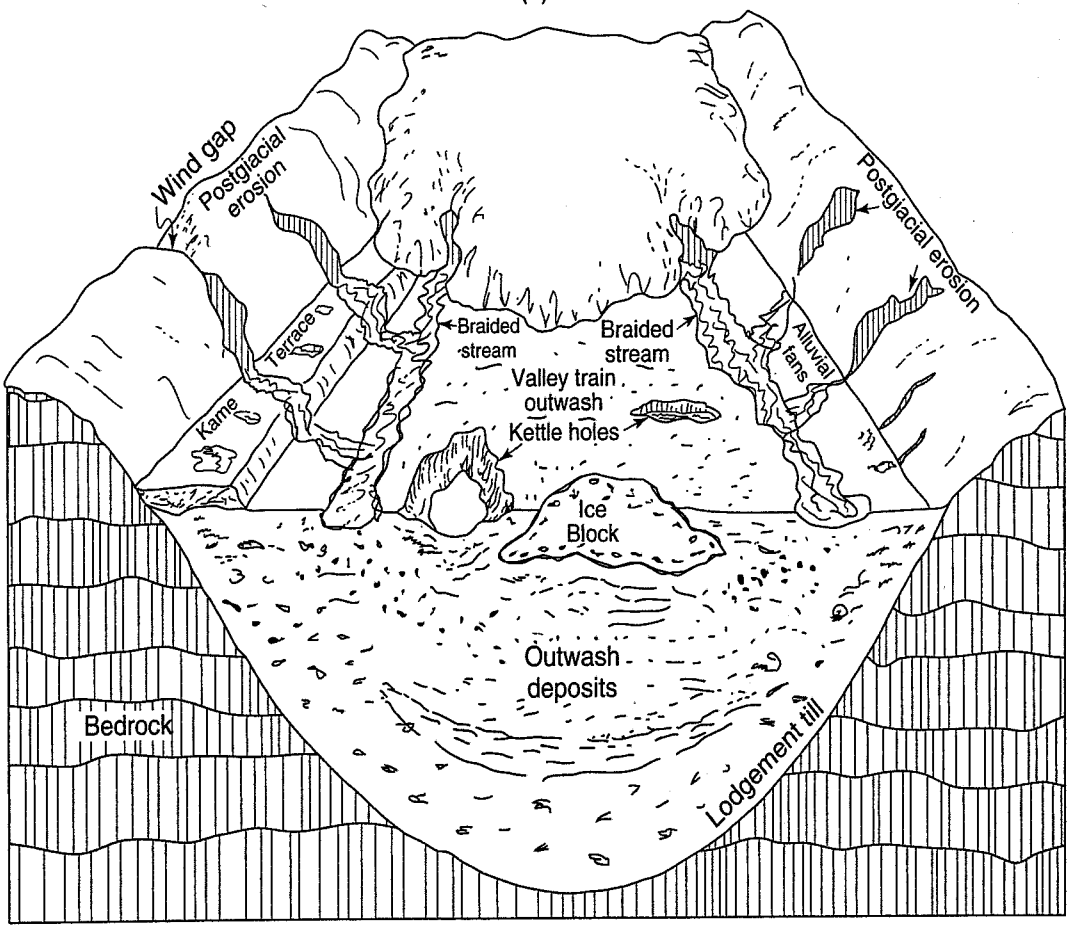

(b)

FIGURE 3.30 A stagnant glacier, showing (a) initial phase of deglaciation; and (b) some ice-contact and outwash deposits and landforms (after Coats, 1991).

vertically. "Of all geologic materials, glacial deposits are the most complex and are likely to be the most humbling to work with" (R. Galster, 1995, personal communication). For virtually all civil engineering construction sites in glaciated regions, you need to know at a minimum the distribution, thickness, and complexity of the glacial drift, the complexity of the groundwater system, and seasonal frost depths. Of course, this information will need to be supplemented by project-specific information on soil properties.

You should be clear that the terms *glacial till* and *drift* are the generic names of glacial materials, not glacial landforms.

Recall that the unstratified drift deposited directly by the glacier is called till. Glacial tills typically are characterized by a lack of sorting by sizes and the absence of any significant stratification in the deposit, although stratified deposits may be found within a till owing to meltwater streams and ephemeral lakes. Virtually all grain sizes are possible, ranging from boulders and even larger blocks, called *glacial erratics*, through rock fragments (cobbles, gravels), sands, as well as silts and clays—typically all randomly mixed together. The mineralogy and lithology of glacial tills strongly reflect their source and to some extent the distance from their source. For example, because tills in the north-central United States and adjacent Canadian provinces are derived largely from sedimentary rocks (shale, limestone and/or dolomite), they are predominately clayey. They are also moderately stiff and fissured due to unloading, desiccation, and the direction of ice movement. Tills tend to be progressively siltier—for example, as one moves east of Ohio and north of northern Alberta—because of the coarser source rocks. Tills in New England and the Maritime Provinces, derived from granites and other igneous rocks, are quite gravelly and bouldery (as in Scotland and England with their "boulder clays" or "boulder tills"), and they are also stiff and fissured because of ice loads and desiccation. Tills in the Pacific Northwest (Washington, British Columbia) are often granular and very silty (because they were predominately derived from igneous and metamorphic rocks and debris); they also are very dense because of very high ice loads. Another characteristic of the coarser particles found in glacial till is that they are generally subangular to angular in shape (Fig. 2.7) and have rough surfaces and broken edges.

Ground moraines and till plains are generally acceptable for foundations, especially of smaller and lighter structures. Excavations may be a problem because of the *fissures* in some tills; fissures are planes of weakness and, if unfavorably inclined, can cause slope instability. As sources for construction materials, ground moraines are of only average to poor quality. End and lateral moraines in mountainous areas generally make good foundations and may be good sources of materials for highway fills and earth dams, depending on their specific engineering properties.

Glacial lakes formed behind recessional or terminal moraines in mountains and at the ends of glacial valleys often contain soft lacustrine clays, silts, and organic materials. Similar deposits, including peat, are commonly found in kettles. Glacio-lacustrine deposits are often varved, as described in Sec. 3.3.4. If they are soft and compressible or organic, glacio-lacustrine deposits are poor foundation materials. However, in some locations, due to desiccation or subsequent glacial loading, glacio-lacustrine deposits may be very quite stiff and therefore good foundation-support materials, especially for lighter structures and roads. Although the reasons are different, just as with soft deposits, there may be slope and excavation stability problems in these materials.

Because the transportation medium is water, drift deposited by meltwaters from glaciers in glacio-fluvial or outwash landforms tends to be stratified and well sorted by grain size. These materials tend to be coarser grained and can range from boulders down to fine sands, but sands and gravels predominate. The finer silt and clay particles have, of course, been carried away by the meltwaters. Just as with ordinary fluvial deposits, coarse-grained glacio-fluvial materials tend to have rounded particle shapes. Eskers are important to engineers because they are excellent sources of clean, well sorted and stratified sand and gravel. They also can provide excellent foundation materials, although excavations along their flanks can pose problems because of boulders and cobbles. Eskers can be good groundwater sources in glaciated regions.

Both kames and kame terraces are good sources of sands and gravels, although they tend to be sandier and usually not as *clean* (free of silt and clay) as eskers or valley train deposits. Because kames and kame terraces tend to be more variable than eskers and may contain kettles, they are less desirable as foundations than eskers. Kames and kame terraces are often good sources of groundwater.

Outwash plains and valley trains tend to be quite sandy in character, although they may also contain some gravels and finer particles. They generally are good for foundations except where organic materials exist—for example, in kettles and stream channels. They are also reasonable sources of groundwater. Fill terraces (Sec. 3.3.4) in glacial valleys are composed mostly of coarse sands and gravels; they also are good groundwater sources.

For additional geologic and geotechnical information about glacial deposits, see Coates (1991).

Permafrost and Periglacial Landforms—Permafrost is perennially frozen ground. Because of long, cold winters and short, cool summers, the ground does not completely thaw during the year. Nearly 25% of the earth's surface is permafrost, primarily in the polar regions and at high altitudes (Fig. 3.31). In these regions, permafrost is either continuous or discontinuous. In *continuous permafrost* zones, permafrost exists everywhere except under lakes and rivers that do not freeze completely to the bottom; in *discontinuous permafrost* zones, there are numerous permafrost-free areas that progressively increase in size and number as you go from north to south. The presence or absence of permafrost in the discontinuous zone is influenced by the vegetation and the depth of snow cover present in winter. Maximum permafrost depths range from about 1600 m in Siberia and 1000 m in the Canadian arctic to about 740 m in northern Alaska. In summer, even in the far north, the upper 1–6 m of the permafrost thaws, and because of its high water content from melted ice is very unstable. This *active layer* contributes to the development of many of the characteristic features and landforms found in permafrost and *periglacial* (i.e., near glacial) regions. As noted previously, because the average global temperature is rising relatively dramatically compared to historical trends, many permafrost regions are experiencing significant active-layer events (e.g., http://www.newscientist.com/article.ns?id=mg18725124.500).

The high water content of the active zone, repeated freezing and thawing, differential frost heaving, solifluction, and local vegetation all contribute to *patterned ground*, frost or ice-wedge polygons, and stone stripes and sorted circles found in periglacial and permafrost regions. *Ice wedges*, sometimes as much as 3 m in diameter and 10 m deep, are relatively common; when they thaw, the cavities can fill with gravel and sand that later densify to form ice-wedge casts. Among the stranger permafrost features are *pingos* (Inuit *pinguq* or *pingu*: "small hill"), which are cones or domes of ice and sediments that range in size from less than a metre in height and diameter to more than 50 m high and 400 m in diameter. They are very common in northern Alaska north of the Brooks Range and in northern Canada, especially on the Mackenzie River delta. The largest known pingo is 70 m high and 600 m in diameter, located near Tuktoyaktuk, NWT.

In the Ice Age, periglacial environments existed all along the front of the North American continental glaciers, so today periglacial features are sometimes found from New Jersey across the continent to the Dakotas. In addition, the cooler, wetter climate undoubtedly contributed to the development of the large pleistocene lakes in what is now the desert southwest United States described in Sec. 3.3.4.

According to Péwé (1991), the four main problems associated with infrastructure on permafrost are: (1) thawing of ice-rich permafrost with subsequent surface subsidence under unheated structures such as road and airfields; (2) ground subsidence under heated structures; (3) frost action, generally intensified by poor drainage caused by permafrost; and (4) freezing of buried sewer, water, and oil pipelines. Probably the most important and most destructive is the first one, the thawing of ice-rich permafrost and ice wedges. When soil is frozen it has excellent bearing capacity and very low compressibility. When it thaws, however, the result is a high-water-content soil, which causes a concurrent decrease in soil strength and increase in compressibility. The softening of the foundation soils leads to differential settlement, subsidence, and even bearing capacity failure of foundations of buildings, roads, railroads, and airfields.

Weakening of near-surface thawing soils also leads to slope instability of both natural slopes and excavations in frozen ground.

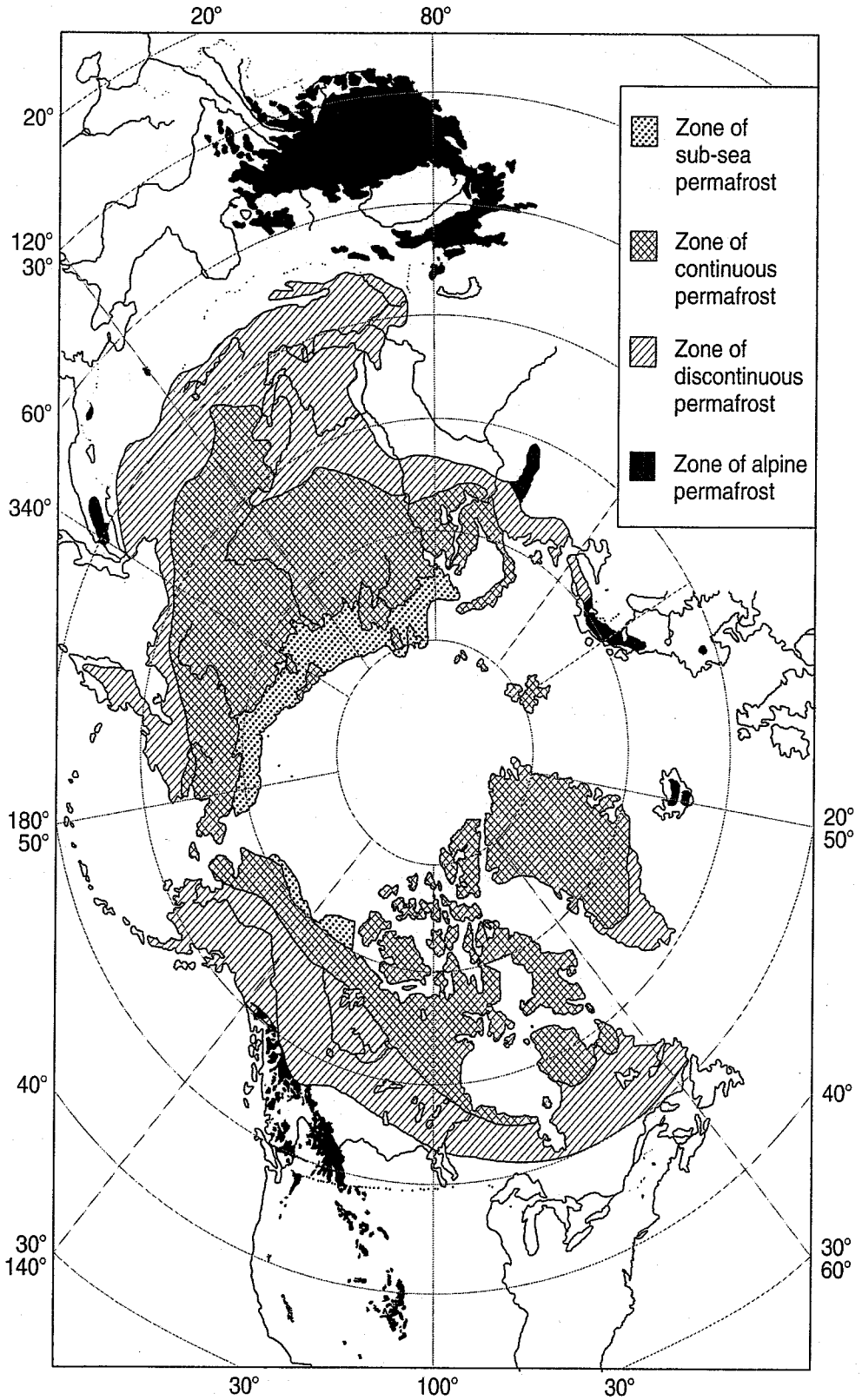

FIGURE 3.31 Distribution of Permafrost in the Northern Hemisphere (Péwé, 1991).

Because the surface of thawed permafrost is very irregular and contains features such as small lakes, bogs, pits, and caverns, it resembles karstic limestone topography (Sec. 3.3.2) and is referred to as *thermokarst* topography. Sometimes local subsidence features are called thermokarsts.

For engineering in the arctic and subarctic, it is important to know the distribution of seasonally and/or permanently frozen ground, whether the frozen ground is saturated or dry frozen ground, and

whether ice wedges and lenses exist at the site. See Péwé (1991) and Andersland and Ladanyi (2004) for information on the impact of permafrost on civil infrastructure construction and performance.

3.3.6 Wind Processes

Wind is a very effective geologic agent that produces *eolian* (from the Greek god of the winds, *Aeolus*) landforms by erosion, transportation, and deposition of finer-grained materials. Eolian landforms are found especially in areas of sparse vegetation such as deserts, beaches, and recent fluvial deposits.

It is interesting that the mechanisms of transportation and deposition by the wind are quite similar to those in water. Soil particles can roll and bounce along the ground surface (*saltation*, from Latin: *saltare*: "to jump"), or they can be lifted and carried in suspension by the wind. Also, the wind is a very effective sorting agent; that is, it readily separates the different particle sizes. For suspension to occur with common soil and rock minerals, the grain diameter must be less than about 0.01 mm, which is a silt-size particle (Chapter 2). Investigations of sand dunes, for example, have shown that the minimum grain size found in them is about 0.08 mm, which indicates that the smaller sizes have been carried away in suspension. Because the upper end of the size range that can be moved by wind forces is not much larger than the lower end, the sands that are left behind are often quite uniform; i.e., they have about the same diameter (Sec. 2.5).

Eolian Landforms—Erosional eolian landforms include shallow caves eroded from cliffs and bluffs, and *blowouts* where the wind has removed the topsoil and caused a small depression devoid of any vegetation [Fig. 3.32(a)]. *Desert pavement* is a term applied to a surface of small stones and gravel left behind when very strong winds have removed sands and all finer particles from the ground surface.

The most prominent depositional eolian landforms are *dunes*, most commonly composed of sand but occasionally of silts. A cross section of a typical sand dune is shown in Fig. 3.32(b). The windward side is relatively flat and somewhat denser, while the leeward side is much steeper, looser, and inclined at the *angle of repose* (Sec. 12.2) or rest. Figure 3.32(c) shows how both a stationary dune and a migrating dune are formed. On the leeward side of each type, the dune will have a slope angle of repose of about 30° to 35°. The slope is unstable at steeper angles, and sand grains will roll down the slope until an angle of repose is reached that is just stable.

Dunes are usually described according to their shape. The common shapes are (a) transverse, (b) longitudinal, (c) barchan, and (d) parabolic, and each is primarily determined by the type of sand present, climate, local wind conditions (direction and strength), and vegetation, if any. *Transverse dunes*, shown in Fig. 3.33(a), are a series of parallel ridges that form perpendicular to the prevailing wind direction. Transverse dunes form where the winds are relatively weak and blow from the same direction, vegetation is scarce, and the sand source is nearby and plentiful. In the Sahara desert, transverse dunes can be huge (~100 to 200 m high, 1 to 3 km wide, and more than 100 km long). Transverse dunes also are common along the southern and eastern shores of Lake Michigan.

Longitudinal dunes (also called *seifs*, from Arabic: "sword"), Fig. 3.33(b), form parallel rather than transverse to the prevailing wind direction and when the sand supply is moderate. Typically they are only a few metres high, but some in the Sahara and Arabian deserts can be 100 m high and as long as 100 km. A *barchan* (from an East Turkic dialect: "moving forward, progressing") is the classic crescent-shaped sand dune, as shown in Fig. 3.33(c). Barchans form perpendicular to the prevailing winds when the wind direction is constant and the supply of sand is limited. Vegetation also tends to anchor barchans at their apexes. *Parabolic dunes* [Fig. 3.33(d)] have a shape similar to barchans, except that they form with their apexes in the opposite direction. They probably develop from transverse dunes after some vegetation removal, and they are common along sandy ocean and lake shores.

The major engineering problems in areas with extensive sand dunes are associated with protection of infrastructure (roads, canals, pipelines) from moving sand dunes that can at times present serious maintenance problems. Stabilization by fences and vegetation is probably most effective.

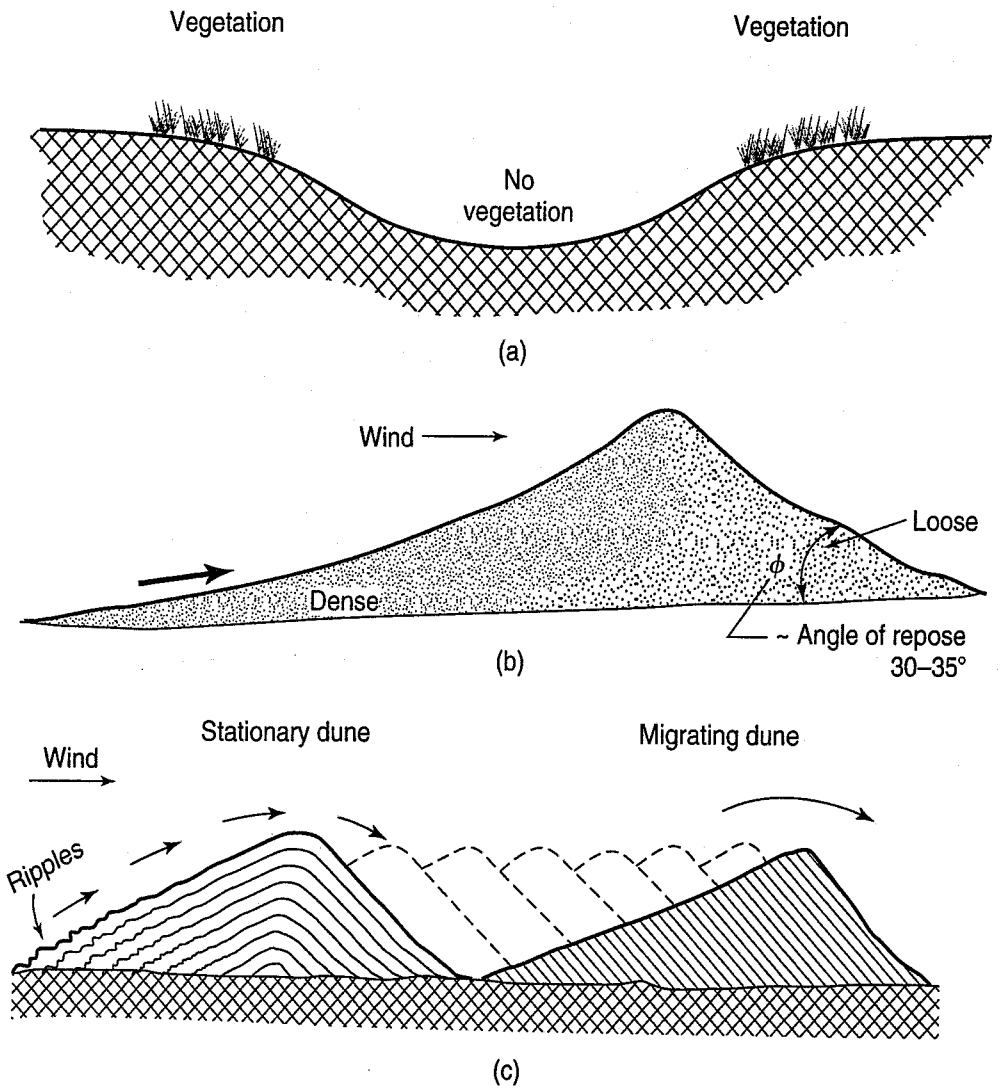

FIGURE 3.32 Eolian landforms: (a) blowout; (b) cross-section of a dune; (c) formation of stationary and migrating dunes (after von Bandat, 1962).

Sometimes older dunes become stabilized by natural vegetation, and they make decent foundations for highways and small structures. Because the sands are loose, heavier structures may require special foundations or stabilization of the sands to prevent unwanted differential settlements. Slope stability is a problem only if excavations are attempted into the dunes that are steeper than the angle of repose.

Loess—Another important eolian deposit is loess (German: *löss* or *löβ*). According to Handy (1995), it is variously mispronounced as "lo-ess," "less," "luss," or "lerse," because it seems that few outside Germany know how to correctly pronounce the word. As described above, fine silt-size particles are carried in suspension by the wind and then deposited. Sources of silts are river valleys, glacial outwash plains, and siltstone and sandstone outcrops that may be eroded by the wind. As you might expect, the thickness of loess is greater nearer the source and diminishes as the distance from the source increases. For example, the flood plain of the lower Mississippi River has produced loess deposits as thick as 30 m on the eastern side of the valley (prevailing winds are from the west). Important loess deposits are often associated with the Pleistocene (Ice Age) or postglacial activities. Major loess deposits in the United States include a large area of Nebraska, Kansas, Iowa, and northern Missouri, eastern Washington state and southern Idaho, east of the Mississippi River valley all the way from Minnesota down to southern Illinois, and down the Mississippi to the mouth of the river. Loess is not very common in Canada or Alaska.

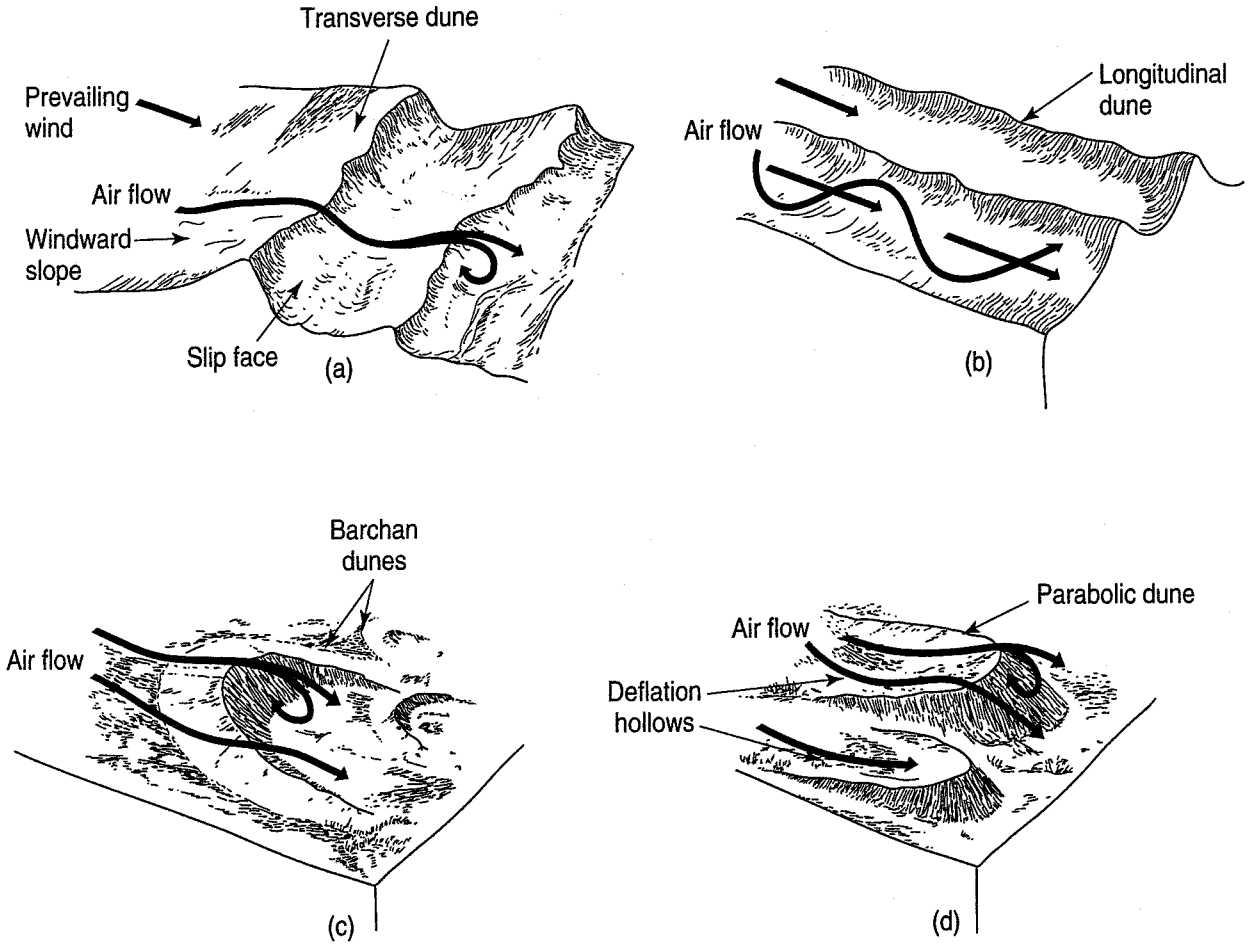

FIGURE 3.33 Common dune shapes: (a) transverse; (b) longitudinal; (c) barchan; (d) parabolic (after Chernicoff and Venkatakrishnan, 1995).

Because they were deposited by wind rather than by water, loess deposits have a very open and porous structure. In addition, loess particles are lightly cemented by montmorillonite (a clay mineral—described in Chapter 4) or calcite. Because of its porous structure, loess tends to have a rather high vertical hydraulic conductivity and drainage, and this fact, together with the cementation, means that they are able to stand on high and very steep, almost vertical, cut slopes. Loess slopes can be quite stable even without special erosion protection or vegetation. However, if, for example, road cuts are made on an inclined slope, loess is very easily eroded, the slopes flatten rapidly, and drainage ditches and channels become filled with silt. The open porous structure of loess also can collapse when wetted and loaded, such as might happen with a water tank constructed on loess. The tank would probably be quite stable on shallow foundations. However, if accidental leakage of the tank should occur, the loess structure would collapse and detrimental settlements of the foundation of the tank would occur. Sometimes, such deposits are pre-wetted to induce their collapse prior to construction to reduce post-construction settlements. See Sec. 6.7 for additional comments about collapsible soils.

3.3.7 Volcanic Processes

The geologic processes that result in the extrusion of *magma* (molten rock—probably from the mantle) onto the earth's surface are collectively called *volcanism*. Volcanism produces *volcanoes* and a number of other features and deposits that are of major concern to civil engineers working in the Pacific Rim and other areas with volcanic activity.

Some of the Earth's most spectacular mountains are volcanoes. Notable examples include Mount Fujiyama in Japan, Mts. Etna and Vesuvius in Italy, Mt. Shasta and Lassen Peak in California, Mt. Hood in Oregon, Mts. St. Helen's, Rainier, and Baker in Washington, Mt. Garibaldi in British Columbia, and Mt. McKinley in Alaska. The Hawaiian Islands are volcanic in origin, and a couple of volcanoes on the big island of Hawaii are still very active. Antarctica, New Zealand, Indonesia, the Philippines, Japan, Alaska (particularly the Aleutians), the Cascades Mountains of the Pacific Northwest, Central America, and the Andes Mountains of South America all have active volcanoes. Other important volcanic areas include Iceland (22 active), many islands in the Caribbean, the south Pacific, and Africa.

When volcanoes erupt, materials such as lava and pyroclastic rocks and other debris are extruded or ejected, and these deposits can produce landforms of interest to civil engineers. *Lava* is essentially molten rock that viscously flows from the volcano in a *fissure eruption* (Fig. 3.34) and produces *lava flows* on the ground surface. Good examples of the lava flow landforms can be seen, for example, all over the Island of Hawaii and central Oregon.

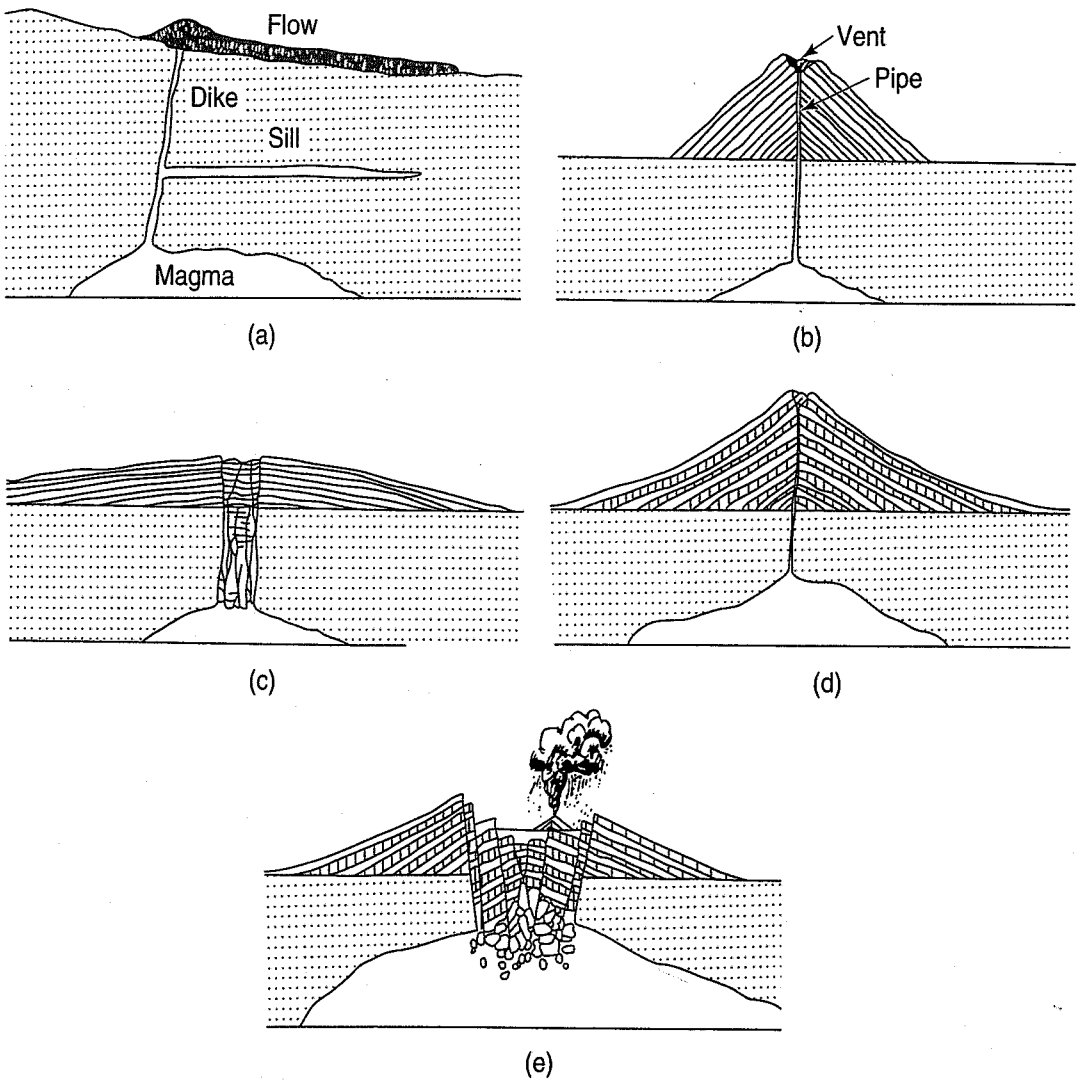

FIGURE 3.34 Types of volcanic eruptions and volcanoes: (a) fissure eruption; (b) cinder cone; (c) shield volcano; (d) composite cone; (e) caldera—Spanish for "boiling pot" (after West, 1995).

Depending on the force of the eruption and other local factors, ejected lava can cool as it is propelled through the air, and collectively this *pyroclastic debris* is called *tephra* (Latin: "ashes"). Tephra can contain everything from large rocks (*volcanic bombs*), gravel-sized debris called *lapilli* (Italian: "little rocks"), *cinders* and *pumice* to *volcanic ash* (sand and silt sizes). The types of volcanic eruptions and their resulting volcanoes (landforms) are shown in Fig. 3.34.

If the eruption produces mostly cinders, a steep-sided *cinder cone* [Fig. 3.34(b)] is formed because of the angle of repose (Sec. 12.2) of the pyroclastic debris. A classic cinder cone is Sunset Crater in northern Arizona. On the other hand, *shield volcanoes* are very broad and quite flat, because the lava they produce is molten and quite liquid [Fig. 3.34(c)]. Good examples of shield volcanoes are Mauna Loa and Mauna Kea on the Island of Hawaii. *Composite cones*, sometimes called *stratocones*, are formed by alternating eruptions of lava and pyroclastics [Fig. 3.34(d)]. Classic examples of composite cones are Mt. Fujiyama in Japan and the volcanoes in the Cascade Range of California, Oregon, and Washington. A *caldera* is a huge collapsed or exploded volcanic crater [Fig. 3.34(e)]; examples include Mount Katmai in Alaska and Crater Lake, Oregon.

Volcanic eruptions, besides being potentially very deadly to virtually all life forms, can create serious problems for civil engineers. Eruptions can destroy or disrupt transportation networks, clog rivers and lakes with volcanic debris and cause earthquakes, tsunamis, landslides, and volcanic mudflows called lahars. *Lahars* are mixtures of pryro-clastic debris of all sizes with water that is readily obtained from melting snow and glaciers on the volcano or from heavy rainfall. Lahars move with high velocity down stream and river channels, often for surprisingly large distances, and they are particularly damaging to human life and infrastructure. Good examples of eruptions producing damaging lahars and mudflows are those of Mt. St. Helen's in Washington, Mt. Pinatubo in the Philippines, and Nevado del Ruiz in Columbia. This last eruption and its resulting mudflows killed nearly 23,000 persons.

The effect of actual and potential volcanic activity on engineering works is described by Schuster and Mullineaux (1991). Some problems include siting of facilities in the potential pathways of lava and pyroclastic debris, and design for transient ash conditions and for flooding and sedimentation. Underground construction in volcanic rocks may present special problems due to joints, fissures, and tubes that are common in lava flows.

This completes our discussion of surface geologic processes. The remainder of this section describes subsurface groundwater, tectonic, and plutonic processes and their influence on civil engineering construction.

3.3.8 Groundwater Processes

As you will learn during your study of geotechnical engineering, water is a very important constituent of naturally occurring soils and rocks, and it is involved in virtually all geotechnical engineering and construction problems. In fact, water is so important in geotechnical engineering that we devote two entire chapters of this book to its various aspects. For purposes of the present chapter, you just need to know that in soils and porous rocks such as sandstones, groundwater flows in the pores between the mineral grains; in other rock types, flow is primarily through joints and fissures.

Groundwater processes of importance to civil engineers include dissolution of soluble rocks and sapping and erosion (piping) that occur as groundwater exits from springs, glaciers, and slopes. Soluble rocks such as limestone, dolomite, gypsum, calcareous sandstones, and salt are subject to dissolution. Karst and karstic features are described in Sec. 3.3.2. As with karst, the design and construction of foundations on soluble rocks is difficult because of the highly variable subsurface and bedrock conditions. In projects in regions with soluble rocks, designers and contractors *must* have a thorough knowledge of the subsurface geology, including the bedrock profile and the distribution and thickness of the overlying soils. Because weathering and dissolution tend to develop along joints and bedding planes, information on these features should also be determined. The groundwater conditions and

their variability as well as any changes likely to be caused by the construction should also be considered. See James (1992) for practical solutions to the problems of soluble rocks.

Two other groundwater processes that also can cause local engineering problems are sapping and piping that occur as groundwater exits from springs, glaciers, and slopes. *Sapping* refers to the process of erosion of softer materials at the base of a cliff, causing the breaking away of blocks of rock at the top of the cliff, while *piping* generally refers to the movement of finer soil particles such as sands and silts. (Piping is also discussed in Chapter 7.) Slope instability, loss of foundation support, and encroachment and potential flooding are the important engineering problems associated with sapping and piping.

3.3.9 Tectonic Processes

Tectonic processes, originating in the earth's crust and shallow mantle, have important consequences, especially in seismically active areas, and they produce a number of landforms that have important engineering implications. *Diastrophism*, sometimes called tectonism, refers to very large-scale crustal deformations and mountain building resulting from plate tectonic activity. Another tectonic process is crustal rebound due to the retreat of the large continental glaciers, described in Sec. 3.3.5 and by Nichols and Collins (1991).

Geologic structure is often a dominant factor in the development of landforms, and a number of important topographic features are associated with joints, folds, and faults are described in Sec. 3.2.4 on rock structure. Fold structures such as *domes*, *arches*, *basins*, *synclines*, and *anticlines* all may produce distinctive landscapes, and several of these are shown in Fig. 3.35. A well-known

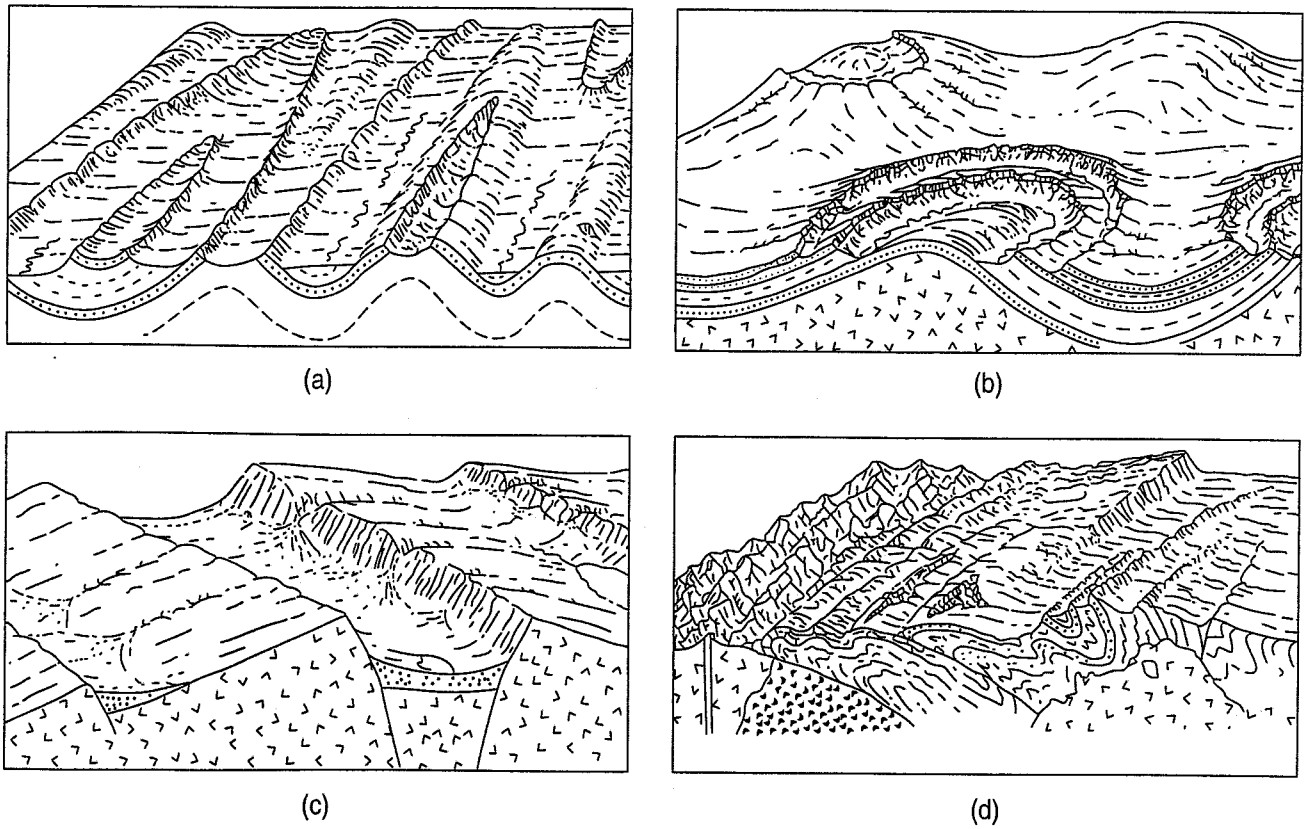

FIGURE 3.35 Geologic structures: (a) folds; (b) domes; (c) fault blocks; and (d) complex structures (after Thornbury, 1954).

example of a dome with a very old crystalline rock core is the Black Hills formation of South Dakota. Good examples of folding with anticlines and synclines are the Appalachian Mountains of the eastern United States.

As you might expect, *faults* also produce distinctive landforms and topographic features. When a normal or thrust fault [Fig. 3.2(a) and (b)] extends to the ground surface, a *fault scarp* is produced (Fig. 3.36). Its height depends, of course, on the amount of displacement, but its appearance today depends on how recently the faulting occurred. Other features that are often evidence of previous faulting include stream offsets, lines of springs, and sag ponds and small lakes that indicate impounded drainage along a fault. Probably the best-known examples of sag ponds are found along the San Andreas Fault in California.

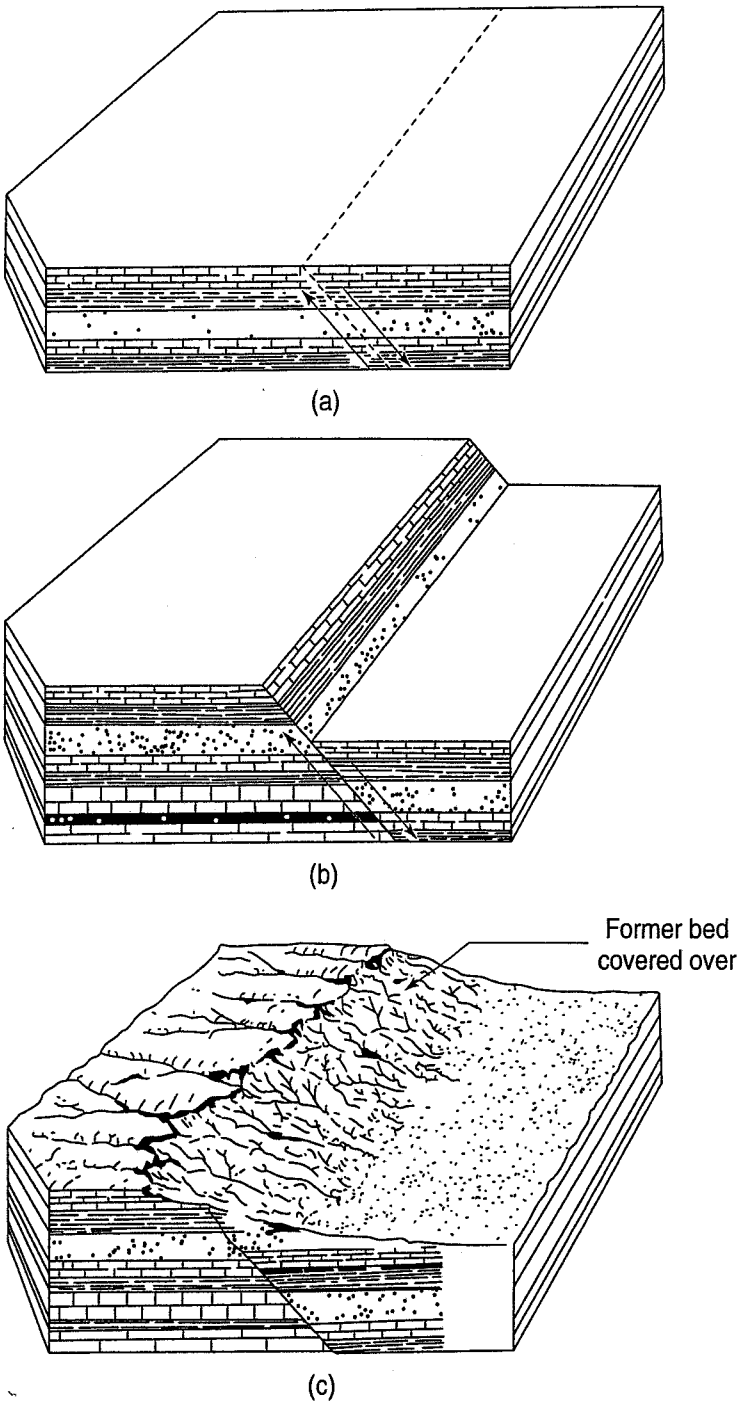

FIGURE 3.36 Fault scarp: (a) before displacement; (b) after displacement; (c) after erosion of the fault scarp (after Emmons et al., 1955).

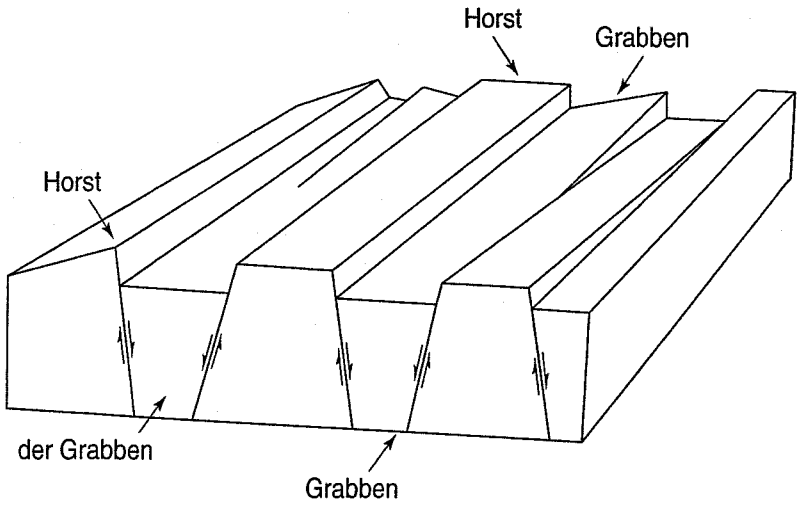

FIGURE 3.37 Block faulting with horsts and grabbens (West, 1995).

When block faulting occurs, a long narrow block of the earth's crust is either uplifted or depressed between two faults along its sides. The higher block is termed a *horst* (German: "refuge") and the lower block a *graben* (German: "ditch" or "trench"), as shown in Fig. 3.37; they occur in almost all intensely faulted regions. Death Valley in southern California, for example, has many such features. If block faulting occurs on a very large scale, block-faulted mountains are produced; these are very common in the Great Basin area of Nevada and Utah.

In seismically active areas the location of faults is important—for two reasons. One is that, if at all possible, you want to avoid locating a structure or facility across a potentially active fault. The other is that faults that have moved in recent geologic time are useful indicators of possible future seismic activity. Thus for the seismic design of civil engineering structures, the distance of a facility from a potentially active fault, the bedrock and surficial geology between the fault and the facility, and the return period of the design earthquake are all used to estimate the intensity of shaking due to an earthquake. These design considerations are even more critical for so-called lifeline facilities (e.g., hospitals) that are potentially important during earthquakes, and for long-lifespan facilities such as waste repositories and nuclear power plants. Kramer (1996) is a good reference on all aspects of geotechnical earthquake engineering.

If you expect to practice in earthquake country, you will need to know something about the regional tectonics, local ground motions and the potential for ground failure, as well as the potential for other seismically induced problems such as landslides, liquefaction (Chapter 7), and subsidence. See Bonilla (1991) for a description of the effects of faulting and earthquakes on dams, power plants, pipelines, and other civil engineering projects.

3.3.10 Plutonic Processes

Subsurface volcanic activity or *plutonism* occurs when magma is intruded into older overlying rocks. Although plutonism produces a number of interesting features (Fig. 3.38), most of them appear at the surface only after the overlying rocks are removed by erosion or other geologic processes. Plutonic rocks and structures may be locally important in the construction of tunnels and underground powerhouses. Plutonic activity may also result in hydrothermal alteration of adjacent rocks and sediments. Hot ascending solutions may alter the minerals in the original rock so that a completely different rock results. *Hydrothermal alteration* can be found in areas of past intrusive activity or of contemporary volcanism. Hydrothermally altered rocks are more erodible, more variable, and weaker than unaltered rocks and thus are poorer foundation and construction materials.

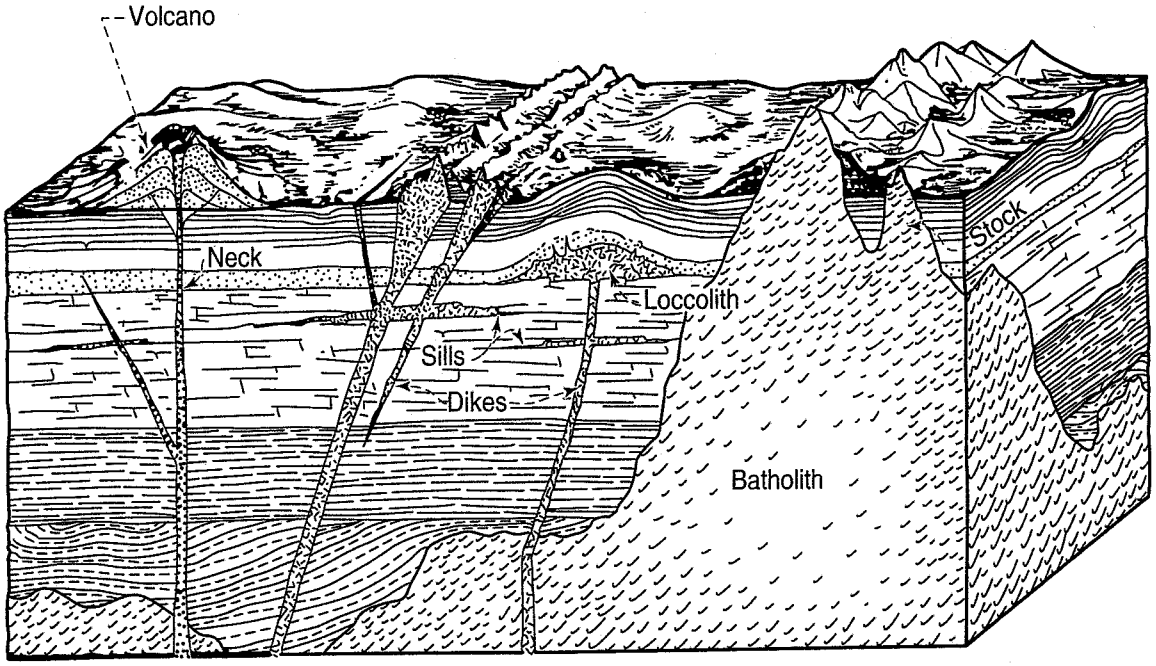

FIGURE 3.38 Plutonic forms (after Krinine and Judd, 1957).

3.4 SOURCES OF GEOLOGIC INFORMATION

Geotechnical engineers use several sources to obtain the geologic information they need in practice. Sometimes this information is available in the context of geographic information systems (GIS), topographic, geologic, and agricultural maps, and aerial photographs and satellite imagery. In addition, valuable information can be obtained from water-well and other subsurface drill logs, reports and papers published by different governmental agencies, and articles in scientific and engineering journals.

To start with, an excellent overall description of the geology and soil deposits of North America has been prepared by Woods, Miles, and Lovell (1962). They also discuss the various types of geologic and pedologic maps as well as the usefulness of aerial photographs. West (1995) has a detailed description of topographic and geologic maps, including valuable information about their use in engineering practice. Goodman (1993) gives information on how geologic maps and aerial photographs can be obtained. An excellent compendium of similar information for Canada is given in the Canadian Foundation Engineering Manual (Canadian Geotechnical Society, 2006). The various state geological surveys are also an excellent source of detailed information. You are probably familiar with topographic maps and how they give you both the geographic location and the elevation of a site. With some experience, you can obtain certain surficial geologic information from topographic maps. The U.S. Geological Survey (USGS) produces 7.5 min quadrangle maps at a scale of 1:24,000 of most of the United States. Topographic maps of all of Canada are available at various scales from the Map Office of the Department of Energy, Mines, and Resources (EMR) in Ottawa. Maps of local areas are also available from various provincial map agencies, departments of natural resources, etc.

Classic geologic maps show the type of rock or rock formation on the bedrock surface as if the surface soils and vegetation were removed. Thick overburden deposits are usually also indicated. Such maps provide very useful information, especially to engineering geologists, about the type and age of the bedrock and general rock properties. They are available from the USGS, various state

geological surveys and departments of natural resources, the Geological Survey of Canada, and a number of provincial agencies and departments (Canadian Geotechnical Society, 2006).

Agricultural soil maps and soil surveys (maps) are prepared by soil scientists and agronomists primarily for agricultural purposes and land use planning; thus they concentrate on the characteristics of the topmost 1 m of the soil surface. Maps are available in the United States generally by county and in Canada by agricultural district. Recent maps also contain some general engineering information such as the soil's suitability for siting homes, septic systems, roads, and landfills. These maps are definitely worth consulting if you have a project in a new area. They are prepared and sold by the Soil Conservation Service (now known as the Natural Resources Conservation Service) of the U.S. Department of Agriculture; in Canada, they are available from the various provincial agricultural departments.

One of the most useful sources of geologic information is aerial photographs. They are typically about 230-mm × 230-mm panchromatic (black and white) photographs, used either as a photomosaic covering a large area or, more commonly, as stereo pairs. In the latter case, with a 60% overlap in the line of flight and 15% side overlaps, adjacent photo pairs can be viewed stereoscopically, yielding a three-dimensional image to aid in geologic interpretation. Airphotos show not only geographic details, but also the tones (the shades of gray), textures, and patterns of the ground surface, which we can use to identify, for example, landforms, soil types, rock outcrops, external and subsurface drainage patterns, seepage zones, organic deposits, aggregate sources, and landslides. Understanding of airphoto interpretation and photogeology is a very valuable tool for a geotechnical engineer.

Traditional air photos covering most of the agricultural United States are available from the USDA; in the American west, the U.S. Forest Service, U.S. Army Corps of Engineers, and Bureau of Land Management are good sources of airphotos. The National Oceanographic and Atmospheric Administration has photos of the U.S. coastlines.

In recent years, color photographs and color infrared (IR) imagery have become available, as have various wave bands (red, green, and two IR bands) of imagery from satellites (LANDSAT). These new interpretive tools have greatly expanded the quantity and quality of information available to geotechnical engineers. LANDSAT information is available from the USGS EROS Data Center. In Canada, LANDSAT imagery is available from the Canada Centre for Remote Sensing in Ottawa and at various regional centers located across the country.

Most parts of the earth are now available through Google Earth and the USA National Atlas Online (http://www.usatlas2000.com), although photo coverage and resolution can vary, even over short distances.

In both the United States and Canada, water-well logs are often available at state and provincial departments of natural resources, environmental protection, water resources, or similar agencies. Well logs can provide much useful information, such as depths to the water table and bedrock, as well as soil and rock types. Sometimes oil and gas logs are also available, although these tend to be proprietary—the property of the company owning the drilling rights. Depending on the site and the engineering problem, you may also want to obtain such things as flood-plain maps, hydrologic information, hydrographic charts, land use and planning surveys and maps, climate and weather records, surface and underground mining reports, and local seismicity records. As you will see in your study of geotechnical engineering, geotechnical engineers need a wide variety of information and resources to assist them in project reconnaissance, planning, design, construction, and occasionally even the maintenance of all types of civil works.

We have emphasized throughout this chapter just how important the knowledge of the geology of a project site is to the successful practice of geotechnical engineering. Knowing where to obtain that geologic information is a key first step in this process.

PROBLEMS

3.1 Go online and find one or more geotechnical and geologic maps that contains your university or home town. Determine from this reference as much geologic and geotechnical information as you can. Comment on possible geotechnical problems likely to occur in your area during the construction of (a) sewer lines, (b) streets and roads, and (c) low-rise commercial buildings. (d) Find a copy of Woods, Miles and Lovell (1962) and compare information from that reference with what you found online.

3.2 Use the web to find the USGS or GSC topographic map that contains your university or home-town location. Write a brief description of the location with sufficient information so that another engineer could easily locate the same map.

3.3 Find geologic maps of your state or province that include the locality of your university or home town. List the bedrock type and units and any other pertinent geologic information about your area.

3.4 Does your state or province require that all water-well drillers record the well logs with an appropriate agency? If so, what is the name of that agency? Find some well logs near your home and report the information. How is this likely to be useful in practice?

3.5 Use Google Earth to locate your university or home town. List as many geologic features as you can that can be seen from the air photos. Comment on the implications of these features for infrastructure construction.

3.6 Locate the most recent USDA or CDA agricultural soil map or soil survey for your home county or district. Does the report give any useful engineering information? If so, comment on how this information would be useful for various types of construction.

3.7 The journal *Environmenal & Engineering Geoscience*, formerly the *Bulletin of the Association of Engineering Geologists*, occasionally publishes articles as part of its "Geology of Cities" series, which describes the geology of the major cities of the world. Find the article for one of these cities and summarize its geology and likely construction problems for (a) urban housing development, (b) tunnels for a mass-transit system, (c) construction of a major wastewater treatment plant, and (d) expansion of either the local airport or harbor.

3.8 Review the geologic processes described in this chapter. Select two or three that are fairly common in the vicinity of your university or home town. For each process, list (a) the common landforms produced, (b) important soils or rock types produced, (c) geologic hazards, if any, associated with each, and (d) engineering problems that may be caused by these hazards.

3.9 Search the library for books and manuals on air photo interpretation. Use a consistent bibliographic citation format, and prepare a list of what you find. Purdue and Cornell Universities have been leaders in the start of air photo interpretation as early as the 1940s. These would be good places to direct a web search to find materials on this topic. Select one of the references and explore the use of API in determining soil types through landform identification. Prepare a one page summary of this information.

3.10 Get online and use the keywords *geology* and *engineering* to open a search. Refine your search as necessary. Prepare a list of websites and links related to geotechnical engineering.

3.11 The mission of the National Earthquake Information Center (NEIC) is to determine rapidly the location and size of all destructive earthquakes worldwide and to immediately disseminate this information to concerned national and international agencies, scientists, and the general public. The NEIC/WDC for Seismology compiles and maintains an extensive, global seismic database on earthquake parameters and their effects. Using links available at the NEIC website http://earthquake.usgs.gov/regional/neic/, find the 10 largest magnitude earthquakes that have occurred in (a) the past week, (b) the previous month, and (c) so far this year. (After S. L. Kramer.)

3.12 For the the earthquakes you located in Problem 3.11, indicate (a) which earthquake you would expect to have produced the strongest ground shaking (on land), and (b) which one you would expect to have produced the greatest financial loss. Explain why you selected those earthquakes. (After S. L. Kramer.)

3.13 Name the appropriate landform or soil feature:

(a) where fish keep their money
(b) where you go for a drink
(c) something a tailor uses
(d) what a weather forecaster might say

(e) what you might use when it's hot
(f) what you use for catching fish
(g) part of a house
(h) where Mr. Spock ("Live long and prosper!") comes from
(i) what tool a mechanic uses (this is a real stretch).

3.14 Anticlines are upfolds and synclines are downfolds. Nevertheless, one often finds synclinal ridges and anticlinal valleys. Explain how each of these could be formed.

3.15 The St. Lawrence River carries much more water to the sea than the Colorado River. Using your knowledge of delta deposition, give two reasons why the St. Lawrence ends in an almost unsedimented estuary whereas the Colorado has been building a huge delta for thousands of years.

3.16 If you were a conservation engineer and had to design a plan for making soil form as quickly as possible on a fresh broken rock rubble left by construction or mining operations, what would you do (without importing any soil from elsewhere)?

3.17 Engineers have made artificial cut-offs (see Fig. P3.17) in the lower Mississippi River and other meandering rivers. Considering the nature of meandering streams, can you suggest reasons for undertaking these projects?

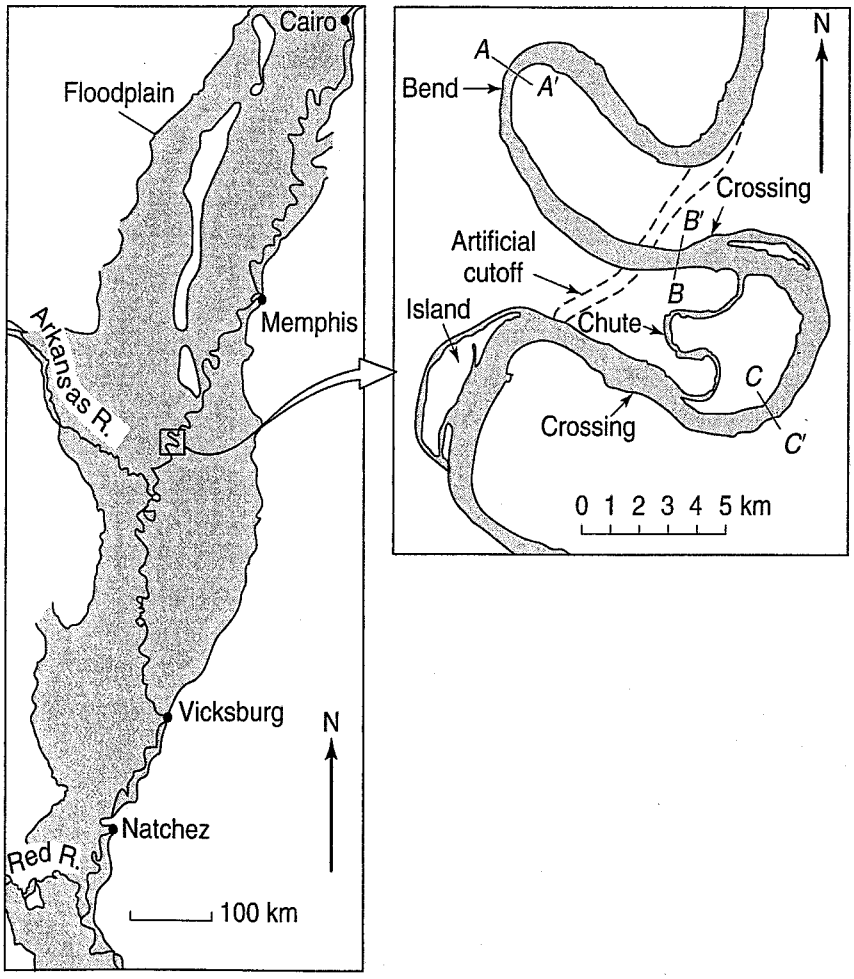

FIGURE P3.17

3.18 A rainwater catch basin is to be built in loess terrain. The basin, which will be asphalt lined, will serve as temporary storage of rainwater from storm sewers before the water flows into the wastewater treatment plant. What major considerations regarding the geotechnical performance of the loess do you have to make:

(a) during the construction of the basin?
(b) during operation of the basin?

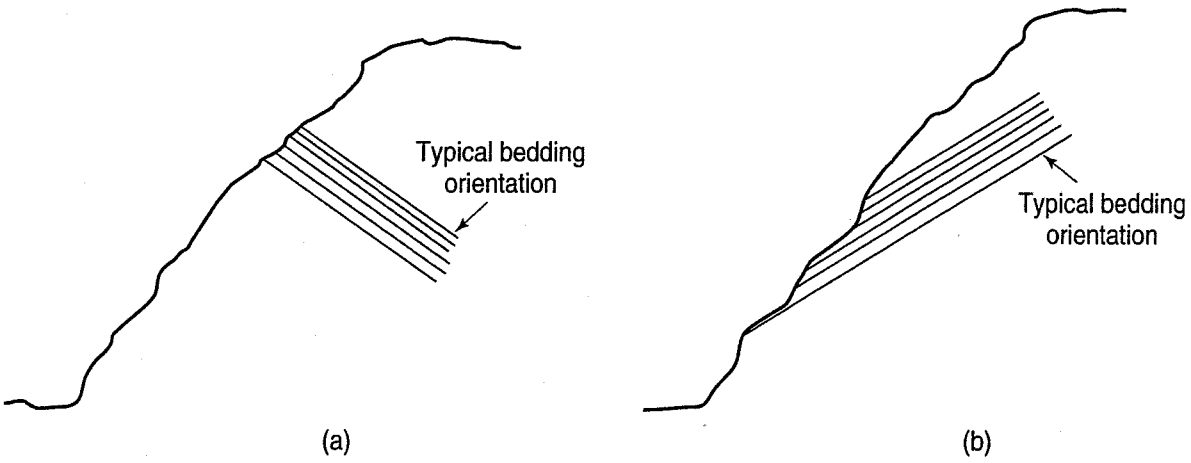

FIGURE P3.19

3.19 You have a choice between two building sites on a natural slope, both underlain by a weak shale. At one site, the beds dip into the hill [Fig. P3.19(a)]; at the other, the beds dip parallel to the slope [Fig. 3.19(b)]. Which do you prefer and why? What precautions will you take to ensure that the slope will not become unstable?

3.20 Predict the probable sequence of events that would follow the building of a dam on a river that has an ample supply of sediment and, prior to the dam installation, has achieved an equilibrium concave-upward shape.

3.21 Why do dune sands tend to vary so little in grain size? Why are they generally free of clay?

3.22 You are assigned to perform a site investigation of a terminal moraine. What characteristics of topography or till composition would you use to distinguish it from a ground moraine on the one hand, and outwash on the other? How might you distinguish it from an esker?

3.23 What, if any, differences do you expect to find in the topography and soils of kames versus kame terraces? In other words, how might their deposition modes affect their characteristics?

3.24 A fjord basin typically has a characteristic rise or sill at its mouth, as shown in Fig. P3.24. Given what you know about their geologic origin, explain how such a sill develops.

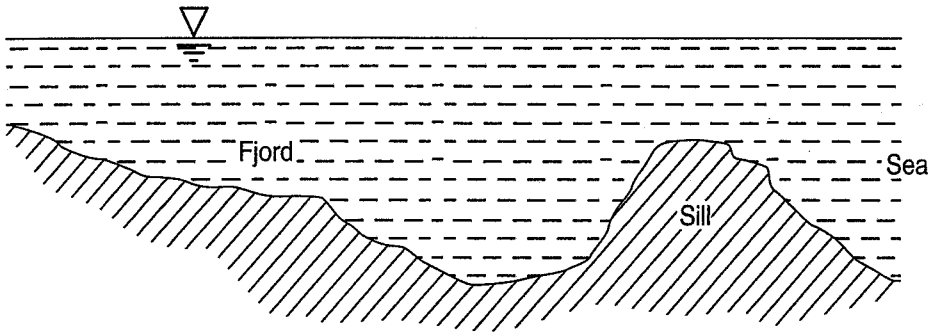

FIGURE P3.24

CHAPTER 4

Clay Minerals, Soil and Rock Structures, and Rock Classification

4.1 INTRODUCTION

In Chapter 3, we described the origin of geomaterials and the landforms where those materials are commonly found. We mentioned that weathering of rocks and other geologic processes results in certain rock structures and discontinuities as well as a wide variety of different soil types. In this chapter, we briefly describe the products of weathering and the important clay minerals that result, how those minerals are identified, and how they interact with water as well as with each other. We also describe some of the latest thinking about soil fabric and structure—concepts fundamental to a good understanding of the behavior of both fine-grained and granular soils.

In this chapter, we also briefly discuss soil profiles and horizons, some special soil deposits that are of interest to geotechnical engineers, and transitional or intermediate geomaterials—those materials that are neither soil nor hard rock. We conclude with a discussion of the properties, macrostructure, and classification of rock masses.

Three new symbols are introduced in this chapter.

Symbol	Dimension	Unit	Definition
A	–	–	Activity - Eq. (4.1)
e_{max}	–	–	Maximum void ratio
e_{min}	–	–	Minimum void ratio

4.2 PRODUCTS OF WEATHERING

In Sec. 3.3.2, we defined *weathering* as the alteration of the composition or structure of rocks because of physical, chemical, or biological processes. Weathering produces all types of soils (called *residual soils* or *residuum*). The mechanical disintegration of rocks by physical weathering tends to produce

coarser-grained soils, ranging in size from boulders and cobbles down to gravel, sands, and even silts. Chemical weathering, on the other hand, tends to produce various types of clay minerals. For example, the hydrolysis of feldspar and mica (biotite) minerals in granitic rocks produces the clay mineral kaolinite, an important constituent of fine-grained soils. Other types of clay minerals are produced from various rock–forming minerals that are subjected to different chemical, climatic, and drainage conditions. Clay minerals are discussed in detail in Sec. 4.3.

In Sec. 2.4, we mentioned that the term *clay* may refer both to a type of soil and to specific clay minerals. Usually, in civil engineering, when we say "clay" we mean a soil that contains some *clay minerals* along with other mineral constituents, is "cohesive" and has plasticity at appropriate water contents, and hardens when dried. But, as Hatheway (2000) has noted, using the word "clay" without a qualifier or modifier is ambiguous and confusing, and may lead to serious misunderstandings.

As we show in the next section, clay minerals are very small, generally crystalline particles that are very active electrochemically. Thus the presence of even a small amount of clay minerals can markedly affect the engineering properties of a soil mass. As the amount of clay increases, the behavior of the soil is increasingly governed by the properties of the clay. When the clay content is about 25% to 35%, the coarser grains (silts, sands, or gravels) are essentially floating in a clay matrix and have little effect on the soil's engineering behavior. Another characteristic of clay soils is that water markedly affects their behavior, but the grain size distribution has relatively little influence.

In contrast, certain characteristics of granular soils, such as the grain size distribution and the grain shape, strongly affect their engineering behavior, but the presence of water, with a few important exceptions, has relatively little effect.

You may recall from Sec. 2.4 that silts are both granular and fine grained. Their individual grains, like those of clays, are invisible to the naked eye, but silts are noncohesive and nonplastic. Water affects their behavior—they are *dilatant*—yet they have little or no plasticity (PI $\cong$ 0), and their strengths, like those of sands, are essentially independent of water content. Rock flour is another example of a very fine-grained cohesionless soil.

This might be a good time to go back to Sec. 2.4 and quickly review the discussion on the influence of water on the behavior of soils.

4.3 CLAY MINERALS

Clay minerals are crystalline substances produced by chemical weathering of certain rock-forming minerals. Chemically, they are *hydrous aluminum silicates* plus other metallic ions, and they belong to the class of minerals called *phyllosilicates*. Their crystals are colloidal sized (diameter less than 1 μm) and can be seen only with an electron microscope. They look like tiny plates or flakes, and from X-ray diffraction studies mineralologists have determined that these flakes consist of many crystal sheets that have a repeating atomic structure. In fact, there are only two fundamental crystal sheets, the *tetrahedral* or *silica* sheet and the *octahedral* or *alumina* sheet. The particular ways in which these sheets are stacked together, with different bonding and different metallic ions in the crystal lattice, characterize the various clay minerals.

The tetrahedral sheet is basically a combination of silica tetrahedral units, consisting of four oxygen atoms at the corners, surrounding a single silicon atom [Fig. 4.1(a)]. Figure 4.1(b) shows how the oxygen atoms at the base of each tetrahedron are combined to form a sheet structure in which all the oxygens at the base of each tetrahedron are in one plane and the apexes of the tetrahedra all point in the same direction. A common schematic representation of the tetrahedral sheet is shown in Fig. 4.1(c). A top view of the tetrahedral (silica) sheet [Fig. 4.1(d)] illustrates how the oxygen atoms at the base of each tetrahedron belong to two tetrahedrons and how adjacent silicon atoms are bonded. Note the hexagonal "holes" in the sheet.

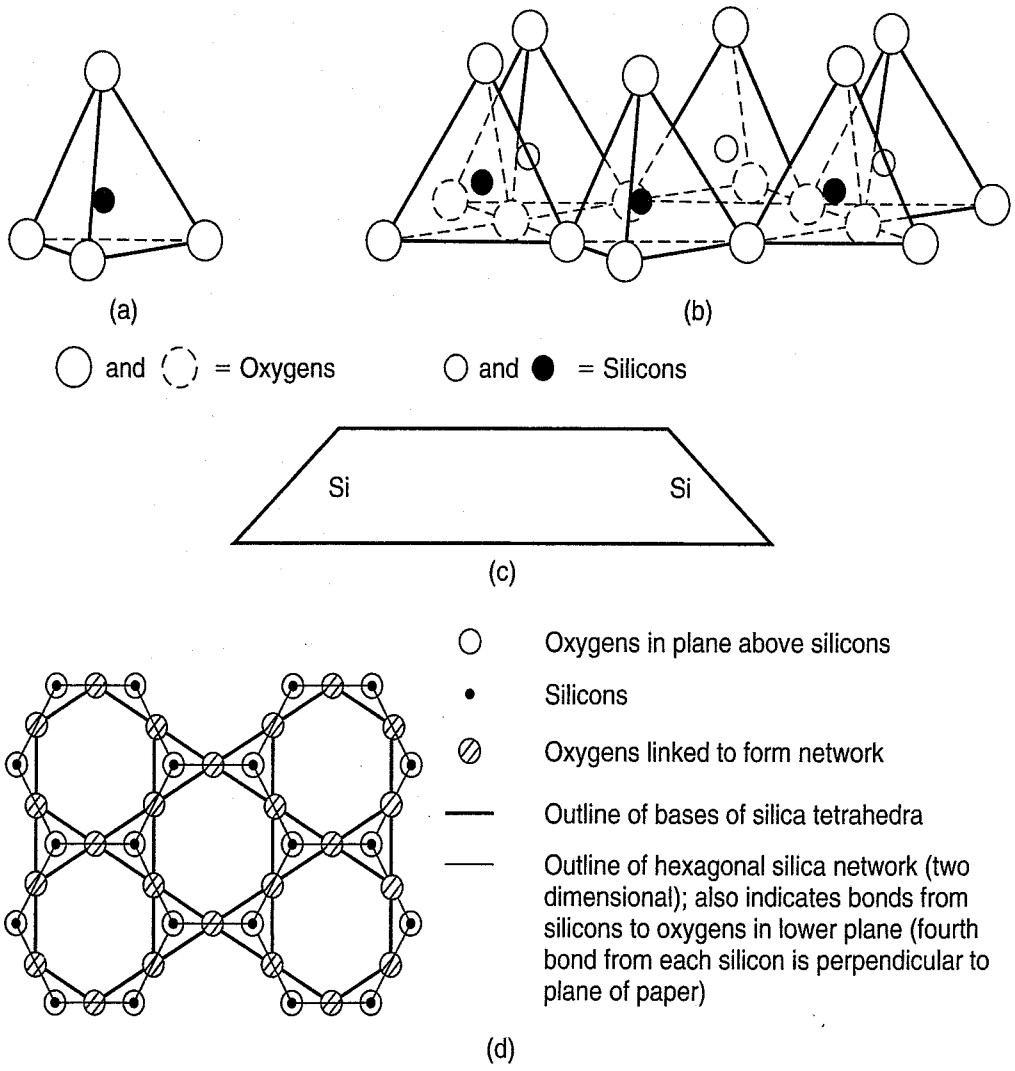

FIGURE 4.1 (a) Single silica tetrahedron (after Grim, 1959). (b) Isometric view of the tetrahedral or silica sheet (after Grim, 1959). (c) Schematic representation of the silica sheet (after Lambe, 1953). (d) Top view of the silica sheet (after Warshaw and Roy, 1961).

The octahedral sheet is basically a combination of octahedral units consisting of six oxygens or hydroxyls enclosing an aluminum, magnesium, iron, or other metallic atom. A single octahedron is shown in Fig. 4.2(a), while Fig. 4.2(b) shows how the octahedrons combine to form a sheet structure. The rows of oxygens or hydroxyls in the sheet are in two planes. Figure 4.2(c) is a schematic representation of the octahedral sheet. For a top view of the octahedral sheet, showing how the different atoms are shared and bonded, see Fig. 4.2(d).

Substitution of different cations in the octahedral sheet is quite common and results in different clay minerals. Since the substituted ions are approximately the same physical size, this substitution is called *isomorphous*. Sometimes not all the octahedrons contain a cation, which results in a somewhat different crystalline structure with slightly different physical properties and a different clay mineral. For example, if all the anions of the octahedral sheet are hydroxyls and two-thirds of the cation positions are filled with aluminum, then the mineral is called *gibbsite*. If magnesium is substituted for the aluminum and it fills all the cation positions, then the mineral is called *brucite*.

All clay minerals consist of the two basic sheets, tetrahedral and octahedral, that are stacked together in certain unique ways and have certain cations present. The variations in the basic sheet structures make up the dozens of clay minerals that have been identified. For engineering purposes it is usually sufficient to describe only a few of the more common clay minerals found in clay soils.

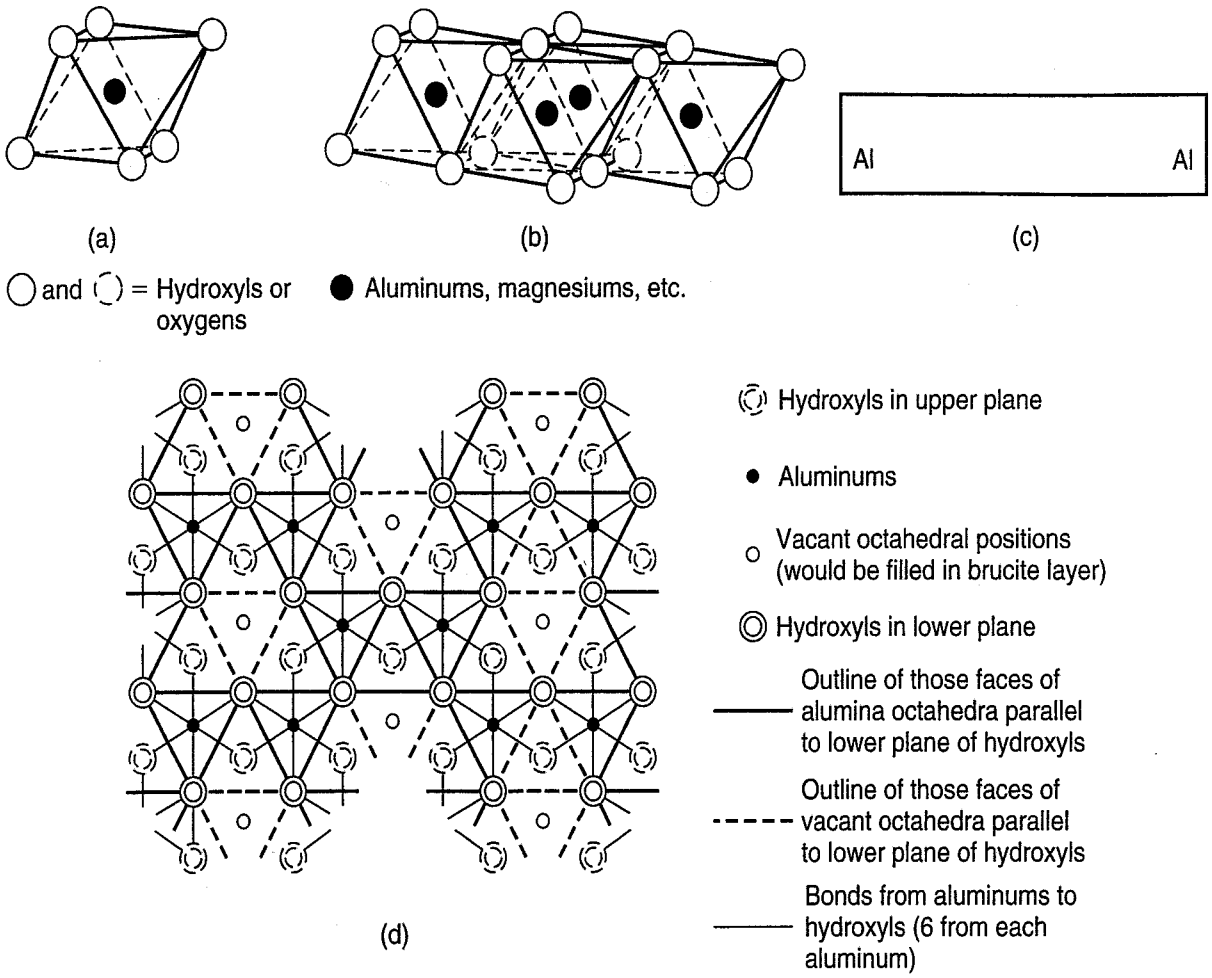

FIGURE 4.2 (a) Single aluminum (or magnesium) octahedron (after Grim, 1959). (b) Isometric view of the octahedral sheet (after Grim, 1959). (c) Schematic representation of the octahedral or alumina (or magnesia) sheet (after Lambe, 1953). (d) Top view of the octahedral sheet (after Warshaw and Roy, 1961).

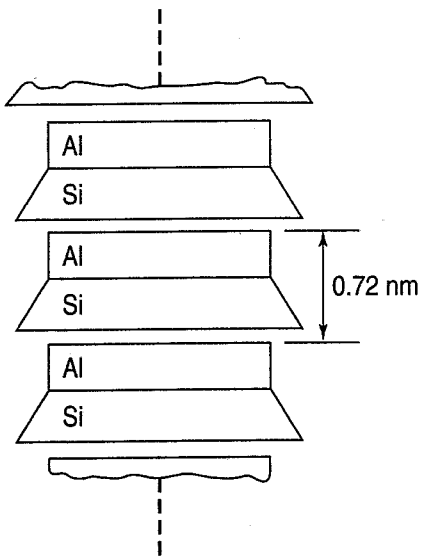

FIGURE 4.3 Schematic diagram of the structure of kaolinite (after Lambe, 1953).

4.3.1 The 1:1 Clay Minerals

The *kaolinite-serpentine* group contains at least 13 different minerals, of which *kaolinite* is the most important. The minerals in this group consist of repeating layers or stacks of one tetrahedral (silica) sheet and one octahedral (alumina or gibbsite) sheet, and thus they are called 1:1 clay minerals (Fig. 4.3). The sheets are held together in such a way that the oxygen atoms at the tips of the silica sheet and one layer of oxygens of the octahedral sheet are shared and form a single 1:1 layer, as shown in Fig. 4.4. This basic layer is about 0.72 nm thick and extends indefinitely in the other two directions. A kaolinite crystal, then, consists of a stack of several layers of the basic 0.72-nm layer. Successive layers of the basic layer are held together by hydrogen bonds between the hydroxyls of the octahedral sheet and the oxygens of the tetrahedral sheet. Since the hydrogen bond is very strong, it prevents hydration and allows the layers to stack up to make a rather large crystal. A typical kaolin crystal can be 70 to 100 layers thick. Figure 4.5 is a scanning electron micrograph (SEM) of kaolinite.

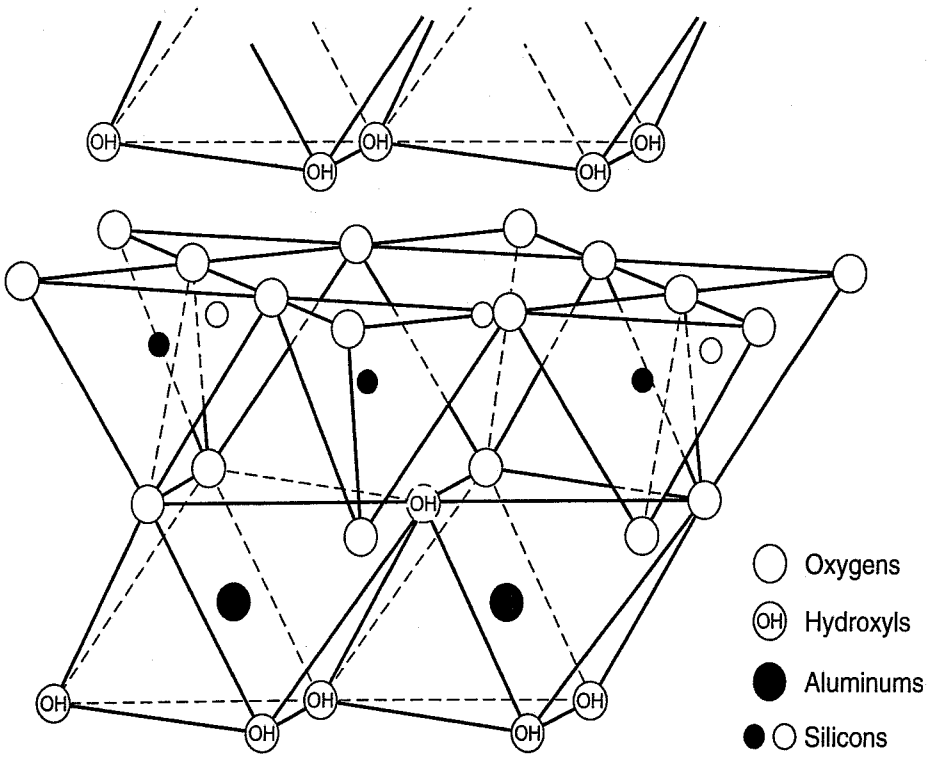

FIGURE 4.4 Atomic structure of kaolinite (after Grim, 1959).

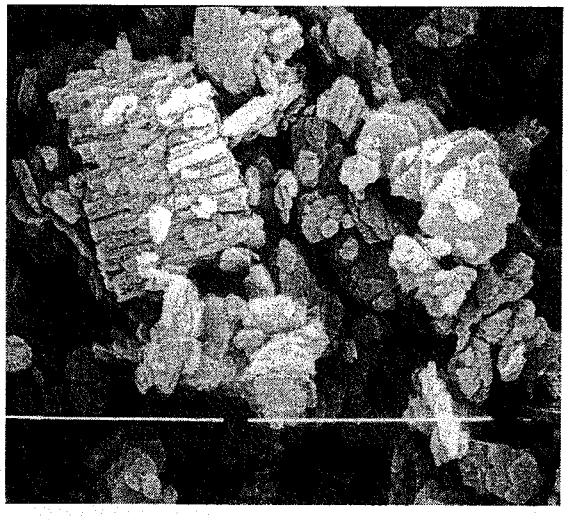

FIGURE 4.5 Scanning electron micrograph of a well-crystallized kaolinite from Georgia. The length of the light bar is 5 μm (photograph by R. D. Holtz).

Kaolinite results from the weathering (hydrolysis and acid leaching) of feldspar and mica (biotite) in granitic rocks. According to Mitchell and Soga (2005), kaolinites tend to develop in areas having relatively high precipitation but good drainage that enables the leaching of Mg, Ca, and Fe cations. In these areas, alumina is abundant and silica is scarce, and the pH and concentration of electrolytes are relatively low. Kaolinite is the primary constituent of china clay, and in fact the name kaolin comes from a hill in Jiangsi Province of China called "Kao-ling" which means "high peak" or "high hill." Kaolinite is also used in the paper, paint, and pharmaceutical industries. For example, as a pharmaceutical it is used in *Kao*pectate and Rolaids. It also is supposed to have health and curative benefits.

Another 1:1 mineral that is occasionally important in practice is *halloysite*. Halloysites are formed by the leaching of feldspar by sulfuric acid, a condition common in areas with volcanic parent materials and high rainfall (Mitchell and Soga, 2005). They differ from kaolinite in that when they form, they somehow become hydrated between layers, distorting the crystal lattice so that the mineral has a tubular shape (Fig. 4.6). The water can easily be driven out by heating or even air drying, so that the tubes unroll and

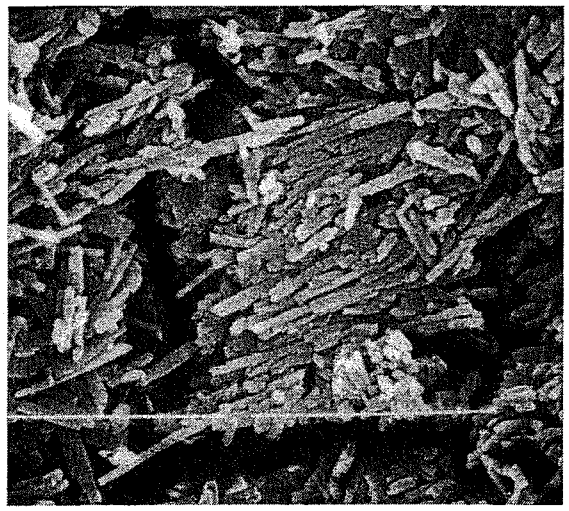

FIGURE 4.6 Scanning electron micrograph of halloysite from Colorado. The length of the light bar is 5 μm (photograph by R. D. Holtz).

look like ordinary kaolinite. The process is irreversible; halloysite will not rehydrate and form into rolls if water is added later. This characteristic occasionally has important consequences in civil engineering practice. Classification and compaction tests (see Chapter 5) on air- or oven-dried samples can give markedly different results than tests on samples at their natural water content. If the soil will not be dried in the field, it is very important for valid results that laboratory tests be carried out at the field water contents.

4.3.2 The 2:1 Clay Minerals

The 2:1 minerals are a large group; more than 40 have been identified. In addition to the clay minerals, probably the best-known members of this group are talc and the two micas, biotite and muscovite. In all cases these minerals are composed of two tetrahedral or silica sheets and one octahedral or alumina (gibbsite) sheet in between (Fig. 4.7). There are three 2:1 subgroups that include fairly to very common clay minerals with important engineering characteristics. One 2:1 subgroup is the *smectites*, and its most important and very common member is *montmorillonite* (named after the village in France,

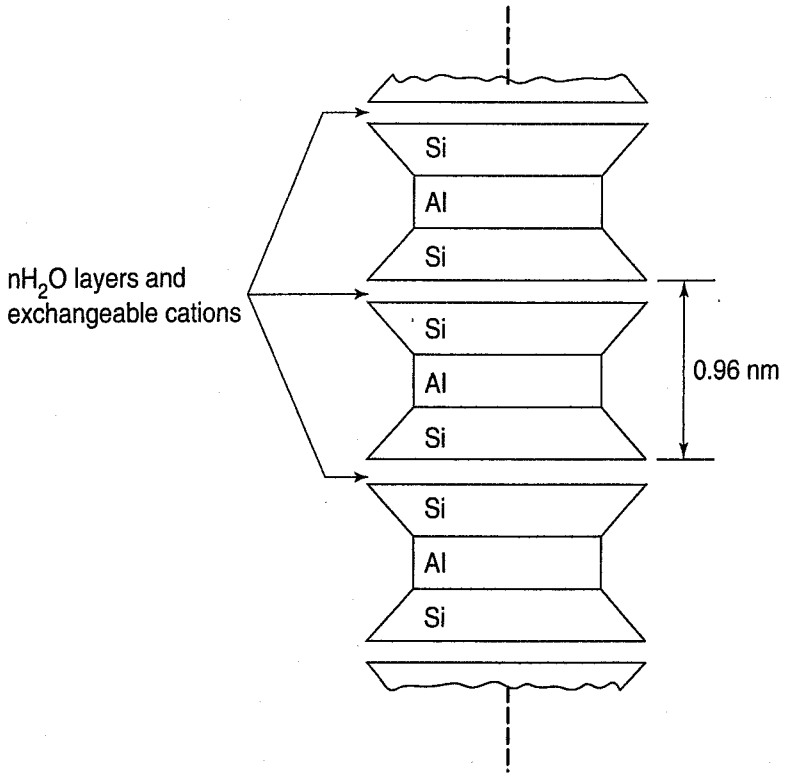

FIGURE 4.7 Schematic diagram of the structure of montmorillonite (after Lambe, 1953).

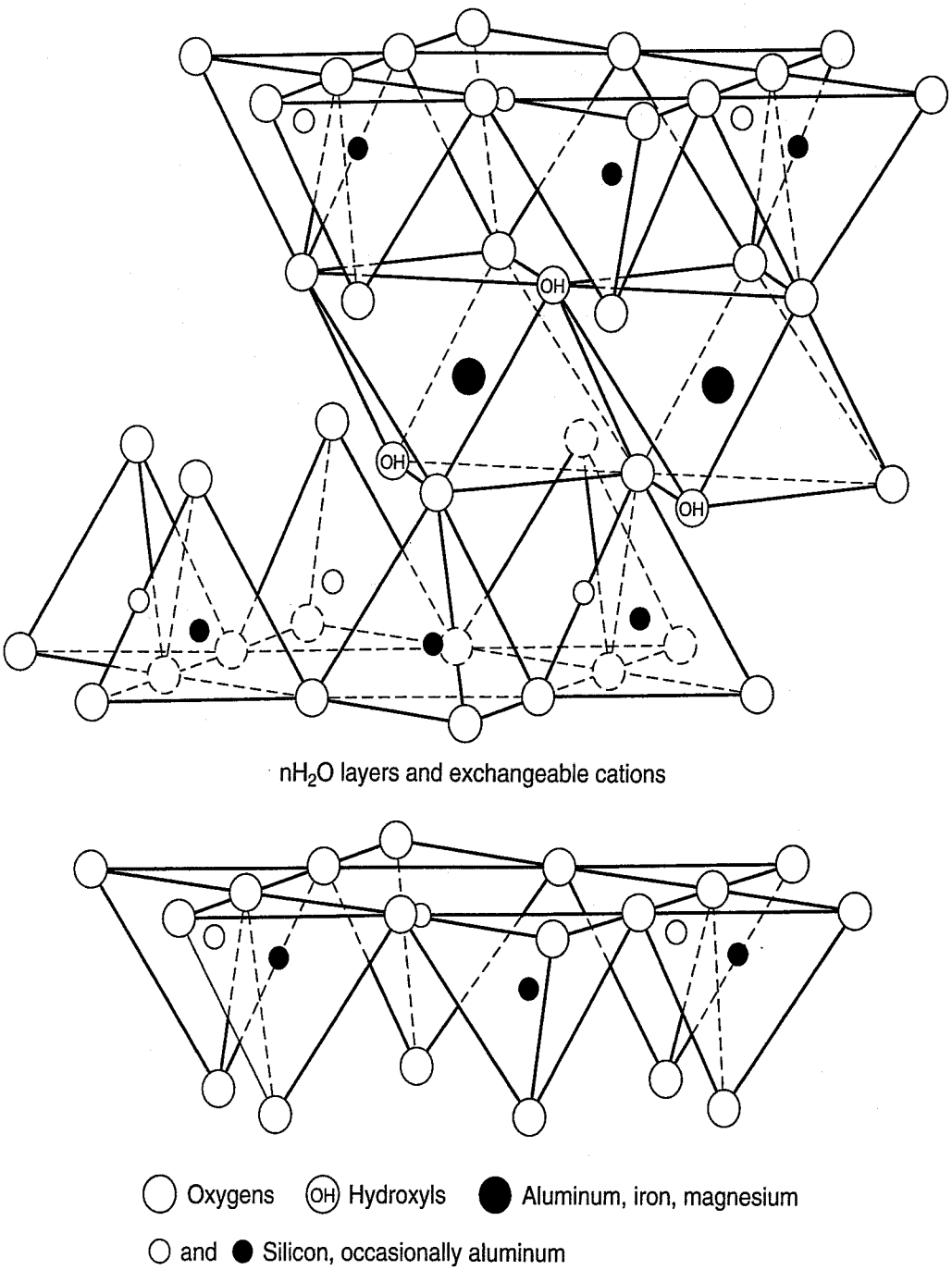

FIGURE 4.8 Atomic structure of montmorillonite (after Grim, 1959).

Montmorillon, where the mineral was first discovered). In montmorillonite, the tips of the tetrahedra share oxygens and hydroxyls with the octahedral sheet to form a single layer, as shown in Fig. 4.8. The thickness of each 2:1 layer is about 0.96 nm, and as in kaolinite the layers extend indefinitely in the other two directions. The bonding (by van der Waals' forces) between the tops of the silica sheets is weak (compared, for example, to the hydrogen bonds in kaolinite), and there is a net negative charge deficiency in the octahedral sheet. Water and exchangeable ions can readily enter and separate the basic layers, as shown schematically in Fig. 4.7. Thus, montmorillonite crystals can be very small (Fig. 4.9), yet they have a very strong attraction for water. Soils containing montmorillonite are very susceptible to swelling as their water content changes (increases), and the swelling pressures developed can easily damage light structures and highway pavements.

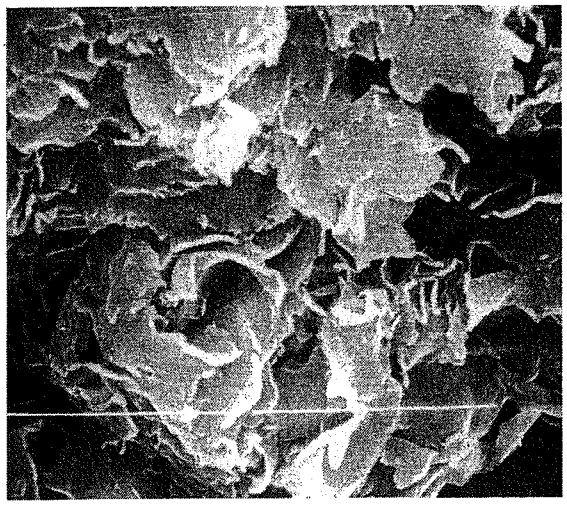

FIGURE 4.9 Scanning electron micrograph of Na-montmorillonite from Wyoming. The length of the light bar is 5 μm (photograph by R. D. Holtz).

According to Mitchell and Soga (2005), smectites tend to form where silica is abundant, the pH and electrolyte content are high, and where there are more Mg^{++} and Ca^{++} than Na^{+} and K^{+} ions. Basic igneous rocks such as gabbro and basalt and volcanic ash can produce smectites in arid or semi-arid areas where evaporation exceeds precipitation and there is poor leaching.

Bentonite is a common name for clays and soft rocks that contain significant amounts of montmorillonite and other smectite minerals. Bentonite is produced by the chemical alteration of volcanic ash. Because of its swelling characteristics, it is used in geotechnical practice as a drilling fluid or "mud" to stabilize boreholes and slurry trenches, to seal boreholes, and to reduce the flow rates through porous soils. For example, when compacted clay liners are used in modern landfill construction, natural clays are often modified with bentonite to reduce their hydraulic conductivity (Chapter 7). Bentonite (montmorillonite) is also the primary constituent in kitty litter, and it has many important industrial and pharmaceutical applications. It is even used in chocolate bars!

Illite, discovered and named by Professor R. E. Grim of the University of Illinois, is another important constituent of clayey soils. It also has a 2:1 structure like that of montmorillonite, but its interlayers are bonded together with a potassium ion. Remember the hexagonal hole in the silica sheet [Fig. 4.1(d)]? The diameter of this "hole" is almost exactly that of a potassium atom, so that when the K^{+} atom just fills the hexagonal hole, it rather strongly bonds the layers together (Fig. 4.10). In addition, there is some isomorphous substitution of aluminum for silicon in the silica sheet.

Illites have a crystal structure similar to that of the mica minerals but with less potassium and less isomorphous substitution; thus they are chemically much more active than the other micas. Figure 4.11 is a SEM of illite. Conditions for forming illites are similar to those for smectites, except that potassium must be abundantly present. Parent materials often include igneous and metamorphic rocks rich in mica. Illites are a very common constituent of clay soils; they are particularly common in the glacio-lacustrine clay deposits in the central North American continent and in the clays found under coal beds in that same area.

Vermiculite is another fairly common 2:1 mineral similar to montmorillonite except that it has only two interlayers of water. After it is dried at high temperature, which removes the interlayer water, "*expanded*" vermiculite makes an excellent insulation material.

4.3.3 Other Clay Minerals

Chlorite is another common mineral found in clay soils, although technically it is a group containing several separate minerals. Chlorite consists of repeating layers of a silica sheet, an alumina sheet, another silica, and then either a gibbsite (Al^{+++}) or brucite (Mg^{++}) sheet (Fig. 4.12). It could be called

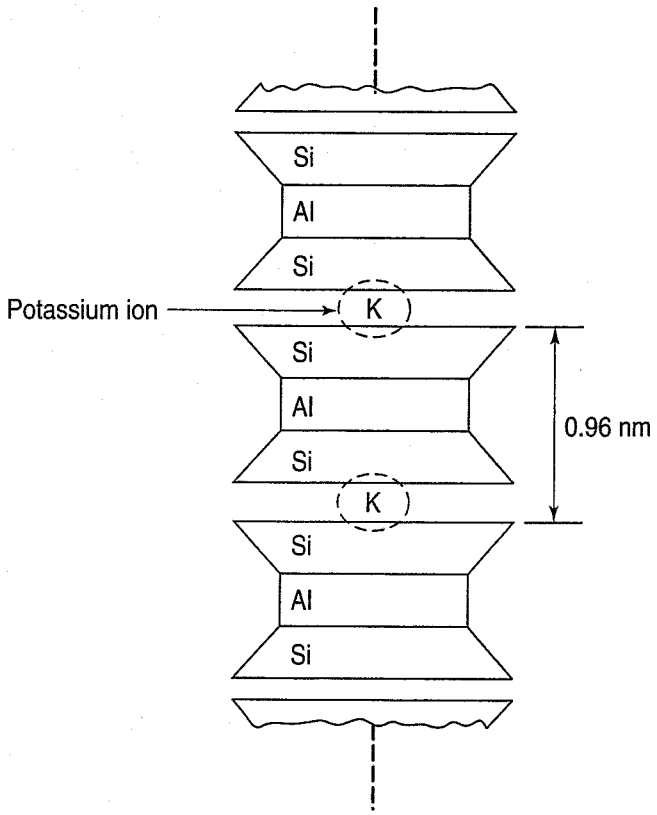

FIGURE 4.10 Schematic diagram of illite (after Lambe, 1953).

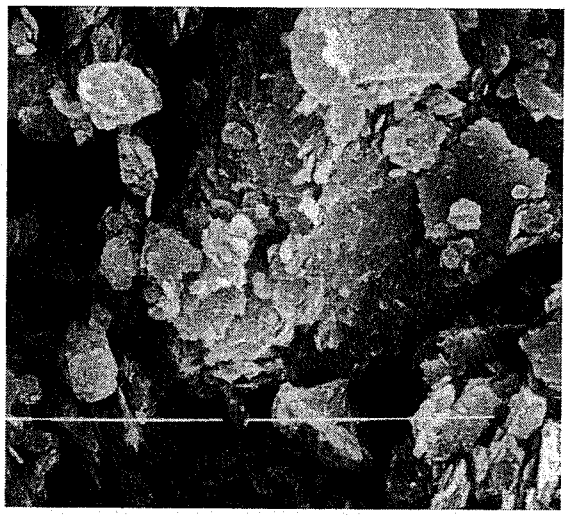

FIGURE 4.11 Scanning electron micrograph of illite from Fithian, Illinois. The length of the light bar is 5 μm (photograph by R. D. Holtz).

a 2:1:1 mineral. Some of the chlorite minerals have considerable isomorphous substitution and are missing an occasional brucite or gibbsite layer; thus they may be susceptible to swelling because water can enter between the sheets. Generally, however, chlorite is significantly less active than montmorillonite and illite. According to Mitchell and Soga (2005), chlorite forms by the alteration of smectite in the presence of sufficient Mg^{++} to form the brucite interlayer. Chlorites are often present in metamorphic rocks and in soils formed from such rocks.

As mentioned above, clay minerals are numerous, and they have virtually every conceivable combination of substituted ions, interlayer water, and exchangeable cations. A few of them are interesting to engineers. *Attapulgite* has a chain rather than a sheet structure; consequently it has a needle- or rodlike appearance (Fig. 4.13). *Mixed-layer* minerals are relatively common; they include, for example, montmorillonite mixed with chlorite or illite. Because *allophane* is a phyllosilicate, it is often classified as a clay mineral. However, it is *amorphous* to X-rays, which means it has no regular crystalline structure.

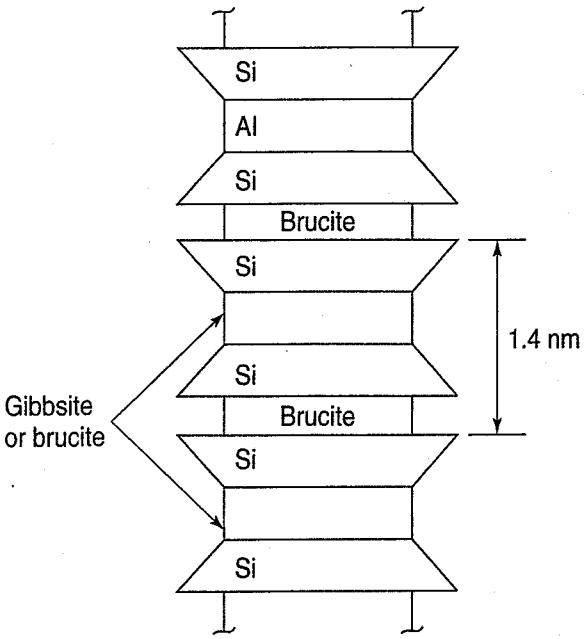

FIGURE 4.12 Schematic diagram of chlorite (after Mitchell and Soga, 2005).

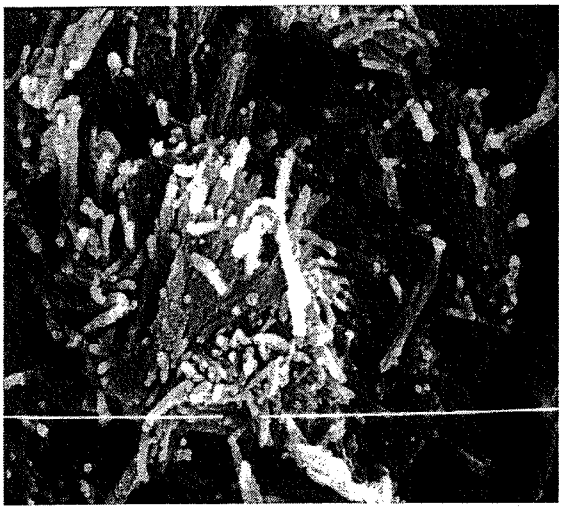

FIGURE 4.13 Scanning electron micrograph of attapulgite from Florida. The length of the space between the bars of light is 0.5 μm (photograph by R. D. Holtz).

Under specialized conditions of weathering (especially of soils of volcanic origin), it may be a locally important constituent of clay soils. Some allophanes have rod- or needle-shaped particles that may make them difficult to compact or stabilize (Sergei Terzaghi, personal communication, 2005).

4.4 IDENTIFICATION OF CLAY MINERALS AND ACTIVITY

Since the clay minerals are so very small, their identification by the usual optical mineralogical techniques used in geology is not possible; thus other means must be employed. From your engineering materials courses, you may remember that materials with regular or repeating patterns of crystal structure will diffract X-rays. Different minerals with different crystalline structures will have different *X-ray diffraction* patterns, and in fact these patterns were used to identify the minerals in the first place. The patterns for the common minerals are published, and it is relatively simple to compare the diffraction pattern of your unknown with those of known minerals. Problems arise, however, with soils that are mixtures of clay minerals, soils that contain organics and other nonclay mineral constituents, and soils with mixed-layer minerals. Usually a detailed quantitative analysis is impossible—about all that one can tell is which minerals are present and roughly how much of each.

Another technique sometimes used to identify clay minerals is *differential thermal analysis* (DTA). A specimen of the unknown soil along with an inert control substance is heated in an electric furnace at a constant rate to several hundred degrees, and the temperature difference between the specimen and the inert substance is measured. Because water losses and phase changes occur at certain unique temperatures for specific clay minerals, the record of these changes may be compared with those of known minerals. In a similar process called *thermal gravimetric analysis* (TGA) the loss in mass of the specimen that occurs during heating is measured. Often both DTA and TGA are conducted in tandem.

Although it is possible to recognize certain clay minerals in micrographs obtained from both transmission and scanning *electron microscopy*, the process is neither easy nor quantitative. See Mitchell and Soga (2005, Chapter 3) for detailed additional information on the identification of clay minerals.

A simple approach, suggested by Professor Casagrande, can also tell you just about as much, at least from an engineering point of view, as the more sophisticated X-ray diffraction and DTA–TGA analyses. The procedure is shown in Fig. 4.14. You simply locate the Atterberg limits of your soil specimen on Casagrande's plasticity chart, then compare its location with those of known minerals. If your sample's Atterberg limits plot high above the A-line near the U-line, chances are it contains a lot of active clay minerals such as montmorillonite. Even if the soil is classified as a CL—for example, a sandy clay—and it still plots near the U-line, then the clay portion of the soil is predominantly montmorillonite. The glacial lake clays from around the Great Lakes region in the United States and Canada are mostly illitic and they plot right above the A-line. Scandinavian marine clays are illitic and they also plot in this region. Kaolinites, which are relatively inactive minerals, plot right below the A-line. Even though they are technically clays, they behave in an engineering sense like ML-MH materials.

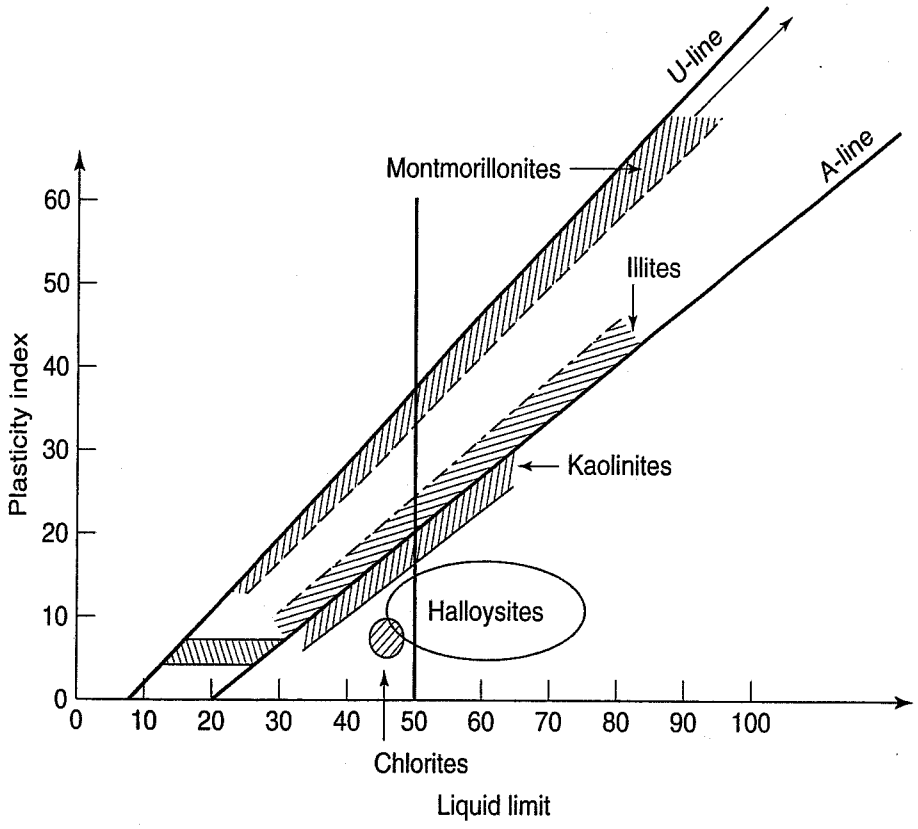

FIGURE 4.14 Location of common clay minerals on Casagrande's plasticity chart (developed from Casagrande, 1948, and data in Mitchell and Soga, 2005).

Skempton (1953) defined the *activity* of a clay as

$$A = \frac{PI}{\text{clay fraction}} \tag{4.1}$$

where the clay fraction is usually taken as the percentage by weight of the soil less than 2 μm. Clays that have an activity around 1 ($0.75 < A < 1.25$) are classified as "normal"; soils with $A < 0.75$ are inactive clays, and those with $A > 1.25$ are active clays.

There is a fair to good correlation between the activity and the type of clay mineral, as shown in Table 4.1. Activity has also been used for certain classification and engineering property correlations, especially for inactive and highly active clays. However, the Atterberg limits alone are usually sufficient for these purposes, and the activity provides no significant new information.

TABLE 4.1 Activities of Various Minerals

Mineral	Activity
Na-montmorillonite	4–7
Ca-montmorillonite	1.5
Illite	0.5–1.3
Kaolinite	0.3–0.5
Halloysite (dehydrated)	0.5
Halloysite (hydrated)	0.1
Attapulgite	0.5–1.2
Allophane	0.5–1.2
Mica (muscovite)	0.2
Calcite	0.2
Quartz	0

After Skempton (1953) and Mitchell and Soga (2005).

4.5 SPECIFIC SURFACE

The ratio of the surface area of a material to either its mass or volume is called the *specific surface*. In terms of volume

$$\text{specific surface} = \text{surface area/unit volume} \tag{4.2}$$

The physical significance of specific surface can be demonstrated using a cube $1 \times 1 \times 1$ cm:

$$\text{specific surface} = \frac{6(1\ \text{cm}^2)}{1\ \text{cm}^3} = 6/\text{cm} = 0.6/\text{mm}$$

If the cube is 1 mm on a side, the specific surface would be

$$\frac{6(1\ \text{mm}^2)}{1\ \text{mm}^3} = 6/\text{mm}$$

If the cube is 1 μm on a side, the specific surface would be

$$\frac{6(1\ \mu\text{m}^2)}{1\ \mu\text{m}^3} = 6/\mu\text{m} = 6000/\text{mm}$$

These three examples illustrate that large particles, whether cubes or soil, have smaller surface areas per unit of volume—and thus smaller specific surfaces—than small particles. To obtain the specific surface in terms of mass, you just divide the value in terms of volume by the mass density ρ_s; units would then be m^2/g or m^2/kg.

Now let us add just enough water to thinly coat the surface area of each cube in the above examples. Note that it will take ten times as much water to wet the surfaces of all the cubes when they are 1 mm on a side than when the same volume is occupied by a single cube of 1 cm^3. Also, if we were trying to remove water, there would be ten times as much to remove from the surfaces of the smaller cubes than those of the larger ones. Or, in energy terms, it would take ten times as much energy to remove the water from the smaller cubes than from the larger ones.

By analogy, the specific surface of a soil is inversely proportional to its grain size. A given amount of soil made up of many small particles would have on average a larger specific surface than that same amount made up of large particles.

Because so many physical processes involving clay and other layer silicate minerals are closely related to their surface area, soil scientists and other Hungarians have developed test procedures to measure the specific surface (Carter et al., 1986). However, in geotechnical engineering, we generally do not need to know a numerical value of the specific surface of a soil—it is the concept that is important. For example, from this concept, we would expect larger water contents for fine-grained soils than for coarse-grained soils, all other things such as void ratio and soil structure being equal.

You may recall from your materials courses that specific surface is a primary factor in concrete and asphalt mix design, because in both cases it is necessary to provide sufficient cement paste or asphalt to coat the aggregate surfaces.

4.6 INTERACTION BETWEEN WATER AND CLAY MINERALS

As mentioned earlier, water usually has little effect on the behavior of granular soils. For example, the shear strength of a sand is approximately the same whether it is dry or saturated. An important exception is the case of loose deposits of saturated sand subjected to dynamic loads such as earthquakes or blasts.

On the other hand, fine-grained soils, especially clay soils, are strongly influenced by the presence of water. The variation of water content gives rise to plasticity, and the Atterberg limits are an indication of this influence. Grain size distribution only rarely governs the behavior of fine-grained soils.

Why is water important in fine-grained soils? From the previous discussion, you know that the smaller the particle, the larger the specific surface. Clay minerals, being relatively small particles, have large specific surfaces, and all else being equal, you might expect them also to have very active surfaces. In fact, the size, specific surface, and activity of clay minerals all relate rather well.

The dimensions and specific surfaces of four common clay minerals are shown in Table 4.2. Kaolinite, the largest clay mineral crystal, has a thickness or edge dimension of roughly 1 μm, while that of montmorillonite, the smallest clay mineral, is only a few nanometres. Since the crystals have roughly the same average "diameter," at least within an order of magnitude, it is not surprising that their specific surfaces are so different. Of course, depending on weathering and other factors, there are rather wide variations in the sizes of the crystals, and Table 4.2 gives only average values. Since surface activity is related to the particle size, you can see why montmorillonite, for example, is much more active than kaolinite. Look again at the activity values in Table 4.1; note that they also roughly relate to mineral size and specific surface. Similarly, the surface activity of a sand or silt grain is extremely low.

For the reasons described below, unbalanced force fields exist at the surfaces of the clay minerals, and this is the physical-chemical basis for the interaction between water, dissolved ions, and clay minerals. The interaction of these force fields leads to various associations or arrangements of soil particles that we call the structure of clay soils, which ultimately controls their engineering behavior.

TABLE 4.2 Typical Dimensions, Specific Surfaces, and Cation Exchange Capacity of the Common Clay Minerals

Clay Mineral	Typical Thickness (nm)	Typical Diameter (nm)	Specific Surface (km^2/kg)	Cation Exchange Capacity[a] (meq/100 g)
Montmorillonite	3	100–1000	0.7–0.84	80–150
Illite	30	10 000	0.065–0.1	10–40
Chlorite	30	10 000	0.08	10–40
Kaolinite	50–2000	300–4000	0.01–0.02	2–15

[a]Defined in Sec. 4.6.2.

After Yong and Warkentin (1975) and Mitchell and Soga (2005).

4.6.1 Hydration of Clay Minerals and the Diffuse Double Layer

As noted by Yong and Warkentin (1975), it seems that clay particles in nature are almost always hydrated; that is, layers of water molecules surround each crystal of clay. This water is called *adsorbed water*. How is water adsorbed on the surface of a clay particle? First, you may recall from chemistry or materials courses that water is a *dipolar* molecule (Fig. 4.15). Even though water is electrically neutral, it has two separate centers of charge, one positive and one negative. Thus the water molecule is electostatically attracted to the surface of the clay crystal. Second, water is held to the clay crystal by *hydrogen bonding* (hydrogen of the water is attracted to the oxygen atoms or hydroxyl molecules on the surface of the clay). Third, the negatively charged clay surface attracts cations present in the water. Since all cations are hydrated to some extent, depending on the ion, cations also contribute to the attraction of water to the clay surface. Of these three factors, hydrogen bonding is probably the most important.

The attraction of water to the clay surface is very strong near the surface and diminishes with distance. It seems that the water molecules right at the surface are very tightly held and strongly oriented. Measurements show that the density and some thermodynamic and electrical properties of the water next to the clay surface are different from those of "free water" (Yong and Warkentin, 1975; Mitchell and Soga, 2005).

What does a clay particle look like with adsorbed water on it? Figure 4.16 shows schematically sodium montmorillonite and kaolinite crystals with layers of *adsorbed* water. Note that the thickness of the adsorbed water is approximately the same, but because of the size differences, it is not surprising that montmorillonite has much greater activity, higher plasticity, greater swelling, more shrinkage, and larger volume change due to loading than kaolinite.

Because the cations in the adsorbed water layers are more concentrated near the surfaces of clay crystals, they thermally diffuse away from the surfaces in an attempt to equalize cation concentrations within the adsorbed water. But this diffusion is counterbalanced by the electrical attraction of the positively charged cations to the negatively charged clay crystal surfaces. These two components—the clay particle surface and the diffuse layer of cations—together form the *diffuse double layer*. The diffuse double layer, shown schematically in Fig. 4.17, also includes anions that are, of course, repelled from the negative force field of the clay crystal.

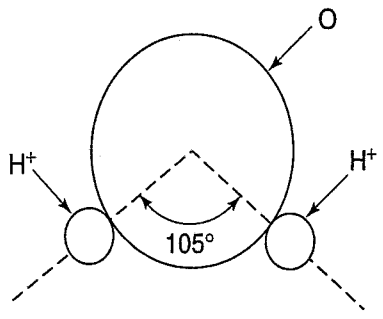

FIGURE 4.15 Schematic diagram of a water molecule (after Lambe, 1953).

The development and the mathematical equations describing the diffuse double layer are given by, among others, Yong and Warkentin (1975), van Olphen (1977), and Mitchell and Soga (2005). They also discuss the influence of such factors as the concentration of the electrolyte, cation valence, dielectric constant of the pore fluid, temperature, ionic size, pH, and anion absorption on

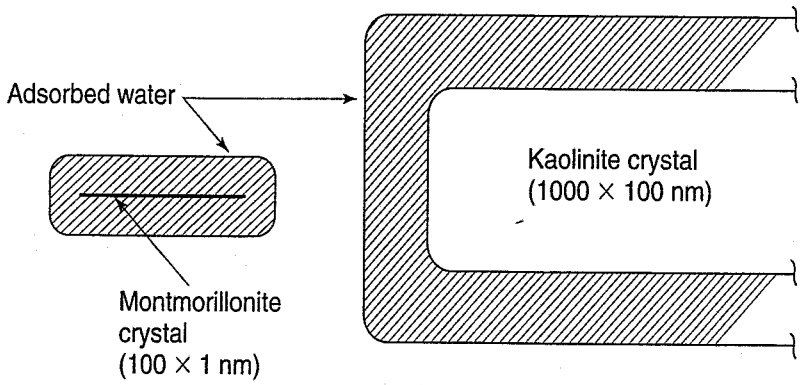

FIGURE 4.16 Relative sizes of adsorbed water layers on sodium montmorillonite and sodium kaolinite (after Lambe, 1958a).

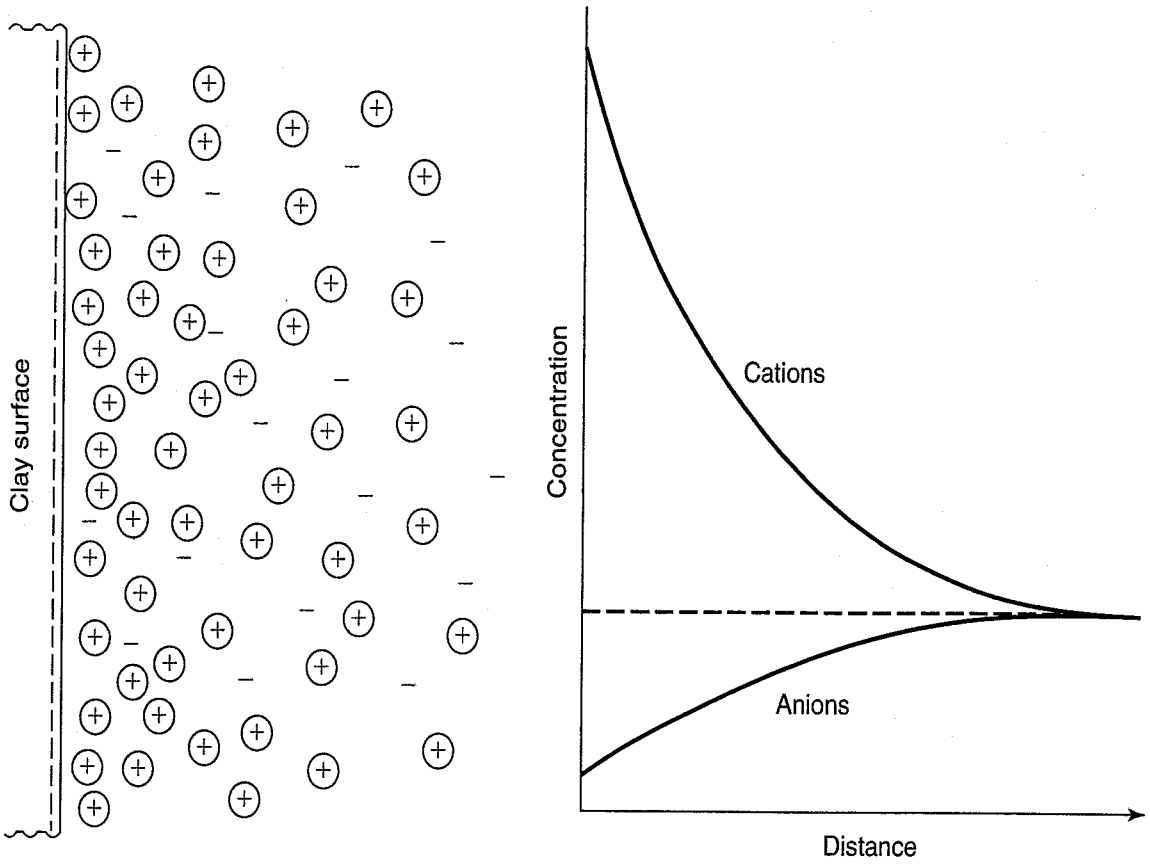

FIGURE 4.17 Diffuse double layer in a clay-water system showing schematically the distribution of ions next to the clay crystal surface (Mitchell and Soga, 2005).

the diffuse double layer. The diffuse double layer is an important concept for understanding the behavior of clay-water-electrolyte systems, and it helps to explain clay properties such as plasticity, swelling, and the interaction of clay particles.

4.6.2 Exchangeable Cations and Cation Exchange Capacity (CEC)

The negative charge at the surface of the clay crystal results from both isomorphous substitution, mentioned earlier, and imperfections in the crystal lattice, especially near the mineral surfaces. "Broken" edges contribute greatly to unsatisfied valence charges at the edges of the crystal. Since the crystal wants

to be electrically neutral, cations in the water may be strongly attracted to the clay, depending on the amount of negative charge present. Different clays have different charge deficiencies and thus different tendencies to attract the exchangeable cations. They are called *exchangeable* because one cation can easily be exchanged with one of the same valence, or with two of one-half the valence, of the original cation. As might be expected from their relative sizes and specific surfaces, montmorillonite has a much greater charge deficiency and thus a much greater attraction for exchangeable cations than kaolinite. Illite and chlorite are intermediate in this respect.

The amount of exchangeable cations can be determined analytically or experimentally (Yong and Warkentin, 1975; van Olphen, 1977; Fang, 1997; and Mitchell and Soga, 2005). The *cation exchange capacity* (CEC) of the clay is usually expressed in units of milliequivalents (meq) per 100 g of dry clay. Sometimes this quantity is referred to as the base exchange capacity (BEC) or the ion exchange capacity (IEC).

So, what is an equivalent? An *equivalent* is the number of ions or electronic charges in one mole of solution, and it equals 6.02×10^{23} charges (you may recall that the number 6.02×10^{23} is *Avocado's number*[1]). The number of equivalents, then, is the weight of an element divided by its atomic weight, times its valence—or, in equation form:

$$\text{one equivalent} = \left(\frac{\text{weight of element}}{\text{atomic weight}}\right)(\text{valence})$$

A milliequivalent (meq) is, of course, 10^{-3} equivalents. Note that 6.02×10^{23} electron charges = 96 500 coulombs = 1 faraday (Leonards, 1962; Mitchell and Soga, 2005).

Typical values of CEC for the common clay minerals are given in Table 4.2. A CEC of 10 meq/100 g means that each 100 g of clay solids is able to exchange $10 \times 10^{-3} \times 6 \times 10^{23} = 6 \times 10^{21}$ electron charges. If the exchangeable ion is monovalent (such as Na^+), then 6×10^{21} sodium ions can be replaced. If it is divalent, such as Ca^{++}, then 3×10^{21} calcium ions can be replaced per 100 g of clay (Leonards, 1962).

Calcium and magnesium are the predominant exchangeable cations in most soils except those of marine origin; potassium and sodium exist but are less common. Aluminum and hydrogen are common in acidic soils. The depositional environment as well as subsequent weathering and leaching will govern what ions are present in a particular soil deposit. As might be expected, the predominant exchangeable cations in marine clays are sodium and magnesium, because these are the most common cations in seawater. Cation exchange or replacement is further complicated by the presence of organic matter. Sulfate, chloride, phosphate, and nitrate are common anions in soils.

In addition to isomorphous substitution and broken bonds or edges, a third source of cation exchange capacity is replacement. The ease of replacement or exchange of cations depends on several factors, primarily the valence of the cation. Higher valence cations easily replace cations of lower valence. For ions of the same valence, the size of the hydrated ion becomes important; the larger the ion, the greater the replacement power. A further complication is the fact that potassium, even though it is monovalent, fits into the hexagonal holes in the silica sheet. Thus it will be very strongly held on the clay surface, and it will have a greater replacement power than sodium, for example, which is also monovalent. The cations can be listed in *approximate* order of their replacement ability. The specific order depends on the type of clay, which ion is being replaced, and the concentration of the various ions in the water. In order of increasing replacement power from left to right, in general the ions are:

$$Li^+ < Na^+ < H^+ < K^+ < NH_4^+ < Mg^{++} < Ca^{++} < Cu^{++} < Al^{+++} < Fe^{+++}$$

[1]Named for Amedeo Avogadro (1776–1856), an Italian mathematician, who proposed that equal volumes of all gases contain the same number of molecules at the same pressure and temperature (Fox and Hill, 2007).

In some instances the specific order may differ slightly, depending on local conditions and variations in concentration. Replacement series may also include different elements such as cesium, barium, thorium, and rubidium.

There are several practical consequences of ion exchange. For one thing, it makes possible the use of chemicals to stabilize or strengthen soils. Lime (CaOH) stabilizes a sodium clay soil by replacing the sodium ions in the clay, because calcium has a greater replacing power than sodium. The swelling of sodium montmorillonitic clays can be significantly reduced by the addition of lime (Chapter 6).

This section has presented only a brief overview of the very complex subject of the interaction between water and clay minerals. For additional information, you should consult Yong and Warkentin (1975), Van Olphen (1977), and Mitchell and Soga (2005) and the references therein.

4.7 INTERACTION OF CLAY PARTICLES

The association of clay minerals and their adsorbed water layers provides the physical basis for soil structure. The individual clay particles interact through their adsorbed water layers, and thus the presence of different ions, organic materials, different concentrations, etc., contribute to the multitude of soil structures found in natural soil deposits. Clay particles can repulse each other electrostatically, but the process depends on the ion concentration, interparticle spacing, and other factors. Similarly, the individual particles can be attracted due to the tendency for hydrogen bonding, van der Waals forces, and other types of chemical and organic bonds. The interparticle force or potential fields decrease with increasing distance from the crystal surface, as shown in Fig. 4.18. The actual shape of the potential curve will depend on the valence and concentration of the dissolved ion, dielectric constant of the pore fluid, temperature, and the nature of the bonding forces.

Particles can flocculate or be repelled (disperse, separate). They can flocculate in several possible configurations; edge-to-face is the most common, but edge-to-edge or face-to-face is also possible. The tendency toward flocculation will depend on *increasing* one or more of the following (Lambe, 1958a, Evans, 1991, Mitchell and Soga, 2005):

- Concentration of the electrolyte
- Valence of the ion

or *decreasing* one or more of the following:

- Dielectric constant of the pore fluid
- Size of the hydrated ion
- pH
- Anion adsorption

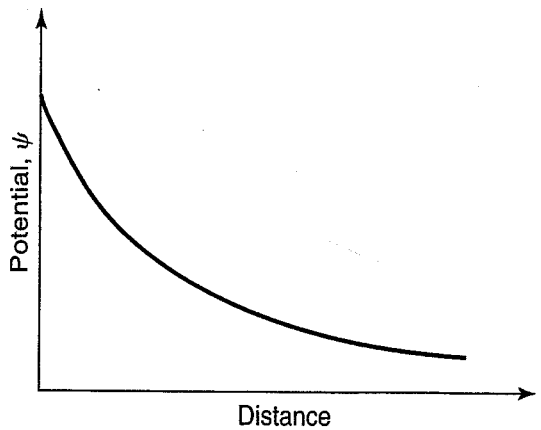

FIGURE 4.18 Chemical, electrostatic, etc., potential versus distance from the clay crystal surface.

The effect of temperature is somewhat ambiguous; in some cases, increasing the temperature results in flocculation, while sometimes the opposite seems to occur.

Just about all naturally occurring clay soils are flocculated to some extent. Only in very dilute solutions (at very high water contents) is dispersion of clay particles possible, and this probably occurs only rarely in nature. However, dispersion is possible in high water content slurries and sludges that are produced as waste products from coal-fired power generation, mineral processing, and other industries.

4.8 SOIL STRUCTURE AND FABRIC OF FINE-GRAINED SOILS

The structure of a fine-grained soil strongly affects—or, some would say, even governs—the engineering behavior of that soil. All the clay structures found in nature and described in the next section result from some combination of the nature of the clay mineral, the geologic environment at deposition, and the subsequent geologic and engineering stress history of the deposit. These are very complicated factors, but we study them because they fundamentally affect the behavior and the engineering properties of soil. When cohesive soils are encountered in engineering practice, geotechnical engineers must consider the soil structure at least qualitatively.

In geotechnical engineering, we define the *structure* of a soil to include the geometric arrangement or *fabric* of the particles or mineral grains as well as the interparticle forces that may act between them. Soil fabric, then, refers only to the geometric arrangement of the particles. Because in granular soils the surface activity of the individual grains is very small, the interparticle forces are also very small. Thus both the fabric and structure of gravels, sands, and to some extent silts are the same. On the contrary, however, interparticle forces are relatively large in fine-grained cohesive soils, and thus the structure of these soils consists of both these forces and the soil fabric.

A complete description of the structure of a fine-grained cohesive soil requires knowledge of both the interparticle forces and the fabric of the particles. Since it is extremely difficult, if not impossible, to directly measure the interparticle force fields surrounding clay particles, most studies of cohesive soil structures involve only fabric. Of course, from the fabric of these soils, certain inferences can be made about their interparticle forces.

How do we observe and study soil fabrics? Because of their relatively large grain sizes, the fabrics of sands and gravels can be visually observed. Sometimes thin sections are prepared from specimens of granular materials stabilized with epoxies or resins and then viewed under an optical microscope. Fine-grained soil fabrics require significant magnification, and many of the methods described in Sec. 4.4 for identifying clay minerals are also used to study clay soil fabrics. None of these procedures is particularly simple, and only a very few provide even crude numerical measures of fabric. See Mitchell and Soga (2005) for detailed description of fabric study using the polarizing microscope, electron microscopy, X-ray diffraction, X-radiography, pore size distribution, and several indirect methods.

4.8.1 Fabrics of Fine-Grained Soils

Although it was generally known that fine-grained soils sometimes behaved differently after remolding (such as reworking a soil by spreading, adding water or drying, and compaction), the influence of soil structure on soil behavior was not considered important until the mid 1920s. Terzaghi (1925a and b) described the process of sedimentation and formation of fine-grained soils, and his models of sedimentation and the structure of fine-grained soils are shown in Fig. 4.19. Casagrande (1932c), building on Terzaghi's concepts, postulated that during sedimentation, clay particles in suspension flocculate and settle to the bottom along with the larger silt grains. As shown in Fig. 4.20(a), the sediments form a honeycomblike open structure with very high water content and void ratio.

With additional deposition, the soil structure compresses at points of high stress concentration, as shown in Fig. 4.20(b) (Casagrande, 1932c). The bonds between the flocculated clay particles are

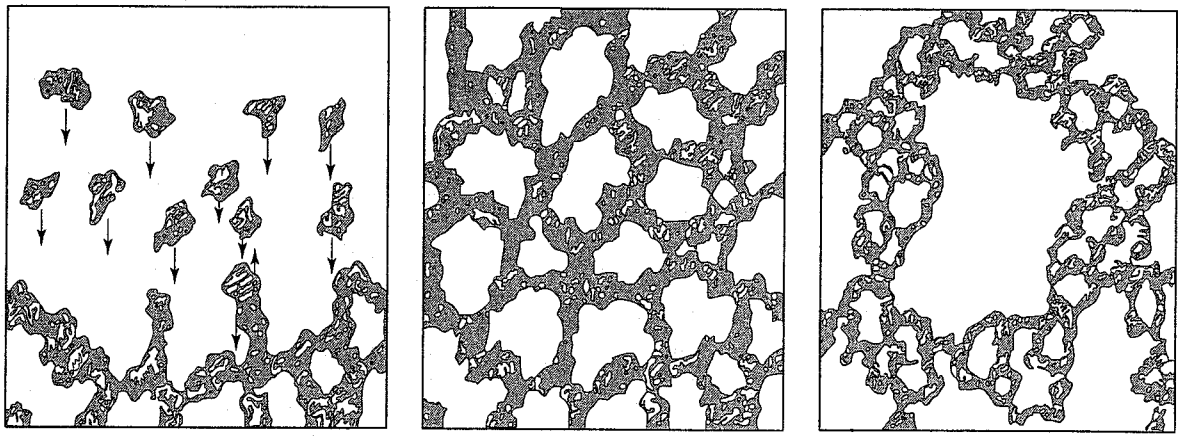

FIGURE 4.19 Terzaghi's (1925b) models for the fabric of fine-grained sediments: (a) process of sedimentation; (b) structure of the flocculated sediment.

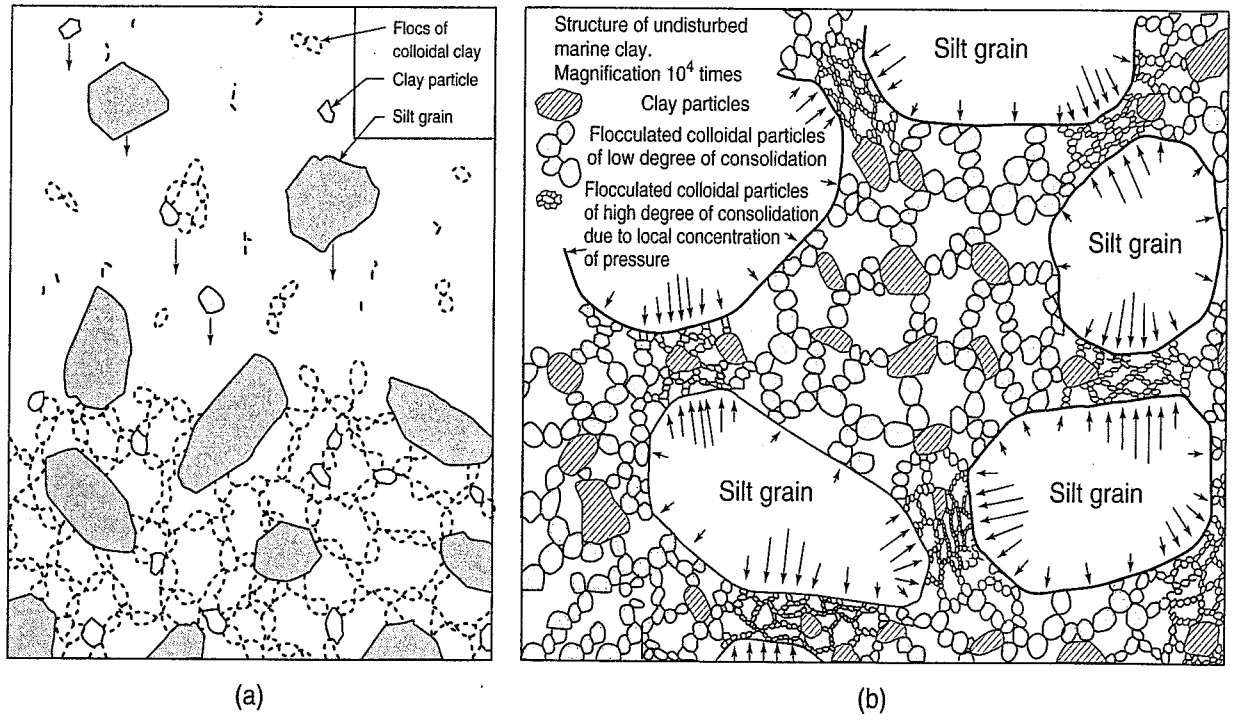

FIGURE 4.20 Casagrande's (1932c) concept of the structure of undisturbed marine clay: (a) during sedimentation; and (b) after compression and densification of the sediment.

quite brittle, especially those formed in seawater; when specimens of these clays are tested in compression, the strain at failure is only 1% or less, and deformations are almost elastic (see Sec. 11.3).

In the 1950s, because of increased interest in the physical-chemical behavior of clay soils, a number of different fabric models were proposed. Two of the best known were by Lambe (1953) and Tan (1957), and they are shown in Figs. 4.21 and 4.22. Representation of fine-grained soil fabrics by only a few clay particles, however, is not very realistic. Single-grain or single-particle units occur only rarely in nature and then only in very dilute clay-water systems under special environmental conditions. From studies of real clay soils with the scanning electron microscope (SEM), the individual clay particles seem to always be aggregated or flocculated together in submicroscopic fabric units called *domains*. Domains in turn group together to form *clusters*, which are large enough to be seen with a visible-light microscope. Clusters group together to form *peds* and even groups of peds. Peds

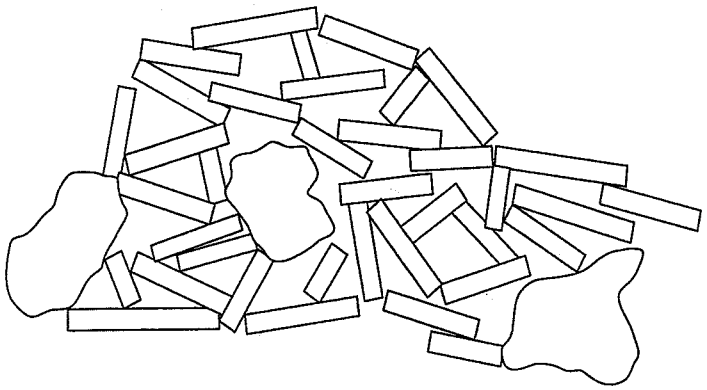

(a)

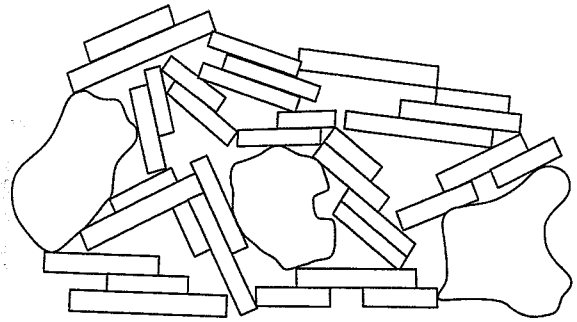

(b)

FIGURE 4.21 Models of undisturbed clays deposited in (a) salt water and (b) fresh water (after Lambe, 1953).

can be seen without a microscope, and they—together with other large visible features such as joints and fissures—constitute the *macrofabric* system of the soil. A schematic sketch of this system proposed by Yong and Sheeran (1973) is shown in Fig. 4.23; a microscopic view of a marine clay is also included (Pusch, 1973).

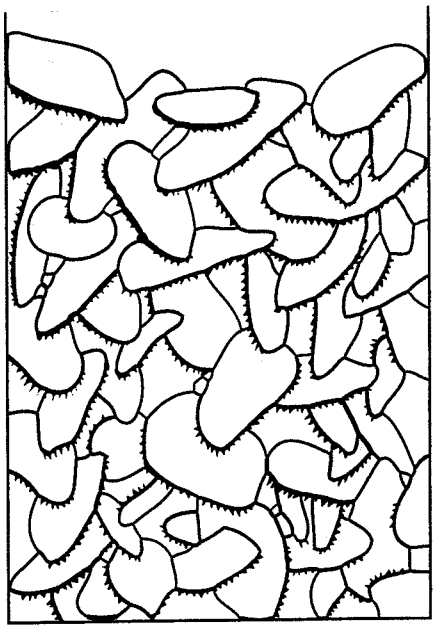

FIGURE 4.22 Schematic diagram of a clay as proposed by Tan (1957).

Collins and McGown (1974) suggest a somewhat more elaborate system for describing macrofabric features in natural soils. They propose three types of features:

1. *Elementary particle arrangements* consisting of single forms of particle interaction at the level of individual clay, silt, or sand particles [Fig. 4.24(a) and (b)] or interaction between small groups of clay platelets [Fig. 4.24(c)] or "clothed" silt and sand particles [Fig. 4.24(d)].
2. *Particle assemblages*, which are units of particle organization having definable physical boundaries and a specific mechanical function. Particle assemblages consist of one or more forms of elementary particle arrangements or smaller particle assemblages, as shown in Fig. 4.25.
3. *Pore spaces* within and between elementary particle arrangements and particle assemblages.

Collins and McGown (1974) show microphotographs of several natural soils that illustrate their proposed system. Other

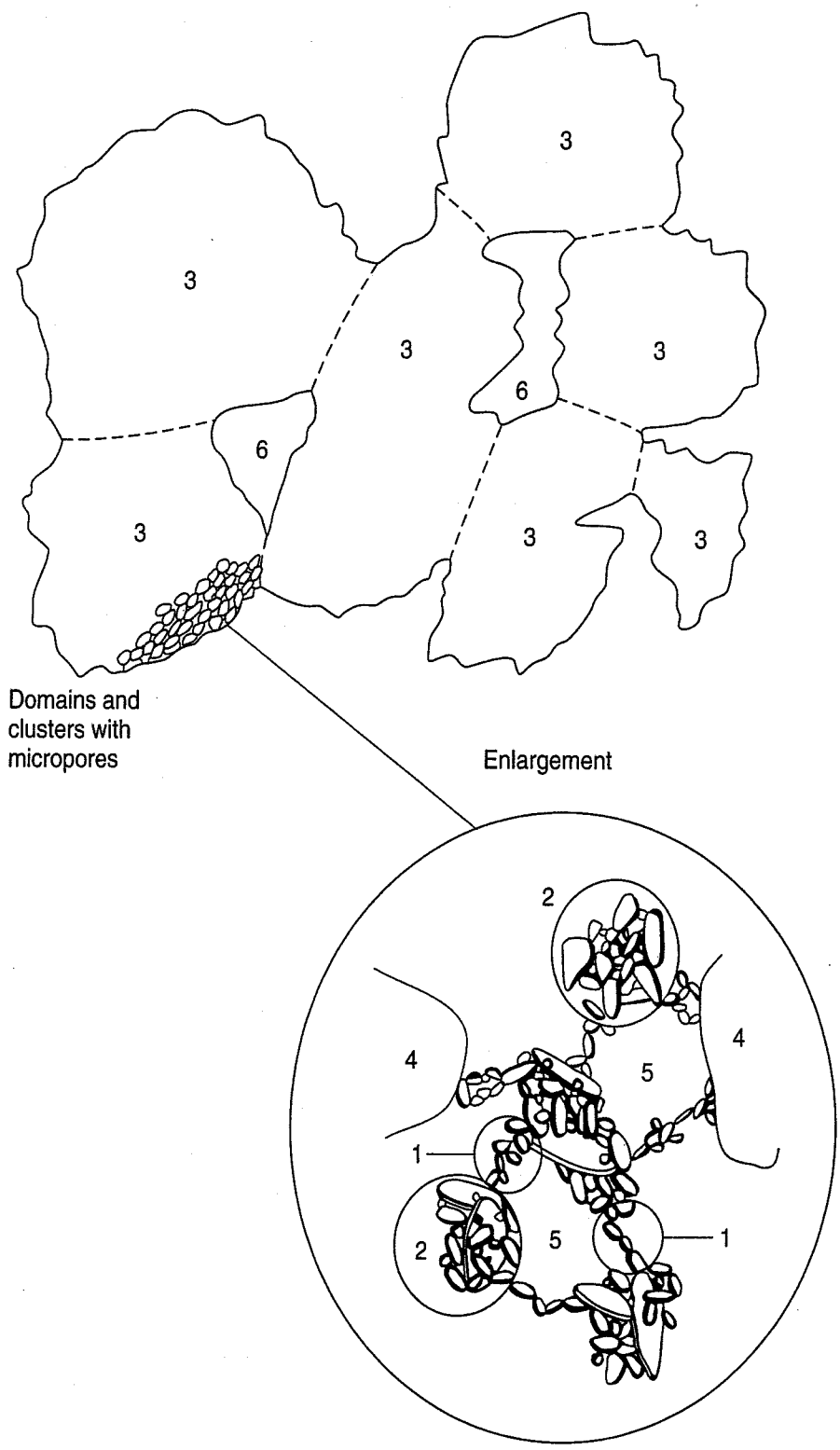

FIGURE 4.23 Schematic diagram of the soil microfabric and macrofabric system proposed by Yong and Sheeran (1973) and Pusch (1973): 1, domain; 2, cluster; 3, ped; 4, silt grain; 5, micropore; and 6, macropore.

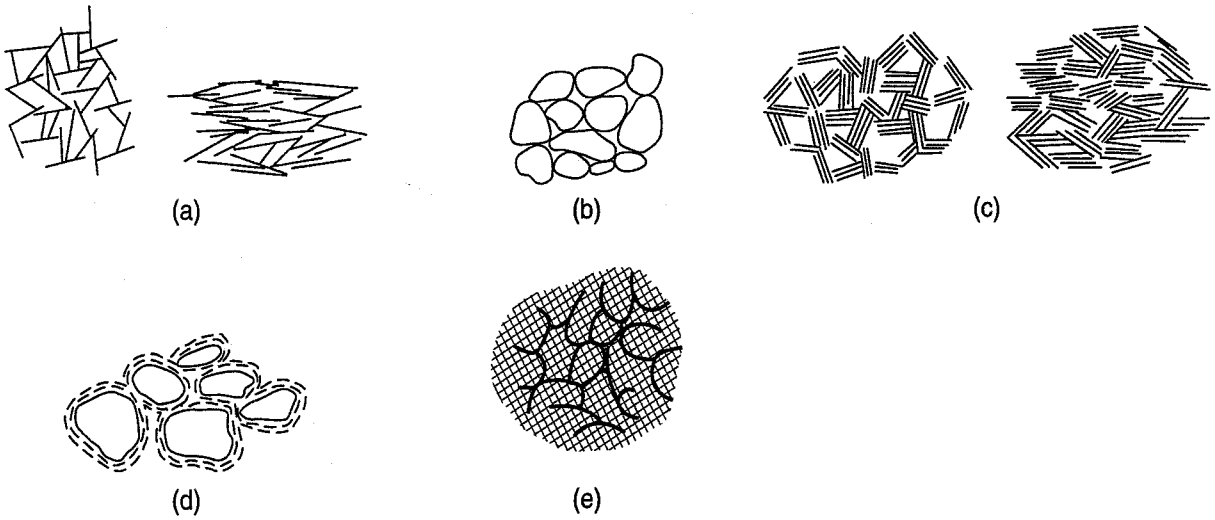

FIGURE 4.24 Schematic representations of elementary particle arrangements: (a) individual clay platelet interaction; (b) individual silt or sand particle interaction; (c) clay platelet group interaction; (d) "clothed" silt or sand particle interaction; (e) partly discernible particle interaction (after Collins and McGown, 1974).

systems for classifying soil structure and fabric have been developed by pedologists and soil scientists. A good example is the system proposed by Brewer (1976).

A SEM microphotograph of a silty clay ped from Norway is shown in Fig. 4.26. Note how complex the structure appears, suggesting that the engineering behavior of this soil is probably also quite complex. Also note how similar this real marine clay looks to the model postulated by Casagrande (1932c) shown in Fig. 4.21(b).

Figure 4.27 shows microphotographs of a compacted clayey silt from France. Figure 4.27(b) is magnified four times larger than Fig. 4.27(a). The large silt grain in the lower left center of Fig. 4.27(b) contains some clay platelets—probably kaolinite, as they are about 5 μm in the major dimension. Coatings of much smaller clay particles are also visible. Again, fabric complexity rather than simplicity is apparent.

Because of their bound water layers, it is difficult to ascertain whether actual mineral contact occurs in clays. However, grain-to-grain contact of silt particles can readily be seen, especially in Fig. 4.27(b) and in Fig. 4.28. It is interesting that many of the fabric models shown in Figs. 4.23, 4.24 and 4.25 can be seen in the SEM microphotographs of Figs. 4.26, 4.27 and 4.28. See Mitchell and Soga (2005) for additional microphotographs of real soil fabrics.

4.8.2 Importance of Microfabric and Macrofabric; Description Criteria

Both the microfabric and macrofabric of a clay deposit reflect the deposit's entire geologic and stress history. This includes its depositional and environmental history, chemical and physical weathering, and stress history—that is, the changes in stress caused both by geological forces and by human activities. Virtually everything that ever happened to that soil is imprinted in some manner on its structure and fabric.

Although microfabric is probably more important from a fundamental than an engineering viewpoint, understanding it improves one's general understanding of soil behavior. For example, clay microfabric research has suggested that the greatest single factor influencing the final structure of a clay soil is the electrochemical environment existing at the time of its sedimentation. Flocculated structures or aggregations of particles (domains and clusters) can result during sedimentation in virtually all depositional environments, whether marine, brackish, or fresh water. Fabric characteristics such as the

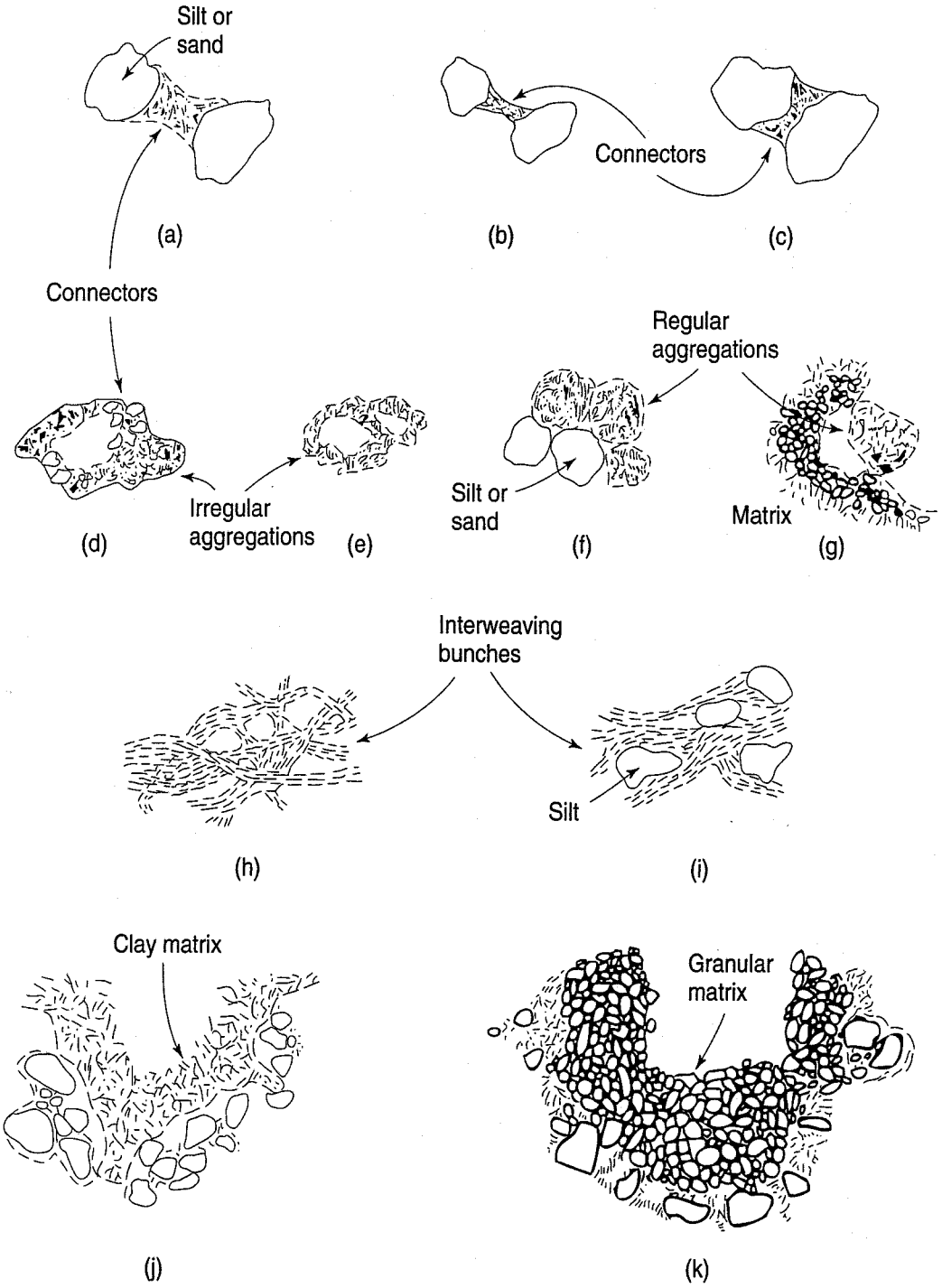

FIGURE 4.25 Schematic representations of particle assemblages: (a), (b), and (c) connectors; (d) irregular aggregations linked by connector assemblages; (e) irregular aggregations forming a honeycomb arrangement; (f) regular aggregations interacting with silt or sand grains; (g) regular aggregation interacting with particle matrix; (h) interweaving bunches of clay; (i) interweaving bunches of clay with silt inclusions; (j) clay particle matrix; (k) granular particle matrix (after Collins and McGown, 1974).

FIGURE 4.26 Drammen silty clay: large ped of silt and clay with weak links to other peds (from Barden and McGown, 1973; photograph courtesy of A. McGown).

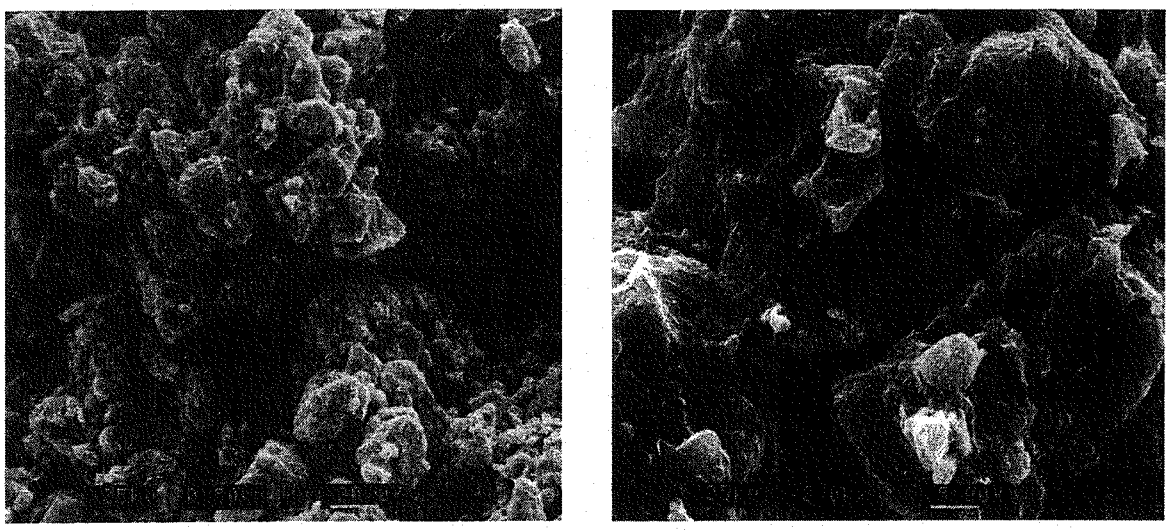

(a) (b)

FIGURE 4.27 Jossigny clayey silt, quasi-statically compacted at 14.9% water content and 16.0 kN/m^3: (a) magnification of 500 times; and (b) magnification of 2000 times (Delage et al., 1996; photograph courtesy of P. Delage).

FIGURE 4.28 SEM of silt grain-to-grain contact in Swedish till (from McGown, 1973).

shape and distribution of pores in the structure are also apparently influenced to a large degree by the clay mineralogy as well as the amount and angularity of silt grains present.

Macrofabric also has an important influence on the engineering behavior of soil deposits, especially those comprised of fine-grained soils. Features such as joints, fissures, intermediate silt and sand seams and layers, root holes, varves, and other "defects" often control the response of the entire soil mass to engineering loads. These features are also a challenge for the geologic and geotechnical investigation that precedes any design and construction. The macrofabric feature may be missed in the investigation, or tests (in situ and laboratory) may not involve the feature and thus the test results will be erroneous. The worst case is, of course, that faulty designs based on this information may result in a failure. Rowe's (1972) Rankine Lecture illustrates the importance of soil macrofabric to geotechnical practice. As a simple example, the strength of a soil mass is significantly reduced along a crack or fissure. If this defect happens to be unfavorably oriented with respect to the applied engineering stress, instability or failure may occur. This is why shallow excavations for pipe trenches, for example, must always be supported. If not, the fissures or defects in the surface soils may result in a collapse of the trench walls—a very dangerous situation for any workers in the trench.

Another example is the influence of a sand or silt layer or seam on the drainage characteristics of a thick clay layer. As we shall see in Chapters 8 and 9, the rate of settlement of the clay layer strongly depends on the distance between drainage layers, and if intermediate drainage layers are missed during the site investigation, erroneous predictions of settlement rates will be made. Accurate settlement predictions are very important in the design of foundations.

Consequently, in engineering problems involving stability, settlements, or drainage, the geotechnical engineer must carefully investigate the macrofabric of the deposit. Criteria have been developed by ASTM, USBR, and the California Department of Water Resources, among others, for describing the macrofabric and structure of intact soils. These criteria are summarized in Table 4.3.

In summary, the fabric of fine-grained soil deposits is highly complex. The engineering behavior of these deposits is strongly influenced by both the micro- and macrofabric. At present, though no established quantitative connection exists between soil fabric and its engineering properties, it is still important to appreciate the complexity of the fabric of fine-grained soils and its relation to the engineering behavior of the deposit.

TABLE 4.3 Criteria for Describing the Structure of Intact Fine-grained Soils

Description	Criteria
Homogeneous	Same color and appearance throughout
Stratified	Alternating layers of varying material or color with layers at least 6 mm thick; note thickness
Laminated	Alternating layers of varying material or color with layers less than 6 mm thick; note thickness
Banded	Layers of same material but with different colors
Fissured	Breaks along definite planes of fracture with little resistance to fracturing
Slickensided	Fracture planes appear polished or glossy, sometimes striated
Blocky	Cohesive soil that can be broken down into small angular lumps that resist further breakdown
Lensed or seamed	Inclusion of small pockets of different soils, such as small lenses of sand scattered through a mass of clay; note thickness and whether seams are continuous
Mottled	Contains color blotches
Honeycombed	Porous or vesicular
Root holes	Note presence of roots or root holes

From ASTM (2010) D 2488; U.S. Dept. of the Interior (1990) 5005; and California DWR (1962) S-4.

4.9 GRANULAR SOIL FABRICS

Do granular materials, sand and gravels, actually have a fabric? At first, you might think that they don't, or if they do, that their fabrics are rather simple in comparison with deposits of fine-grained soils. In turns out that when granular materials are deposited either by wind or in water, they can have rather complex fabrics that in some cases significantly influence their engineering behavior. Go back and review the appropriate sections of Chapter 3 for a description of soil deposition by water (rivers, beaches, etc.) and wind (loess deposits and sand dunes; grain sizes generally < 0.05 mm) and the landforms that result from these geologic processes.

Grains of soil larger than 0.01 to 0.02 mm settle out of a soil-fluid suspension independently of other particles, because their weight causes them to settle and come to equilibrium in the bottom of the fluid as soon as the velocity can no longer support them in suspension. In this case, their fabric is *single grained.* This is the fabric of, for example, a sand or gravel pile, and some sand-silt mixtures. Single-grained fabrics may be "loose" (high void ratio or low density), as shown in Fig. 4.29(a), or "dense" (low void ratio or high density), as shown in Fig. 4.29(b). Under some conditions of deposition a granular material can achieve a very open or "honeycomb" fabric [Fig. 4.29(c)], with a very high void ratio

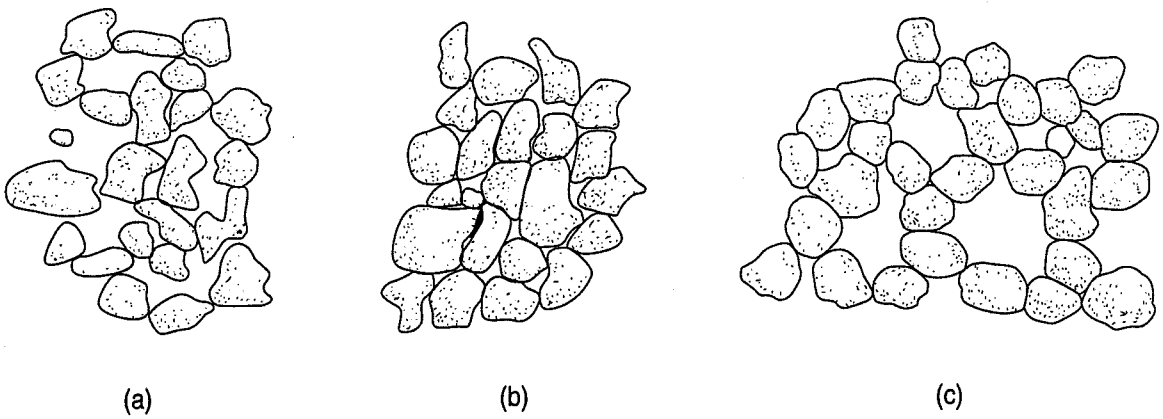

FIGURE 4.29 Single-grained soil structures: (a) loose; (b) dense; and (c) honeycomb.

and low density. A honeycomb fabric is metastable; that is, the grain arches can support static loads, but the structure is very sensitive to collapse, especially when vibrated or loaded dynamically. The presence of water in very loose granular fabrics also can significantly influence their engineering behavior. Good examples are *bulking*, a capillary phenomenon discussed in Chapter 6, and *quicksand* and *liquefaction*, described in Chapter 7.

The fabrics of natural deposits of granular soils are often much more complex than those shown in Fig. 4.29. Consequently, just as with the structure of fine-grained soil deposits, the geotechnical engineer must carefully investigate the macrofabric or structure of granular soil deposits. Descriptive criteria are summarized in Table 4.4.

Depending on the shape of the grains, the grain size distribution, and the packing or arrangement of the grains (fabric), granular soils can have a rather wide range of void ratios. The greatest possible void ratio or loosest possible condition of a soil is called the *maximum void ratio* (e_{max}). Similarly, the *minimum void ratio* (e_{min}) is the densest possible condition that a given soil can attain. The ranges of possible void ratios and porosities for typical granular soils are shown in Table 4.5. The maximum and minimum void ratios are usually determined in the laboratory using test procedures discussed in Chapter 5.

Void ratio or density alone is not sufficient to accurately characterize the fabric, and thus the engineering properties, of granular soils. It is possible, for example, for two sands to have the same void ratio

TABLE 4.4 Criteria for Describing the Structure of Coarse-Grained Soils in their Natural or In-Place Condition

Uniform	Particles of the same size
Heterogeneous	Mixture of different sizes, shapes, hardness, or mineral composition
Stratified	Layers of different soils; note thickness, strike, and dip of beds/layers
Lenses or seams	Thin layer or strata; note thickness
Cementation	Detected by visual-manual inspection and/or the acid test
Degree of "compactness"	Loose (high voids, settles with jarring); dense (no movement with vibration)

From California DWR (1962).

TABLE 4.5 Typical Values of Void Ratio and Porosity of Granular Soils

	Particle Size and Gradation				Void Ratio		Porosity (%)	
	≈ Size Range (mm)							
Soil Type	D_{max}	D_{min}	$\approx D_{10}$	$\approx C_u$	e_{max} (loose)	e_{min} (dense)	n_{max} (loose)	n_{min} (dense)
1. Uniform materials:								
(a) Equal spheres	—	—	—	1.0	0.92	0.35	48	26
(b) Standard Ottawa sand	0.84	0.59	0.67	1.1	0.80	0.50	44	33
(c) Clean, uniform sand (fine or medium)	—	—	—	1.2 to 2.0	1.0	0.40	50	29
(d) Uniform, inorganic silt	0.05	0.005	0.012	1.2 to 2.0	1.1	0.40	52	29
2. Well-graded materials:								
(a) Silty sand	2.0	0.005	0.02	5 to 10	0.90	0.30	47	23
(b) Clean, fine to coarse sand	2.0	0.05	0.09	4 to 6	0.95	0.20	49	17
(c) Micaceous sand	—	—	—	—	1.2	0.40	55	29
(d) Silty sand and gravel	100	0.005	0.02	15 to 300	0.85	0.14	46	12

After Hough (1969).

but significantly different fabrics (and different relative densities; see Chapter 5) and thus significantly different engineering behavior. Figure 4.30 shows a couple of two-dimensional examples of what we mean. Both "sands" in Figs. 4.30(a) and (b) are identical—they have the same grain size distribution and the same void ratio, but their particle arrangements or fabrics are obviously very different. Figures 4.30(c) and (d) show the effect of particle shape and orientation. Again, both "sands" have the same grain-size distribution and the same void ratio, but the orientation of their particles and their fabrics are obviously very different. If the materials illustrated in Fig. 4.30 were real sands, their engineering properties—such as hydraulic conductivity, compressibility, and shear strength—would undoubtedly be very different.

Finally, stress history is another factor that must be considered when dealing with sands and gravels in engineering practice. Deposits of granular materials that have been preloaded by nature or human activities will have very different stress-strain properties and therefore very different compressibility and settlement response (Lambrechts and Leonards, 1978; Holtz, 1991).

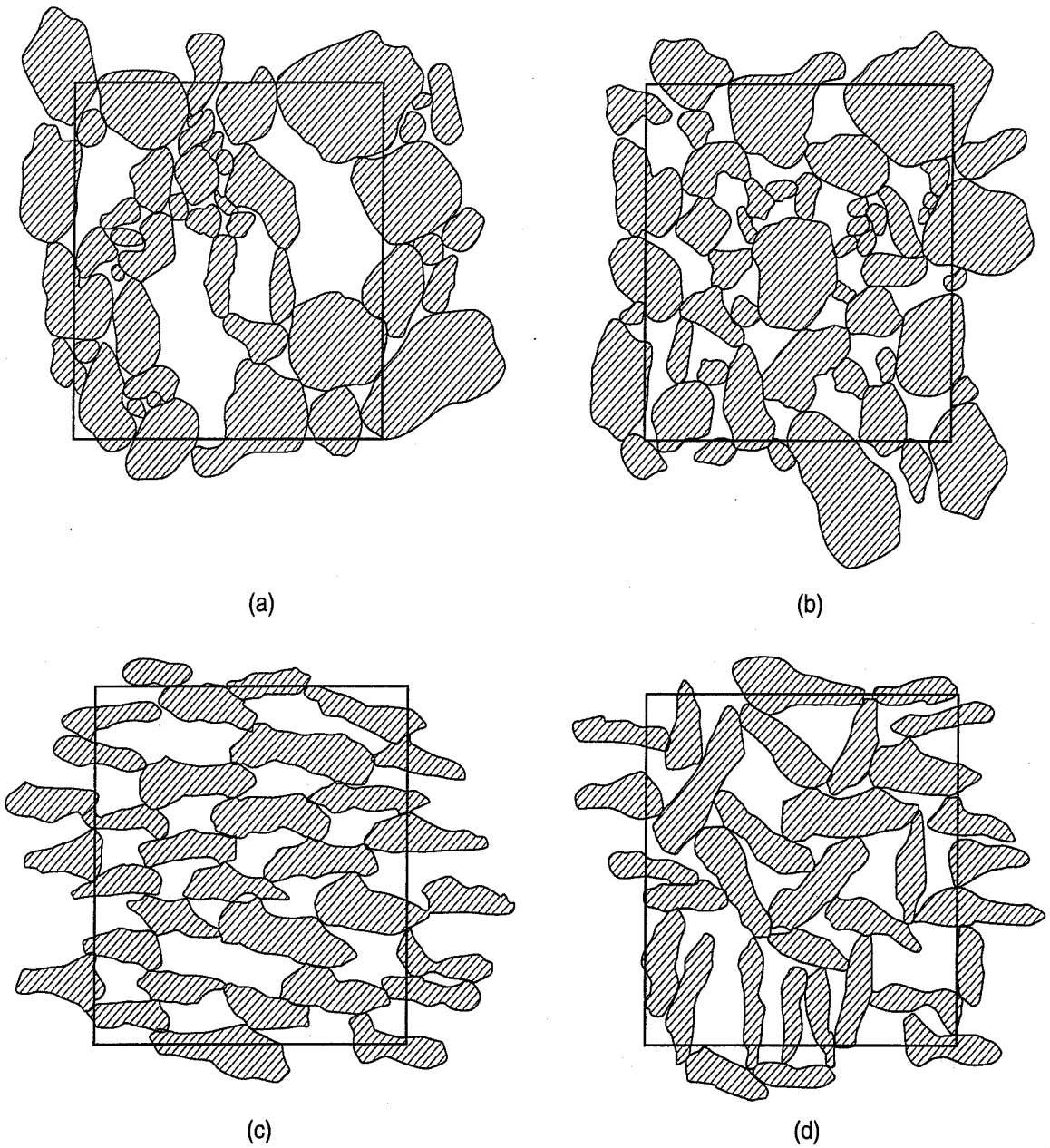

FIGURE 4.30 Potential ranges in packing of identical particles at the same relative density (a) versus (b) (G. A. Leonards, 1976, personal communication) and particle orientations (c) versus (d) of identical particles at the same void ratio (after Leonards et al., 1986).

4.10 SOIL PROFILES, SOIL HORIZONS, AND SOIL TAXONOMY

Many times, after a geologic process (Chapter 3) has taken place, a fresh rock surface or freshly transported rock and soil materials are exposed to the atmosphere and thus are subjected to weathering. As discussed in Sec. 3.3.2, weathering causes changes in the character of the topmost soil and rock layers. Depending on the time, climate (temperature, precipitation, and so on), topography, and vegetation, if any, a *soil profile* or *weathering profile* is formed. The most important factors in soil profile development are the parent material, climate, and time, although topography and the presence of vegetation also contribute.

The soil profile typically develops several distinct zones or *horizons* with specific characteristics:

- The *O horizon* contains organic matter, both fresh and decomposed.
- The *A horizon*, sometimes called *topsoil*, is rich in humus and organic plant residues; therefore it is generally dark brown or black in color. This horizon is also a zone of leaching, where some clay minerals and soluble mineral salts have been leached out by rainwater.
- The *B horizon* is the zone of accumulation because materials leached out of the A-horizon accumulate in this horizon. In temperate climates, the B-horizon is often clayey and has a blocky texture (because of periodic wetting and drying).
- The *C horizon* is also called the *parent material*, because it is generally assumed that the materials in the A and B horizons are weathered from this horizon.
- The completely *unweathered* and unaltered bedrock is called the R-horizon.

Both the O and A horizons have very poor engineering properties because of the organic materials present. They generally are loose and therefore highly compressible, and they have a low density and shear strength. In temperate regions, because of the organic matter, the O and A horizons are used for agricultural purposes. In desert regions, however, due to the lack of rainfall to support vegetation, there is no O horizon and no humus in the A horizon. Even though a relatively large amount of organic matter is generated in hot, humid tropical regions, rapid oxidation of organic matter means that tropical soils are generally not very good agricultural soils.

The B horizon can be a problem for engineers in some areas because the clay minerals present may be montmorillonitic and therefore swelling (Chapter 6). If clay is needed, for example, to decrease the hydraulic conductivity of a dike or of the liner for a waste containment system, then the B horizon may be a good source of material for this purpose.

The C material is only slightly weathered, if at all, especially in temperate regions. However, in areas of intense weathering, such as the tropics, it may accumulate weathering products from the B horizon. Parent material may be bedrock or freshly deposited alluvium, glacial till, loess, etc.

Knowledge of the characteristics of these various soil layers is very often important in civil engineering practice, because much of the civil infrastructure is relatively shallow and its development occurs in or on one of these layers, especially in the B and C horizons. Examples include the foundations of small structures, roads and airfields, and water and sewer lines.

Another view of the *soil profile* is a vertical cross-section through the soil deposit, usually determined by means of a geologic investigation and soil borings, or other subsurface exploration techniques. In foundation engineering, the soil profile is usually illustrated in a drawing or plot that shows the various layers and types of soils at the location or site of interest. Sometimes engineering properties are also shown on the same plot. Section 8.11 shows some typical soil profiles.

Soil scientists have developed a comprehensive system of soil classification called *soil taxonomy* that is reasonably objective, semi-quantitative, and universally applicable. The system was designed to be independent of the classifier and presumably useful for both agricultural and engineering purposes, although it is probably too detailed for most geotechnical engineering applications. However, you should know that such a system exists, so that if you see these names on soil maps or in a soils report, you won't panic! For detailed descriptions of the system, see the papers in TRB (1977), particularly

Fernau (1977). SMSSSS (1990), PCA (1992) and Mitchell and Soga (2005) are also recommended. If you are working in Canada, then the Canadian System of Soil Classification by the Soil Classification Working Group (1998) is very useful.

4.11 SPECIAL SOIL DEPOSITS

In Chapter 3, we described a number of different soils and soil deposits associated with a specific landform or geologic process. For example, when we discussed weathering (Sec. 3.3.2), we briefly described residual and tropical soils and provided references for additional information on the engineering characteristics of these soils. In our discussion of eolian landforms (Sec. 3.3.6), we described some of the engineering problems associated with foundations on loess, and so on.

There are a few soil deposits that are not really associated with a specific landform or process, yet they are of interest to geotechnical engineers since they present challenging design and construction problems. If you ever have a project in these areas, you will at least have some idea where to go for additional information. Collapsing and swelling soils are discussed in Chapter 6.

4.11.1 Organic Soils, Peats, and Muskeg

You may recall from Chapter 2 that organic soils are silts or clays with sufficient organic content to influence their engineering properties (USCS symbol *OL* or *OH*). Soils consisting primarily of organic matter are called peats (USCS symbol *Pt*). Depending on how much decomposition has occurred since deposition, peats can range in texture from fibrous to amorphous. ASTM (2010) standard D 4427 classifies peats depending on their fiber content, ash content after burning a specimen to constant weight at 440°C, water-holding capacity, and, if appropriate, their botanical composition. There are standard tests for these characteristics.

We mentioned several landforms in Chapter 3—among them fluvial, coastal, glacial, and lacustrine—that may have organic soils or peat associated with them. Thus it is important, if your project is located in these areas, that you look for these materials at your site. Identification and characterization of deposits of peat and organic soils is important, because these deposits tend to have very poor engineering properties. They are often soft and weak, and thus the stability of embankments and foundations constructed on them may be marginal. Furthermore, they are highly compressible, so even lightweight structures and low embankments may experience large and undesirable settlements, which can continue for a very long time. These deposits are often very acidic and thus corrosive to buried steel pipes, piles, anchors, and the like. Finally, underground construction in organic soils can be dangerous because of trapped methane in the soil.

Muskeg is a term applied to relatively flat and mostly treeless areas consisting of mostly decaying and decayed grasses and plants that thrive in wet, acid soil in areas of abundant rain and cool summers. The origin of the term muskeg is somewhat obscure, but it is thought to be derived from an Ojibwa word "mashkig," meaning swamp or marsh (Pihlainen, 1963). The term muskeg may be applied to an "organic terrain" or *peat bog*, and sometimes it refers to the organic materials in the bog, which means basically it is synonymous with peat. Sphagnum moss is the main constituent of muskeg. Muskeg covers about 10% of southeast Alaska and about 15% of Canada. Construction on muskeg, especially in the summer months, is problematic, to say the least, and often some type of "floating" foundation is necessary.

4.11.2 Marine Soils

Because an important part of geotechnical practice is near or offshore in a marine environment, we need to be able to classify marine soils as well as to have some idea of their engineering characteristics. Our discussion in Sec. 3.3.4 emphasized the soil types most commonly encountered in coastal landforms, but what do you do if, for example, your project is to build a dock and quay, an oil exploration or production platform, or a moorage or ship anchorage facility in deep water?

Noorany (1989) has devised a classification system for marine sediments that includes both their composition and depositional characteristics. There are three main classes of sediments: *lithogenous*, *hydrogenous*, and *biogenous*. Lithogenous sediments come from the land, while hydrogenous sediments are mostly precipitates that include oolitic sands, nonskeletal carbonates, etc. Biogeneous sediments come from marine organisms and include calcareous and siliceous oozes and bioclastic granular materials. Details are given in Noorany (1989).

One deposit that presents problems for offshore platform construction is that of calcareous sand materials. Formed from the calcareous skeletal remains of coral, mollusks, and algae, these materials are found in large areas offshore of North Africa in the Mediterranean Sea, as well as offshore of Southeast Asia, Brazil, and Australia. During site exploration, they appear to be fairly strong, almost a soft rock. However, because these sands are biogenic in origin, they are only weakly cemented, and they easily crush when large-diameter piles, for example, are driven into them. Thus, pile capacities are often much lower than predicted by common onshore methods (Murff, 1987, and Poulos, 1988a).

For a good description of the engineering properties of marine soils, see Noorany and Gizienski (1970), Poulos (1988b), and Noorany (1989).

4.11.3 Waste Materials and Contaminated Sites

Waste materials and contaminated sites pose special problems for civil engineering construction. They are often encountered in urban areas. Even in rural areas, however, there are old landfills, dumps, and abandoned mines or other industrial sites, and you need to be aware of any applicable environmental regulations as well as the geotechnical conditions at these areas. It is important that any potential construction site be thoroughly investigated as to its previous uses and possible contamination. Many otherwise fine construction sites have been spoiled by the discovery of contaminants in the subsurface soils, and if construction has already started, expensive delays can result and construction costs can increase enormously.

Landfills and dumps are highly variable in their material properties, depending on how old the landfill is and how it was operated. Older facilities with loosely dumped municipal wastes can experience large total and differential settlements under new construction. Some sort of improvement is normally required at these sites for virtually all except the lightest structures. Other factors that make construction work difficult include foul odors, flammable gases, rodents and other pests, and exposure to potentially hazardous materials. In rural areas, you may encounter illegally discarded garbage, used appliances, wrecked cars, used tires, and the like that have been dumped in ravines, swamps, and tidal flats, on river and stream banks, etc.

Other wastes sometimes of concern to civil engineers include industrial byproducts such as slags, bottom and fly ashes, and inorganic sludges as well as sediments dredged from harbors and rivers. If these materials are contaminated with organics or heavy metals, they require special handling and treatment. In any event, geotechnical design and construction at sites with these materials is neither simple nor inexpensive. (See the U.S. Environmental Protection Agency: http://www.epa.gov/ for additional information.)

Both surface and underground mining operations typically leave rather unusual deposits and conditions that may cause foundation subsidence or slope instability in the area. Special treatment of loosely dumped spoil materials from strip mines is required for foundations at these sites. Mineral processing operations produce wastes in the form of tailings and slurries (slimes) that, if encountered, are very difficult to stabilize. At all such sites, be sure that all environmental regulations are strictly followed.

4.12 TRANSITIONAL MATERIALS: HARD SOILS VERSUS SOFT ROCKS

Geotechnical engineers commonly think of soils and rock as two distinctly different materials, even though the line between hard soils and soft rocks is quite fuzzy. Traditionally, soil mechanics and soil engineering differ from rock mechanics and rock engineering, although they may use the same engineering mechanics, theories of elasticity and plasticity, seepage through porous media, principle of

effective stress, and other theoretical concepts. The world is not composed of only recent deposits of soft clays or old intact hard rock. There are a wide range of geo-materials in that transitional area between soil and rock, and their engineering properties and behavior are often quite ambiguous. Sometimes these transitional materials are called *intermediate geo-materials*. For example, when transitional or intermediate geo-materials are loaded in shear, their failure is neither brittle (occurring at small strains) nor ductile (occurring at large strains). Do excavations in these materials require drilling and blasting, or can they be excavated by machinery? With regard to stability and seepage problems, the influence of joints and fissures in transitional materials may or may not dominate their behavior. Treating these materials as traditional soft soils or hard rocks is totally inappropriate. It is better to think of the geotechnical world as consisting of the entire range of possible geologic materials, with most materials somewhere between soft soil and hard rock. The geotechnical profession is well aware of the gap between soils and rock engineering, and a number of conferences and symposia have dealt with this problem. The papers and special reports in Kane and Amadei (1991), Anagnostopolous et al. (1993), and Santi and Shakoor (1997) are especially recommended.

Examples of the transition between soil and rock can be found particularly in residual and tropical soil profiles (see Sec. 3.3.2). In these profiles it can sometimes be difficult to determine when the soil ends and rock begins, because the profile gradually transitions between softer soils at the top, becoming harder with depth, perhaps with more and more highly fractured and weathered rock that may be rather weak and soft, and finally becoming less and less weathered and harder with depth. An example is shown in Fig. 4.31.

Kane and Amadei (1991) and the papers therein deal specifically with the soil-rock interface—how it is detected, specified, and handled during construction. Particularly valuable in this regard are Kulhawy et al. (1991) and Smith et al. (1991).

The soil-rock interface is an area of major and often costly disputes between design engineers and contractors, because what is shown on the plans and given in the specifications may be very different than what is actually found at the project site. There are frequent disputes about the depth to rock shown on the plans and about the strength, jointing, and nature of the interface, as well as about the problem of rock versus soil excavation—whether drilling and blasting are required or machine excavation can be used. The cost difference between soil and rock excavation may be a factor of five to ten or more, so large amounts of money can be involved, depending on the size of the project, depth and amount of excavation, and contract details.

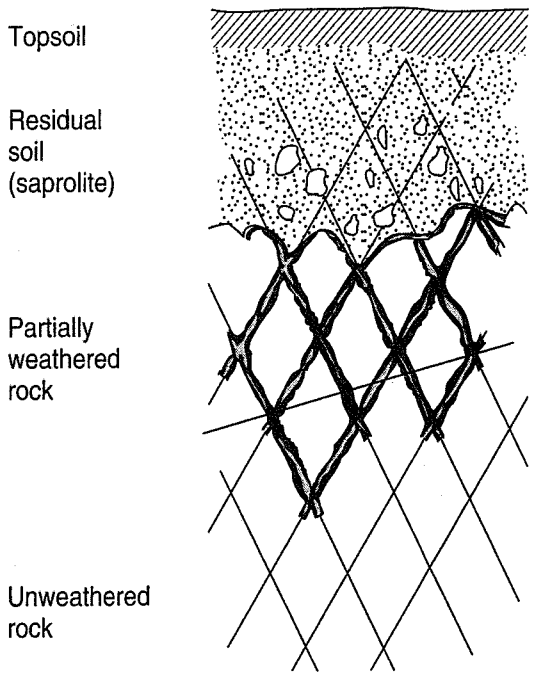

FIGURE 4.31 Schematic of a residual soil and weathered rock profile (adapted from Kulhawy et al., 1991). (See also Fig. 3.6.)

4.13 PROPERTIES, MACROSTRUCTURE, AND CLASSIFICATION OF ROCK MASSES

Similar to soil deposits, the macrostructure of a rock mass has an important influence on its engineering behavior. This is because rock masses almost always contain discontinuities and other "defects" that, depending on their physical and geometric characteristics, can have a major influence on stability and performance. Whenever we construct a foundation on rock or excavate a tunnel in rock, the stability and performance of that foundation or tunnel is strongly influenced by the characteristics of the *discontinuities* in the rock. (Discontinuities include joints, faults, bedding planes, cleavage planes, shear zones, solution cavities, and so on, and they constitute planes or zones of weakness that may significantly reduce the strength and deformability of the rock mass.) Even if the intact rock is very strong, overall behavior of the foundation or tunnel is controlled by the discontinuities. They must be located and their characteristics determined as part of the geologic and geotechnical investigations that precede design and construction. If these discontinuities are missed in the site investigation or not properly considered in design, failures may occur.

In this section, we describe some of the engineering properties of rock masses, some of the characteristics of discontinuities in rock, and finally how engineers consider properties and discontinuities in the classification of rock masses.

4.13.1 Properties of Rock Masses

The determination of the strength, modulus, and other engineering properties of intact rock is a well-developed part of rock mechanics and geotechnical engineering. Most of the common rock mechanics tests are now ASTM standard tests, and they are discussed in Chapter 12.

Intact rocks can be classified according to their geologic characteristics (type, mineralogy, crystallography, texture, etc.—see Sec. 3.2.3) and/or their engineering properties (compressive strength and modulus). Usually only the compressive strength is used to classify intact rock, and Table 4.6 presents the International Society for Rock Mechanics (ISRM) grade, strength classification, field identification, and approximate range of uniaxial compressive strength of intact rock.

You may recall from our discussion of rock structure in Sec. 3.2.4 that folding, shifting, or faulting of rock masses results in structural features such as joints, folds, and faults. (Rock structures also produce several interesting landforms, as discussed in Sec. 3.3.9.) In any event, the rock mass includes the blocks of intact material as well as structural features and discontinuities.

4.13.2 Discontinuities in Rock

Joints are by far the most common discontinuity in rock masses, and a knowledge of their orientation, length, spacing, surface characteristics, and the nature of any infilling is essential for any rock engineering design. Goodman (1989) and Wyllie (1999) give details as to how rock joints are observed, measured, and tested for strength and frictional characteristics. The International Society for Rock Mechanics (1981) developed a very a comprehensive procedure for quantitatively describing a rock mass (see also Wyllie, 1999, and Sabatini et al., 2002). The procedure gives details on five items:

1. Rock material
   - Type
   - Compressive strength
   - Degree of weathering
2. Discontinuities
   - Type (e.g., fault, bedding, foliation, cleavage, schistosity, joints)
   - Orientation (dip angle and direction)

TABLE 4.6 Strength of Intact Rock

ISRM Grade	Description or Classification	Approximate Range of Uniaxial Compressive Strength		Point Load Index		Field Estimate of Strength	Examples
		MPa	psi	MPa	psi		
R6	Extremely strong rock	>250	>36 000	>10	>1500	Rock can only be chipped by a geologic hammer	Fresh basalt, chert, diabase, gneiss, granite, quartzite
R5	Very strong rock	100–250	15 000–36 000	4–10	600–1500	Requires many blows of geological hammer to cause fracture	Amphibolite, sandstone, basalt, gabbro, gneiss, granodirite, peridotite, rhyiolite, tuff
R4	Strong rock	50–100	7000–15 000	2–4	300–600	Requires more than one hammer blow to cause fracture	Limestone, marble, sandstone, schist
R3	Medium strong rock	25–50	3500–7000	1–2	150–300	Cannot be scraped or peeled with a pocket knife; can be fractured with a single blow of geologic hammer	Concrete, phyllite, schist, siltstone
R2	Weak rock	5.0–25	725–3500	[a]	[a]	Can be peeled by a pocket knife with difficulty; shallow indentations made by blow with point of geologic hammer	Chalk, claystone, potash, marl, siltstone, shale, rocksalt
R1	Very weak rock	1.0–5.0	150–725	[a]	[a]	Crumbles under firm blows with point of geological hammer	Highly weathered or altered rock, shale
R0	Extremely weak rock	0.25–1.0	35–150	[a]	[a]	Indented by thumbnail	Stiff fault gouge

[a]Point load test results on rock with an uniaxial compressive strength less than about 25 MPa (3600 psi) are highly ambiguous.

After International Society for Rock Mechanics (1979 and 1981), Wyllie (1999), Marinos and Hoek (2001), and Canadian Geotechnical Society (2006).

- Roughness (e.g., smooth, slickensided, stepped, undulating, etc.)
- Aperture width (whether open or closed, etc.)

3. Nature of the infilling (type/width)
   - Mineralogy, particle sizes, water content, hydraulic conductivity, fracturing of rock walls, etc.
4. Rock mass description (e.g., massive, blocky, tabular, columnar, crushed, etc.)
   - Joint spacing (close, moderate, wide, etc.)
   - Persistence (areal extent or size within a plane area)
   - Number of joint sets
   - Block size and shape (small to large)
5. Groundwater (seepage) conditions (quantities from joints and the rock mass)

As an example, Table 4.7 gives the terms used to describe the spacing of joints in a rock mass. The ISRM procedure does this for all of the above items, but the table will show you how the system works.

TABLE 4.7 Spacing of Discontinuities in Rock Masses

Description	Spacing (m)
Extremely wide	>6
Very wide	2–6
Wide	0.6–2
Moderate	0.2–0.6
Close	0.06–0.2
Very close	0.02–0.06
Extremely close	<0.02

After International Society for Rock Mechanics (1981), Wyllie (1999).

4.13.3 Rock Mass Classification Systems

A number of systems have been developed for classifying rock masses. The ASTM (2010) standard guide D 5878 for rock mass classification lists eight such systems, and one of those—the Japanese Society of Engineering Geology system—has seven subsystems depending on the specific application (e.g., railway tunnels, highway tunnels and slopes, water tunnels). Perhaps the development of so many classification systems is not surprising, given the variety of geologic conditions likely to be encountered in practice, the different excavation and exploration procedures in common use, and the specific engineering applications (tunnels, foundations, excavations, mining, etc.).

The *rock quality designation* or RQD attempts to quantify the degree of fracturing and other alteration of the original rock mass. The RQD was developed by Professor Don Deere of the University of Illinois in the early 1960s (Deere, 1963). It is based on the rock cores recovered from core barrels taken during the exploration program. The rock cores are obtained by diamond drilling (preferably with a "triple tube" core barrel to get the best-quality rock cores). The cores are placed in core boxes, an example of which is shown in Fig. 4.32. Then the intact fragment lengths are measured and the RQD is obtained by summing up the total length of the core pieces that are 10 cm (4 in.) or greater in length, and dividing that sum by the length of the core run. It is usually expressed as a percentage.

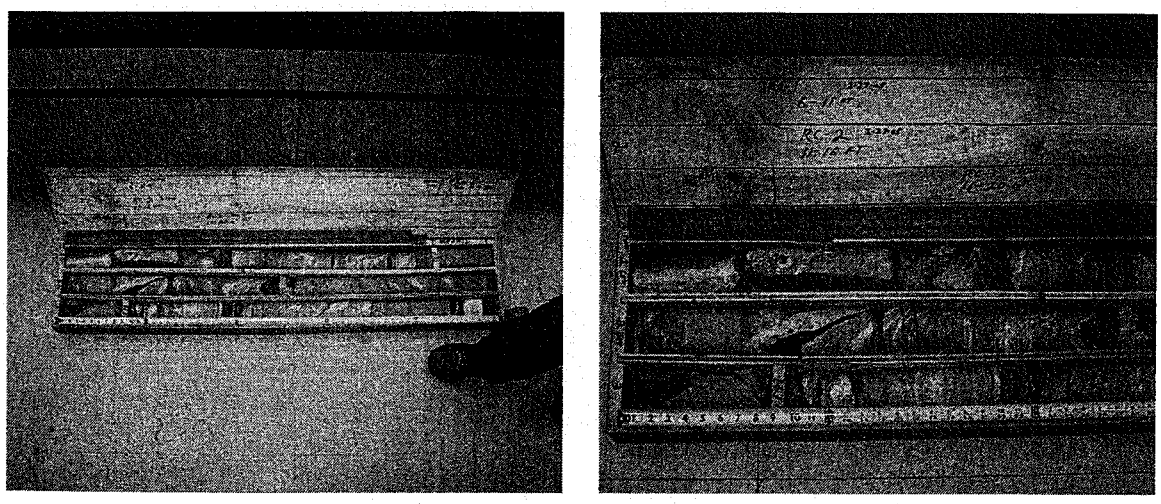

(a) (b)

FIGURE 4.32 (a) Rock core box from Cumberland, Rhode Island showing degree of weathering and fracture from (foot by Kevin Broccolo); (b) close-up of rock core box.

Figure 4.33(a) illustrates the process; care should be taken to distinguish between natural discontinuities and those caused by the drilling process. As shown in Figs. 4.32(b) and 4.33, sometimes rock defects are at an angle with the direction of drilling, and thus it may be difficult to decide what core length actually is. Figure 4.33(b) shows how to make correct length measurements for the RQD. Deere and Deere (1988) give some additional background and engineering uses of the RQD. The standard test method for determining the RQD of rock cores is ASTM (2010) D 6032.

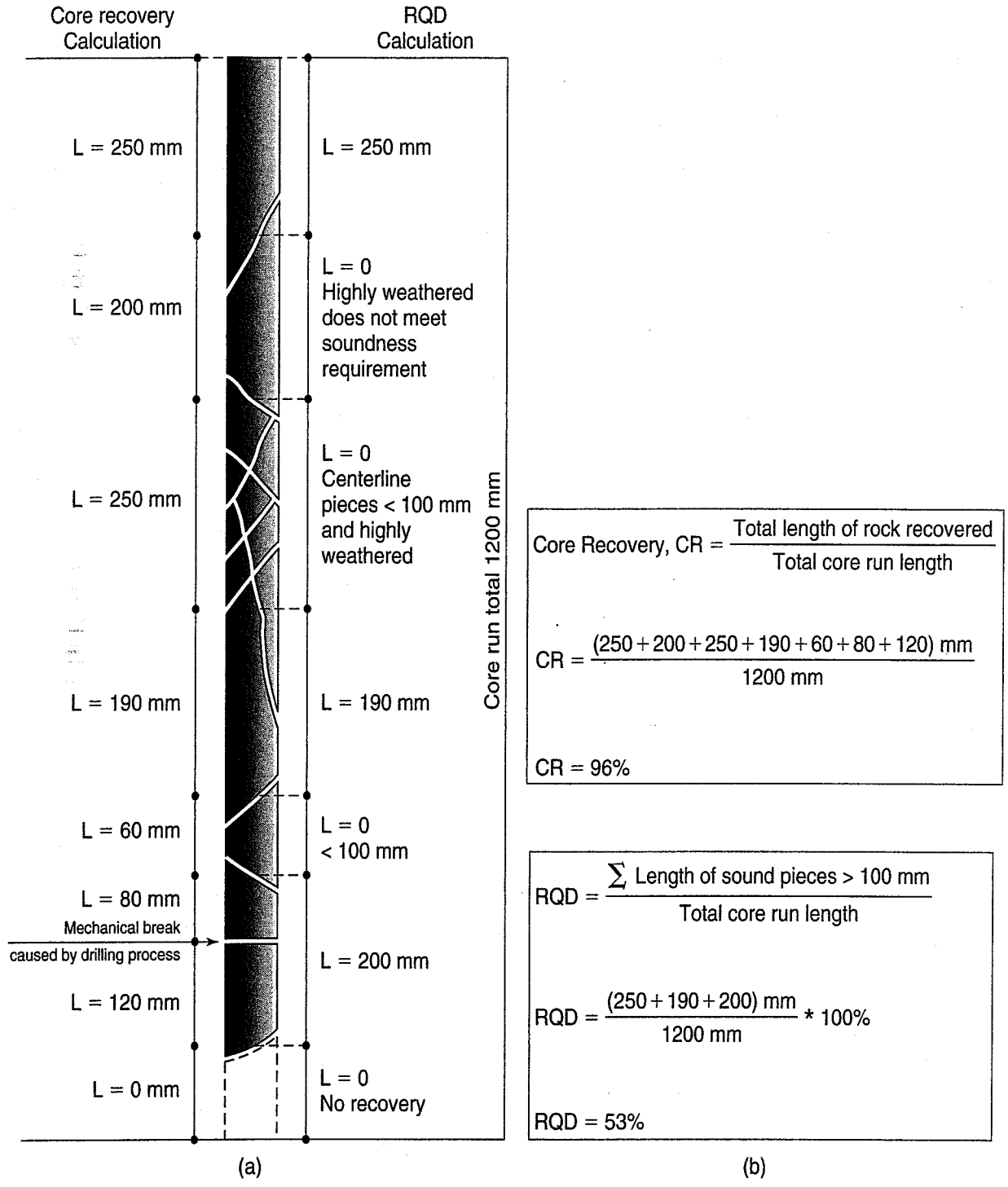

FIGURE 4.33 (a) Illustration of how RQD is determined; (b) core length determination (after Samtani and Nowatski, 2006).

Example 4.1

Given:

A core box containing a run of 4.7 ft (1433 mm) of rock core, as shown in Fig. Ex. 4.1.

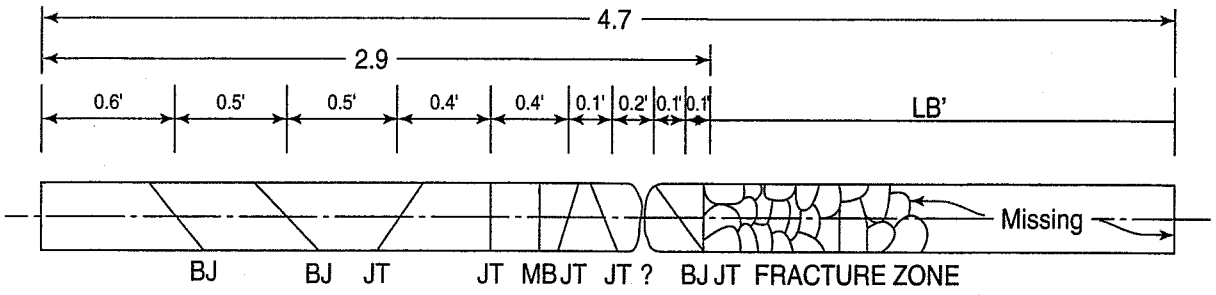

FIGURE Ex. 4.1 (After U.S. Dept. of Interior, 1998.)

Required

Compute the RQD.

Solution: Data from the field is shown in Fig. Ex. 4.1. Note the symbols used: BJ (bedding joint), JT (joint), MB (mechanical break), and FZ (fracture zone). Other symbols that may be used are: IJ (incipient joint), IF (incipient fracture), and RF (random fracture).

$$\text{RQD} = \frac{\text{Sum of length of pieces} \geq 0.33 \text{ ft (4 in.)}}{\text{(total length of core run)}} \times 100 = \frac{2.4}{4.7} \times 100 = 51\%$$

From Fig. Ex. 4.1, the lengths of core along the centerline greater than 4 in. (100 mm) are 0.6 + 0.5 + 0.5 + 0.4 + 0.4, or a total of 2.4 ft. With a total core run of 4.7 ft, the RQD is 2.4/4.7 × 100 = 51%.

Hunt (2005) grouped rock classification systems into those that are relatively simple, dependent on one or two properties, and those with more complex algorithms. The "simple" classification systems depend primarily on rock quality designation and velocity index. The *velocity index* is computed by dividing the in situ velocity (reduced by rock defects) by the laboratory-measured seismic velocity on an intact piece of the rock, and squaring this ratio. This ratio and thus its square will be less than or equal to unity. There is a reasonably well-defined relationship between the velocity index and RQD. Table 4.8 shows typical classifications based on RQD and velocity index. Recognize that these types of general classifications cannot be used for any detailed evaluation of rock engineering properties.

Prior to developing the ASTM (2009) Standard Guide D 5878, ASTM sponsored a symposium focused on the different rock mass classification systems in use at that time (Kirkaldie, 1988). The rationale for each system was explained by its developers, and its strong points as well as its weaknesses were described. In this section we summarize four such systems. For details, see ASTM (2009) standard guide D 5878 and the papers in Kirkaldie (1988).

TABLE 4.8 Rock Mass Classifications Based on RQD and Velocity Index

RQD, %	Velocity Index	Description of Rock Quality
90–100	0.80–1.00	Excellent
75–90	0.60–0.80	Good
50–75	0.40–0.60	Fair
25–50	0.20–0.40	Poor
0–25	0–0.20	Very poor

After Hunt (2005).

The Unified Rock Classification System (URCS) was patterned after the Unified Soil Classification System (Williamson and Kuhn, 1988), and it relies on four fundamental properties: degree of weathering, uniaxial compressive strength, discontinuities, and density. Although it ignores the relationship between geologic structure and slope or excavation orientation, the URCS has apparently been successfully applied to excavations and slopes, as well as to foundations and the blasting characteristics of earthen materials. Basic elements of the URCS are given in ASTM (2010) D 5878.

The Rock Mass Rating system (RMR)—sometimes called the Geomechanics Classification—was developed by Professor Z. T. Bieniawski in the early 1970s (Bieniawski, 1988). The RMR is based on six parameters: uniaxial compressive strength of the rock, RQD, spacing, condition and orientation of discontinuities, and groundwater conditions. For each category a point total or rating is assigned, and this is used to categorize the rock. The RMR rating can then be correlated to ground engineering practices, such as requirements for excavation support and tunnel support, as well as rock strength parameters. It was originally developed for tunneling, but has also been successfully applied to mining, slopes, foundations, ripability, and rock bolting. The RMR classification system also includes adjustments that consider the effect of the orientations of strike and dip in tunneling and adjustments for mining applications.

The Q-system or NGI System was developed by N. Barton at the Norwegian Geotechnical Institute for selection of reinforcement and support systems for tunnels in rock. The "Q" comes from the rock mass quality (Q) and is based on six input parameters: RQD, number of joint sets, joint roughness, joint alteration (filling), amount of water, and a stress reduction factor. The Q-system was developed from case histories of tunnels in Scandinavia where the rock is mostly granitic, but it has also been used for underground chamber support requirements, seismic stability of roof rock, and ripability and excavatability of softer rocks.

Marinos and Hoek (2004) note that RMR and Q are quite OK when behavior is controlled by sliding and rotation on discontinuity surfaces with relatively little failure of the intact rock. These authors, however, were less successful in applying these classification systems to massive rock at great depths and also to very weak rock masses. They suggest that the Geological Strength Index (GSI) provides more reliable estimates of the strength and deformability of rock masses for tunnels.

The GSI system, developed by Hoek and Brown (1997) and extended by Marinos and Hoek (2000), is based on a matrix of rock structure versus surface conditions. As shown in Table 4.9, a rock mass is characterized according to the intersection of these two criteria. *Structure* is defined as the degree of interlocking among rock pieces, and these "pieces" may include relatively intact rock with only planes of discontinuity separating them. Surface conditions have to do with the roughness, degree of weathering, and nature of any fillings (e.g., broken rock or clay) in fractures.

An excellent example of the use of the GSI for a heterogeneous rock mass (flysch) is given by Marinos and Hoek (2000) and Hoek (2007).

TABLE 4.9 Geological Strength Index Classification System

GEOLOGICAL STRENGTH INDEX FOR JOINTED ROCKS (Hoek and Marinos, 2000)

From the lithology, structure and surface conditions of the discontinuities, estimate the average value of GSI. Do not try to be too precise. Quoting a range from 33 to 37 is more realistic than stating that GSI = 35. *Note that the table does not apply to structurally controlled failures.* Where weak planar structural planes are present in an unfavourable orientation with respect to the excavation face, these will dominate the rock mass behaviour. The shear strength of surfaces in rocks that are prone to deterioration as a result of changes in moisture content will be reduced if water is present. When working with rocks in the fair to very poor categories, a shift to the right may be made for wet conditions. Water pressure is dealt with by effective stress analysis.

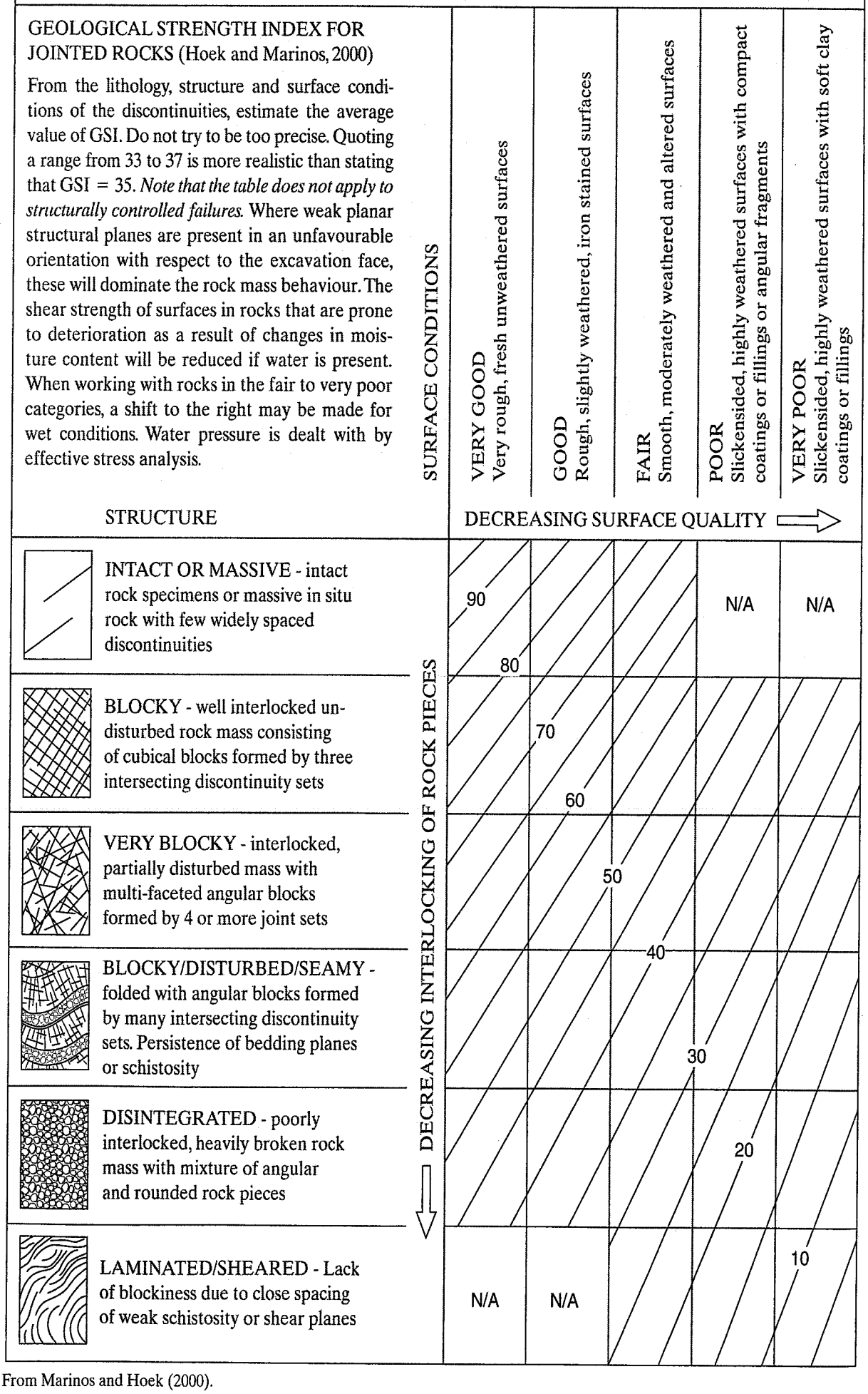

From Marinos and Hoek (2000).

PROBLEMS

4.1 Calculate the specific surface of a cube (a) 10 mm, (b) 1 mm, (c) 1 μm, and (d) 1 nm on a side. Calculate the specific surface in terms of both areas and m^2/kg. Assume for the latter case that $\rho_s = 2.65\ Mg/m^3$.

4.2 Calculate the specific surface of (a) tennis balls, (b) ping pong balls, (c) ball bearings 1.5 mm in diameter, and (d) fly ash with approximately spherical particles 60 μm in diameter.

4.3 Describe briefly the crystalline or atomic structure of the following ten minerals. Also list any important distinguishing characteristics.

(a) Smectite
(b) Brucite
(c) Gibbsite
(d) Attapulgite
(e) Bentonite
(f) Allophane
(g) Halloysite
(h) Illite
(i) Mica
(j) Chlorite

4.4 Describe the following types of bonding agents found with clay minerals.

(a) Hydrogen bond
(b) Covalent bond
(c) van der Waals forces
(d) James bond
(e) Ward Bonds
(f) War Bonds

4.5 Verify that the maximum and minimum void ratios for perfect spheres given in Table 4.5 are reasonable.

4.6 Which sheet, silica or alumina, would you wear to a toga party? Why?

4.7 A specially processed clay has particles that are 500 nm thick and 10 000 nm × 10 000 nm wide. The specific gravity of solids is 2.80. The particles lie perfectly parallel with an edge-to-edge spacing of 400 nm (i.e., they look like thin bricks stacked perfectly parallel).

(a) Initially, the cation valence in the double layer is +1, resulting in a face-to-face spacing of 1500 nm. How many particles per cm^3 will there be at this spacing? What are the void ratio and water content, assuming that the soil is at 100% saturation?

(b) Another sample of the clay is mixed such that the cation valence is +2. What are the new void ratio and water content under these conditions? Assume the edge-to-edge spacing remains 400 nm and that $S = 100\%$. (After C. C. Ladd.)

4.8 Let T be the layer thickness of a deposit of illite mixed with kaolinite that deposited in fresh water at pH = 7. What would be the effect on T (increase, decrease, remain the same) if the mixture had been deposited in salt water having a high pH? Determine the effect on T by looking at the individual effects on the illite and kaolinite. Explain your answer.

4.9 Given the particles in Fig. 4.30, is it realistic to show that all the particles are in contact with each other for this given plane? Any given plane? Why?

4.10 A client has a property that she thinks contains clay minerals of sufficient quality and quantity that it may be possible to mine the clays, process them, and sell them commercially. She requests that you visit the property, obtain samples, determine the type of clay or clays present, and estimate the approximate quantity of clay available. With what you know so far from the first four chapters, (1) outline the field and laboratory procedures that you would use to find the clay type, and (2) outline the procedures you would use to find the extent of the clay materials on the property.

4.11 At a site near San Francisco Bay, Bay Mud has been dredged and redeposited as a slurry, and it is desirable now to strengthen the dredged material. What chemical(s) additives could be used to improve the strength and other engineering characteristics of this slurry?

4.12 In many areas of the world, soft clays are dredged from a coastal area near the sea and placed inside containment dikes with wiers for water to escape. The idea is to develop areas above the water surface for future construction. What chemicals could be added to the slurry to enable it to gain in strength in a shorter time than would be possible without the chemicals?

4.13 Describe the fabric of a relict structure soil. In what part of North America would such structures most likely be found?

4.14 Can a soil have a *low* void ratio and a *high* density at the same time? Explain.

4.15 Three sections of rock core are shown in Fig. 4.32. The rock comes from near Cumberland, RI, and is called Corbormite (Capt. James T. Kirk, personal communication, 2007). The length of the first (top) run is 56 in. and the computed RQD is 82%. For the second run (middle), a length of 60 in. was recovered and the RQD is 100%. Finally, the third run (bottom) is also 5 ft long and the RQD is 95%. Verify that the calculated RQD values for the top and bottom runs are correct.

4.16 In one core run of 1500 mm selected from cores obtained during drilling for a bridge foundation in hard limestone, the following core recovery information was obtained:

Core Recovery (mm)	Length of Core Pieces > 100 mm
250	150
50	
50	
75	
100	100
125	125
75	
100	100
150	150
100	100
50	
125	125
Sum =	Sum =

Determine (a) the percent core recovery, and (b) the RQD. Based on this RQD, what is the rock quality? Why?

CHAPTER 5

Compaction and Stabilization of Soils

5.1 INTRODUCTION

Often in civil engineering practice the soils at a given site are less than ideal for the intended construction. They may be weak, highly compressible, or have a higher hydraulic conductivity than desirable from an engineering or economic point of view. It would seem reasonable in such instances to simply relocate the structure or facility. However, considerations other than geotechnical often govern the location of a structure, and the civil engineer is forced to design for the site at hand. One possibility is to adapt the structure's foundations to the geotechnical conditions at the site. Another possibility is to try to *stabilize* or improve the engineering properties of the soils at the site. Which approach provides the most economical solution will depend on the specific circumstances of the project.

Stabilization methods are usually *mechanical* or *chemical*, but even thermal and electrical stabilization have occasionally been used or considered. In this chapter we are primarily concerned with mechanical stabilization or densification, also called *compaction*. Chemical stabilization includes the injecting or mixing into the soil of chemical substances such as Portland cement, lime, asphalt, or calcium chloride. Chemical soil stabilization is usually covered in advanced courses in highway and airfield pavement engineering and graduate-level geotechnical engineering. Methods for stabilizing poor foundation soils will be briefly described at the end of this chapter.

Compaction and stabilization are especially important when soil is used as an engineering material; that is, the structure itself is made of soil. Examples of *earth structures* include highway and railroad embankments and fills, earth dams, and levees along rivers. If soils or rocks are loosely dumped or otherwise placed at random in a fill, the resulting embankment will have poor stability and probably will experience large and undesirable settlements. In fact, prior to the 1920s, embankments were usually constructed by end-dumping soils from wagons or trucks. There was very little attempt to compact or densify the soils and rocks, and failures of even moderately high embankments were common. Of course, earthworks such as levees and diversion dams have been built for thousands of years. However, these structures, for example in ancient China or India, were constructed by people carrying small baskets of earth and dumping them in the embankment. People walking over the dumped materials compacted and thus densified the soils. In some countries even

elephants have been used to compact soils, but research has shown that they are not very good at it (Meehan, 1967).

The following symbols are introduced in this chapter.

Symbol	Dimension	Unit	Definition
g	L/T^2	m/s^2	Acceleration due to gravity, 9.80665 m/s^2
D	L	M	Depth of soil improvement for dynamic compaction
D_r	–	(%)	Relative density - Eq. (5.4)
H	L	M	Drop height for dynamic compaction
I_d	–	(%)	Index density or index unit weight - Eqs. (5.6) and (5.7)
RC	–	(%)	Relative compaction - Eq. (5.9)
w_{opt} *or* OMC	–	(%)	Optimum water content; sometimes called the optimum moisture content (OMC)
$\rho_{d\,max}$	M/L^3	Mg/m^3	Maximum dry density
$\rho_{d\,field}$	M/L^3	Mg/m^3	Field dry density

5.2 COMPACTION AND DENSIFICATION

Compaction is the densification of soils and rocks by the application of mechanical energy. It may also involve a modification of the water content as well as the gradation of the soil. Granular soils are most efficiently compacted by vibration. In the field, hand-operated vibrating plates and motorized vibratory rollers of various sizes are very good at compacting sand and gravel soils. Rubber-tired equipment can also be used to densify sands. Even large free-falling weights have been used to dynamically compact loose granular deposits and fills. These techniques are described later in this chapter (Secs. 5.5 and 5.9).

Fine-grained soils may be compacted in the laboratory by falling weights and hammers and by special "kneading" compactors and may even be statically compressed in a laboratory press or loading machine. In the field, common compaction equipment includes hand-operated tampers, "sheepsfoot" rollers, rubber-tired rollers, and other types of motorized compaction equipment (Sec. 5.6). Considerable compaction can also be obtained by proper routing of the hauling equipment over the embankment during construction.

The overall objective of compaction is the improvement of the engineering properties of the soil mass. Specifically, by compaction:

- Detrimental settlements can be reduced or prevented.
- Soil strength can be increased and slope stability improved.
- Bearing capacity of pavement subgrades can be increased.
- Hydraulic conductivity can be decreased.
- Undesirable volume changes—caused, for example, by frost action, swelling, and shrinkage of fine-grained soils—may be controlled.

5.3 THEORY OF COMPACTION FOR FINE-GRAINED SOILS

Our understanding of the fundamentals of compaction of fine-grained soils is relatively new. R. R. Proctor in the early 1930s was building dams for the old Bureau of Waterworks and Supply for the City of Los Angeles, and he developed the principles of compaction in a series of articles in *Engineering News-Record* (Proctor, 1933). In his honor, the standard laboratory compaction test that he developed is commonly called the *Proctor* test.

Proctor noted that compaction is a function of four variables: (1) dry density ρ_d, (2) water content w, (3) compactive effort, and (4) soil type (gradation, presence of clay minerals, etc.). Dry density and water content you already know from Chapter 2. They are determined in the laboratory and in the field as required.

Compactive effort is a measure of the mechanical energy applied to a soil mass. It has units of energy per unit volume, or N-m/m^3 (*Note:* 1 N-m = 1 joule.) In British engineering units, compactive effort is ft-lbf/ft^3. In the field, compactive effort is the number of passes or "coverages" of the roller of a certain type and weight on a given volume of soil. In the laboratory, *static*, *vibratory*, *impact* (or *dynamic)*, or *kneading* compaction is usually employed. During *impact* compaction, the most common laboratory type, a steel rammer is dropped several times on a soil specimen in a mold. The mass of the rammer, height of drop, number of drops per layer, number of layers of soil, and the volume of the mold are specified, so compactive effort is easily calculated, as shown below in Example 5.1. First, you should know that there are two standard laboratory compaction tests in common use: the *standard Proctor* test and the *modified Proctor* test. The ASTM specifications for each test are given in Table 5.1. The modified test was developed during World War II by the U.S. Army Corps of Engineers to better represent the compaction required for airfields to support heavy aircraft.

As indicated in Table 5.1, the standard and modified tests differ only in terms of the rammer weight, height of drop, and number of layers of soil placed in the mold. Methods A, B, and C depend only on the gradation of the soils to be compacted. AASHTO (2010) also has two standard compaction tests, Designation T 99 and T 180, that are very similar to the two ASTM compaction tests, D 698 and D 1557, for standard and modified effort, respectively. Instead of three methods (A–C), AASHTO has four methods (A–D) for different mold sizes and maximum particle size of the soil sample. See AASHTO (2010) for details.

TABLE 5.1 Specifications for the Two Proctor Laboratory Compaction Tests

Test	Standard Effort (ASTM Test Method D 698)			Modified Effort (ASTM Test Method D 1557)		
Method	A	B	C	A	B	C
Rammer weight	5.5 lbf (24.4 N)	5.5 lbf (24.4 N)	5.5 lbf (24.4 N)	10 lbf (44.5 N)	10 lbf (44.5 N)	10 lbf (44.5 N)
Height of drop	12 in. (305 mm)	12 in. (305 mm)	12 in. (305 mm)	18 in. (457 mm)	18 in. (457 mm)	18 in. (457 mm)
Mold diameter	4 in. (102 mm)	4 in. (102 mm)	6 in. (152 mm)	4 in. (102 mm)	4 in. (102 mm)	6 in. (152 mm)
Mold volume	0.0333 ft^3 (944 cm^3)	0.0333 ft^3 (944 cm^3)	0.075 ft^3 (2124 cm^3)	0.0333 ft^3 (944 cm^3)	0.0333 ft^3 (944 cm^3)	0.075 ft^3 (2124 cm^3)
Material	Passing No. 4 (4.75 mm) sieve	Passing 3/8 in. (9.5 mm) sieve	Passing 3/4 in. (19 mm) sieve	Passing No. 4 (4.75 mm) sieve	Passing 3/8 in. (9.5 mm) sieve	Passing 3/4 in. (19 mm) sieve
Layers	3	3	3	5	5	5
Blows per layer	25	25	56	25	25	56
Compactive effort	12 400 ft-lbf/ft^3 (600 kN-m/m^3)	12 400 ft-lbf/ft^3 (600 kN-m/m^3)	12 400 ft-lbf/ft^3 (600 kN-m/m^3)	56 000 ft-lbf/ft^3 (2700 kN-m/m^3)	56 000 ft-lbf/ft^3 (2700 kN-m/m^3)	56 000 ft-lbf/ft^3 (2700 kN-m/m^3)
Use	≤25% by mass retained on No. 4 sieve	≤25% by weight retained on 9.5 mm sieve	≤30% by weight retained on 19 mm sieve	≤25% by mass retained on No. 4 sieve	≤25% by mass retained on 9.5 mm sieve	≤30% by weight retained on 19 mm sieve

After ASTM (2010).

ASTM Standard Practice D 4718 discusses how to calculate the densities and water contents of soils containing oversize particles when you know the data for the soil fraction with oversize particles removed. Sometimes this is called the "rock correction" factor. The practice is valid for soils with up to 40% retained on the No. 4 sieve, and it may also apply to soils with up to 30% retained on the 19-mm sieve (ASTM, 2010).

Example 5.1

Given:

Standard Proctor test specifications (see Table 5.1).

Required:

Calculate the compactive effort in both SI and British Engineering units. Do this for the 102 mm diameter mold.

Solution: See Table 5.1 for appropriate dimensions and Appendix A for relevant unit conversion factors.

a. SI units:
From Table 5.1, we know that the weight of the rammer is 24 N (rammer mass is 2495 kg × 9.81 m/s^2 = 24 N), and the height of drop of the rammer is 305 mm. The soil is placed in three layers, and each layer is tamped 25 times. The volume of the 102 mm diameter mold is 944 cm^3. Therefore the compactive effort is

$$\frac{(24\text{ N})(305\text{ mm})(3\text{ layers})(25\text{ blows/layer})}{944\text{ cm}^3} = 591\text{ kN-m/m}^3$$

or, as ASTM calls it, 600 kN-m/m^3. This is, of course, equivalent to 600 kJ/m^3.

b. British engineering units:

$$\text{compactive effort} = \frac{5.5\text{ lbf}\,(1\text{ ft})(3)(25)}{0.0333\text{ ft}^3} = 12{,}375\text{ ft-lbf/ft}^3$$

or, as ASTM calls it, 12,400 ft-lbf/ft^3.

For other types of compaction, the calculation of compactive effort is not so simple. In kneading compaction, for example, the tamper applies a given pressure for a fraction of a second. The kneading action is supposed to simulate the compaction produced by a "sheepsfoot" roller and other types of field compaction equipment. In *static compaction*, the soil is simply pressed into a mold under a constant static stress in a laboratory testing machine.

5.3.1 Process of Compaction

The process of compaction of fine-grained soils can best be understood by looking at the common laboratory compaction or Proctor test. Several specimens from the same soil sample are prepared at different water contents. Then each specimen is compacted according to the Proctor compaction test specifications given in Table 5.1. Typically, the total or wet density and the actual water content of each compacted specimen are measured. The dry density for each sample can then be calculated from phase relationships we developed in Chapter 2.

$$\rho = \frac{M_t}{V_t} \tag{2.6}$$

$$\rho_d = \frac{\rho}{1 + w} \tag{2.14}$$

When the dry densities of each specimen are determined and plotted versus their respective water contents, then a curve called a *compaction curve* for the particular Proctor compactive effort is obtained. For example, in Fig. 5.1, curve A shows the results of a standard Proctor test conducted on a sample of glacial till from Indiana. Each data point on the curve represents a single compaction test, and usually at least four or five individual compaction tests are required to completely determine the compaction curve. This curve is unique for a given soil type, method of compaction, and (constant) compactive effort. The peak point of the compaction curve is an important point. The water content corresponding to the *maximum dry density* is known as the *optimum water content* (also known as the optimum moisture content, OMC). Note that the maximum dry density is only a maximum for a specific compactive effort and method of compaction. This does not necessarily reflect the maximum dry density that can be obtained in the laboratory or in the field.

Curve B in Fig. 5.1 is the compaction curve obtained by the *modified* Proctor compaction test on that same glacial till soil. Recall from Table 5.1 that this test utilizes a heavier hammer (4.5 kg or 10 lb), a greater height of fall (457 mm or 18 in.), and five layers tamped 25 times into either a 102 mm (4 in.) or 152 mm (6 in.) diameter Proctor mold. Note that increasing the compactive effort increases the maximum dry density, as expected, but at the same time the optimum water content decreases. This is an important observation that we will use later in this chapter.

Why do we get compaction curves such as those shown in Fig. 5.1? Starting at a low water content, as the water content increases, larger and larger water films develop around the soil particles. This process tends to "lubricate" the particles and makes it easier for them to be moved about and reoriented into a denser configuration. However, we eventually reach a water content where the density does not increase any further. At this point, water starts to replace soil particles in the mold, and since $\rho_w \ll \rho_s$, the dry density curve starts to fall off, as shown in Fig. 5.2.

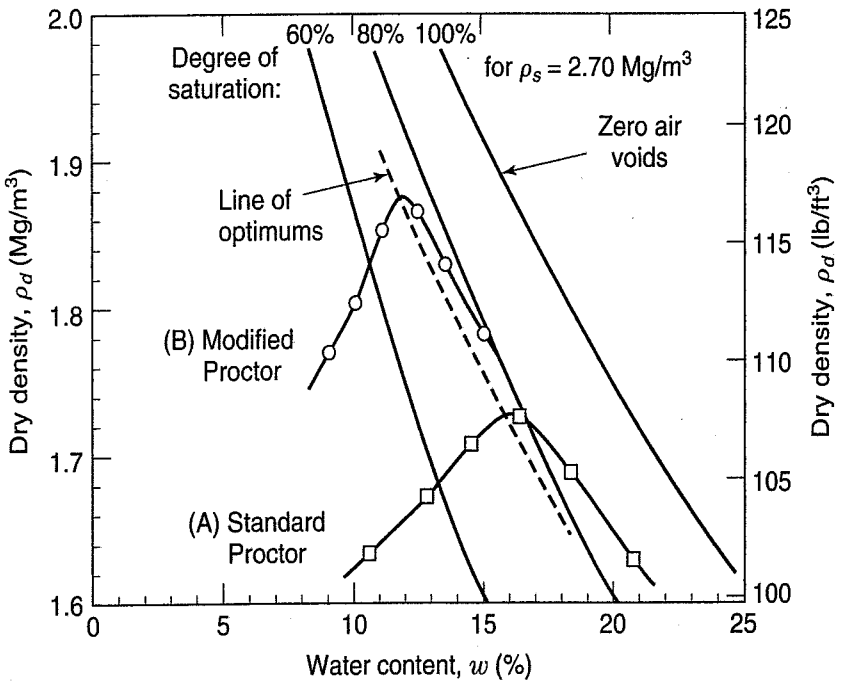

FIGURE 5.1 Standard and modified Proctor compaction curves for Crosby B till.

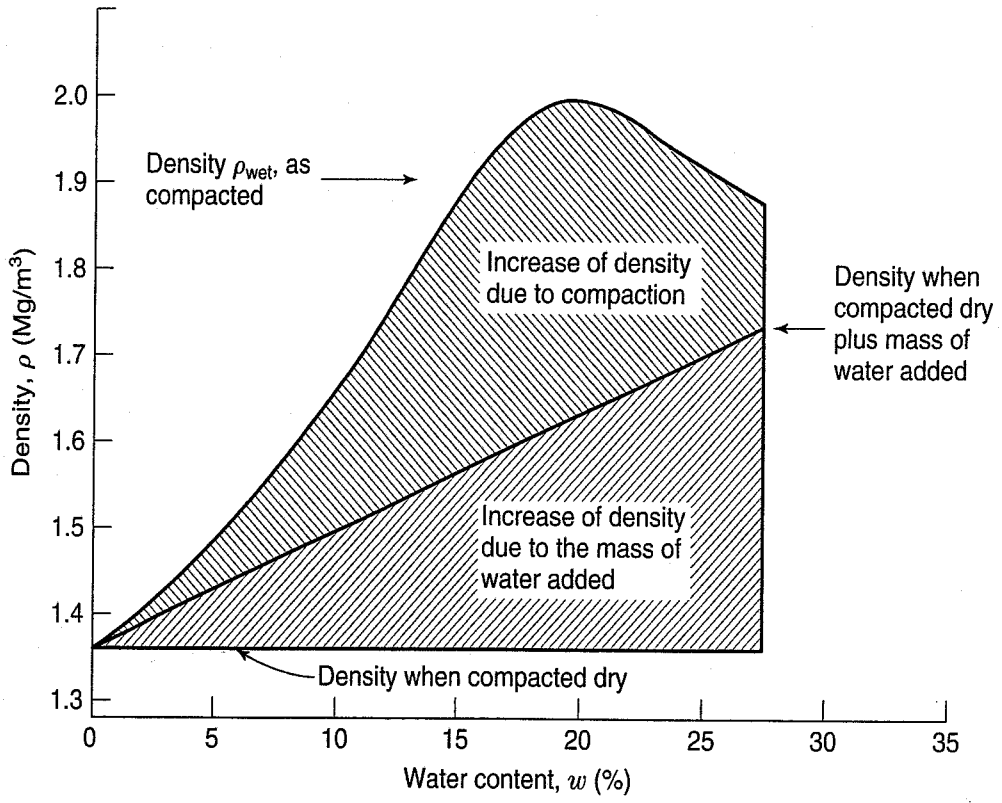

FIGURE 5.2 The water content-density relationship indicating the increased density resulting from the addition of water and that due to the applied compaction effort. Soil is a silty clay, LL = 37, PI = 14, standard Proctor compaction (after Johnson and Sallberg, 1960).

5.3.2 Typical Values; Degree of Saturation

Typical values of maximum dry density are around 1.6 to 2.0 Mg/m^3 (100 to 125 lbf/ft^3) with the maximum range from about 1.3 to 2.4 Mg/m^3 (80 to 150 lbf/ft^3). (Densities are also given in British engineering units, because you are likely to encounter them in United States practice.) Typical optimum water contents are between 10% and 20%, with an outside maximum range of about 5% to 40%.

Also shown on Fig. 5.1 are curves representing different *degrees of saturation* of the soil. From Eqs. (2.12) and (2.15), we can derive the equation for these theoretical curves.

$$\rho_d = \frac{\rho_w S}{w + \frac{\rho_w}{\rho_s} S} \tag{5.1}$$

The exact position of the degree of saturation curves depends only on the value of the density of the soil solids ρ_s. Note that at optimum water content for the soil in Fig. 5.1, S is about 75%. Note, too, that the compaction curve, even at high water contents, never actually reaches the curve for "100% saturation" (traditionally called the *zero air voids* curve). And this is true even for higher compactive efforts—for example, curve B in Fig. 5.1. Even if you keep adding water to the sample, it will never quite become completely saturated.

Also shown in Fig. 5.1 is the *line of optimums* (LOO). This is the line or curve drawn through the *peak* points of the compaction curves determined at different compactive efforts, but on the same soil. The LOO line will be almost parallel to the 100% S curve.

Often in geotechnical practice, compaction properties are given in terms of unit weights rather than densities. In fact, both terms may be used interchangeably, especially in discussions of field compaction and testing. Using the principles given in Sec. 2.3.2, you can convert the density equations given above to equivalent unit weight equations. For example, Eq. (2.6) becomes $\gamma = W_t/V_t$ [Eq. (2.20)], and Eq. (2.14) becomes $\gamma_d = \gamma/(1 + w)$.

Another way to determine the water-content density relations is the chart shown in Fig. 5.3. The ordinates are in terms of both density and unit weight. On this figure, relationships for 0%, 10% and 20%

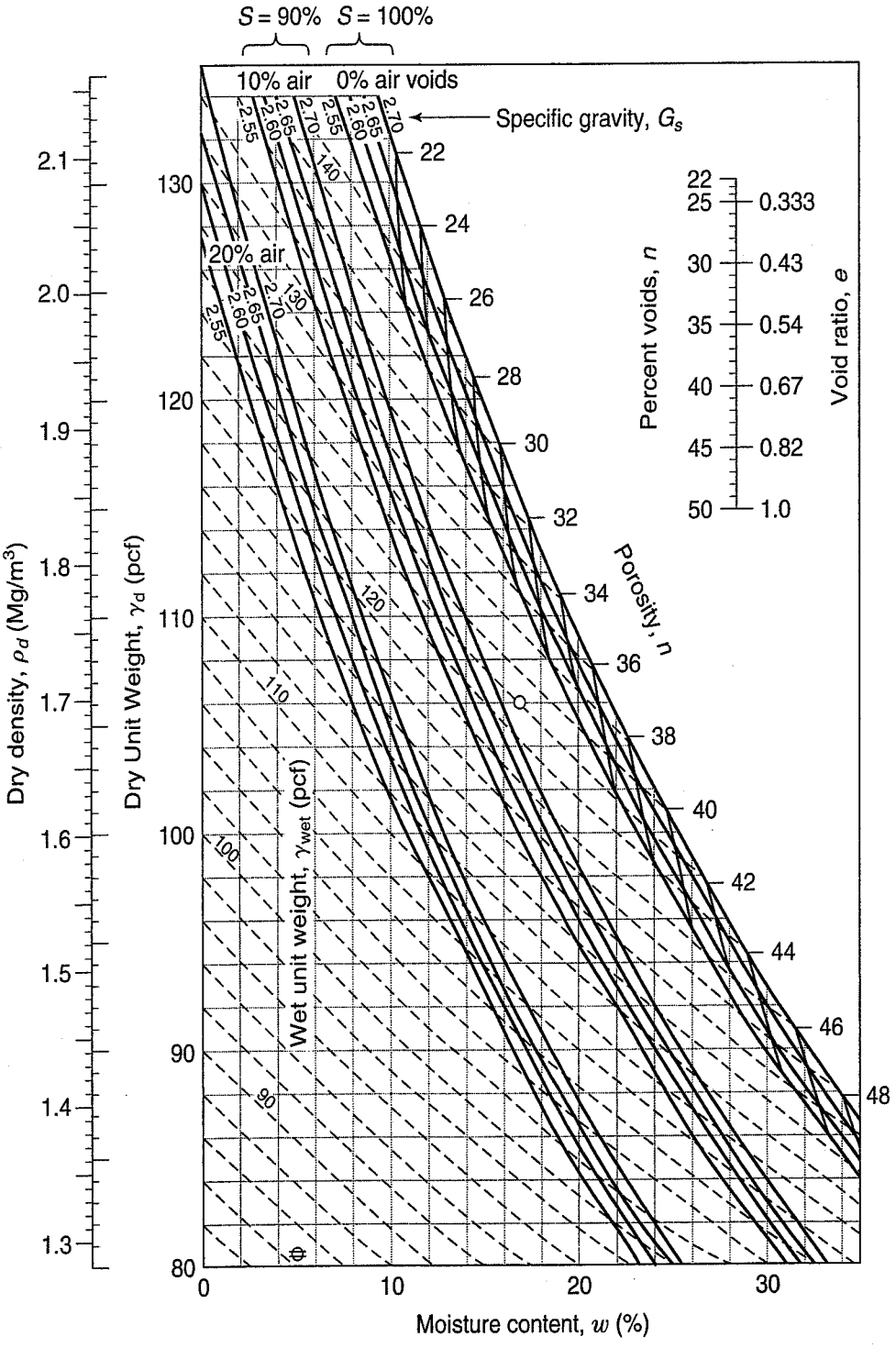

FIGURE 5.3 Solution of the soil solids water-voids relationships of soil masses (Bureau of Public Roads, now the Federal Highway Administration).

air voids (S = 100%, 90%, and 80%) are plotted for specific gravities G_s of 2.55, 2.60, 2.65, and 2.70. Also contained on this figure are lines of wet unit weight and porosity.

To use this figure, plot your compaction curve and determine the maximum dry density and optimum water content as usual. Assume you obtain the values at point O, or a water content of 17% and a dry density of 106 pcf. Also assume that the specific gravity G_s is 2.70 for this soil. Then use the dashed lines to find that the wet density is 124 pcf. Now for this point, interpolate for the percent air voids between 0% and 10% and find the percent air voids equal to ~8%. Also, for point O, the porosity, n, on the 0% air voids curve (or the 100% saturation curve) is ~37%. Using the nomograph in the upper right of the figure, find the void ratio equal to ~0.59. You can use Fig. 5.3 to solve for similar compaction problems.

Other useful equivalent equations are developed in Example 5.2.

Example 5.2

Given:

Equations (2.12) and (5.1).

Required:

Convert these equations to their equivalents using unit weights.

Solution: For Eq. (2.12), go back and look at Example 2.10. Or

$$\gamma_d = \frac{G_s \gamma_w}{1 + e} \tag{2.28a}$$

To convert Eq. (5.1), use the basic relationships for ρ and γ developed in Sec. 2.3.2,

$$\rho_d = \frac{\rho_w + S}{w + \frac{\rho_w}{\rho_s} S} = \frac{\gamma_d}{g} = \frac{\frac{\gamma_w}{g} S}{w + \frac{\frac{\gamma_w}{g}}{G_s \left(\frac{\gamma_w}{g}\right)} S} = \gamma_d = \frac{\gamma_w S}{w + \frac{S}{G_s}} \tag{5.2}$$

If S = 100%, Eq. (5.2) becomes

$$\gamma_d = \frac{\gamma_w G_s}{w_{\text{sat}} G_s + 1} \tag{5.3}$$

Equations (5.2) and (5.3) can be easily rearranged to give useful relationships for w_{sat} as a function of γ_d, γ_w, G_s, and S.

5.3.3 Effect of Soil Type and Method of Compaction

Typical compaction curves for different types of soil are illustrated in Fig. 5.4. Notice how a well-graded sand with silt (SW-SM soil, No. 1) has a higher dry density than a more uniform sand (SP, No. 8). For clayey soils, the maximum dry density tends to decrease as plasticity increases.

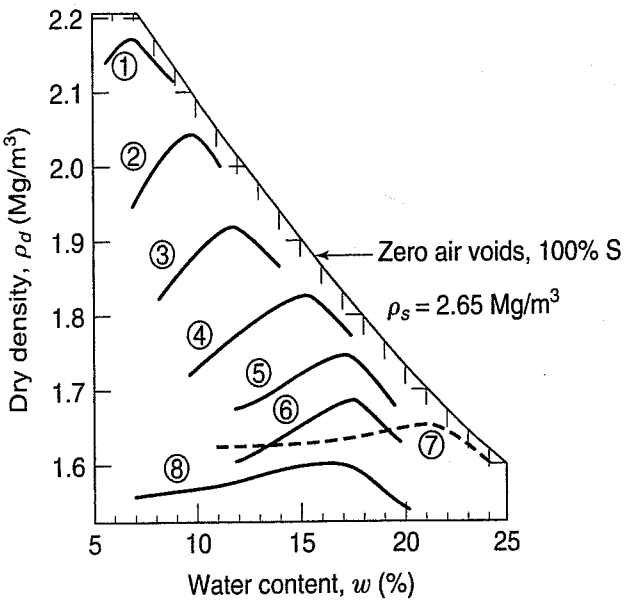

FIGURE 5.4 Water content-dry density relationships for eight soils compacted according to the standard Proctor method (after Johnson and Sallberg, 1960).

Soil No.	Description and USCS Symbol	Sand	Silt	Clay	LL	PI
1	Well-graded sand with silt SW-SM	88	10	2	16	NP
2	Well-graded silt SM	72	15	13	16	NP
3	Clayey sand SC	73	9	18	22	4
4	Sandy lean clay CL	32	33	35	28	9
5	Lean silty clay CL	5	64	31	36	15
6	Loessial silt ML	5	85	10	26	2
7	Fat clay CH	6	22	72	67	40
8	Poorly graded sand SP	94	6	—	NP	—

Go back at look again at Table 5.1 and note the limitations in terms of particle sizes for the use of the Proctor compaction tests (last row of the table). What do you do if the percentage of coarse or "oversize" material is greater 30%? One possibility is to use the compaction test procedure developed by the U.S. Bureau of Reclamation, method USBR 5515, that uses a large compaction mold with a volume of about 0.04 m^3 (U.S. Dept. of the Interior, 1990). You should never replace the coarser fraction with an equivalent mass of finer-grained soil, as this will give incorrect results (Torrey and Donaghe, 1994). The presence of a significant amount of oversize material in earth and earth-rock fills causes problems both in tests for design and in compaction control in the field (discussed in Sec. 5.7.2).

Another problem with compaction tests on especially coarser-grained residual soils (see Secs. 3.3.2 and 4.12), is that the soil particles break down or degrade due to the impact of the Proctor hammer during compaction. This phenomenon causes an increase in maximum dry density as the material becomes finer grained. The problem is that the test value may not be representative of field conditions. Parenthetically this is the reason why both ASTM D 698 and D 1557 specify that compacted soil cannot be reused for subsequent compaction testing. Gap-graded soils also present problems for compaction tests and their interpretation.

Compaction behavior of fine-grained soils as described in Sec. 5.3.1 is typical for both field and laboratory compaction. The curves will have different shapes and positions on the ρ_d versus w plot, but in general the response will be similar to that shown in Fig. 5.5, in which the same soil is compacted under different conditions. The standard and modified Proctor laboratory tests were developed as a standard of comparison for field compaction—that is, to see if the rolling or compaction was sufficient.

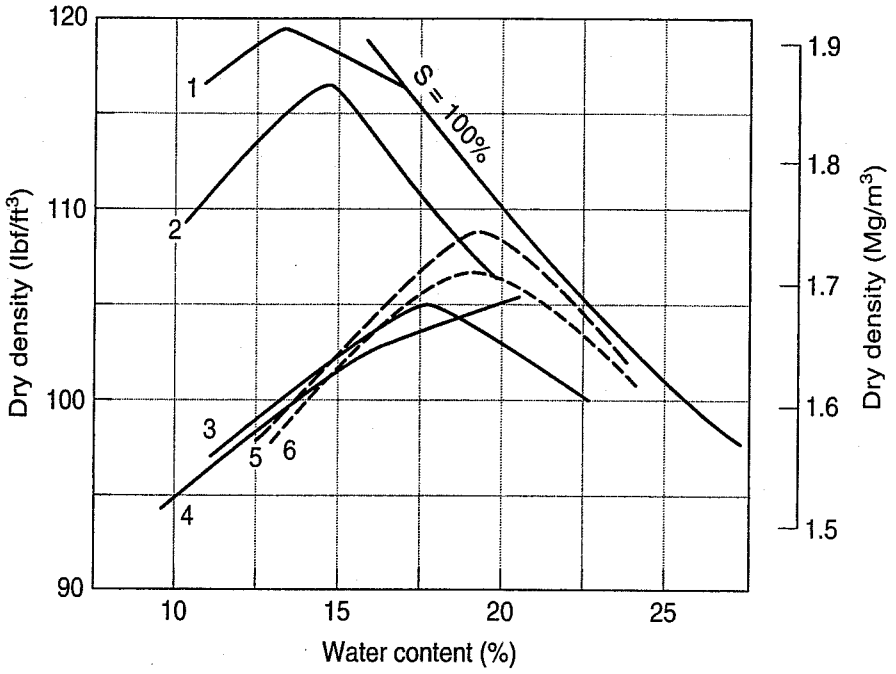

FIGURE 5.5 Comparison of field and laboratory compaction. (1) Laboratory static compaction, 2000 psi; (2) modified Proctor; (3) standard Proctor; (4) laboratory static compaction, 200 psi; (5) field compaction, rubber-tired load, 6 coverages; (6) field compaction, sheepsfoot roller, 6 passes. *Note:* Static compaction from top and bottom of soil sample. (After Turnbull, 1950, and as cited by Lambe and Whitman, 1969.) (See also USAE WES 1949.)

The approximation to field compaction is not exact, as mentioned, because the standard laboratory compaction is a dynamic-impact type, whereas field compaction is essentially a kneading-type compaction. This difference led to the development of the Harvard miniature compactor (Wilson, 1970; U.S. Dept. of the Interior, 1990, Procedure 5510) as well as larger laboratory kneading compactors. Field compaction control procedures are described in Sec. 5.7.

5.4 STRUCTURE OF COMPACTED FINE-GRAINED SOILS

The structure that results from the compaction of fine-grained soils depends on the method or type of compaction, the compactive effort applied, the soil type, and on the molding water content. Usually the water content of compacted soils is referenced to the optimum water content for a given type of compaction. Depending on their position on the compaction curve, soils are called *dry of optimum*, *near or at optimum*, or *wet of optimum*. Research on compacted clays has shown that when they are compacted dry of optimum, the soil structure is essentially independent of the type of compaction (Seed and Chan, 1959). Wet of optimum, however, the type of compaction has a significant effect on the soil structure and thus on the resulting engineering properties of the soil.

The real structure and fabric of compacted clays is about as complex as the fabric of natural clays described in Chapter 4. At the same compactive effort, as the water content increases, the soil fabric becomes increasingly oriented. Dry of optimum fine-grained soils are always *flocculated*, whereas wet of optimum the fabric becomes more oriented or *dispersed*. In Fig. 5.6, for example, the fabric at point C is more oriented than at point A. Now, if the compactive effort is increased, the soil tends to become more oriented, even dry of optimum. Again, referring to Fig. 5.6, a sample at point E is more oriented than at point A. Wet of optimum, the fabric at point D will be somewhat more oriented than at point B,

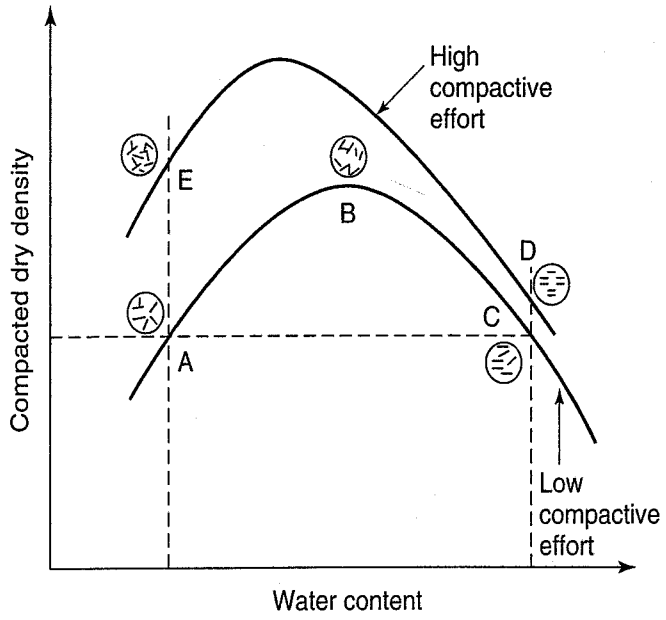

FIGURE 5.6 Effect of compaction on soil structure (after Lambe, 1958a).

although the effect is less significant than dry of optimum. Because a clayey soil compacted dry of optimum has a water deficiency, its structure is more sensitive to change than if it were compacted wet of optimum.

The engineering properties of compacted fine-grained soils depend greatly on the structure and fabric of the soil, because, as we have seen, the structure depends on the molding water content, compactive effort , and type of compaction. We discuss the effects of compaction on shrinkage and swelling characteristics of soils in Chapter 6. Hydraulic conductivity of compacted clays is described in Chapter 7, while the compressibility of compacted clays is discussed in Chapter 8. Finally, the shear strength properties of fine-grained soils are discussed in Chapter 12.

5.5 COMPACTION OF GRANULAR SOILS

We mentioned earlier in this chapter that granular soils are most efficiently compacted or densified by vibration. This is true both in the laboratory and in the field. These particles have no inherent cohesion; they are large enough so that gravity forces between particles are greater than surface forces (Chapter 4). They are easily moved from a looser into a denser configuration or packing through vibration.

The variables that influence vibratory densification are the characteristics of the (1) soil and (2) equipment, and (3) procedures used in the field. Soil characteristics include the initial density, grain size distribution and particle shape, and water content. From our discussion of granular soil fabrics in Sec. 4.10, it should be obvious that densification applies only to loose granular materials; dense materials ordinarily do not need additional compaction. Well-graded materials are generally easier to compact than uniform materials; similarly, dry soils are easier to densify than wet soils. The thickness of the layer or deposit also influences densification.

Equipment characteristics include the mass and size of the vibratory equipment and its frequency and amplitude of vibration. Sometimes the frequency and amplitude of vibration are varied to improve densification. Field compaction equipment is discussed in Sec. 5.6.

For compacted fills, field procedures include the number of passes of the vibratory equipment, thickness of the *lift* or layer being compacted, frequency of the vibrator, and the towing speed. Several different procedures are available for densification of deep deposits of granular materials, and these are briefly described in Sec. 5.5.2. Compaction of rock fills is discussed in Sec. 5.5.3.

5.5.1 Relative or Index Density

Recall from Sec. 4.10 that granular soils can have a rather wide range of void ratios and densities. The actual range depends on the grain shape, grain size distribution, and the fabric of the soils. We also defined maximum void ratio (e_{max}) or minimum density ($\rho_{d\,min}$) as the loosest possible condition of a dry granular soil. The corresponding densest possible condition of that soil is the minimum void ratio (e_{min}) and maximum dry density ($\rho_{d\,max}$).

Determination of the maximum and minimum values is not so easy. Laboratory test results are often highly variable and operator-dependent (Selig and Ladd, 1973). Even the ASTM (2010) tests, D 4253 for maximum density and D 4254 for minimum density, do not necessarily give the absolute maximum or minimum density values; thus they are called maximum and minimum *index* densities. The corresponding void ratios are e_{min}, the minimum *index* void ratio and e_{max}, the maximum *index* void ratio. For completeness, the maximum and minimum index unit weights are also defined.

Often in practice it is useful to know just how loose or how dense a sand specimen or granular soil deposit is *relative* to the maximum and minimum possible conditions. This leads to the concept of *index density* (or *index unit weight*), also commonly referred to as *relative density*. The index density D_r is used to compare the void ratio e of a given soil with the maximum and minimum void ratios. Index density is defined as

$$D_r = \frac{e_{max} - e}{e_{max} - e_{min}} \times 100\,(\%) \tag{5.4}$$

It is usually expressed as a percentage. Index or relative density can also be stated in terms of maximum and minimum index densities and index unit weights as

$$D_r = \frac{1/\rho_{d\,min} - 1/\rho_d}{1/\rho_{d\,min} - 1/\rho_{d\,max}} \times 100 = \frac{\gamma_d - \gamma_{d\,min}}{\gamma_{d\,max} - \gamma_{d\,min}}\left(\frac{\gamma_{d\,max}}{\gamma_d}\right) \times 100 \tag{5.5}$$

The parameters $\rho_{d\,max}$ and $\rho_{d\,min}$ are, respectively, the maximum and minimum dry density of a soil obtained from ASTM standards D 4253 and D 4254. The $\rho_{d\,max}$ corresponds to the minimum void ratio (e_{min}), and $\rho_{d\,min}$ to the maximum void ratio (e_{max}). The density index I_d is the ratio, expressed as a percentage, of the difference between the value of any given dry density (or unit weight) and the minimum dry density (or unit weight) to the difference between its maximum and minimum dry densities (or unit weights). In equation form:

$$I_d = \frac{\rho_d - \rho_{d\,min}}{\rho_{d\,max} - \rho_{d\,min}} \times 100\,(\%) \tag{5.6}$$

or

$$I_d = \frac{\gamma_d - \gamma_{d\,min}}{\gamma_{d\,max} - \gamma_{d\,min}} \times 100\,(\%) \tag{5.7}$$

The maximum-minimum index density tests are applicable to clean, free-draining granular soils containing a maximum of 15% passing the 75 μm or the No. 200 sieve. An approximate density classification based on D_r is: for $D_r < 15\%$, the soil is classified as very loose; for 15–35%, loose; 35–65%, medium dense; 65–85%, dense; and >85%, very dense.

The relative density of a natural soil deposit very strongly affects its engineering behavior. Consequently, it is important to conduct laboratory tests on specimens of the sand at the same relative density as in the field. Sampling of loose granular materials, especially at depths greater than a few metres, is very difficult. Since these materials are very sensitive to even the slightest vibration, one is never sure the sample has the same density as the natural soil deposit. Therefore, different kinds of penetrometers are used in engineering practice that test the soil while it is still in the ground (or in situ), under the assumption that it has not been significantly disturbed. The penetration resistance values are roughly

correlated with relative density. For deposits at shallow depths where direct access is possible, other techniques have been developed to measure the in-place density of compacted soils. These techniques are discussed in detail in Sec. 5.7.

5.5.2 Densification of Granular Deposits

When structures are to be founded on deep deposits of loose granular materials, settlements usually control the design. In earthquake-prone areas if the groundwater table is high, these deposits are susceptible to liquefaction (Chapter 7). Deep foundations can always be used, but they are relatively expensive, and it is often more economical to densify the subsoils to decrease settlements and mitigate liquefaction potential. Because densification by heavy surface vibratory rollers is usually insufficient, as we shall see in the next section, other techniques must be employed that carry the vibratory energy to greater depths. These techniques include dynamic compaction, densification by blasting, vibro-compaction and vibro-replacement techniques, inundation with water (for collapsible deposits, Chapter 6), and compaction piles. All these techniques are obviously applicable only to new construction, and blasting is used only at very remote sites needing densification.

In this section, we discuss only the most common techniques: dynamic compaction, vibro-compaction, and vibro-replacement. For a detailed discussion of these and other soil improvement methods, see Hausmann (1990) and Holtz et al. (2001), among others.

Dynamic Compaction—The method basically consists of repeatedly dropping a very heavy weight (10 to 40 tons mass) some height (10 to 40 m) over the site. The impact produces shock waves that cause densification of unsaturated granular soils. In saturated granular soils, the shock waves can produce partial liquefaction of the sand, a condition similar to quicksand (discussed in Chapter 7), followed by consolidation (discussed in Chapter 8) and rapid densification. The variables include energy (drop height and weight of pounder), the number of drops at a single point (3 to 10), and the pattern of the drops at the surface (5 to 15 m center-to-center). Figure 5.7 shows a pounder just impacting the surface of a loose sand layer. Eventually this site will look like a set of organized moon craters. The craters can be filled with sand and additionally tamped, or the area between them can be smoothed out by the pounder itself.

Dynamic compaction was apparently first used in Germany in the mid-1930s during construction of the Autobahns (Loos, 1936). It has also been used in the USSR to compact loessial soils up to 5 m deep (Abelev, 1957). In the United States, Bob Lukas of STS Consultants about 1970 used a wrecking ball to compact loose building rubble in Chicago. He soon found that a flat-bottom weight (either a stack of steel plates, or a steel box filled with concrete) was more effective. About the same time, dynamic compaction was further refined and promoted in France and elsewhere by Louis Ménard (Ménard and Broise, 1975). Ménard also developed very heavy pounders (up to 200 metric tons mass) and massive tripod cranes for lifting them to drop heights up to 40 m. Improvement is claimed to depths down to 40 m. In North America, dynamic compaction has been used on a more modest scale by contractors using ordinary equipment (Leonards et al., 1980; Lukas, 1980 and 1995). Modest depths can be densified by ordinary construction cranes, but for heavier weights and great drop heights, special cables, crane clutches, and stronger booms are required to avoid damaging the crane.

The depth of influence D, in metres, of the soil undergoing compaction is given by Lukas (1995) as

$$D = n(W \times H)^{1/2} \tag{5.8}$$

where D = depth of improvement in metres,
n = an empirical coefficient that is less than 1.0,
W = mass of tamper in megagrams,
H = drop height in metres.

The value of n varies from about 0.35 to 0.6 depending on the soil type, the ease with which water will flow through the soils, and the degree of saturation. Leonards et al. (1980) recommended $n = 0.5$.

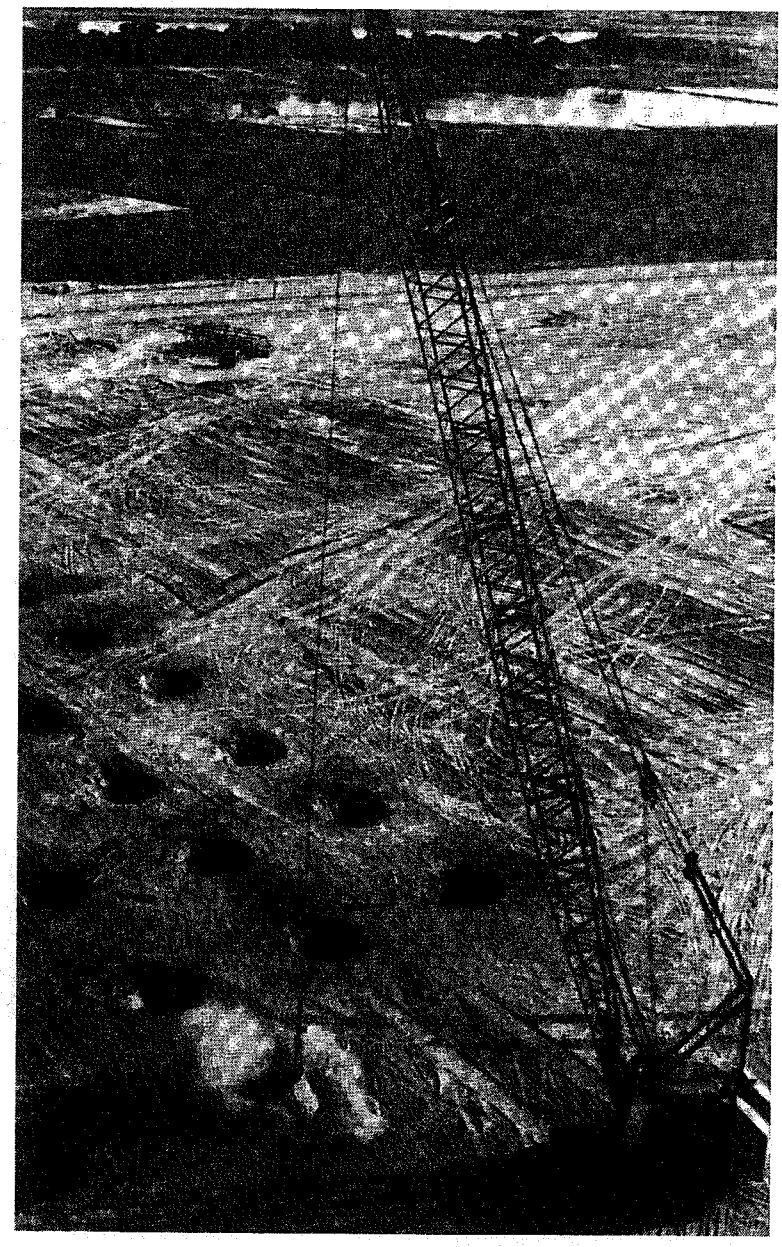

FIGURE 5.7 Dynamic compaction at a site in Bangladesh. The 100-ton crane is dropping a 16-metric-ton weight 30 m (courtesy of S. Varaksin, Techniques Louis Ménard, Longjumeau, France).

The heavier the weight and/or the greater the drop height, the greater the depth of compaction, and several researchers have tried to develop relationships between applied energy and surface area treated. Leonards et al. (1980) also found that the amount of improvement due to compaction in the zone of maximum improvement correlates best with the product of the energy per drop times the total energy applied per unit of surface area. Lukas (1995) noted that the mass of the tamper, drop height, grid spacing, and the number of drops at each grid point location all influenced the applied energy and therefore the effectiveness of the densification. Research has shown that there is a limit to how much improvement is possible, even with heavier weights and greater drop heights.

Not all soil deposits are conducive to dynamic compaction, especially if a significant percentage of fines is present or if the soils have some plasticity. Clean granular deposits, mine spoils, loosely dumped fills, and even garbage dumps have been successfully densified with dynamic compaction. Treatment of silt deposits has been less successful and the method is not recommended for clay or peat deposits. Densification of stratified sites also has not been very successful. For example, even a thin clay layer will absorb much of the dynamic energy and prevent densification of the loose sands below it.

Lukas (1995) gives detailed information on the design of dynamic compaction. Actual construction is most often done by specialty foundation contractors.

Vibro-Compaction—Vibro-compaction refers to the densification of granular deposits with some type of a vibrating probe that is vibrated, jetted, or otherwise inserted into the ground. Probes are usually supported by a crane, and several different types have been developed by contractors and engineers. They can be tubes or pipes, both closed and open ended, rods with wings or blades attached, or beams or plates of various shapes, some with holes in the web. Cylindrical probes have typical diameters of 300 to 450 mm, and that is the approximate width of the plate and wing-type probes. Some systems have the vibrating engine in the bottom of the probe, while others have the vibrator attached to the top of the unit. Most systems use a constant-frequency vibrator, typically 12–20 Hz, but a few have variable vibrators that allow the engineer to match the frequency to the resonance of the sand deposit.

Often a cone of settlement occurs at the ground surface around the probe due to densification, so the contractor adds clean sand to fill the area around the probe. As sand is added, the probe is repeatedly raised and lowered into the probe hole, and it is gradually withdrawn as the added sand and the area around the probe densifies.

Vibro-floatation, probably the oldest vibro-compaction system, was developed in Germany in the 1930s for the construction of the Berlin subway. It has a vibrator at the bottom of the probe and uses water jets to excavate the hole ahead of the probe. Until the 1970s, Vibro-floatation was the only vibro-compaction system available. Since then, a number of systems have been developed in Japan (Fudo Compozer sand piles; Vibrorod), Sweden (Vibrowing), Belguim (Franki Y-probe), Germany (Müller resonant compaction, MRC), and the United States (Terraprobe), among others.

Applicable soil deposits for vibro-compactions include sands and gravels with less than about 20% fines, mine spoils, and dumped fills, depending on the nature of the fill. It is less successful in silty deposits, and it is not appropriate for clays, peats, and garbage.

Design begins with a thorough geotechnical site investigation and laboratory testing program to determine the gradation of the soils and their variability including macrofabric (Chapter 4). From a settlement analysis, the geotechnical engineer establishes the compaction requirements, including numerical performance predictions, and develops the vibro-compaction scheme. For example, do you densify the entire area, or only under columns and footings? This pattern and the desired degree of improvement will depend on the project requirements and the experience and judgment of the geotechnical engineer. The final step is to develop QC/QA plans, and this typically involves the common in situ tests (discussed later in this book).

Typical spacing of the vibro-centers is from about 1 m up to 3.5 m. Density will, of course, be increased as the vibro-center spacing is decreased. Probe pattern is either square or triangular. The depth of improvement will depend on the need and the capability of the equipment, but typical depths are 10 to 20 m. Vibro-compaction is most often done by contractors who specialize in this type of work.

Vibro-Replacement—Vibro-replacement is a little more complicated than vibro-compaction because some of the less desirable subsoil is actual replaced—or displaced—with high-quality granular materials or even concrete. Depending on the site conditions and economics, replacement can be with sand only (sand columns), sand and gravel (sand-gravel columns), gravel columns, often called *stone columns*, and concrete columns (vibro-concrete columns).

Vibro-replacement is often used at sites where vibration alone will not work. It seems especially appropriate for deposits of loose stratified sands and silts to mitigate liquefaction potential. It is also applicable to sites with predominantly cohesive soils, because the added coarser materials reinforce the subsoil and increase strength and decrease compressibility and settlements. However, if the subsoils are very soft (e.g., very soft sensitive clays, organic soils and peats), stone columns can get very expensive, because they can require so much stone that the soft materials are displaced rather than replaced. Stone columns are also good for mine spoils and dumped fills but inappropriate for garbage dumps. To provide some additional compressive strength, sometimes Portland cement is added to the stone to make vibro-concrete columns.

Design of vibro-replacement is very similar to vibro-compaction design described above: perform a geotechnical site investigation and laboratory testing program; predict settlements and liquefaction

potential, if appropriate; establish the improvement requirements, including numerical performance predictions; design the vibro-replacement scheme; and establish the QA/QC criteria for the contractor.

Design of the vibro-replacement scheme (pattern, spacing, depth, replacement ratio, etc.) is often done by a specialty contractor as part of a design-build project or as a subcontractor. In this case, the project geotechnical engineering should be closely involved, as the desired degree of improvement will depend on the project requirements. On typical stone column projects, between 15% and 35% of soil volume is replaced. As before, columns are installed in a triangular or rectangular pattern at a typical center-to-center spacing of 1.5 to 3.5 m. Lengths of columns are commonly 6–12 m, but they can be installed up to 20 m.

Successful installation of stone columns usually requires the services of an experienced specialty foundation contractor. The probes are typically 300 to 450 mm in diameter and are basically of two types—top feed or bottom feed. With top feed, the stone and sand is fed into the hole from the top and then vibrated to densify the loose materials and expand the column laterally into surrounding soft or loose soils. At a site where the hole can be drilled and will remain open for some time, small charges of stone are repeatedly dumped into the hole and vibrated with equipment inserted into the hole until the column is completed. With the bottom-feed method, stone and sand are fed into a chamber at the top of the probe via a hopper hoisted by a crane. The chamber is closed, and air pressure is used to feed the stone out the bottom through a valve into the hole (dry method). Sometimes water jetting is used similar to vibro-floatation to aid in advancing the probe (wet method). The treated columns are typically 0.6 to 1.2 m in diameter.

5.5.3 Rock Fills

As with rock classification systems (Sec. 4.14), the definitions and methodologies related to rock fills have evolved considerably over the past 40 years. Today, rock fills are defined as those granular fills that have at least 30% by dry weight of clean rock (i.e., excluding fines and organics) retained on the $\frac{3}{4}$ in. (19 mm) sieve, and that contain less than 15% minus No. 200 (0.075 mm) material (Breitenbach, 1993 and 2010). The goal is a free-draining rock fill with a rock-to-rock contact structure that will be effectively compacted by vibratory compaction devices (Sec. 5.6.2). Rock fill materials are usually obtained by ripping or blasting rock deposits, or they can be derived from mine waste rock, referred to as tailings. Like other compacted fills, well-graded rock fills will tend to provide the densest, and therefore most stable, structure that is least prone to future settlements.

Early embankments made of rock fill were often placed in large single lifts 10 to 50 m (35 to 165 ft) in depth, which were not mechanically compacted but then were flooded with water in an attempt to densify them. This so-called "sluicing" method probably had its origins in the California gold-mining era of the 1850s (Sherard et al., 1963). The other method that became common with the advent of compaction equipment was placing the rock in 1 to 1.5 m (3 to 5 ft) thick lifts that were compacted by a nonvibrating steel drum or rubber-tired rollers. In the early 1960s, the Corps of Engineers performed tests on rock fills compacted using vibratory compactors at the 136 m (445 ft) high Cougar Dam near Eugene, Oregon. This testing led to more objective rock fill gradation classifications and also provided performance data on the use of smaller lift thicknesses for compacted rock fills. Today, rock fill is placed in even thinner lifts of 0.3 to 0.9 m (1 to 3 ft), and vibratory rollers are used for the most effective compaction results. This stabilization of rock fills results in safer and more economical embankment designs.

5.6 FIELD COMPACTION EQUIPMENT AND PROCEDURES

5.6.1 Compaction of Fine-Grained Soils

Soil to be used in a compacted fill is excavated from a *borrow area*. *Power shovels*, *draglines*, and self-propelled *scrapers* or "*pans*" are used to excavate the borrow material. A self-loading scraper is shown in Fig. 5.8(a) and an elevating scraper in Fig. 5.8(b). Sometimes "dozers" are necessary to help load the

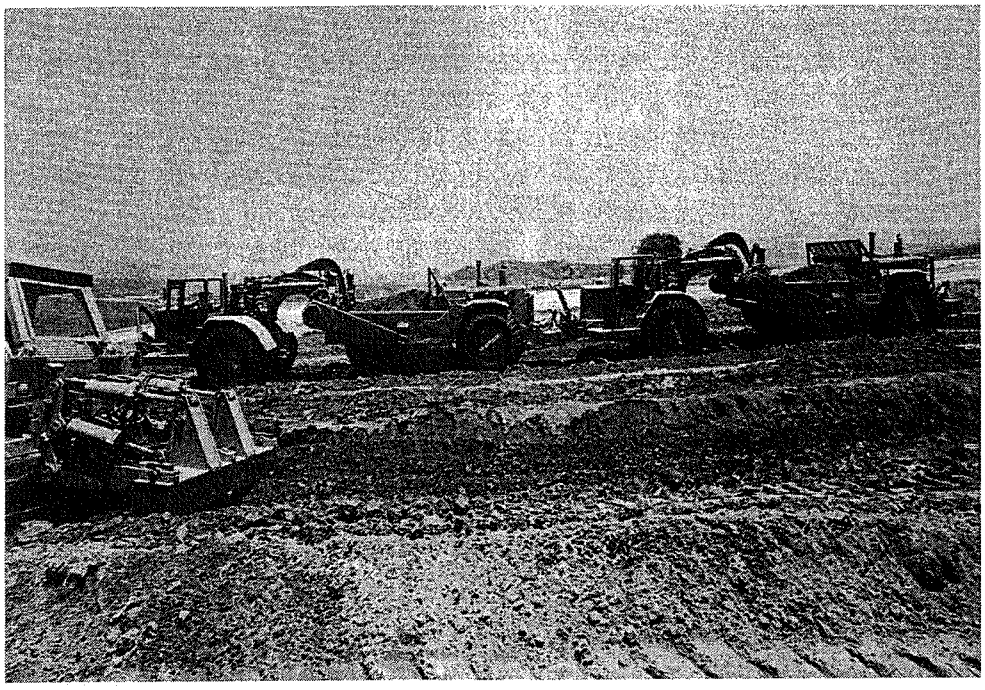

(a)

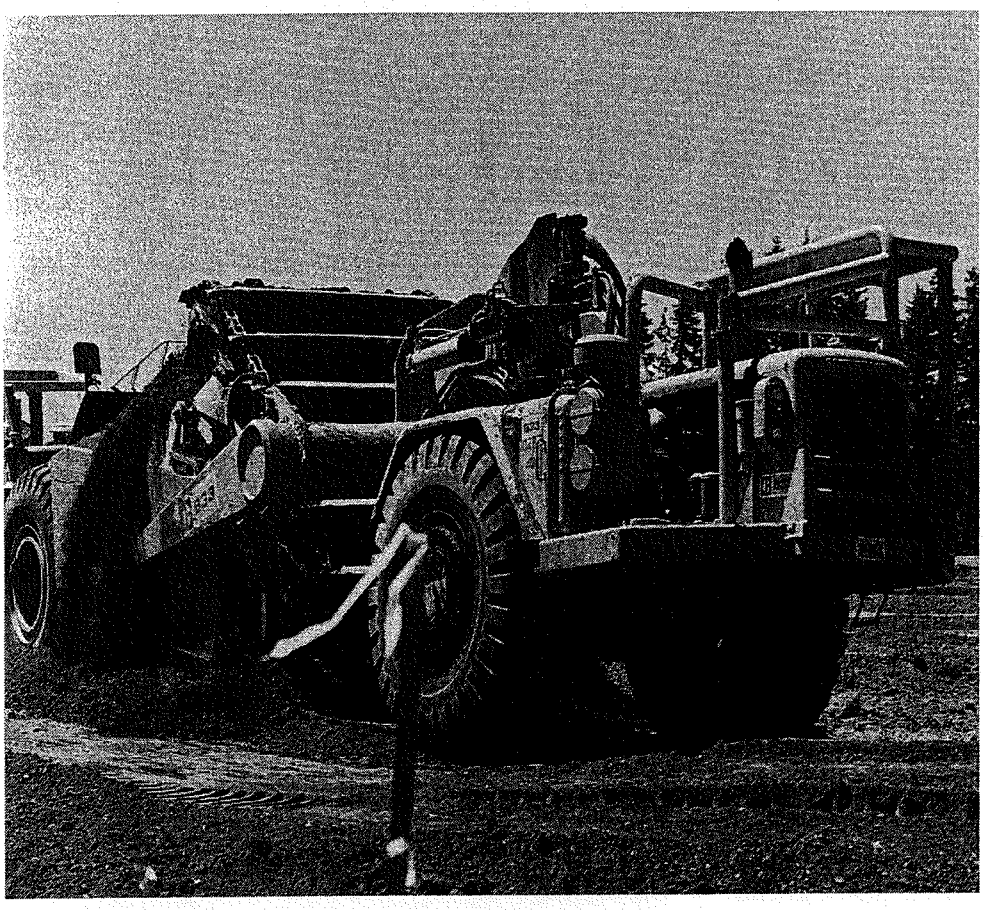

(b)

FIGURE 5.8 Two types of scrapers: (a) conventional or self-loading scraper. Sometimes a "dozer" or two helps push the "pan" to load up; (b) elevating scraper, where the elevating machine loads by itself and eliminates the need for a pusher (photographs courtesy of Caterpillar Inc.).

scraper. Scrapers may cut through layers of different materials, allowing soil types to be mixed, for example. The power shovel mixes the soil by digging along a vertical surface, whereas the scraper mixes the soil by cutting across a sloping surface where different layers may be exposed.

The borrow area may be on site or several kilometers away. Scrapers, which can operate on and off the road, are often used to transport and spread the soil in layers called *lifts* on the fill area. Trucks may be used as well, on or off the highway, and they may *end dump*, *side dump*, or *bottom dump* the fill material [Fig. 5.9(a)]. The hauling contractor usually tries to spread the fill material when dumping in order to reduce the spreading time. Where possible, the contractor directs the earth-moving equipment over previously uncompacted soil, thereby reducing the amount of compactive effort required later.

Once borrow material has been transported to the fill area, *bulldozers*,* front loaders, and *motor graders*, called *blades* [Fig. 5.9(b)], spread the material to the desired lift thickness. Lift thickness may range from 150 to 500 mm (6 to 18 in.) or so, depending on the size and type of compaction equipment and on the maximum grain size of the fill. Unless the borrow materials are already within the desired

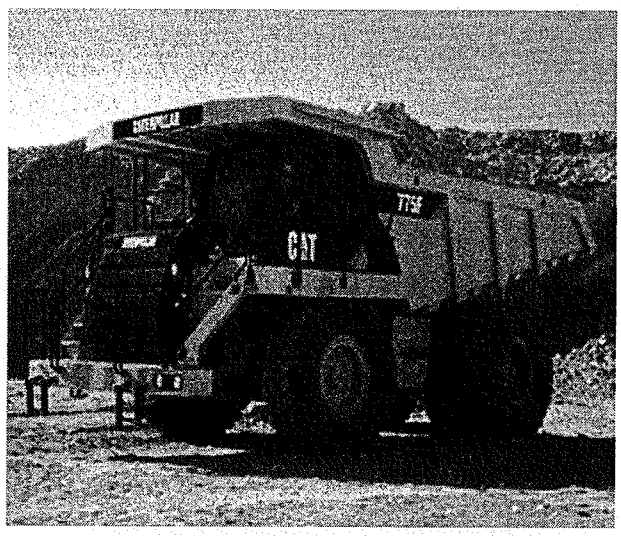

(a)

(b)

FIGURE 5.9 Examples of equipment used for hauling and spreading fill materials: (a) fill material being hauled by end dump truck; (b) motor grader spreading and preparing fill subgrade (photographs courtesy of Caterpillar, Inc.).

**Genus bovinas masculinus sonambulorum.*

water content range, the soil may need to be wetted, dried, or otherwise reworked. Usually motor graders and dozers are used to spread the soil to facilitate drying or mixing, although occasionally contractors use farm implements such as disc harrows for this purpose.

The kind of compacting equipment or *rollers* used on a job will depend on the type of soil to be compacted. Equipment is available to apply pressure, impact, vibration, and kneading. Figure 5.10 shows two types of rollers.

(a)

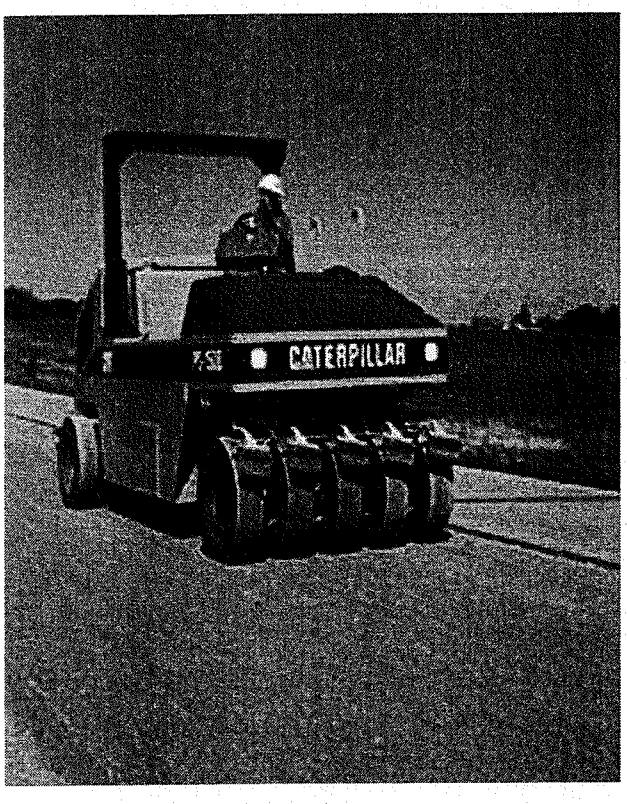

(b)

FIGURE 5.10 Types of rollers: (a) smooth-wheel roller; (b) rubber-tired roller (photographs courtesy of Caterpillar Inc.).

A *smooth-wheel*, or *drum*, *roller* [Fig. 5.10(a)] supplies 100% coverage under the wheel, with ground contact pressures up to 400 kPa (55 psi), and may be used on all soil types except rocky soils. The most common use for large, smooth-wheel rollers is for *proofrolling* subgrades and compacting asphalt pavements. The *pneumatic* or *rubber-tired roller* [Fig. 5.10(b)] has about 80% coverage (80% of the total area is covered by tires), and tire pressures may be up to about 700 kPa (100 psi). A heavily loaded wagon with several rows of four to six closely spaced tires is self-propelled or towed over the soil to be compacted. Like the smooth-wheel roller, the rubber-tired roller may be used for both granular and fine-grained earthfills, as well as for earth dam construction.

Probably the first roller developed and perhaps the most common type of compactor used today for fine-grained soils is the *sheepsfoot roller*. These rollers are usually towed in tandem by crawler tractors or are self-propelled, as shown in Fig. 5.11. The sheepsfoot roller, as its name implies, has many round or rectangular shaped protrusions or "feet" attached to a steel drum. The area of each protrusion ranges from 30 to 80 cm^2 (5 to 12 $in.^2$). Because of the 8% to 12% coverage, very high contact pressures are possible, ranging from 1400 to 7000 kPa (200 to 1000 psi), depending on the drum size and whether the drum is filled with water. The drums come in several diameters and weights. The sheepsfoot roller starts compacting the soil below the bottom of the feet (projecting about 150 to 250 mm from the drum) and works its way up the lift with each successive pass of the roller. Eventually the roller "walks out" of the fill as the upper part of the lift is compacted. The sheepsfoot roller is best suited for compacting fine-grained soils.

Other rollers with protrusions have also been developed to obtain high contact pressures for better crushing, kneading, and compacting of a rather wide variety of soils. These rollers can be either towed or self-propelled. *Tamping foot rollers* (Fig. 5.12) have approximately 40% coverage and generate high contact pressures ranging from about 1500 to 8500 kPa (200 to 1200 psi), depending on the size of the roller and whether the drum is filled for added weight. The special hinged feet of the tamping foot roller apply a kneading action to the soil. These rollers compact similarly to the sheepsfoot in that the roller eventually "walks out" of a well-compacted lift. Tamping foot rollers are best for compacting fine-grained soils.

Still another type is the *mesh*, or *grid pattern*, *roller* with about 50% coverage and pressures from about 1500 to 6500 kPa (200 to 900 psi) (Fig. 5.13). The mesh roller is ideally suited for compacting rocky soils, gravels, and sands. With high towing speed, the material is vibrated, crushed, and impacted. Another development also suitable for a wide variety of material is the "square" or impact roller developed in Australia by Broons. The compactors weigh 13 800 to 18 200 kg and are 1.3 to 1.95 m wide, all designed to be towed by a tractor.

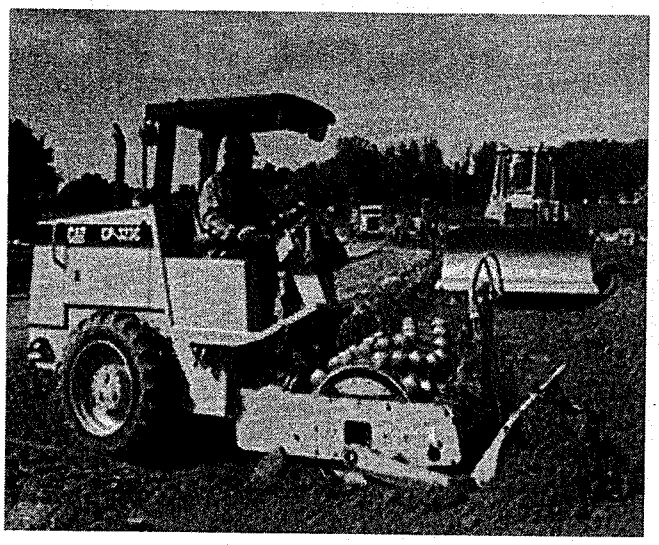

FIGURE 5.11 Self-propelled sheepsfoot roller (photograph courtesy of Caterpillar Inc.).

FIGURE 5.12 Self-propelled tamping foot compactor (photograph courtesy of Caterpillar, Inc.).

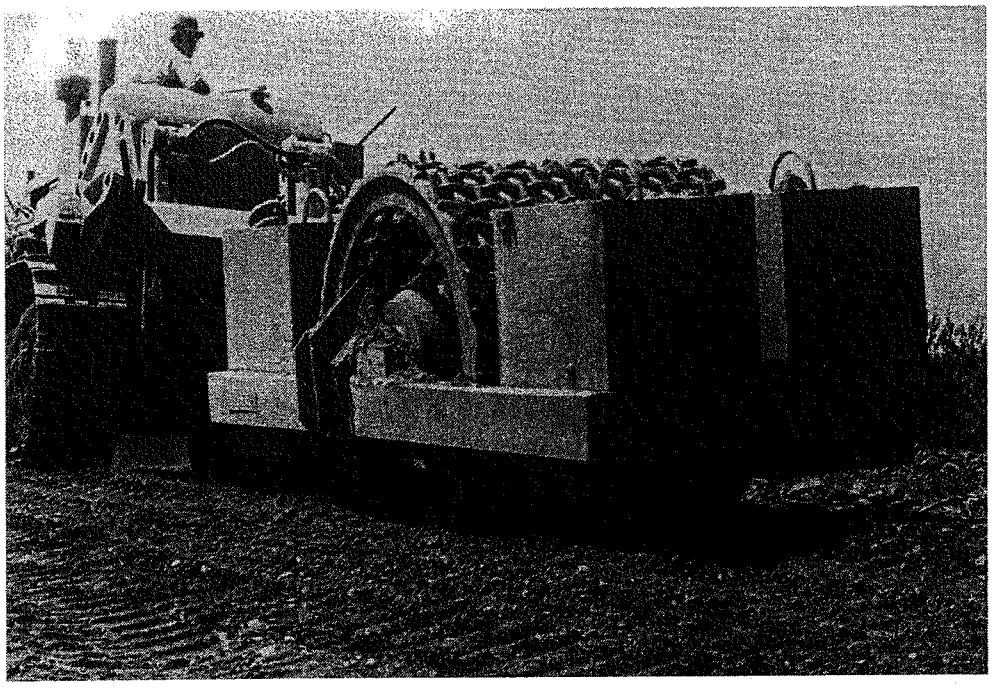

FIGURE 5.13 Mesh or grid roller (photo courtesy of BOMAG Americas, Inc.).

5.6.2 Compaction of Granular Materials

Several compaction equipment manufacturers have attached vertical vibrators to smooth-wheel and tamping foot rollers to make them more suitable for densifying granular soils. Figure 5.14 shows a vibrating drum on a smooth-wheel roller compacting a gravelly material. In areas where the larger rollers cannot operate, compaction is accomplished by *rammers* ("*jumping jacks*") and *vibrating plates* of various sizes and weights. Rammers are motorized but hand guided and weigh between 50 and 150 kg; they have a compacting plate of about 60 to 100 cm^2. Self-propelled but hand-guided plate vibrators weigh from 50 to 3000 kg (100 to 6000 lb) and have a typical plate areas of 0.4 m^2 to 1 m^2. Effective compaction depth for even the larger plates is less than 1 m.

Broms and Forssblad (1969) have listed the different types of vibratory soil compactors, their mass and frequency of operation, and their practical applications (Table 5.2).

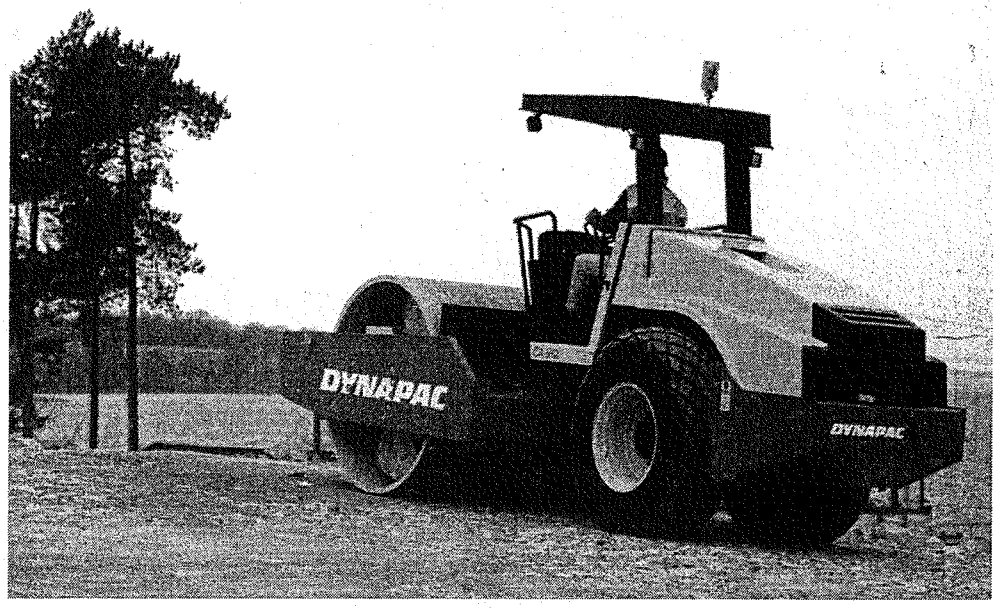

FIGURE 5.14 Vibratory roller (photograph courtesy of Dynapac, Inc.).

TABLE 5.2 Types and Applications of Vibratory Soil Compactors

Type of Machine	Mass, kg (Weight, lb)	Frequency (Hz)	Applications
Vibrating tampers (rammers):			
Hand-guided	50–150 (100–300)	≈10	Street repair. Fills behind bridge abutments, retaining and basement walls, etc. Trench fills.
Vibrating plate compactors:			
Self-propelled, hand-guided	50–3000 (100–600)	12–80	Base and subbase compaction for streets, sidewalks, etc. Street repair. Fills behind bridge abutments, retaining and basement walls, etc. Fills below floors. Trench fills.
Multiple-type, mounted on tractors, etc.	200–300 (400–600)	30–70	Base and subbase compaction for highways.
Crane-mounted[a]	Up to 20 000 (20 tons)	10–15	
Vibrating rollers:			
Self-propelled, hand-guided (one or two drums)	250–1500 (500–3000)	40–80	Base, subbase, and asphalt compaction for streets, sidewalks parking areas, garage driveways, etc. Fills behind bridge abutments and retaining walls. Fills below floors. Trench fills.
Self-propelled, tandem-type	700–10 000 (0.7–10 tons)	30–80	Base, subbase, and asphalt compaction for highways, streets, sidewalks, parking areas, garage driveways, etc. Fills below floors.
Self-propelled, rubber tires	4000–25 000 (4–25 tons)	20–40	Base, subbase, and embankment compaction for highways, streets, parking areas, airfields, etc. Rock-fill dams. Fills (soil or rock) used as foundations for residential and industrial buildings.
Tractor-drawn	1500–15 000 (1.5–15 tons)	20–50	Base, subbase, and embankment compaction on highways, streets, parking areas, airfields, etc. Earth- and rock-fill dams. Fills (soil or rock) used as foundations for residential and industrial buildings. Deep compaction of natural deposits of sand.

[a]Only limited use.

After Broms and Forssblad (1969).

As discussed in Sec. 5.5, several variables control the vibratory compaction and densification of granular soils. They include:

1. Characteristics of the compactor
   - Mass
   - Size
   - Operating frequency and frequency range
   - Amplitude of vibration
2. Characteristics of the soil
   - Initial density
   - Grain size distribution
   - Grain shape
   - Water content
3. Construction procedures:
   - Number of passes of the roller
   - Lift thickness
   - Modification of the vibrator frequency during compaction
   - Towing speed

The compactor characteristics influence the stress level, density increase, and depth of influence of the dynamic force. For example, as shown in Fig. 5.15, when oscillation is added to a static component, the density is significantly increased. The influence of operating frequency for various soil types is shown in Fig. 5.16. Note how a peak in the density-frequency curve develops for most of the soils, even clays. The frequency at which a maximum density is achieved is called the *optimum frequency*. It is a function of the compactor-soil system, and it changes as the density increases during the process of compaction. It is desirable for a compactor to have the capability to vary its operating frequency and to have the range required to obtain maximum density. However, the peaks are gentle, and, on a percentage basis, a wide frequency range is not all that important.

Soil conditions are also important. The initial density in particular strongly influences the final density. For example, the upper 300 mm of medium dense sand may never become denser than the initial density, whereas dense sands will become looser in the upper 300 mm. This phenomenon is also illustrated below.

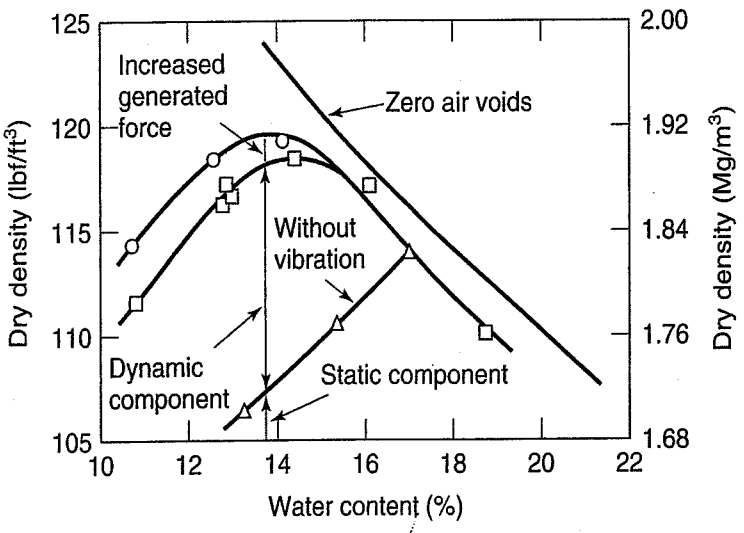

FIGURE 5.15 Compaction results on 30 cm (12 in.) layers of silty sand, with and without vibration, using a 7700 kg (17 000 lb) towed vibratory roller (after Parsons et al., 1962, as cited by Selig and Yoo, 1977).

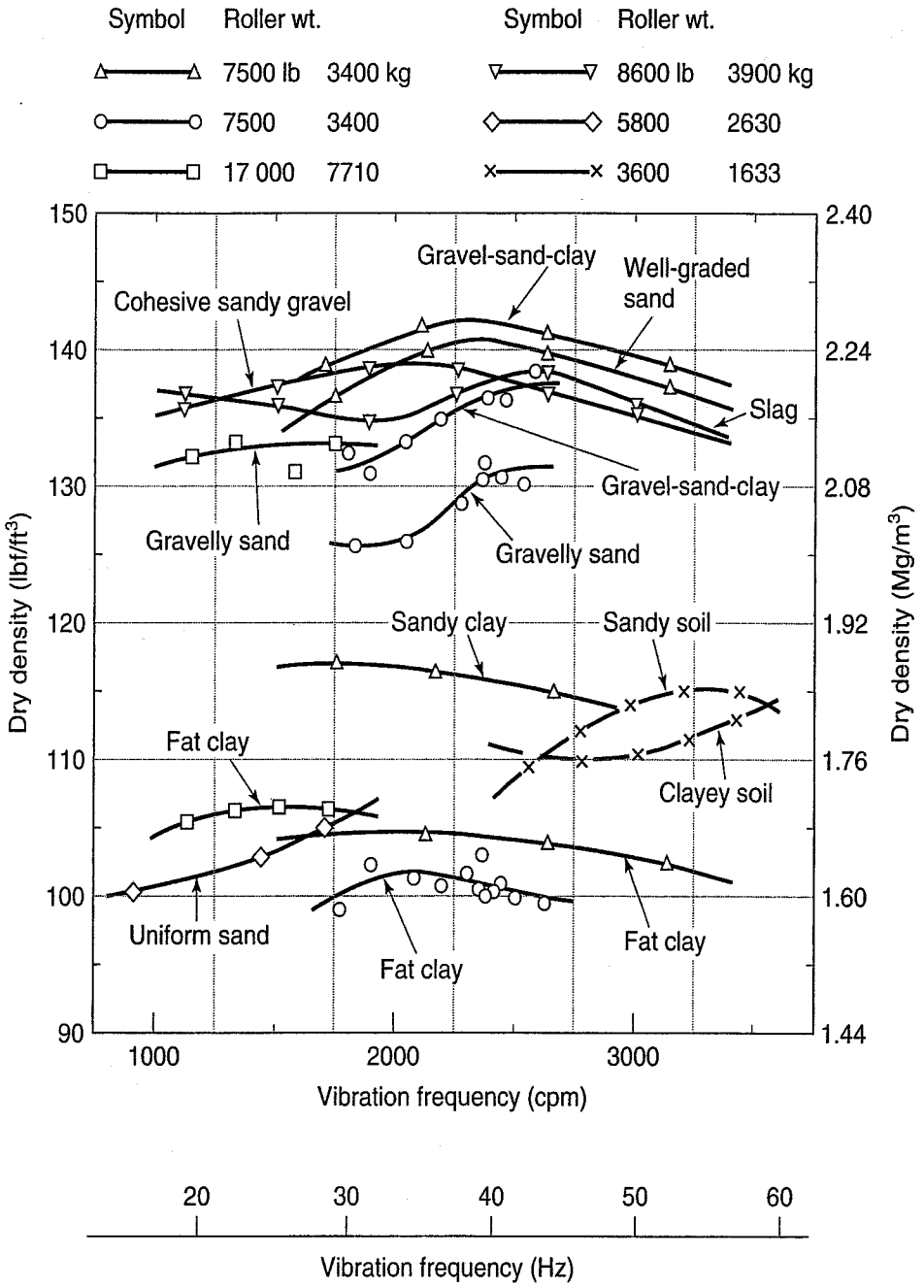

FIGURE 5.16 Variation with frequency of compaction by smooth-drum vibratory rollers (after several sources as cited by Selig and Yoo, 1977).

After the compactor is chosen, construction procedures essentially govern the results. The influence of the number of passes of a roller and the towing speed is shown in Fig. 5.16 for a 7700 kg roller compacting a fat (high LL) clay and a well-graded sand. Notice how the density increases as the number of passes or coverages increases, up to a point. Not so obvious is that, for a given number of passes, a higher density is obtained if the vibrator is towed more slowly! The results in both Figs. 5.16 and 5.17 indicate that vibratory compaction can work even in materials with some clay fines (Selig and Yoo, 1977). Also, for soils compacted on the dry side of optimum, adding the dynamic component results in increased density.

The effect of lift thickness may be illustrated by the work of D'Appolonia et al. (1969), shown in Fig. 5.18. A 5670 kg roller operating at a frequency of 27.5 Hz was used to compact a 2.40 m thick layer

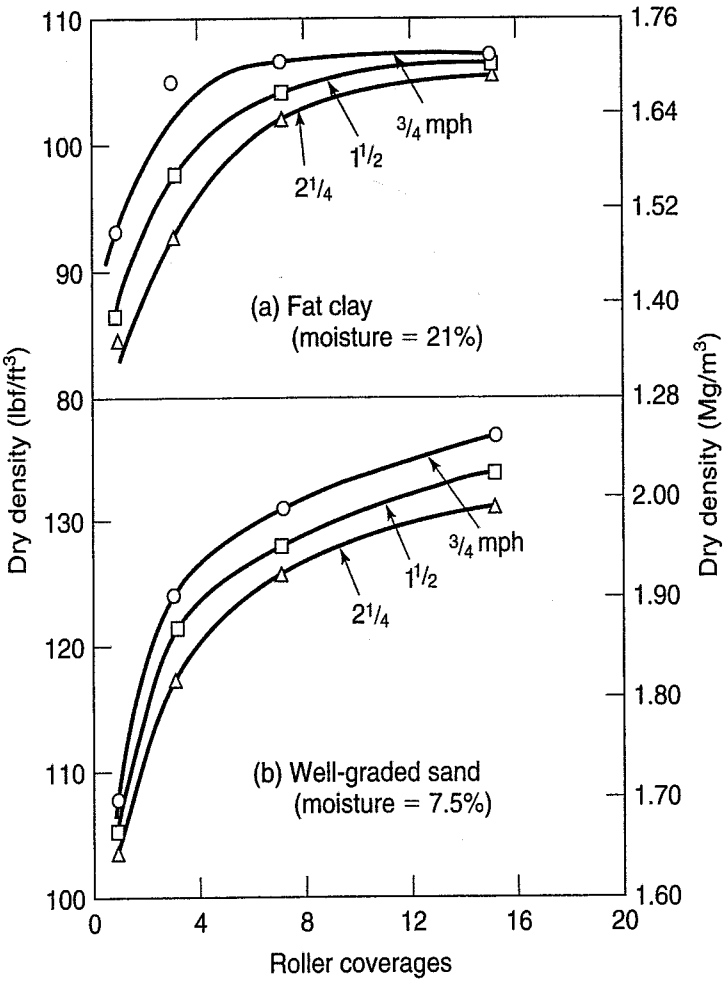

FIGURE 5.17 Effect of roller travel speed on amount of compaction with 7700 kg (17 000 lb) towed vibratory roller (after Parsons et al., 1962, as cited by Selig and Yoo, 1977).

of northern Indiana dune sand. The initial relative density was about 50% to 60%. Field density tests were made in test pits before and after compaction. Note how the density varied with depth. In the upper 150 mm (6 in.), the soil is vibrated loose, whereas the soil reaches its maximum density for a given number of coverages at about 45 cm; thereafter the increase in density tapers off. When compacting past five or so coverages, there is not a great increase in density.

Example 5.3

Given:

Five coverages of a certain roller and operating frequency.

Required:

Determine the maximum lift thickness required to obtain a minimum relative density of 75%.

Solution: Using the data shown in Fig. 5.18, trace the relative density versus depth curve for five passes. Superimpose that drawing over the original one, and slide it up and down until the desired relative density of 75% is obtained (shown in Fig. Ex. 5.3). About 0.45 m (18 in.) is indicated as the maximum thickness. Actually, however, the lift thickness could be greater, as compaction of the top layer densifies the lower layer with successive passes.

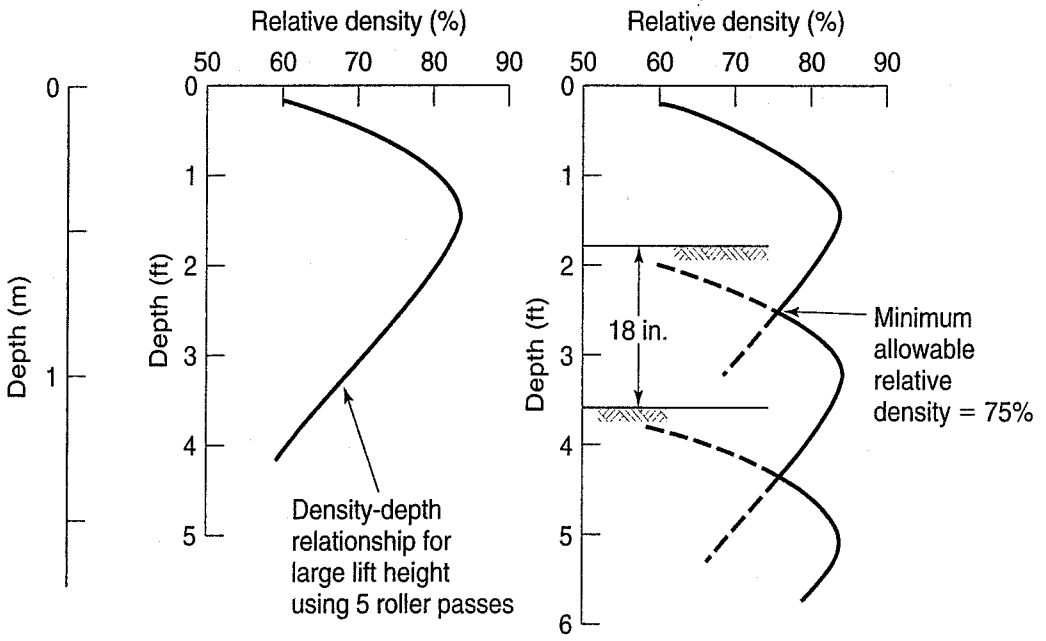

FIGURE Ex. 5.3 Approximate method for determining lift thickness required to achieve a minimum compacted relative density of 75% with five roller passes, using data for a large lift thickness (after D'Appolonia et al., 1969).

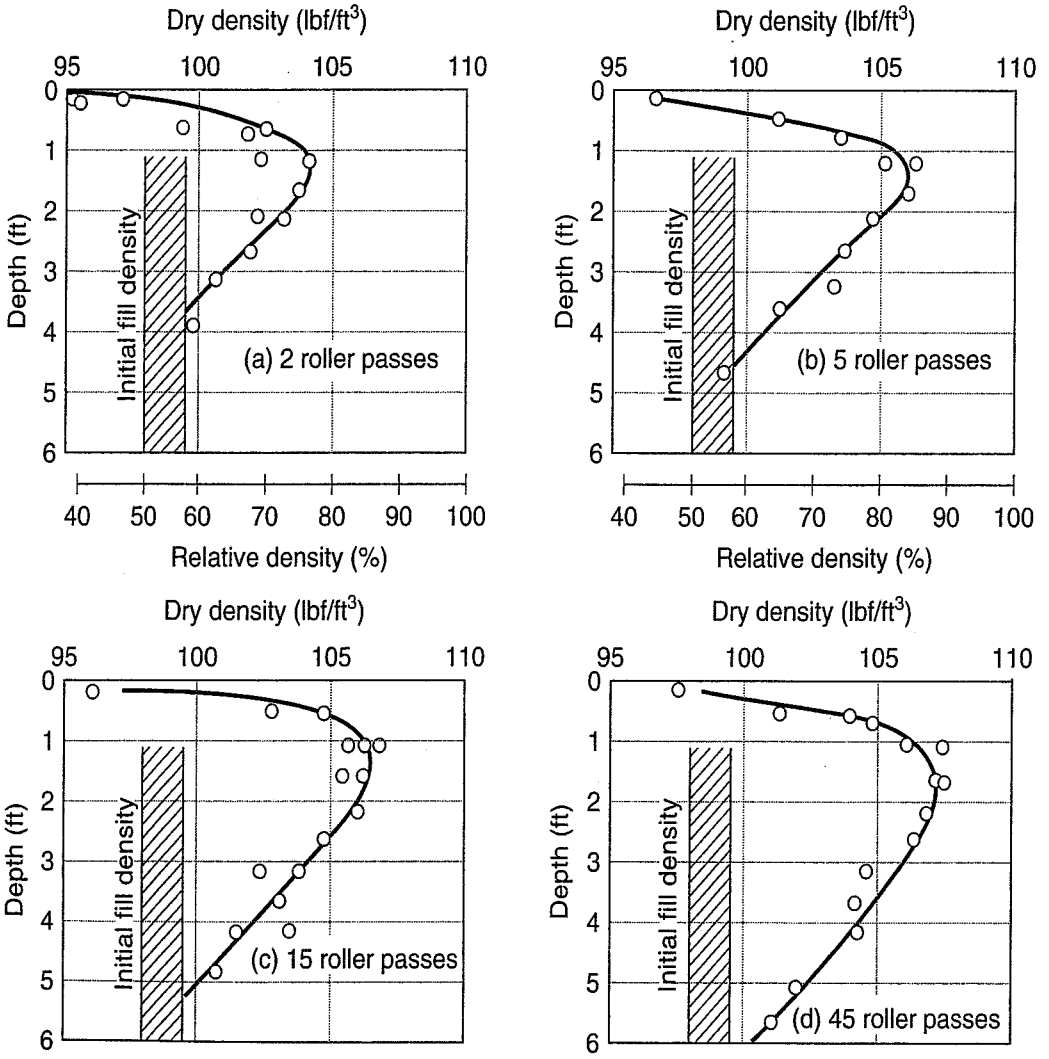

FIGURE 5.18 Density-depth relationship for a 5670 kg (12 500 lb) roller operating at 27.5 Hz for a 240 cm (94.5 in.) lift height.

5.6.3 Compaction Equipment Summary

Figure 5.19 summarizes the applicability of various types of compaction equipment as a function of soil type, expressed as percentages of clay to sand to rock. These "zones" are not absolute, and it is possible for a given piece of equipment to compact satisfactorily outside the given zone.

5.6.4 Compaction of Rockfill

If available, sound, hard, and durable rock is best for rockfills. However, when properly compacted, satisfactory embankments have been constructed of poorer quality rock. Shales and other softer or poorly cemented sedimentary rocks may be susceptible to weathering and degradation in service, even when they appear to be sound at the time of excavation and placement. Such materials need to be identified early on, and avoided if possible.

As discussed in Sec. 5.5.2, the methods for placing and compacting rock fills have evolved considerably in the past 40 years, primarily due to the development of vibratory compactors. This equipment enables engineers to produce more stable embankments by increasing fill strength. Loose lift thicknesses (i.e., after placement and prior to compaction) are typically 0.3 to 0.9 m (1 to 3 ft), but should be thicker than the nominal diameter of the maximum rock size. A rule of thumb is that the maximum rock size should be two-thirds of the loose lift thickness. Vibratory smooth steel drum rollers have been found to be most effective for compacting rock fills, operating at 20 to 25 Hz and at a roller speed of about 3 kph (Breitenbach, 1993). Further, static roller weights of 8000 kg on level ground, and a minimum dynamic force of 80 000 kN, are recommended, with 4 to 6 passes per lift section as the optimum coverage. Equipment recently developed in Europe by LandPac specifically for compaction of rockfill is a towed 12 Mg compactor with a noncylindrical roller. The roller has three lobes, and the shape is reminiscent of a three-leaf clover. Improvement is claimed as deep as 5 m.

For additional information on the treatment of rock fills, see U.S. Dept. of the Interior (1987, 1998), Hilf (1991), Jansen (1988), and U.S. Army Corps of Engineers (1999).

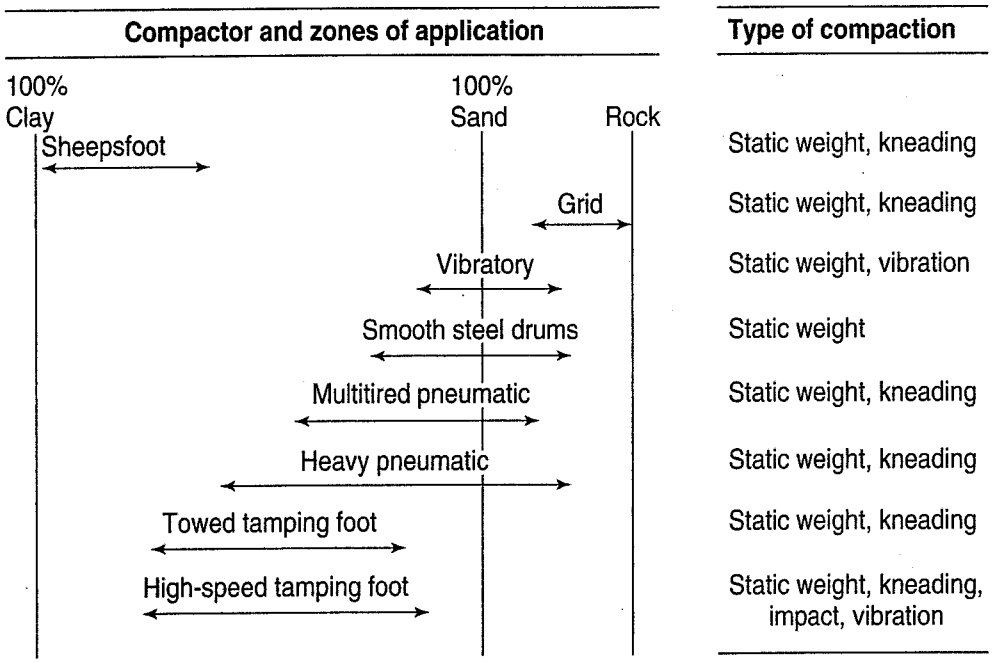

FIGURE 5.19 Applicability of various types of compaction equipment for a given soil type (modified after Caterpillar, Inc., 1977).

5.7 SPECIFICATIONS AND COMPACTION CONTROL

For earthwork and other types of compaction, control of the contractor's compaction process is essential to obtain a satisfactory design and the desired performance of the project. Appropriate control of the compaction process depends on the compaction specifications, and it is the design engineer's responsibility to prepare specifications for the project. The design engineer should also be responsible for the construction, inspection, and quality assurance (QA) of the compaction to ensure that the contractor has in fact satisfactorily performed the compaction work.

Figure 5.20 illustrates the "system" commonly used today for earthwork and other types of compaction projects. Depending on the design problem, certain laboratory tests are conducted on samples of the proposed borrow materials to define the engineering properties required for design of the embankment or other earth structure. After the earth structure is designed, the engineer also prepares earthwork and compaction specifications that control the construction processes and procedures. Good specifications will assure the engineer (and thus the owner) that a satisfactory embankment will be constructed. The specifications also include field *compaction control tests*, and the results of these tests become the standard for controlling the project. Construction control inspectors then conduct these tests to insure that the contractor actually adheres to the compaction specifications. The two-way arrows between some boxes in Fig. 5.20 indicate that these items are interdependent and that two-way communication is essential to have a successful project.

As you may know, there is a difference between quality assurance and quality control (QC). QA is done by the engineer as a representative of the owner to assure that the contractor is doing a good job. If the contractor did their own tests to be sure their compaction procedures were OK, that would be an example of QC. QA only is common for most compaction jobs, but on some large earthwork projects such as levees and earthdams, both are done.

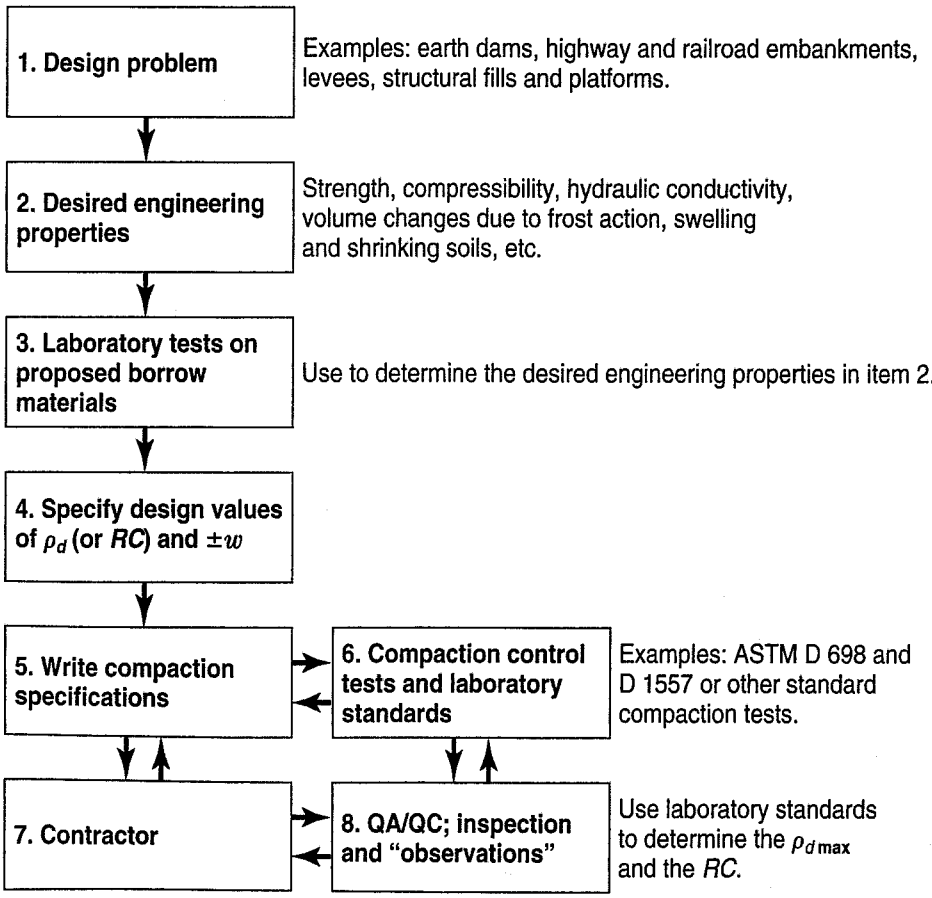

FIGURE 5.20 The compaction "system" in civil engineering practice.

In this section, we discuss the types of compaction specifications and the field tests used to control compaction. Then we give you, if you are a contractor, some suggestions for achieving the most efficient compaction, and we briefly describe the phenomenon of overcompaction and QA/QC for rockfills. Finally we briefly tell you about compaction in trenches.

5.7.1 Specifications

There are basically two types of earthwork specifications: (1) *method* or *procedure* specifications, and (2) *end-product* specifications, sometimes called *performance* specifications. With both types, requirements for site preparation, also known as *clearing and grubbing*, treatment of tree stumps and roots, other organic materials, boulders, etc., are often the same. A maximum allowable size of material to be compacted as well as a maximum thickness of the uncompacted lift may also be specified. Peripheral construction requirements—for example, site drainage and runoff control, hours of work, and other contractual requirements—may also be similar.

Method Specifications—With method specifications, the type and weight of compactor or roller, the number of passes of that roller, as well as the lift thicknesses are specified by the engineer. A maximum allowable size of material may also be specified. With method specifications the responsibility for the quality of the earthwork rests with the owner or owner's engineer. If compaction control tests (discussed in Sec. 5.7.2) performed by the engineer fail to meet a certain standard, then the contractor is paid extra for the additional compaction.

Method specifications require prior knowledge of the borrow materials so as to be able to predict in advance how many passes of, for example, a certain type of roller will produce adequate compaction and fill performance. This means that during design, test fills or test sections must be constructed of the proposed borrow materials using different equipment, compactive efforts, lift thicknesses, etc., in order to determine which equipment and procedures will be the most efficient in producing the desired properties. Because test programs are expensive, method specifications can be justified only for very large compaction projects such as earth and rockfill dams. However, considerable savings in earthwork construction unit costs result, because a major part of the uncertainty associated with compaction will be eliminated for the contractor. The contractor can estimate quite well in advance just how much the construction will cost, and she knows that if extra rolling is required, she will be adequately compensated.

See U.S. Dept. of the Interior (1998) and U.S. Army Corps of Engineers (1999) for a discussion of test fills and sections for designing compaction specifications.

There are two other situations where a method specification is appropriate. One is where a geotechnical engineer has considerable knowledge of the local soils in an area and knows by experience that he will get satisfactory performance after a certain amount and type of compaction. The other situation is for compacting backfills in utility trenches.

End-Product Specifications and Relative Compaction—*End-product* specifications, sometimes called *performance* specifications, are commonly used for highway and building foundation embankments. With this type of specification, the contractor is required to obtain a certain *relative compaction*, or *percent compaction*. Relative compaction, *RC*, is defined as the ratio of the field dry density, $\rho_{d\,\text{field}}$ to the laboratory maximum dry density, $\rho_{d\,\max}$, expressed as a percentage, or

$$\text{relative or percent compaction } (RC) = \frac{\rho_{d\,\text{field}}}{\rho_{d\,\max}} \times 100\,(\%) \tag{5.9}$$

The maximum dry density is determined by a specified laboratory standard compaction test, such as the standard Proctor or the modified Proctor test. Obviously the specified lab test is conducted on the same soil as that to be compacted in the field. Typical values for relative compaction are 90% or 95% of the laboratory maximum; the specific value depends on the nature of the project, location of the fill being compacted, experience, and tradition. As mentioned above, the lift thickness and maximum allowable size of material to be compacted are also included in end-product specifications.

With this type of specification, as long as the contractor is able to obtain the minimum specified relative compaction, it shouldn't matter what equipment or procedures are used. The economics of the project supposedly ensure that the contractor will utilize the most efficient compaction procedures (discussed below).

How the field dry density and relative compaction are obtained in practice is described in Sec. 5.7.2.

Relative Compaction versus Relative Density—What is the difference between relative compaction and relative density? Despite similar names, they are not the same. We defined the relative or index density D_r and density index I_d in Sec. 5.5. You may recall that relative and index density applies only to granular soils. If some fines are present, it is sometimes difficult to decide which type of test—index density or the Proctor—is applicable as a standard test. The ASTM (2010) index density tests, D 4253 and D 4354, are applicable to soils with less than 15% fines (passing the 75 μm or No. 200 sieve); otherwise a Proctor compaction test should be used. In borderline cases, it is a good idea to perform both tests. This will usually indicate which test is most appropriate for your material. For control of the densification of granular fills, the use of the relative density or density index is, of course, very appropriate.

A relationship between relative density and relative compaction is shown in Fig. 5.21. A statistical study of published data on 47 different granular soils indicated that the relative compaction corresponding to zero relative density is about 80%.

5.7.2 Compaction Control Tests

As noted in Fig. 5.20, virtually all compaction projects require some type of quality control testing to be performed to determine whether the fill has been properly compacted. The results of these tests give the field dry density, $\rho_{d\,\text{field}}$. Then the relative compaction of the fill can be determined by Eq. (5.9).

The testing procedure is as follows: A test site is selected that is representative or typical of the compacted lift and borrow material. Typical specifications call for a field test to be conducted every 1000 to 3000 m^3 (1500 to 4000 yd^3) or so, or when the borrow material changes significantly. It is also advisable to perform the test at least one or maybe two compacted lifts below the already compacted ground surface, especially when sheepsfoot rollers are used, or in granular soils. Because the objective of compaction is to stabilize soils and to improve their engineering behavior, it is important to keep in mind the desired engineering properties of the fill, not just its dry density and water content. This point is often lost in earthwork construction control. Major emphasis is usually placed on achieving the specified dry density and relative compaction, and little consideration is given to the desired engineering properties of the compacted fill. Dry density and water content correlate well with the engineering properties, and thus they are convenient construction control parameters.

Compaction control tests can either be *destructive* or *nondestructive*. Destructive tests involve excavation and removal of some of the fill material, whereas nondestructive tests indirectly determine the density and water content of the fill.

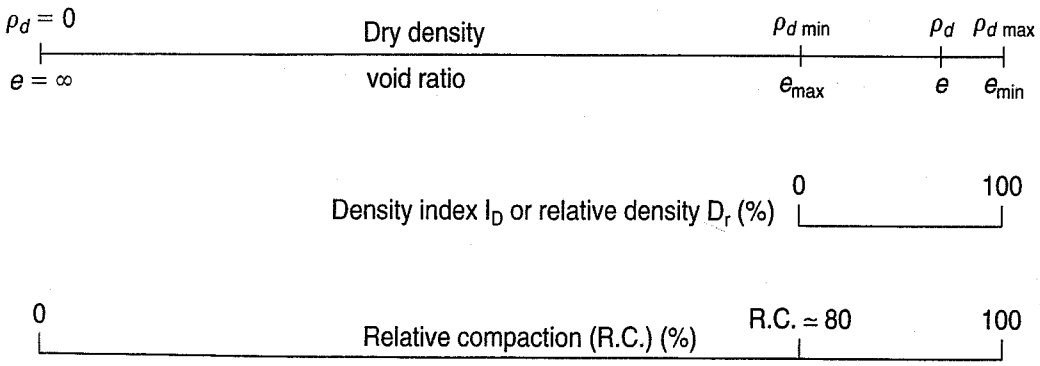

FIGURE 5.21 Relative density and relative compaction concepts (after Lee and Singh, 1971).

Destructive Compaction Control Tests—The steps required for the common destructive tests are:

1. Excavate a hole in the compacted fill at the desired sampling elevation. The size of the hole will depend on the maximum size of material in the fill and the equipment used to measure the volume of the hole. Determine the *mass* M_t of the excavated material.
2. Take a water content sample and determine the water content of the soil in the fill. This value is the *field water content* w_{field}.
3. Measure the *volume* V of the excavated material.
4. Compute the *total density*. Knowing M_t, the total mass of the material excavated from the hole, and the volume V of the hole, we can compute the field total density ρ_{field}. Since we also know the field water content w_{field}, we can obtain the field dry density of the fill $\rho_{d\,\text{field}}$, from Eq. (2.14).
5. Compare $\rho_{d\,\text{field}}$ with $\rho_{d\,\max}$ and calculate the relative compaction using Eq. (5.9).

The required measurements are usually made by a field inspector or materials engineer. On large projects, with fully equipped field laboratories at or near the job site, field personnel perform the excavation and volume measurements on the compacted fill. After placing the excavated material in sealed containers, they return to the lab, weigh the excavated material, and determine its water content. On smaller projects, field inspectors may have a van or other vehicle that serves as a mobile laboratory. In both cases, ordinary laboratory balances or scales are used to determine the mass of the excavated material.

The water content of the excavated soil can be determined by conventional oven drying (ASTM D 2216), as described in Chapter 2. Although this procedure is the standard, it is slow—it often takes 16 to 24 hr to obtain a constant dry weight of specimen. Another disadvantage for mobile laboratories is that laboratory ovens are usually electrical. For these reasons, sometimes rapid water content methods are used in the field (e.g., propane gas heaters; Sec. 5.7.3) instead of oven drying.

Techniques commonly employed to measure the volume of the hole include the sand cone, the balloon method, or pouring water or oil of known density into the hole (Fig. 5.22). In the sand cone method, dry sand of known dry density is allowed to flow through a cone-shaped pouring device into the hole. The volume of the hole can then easily be determined from the weight of sand in the hole and the dry density of the poured sand (requires calibration). In the balloon method, the volume is determined directly by the expansion of a balloon in the hole [Fig. 5.22(b)]. Other methods for determining the volume of the excavated hole are discussed later in this section.

Example 5.4

Given:

A field density test is performed by the balloon method [Fig. 5.22(b)]. The following data are obtained from the test:

Mass of soil removed + pan = 1590 g
Mass of pan = 125 g
Balloon readings:
Final = 1288 cm^3
Initial = 538 cm^3
Water-content information:
Mass of wet soil + pan = 404.9 g
Mass of dry soil + pan = 365.9 g
Mass of pan = 122.0 g

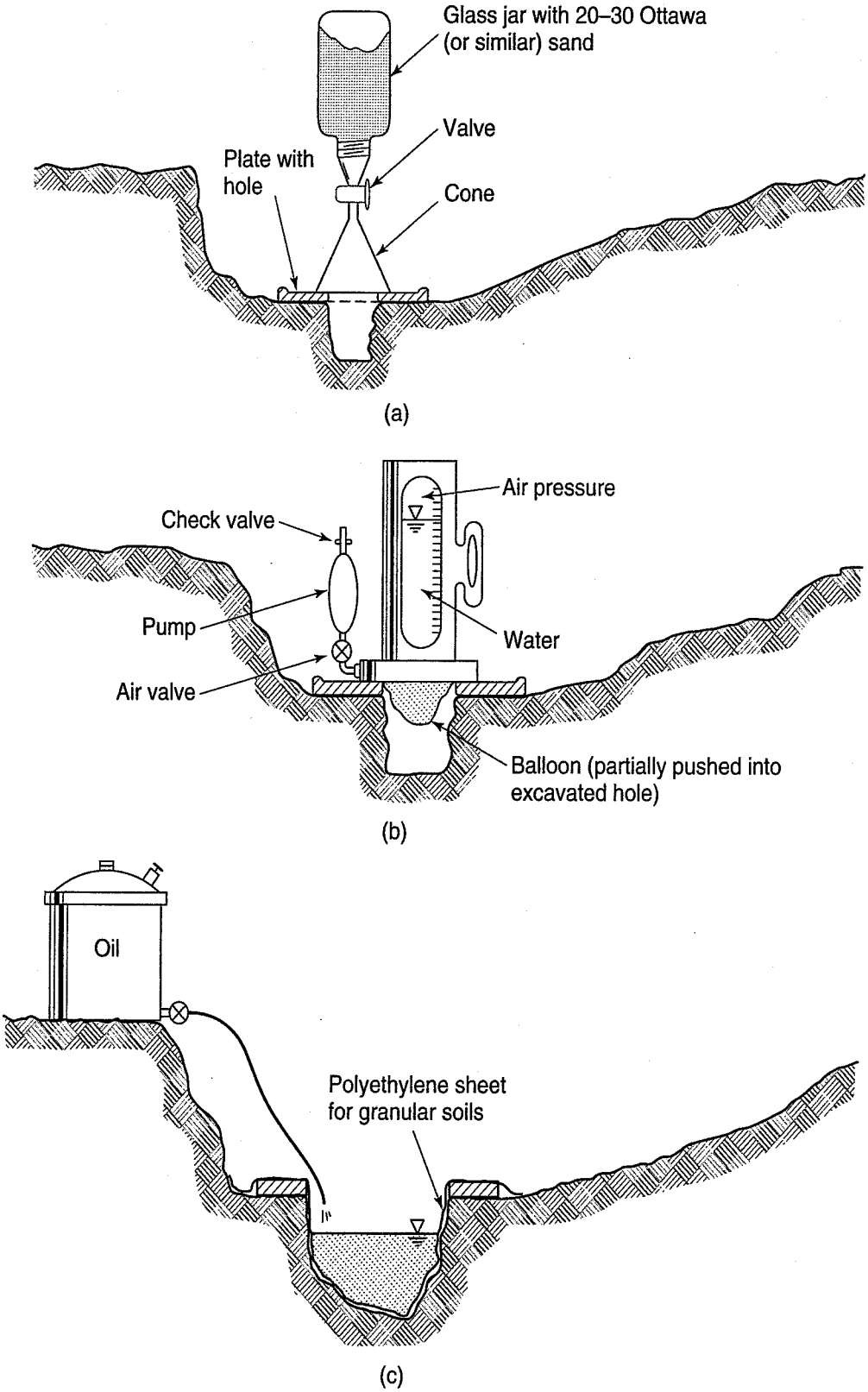

FIGURE 5.22 Some in-place destructive methods for determining density in the field: (a) sand cone; (b) balloon; (c) oil (or water) method.

Required:

a. Compute the dry density and water content of the soil.

b. Using curve B of Fig. 5.1 as the laboratory standard, compute the relative compaction.

Solution:

a. Compute the wet density, $\rho = \dfrac{M_t}{V_t}$

$$\rho = \frac{1590 - 125\text{ g}}{1288 - 538\text{ cm}^3} = \frac{1465\text{ g}}{750\text{ cm}^3} = 1.95\text{ g/cm}^3 = 1.95\text{ Mg/m}^3$$

Water content determination:

1. Mass of wet soil + pan = 404.9 g
2. Mass of dry soil + pan = 365.9 g
3. Mass of water M_w (**1** − **2**) = 39.0 g
4. Mass of pan = 122.0 g
5. Mass of dry soil M_s (**2** − **4**) = 243.9 g
6. Water content $(M_w/M_s) \times 100$ (**3** ÷ **5**) = 16%

For calculation of dry density, use Eq. (2.14):

$$\rho_d = \frac{\rho}{1 + w} = \frac{1.95\text{ Mg/m}^3}{1 + 0.16} = 1.68\text{ Mg/m}^3$$

b. For calculation of relative compaction, use Eq. (5.9):

$$\text{R.C.} = \frac{\rho_{d\,\text{field}}}{\rho_{d\,\max}} = \frac{1.68}{1.86} \times 100 = 90.3\%$$

Nondestructive Methods—Because of some of the problems with destructive field tests, nondestructive density and water-content testing using radioactive isotopes have become quite popular during the past 40 years. Nuclear methods have several advantages over the traditional destructive techniques. Nuclear tests can be conducted rapidly and results obtained within minutes. Erratic results can be easily and quickly double-checked. Therefore the contractor and engineer know the test results quickly, and corrective action can be taken before too much additional fill has been placed. Because nuclear tests can be performed so quickly and easily, more tests can be conducted, and better statistical quality control of the fill is provided. An average value of the density and water content is obtained over a significant volume of fill, and therefore the natural variability of compacted soils can be considered to some degree.

Disadvantages of nuclear methods include the relatively high initial cost of the equipment, regulatory documentation required to own a piece of equipment containing nuclear material, and the potential danger to field personnel of exposure to radioactivity. Strict radiation safety standards must be enforced when nuclear devices are used, and only properly trained and licensed operators are permitted to use nuclear density equipment. On the other hand, in modern nuclear equipment, the radioactive sources are well shielded and protected by very strong cases, so nuclear testing is no more dangerous than any other construction monitoring activity.

Basically, two types of sources or emitters are necessary to determine both the density and the water content. Gamma radiation, as provided by radium or a radioactive isotope of cesium, is scattered by the soil particles; the amount of scatter is proportional to the total density of the material. The spacing

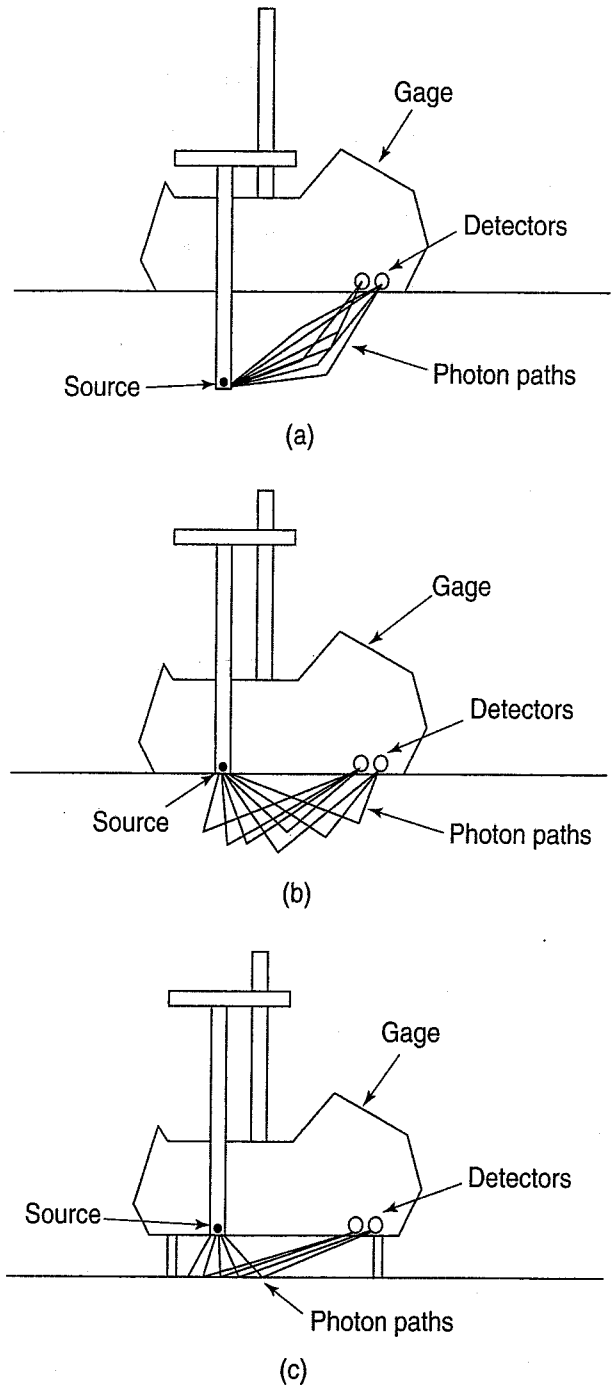

FIGURE 5.23 Nuclear density and water content determination: (a) direct transmission; (b) backscatter; and (c) air gap (after Troxler Electronic Laboratories, Inc., Research Triangle Park, North Carolina).

between the source and pickup, usually a scintillation counter or a Geiger counter, is constant. Hydrogen atoms in the pore water scatter neutrons, providing a means whereby water content can be determined. Typical neutron sources are americium-beryllium isotopes.

Nuclear test instruments must be properly calibrated, both internally (system and factory calibration) and against materials of known density. Materials can be compacted soils or asphalt concrete, or even Portland cement concrete. Three nuclear techniques in common use are shown in Fig. 5.23. The *direct transmission* method is illustrated schematically in Fig. 5.23(a) and the *backscatter* technique in Fig. 5.23(b). The less common *air-gap* method [Fig. 5.23(c)] is sometimes used when the composition of the near-surface materials adversely affects the density measurement. However, the presence of an uncontrolled air gap on the material surface can significantly affect the measurements. Filling the gap with dry sand helps reduce but does not eliminate this effect.

The presence of oversize particles may adversely influence the results, especially if a density test is performed using the backscatter technique directly over a large cobble or boulder. Structures, buried pipes, and cables closer than 3 m from the test point may also give false readings if not correctly adjusted for. Another factor that can adversely influence results is the presence of certain water-bearing minerals such as gypsum and other evaporates in the soil, a rather common occurrence throughout the drier regions of western North America. The measured nuclear water content will be much greater than the oven dry water content, and unless properly calibrated, the gage will give an incorrect reading of relative compaction (R. L. Lytton, personal communication, 2010).

Detailed calibration and test procedures are given in ASTM (2010) D 6938. The corresponding numbers for AASHTO (2010) are Designation T 238 for density and T 239 for water content. The USBR test procedure is 7230.

Because of health and safety concerns associated with nuclear densometers, as well as the administrative overhead required to document their ownership, there has been considerable recent development of new, alternative field compaction control devices. Two primary types of devices have been developed. The first is a soil stiffness measurement device that uses geophysical technology to

determine the modulus of compacted materials. This device had its origins in landmine detection devices used by the military (Sawangsuriya et al., 2003). Stress waves are generated by a device placed on the surface of the compacted material. Soil deflections and other stress wave responses from the soil are used to compute the soil stiffness or modulus. However, dry density of the compacted material can be obtained only when an independent moisture content measurement is also obtained, either by using a nuclear gauge or by taking soil samples (Edil and Sawangsuriya, 2006).

The other type of nondestructive device that has been adapted for field compaction control is based on time domain reflectometry (TDR). This is an electromagnetic technique that measures the soil's apparent dielectric constant, which is a measure of how well the soil can polarize an electric field (Benson and Bosscher, 1999). Much like the nuclear and geophysical methods, TDR involves transmission of a pulse (in this case, an electromagnetic one) and monitoring the velocity with which reflections return to the source of the transmission. For some applications, this can be done using a coaxial cable, so that when the pulse reaches a change in the cable's properties due to bending (for example, if it's being used to detect movement of a rock fault), part of the pulse reflects back to the generator.

To imitate a coaxial cable in compacted soils, a three- or four-spike probe is placed in the soil, as shown in Fig. 5.24. The center spike is the central conductor in the coaxial cable, the soil is the dielectric medium surrounding it, and the two or three outer spikes serve as the shield conductor. Correlation equations have been developed to provide water content and dry density from this measurement. However, there are still limits on the types of soils for which this method yields valid results (Yu and Drnevich, 2004). This method also requires making field measurements of ground temperature and performing laboratory compaction tests to obtain calibration constants needed to analyze TDR data. To use TDR for field compaction control, see ASTM D 6780.

It is worth mentioning that "smart" vibratory compactors have been developed that may eventually replace manual methods of compaction control. These compactors are based on the principles of stress wave mechanics, and they automatically adjust their vibratory characteristics based on soil response and input project specifications. Proponents point to gains in construction productivity, since this optimizes equipment performance and reduces repeated compaction of soil that meets or exceeds project specifications.

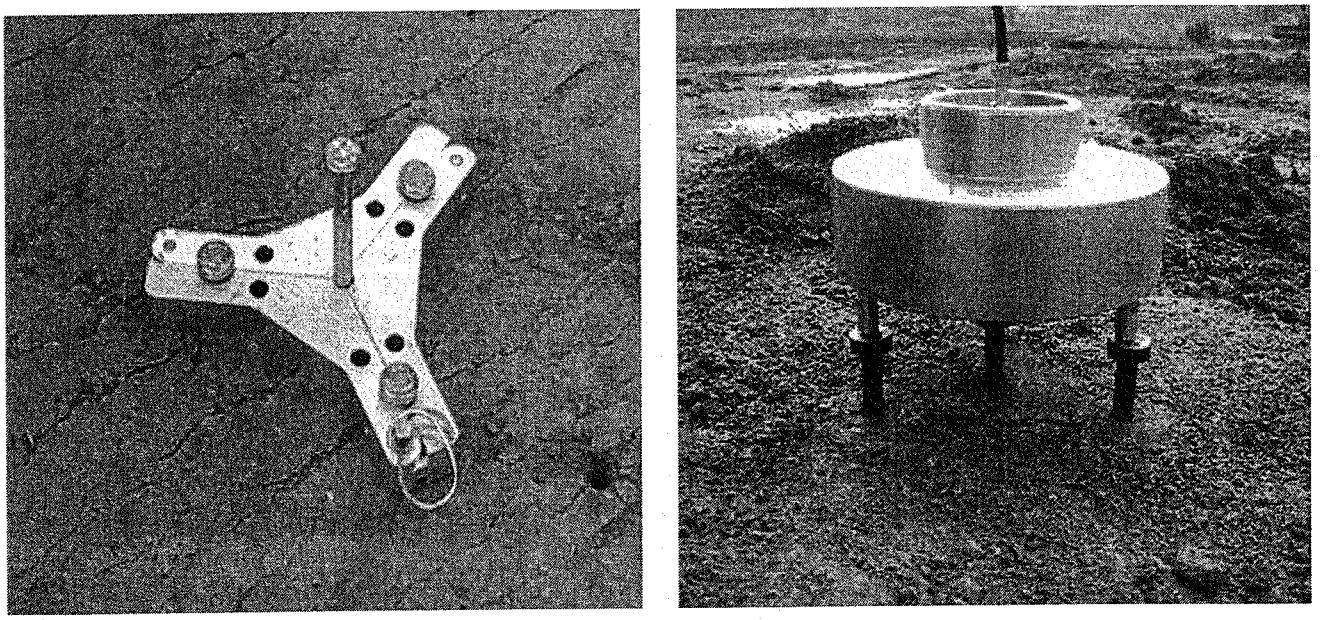

(a) (b)

FIGURE 5.24 Field test procedures using TDR probes: (a) spikes being driven through template into soil surface; (b) multiple rod probe head in contact with spikes for measurement (from Yu and Drnevich, 2004).

5.7.3 Problems with Compaction Control Tests

Problems associated with field density tests include:

- Statistical quality control of compaction
- Presence of oversize particles
- Lack of knowledge of the laboratory standard dry density

These next two problems apply to destructive tests only:

- Time required to obtain the field water content
- Incorrect determination of the volume of the excavated hole

Since the days of R. R. Proctor, geotechnical engineers have developed solutions to these problems, and these are discussed in the following sections.

Statistical Quality Control of Compaction—First, it is difficult and expensive with destructive testing to conduct a sufficient number of tests for a proper statistical analysis of the compaction test results. Second, the volume of material involved in each test is an extremely small percentage of the total volume of fill being controlled (typically one part in 100 000, or even less). One solution to the problem of too few tests is nondestructive testing. With these methods, it is possible to conduct the number of tests necessary for statistical quality control of the compaction. Even though this is possible, it is not commonly done in practice.

Presence of Oversize Particles—You may recall from Sec. 5.3 that the presence of a significant amount of gravel and cobbles in earth fill causes problems with laboratory compaction tests. Consequently, the standard procedures limit the amount of oversize particles permitted (Table 5.1).

Field compaction control tests have similar problems, as mentioned briefly above in the discussion of the nuclear density test. If there is too high a percentage of oversize material, the laboratory density will be less than that obtained in the field. One possibility is to use a test fill to determine field compaction procedures and then use a method specification to control compaction, or to use the procedures suggested for controlling rockfills in Sec. 5.7.6. You can also correct the compaction test results for up to about 50% gravel by using a procedure suggested by the AASHTO (2010) Method T 224.

Another problem with destructive quality control tests in earth fill containing oversize material is the size of the excavated hole and how to determine its volume. One solution is to use test pits between 0.03 and 2.55 m^3 (1 and 90 ft^3) in volume, which are excavated by hand or machine. The volume of the excavated material is determined either by the sand replacement method, ASTM standard D 4914, or the water replacement method, D 5030 (ASTM, 2010). Although these are standard procedures, neither is cheap or simple to perform.

When controlling sandy or fine gravelly fills with less than 5% fines and a maximum particle size of 19 mm, the sleeve method, ASTM D 4564, is applicable. Of course, for quality control of granular fills, the use of the relative density or density index as the compaction standard is appropriate.

Lack of Knowledge of the Laboratory Standard Density—Ideally, it is desirable to have the complete compaction curve for each field test, but this is time consuming and expensive. Consequently, the laboratory maximum density may not be known exactly. It is not uncommon, especially in highway construction, for a series of laboratory compaction tests to be conducted on representative samples of the borrow materials for the highway. Then, when the field compaction control test is conducted, its result is compared with the results of one or more of these project "standard" soils. If the soils at the site are highly variable, this is a poor procedure.

Alternatively, you can use the "family of curves—one-point method" (AASHTO Designation T 272), sometimes called the *field check point* method. This method gives a fairly rapid determination of the maximum density and optimum water content of the soil excavated during the field density test. In this approach, a family of compaction curves is developed for the project by combining a series of Proctor curves for the various soils found in the project borrow areas. An extra amount of soil sufficient to

perform a single laboratory compaction test is removed from the compacted fill during the field density test. Then a one-point Proctor test is conducted on this material, and the results provide the field "check point." The only restrictions necessary to determine the field check point are that:

1. During compaction, the mold must be placed on a smooth solid mass of at least 100 kg, a requirement which may be difficult to achieve in the field. Asphalt pavement or compacted soil should *not* be used. (This is good practice no matter where you do the compaction test.)
2. The soil to be compacted must be dry of optimum (AASHTO recommends about 4% dry) for the compactive effort used, and knowing when the soil is dry of optimum takes some experience.

How the one-point method works is shown in Fig. 5.25. Three compaction curves are shown for soils A, B, and C from a given construction job borrow area. The soil just tested for field density, as identified by the field engineer, does not match any soils for which project compaction curves exist, so a field "check point" compaction test is run. If the soil after excavation is not well dry of optimum, then it will need to be dried, thoroughly remixed, and compacted appropriately. The field "check point" test result is plotted as point X on the graph. By drawing a line parallel to the dry side of optimum of curves A, B, and C and reaching a maximum at the "line of optimums," a reasonable approximation of the maximum dry density may be obtained. If the soil was too wet when compacted, a point such as Y would be obtained. Then it would be difficult to distinguish which laboratory curve the soil belonged to, and an estimate of the maximum dry density would be almost impossible. Some experience is required to develop a "feel" for when the soil is dried out enough for the field check point water content to be less than the OMC.

Another method for quickly and efficiently determining the relative compaction of fine-grained soils is the *rapid method*. Developed in the 1950s by the U.S. Bureau of Reclamation (Hilf, 1961 and 1991), it is now a standard ASTM (2010) test method, D 5080; the corresponding U.S. Dept. of the Interior (1990) number is 7240. The rapid method makes it possible to determine accurately the relative compaction of a fill as well as a very close approximation of the difference between the optimum water content and the fill water content without oven drying. Experience has shown that it is possible to obtain the values required for control of construction in about 1 to 2 h from the time the field density test is first performed.

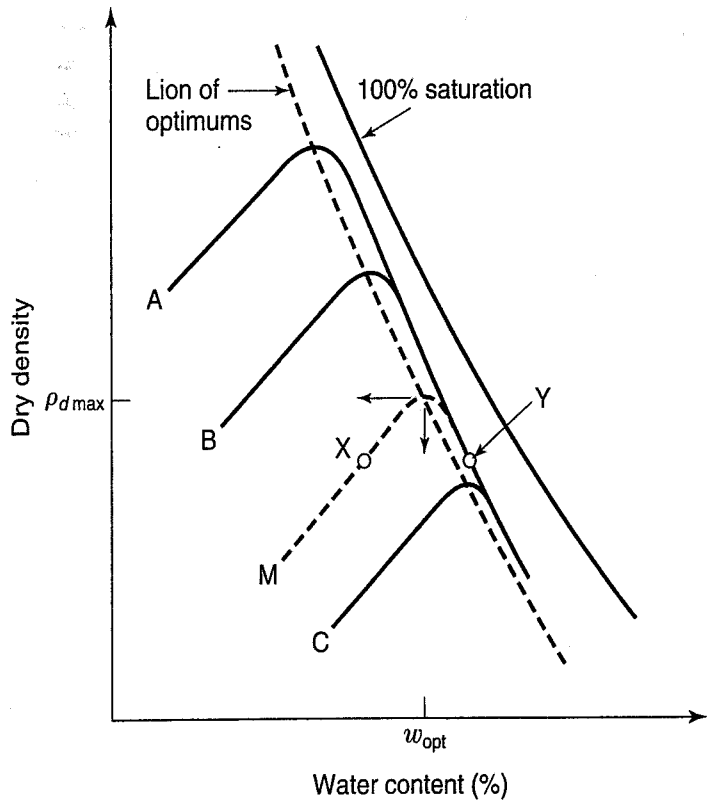

FIGURE 5.25 Principle of the check point test.

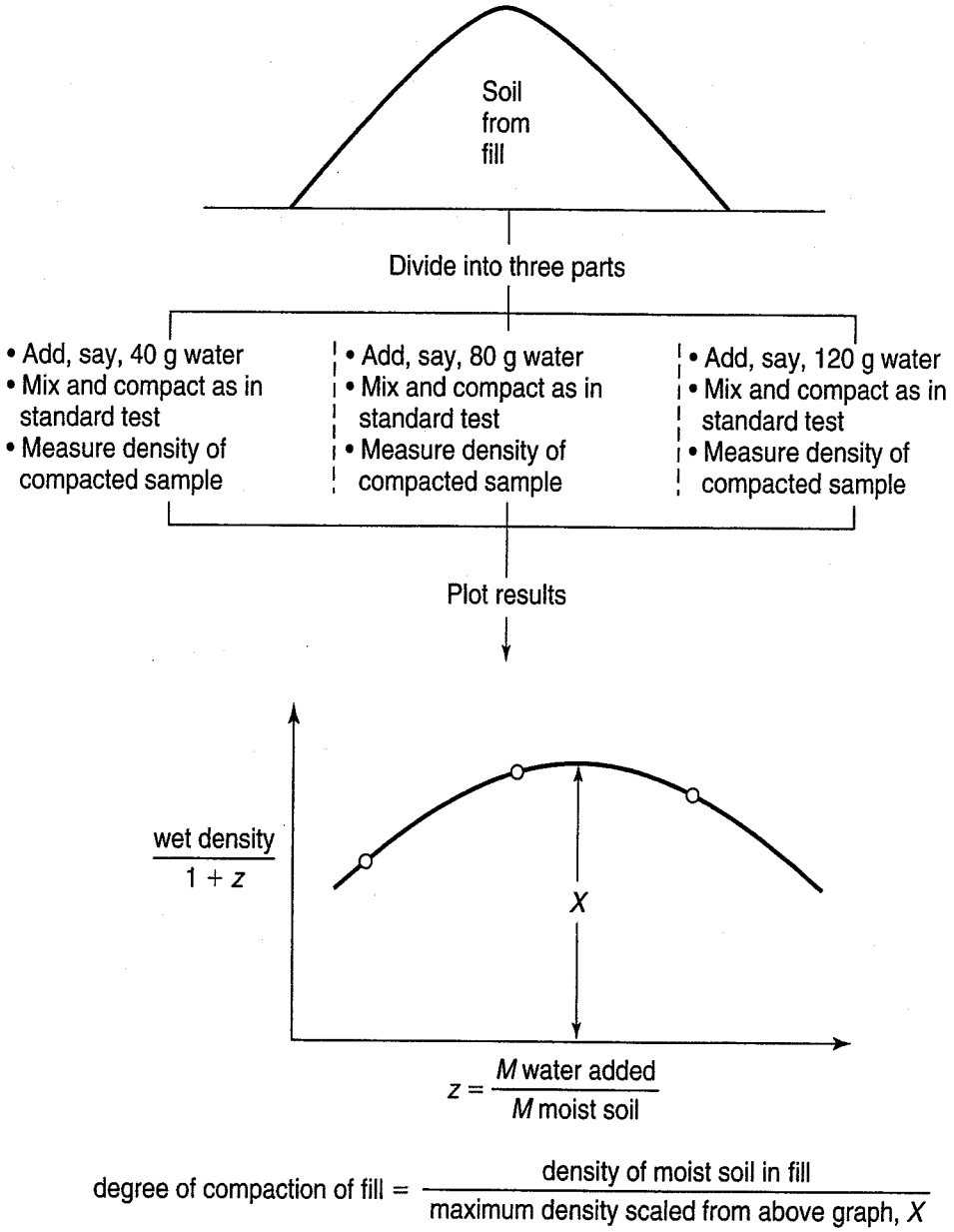

FIGURE 5.26 Procedure for rapid method of determining degree of compaction of fill (after Seed, 1959).

Briefly, the procedure is as follows: Specimens of the fill material are compacted according to the desired laboratory standard at the fill water content and, depending on an estimate of how close the fill soil is to optimum, water is either added or subtracted from the specimen (see Fig. 5.26). With a little experience, it is relatively easy to estimate whether the fill material is about optimum, slightly wet, or slightly dry of optimum. From the wet density curve, the exact percent relative compaction based on dry density may be obtained. Only one water content, the fill water content, need be determined and then only for record purposes. The main advantage of the *rapid method* is that the contractor has the compaction results in a relatively short time.

Time Required to Determine the Water Content—One major problem with the common destructive density test procedures is that determining the field water content takes time (several hours or overnight according to ASTM D 2216). Time is always of the utmost value on a compaction project, and if it takes a day or even several hours before the compaction test results are available, several lifts of fill may have been placed and compacted over the "bad" or "failing" test area. Then the engineer has to require the contractor to tear out a lot of possibly good fill to ensure that the relative compaction of the

TABLE 5.3 Procedures for Determining Water Content of Excavated Material

Test Method	ASTM	AASHTO	USBR	Remarks and Limitations
Oven drying	D 2216	T 265	5300	The standard against which all other methods are judged
Direct heating	D 4959	—	—	Should not be used for soils containing significant amounts of halloysite, montmorillonite, or gypsum; highly organic soils, or marine deposits
Calcium carbide gas-pressure tester	D 4944	T 217	5310	Should not be used for highly plastic clays; organic soils, gypsum
Microwave oven	D 4643	—	5315	Should not be used for soils containing significant amounts of halloysite, montmorillonite, or gypsum; highly organic soils, hydrocarbon-contaminated soils; marine soils

After ASTM, AASHTO, and USBR Standards.

"bad" lift meets contract specifications. Contractors understandably are very hesitant to do this, and yet how many zones of bad compaction should be allowed in an embankment? None, of course!

Because determination of the water content takes the most time, several methods have been proposed to obtain it more rapidly, and these along with the standard oven drying method are listed in Table 5.3. In the direct heating method, the water content specimen is subjected to a source of heat provided by, for example, portable gas stoves, hair driers, blow torches, or heat lamps. Care must be taken to apply the heat uniformly and avoid overheating the specimen. By applying the heat incrementally, carefully stirring the specimen, and repeatedly weighing the specimen until a constant dry mass is obtained, satisfactory results can be obtained. With experience, one could judge when the soil is dry by its color and by weighing it several times to a point when the weight does not vary. Table 5.3 lists some limitations of direct heating.

Alternatively, a calcium carbide gas-pressure meter, the "speedy" moisture meter, can be used. The water in the soil reacts with calcium carbide to produce acetylene gas, and the gas pressure shown on a calibrated gage is proportional to the water content. Burning with methanol and the special alcohol-hydrometer method are also sometimes used. For these two methods, the correlation with standard oven drying is approximate—generally satisfactory for silts and lean clays but poor for organic soils and fat clays.

If electricity is available at the field control laboratory, an ordinary microwave oven can be used to rapidly determine the water content. According to ASTM D 4643, microwave drying is not intended as a replacement for convection oven drying, but it can be used as a supplementary method when rapid results are required. As with direct heating, an incremental approach is taken to avoid overheating the specimen. The method appears to be satisfactory for most soils unless they contain a significant amount of the minerals and substances listed in Table 5.3. Small, porous pebbles in the soil sample may explode when rapidly heated; therefore, soil containers should be covered with heavy paper towels to prevent damage or injuries.

Incorrect Determination of the Volume of the Excavated Hole—The other problems with destructive field tests are often associated with determining the volume of the excavated material. Standard procedures are listed in Table 5.4; three of them are shown schematically in Fig. 5.22. Historically, the sand cone was often taken as the "standard" volumetric procedure, but this test has its limitations and is subject to errors. For example, vibration from nearby working equipment will increase the density of the sand in the hole, which gives a larger hole volume than it should; this results in a lower field density. A higher density will result if the field technician stands too close to the hole and causes soil to squeeze into it during excavation. Any kind of unevenness in the walls of the hole causes a significant error in the balloon method. If the soil is coarse sand or gravel, neither of the liquid methods works well, unless the hole is very large, which means using one of the two test-pit methods with a polyethylene

TABLE 5.4 Procedures for Determining the Volume of the Excavated Hole in Destructive Field Density Tests

Test Method	Designations According to: ASTM	AASHTO	USBR	Limitations
Sand-cone	D 1556	T 191	7205	For fine-grained soils without appreciable coarse gravel
Rubber balloon	D 2167	T 205	7206	For fine-grained soils without sharp angular aggregate
Drive cylinder	D 2937	T 204		For fine-grained soils with gravel
Sleeve	D 4564		7215	For granular materials without fines
Sand replacement in test pit	D 4914		7220	For soils with gravel and cobbles
Water replacement in test pit	D 5030		7221	For soils with gravel and cobbles

sheet to contain the water or oil. All of the common volumetric methods are subject to error if the compacted fill contains gravel and cobbles, although the two test pit procedures are attempts to minimize this effect (see the previous discussion of "oversize particles").

5.7.4 Most Efficient Compaction

The most efficient and therefore the most economical compaction conditions are illustrated in Fig. 5.27. Three hypothetical field compaction curves of the same soil but at different compactive efforts are shown. Assume that curve ① represents a compactive effort that can easily be obtained by existing compaction equipment. Then to achieve, say, 90% relative compaction, the placement water content of the compacted fill must be greater than water content **a** but less than water content **c**. These points are found where the 90% R.C. line intersects compaction curve ①. If the placement water content is outside the range **a** to **c**, then it will be very difficult, if not impossible, to achieve the required percentage relative compaction specified, no matter how much the contractor compacts that lift. This is why it may be necessary to wet or dry (rework) the soil prior to rolling in the field.

Now that we have established the range of placement water contents, the contractor might ask: "What is the best placement water content to use?" From a purely economical viewpoint, the most efficient water content would be at **b**, where the contractor provides the *minimum* compactive effort to attain the required 90% relative compaction. To consistently achieve the minimum relative compaction for the project, the contractor will usually use a slightly higher compactive effort, for example as shown by curve ② of Fig. 5.27. Thus, the most efficient placement water contents exist between the optimum water content and **b**.

However, what may be best from the contractor's viewpoint may not result in a fill with the desired engineering properties. Compacting a soil on the wet side generally results in a lower strength and a higher compressibility, for example, than compacting the soil on the dry side of the optimum water content. Other characteristics such as permeability and shrink-swell potential will also be different. Thus, a *range of placement water contents* should also be specified by the designer, in addition to the percent relative compaction. This point illustrates why the desired engineering performance of the fill rather than just the percentage of compaction must be kept in mind when writing compaction specifications and designing field control procedures (see Fig. 5.19).

5.7.5 Overcompaction

Figures 5.27 and 5.1 illustrate that specified densities can be achieved at higher water contents if more compactive effort is applied, by using either heavier rollers or more passes of the same roller. But, as mentioned above, at higher water contents, e.g., wet of optimum, a lower strength will be obtained with

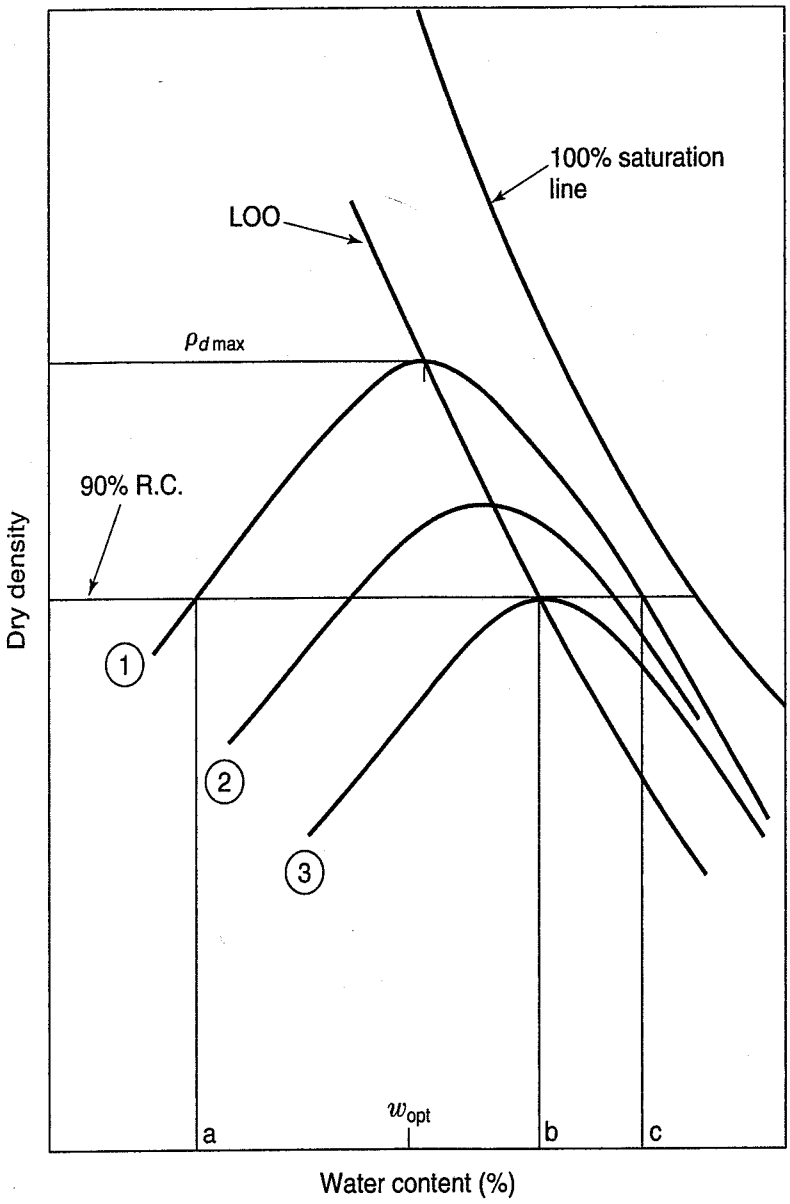

FIGURE 5.27 Dry density versus water content, illustrating the most efficient conditions for field compaction (after Seed, 1964).

higher compaction energies. This effect is known as *overcompaction*. Overcompaction can occur in the field when wet of optimum soils are *proofrolled* with a very heavy, smooth-wheeled roller [Fig. 5.10(a)], or an excessive number of passes are applied to the lift (Mills and DeSalvo, 1978). Thus, even good material can become weaker. You can also detect overcompaction in the field by careful observation of the soil immediately under the compactor or the wheels of a heavily loaded scraper. If the soil is too wet and the energy applied is too great, "*pumping*" or *weaving* of the fill will result as the compactor or wheels shove the wet weaker fill ahead of itself. Also, sheepsfoot rollers won't be able to "walk out" of wet or overcompacted soil. This is another reason that observation of the compaction process should be done by competent and experienced field inspectors.

5.7.6 Rock Fill QA/QC

Quality control of compacted rock fills can be accomplished using a field bulk density test, which is simply a large-scale version of the volume replacement tests used in compacted soil fills (Fig. 5.22 and Table 5.4). As shown in Fig. 5.28(a), a plywood ring is placed on the compacted rock fill surface with a typical opening diameter of 3 ft (0.9 m). Prior to any excavation of the compacted fill, the volume of

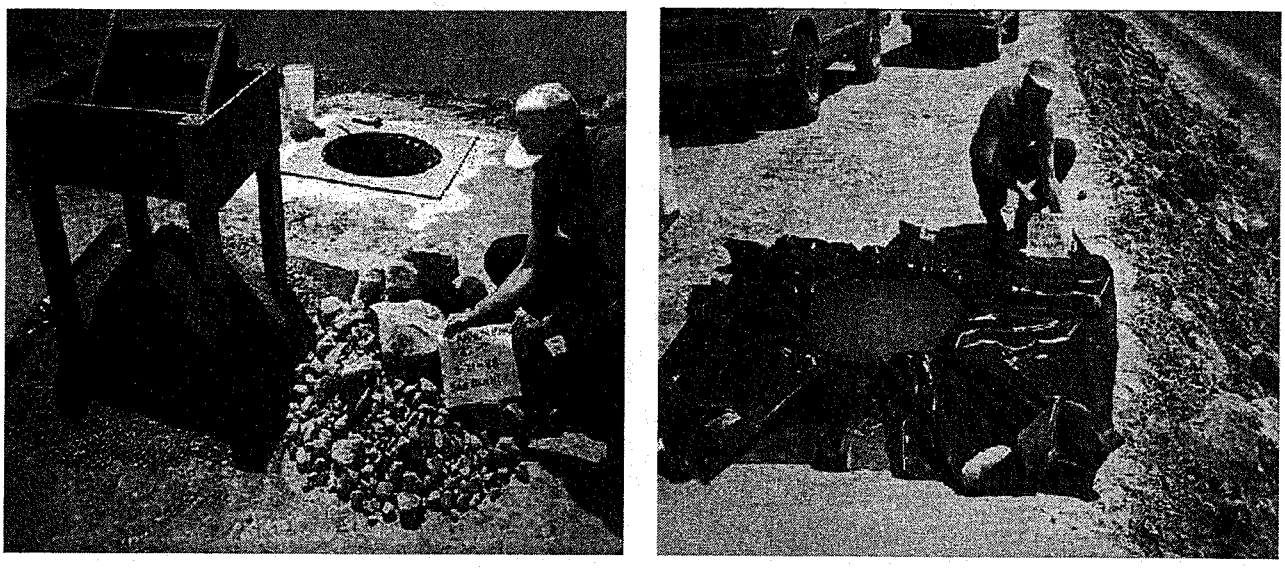

(a) (b)

FIGURE 5.28 Water replacement test to determine the in-place density of rock fill: (a) plywood ring for use as hole template; (b) plastic-lined hole filled with water for volume determination (photographs by A. Breitenbach from www.geoengineer.org/rockfill.htm).

the ring above the compacted rock fill is determined, to be subtracted later from the total volume of the ring and excavated hole (this can sometimes be significant due to the irregularity of the rock fill surface). This is done by anchoring a plastic liner in the ring and measuring the water volume needed to fill it. Material is then hand excavated within the ring diameter down to a depth of about 0.8 to 1 m (2.5 to 3 ft), so that about 500 to 700 kg (1000 to 1500 lb) of material is obtained. The plastic liner is placed in the excavated hole and anchored at the ring, and the lined excavation is filled with a measured volume of water [Fig. 5.28(b)]. Once the in-place total density is determined, the in-place dry density can be computed. For most rock fills, the moisture content of the plus 19 mm (+¾-in.) rock is insignificant, so that the moisture content can be computed based on the minus 19 mm portion of the rock fill [Fig. 5.28(a) shows the field sieve used to separate the fractions]. The resulting expression is

$$\begin{aligned}\rho_d &= \text{total moist mass of rock fill material} \\ &= 1 + (w_{-3/4}/100) \times (\%\ \text{passing}\ 3/4\ \text{in.}/100)\end{aligned} \tag{5.10}$$

where $w_{-3/4}$ = water content of the minus 19 mm material. Breitenbach (1993) discusses dry density calculations for rock fills in which the plus 19 mm materials have some appreciable moisture content, such as weathered rock, shales, claystones, or other absorptive rock types.

5.7.7 Compaction in Trenches

Besides compacting for fills and for preparing the ground to support foundations, it is equally important to compact backfills used in utility trenches. These backfills cover pipes, cables, or other utilities and provide protection from surface loadings and erosion. In addition, the backfill usually serves as a road subbase if it is paved over. Unfortunately, backfilling often is done quickly after utility installation or repair to minimize traffic impacts, and may be done by the contractor without inspection. This can lead to pavement irregularities and other problems with trench backfills.

What exactly is a *trench?* OSHA (Occupational Safety and Health Administration) defines a trench as a narrow underground excavation that is *deeper than it is wide*, and no wider than 4.5 m. The width of a trench is governed by the width of what is placed at the bottom and to some extent by the width of the excavation equipment. In addition to stability and settlement after backfilling, the main geotechnical concern is the stability of an open excavation. If you do a web search on 29 CFR 1926.652, it will bring you to the U.S. Federal regulations regarding excavations that apply to depths greater than 4 ft or 1.2 m. The 1.2 m figure is a reasonable depth not to be exceeded when workers are installing utilities in a trench at least 2 ft or 0.6 m wide. The regulations impose restrictions for deeper trenches and are important from a safety and legal point of view. If you are involved with a trench excavation, you need to be aware of these safety considerations and strictly follow the law.

For a trench less than about a metre wide, it is recommend that it be filled with material that will "flow" as opposed to chunky clayey clumps. Gravels and sands are the best backfill materials and should be compacted in lifts no more than about 15 to 30 cm. It is helpful, too, if the water content is a few percent above optimum. There should be at least 85% relative compaction based on the modified method (ASTM D 1557), 60 cm below the final ground surface, and at least 90% relative compaction in the upper 60 cm of the trench. Flooding of the backfill material is *not* recommended as a way to "compact" the soil. You will end up with a saturated, compressible layer at about 85% relative compaction, which corresponds to a very low relative density and is not adequate (see Fig. 5.21).

For trenches wider than about 1 m, the minimum compaction should be at least 90% relative compaction for all depths, exclusive of the top 15 cm (6 in.) below the pavement and the base course of a pavement, if the trench surface will be paved over. Therefore, the top 15 cm should be recompacted to at least 95% relative compaction based on the modified method. If these recommendations are followed, there should be little if any movement of the former trench area. The layers in the trench may be compacted with vibrating plate compactors, pneumatic compactors, and the like. Compaction recommendations for trenches when the depth/width ratio is ≥2 are shown in Fig. 5.29.

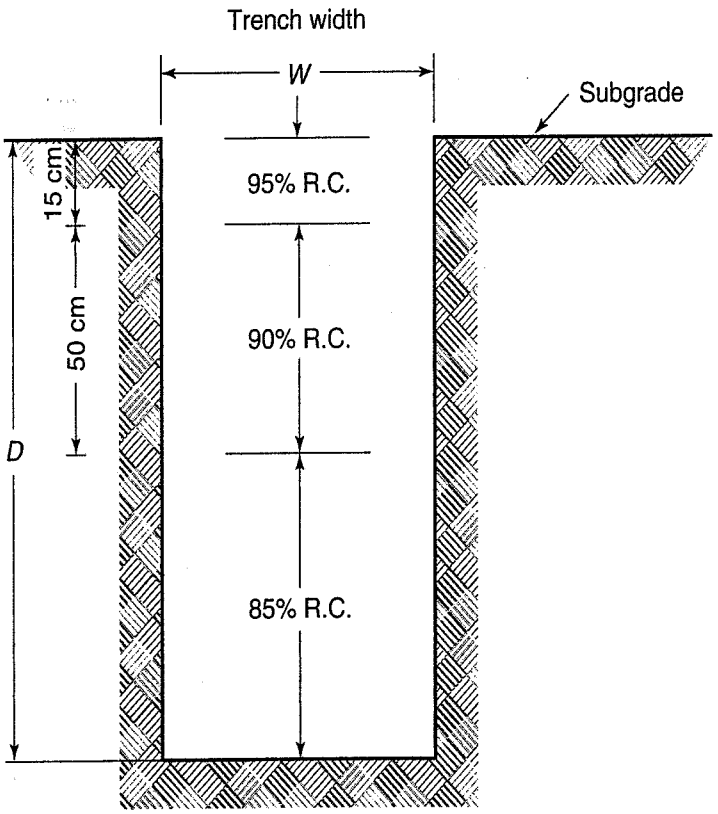

FIGURE 5.29 Minimum compaction requirements for utility trenches for $D/W > 2$.

Because of quality control and concerns about pavement settlements, many municipalities now require contractors to use "flowable fill," a very low strength concrete, to backfill utility trenches. These materials have sufficient compressive strength (about 1–1.5 MPa) to withstand traffic loads, but are weak enough to be excavated in the future if the utility line needs to be exposed for other repairs.

5.8 ESTIMATING PERFORMANCE OF COMPACTED SOILS

How will a given soil behave in a fill, supporting a foundation, holding back water, or under a pavement? Will frost action be a critical factor? For future reference, we present the experience of the U.S. Army Corps of Engineers on compaction characteristics applicable to roads and airfields (Table 5.5) and the experience of the U.S. Department of the Interior, Bureau of Reclamation, for several types of earth structures.

In Table 5.5, the terms *base*, *subbase*, and *subgrade* [Columns (7), (8), and (9)] refer to components of a pavement system, and they are defined in Fig. 5.30. In Column (16), the term CBR represents the California bearing ratio. The CBR is used by the Corps of Engineers for the design of *flexible* pavements. They use the modulus of subgrade reaction [Column (17)] for *rigid* pavement design. The

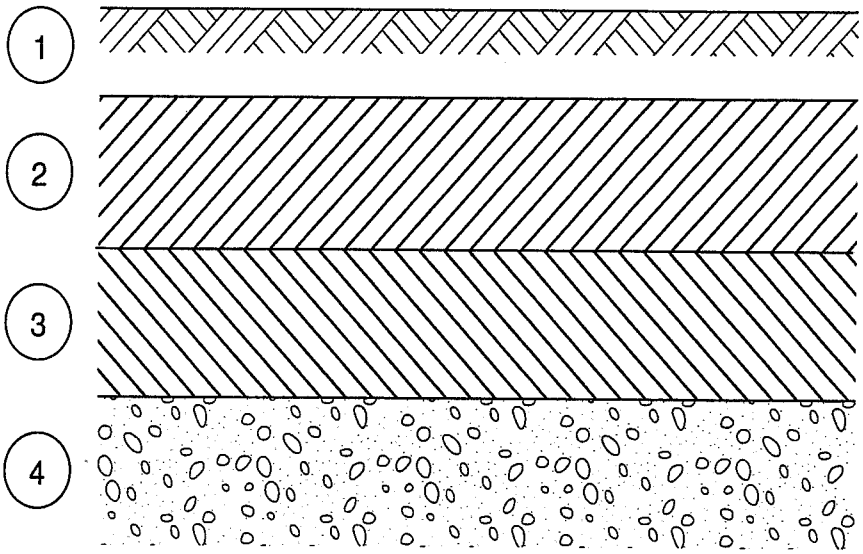

(1) Wearing surface: 20–25 cm Portland cement or 2–8 cm asphaltic concrete.

(2) Base: 5–10 cm asphaltic concrete, 15–30 cm sand-gravel base, 20–30 cm soil-cement, or 15–20 cm asphalt stabilized sand.

(3) Subbase material (this layer may be omitted): 15–30 cm sand-gravel.

(4) Subgrade: The natural soil at the site. The top 0.15–0.5 m is usually compacted prior to the placement of the other layers of the pavement.

FIGURE 5.30 Definitions of terms common to pavement systems, with typical dimensions and materials for each component.

upper layers of flexible pavements usually are constructed of asphaltic concrete, whereas rigid pavements are made of Portland cement concrete. A good reference for the design of pavements is the book by Papagiannakis and Masad (2008).

The use of these tables in engineering practice is best shown by an example. They are very helpful for preliminary design purposes, for choosing the most suitable compaction equipment, and for rapid checking of field and laboratory test results.

Example 5.5

Given:

A soil, classified as a CL according to the USCS, is proposed for a compacted fill.

Required:

Consider the soil to be used as:

a. Subgrade
b. Earth dam
c. Foundation support for a structure

Use Table 5.5 and comment on:

1. The overall suitability of the soil
2. Potential problems of frost
3. Significant engineering properties
4. Appropriate compaction equipment to use

Solution:

	a. Subgrade	**b.** Earth Dam	**c.** Structural Foundation
1. Suitability	Poor to fair	Useful as central core	Acceptable if compacted dry of optimum and if not saturated during service life
2. Frost potential	Medium to high	Low if covered by non-frost-heaving soil of sufficient depth	Medium to high if not controlled by temperature and water availability
3. Engineering properties	Medium compressibility fair strength CBR $\leq$ 15	Low permeability, compact for low permeability and high strength but also for flexibility	Potential for poor strength and therefore poor performance
4. Appropriate compaction equipment	Sheepsfoot and/or rubber-tired roller	Sheepsfoot and/or rubber-tired roller	Sheepsfoot and/or rubber-tired roller

Note: After you have finished this book and a course in foundation engineering, you can readily expand the information in this table.

TABLE 5.5 Characteristics Pertinent to Roads and Airfields

Major Divisions (1)	(2)	Symbol Letter (3)	Hatching (4)	Color (5)	Name (6)	Value as Subgrade When not Subject to Frost Action (7)	Value as Subbase When not Subject to Frost Action (8)	Value as Base When not Subject to Frost Action (9)
COARSE-GRAINED SOILS	GRAVEL AND GRAVELLY SOILS	GW		Red	Well-graded gravels or gravel-sand mixtures, little or no fines	Excellent	Excellent	Good
		GP			Poorly graded gravels or gravel-sand mixtures, little or no fines	Good to excellent	Good	Fair to good
		GM d		Yellow	Silty gravels, gravel-sand-silt mixtures	Good to excellent	Good	Fair to good
		GM u				Good	Fair	Poor to not suitable
		GC			Clayey gravels, gravel-sand-clay mixtures	Good	Fair	Poor to not suitable
	SAND AND SANDY SOILS	SW		Red	Well-graded sands or gravelly sands, little or no fines	Good	Fair to good	Poor
		SP			Poorly graded sands or gravelly sands, little or no fines	Fair to good	Fair	Poor to not suitable
		SM d		Yellow	Silty sands, sand-silt mixtures	Fair to good	Fair to good	Poor
		SM u				Fair	Poor to fair	Not suitable
		SC			Clayey sands, sand-clay mixtures	Poor to fair	Poor	Not suitable
FINE-GRAINED SOILS	SILTS AND CLAYS LL IS LESS THAN 50	ML		Green	Inorganic silts and very fine sands, rock flour, silty or clayey fine sands or clayey silts with slight plasticity	Poor to fair	Not suitable	Not suitable
		CL			Inorganic clays of low to medium plasticity, gravelly clays, sandy clays, silty clays, lean clays	Poor to fair	Not suitable	Not suitable
		OL			Organic silts and organic silt-clays of low plasticity	Poor	Not suitable	Not suitable
	SILTS AND CLAYS LL IS GREATER THAN 50	MH		Blue	Inorganic silts, micaceoas or diatomaceous fine sandy or silty soils, clastic silts	Poor	Not suitable	Not suitable
		CH			Inorganic clays of high plasticity, fat clays	Poor to fair	Not suitable	Not suitable
		OH			Organic clays of medium to high plasticity, organic silts	Poor to very poor	Not suitable	Not suitable
HIGHLY ORGANIC SOILS		Pt		Orange	Peat and other highly organic soils	Not suitable	Not suitable	Not suitable

After U.S. Army Waterways Experiment Station (1960).

Notes:

1. In Column (3), division of GM and SM groups into subdivisions of d and u are for roads and airfields only. Subdivision is on basis of Atterberg limits; suffix d (e.g., GMd) will be used when the liquid limit is 25 or less and the plasticity index is 5 or less; the suffix u will be used otherwise.
2. In Column (13), the equipment listed will usually produce the required densities with a reasonable number of passes when moisture conditions and thickness of lift are properly controlled. In some instances, several types of equipment are listed, because variable soil characteristics within a given soil group may require different equipment. In some instances, a combination of two types may be necessary.
   a. *Processed base materials and other angular materials.* Steel-wheeled and rubber-tired rollers are recommended for hard, angular materials with limited fines or screenings. Rubber-tired equipment is recommended for softer materials subject to degradation.
   b. *Finishing.* Rubber-tired equipment is recommended for rolling during final shaping operations for most soils and processed materials.

Potential Frost Action (10)	Compressibility and Expansion (11)	Drainage Characteristics (12)	Compaction Equipmen (13)	Unit Dry Densities		Typical Design Values	
				lbf/ft^3 (14)	Mg/m^3 (15)	CBR (16)	Subgrade Modulus k (1bf/in.^{3}) (17)
None to very slight	Almost none	Excellent	Crawler-type tractor, rubber-tired roller, steel-wheeled roller	125–140	2.00–2.24	40–80	300–500
None to very slight	Almost none	Excellent	Crawler-type tractor, rubber-tired roller, steel-wheeled roller	110–140	1.76–2.24	30–60	300–500
Slight to medium	Very slight	Fair to poor	Rubber-tired roller, sheepsfoot roller; close control of moisture	125–145	2.00–2.32	40–60	300–500
Slight to medium	Slight	Poor to practically impervious	Rubber-tired roller, sheepsfoot roller	115–135	1.84–2.16	20–30	200–500
Slight to medium	Slight	Poor to practically impervious	Rubber-tired roller, sheepsfoot roller	130–145	2.08–2.32	20–40	200–500
None to very slight	Almost none	Excellent	Crawler-type tractor, rubber-tired roller	110–130	1.76–2.08	20–40	200–400
None to very slight	Almost none	Excellent	Crawler-type tractor, rubber-tired roller	105–135	1.68–2.16	10–40	150–400
Slight to high	Very slight	Fair to poor	Rubber-tired roller, sheepsfoot roller; close control of moisture	120–135	1.92–2.16	15–40	150–400
Slight to high	Slight to medium	Poor to practically impervious	Rubber-tired roller, sheepsfoot roller	100–130	1.60–2.08	10–20	100–300
Slight to high	Slight to medium	Poor to practically impervious	Rubber-tired roller, sheepsfoot roller	100–135	1.60–2.16	5–20	100–300
Medium to very high	Slight to medium	Fair to poor	Rubber-tired roller, sheepsfoot roller; close control of moisture	90–130	1.44–2.08	15 or less	100–200
Medium to high	Medium	Practically impervious	Rubber-tired roller, sheepsfoot roller	90–130	1.44–2.08	15 or less	50–150
Medium to high	Medium to high	Poor	Rubber-tired roller, sheepsfoot roller	90–105	1.44–1.68	5 or less	50–100
Medium to very high	High	Fair to poor	Sheepsfoot roller, rubber-tired roller	80–105	1.28–1.68	10 or less	50–100
Medium	High	Practically impervious	Sheepsfoot roller, rubber-tired roller	90–115	1.44–1.84	15 or less	50–150
Medium	High	Practically impervious	Sheepsfoot roller, rubber-tired roller	80–110	1.28–1.76	5 or less	25–100
Slight	Very high	Fair to poor	Compaction not practical				

c. *Equipment size.* The following sizes of equipment are necessary to assure the high densities required for airfield construction:

Crawler-type tractor—total weight in excess of 30 000 lb (14 000 kg).

Rubber-tired equipment—wheel load in excess of 15 000 lb (7000 kg); wheel loads as high as 40 000 lb (18 000 kg) may be necessary to obtain the required densities for some materials (based on contact pressure of approximately 65 to 150 psi or 450 kPa to 1000 kPa).

Sheepsfoot roller—unit pressure (on 6 to 12 in.^{2} or 40 to 80 cm^2 foot) to be in excess of 250 psi (1750 kPa); unit pressures as high as 650 psi (4500 kPa) may be necessary to obtain the required densities for some materials. The area of the feet should be at least 5% of the total peripheral area of the drum, using the diameter measured to the faces of the feet.

3. In Columns (14) and (15), densities are for compacted soil at optimum water content for modified AASHTO compaction effort.
4. In Column (16), the maximum value that can be used in design of airfields is, in some cases, limited by gradation and plasticity requirements.

PROBLEMS

5.1 For the data in Fig. 5.1:

(a) Estimate the maximum dry density and optimum water content for both the standard curve and the modified Proctor curve.

(b) What is the placement water content range for 90% relative compaction for the modified Proctor curve and 95% relative compaction for the standard Proctor curve?

(c) For both curves, estimate the maximum placement water content for the minimum compactive effort to achieve the percent relative compaction in part (b).

5.2 The natural water content of a borrow material is known to be 8%. Assuming 5500 g of *wet* soil is used for laboratory compaction test points, compute how much water is to be added to other 5500 g samples to bring their water contents up to 11%, 15%, 18%, 22%, and 26%.

5.3 For the soil shown in Fig. 5.1, a field density test provided the following information:

Water content = 13%

Wet density = 1.84 Mg/m^3 (115 lbf/ft^3)

Compute the percent relative compaction based on the modified Proctor and the standard Proctor curves.

5.4 For the data given below (ρ_s = 2.68 Mg/m^3):

(a) Plot the compaction curves.

(b) Establish the maximum dry density and optimum water content for each test.

(c) Compute the degree of saturation at the optimum point for data in Column A.

(d) Plot the 100% saturation (zero air voids) curve. Also plot the 70%, 80%, and 90% saturation curves. Plot the line of optimums.

A (modified)		B (standard)		C (low energy)	
ρ_d (Mg/m^3)	w (%)	ρ_d (Mg/m^3)	w (%)	ρ_d (Mg/m^3)	w (%)
1.873	9.3	1.691	9.3	1.627	10.9
1.910	12.8	1.715	11.8	1.639	12.3
1.803	15.5	1.755	14.3	1.740	16.3
1.699	18.7	1.747	17.6	1.707	20.1
1.641	21.1	1.685	20.8	1.647	22.4
		1.619	23.0		

5.5 The following moisture-density data are results from laboratory compaction tests on a given soil using the same compactive effort:

Water Content (%)	Dry Unit Weight (lb/ft^3)
8	111
11	113
14	115
17	114
20	109

Note: G_s = 2.70.

(a) On a suitable graph or using a spreadsheet, plot the curve of dry unit weight versus water content and indicate the maximum dry unit weight and the optimum water content.

(b) What range of water contents would be acceptable if the specifications call for 98% relative compaction and water content should be dry of optimum? Show how you calculated the relative compaction and show on the plot the range of water contents.

(c) What is the maximum saturation level achieved during compaction tests that were performed?

5.6 A Proctor test was performed on a soil which has a specific gravity of solids of 2.71. For the water content and total unit weight (γ_t) data below:

(a) Plot the moisture-dry density curve.

(b) Find the maximum dry density and optimum moisture content.

(c) Determine the moisture range permitted if a contractor must achieve 90% relative compaction.

(d) What volume of water, in ft^3, must be added to obtain 1 yd^3 of soil at the maximum dry density if the soil is originally at 10% water content?

Water Content (%)	Wet Density (pcf)
10	98
13	106
16	119
18	125
20	129
22	128
25	123

5.7 Two choices for borrow soil are available:

Borrow A		Borrow B
115 pcf	Density in place	120 pcf
?	Density in transport	95
0.92	Void ratio in transport	?
25%	Water content in place	20%
\$0.20/yd^3	Cost to excavate	\$0.10/yd^3
\$0.30/yd^3	Cost to haul	\$0.40/yd^3
2.7	G_s	2.7
112 pcf	Maximum Proctor dry density	110

Note: "In place" indicates when the soil was in its original, natural location.

It will be necessary to fill a 200 000 yd^3 depression, and the fill material must be compacted to 95% of the standard Proctor (maximum) density. A final 10% moisture content is desired in either case. (a) What is the minimum volume of borrow from each site needed to fill the depression? (b) What is minimum quantity (volume) of material from each site to haul? (c) What soil would be cheaper to use?

5.8 Refer to the following data: γ_d in borrow pit, 87.0 pcf; W in borrow pit, 13.0%; G_s, 2.70; Modified Proctor w_{opt}, 14.0%; Modified Proctor $\gamma_{d_{max}}$, 116.0 pcf. Assume that 50 000 yd^3 of the soil from the borrow pit is to be delivered to an embankment at a construction site. By the time it reaches the site, the water content is 9%. It will be compacted to a minimum of 90% of modified Proctor maximum dry density. Determine the total volume of water (in ft^3) that must be added to the soil to increase the moisture content to the optimum level.

5.9 The values of e_{min} and e_{max} for a pure silica sand $\rho_s = 2.70$ Mg/m^3 were found to be 0.42 and 0.71, respectively. (a) What is the corresponding range in dry density? (b) If the in situ void ratio is 0.58, what is the relative density?

5.10 The wet density of a sand in an embankment was found to be 1.85 Mg/m^3 and the field water content was 12%. In the laboratory, the density of the solids was found to be 2.71 Mg/m^3, and the maximum and minimum void ratios were 0.65 and 0.38, respectively. Calculate the relative density of the sand in the field.

5.11 The laboratory test results on a sand are $e_{max} = 0.91$, $e_{min} = 0.48$, and $G_s = 2.67$.

(a) What is the dry unit weight (in lb/ft^3) of this sand when its relative density is 67% and its water content is 10%?

(b) How would you classify the density of this soil?

5.12 Based on field data, you have determined that a sand's relative density is on the borderline between "medium" and "dense," and its void ratio is 0.93. For this soil, if the difference between e_{min} and e_{max} is 0.3, what is e_{min}?

5.13 For a granular soil, given $\gamma_t = 108$ pcf, $D_r = 82\%$, $w = 8\%$, and $G_s = 2.65$. For this soil, if $e_{min} = 0.44$, what would be the dry unit weight in the "loosest" state?

5.14 The laboratory test results on a sand are as follows: $e_{max} = 0.91$, $e_{min} = 0.48$, and $G_s = 2.67$. What would be the dry and moist unit weights of this sand, in lb/ft^3, when densified at a moisture content of 10% to a relative density of 65%?

5.15 A sample of sand has a relative density of 40% with a specific gravity of solids of 2.65. The minimum void ratio is 0.45 and the maximum void ratio is 0.97.

(a) What is the unit weight (in units of lb/ft^3) of this sand in the saturated condition?

(b) If the sand is compacted to relative density of 65%, what will be the decrease in thickness of a 4 ft. thick layer?

5.16 A field compaction control test was conducted on a compacted lift. The mass of the material removed from the hole was 1820 g and the volume of the hole was found to be 955 cm^3. A small sample of the soil lost 17 g in the drying test and the mass remaining after drying was 94 g. The laboratory control test results are shown in Fig. P5.16.

(a) If end-product specification requires 100% relative compaction and w = (optimum − 3%) to (optimum + 1%), determine the acceptability of the field compaction and state why this is so.

(b) If it is not acceptable, what should be done to improve the compaction so that it will meet the specification?

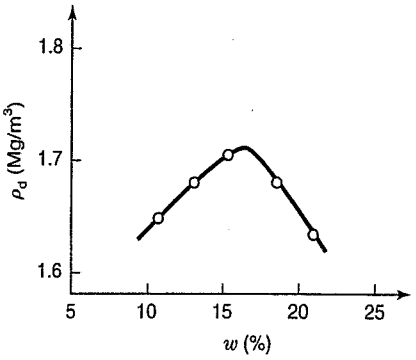

FIGURE P5.16

5.17 Calculate the compactive effort of the modified Proctor test in both (a) SI and (b) British engineering units.

5.18 Why does the relative compaction decrease if there is vibration during the sand-cone test?

5.19 In a field density test, using the oil method, the wet mass of soil removed from a small hole in the fill was 1.65 kg. The mass of oil (specific gravity = 0.92) required to fill the hole was 0.75 kg, and the field water content was found to be 22%. If the ρ_s of the soil solids is 2650 kg/m^3, what are the dry density and degree of saturation of the fill?

5.20 You are an earthwork construction control inspector checking the field compaction of a layer of soil. The laboratory compaction curve for the soil is shown in Fig. P5.20. Specifications call for the compacted density to be at least 95% of the maximum laboratory value and within ±2% of the optimum water content. When you did the sand cone test, the volume of soil excavated was 1165 cm^3. It weighed 2230 g wet and 1852 g dry.

(a) What is the compacted dry density?

(b) What is the field water content?

(c) What is the relative compaction?

(d) Does the test meet specifications?

(e) What is the degree of saturation of the field sample?

(f) If the sample were saturated at constant density, what would be the water content?

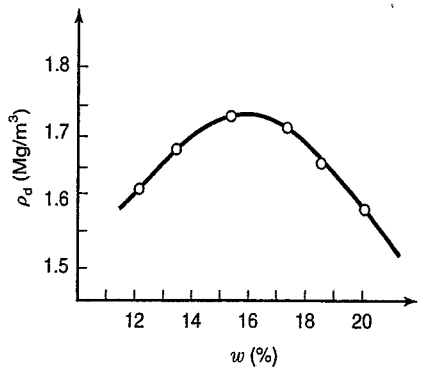

FIGURE P5.20

5.21 You are checking a field-compacted layer of soil. The laboratory control curve has the following values:

ρ_d (lb/ft^3)	w (%)
104	14
105.5	16
106	18
105	20
103.5	22
101	24

The specification for compaction states that the field-compacted soil must be at least 95% of the maximum control density and within of the optimum moisture for the control curve. You dig a hole of 1/30 ft^3 in the compacted layer and extract a sample that weighs 3.8 lb wet and 3.1 lb dry.

(a) What is the compacted ρ_d? The compaction w? The percent compaction? Does the sample meet the specifications?

(b) If the density of solids is 2.68 Mg/m^3, what is the compacted degree of saturation? If the sample were saturated at constant density, what would be the water content? (After C. W. Lovell.)

5.22 A mixture contains 28% by *dry weight* fines and 72% coarse. When the coarse material has a $w = 3\%$, its affinity for water is completely satisfied. The fines have a PL = 22 and an LL = 34. This mixture is *compacted* by rolling to $\rho_d = 128$ pcf and $w_{mix} = 13\%$. What is the water content of the *fines* in the compacted mass? What is the liquidity index of the fines in the compacted mass? (After C. W. Lovell.)

5.23 A soil proposed for a compacted fill contains 38% fines and 62% coarse material by *dry weight*. When the coarse fraction has $w = 2.0\%$, its affinity for water is completely satisfied (that is, it is saturated but surface dry). The Atterberg limits of the fines are LL = 31 and PL = 13. The soil is compacted by rolling to a $\rho_d = 1.95$ Mg/m^3 at $w = 15\%$. *Note:* This is the water content of the entire soil mixture.

(a) What is the water content of the *fines* in the compacted mass?

(b) What is the likely classification of the soil? (Give both the Unified and the AASHTO classifications.)

(c) What is the liquidity index of the fines?

(d) What can you say about the susceptibility of the fill to

(1) shrinkage-swelling potential?

(2) potential for frost action?

(e) Is there a certain type of compaction equipment you would especially recommend for this job? Why?

5.24 A fine sand with poor gradation is to be used as a subgrade for a flexible pavement. Give as much information as you can about the suitability of this soil as a pavement subgrade.

5.25 What soils, if properly compacted, would make the best foundation material for a structure? Give your answers in terms of the Unified Soil Classification System symbols.

5.26 The same as Problem 5.25, for an earth dam.

5.27 Given: The data shown in Fig. 5.4. Soil types 3 and 4 are mixed in the borrow area to some unknown extent. After a representative sample of the combined material is air dried to a uniform water content (hopefully on the dry side of optimum), a compaction test is performed and a value of 1.85 Mg/m^3 dry density at 12.5% water content is obtained.

(a) Estimate the maximum dry density of the combined soils.

(b) If a field dry density of 1.54 Mg/m^3 is obtained after compaction by a sheepsfoot roller, compute the relative compaction.

5.28 The core of an earth dam is to be compacted on the wet side of optimum so as to ensure low permeability and flexibility (a nonbrittle stress-strain relationship). You have the choice of using a sheepsfoot roller or a smooth-wheel roller to compact the soil. To reduce potential shrinkage of the dam core, which is the best piece of equipment to use? If the soil were to be compacted dry of optimum, would it matter?

5.29 A contractor is placing soil in 10-in. loose lifts, each at about 85 pcf. The moisture content is 8% at the time of placement. The optimum water content for this soil is 10%. The contractor has a water truck with a spray bar on the back. She will use it to drive over the dry soil, with the spray bar running, to increase the water content. How fast should the truck move with the spray running at some flow rate?

Make a plot of gal/min from the spray bar (ordinate) versus speed of the truck in mph (abscissa) for the driver to use. The plot must have a family of curves on it, one each for water contents between 5% and 14% for this soil, including 10%. Use a spreadsheet to create the data and corresponding plots. Submit sample calculations, the plot, and an explanation of how to use the plot, to be given to the contractor.

Extra credit: Make a similar plot, for a soil with a 6% initial water content. (After D. Elton.)

CHAPTER 6

Hydrostatic Water in Soils and Rocks

6.1 INTRODUCTION

From previous discussions on the Atterberg limits, classification of soils, geologic processes, and soil and rock structures, you should now realize that the presence of water in soils and rocks is very important. Water very strongly affects the engineering behavior of most soils, especially fine-grained soils, as well as many rock masses. Water is an important factor in most geotechnical engineering design and construction projects. A few examples include capillarity, swelling, and frost action in soils, discussed in this chapter, and seepage of water through dams and levees and toward wells, as discussed in Chapter 7. As an indication of the practical importance of water in geotechnical engineering, it has been estimated that more people have lost their lives as a result of failures of dams and levees due to seepage and "piping" (Chapter 7) than to all the other failures of civil engineering works combined. In North America, damage from swelling (expansive) soils causes a greater economic loss annually than floods, hurricanes, tornadoes, and earthquakes combined.

In general, water in soils can be thought of as either static or dynamic. The groundwater table, even though it actually fluctuates throughout the year, is considered to be static for most engineering purposes. Adsorbed water (Chapter 4) is generally static. Similarly, capillary water is usually taken to be static, although it too can fluctuate, depending on climatic conditions and other factors. In this chapter we shall concentrate on hydrostatic water problems in geotechnical engineering.

The following notation is introduced in this chapter.

Symbol	Dimension	Unit	Definition
C	1/m	1/m	Empirical capillary coefficient - Eq. (6.7)
D	L	m, mm	Diameter
d	L	m, mm	Capillary diameter - Eq. (6.4b)
F	MLT^{-2}	N	Force
h_c	L	m	Height of capillary rise - Eqs. (6.4c) and (6.5)
I_c	—	(%)	Collapse potential

(Continued)

Symbol	Dimension	Unit	Definition
P_{atm}	$ML^{-1}T^{-2}$	kPa	Atmospheric pressure
r_m	L	m, mm	Radius of meniscus
SL	–	(%)	Shrinkage limit - Eq. (6.9)
T	MT^{-2}	N/m	Surface tension
u	$ML^{-1}T^{-2}$	kPa	Pore water pressure
u_c	$ML^{-1}T^{-2}$	kPa	Capillary pressure - Eq. (6.6b)
α	–	degree	Contact angle
σ	$ML^{-1}T^{-2}$	kPa	Total stress
σ'	$ML^{-1}T^{-2}$	kPa	Effective or intergranular stress - Eq. (6.8)
σ_h	$ML^{-1}T^{-2}$	kPa	Total horizontal stress - Eq. (6.19)
σ'_h	$ML^{-1}T^{-2}$	kPa	Effective horizontal stress - Eq. (6.20)
σ_v	$ML^{-1}T^{-2}$	kPa	Total vertical stress - Eq. (6.19)
σ'_v	$ML^{-1}T^{-2}$	kPa	Effective vertical stress - Eq. (6.20)

6.2 CAPILLARITY

Capillarity arises from a fluid property known as *surface tension*, which occurs at the interface between different materials. For soils and rocks, it occurs between surfaces of water, mineral grains, and air. Fundamentally, surface tension results from differences in forces of attraction between the molecules of the materials at the interface.

The phenomenon of capillarity may be demonstrated in many ways. Placing the end of a dry towel in a tub of water will eventually result in a saturated towel. To illustrate the effects of capillarity in porous materials such as soils and rocks, we can use the analogy of small-diameter glass tubes to represent the voids between the mineral grains. Capillary tubes demonstrate that the adhesion forces between the glass walls and water cause the water to rise in the tubes and form a meniscus[1] between the glass and the tube walls. The height of rise is inversely proportional to the diameter of the tubes; the smaller their inside diameter, the greater the height of capillary rise. The meniscus formed is concave upward with the water "hanging," so to speak, on the walls of the glass tube [Fig. 6.1(a)]. With some

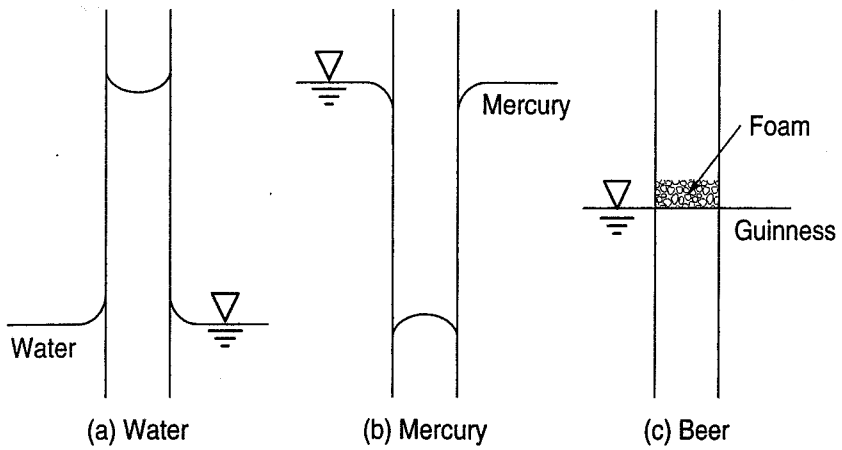

FIGURE 6.1 Menisci in glass tubes in (a) water, (b) mercury, and (c) beer.

[1]After Giacomo Meniscus (1449–1512), a Venetian physician and friend of Leonardo da Vinci. (We are indebted to Prof. M. E. Harr, Professor Emeritus, Purdue University, for this little known fact.) (From the Greek, μενισκοσ = "small moon" or "crescent.")

materials the internal cohesion forces are greater than the adhesion forces, and the substance will not "wet" the glass tube. Mercury, for example, has a depressed meniscus; its shape is convex [Fig. 6.1(b)].

If we look more closely at the meniscus geometry for water in a fine capillary tube (Fig. 6.2), we can write equations for the forces acting in the water column. The force acting downward, considered positive, is the weight W of the column of water, or

$$\sum F_{\text{down}} = W = \text{volume}(\rho_w)g = h_c\left(\frac{\pi}{4}d^2\right)\rho_w g \tag{6.1}$$

The upward force is the vertical component of the reaction of the meniscus against the tube circumference, or

$$\sum F_{\text{up}} = \pi d T \cos\alpha \tag{6.2}$$

where T is the *surface tension* of the water-air interface which acts around the circumference of the tube. The surface tension has dimensions of force/unit length. The other terms are functions of the geometry of the system and are defined in Fig. 6.2.

For equilibrium $\sum F_v = 0$, and

$$-(h_c)\frac{\pi}{4}d^2\rho_w g - \pi d T \cos\alpha = 0 \tag{6.3}$$

Solving for the height of capillary rise, h_c, we obtain

$$h_c = \frac{-T\cos\alpha}{d\rho_w g} \tag{6.4a}$$

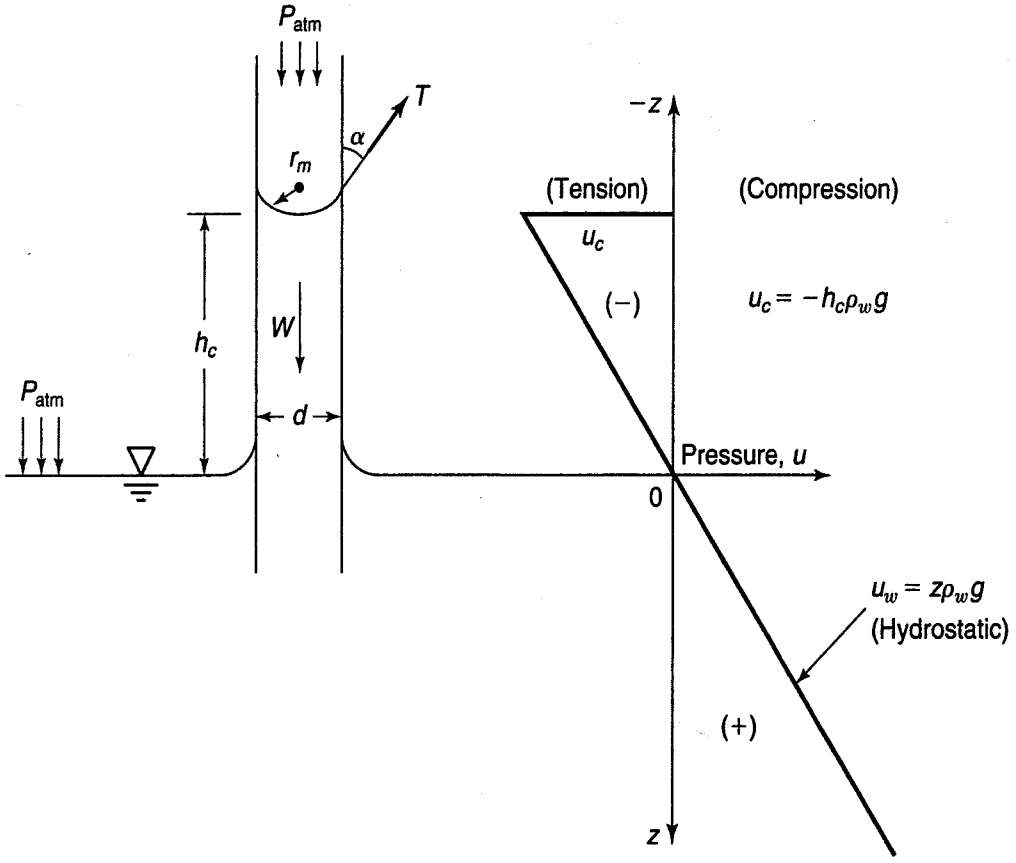

FIGURE 6.2 Meniscus geometry of capillary rise of water in a glass tube.

where

$$d = 2 \cos \alpha \, r_m \tag{6.4b}$$

For clean glass tubes and pure water, $\alpha \rightarrow 0$ and $\cos \alpha \rightarrow 1$,

$$h_c = \frac{-4T}{d\rho_w g} \tag{6.4c}$$

The capillary rise is upward, above the *free water surface*, but it has a negative value because of the sign convention shown in Fig. 6.2. Surface tension T is a physical property of water. From the *Handbook of Chemistry and Physics* (2008), at 20°C, T is about 73 dynes/cm or 73 mN/m. Since $\rho_w = 1000$ kg/m^3 and $g = 9.81$ m/s^2, for pure water in clean glass tubes Eq. (6.4) reduces to

$$h_c = \frac{-0.03}{d} \tag{6.5}$$

where h_c = height of capillary rise, m, and

d = diameter of capillary tube, mm

This formula is easy to remember. For the height of capillary rise in metres, divide 0.03 by the diameter in millimetres.

All the preceding discussion is for clean glass tubes and pure water under laboratory conditions. In reality, the actual height of capillary rise is likely to be somewhat less due to the presence of impurities and imperfectly clean surfaces.

Example 6.1

Given:

The diameter of a clean glass capillary tube is 0.1 mm.

Required:

Expected height of capillary rise of water.

Solution: Use Eq. (6.5).

$$h_c = \frac{0.03}{0.1 \text{ mm}} = 0.3 \text{ m}$$

Also shown in Fig. 6.2 is the pressure or stress distribution in the water. Below the surface of the water reservoir, the pressure increases linearly with depth (hydrostatic pressure), or

$$u_w = z\rho_w g \tag{6.6a}$$

where u_w = water pressure at some depth, and

z = depth below free water surface.

Above the reservoir surface, the water pressure in the capillary tube is negative or less than zero gage pressure (referenced to atmospheric pressure). From Eq. (6.4c), the magnitude of the capillary pressure u_c is

$$u_c = -h_c \rho_w g = -\frac{4T}{d} = -\frac{2T}{r_m} \tag{6.6b}$$

The shape of the meniscus is actually spherical (a minimum energy condition) with radius r_m (Fig. 6.2). The radius is greater than or equal to the radius of the tube, depending on the contact angle α. When α is approximately zero, then $r_m = d/2$.

What is the maximum negative pressure that can be attained? In large tubes, the limitation is the vapor pressure of water. As the pressure becomes increasingly negative (that is, less than atmospheric), water will cavitate or "boil" when the ambient pressure reaches the vapor pressure. This occurs when the water column is about 10 m in length, which is about the maximum height that a suction pump can draw. When the water "boils" at the vapor pressure, or about −1 atm pressure, then bubbles of water vapor form, and the column of water is broken. In absolute terms, the vapor pressure of water is 17.54 mm Hg or 2.34 kPa absolute at 20°C [from the *Handbook of Chemistry and Physics* (2008)].

The relationships between absolute, gage, and vapor pressure of water are shown in Fig. 6.3. The equivalent capillary tube diameter at the vapor pressure is about 3 μm. Now, if the tube is smaller than this diameter, then the water cannot cavitate because the surface tension is too high and a bubble cannot form. In this case, the height of capillary rise in smaller tubes depends only on the tube diameter, and thus the rise may be much greater than 10 m. Similarly, the capillary pressure (pore water tension) in this case may be much greater than −1 atm or −100 kPa.

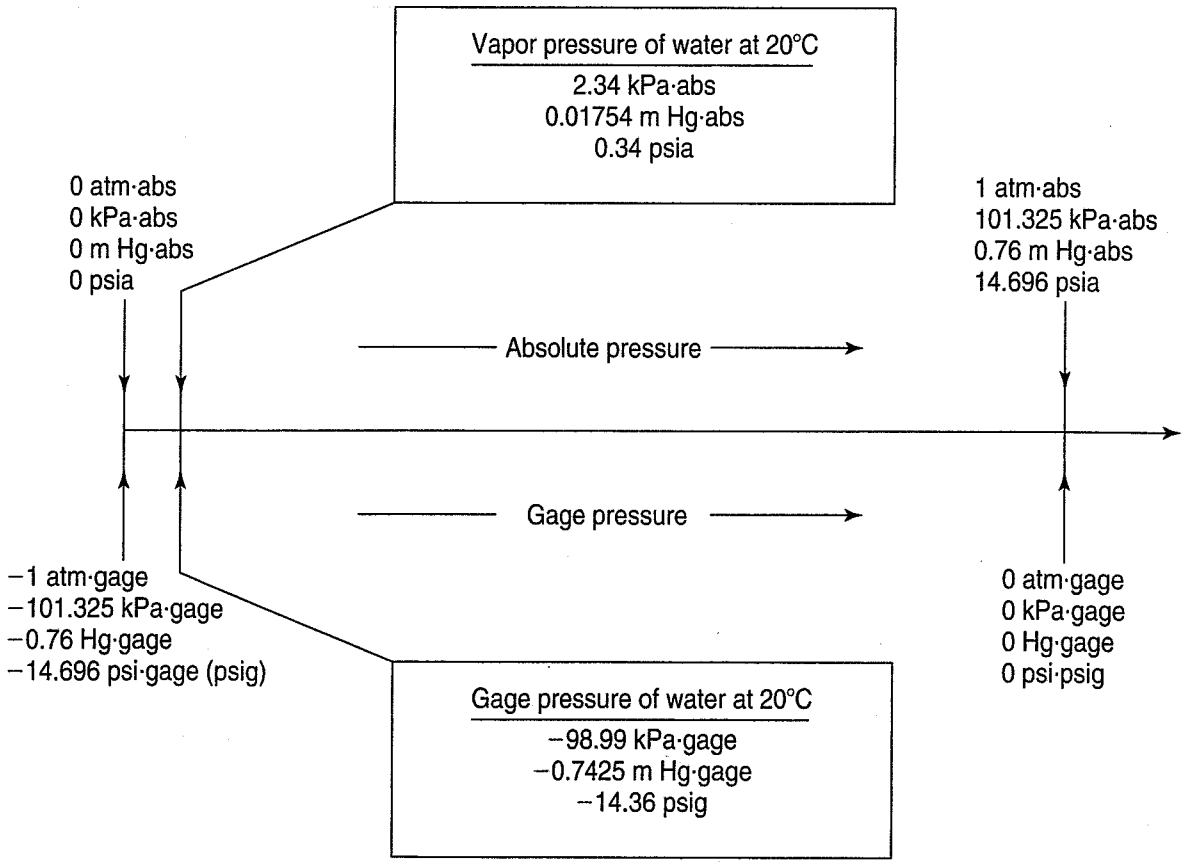

FIGURE 6.3 The relationship between atmospheric and vapor pressures of water in terms of absolute and gage pressures.

In summary, remember that for *large tubes* the maximum allowable tension or suction in water depends only on the atmospheric pressure and has nothing to do with the diameter of the tube. Capillary rise in *small tubes*, on the other hand, is a function of the tube diameter only and has no relation to atmospheric pressure (Terzaghi and Peck, 1967; Sowers, 1979).

Example 6.2

Given:

The pressure relationships shown in Fig. 6.3.

Required:

a. Show that the maximum height of a water column in a large tube is about 10 m.

b. Show that the equivalent pore diameter at the vapor pressure is about 3 μm.

Solution:

a. In large tubes, the maximum height of a water column is governed by the vapor pressure or the maximum negative pressure in the water. From Fig. 6.3, at the vapor pressure, the pressure is −98.99 kPa. Because 1 kPa = 10^3 kg · m/s^2/m^2 (Appendix A), and using Eq. (6.6), we have

$$h_c = \frac{u_c}{\rho_w g} = \frac{-98.99 \text{ kPa}}{(1000 \text{ kg/m}^3)(9.81 \text{ m/s}^2)}$$
$$= -10.1 \text{ m (rise)}$$

b. Use Eq. (6.5) and solve for d_c

$$d_c = \frac{-0.03}{h_c} = \frac{-0.03}{-10.1 \text{ m}} = 3(10^{-3}) \text{ mm} = 3(10^{-6}) \text{ m}$$

6.2.1 Capillary Rise and Capillary Pressures in Soils

Although soils are random assemblages of particles, and the resulting voids are similarly random and highly irregular, the capillary tube analogy, although imperfect, helps explain capillary phenomena observed in real soils.

In principle, capillary or negative pressures and capillary rise will be similar in soils and in glass tubes. Let's look at a series of capillary tubes in Fig. 6.4. Tube 1 has a diameter d_c, and thus the corresponding height of capillary rise is h_c. The fully developed meniscus has a radius r_c. In tube 2, $h < h_c$; the water will try to rise to h_c, but it cannot. Consequently, the radius of the meniscus in tube 2 will be *greater* than r_c, since it is physically impossible for the corresponding capillary pressure (and therefore the r_c) to develop. In tube 3, a large bubble or void exists, and there is no way for the water to be pulled above a void with diameter greater than d_c. If, however, as shown in tube 4, water enters from the top, then it is possible for the meniscus at the top of the tube to support the entire column of water of diameter d_c. The walls of the void support the water in the void outside the column of water. Tube 5 is filled with soil, and the water rises to the surface of the soil, since the average or *effective* pore diameter of the soil is much less than d_c. The capillary menisci hang on the particles, which pull the grains together, causing an *intergranular* stress to act at the contact between the two grains. A magnified picture of two sand particles connected by menisci of radius r_m is shown in Fig. 6.5.

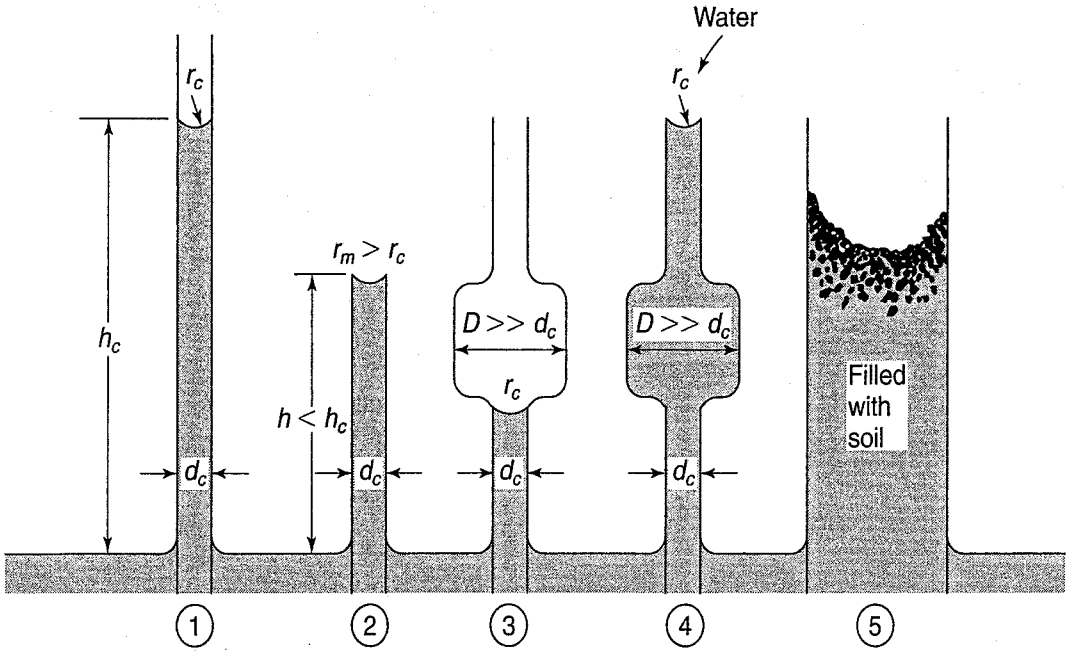

FIGURE 6.4 Capillary rise in tubes of different shapes (after Taylor, 1948).

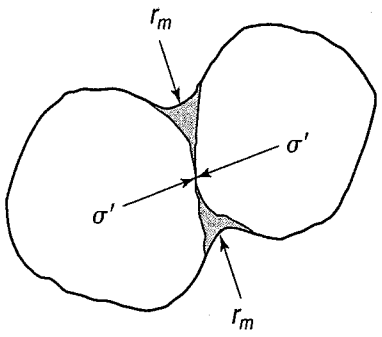

FIGURE 6.5 Two soil grains held together by a capillary film.

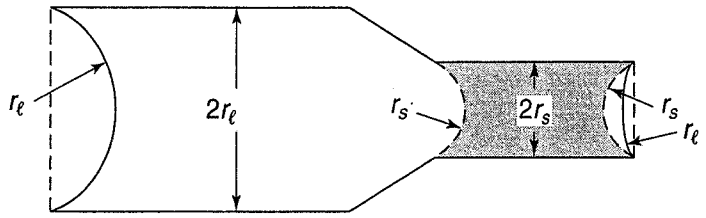

FIGURE 6.6 Capillarity in a tube of unequal radii (after A. Casagrande).

Another analogy illustrating the development of menisci in soils is shown by the tube in Fig. 6.6. The tube initially is completely filled with water. As evaporation occurs, the menisci begin to form, and, at the beginning, the largest possible radius is that of the larger end, r_ℓ. At the smaller end, the radius is also equal to r_ℓ. It cannot be any smaller, because then the pressure would have to be lower (more negative), and that cannot happen. By hydrostatics, the pressure in the water must be the same at both ends, otherwise flow would occur toward the end with the lower (more negative) pressure. As evaporation continues, the menisci retreat until the condition indicated by the cross-hatched section of the tube occurs. At this time, the menisci have radii equal to r_s, the radius of the smaller section of the capillary tube. The capillary pressure can go no lower (i.e., no more negative), and it corresponds to the pressure which can be supported by the smaller diameter radii. This pressure is given by Eq. (6.6). If evaporation continues, the tube will eventually become empty.

Although the capillary tube analogy is imperfect, it is still useful, because it recognizes that capillary phenomena depend on the pore sizes or pore volumes and their distribution in soils. There is an ASTM standard (D 4404) for the determination of pore volume and pore volume distribution by mercury intrusion porosimetry. However, because this determination requires special equipment and procedures, it is not routinely done. It is easier to measure the grain sizes in soils, so we usually use the effective grain size D_{10} and assume that the effective pore diameter is some fraction of the D_{10}. For example, Sowers (1979) suggests using about 20% of the effective grain size. Using this assumption and Eqs. (6.5) and (6.6), we can estimate a theoretical height of capillary rise and the corresponding capillary pressure in a fine-grained soil.

Alternatively, we could use an equation suggested by Terzaghi et al. (1996) for the height of capillary rise h_c (m) that depends on the D_{10} (mm) and void ratio e, or

$$h_c = \frac{C}{eD_{10}} \tag{6.7}$$

The empirical coefficient C varies between 0.01 and 0.05 and is a function of the grain shape and surface impurities (Terzaghi et al., 1996).

Example 6.3

Given:

A sample of clay soil with a D_{10} of 1 μm and a void ratio of 0.4.

Required:

a. Calculate the theoretical height of capillary rise in the clay.

b. Estimate the capillary pressure in the clay.

Solution: Assume the effective pore diameter is about 20% of D_{10}. Thus,

$$D_{\text{pore}} \approx 0.2(D_{10}) = 0.2\ \mu\text{m} = 0.2 \times 10^{-3}\ \text{mm}$$

a. Capillary rise [Eq. (6.5)]:

$$h_c = \frac{-0.03\ \text{m}}{0.2 \times 10^{-3}\ \text{mm}} = -150\ \text{m (about 500 ft)}$$

If we use Eq. (6.7), we need to assume a value of C. For this example, let's use the mean value or 0.03.

$$h_c = \frac{C}{eD_{10}} = \frac{0.03}{(0.4)(1\ \mu\text{m})} = 62.5\ \text{m}$$

b. Capillary pressure [Eq. (6.6b)]:

$$u_c = h_c\rho_w g = -150\ \text{m}\ (1000\ \text{kg/m}^3)(9.81\ \text{m/s}^2)$$

$$\approx -1500\ \text{kPa} \approx -15\ \text{atm} \approx -225\ \text{psi}$$

Although theoretically possible, rarely in natural soil deposits do the heights of capillary rise actually reach those suggested by Example 6.3. Some of the voids in natural soils are large enough so that the water can vaporize and form bubbles. This results in the menisci being destroyed and the actual height of capillary rise being reduced. Still, heights of capillary rise can be significant in especially fine-grained soils. Table 6.1 lists some typical heights of capillary rise for some soil types.

The capillary pressures we estimated in Example 6.3 are very large indeed, but they are definitely possible in the very small pores of soils and rocks. This means, too, that the resulting *intergranular stress* acting between the soil grains is of the same order of magnitude. Recall the magnified picture of the two sand grains connected by menisci shown in Fig. 6.5. In this figure, the intergranular contact stress is given the symbol σ'. This stress, called the *effective stress*, has special significance in geotechnical engineering, and it is discussed in more detail later in the chapter. For now, let us just define the effective stress as the total stress σ minus the pore water pressure u,

$$\sigma' = \sigma - u \tag{6.8}$$

In Example 6.3, the sample of clay, if it is in the laboratory, is acted on by atmospheric pressure, or in this case, the total stress $\sigma = 0$ (zero gage pressure). Then, from Eq. (6.8), $\sigma' = -(-u_c) = u_c$, or for the conditions in Example 6.3, $\sigma' \approx +1500$ kPa. Thus the effective stress in materials with small pores can be very large, owing to the capillary pressures essentially "pulling" the particles together.

At the top of a soil-water column—for example, in tube 5 of Fig. 6.4—the capillary menisci pull the grains of soil together, as sketched in Fig. 6.5. The smaller the meniscus, the larger the capillary tension, and the larger the intergranular contact stress between the particles. Intergranular contact stress causes a frictional resistance to develop between the grains. The effect is similar to what happens when some sand is placed in a rubber membrane, sealed, and a vacuum applied to the specimen. The pressure difference between the external atmospheric pressure (zero gage pressure) and the applied vacuum (some value of negative gage pressure) holds the grains tightly together and thereby increases their frictional resistance considerably. In this case, the larger the applied vacuum, the greater the frictional resistance.

Another important consequence of the increase in intergranular or effective stress that occurs due to capillarity is illustrated by the racetrack at Daytona Beach, Florida (Fig. 6.7). The sands are very fine and have been densified somewhat by wave action. The capillary zone, which is relatively wide due to the flat slope of the beach, provides excellent driving conditions due to high capillary pressures. Just as in tube 5 of Fig. 6.4, the confining pressure results from the columns of water hanging on the menisci at the surface of the beach. Where the ocean water destroys the menisci, the bearing capacity is very poor, as anyone knows who has ever tried to escape a rising tide at a beach in a car!

Similarly, above the zone of capillary rise, the sand is dry and has relatively poor bearing capacity, especially for moving vehicles. The relative density throughout the beach zone is essentially the same, yet the bearing capacity is significantly different simply due to capillarity.

TABLE 6.1 Approximate Height of Capillary Rise in Different Soils

	Grain Size Range (mm)	Loose	Dense
Coarse sand	2–0.6	0.03–0.12 m	0.04–0.15 m
Medium sand	0.6–0.2	0.12–0.50 m	0.35–1.10 m
Fine sand	0.2–0.06	0.30–2.0 m	0.40–3.5 m
Silt	0.06–0.002	1.5–10 m	2.5–12 m
Clay	< 0.002	≥ 10 m	

After Beskow (1935) and Hansbo (1975 and 1994).

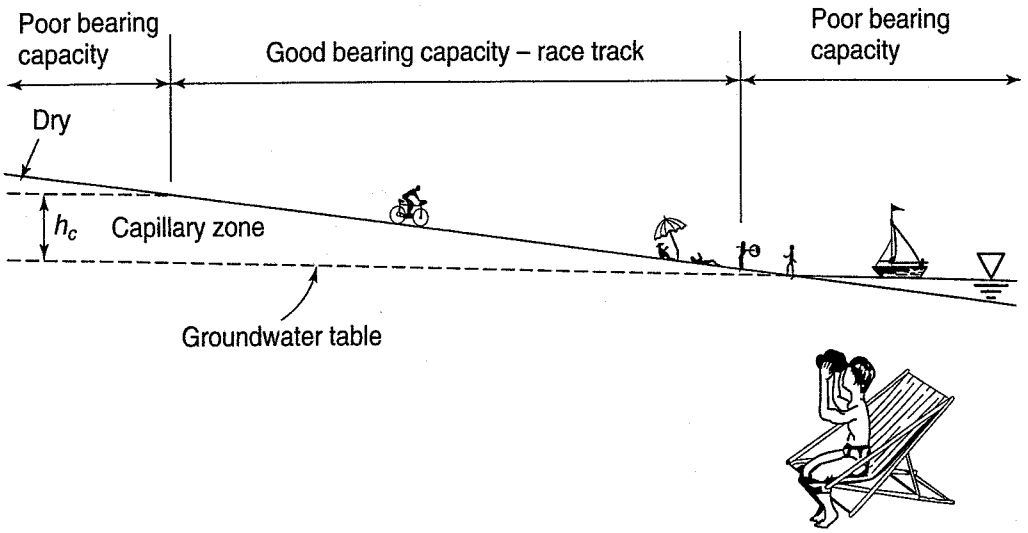

FIGURE 6.7 Cross section of racetrack at Daytona Beach, Florida.

Keep in mind that we have simplified our discussion by assuming that the capillary rise represents a boundary between completely saturated soil and completely dry soil. In fact, if the soil is originally dry, and then is exposed to a phreatic surface (for example, by placing a tube full of dry soil in a water bath), the degree of saturation may not be 100% *at any point* in the capillary zone, since soil voids are typically discontinuous, impeding the path of water migrating from the phreatic surface up through the soil. For example, in special capillary tests on fine sand that was originally dry, Lambe (1950) found that the degree of saturation was about 75% in the capillary zone except near the capillary boundary, where it dropped to about 65%. On the other hand, if the soil is originally saturated or wetted from above (as from rainfall), these values will be completely different and generally higher (Terzaghi 1943; Lambe and Whitman 1969).

6.2.2 Measurement of Capillarity; Soil-Water Characteristic Curve

In a number of applications, it is important to measure various aspects of capillarity in soils, since it can play an important role in their susceptibility to swelling and shrinkage, frost action, and flow through embankments and earth dams, among other phenomena. The earliest measures of capillary rise in soils were made using a device called a *capillarimeter*, which measures the ability of the soil to take in air under tension (Fredlund and Rahardjo, 1993). Lane and Washburn (1946) used both capillarimeters and soil in tubes to measure capillarity in soils.

ASTM standards D 2325 (for medium- to coarse-grained soils) and D 3152 (for fine-grained soils) are test methods for measuring the relationship between water content in a soil and the negative or capillary pressure (referred to as *matric suction*) applied to the pore water system. While the equipment for the test methods is different, the concepts are fundamentally the same. A saturated soil specimen and adjacent porous element are placed in a sealed chamber. The side of the porous element opposite to that in contact with the soil is exposed to atmospheric pressure and a positive pressure applied to the top of the soil. Water is allowed to drain out of the specimen until equilibrium is established between this applied gradient and the internal soil suction. At this point, the moisture content of the soil is measured. USBR procedure 5735 is similar, except that it specifies measurement of pore pressure at the end bearing plate, which will be negative until enough positive pressure is applied to the soil. Results of the ASTM tests plot tension as height above water table in metres versus volumetric water content. The volumetric water content can be related to the mass water content if the G_s and the degree of saturation are known.

Fredlund and Rahardjo (1993) provide details on two other methods for measuring matric suction. A *tensiometer* is a field device that uses an applied vacuum to draw water from the soil to determine the matric suction. In this way, the mechanics are similar to those in the two ASTM standards (D 2325 and D 3152) and the USBR 5735 standard. An indirect method for measuring matric suction is known as the axis translation technique. This involves the use of a porous block made from a material which has a known water content-suction relationship. The porous block is brought into contact with the soil, and equilibrium is achieved between the matric suction of the block and the soil. By measuring the water content of the block, one can infer the matric suction based on the block's calibration curve.

The matric suction is equal to the quantity $(u_a - u)$, where u_a is the pore air pressure and u is the pore water pressure. The matric suction is of course negative or less than zero gage pressure (Fig. 6.3), except when the soil is saturated. One way to visualize matric suction is the *soil-water characteristic curve*, shown schematically in Fig. 6.8(a). According to Fredlund and Rahardjo (1993), the matric suction tends to a limiting value of about 590 MPa at zero water content for many soils. At the other end of the curve when the matric suction is zero, the soil is saturated. Because especially fine-grained soils contain a large number of very different pore sizes and pore volumes, the water content changes in a very nonlinear fashion as the suction increases. Also as a dry soil saturates or a saturated soil drains, it does

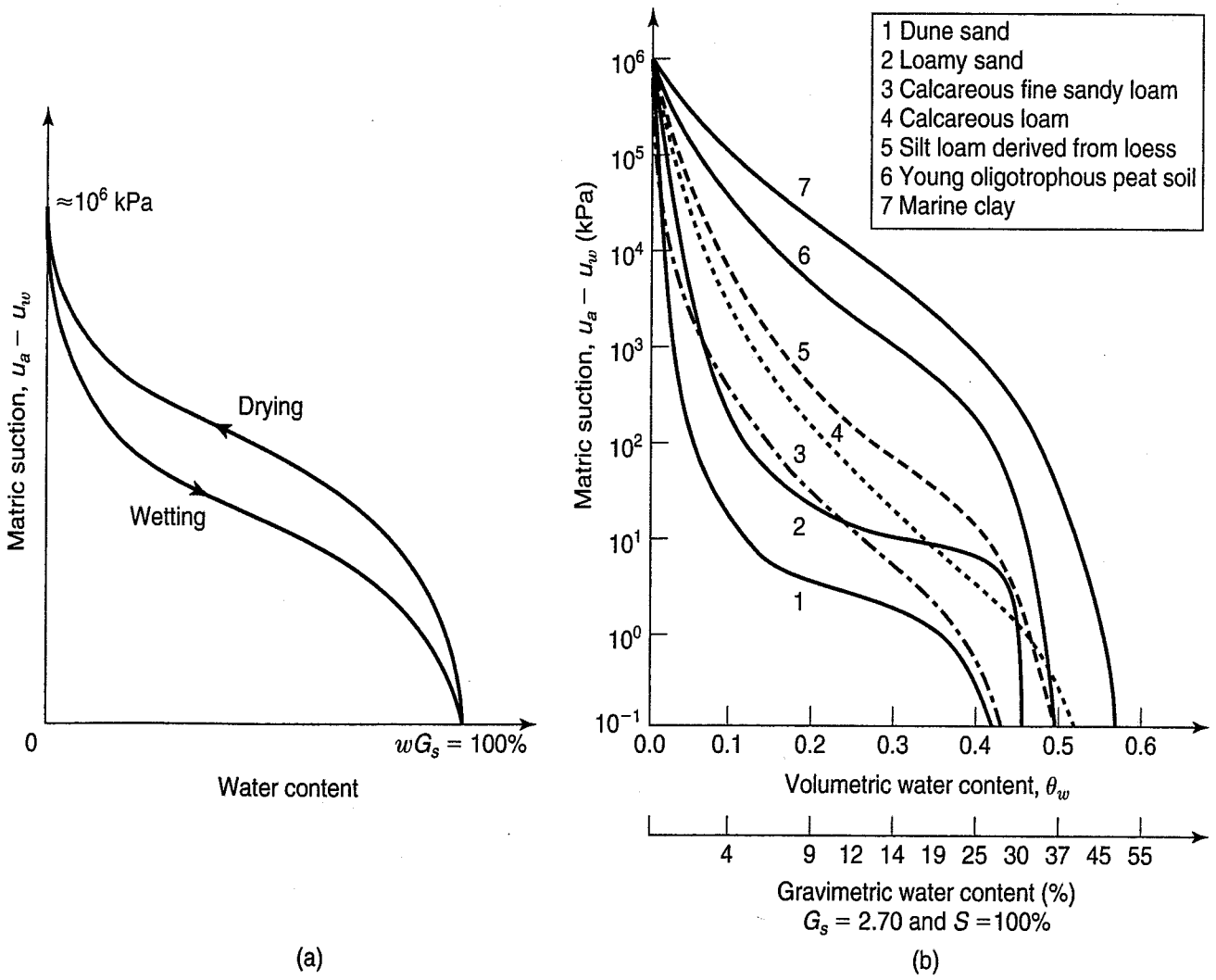

FIGURE 6.8 Soil-water characteristic curve—matric suction versus water content: (a) schematic for a plastic clay showing hysteresis due to wetting and drying (after Blight, 1980); (b) curves for different soils (after Koorevaar et al., 1983, as cited by Mitchell and Soga, 2005).

not follow the same curve as shown in Fig. 6.8(a). Mitchell and Soga (1995) give a detailed explanation for this hysteretic behavior.

As shown in Fig. 6.8(b), the actual shape of the soil-water characteristic curve depends on the soil type. The grain size distribution, soil fabric, and contact angle (Fig. 6.2) also influence the shape. Note that the abscissa of Fig. 6.8(b) is the *volumetric water content*, θ_w, which is defined as the V_w/V. Obviously θ_w is not the same as the water content used in geotechnical engineering (soil scientists call our water content the *gravimetric water content.*) From phase relations and Eq. (2.28b) ($Se = wG_s$), the relationship between the two water contents is

$$\theta_w = \frac{SwG_s}{S + wG_s} \tag{6.9}$$

An approximately equivalent gravimetric water content for the soils in Fig. 6.8(b) is shown below the volumetric water content scale. It was calculated for a $G_s = 2.70$ and $S = 100\%$.

6.2.3 Other Capillary Phenomena

Another phenomenon caused by capillarity is *bulking*. When moist sand is loosely dumped, it forms a very loose honeycombed structure [similar to Fig. 4.29(c), as shown in Fig. 6.9]. The grains are all held together by capillary films, and the moisture film surrounding the individual grains causes an "apparent cohesion." It is not true cohesion in a physical sense. The resulting structure, although it has a very low relative density, is fairly stable as long as the capillary menisci are present. If they are destroyed—for example, by flooding or evaporation—then the honeycomb structure collapses and the volume of the sand decreases significantly. As long as there is some moisture present, however, the sand will bulk and occupy a larger volume than it would if dry. Bulking can occur with water contents of only a few percent up to about 15 or 20 percent, depending on the grain size distribution and silt content of the sand. Figure 6.8 also shows why it is not a good idea to purchase moist sand by the volume—one may end up buying a lot of air!

Because bulked sands have a loose honeycombed structure, they are very compressible and may even be susceptible to collapse (discussed in Sec. 6.7). If they are used for backfill, for example, they have to be densified to avoid unwanted postconstruction settlements. You may recall from Sec. 5.5 that sands are most effectively densified by vibration. Bulked moist sands will require more energy to densify than dry sands, because it takes additional energy to destroy the capillary films surrounding the sand grains. Sometimes contractors will try to use flooding to destroy the menisci, but flooding is not a very good way to increase the density of a sand fill. The relative density of flooded fills will still be only 40% or 50% and thus they will still be susceptible to significant settlements if loaded or vibrated.

You can demonstrate bulking of sands in a simple laboratory experiment. Fill an ordinary Proctor compaction mold with dry sand, vibrate it by tapping the side of the mold, and then strike it off level at

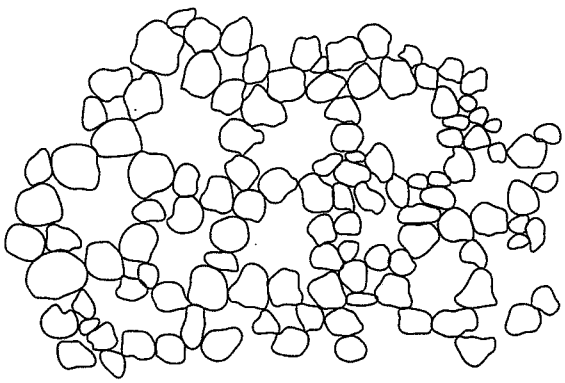

FIGURE 6.9 Bulking structure in sand.

the top. Dump the sand into a large pan and, with a spray bottle, add a small amount of water to the sand and mix it thoroughly. Then try to put the moist sand back into the mold. You will find that its volume has expanded significantly. Even if you compact the sand in layers in the mold, it will be very difficult to achieve the original density. Capillarity also allows excavations to be constructed at very steep slopes in silts and very fine sands—materials that, if dry, would readily fall to their natural *angle of repose* (Sec. 12.2), which is much flatter.

If you have ever played at the beach, you probably took advantage of capillarity to construct, for example, sand castles or other similar features from moist sand. Excavations made below the water table will collapse, because the menisci obviously do not exist there! Above the groundwater table and within the zone of capillarity, capillary menisci at the surface of the excavation provide the stability for the cut. However, such excavations are very unstable. At the beach, it is not so serious if an excavation collapses, but excavations of utility trenches, for example, are another matter. Unsupported excavations in silts and sands have been known to collapse due to very slight vibrations, such as from trucks on adjacent streets or nearby construction operations such as pile driving. This is why it is necessary to externally support all vertical excavations more than a meter or so deep, especially if people are working in the excavation. Lateral support or laying back the slope to a flatter angle is necessary even if the soils appear to be stable when first excavated.

Another phenomenon that depends on capillarity is *slaking*, which occurs when a lump of dry soil is immersed in a beaker of water. The lump immediately starts to disintegrate, and with some soils the disintegration is so rapid that the soil appears to almost explode. Slaking is a very simple way to distinguish between hard piece of soil and a small rock; rocks don't slake, whereas soils do. The soil lump has to be dry, so that the soil-water surface tension tends to pull water into the pores. Air bubbles trapped in the voids are compressed by the menisci, and if the internal air pressure is high enough to exceed the tensile strength of the soil, the soil lump collapses. In a rock fragment, the internal cohesion is sufficiently strong to resist these resulting entrapped air pressures, and slaking cannot occur.

Terzaghi (1943) used the capillary tube analogy to illustrate slaking. The capillary tubes are initially dry and then submerged; the capillary menisci now try to pull water into the voids, as shown in Fig. 6.10. By drawing a free-body diagram of the tube walls, you can see that the walls are in tension, and if the tensile strength is less than the tension applied by the menisci, the walls will fracture, which is exactly what occurs when a soil slakes.

Capillarity also plays an important role in the formation of ice lenses in fine-grained soils. The result can be significant volume changes that can damage infrastructure (particularly roads that are susceptible to so-called "frost heaving"), even in areas where the groundwater table is well below the ground surface. Frost action is discussed later in this chapter.

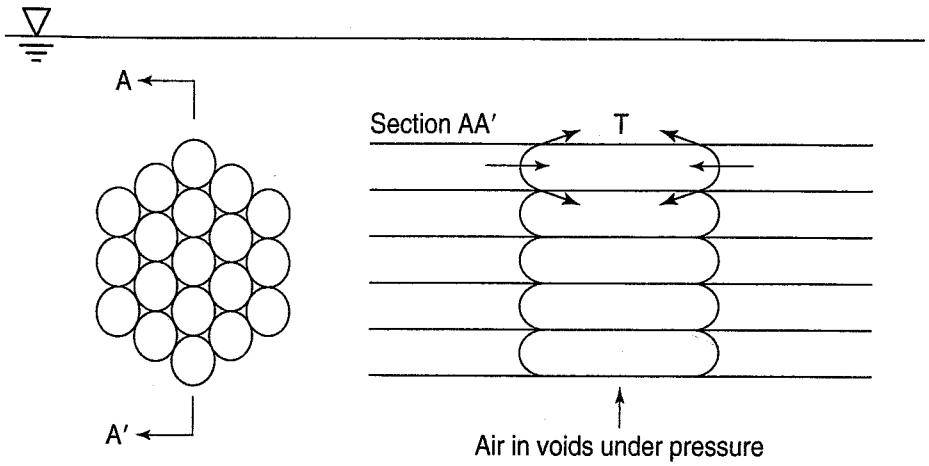

FIGURE 6.10 Capillary tube analogy for slaking (after Terzaghi, 1943).

6.3 GROUNDWATER TABLE AND THE VADOSE ZONE

6.3.1 Definition

From a geotechnical perspective, the *groundwater table* can be defined as the steady state or equilibrium elevation of free standing water in an excavated or drilled exploration hole. More specifically, it is the steady state elevation at which the pore water pressure is equal to the atmospheric pressure. Recognize that it is not really a table, but a surface of atmospheric pressure (zero gage pressure), but that is what it is commonly called. Below the groundwater table the degree of saturation is assumed to be (and usually is) 100%. Depending on the grain size of the soil above the groundwater table, the soil may be saturated because of capillarity, or it may become unsaturated nearer the ground surface. Above the zone of capillarity, the soil is *unsaturated*. The degree of saturation may range from 100% down to nearly zero if the soil is almost dry near the ground surface. The soil above the groundwater table is called the *vadose zone* (pronounced *vay-dose*), so it includes the *capillary zone* or *capillary fringe* (if any exists) and soils with other moisture conditions above that. These definitions are illustrated in Fig. 6.11. Note that the capillary zone is still considered part of the vadose zone.

6.3.2 Field Determination

There are several methods to measure the level of the groundwater table and hence the thickness of the vadose zone. The first and simplest way is just to establish an open exploration pit or borehole from which the level of the free water surface is measured relative to the ground surface or some other datum. This is often referred to as an *observation well*. A test or exploration pit is, of course, useful only if the groundwater table is near the ground surface. More commonly, a borehole anywhere from 50 to 100 mm in diameter is drilled deep enough to intercept the groundwater level (the depth can be estimated based on experience or by researching local geological maps). Usually a small perforated pipe or casing is installed in the borehole, because otherwise it may collapse with time. This type of observation well is an open-tube standpipe, and the depth to the water table is determined by a simple tape

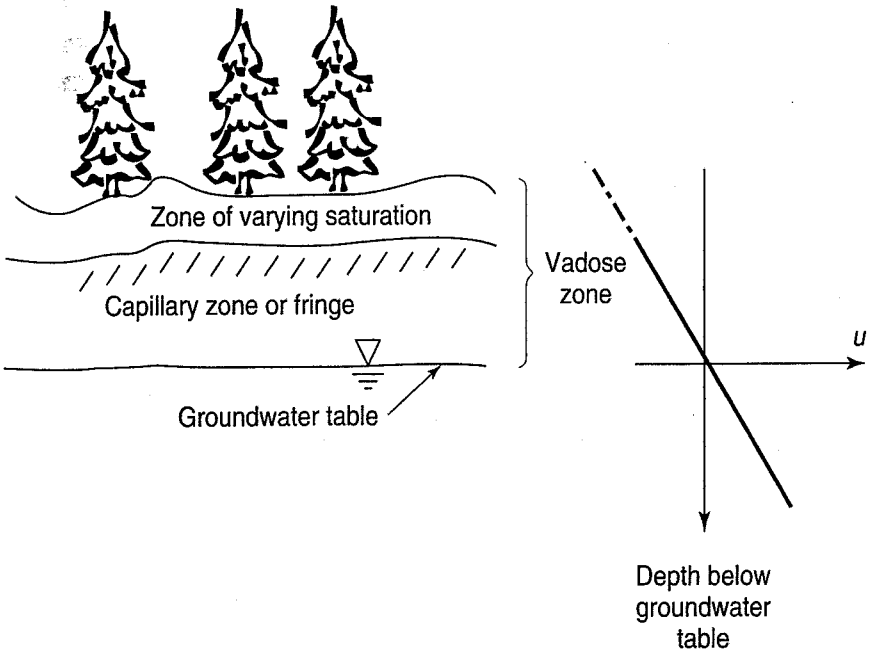

FIGURE 6.11 Illustration of vadose zone located above the groundwater table and the pore pressure distribution with depth.

measurement. Another method is to install a *piezometer* in the borehole that measures the water pressure at the depth of the piezometer point. Note that the piezometer point must be sealed from other water pressure sources in order to determine the water pressure at the point of installation. A piezometer can be a hydraulic or open standpipe (e.g., a Casagrande-type piezometer, which is a porous tipped tube) that allows water to rise to a certain level in an open pipe from a sealed tip, from which water pressure at the tip location can be deduced. Today, most piezometers are electro-mechanical devices that produce electrical signals proportional to the water pressure at the point of measurement. Dunnicliff (1993) provides an extensive survey of pore pressure measurement devices.

Example 6.4

Given:

The groundwater elevation in a loess deposit is determined by a standpipe piezometer to be at a depth of 4.5 m. Laboratory tests on samples of the loess show typical grain size distribution curves similar to Curve A in Fig. Ex. 6.4a (after U.S. Dept. of the Interior, 1990).

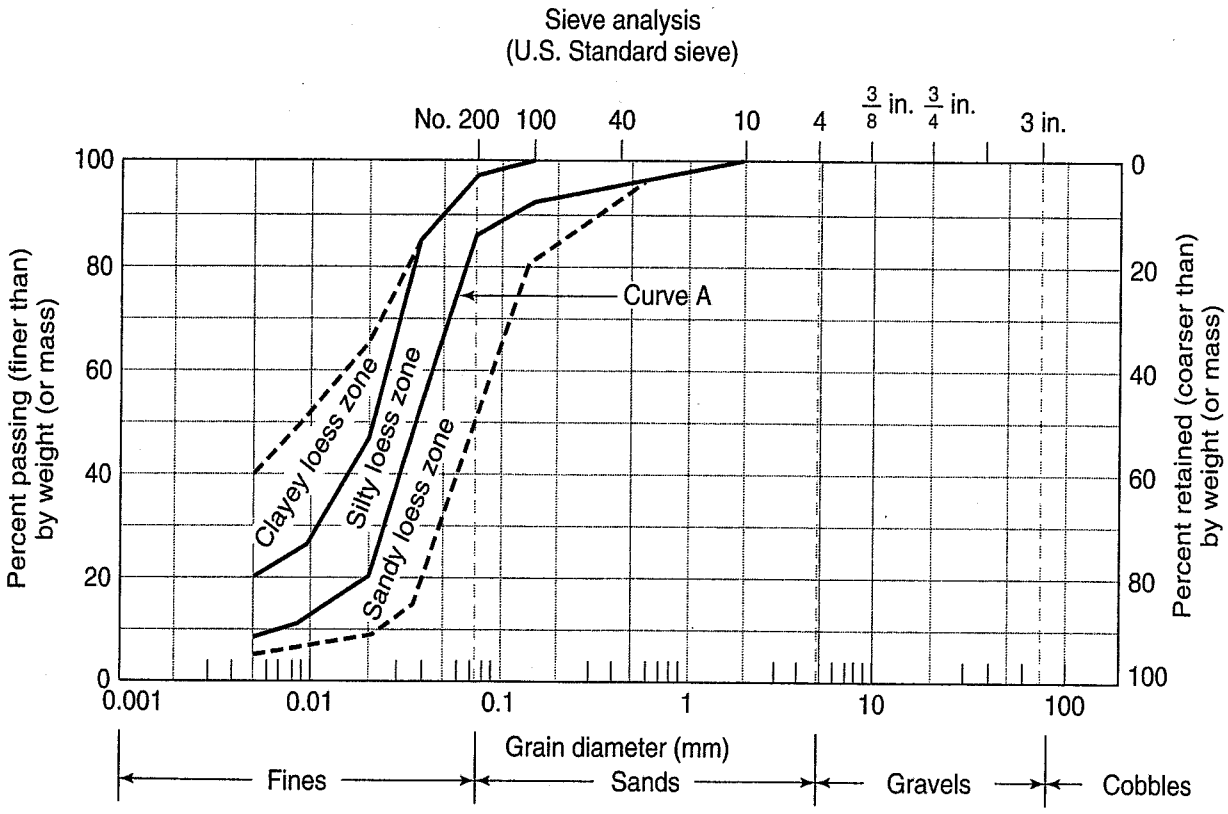

FIGURE Ex. 6.4a

Required:

a. Estimate the capillary rise in metres.

b. Plot the static water pressure distribution from the ground surface to a depth of 8 m.

Solution:

a. Recall from Sec. 6.2.2 that the effective pore size is commonly assumed to be 20% of the D_{10}. From Fig. Ex. 6.4a, D_{10} is estimated to be about 0.008 mm. Therefore, $0.2 \times 0.008 = 1.6 \times 10^{-3}$ mm. Using Eq. (6.5), the height of capillary rise is approximately

$$h_c = -0.03/d \text{ (in mm)} = -0.03/(1.6 \times 10^{-3} \text{ mm}) = 18.75 \text{ m}$$

Since the groundwater table is only 4.5 m below the ground surface, the loess above the groundwater table must be saturated or nearly so. However, near the ground surface, the soils may be unsaturated because of evaporation.

b. Use Eq. (6.6a) to determine the distribution of water pressure with depth below the groundwater table. Remember that the depth of the groundwater table is at −4.5 m. So at a depth of 8 m, $z = z_w = 3.5$ m, and

$$u_w = z_w \rho_w g = 3.5 \text{ m} \times 1 \text{ Mg/m} \times 9.8 \text{ m/s}^2 = 34 \text{ kPa}$$

At $z = -4.5$ m, u_w is, of course, equal to zero, and the pressure distribution is linear.

Is there a water pressure above the groundwater table? Yes, but it is negative due to capillarity. We may calculate it using Eq. (6.6b). With the height of capillary rise $h_c = 4.5$ m, the maximum capillary pressure is

$$u_c = h_c \rho_w g = -4.5 \text{ m} \times 1 \text{ Mg/m}^3 \times 9.8 \text{ m/s}^2 = -44 \text{ kPa}$$

The complete pressure diagram is shown in Fig. Ex. 6.4b.

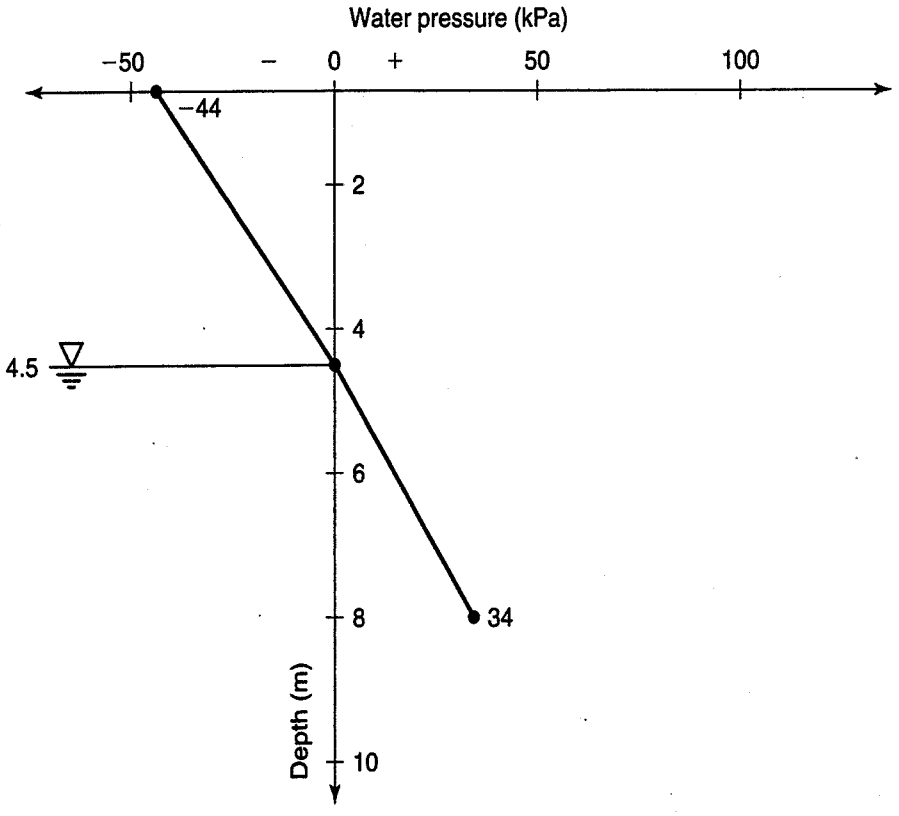

FIGURE Ex. 6.4b

For more detailed information on groundwater and the vadose zone, consult Freeze and Cherry (1979), Todd (1980), Cedergren (1989), and U.S. Department of the Interior (1995). As mentioned, Dunnicliff (1993) is a good reference on piezometric instrumentation and measurements.

6.4 SHRINKAGE PHENOMENA IN SOILS

Shrinkage of fine-grained soils can be of considerable practical significance. Cracks and fissures caused by soil shrinkage are zones of weakness that can greatly reduce the stability of clay slopes and the bearing capacity of foundations. The volume changes caused by evaporation and desiccation can damage small buildings and highway pavements. Shrinking soils can also increase in volume or expand if they have access to water, possibly causing more damage. Swelling soils are discussed in the next section of this chapter. Shrinking and swelling cause *billions* of dollars of damage annually in North America.

6.4.1 Capillary Tube Analogy

We can get an idea of how capillary stresses cause shrinkage in clay soils by studying the analogy of a horizontal tube with compressible elastic walls (Terzaghi, 1927). In Fig. 6.12(a) the tube at the beginning is completely filled with water and the radii of the menisci, which haven't reached their final shape yet, are very large. As evaporation occurs, pressure in the water decreases and the menisci start to form [Fig. 6.12(b)]. As evaporation continues, the radii become smaller and smaller, compression in the compressible walls of the tube increases, and the tube shrinks in length and diameter. The limiting case, shown in Fig. 6.12(c), is when the radii of the menisci are at the minimum (equal to one-half the diameter of the tube) and are fully developed. The negative pressure in the capillary tube is then equal to the value computed from Eq. (6.6b), and the walls of the tube have shrunk to an equilibrium condition between the stiffness of the walls and the capillary forces. If the tube is immersed in water, the menisci are destroyed, and the tube can expand because the capillary forces are no longer acting on the tube walls.

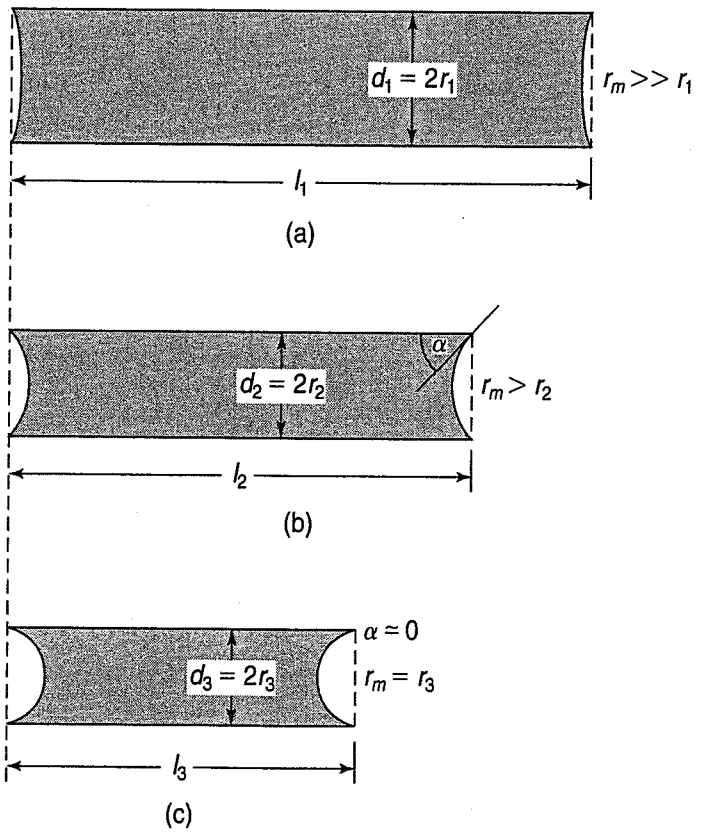

FIGURE 6.12 Compressible elastic capillary tube shrinking due to evaporation and surface tension (after Terzaghi, 1927).

Unless the walls of the tube are perfectly elastic, the tube will not return completely to its original length and diameter.

Another simple analogy was used by Terzaghi to illustrate the effects of capillary pressures in a porous material (Casagrande, 1938). A loose ball of absorbent cotton is submerged in a beaker and allowed to completely saturate. If the ball is compressed and then released, the fibers will quickly swell again. However, if the compressed ball is removed from the water and released, it will essentially retain its compressed shape because of the capillary menisci that form around the fibers. In fact, the ball will be rather firm as long as it doesn't dry out too much. If the cotton ball is again immersed in water, the menisci are destroyed and the fibers again become extremely loose and soft. Similar behavior results when dry cotton is compressed; it is quite elastic and becomes loose once the compressive forces are released.

Take another look at the tube shown in Fig. 6.6. If it is assumed to have compressible walls, then the analogy with shrinking soils is very useful. A soil sample slowly drying (that is, undergoing desiccation) will form capillary menisci between the individual soil grains. As a result, the stresses between the grains (intergranular or effective stresses) will increase, and the soil will decrease in volume. As shrinkage continues, the menisci become smaller, the capillary stresses increase, and the volume further decreases. A point is reached where no further volume decrease occurs, but the degree of saturation is still essentially 100%. The water content at which this occurs is defined as the *shrinkage limit* (SL or w_S), and it is one of the Atterberg limits mentioned in Sec. 2.7. At this point, the capillary menisci just begin to retreat below the soil surface, and the color of the surface changes from a shiny to a dull appearance. (The same effect is observed when a dilatant soil is stressed—the menisci retreat below the surface, which becomes dull in appearance because the reflectivity of the surface changes. See Sec. 2.9.1.)

6.4.2 Shrinkage Limit Test

How is the shrinkage limit determined? Atterberg's (1911) original work was with small bars or prisms of clay that he allowed to dry slowly. He observed the point at which the color changed, and at the same time he noted that the length was essentially a minimum at that point. Terzaghi figured out that one could just as well measure the dry volume and dry mass and back calculate the water content at the point of minimum volume. Figure 6.13 illustrates this procedure. A small amount of soil of total mass M_i is placed in a small dish of known volume V_i and allowed to dry slowly. After the oven dry mass M_s is obtained, the volume of the dry soil V_{dry} is determined, and the shrinkage limit SL is calculated from

(a)
$$\text{SL} = \left(\frac{V_{\text{dry}}}{M_s} - \frac{1}{\rho_s}\right)\rho_w \times 100\,(\%) \tag{6.10}$$

or

(b)
$$\text{SL} = w_i - \left(\frac{(V_i - V_{\text{dry}})\rho_w}{M_s}\right) \times 100\,(\%) \tag{6.11}$$

The two equations correspond to the two parts of Fig. 6.13. Both may be readily derived from the figure and the phase relationships of Chapter 2.

Although the shrinkage limit was a popular classification test during the 1920s, it is subject to considerable uncertainty and thus is no longer commonly conducted. In the discontinued standard ASTM test D 427, the volume of the dry soil specimen is determined by weighing the amount of mercury the dry specimen displaces. Because mercury is a hazardous substance, special laboratory

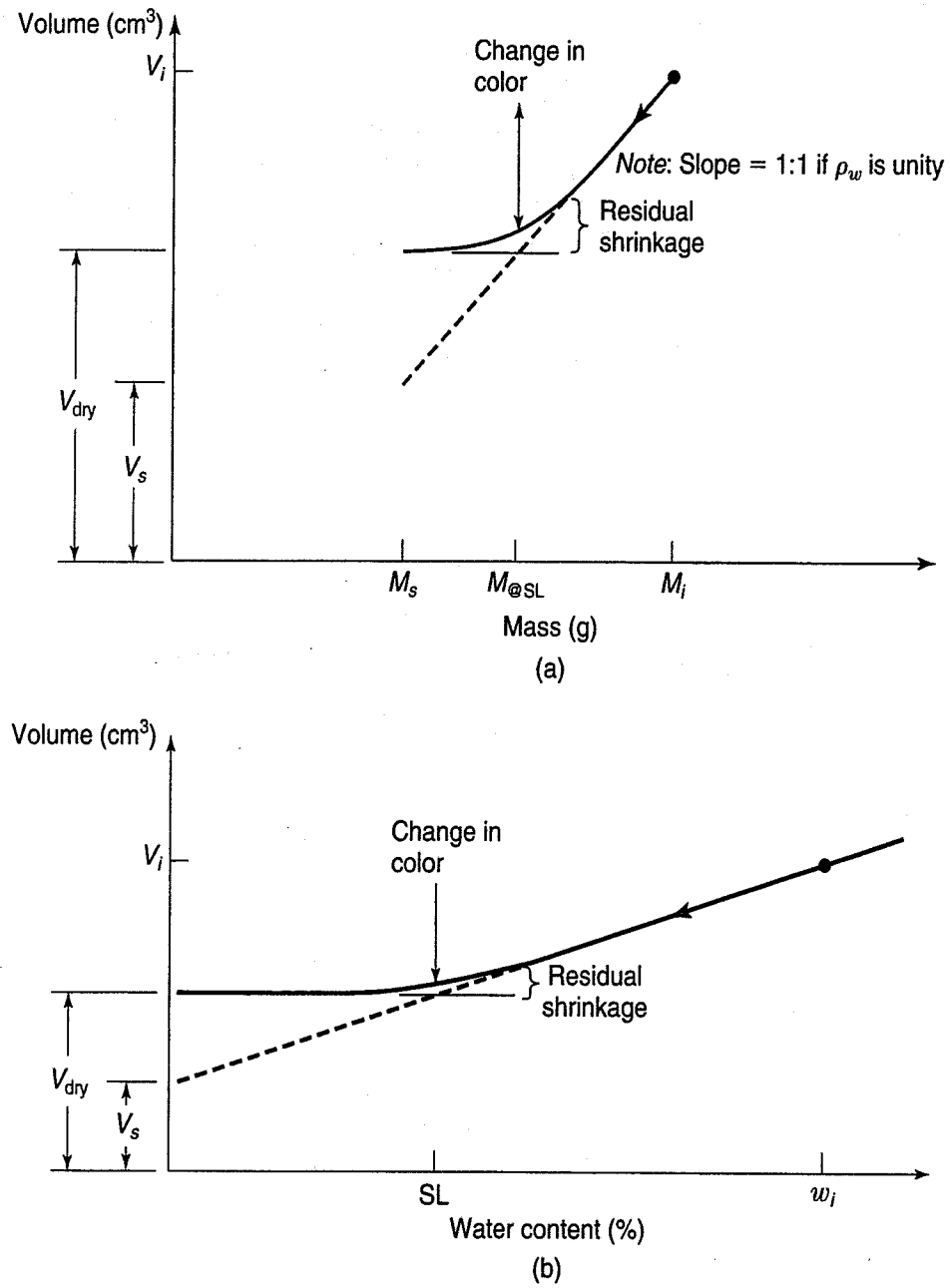

FIGURE 6.13 Determination of the shrinkage limit based on (a) total mass; and (b) water content.

handling and disposal procedures are required. Consequently, a wax-displacement procedure was developed and standardized in 1989 (ASTM D 4943). To prevent water absorption by the dry soil specimen, it is first coated with wax before being submerged in water to determine its dry volume. The British Geological Survey has developed an automated apparatus called a "Shrinkit" that uses a laser, a 3D moving platform, and a digital balance to measure the 3D shrinkage of a specimen 100 mm high and 100 mm in diameter (Hobbs and Jones, 2006).

One of the biggest problems with both shrinkage limit tests is that the amount of shrinkage and therefore the SL depends on the initial fabric of the soil. The standard procedures start with the water content above the liquid limit. However, especially with sandy and silty clays, this often results in a shrinkage limit greater than the plastic limit, which is meaningless, since the SL should be less than the PL (Fig. 2.8). Casagrande suggested that the initial water content be slightly greater than the PL, if

possible, but admittedly it is difficult to avoid entrapping air bubbles in soils at lower water contents. Besides air bubbles entrapped in the dry soil specimen, other problems with the SL test include errors resulting from specimen cracking during drying as well as weighing and other measurement errors.

If one follows Casagrande's advice and begins the test slightly above the plastic limit, then the Atterberg limits for the soil plot near the A-line on the plasticity chart (Fig. 2.13) and the shrinkage limit is very close to 20. If the limits plot above the A-line, then the SL is less than 20 by an amount approximately equal to the vertical distance (Δp_i) above the A-line. Similarly, for ML and MH (and OL and OH) soils, the shrinkage limit is greater than 20 by an amount approximately equal to Δp_i below the A-line where the limits plot. Therefore, the

$$\text{SL} = 20 \pm \Delta p_i \tag{6.12}$$

This procedure and equation have been found to be about as accurate as the shrinkage limit test itself because of all the problems with the test.

An even simpler procedure was suggested by Prof. A. Casagrande in his lectures at Harvard University. If the U-line and A-line of the plasticity chart (Fig. 2.13) are extended, they converge at a point with coordinates (−43.5, −46.4), as shown in Fig. 6.14. Then if a line is extended from that point to the coordinates of the liquid limit and plasticity index plotted on the plasticity chart, where that line crosses the liquid limit axis is approximately the shrinkage limit. Although not an exact procedure, it is close enough, considering the other inaccuracies we typically deal with as geotechnical engineers as well as the approximate nature of the shrinkage limit test. If you can obtain a reasonable estimate of the shrinkage limit from the plasticity chart, then the shrinkage limit test need not be performed, since it provides no additional information of value.

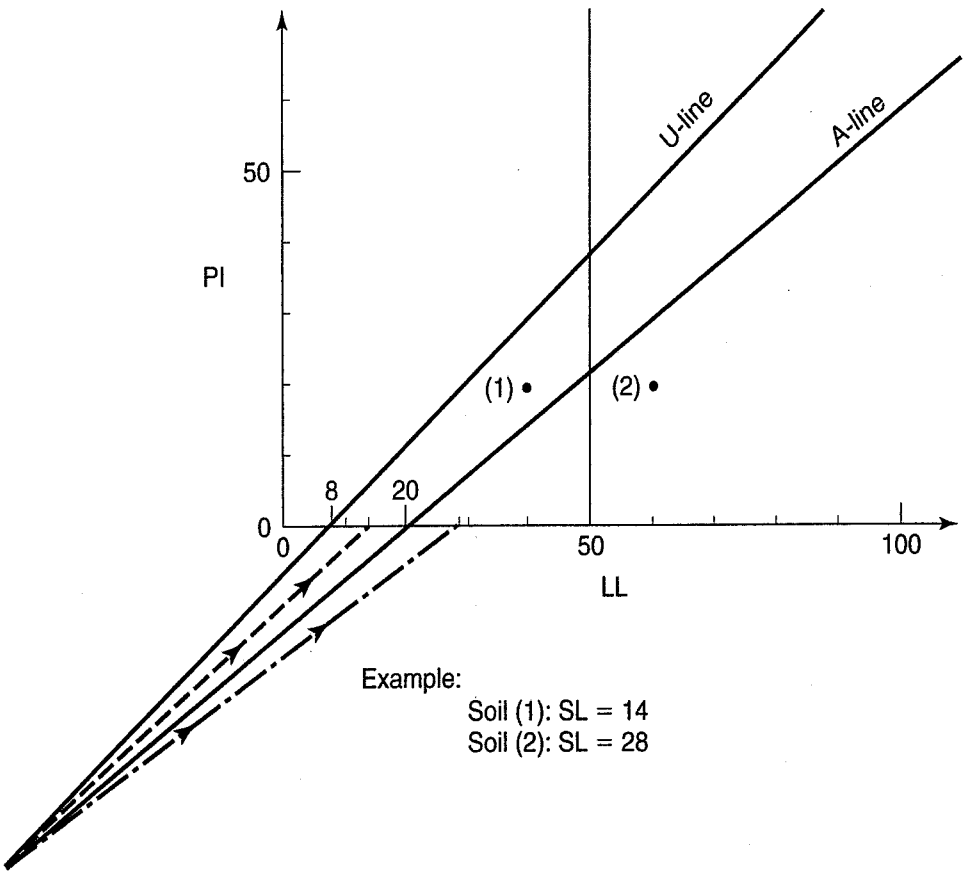

FIGURE 6.14 Casagrande's procedure for estimating the shrinkage limit.

Note that when their water contents are near the SL, very fine-grained clay soils with highly active clay minerals (those that plot near the U-line) experience very large capillary pressures. These soils will have shrinkage limits around 8, according to the Casagrande procedure. In fact, Prof. Casagrande observed shrinkage limits as low as 6 for montmorillonitic clays. Soils at the shrinkage limit will have a very low void ratio because the capillary pressures are so large; these pressures are, for example, much greater than can be achieved by compaction.

Example 6.5

Given:

A clay soil with a shrinkage limit of eight.

Required:

Assuming $\rho_s = 2.70\ \text{Mg/m}^3$ and $S = 100\%$, calculate the void ratio and dry density of the soil.

Solution: Use Eqs. (2.12) and (2.15)

$$e = \frac{w\rho_s}{\rho_w} = \frac{0.08(2.70\ \text{Mg/m}^3)}{1\ \text{Mg/m}^3} = 0.22$$

$$\rho_d = \frac{\rho_s}{1+e} = \frac{2.70\ \text{Mg/m}^3}{1.22} = 2.21\ \text{Mg/m}^3 = 137.9\ \text{lbf/ft}^3$$

The density of concrete is about 2.4 Mg/m^3. Thus you can see that the capillary pressures must be very large to cause soil to become so dense at the SL. It should not be surprising, then, that some clay soils have very high dry strengths, and that dry strength is a good indicator of the presence of active clay minerals. In fact, in Sec. 2.9.1 on visual-manual soil classification, we said that high dry strength is characteristic of a CH clay.

One way to show that high capillary pressures can exist in soils is to allow a fat (CH) clay soil at a high water content to dry slowly on your skin. The high shrinkage pressures will actually cause some pain; in fact, this process was used during ancient times as a torture system. A human body covered with clay drying slowly in the sun has ultimately very little resistance to pressures that can reach several atmospheres! (See Example 6.3.)

6.4.3 Shrinkage Properties of Compacted Clays

As shown in Fig. 6.15, soil specimens compacted wet of optimum have greater shrinkage than those compacted dry of optimum. As illustrated in the upper part of the figure, different methods of compaction influence the magnitude of shrinkage, because they produce different soil fabrics. Go back and reread Sec. 5.4 on the structure of compacted clays.

Results of shrinkage tests performed on a compacted silt and a glacial till are shown in Fig. 6.16 (Ho and Fredlund, 1989). By plotting void ratio e versus the product of water content and specific gravity wG_s, this figure shows that shrinkage is occurring as the water content and degree of saturation decrease. Note too that the amount of shrinkage depends on the soil type and on the initial water content. The higher PI glacial till shrinks more than the silt, and both soils have more shrinkage when compacted at optimum water content than when compacted dry of optimum. For additional information on shrinkage and shrinkage test procedures, see Fredlund and Rahardjo (1993).

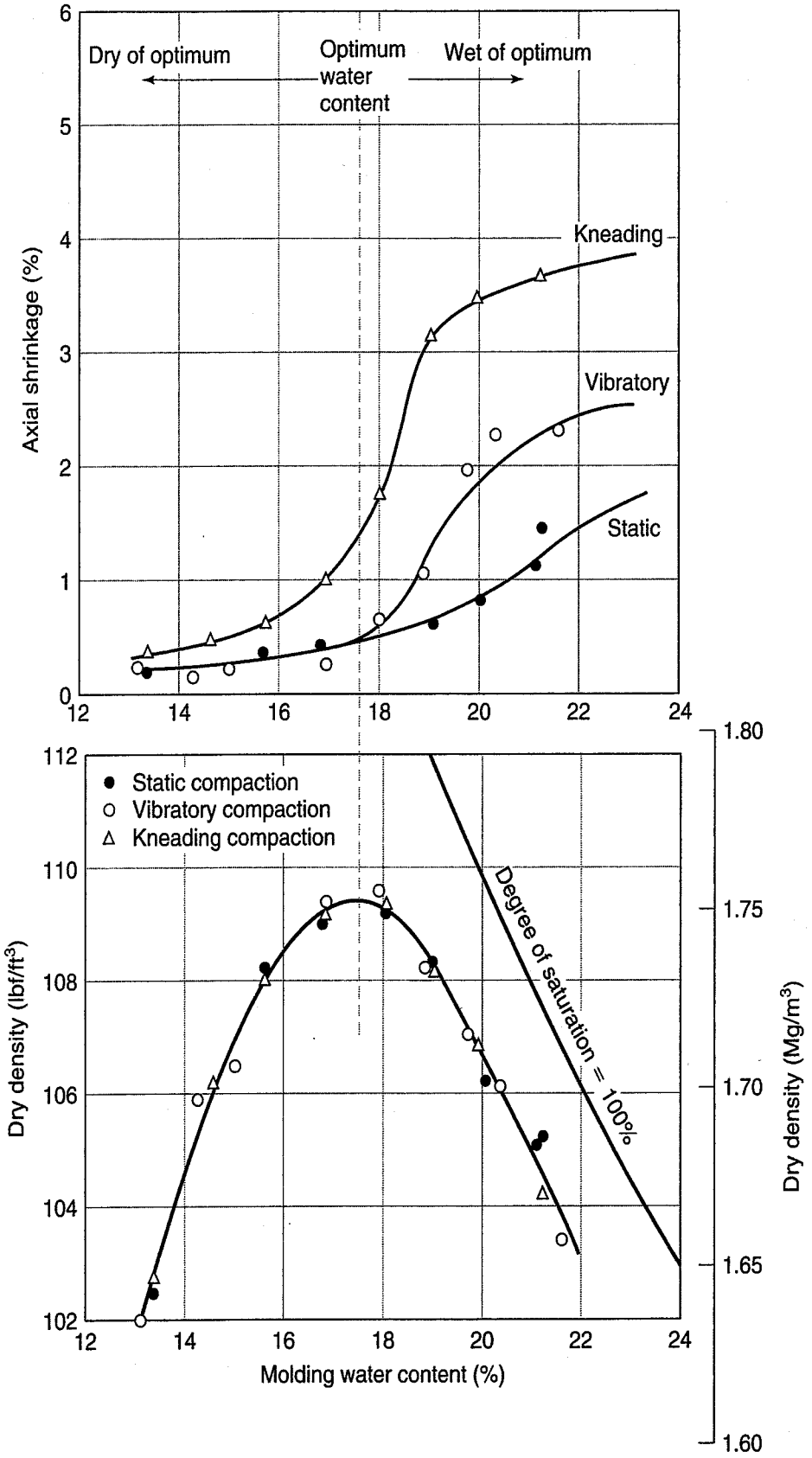

FIGURE 6.15 Shrinkage as a function of water content and type of compaction (after Seed and Chan, 1959).

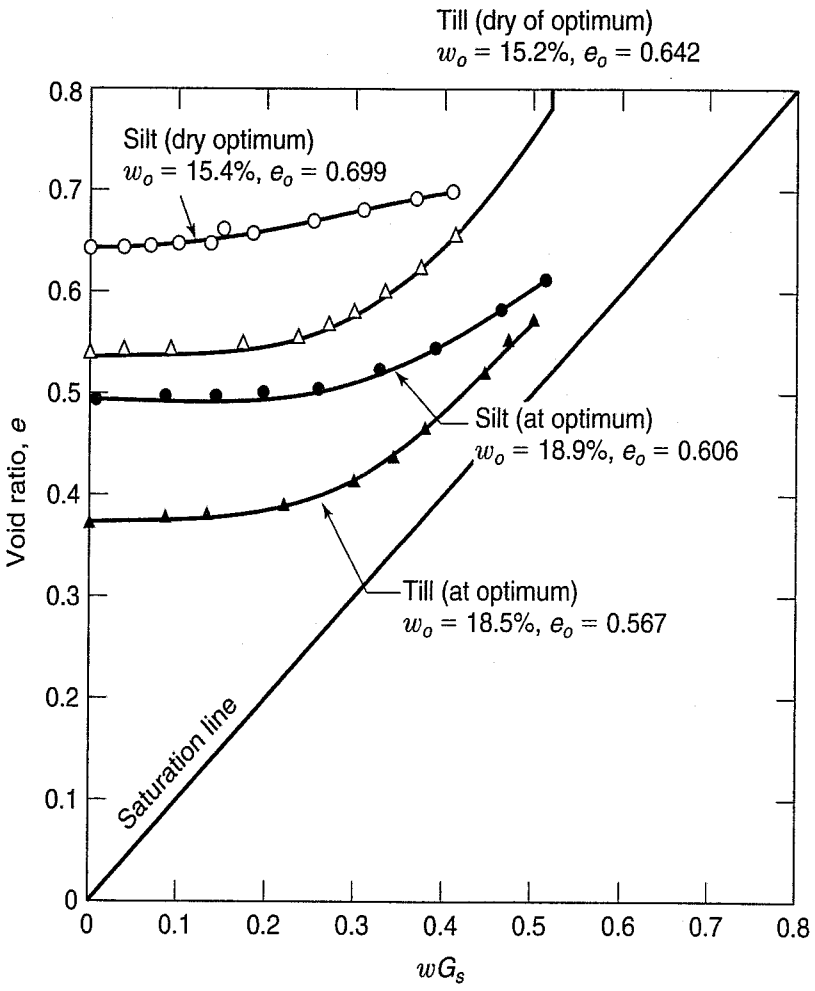

FIGURE 6.16 Shrinkage characteristics of a compacted silt and glacial till (Ho and Fredlund, 1989).

6.5 EXPANSIVE SOILS AND ROCKS

Any soil or rock material that has the potential for significant volume change because of an increase in water content is called an *expansive soil* (Nelson and Miller, 1992). Sometimes these materials are called *swelling* soils or rocks. As mentioned above, in areas where they are locally abundant, expansive soils cause literally billions of dollars of damage each year to light structures and pavements. Expansive rocks also cause serious problems during construction of excavations and tunnels.

Expansive soils are found throughout the world. They are very common in large areas of the North American continent, southern as well as sub-Saharan Africa, large parts of Australia, western India, and the Mideast. In the United States, expansive soils are important in areas of desiccated and highly overconsolidated fine-grained soils and weathered shales. This includes the Dakotas, Montana, eastern Wyoming and Colorado, the four-corners area of the Southwest, parts of California, and East Texas. In the western provinces of Canada between the Rocky Mountains and the Great Lakes are huge areas of Cretaceous clay-shales and clays that contain significant amounts of active clay minerals, particularly smectite. These deposits are often highly expansive, as are the lacustrine clay deposits found in the large Pleistocene glacial lakes, such as Glacial Lakes Agazziz and Regina in Saskatchewan and Manitoba.

Because the climate in most of the central North American continent is arid or semi-arid, the natural water content regime is often changed by human development and construction, irrigation, and vegetation, and this leads to problems with light structures and pavements.

Figure 6.17 shows the extent of potentially expansive soils in the United States. Because of their small scale, these maps can give only a very general idea of potential problem areas, but at least you

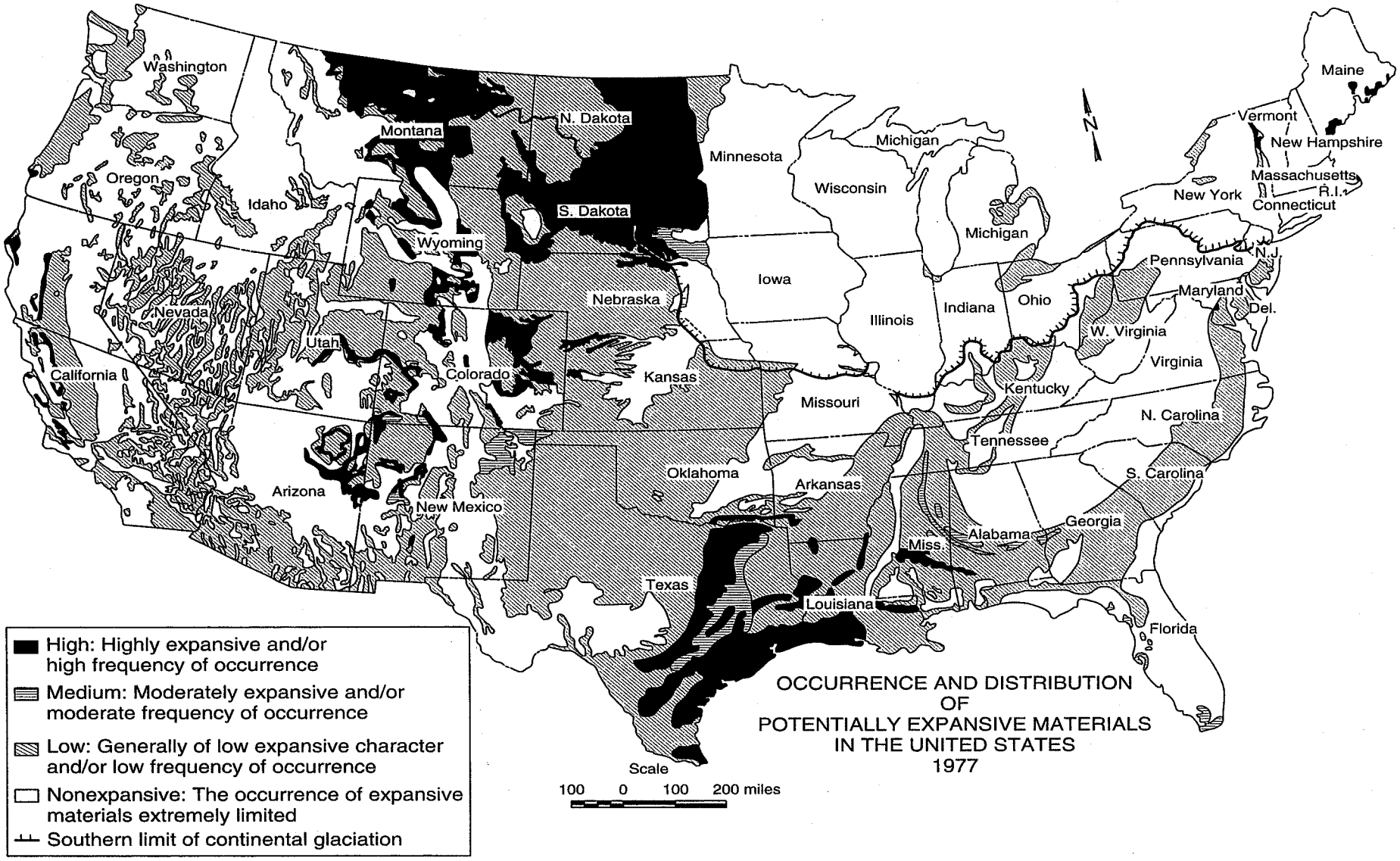

FIGURE 6.17 Occurrence and distribution of potentially expansive soils in the United States (after U.S. Army Engineer Waterways Experiment Station as presented by Nelson and Miller, 1992).

can see that for many localities, swelling soils can be a serious problem. Thus it is important that you understand some of the characteristics of swelling soils, how to identify them, and what to do about them if you are unfortunate enough to find them on one of your projects.

6.5.1 Physical-Chemical Aspects

Although fundamentally related to shrinkage, swelling soils are usually treated as a separate subject, largely because swelling is a somewhat more complex process than shrinkage (Yong and Warkentin, 1975). Remember that for a soil to shrink, it has to lose water through desiccation. It is just the opposite for a swelling soil–it has to have access to water and contain minerals that will imbibe water.

Swelling soils usually contain clay minerals of the smectite group such as montmorillonite and vermiculite (Chapter 4), although other active minerals such as mixed layer minerals may also contribute to swelling. These soils exhibit a very high dry strength and high plasticity, are often shiny in appearance when cut by a knife blade, have relatively deep shrinkage cracks, and when wet have a very low shear strength (Chapter 12). All of these conditions are indicative of a potentially swelling soil.

The amount of swelling and the magnitude of the resulting swelling pressure depend on the clay minerals present in the soil, the soil structure and fabric, and several physical-chemical aspects of the soil that were discussed in Chapter 4. These include factors such as the cation exchange capacity, cation valence, salt concentration, cementation, and presence of organic matter. Everything else being equal, montmorillonites swell more than illites, which swell more than kaolinites. Soils with random fabrics tend to swell more than soils with oriented fabrics. Disturbance of or remolding of old natural clays may increase the amount of swelling. Monovalent cations in a clay (for example, sodium montmorillonite) will swell more than divalent cations (for example, calcium montmorillonite). Cementation and organic substances tend to reduce swelling.

Practically speaking, the three ingredients necessary for potentially damaging swelling to occur are (1) presence of expansive clay minerals, especially montmorillonite, in the soil, (2) the natural water content at approximately the PL, and (3) a source of water for the potentially swelling clay (Gromko, 1974). Nelson and Miller (1992) also point out that swelling potential is enhanced by the presence of salt cations (e.g., sodium, calcium, magnesium, and potassium) in the pore water, because the hydration of these cations can lead to large amounts of water between clay particles. For additional information on the physical-chemical aspects of expansive clays, see Mitchell and Soga (2005) and Fredlund and Rahardjo (1993).

6.5.2 Identification and Prediction

How do engineers know if the soils and rocks at a site are expansive? Many methods and procedures have been developed over the years to identify expansive geo-materials and to predict their potential for swelling. These methods include chemical and mineralogical analyses, correlations with the classification and index properties, and laboratory tests that measure swelling pressure and volume changes.

We mentioned above that the smectite minerals (e.g., montmorillonite, vermiculite) are the most highly expansive, and as described in Sec. 4.4, these minerals can be identified by X-ray diffraction, differential thermal analyses, electron microscopy, and cation exchange capacity. Soils that contain these minerals usually plot high above the A-line and just below the U-line on the plasticity chart (Fig. 4.14).

Once identified, it is important to assess their swelling potential, and probably the most common way to do this is to use classification and index tests. Table 6.2 summarizes the experience of the U.S. Dept. of the Interior based on their research on swelling clays and expansive soils (Holtz, 1959). Figure 6.18 shows four other expansion prediction procedures based on index and other properties. For example, Kay (1990) showed that the percent expansion correlated quite well with the liquid limit (range: $20 < LL < 100$) for expansive soils in southeastern Australia. Gromko (1974) and Nelson

TABLE 6.2 Expansion Potential from Classification Test Data

Degree of Expansion	Probable Expansion as a Percent of Total Volume Change (Dry to Saturated Condition)†	Colloidal Content (% −1 μm)	Plasticity Index, PI	Shrinkage Limit, SL
Very high	>30	>28	>35	<11
High	20–30	20–31	25–41	7–12
Medium	10–20	13–23	15–28	10–16
Low	<10	<15	<18	>15

†Under a surcharge of 6.9 kPa (1 psi).

After Dept. of the Interior (1998) and Holtz (1959).

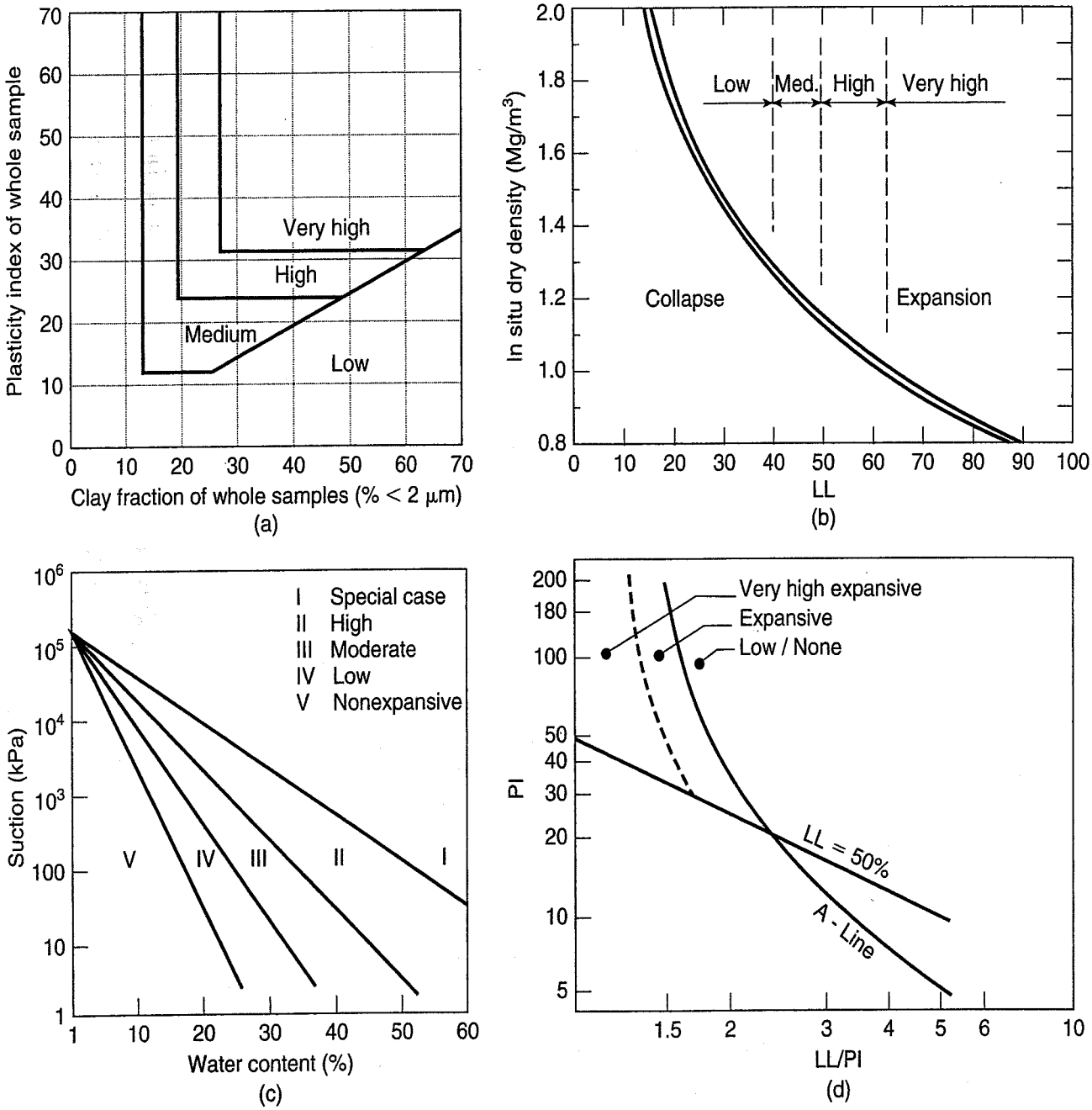

FIGURE 6.18 Soil expansion prediction based on: (a) activity (van der Merwe, 1964); (b) in situ dry density and liquid limit (adapted from Mitchell and Gardner, 1975, and Gibbs, 1969); (c) suction versus water content (McKeen, 1992); (d) log PI versus log LL/PI (Marin-Nieto, 1997 and 2007).

and Miller (1992) provide additional correlations with soil classification properties that have been successfully used to predict swelling potential.

Several laboratory tests have been developed to measure soil expansion in both compacted soils as well as in specimens of undisturbed or natural soils. We will describe only a few of the more common tests; for details about other laboratory tests, see Nelson and Miller (1992).

One fairly simple swelling identification test is the *free-swell test* developed by the U.S. Bureau of Reclamation (Holtz and Gibbs, 1956). The test is performed by slowly pouring 10 cm^3 of dry soil, which has passed the 425 mm (No. 40) sieve, into a 100 cm^3 graduated cylinder filled with water, and observing the equilibrium swelled volume. Free swell, expressed as a percentage, is defined as

$$\text{free swell} = \frac{(\text{final volume}) - (\text{initial volume})}{\text{initial volume}} \times 100\,(\%) \tag{6.13}$$

For comparison, highly swelling bentonites (mostly Na-montmorillonite) will have free-swell values of greater than 1200%. Even soils with free swells of 100% may cause damage to light structures when they become wet; soils with free swells less than 50% have been found to exhibit only small volume changes.

Although the free swell test seems to be very simple, it has some problems, and it is no longer a standard USBR test. Sridharan and Prakash (2000) point out that obtaining exactly 10 cm^3 of soil is not easy, and they suggest using 10 g of dry soil in carbon tetrachloride or kerosene as well as distilled water for comparison.

The *expansion index (EI) test* was developed for compacted soils in southern California, and it is the basis for ASTM (2010) standard D 4829. The soil is passed through the No. 4 sieve and moistened to a water content close to its optimum. It is compacted in a very stiff steel ring about 25 mm high by 100 mm in diameter, and a vertical confining pressure of 6.9 kPa (1 psi) is applied to it; then the soil specimen is inundated with distilled water. The deformation (expansion) of the specimen is recorded for 24 hr, or until the rate of deformation reaches a minimum value. The expansion index, EI, is defined as 1000 times the change in height of the specimen divided by the initial height. Table 6.3 gives the expansion potential for various expansion index (EI) ranges.

ASTM (2010) standard D 4546 is another test for determining the swell potential of compacted soil specimens as well as undisturbed soil samples. This test permits either constant or varying applied vertical pressures and different inundation times. The apparatus used is the one-dimensional consolidometer described in Chapter 8. A specimen of soil is confined in a stiff brass or stainless steel ring, usually about 20 to 25 mm high and 50 to 100 mm in diameter. For the free-swell test, the specimen is loaded with a small seating load of 1 kPa, inundated, and the change in height is observed. The results are reported as "free-swell" strain for a given vertical pressure.

A variation of the free-swell test is to keep loading the specimen after it is inundated so that the height of the specimen remains constant and measure the pressure required to maintain a constant

TABLE 6.3 Expansion Potential for Given Expansion Index Ranges

EI	Expansion Potential
0–20	Very low
21–50	Low
51–90	Medium
91–130	High
>130	Very high

After ASTM (2010), Nelson and Miller (1992).

volume. Still another variation is to apply an initial stress equal to the estimated in situ vertical pressure and then, after inundation, apply increments of load required to prevent any change in specimen height. The vertical stress necessary to maintain zero volume change is reported as the *swelling pressure*. USBR tests 5705 and 5715 are similar in concept to ASTM D 4546, but they differ in some details such as loading and unloading procedures.

Another method for quantifying the expansion potential of soils is through the use of the *coefficient of linear extensibility* (COLE) test, described by Nelson and Miller (1992) and used by the U.S. Natural Resources Conservation Service. This test basically determines the linear strain (shrinkage or expansion) of a natural clay specimen dried in unconfined conditions from 33 kPa (5 psi) suction to oven-dry suction ($\approx$1000 MPa). The COLE value, expressed as a percentage, is used to predict expansion potential of soils with active clay minerals.

6.5.3 Expansive Properties of Compacted Clays

The swelling behavior of compacted fine-grained soils is not so simple. As with natural soil deposits, the tendency of compacted soils to expand depends on their fabric, and their fabric depends on whether they are compacted wet or dry of the optimum water content. You will recall from Chapter 5 that the optimum water content is a function of the mechanical energy applied ("compactive effort") during compaction. Generally, a soil compacted dry of optimum will have a more random (or flocculated) fabric than those compacted wet of optimum. However, the fabric also depends on the method of compaction. If the soil is repeatedly sheared during compaction—e.g., in impact (Proctor) compaction, rather than simply compressed statically, then the fabric tends to be more oriented than random, and this happens more when the soil is wet of optimum than dry.

So how does all this affect swelling? Fine-grained soils compacted dry of optimum expand more than if they are compacted wet. This is because they have a relatively greater water deficiency, and thus they have a greater tendency to adsorb water and swell more. Greater capillary pressures in the macropores of a random fabric of a soil dry of optimum also play a role. If the soil is compacted wet of optimum, expansion will be about the same (i.e., a random fabric will behave similarly to an oriented fabric), because the affinity for water is already satisfied. Therefore, there is generally less swelling on the wet than on the dry (flocculated) side, and this is shown in Fig. 6.19 for a high plasticity soil compacted at standard Proctor compaction. Soils compacted dry of optimum are in general more sensitive to environmental changes, such as changes in water content. The amount of expansion also depends on whether the clay is surcharged and on the magnitude of the load relative to the swelling pressure. This is shown in test results on compacted specimens of a highly expansive clay from the central valley of California (Fig. 6.20).

Seed, Woodward, and Lundgren (1962) developed the relationships shown in Fig. 6.21 for artificial mixtures of sands and clays compacted to maximum density by standard Proctor compaction and allowed to swell against a 6.9 kPa (1 psi) surcharge. These relationships between activity and percent clay sizes have also been shown to be fairly good for many natural soils. The purpose of Fig. 6.21 is to identify a compacted soil that is potentially swelling and that may require further investigation and laboratory testing. Figure 6.21 should not be used for design.

6.5.4 Swelling Rocks

According to Goodman (1989), only a few minerals are responsible for swelling in rocks and associated engineering problems. As you might expect, the clay minerals montmorillonite and vermiculite are problems when they are found in rock joints. Another problem mineral is anhydrite (or, more accurately, anhydrous calcium sulfate, $CaSO_4$). In addition, some basalts (fine-grained volcanic rock) and salts found in evaporite deposits can swell sufficiently to create problems for overlying or adjacent structures. We are already familiar with montmorillonite (Chapter 4) and its ability to adsorb water

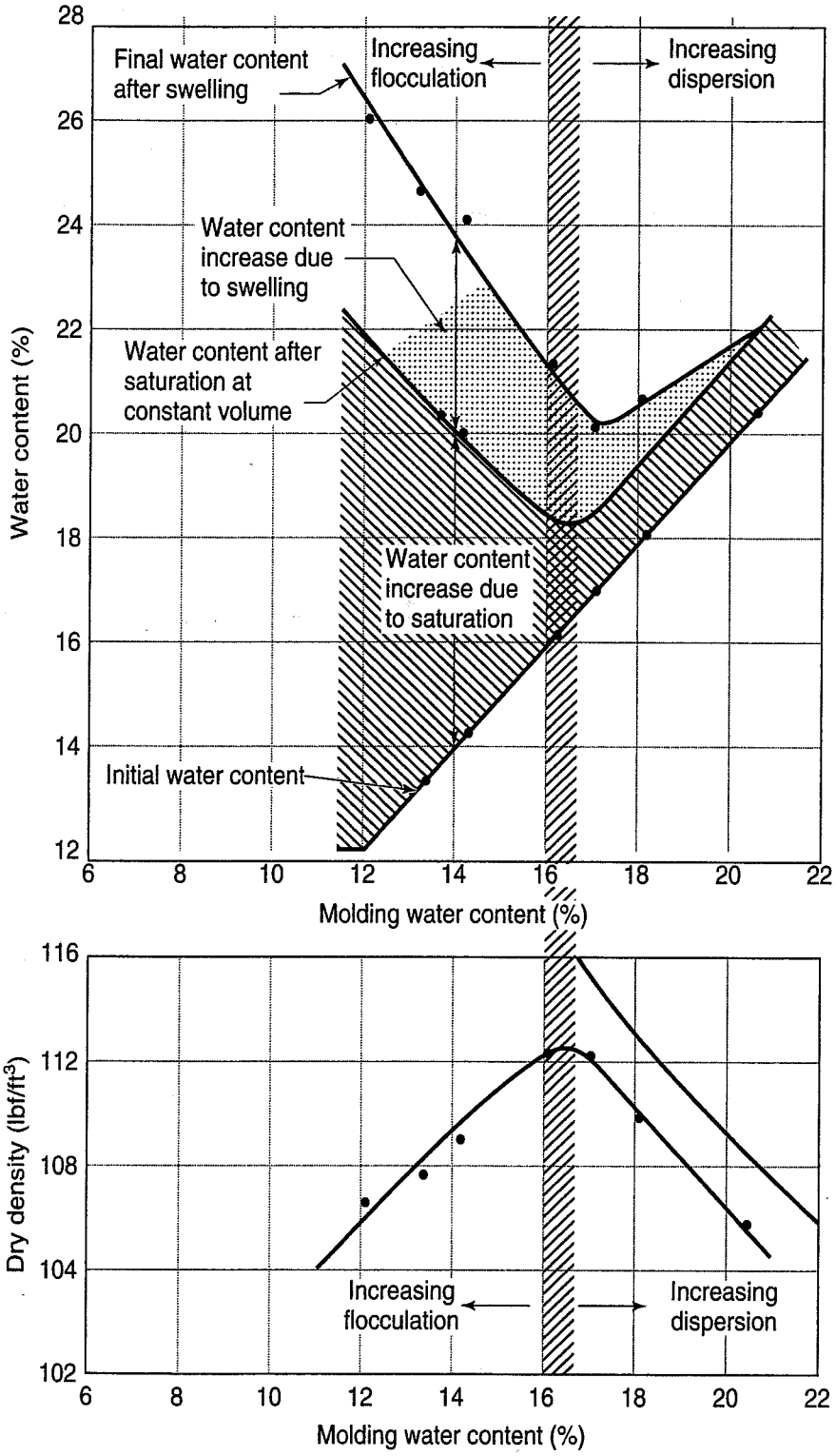

FIGURE 6.19 Influence of molding water content and soil structure on the swelling chartacteristics of a sandy clay (Seed and Chan, 1959).

many times its own particle thickness (see Fig. 4.16). When montmorillonite is the principal clay mineral in claystone and shale, and it has access to an adequate supply of water, it can overcome cementation forces and expand considerably. Anhydrite is contained in deposits of galena and pyrite, among other rock types, and converts to gypsum when exposed to water. Vermiculite results from hydration of certain basalts and has a variety of commercial applications.

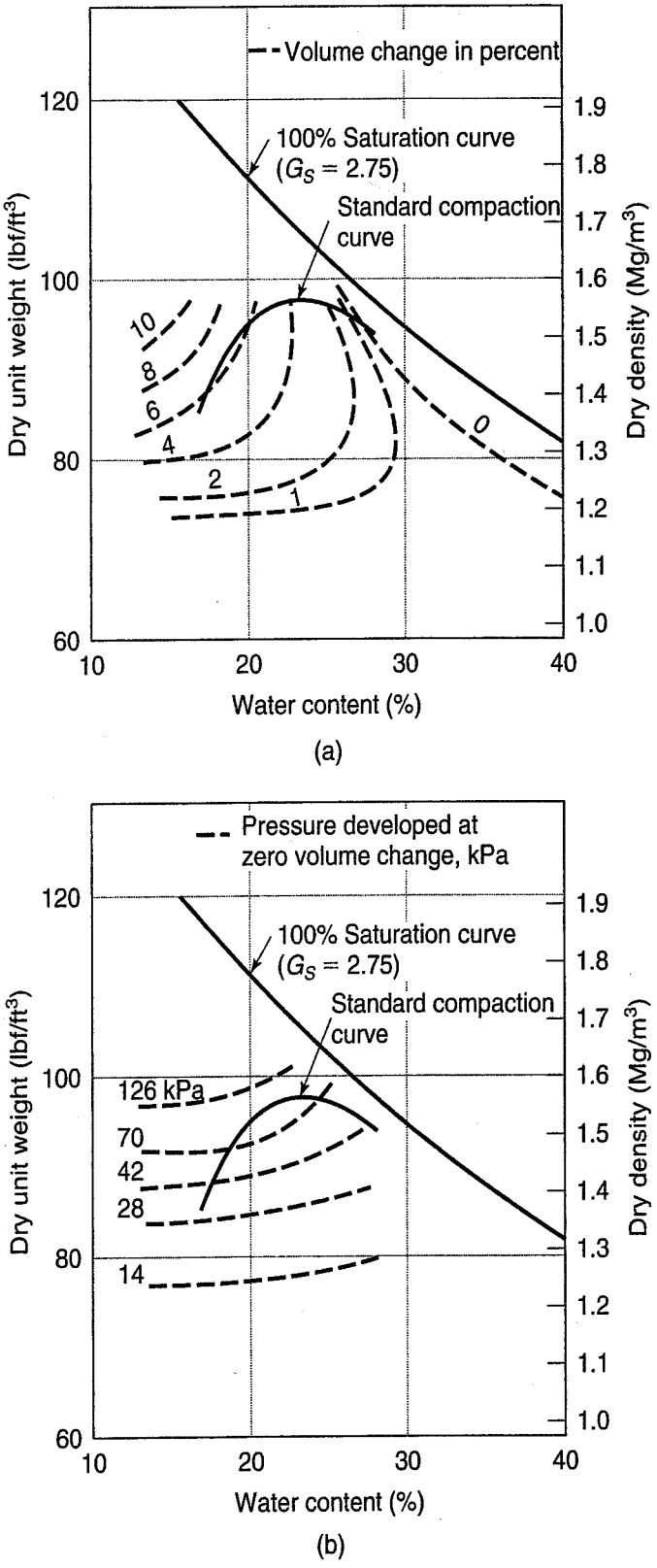

FIGURE 6.20 Effects of placement water content and dry density on the expansion characteristics of a CH clay from the Delta-Mendota Canal, California: (a) percent expansion for various placement conditions under 7 kPa; (b) total uplift pressure at zero volume change caused by wetting for various placement conditions (U.S. Dept. of the Interior, 1998).

Rock can be tested for its swelling potential in a manner similar to that for clays, as described in the preceding section. Goodman (1989) suggests placing a dry rock specimen in a stiff consolidometer ring with some initial vertical stress applied to it, and then exposing it to water, during which the vertical stress and deformation are monitored. Figure 6.22 shows the results from swelling tests on two rock types, the well-known Bearpaw shale from Montana and Wyoming and a Norwegian "fault gouge" (the pulverized rock produced when two sides of a fault move past each other).

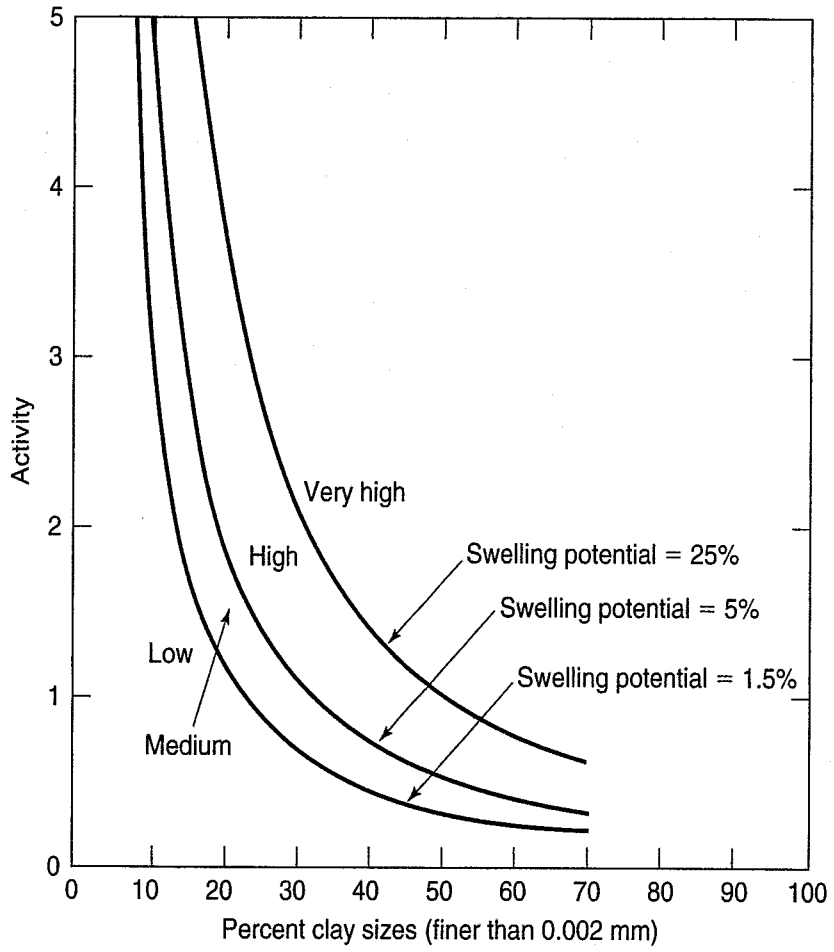

FIGURE 6.21 Classification chart for swelling potential of compacted clays (after Seed et al., 1962).

6.6 ENGINEERING SIGNIFICANCE OF SHRINKAGE AND SWELLING

Several times in this chapter we have mentioned the enormous costs of damage caused by shrinking and swelling soils to pavements, light structures such as houses, and other infrastructure. The damage is rarely life threatening, but nonetheless it is important because of compromised serviceability, aesthetics, and the costs of repair and maintenance. Estimates of the damage costs caused by shrinking and swelling soils range from about $10 to as much as $13 *billion* annually in the United States alone. To put this in perspective, this cost is more than twice the annual cost of damage from floods, hurricanes, tornadoes, and earthquakes combined!

The volume changes resulting from both shrinkage and swelling of fine-grained soils are often large enough to seriously damage small buildings and highway pavements. A common occurrence is that a pavement or building is constructed when the top soil layer is relatively dry. The structure covering the soil prevents further evaporation, and the soil increases in water content due to capillarity. If the soil is expansive, it may swell, and if the vertical stress exerted by the pavement or building is less than the swelling pressure, heave will result. Heave is usually uneven and differential, and often cosmetic or even structural damage results.

The effects of shrinkage of fine-grained soils can be significant from an engineering point of view. Shrinkage cracks can occur locally when the capillary pressures exceed the tensile strength of the soil. These cracks, part of the clay macrostructure (Chapter 4), are zones of weakness that can reduce the overall strength of a soil mass and affect, for example, the stability of clay slopes and the bearing capacity of foundations. The desiccated and cracked dry crust usually found over deposits of soft clay affects the stability of highway and railroad embankments constructed on these deposits. Shrinkage and shrinkage cracks are caused by evaporation from the surface in dry climates, lowering

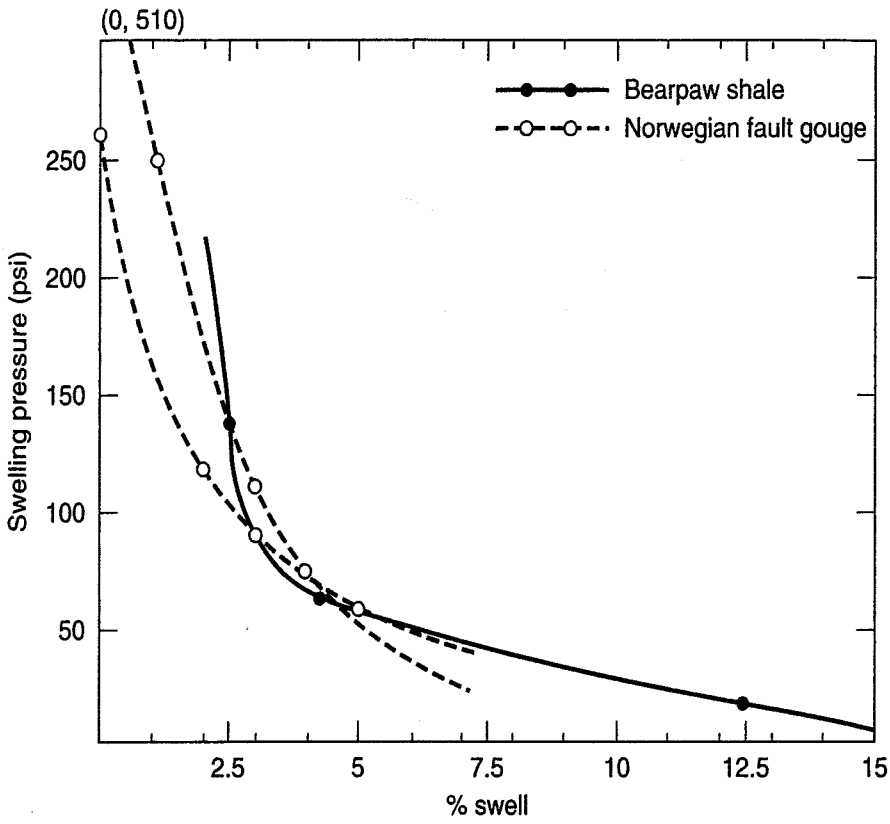

FIGURE 6.22 Swelling test results for Bearpaw shale and fault gouge from Norway (Goodman, 1989).

of the groundwater table, and even desiccation of soil by trees and shrubs during temporary dry spells in otherwise humid climates. When the climate changes and the soils have access to water again, they tend to increase in volume or swell. Bozozuk (1962) describes several examples of the type of damage to structures on clay foundations caused by soil shrinkage, including that caused by trees and vegetation. Because of transpiration, water is drawn from the surrounding soils by the plants' root systems, and this causes soil shrinkage and differential settlements. For case histories of successful treatment of settlement problems caused by vegetation, see Wallace and Otto (1964) and several papers in Vipulanandan et al. (2001).

Swelling, like shrinkage, is generally confined to the upper portions of a soil deposit. Thus, swelling damages light structures such as small buildings, highway pavements, and canal linings. Swelling pressures as high as 1000 kPa have been measured, which is equivalent to an embankment thickness of 40 to 50 m. Ordinarily, such high pressures do not occur, but even with more modest swelling pressures of 100 or 200 kPa, for example, an embankment of 5 or 6 m would be required to prevent all swelling of the subgrade. (For comparison, an ordinary building imposes a stress something on the order of 10 kPa per story.)

The process of shrinking and swelling is not completely reversible—the soil always has a memory of its stress history and will show the effects of previous shrinkage and drying cycles. Thus soft clays become what is called *overconsolidated* and less compressible because of the increase in effective stress caused by capillary action. Overconsolidation is discussed in Chapter 8.

Since the potential damage to light structures and pavements due to shrinkage and swelling of soils is so great, the engineer must pay special attention to this problem, if it is suspected that such soils exist at a site.

What can engineers do to prevent damage to structures from shrinking and swelling soils? If it is impractical to simply avoid swelling soils or to excavate and replace them with a suitable nonswelling fill, then your alternatives are (1) structural or (2) some type of soil treatment. The structural alternative is either a foundation design that isolates the superstructure from soil deformations, or a foundation

that is stiff enough to resist differential settlements that might damage the superstructure. For example, the structure can be placed on driven or bored piles that extend through the expansive soil to a stable, underlying stratum. Sometimes the bored piles are "belled" or widened at the bottom to serve as anchors to prevent the foundation from lifting up during expansion of the overlying soil. To reduce uplift shear stresses on the upper part of the piles, they may be isolated from the swelling zone. Also a gap is sometimes built between this type of foundation and the structure to allow the ground surface to move without taking the superstructure with it.

As for soil treatment, there are three ways to modify the behavior of expansive soils: (1) moisture control, (2) prewetting, and (3) chemical stabilization. If expansive soils deform due to seasonal moisture fluctuations, then one way to minimize this movement is to use a system of drains around the foundation to channel surface and groundwater away from the area. Horizontal and/or vertical barriers can also be installed to minimize water movement into the problem soil. Prewetting suspected problem soils will allow potentially damaging swelling to take place prior to construction. Moisture barriers and waterproof membranes have been used to prevent water from reaching the swelling soil. Chemical stabilization, most commonly with lime (CaO), has also been successfully employed to reduce swelling, especially of sodium montmorillonitic clays. The reason why it works is discussed in Chapter 4. Other stabilizing agents such as Portland cement are sometimes used. You should be aware, however, that not all lime and cement stabilization is successful, especially if sulfates are also present in the expansive soils. A crystalline substance called *ettringite* is produced, and this causes subsequent undesirable heaving in floor slabs and other light structures (Puppala et al., 2005). The heaving can occur months or even years after an apparently successful stabilization of the foundation.

For additional practical information about all types of construction on expansive soils, see Chen (1988), Nelson and Miller (1992), U.S. Department of the Army (1983), and Noe et al. (2007).

6.7 COLLAPSIBLE SOILS AND SUBSIDENCE

Some soils exist that are stable and able to support significant structural loads when dry. But if their water content increases significantly, they undergo a very large decrease in volume, even without a change in the surface load. These soils are called *collapsible soils*. As you might imagine, sudden unexpected settlements can be very detrimental to structures founded on collapsible soils. Thus, it is important in advance of construction to identify sites that are likely have collapsible soils so that appropriate treatment measures can be instituted.

Examples of collapsible soils include loess (windblown silts and sands, Sec. 3.3.6), weakly cemented sands and silts, and certain residual soils. Other collapsible soils are found in alluvial flood plains and fans as the remains of mudflows and slope wash and colluvial slopes. Many but not all collapsible soil deposits are associated with arid or semi-arid regions (such as the southwest United States and California). Some dredged materials are collapsible, as are those deposited under water, in which the sediment forms at very slow rates of deposition (Rogers, 1994). As a consequence of their deposition, these deposits have unusually high void ratios and low densities. All soil deposits with collapse potential have one thing in common. They possess a loose, open, *honeycomb* structure [Fig. 4.29(c)] in which the larger bulky grains are held together by capillary films, montmorillonite or other clay minerals, or soluble salts such as halite, gypsum, or carbonates.

An example of collapsing soil behavior is shown in Fig. 6.23. Two specimens of loess, one at a low dry density and one at a higher dry density, are gradually loaded to about 700 kPa. Then water is added, and as shown in the figure, collapse occurs. This results in a large decrease in void ratio and a concurrent increase in dry density. As expected, the lower-density specimen experiences larger settlements than the denser specimen.

One way to assess the collapse potential of various soils, based on USBR experience, is shown in Fig. 6.24. Soils with an in situ dry density ρ_d and a liquid limit LL to the left of the two lines should be

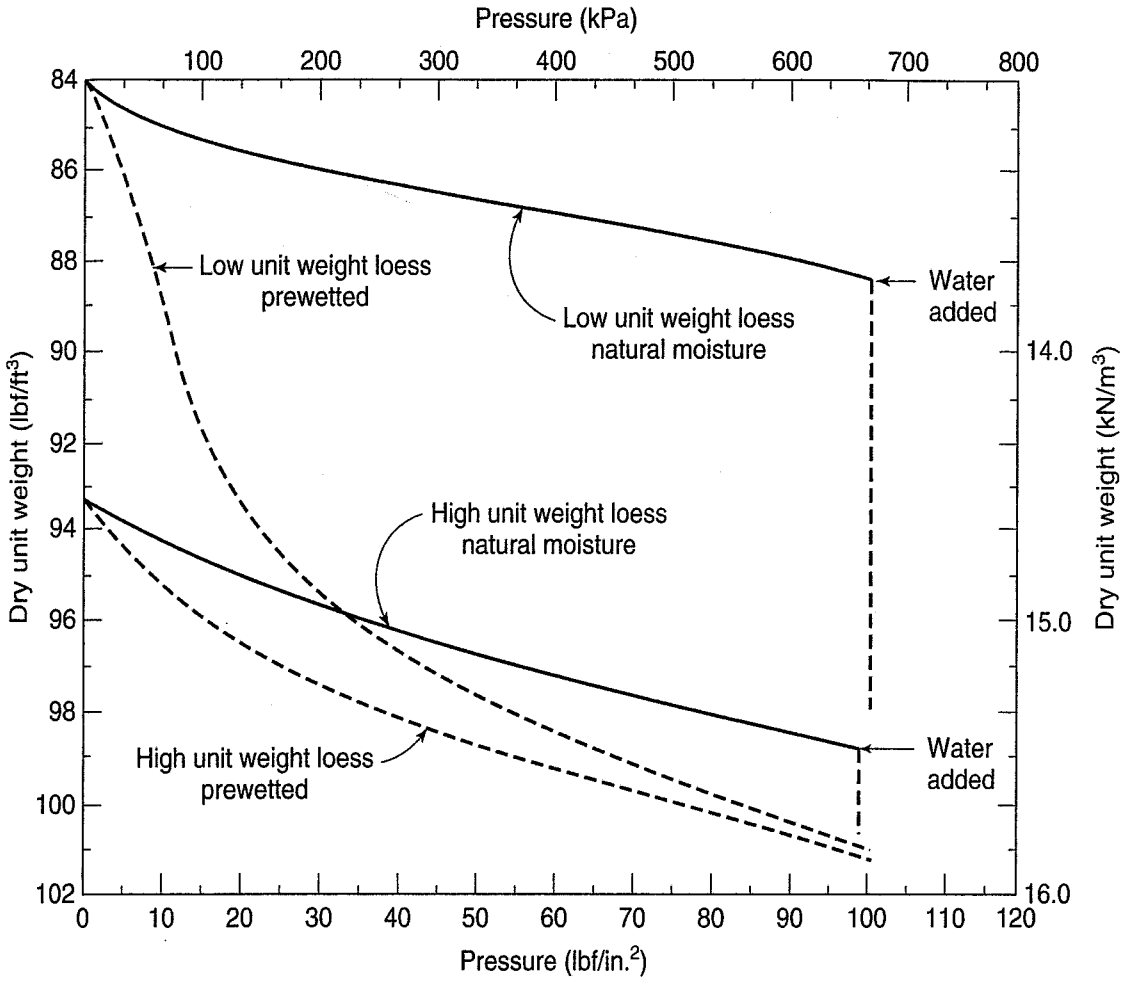

FIGURE 6.23 Effect of loading and wetting high and low unit weight loess soil foundations (U.S. Dept. of the Interior, 1998).

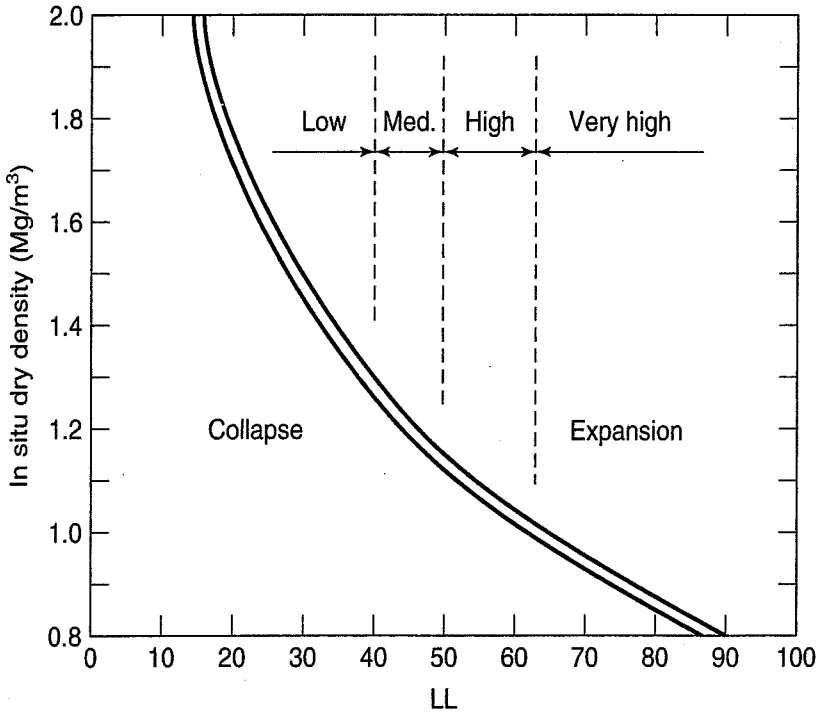

FIGURE 6.24 Collapsibility based on in situ dry density and liquid limit (adapted from Mitchell and Gardner, 1975, and Gibbs, 1969).

investigated further for their collapse potential. The lower curve is for soils with a specific gravity G_s of 2.60 and the upper curve is for $G_s = 2.70$.

Collapse potential of a natural soil can be determined by a ASTM (2010) standard D 5333, which is fundamentally the same as the one-dimensional swell test D 4829 described in Sec. 6.5.2. However, in the case of the collapse potential test, an undisturbed soil sample at its natural water content is placed in the consolidometer ring (Chapter 8), and vertical stress increments are applied each hour until the design stress is achieved. Then the specimen is flooded with water, and the *reduction* in specimen height is measured (versus the increase in height that occurs in the swelling test). The *collapse potential*, I_c(%), is simply the percent strain at the stress level tested, or sometimes the *collapse index* is used, which is defined as the relative magnitude of strain at 200 kPa. The collapse index can be correlated to the degree of specimen collapse, as given in Table 6.4. Another way to identify collapsible soils is by the fall cone test (Ayadat and Hanna, 2007).

An extensive review of the identification and treatment of collapsible soils is given by Dudley (1970) and by Houston and Houston (1989). El-Ehwany and Houston (1990) provide recommendations for site investigations for collapsible soil deposits. Bara (1978) also summarizes some of the methods for predicting the decrease in void ratio upon wetting, as do Clemence and Finbarr (1981) and Houston et al. (1988). A useful case history involving the prediction of a collapsible compacted fill is given by Kropp et al. (1994) and by Noorany and Stanley (1994).

If a site is identified that has significant collapse potential, what can engineers do to improve the soils at the site and reduce the impact of potential collapse? Choice of method depends on depth of treatment required and the nature of the cementation or bonding between soils grains. For modest depths, compacting with rollers, inundation, or overexcavation and recompaction, sometimes with chemical stabilization, are often used. Dynamic compaction (Sec. 5.5.2) would also be feasible. For deeper deposits, ponding or flooding is effective and often the most economical treatment method (Bara, 1978). Depending on the nature of the bonding between soil grains, inundation can result in a compression of up to 8% or 10% of the thickness of the collapsible soil layer. Dynamic compaction, blasting, vibro compaction-replacement, and grouting are potentially feasible improvement techniques. Much of this work is summarized by Holtz (1989) and Holtz et al. (2001).

Another geohazard is subsidence, which can result in major damage to structures and other infrastructure at or near the ground surface. One important type of subsidence occurs on karst terrain, and you may recall from Sec. 3.3.2 that karstic features are associated with limestone bedrock. Underground solution cavities can collapse and cause large sinkholes in built-up areas that can be very destructive to surface structures. Karst terrain presents complex and challenging problems in site exploration, foundation design and construction, and for the remediation of damaged existing structures (Sitar, 1988; Sowers, 1996). Another source of subsidence is the collapse of abandoned underground mines.

Regional subsidence due to compaction of unconsolidated sediments caused by withdrawal of underground fluids (water, oil, and gas) can be very detrimental to structures and other infrastructure at the surface. Mexico City is the classic case in geotechnical engineering because large areas of the city have settled more than 10 m due to pumping of groundwater from an aquifer found conveniently

TABLE 6.4 Classification of Collapse Index (ASTM, 2010)

Collapse Index	Degree of Specimen Collapse
0	None
0.1 to 2.0	Slight
2.1 to 6.0	Moderate
6.1 to 10.0	Moderately severe
>10	Severe

about 30 m below the city. The reasons for such large settlements are explained in Chapter 8. Less dramatic but nonetheless locally important subsidence has occurred in Bangkok, Thailand, and Las Vegas, Nevada, but due to groundwater pumping. Regional subsidence due to pumping of oil and gas caused significant subsidence to Long Beach, California, in the 1920s. For additional information on regional land subsidence, see Holzer (1991) and Borchers (1998).

6.8 FROST ACTION

Whenever the air temperature falls below freezing, especially for more than a few days, it is possible for the pore water in soils to freeze. Frost action in soils can have several important engineering consequences. First, the volume of the soil can immediately increase about 10% just due to the volumetric expansion of water upon freezing. A second but significantly more important factor is the formation of ice crystals and lenses in the soil. These lenses can even grow to several centimetres in thickness and cause heaving and damage to light surface structures such as small buildings and highway pavements. If soils simply froze and expanded uniformly, structures would be evenly displaced, since the frozen soil is quite strong and easily able to support light structures. However, just as with swelling and shrinking soils, the volume change is usually uneven, and this is what causes structural and other damage.

The problems do not end here. During the spring, the ice lenses melt and greatly increase the water content and decrease the strength of the soil. Highway pavements especially can suffer serious structural damage during the spring thaw (called, for obvious reasons, the "spring breakup").

Our understanding of the mechanism of ice lens formation as well as the conditions necessary for detrimental frost action occurred relatively recently. Prior to the 1920s and the rapid development of automobile traffic, roads were left snow covered for sleds during the winter. Since snow is a good insulator, depths of frost penetration were limited and rarely was frost heave a problem. Because the traffic loads were light, there were also few problems during the spring thaw. The problems began when it became necessary to remove snow for cars. At first, frost heave was attributed solely to the 10% volumetric expansion of water upon freezing. But some enterprising young engineers made some measurements, both of the magnitude of heave and of the water content of highway subgrades. Professor Casagrande relates that, on one stretch of badly frost-heaving road in New Hampshire, measurements during the winter of 1928–29 showed that the depth of frost penetration was about 45 cm, and the total surface heave was about 13 cm. The water content, normally between 8% and 12%, had increased significantly and ranged between 60% and 110%. When a test pit was excavated, the subgrade was full of ice lenses with a total thickness of (you guessed it!) 13 cm! The water table had been located at some 2 m depth in the autumn, yet during the spring it was right below the pavement. When the soil began to thaw in the spring, the upper layers became water saturated and very soft—the water was trapped in the subgrade between the thawed surface layer and the top of the still frozen soil below.

Now the question was: how did the water get there? It wasn't there before the winter season. Also, the observation was made that there was very little ice in clean sands and gravels. But with silty soils, ice lenses were plentiful, and this fact suggested that capillarity was somehow involved. Further investigations showed that the formation of ice lenses also depended on the rate of freezing of the soil. If the soil froze rapidly, as might occur during a cold snap early in the winter before there was significant snow, then fewer ice lenses tended to form. With a slower rate of freezing, there were more ice lenses, and thicker lenses tended to form nearer the bottom of the frozen layer. So, one condition for ice lens formation must be that there is a source of water nearby. All these factors are discussed in the following sections.

Research during the past 80 years has explained many of the observed phenomena associated with soil freezing and frost action. As might be expected, the process, especially with fine-grained soils, is a rather complicated heat-diffusion (thermodynamic) and pore water-chemistry problem and is related to the soil-water potential and water movement in frozen soils (Yong and Warkentin, 1975; Mitchell and Soga, 2005).

The early history of research on frost action and frost heave is now in a U.S. Army Cold Regions Research & Engineering Laboratory (CRREL) special report (Black and Hardenberg, 1991). This report has reprints of the early work by Beskow in Sweden and Taber in the United States.

6.8.1 Terminology, Conditions, and Mechanisms of Frost Action

Common terminology for frozen ground is defined in ASTM (2010) D 4083, and some of these terms are shown in Fig. 6.25.

Basically, three conditions must exist for frost action and the formation of ice lenses in soils:

1. Temperatures below freezing.
2. Source of water close enough to supply capillary water to the frost line.
3. Frost-susceptible soil type and grain (pore) size distribution.

Freezing temperatures depend, of course, on the climatic conditions in the area. If the maximum depth of frost penetration during the coldest part of the winter is less than about 300 mm, it does not affect infrastructure sufficiently to be of concern. However, much of the North American continent has sufficiently cold winters that frost penetration occurs to depths great enough to be of interest to engineers. Figure 6.26 shows typical depths of frost penetration in the continental United States.

Although our discussion has focused on the effects of frost action on roads and highways, other infrastructure such as water mains and footings for small structures can also be adversely affected if they are not located well below the depth of frost penetration. For both these situations, it is a good idea to conservatively follow local experience and building codes.

Even if the winter air temperatures are above freezing during the day, the subsoil can remain frozen during much of the winter because of the low thermal conductivity of the soil-water system. The common measure of severity of the winter temperatures is the *freezing index*, which is defined as the number of degree-days below freezing. In addition to the freezing index, ground cover, topography, presence of snow, and other factors locally affect the rate and depth of frost penetration. The maximum frost depths in Fig. 6.26 are for extremely cold winters without much snow cover. If there is some snow, especially early in the winter, then the frost depth will be much less.

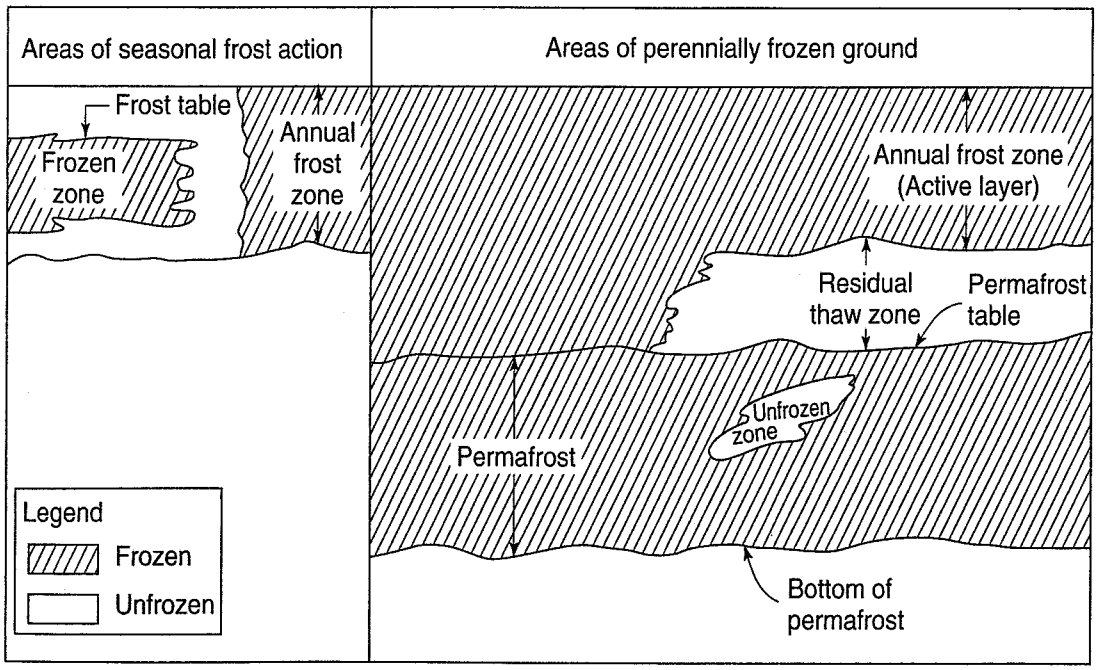

FIGURE 6.25 Frozen-ground terminology (ASTM, 2010).

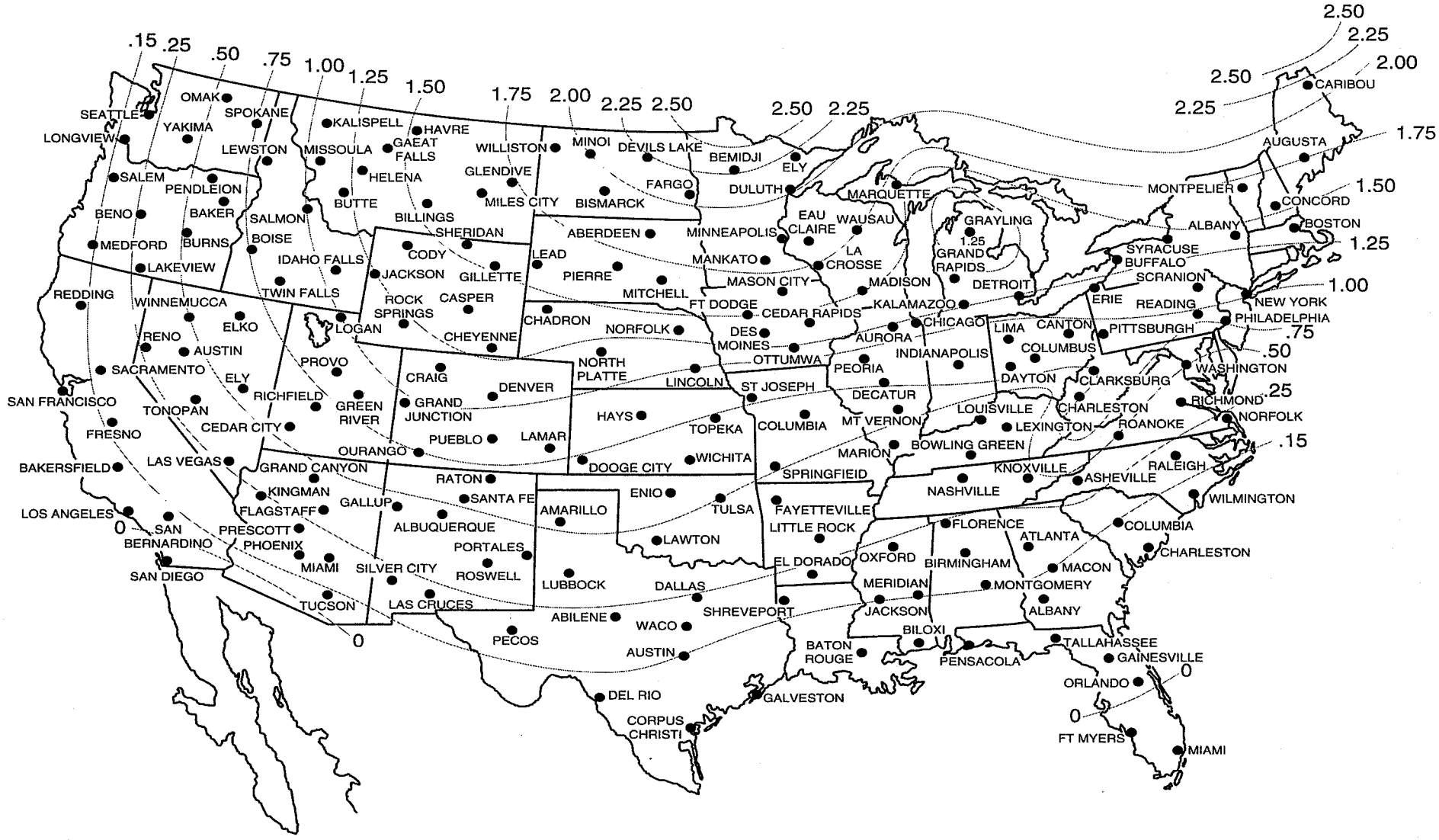

FIGURE 6.26 Maximum depths in metres of frost penetration in the continental United States (from Floyd, 1979).

The maximum frost depths in Fig. 6.26 are obviously much greater north of the U.S. border and in most of Alaska. Higher elevations of the Rockies, the Sierras, and the Cascades also have local areas of deep frost penetration. If you are working in Canada, you can estimate maximum frost depth from the *freezing index*, as explained in Burn (1976).

As indicated on Fig. 3.31, a large part of the Northern Hemisphere including Canada and Alaska contains areas of permanently frozen ground called *permafrost*. Permafrost can be *continuous* or *discontinuous* and is shown in Figs. 6.25 and 3.31. Construction in permafrost areas is particularly challenging and requires special design and construction procedures. For further information, see U.S. Department of the Army (1987), Davis (2001), and Andersland and Ladanyi (2004).

Besides freezing temperatures, a source of groundwater within the height of capillary rise provides the water necessary to feed growing ice lenses. The soil must be fine enough for relatively high capillary pressures to develop and yet not so fine that the flow of water in the soil pores is restricted. As discussed in the next chapter, the hydraulic conductivity or permeability of clay soils is very low. Even though the capillary pressures are very high, unless the clay is relatively sandy or silty, the amount of water that can flow during a freezing spell is so small that ice lenses have little chance to form. However, practically speaking, clay soils near the surface are often cracked and fissured, as described previously, which may allow some water movement to the frost line.

As with other capillary phenomena, it is the pore sizes and not the grain sizes that really control frost action. Reed et al. (1979) have shown that an intrinsically frost-susceptible soil, as predicted by texture and/or gradation, can actually have many levels of susceptibility that depend on the fabric of the soil resulting from compaction.

Figure 6.27 shows a sample of fissured clay that froze down from the top. Note how the water content increased within the frozen zone and how this compared with the value before freezing. Since

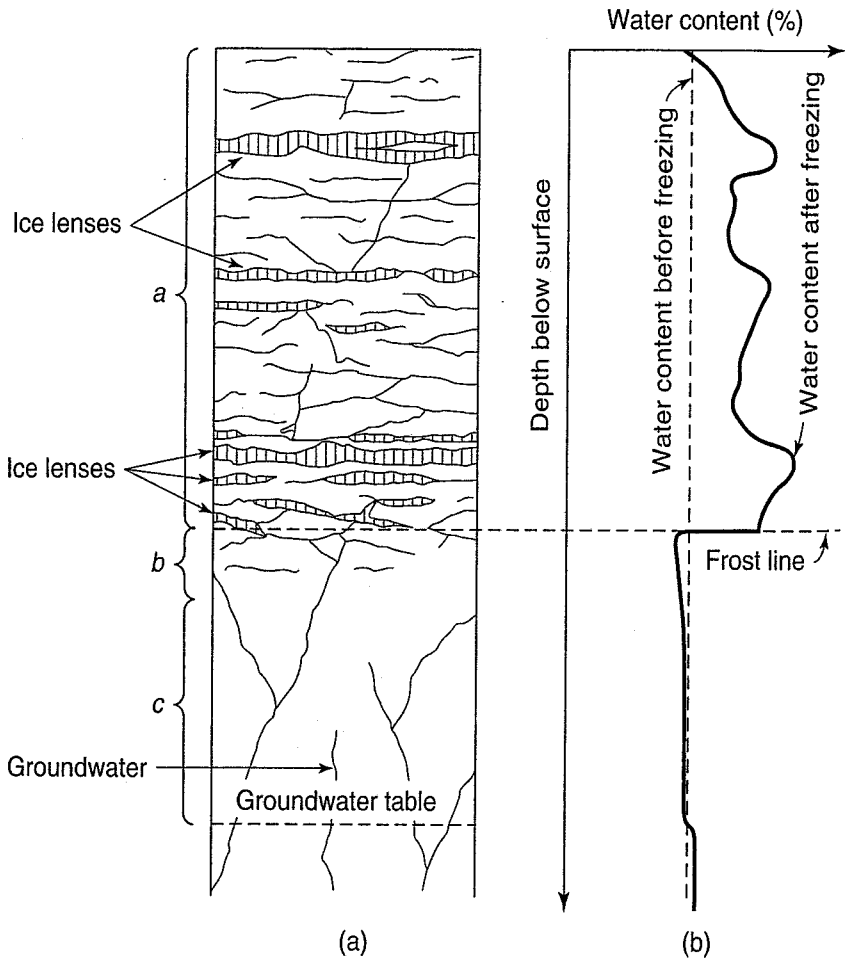

FIGURE 6.27 Diagram showing the relation between different ice layers in frozen soil (a) and the water content distribution curve (b). The soil is assumed to be a medium clay with permanent cracks: *a* = frozen part; *b* = dried-out zone below the frost line (after Beskow, 1935).

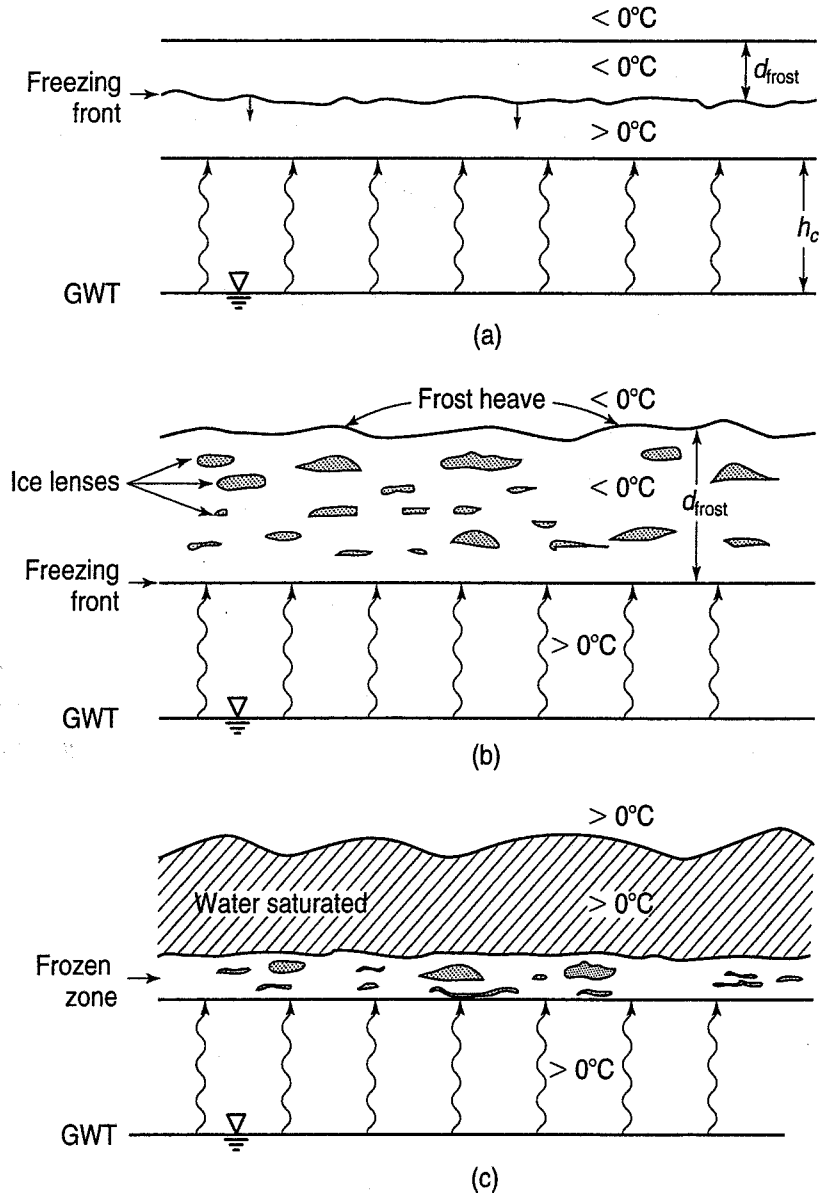

FIGURE 6.28 Schematic diagram of the formation of ice lenses and frost heaving in the (a) fall; (b) winter; and (c) spring.

the clay contains permanent cracks, the groundwater surface is real—that is, the level where the cracks contain free water—and is therefore noticed as a kink in the water distribution curve. Note, too, how the ice lenses developed in the frozen zone. They were continually supplied from the water table through the fissures and cracks in the clay.

What is the process that allows ice lenses to form and frost heaving to occur in the field? Assume we have a site with frost-susceptible soils. Figure 6.28(a) shows conditions during the fall season after some nights with temperatures below freezing. (Also shown is the groundwater table GWT and the height of capillary rise h_c.) The upper layers of soil are frozen, but below the freezing front, the temperature is still above freezing and soil is unfrozen. During this period, the water content and other soil properties of the upper soil layers are unchanged. This is not the situation, however, as winter weather continues [Fig. 6.28(b)]. The freezing front is now below the height of capillary rise, h_c, and water is continually drawn by capillarity up to the freezing front. This is why the water content in the upper layers increases so dramatically and frost heaving continues to occur throughout the winter. In the spring, the weather warms and the top layer starts to thaw [Fig. 6.28(c)]. Because the water content of the upper soils is now so high, its strength is significantly less. This is the cause of the "spring breakup" that occurs in pavements and is the reason why load restrictions are often imposed. Also, lightweight structures may not be able to tolerate the differential heaving and settlement caused by frost action.

6.8.2 Prediction and Identification of Frost-Susceptible Soils

What are frost-susceptible soils? As suggested above, ice lenses will simply not form in coarse-grained soils, because the height of capillary rise in these soils is too small. Casagrande (1932a) and other researchers like Beskow (1935) in Sweden found that ice lens formation in fine-grained soils depended on both a critical grain size and the grain size distribution of the soil. Beskow found 0.1 mm to be the maximum size that would permit ice lens formation under any conditions. Casagrande found 0.02 mm to be a critical grain size; even gravels with only 5% to 10% of 0.02 mm silt were frost-susceptible. Casagrande also found that with well-graded soils, only 3% of the material finer than 0.02 mm was required to produce frost heaving, whereas fairly uniform soils must have at least 10% of that size to be problematic. It seems that soils with less than 1% smaller than 0.02 mm also rarely frost heaved.

These criteria apparently do work. For example, after Rhode Island DOT started limiting the amount of 0.02 mm permitted to 1% or less, they have had no further frost-heave problems (Chamberlain et al., 1982).

Beskow's (1935) limiting grain size curves are shown in Fig. 6.29 for Swedish glacial tills and similar soils. Soils between the curves were found to be frost heaving; those below the bottom curve never heaved.

Table 6.5 presents the U.S. Army Corps of Engineers frost design classification system based upon work by Casagrande (1932a). This is why the criterion of the percent finer than 0.02 mm is used. Based upon typical percentages of this grain size, a good estimate of the soil type and hence the Unified Soil Classification System symbol is given. The classification system was developed by the Corps for pavement design, and it is in order of increasing frost susceptibility and loss of subgrade strength upon thawing. There is some overlapping of frost susceptibility between groups in Table 6.5. For example, soils in Groups F1 and F2 are similar, but F2 soils are more likely to have a lower strength

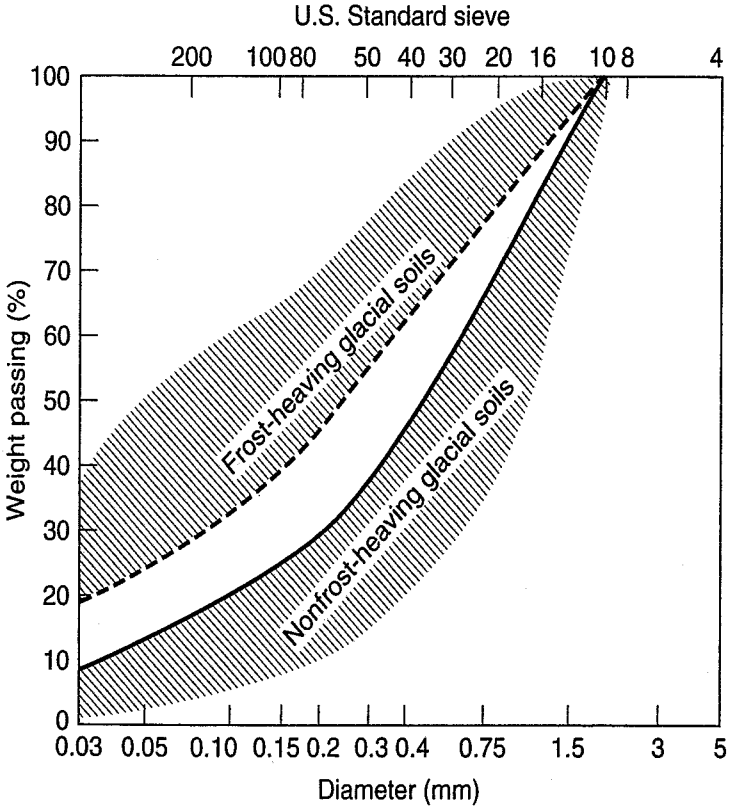

FIGURE 6.29 Limits between frost-susceptible and non-frost-susceptible mixtures of glacial tills or similar mixtures (after Beskow, 1935).

TABLE 6.5 U.S. Army Corps of Engineers Frost Design Soil Classification

Frost Group	Frost Susceptibility	Soil Type	Percent Finer than 0.02 mm	Typical USCS Classification
NFS[a]	Negligible to low	a. Gravels, crushed stone, crushed rock	0–1.5	GW, GP
		b. Sands	0–3	SW, SP
PFS[b]	Possibly	a. Gravels, crushed stone, crushed rock	1.5–3	GW, GP
		b. Sands	3–10	SW, SP
S1	Very low to medium	Gravelly soils	3–6	GW, GP, GW-GM, GP-GM
S2	Very low to medium	Sandy soils	3–6	SW, SP, SW-SM, SP-SM
F1	Very low to high	Gravelly soils	6–10	GM, GW-GM, GP-GM
F2	Medium to high	a. Gravelly soils	10–20	GM, GM-GC, GW-GM, GP-GM
	Medium to high	b. Sands	6–15	SM, SW-SM, SP-SM
F3	Medium to very high	a. Gravelly soils	>20	GM, GC
	Medium to very high	b. Sands except very fine silty sands	>15	SM, SC
	Low	c. Clays, PI > 12	–	CL, CH
F4	Low to very high	a. All silts	–	ML, MH
	Low to very high	b. Very fine silty sands	>15	SM
	Low to high	c. Clays, PI < 12	–	CL, CL-ML
	Very low to very high	d. Varved clays and other fine-grained banded sediments	–	CL and ML; CL, ML and SM; CL, CH and ML; CL, CH, ML and SM

[a]Not frost-susceptible.
[b]Possibly frost-susceptible, but requires a laboratory test to determine design frost soil classification.

After Johnson et al. (1986), U.S. Department of the Army (1987), and Andersland and Ladanyi (2004).

during thaw. Soils in group F4 are especially highly frost susceptibile. Potentially frost-susceptible soils in Table 6.5 are likely to develop significant ice segregation if frozen at rates that are commonly observed in pavement systems (2.5 to 25 mm/day) and if free water is available (less than 1.5 to 3 m below the freezing front).

Figure 6.30 shows rates of frost heave versus percent finer than 0.02 mm for the soil types and frost groups in Table 6.5. Figure 6.30 is based on laboratory tests on remolded samples, and there is considerable overlap among the various soil types and groups. Because laboratory tests are quite rigorous, the predicted rates of heave shown in Fig. 6.30 are generally greater than expected under normal field conditions. Soils that heave in standard laboratory tests at average rates of up to 1 mm/day are probably acceptable for use under pavements in frost areas, unless unusually severe conditions are anticipated. Even the soils that approach heave rates of 1 mm/day in laboratory tests are probably going to show some measurable frost heave under average field conditions. Keep these facts in mind if you are faced with out-of-the-ordinary pavement practice, and remember that good pavement drainage is essential for good performance.

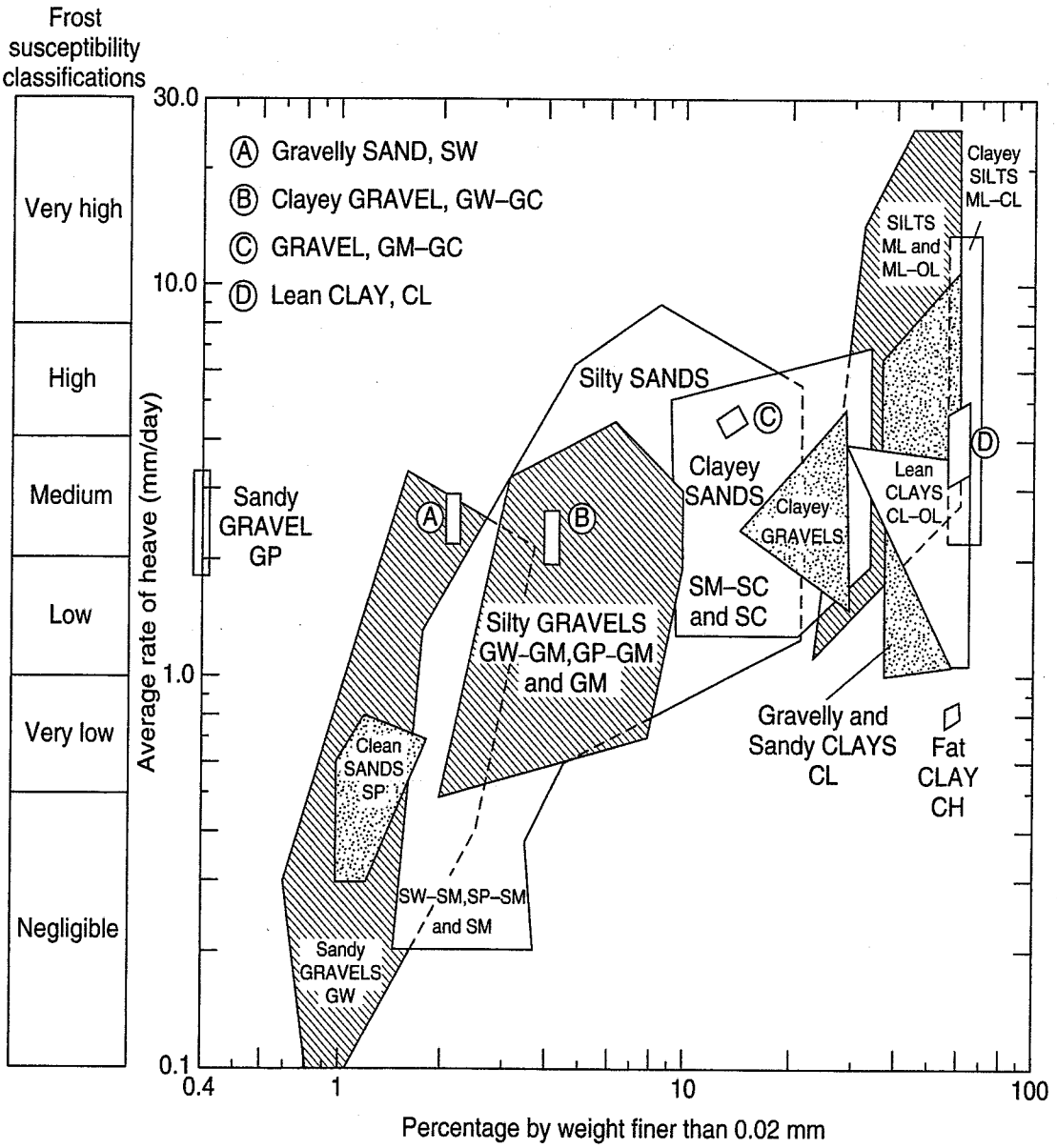

FIGURE 6.30 Rates of heave in laboratory freezing tests on remolded soils (U.S. Department of the Army, 1984).

6.8.3 Engineering Significance of Frozen Ground

Just as with swelling and shrinking soils, frost action can seriously affect structures such as small buildings and highway pavements that are founded directly on the ground surface. Differential heave during the winter can result in undesirable deformations and distortion of the structure. Then when the spring thaw occurs, strength loss can be a serious problem, especially in highway pavements.

Damage to highways in the United States and Canada because of frost action is estimated to amount to millions of dollars annually. But because of the fundamental understanding of the factors involved in frost action and heave, engineers have developed relatively successful methods for dealing with these problems. Load restrictions on secondary roads during the spring "breakup" are common in the northern United States and in Canada. Probably the most common way to deal with the potential damage due to frost-susceptible subgrade soils is to excavate and replace them with non-frost-susceptible materials. Although probably not very economical for highways, it might be possible to lower the groundwater table. Impervious membranes, capillary breaks of coarse gravel or geo-composites, chemical additives, and even foamed insulation (expanded polystyrene, EPS) have been successfully used in

special cases. EPS, however, has been blamed for traffic accidents, because water on the pavement surface may freeze unexpectedly, similar to what happens at certain times of the year to bridge decks.

Frost penetration can seriously affect building foundations and water lines. Footings and basements, as well as water mains, must be founded well below the maximum depth of frost penetration for the locality. Special construction techniques must be used in arctic climates. For details, see the U.S. Department of the Army (1987), Andersland and Ladanyi (2004), and Canadian Geotechnical Society (2006). As mentioned, adequate performance of any type of infrastructure in permafrost regions requires very special design, construction, and maintenance procedures. For good sources of information see the above references and Davis (2001).

6.9 INTERGRANULAR OR EFFECTIVE STRESS

The concept of intergranular or *effective stress* was introduced in Sec. 6.2.1. By definition,

$$\sigma = \sigma' + u \tag{6.14}$$

where σ = total normal stress,

σ' = intergranular or effective normal stress, and

u = pore water or neutral pressure.

When the densities and thicknesses of the soil layers and location of the groundwater table are known, both the total stress and pore water pressure may readily be estimated or calculated. The effective stress cannot be measured; it can only be calculated!

The total vertical stress is called the *body stress*, because it is generated by the mass (acted upon by gravity) in the body. To calculate the total vertical stress σ_v at a point in a soil mass, you simply sum up the densities of all the material (soil solids + water) above that point multiplied by the gravitational constant g, or

$$\sigma_v = \int_0^h \rho g \, dz \tag{6.15a}$$

If ρg is a constant throughout the depth, then

$$\sigma_v = \rho g h \tag{6.15b}$$

Typically, we divide the soil mass into n layers and evaluate the total stress incrementally for each layer, or

$$\sigma_v = \sum_{i=1}^{n} \rho_i g z_i \tag{6.15c}$$

As an example, if a soil could have zero voids, then the total stress exerted on a particular plane would be the depth to the given point times the density of the material—or, in this case, ρ_s times the gravitational constant g. If the soil were dry, then you would use ρ_d instead of ρ_s.

The neutral stress or pore water pressure is similarly calculated for static water conditions. It is simply the depth below the groundwater table to the point in question, z_w, times the product of the density of water ρ_w and g, or

$$u = \rho_w g z_w \tag{6.16}$$

In solid mechanics, the pore water pressure u is referred to as the *neutral stress* because it has no shear component. Recall from fluid mechanics that by definition a liquid cannot support static shear stress. It has only normal stresses, which act equally in all directions. On the other hand, total and

effective stresses can have both normal and shear components. By Eq. (6.8), the effective stress σ' is simply the difference between the total and neutral stresses.

What is the physical meaning of effective stress? First, lettuce discuss the concept of stress itself. You may recall from basic mechanics that stress is really a fictitious quantity. It is defined as a differential force divided by a differential area, as the area shrinks to a point in the limit. This concept is useful, even though in reality, on the micro scale, it has no meaning physically. For example, what would happen in a sand or gravel when the particular differential area you chose ended up in a void? Of course, the stress would have to be zero. Yet right next door, where two gravel particles might be in point-to-point contact, the contact stress might be extremely high; it could even exceed the crushing strength of the mineral grains. Stress then really calls for a continuous material, whereas depending on the scale, real materials are not really continuous. Soils, especially, are not continuous, as we have seen in Chapter 4. Even fine-grained clay soils are collections of discrete mineral particles held together by gravitational, chemical, ionic, van der Waals, and many other kinds of forces. Still, the concept of stress on a macroscale is useful in engineering practice, and that is why we use it.

So, what does effective stress mean physically? In a granular material such as a sand or gravel, it is sometimes called the *intergranular stress*. However, it is not really the same as the grain-to-grain contact stress, since the contact area between granular particles can be very small. In fact, with rounded or spherical grains the contact area can approach a point. Therefore, the actual contact stress can be very large. Rather, the intergranular stress is the sum of the contact forces divided by the total or gross (engineering) area, as shown in Fig. 6.31. If we look at forces, the total vertical force or load P can be considered to be the sum of the intergranular contact forces P' plus the hydrostatic force $(A - A_c)u$ in the pore water. Since the neutral stress can obviously act only over the void or pore area, to get *force* the neutral stress u must be multiplied by the area of the voids $A - A_c$, or

$$P = P' + (A - A_c)u \tag{6.17a}$$

where A = total or gross (engineering) area, and

A_c = contact area between grains.

Dividing by the gross area A to obtain stresses, we have

$$\frac{P}{A} = \frac{P'}{A}\left(\frac{A - A_c}{A}\right)u \tag{6.17b}$$

or

$$\sigma = \sigma' + \left(1 - \frac{A_c}{A}\right)u \tag{6.17c}$$

or

$$\sigma = \sigma' + (1 - a)u \tag{6.17d}$$

where a = contact area between particles per unit gross area of the soil (Skempton, 1960).

In granular materials, since the contact areas approach point areas, a approaches zero. Thus Eq. (6.17d) reduces to Eq. (6.8), or $\sigma = \sigma' + u$. This equation, which defines effective stress, was first proposed in the 1920s by Terzaghi, who is considered to be the father of soil mechanics. Equation (6.8) is extremely useful and important. It is generally accepted that the effective stresses in a soil mass actually control or govern the engineering behavior of that mass. The response of a soil mass to changes in applied stresses (compressibility and shearing resistance) depend almost exclusively on the effective stresses in that soil mass. The principle of effective stress is probably the single most important concept in geotechnical engineering.

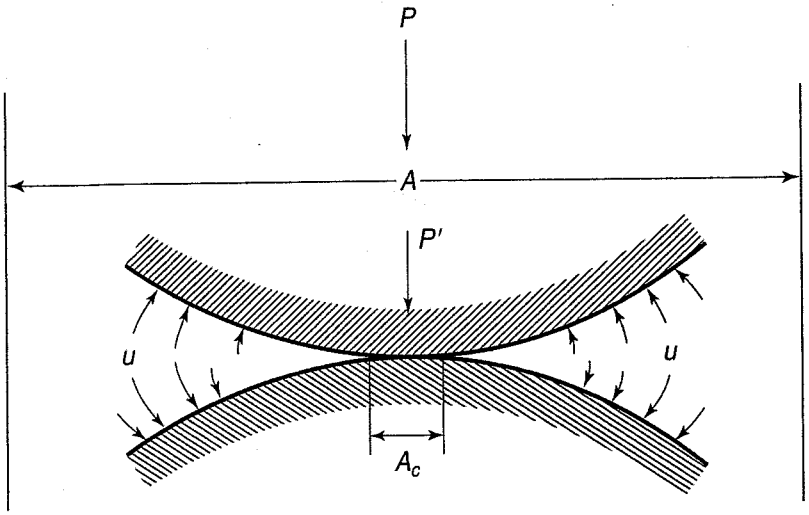

FIGURE 6.31 Particles in solid contact (after Skempton, 1960).

We have discussed effective stresses for granular particulate materials. What does the concept mean for fine-grained cohesive soils? From the discussion in Chapter 4, it is doubtful that the mineral crystals are in actual physical contact, since they are surrounded by a tightly bound water film. On the micro scale, the interparticle force fields that would contribute to effective stress are extremely difficult to interpret and philosophically impossible to measure. Any inference about these force fields comes from a study of the fabric of the soil. So, in view of this complexity, what place does so simple an equation as 6.8 have in engineering practice? Experimental evidence as well as a careful analysis by Skempton (1960) has shown that for saturated sands and clays the principle of effective stress is an excellent approximation to reality. It is not so good, however, for unsaturated soils or saturated rocks and concrete. Whatever it is physically, effective stress is *defined* as the difference between an engineering total stress and a measurable neutral stress (pore water pressure). The concept of effective stress, as we shall see in later chapters, is extremely useful for understanding soil behavior, interpreting laboratory test results, and making engineering design calculations. The concept works, and that is why we use it.

Now we shall work through some examples to show you how to calculate the total stress, pore pressure, and effective stress in soil masses.

Example 6.6

Given:

The container of soil shown in Fig. Ex. 6.6. The saturated density is 2.0 Mg/m^3.

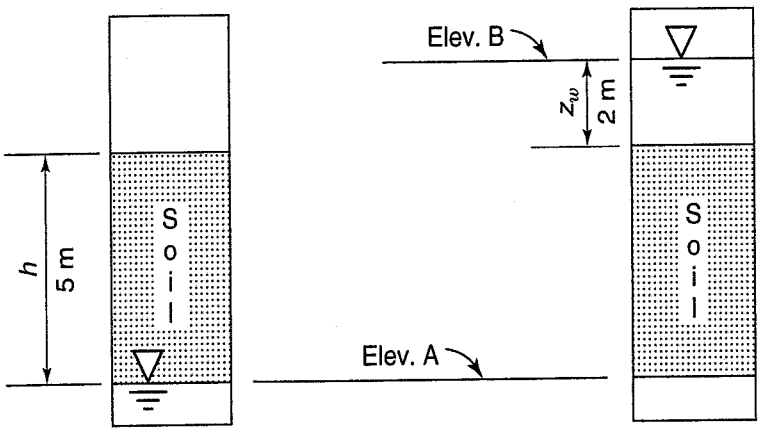

FIGURE Ex. 6.6 (a) Saturated (b) Submerged

Required:

Calculate the total stress, pore pressure, and effective stress at elevation A when (a) the water table is at elevation A and (b) the water table rises to elevation B.

Solution:

a. Assume the soil in the container is initially *saturated* (but not submerged). The water table is located at elevation A. Use Eqs. (6.15b), (6.16), and (6.8) to calculate the stresses at elevation A.

Total stress [Eq. (6.15b)]:

$$\sigma = \rho_{sat} g h = 2.0\ \text{Mg/m}^3 \times 9.81\ \text{m/s}^2 \times 5\ \text{m}$$
$$= 98\,100\ \text{N/m}^2 = 98.1\ \text{kPa}$$

Pore pressure [Eq. (6.16)]:

$$u = \rho_w g z_w = 1\ \text{Mg/m}^3 \times 9.81\ \text{m/s}^2 \times 0 = 0$$

From Eq. (6.8):

$$\sigma' = \sigma = 98.1\ \text{kPa}$$

Recall that $1\ \text{N} = 1\ \text{kg} \cdot \text{m/s}^2$ and that $1\ \text{N/m}^2 = 1\ \text{Pa}$ (Appendix A).

b. If we raise the water table to elevation B, a change in effective stresses at elevation A occurs, since the saturated soil becomes submerged or buoyant. The stresses at elevation A due to the soil and water above are as follows:

Total stress:

$$\sigma = \rho_{sat} g h + \rho_w g z_w$$
$$= (2.0 \times 9.81 \times 5) + (1 \times 9.81 \times 2)$$
$$= 117.7\ \text{kPa}$$

Pore pressure:

$$u = \rho_w g (z_w + h)$$
$$= 1 \times 9.81 \times (2 + 5)$$
$$= 68.7\ \text{kPa}$$

Effective stress at elevation A:

$$\sigma' = \sigma - u = (\rho_{sat} g h + \rho_w g z_w) - \rho_w g (z_w + h)$$
$$= 117.7 - 68.7 = 49.0\ \text{kPa}$$

There are several things that you should know about this example. First, the example may not be very realistic, because it is unlikely that the entire 5 m of sand above the water table would be completely saturated. But assuming so makes the calculations easier. Second, the significant figures used are probably unrealistic. After all, 1 kPa is a very small stress, and in geotechnical practice, we rarely know the soil properties and depths very accurately. In fact, it is often assumed in practice that $g \approx 10\ \text{m/s}^2$, so in this example, the total stress in part **a** would be 100 kPa. Similarly, the total stress in part **b** would be 120 kPa. And so on.

Note also that raising the elevation of the groundwater table *decreases* the intergranular pressure or effective stress in Example 6.6 from 98 kPa to 49 kPa, or a reduction of 50%! When the groundwater table is *lowered*, the reverse occurs and the soil is subjected to an *increase* in effective stress. This overall

increase in vertical stress may lead to substantial areal subsidence, as is occurring, for example, in Mexico City and Las Vegas. As was discussed in Sec. 6.8, in these rapidly growing cities, groundwater is being pumped for municipal water supply, and the resulting settlements have caused substantial damage to streets, buildings, and underground utilities.

Another way to calculate the effective stress in part **b** of Example 6.6 is to use the submerged or buoyant density [Eq. (2.11)]. Note that

$$\begin{aligned}\sigma' &= (\rho_{sat}gh + \rho_w g z_w) - \rho_w g(z_w + h)\\ &= (\rho_{sat} - \rho_w)gh\\ &= \rho' gh\end{aligned} \tag{6.18}$$

Example 6.7

Given:

The data of Example 6.6.

Required:

Use Eq. (6.18) to compute the effective stress at elevation A when the water table is at elevation B.

Solution:

$$\rho' = \rho_{sat} - \rho_w = 2.0 - 1.0 = 1.0\ \text{Mg/m}^3$$
$$\sigma' = \rho' gh = 1.0 \times 9.81 \times 5 = 49.0\ \text{kPa}$$

Assuming $g \approx 10\ \text{m/s}^2$, then $\sigma' = 50\ \text{kPa}$.

Example 6.8

Given:

The soil profile as shown in Fig. Ex. 6.8

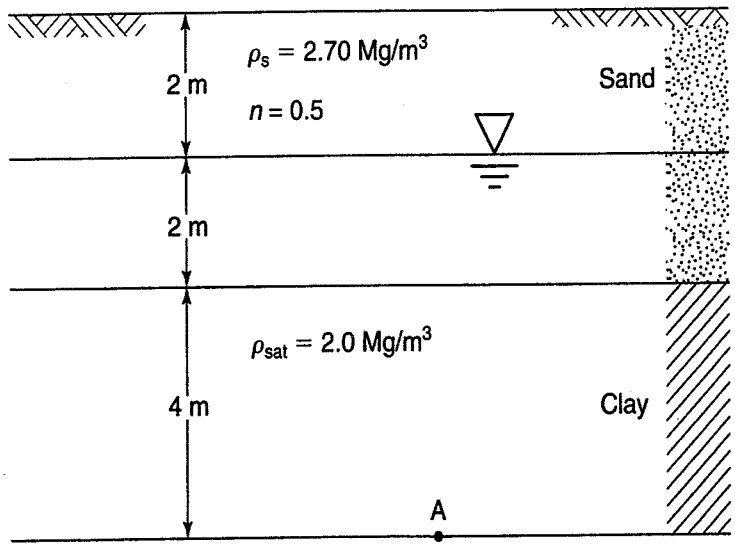

FIGURE Ex. 6.8

Required:

What are the total and effective stresses at point A?

Solution: First find ρ_d and ρ_{sat} of the sand. This will be a review of phase relations. Let $V_t = 1\ m^3$; therefore $n = V_v$, and

$$V_s = 1 - V_v = 1 - n$$

From Eq. (2.7),

$$M_s = \rho_s(1 - n)$$

$$M_s = 2.70\ Mg/m^3\ (1 - 0.5)m^3 = 1.35\ Mg\ (or\ 1350\ kg)$$

$$\rho_d = \frac{M_s}{V_t} = \frac{1.35\ Mg}{1\ m^3} = 1.35\ Mg/m^3\ (or\ 1350\ kg/m^3)$$

$$\rho_{sat} = \frac{M_s + M_w}{V_t} = \frac{M_s + \rho_w V_u}{V_t}$$

$$\rho_{sat} = \frac{1.35\ Mg + 1\ Mg/m^3\ (0.5\ m^3)}{1\ m^3} = 1.85\ Mg/m^3$$

The total stress at A is $\sum \rho_i g h_i$:

$$\begin{aligned} 1.35\ Mg/m^3 \times 9.81\ m/s^2 \times 2\ m &= 26.49\ kN/m^2 \\ +\ 1.85\ Mg/m^3 \times 9.81\ m/s^2 \times 2\ m &= 36.30\ kN/m^2 \\ +\ 2.0\ Mg/m^3 \times 9.81\ m/s^2 \times 4\ m &= \underline{78.48\ kN/m^2} \\ &\quad 141.27\ kN/m^2, \text{ or } 141.3\ kPa \end{aligned}$$

The effective stress at A is

$$\sigma' = \sigma - \rho_w g h$$

$$= 141.3 - (1\ Mg/m^3 \times 9.81\ m/s^2 \times 6\ m) = 82.4\ kPa$$

The effective stress may also be computed by the $\sum \rho g h$ above the water table and the $\sum \rho' g h$ below the water table, or

$$\begin{aligned} 1.35\ Mg/m^3 \times 9.81\ m/s^2 \times 2\ m &= 26.49\ kPa \\ +(1.85 - 1.0) \times 9.81 \times 2\ m &= 16.68\ kPa \\ +(2.0 - 1.0) \times 9.81 \times 4\ m &= \underline{39.24\ kPa} \\ &\quad 82.41\ kPa\ (checks) \end{aligned}$$

It is important to note that, although we carry this many decimal places in example and homework problems, computations would probably be carried out in practice only to the nearest whole kPa (in this case, the effective stress would be reported as 82 kPa).

6.10 VERTICAL STRESS PROFILES

In foundation engineering, it is often useful to have a plot of the total stress, pore pressure, and effective stress with depth at a site. Such plots are used for evaluation of bearing capacity and settlement of shallow and deep foundations, as well as the stability of excavations. Because these profiles are indeed

important in geotechnical practice, you should become proficient in computing them. The following examples illustrate how these profiles are established and some of the very useful information that can be obtained from them.

Example 6.9

Given:

The soil profile of Example 6.8.

Required:

Plot the total stress, pore pressure, and effective stress with depth for the entire soil profile.

Solution: See Fig. Ex. 6.9. You should verify that the numerical values shown on the figure are correct. As in the previous example, computations to the nearest whole kPa are generally accurate enough.

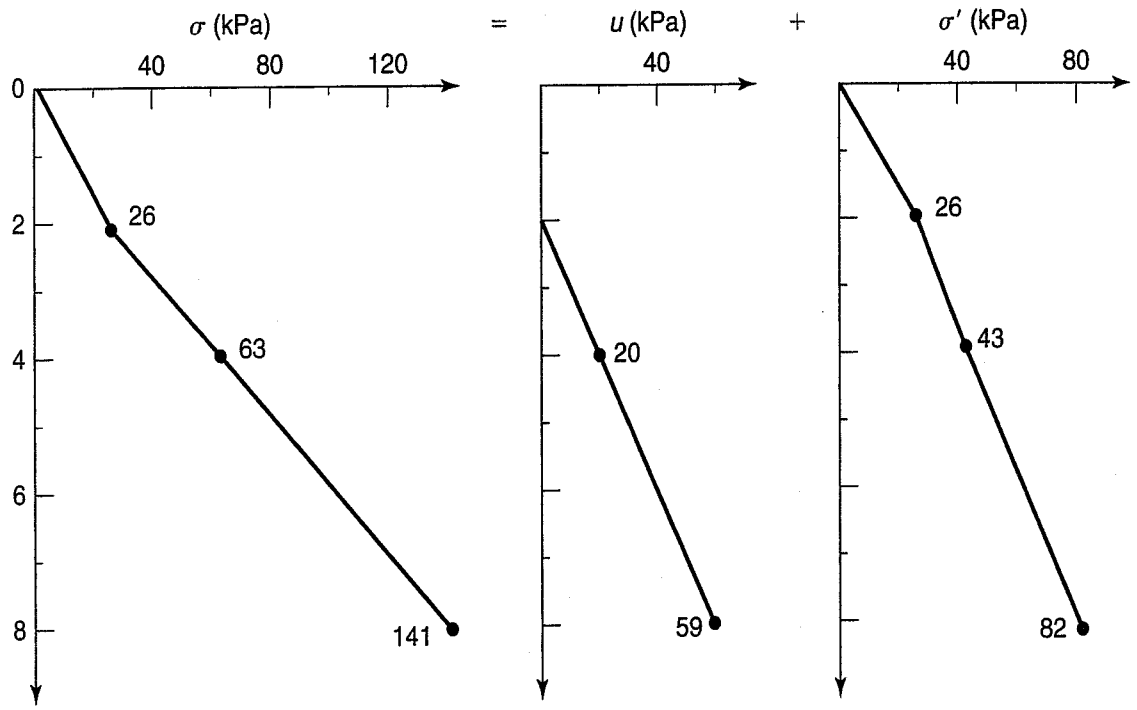

FIGURE Ex. 6.9

Note how the slopes of the stress profiles change as the density changes. In geotechnical practice, the basic soils information comes from site investigations and borings, which determine the thicknesses of the significant soil layers, the depth to the water table, and the water contents and densities of the various materials. Stress profiles are also useful for illustrating and understanding what happens to the stresses in the ground when conditions change—for example, when the groundwater table is raised or lowered as a result of some construction operation, pumping, or flooding. Some of these effects are illustrated in the following examples.

Example 6.10

Given:

The soil profile of Example 6.8.

Required:

Plot the total stress, pore pressure, and effective stress with depth if the groundwater table rises to the ground surface.

Solution: See Fig. Ex. 6.10.

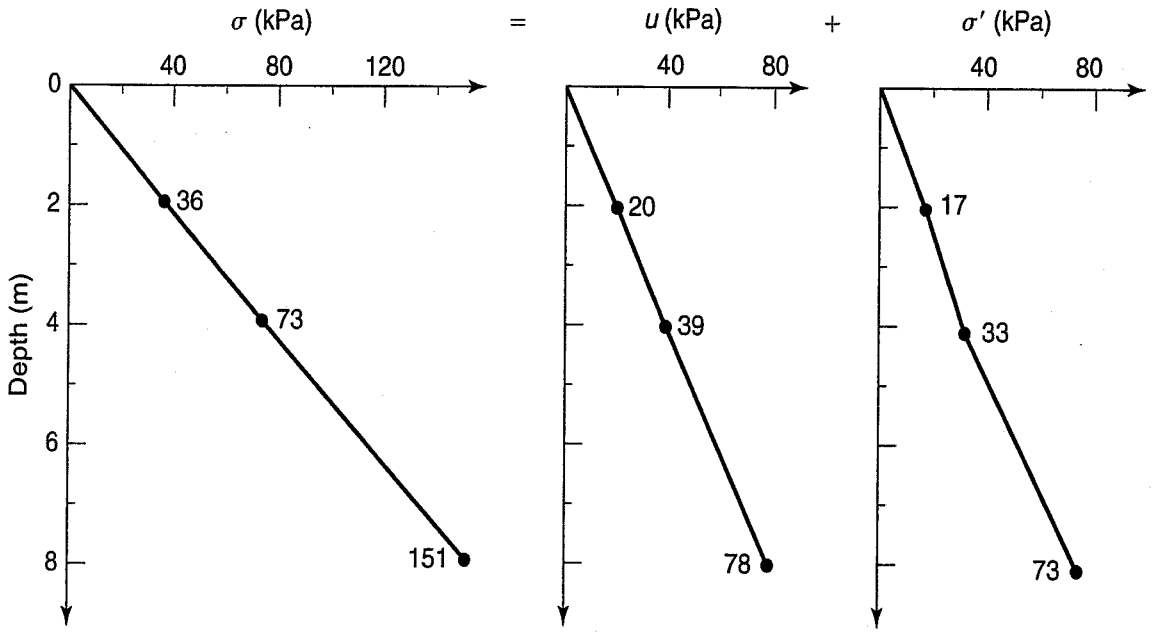

FIGURE Ex. 6.10

Note that the effective stress at point A (at $z = 8$ m) is *reduced*! Had the groundwater table dropped below its original elevation, the effective stress at point A would have increased.

Example 6.11

Given:

The soil profile of Example 6.8.

Required:

Plot the total stress, pore pressure, and effective stress with depth for the case where the groundwater table is 2 m *above* the ground surface.

Solution: See Fig. Ex. 6.11.

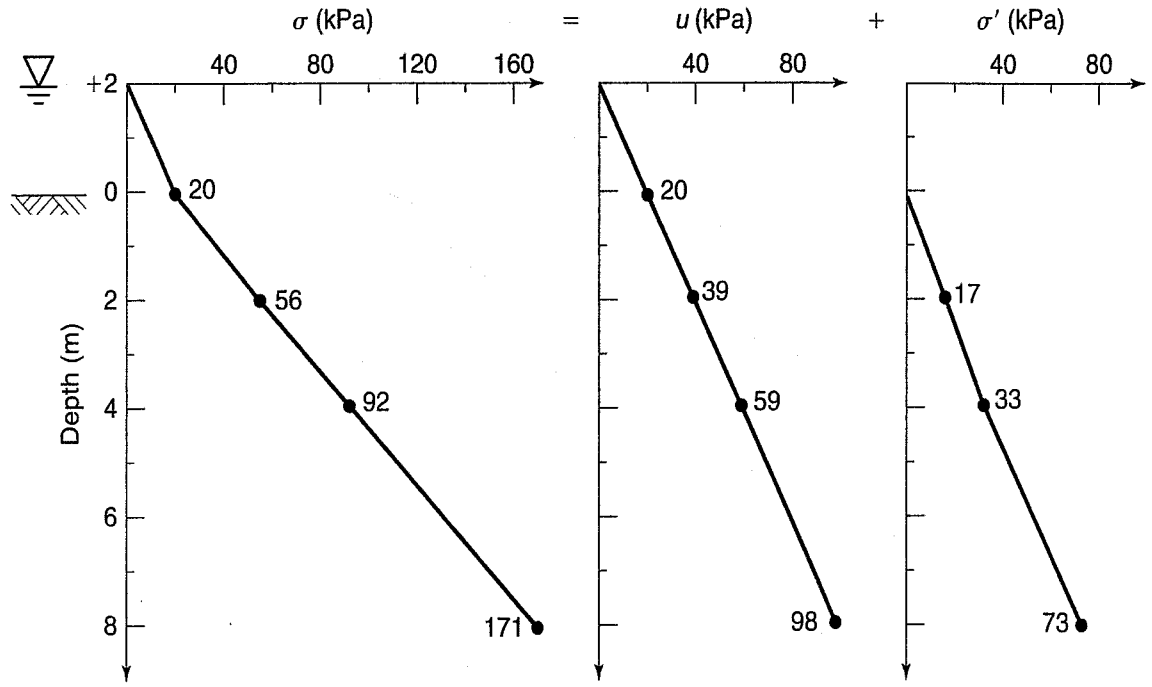

FIGURE Ex. 6.11

Consider carefully how the stress profiles change as the water table elevation changes. Note especially how the effective stresses decrease as the water table rises (Example 6.9 versus 6.10) and then how the effective stress is not changed even when the groundwater table is above the ground surface (Example 6.11). Of course, in that case both the total stress and pore pressure increase as the water table rises above the ground surface, but the effective stresses remain *unchanged*. The reason why the effective stresses remain unchanged is a very important concept, and you should be sure you understand why it happens.

Similar but opposite changes in effective stresses occur when the groundwater table is lowered. This might occur because of a drought, the pumping of water from the sand layer, or even an excavation nearby that could drain the sand. We discuss some of these conditions in Chapter 7. The point here is that if the groundwater table is lowered, you might expect the effective stresses in the clay layer to actually *increase*. If the clay is compressible, an increase in effective stresss causes surface settlements. This process doesn't happen overnight; in fact it may take several decades for the compression and settlement to occur. These processes are discussed in detail in Chapters 8 and 9.

Example 6.12

Given:

The soil profile of Example 6.8.

Required:

a. Find the total stress, pore pressure, and effective stress at point A when the groundwater table is lowered 2 m to the top of the clay layer. Assume for simplicity that the entire sand layer is now dry.

b. Compare the effective stress at point A with the result in Example 6.8 and comment on the results.

Solution:

a. As in the previous examples, to get the total stress σ at point A, we simply sum up the total stress for the soil layers above the point, or

Sand: $\sigma = 1.35\ \text{Mg/m}^3 \times 9.81\ \text{m/s}^2 \times 4\ \text{m} = 53\ \text{kPa}$

Clay: $\sigma = 2.0\ \text{Mg/m}^3 \times 9.81\ \text{m/s}^2 \times 4\ \text{m} = 78\ \text{kPa}$

Total stress at point A: $\sigma = 53 + 78 = 131\ \text{kPa}$

With the groundwater table at the top of the clay layer, the pore pressure u at that point is 39 kPa. Therefore the effective stress σ' at point A is $131 - 39 = 92$ kPa.

As in Example 6.8, the effective stress at point A may also be computed by the $\Sigma \rho gh$ above the water table and the $\Sigma \rho' gh$ below the water table, or

Sand: $\sigma = \sigma' = 53\ \text{kPa}$

Clay: $\sigma' = 131 - (1 \times 9.81 \times 4\ \text{m}) = 92\ \text{kPa}$ (checks)

b. Comparing the numerical values with those of Ex. 6.8, we find that the effective stress at point A *increases* from 82 kPa to 92 kPa, or an *increase* of 10 kPa. Comment: lowering the groundwater table will cause an increase in effective stress.

Other stress profiles of geotechnical interest arise during steady-state pumping from a pervious layer or *aquifer* below the clay layer. An aquifer is simply a source of groundwater that may be taken by pumping from wells (Chapter 7). Sometimes the water pressure in the aquifer is greater than the head caused by the local groundwater table; this is called an *artesian* condition. To know the actual groundwater conditions at a site, we would need to use a piezometer to measure the value of the pore water pressure at a given elevation.

We have already mentioned the potential detrimental effect of the lowering of the groundwater level due to pumping because of the increase in the effective stress. In the case of an artesian condition, the initial pore water pressure is *above* the static water table. Because of the increased pore water pressure, a corresponding *decrease* in effective stress occurs, and this can result in a loss of stability of a slope or foundation.

6.11 RELATIONSHIP BETWEEN HORIZONTAL AND VERTICAL STRESSES

You may recall from hydrostatics that the pressure in a liquid is the same in any direction—up, down, sideways, or at any inclination. However, this is not true in soils. Rarely in natural soil deposits is the horizontal stress in the ground exactly equal to the vertical stress. In other words, the stresses in situ are not necessarily hydrostatic. We can express the ratio of the horizontal to vertical stress in the ground as

$$\sigma_h = K\sigma_v \tag{6.19}$$

where K is an *earth pressure coefficient.*

Since the groundwater table can fluctuate and the total stresses can change, the coefficient K is *not* a constant for a particular soil deposit. However, if we express this ratio in terms of effective stresses, we take care of the problem of a variable water table, or

$$\sigma'_h = K_o\sigma'_v \tag{6.20}$$

The parameter K_o is a very important coefficient in geotechnical engineering. It is called the *coefficient of lateral earth pressure at rest.* It expresses the stress conditions in the ground in terms of *effective stresses*, and it is independent of the location of the groundwater table. Even if the depth

changes, K_o will be a constant as long as we are in the same soil layer and the density remains the same. However, this coefficient is very sensitive to the geologic and engineering stress history, as well as to the densities of the overlying soil layers (see, for example, Massarsch et al., 1975). The value of K_o is important in stress analyses, in assessing the shearing resistance of particular soil layers, and in such geotechnical problems as the design of earth-retaining structures, earth dams and slopes, and many foundation engineering problems.

The K_o in natural soil deposits can be as low as 0.4 or 0.5 for sedimentary soils that have never been preloaded or up to 3.0 or greater for some very heavily preloaded deposits. Typical values of K_o for different geologic conditions are given in Chapter 11.

Example 6.13

Given:

The stress conditions of Example 6.8. Assume K_o for this soil deposit is 0.6.

Required:

Calculate both the horizontal total and effective stresses at depths of 4 m and 8 m in the deposit. Also, determine the value of K at these depths.

Solution: From Fig. Ex. 6.9, at 4 m, σ'_v is 43 kPa. From Eq. (6.19), $\sigma'_h = 0.6 \times 43$ kPa $= 26$ kPa. At 8 m, $\sigma'_h = 0.6 \times 82 = 49$ kPa. For the total horizontal stresses, we cannot use Eq. (6.18) directly, because we do not know K. So we use Eq. (6.8) to get σ_h, or $\sigma_h = \sigma'_h + u$. At 4 m, $\sigma_h = 26 + 20 = 46$ kPa. At 8 m, $\sigma_h = 49 + 59 = 108$ kPa. Using Eq. (6.18), we can determine the value of the total stress coefficient K.

At 4 m,

$$K = \frac{\sigma_h}{\sigma_v} = \frac{46}{63} = 0.73$$

At 8 m,

$$K = \frac{\sigma_h}{\sigma_v} = \frac{108}{141} = 0.77$$

Note that K is *not* necessarily equal to K_o. To get K, we have to go through K_o and add the pore water pressure to the effective stress for the depth in question.

PROBLEMS

6.1 The end of a clean glass tube is inserted in pure water. What is the height of capillary rise if the tube is (a) 0.15 mm, (b) 0.015 mm, and (c) 0.0015 mm in diameter?

6.2 Calculate the maximum capillary pressure for the tubes in Problem 6.1.

6.3 Calculate the theoretical height of capillary rise and the capillary tension of the three soils whose grain size distribution is shown in Fig. 2.6.

6.4 A tube, similar to that shown in Fig. 6.12, has a 0.0025-mm inside diameter and is open at both ends. The tube is held vertically and water is added to the top end. What is the maximum height h of the column of water that will be supported? (*Hint:* A meniscus will form at the top and at the bottom of the column of water, as shown in Fig. P6.4.) (After Casagrande, 1938.)

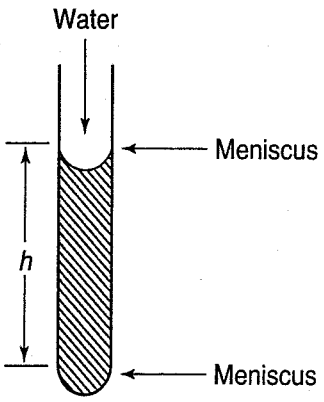

FIGURE P6.4 (After Casagrande, 1938.)

6.5 The tube shown in Fig. 6.6 is filled with water. When evaporation takes place, the meniscus will first form at the larger end, as explained in the text. Assuming this meniscus to be fully formed, derive an expression for the contact angle at the other end of the tube in terms of the two radii, r_l and r_s.

6.6 Figure P6.6 shows an angled, glass capillary tube with diameter 110 μm. Other dimensions are shown.

(a) Where will the top of the capillary rise be?

(b) What is the water pressure in the horizontal section of the tube, in kPa?

(c) What air pressure should be applied to the top opening in the tube to cause the water level to be at 10 cm above the free water surface?

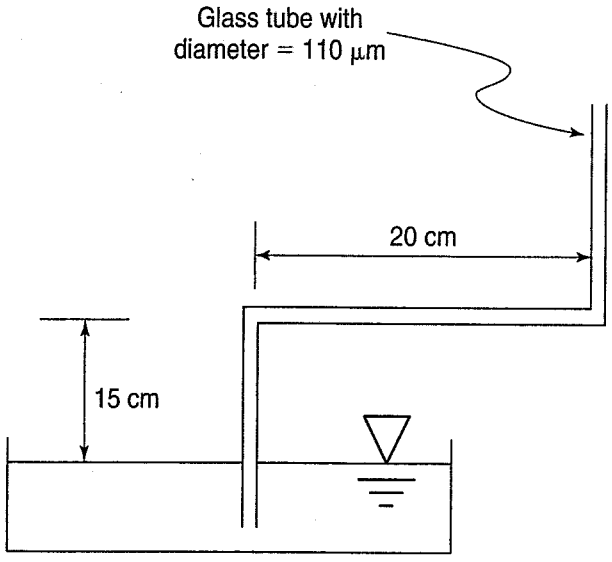

FIGURE P6.6

6.7 A glass tube with inside diameter 150 μm is placed in a water bath.

(a) How high will the water rise inside the tube? Give your answer in cm.

(b) What will the water pressure be halfway between the free water surface and the water level in the tube (i.e., at $h_c/2$)? Give your answer in kN/m^2.

(c) If the tube is intended to model soil void size, what would the effective grain size of the soil be?

(d) What air pressure (+ or −) would have to be applied to the tube to get the water in the tube to rise 25 cm above the free water surface? Give your answer in kN/m^2.

6.8 Figure P6.8 shows a tube with two sections, each with a different diameter, d_1 and d_2. The tube is placed in the water bath as shown.

(a) How high above the phreatic surface will the water rise in the tube due to capillarity? What is the pore pressure at the surface of the capillary rise?

(b) If the capillary rise you found in part (a) occurred in a soil, what would you estimate as the soil's D_{10}?

6.9 Figure P6.9 shows a long, thin tube which was filled with a clay and placed in a water bath. The D_{10} for the clay is shown.

(a) How high, h_c, will the water rise in the tube?

(b) What is the capllary pressure at h_c, in kN/m^2?

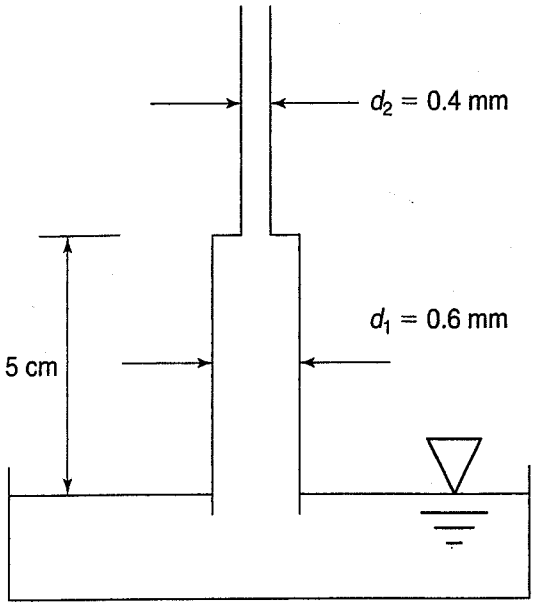

FIGURE P6.8

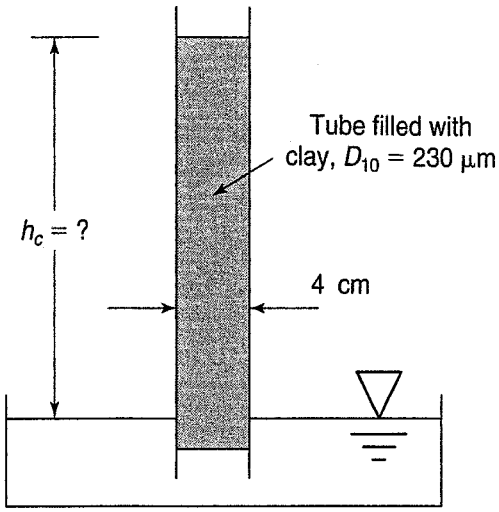

FIGURE P6.9

6.10 **(a)** Would the shrinkage limit of a clay be different if the water in the voids were replaced by some other liquid with a *smaller* surface tension? Why?
(b) Would there be more or less shrinkage? Why?

6.11 Assume that equations developed for height of capillary rise in constant-diameter tubes can be applied. Calculate the *net* compressive stress on a soil pat at the shrinkage limit where the average diameter of the surface pores is 0.0012 mm.

6.12 Estimate the shrinkage limits of the soils A–F in Problem 2.58.

6.13 During a shrinkage limit test on a silty clay, the volume of the dry soil pat was found to be 11.02 cm^3 and its dry mass was 22.78 g. If the shrinkage limit was 10.9, what is the density of the soil solids?

6.14 Estimate the volume change of an organic silty clay with LL = 65 and PL = 38, when its water content reduced from 48% to 18%.

6.15 Comment on the validity of Casagrande's procedure (Fig. 6.14) for estimating the shrinkage limit for undisturbed soils. Does it matter whether the soils are sensitive or not? Why?

6.16 A saturated sample of clay with an SL of 20 has a natural water content of 32%. What would its dry volume be as a percentage of its original volume if ρ_s is 2.67?

6.17 A sample of clayey silt is mixed at about its LL of 43. It is placed carefully in a small porcelain dish with a volume of 18.9 cm^3 and weighs 33.89 g. After oven drying, the soil pat displaces 212.4 g of mercury. (a) Determine the SL of the soil sample. (b) Estimate the ρ_s of the soil.

6.18 The LL of a bentonitic clay is 442 and the PL is 69. The SL was determined to be about 9. Calculate the expected volumetric decrease when a sample of this bentonite is dried, if its natural water content was 91%.

6.19 The shrinkage limit of a 0.12 m^3 sample of a clay is 13 and its natural water content is 29%. Assume the density of the soil solids is 2.70 Mg/m^3, and estimate the volume of the sample when the water content is 11.8%.

6.20 During the determination of the shrinkage limit of a sandy clay, the following laboratory data was obtained:

Wet wt. of soil + dish = 91.04 g
Dry wt. of soil + dish = 78.22 g
Wt. of dish = 51.55 g
Volumetric determination of soil pat:
Wt. of dish + mercury = 430.80 g
Wt. of dish = 244.62 g

Calculate the shrinkage limit of the soil, assuming ρ_s = 2.65 Mg/m^3.

6.21 The LL of a medium sensitive Swedish postglacial clay is 61 and the PI is 32. At its natural water content, the void ratio is 0.99, while after shrinkage the minimum void ratio is 0.69. Assuming the density of the soil solids is 2.69, calculate the shrinkage limit of the clay.

6.22 Derive Eqs. (6.9) and (6.10) for the shrinkage limit, using phase relationships. Show that they are identical.

6.23 Estimate the swelling potential of soils A–F, Problems 2.56 and 2.58. Use both Table 6.2 and Fig. 6.21.

6.24 Estimate the frost susceptibility of soils A–F, Problems 2.56 and 2.58, according to Beskow (Fig. 6.29) and U.S. Army Corps of Engineers frost design classification system (Table 6.5).

6.25 Obtain two lemon-sized chunks of soil from the field. Put one in the lab oven to dry out. Place it and the field water-content sample in small jars and cover them both with water. Observe the behavior and record your observations.

6.26 What is the estimated frost penetration for your home town?

6.27 A soil has the following profile with depth:

0–10 ft	γ_t = 110 pcf
10–25 ft	γ_t = 95 pcf
25–50 ft	γ_t = 113 pcf

The water table is at a depth of 10 ft. Plot the total stress, effective stresses, and pore pressure versus depth. Show all of your calculations. Assume that there is no capillarity.

6.28 Figure P6.28 shows the soil profile at the site of an existing warehouse (i.e., covers a large area) that causes a surface loading of 2000 psf. Draw the σ_v, σ'_v and u profiles with depth. Show values at 0, 12, 25, 38 and 48 ft. depth.

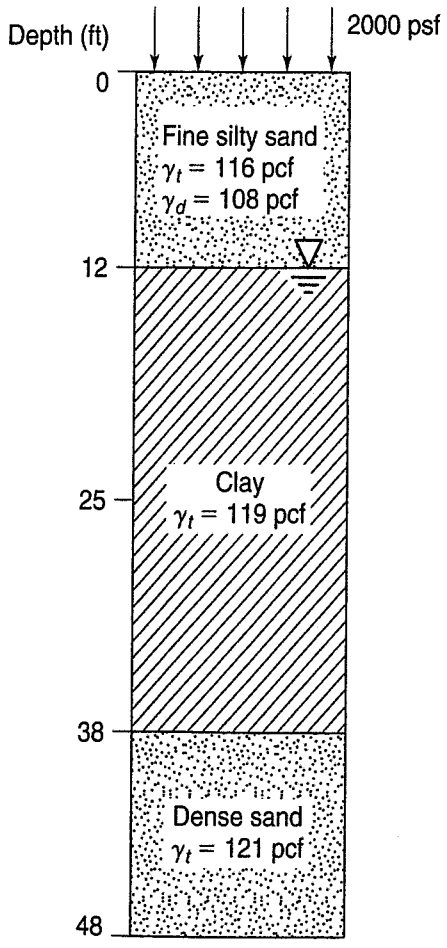

FIGURE P6.28

6.29 **(a)** For the conditions shown, compute the σ_v, u, and σ'_v values at the ground surface, water table, and at all soil layer interfaces. Refer to the soil profile shown in Fig. P6.29.

(b) During the spring, the water rises to 4 ft above the ground surface. Determine the σ_v, u, and σ'_v values at depth 25 ft for this condition. You do not need to compute values at other depths.

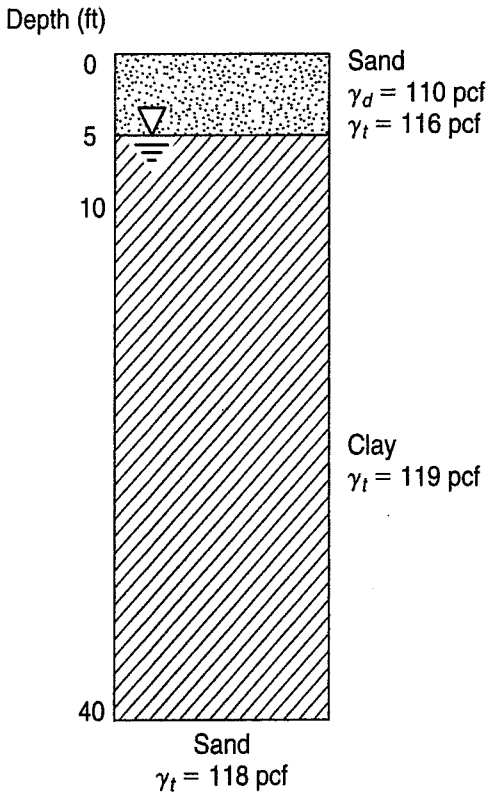

FIGURE P6.29

6.30 For the soil profile of Example 6.8 plot the total, neutral, and effective stresses with depth if the groundwater table is *lowered* 4 m below the ground surface.

6.31 Soil borings made at a site near Chicago indicate that the top 6 m is a loose sand and miscellaneous fill, with the groundwater table at 3 m below the ground surface. Below this is a fairly soft blue-gray silty clay with an average water content of 30%. The boring was terminated at 16 m below the ground surface when a fairly stiff silty clay was encountered. Make reasonable assumptions as to soil properties and calculate the total, neutral, and effective stresses at 3, 7, 12, and 16 m below the ground surface.

6.32 Plot the soil profile of Problem 6.31 and the total, neutral, and effective stresses with depth.

6.33 A soil profile consists of 5 m of compacted sandy clay followed by 5 m of medium dense sand. Below the sand is a layer of compressible silty clay 20 m thick. The initial groundwater table is located at the bottom of the first layer (at 5 m below the ground surface). The densities are 2.05 Mg/m^3 (ρ), 1.94 Mg/m^3 (ρ_{sat}), and 1.22 Mg/m^3 (ρ') for the three layers, respectively. Compute the effective stress at a point at middepth in the compressible clay layer. Then, assuming that the medium dense sand remains *saturated*, compute the effective stress in the clay layer at midpoint again, when the groundwater table drops 5 m to the top of the silty clay layer. Comment on the difference in effective stress.

6.34 Specify the conditions under which it is possible for K_o to equal K.

6.35 For the soil profile of Problem 6.31, calculate the horizontal, total, and effective stresses at depths of 3, 7, 12, and 16 m, assuming (a) K_o is 0.45 and (b) K_o is 1.6.

6.36 The value of K_o for the compressible silty clay layer of Problem 6.33 is 0.68. What are the total and effective horizontal stresses at middepth of the layer?

CHAPTER 7

Fluid Flow in Soils and Rock

7.1 INTRODUCTION

The importance in civil engineering of water in soils is mentioned at the beginning of Chapter 6. Most geotechnical engineering problems somehow have water associated with them, due to either water flowing through the voids and pores in the soil mass or to the state of stress or pressure in the water in the pores. In Chapter 6 we described the effects of static water on soil and rock properties (hence the name *hydrostatic*), and in this chapter we describe the effects of water flow through soils and rock on their properties and engineering behavior. Note that we don't use the corresponding term *hydrodynamic*, since in most situations involving geomaterials, water moves relatively slowly.

The following notation is introduced in this chapter.

Symbol	Dimension	Unit	Definition
A	L^2	m^2	Area
h	L	m	Energy or head, head loss (also with subscripts f, L, m), layer thickness
h_p	L	m	Pressure head - Eq. (7.4)
i	—	—	Hydraulic gradient - Eq. (7.1)
i_c	—	—	Critical hydraulic gradient - Eq. (7.15)
i_E	—	—	Exit gradient
j	$ML^{-2}T^{-2}$	kN/m^3	Seepage force per unit volume - Eq. (7.17)
k	LT^{-1}	m/s	Darcy coefficient of permeability - Eqs. (7.2), (7.5)
$k_{equivalent}$	LT^{-1}	m/s	Equivalent Darcy coefficient of permeability for multiple soil layers - Eqs. (7.22), (7.23)
K_i	L^2	m^2	Intrinsic permeability - Eq. (7.6)
L	L	m	Length of sample
l	L	m	Unit or characteristic length
N_d	—	—	Number of equipotential "drops" in a flow net - Eq. (7.21)
N_f	—	—	Number of flow channels in a flow net - Eq. (7.21)
p	$ML^{-1}T^{-2}$	kPa	Pressure - Eq. (7.4)
q	L^3T^{-1}	m^3/s	Flow rate (sometimes per unit width) - Eqs. (7.3), (7.5)

(Continued)

Symbol	Dimension	Unit	Definition
Q	L^3	m^3	Volume of flow - Eq. (7.8)
r	L	m	Radial distance from well centerline - Eq. (7.24)
T	L	m	Thickness of layer
u	$ML^{-1}T^{-2}$	kPa	Pore water pressure
v	LT^{-1}	m/s	Velocity - Eq. (7.2)
v_s	LT^{-1}	m/s	Seepage velocity - Eq. (7.8)
z	L	m	Potential head; depth
μ	$ML^{-1}T^{-1}$	Pa-s	Absolute or dynamic viscosity - Eq. (7.6)
ν	L^2T^{-1}	m/s	Kinematic viscosity, μ/ρ - Eq. (7.6)

7.2 FUNDAMENTALS OF FLUID FLOW

Fluid flow, as you may recall from your basic fluid mechanics courses, can be described or classified in several different ways. Flow can be *steady* or *unsteady*, corresponding to conditions that are constant or vary with time. Flow can also be classified as *one-*, *two-*, or *three-dimensional.* In one-dimensional flow, all the fluid parameters—pressure, velocity, temperature, etc.—are constant in any cross section perpendicular to the direction of flow. Of course, these parameters can vary from section to section along the direction of flow, as in the vertical percolation of rain water down through a soil. In two-dimensional flow (for example, flow under a dam), the fluid parameters are the same in parallel planes, so that a "slice" through any part of the soil profile gives the same flow pattern. In three-dimensional flow, the fluid parameters vary in the three coordinate directions. For example, when a contaminant plume spreads out from a concentrated source, such as a leaking underground storage tank, there is typically both areal and vertical expansion of the plume. However, for purposes of analysis, most flow problems in geotechnical engineering are usually assumed to be either one- or two-dimensional, which is usually adequate for practical cases.

Because density changes can be neglected at ordinary stress levels for most geotechnical engineering applications, flow of water in soils can be considered *incompressible.*

Flow can also be described as *laminar*, where the fluid flows in parallel layers without mixing, or *turbulent*, where random velocity fluctuations result in mixing of the fluid and internal energy dissipation. There can also be intermediate or *transition* states between laminar and turbulent flow. These states are illustrated in Fig. 7.1, which shows how the *hydraulic gradient* changes with increasing velocity of flow. Hydraulic gradient i, a very important concept, is defined as the energy or *head loss* h per unit length l, or

$$i = \frac{h}{l} \tag{7.1}$$

The energy or head loss increases linearly with increasing velocity as long as the flow is laminar. Once the transition zone is passed, because of internal eddy currents and mixing, energy is lost at a much greater rate (zone III, Fig. 7.1) and the relationship is nonlinear. Once in the turbulent zone, if the velocity is decreased, the flow remains turbulent well into transition zone II until the flow again becomes laminar.

Flow in most soils is so slow that it can be considered laminar. Thus, from Fig. 7.1, we could write that v is proportional to i, or

$$v = ki \tag{7.2}$$

Equation (7.2) is an expression for *Darcy's law*, which is discussed later in this chapter.

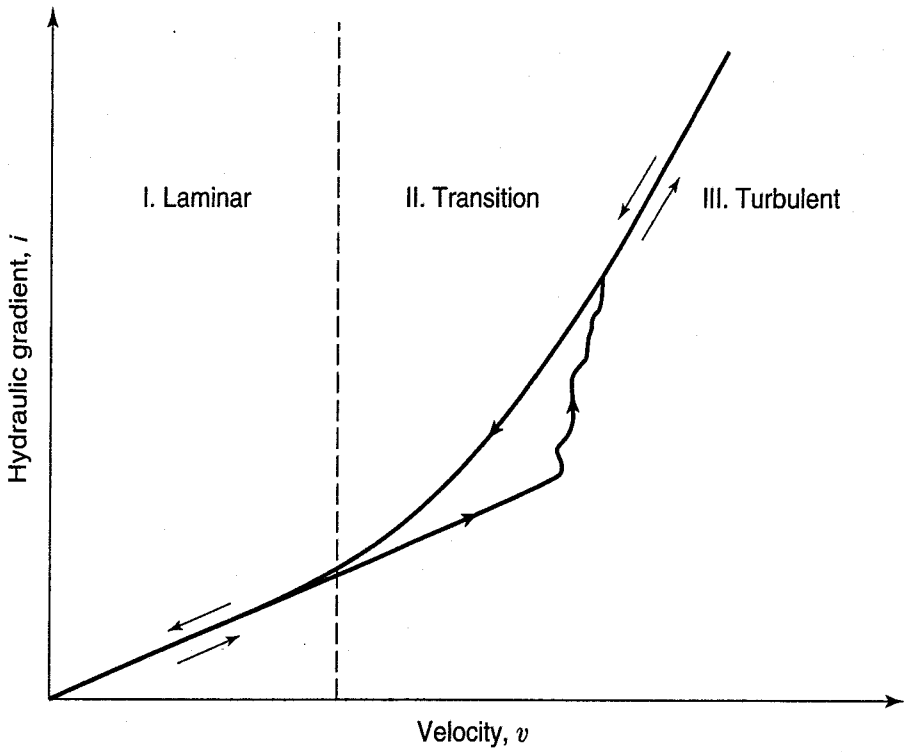

FIGURE 7.1 Zones of laminar and turbulent flow (after Taylor, 1948).

Another important concept from fluid mechanics is the *law of conservation of mass*. For incompressible steady flow, this law reduces to the *equation of continuity*, or, when one considers the flow rate at any two points or sections in the flow path,

$$q = v_1 A_1 = v_2 A_2 = \text{constant} \tag{7.3}$$

where q = rate of discharge (units: volume/time, m^3/s),

v_1, v_2 = velocities at sections 1 and 2, and

A_1, A_2 = the cross-sectional areas at sections 1 and 2.

The other well-known equation from fluid mechanics that we shall use is the *one-dimensional energy equation* (sometimes incorrectly called the Bernoulli equation) for incompressible steady flow of a fluid:

$$\frac{v_1^2}{2} + \frac{p_1}{\rho_w} + gz_1 = \frac{v_2^2}{2} + \frac{p_2}{\rho_w} + gz_2 = \text{constant energy} \tag{7.4a}$$

where v_1, v_2 = velocities at sections 1 and 2,

g = acceleration of gravity,

ρ_w = density of the fluid (water),

p_1, p_2 = pressures at sections 1 and 2, and

z_1, z_2 = distance above some arbitrary datum plane at sections 1 and 2.

This equation is the steady-flow energy equation in terms of energy per unit of mass of fluid (units: J/kg). In hydraulics, however, it is more common to express Eq. (7.4a) in terms of energy per unit weight by dividing each term in the equation by g, the acceleration of gravity, or

$$\frac{v_1^2}{2g} + \frac{p_1}{\rho_w g} + z_1 = \frac{v_2^2}{2g} + \frac{p_2}{\rho_w g} + z_2 = \text{constant total head} \tag{7.4b}$$

Equation (7.4b) states that the *total energy* or *head* in the system is the sum of the *velocity head*, $v^2/2g$, the *pressure head* $p/\rho_w g$ $(= P/\gamma_w)$, and the *potential (position) head* z. Whether the flow is in pipes, open channels, or through porous media, energy or head losses occur. Usually a loss term h_f is added to the second part of Eq. (7.4b); thus

$$\frac{v_1^2}{2g} + \frac{p_1}{\rho_w g} + z_1 = \frac{v_2^2}{2g} + \frac{p_2}{\rho_w g} + z_2 + h_f \tag{7.4c}$$

Why do we say *head* for each term in the one-dimensional energy equation? Because each term has units of length, and each is called the velocity head, pressure head, or potential head, as the case may be. For most soil flow problems, the velocity head is comparatively small and is usually neglected.

7.3 DARCY'S LAW FOR FLOW THROUGH POROUS MEDIA

We have already mentioned that in most cases the flow of water through the pores or voids in a soil mass can be considered laminar. We also stated that for laminar flow the velocity is proportional to the hydraulic gradient, or $v = ki$ [Eq. (7.2)]. A French waterworks engineer named Darcy[1] (1856) showed experimentally that the rate of flow in *clean sands* was proportional to the hydraulic gradient [Eq. (7.2)]. Equation (7.2) is usually combined with the continuity equation [Eq. (7.3)] and the definition of hydraulic gradient [Eq. (7.1)]. Using the notation as defined in Fig. 7.2, *Darcy's law* is usually written as

$$q = vA = kiA = k\frac{\Delta h}{L}A \tag{7.5}$$

where q is the total rate of flow through the cross-sectional area A, and the proportionality constant k is called the *Darcy coefficient of permeability*. Commonly, in civil engineering, it is called simply the *coefficient of permeability* or, even more simply, the *permeability*.

In the fields of geology, geohydrology, and hydrogeology our (geotechnical engineering) permeability is referred to as the *hydraulic conductivity*. The term "permeability" in these other fields refers to the *intrinsic permeability*, K_i, which has units of length squared (m^2) and is given by

$$K_i = \frac{k\mu}{\rho g} = \frac{k\mu}{\gamma} = \frac{k\nu}{g} \tag{7.6}$$

where g = gravitational constant, 9.8 m/s^2,

k = permeability or hydraulic conductivity, m/s,

γ = unit weight per volume, N/m^3,

μ = absolute or dynamic viscosity, Pa-s,

ν = kinematic viscosity, μ/ρ, m^2/s,

ρ = density, kg/m^3.

[1]Henry Darcy (1803–1858) was responsible for the water supply for the city of Dijon in southern France in the 1830s and 40s. Today, Dijon is better known for Grey Poupon mustard. See Philip (1995) for an interesting history of Darcy and his many important contributions.

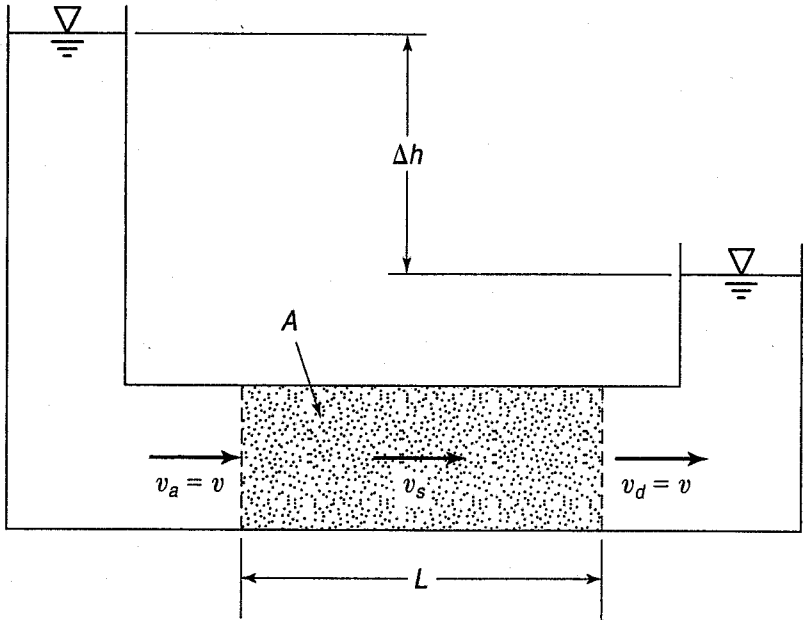

FIGURE 7.2 Superficial and seepage velocities in uniform flow (after Taylor, 1948).

In recent years, as geotechnical engineers have become involved in the cleanup of contaminated soils and groundwater, design of waste containment facilities, and other geoenvironmental problems, the term hydraulic conductivity has become almost synonymous with permeability in geotechnical practice. Using hydraulic conductivity instead of permeability also avoids misunderstanding by people who are not civil engineers.

The coefficient of permeability, k, of soil and rock is a function of the soil properties (density and void ratio) and of the density and viscosity of the pore fluid (water, oil, a chemical contaminant), which are temperature dependent. Other factors that influence k are discussed below.

Why do we use the total cross-sectional area in Eq. (7.5)? Obviously, the water cannot flow through the solid particles but only through the voids or pores between the grains. So why don't we use that area and compute the velocity based on the area of the voids? It would be relatively easy to compute the area of the voids from the void ratio e [Eq. (2.1)], even though e is a volumetric ratio. For a unit width of sample in Fig. 7.2, we can write $e = V_v/V_s = A_v/A_s$.Now the approach velocity v_a and the discharge velocity v_d in Fig. 7.2 both equal $v = q/A$, the discharge q divided by the total cross-sectional area A. Thus the v in this relationship is really a *superficial* or macroscale velocity, a fictitious but statistically convenient "engineering" velocity. The actual *seepage* velocity v_s, which is the actual velocity of the water flowing in the voids, is greater than the superficial velocity. We can show this by applying our continuity-of-flow principle in a different way:

$$q = v_a A = v_d A = vA = v_s A_v \tag{7.7}$$

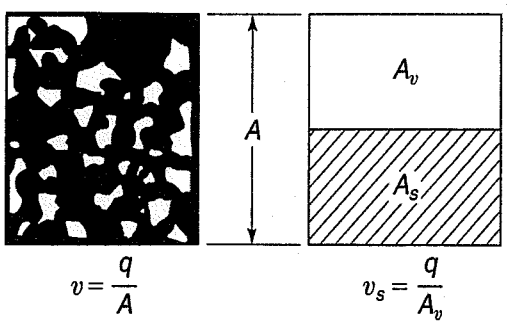

FIGURE 7.3 Phase diagram for seepage and superficial velocities of flow (flow is perpendicular to page).

From Fig. 7.3 and Eq. (2.2), $A_v/A = V_v/V = n$; then

$$v = nv_s \tag{7.8}$$

Since $0\% \leq n \leq 100\%$, it follows that the seepage velocity is always greater than the superficial or discharge velocity.

From the preceding discussion you can see that the void ratio or porosity of a soil affects the way water flows through it and thus the value of the permeability of a particular soil. From theoretical relationships for flow through capillary tubes developed by Hagen and

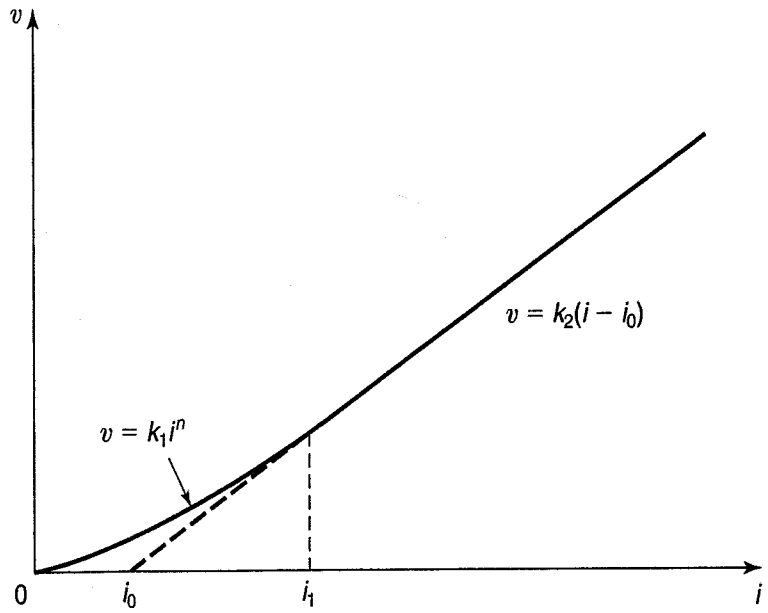

FIGURE 7.4 Deviation from Darcy's law observed in Swedish clays (after Hansbo, 1960).

Poiseuille about 1840 and from the more recent hydraulic radius models of Kozeny and Carman, we know that several other factors also affect permeability. (Leonards, 1962, Chapter 2, provides an excellent summary of these developments.) The effective grain size (or, better, the effective pore size) has an important influence here, much as it does on the height of capillary rise (Sec. 6.2). The shapes of the voids and flow paths through the soil pores, called *tortuosity*, also affect k. All of the previous discussion of permeability was for saturated soils only, so the degree of saturation S must influence the actual permeability. Finally, as noted previously, flow is affected also by the properties of the fluid, such as viscosity (which depends on the temperature) and fluid density.

Darcy originally developed his relationship for clean sands; how valid is it for other soils? Careful experiments have shown that Eq. (7.5) is valid for a wide range of soil types at reasonable, engineering hydraulic gradients. In very clean gravels and open-graded rock fills under relatively high gradients, flow may be turbulent and Darcy's law would be invalid. At the other end of the spectrum, careful investigations by Hansbo (1960) found that in clays at very low hydraulic gradients the relationship between v and i is nonlinear (Fig. 7.4). Field measurements (Holtz and Broms, 1972) showed that the exponent n has an average value of about 1.5 in typical Swedish clays. By no means, however, is there complete agreement with the concept shown in Fig. 7.4. Mitchell and Soga (2005) summarize several investigations about this point, and they conclude that "Darcy's law is valid, *provided that all system variables are held constant.*"

7.4 MEASUREMENT OF PERMEABILITY OR HYDRAULIC CONDUCTIVITY

How is the coefficient of permeability or the hydraulic conductivity of a soil or rock determined? A device called a *permeameter* is used in the laboratory, and either a *constant-head test* or a *falling-head test* is conducted [Figs. 7.5(a) and (b)]. In the field, pumping tests or infiltration tests are used to measure permeability. Infiltration tests can be either constant head or falling head, while the other types are a bit more complicated.

In the basic, one-dimensional, constant-head test, the volume of water Q collected in time t [Fig. 7.5(a)] is

$$Q = Avt$$

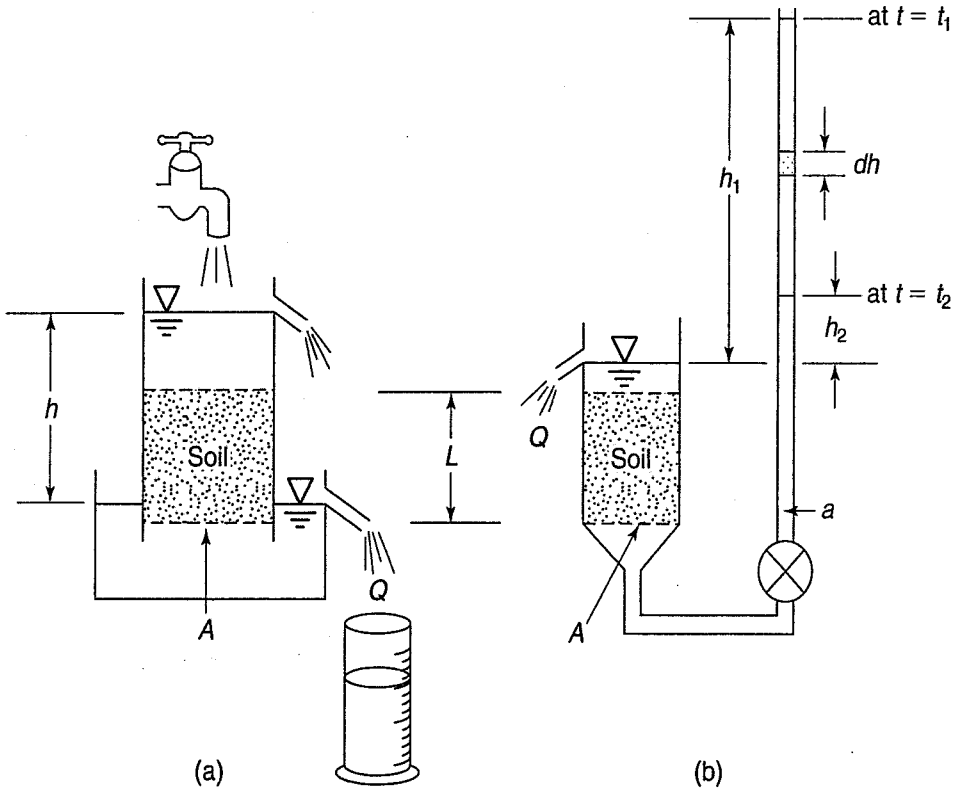

FIGURE 7.5 Determining the coefficient of permeability by the laboratory: (a) constant-head test; (b) falling-head test.

From Eq. (7.5),

$$v = ki = k\frac{h}{L}$$

so

$$k = \frac{QL}{hAt} \tag{7.9}$$

where Q = total discharge volume, m^3, in time t, s, and
A = cross-sectional area of soil sample, m^2.

Example 7.1

Given:

A cylindrical soil sample, 7.3 cm in diameter and 16.8 cm long, is tested in a constant-head permeability apparatus. A constant head of 75 cm is maintained during the test. After 1 min of testing, a total of 945.7 g of water was collected. The temperature was 20°C. The void ratio of the soil was 0.43.

Required:

Compute the coefficient of permeability in centimetres per second and in furlongs per fortnight.

Solution: First, calculate the cross-sectional area of the sample:

$$A = \frac{\pi D^2}{4} = \frac{\pi}{4}(7.3\text{ cm})^2 = 41.9\text{ cm}^2$$

From Eq. (7.9), solve for k:

$$\begin{aligned} k &= \frac{QL}{hAt} \\ &= \frac{945.7\text{ cm}^3 \times 16.8\text{ cm}}{75\text{ cm} \times 41.9\text{ cm}^2 \times 1\text{ min} \times 60\text{ s/min}} \\ &= 0.08\text{ cm/s} \end{aligned}$$

To convert to furlongs per fortnight (see Appendix A):

$$\begin{aligned} k = &\left(0.08\frac{\text{cm}}{\text{s}}\right)\left(60\frac{\text{s}}{\text{min}}\right)\left(60\frac{\text{min}}{\text{h}}\right)\left(24\frac{\text{h}}{\text{d}}\right)\left(14\frac{\text{d}}{\text{fortnight}}\right) \\ &\times \left(\frac{1\text{ in.}}{2.54\text{ cm}}\right)\left(\frac{1\text{ ft}}{12\text{ in.}}\right)\left(\frac{\text{mi}}{5280\text{ ft}}\right)\left(\frac{8\text{ furlongs}}{\text{mi}}\right) \\ = &\ 4.8\frac{\text{furlongs}}{\text{fortnight}} \end{aligned}$$

For the falling-head test [Fig. 7.5(b)] the velocity of fall in the standpipe is

$$v = -\frac{dh}{dt}$$

and the flow into the sample is

$$q_{\text{in}} = -a\frac{dh}{dt}$$

From Darcy's law [Eq. (7.5)], the flow out is

$$q_{\text{out}} = kiA = k\frac{h}{L}A$$

By Eq. (7.3) (continuity), $q_{\text{in}} = q_{\text{out}}$, or

$$-a\frac{dh}{dt} = k\frac{h}{L}A$$

Separating variables and integrating over the limits,

$$a\int_{h_2}^{h_1}\frac{dh}{h} = k\frac{A}{L}\int_{t_1}^{t_2} dt$$

we obtain

$$k = \frac{aL}{A\,\Delta t}\ln\frac{h_1}{h_2} \tag{7.10a}$$

where $\Delta t = t_2 - t_1$. In terms of $\log_{10}$,

$$k = 2.3\frac{aL}{A\,\Delta t}\log_{10}\frac{h_1}{h_2} \tag{7.10b}$$

where a = area of standpipe,
A, L = soil sample area and length,
Δt = time for standpipe head to decrease from h_1 to h_2.

Example 7.2

Given:

A laboratory falling-head permeability test is performed on a light-gray gravelly sand (SW), and the following data is obtained:

$a = 6.25\ \text{cm}^2$
$A = 10.73\ \text{cm}^2$
$L = 16.28\ \text{cm}^2$
$h_1 = 160.2\ \text{cm}$
$h_2 = 80.1$ cm, and
$\Delta t = 90$ s for the head to fall from h_1 to h_2.

Water temperature = 20°C.

Required:

Compute the coefficient of permeability in cm/s.

Solution: Use Eq. (7.10b) and solve for k

$$k = 2.3 \times \frac{6.25}{10.37} \times \frac{16.28}{90}\log\frac{160.2}{80.1}$$
$$= 0.07\ \text{cm/s at } 20°\text{C}$$

Note: If the water temperature is different than 20°C, a correction for differences in the value of the viscosity is made.

7.4.1 Laboratory and Field Hydraulic Conductivity Tests

Although the two examples given above are for laboratory tests, the basic equations for constant and falling head tests also apply to field tests. This section gives the common laboratory and field k tests standardized by ASTM.

The standard laboratory constant head permeability test is D 2434 (ASTM, 2010). This test uses a rigid wall permeameter and consequently is appropriate only for granular soils. For fine-grained soils, ASTM (2010) D 5084 is the appropriate laboratory test, because it uses a flexible wall permeameter that eliminates the tendency for flow to occur between the test specimen and the permeameter wall. Also, the test specimen can be saturated by the use of backpressure (Chapter 12). Test standard D 5084 has six parts: constant head; falling head—constant tailwater elevation; falling head—rising tailwater elevation; constant rate of flow; and two constant volume methods using special mercury tube measurement devices.

Because of recent developments in geoenvironmental engineering and groundwater monitoring for environmental purposes, ASTM has developed numerous procedures and tests for groundwater monitoring and vadose-zone investigations. Guides for comparison of these field methods, including pumping and slug tests, are in ASTM (2010) D 4043, D 4044, and 5126.

In field pumping tests, which are typically conducted in boreholes, water is withdrawn from a central well at a constant rate, and groundwater levels at various distances from the central well are monitored in wells or by piezometers. In a slug test, a volume of water is either removed from or added to a groundwater well, and the change in water level with time is monitored (this is also referred to as a "perc" test, since it measures the percolation of water into or out of the soil). Pumping tests are a more complex version of the one-dimensional, constant-head test, and slug tests are similarly a three-dimensional version of the falling-head test. Another type of field permeability test is the ring infiltrometer test (D 3385), which can be conducted either constant head or falling head on soils at or near the ground surface.

7.4.2 Factors Affecting Laboratory and Field Determination of *k*

Several factors influence the reliability of the permeability test in the laboratory. Air bubbles may be trapped in the test specimen, or air may come out of solution from the water. The degree of saturation could thus be less than 100%, which would affect the test results significantly. Deaired water and not tap water should always be used for laboratory k tests. In constant head tests on granular soils, several pore volumes of deaired water should be passed through the specimen until a constant value of k is obtained. In the flexible wall hydraulic conductivity test, the specimen can be saturated by the use of backpressure (discussed in Chapter 12). Migration of fines in testing sands and silts affects the measured values. Especially when testing very loose granular specimens, it is difficult to maintain a constant void ratio, but if the void ratio changes during the test, the measured values are obviously incorrect. Temperature variation, especially in tests of long duration, may affect the measurements, and if the ground temperature is significantly less than the laboratory test temperature, a viscosity correction should be made.

Although the small samples used in the laboratory are assumed to be representative of field conditions, it is difficult to duplicate the in situ soil structure, especially of granular deposits and of stratified and other nonhomogeneous materials. (Remember what you have read in Chapters 3 and 4.) To properly account for the natural variability and inhomogeneity of soil deposits and for difficulties in laboratory tests, field pumping tests from wells or infiltration tests are commonly used to measure the overall average coefficient of permeability. These tests have their own problems, including costs, but the advantage of obtaining an overall average measure of hydraulic conductivity at a site makes field tests often worth the time and expense.

The coefficient of permeability may also be obtained indirectly by performing a laboratory one-dimensional compression (consolidation) test (Chapter 8), or by testing a soil sample in the triaxial cell, a variation of the ASTM D 5084 flexible wall k test. Triaxial tests are discussed in Chapter 11.

7.4.3 Empirical Relationships and Typical Values of *k*

Besides the direct determination of permeability or hydraulic conductivity in the laboratory, useful empirical formulas and tabulated values of k exist for various soil and rock types.

One very popular empirical equation relates the coefficient of permeability to D_{10}, the *effective grain size*. This relationship was proposed by A. Hazen (1911) for *clean* sands (with less than 5% passing the No. 200 sieve) and with D_{10} sizes between 0.1 and 3.0 mm, or

$$k = CD_{10}^2 \tag{7.11}$$

where the units of k are in cm/s and those of the effective grain size are in mm. The constant C varies from 0.4 to 1.2, so an average value of 1 is commonly assumed, and this constant takes into account the conversion of units. The equation is valid for $k \geq 10^{-3}$ cm/s.

As mentioned, the Hazen equation is very popular and often applied to soils well outside its specified limitations. Carrier (2003) proposed an alternative that is based on the more fundamental Kozeny–Carmen equation mentioned above. Although Carrier's approach is somewhat more complicated than the simple Hazen equation, it is more accurate because it takes into account the complete grain size distribution (not just D_{10}), the particle shape, and the void ratio of the soil. A small but interesting point: Carrier (2003) notes that Hazen developed his equation for use at at 10°C and not 20°C as commonly assumed; thus we really should multiply C in Eq. (7.11) by 1.3.

To estimate k at void ratios other than the test void ratio, Taylor (1948) offers the relationship

$$k_1 : k_2 = \frac{C_1 e_1^3}{1 + e_1} : \frac{C_2 e_2^3}{1 + e_2} \tag{7.12}$$

where the coefficients C_1 and C_2, which depend on the soil structure, must be determined empirically. *Very approximately for sands*, $C_1 \approx C_2$. This means that if one has determined C for a particular sand using Eq. (7.11), it can be assumed to be about the same for another similar sand. Another relationship found useful for sands is

$$k_1 : k_2 = C_1' e_1^2 : C_2' e_2^2 \tag{7.13}$$

As before, *approximately for sands*, $C_1' \approx C_2'$.

For silts and clays, none of these three relationships, Eqs. (7.11) to (7.13) works very well. For kaolinites over a rather *narrow* range of permeabilities (say one order of magnitude), e versus $\log_{10} k$ has been found to be approximately linear, all other factors being equal (Taylor, 1948; Mesri et al., 1994). For compacted silts and silty clays, however, Garcia-Bengochea et al. (1979) found that the relationship between void ratio e and the logarithm of permeability k is far from linear (Fig. 7.6). They showed that pore size distribution parameters provide a better relationship with the ratio for some compacted soils.

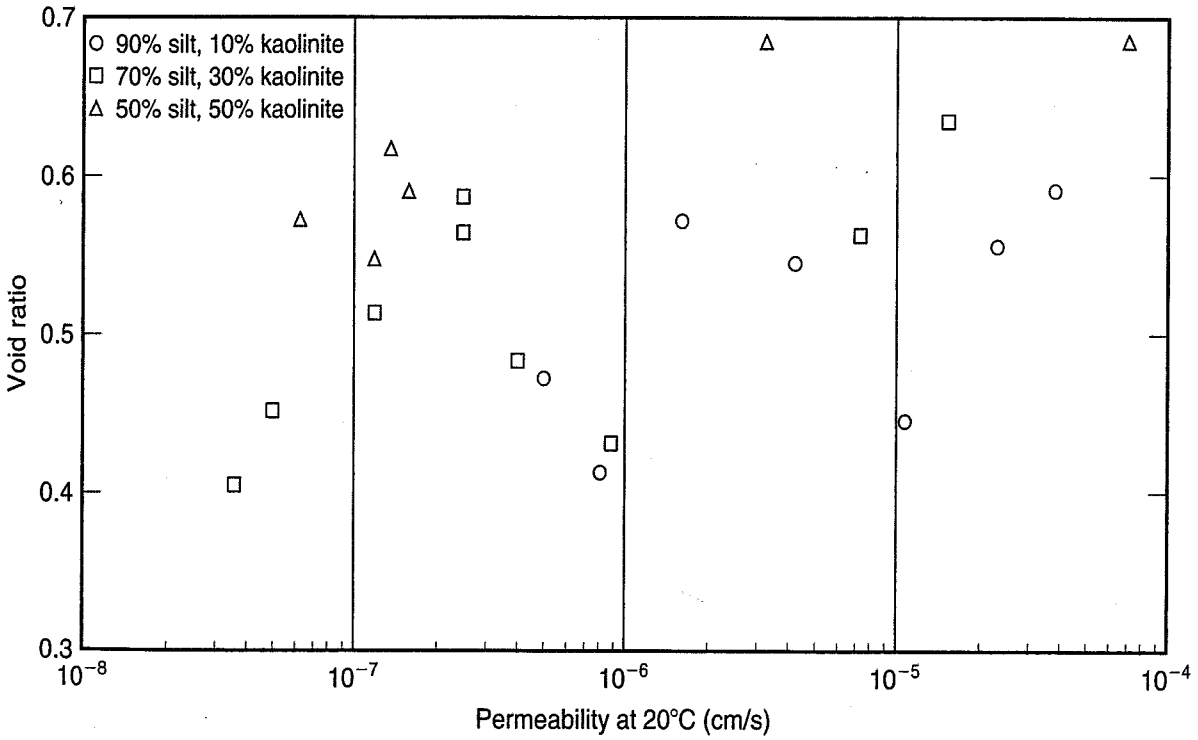

FIGURE 7.6 Void ratio e versus permeability k for several compacted soils (after Garcia-Bengochea et al., 1979).

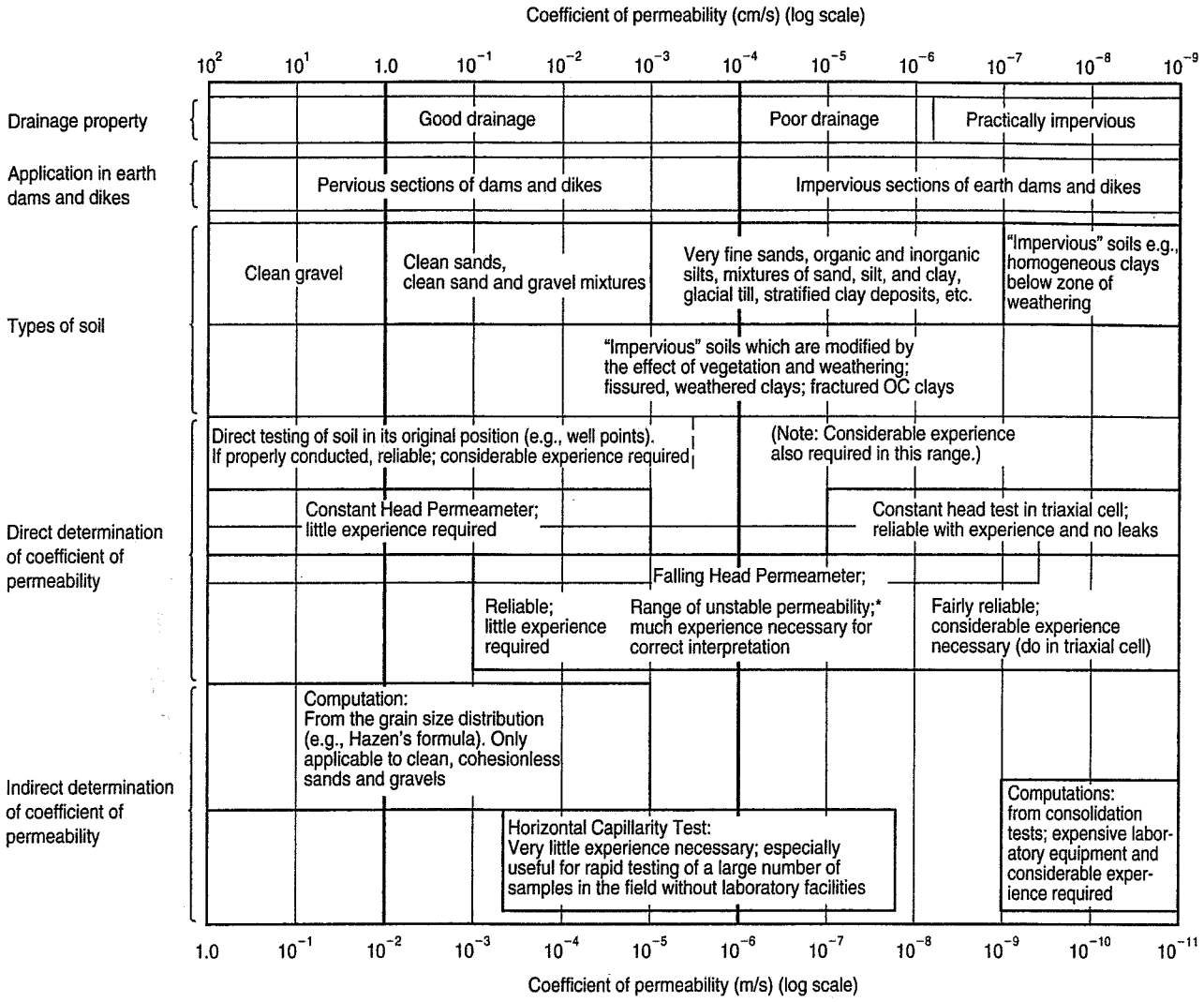

*Due to migration of fines, channels, and air in voids.

FIGURE 7.7 Permeability, drainage, soil type, and methods to determine the coefficient of permeability (after A. Casagrande, 1938, with minor additions).

For example, Fig. 7.7 is useful. The coefficient of permeability is plotted here on a log scale, since the range of permeabilities in soils is so large. Note that certain values of k—1.0, 10^{-4}, and 10^{-9} cm/s (10^{-2}, 10^{-6}, and 10^{-11} m/s)—are emphasized. These are Casagrande's *benchmark values* of permeability, and they are useful reference values for engineering behavior. For example, 1.0 cm/s (10^{-2} m/s) is the approximate boundary between laminar and turbulent flow and separates clean gravels from clean sands and sandy gravels. A k of 10^{-4} cm/s or 10^{-6} m/s is the approximate boundary between pervious and poorly drained soils under low gradients. Soils around this value are also highly susceptible to migration of fines or *piping*. The next boundary, 10^{-9} cm/s (10^{-11} m/s), is approximately the lower limit of the permeability of soils and concrete, although some recent measurements have found permeabilities as low as 10^{-13} m/s for highly plastic clays at the shrinkage limit. Professor Casagrande recommended that k be related to the nearest benchmark value—for example, 0.01×10^{-4} cm/s rather than 1×10^{-6} cm/s—but that recommendation has not been especially popular. For various soil and rock types, Fig. 7.7 also indicates their general drainage properties, applications to earth dams and dikes, and the means for direct and indirect determination of the coefficient of permeability.

For compacted clays, permeability at constant compactive effort decreases with increasing water content and reaches a minimum at about the optimum. Figure 7.8 shows that the permeability is about an order of magnitude higher when this soil is compacted dry of optimum than when compacted wet of

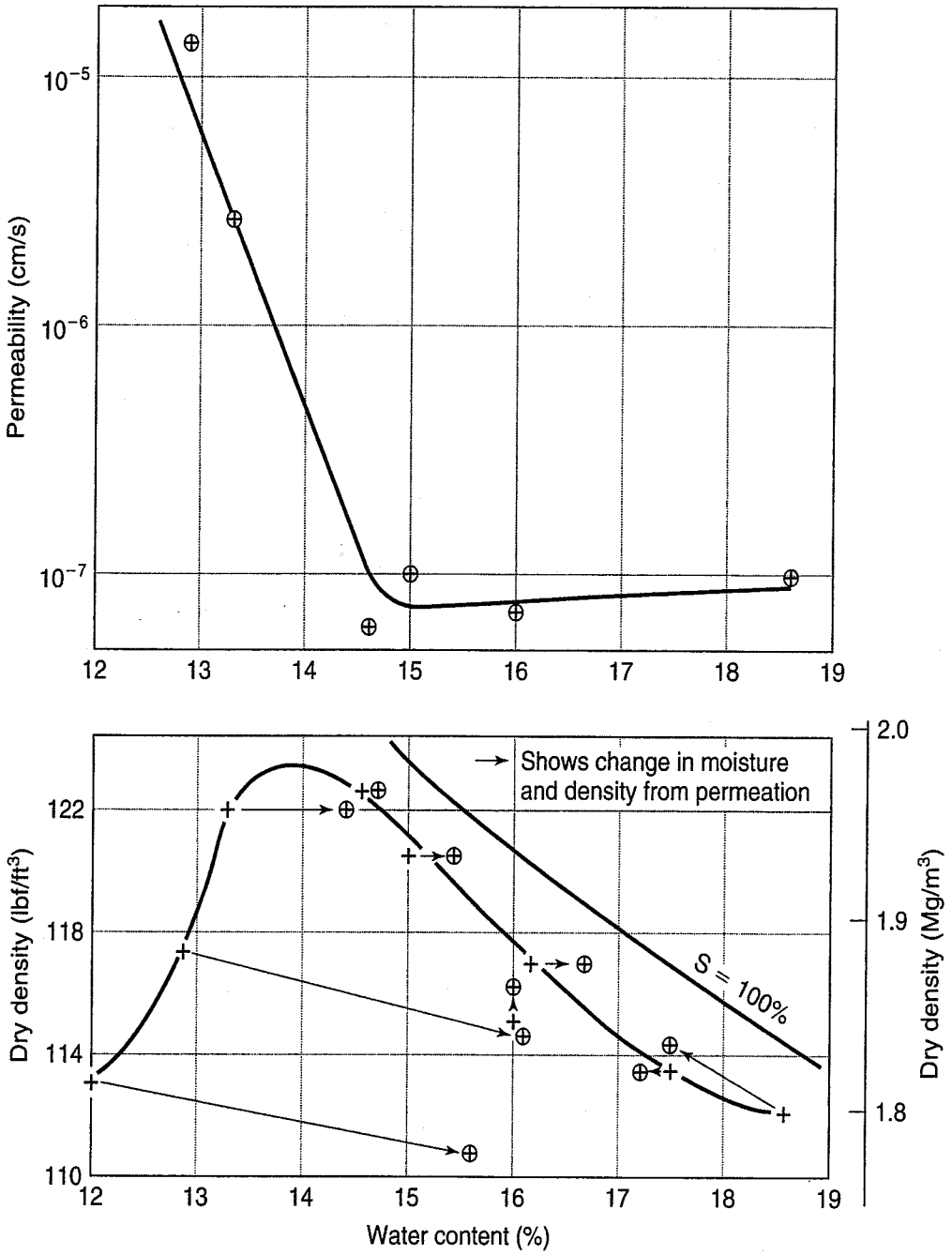

FIGURE 7.8 Change in permeability with molding water content (after Lambe, 1958b).

optimum. If the compactive effort is increased, the coefficient of permeability (hydraulic conductivity) decreases, because the void ratio decreases (increasing dry density or unit weight). According to Lambe (1958b), the permeability of soils compacted on the dry side of optimum reduces with time due to permeation, whereas for soils compacted wet of optimum, the permeability remains more or less constant with time.

Table 7.1 gives some additional values of the hydraulic conductivity for different rock types. Recognize that hydraulic conductivity is one of the most difficult properties to determine, especially for rock, and that the values in Table 7.1 are only a rough approximation and should be used with caution. Very often, the joints and fractures control the in situ hydraulic conductivity and not the intact rock itself.

TABLE 7.1 Typical Values of the Hydraulic Conductivity for Rocks

Rock Type	Hydraulic Conductivity (m/s)
Basalt	1.2×10^{-7}
Dolomite	1.2×10^{-8}
Gabbro, weathered	2.3×10^{-6}
Granite, weathered	1.6×10^{-5}
Limestone	1.1×10^{-5}
Sandstone, fine grained	2.3×10^{-6}
Sandstone, medium grained	3.6×10^{-5}
Schist	2.3×10^{-6}
Slate	9.3×10^{-10}
Tuff	2.3×10^{-6}

Modified after Morris and Johnson (1967).

7.5 HEADS AND ONE-DIMENSIONAL FLOW

Early in this chapter we mentioned the three types of heads associated with the one-dimensional energy equation [Eq. (7.4)]—the velocity head $v^2/2g$, the pressure head $h_p = p/\rho_w g$, and the position or elevation head z. We discussed why the energy per unit mass (or weight) was called head and had units of length. And we also stated that, for most seepage problems in soils, the velocity head was small enough to be neglected. Thus total head h becomes the sum of the pressure head and the elevation head, or $h = h_p + z$. In fluid mechanics, h is referred to as the piezometric head. However, in soil mechanics, h_p only is called the *piezometric* head. This is because it is the height of water that would be found in an open standpipe or determined by a piezometer, as measured from the elevation at point X where the standpipe or piezometer inlet is located. The pore water pressure, u_x, at point X divided by the unit weight of water ($\rho_w g$) equals the piezometric head.

The elevation head at any point is the vertical distance above or below some reference elevation or datum plane. It is most often convenient to establish the datum plane for seepage problems at the tailwater elevation (the elevation at the lower of the two phreatic surfaces), but you could just as well use the bedrock or some other convenient elevation as the datum. The advantage of using a datum at the lower phreatic surface is that water at this location will have zero total head ($h_p = 0$ and $z = 0$). Pressure head is simply the water pressure divided by $\rho_w g$ [Eq. (7.4)].

These concepts are illustrated in Fig. 7.9. Here we have an open-ended cylinder of soil similar to the permeameter of Fig. 7.5(a). The flow into the cylinder is sufficient to maintain the water elevation at A, and the tail water is constant at elevation E. All energy or head is lost in the soil.

Note that for piezometer c in the figure, the pressure head h_p is the distance AC and the elevation head z is the distance CE. Thus the total head at point C is the sum of these two distances, or AE. Determinations of the piezometric heads at the other points in Fig. 7.9 are made in a similar manner, and these are shown in the table below the figure. Be sure you understand how each of the heads, including the head loss through the soil, is obtained in Fig. 7.9. Note that it is possible for the elevation head (as well as the pressure head) to be negative, depending on the geometry of the problem. The important thing is that the total head must equal the sum of the pressure and elevation head at all times.

As mentioned, we assume that all the energy or head lost in the system is lost in flowing through the soil sample of Fig. 7.9. Thus at elevation C no head loss has yet occurred; at D, the midpoint of the sample, half the head is lost (½ AE); and at F, all of the head has been lost (AE).

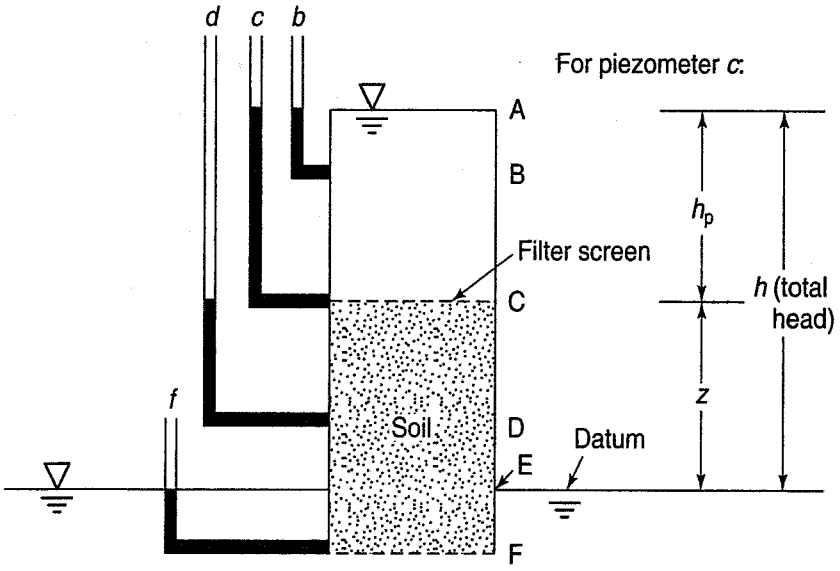

Point	Pressure Head	Elevation Head	Total Head	Head Loss through Soil
B	AB	BE	AE	0
C	AC	CE	AE	0
D	CD	DE	CE	$^1/_2$AE
F	EF	−EF	0	AE

FIGURE 7.9 Illustration of types of head (after Taylor, 1948).

The following examples illustrate how you determine the various types of heads and head loss in some simple one-dimensional flow systems.

Example 7.3

Given:

The test setup of Fig. 7.9 has the dimensions shown in Fig. Ex. 7.3a.

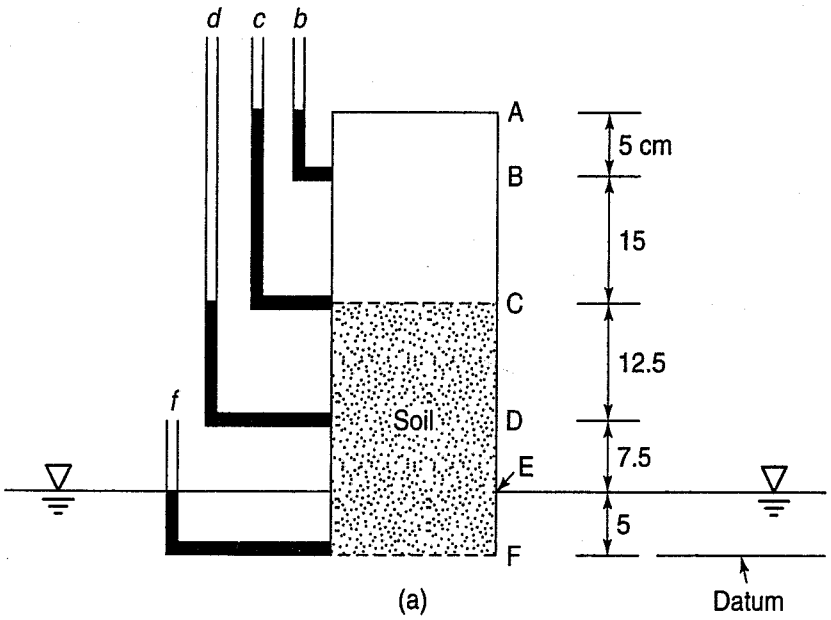

FIGURE Ex. 7.3a

Required:

a. Calculate the magnitude of pressure head, elevation head, total head, and head loss at points B, C, D, and F, in centimetres of water.

b. Plot the heads versus the elevation.

Solution:

a. List dimensions and heads in a table as in Fig. 7.9, as shown below; the heads are in units of centimetres of water.

Point	Pressure Head	Elevation Head	Total Head	Head Loss
B	5	35	40	0
C	20	20	40	0
D	12.5	7.5	20	20
F	5	−5	0	40

b. See Fig. Ex. 7.3b.

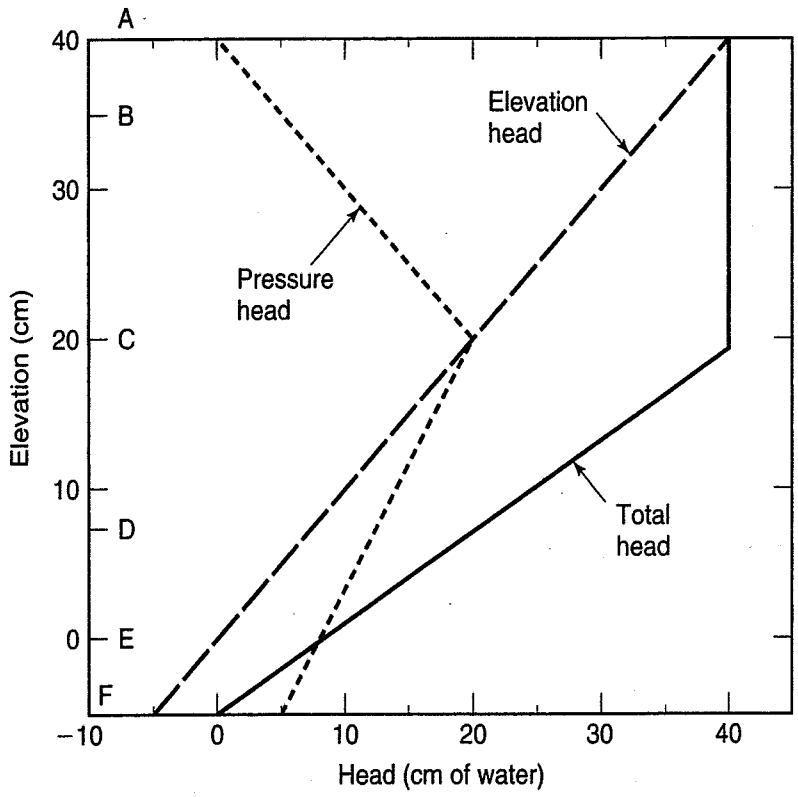

(b)

FIGURE Ex. 7.3b

Example 7.4

Given:

The cylinder of soil and standpipe arrangement shown in Fig. Ex. 7.4.

Required:

Determine the pressure head, elevation head, total head, and head loss at points B, C, and D. BC = CD.

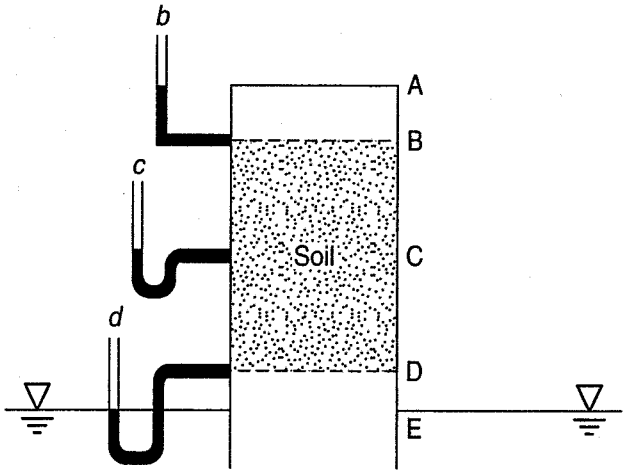

FIGURE Ex. 7.4 (After Taylor, 1948).

Solution: Set up a table similar to that of Fig. 7.9 and Example 7.3.

Point	Pressure Head	Elevation Head	Total Head	Head Loss
B	AB	BE	AE	0
C	0	CE	CE	½ AE
D	−DE	DE	0	AE

Example 7.5

Given:

The horizontal cylinder of soil as shown in Fig. 7.2. Assume $L = 10$ cm, $A = 10$ cm^2, and $\Delta h = 5$ cm. Tailwater elevation is 5 cm above the centerline of the cylinder. The soil is a medium sand with $e = 0.68$.

Required:

Determine the pressure, elevation, and total head at sufficient points to be able to plot them versus horizontal distance.

Solution: Redraw Fig. 7.2 in Fig. Ex. 7.5a with the key dimensions. Estimate the other required dimensions. Label the key points as shown. Assume the datum is the elevation of the tailwater. Set up a table as in Fig. 7.9, and fill in the blanks. The units are in centimetres of water.

Point	Pressure Head	Elevation Head	Total Head	Head Loss
A	10	−5	5	0
B	10	−5	5	0
C	7.5	−5	2.5	2.5
D	5	−5	0	5
E	5	−5	0	5

The plot of heads versus horizontal distance is in Fig. 7.5(b) for the centerline of the cylinder.

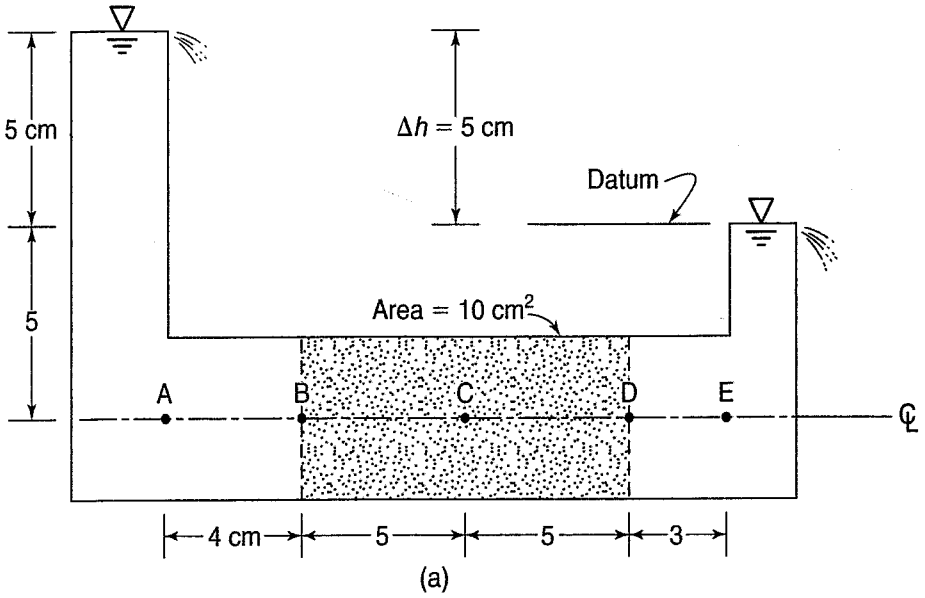

FIGURE Ex. 7.5a

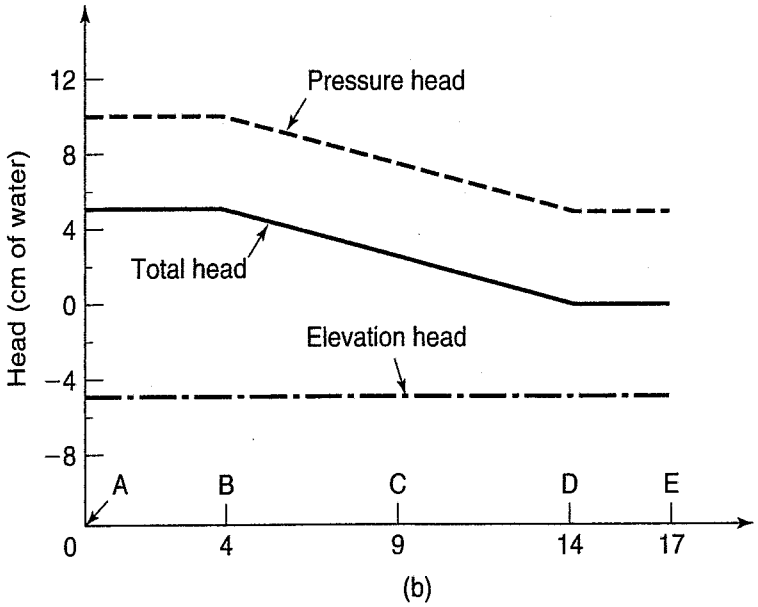

FIGURE Ex. 7.5b

Example 7.6

Given:

A cylinder similar to Ex. 7.5 except the line A–E slopes downward at 2H:1V.

Required:

Determine the pressure, elevation, and total head at sufficient points to be able to plot them versus horizontal distance.

Solution: Redraw Fig. 7.2 in Fig. Ex. 7.6a at the appropriate slope. Estimate the other required dimensions. Label the key points as shown. Assume the datum runs through point E. Set up a table as in Fig. 7.9 and fill in the blanks. The units are in centimetres of water. The plot of heads versus horizontal distance is in Fig. Ex. 7.6b for the centerline of the cylinder.

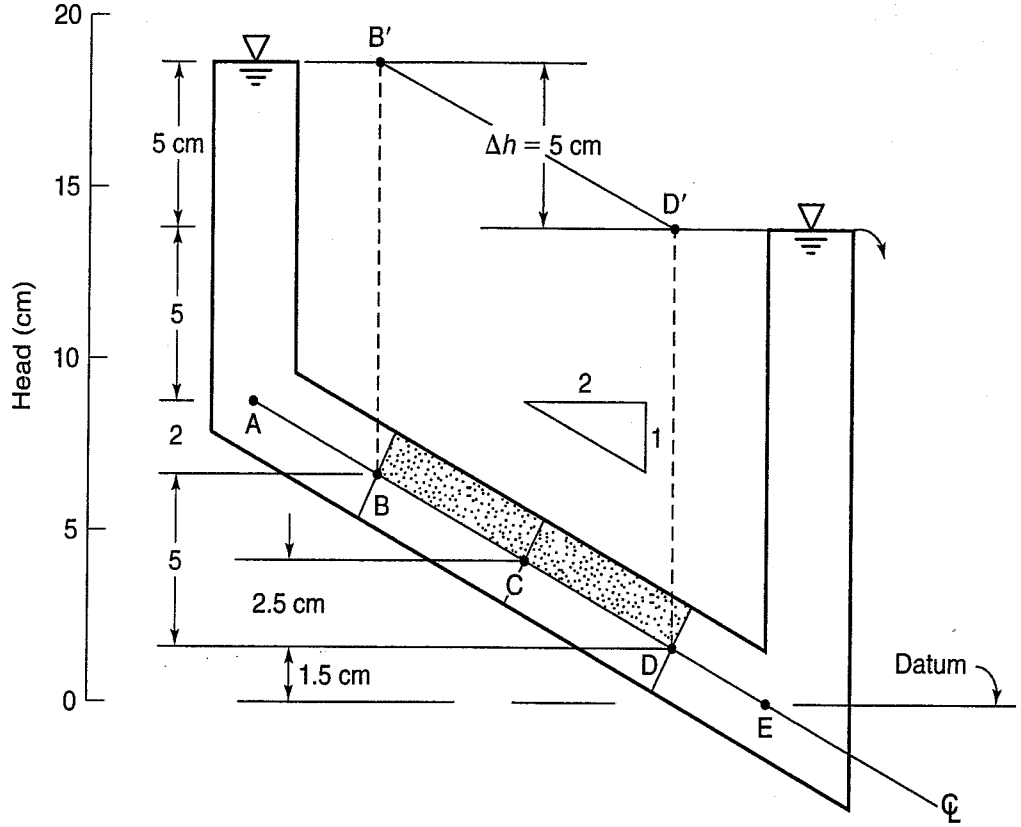

FIGURE Ex. 7.6a

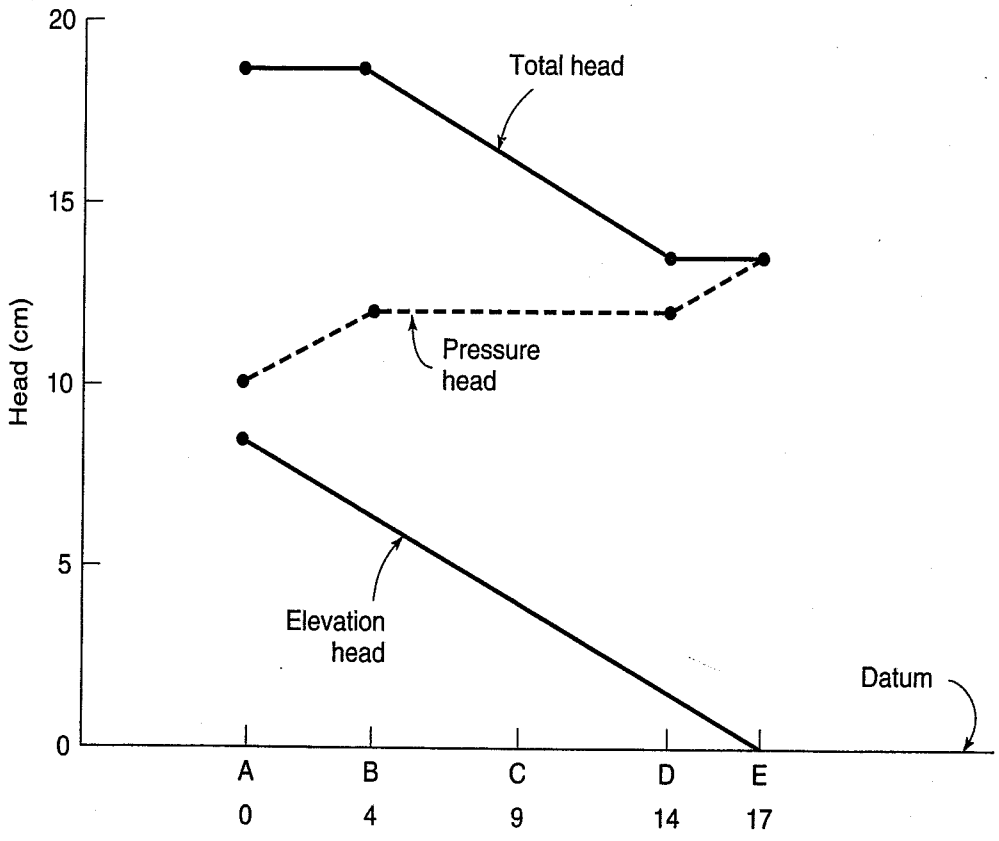

FIGURE Ex. 7.6b

Point	Pressure Head (cm)	Elevation Head (cm)	Total Head (cm)	Head Loss (cm)
A	10	8.5	18.5	0
B	12	6.5	18.5	0
C	12	4	16	2.5
D	12	1.5	13.5	5
E	13.5	0	13.5	5

Example 7.7

Given:

Similar setup as Ex. 7.5 with two exceptions: (1) units are in *metres*, and (2) the two soils in the horizontal cylinder have different permeabilities, and $k_1 = 10k_2$. Assume that $L_1 = 4$ m and $L_2 = 6$ m. Note that the head loss over the full length of soil will not be linear.

Required:

Determine the pressure, elevation, and total head at sufficient points to be able to plot them versus horizontal distance.

Solution: Redraw Fig. 7.2 as in Fig. Ex. 7.7a. Estimate the other required dimensions. Label the key points as shown. Assume the datum runs through points A–E. Set up a table as in Fig. 7.9 and fill in the blanks. The units are in metres of water. The plot of heads versus horizontal distance is in Fig. Ex. 7.7b for the centerline of the cylinder.

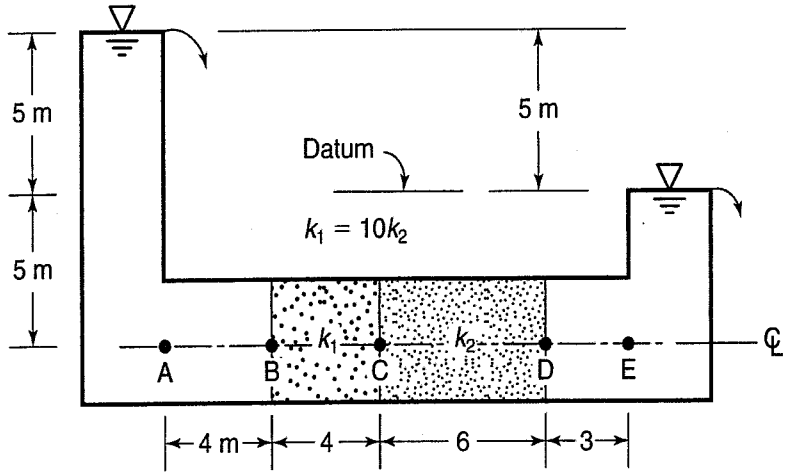

FIGURE Ex. 7.7a

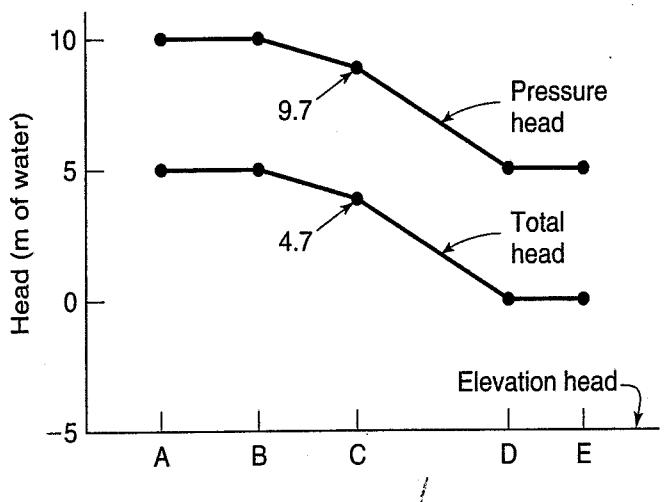

FIGURE Ex. 7.7b

We now have the tools to solve this problem. Use Eq. (7.5), and recognize that the flow is in series. Thus the quantity of flow in one soil has to be the same as in the second soil. So,

$$q_1 = k_1 i_1 A_1 = q_2 = k_2 i_2 A_2$$

Since the areas are the same, $q_{1,2} = k_1 i_1 = k_2 i_2$ with $k_1 = 10k_2$ and $i = \Delta h/l$.
Substituting,

$$q_{1,2} = 10k_2 \frac{\Delta h_1}{L_1} = k_2 \frac{\Delta h_2}{L_2}$$

Also, the total head loss, $\Delta h = \Delta h_1 + \Delta h_2$. So, $\Delta h_1 = \Delta h - \Delta h_2$, and we obtain

$$q_{1,2} = 10k_2 \frac{(\Delta h - \Delta h_2)}{L_1} = k_2 \frac{\Delta h_2}{L_2}$$

Rearranging and multiplying out,

$$L_2 10k_2 \Delta h - L_2 10k_2 \Delta h_2 = k_2 \Delta h_2 L_1$$

Rearranging and canceling out the k_2's,

$$10L_2 \Delta h = \Delta h_2 (L_1 + 10L_2)$$

Solving for Δh_2,

$$\Delta h_2 = \frac{10L_2 \Delta h}{L_1 + 10L_2}$$
$$= \frac{10 \times 6\,\text{m} \times 5\,\text{m}}{(4\,\text{m} + 10 \times 6\,\text{m})} = \frac{300\,\text{m}^2}{64\,\text{m}}$$
$$= 4.69\,\text{m}$$
$$\therefore \Delta h_1 = \Delta h - \Delta h_2 = 5 - 4.69 = 0.31\,\text{m}$$

Point	Pressure Head (m)	Elevation Head (m)	Total Head (m)	Head Loss (m)
A	10	−5	5	0
B	10	−5	5	0
C	9.7	−5	4.7	0.31
D	5	−5	0	5
E	5	−5	0	5

Because the permeability of soil 2 is so much less than that of soil 1, most of the head is lost in soil 2.

Example 7.8

Given:

Same physical setup as in Ex. 7.7 except the two soils are parallel to each other. Let $k_1 = 5k_2$, and of course, $L_1 = L_2$. Soil 1 has area A_1 and soil 2, A_2. Note that the datum in Fig. Ex. 7.8 is at the centerline of the cylinder and goes through points A–E.

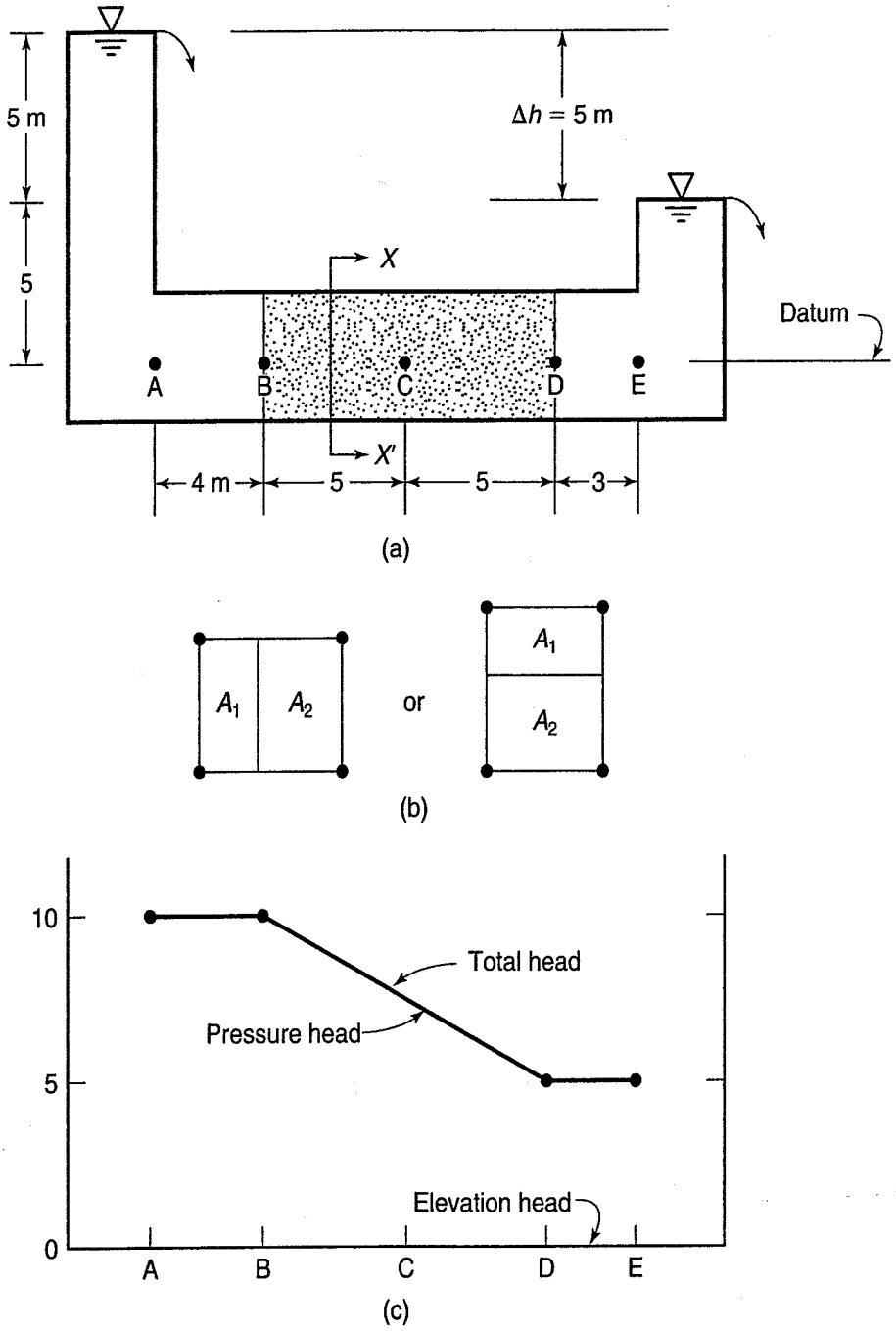

FIGURE Ex. 7.8

Required:

Determine the pressure, elevation, and total head at sufficient points to be able to plot them versus horizontal distance. Determine the quantity of flow in each soil.

Solution: In this problem, unlike the previous example, the gradient is the same but the quantity of flow is different in the two soils because of the different permeabilities. The physical setup is shown in Fig. Ex. 7.8a, while a cross section $(X-X')$ is given in Fig. Ex. 7.8b. Regardless of the way we assume the layering (side-by-side vertically or horizontally), let's assume that the datum is along the centerline between the two soils. This eliminates the need for two separate solutions.

From Fig. Ex. 7.8a, estimate the other required dimensions. Label the key points as shown. Set up a table as in Fig. 7.9 and fill in the blanks. The units are in metres of water. The plot of heads versus

horizontal distance is in Fig. Ex. 7.8c for the centerline of the cylinder. Because the two soils are parallel to each other with different permeabilities, the total flow in each soil layer will be the sum of q_1 and q_2. The amount of flow in each soil layer is given by

$$q_1 = k_1 i A_1 \quad \text{and} \quad q_2 = k_2 i A_2$$

And

$$q = q_1 + q_2$$

In this example, the k's and A's are different but the gradient is the same. We cancel the i's and substitute $k_1 = 5k_2$, or

$$q_1 = k_1 i A_1$$
$$q_2 = k_2 i A_2$$
$$q = (q_1 = 5k_2 A_1) + (q_2 = k_2 A_2)$$
$$q = 5k_2 A_1 + k_2 A_2 + k_2(5A_1 + A_2)$$

Each soil type has the same head loss, but soil 1 has five times the amount of flow as soil 2. So, we can just draw in the rest of the head loss between points B and D with a straight line. Because the datum is along the "centerline" of the two soils, the total head equals the pressure head.

Point	Pressure Head (m)	Elevation Head (m)	Total Head (m)	Head Loss (m)
A	10	0	10	0
B	10	0	10	0
C	7.5	0	7.5	2.5
D	5	0	5	5
E	5	0	5	5

If you understand the above examples, you should be able to solve a wide variety of head and one-dimensional flow problems, such as horizontal and inclined flow systems, multiple soil layers in either series or parallel, or combinations of these.

7.6 SEEPAGE FORCES, QUICKSAND, AND LIQUEFACTION

When water flows through soils (such as in the permeability tests already discussed), it exerts *seepage forces* on the individual soil grains. And, as you might imagine, seepage forces affect the intergranular or effective stresses in the soil mass, which under certain conditions can have important practical consequences. If the seepage forces are large enough, the effective stress can go to zero and the soil becomes essentially a dense liquid called *quicksand*. Another important consequence is *liquefaction* caused by vibrations from earthquakes and other dynamic sources. In this section we discuss seepage forces, how they are calculated, and the phenomena of quicksand and liquefaction.

7.6.1 Seepage Forces, Critical Gradient, and Quicksand

Let us reconsider the 5 m column of soil of Example 6.6. By connecting a riser tube to the bottom of the sample, we can flow water into the column of soil, as shown in Fig. 7.10. When the water level in the riser tube is at elevation B, we again have the static case and all the standpipes are at elevation B. If the

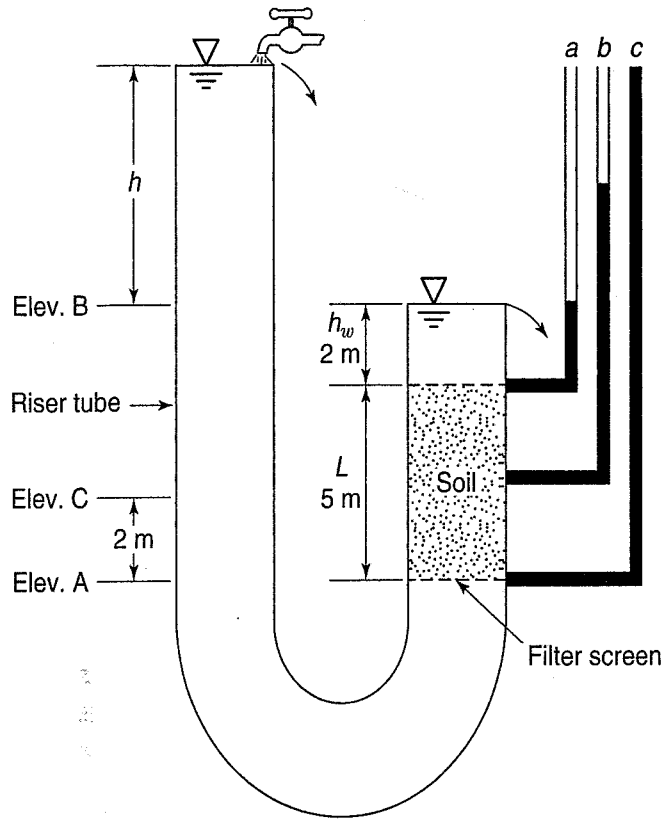

FIGURE 7.10 Sample of soil from Example 6.6, but with a riser tube connected to the bottom of the sample. Standpipes are shown for the case where the water level in the riser pipe is at a distance h above elevation B.

water in the riser tube is below elevation B, water will flow *downward* through the soil; when it is above elevation B, the reverse is true. This is the same case as the falling-head permeameter test setup of Fig. 7.5(b) in which water flows *upward* through the soil: when this happens, the water loses some of its energy through friction. The greater the head h above elevation B in Fig. 7.10, the larger the energy or head loss and the larger the seepage forces transmitted to the soil. As the seepage forces increase, they gradually overcome the gravitational forces acting on the soil column, and eventually a *quick* condition (in this case, "quick" means "alive" or "living") or *boiling* will occur. Another name for this phenomenon is *quicksand*. To have a sand mass in a quick condition, the effective stresses throughout the sample must be zero.

At what height h above elevation B does the soil become quick? First, from Fig. 7.10 we can calculate the total, neutral, and effective stress at elevation A when the water level in the riser tube is at elevation B. We will neglect any friction losses in the riser tube. Total stress at the bottom of the sample (elevation A) is

$$\sigma = \rho_{sat} g L + \rho_w g h_w = \rho' g L + \rho_w g (L + h_w) \tag{a}$$

The pore pressure at that point is

$$u = \rho_w g (L + h_w) \tag{b}$$

Therefore the effective stress is [Eqs. (a) − (b)]:

$$\sigma' = \sigma - u = \rho' g L \tag{c}$$

Let the water level rise a distance h *above* elevation B (Fig. 7.10). Now the pore water pressure at the bottom of the sample is

$$u = \rho_w g (L + h_w + h) \tag{d}$$

or the pore pressure difference acting at the bottom of the sample is [Eqs. (d) − (b)]:

$$\Delta u = \rho_w g h \tag{e}$$

The effective stress at the bottom of the soil column (elevation A) is now [Eqs. (a) − (d)]:

$$\sigma' = [\rho' g L + \rho_w g(L + h_w)] - [\rho_w g(L + h_w + h)]$$

or

$$\sigma' = \rho' g L - \rho_w g h \tag{f}$$

Thus the effective stress has decreased by exactly the increase in pore water pressure Δu at the base of the sample [Eqs. (f) − (c) = (e)].

What happens when the effective stress at the bottom of the soil column is zero? (Note that σ' cannot be less than zero.) Set Eq. (f) equal to zero and solve for Eq. (h), which is the head above elevation B to cause a *quick* condition, or

$$h = \frac{L\rho'}{\rho_w}$$

Rearranging,

$$\frac{h}{L} = i = \frac{\rho'}{\rho_w} = i_c \tag{7.14}$$

By Eq. (7.1), the head h divided by the sample length L equals the hydraulic gradient i. The value i when a quick condition occurs is called the *critical hydraulic gradient* i_c.

In Sec. 2.3.1 we obtained the following relationship for the submerged density ρ':

$$\rho' = \frac{\rho_s - \rho_w}{1 + e} \tag{2.19}$$

Combining Eqs. (7.14) and (2.19), we obtain an expression for the critical hydraulic gradient necessary for a quick condition to develop:

$$i_c = \frac{\rho_s - \rho_w}{(1 + e)\rho_w} \tag{7.15}$$

or

$$i_c = \frac{1}{1 + e}\left(\frac{\rho_s}{\rho_w} - 1\right) \tag{7.16}$$

The approach just used to obtain i_c is based on the premise that quick conditions occur when the effective stress at the bottom of the soil column is zero.

Another way to obtain the formula for the critical gradient is to consider the *total boundary pore water pressure* and the *total weight* of all the material above that boundary. Quick conditions then occur if these forces are just equal. From Fig. 7.10, the upward force equals the pore water pressure acting on the filter screen at elevation A on the bottom of the soil column, or

$$F_{\text{water}} \uparrow = (h + h_w + L)\rho_w g A$$

where A is the cross-sectional area of the sample.

TABLE 7.2 Typical Values of i_c for $\rho_s = 2.68$ Mg/m^3

Void Ratio	Approximate Relative Density	i_c
0.5	Dense	1.12
0.75	Medium	0.96
1.0	Loose	0.84

The total weight of soil and water acting downward at the bottom of the sample (elevation A) is

$$F_{\text{soil + water}} \downarrow = \rho_{\text{sat}} gLA + \rho_w g h_w A$$

Equating these two forces, we obtain

$$(h + h_w + L)\rho_w gA = \rho_{\text{sat}} gLA + \rho_w g h_w A \tag{g}$$

Use Eq. (2.17) for ρ_{sat} and do the algebra to satisfy yourself that Eq. (g) reduces to Eq. (7.15). Therefore both approaches, total and effective, will give the same results.

We can compute typical values of the critical hydraulic gradient, assuming a value of $\rho_s = 2.68$ Mg/m^3 and void ratios representative of loose, medium, and dense conditions. The values of i_c are presented in Table 7.2. Thus, for estimation purposes, i_c is often taken to be about unity, which is a relatively easy number to remember.

Example 7.9

Given:

The soil sample and flow conditions of Fig. 7.10 and Example 6.6.

Required:

a. Find the head required to cause quick conditions.

b. Find the critical hydraulic gradient.

Solution:

a. From Eq. (7.14),

$$h = \frac{\rho' L}{\rho_w} = \frac{\rho_{\text{sat}} - \rho_w}{\rho_w} L$$
$$= \left(\frac{2.0 - 1.0}{1.0}\right) 5 \text{ m} = 5.0 \text{ m}$$

b. The critical hydraulic gradient [Eq. (7.14)] is

$$i_c = \frac{\rho'}{\rho_w} = \frac{(2.0 - 1.0)}{1.0} = 1.0$$

We could also use Eq. (7.15) if we knew the value of ρ_s and e. Assume $\rho_s = 2.65$ Mg/m^3. Using Eq. (2.17), solve for $e = 0.65$. Therefore,

$$i_c = \frac{(2.65 - 1.0)}{(1 + 0.65)(1.0)} = 1.0$$

Seepage forces, which may cause quicksand to develop (but not necessarily), are always present in soils where there is a gradient causing the flow of water. Seepage forces affect sands more than clays, because sands are cohesionless whereas clay soils have some inherent cohesion which holds the particles together. To evaluate the seepage forces, lettuce look again at Fig. 7.10. For quick conditions to develop, the upward force of water due to the head h on the left side of the figure must just equal the *effective* downward force exerted by the submerged soil column on the right side of the figure, or

$$\text{upward force} = \text{downward force}$$

$$\rho_w g h A = \rho' g L A \tag{7.17a}$$

Substituting Eq. (2.18) into this equation, we get

$$\rho_w g h A = \frac{\rho_s - \rho_w}{1 + e} g L A \tag{7.17b}$$

After algebraic manipulation, this equation is identical to Eq. (7.16). In uniform flow the upward force $\rho g h A$ on the left-hand side of Eq. (7.17a) is distributed (and dissipated) uniformly throughout the volume LA of the soil column. Thus

$$\frac{\rho_w g h A}{L A} = \rho_w g i = j \tag{7.17c}$$

The term $i\rho_w g$ is the *seepage force per unit volume*, commonly represented by the symbol j. The value of this force at quick conditions equals $i_c \rho_w g$, and it acts in the direction of fluid flow in an isotropic soil. If the right-hand side of Eq. (7.17a) is divided by LA, the unit volume, then we have

$$j = \rho' g \tag{7.17d}$$

These expressions, Eqs. (7.17c) and (7.17d), can be shown to be identical when quick conditions occur [see Eq. (7.15)].

Example 7.10

Given:

The soil sample and flow conditions of Fig. 7.10 and Example 6.6.

Required:

a. Find the head required to cause a quick condition.
b. Compute the seepage force per unit volume at quick conditions.
c. Using seepage forces, show that quick conditions really develop under the head of part **a**.
d. Compute the total seepage force at elevation A.

Solution:

a. From Example 7.9, h above elevation B to cause a quick condition is 5.0 m.

b. The seepage force per unit volume is computed from Eq. (7.17c).

$$j = i\rho_w g = \frac{5\text{ m}}{5\text{ m}} \times 1\frac{\text{Mg}}{\text{m}^3} \times 9.81\frac{\text{m}}{\text{s}^2} = 9.81\frac{\text{kN}}{\text{m}^3}$$

We also could use Eq. (7.17d) if we knew the value of ρ_s or e. Assume, as in Example 7.9, $\rho_s = 2.65\ \text{Mg/m}^3$. Then $e = 0.65$.

Therefore

$$j = \frac{2.65 - 1.0}{1.65} g = 9.81 \frac{\text{kN}}{\text{m}^3}$$

Note that the units check ($F/L^3 = ML^{-2}T^{-2}$).

c. Quick conditions develop when the upward seepage force just equals the downward buoyant force of the soil. Or, from Eqs. (7.17c) and (d):

$$\frac{j}{\text{vol}}(\text{vol}) \uparrow = \rho' g(\text{vol}) \downarrow$$

$$9.81 \frac{\text{kN}}{\text{m}^3} \times 5\,\text{m} \times 1\,\text{m}^2 = (2.0 - 1.0) \frac{\text{Mg}}{\text{m}^3} \times 9.81 \frac{\text{m}}{\text{s}^2} \times 5\,\text{m} \times 1\,\text{m}^2$$

$$49.05\,\text{kN} \uparrow = 49.05\,\text{kN} \downarrow$$

d. The total seepage force at elevation A is

$$j(\text{vol}) = 9.81 \frac{\text{kN}}{\text{m}^3} \times 5\,\text{m} \times 1\,\text{m}^2 = 49\,\text{kN}$$

This force is distributed uniformly through the volume of the soil column.

The seepage force is a real force, and it is added vectorially to the body or gravitational forces to give the net force acting on the soil particles. We can represent these forces in two different ways that give identical results. In Example 7.10 we treated the problem considering seepage forces and submerged densities. A quick condition resulted because the effective or buoyant density of the soil volume (acting downward) just equaled the seepage force (acting upward). This is sometimes referred to as the *internal solution method* for obtaining the solution, since it is based on a seepage force acting within the soil.

An alternative approach is to consider the *total* saturated weight of soil and the boundary water forces acting on the soil, top and bottom, as shown in Example 7.11. This is sometimes called the *external solution method*, since it is based on boundary forces acting outside the soil.

Example 7.11

Given:

The soil sample and conditions of Fig. 7.10 and Examples 6.6 and 7.10.

Required:

Show, using total (saturated) weight of the soil above elevation A and the boundary water forces, that quick conditions develop when the head h is 5 m.

Solution: For a quick condition, $\sum F_v = 0$.

$$F_{\text{soil}} \downarrow = \rho_{\text{sat}} g L A$$

$$= 2.0 \frac{\text{Mg}}{\text{m}^3} \times 9.81 \frac{\text{m}}{\text{s}^2} \times 5\,\text{m} \times 1\,\text{m}^2 = 98.1\,\text{kN}$$

$$F_{\text{water top}} \downarrow = \rho_w g h_w A$$
$$= 1\frac{\text{Mg}}{\text{m}^3} \times 9.81\frac{\text{m}}{\text{s}^2} \times 5\,\text{m} \times 1\,\text{m}^2 = 19.6\,\text{kN}$$
$$F_{\text{water bottom}} \uparrow = \rho_w g(L + h_w + h)A$$
$$= 1\frac{\text{Mg}}{\text{m}^3} \times 9.81\frac{\text{m}}{\text{s}^2} \times (5 + 2 + 5)\,\text{m}$$
$$= 118\,\text{kN}$$

Therefore $\sum F_{\text{down}} = \sum F_{\text{up}}$ for a quick condition (i.e., 118 kN = 118 kN).

Example 7.12

Given:

The soil and flow conditions of Fig. 7.10, except that the left-hand riser tube is at elevation C, or 2 m above elevation A. Assume the water level is maintained constant at elevation C.

Required:

Compute: **a.** the hydraulic gradient, **b.** effective stress, and **c.** seepage force at elevation A.

Solution: In this case the flow of water is downward through the soil. Assume the datum plane is at the tail water elevation, or at elevation B.

a. Use Eq. (7.1); since the head loss is −5 m (below elevation B),

$$i = \frac{H}{L} = \frac{-5}{5} = -1$$

b. The effective stress at elevation A may be computed in the two ways just described.

1. Using *boundary* water forces and saturated densities, we get (units are the same as in Example 7.11)

$$F_{\text{soil}} \downarrow = \rho_{\text{sat}} g L A$$
$$= 2.0(9.81)(5)(1) = 98.1\,\text{kN} \downarrow$$
$$F_{\text{water top}} \downarrow = \rho_w g h_w A$$
$$= 1(9.81)(2)(1) = 19.6\,\text{kN} \downarrow$$
$$F_{\text{water bottom}} \uparrow = \rho_w g h A$$
$$= 1(9.81)(2)(1) = 19.6\,\text{kN} \uparrow$$
$$\sum F_{v_A} = 19.6 + 98.1 - 19.6$$
$$= 98\,\text{kN} \downarrow \text{ (net or effective force)}$$
$$\text{effective stress} = \frac{F}{A} = 98\,\text{kN/m}^2$$

Thus the filter screen at elevation A must support a force of 98 kN per unit area or a stress of 98 kN/m^2 in this case.

2. The other way to compute the effective stress at elevation A is to use seepage forces, buoyant densities, and Eq. (7.17). Note that $h = -5$ m referenced to elevation B.

$$j = \rho_w gi(\text{vol}) = 1(9.81)\left(\frac{-5}{5}\right)(5)(1)$$
$$= 49 \text{ kN acting down in the direction of flow}$$

To this we add the effective or buoyant weight:

$$F_{\text{down}} \downarrow = \rho' gLA = (\rho_{\text{sat}} - \rho_w)gLA$$
$$= (2.0 - 1)(9.81)(5)(1) = 49.05 \text{ kN} \downarrow$$

Therefore, adding vectorially these two forces, we get the seepage force plus the effective soil force acting on area A, or 49 + 49 = 98 kN per unit area, as before. Or the effective stress at A = 98 kN/m^2. Note that this second approach also automatically gives the solution to part **c**, the seepage force at A. Note that the seepage force at the top of the soil is zero and increases linearly to 49 kN at elevation A.

7.6.2 Quicksand Tank

An apparatus sometimes used in soil mechanics teaching laboratories to demonstrate the phenomenon of quicksand is shown in Fig. 7.11. Instead of a standpipe, as in Fig. 7.10, a pump is used to create the upward flow in the quicksand tank. The water flows through a porous stone to distribute the pressure evenly on the bottom of the sand mass. Piezometers at various levels on the tank enable heads to be observed and measured. As valve 1 is gradually opened, the head applied to the bottom of the sand mass increases, eventually becoming sufficient to cause the entire sand mass to boil or *liquefy*. As in Examples 7.10 and 7.11, the seepage forces are acting upward and just balance the downward-acting gravitational forces. The effective stresses between the sand grains are zero, and the soil has no shear resistance. As long as the pump is running, the soil mass can easily be stirred with a rod or metre stick, and it acts like a dense liquid [Fig. 7.12(a)]. Notice the elevations of the water in the piezometer tubes A, B, and C are at locations 1, 2, and 3 during upward flow. They are considerably higher than the elevation of the free water surface. The difference in elevation of the water level between points 1 and 3 is due to the head loss when flow occurs between points A and C.

Next we shut off the pump, close valve 1, and open valve 2. Now the direction of the water flow is reversed, and the seepage forces act downward along with gravity and increase the effective stresses. A rod or metre stick left buried in the sand has resistance to movement, and the sand mass can no longer be stirred easily. Even though the sand is very loose, it can support some static loads at the surface, as shown in Fig. 7.12(b). This case is similar to Example 7.12. Therefore, depending on their direction, seepage forces can significantly increase the effective stresses and the strength of the soil mass. In the case of downward flow, the pore water pressures at piezometer tubes A through C are shown by the elevations of the water level at points 4, 5, and 6 in Fig. 7.12(b). The effective stress at point A must be higher now with downward flow. This is shown by the water elevation of point 6, which is below the elevation of the water table.

Some practical examples of quick conditions include excavations in granular materials behind cofferdams alongside rivers. To excavate and proceed with construction, the water table at the site is lowered by a system of wells and pumps. Water from the river invariably seeps into the excavation and must be pumped out to keep the excavation dry. If upward gradients approach unity, the sand can become quick and the cofferdam can fail. Such failures are usually catastrophic, so high safety factors must be used in design. Example 7.13 is a simple example to illustrate this situation.

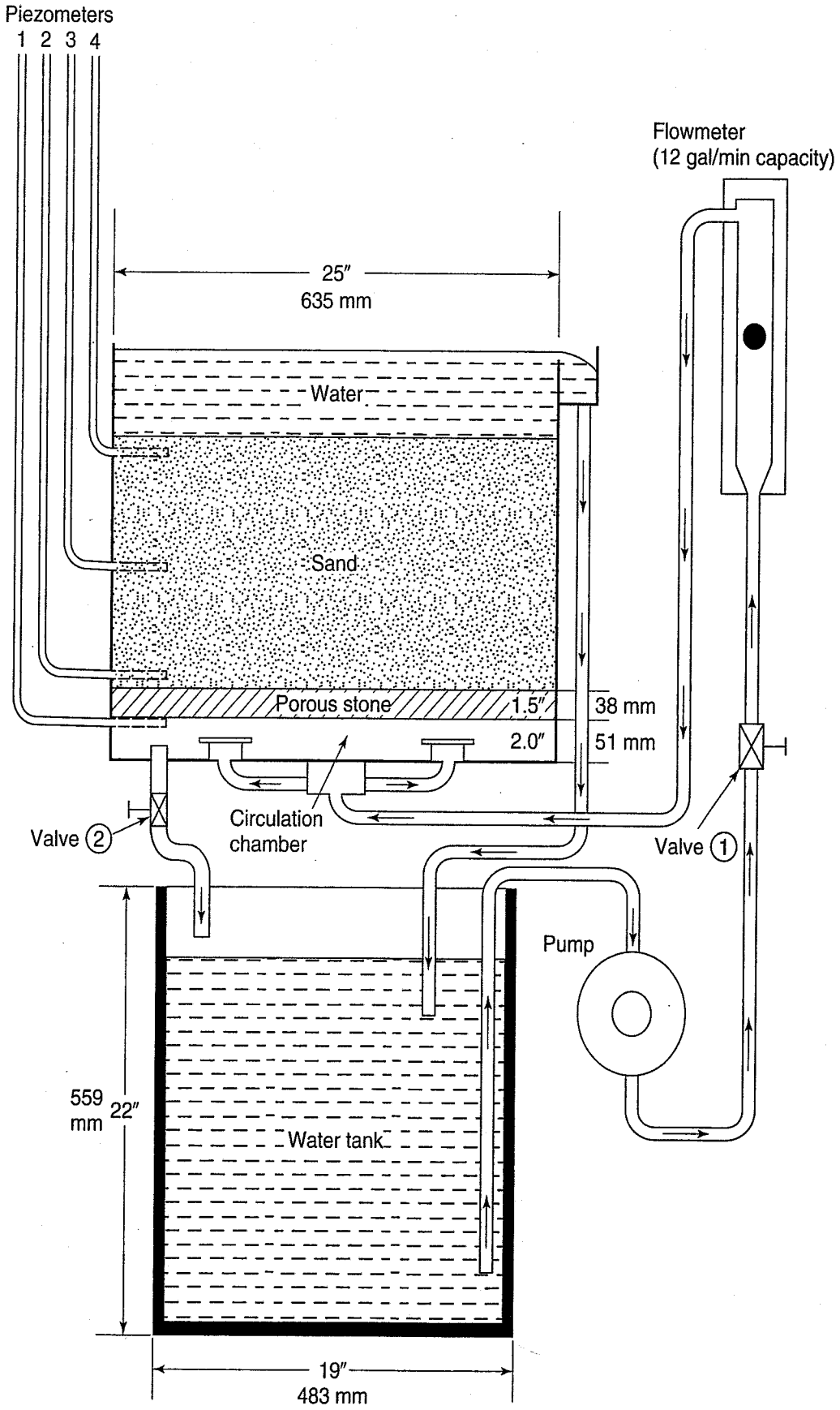

FIGURE 7.11 Diagram of a quicksand tank (courtesy J. O. Osterberg, Northwestern University).

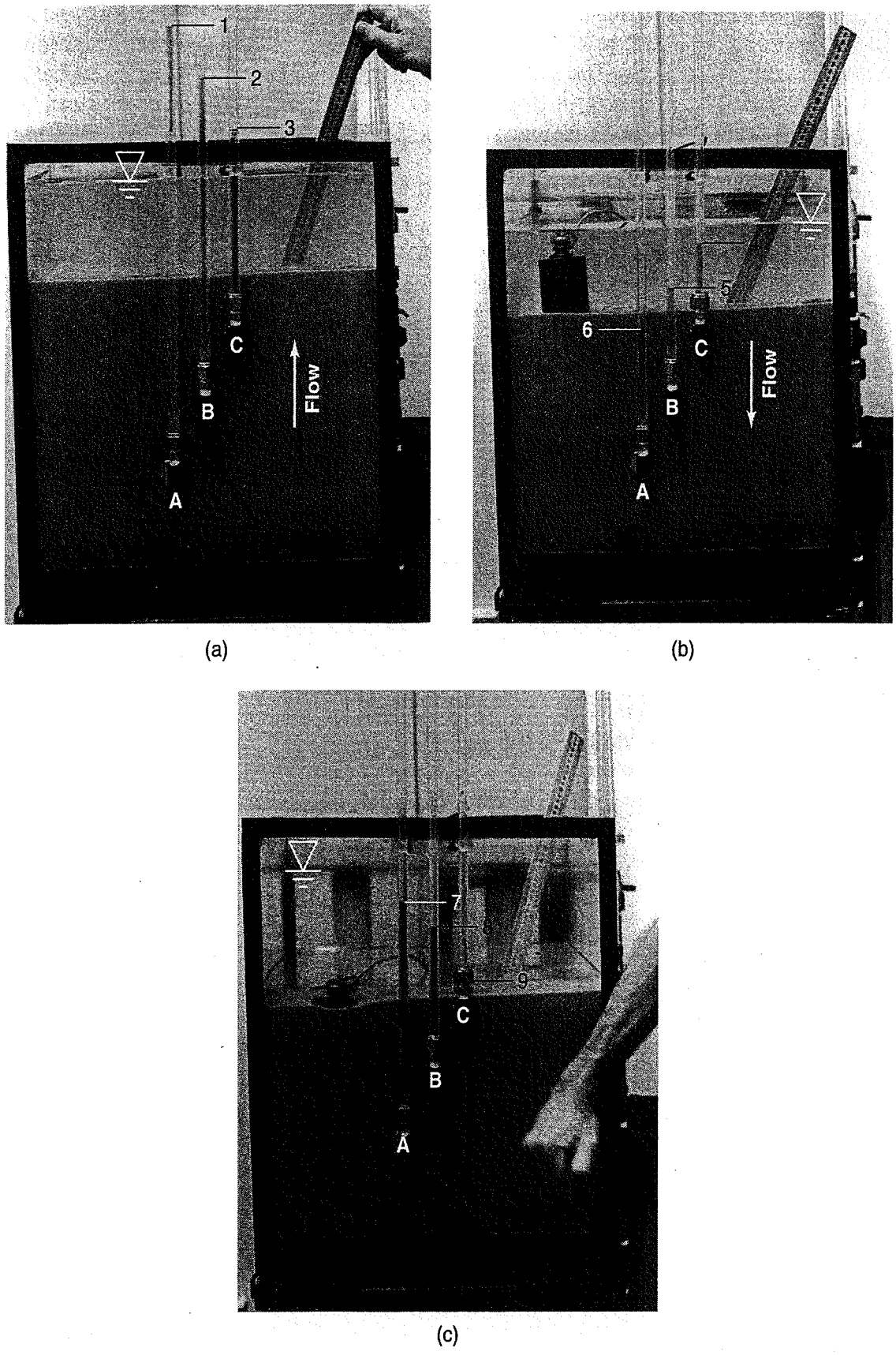

FIGURE 7.12 Quicksand tank: (a) under an upward gradient, the sand mass is easily stirred with a metre stick; (b) gradient is downward; sand is able to support a static load; (c) after a shock load is applied to the side of the tank, the sand mass liquefies and momentarily loses all bearing capacity. Notice water level in piezometers (photograph by M. Surendra; hand by R. D. Holtz).

Another place where quick conditions often occur is behind levees during floods. The water seeps under the levee and, as in the case of the cofferdam, if the gradient is high enough, localized quick conditions can occur. This phenomenon is known as a *sand boil* and must be halted quickly (usually by stacking sandbags in a ring around the boil); otherwise the erosion can spread and undermine the levee. Quick conditions are also possible almost anywhere that *artesian* pressures exist—that is, where the head is greater than the usual static water pressure. Such pressures occur where a pervious underground stratum is continuous and connected to a place where the head is higher.

Contrary to popular belief, it is not possible to drown in quicksand, unless you really work at it, because the density of quicksand is much greater than that of water. Since you can almost float in water, you should easily be able to float in quicksand.

Example 7.13

Given:

The conditions as shown in Fig. Ex. 7.13. The silty clay acts as an impervious layer and prevents flow of water up from the fine sand layer below it. Because of a river nearby, the fine sand layer is under a head of water greater than the existing ground surface (artesian conditions). A standpipe or piezometer installed through the silty clay layer rises to a distance h above the top of the sand layer, as shown in the figure. An excavation is made in the silty clay to within a distance H_s above the top of the sand layer.

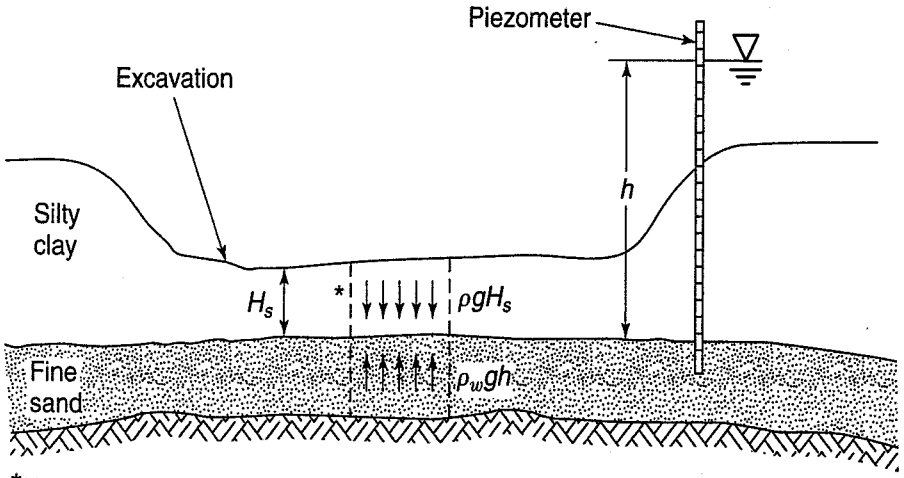

*Neglect shear along sides.

FIGURE Ex. 7.13

Required:

How deep an excavation can be made so that the uplift pressure in the middle of the excavation will not cause the bottom of the excavation to "blow up"? Determine the thickness of the silty clay layer H_s in terms of the soil properties and geometry given in Fig. Ex. 7.13. Assume that the shear force on the sides of the soil plug can be neglected.

Solution: At equilibrium, $\sum F_v = 0$

$$H_s \rho g = \rho_w g h$$

or

$$H_s = \frac{\rho_w g h}{\rho g}$$

Failure will occur if $H_s < \rho_w gh/\rho g$. If $H_s > \rho_w gh/\rho g$, then failure cannot happen, and the factor of safety is greater than unity. In practice, the factor of safety against catastrophic failure should be rather high, since, if it occurs, it can be devastating. You must be very conservative in designing such situations because of the possible consequences.

7.6.3 Liquefaction

Another phenomenon related to quicksand is *liquefaction*, which can be demonstrated in a quicksand tank [Fig. 7.12(c)]. After the sand is made quick and is in a very loose state, the flow is reversed and the water level decreases. When the water level in the tank reaches just below the surface of the sand, all the valves are shut and all flow ceases. We now have a deposit of *loose*, *saturated sand* ready for an earthquake! If we apply a sharp blow to the side of the tank, instantly the entire soil mass liquefies and the sand loses all bearing capacity [Fig. 7.12(c)]. Notice that the kilogram weight sank, the water level rose a few centimeters above the ground surface (shown), and water levels in the piezometer tubes A through C rose to points 7, 8, and 9.

The reaction in Fig. 7.12(c) is exactly what happens when a loose, saturated sand deposit is subjected to loads of very short duration, such as occur during earthquakes, pile driving, and blasting. The loose sand tries to densify during shear, and this tends to squeeze the water out of the pores. Normally, under static loading, the sand has sufficient permeability so the water can escape and any induced pore water pressures can dissipate. But in a dynamic situation, because the loading occurs in such a short time, the water doesn't have time to escape and the pore water pressure increases. Since the total stresses have not increased during loading, the effective stresses then tend toward zero [by Eq. (6.8)], and the soil loses all strength. Note the position of the water level in the standpipes of Fig. 7.12(c). The photograph was taken just after a sharp blow against the side of the tank.

The presence of excess pore water pressure below the ground surface indicates that *upward flow* is taking place, and liquefaction occurs. All these events happen almost simultaneously. During and immediately after many earthquakes, water has been observed squirting up through the ground to a metre or so in height, sometimes up to 20 minutes after the initial shock waves. Thus *sand boils* are created where the upward flow of water carries sand with it to the ground surface.

Casagrande (1936a) was the first to explain liquefaction in terms of soil mechanics, and he also describes (1950, 1975) some situations in practice where liquefaction has occurred. Among these are the failure of Ft. Peck Dam in Montana in 1938 and *flow slides* along the lower Mississippi River. Here sands are deposited during floods in a very loose state. Somehow strains are induced in these deposits, and it seems that they almost spontaneously liquefy and flow out into the river. The problem is that they often take levees and other flood protection works along with them, and repairs are expensive. Bank erosion leading to progressive liquefaction, seepage pressures from high water tables, and even traffic vibrations have been blamed for flow slides. Flow slides also occur in mine tailings dams. These structures are often very large and constructed hydraulically of very loose sands and silts. Since they are essentially waste dumps, often with very fast rates of deposition, and with inadequate engineering and construction inspection, failures are relatively common. This type of liquefaction is sometimes called *static liquefaction*.

Since the Niigata, Japan, and the Anchorage, Alaska, earthquakes of 1964, where severe damage occurred due to liquefaction, there has been increasing interest in liquefaction. It has been found to occur in the laboratory in even moderately dense sands after repeated or cyclic application of shear

stress, which means that if an earthquake lasted long enough, then even moderately dense saturated sands might liquefy. This phenomenon is sometimes called *cyclic mobility*.

For some historical background on liquefaction and cyclic mobility, see Casagrande (1975) and Seed (1979). Kramer (1996) is an excellent textbook on geotechnical earthquake engineering.

7.7 SEEPAGE AND FLOW NETS: TWO-DIMENSIONAL FLOW

The concept of head and energy loss as water flows through soils has been mentioned several times in this chapter. When water flows through a porous medium such as soil, energy or head is lost through friction, much as in flow through pipes and in open channels. As in the laboratory permeability test described earlier, for example, similar energy or head losses occur when water seeps through an earth dam or under a sheet pile cofferdam (Fig. 7.13).

Two types of flow conditions, *confined* and *unconfined*, are illustrated in Fig. 7.14. Notice that the phreatic surface is not "confined" in layer A by an impervious boundary but is free to seek its own location. On the other hand, layer B is an example of confined flow, because the *aquifer* (a layer or formation of high permeability) and the phreatic surface are confined by an *aquiclude* (a layer of much lower permeability). An aquifer readily permits flow under normal gradients, while an aquiclude does not and is, in effect, impervious. In terms of relative difficulty of pumping water from a geologic formation (soil or rock layer(s)), an *aquitard*[2] is less pervious than an aquifer but more so than an aquiclude. Note the different groundwater elevations in the two piezometers in Fig. 7.14. If the B layer were under artesian conditions, the water level in the B piezometer could be well above the ground surface. Note that all the examples in Sec. 7.5 were confined because their boundaries were impervious.

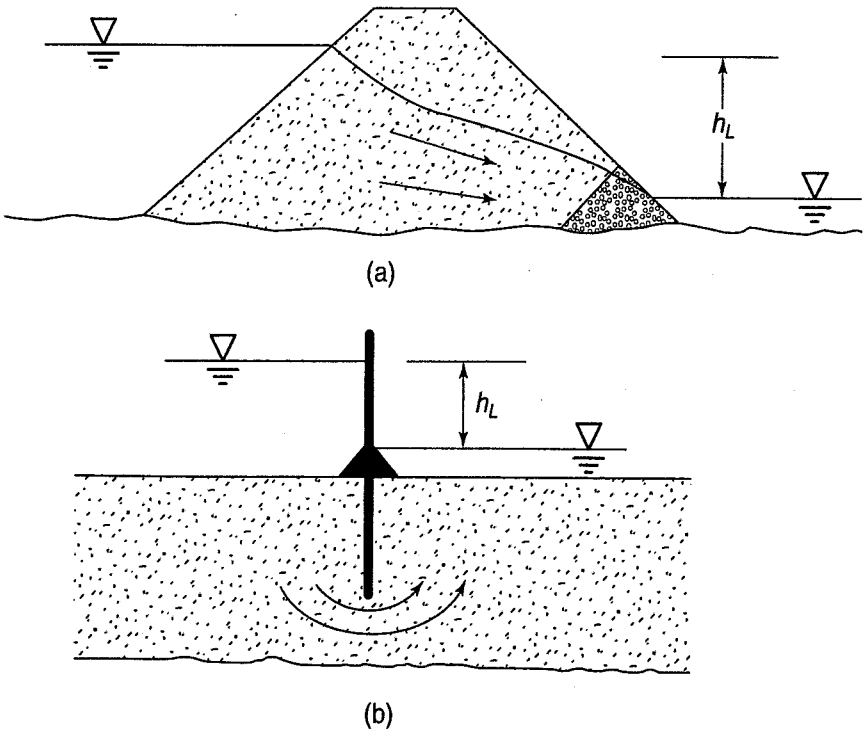

FIGURE 7.13 Engineering examples of head loss because of seepage through soils.

[2]Not to be confused with an *aquitart*, a waterborne inhabitant of a light district where the predominant wavelength is around 750 nm.

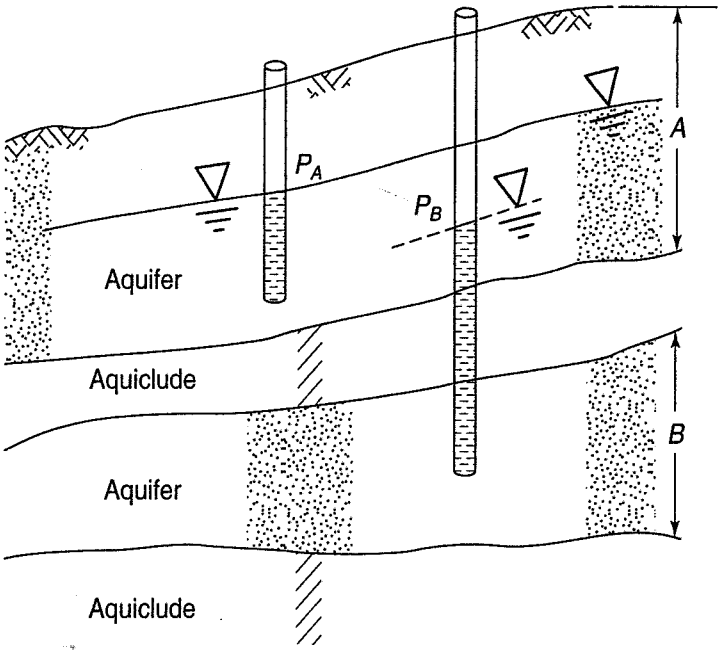

FIGURE 7.14 Examples of unconfined flow in aquifer A and confined flow in aquifer B.

Pumping from aquifers can be either unconfined or confined, depending on the geology. If a well penetrates only layer A in Fig. 7.14, flow toward the well is unconfined. On the other hand, if the well penetrates into the aquifer of layer B, seepage to the well is confined. Seepage toward wells is described in Sec. 7.8. When water seeps through earth dams and levees, as shown in Fig. 7.13(a), flow is definitely unconfined, because there is a free surface at atmospheric pressure. As explained in Sec. 7.9, the primary design problem is to establish the shape of the top line of seepage.

Different kinds of heads and head losses were described in Sec. 7.5, and it might be a good idea to review that material before proceeding further in this section.

Figure 7.15 shows how the total head $(h_p + z)$ might be determined from the positions and elevations of the water levels in the standpipes. Also shown in this figure is how energy or head is lost in flowing under a dam. Note how the water levels in each successive piezometer decrease as water flows from the heel to the toe of the dam. Example 7.15 explains in detail how head computations are made.

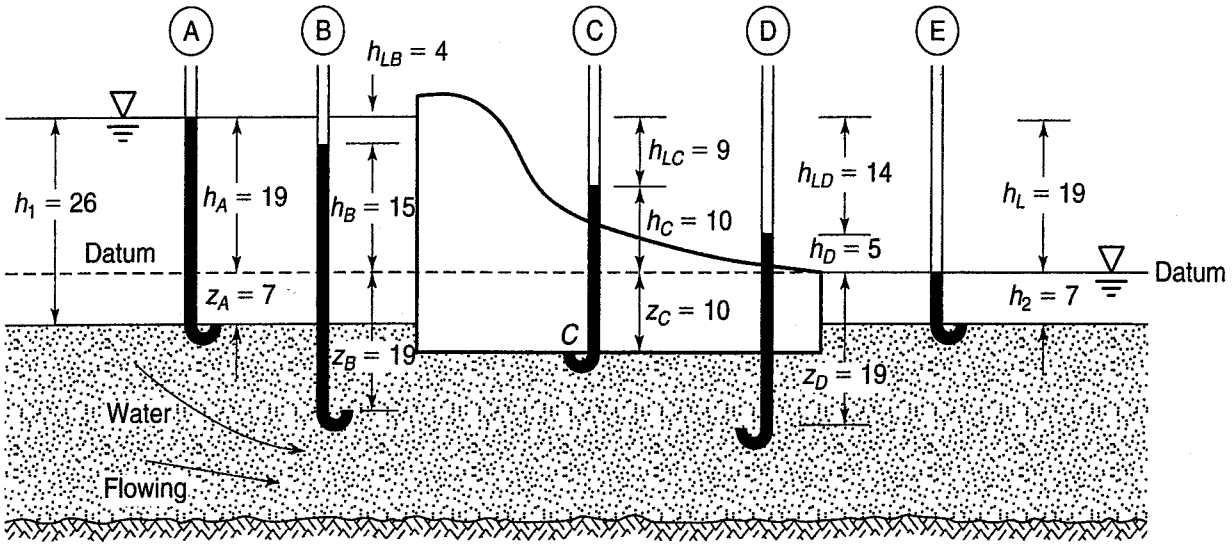

FIGURE 7.15 Example of heads and head loss due to seepage under a dam. All dimensions in metres.

Example 7.14

Given:

The dam with piezometers shown in Fig. 7.15. The total head loss is 19 m (h_L).

Required:

a. Calculate the pressure heads h_p and the total heads h for piezometers A through E.
b. Determine the uplift pressure acting on the base of the dam at point C.

Solution:

a. Pressure and total heads.

Piezometer A: The pressure head is the length of the column of water in the standpipe, or

$$h_P = h_A + z_A = h_1 = 19 + 7 = 26\,\text{m}$$

Note that this dimension is also numerically equal to

$$h_L + h_2 = 19 + 7 = 26\,\text{m}$$

The total head is

$$h = (h_P + z) = 26 - 7 = 19\,\text{m}$$

which is the height of rise above the datum.

Piezometer B:

$$h_P = h_B + z_B = 15 + 19 = 34\,\text{m}$$
$$h = (h_P + z) = 34 - 19 = 15\,\text{m}$$

Note that h is also numerically the same as

$$h_L - h_{LB} \quad \text{or} \quad h = 19 - 4 = 15\,\text{m}$$

Piezometer C:

$$h_p = h_C + z_C = 10 + 10 = 20\,\text{m}$$

(We will use this pressure head to compute the uplift pressure at point C, below.)

$$h = (h_p + z) = 20 - 10 = 10\,\text{m}$$

(Check: $h = h_L - h_{LC} = 19 - 9 = 10\,\text{m}$.)

Piezometer D:

$$h_P = h_D + z_D = 5 + 19 = 24\,\text{m}$$
$$h = h_D + z_D - z_D = 5\,\text{m}$$

(Check: $h = h_L - h_{LC} = 19 - 14 = 5$ m.)

Piezometer E:

$$h_P = h_2 = 7 \text{ m}$$
$$h = h_P - z_E = 7 - 7 = 0$$
$$h_L = 19 \text{ m}$$

Note that at the tailwater all of the head has been lost. Thus the total head at this point is zero.

b. Uplift pressure at point C:

$$p_C = h_p \rho_w g = (h_C + z_C)\rho_w g = (h_L - h_{LC} + z_C)\rho_w g$$
$$= 20 \text{ m } (1000 \text{ kg/m}^3)(9.81 \text{ m/s}^2) = 196 \text{ kPa}$$

7.7.1 Flow Nets

We could represent the flow of water through the foundation under the dam in Fig. 7.15 by *flow lines*, which would represent an average flow path of a particle of water from the upstream reservoir down to the tail water. Similarly, we could represent the energy of flow by lines of equal potential, called, naturally, *equipotential lines*, or contours of constant total head. Along any equipotential line, the energy available to cause flow is the same; conversely, the energy lost by the water in getting to that line is the same all along the line. The network of flow lines and equipotential lines is called a *flow net*, a concept that illustrates graphically how the head or energy is lost as water flows through a porous medium, as shown in Fig. 7.16.

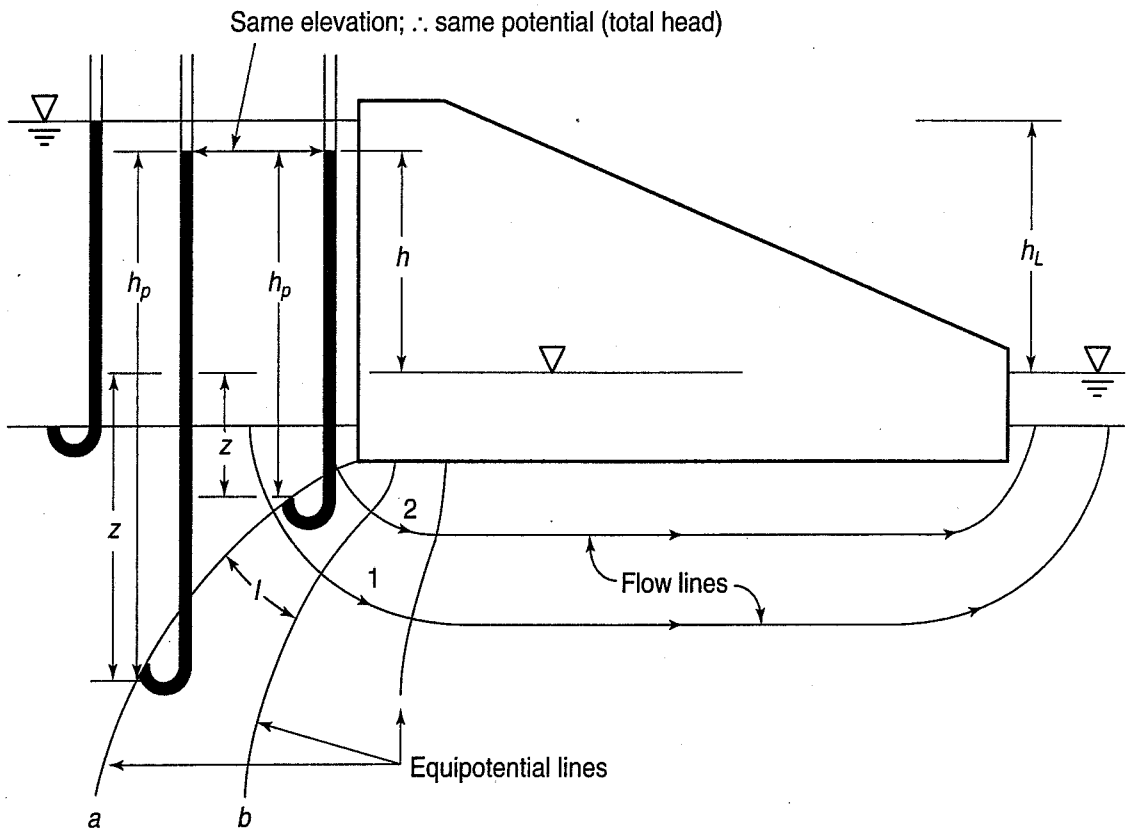

FIGURE 7.16 Equipotential and flow lines (only a few shown).

You probably can see that we could, if we wanted to, draw an infinite number of flow lines and equipotential lines to represent the seepage shown in Fig. 7.16, but it is more convenient to select only a few representative lines of each type. The hydraulic gradient between any two adjacent equipotential lines is the drop in potential (head) between those lines divided by the distance traversed. Or, in Fig. 7.16 along flow line 2, the gradient between equipotential lines a and b is the head drop between those lines divided by l. Because in an *isotropic* soil the flow must follow paths of the largest gradient, the flow lines have to cross the equipotential lines at right angles, as shown in Fig. 7.16. Note that, as the equipotential lines become closer together, l decreases and the gradient increases [Eq. (7.1)].

Figure 7.16 represents a typical cross section of the dam and foundation. Thus, as in all seepage problems considered in this text, the flow condition is *two dimensional*. Three-dimensional flow is the more general situation in many geotechnical problems, but seepage analyses of these problems are just too complicated to be practical, so we usually simplify the problem to two dimensions.

Flow nets are very useful in solving seepage problems in engineering practice—for example, to estimate seepage losses from reservoirs, uplift pressures under dams, and check points of potential detrimental erosion where $i \rightarrow i_{cr}$. We shall explain the techniques in this section.

A flow net is actually a graphical solution of *Laplace's equation* in two dimensions,

$$\frac{\partial^2 h}{\partial x^2} + \frac{\partial^2 h}{\partial y^2} = 0 \tag{7.18}$$

where x and y are the two coordinate directions, and h is the head at any point (x, y). Laplace's equation, derived in Appendix B, is very important in mathematical physics; it represents the energy loss through any resistive medium. For example, besides the flow of water through soils, it describes electron flow, the flow of people to hospitals, and so on. If the *boundary conditions* (geometry, flow conditions, and head conditions at the boundaries) are simple, then it is even possible to solve the equation in closed form—that is, exactly. But for most practical engineering problems, it is usually easier to solve seepage problems either graphically or using numerical methods. Both flow nets and numerical solutions are not exact solutions to Laplace's equation for a given set of boundary conditions, but if done properly, they are quite satisfactory.

How do you make a flow net? Traditionally, they were sketched by hand, and students learned by experience, drawing flow nets for a variety of flow and boundary conditions. However, this is a dying art, having been replaced by finite element or finite difference computer programs. For relatively simple boundary conditions, though, you should still have an idea of how to sketch flow nets—for three reasons. First, learning to draw flow nets helps you to understand how water flows through soils and how that flow might impact your design. Second, you may need to get only an approximate idea of flow rate and other flow parameters (e.g., critical gradient) to cross-check field measurements or to get an estimate of flow. Time and budget constraints may not warrant a full computer analysis for such an approximation. The third reason is to check computer analyses for gross errors. We all know that just because it is a computer solution doesn't mean it is accurate.

To start sketching a flow net for two-dimensional steady-state problems, you simply draw the medium with its boundaries to some convenient scale (draw this part in ink, since you may end up erasing the flow net a lot to get it right). By trial and error (mostly error, until you get some practice!) sketch a network of flow lines and equipotential lines spaced so that the enclosed figures resemble "squares" (you won't be able to avoid having many elements that have curved sides or corners that aren't exactly at 90°). Their sides intersect at right angles. Look again at Fig. 7.16, specifically the "square" enclosed by flow lines 1 and 2 and equipotential lines a and b. Not all the "squares" in a flow net have to be the same size, either. Note that a flow line cannot intersect an impervious boundary; in fact, an impervious boundary is a flow line. Note, too, that all equipotential lines must meet impervious boundaries at right angles. Neither the number of *flow channels* (channels between flow lines) nor the number of *equipotential drops* (a *drop* is the decrease in head Δh from one equipotential line to the next) needs to be a whole number; fractional squares are allowed.

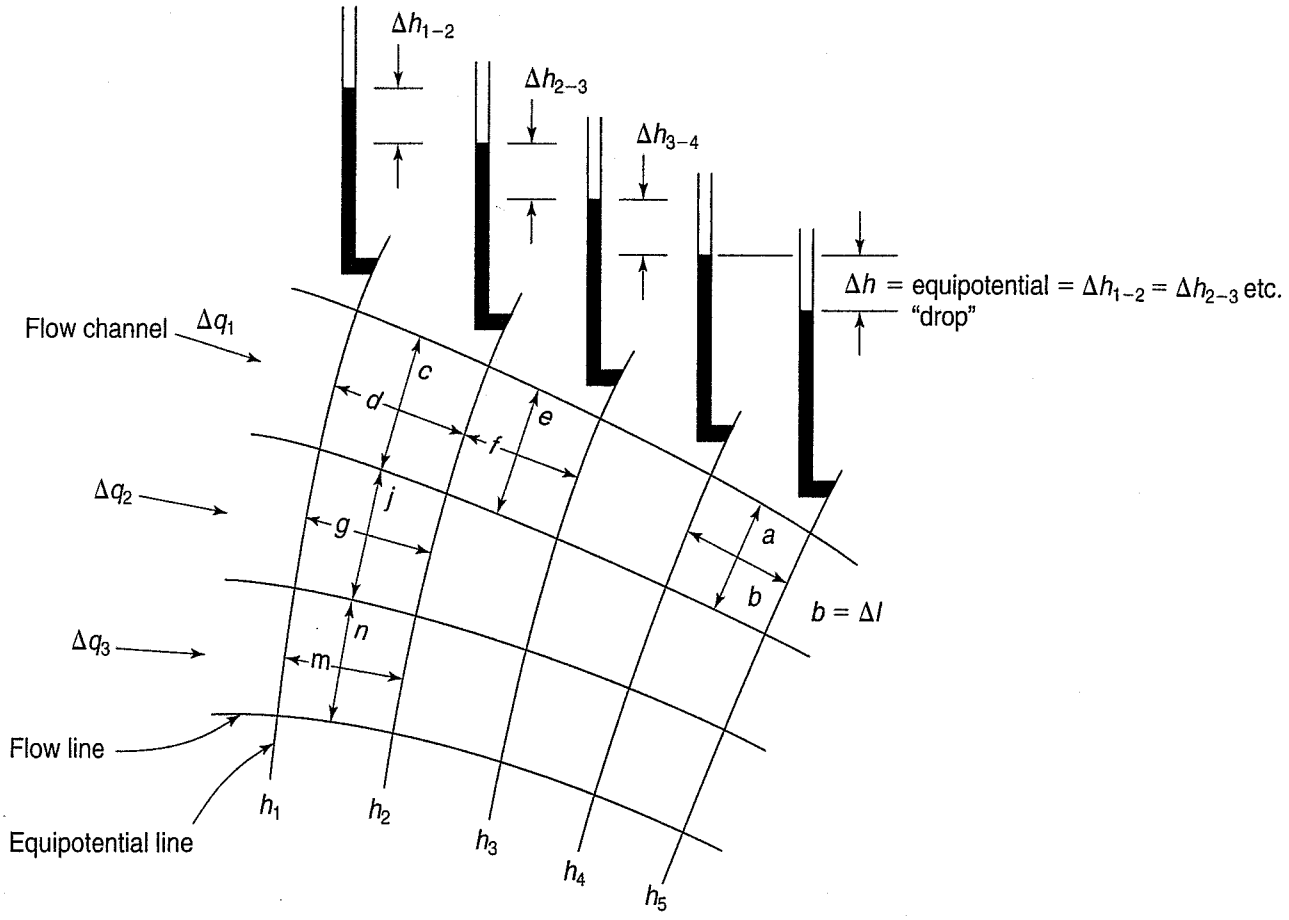

FIGURE 7.17 Flow net illustrating some definitions.

Figure 7.17 explains some of the terms associated with flow nets. Look at the "square" with dimensions $a \times b$. Note that the gradient is

$$i = \frac{\Delta h}{\Delta l} = \frac{\Delta h_{1-2}}{d} = \frac{\Delta h_{2-3}}{f} = \frac{\Delta h_{4-5}}{b} = \frac{h_L/N_d}{b} \tag{7.19a}$$

where the length of the flow path in one square is $b = \Delta l$. The equipotential drop between two flow lines is $\Delta h = h_L/N_d$, where N_d is the total number of potential drops, and h_L is the total head lost in the system.

From Darcy's law and Fig. 7.17 we know that the flow in each flow channel is

$$\begin{aligned} \Delta q_1 &= k\frac{\Delta h_{1-2}}{d} \\ \Delta q_2 &= k\frac{\Delta h_{1-2}}{g} \\ \Delta q_3 &= k\frac{\Delta h_{1-2}}{m} \end{aligned} \tag{7.19b}$$

or, in general,

$$\Delta q = k\frac{\Delta h}{\Delta l}A = k\left(\frac{h_L/N_d}{b}\right)a \tag{7.19c}$$

and the total discharge q per unit depth (perpendicular to the paper) is

$$q = q_1 + q_2 + q_3 + \cdots \tag{7.19d}$$

$$q = \Delta q N_f = k h_L \left(\frac{a}{b}\right)\left(\frac{N_f}{N_d}\right) \tag{7.19e}$$

where N_f is the total number of flow channels in the flow net. If we sketched "squares" in our flow net, then $a = b$. Thus, we can readily estimate the quantity of flow q by simply counting the number of potential drops N_d and the number of flow channels N_f, if we know the k of the material, and the total head loss h_L. Equation (7.19e) becomes

$$q = k h_L \frac{N_f}{N_d} \tag{7.20}$$

The ratio N_f/N_d is called the *shape factor*, because it depends only on the geometry of the problem. Besides quantity of flow, other products of flow nets are described in Sec. 7.7.2.

With confined flow problems, where there is no phreatic (free) surface, sketching a flow net is not so difficult. Start with a sketch, to scale, of the soil mass, boundaries, and so on. Keep the sketch small so you can observe the entire picture as it develops. Use good-quality paper, a soft pencil, and have a good eraser handy—you'll need it! Draw the boundaries in ink on the reverse side of the sheet. Start with, at most, only three or four lines. By trial and error, sketch the net (lightly) until you get "squares" throughout the region of flow. It's easier if you can manage to keep the number of flow channels to a whole number. The flow lines and equipotential lines should be smooth, gradual curves, all intersecting at right angles. As mentioned, you should be able to subdivide each square to make additional small squares. The flow net shown in Fig. 7.18 is an example of a fairly well-drawn flow net for confined flow.

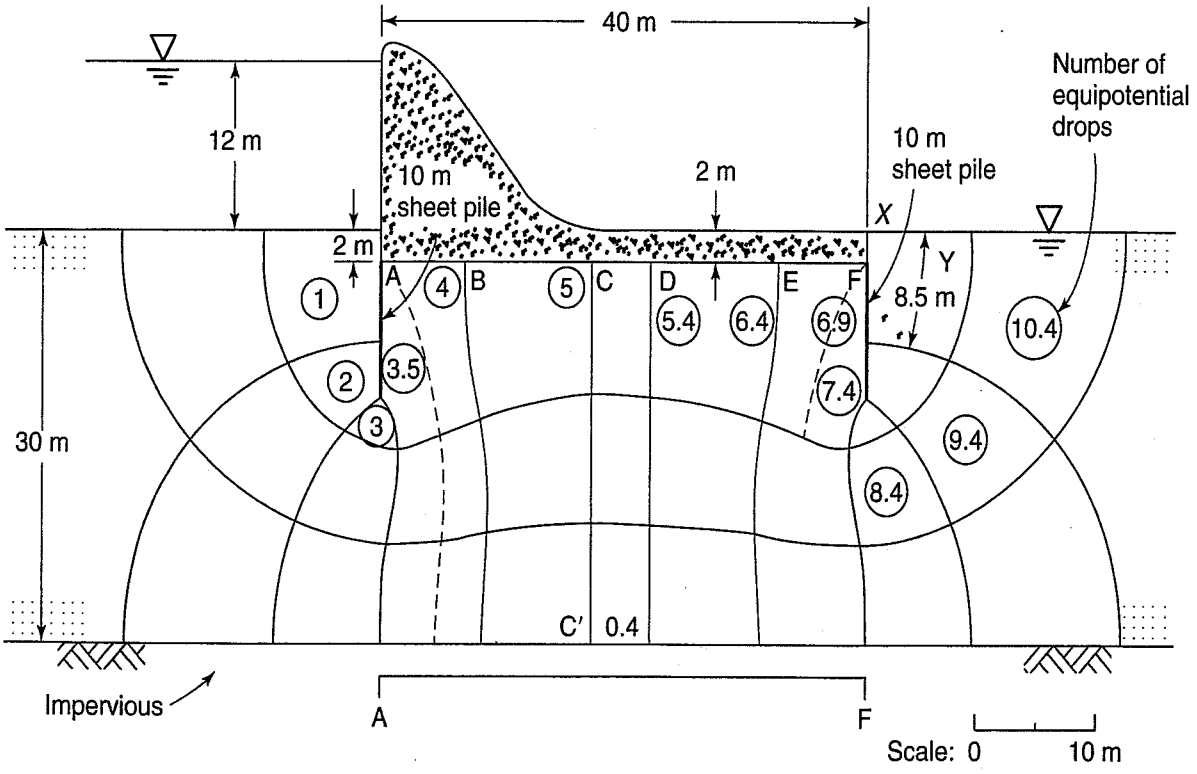

FIGURE 7.18 Example of a reasonably well-drawn flow net for confined flow.

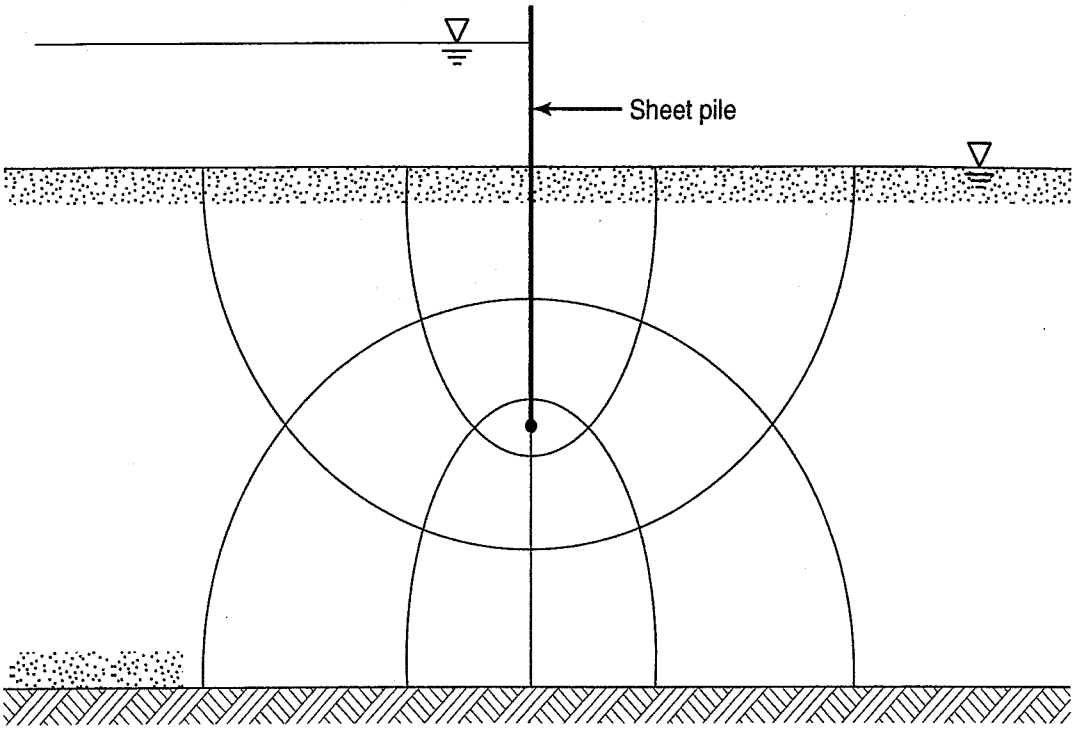

FIGURE 7.19 Symmetrical flow net example showing a sheet pile driven half way into an aquifer. Note that the number of flow channels N_f is 3 and the number of equipotential drops N_d is 6 (modified after Casagrande, 1937, drawn by W. Kovacs).

An example of unconfined flow with a sheet pile driven halfway into an aquifer is shown in Fig. 7.19. The flow net is horizontally symmetrical, providing that the top and bottom flow lines (borders) are parallel and the penetration of the sheet pile is exactly one-half the depth of the aquifer. Note that the number of flow channels N_f is 3 and the number of equipotential drops N_d is 6. Regardless of how many flow channels you use, the N_f/N_d ratio, or the shape factor, will always be $\frac{1}{2}$ for the geometry of this example! If the geometry is different, you will have a different solution, and the N_f/N_d ratio will not necessarily be the same.

Another characteristic of a correct flow net is that you can inscribe a circle inside each "square" and it will be tangent to all four sides. As soon as you change any of the boundary conditions, you change the flow net solution. For any given set of boundary conditions, *there is only one solution to the problem!*

7.7.2 Quantity of Flow, Uplift Pressures, and Exit Gradients

We showed in the development of Eq. (7.20) that the quantity of seepage or the flow rate is easily obtained from a properly constructed flow net. Even a crude flow net provides a fairly accurate estimate of the flow quantities! This is because we usually do not know the hydraulic conductivity k, especially in the field, with any degree of accuracy.

Example 7.14 indicates how the uplift pressures under a dam are calculated. From the flow net, it is not difficult to determine the h_p at various points at the bottom of the dam. Then the distribution of uplift pressures can be drawn. This distribution is important for analyzing the stability of concrete gravity dams. The procedure is illustrated in Example 7.15.

Another important use of flow nets is to determine gradients, especially at certain critical points—for example, at the toe of a dam or any place where seepage water exits. From Sec. 7.6 you

know that when the gradient approaches unity, critical conditions can occur, which leads to *piping* and *erosion* and possibly complete failure of the structure. Piping is a phenomenon where seeping water progressively erodes or washes away soil particles, leaving large voids (pipes) in the soil. These voids simply continue to erode and work their way backward under the structure, or they may collapse. Either way, if piping is not stopped promptly, failure is imminent. The critical place for piping is usually right at the corner of the toe of a dam. We can see why if we study an enlargement of the flow net at the toe (Fig. 7.20).

For the case of the dam placed (foolishly) right on the ground surface [Fig. 7.20(a)], if we keep subdividing the squares, l rapidly approaches zero while Δh is still finite. Thus, the gradient rapidly increases and reaches the critical gradient i_{cr}. If this actually happened in a real structure, piping and probably failure of the structure (by undermining) would occur.

For the example shown in Fig. 7.20(b), the dam is somewhat safer than in Fig. 7.20(a), since, for typical cases, the exit gradient is much less than critical. From Eq. (7.19a), the exit gradient i_E equals $\Delta h_L/\Delta l$, where Δh_L equals the head loss h_L divided by the number of equipotential drops N_d. Thus, if all other things are the same, an embedded foundation will have more equipotential drops and a lower exit gradient. Remember that the flow net in its enlarged condition in Fig. 7.20 merely shows the *concentration* of flow. As the squares get smaller and smaller, the tendency is to think that the exit gradient is steadily increasing! This is not so. As the number of equipotential drops increases, Δh_L also decreases per drop, and the ratio of $\Delta h_L/\Delta l$ remains about the same. For this example, too, you can see why the critical place is right next to the

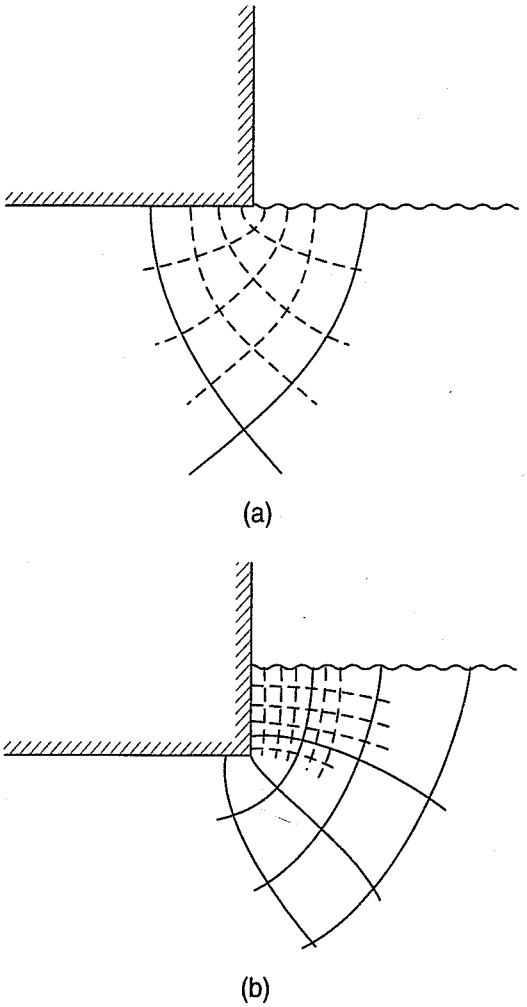

FIGURE 7.20 Exit gradients at toe of dams: (a) dam constructed directly on ground surface; (b) dam placed below the ground surface.

downstream toe. There, the Δl is the smallest for a given Δh_L. The next flow channel over, for example, is safer since the same head (Δh_L) is lost over a greater length (greater distance between equipotential lines).

For practical problems, where there is a danger that i could approach i_c, you should be very conservative in your design. Use a factor of safety of at least 5 or 6 for such cases. For one thing, failure is usually catastrophic and occurs rapidly and with little warning. For another, it is extremely difficult to know exactly what is going on underground, especially locally. Local defects, gravel pockets, etc., can significantly alter the flow regime and concentrate flow, for example, where you might not want it and not be prepared for it. Concentration of flow occurs, too, at corners of temporary structures like cofferdams. As Terzaghi (1929) and Taylor (1948) point out, the entire flow regime may be widely different from that assumed in our (idealized) flow net. Great variation in horizontal and vertical permeability may exist from point to point under a foundation; the flow may not be entirely two-dimensional; geologic defects in the underlying subsoils may provide preferential routes for the water to concentrate and seep under and out of a foundation. If sheet piling is used, cutoff is often uncertain (for example, piling unknowingly driven into boulders), and you would be wise to assume that the worst possible conditions could happen—then prepare for such eventualities. Since failure of cofferdams is often catastrophic, it is extremely important that large factors of safety be used, especially where people's lives are at stake. Failures of earth structures resulting from piping have caused more deaths than all other failures of civil engineering structures combined. Therefore, your responsibility is clear—be careful and conservative, and be sure of your ground conditions and design.

Example 7.15

Given:

The dam and flow net shown in Fig. 7.18. The dam is 120 m long and has two 10 m sheet piles driven partially into the granular soil layer. Datum is at tailwater elevation.

Required:

a. The quantity of seepage loss under the dam when $k = 20 \times 10^{-4}$ cm/s.

b. The exit gradient (at point X).

c. The pressure distribution on the base of the dam.

d. The factor of safety with respect to piping.

Solution:

a. From Eq. (7.20), the quantity of seepage is

$$q = kh_L\left(\frac{N_f}{N_d}\right) \times \text{length}$$

$$= \left(20 \times 10^{-4}\frac{\text{cm}}{\text{s}}\right)\left(\frac{\text{m}}{100\ \text{cm}}\right) 12\ \text{m}\frac{3}{10.4}120\ \text{m}$$

$$= 8.3 \times 10^{-3}\ \text{m}^3/\text{s}$$

b. At point X, the exit gradient is

$$i_E = \frac{\Delta h_L}{L} = \frac{1.15}{8.5} = 0.14, \text{ which is not critical}$$

Note: $\Delta h_L = h_L/N_d = 12\text{ m}/10.4 = 1.15\text{ m}$. $L = 8.5\text{ m}$, scaled from Fig. 7.18, is the length of square Y.

c. Pressure heads are evaluated for points A through F along the base of the dam in Fig. Ex. 7.15.

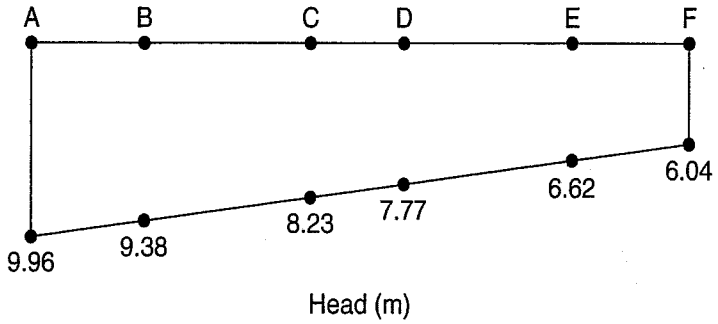

FIGURE Ex. 7.15 Pressure head for locations A through F.

The pressure head at point A, at the base of the dam and just to the right of the left sheet pile, is found this way: the percentage of the head loss is proportional to the number of equipotential drops. Of the total of 10.4 drops for the entire flow net, only 3.5 have occurred by point A. Thus the pressure head at point A is

$$h_A = 12\text{ m} - 12\text{ m} \times \frac{3.5}{10.4} + 2\text{ m}$$
$$= 12 - 4.04 + 2 = 9.96\text{ m}$$

The extra 2 m brings the head from the water-soil interface down to the base of the dam.

In a similar manner, we can calculate the head at point D:

$$h_D = 12 - 12 \times \frac{5.4}{10.4} + 2 = 7.77\text{ m}$$

The heads at all the points under the dam are as follows:

Location	Head (m)	Pressure (kPa)
A	9.96	98
B	9.38	92
C	8.23	81
D	7.77	76
E	6.62	65
F	6.04	59

These values of head are plotted in Fig. Ex. 7.15. To compute the *uplift pressures* on the base of the dam, we multiply the head times the product $\rho_w g$. The pressures are given above. If the density of concrete is 2.4 Mg/m^3, then the pressure exerted by 2 m of concrete is

$$2.4\ \text{Mg/m}^3 \times 9.81\ \text{m/s}^2 \times 2\ \text{m} = 47\ \text{kPa}$$

Thus at any point along the base of the dam from point C through F the uplift force exceeds the weight of the dam, so the dam is *unstable* with this design.

d. The factor of safety with respect to piping is given by

$$\text{F.S.} = \frac{i_c}{i_E}$$

where i_c = the critical gradient, Eq. (7.15), and is approximately equal to unity. With the exit gradient found in part **b**, we find the factor of safety is

$$\text{F.S.} = \frac{1}{0.14} = 7$$

Example 7.16

Given:

The flow net in Fig. 7.19. Assume the hydraulic conductivity is 10^{-4} cm/sec. The sheet pile is 13 m long (into the paper). The thickness of the soil layer is 10 m and the sheet pile penetrates halfway through. A head of 5 m (h_L) of water separates both sides of the sheet pile.

Required:

a. Compute the amount of flow under the sheet pile for its full length in units of m^3/s.

b. Evaluate the exit gradient and compute the factor of safety with respect to a quick condition

c. Comment on what options a designer has to increase the factor of safety in part **b**.

Solution:

a. The amount of flow is given by Eq. (7.20).

$$q = k\,\Delta h \frac{N_f}{N_d}\ \text{per m of wall} \times \text{wall length}$$

$$q = 10^{-4}\ \text{cm/sec} \times 0.01\ \text{m/cm} \times 5\ \text{m} \times \frac{3}{6} \times 13\ \text{m}$$

$$q = 3.25 \times 10^{-5}\ \text{m}^3\text{/sec} = 2.8\ \text{m}^3\text{/day}$$

b. The exit gradient is given by

$$i_E = \frac{\Delta h}{L} = \frac{h_L/N_d}{L}$$

$$i_E = \frac{5 \text{ m/6 drops}}{2.5 \text{ m}}$$

$$i_E = \frac{1}{3}$$

where L = the scaled length taken from Fig. 7.19. The distance, L, is shown just below E–F and is approximately 2.5 m. The factor of safety with respect to boiling or quicksand is

$$\text{F.S.} = \frac{i_c}{i_E}$$

where i_c is the critical gradient as given in Eq. (7.15) or (7.16). The approximate value of the critical gradient is unity. So,

$$\text{F.S.} = \frac{1}{1/3} = 3$$

c. Options available to increase the factor of safety in part **b**.

First, is the factor of safety adequate? If it is greater than one, is that OK? Because we do not know all the details about the subsurface soil properties and potential geologic "defects," not to mention the consequences of failure, designers should be very conservative in this situation. A factor of safety of 5 to 10 would not be unreasonable.

7.7.3 Other Solutions to Seepage Problems

A number of methods other than sketching to obtain flow nets have been developed to find solutions to seepage problems. They include exact and approximate mathematical solutions for Laplace's equation (Harr, 1962), viscous flow (Hele–Shaw) models, small-scale laboratory flow models, electrical analog models, and the method of fragments (Harr, 1962 and 1977). This last method is so simple and practical that we present it in Appendix C.

However, by far the most common approach that practitioners take today to obtain flow nets and solve seepage problems under a variety of complex boundary conditions and variable soil properties is the use of finite element or finite difference computer programs. A number of these programs, some with student versions, are commercially available for download from company websites.[3] The output from these programs usually includes flow rates, heads, gradients, uplift pressures and other useful information. Figure 7.21 is a computer analysis of the dam in Fig. 7.18 and Example 7.15. The flow value computed at the section at 50 m is 6.9×10^{-5} m^3/s/m of cross-section. If you multiply this value by the dam length of 120 m, you get a total flow of 8.28×10^{-3} m^3/s, which is very close to the value obtained from the flow net analysis in Example 7.15.

[3]Examples include SEEP/W (www.geo-slope.com), SEEP2D (www.seepage-analysis.com), and SVFlux2D (www.scisoftware.com).

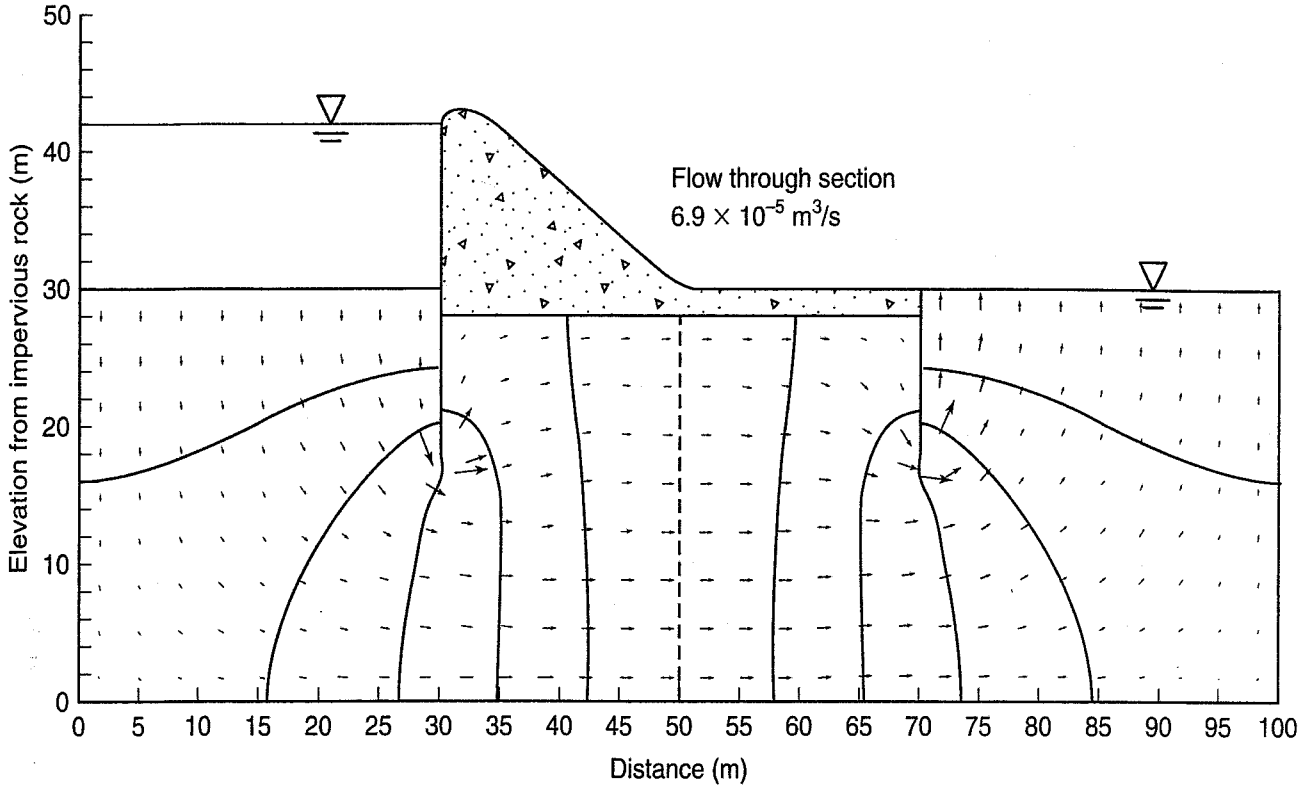

FIGURE 7.21 Example of output from a SEEP/W analysis of the dam in Fig. 7.18.

7.7.4 Anisotropic and Layered Flow

We mentioned earlier that flow nets are valid for isotropic soils only, a condition that is unlikely in natural soil deposits or even in earth dams. However, it is easy to take the directional difference in permeability into account by transforming the scale to which you draw the flow net. For example, if the horizontal permeability is much greater than the vertical, then you shorten the horizontal dimensions of the problem by the ratio $\sqrt{k_h/k_v}$. The proof of this transformation, as well as examples for its use, are shown in Taylor (1948). Equation (7.20) for the quantity of seepage then becomes

$$q = \sqrt{k_v k_h} \cdot h_L \frac{N_f}{N_d} \tag{7.21}$$

In some sedimentary soil deposits, because of the different strata and soil layering, the hydraulic conductivity and thus the flow in the perpendicular (usually vertical) direction will be different and likely less than in the parallel (usually horizontal) direction. Varved clays, mentioned in Chapter 3, are good examples of this. If such soils are encountered, it is necessary to obtain some *equivalent* permeability in both the parallel and perpendicular directions. Figure 7.22 illustrates two possible flow conditions in multilayered soils. In the horizontal case, the average or equivalent flow is given by

$$q_{h\,\text{equivalent}} = k_{h\,\text{equivalent}}\, iH = k_{1h} iH_1 + k_{2h} iH_2 + \cdots$$

where the k's and H's are defined in Fig. 7.22. Because the gradient across each layer is equal, it cancels out, leaving

$$k_{h\text{equivalent}} H = k_1 H_1 + k_2 H_2 + \cdots$$

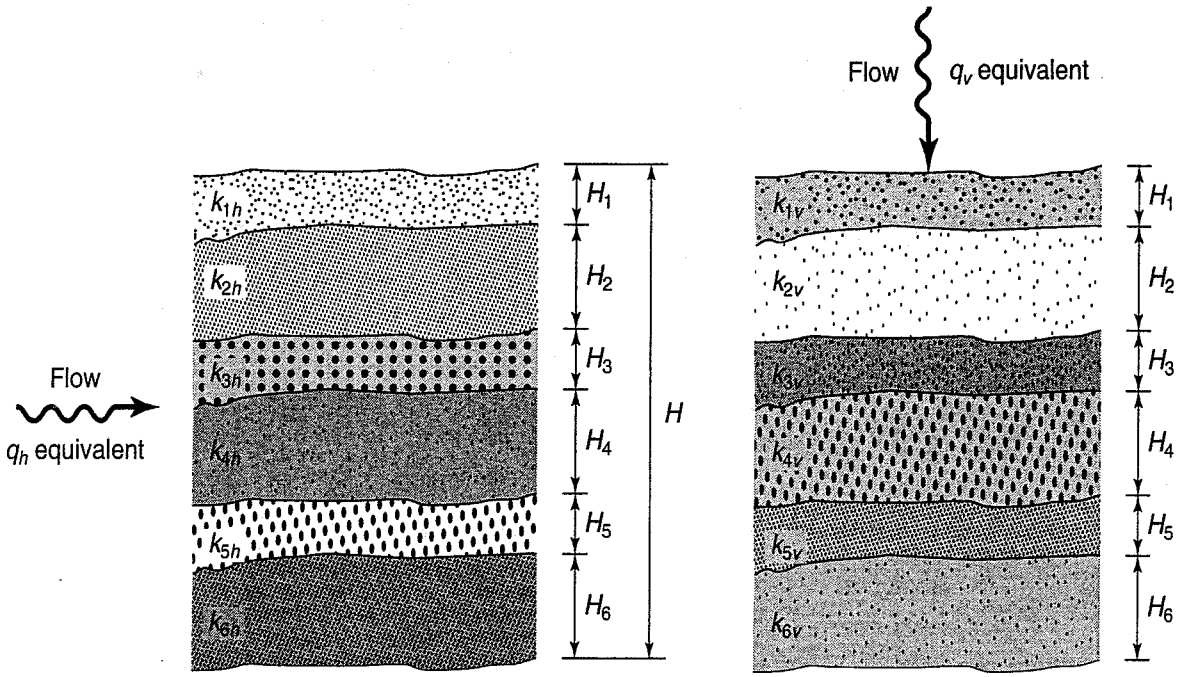

FIGURE 7.22 Two flow conditions in multilayered soils: (a) horizontal flow; (b) vertical flow.

or

$$k_{h\,\text{equivalent}} = \frac{\sum_{i=1}^{n} k_i H_i}{\sum_{i=1}^{n} H_i} \tag{7.22}$$

When the flow is perpendicular to the soil layers, as in Fig. 7.22(b), the velocity will be the same in each layer but the gradient across each layer will be different. So,

$$v = ki = k_{v\,\text{equivalent}} \frac{\Delta h}{H} = k_{v1} \frac{\Delta h_1}{H_1} = k_{v2} \frac{\Delta h_2}{H_2} = \cdots = k_{vn} \frac{\Delta h_n}{H_n}$$

and

$$\Delta h = \Delta h_1 + \Delta h_2 + \cdots + \Delta h_n$$

where

$$\Delta h_n = k_{v\,\text{equivalent}} \frac{H_n}{k_{vn}} \frac{\Delta h}{H}$$

Combining these three equations, we get

$$k_{v\,\text{equivalent}} = \frac{\sum_{i=1}^{n} H_i}{\sum_{i=1}^{n} \frac{H_i}{k_{vi}}} \tag{7.23}$$

With the above equations, we can determine the equivalent coefficient of permeability or hydraulic conductivity of a layered soil deposit, once the thickness and k of the individual layers are known.

Example 7.17

Given:

A multilayer soil similar in appearance to Fig. 7.22. It has a total layer thickness of 1.8 m and is composed of four layers. The layers are 0.8, 0.5, 0.3, and 0.2 m, respectively. The isotropic hydraulic conductivities are 10^{-7}, 10^{-6}, 10^{-5}, and 10^{-4} m/s, respectively.

Required:

Evaluate the equivalent hydraulic conductivities in both the vertical and horizontal directions.

Solution: Use Eq. (7.22) to determine the equivalent horizontal permeability.

$$k_{h\,\text{equivalent}} = \frac{\sum_{i=1}^{n=4} k_j H_j}{\sum_{i=1}^{n=4} H_j}$$

$$= \frac{10^{-7}\ \text{m/s} \times 0.8\ \text{m} + 10^{-6}\,0.5 + 10^{-5}\,0.3 + 10^{-4}\,0.2}{0.8\ \text{m} + 0.5 + 0.3 + 0.2}$$

$$= 1.3 \times 10^{-5}\ \text{m/s}$$

Use Eq. (7.23) to find the equivalent vertical permeability,

$$k_{v\,\text{equivalent}} = \frac{\sum_{i=1}^{n} H_i}{\sum_{i=1}^{n} \frac{H_n}{k_{vn}}}$$

$$= \frac{1.8\ \text{m}}{\left(\frac{0.8\ \text{m}}{10^{-7}\ \text{m/s}} + \frac{0.5}{10^{-6}} + \frac{0.3}{10^{-5}} + \frac{0.2}{10^{-4}}\right)}$$

$$= 2.1 \times 10^{-7}\ \text{m/s}$$

Note that the perpendicular hydraulic conductivity will always be less than the parallel hydraulic conductivity.

7.8 SEEPAGE TOWARD WELLS

We mentioned in Sec. 7.4.1 that wells are used to determine the in situ hydraulic conductivity or coefficient of permeability k of the soils at a site. Wells are also commonly used to provide for domestic and irrigation water supply. At sites with a high water table, wells are used to dewater the site so that construction may take place in the dry. In siting a dam on an alluvial foundation, if there is concern that too much water would flow under the dam, the water flow could be calculated, provided the coefficient of permeability is known. Tests on laboratory samples are useful, but these relatively small samples represent only, perhaps,

one-millionth of the amount of soil that will take part in the flow of water. So, a full-scale field pumping test would provide a useful way to estimate the overall value of k.

To determine the hydraulic conductivity, a well-pumping test is performed. A well is installed (see Driscoll, 1986, for details) and is then pumped until steady state conditions are reached. Water level readings are taken from nearby observation wells. The *drawdown* of the initial groundwater table in the observation wells is used in an appropriate formula to compute the in situ hydraulic conductivity.

Although formulations are available for steady state and transient conditions, for unconfined and confined radial flow to a wells and slots, only two simple steady state and radial flow situations are presented in this section.

A typical cross section illustrating the steady state flow in an *unconfined* aquifer is shown in Fig. 7.23. The quantity of flow is obtained using Darcy's law [Eq. (7.5)], but with appropriate boundary conditions, or

$$q = kiA = k\frac{dh}{dr}2\pi rh$$

Rearranging

$$\frac{dr}{r} = \frac{k}{q}2\pi h\, dh$$

Integrating between the limits of r from r_1 to r_2 and of h from h_1 to h_2 (refer to Fig. 7.23 for definitions of these parameters), and solving for k, we obtain

$$\ln\frac{r_2}{r_1} = \frac{k\pi}{q}(h_2^2 - h_1^2)$$

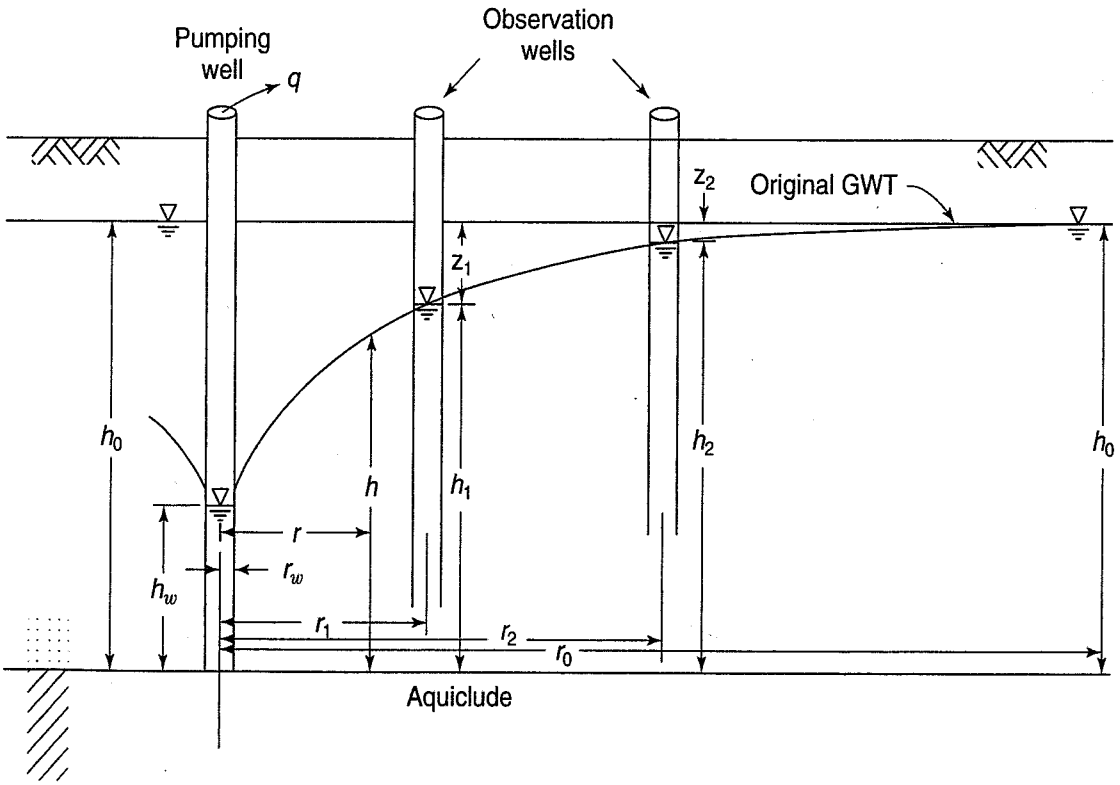

FIGURE 7.23 Unconfined radial flow.

Solving for k,

$$k = \frac{q}{\pi} \frac{\ln \frac{r_2}{r_1}}{(h_2^2 - h_1^2)} = \frac{2.3q}{\pi} \frac{\log \frac{r_2}{r_1}}{(h_2^2 - h_1^2)} \tag{7.24}$$

The observation wells are often constructed on a radial line from the pumping well.

Example 7.18 (After U.S. Dept. of the Interior, 1995.)

Given:

An unconfined aquifer with a saturated thickness of 15 m (h_o). Observation wells are located distances of 30, 60, and 120 m from the pumping well. Water is pumped from the well at a rate of 0.08 m^3/s. After pumping 16 hr, the following drawdown information was collected: at $r_1 = 30$ m, $z_1 = 0.58$ m; at $r_2 = 60$ m, $z_2 = 0.41$ m; at $r_3 = 120$ m, $z_3 = 0.24$ m.

Required:

Evaluate the hydraulic conductivity in m/s.

Solution: Using Eq. (7.24) and inserting the appropriate values,

$$k = \frac{2.3q}{\pi} \frac{\log \frac{r_2}{r_1}}{(h_2^2 - h_1^2)}$$

$$= \frac{2.3}{\pi} \times 0.08 \frac{m^3}{sec} \frac{\log \frac{60}{30}}{(14.59^2 - 14.42^2)\ m^2}$$

$$= 0.003 \text{ m/s}$$

Where did the 14.59 come from? You take the thickness of the layer (15 m), subtract the drawdown (0.41 m), and obtain h_2. See Fig. 7.23 for the definition of h_2.

Another typical situation is performing a pumping test in a *confined* aquifer. The drawdown curve must always be above the confining layer. Using the definitions from Fig. 7.24 as a guide and starting with Darcy's law, Eq. (7.5) (again), and with appropriate boundary conditions, we obtain

$$q = ki(A) = k\frac{dh}{dr}(2\pi rt)$$

Rearranging

$$\frac{dr}{r} = k2\pi t\, dh$$

Integrating and inserting the boundary conditions of when $h = h_w, r = r_o$, and when $h = h_o, r = r_o$, we obtain

$$\ln \frac{r_2}{r_1} = \frac{k2\pi t}{q}(h - h_w)$$

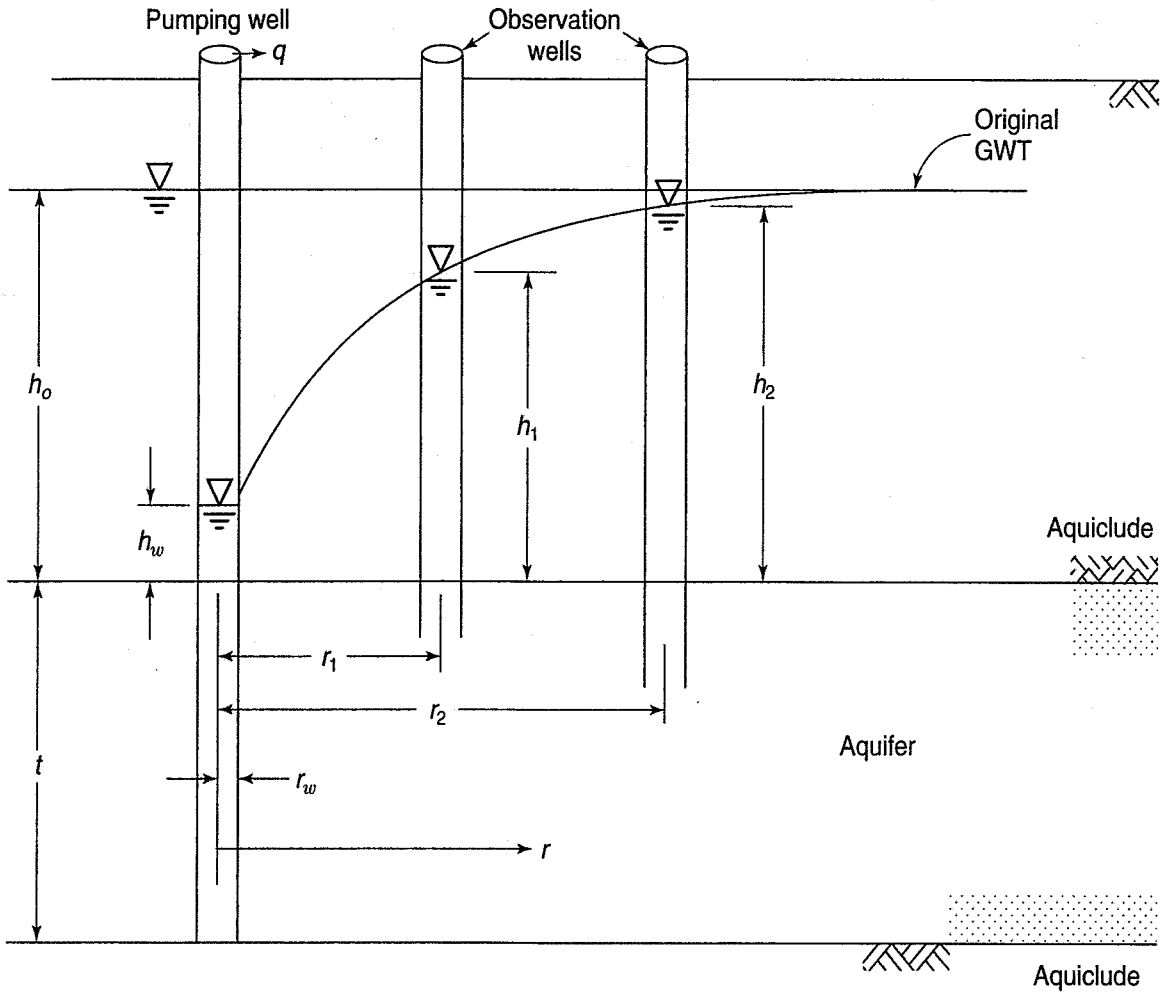

FIGURE 7.24 Radial flow in a confined aquifer with a fully penetrating well.

Solving for k,

$$k = \frac{q}{2\pi t} \frac{\ln \frac{r_o}{r_w}}{(h_o - h_w)}$$

For the general case:

$$k = \frac{q}{2\pi t} \frac{\ln \frac{r_2}{r_1}}{(h_2 - h_1)} \tag{7.25}$$

If we multiply both sides of Eq. (7.25) by t, the product of $k \times t$ becomes the *transmissivity* (or transmissibility) T, with units L^2/T or m^2/day. Transmissivity and *storativity* are terms that you will use in groundwater hydrology courses and references.

So far we have discussed only steady state pumping for radial flow and fully penetrating wells. Solutions are available for other situations and conditions—for example, flow to slots and trenches and partially penetrating wells. Unsteady or transient flow also may occur at times, and we must use other mathematical models, such as the Theis method, for solving these problems. For these and other non-ideal pumping conditions, see Mansur and Kaufman (1962), Departments of the Army, Navy, and Air Force (1971), Driscoll (1986), Freeze and Cherry (1979), U.S. Dept. of the Interior (1995), Reddi (2003), and Todd and Mays (2004).

7.9 SEEPAGE THROUGH DAMS AND EMBANKMENTS

Thus far we have been discussing mostly seepage problems in which the boundary conditions have been known. In the case of seepage through a homogenous earth dam, the upper or *top line of seepage* is not known and must be found usually by trial and error (Casagrande, 1937).

Figure 7.25 illustrates some constraints that must be satisfied simultaneously in order for the top line of seepage to be drawn correctly. For any given earth dam geometry, we choose some whole number of flow channels. Then there is only *one* flow net solution for this situation. (Change the number of flow channels and you have a different solution.) The line XY in Fig. 7.25 is an equipotential line, while line XZ is a flow line. All flow lines emanating from an equipotential line must be at right angles; see points a, b, and c. The line of seepage will intersect the downstream slope someplace between points D and Z, such that the head will be divided equally from point Y to point Z, the tailwater. Finally—and this is the difficult part when drawing a flow net—the resulting equipotential lines that emanate from the line of seepage must intersect the line of seepage at right angles. Now add the fact that the flow lines (from points a, b, and c, for example) must all intersect those equipotential lines at right angles as well. Figure 7.26 from Casagrande (1937) illustrates these constraints.

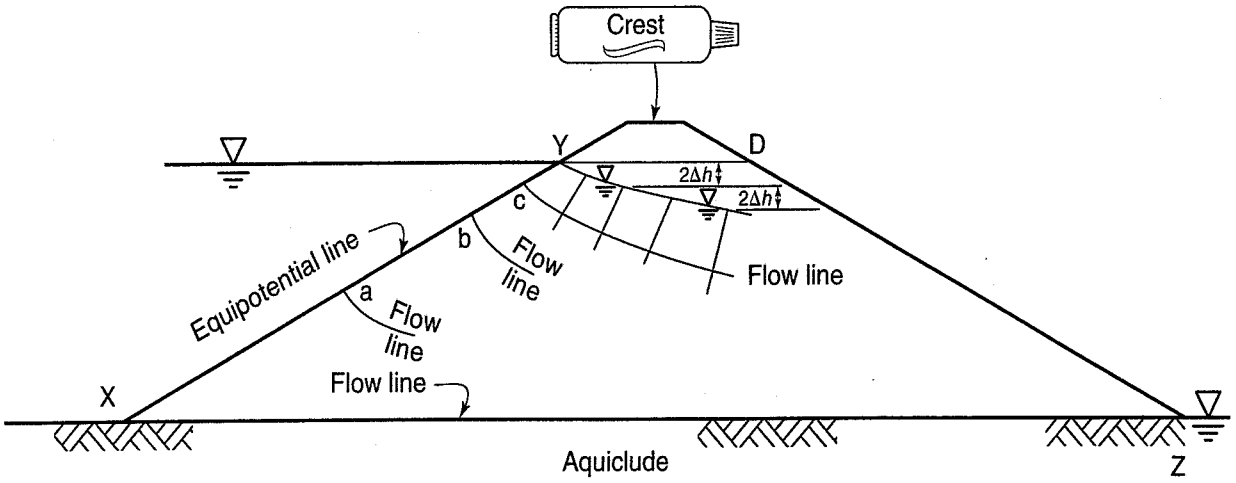

FIGURE 7.25 Example of the start of flow net construction through a homogenous earth dam on an impervious foundation.

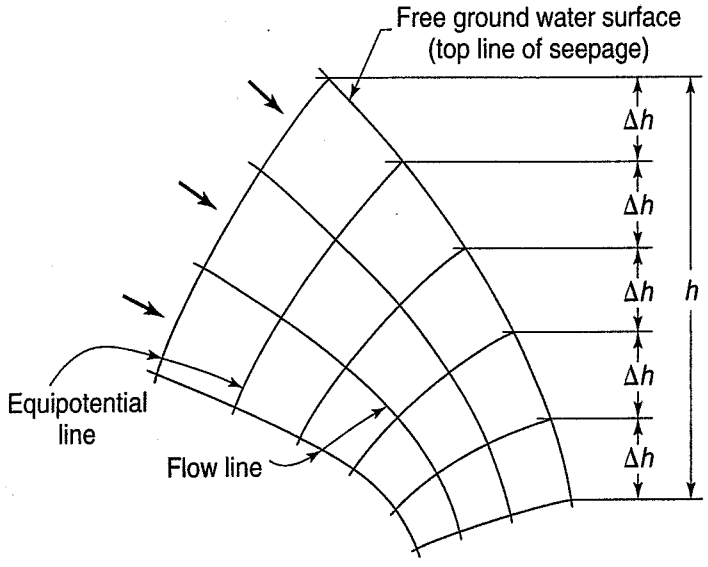

FIGURE 7.26 General conditions for the top line of seepage for unconfined flow (after Casagrande, 1937).

After the flow net is properly constructed, the exit point along the downstream surface is found. When you think of it, you don't want the exit point along the line DZ. As mentioned in Sec. 7.7.2, internal erosion or piping will take place on the downstream face, and the dam may eventually fail. Therefore, internal filters or special drainage features are constructed within the dam so that the line of seepage will emerge well below the top surface of the dam. Figure 7.27 illustrates some of these drainage features that allow seepage to exit without erosion. Notice how the various drains (toe filter, horizontal drain blanket, and chimney drain) alter the phreatic surface to a position well

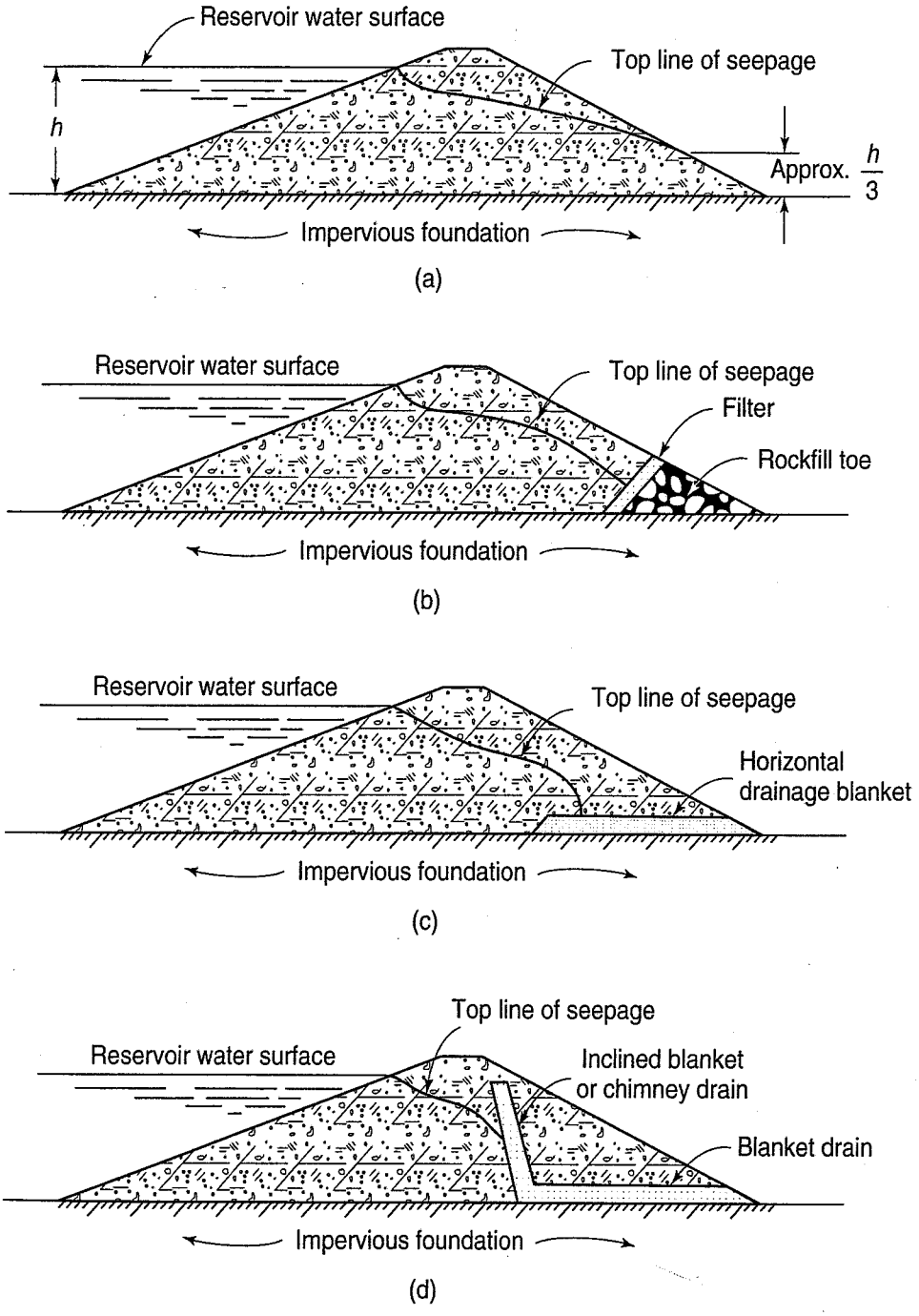

FIGURE 7.27 Effect of internal drainage devices on the line of seepage in a homogenous earth dam: (a) without internal drain; (b) with a rockfill toe; (c) with a horizontal drainage blanket; (d) with a chimney drain (after U.S. Dept. of the Interior, 1987).

below the downstream surface. The dam may leak like crazy (not necessarily economical), but as long as the water is clear, there is no erosion and therefore the dam is safe in that respect.

Casagrande (1937) is considered the classic reference for flow nets for earth dams, and it has many examples. See also Taylor (1948), Perloff and Baron (1976), and Cedergren (1989). From an engineering point of view, the flow net does not have to be perfect to obtain a reasonable estimate of the quantity of flow or the uplift pressures below a structure. On the other hand, you really need a very good solution in order to evaluate the factor of safety with respect to *piping or boiling*. Small differences in the critical exit "square" may make large differences in the factor of safety. It all goes back to: what are the consequences of failure? Typically, earth structures are seldom homogenous but are composed of various sections of different permeability (see Sec. 7.7.4). Usually the horizontal permeability is larger than the vertical permeability. Equation (7.26) may be used to prepare a transformed section whereby the horizontal dimensions are reduced, the flow net is drawn, and then it is redrawn to the original expanded size:

$$\text{shape factor} = \sqrt{\frac{k_v}{k_h}} \tag{7.26}$$

where k_v = vertical permeability,
k_h = horizontal permeability.

Figure 7.28 illustrates the case where flow is below a dam structure. The horizontal permeability is three times the vertical permeability. The true section is shown in Fig. 7.28(a). A transformed section is made by selecting some point (A) and reducing the horizontal distance to any other point by the shape factor—in this case, $1/3$. Figure 7.28(b) shows the transformed section with the flow net drawn as usual. Notice the horizontal and vertical symmetry of the flow net. The amount of flow and uplift pressures may be obtained from either Fig. 7.28(b) or (c). However, when the flow net is expanded back to the original size, only this true section will give the actual factor of safety with respect to piping or boiling, using the equation given in Example 7.15. In the event that the anisotropic permeabilities are not parallel to the horizontal and vertical axis but are inclined, the transformed section would be drawn at some angle parallel to the *inclined* permeabilities.

7.10 CONTROL OF SEEPAGE AND FILTERS

In the discussion of seepage forces and flow nets, piping and erosion were mentioned as a possibility if, somewhere in the porous medium, the gradient exceeded the critical gradient. Piping can occur anyplace in the system, but usually it occurs where the flow is concentrated, as shown in Fig. 7.20, or if the flow exits at the top surface of an earth dam. When the seepage forces are large enough to move particles, piping and erosion can start, usually continuing until either all the soils in the vicinity are carried away or the structure collapses. Cohesionless soils, especially silty soils, are highly susceptible to piping, and if you must use such soils in an embankment dam, for example, then you must be very careful to see that the seepage is controlled and that the chance for piping to occur is very small.

How is seepage controlled? The choice of methods depends on the situation, but sometimes a cutoff wall or trench is constructed to completely block the seeping water. Sometimes the drainage path is lengthened by an impervious blanket, so that more of the head is lost and thus the gradient in the critical region is reduced. If properly designed and constructed, relief wells and other kinds of drains can be used to positively relieve high uplift pressures at the base of hydraulic structures (Cedergren, 1989).

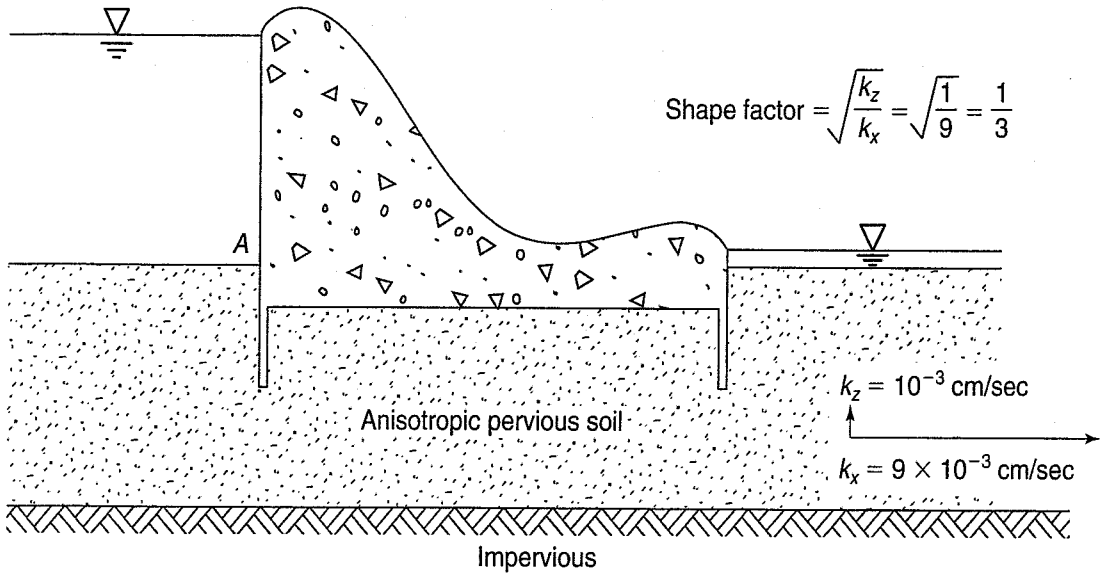

(a) Sketch of problem

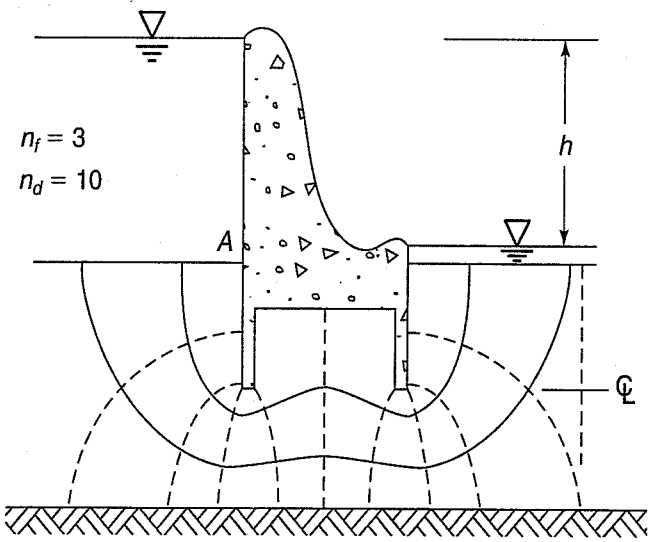

(b) Transformed flow reduced to one-third of actual net-horizontal dimensions

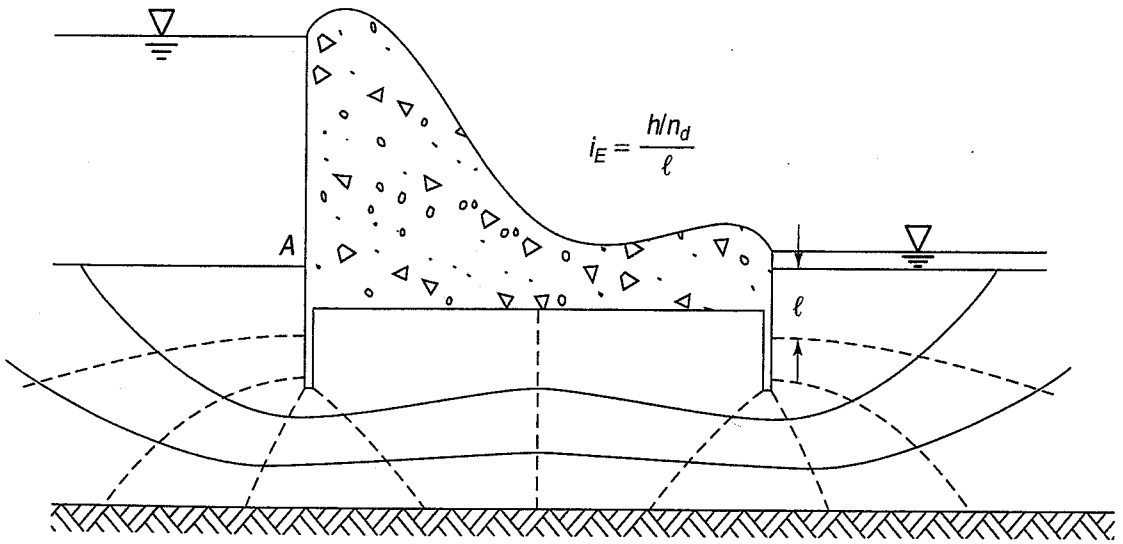

(c) Final flow net

FIGURE 7.28 Use of a transformed flow net to account for anisotropic permeability in a dam foundation: (a) problem; (b) transformed flow net; (c) final flow net (after Perloff and Baron, 1976).

Another way to prevent erosion and piping, reduce potentially damaging exit gradients, and reduce uplift pressures is to use a *protective filter*. Traditionally, filters consisted of one or more layers of free-draining granular materials are placed in less pervious foundation or base materials to prevent the movement of soil particles susceptible to piping. Filters allow the seepage water to escape with relatively little head loss, thus reducing the seepage forces within the filter itself. Today, especially for routine drainage applications, filters of nonwoven geotextiles and geocomposite drainage products are commonly used to replace granular filters. However, in earth dams and other important water retention structures, most designs still call for graded granular filters. In any case, to properly design both types of filters, you need to understand basic filtration principles.

Hazen (1911), while working with water treatment filters around the turn of the last century, found that the *effective size* of a filter was the D_{10} [for example, Eq. (7.11)]; that is, this size controlled the performance of a filter sand as much as the remaining 90% of the sizes.

7.10.1 Basic Filtration Principles

In 1922, Terzaghi delineated the requirements for a graded granular filter based on the grain size distributions of both the filter and the material to be protected. Although the requirements have been modified slightly based on laboratory tests by the U.S. Army Corps of Engineers and the U.S. Bureau of Reclamation, the basic principles are still the same. The filter must be able to:

1. retain the soil particles in place and prevent their migration (piping) through the filter (if some soil particles do move, they must be able to pass through the filter without clogging the drain during the life of the project); and
2. allow water to flow through the filter into the drain throughout the life of the project.

The first criterion is called the retention or piping criterion, and the second is the permeability or flow criterion. The subsidiary criterion that the long-term performance must be maintained is sometimes referred to as the durability or clogging criterion, because if the filter clogs, the flow capacity will be reduced, and instability may result. These principles apply to graded granular filters as well as geotextile filters. Both require proper engineering design, or the filter and drain may not perform as desired.

Figure 7.29 illustrates the principle of the first requirement, that of retention or prevention of piping. As a crude approximation, let us model the filter and soil as perfect spheres. If three equal spheres of the filter just touch, as shown in Fig. 7.29, then they are 6.5 times larger than the largest soil particle that can just pass in between them. This model is for dense packing or dense conditions. If the soil to be filtered were looser, you would think that even larger soil particles would be able to pass through the filter. However, laboratory tests have shown that the grain size of a uniform filter material can be as large as 10 times the grain size of a uniform foundation soil and still prevent particle movement. This is probably because two particles of the same size cannot pass the filter at the same time, and the larger soil particles form a *filter bridge* over the hole, which in turn filters smaller particles of soil, which then retain the soil and prevent piping. Other factors such as particle shape, relative density, and the porosity of the filter material also affect the limiting size. For design, it is probably best to limit this number to 4 or 5. At least that is what Terzaghi did (Taylor, 1948). Because it is easier to obtain the grain sizes of a soil than the pore sizes, we use the grain sizes as a surrogate for the pore sizes in developing filter criteria.

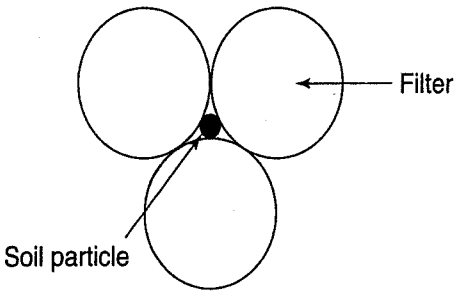

FIGURE 7.29 Soil particle retained by an ideal filter.

7.10.2 Design of Graded Granular Filters

The Terzaghi retention (piping) criterion is

$$D_{15\,\text{filter}} < (4 \text{ to } 5)D_{85\,\text{soil}} \tag{7.27}$$

and the Terzaghi permeability criterion is

$$D_{15\,\text{filter}} > (4 \text{ to } 5)D_{15\,\text{soil}} \tag{7.28}$$

where D_{15} and D_{85} are the 15% and 85% size passing, respectively, for the filter and the soil to be protected.

Recall that the effective size is D_{10}, not D_{15}, but it doesn't really matter which one you use. The important thing is to recognize that the finer portion of the gradation controls the hydraulic conductivity of the drain and filter. The permeability criterion insures that there is adequate flow *through* the filter and that any seepage forces that develop are small. The number "4 to 5" is really a safety factor on the hydraulic conductivity, because all we really need is for the k of the filter to be slightly greater than that of the soil. But a difference in k of four or five times is that much safer, and we probably know the value of k only to the nearest order of magnitude anyway (Sec. 7.4). The Bureau of Reclamation also specified that the filter as constructed should contain no more than 5% passing the 0.075-mm sieve (U.S. Dept. of the Interior, 1987). Further, they recommend that the filter should be *uniformly* graded.

Because filters are often used adjacent to slotted or perforated pipe drains, the Bureau of Reclamation added the following criterion:

$$D_{85\,\text{filter}} \geq 2 \times \text{maximum openings in pipe} \tag{7.29}$$

The U.S. Army Corps of Engineers criterion for slotted and circular hole pipes is somewhat more conservative than the Bureau's, according to Cedergren (1989). For slotted pipe

$$D_{85\,\text{filter}} \geq 1.2 \times \text{slot width} \tag{7.30}$$

$$D_{85\,\text{filter}} \geq 1 \times \text{hole diameter for circular holes} \tag{7.31}$$

Example 7.19 (From U.S. Dept. of the Interior, 1998.)

Given:

The grain size distribution curve A, shown in Fig. Ex. 7.19.

Required:

Design Filter 1 to protect the base soil, curve (range) A, and design Filter 2 to protect Filter 1. A plastic pipe (a "geopipe") with circular openings of 6.4 mm will be used to drain the water away from the filters.

Solution: The ranges of the completed grain size curves are also shown in Fig. Ex. 7.19. You have to start with a *base* soil or the *soil to be protected.* Sometimes this is called the *foundation soil.* The base soil can be a single line on a grain size distribution curve or a range as shown in the figure. From this figure, find minimum D_{85} of the soil or base = 0.10 mm. On the same curve, find D_{15} = 0.03 mm. Note that the D_{15} is on the *larger* size of the curve. Why? Because if the hydraulic conductivity of the filter is OK for the larger D_{15}, then it certainly is OK for the finer-grained soil. You need to start with those two points (D_{85} and D_{15}) in order to design a filter. Using Eqs. (7.27) and (7.28), solve for D_{15} of Filter 1.

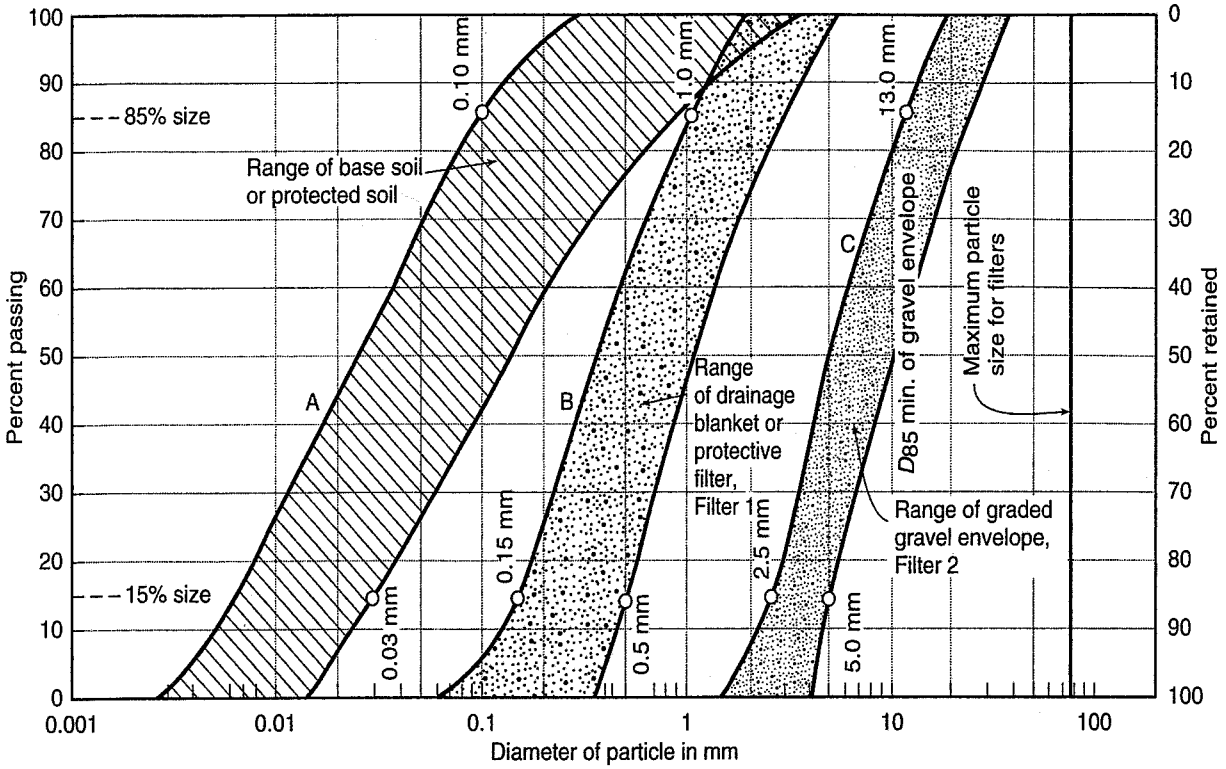

FIGURE Ex. 7.19

The *maximum* value of D_{15} is given by

$$\begin{aligned} D_{15\,\text{filter}} &\leq 5D_{85\,\text{soil}} \\ &\leq 5 \times 0.10\ \text{mm} \\ &\leq 0.50\ \text{mm (upper limit)} \end{aligned}$$

The D_{15} of Filter 1 represents the *minimum* value

$$\begin{aligned} D_{15\,\text{filter}} &\geq 5 \times D_{15\,\text{soil}} \\ &\geq 5 \times 0.03\ \text{mm} \\ &\geq 0.15\ \text{mm (lower limit)} \end{aligned}$$

Plot these values on Fig. Ex. 7.19, and with the *range* of grain size curves drawn (with some license) to be generally parallel to the soil the filter is to protect. For a soil to be considered well graded, the uniformity coefficient [Eq. (2.34)] lies in the range of 1.5 to 8. For Filter 1, $C_u = D_{60}/D_{10} = 0.45\ \text{mm}/0.12\ \text{mm} = 4$, therefore it is acceptable. Notice that <5% passes the 0.075 mm sieve.

Equation (7.29) indicates that Filter 1 must have a $D_{85} = 2 \times$ hole opening of 6.4 mm or about 13 mm. Figure Ex. 7.19 shows that D_{85} of Filter 1 is a mere 0.10 mm. (Remember that the resulting D_{85} on the left of the range of Filter 1, or range of B, is because range B was drawn using some artistic license to make it somewhat parallel to curve A.) Therefore a second filter, Filter 2, is needed.

Repeating the above equations, the maximum value of D_{15} is

$$\begin{aligned} D_{15}\,(\text{of Filter 2}) &\leq 5 \times D_{85}\,(\text{soil} = \text{Filter 1}) \\ &\leq 5 \times 1.0\ \text{mm} \\ &\leq 5.0\ \text{mm (upper limit)} \end{aligned}$$

The minimum D_{15} of Filter 2 is

$$\begin{aligned} D_{15}\,(\text{of Filter 2}) &\geq 5 \times D_{15}\,(\text{soil} = \text{Filter 1}) \\ &\geq 5 \times 0.5\ \text{mm} \\ &\geq 2.5\ \text{mm (lower limit)} \end{aligned}$$

For the drain pipe with 6.4 mm holes, use Eq. (7.29), or D_{85} (of Filter 2) $\geq$ 13 mm. This value of D_{85} becomes the minimum value. Review Fig. Ex. 7.19 for the location of all these points. Make sure you understand where all the values came from.

In the early 1990s, the Bureau of Reclamation changed their filter criteria. They established four categories of filter design, depending on the amount of "base" soil (or soil to be protected) that passes the No. 200 (75 μm) sieve. The criteria are given in U.S. Dept. of the Interior (1994).

As you can see, the design of graded granular filters is simple. You just have to follow the recipes. Note that filters may have their own filter, so as to satisfy the two requirements of not clogging the filter but at the same time allowing flow through the filter. A *strong* word of caution: *filter design is very important.* As you observe construction, you will notice lots of carelessness when it comes to placing crushed gravel over fine-grained soils, supposedly designed as a filter. With time, the crushed rock will get clogged and pore water will build up, perhaps leading to failure. On the other hand, flow can be restricted with the same result. If granular filters are deposited below water, the heavier particles settle out first, which ruins carefully designed filter gradations. More foundation failures are due to water than to other causes.

7.10.3 Geotextile Filter Design Concepts

Designing geotextile filters is very similar to designing graded granular filters. A geotextile is similar to a soil in that it has voids (pores) and particles (filaments and fibers). However, because of the shape and arrangement of the filaments and the geotextiles' compressible structure, the geometric relationships among filaments and voids are more complex than in soils. Since it is possible to measure pore sizes of geotextiles directly, at least in theory, relatively simple relationships between the pore sizes of the geotextile and particle sizes of the soil to be retained have been developed for design.

The basic filtration principles stated in Sec. 7.10.1 are the basis for design of geotextile filters. Specifically, the geotextile must retain the soil particles (*retention criterion*) while allowing water to pass (*permeability criterion*) throughout the life of the structure (*clogging resistance criterion*). To perform effectively, the geotextile must also survive installation (*survivability or constructability criterion*) and last throughout the life of the project or system (*durability criterion*).

Based on a detailed study of both North American and European research on filters, Christopher and Holtz (1985) developed what is now called the FHWA (U.S. Federal Highway Administration) filter design procedure for geotextile filters used in drainage and erosion control applications. The level of design and testing required depends on the critical nature of the project and the severity of the hydraulic and soil conditions (Table 7.3). Especially for critical projects, consideration of the risks and the consequences of a geotextile filter failure require great care in selecting the appropriate geotextile. For such projects, and for severe hydraulic conditions, we recommend you use very conservative designs. Because the cost of the geotextile is usually small compared to that of the other components and the construction costs of a drainage system, do not try to save money by selecting a cheaper geotextile or eliminating laboratory soil-geotextile performance testing when it is required by the FHWA design procedure.

TABLE 7.3 Guidelines for Evaluating the Critical Nature or Severity of Drainage and Erosion Control Applications

A. Critical Nature of the Project		
Item	Critical	Less Critical
1. Risk of loss of life and/or structural damage due to drain failure:	High	None
2. Repair costs versus installation costs of drain:	Very much greater	Less than or equal to
3. Evidence of drain clogging before potential catastrophic failure:	None	Yes
B. Severity of the Conditions		
Item	Severe	Less Severe
1. Soil to be drained:	Gap-graded, pipable, or dispersible	Well-graded or uniform
2. Hydraulic gradient:	High	Low
3. Flow conditions:	Dynamic, cyclic, or pulsating	Steady state

After Carroll (1983).

7.10.4 FHWA Filter Design Procedure

Based on the concepts just described, the FHWA filter design procedure has three criteria: retention, permeability, and clogging resistance. Survivability and durability also are part of the design.

Retention Criterion—Because they put different demands on the geotextile filter, two flow conditions, (1) steady state and (2) dynamic, are considered for retention.

1. For *steady state flow conditions:*

$$AOS \text{ or } O_{95\ \text{geotextile}} \leq BD_{85\ \text{soil}} \tag{7.32}$$

where AOS = apparent opening size (mm); see ASTM (2010) D 4751,
O_{95} = opening size in the geotextile for which 95% are smaller (mm); $AOS \approx O_{95}$,
B = a coefficient (dimensionless), and
D_{85} = soil particle size for which 85% are smaller (mm).

The coefficient B ranges from 0.5 to 2 and is a function of the type of soil to be filtered, its density, the uniformity coefficient C_u if the soil is granular, the type of geotextile (woven or nonwoven), and the flow conditions.

For *sands*, *gravelly sands*, *silty sands*, and *clayey sands* (soils with less than 50% passing the 0.075 mm sieve), B is a function of the uniformity coefficient, C_u. Therefore, for

$$C_u \leq 2 \text{ or } \geq 8: \quad B = 1 \tag{7.33a}$$

$$2 \leq C_u \leq 4: \quad B = 0.5C_u \tag{7.33b}$$

$$4 < C_u < 8: \quad B = 8/C_u \tag{7.33c}$$

Recall that $C_u = D_{60}/D_{10}$.

Sandy soils that are not uniform tend to bridge across the openings; thus, the larger pores may actually be up to twice as large ($B \leq 2$) as the larger soil particles, because, quite simply, two particles

cannot pass through the same hole at the same time. Therefore, use of the criterion $B = 1$ would be quite conservative for retention, and in fact this criterion has been used by the U.S. Army Corps of Engineers. If the protected granular soils contain appreciable fines, use only the portion passing the 4.75 mm sieve for selecting the geotextile (i.e., screen off the + 4.75 mm material and just use the GSD for the remainder of the soil in your calculations).

For *silts and clays* (soils with more than 50% passing the 0.075 mm sieve), B is a function of the type of geotextile:

for woven geotextiles, $B = 1$: $O_{95} < D_{85}$ (7.34)

for nonwoven geotextiles, $B = 1.8$: $O_{95} < 1.8D_{85}$ (7.35)

and for both: AOS or $O_{95} < 0.3$ mm (7.36)

Due to their random pore characteristics and feltlike surface, some types of nonwoven geotextiles will generally retain finer particles than a woven geotextile of the same AOS. Therefore, the use of $B = 1$ will be even more conservative for nonwoven geotextiles. If you need a review of geotextile types and properties, see Holtz et al. (1997 and 2008) and Koerner (2006).

2. For *dynamic flow conditions:*

If the geotextile is not properly weighted down and in *intimate contact* with the soil to be protected, or if dynamic, cyclic, or pulsating loading conditions produce high localized hydraulic gradients, then soil particles can move behind the geotextile. Thus, the use of $B = 1$ is not conservative, because the bridging network will not develop and the geotextile will be required to retain even finer particles. When retention is the primary criterion, B should be reduced to 0.5, or:

$$O_{95} \leq 0.5D_{85} \tag{7.37}$$

Dynamic flow conditions can occur in pavement drainage applications and in some erosion control situations. For reversing inflow-outflow or high-gradient situations, be sure that sufficient weight is maintained on the geotextile filter to prevent it from moving.

The above retention criterion assumes that the soil to be filtered is internally stable—it will not pipe internally. If *unstable* soil conditions are encountered, performance tests should be conducted to select suitable geotextiles. According to Kenney and Lau (1985, 1986) and LaFleur et al. (1989), broadly graded ($C_u > 20$) soils with concave upward grain-size distributions tend to be internally unstable.

Permeability Criterion—We consider two conditions when designing for permeability: (1) less critical/less severe and (2) critical/severe conditions.

1. For *less critical applications* and *less severe conditions:*

$$k_{\text{geotextile}} \geq k_{\text{soil}} \tag{7.38a}$$

2. For *critical applications* and *severe conditions:*

$$k_{\text{geotextile}} \geq 10\, k_{\text{soil}} \tag{7.38b}$$

where $k_{\text{geotextile}}$ = the geotextile's Darcy coefficient of permeability (m/sec).

For actual flow capacity, the permeability criterion for noncritical applications is conservative, since an equal quantity of flow takes significantly less time through a relatively thin geotextile than through a thick granular filter. Even so, some pores in the geotextile may become blocked or plugged with time. Therefore, for critical or severe applications, use Eq. (7.38b), because with a factor of safety of 10, it provides an additional degree of conservatism. Equation (7.38a) may be used where flow reduction is judged not to be a problem, such as in clean, medium to coarse sands and gravels.

Additional geotextile qualifiers such as the *permittivity* are often used in filtration and drainage design (Holtz et al., 1997 and 2008). Permittivity, defined as the Darcy coefficient of permeability divided by the geotextile thickness, is a good indicator of flow capacity, and thus it is useful for making sure the geotextile filter has sufficient flow capacity for a given soil in a particular application. Many manufacturers give the permittivity value for their products according to ASTM (2010) D 4491, and products are available that meet or exceed recommended permittivity values in Holtz et al. (1997 and 2008).

Clogging Resistance—For clogging resistance, we consider the same two conditions as we did for the permeability criteria: (1) less critical/less severe and (2) critical/severe conditions.

1. For *less critical/less severe* conditions:

$$O_{95\ \text{geotextile}} \geq 3D_{15\ \text{soil}} \tag{7.39}$$

Equation (7.39) applies to soils with $C_u > 3$. For $C_u \leq 3$, select a geotextile with the maximum *AOS* value based on retention. In situations where clogging is a possibility (e.g., gap-graded or silty soils), the following *optional* qualifiers may be applied:

For *nonwoven* geotextiles:

$$\text{porosity of the geotextile, } n \geq 50\% \tag{7.40}$$

For *woven monofilament* geotextiles:

$$\text{percent open area, } POA \geq 4\% \tag{7.41}$$

Most common nonwoven geotextiles have porosities much greater than 70%, and most woven monofilaments easily meet the criterion of Eq. (7.41). Woven slit films do not and are therefore not recommended for subsurface drainage applications.

For *less critical/less severe* conditions, a simple way to avoid clogging, especially with silty soils, is to allow fine particles already in suspension to pass through the geotextile. Then the filter bridge mentioned earlier formed by the larger particles retains the smaller particles. The filter bridge should develop rather quickly, and the quantity of fine particles actually passing through the geotextile is ordinarily relatively small. This is why the less critical/less severe clogging resistance criterion requires an *AOS* (O_{95}) sufficiently larger than the finer soil particles (D_{15}). Those are the particles that will pass through the geotextile. Unfortunately, the *AOS* value indicates only the size and not the number of O_{95}-sized holes available. Thus, the finer soil particles will be retained by the smaller holes in the geotextile, and, if there are sufficient fines, a significant reduction in flow rate can occur.

Consequently, to control the number of holes in the geotextile, it may be desirable to increase other qualifiers such as the porosity and open area requirements. There should always be enough holes in the geotextile to maintain permeability and drainage, even if some of them clog. Filtration tests provide another option to be considered, especially by inexperienced users.

2. For *critical/severe* conditions:

For critical/severe conditions, first select geotextiles that meet the retention and permeability criteria above. Second, perform laboratory filtration tests that simulate or model field hydraulic conditions and use samples of on-site soils. These are called *performance* tests, because they model the actual performance of the geotextile and soil under realistic field conditions.

For sandy soils with $k > 10^{-6}$ m/sec, we recommend the gradient ratio test, ASTM (2010) D 5101. This test uses a rigid-wall permeameter with piezometer taps that allow for simultaneous measurement of the head losses in the soil and the head loss across the soil/geotextile interface (Fig. 7.30). The ratio of the head loss across this interface (nominally 25 mm) to the head loss across 50 mm of soil is termed the gradient ratio. If fine soil particles move and clog the geotextile filter, then the gradient ratio (*GR*) will increase above the maximum recommended value of three. Experience has shown that as long as the *GR* is less than three, satisfactory long-term performance will occur.

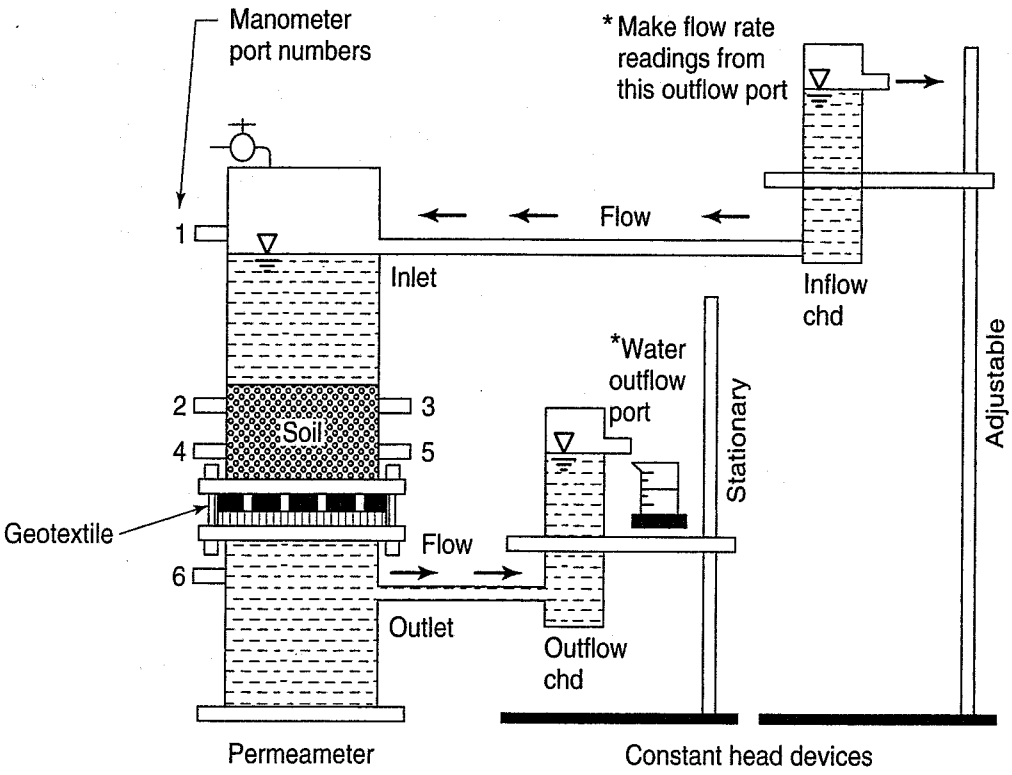

FIGURE 7.30 U.S. Army Corps of Engineers gradient ratio test device (Holtz et al., 2008).

For soils with a permeability less than about 10^{-6} m/sec, filtration tests should be conducted in a flexible wall apparatus to insure that the specimen is 100% saturated and that flow is through the soil rather than along the sides of the specimen. The flexible-wall GR test combines the best features of the GR test (ASTM standard D 5101) and the flexible wall permeability test (D 5084). Just as with the GR test, multiple ports along the soil column accurately determine head losses. Research by Harney and Holtz (2001) and Bailey et al. (2005) indicated that the FWGR yielded consistent and accurate results, and in significantly less time than the GR.

Survivability and Durability Criteria—We mentioned earlier that survivability and durability are a part of geotextile filter design. To be sure that the geotextile will survive the construction process and not deteriorate in the field environment, certain strength and durability properties are required. Probably the best material specifications available for geotextile filters are the AASHTO (2006) Standard Specifications for Geotextiles—M 288. Minimum values for tensile strength and tear and puncture resistance are specified for different field conditions, such as the condition of the subgrade, angularity of the aggregate, and the way the drain and backfill materials are installed and compacted. ASTM standard tests are available for all the required survivability properties.

Geotextile durability relates to its longevity. Geotextiles have been shown to be basically inert materials for most environments and applications. However, certain applications may expose the geotextile to chemical or biological activity that could drastically influence its filtration properties or durability. For example, in drains, granular filters and geotextiles can become chemically clogged by iron or carbonate precipitates, and biologically clogged by algae, mosses, and so on. Biological clogging is a potential problem when filters and drains are periodically inundated, then exposed to air. Excessive chemical and biological clogging can significantly influence filter and drain performance. These conditions are present, for example, in municipal solid waste landfills.

For additional information about the survivability and durability tests, see Koerner (2006) and Holtz et al. (1997 and 2008).

Example 7.20 (After Holtz et al., 1997 and 2008.)

Given:

Undesirable seepage and occasional shallow slope failures are currently a maintenance problem for a rural two-lane highway. The proposed solution is to construct an interceptor drain at the toe of the slope in order to permanently lower the high groundwater table. A geotextile-wrapped trench drain about 1 m deep is proposed, and representative soil samples were obtained along the proposed drain alignment. All three soil samples were nonplastic. Gradations of three samples are given in the table and shown on Fig. Ex. 7.20.

Required:

Use the FHWA geotextile filter design procedure to design the geotextile filter for the drain.

Sieve Size (mm)	Percent Passing, By Weight		
	Sample A	Sample B	Sample C
25	99	100	100
13	97	100	100
4.76	95	100	100
1.68	90	96	100
0.84	78	86	93
0.42	55	74	70
0.15	10	40	11
0.074	1	15	0

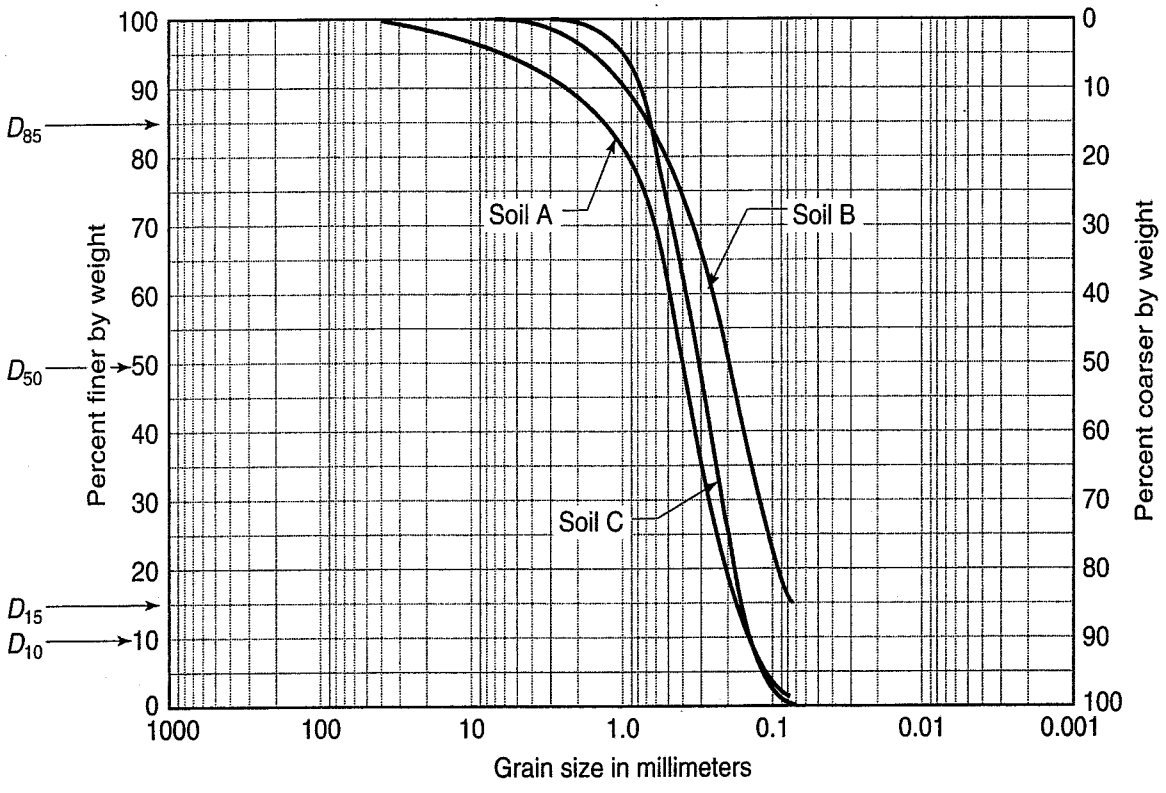

FIGURE Ex. 7.20 Grain size distribution curve for soils A, B, and C.

Solution: Determine the geotextile properties required for apparent opening size (AOS) and permeability. For the example, we will assume that the survivability properties can be obtained from the AASHTO (2006) M-288 specifications.

From given data, this is a noncritical application. Soils are reasonably well graded, the hydraulic gradients are low, and flow conditions are steady state for this type of application.

For retention, we use the grain size analyses in Fig. Ex. 7.20 to determine the D_{60}, D_{10}, and D_{85} sizes for Samples A, B, and C. Determine uniformity coefficient, C_u, coefficient B, and the maximum AOS. From the following table, note that the worst case soil for retention (i.e., smallest $B \times D_{85}$) is Soil C. Any geotextile that retains Soil C will also retain Soils A and B. So for the geotextile requirements, AOS $\leq$ 0.72 mm.

Soil Sample	$D_{60} \div D_{10} = C_u$	B	AOS (mm) $\leq B \times D_{85}$
A	$0.48 \div 0.15 = 3.2$	$0.5C_u = 0.5 \times 3.2 = 1.6$	$1.6 \times 1.0 = 1.6$
B	$0.25 \div 0.06 = 4.2$	$8C_u = 8 \times 4.2 = 1.9$	$1.9 \times 0.75 = 1.4$
C	$0.36 \div 0.14 = 2.6$	$0.5C_u = 0.5 \times 2.6 = 1.3$	$1.3 \times 0.55 = 0.72$

Because this is a noncritical application and the soils are predominantly sandy, we can use the Hazen equation [Eq. (7.11)] to estimate the permeability. The largest D_{10} controls permeability; therefore Soil A with $D_{10} = 0.15$ mm controls

$$k \approx (D_{10})^2 = (0.15)^2 \approx 2(10)^{-2} \text{ cm/sec} = 2(10)^{-4} \text{ m/sec}$$

Because this application is a less critical/less severe, $k_{\text{geotextile}} \geq k_{\text{soil}}$. So, $k_{\text{geotextile}}$ just needs to be greater than $2(10)^{-4}$ m/sec.

For clogging, because this is a less critical/less severe application and Soils A and B have a C_u greater than 3. Therefore, for Soils A and B, $O_{95} \geq 3D_{15}$. So

$$O_{95} \geq 3 \times 0.15 = 0.45 \text{ mm for Sample A}$$
$$\geq 3 \times 0.075 = 0.22 \text{ mm for Sample B}$$

Soil A controls, although—because sand-size particles typically do not create clogging problems—Soil B could have been used as the design control. So, using Soil A, AOS $\geq$ 0.45 mm. For Soil C, a geotextile with the maximum AOS value determined from the retention criteria should be used. Therefore AOS $\approx$ 0.72 mm. Also, additional qualifiers are that the nonwoven porosity is greater than 50% and the woven percent open area is greater than 4%.

In summary, for the filtration, the geotextile should have 0.45 mm $\leq$ AOS $\leq$ 0.72 mm; and $k_{\text{geotextile}} \geq 2(10)^{-2}$ cm/sec. Woven slit film geotextiles are not allowed.

For survivability, use the AASHTO (2006) M-288 specifications.

PROBLEMS

7.1 A clean sand having a permeability of 4.5×10^{-3} cm/s and a void ratio of 0.45 is placed in a horizontal permeability apparatus, as shown in Fig. 7.2. Compute the discharge velocity and the seepage velocity as the head Δh goes from 0 to 80 cm. The cross-sectional area of the horizontal pipe is 95 cm^2, and the soil sample is 0.65 m long.

7.2 A sample of medium quartz sand is tested in a constant head permeameter. The sample's diameter is 60 mm and its length is 130 mm. Under an applied head of 60 cm, 119 cm^3 flows through the sample in 5 min. The M_s

of the sample is 410 g. Calculate (a) the Darcy coefficient of permeability, (b) the discharge velocity, and (c) the seepage velocity. (After A. Casagrande.)

7.3 A permeability test was run on a compacted sample of dirty sandy gravel. The sample was 175 mm long and the diameter of the mold 175 mm. In 90 s the discharge under a constant head of 38 cm was 405 cm^3. The sample had a dry mass of 4950 g and its ρ_s was 2710 kg/m^3. Calculate (a) the coefficient of permeability, (b) the seepage velocity, and (c) the discharge velocity during the test.

7.4 During a falling-head permeability test, the head fell from 49 to 28 cm in 4.7 min. The specimen was 8 cm in diameter and had a length of 85 mm. The area of the standpipe was 0.45 cm^2. Compute the coefficient of permeability of the soil in cm/s, m/s. and ft/d. What was the probable classification of the soil tested? (After A. Casagrande.)

7.5 A falling-head permeability test is to be performed on a soil whose permeability is estimated to be 2.8×10^{-6} m/s. What diameter standpipe should you use if you want the head to drop from 31.2 cm to 19.4 cm in about 5 min? The sample's cross section is 12 cm^2 and its length is 7.4 cm. (After Taylor, 1948.)

7.6 Show that the units of Eq. (7.4a) are in fact energy/mass. Show that Eq. (7.4b) has units of energy/weight, and that this comes out as a length (head).

7.7 Briefly describe exactly how you make a correction for temperature in a permeability test if the water is not exactly 20°C. State your reference.

7.8 In Example 7.1, the void ratio is specified as 0.43. If the void ratio of the same soil were 0.35, evaluate its coefficient of permeability. First estimate in which direction k would go, higher or lower; then proceed.

7.9 A falling-head permeability test on a specimen of fine sand 12.5 cm^2 in area and 10 cm long gave a k of 6.2×10^{-4} cm/s. The dry mass of the sand specimen was 195 g and its ρ_s was 2.71 Mg/m^3. The test temperature was 23°C. Compute the coefficient of permeability of the sand for a void ratio of 0.67 and the standard temperature of 20°C. (After A. Casagrande.)

7.10 A constant head permeability test is performed on a soil that is 2 cm × 2 cm square and 2.5 cm long. The head difference applied during the test is 18 cm, and 5 cm^3 is collected over a time of 100 sec.

(a) Compute the permeability based on these test conditions and results.

(b) A falling head test is to be done on the same soil specimen in the same time ($t_1 - t_2 = 100$ sec), and the standpipe diameter is 0.8 cm. If the average head during the test should be 18 cm [$\frac{1}{2}(h_1 + h_2) = 18$], what are h_1 and h_2?

7.11 The coefficient of permeability of a clean sand was 389×10^{-4} cm/s at a void ratio of 0.38. Estimate the permeability of this soil when the void ratio is 0.61.

7.12 Permeability tests on a soil supplied the following data:

Run No.	e	Temp. (°C)	k (cm/s)
1	0.70	25	0.32×10^{-4}
2	1.10	40	1.80×10^{-4}

Estimate the coefficient of permeability at 20°C and a void ratio of 0.85. (After Taylor, 1948.)

7.13 For the initial case in Problem 6.33, compute the head of water required at the top of the silty clay layer to cause a quick condition.

7.14 Sand is supported on a porous disc and screen in vertical cylinder, as shown in Fig. P7.14. These are equilibrium conditions.

(a) For each of the five cases, plot the total, neutral, and effective stresses versus height. These plots should be approximately to scale.

(b) Derive formulas for those three stresses in terms of the dimensions shown and e, ρ_s, and ρ_w for each case at both the top and bottom of the sand layer. For case IV, assume the sand is 100% saturated to the upper surface by capillarity. For case V, assume the sand above level h_c is completely dry and below h_c is completely saturated. (After A. Casagrande.)

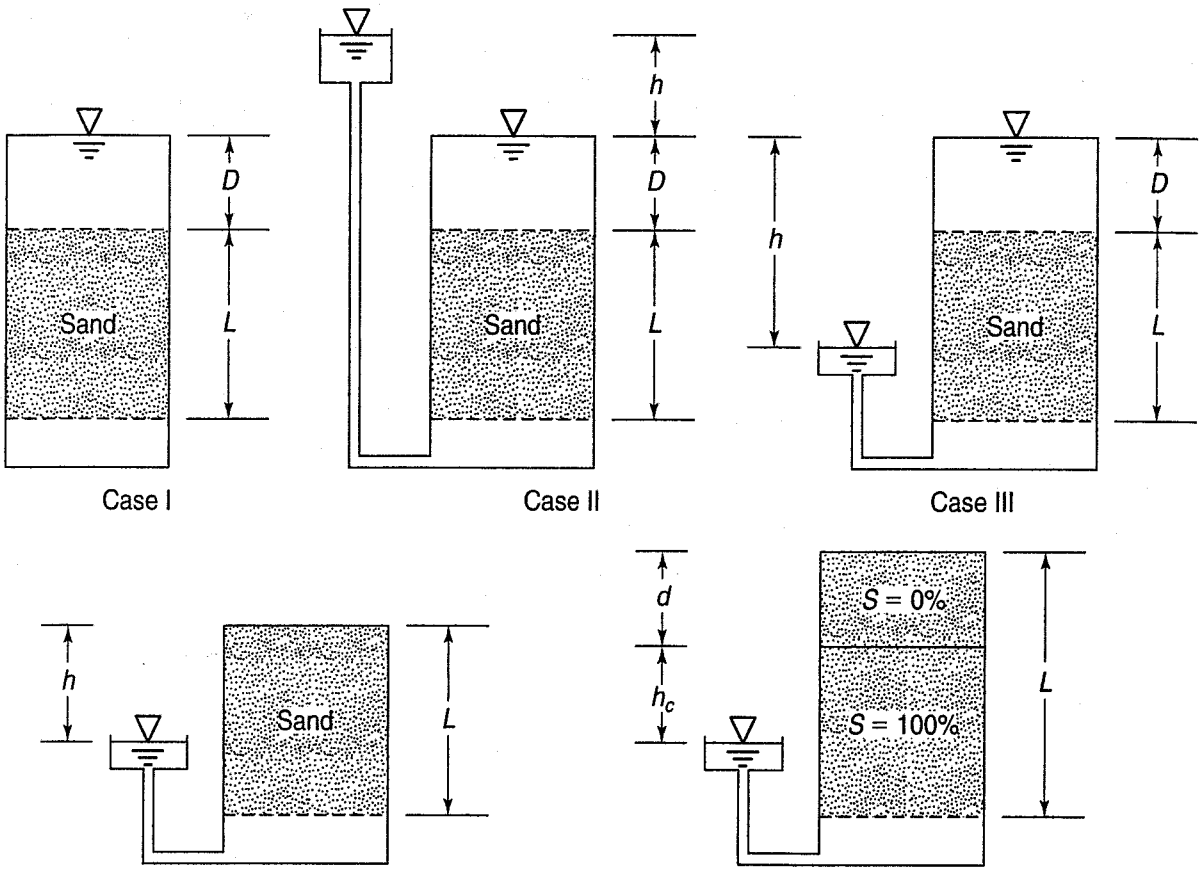

FIGURE P7.14

7.15 Given the soil cylinder and test setup of Example 7.4, with actual dimensions as follows: $AB = 5$ cm, $BC = 10$ cm, $CD = 10$ cm, and $DE = 5$ cm. Calculate the pressure, elevation, and total heads at points A through E in centimetres of water, and plot these values versus elevation.

7.16 For each of the cases I, II, and III of Fig. P7.16, determine the pressure, elevation, and total head at the entering end, exit end, and point A of the sample. (After Taylor, 1948.)

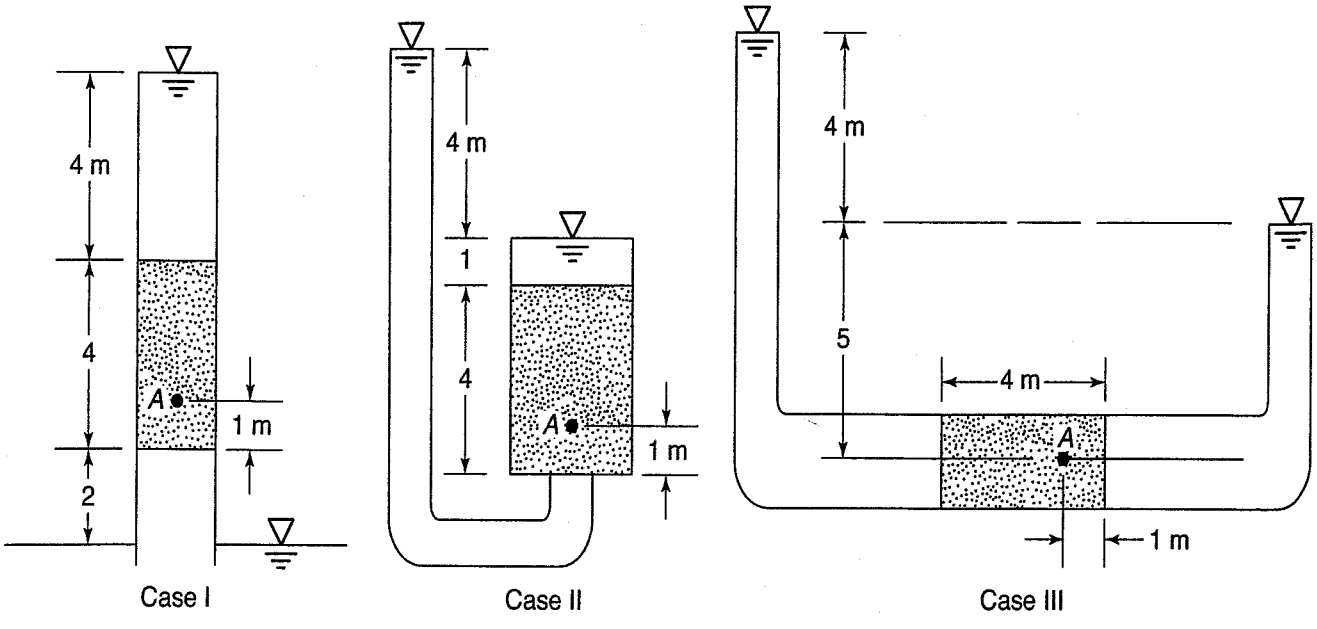

FIGURE P7.16

7.17 For each of the cases shown in Fig. P7.16, determine the discharge velocity, the seepage velocity, and the seepage force per unit volume for (a) a permeability of 0.14 cm/s and a porosity of 46% and (b) a permeability of 0.0013 cm/s and a void ratio of 0.71. (After Taylor, 1948.)

7.18 An inclined permeameter tube is filled with three layers of soil of different permeabilities as in Fig. P7.18. Express the head at points A, B, C, and D (with respect to the datum indicated) in terms of the different dimensions and permeabilities. (a) Work the problem first assuming $k_1 = k_2 = k_3$. (b) Then work it assuming $3k_1 = k_2 = 2k_3$. Plot the various heads versus horizontal distance for both parts (a) and (b). (After A. Casagrande.)

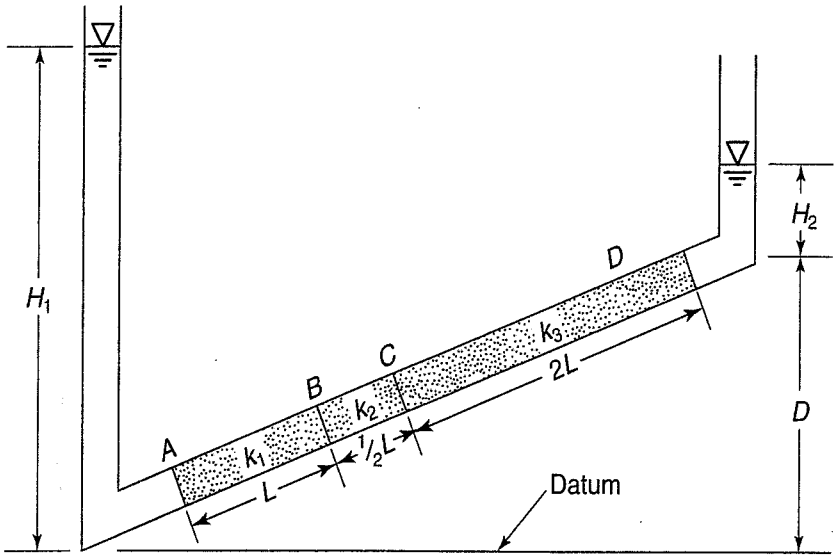

FIGURE P7.18

7.19 Assume the soil of Fig. 7.10 has a saturated density of 1.89 Mg/m^3. If the head of water h above elevation B is 2.45 m, compute the effective stress at elevation A at the bottom of the soil sample during flow. What is the effective stress under these conditions at midheight in the soil column during steady-state flow?

7.20 The foundation soil at the toe of a masonry dam has a porosity of 38% and a p_s of 2.73 Mg/m^3. To assure safety against piping, the specifications state that the upward gradient must not exceed 30% of the gradient at which a quick condition occurs. What is the maximum permissible upward gradient? (After Taylor, 1948.)

7.21 Show that it is impossible to drown in quicksand. (*Hint:* Calculate the density of the quicksand.)

7.22 Use Eq. (2.17) for ρ_{sat} and do the algebra to satisfy yourself that Eq. (g) in Sec. 7.6.1 reduces to Eq. (7.15).

7.23 A contractor plans to dig an excavation as show in Fig. P7.23. If the river is at level A, what is the factor of safety against quick conditions? Neglect any vertical shear. To what elevation can the water rise before a quick condition will develop? (After D. N. Humphrey.)

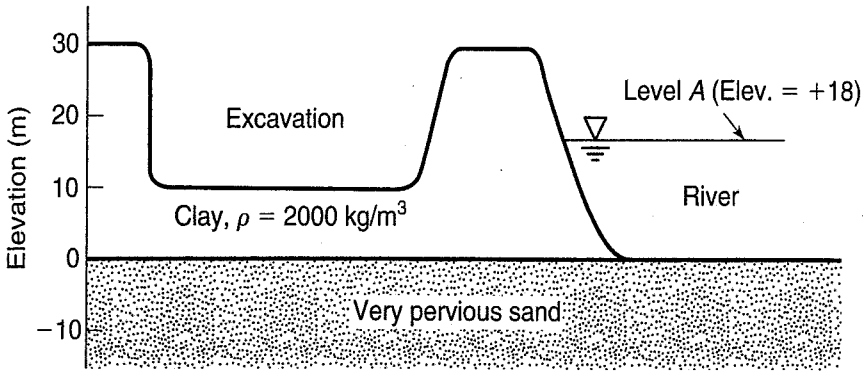

FIGURE P7.23

7.24 Given the excavation as shown in Example 7.13, with h = 18 m and ρ = 1915 kg/m^3, calculate the minimum allowable H_s.

7.25 A sheet pile wall has been installed partially through a silty sand layer, similar to the one shown in Fig. 7.13(b). Assume a sheet pile 12 m long penetrates 6 m (halfway) into the silty sand layer of thickness 12 m. For this condition:

(a) Draw a flow net using three (or four at most) flow channels. Note that the flow net is completely symmetrical about the bottom of the sheet pile. (This part is needed for the solution of Problem 7.31.)

(b) If the water height on the upstream side is 5 m and on the downstream side 1 m, compute the amount of water flowing under the sheet pile per metre of wall if the coefficient of permeability is 3.1×10^{-4} cm/s.

(c) Compute the maximum hydraulic gradient at the downstream side of the sheet pile.

7.26 Using the data of Fig. 7.18, compute the total head, piezometric head, pressure head, and elevation head for points C and C′. Assume any convenient datum.

7.27 Assuming that you have completed the flow net of Problem 7.25, compute the total head, piezometric head, pressure head, and elevation head for a point halfway up the sheet pile from its base, on either side of the sheet pile. Assume the datum is at the bottom of the silty sand layer. Plot gradient versus depth of piling and extrapolate to find the exit gradient.

7.28 Develop a flow net for the case shown in Fig. P7.28 using either manual methods or flow net software. Assume three or four flow channels.

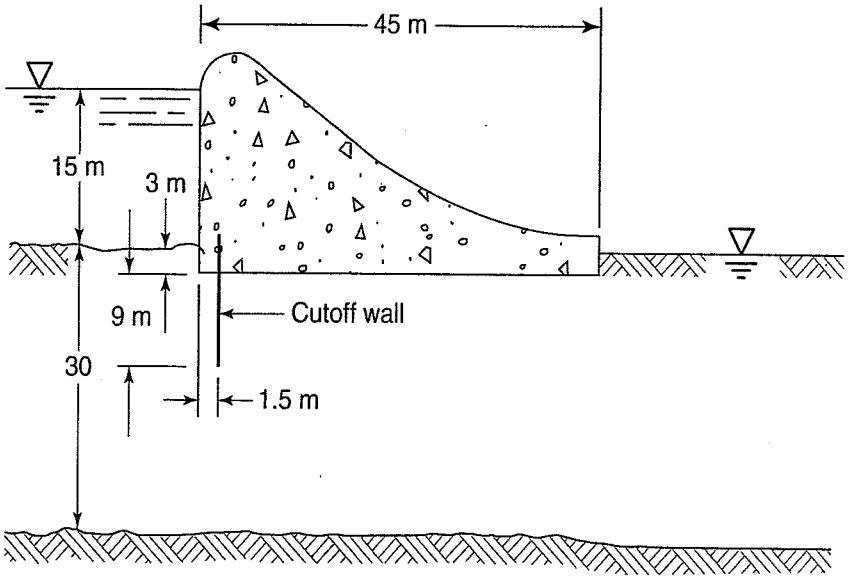

FIGURE P7.28 (Adapted from Taylor, 1948.)

7.29 Develop a flow net for the case shown in Fig. P7.29 using either manual methods or flow net software.

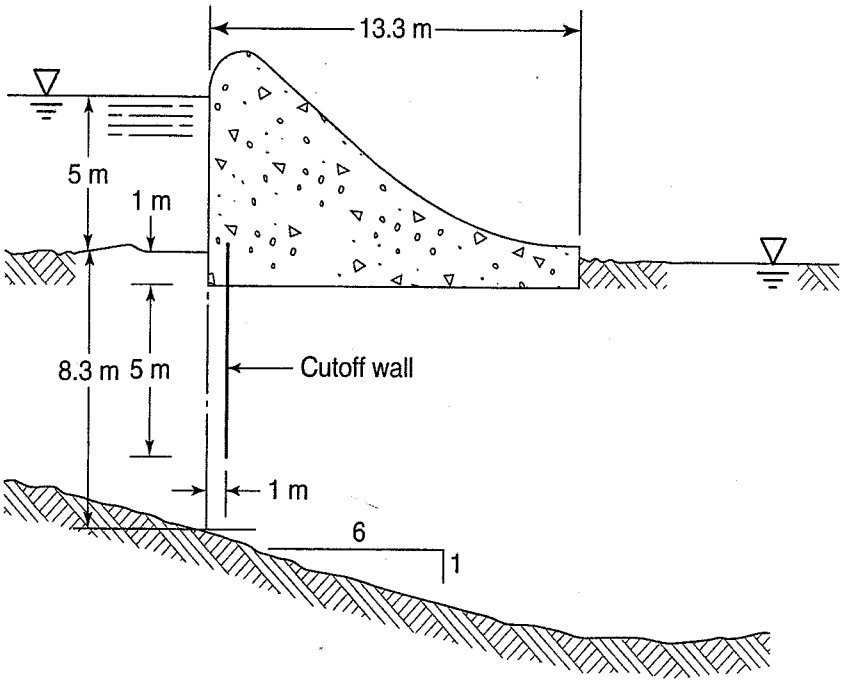

FIGURE P7.29 (Adapted from Taylor, 1948.)

7.30 For the completed flow net of Fig. P7.30, compute the flow under the dam per meter of dam if the coefficient of permeability is 4.2×10^{-4} cm/s.

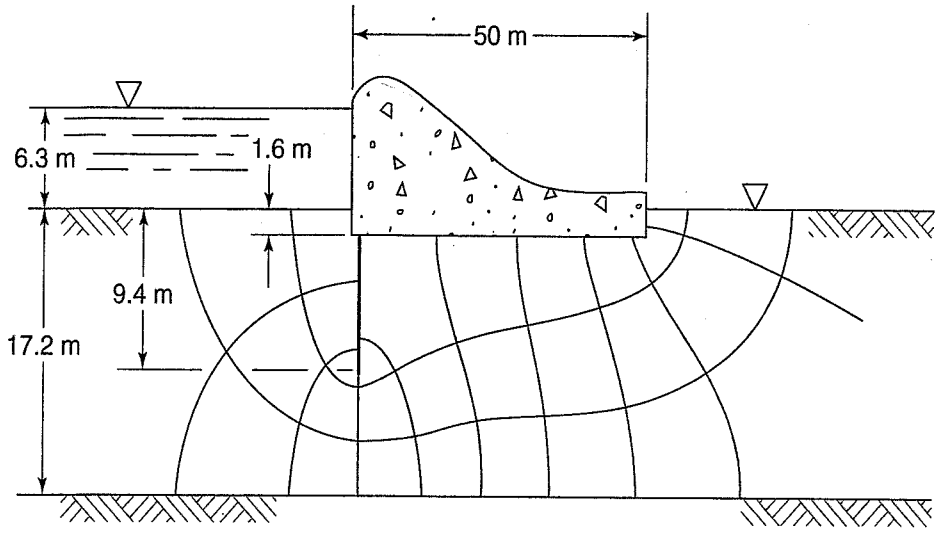

FIGURE P7.30 (Adapted from Taylor, 1948.)

7.31 Given the data of Problem 7.25. Using the method of fragments (see Appendix C), determine:

(a) The amount of water flowing under the sheet pile per metre of wall.

(b) The exit gradient.

7.32 For the dam of Fig. 7.15 set up the problem and solve as far as you can by the method of fragments (see Appendix C).

7.33 If one of the rows of sheet piles had to be removed for the problem given in Fig. Ex. 7.20a, which one when removed would cause the least reduction in flow?

7.34 Same as Problem 7.33, but solve for the least amount of uplift pressure. Give your answer in terms of metres of head.

7.35 Assume a row of sheet piles as shown in Fig. Ex. 7.29a. The total thickness of the soil layer is 18 m, while the difference between the head and tailwater is 12 m. Plot a graph showing how the flow under the sheet pile varies when the depth of the sheet pile goes from 8 m to 18 m. Ignore problems associated with the exit gradient.

7.36 Suppose there is a problem with the exit gradients, as in Problem 7.35. One solution would be to place a horizontal filter over the soil where the water exits. How does this help? Is it better for the filter to have a similar coefficient of permeability? One that is much smaller? Or one that is much larger? Explain which one is most desirable.

7.37 A protective three-layer filter is proposed between the foundation and rock drain located near the toe of a compacted earth-fill dam. Samples were taken and the grain sizes of the materials were determined to be as follows:

	D_{15} (mm)	D_{85} (mm)
Foundation, finest samples	0.024	0.1
Foundation, coarsest samples	0.12	0.9
Filter layer No. 1	0.3	1.0
Filter layer No. 2	2.0	3.5
Filter layer No. 3	5.0	10.0
Rock drain	15.0	40.0

Is this filter acceptable. If not, comment on any practical consequences. (After Taylor, 1948.)

7.38 In an attempt to reduce minor surface instability and maintenance problems on the backslopes of a rural highway, interceptor trench drains are to be installed at the top of the slope to intercept surface and infiltrating groundwater from the hillsides above the road. The drains are 1 to 1.5 m deep, and the drainage trench lined with a geotextile filter. A perforated drain pipe is placed in the bottom of the trench, and the trench is backfilled with coarse drainage aggregate.

Sieve analyses were performed on samples of soils typical of the problem areas along the highway alignment, and the following average data (percent passing) were obtained:

	Soils		
U.S. Standard Sieve No.	A	B	C
¾ in.	99	100	100
⅜ in.	88	100	99
No. 4	68	96	78
10	52	57	65
20	34	5	62
40	21	1	61
100	6	0	25
200	1	0	20

Design the geotextile filter for the interceptor drains. Extra credit: prepare material and construction specifications for this project.

CHAPTER 8

Compressibility of Soil and Rock

8.1 INTRODUCTION

You are undoubtedly aware that when materials are loaded or stressed, they deform or strain. Deformations can be either a change in shape (*distortion*) or a change in volume (usually *compression* in soils). While in some materials the deformation or strain occurs immediately upon loading, in others, this response may require a relatively long time. In geotechnical engineering, this second, time-dependent response is especially true for clay soils. Most of this chapter is devoted to the compressibility of these kinds of soils.

The simplest type of stress-strain relationship applies to *elastic* materials, in which the stresses and strains occur simultaneously, and if the load is removed, the material returns to its original shape. Elastic stress-strain relationships can be either *linear* (as in Hooke's law for a spring) or nonlinear. Some special elastic materials do not respond immediately to loading, and these are referred to as *visco-elastic*, where "visco" refers to the influence of time on the response. Typically, the faster a visco-elastic material is loaded, the stiffer it becomes; or stated another way, when a load is applied rapidly to a visco-elastic material, it deforms less than when the load is applied more slowly. But soils are even more complicated than this—most do not return to their original shape when they are unloaded, but retain some permanent deformation or strain. This is referred to as *plastic* behavior. For example, Silly Putty™ is material that is almost perfectly plastic—when it is loaded enough to cause some deformation, then unloaded, almost no strain is recovered, and it retains its deformed shape.

Another important characteristic of soils is that they are *nonconservative* materials, which means in engineering mechanics terminology that they have a "memory." If a soil is loaded and then unloaded, it retains part of that *stress history*, which can influence the soil's behavior if it is later reloaded.

Soils are therefore extremely complex materials in terms of their stress-strain-time behavior. As a result they have been among the most difficult engineering materials to model, both mechanically or in computer codes, because they often have all of the characteristics we've just mentioned. In summary, soils have

- nonlinear stress-strain relationships;
- time-dependent response to loading (the visco-part);

- some recoverable deformations when loaded and then unloaded (elastic);
- some irrecoverable deformations when loaded and unloaded (plastic); and
- a memory, a result of their stress history.

This chapter deals with all of the mechanical and behavioral issues we've just mentioned: nonlinearity, time dependence, and elastic and plastic response to loading-unloading, and the effect of stress history. Since most settlement problems in geotechnical practice are associated with clay soils, they will be the primary focus of this chapter.

The following notation is introduced in this chapter.

Symbol	Dimension	Unit	Definition
a_v	$M^{-1}LT^2$	$(kPa)^{-1}$	Coefficient of compressibility - Eq. (8.5)
C_c	—	—	Compression index - Eq. (8.7)
C_c^*	—	—	Burland's intrinsic compression index - Eq. (8.30)
C_{ce}	—	—	Modified compression index - Eq. (8.8)
C_r	—	—	Recompression index - Eq. (8.15)
C_{re}	—	—	Modified recompression index
D	$ML^{-1}T^{-2}$	kPa	Constrained modulus - Eq. (8.6)
e_o	—	(decimal)	Initial or in situ void ratio
e_{100}^*	—	—	Burland's intrinsic void ratio, e, at σ'_v = 100 kPa
e_{1000}^*	—	—	Burland's intrinsic void ratio, e, at σ'_v = 1000 kPa
Δe	—	(decimal)	Change in void ratio
H_o	L	m	Original thickness of a soil layer - Eq. (8.3)
ΔH	L	m	Change in thickness of a soil layer - Eq. (8.3)
I_v	—	—	Burland's void index - Eq. (8.29)
LIR	—	—	Load increment ratio - Eq. (8.27)
m	—	—	Dimensionless modulus number - Eq. (8.21)
M	$ML^{-1}T^2$	kPa	Tangent modulus - Eq. (8.21)
m_v	$M^{-1}LT^2$	$(kPa)^{-1}$	Coefficient of volume change - Eq. (8.6)
OCR	—	—	Overconsolidation ratio - Eq. (8.2)
s	L	m	Settlement - Eq. (8.4)
s_c	L	m	Consolidation settlement - Eq. (8.1)
s_i	L	m	Immediate or distortion settlement - Eq. (8.1)
s_s	L	m	Secondary compression - Eq. (8.1)
s_t	L	m	Total settlement - Eq. (8.1)
u	$ML^{-1}T^{-2}$	kPa	Pore water pressure
u_o	$ML^{-1}T^{-2}$	kPa	Initial or hydrostatic pore water pressure
z	L	m	Depth
α	—	—	Dimensionless stress exponent - Eq. (8.21)
ε_v	—	(%)	Vertical strain - Eq. (8.3)
σ'_{vc}	$ML^{-1}T^{-2}$	kPa	Vertical effective consolidation stress
σ'_p	$ML^{-1}T^{-2}$	kPa	The preconsolidation stress or maximum past vertical effective stress - Eq. (8.2); p'_c and σ'_{vm} are sometimes used
σ'_{ref}	$ML^{-1}T^2$	kPa	Reference stress = 100 kpa - Eq. (8.21)
σ'_{vo}	$ML^{-1}T^{-2}$	kPa	Vertical (effective) overburden stress - Eq. (8.2)
τ_f	$ML^{-1}T^2$	kPa	Undrained shear strength - Eq. (8.34)

8.2 COMPONENTS OF SETTLEMENT

When a soil deposit is loaded—for example, by a structure or a man-made fill—deformations occur. The total vertical deformation at the surface resulting from the load is called *settlement*. The movement may be downward with an increase in load or upward (called *swelling*) with a decrease in load. Temporary construction excavations and permanent excavations such as highway cuts will cause a reduction in the stress, and swelling may result. As shown in Chapter 6, a lowering of the water table will also cause an increase in the effective stresses within the soil, which will lead to settlements. Another important aspect about settlements, especially in fine-grained soils, is that they are often time dependent.

In the design of foundations for engineering structures, we are interested in how much settlement will occur and how fast it will occur. Excessive settlement may cause structural as well as other damage, especially if such settlement occurs rapidly. The total settlement, s_t, of a loaded soil has three components, or

$$s_t = s_i + s_c + s_s \tag{8.1}$$

where s_i = the *immediate* settlement,
s_c = the consolidation (time-dependent) settlement, and
s_s = the secondary compression (also time-dependent).

The immediate settlement, although not actually elastic, is usually estimated by using elastic theory in clay soils. The equations for this component of settlement are in principle similar to those for the deformation of a column under an axial load P, where the deformation is equal to PL/AE. In most foundations, however, the loading is usually three dimensional, causing some distortion of the foundation soils, which is why this is sometimes called the *distortion* settlement.

Most settlements that occur in coarse-grained soils are immediate. The reason is that these soils typically have such a high permeability that any water or air that needs to escape in order for the soil to compress can do so very rapidly. Distortion settlement can be appreciable in certain fine-grained soils even though no compression is occurring—the permeability is too low for water to escape quickly and allow the soil to compress. Immediate settlements must be considered in the design of shallow foundations, especially for structures that are sensitive to rapid settlements. A brief introduction to estimating the immediate settlement of shallow foundations on clay soils is given in Sec. 10.4.

The consolidation settlement is a time-dependent process that occurs in saturated fine-grained soils that have a low coefficient of permeability. The rate of settlement depends on the rate of pore water drainage. Secondary compression, which is also time dependent, occurs at constant effective stress and with no subsequent changes in pore water pressure. Compressibility of geo-materials is discussed in this chapter, while the time rate of consolidation and secondary compression are discussed in Chapter 9. We show you how to make settlement computations in Chapter 10.

8.3 COMPRESSIBILITY OF SOILS

Assume for the time being that the deformations of our compressible soil layer will occur in only one dimension. An example would be the deformation caused by an earthfill covering a very large area. Later on we shall discuss what happens when a structure of finite size loads the soil and produces deformation.

When a soil is loaded, it will compress because of:

1. deformation of soil grains,
2. compression of air and water in the voids, and/or
3. squeezing out of water and air from the voids.

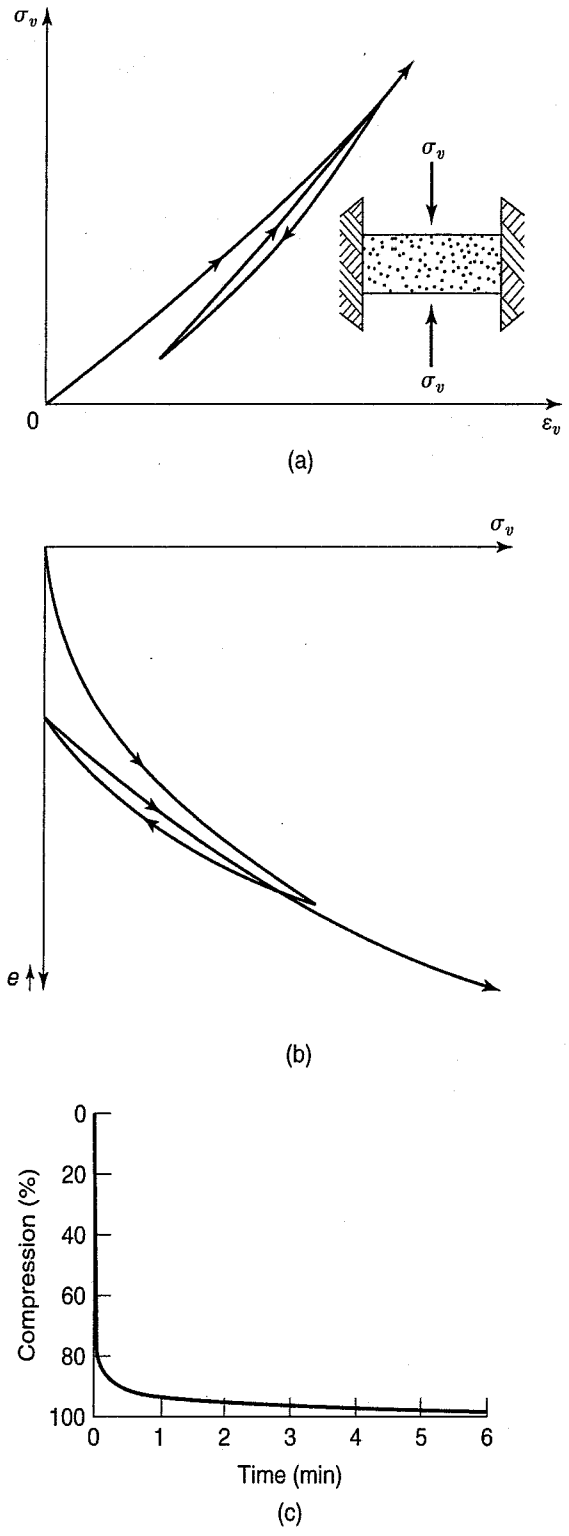

FIGURE 8.1 Stress-strain and stress-time curves for a typical sand: (a) stress versus strain; (b) void ratio versus pressure; (c) compression versus time (after Taylor, 1948).

At typical engineering loads, the amount of compression of the soil mineral grains themselves is small and usually can be neglected. Often, compressible soils are found below the water table, and they can be considered fully saturated (at least we usually assume 100% saturation for most settlement problems). Thus the compression of the pore fluid can be neglected. Therefore, the last item contributes the most to the volume change of loaded soil deposits. As the pore fluid is squeezed out, the soil grains rearrange themselves into a more stable and denser configuration, and a decrease in volume and surface settlement results. How fast this process occurs depends primarily on the permeability of the soil. How much rearrangement and compression takes place depends on the rigidity of the soil skeleton, which is a function of the structure of the soil. Soil structure, as discussed in Chapter 4, depends on the geologic and engineering history of the deposit.

Consider the case where granular materials are one-dimensionally compressed. The curve shown in Fig. 8.1(a) is typical for sands in compression in terms of stress-strain; Fig. 8.1(b) shows the same data as a void-ratio-versus-pressure curve. Note that it is common to rotate the coordinate axes 90° when plotting e versus σ_v data. Figure 8.1(c) shows the compression versus time; note how rapidly compression occurs. The deformations take place in a very short time due to the relatively high permeability of granular soils. It is very easy for the water (and air) in the voids to squeeze out. Many times, for all practical purposes, the compression of sands occurs during construction and, as a result, most of the settlements have taken place by the time the structure is completed. However, because they occur so fast, even the relatively small total settlements of granular layers may be detrimental to a structure which is particularly sensitive to rapid settlements. The settlement of granular soils is estimated by using Eq. (8.1) with s_c and s_s neglected. Details of these analyses can be found in books on foundation engineering.

When clays undergo loading, because of their relatively low permeability, their compression is controlled by the rate at which water is squeezed out of the pores. This process, called *consolidation*, is a stress-strain-time phenomenon. Deformation may continue for months, years, or even decades. This is the fundamental and only difference between the compression of granular materials and the consolidation of cohesive soil: compression of sands occurs almost instantly, whereas

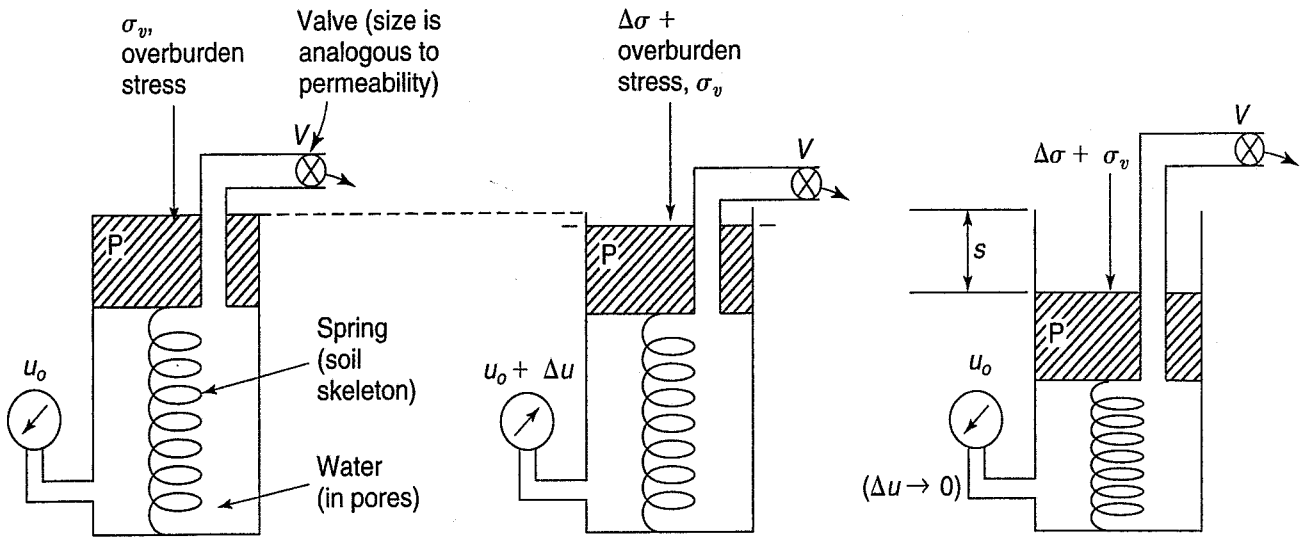

FIGURE 8.2 Spring analogy as applied to consolidation.

consolidation is a very time-dependent process. The difference in settlement rates depends on the difference in permeabilities.

The consolidation of clay is readily explained by the *spring analogy* shown in Fig. 8.2. A piston P is loaded by a vertical stress (σ_v) and compresses a spring inside the chamber, which is filled with water. The spring is analogous to the soil mineral skeleton, while the water in the cylinder represents the water in the soil voids. The valve V at the top of the piston represents the soil permeability. At equilibrium, when the valve is open, no water flows out because the spring is supporting the stress completely. This is analogous to the situation where a soil layer is at equilibrium with the weight of all soil layers (called *overburden*) above it. A pressure gage is connected to the cylinder, and it shows the hydrostatic pressure u_o at this particular location in the soil. Now the soil layer is loaded by an additional stress increment, $\Delta\sigma$, Fig. 8.2(b). At the start of the consolidation process, let us assume that the valve V is initially closed. Upon application of the stress, the pressure is immediately transferred to the water inside the cylinder. Since the water is relatively incompressible and the valve is closed so that no water can get out, there is no deformation of the piston, and the pressure gage reads $u_o + \Delta u$, where $\Delta u = \Delta\sigma$, the additional stress added [Fig. 8.2(b)]. The pore water pressure Δu is called the *excess pore water pressure*, since it is in excess of the original hydrostatic pressure u_o.

To simulate a fine-grained cohesive soil with its low permeability, we can open the valve and allow water to slowly leave the cylinder under the initial excess pressure Δu. With time, as water flows out, the water pressure decreases and gradually the stress $\Delta\sigma$ is transferred to the spring, which compresses under that stress. Finally, at equilibrium [Fig. 8.2(c)] no further water is squeezed out of the cylinder, the pore water pressure is again hydrostatic, and the spring is in equilibrium with the overburden and applied stress, $\sigma_v + \Delta\sigma$.

Although the model is rather crude, the process is analogous to what happens when cohesive soils in the field and laboratory are loaded. Initially, all of the external stress is transferred into excess pore water pressure. Thus, at first there is no change in the effective stress in the soil, since the additional total stress is exactly equal to the amount of additional pore pressure [Eq. (6.8)]. Gradually, as the water is squeezed out under a pressure gradient, the soil skeleton compresses and the effective stresses increase. The compressibility of the spring is analogous to the compressibility of the soil skeleton. Eventually the excess pore pressure becomes zero, and the pore water pressure is the same as the hydrostatic pressure prior to loading.

8.4 ONE-DIMENSIONAL CONSOLIDATION TESTING

When soil layers covering a large area are loaded vertically, the compression can be assumed to be one-dimensional. To simulate one-dimensional compression in the laboratory, we compress the soil in a special device called a *consolidometer* (sometimes confusingly referred to as an *oedometer*). Principal components of two types of consolidometers are shown in Fig. 8.3.

An undisturbed soil specimen, which represents an element of the compressible soil layer under investigation, is carefully trimmed and placed into the confining ring. The ring is relatively rigid so that no lateral deformation takes place. On the top and bottom of the specimen are porous "stones" which allow drainage during the consolidation process. These stones are actually discs made of sintered corundum or brass that is very porous. Ordinarily, the top porous stone has a diameter approximately 0.5 mm smaller than the ring, so that it does not drag along the side of the ring when the specimen is being loaded. Usually the ratio of the diameter to height of the specimen is between 2.5 and 5, and the diameter depends on the diameter of the undisturbed soil samples tested. There is more trimming disturbance with thinner and to a lesser extent smaller-diameter specimens; on the other hand, taller specimens have greater side friction. Side friction can be reduced to some extent by the use of ceramic or Teflon-lined rings or by application of a lubricant such as molybdenum disulphide.

In the *floating-ring test* [Fig. 8.3(a)] the compression takes place from both faces of the soil specimen. It can be shown (Lambe, 1951) that the ring friction is somewhat less in this test in a *fixed-ring test* [Fig. 8.3(b)], in which all movement is downward relative to the ring. The primary advantage of the fixed-ring test is that drainage from the bottom porous stone may be measured or otherwise controlled. In this manner, for example, permeability tests may be conducted in the consolidometer.

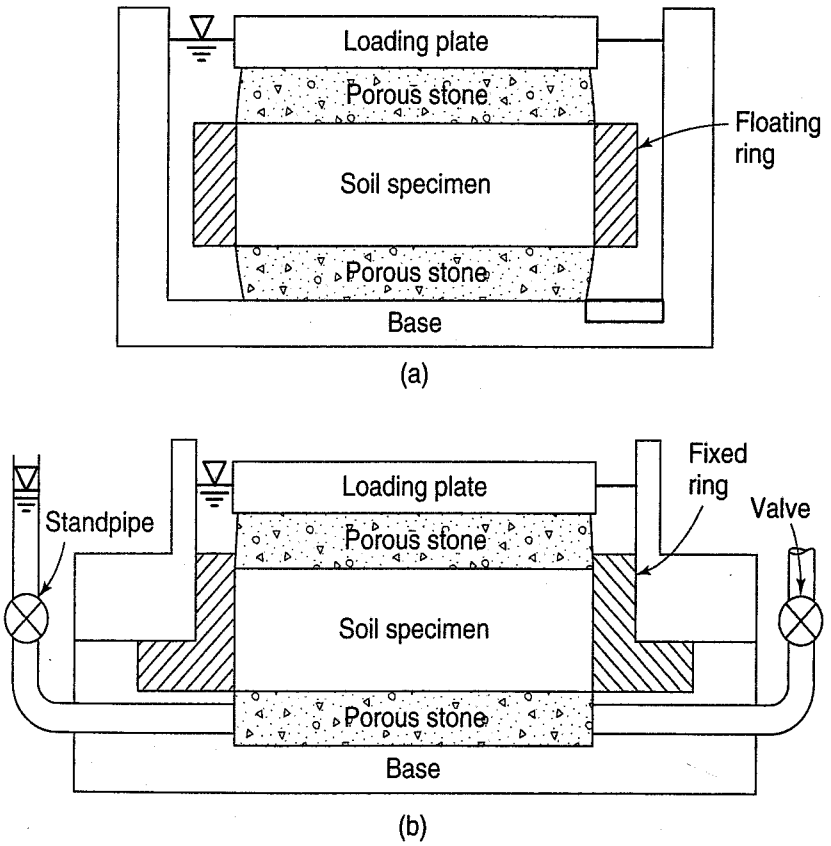

FIGURE 8.3 Schematic cross-section of the consolidation test apparatus, or a consolidometer: (a) floating-ring consolidometer; (b) fixed-ring consolidometer (after U.S. Army Corps of Engineers, 1986).

During the consolidation test, to establish the relationship between load and deformation for the soil being tested, the applied load and specimen deformation are carefully measured. Stress is, of course, computed by dividing the applied load by the area of the specimen. It is common practice in North America to load the specimen incrementally, either through a mechanical lever-arm system or by an air or air-hydraulic pressure cylinder. This test is called an *incremental load consolidation test*, and the standard procedure is ASTM (2010) D 2435. After each stress increment is applied, the specimen is allowed to consolidate and come to equilibrium with little or no further deformation and with the *excess* pore water pressure within the specimen approximately equal to zero. Thus the final or equilibrium stress is an *effective stress*. The process is repeated, usually by doubling the previously applied increment, until sufficient points are obtained to adequately define the stress-deformation curve.

The *constant rate of strain consolidometer* can also be used to determine consolidation properties (ASTM, 2010, D 4186; Gorman et al., 1978). In this device, the specimen is loaded continuously at a constant rate of deformation or strain, and drainage is typically allowed only at the top of the specimen. As a result, excess pore pressure exists at the base and gradually diminishes to zero at the top surface. The rate of deformation is controlled so that the pore pressure at the base is between 3% and 15% of the applied load at the end of loading. The load, deformation, and base excess pore pressure are measured, and analytical methods exist (Smith and Wahls, 1969; Wissa et al., 1971) to interpret the results. However, this test has certain limitations in the type of data that can be extracted. We will focus on the incrementally loaded test.

The object of the consolidation test is to simulate the compression of the soil under given external loads. What we are in fact measuring is the modulus of the soil in confined compression [Fig. 8.1(a)]. By evaluating the compression characteristics of an *undisturbed representative* sample, we can predict the settlement of the soil layer in the field.

Engineers use several methods to present stress-deformation data. Two methods are shown in Fig. 8.4. In the first, *percent consolidation* or *vertical strain* is plotted versus the equilibrium or *effective consolidation stress* σ'_{vc}. (The subscripts *vc* refer to vertical consolidation, and the prime mark indicates

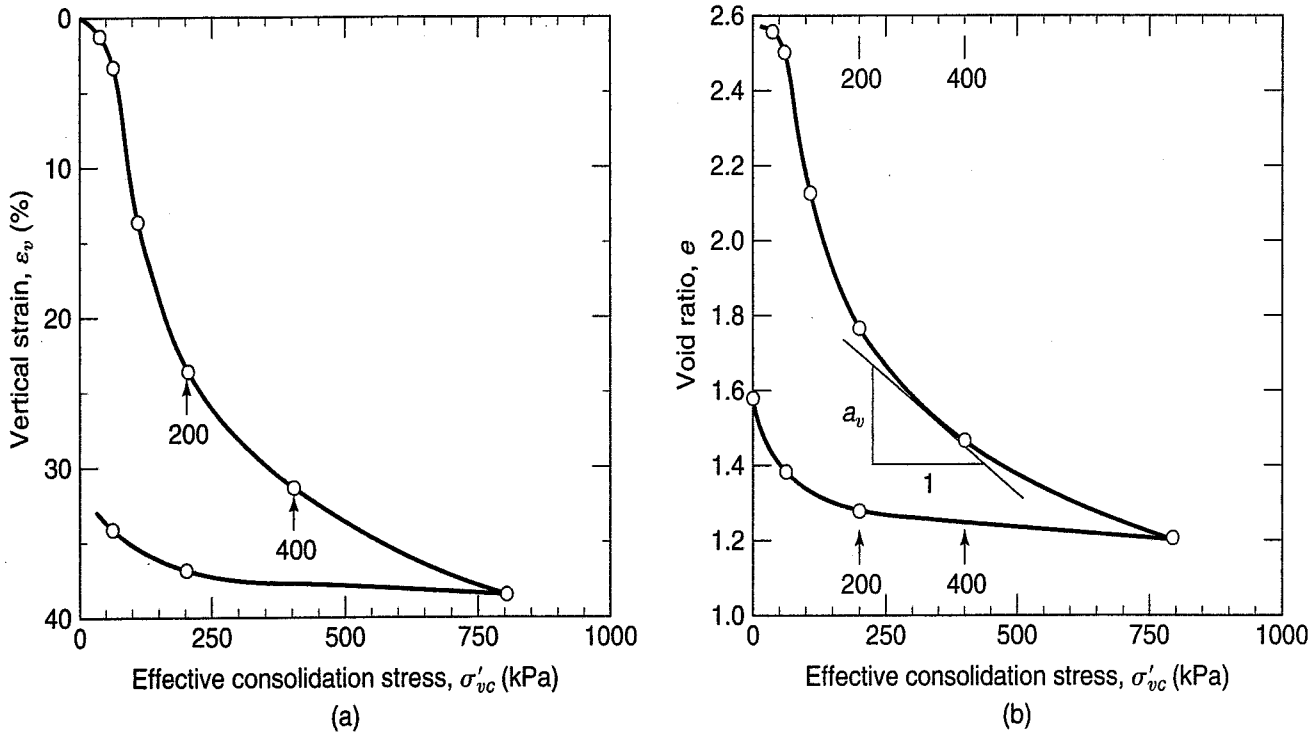

FIGURE 8.4 Two ways to present consolidation test data: (a) percent consolidation (or strain) versus effective stress; (b) void ratio versus effective stress. Test on a specimen of San Francisco Bay mud from −7.3 m.

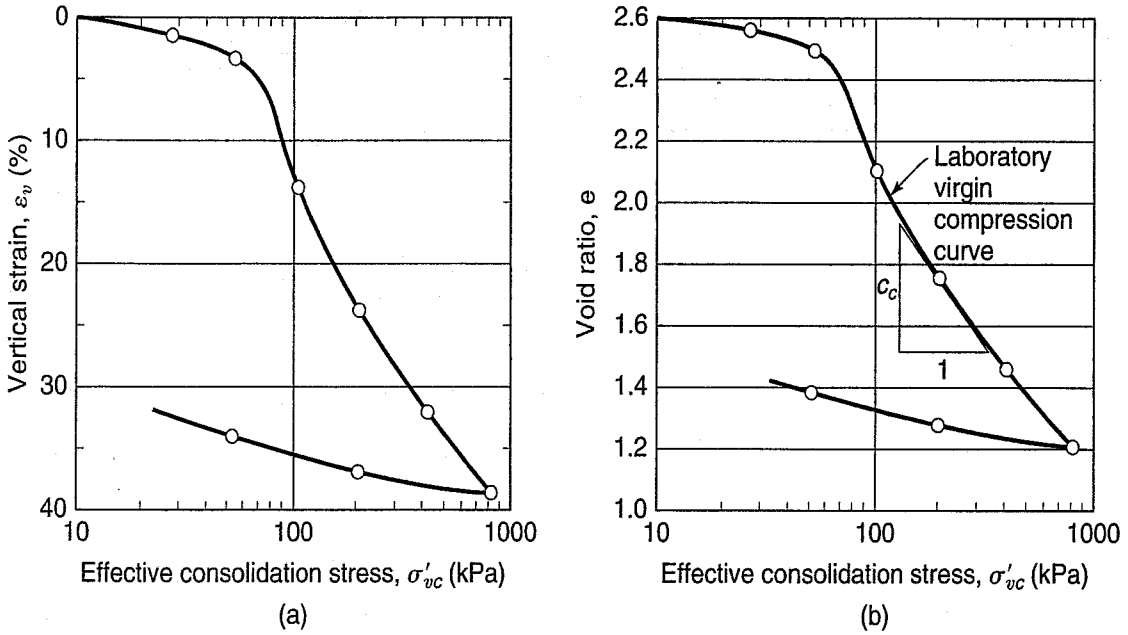

FIGURE 8.5 Consolidation test data presented as: (a) percent consolidation (or strain) versus log effective stress; (b) void ratio versus log effective stress (same data as in Fig. 8.4).

effective stress.) A second way to present stress-deformation data is to relate the *void ratio* to the *effective consolidation stress*. Both of these graphs show that soil is a strain hardening material; that is, the (instantaneous) modulus increases as the stresses increase.

Since the stress-strain relationships shown in Fig. 8.4 are highly nonlinear, more common ways to present the results of a consolidation test are shown in Fig. 8.5. The data shown in Fig. 8.4 are now presented as percent consolidation (or vertical strain) and void ratio versus the *logarithm* (base 10) of effective consolidation stress. It can be seen that both plots have two approximately straight line portions connected by a smooth transitional curve. The stress at which the transition or "break" occurs in the curves shown in Fig. 8.5 is an indication of the *maximum* vertical overburden stress that this particular sample has sustained in the past; this stress, which is very important in geotechnical engineering, is known as the *preconsolidation pressure*, σ'_p. Sometimes the symbol p'_c or σ'_{vm} is used, where the subscript m indicates maximum past pressure. The σ'_p in soils is analogous to the yield stress in metals.

8.5 PRECONSOLIDATION PRESSURE AND STRESS HISTORY

We have mentioned that soils have a "memory," so to speak, of the stress and other changes that have occurred since they were deposited. These changes are part of the soil's stress history and they are preserved in its structure (Casagrande, 1932c). When a laboratory specimen or a soil deposit in the field is loaded to a stress level greater than it has ever experienced in the past, the soil structure is no longer able to sustain the increased load and it starts to break down. Depending on the type of soil and its geologic history, this breakdown may result in quite a drastic difference in the slopes of the two portions of the consolidation curve. In other words, the transition region may be small, and such soils are often very sensitive to even small changes in the applied stresses. With other less sensitive soils, such as silty soils, there never really is a "break" in the curve, because the fabric gradually alters and adjusts as the applied stress increases. The initial, flatter portion of the void ratio-log pressure consolidation curve is termed the *reconsolidation* portion, and the part after the change in slope is called the *virgin compression* portion [Fig. 8.5(b)]. As the latter name implies, the soil has never before experienced a stress greater than the preconsolidation stress or pressure.

8.5.1 Normal Consolidation, Overconsolidation, and Preconsolidation Pressure

We say that a soil is *normally consolidated* when the preconsolidation pressure σ'_p just equals the currently existing effective vertical overburden pressure σ'_{vo} (that is, $\sigma'_p = \sigma'_{vo}$). If we have a soil whose preconsolidation pressure is *greater* than the existing overburden pressure (that is, $\sigma'_p > \sigma'_{vo}$), then we say the soil is *overconsolidated* (or *preconsolidated*). We can define the *overconsolidation ratio*, OCR, as the ratio of the preconsolidation stress to the existing vertical effective overburden stress, or

$$\text{OCR} = \frac{\sigma'_p}{\sigma'_{vo}} \tag{8.2}$$

Soils that are normally consolidated have an OCR = 1, and soils with an OCR > 1 are overconsolidated. It is also possible to find a soil that has an OCR < 1, in which case the soil would be *underconsolidated*. Underconsolidation can occur, for example, in soils that have only recently been deposited, either geologically or by human activity, and are still consolidating under their own weight. For example, geologically recent submarine landslides, mine tailings, and sludge ponds are often underconsolidated. If the pore water pressure were measured under conditions of underconsolidation, the pressure would be in excess of hydrostatic.

There are many reasons why a soil may be overconsolidated. The cause could be either a change in the total stress or a change in pore water pressure; both changes would alter the effective stress. Geologic deposition followed by subsequent erosion is an example of a change in the total stress that will preconsolidate the underlying soils. Desiccation of the upper layers due to surface drying will also produce overconsolidation. Sometimes an increase in σ'_p occurs due to changes in the soil structure and alterations of the chemical environment of the soil deposit. Table 8.1 lists some of the mechanisms leading to preconsolidation of soils (see also Holtz, 1991).

8.5.2 Determining the Preconsolidation Pressure

How is the preconsolidation pressure determined? Several procedures have been proposed to determine the value of σ'_p. The most popular is the Casagrande (1936b) construction, illustrated in Fig. 8.6, where a typical void-ratio-versus-log-pressure curve is plotted for a clay soil. The procedure is also applicable to ε_v-versus-log-σ'_{vc} curves. The Casagrande procedure is as follows:

1. Choose by eye the point of minimum radius (or maximum curvature) on the consolidation curve (point A in Fig. 8.6).
2. Draw a horizontal line from point A.
3. Draw a line tangent to the curve at point A.
4. Bisect the angle made by steps 2 and 3.
5. Extend the straight-line portion of the *virgin* compression curve up to where it meets the bisector line obtained in step 4. The point of intersection of these two lines is the preconsolidation stress (point B of Fig. 8.6).

An even simpler method for estimating the preconsolidation stress is used by some engineers. The two straight-line portions of the consolidation curve are extended; their intersection defines another "most probable" preconsolidation pressure (point C of Fig. 8.6). If you think about it, the maximum possible σ'_p is at point D, the minimum possible σ'_p is at point E, the intersection of the virgin compression curve with a horizontal line drawn from e_o.

Sällfors (1975) provides an alternative method to evaluate the preconsolidation pressure. It is graphical like Casagrande's and has field evidence to back it up. The procedure uses the void ratio-linear

TABLE 8.1 Mechanisms Causing Preconsolidation

Mechanism	Remarks and References
Change in total stress due to:	
Removal of overburden	Geologic erosion or excavation by man
Past structures	
Glaciation	
Change in pore water pressure due to:	
Change in water table elevation	Kenney (1964) gives sea level changes
Artesian pressures	Common in glaciated areas
Deep pumping; flow into tunnels	Common in many cities
Desiccation due to surface drying	May have occurred during deposition
Desiccation due to plant life	May have occurred during deposition
Change in soil structure due to:	
Secondary compression (aging)[a]	Raju (1956) Leonards and Ramiah (1959) Leonards and Altschaeffl (1964) Bjerrum (1967, 1972)
Environmental changes such as pH, temperature, and salt concentration	Lambe (1958a and b)
Chemical alterations due to weathering, precipitation, cementing agents, ion exchange	Bjerrum (1967)
Change of strain rate on loading[b]	Lowe (1974)

[a]The magnitude of σ'_p/σ'_{vc} related to secondary compression for mature natural deposits of highly plastic clays may reach values of 1.9 or higher.
[b]Further research is needed to determine whether this mechanism should take the place of secondary compression.
After Brumund, Jonas and Ladd (1976).

or arithmetic pressure curve [like Fig. 8.5(a), although it appears that the early load increments are too high to effectively establish the preconsolidation pressure]. Follow these steps to find σ'_p using Fig. 8.7:

1. Extend the straight-line portions of the e–log σ'_v curve at the break in the curve (around the preconsolidation pressure), as lines 1 and 2.
2. Place a line *tangent* to the data curve and adjust it until you make an isosceles triangle with its two sides of length x. (See below.)
3. Extend the left side of the tangent line until it intersects with the top data line, line 1. The preconsolidation pressure is equal to the pressure at this intersection point.

Butterfield (1979) advocated plotting the natural logarithm of $(1 + e)$ versus log σ'_v, with the σ'_p defined at the intersection of the straight-line extensions of the recompression and virgin compression lines. Becker et al. (1987) plotted the *strain energy* or "work" done to compress the soil during consolidation and plotted this cumulative work (W) versus log σ'_v. The break in the W–log σ'_v curve defines the preconsolidation pressure. For additional information on this method and several others, see Holtz (1991).

Hansbo (1994) points out that using the e-log σ'_v curves may give a σ'_p that may not actually exist, even though there is a change in slope of the consolidation curve. The logarithmic scale chosen also determines the value of σ'_p. Therefore, one should check to see if a preconsolidation pressure exists by redrawing the data on a void ratio (or percent strain) versus (arithmetic) pressure curve. The tangent modulus method described in Sec. 8.8 also can be used to estimate the preconsolidation pressure, as can a method by Schmertmann (1955) described in Sec. 8.10.

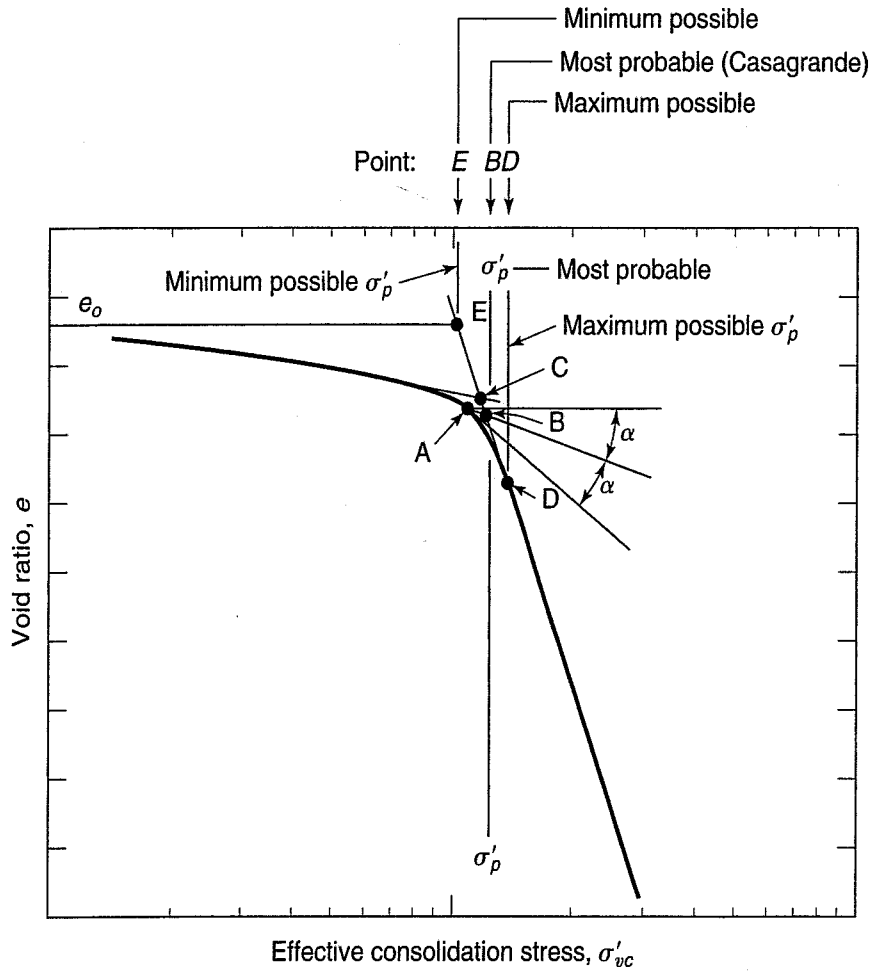

FIGURE 8.6 The Casagrande (1936b) construction for determining the preconsolidation stress. Also shown are the minimum possible, the most probable, and the maximum possible preconsolidation stresses.

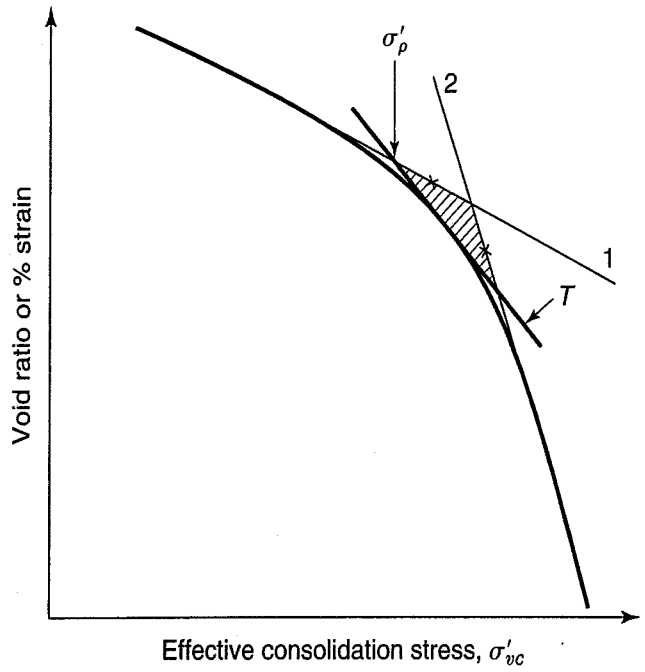

FIGURE 8.7 Determination of the preconsolidation pressure, σ'_p, using void ratio or percent consolidation versus linear effective stress (Sällfors, 1975).

8.5.3 Stress History and Preconsolidation Pressure

How is it possible that the simple graphical procedures described above predict the preconsolidation pressure? To understand the reason, let us follow the complete stress-strain history of a sedimentary clay soil during deposition, sampling, and finally reloading in the laboratory by the consolidation test. This history is shown in Fig. 8.8. The line OA represents the relationship between the void ratio and the logarithm of effective stress of a particular element in the ground during deposition. In this case, additional material is deposited above our element, and the process consolidates the element to point A. This point represents the in situ e versus log σ'_{vc} coordinates of the normally consolidated clay element. When a boring is made to sample the soil, the overburden stresses are removed by the sampling operation, and the sample rebounds or swells along the (dashed) curve AB.

When the soil specimen is transferred from the sampling tube into a consolidometer ring and then reloaded in the consolidation test, the (solid) reloading curve BC is obtained. About point C, the soil structure starts to break down, and if loading continues, the laboratory virgin compression curve CD is obtained. Eventually the field and laboratory curves OAD and BCD will converge beyond point D. If you perform the Casagrande construction on the curve in Fig. 8.8, you will find that the most probable preconsolidation pressure is very close to point A on the graph, which is the actual maximum past pressure. Observations of this sort enabled Casagrande to develop his graphical procedure to find the preconsolidation

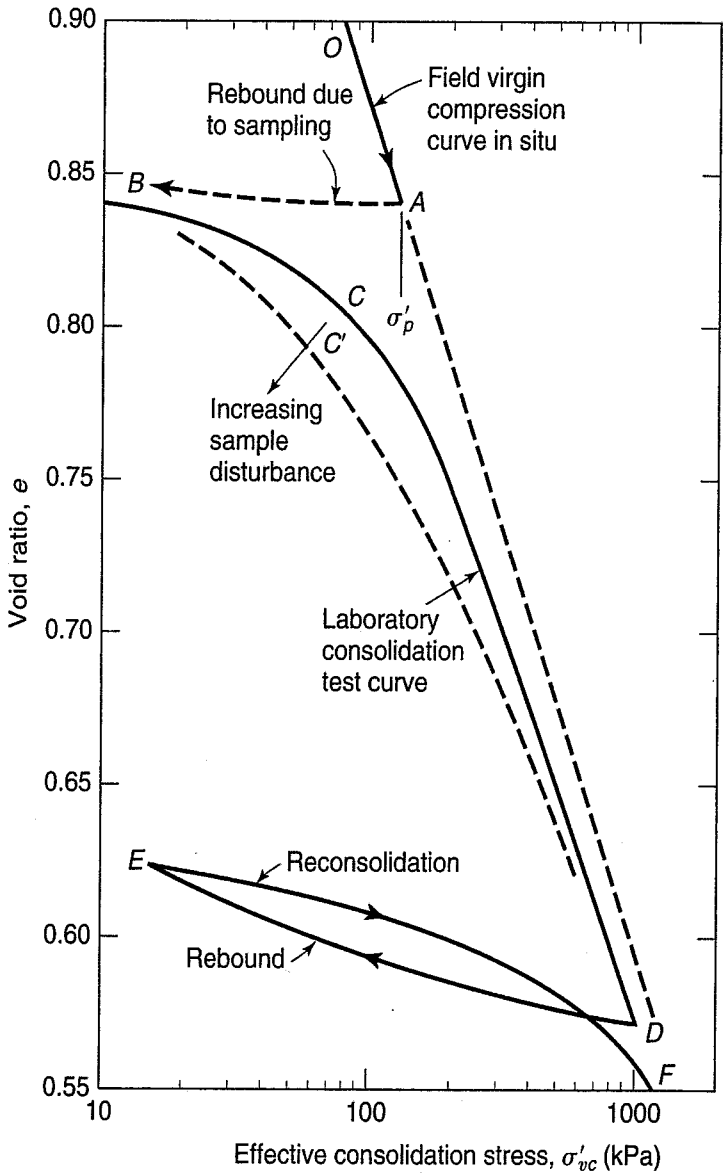

FIGURE 8.8 Void ratio versus log effective consolidation stress curve illustrating deposition, sampling (unloading) and reconsolidation in the consolidation test apparatus.

stress. If the sampling operation was of poor quality and mechanical disturbance to the soil structure occurred, a different curve BC'D (long dashes) would result upon reloading of the sample in the consolidometer. Note that with the "disturbed" curve, the preconsolidation stress has all but disappeared with increasing mechanical disturbance; the reloading curve will move away from point A in the direction of the arrow. The preconsolidation pressure is much more difficult to define, because sample disturbance has altered the soil structure and the "break point" in the consolidation curve becomes more obscure.

In the consolidation test, after the maximum stress is reached, the specimen is rebounded incrementally to essentially zero stress (points D to E of Fig. 8.8). This process allows you to determine the final void ratio, which you need in order to plot the entire e versus log σ'_c curve. Sometimes another reload cycle is applied, like curve E to F of Fig. 8.8. Just as with the initial reconsolidation curve (BCD), this loading curve eventually rejoins the virgin compression curve.

Example 8.1

Given:

The results of the laboratory consolidation test of Fig. 8.8.

Required:

For the laboratory compression curve (BCD), (a) determine the preconsolidation stress using the Casagrande procedure; (b) find both the minimum and maximum possible values of this stress; and (c) determine the OCR if the in situ effective overburden stress is 80 kPa.

Solution:

a. Go through the steps of the Casagrande construction as shown on Fig. 8.6. The σ'_p is about 130 kPa.

b. Assume $e_o = 0.84$. Minimum possible σ'_p is about 90 kPa, and the maximum possible σ'_p is about 200 kPa.

c. Use Eq. (8.2)

$$\text{OCR} = \frac{\sigma'_p}{\sigma'_{vo}} = \frac{130}{80} = 1.6$$

Because of the uncertainties in determining both σ'_p and σ'_{vo}, OCRs are usually given to only one decimal place.

8.6 CONSOLIDATION BEHAVIOR OF NATURAL AND COMPACTED SOILS

Typical consolidation curves for a wide variety of soils are presented in Figs. 8.9(a) through 8.9(j). You should become familiar with the general shapes of these curves, especially around the preconsolidation stress, for the different soil types. Also, study the amount of compression Δe as well as the slopes of the various curves.

The test results in Fig. 8.9(a) are typical of soils from the lower Mississippi River Valley near Baton Rouge, Louisiana. These soils, primarily silts and sand silts with clay strata, are slightly overconsolidated due to wetting and drying cycles during deposition (Kaufman and Sherman, 1964). Figures 8.9(b) and 8.9(c) show test results from heavily overconsolidated clays. Note the very low void ratios for the precompressed glacial till soils from Canada in Fig. 8.9(b) (MacDonald and Sauer, 1970).

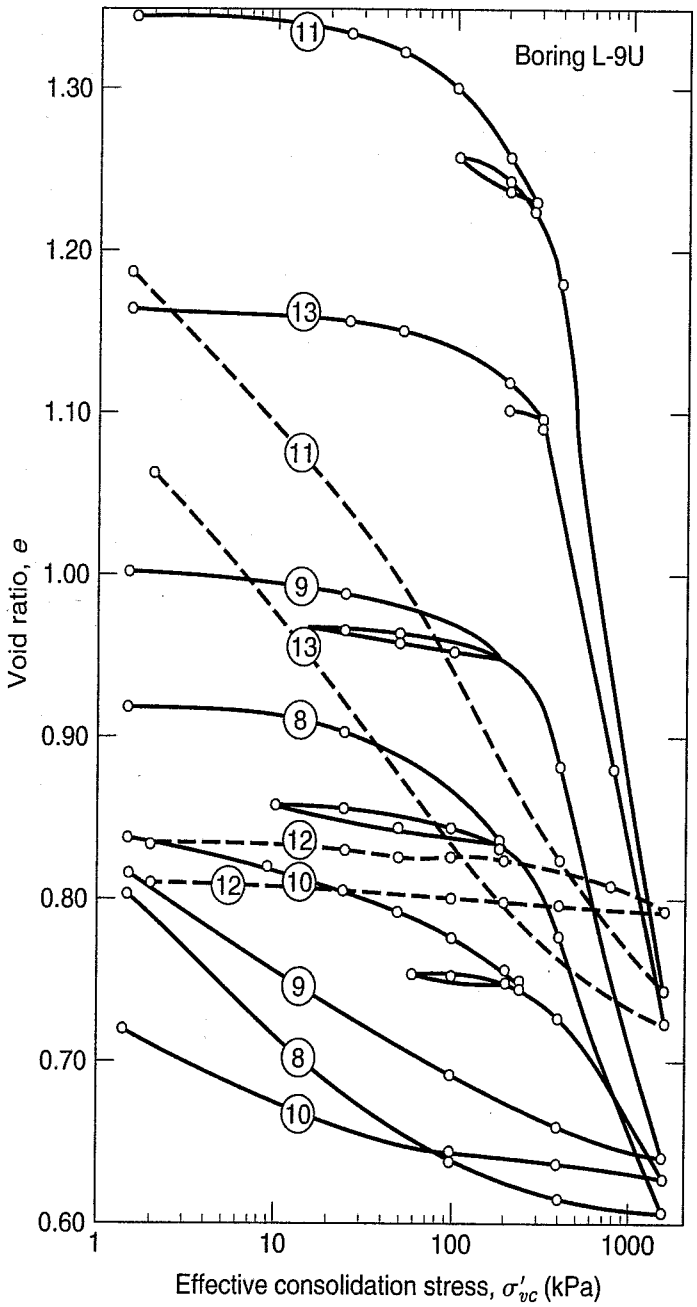

Test No.	Elev. (m)	Classification	Atterberg limits			w_n (%)	e_o	σ'_{vo} (kPa)	σ'_p (kPa)	C_c
			LL	PL	PI					
8	−8.8	CL-clay, soft	41	24	17	34.0	0.94	160	200	0.34
9	−9.8	CL-clay, firm	50	23	27	36.4	1.00	170	250	0.44
10	−17.1	ML-sandy silt	31	25	6	29.8	0.83	230	350	0.16
11	−20.1	CH-clay, soft	81	25	56	50.6	1.35	280	350	0.84
12	−23.2	SP-sand		Nonplastic		27.8	0.83	320	–	–
13	−26.2	CH-clay w/silt strata	71	28	43	43.3	1.17	340	290	0.52

(a)

FIGURE 8.9(a) Nearly normally consolidated clays and silts (after Kaufman and Sherman, 1964).

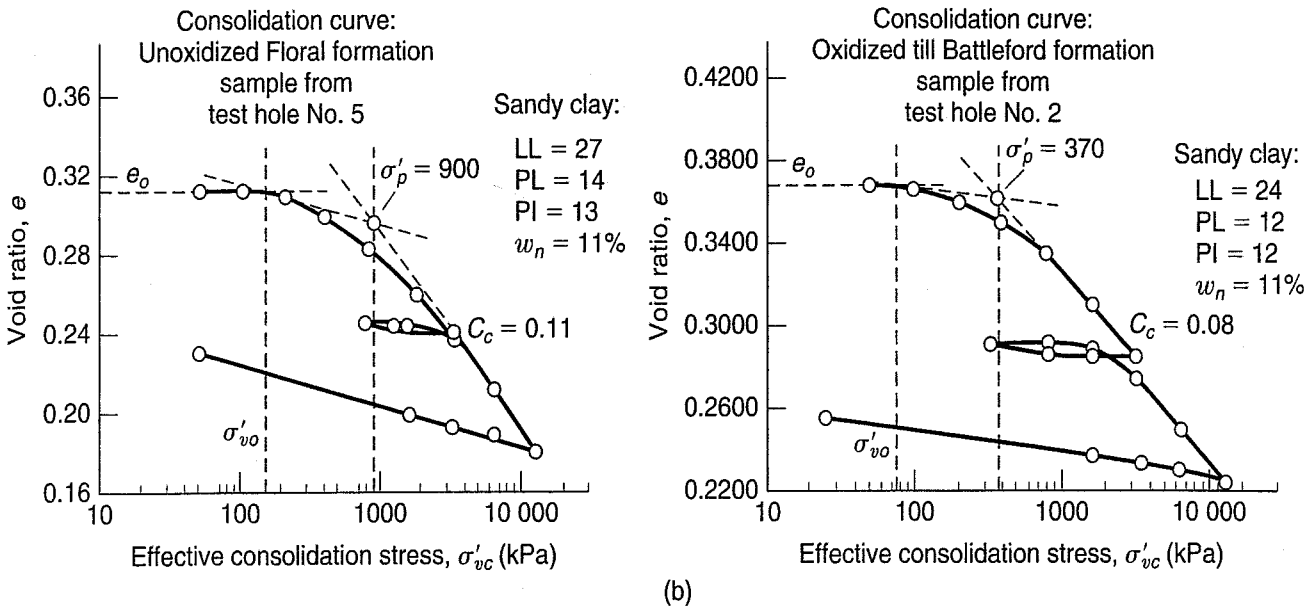

(b)

FIGURE 8.9(b) Overconsolidated clay tills (after MacDonald and Sauer, 1970).

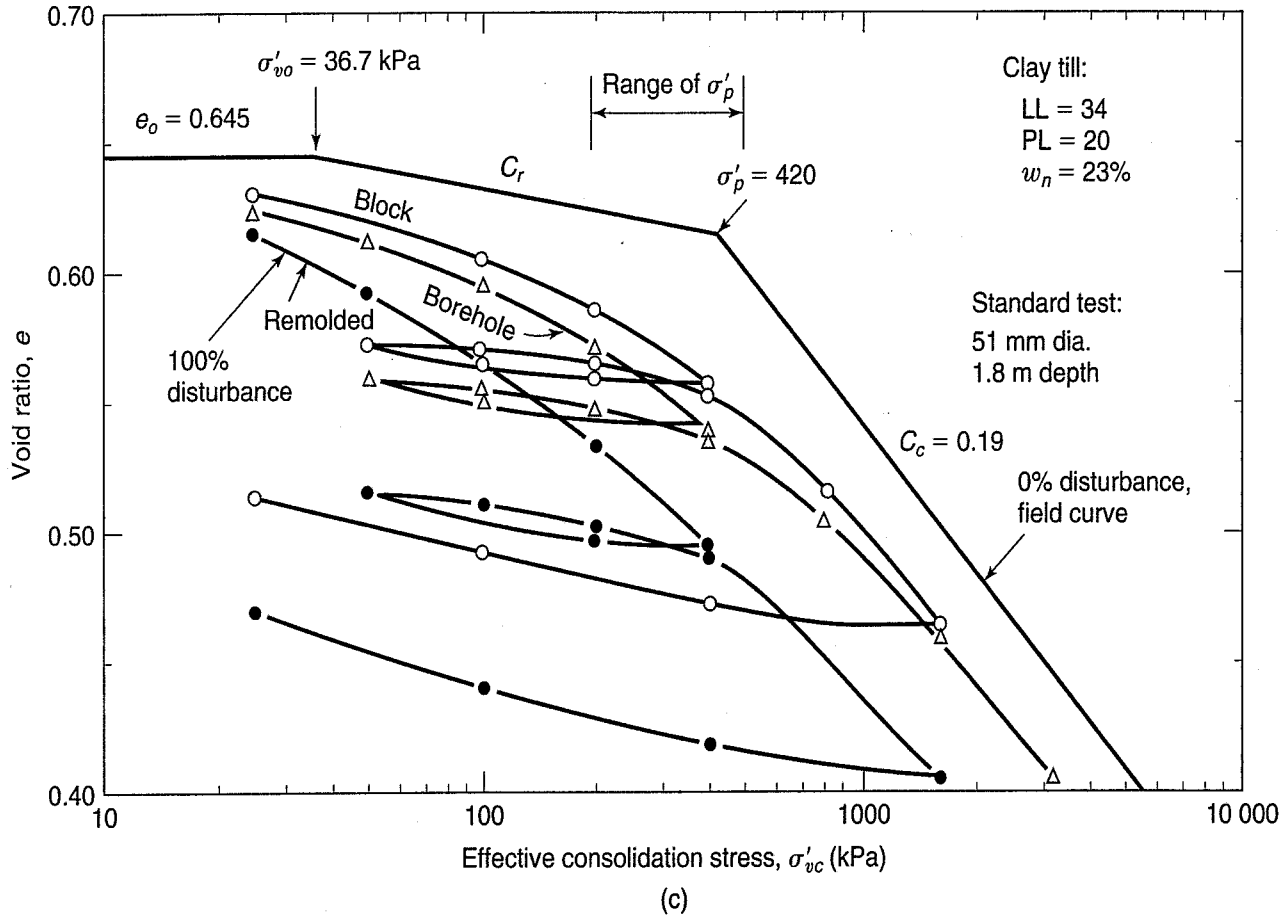

(c)

FIGURE 8.9(c) Overconsolidated clay tills, showing effects of different types of sampling (after Soderman and Kim, 1970).

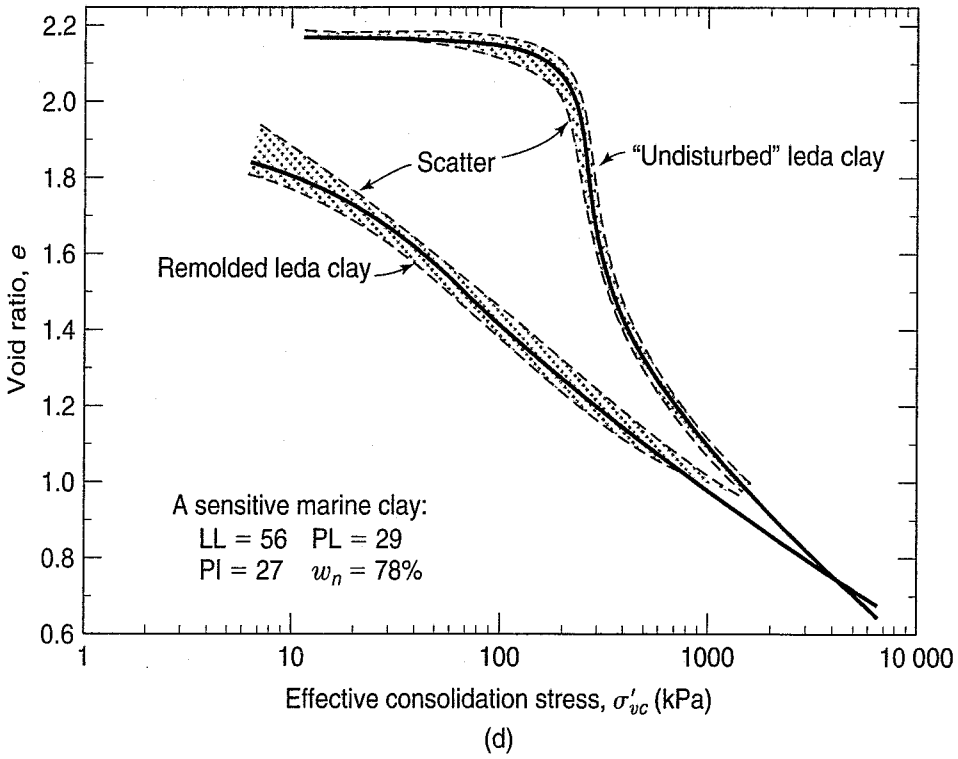

FIGURE 8.9(d) Leda clay (after Quigley and Thompson, 1966).

The effects of sample disturbance on clay tills are shown in Fig. 8.9(c). Note how the consolidation curves move downward and to the left (see Fig. 8.8) as disturbance increases (Soderman and Kim, 1970).

Compression curves for another Canadian clay, a sensitive marine clay called *Laurentian* or *Leda clay*, are shown in Fig. 8.9(d) (Quigley and Thompson, 1966). Both the undisturbed and remolded curves are shown. The very sharp "break" or drop-off in the undisturbed curve at the preconsolidation stress is typical of highly sensitive clays. Until then the compression curve is very flat, but once this "critical" or yield stress is reached, the soil structure breaks down quickly and dramatically.

Figure 8.9(e) shows the consolidation characteristics of Mexico City clay (Rutledge, 1944). This sediment is not a mineral-based clay but is composed primarily of microfossils and diatoms. The porous structure of the fossils gives the soil a very high void ratio, natural water content, and compressibility. Mexico City clay was previously thought to be composed primarily of volcanic ash that weathered to allophane (Chapter 4), since it is appears amorphous in X-rays. Also, see how the compression increases markedly after the preconsolidation stress is reached. As expected, remolding almost completely destroys the preconsolidation effect (see the dashed curve).

Figure 8.9(f) shows the consolidation curves for two typical glacial lake clays (Rutledge, 1944). Both of these clays are rather silty and have much lower in situ void ratios and natural water contents than either the Leda or Mexico City clays.

Highly expansive or swelling clays from the southwest United States have compression curves like those shown in Fig. 8.9(g). Soils in both tests started out at about the same void ratio and water content. Both were initially loaded so that the void ratios remained constant. Then the sample marked (1) was loaded incrementally and continuously in the conventional manner; the other was repeatedly rebounded and reloaded. Notice how much rebound (swell) occurred and also that the cyclic test marked (2) had essentially the same compression characteristics as the conventional test. These variations probably occurred because the samples had a long history of alternate wetting and drying (desiccation) that caused the soils to be heavily overconsolidated (Chapter 6 and Table 8.1).

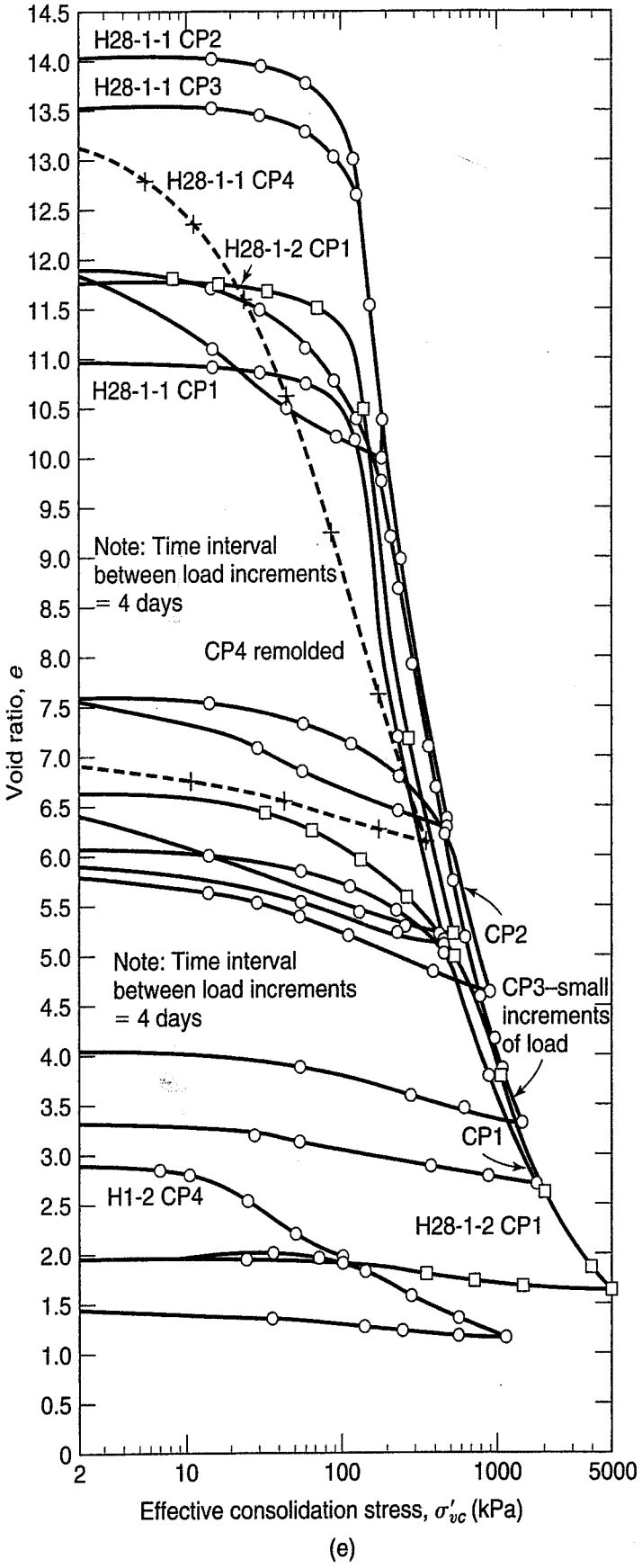

FIGURE 8.9(e) Mexico City clay (after Rutledge, 1944).

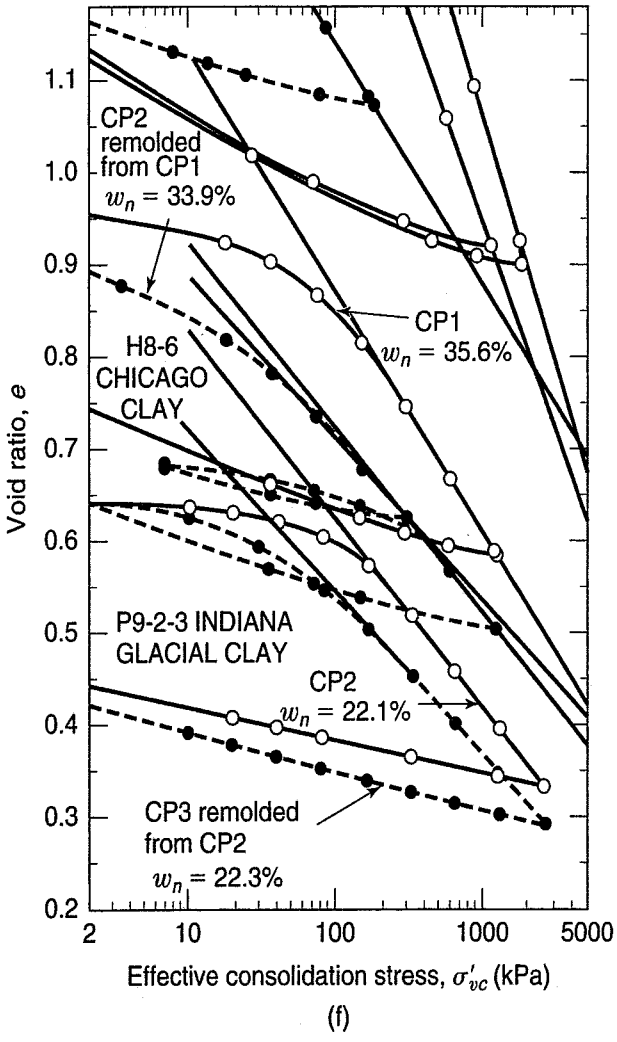

FIGURE 8.9(f) Chicago and Indiana glacial clay (after Rutledge, 1944).

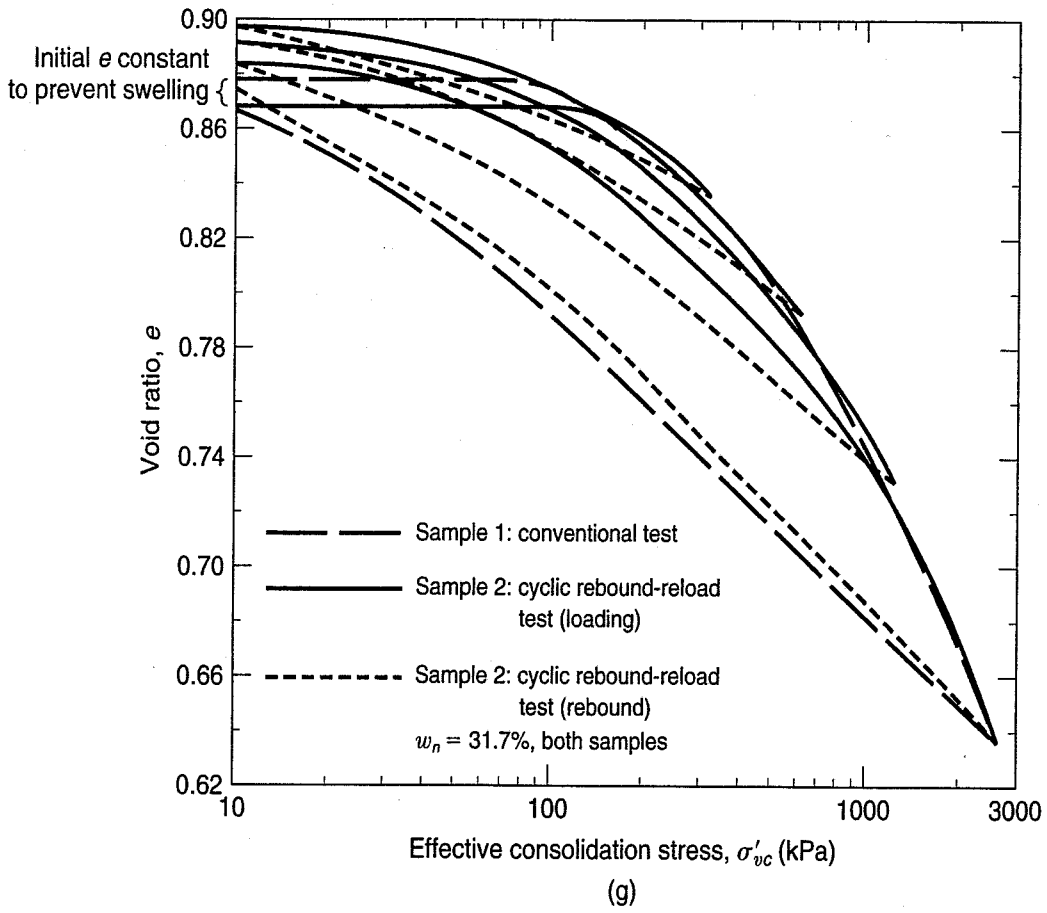

FIGURE 8.9(g) Swelling clays from Texas (after Dawson, 1944).

Consolidation curves for windblown silts (loess) are shown in Fig. 8.9(h). The first figure from Clevenger (1958) shows dry density versus applied load (arithmetic) for an initially low and an initially high density sample. The second figure shows the same data conventionally plotted as an e versus log σ'_{vc} curve. Notice what happens when the samples are prewetted. In its natural state, loess is typically partially saturated, and when it is submerged or inundated, collapse of the soil structure occurs. This condition is shown by the prewetted (dashed) curves of Fig. 8.8(h). The amount of collapse upon wetting depends, as you might expect, on the initial density. Had the water not been added, the consolidation would have followed the upper curve. Sometimes prewetting loessial soils may be desirable to reduce settlements after construction.

Consolidation characteristics of another undisturbed silt are shown in Fig. 8.9(i). Notice the lack of a "break" in the curve; this is typical of silty soils, and it makes determination of the preconsolidation stress difficult in practice.

Besides Mexico City clay, peats and other highly organic soils also have high void ratios and high natural water contents. The very high void ratio and concave upward shape of the compression curve is typical for peat, as shown in Fig. 8.9(j). Just as with silts, determination of the preconsolidation stress is often difficult for such soils.

Compressibility of compacted clays is a function of the stress level imposed on the soil mass. At relatively low stress levels, clays compacted wet of optimum are more compressible. At high stress levels, the opposite is true. In Fig. 8.10 it can be seen that a larger change in void ratio (a decrease) takes place in the soil compacted dry of optimum for a given change (increase) in applied pressure.

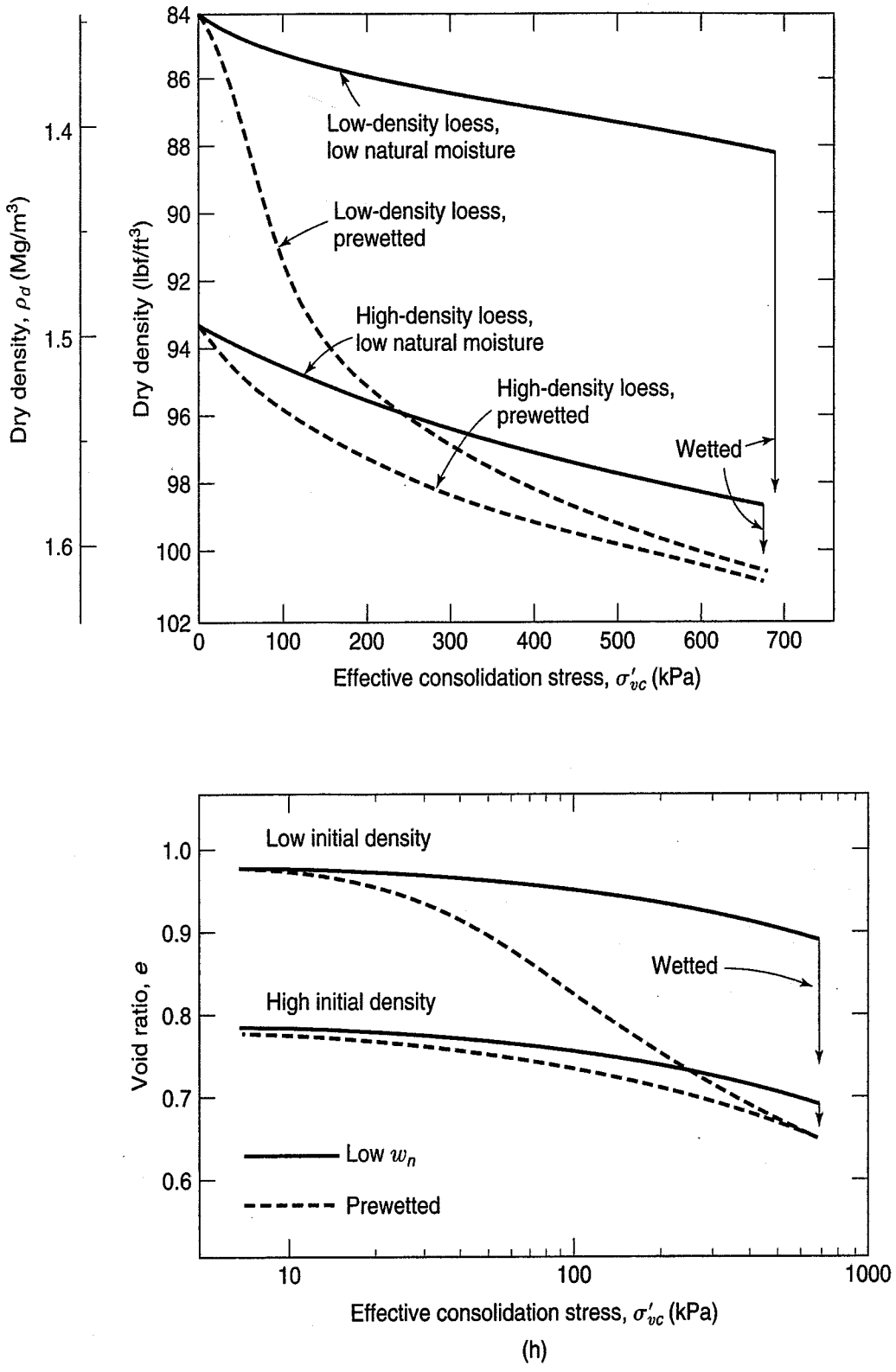

FIGURE 8.9(h) Loessial soils from the Missouri River Basin, showing effect of prewetting on consolidation. Note the drastic reduction in the void ratio when the low natural water content soil is wetted (after Clevenger, 1958).

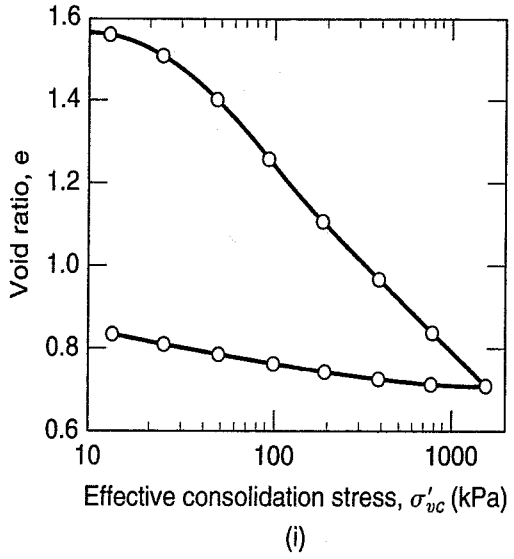

FIGURE 8.9(i) Newfoundland silt (after Taylor, 1948).

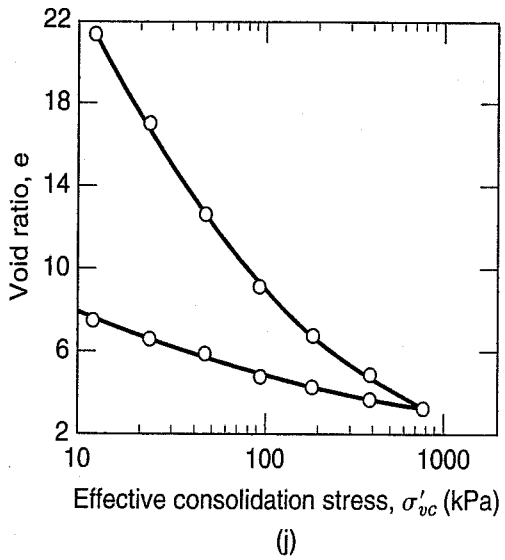

FIGURE 8.9(j) Newfoundland peat (after Taylor, 1948).

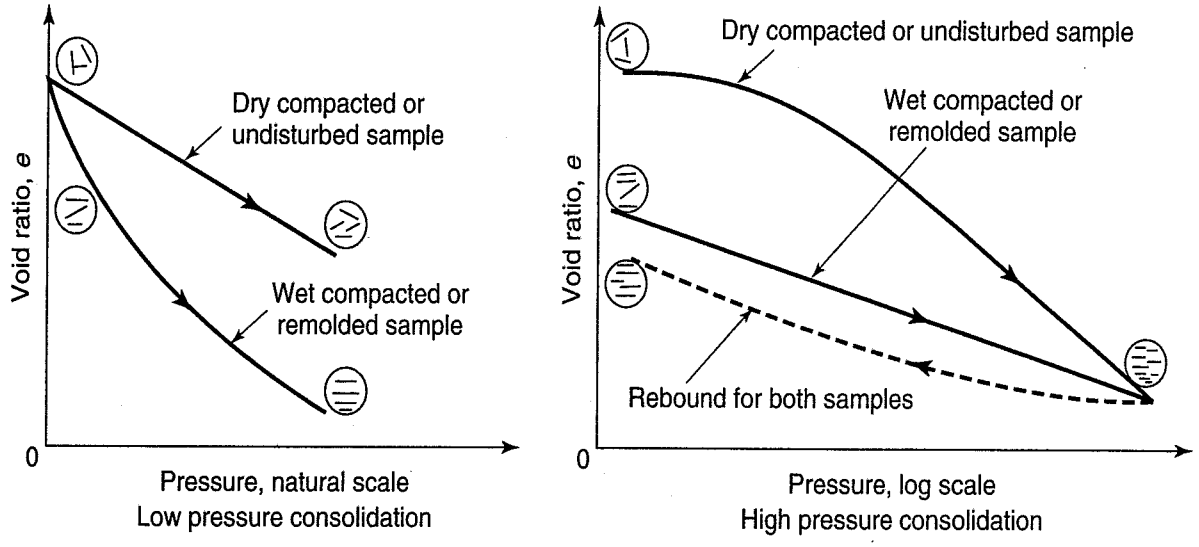

FIGURE 8.10 Change in compressibility with molding water content (after Lambe, 1958b).

8.7 SETTLEMENT CALCULATIONS

How are settlements calculated? Figure 8.11 shows a soil layer of height H that is composed of both solids and voids, as shown in the middle of the figure. From the phase relationships described in Chapter 2, we can assume that the volume of solids V_s is equal to unity, and therefore the volume of voids is equal to e_o, the initial or original void ratio. Finally, upon completion of consolidation, the column of soil would look like that shown at the right side of Fig. 8.11 The volume of solids remains the same, of course, but the void ratio has decreased by the amount Δe. As you know, linear strain is defined as a change in length divided by the original length. Likewise, we may define the vertical strain in a soil layer as the ratio of the change in height to the original height of our soil column. Vertical strain, ε_v, may be related to void ratio by using Fig. 8.11, or

$$\varepsilon_v = \frac{\Delta L}{L_o} \text{ or } \frac{\Delta H}{H_o} = \frac{s}{H_o} = \frac{\Delta e}{1 + e_o} \tag{8.3}$$

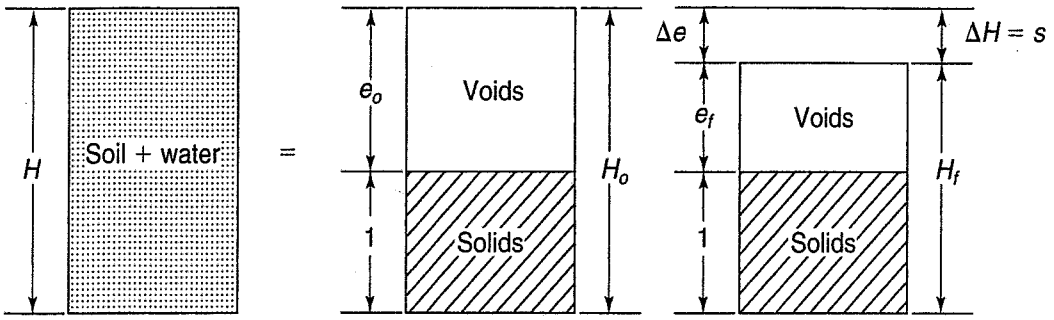

FIGURE 8.11 Calculation of settlement from the phase diagram.

Solving for the settlement s in terms of the void ratio, we obtain:

$$s = \frac{\Delta e}{1 + e_o} H_o = \varepsilon_v H_o \tag{8.4}$$

Note that Eq. (8.4) is based only on phase relationships and applies to all soil types.

Example 8.2

Given:

Prior to placement of a fill covering a large area at a site, the thickness of a compressible soil layer was 10 m. Its original in situ void ratio was 1.0. Some time after the fill was constructed, measurements indicated that the average void ratio was 0.8.

Required:

Estimate the settlement of the soil layer.

Solution: Use Eq. (8.4)

$$s = \frac{\Delta e}{1 + e_o} H_o = \frac{1.0 - 0.8}{1 + 1.0} 10\,\text{m} = 1.0\,\text{m}$$

When we know the relationship between void ratio and effective stress, we can compute the settlement of a compressible layer due to the applied stress. This relationship is, of course, determined from a one-dimensional compression or consolidation test, and we have already shown several ways to display the test results. The slope of the compression curve, when the results are plotted arithmetically, is called the *coefficient of compressibility*, a_v, or

$$a_v = \frac{-de}{d\sigma'_v} \tag{8.5a}$$

Since the curve is not linear [see Figs. 8.1(b) and 8.4(b)], a_v is approximately constant over only a small pressure increment, σ'_1 to σ'_2; or

$$a_v = \frac{-\Delta e}{\Delta \sigma'_v} = \frac{e_1 - e_2}{\sigma'_2 - \sigma'_1} \tag{8.5b}$$

where the void ratios e_1 and e_2 correspond to the respective pressures σ'_1 and σ'_2.

Example 8.3

Given:

The compression curve shown in Fig. 8.4(b).

Required:

Compute the coefficient of compressibility a_v for the stress increment from 200 to 400 kPa.

Solution: From Fig. 8.4(b), we find the void ratios corresponding to these stresses are $e_1 = 1.76$ and $e_2 = 1.47$. Using Eq. (8.5b), we have

$$a_v = \frac{1.47 - 1.76}{400 - 200} = -0.0015 \text{ per kPa}$$

Note that the units of a_v are the *reciprocal* of those for stress, or 1/kPa or m^2/kN; a_v could be reported as 1.5 m^2/N.

When the test results are plotted in terms of the percent consolidation or strain as in Fig. 8.4(a), then the slope of the compression curve is the *coefficient of volume change*, m_v, or

$$m_v = \frac{d\varepsilon_v}{d\sigma'_v} = \frac{\Delta\varepsilon_v}{\Delta\sigma'_v} = \frac{a_v}{1 + e_o} = \frac{1}{D} \tag{8.6}$$

where ε_v is the vertical compression or strain [Eq. (8.3)], and D is the *constrained modulus*. In one-dimensional compression, ε_v is equal to $\Delta e/(1 + e_o)$.

Example 8.4

Given:

The compression curve shown in Fig. 8.4(a).

Required:

a. Compute the coefficient of volume change m_v for the stress increment from 200 to 400 kPa.

b. Determine the constrained modulus D.

Solution:

a. From Fig. 8.4(a), the ε_v corresponding to σ'_v of 200 kPa is 23.7% and the ε_v corresponding to 400 kPa is 31.4%. Use Eq. (8.6)

$$m_v = \frac{0.314 - 0.237}{400 - 200} = 0.0004 \text{ per kPa}$$

As with a_v, the units of m_v are the reciprocal of those for stress.

b. The constrained modulus is the reciprocal of m_v, or

$$D = 2600 \text{ kPa}$$

Example 8.5

Given:

The results of Examples 8.3 and 8.4.

Required:

Show that $m_v = a_v/(1 + e_o)$ for the increment 200 to 400 kPa.

Solution: From Examples 8.3 and 8.4, $a_v = 0.0015$ per kPa and $m_v = 0.0039$ per kPa. From Fig. 8.4(b), $e_o = 2.60$

$$m_v = \frac{a_v}{1 + e_o} = \frac{0.0015}{1 + 2.6} = 0.0004, \text{ or the same as above.}$$

When test results are plotted in terms of the void ratio versus the *logarithm* of effective stress [Fig. 8.5(b)], then the slope of the virgin compression curve is called the *compression index*, C_c, or

$$C_c = \frac{-de}{d \log \sigma_v} = \frac{e_1 - e_2}{\log \sigma_2' - \log \sigma_1'} = \frac{e_1 - e_2}{\log \dfrac{\sigma_2'}{\sigma_1'}} \tag{8.7}$$

Example 8.6

Given:

The consolidation test data of Fig. 8.5(b).

Required:

Determine the compression index of this soil (a) by Eq. (8.7) and (b) graphically.

Solution:

a. The virgin compression curve of Fig. 8.5(b) is approximately linear from 100 to 800 kPa. At least we can determine the average slope between these two points. Therefore from Eq. (8.7) we have

$$C_c = \frac{2.10 - 1.21}{\log \dfrac{800}{100}} = 0.99$$

Note that C_c is dimensionless.

b. To determine the C_c graphically, we note that

$$\log \frac{\sigma_2'}{\sigma_1'} = \log \frac{1000}{100} = \log 10 = 1$$

Therefore if we find the difference in void ratio of the virgin compression curve over *one log cycle*, we automatically have the C_c (because the denominator of Eq. (8.7) is one). If you do this for

the log cycle 100 to 1000 kPa, for example, you find that Δe is slightly less than 1.0 for a line parallel to the average slope between 100 and 800 kPa. Therefore C_c is slightly less than 1.0, which checks the calculation of part **a**.

Example 8.7

Given:

The consolidation test data of Fig. 8.9(a).

Required:

Determine the C_c of tests 9 and 13.

Solution: We can either use Eq. (8.7) or do this graphically. For test 9, using Eq. (8.7),

$$C_c = \frac{0.88 - 0.64}{\log \dfrac{1500}{400}} = 0.42$$

This is close to what Kaufman and Sherman (1964) obtained (0.44), as shown in Fig. 8.9(a). Since the virgin compression curve is not exactly a straight line beyond σ'_p, the value of C_c depends on where you determine the slope.

For test 13, find Δe for the log cycle from 300 to 1000 kPa

$$\Delta e = 1.09 - 0.83 = 0.26; \quad \text{so} \quad C_c = 0.50$$

The slope of the virgin compression curve when the test results are plotted as percent consolidation or vertical strain versus *logarithm* of effective stress [Fig. 8.5(a)] is called the *modified compression index*, $C_{c\varepsilon}$. It is expressed as

$$C_{c\varepsilon} = \frac{\Delta \varepsilon_v}{\log \dfrac{\sigma'_2}{\sigma'_1}} \tag{8.8}$$

Sometimes $C_{c\varepsilon}$ is called the *compression ratio*. The relationship between the modified compression index $C_{c\varepsilon}$ and the compression index C_c is given by

$$C_{c\varepsilon} = \frac{C_c}{1 + e_o} \tag{8.9}$$

Note that there is really nothing "modified" about $C_{c\varepsilon}$; rather the term is used to differentiate it from the compression index, C_c. The term "modified" comes from California soil mechanics practice in the early 1940s.

Example 8.8

Given:

The consolidation data of Fig. 8.5(a).

Required:

Determine the modified compression index of this soil (a) by Eq. (8.8) and (b) graphically. (c) Check the C_c from Example 8.6 by Eq. (8.9).

Solution: Do this problem just like Example 8.6.

a. Consider the virgin compression curve to be approximately a straight line over the stress range 100 to 800 kPa. Thus, using Eq. (8.8), we have

$$C_{c\varepsilon} = \frac{0.38 - 0.14}{\log \dfrac{800}{100}} = 0.27$$

b. To find $C_{c\varepsilon}$ graphically, choose any convenient log cycle; in this case use the cycle 100 to 1000 kPa. Then the $\Delta\varepsilon_v$ for this cycle is 38 − 10 = 28%, or $C_{c\varepsilon}$ = 0.28, which checks part **a** adequately.

c. Assume e_o = 2.60 from Fig. 8.5(b). Use Eq. (8.9). Therefore

$$C_c = C_{c\varepsilon}(1 + e_o) = 0.27(1 + 2.6) = 0.97$$

which is close to the C_c value from Example 8.6.

Example 8.9

Given:

The void ratio versus log effective pressure data shown in Fig. Ex. 8.9.

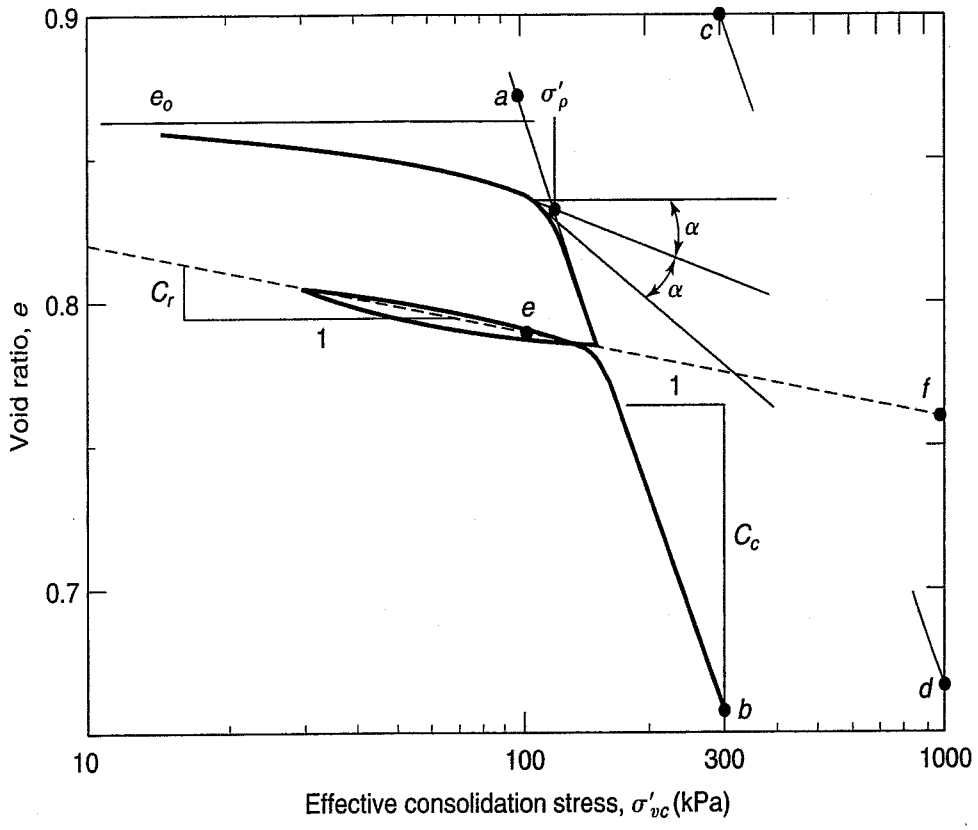

FIGURE Ex. 8.9

Required:

Determine (a) the preconsolidation pressure σ'_p, (b) the compression index C_c, and (c) the modified compression index $C_{c\varepsilon}$.

Solution:

a. Perform the Casagrande construction according to the procedure outlined in Sec. 8.5, and find $\sigma'_p \approx 120$ kPa.

b. By definition [Eq. (8.7)],

$$C_c = \frac{\Delta e}{\log \dfrac{\sigma'_2}{\sigma'_1}}$$

Using the points a and b of Fig. Ex. 8.9, $e_a = 0.87$, $e_b = 0.66$, $\sigma'_a = 100$ kPa, and $\sigma'_b = 300$ kPa. Therefore,

$$C_c = \frac{e_a - e_b}{\log \dfrac{\sigma'_b}{\sigma'_a}} = \frac{0.87 - 0.66}{\log \dfrac{300}{100}} = \frac{0.21}{0.477} = 0.44$$

A second graphical way is to find Δe over *one* cycle; for example,

$$\log \frac{1000}{100} = \log 10 = 1$$

When this is done, $C_c = \Delta e$. In Fig. Ex. 8.9 the vertical scale is not sufficient to extend a slope over $\Delta\sigma' = 1$ log cycle to compute C_c, but it can be done in two steps, e_a to e_b and e_c to e_d. (To extend the line $\overline{e_a e_b}$ to one full log cycle on the *same* graph, choose e_c at the same pressure as e_b. Then draw the line $\overline{e_c e_d}$ parallel to $\overline{e_a e_b}$. This second line is merely the extension of $\overline{e_a e_b}$ if the graph paper extended lower than shown.) Or,

$$\begin{aligned} \Delta e = C_c &= (e_a - e_b) + (e_c - e_d) \\ &= (0.87 - 0.66) + (0.90 - 0.66) \\ &= 0.215 + 0.236 \\ &= 0.45, \text{ or about the same as above} \end{aligned}$$

c. The modified compression index $C_{c\varepsilon}$ is

$$C_{c\varepsilon} = \frac{C_c}{1 + e_o} = \frac{0.45}{1 + 0.87} = 0.24$$

8.7.1 Consolidation Settlement of Normally Consolidated Soils

To calculate consolidation settlement, Eqs. (8.5), (8.6), or (8.7) and (8.8) may be combined with Eq. (8.4). For example, using Eqs. (8.7) and (8.4), we obtain

$$s_c = C_c \frac{H_o}{1 + e_o} \log \frac{\sigma'_2}{\sigma'_1} \tag{8.10}$$

If the soil is normally consolidated, then σ'_1 would be equal to the existing vertical overburden stress σ'_{vo}, and σ'_2 would include the additional stress $\Delta\sigma_v$ applied by the structure, or

$$s_c = C_c \frac{H_o}{1 + e_o} \log \frac{\sigma'_{vo} + \Delta\sigma_v}{\sigma'_{vo}} = C_c \frac{H_o}{1 + e_o} (\log \sigma'_{vf} - \log \sigma'_{vo}) \tag{8.11}$$

When computing the settlement by means of the percent consolidation versus log effective stress curve, Eq. (8.8) is combined with Eq. (8.4) to get

$$s_c = C_{c\varepsilon} H_o \log \frac{\sigma'_2}{\sigma'_1} \tag{8.12}$$

or, analogous to Eq. (8.11), for normally consolidated clays,

$$s_c = C_{c\varepsilon} H_o \log \frac{\sigma'_{vo} + \Delta\sigma_v}{\sigma'_{vo}} = C_{c\varepsilon} H_o (\log \sigma'_{vf} - \log \sigma'_{vo}) \tag{8.13}$$

Other similar settlement equations can be derived using a_v and m_v. In this case the average stress for a given stress increment must be used, since the compression curves are nonlinear.

Example 8.10

Given:

Test results shown in Fig. 8.4 and 8.5 are representative of the compressibility of a 10 m layer of normally consolidated San Francisco Bay mud. The initial void ratio is about 2.5.

Required:

Estimate the consolidation settlement of a large fill on the site if the average total stress increase on the clay layer is 10 kPa.

Solution: First estimate the preconsolidation stress to be about 70 kPa. Since the clay is normally consolidated, $\sigma'_p \approx \sigma'_{vo}$. Use the results of Examples 8.6 and 8.8. C_c is 0.99 and $C_{c\varepsilon}$ is 0.27. Use Eq. (8.11)

$$s_c = 0.99\left(\frac{10\text{ m}}{1 + 2.5}\right) \log \frac{70 + 10}{70} = 0.16\text{ m}$$

Use Eq. (8.13)

$$s_c = 0.27(10\text{ m}) \log \frac{70 + 10}{70} = 0.16\text{ m}$$

With a high water table, the actual settlement would be even slightly less, since fill that was above the water table would soon become submerged. Thus the resulting fill load would be reduced. To take this aspect into account, trial and error computations are required.

There are a couple of reasons for the popularity in engineering practice of using the percent consolidation or vertical strain versus log effective stress curve to compute settlements. First, estimating

field settlements is simple. You can read the percent compression directly from the graph, once you have a good estimate of the in situ vertical overburden stress.

Another reason the percent consolidation versus log effective stress plots are popular is that *during* the consolidation test it is often desirable to know what the shape of the compression curve is, so as to be able to obtain an early evaluation of the preconsolidation pressure. The void ratio versus log effective stress curve cannot be plotted during the test, because we must know both the initial and final values of the void ratio. This calculation requires the determination of the dry mass of solids, which can be determined only at the *end* of the test. Therefore the e versus log σ'_{vc} curve cannot be plotted during the test. However, the percent consolidation versus log pressure curve can be plotted while the test is *being* performed. Another advantage is that when the preconsolidation pressure is being approached, the load increments placed on the sample can be reduced so as to define more carefully the transition between the reloading curve and the virgin compression curve. Also, the test can be stopped when two or three points define the straight line portion of the virgin compression curve. Finally, as Ladd (1971a) pointed out, two samples may show very different e versus log σ'_{vc} plots but have similar vertical strain versus log effective stress curves because of differences in initial void ratio.

Example 8.11

Given:

The data of Example 8.10.

Required:

Estimate the settlement *directly* from Fig. 8.5(a).

Solution: If the preconsolidation stress is about 70 kPa, the final stress after loading is 80 kPa. Refer to Fig. 8.5(a). At the σ'_p (which is equal to σ'_{vo}, since it is normally consolidated), ε_v is about 5.5%. At $\sigma'_v = 80$ kPa, ε_v is about 7.5%. Therefore $\Delta\varepsilon_v$ is 2%, so the estimated settlement will be

$$s_c = 0.02(10\text{ m}) = 0.2\text{ m}$$

The settlement is greater in this example because the slope of the virgin compression curve is steeper from 70 to 80 kPa than from 10 to 80 kPa (see Example 8.6).

All the equations for settlement presented above were for a single compressible layer. When the consolidation properties or the void ratio vary significantly with depth or are different for distinct soil layers, then the total consolidation settlement is merely the sum of the settlements of the individual layers, or

$$s_c = \sum_{i=1}^{n} s_{ci} \tag{8.14}$$

where s_{ci} is the settlement of the ith layer of n total layers as calculated by Eqs. (8.10) through (8.13).

8.7.2 Consolidation Settlement of Overconsolidated Soils

What happens if the soil is overconsolidated? You will recall that an overconsolidated soil is one in which the present vertical effective stress is less than σ'_p. Overconsolidated soils are encountered more often in engineering practice than normally consolidated soils, so it is important to know how to make settlement calculations for this important class of soil deposits.

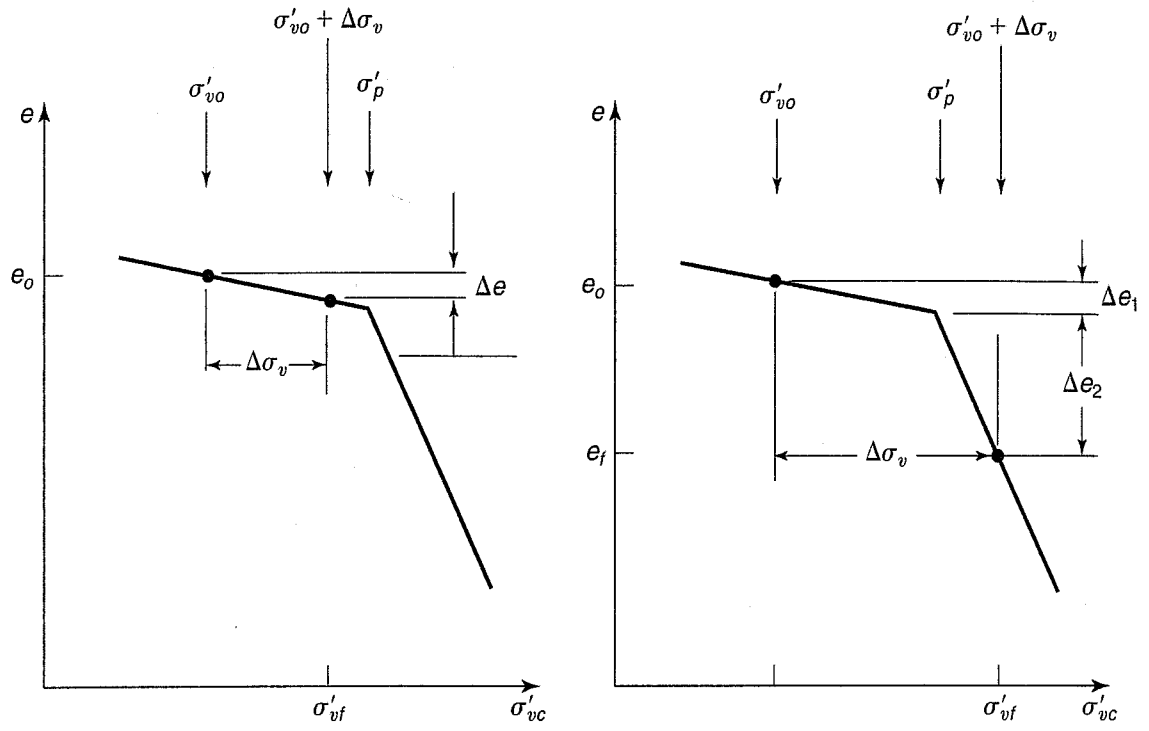

FIGURE 8.12 Principle of settlement calculations for overconsolidated soils (after Perloff and Baron, 1976).

The first thing to do is to check whether the soil is *preconsolidated*. You do this by comparing the preconsolidation pressure σ'_p from a laboratory consolidation test to the existing computed vertical effective overburden pressure, σ'_{vo}. You already know from Chapter 6 how to calculate σ'_{vo}. If the soil layer is definitely overconsolidated, then you have to check to see if the stress added by the engineering structure, $\Delta\sigma_v$, plus the σ'_{vo} exceeds the preconsolidation pressure σ'_p. Whether or not it does can make a large difference in the amount of settlement calculated, as shown in Fig. 8.12. Note that the ordinates in Fig. 8.12 could just as well be vertical strain.

If you have the case shown in Fig. 8.12(a)—that is, if $\sigma'_{vo} + \Delta\sigma_v \leq \sigma'_p$—then use either Eq. (8.11) or (8.13), but with the recompression indices C_r or $C_{r\varepsilon}$ in place of C_c and $C_{c\varepsilon}$, respectively. The *recompression index*, C_r, is defined just like C_c, except that it is the average slope of the recompression part of the e versus log σ'_{vc} curve (Fig. 8.8). If the data are plotted in terms of σ_v versus log σ'_{vc}, then the slope of the recompression curve is called the *modified recompression index* $C_{r\varepsilon}$ (sometimes called the *recompression ratio*). C_r and $C_{r\varepsilon}$ are related just like C_c and $C_{c\varepsilon}$ [Eq. (8.9)], or

$$C_{r\varepsilon} = \frac{C_r}{1 + e_o} \tag{8.15}$$

Example 8.12

Given:

The void ratio versus log effective stress data shown in Fig. Ex. 8.9.

Required:

Calculate (a) the recompression index C_r and (b) the modified recompression index $C_{r\varepsilon}$.

Solution:

a. The recompression index C_r is found in a similar manner to the C_c [Eq. (8.7)]. Using the points e and f over 1 log cycle, we find that

$$C_r = e_e - e_f = 0.79 - 0.76 = 0.03$$

b. The modified recompression index $C_{r\varepsilon}$ is found from Eq. (8.15)

$$C_{r\varepsilon} = \frac{C_r}{1 + e_o} = \frac{0.030}{1 + 0.87} = 0.016$$

Note that neither of these terms has units.

To calculate settlements of overconsolidated clays, Eqs. (8.11) and (8.13) become

$$s_c = C_r \frac{H_o}{1 + e_o} \log \frac{\sigma'_{vo} + \Delta\sigma_v}{\sigma'_{vo}} = C_r \frac{H_o}{1 + e} (\log \sigma'_{vf} - \log \sigma'_{vo}) \tag{8.16}$$

$$s_c = C_{r\varepsilon} H_o \log \frac{\sigma'_{vo} + \Delta\sigma_v}{\sigma'_{vo}} = C_{r\varepsilon} H_o (\log \sigma'_{vf} - \log \sigma'_{vo}) \tag{8.17}$$

when $\sigma'_{vo} + \Delta\sigma_v \leq \sigma'_p$. Since C_r is usually much smaller than C_c, the settlements occurring when $\sigma'_{vo} + \Delta\sigma_v \leq \sigma'_p$ are much less than if the soil were normally consolidated.

If the added stress caused by the structure exceeds the preconsolidation stress, then much larger settlements would be expected. This is because the compressibility of the soil is much greater on the virgin compression curve than on the recompression curve, as was shown, for example, in Fig. 8.8. For the case, then, where $\sigma'_{vo} + \Delta\sigma_v > \sigma'_p$, the settlement equation consists of two parts: (1) the change in void ratio or strain on the recompression curve from the original in situ conditions of (e_o, σ'_{vo}) or $(\varepsilon_{vo}, \sigma'_{vo})$ to σ'_p; and (2) the change in void ratio or strain on the virgin compression curve from σ'_p to the final conditions of (e_f, σ'_{vf}) or $(\varepsilon_{vf}, \sigma'_{vf})$. Note that $\sigma'_{vf} = \sigma'_{vo} + \Delta\sigma_v$. These two parts are shown graphically in Fig. 8.12(b). The complete settlement equation then becomes

$$s_c = C_r \frac{H_o}{1 + e_o} (\log \sigma'_p - \log \sigma'_{vo}) + C_c \frac{H_o}{1 + e_o} (\log \sigma'_f - \log \sigma'_p) \tag{8.18a}$$

This equation can also be written as

$$s_c = C_r \frac{H_o}{1 + e_o} \log \frac{\sigma'_p}{\sigma'_{vo}} + C_c \frac{H_o}{1 + e_o} \log \frac{\sigma'_{vo} + \Delta\sigma_v}{\sigma'_p} \tag{8.18b}$$

One could argue that in the right-hand term of Eq. (8.18) the void ratio corresponding to the preconsolidation pressure on the true virgin compression curve should be used. Although this is technically correct, it doesn't make any significant difference in the answer.

In terms of the modified indices, we have

$$s_c = C_{r\varepsilon} H_o (\log \sigma'_p - \log \sigma'_{vo}) + C_{c\varepsilon} H_o (\log \sigma'_f - \log \sigma'_p) \tag{8.19a}$$

$$s_c = C_{r\varepsilon} H_o \log \frac{\sigma'_p}{\sigma'_{vo}} + C_{c\varepsilon} H_o \log \frac{\sigma'_{vo} + \Delta\sigma_v}{\sigma'_p} \tag{8.19b}$$

Sometimes the degree of overconsolidation varies throughout the compressible layer. You could apply Eq. (8.16) or (8.17) to the part where $\sigma'_{vo} + \Delta\sigma_v < \sigma'_p$ and Eq. (8.18) or (8.19) to the part where $\sigma'_{vo} + \Delta\sigma_v > \sigma'_p$. In practice, however, it is usually easier simply to divide the entire stratum into

several layers, apply the appropriate equation to calculate the average settlement for each layer, and then sum up the settlements by Eq. (8.14).

8.7.3 Determining C_r and $C_{r\varepsilon}$

What is the best way to get C_r and $C_{r\varepsilon}$ for use in Eqs. (8.16) through (8.19)? Because of sample disturbance, the slope of the initial recompression portion of the laboratory consolidation curve (Fig. 8.8) is too steep and would yield values that are too large for these indices. Leonards (1976) offers the reasons why in situ values are generally smaller than those obtained from laboratory measurements: (1) disturbance during sampling, storage, and preparation of test specimens; (2) recompression of gas bubbles in the voids; and (3) errors in test procedures and methods of interpreting test results. This latter item includes the problem of reproducing the in situ state of stress in the specimen.

Leonards recommends that the σ'_{vo} be applied to the specimen and that it be inundated and then allowed to come to equilibrium for at least 24 hours before starting the incremental loading. Any tendency to swell should be controlled. Then the consolidation test is continued with relatively large load increments. To reproduce as closely as possible the in situ stress state, the specimen should be consolidated to slightly less than the σ'_p and then allowed to rebound. This is the first cycle shown in Fig. 8.13. If you don't have a good idea of the σ'_p, then consolidate initially to $\sigma'_{vo} + \Delta\sigma_v$ only, which is presumably less than σ'_p. The determination of C_r or $C_{r\varepsilon}$ is over the range of $\sigma'_{vo} + \Delta\sigma_v$, as shown in Fig. 8.13. (The $\Delta\sigma_v$ is the estimated stress applied by the structure). It is common practice to take the average slope of the two curves. From the typical test results shown in Fig. 8.13, you can see that the actual values of the recompression index depend on the stress at which the rebound-reload cycle starts, especially whether it starts at a stress less than or greater than the σ'_p. See the difference in slopes of the rebound curves shown in the figure. The value of C_r also depends on the OCR to which rebounding and

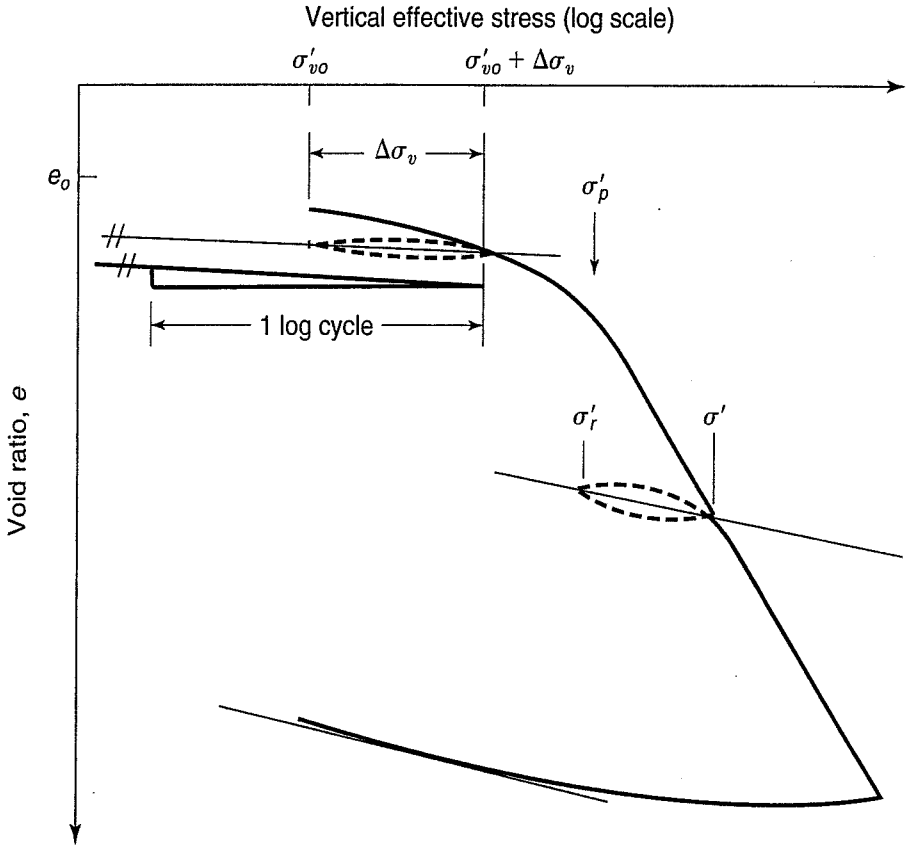

FIGURE 8.13 Typical consolidation curve showing the recommended procedure for determining the C_r (after Leonards, 1976).

reloading take place—for example, the ratio of σ'/σ'_r in Fig. 8.13. The final consideration affecting the value of C_r is the presence of gas bubbles in the pores of the soil. Use of backpressure (Chapter 12) can sometimes take care of this problem.

Example 8.13

Given:

The data in Example 8.1 and Fig. 8.8 is representative of a layer of silty clay 10 m thick.

Required:

Estimate the consolidation settlement if the structural loads at the surface will increase the average stress in the layer by 35 kPa.

Solution: From Example 8.1, we know that the σ'_{vo} is 80 kPa and the σ'_p is about 130 kPa; e_o is about 0.84. Since the applied stress is 35 kPa, the $\sigma'_{vo} + \Delta\sigma_v = 115$ kPa < 130 kPa. Therefore, use Eq. (8.16). To get C_r, we will take the average slope of the two curves DE and EF near the bottom of Fig. 8.8. C_r is approximately 0.03. Now use Eq. (8.16)

$$s_c = 0.03\frac{10\text{ m}}{1 + 0.84}\log\frac{80 + 35}{80} = 0.026\text{ m or }26\text{ mm}$$

From the preceding discussion, the C_r in this example is probably too large, since we determined it from an unload-reload cycle well beyond the σ'_p. It is therefore very likely that the settlements in the field will be less than 26 mm.

Example 8.14

Given:

The data in Example 8.13, except that the structural engineer made an error in computing the loads; the correct loads now will produce an average stress increase of 90 kPa in the silty clay layer.

Required:

Estimate the consolidation settlement due to the new loads.

Solution: Now, the applied stress is much greater than $\sigma'_{vo} + \Delta\sigma_v$, or $80 + 90 = 170 > 130$ kPa. Therefore we must use Eq. (8.18). In addition to the C_r, we need the compression index C_c. From Fig. 8.8 we find that C_c is about 0.25. Substitution into Eq. (8.18b) gives

$$\begin{aligned} s_c &= 0.03\frac{10\text{ m}}{1 + 0.84}\log\frac{130}{80} + 0.25\frac{10\text{ m}}{1 + 0.84}\log\frac{80 + 90}{130} \\ &= 0.034\text{ m} + 0.158\text{ m} \\ &= 0.193\text{ m} \end{aligned}$$

This value should be reported as "about 20 cm" due to the uncertainties in sampling, testing, and in estimating the σ'_p, the applied stress increase, and C_r and C_c.

8.8 TANGENT MODULUS METHOD

The tangent modulus method was developed by Janbu in the early 1960s and is summarized by Janbu (1998). The approach is based upon the simple premise that the modulus of a material is given by stress divided by strain. Knowing the modulus, obtained from laboratory tests performed on high quality undisturbed specimens, and the resulting stress imposed upon the soil by the foundation, one can readily compute the strain and the resulting settlement.

Go back and look again at Figs. 8.1(b) and 8.4(a). They show that as the stress increases, the strain also increases, but at a decreasing rate. The slope of this curve at any point is the *tangent modulus* M_t, and is given by

$$M_t = \frac{d\sigma'}{d\varepsilon} \tag{8.20}$$

where $d\sigma'$ = increment of effective stress,
$d\varepsilon$ = increment of strain.

Janbu also gives the following empirical equation for the tangent modulus:

$$M_t = m\sigma_{\text{ref}}\left(\frac{\sigma'}{\sigma_{\text{ref}}}\right)^{1-\alpha} \tag{8.21}$$

where M_t = tangent modulus in kPa or MPa,
σ_{ref} = reference stress = 100 kPa = 0.1 MPa,
σ' = effective stress in the ε direction in kPa or MPa,
m = dimensionless modulus number,
α = dimensionless stress exponent.

The reference stress is included to make Eq. (8.21) dimensionally correct. Both the modulus number and the stress exponent depend on the material type. So, for settlement calculations, the strain of a typical element can be expressed as

$$\varepsilon = \int_{\sigma'_{vo}}^{\sigma'_f} \frac{1}{M_t} d\sigma' \tag{8.22}$$

Combining Eqs. (8.21) and (8.22) and solving for the strain gives

$$\varepsilon = \frac{1}{m\,\alpha}\left[\left(\frac{\sigma'_f}{\sigma_{\text{ref}}}\right)^{\alpha} - \left(\frac{\sigma'_{vo}}{\sigma_{\text{ref}}}\right)^{\alpha}\right] \tag{8.23}$$

where $\sigma'_f = \sigma'_{vo} + \Delta\sigma'$,
σ'_{vo} = vertical effective overburden stress.

Of course, α may not be zero in Eq. (8.23), and if we have the strain, we can readily get the settlement from Eq. (8.4).

Equation (8.23) is applicable to all types of geologic materials from normally and overconsolidated clays, old and young silts and sands, rock, and normally and overconsolidated quick clays. What differentiates these materials is their modulus number m and the dimensionless stress exponent α. For overconsolidated soils and rock, $\alpha = 1.0$, and for sands and silts, $\alpha = 0.5$. For normally consolidated clays, $\alpha = 0$, although for normally consolidated extra sensitive Scandinavian clays (quick clays), $\alpha = -0.5$, and some Canadian quick clays may be even as low as -0.7.

When these values of α are inserted into Eq. (8.23) for the four different material types, the following equations result.

For $\alpha = 1$:

$$\varepsilon = \frac{\Delta\sigma'}{m\,\sigma_{\text{ref}}} \tag{8.24a}$$

where $\Delta\sigma'$ = incremental effective stress in kPa or MPa.

When $\alpha = 0.5$ for normally consolidated sands and silts, Eq. (8.23) becomes

$$\varepsilon = \frac{2}{m}\left[\sqrt{\frac{\sigma'_p + \Delta\sigma'}{\sigma_{\text{ref}}}} - \sqrt{\frac{\sigma'_p}{\sigma_{\text{ref}}}}\right] \tag{8.24b}$$

When $\alpha = 0$ for normally consolidated clays, Eq. (8.23) becomes

$$\varepsilon = \frac{1}{m}\ln\frac{\sigma'_p + \Delta\sigma'}{\sigma'_p} \tag{8.24c}$$

Finally, for normally consolidated extra-sensitive clays, with $\alpha = -0.5$, Eq. (8.23) is given by

$$\varepsilon = \frac{2}{m}\left[\sqrt{\frac{\sigma_{\text{ref}}}{\sigma'_p}} - \sqrt{\frac{\sigma_{\text{ref}}}{\sigma'_p + \Delta\sigma'}}\right] \tag{8.24d}$$

Typical values of α and the modulus number m are in Table 8.2. Figure 8.14 shows schematically moduli for elastic, elastoplastic, and plastic materials.

TABLE 8.2 Typical Stress Exponents and Modulus Numbers

Soil or Rock	Type	Stress Exponent, α	Modulus Number, m
Rock	High strength	1	1000 to 1 000 000
	Low strength	1	300 to 1000
Tills	Dense–very dense	1	300 to 1000
Gravel		0.5	40 to 400
Sand	Dense	0.5	250 to 400
	Medium dense	0.5	150 to 250
	Loose	0.5	100 to 150
Silt	Dense	0.5	80 to 200
	Medium dense	0.5	60 to 80
	Loose	0.5	40 to 60
Silty clay and clayey silt	Hard, stiff	0	20 to 60
	Stiff–firm	0	10 to 20
	Firm–soft	0	5 to 10
Clays	Soft marine and organic clays	0	5 to 20
Peat		0	1 to 5

After Fellenius (2009).

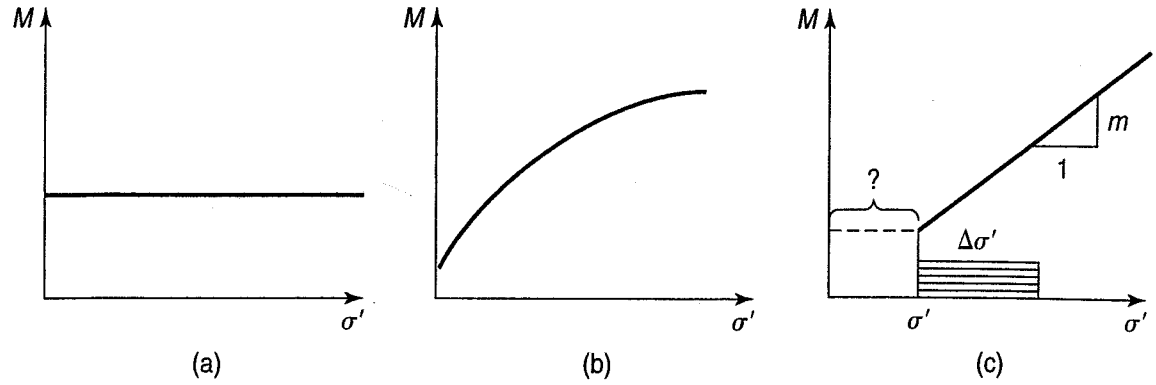

FIGURE 8.14 Moduli for (a) equivalent elastic ($\alpha = 1.0$); (b) elastoplastic ($\alpha \simeq 0.5$); and (c) plastic materials ($\alpha = 0$) (from Holtz, 1991).

Now comes the good part. We merely sum up the individual compressions of the thin layers of thickness dz between the depths $z = 0$ to $z = H$ by

$$\Delta h = \int_0^H \varepsilon \, dz \tag{8.25}$$

where Δh = consolidation settlement,
ε = vertical strain from Eq. (8.3),
H = layer thickness.

Recognize that Eq. (8.25) may take into account a multilayer deposit with different values of α and modulus number m.

If a conventional consolidation test is performed, then the value of m may be obtained from the e log σ'_v curve by the following equation for normally consolidated clays:

$$m = 2.3\frac{1 + e_o}{C_c} \tag{8.26a}$$

where C_c = compression index.

For overconsolidated clays, m may be given by

$$m_r = 2.3\frac{1 + e_o}{C_r} \tag{8.26b}$$

where m_r = rebound or recompression modulus,
C_r = recompression index.

Example 8.15

Given:

The data in Fig. 8.5(a).

Required:

Evaluate the modulus number by means of Eq. (8.26a) and compare with values for normally consolidated clays in Table 8.2.

Solution: Using Eq. (8.26a), we find

$$m = 2.3\frac{1 + e_o}{C_c} = 2.3\frac{1 + 2.6}{0.986} = 8.4$$

This value compares well with the value of m for soft clays in Table 8.2.

During our discussion of the preconsolidation pressure in Sec. 8.5.2 we saw that the tangent modulus method can also be a way to find the σ'_p. If you plot modulus versus average stress, the modulus tends to reach a minimum value that seems to represent the preconsolidation pressure.

8.9 FACTORS AFFECTING THE DETERMINATION OF σ'_p

Brumund et al. (1976) discuss three factors which significantly influence the determination of σ'_p from laboratory consolidation tests (Table 8.1). We have already mentioned one—the effect of sample disturbance on the shape of the consolidation curve (Fig. 8.8). We showed how the "break" in the curve became less well-defined with increasing disturbance. You can see these effects in Fig. 8.15(a). With sensitive clays especially [for example, Figs. 8.9(d) and 8.9(e)], increasing sample disturbance lowers the value of the σ'_p. At the same time, the void ratio is decreased (or the strain increased) for any given value of σ'_{vc}. As a consequence, the compressibility is decreased when $\sigma'_{vc} < \sigma'_p$, and the compressibility is increased when $\sigma'_{vc} > \sigma'_p$.

The load increment ratio (LIR) used in incremental loading consolidation testing is important for valid measurement of consolidation properties. The LIR is defined as the change in pressure or the pressure increment divided by the initial pressure before the load is applied. This relationship is as follows:

$$\text{LIR} = \frac{\Delta\sigma}{\sigma_{\text{initial}}} \tag{8.27}$$

where $\Delta\sigma$ is the incremental stress, and σ_{initial} is the previous stress. An LIR of unity, which is a typical value, means that the load is doubled each time. This procedure results in evenly spaced data points on the void ratio versus log effective stress curve, such as shown in Fig. 8.5(b).

Experience with soft, sensitive clays [Fig. 8.9(d)] has shown that a small stress change or even vibration may drastically alter the soil structure. For such soils an LIR of unity may not accurately define the value of the preconsolidation stress, so an LIR of less than one is often used. The influence of varying the LIR on the compressibility as well as on the σ'_p of a typical clay is shown in Fig. 8.15(b). The effect of the duration of the load increment is shown in Fig. 8.15(c). The common procedure (ASTM D 2435) is for each increment to be left on the sample for 24 hours. Note how this procedure affects the σ'_p. Some of the terminology used for these figures will become clearer after you read Chapter 9.

8.10 PREDICTION OF FIELD CONSOLIDATION CURVES

Since the consolidation test really is a reloading of the soil (shown by curve BCD of Fig. 8.8), even with high-quality sampling and testing the actual recompression curve has a slope which is somewhat *less* than that of the *field virgin compression curve* (OAD in Fig. 8.8). Schmertmann (1955) developed a graphical procedure to evaluate the slope of the field virgin compression curve. The procedure for this

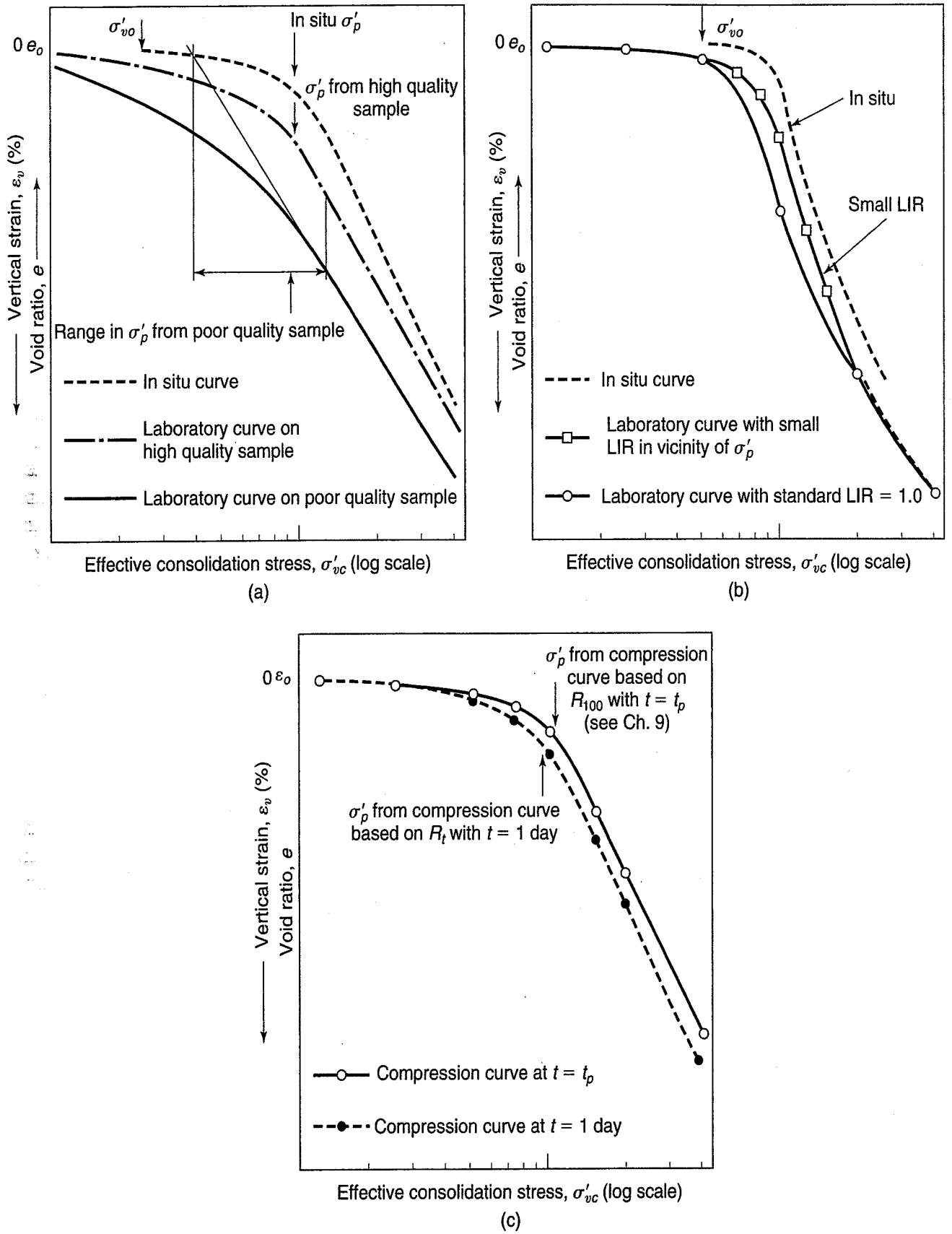

FIGURE 8.15 Factors affecting the laboratory determination of σ'_p: (a) effect of sample disturbance; (b) effect of load increment ratio; (c) effect of load increment duration (after Brumund et al., 1976).

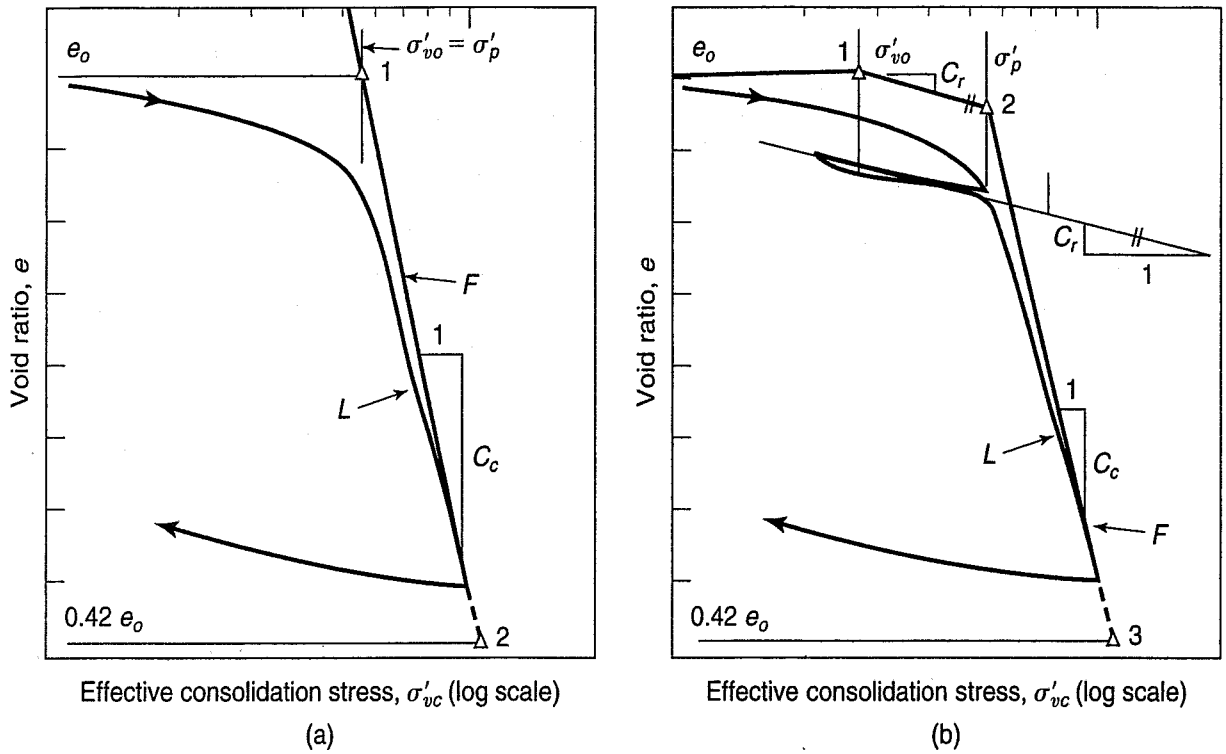

FIGURE 8.16 Illustration of the Schmertmann (1955) procedure to obtain the field virgin compression curve: (a) normally consolidated soil; (b) overconsolidated soil.

construction technique is illustrated in Fig. 8.16, where typical void ratio versus log effective stress curves are plotted. To correct the laboratory virgin compression curve for a normally consolidated soil in the field, proceed as follows:

1. Perform the Casagrande construction and evaluate the preconsolidation pressure σ'_p.
2. Calculate the initial void ratio e_o. Draw a horizontal line from e_o, parallel to the log effective stress axis, to the preconsolidation pressure σ'_p. This defines control point 1, illustrated by the small triangle 1 in Fig. 8.16(a).
3. From a point on the void ratio axis equal to $0.42e_o$, draw a horizontal line, and where the line meets the extension of the laboratory virgin compression curve L, define another control point, as shown by the small triangle 2. You should note that the coefficient of e_o is not a "magic number" but is a result of many observations on different clays.
4. Connect the two control points by a straight line. The slope of this line, F, defines the compression index C_c that most probably exists in the field. Line F is the *field virgin compression curve*. The Schmertmann correction allows for disturbance of the clay due to sampling, transportation, and storage of the sample plus subsequent trimming and reloading during the consolidation test.

Example 8.16

Given:

The e versus log σ data of Fig. Ex. 8.16. This consolidation data is from an undisturbed clay sample taken from the midpoint of a compressible layer 10 m thick. The OCR = 1.0.

Required:

a. Determine the slope of the field virgin compression curve using the Schmertmann procedure.

b. Compute the settlement of this clay layer if the stress increases from 275 to 800 kPa. Use both the laboratory and field virgin compression curves.

c. Comment on the difference, if any, in the calculated settlement.

Solution:

a. First, establish the field virgin compression curve according to the Schmertmann procedure outlined above. Perform the Casagrande construction on the curve shown in Fig. Ex. 8.16 to obtain the preconsolidation pressure to be about 275 kPa. Draw a horizontal line from $e_o = 0.91$ to the point where it intersects the preconsolidation pressure to establish control point 1, shown by triangle 1. Extend the virgin compression curve to $0.42e_o$ (0.42×0.91) or 0.38, to establish control point 2. Connecting the two control points 1 to 2 creates the field virgin compression curve.

You determine the value of C_c from the field virgin compression curve just as you did for the laboratory consolidation curve (see Examples 8.6, 8.7, and 8.9). For the log cycle from 1000 to 10 000 kPa, $e_{1000} = 0.705$ and $e_{10,000} = 0.329$; therefore $C_c = 0.705 - 0.329 = 0.376$. The slope of the laboratory virgin compression curve is found in the same way and equals 0.31. We'll need this value later.

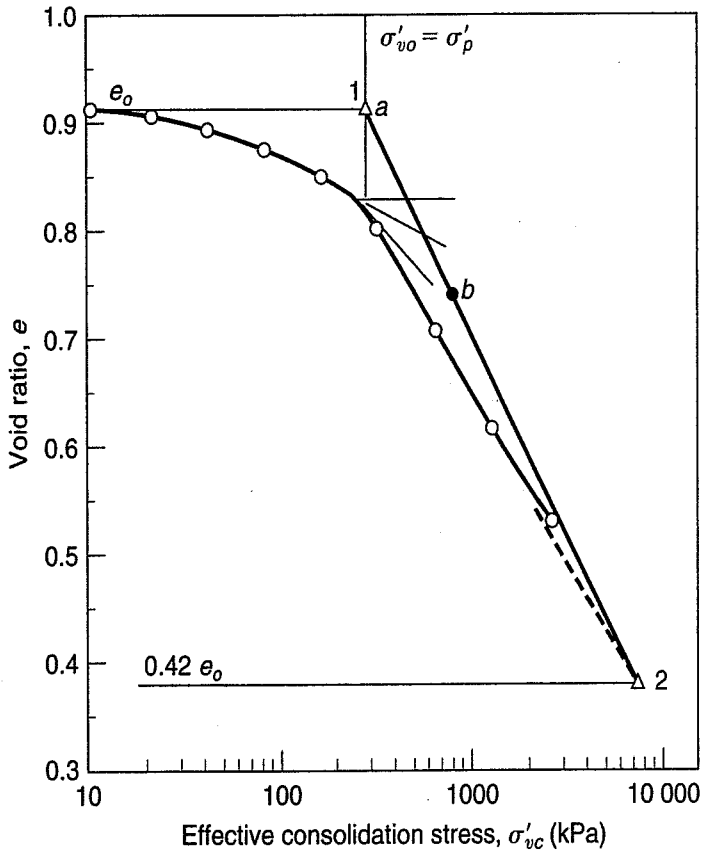

FIGURE Ex. 8.16

b. To compute the settlement, we may use either Eq. (8.4) or (8.11). Use Eq. (8.4) first:

$$s_c = \frac{\Delta e}{1 + e_o} H_o$$

The change in void ratio, Δe, is merely the difference in void ratio for $\sigma = 275$ kPa and $\sigma = 800$ kPa. These values are 0.912 at point *a* and 0.744 at point *b* in Fig. Ex. 8.16 on the field virgin compression curve. Therefore,

$$s_c = \frac{0.912 - 0.744}{1 + 0.912} 10\text{ m} = 0.88\text{ m}$$

Using Eq. (8.11):

$$s_c = \frac{C_c}{1 + e_o} H_o \log \frac{\sigma'_{vo} + \Delta\sigma_v}{\sigma'_{vo}}$$

$$= \frac{0.376}{1 + 0.912} (10\text{ m}) \log \frac{800}{275} = 0.91\text{ m}$$

The slight difference in the calculated values of the consolidation settlement s_c is due to small errors in reading data points from Fig. Ex. 8.16.

If we calculate the consolidation settlement using the laboratory virgin compression curve to establish C_c, we obtain [Eq. (8.11)]:

$$s_c = \frac{0.31}{1 + 0.912} (10\text{ m}) \log \frac{800}{275} = 0.75\text{ m, or 16\% lower}$$

c. Comment on the difference. Sixteen percent could be significant in some cases, especially if the proposed structure is particularly sensitive to settlements. Ladd (1971a) has found the Schmertmann correction will increase compression indices about 15% for fairly good samples of soft to medium clay. Since the procedure is simple, it would seem prudent to use it to make the best possible estimates of field compressibility. On the other hand, beware of too much precision in settlement calculations. When foundation engineers present their results in an engineering report, they commonly report the expected settlement as, for example, "approximately 0.9 m," because including more significant figures would imply more than the actual precision. It is often even better to give a range of settlements possible, along with your calculated "most probable" predicted value.

The Schmertmann procedure for an overconsolidated soil is illustrated in Fig. 8.16(b). If it is suspected that an overconsolidated soil is being tested, then it is good practice to follow the test procedure suggested in Sec. 8.7 and Fig. 8.13. A cycle of partial unloading and reloading is shown in Fig. 8.16(b) and in Figs. 8.9(a), (b), and (c). The average slope of the rebound-reload curve establishes C_r. The remaining steps in the Schmertmann procedure are as follows:

1. Calculate the initial void ratio e_o. Draw a horizontal line from e_o, parallel to the log effective stress axis, to the existing vertical overburden pressure σ'_{vo}. This establishes control point 1, as shown by the small triangle 1 in Fig. 8.16(b).
2. From control point 1, draw a line parallel to the rebound-reload curve to the preconsolidation pressure σ'_p. This will establish control point 2, as shown by the small triangle 2 in Fig. 8.16(b).
3. In a manner similar to that used for the normally consolidated soil, draw a horizontal line from a void ratio equal to $0.42e_o$. Where this line intersects the laboratory virgin compression curve L, establish a third control point, as shown by triangle 3 in Fig. 8.16(b). Connect control points 1 and 2, and 2 and 3, by straight lines. The slope of the line F joining control points 2 and 3 defines the compression index C_c for the field virgin compression curve. The slope of the line joining

control points 1 and 2 of course represents the recompression index C_r. An example of a field compression curve is shown in Fig. 8.9(c).

Example 8.17

Given:

The void ratio versus pressure data shown below. The initial void ratio is 0.725, and the existing vertical effective overburden pressure is 130 kPa.

Void Ratio	Pressure (kPa)
0.708	25
0.691	50
0.670	100
0.632	200
0.635	100
0.650	25
0.642	50
0.623	200
0.574	400
0.510	800
0.445	1600
0.460	400
0.492	100
0.530	25

Required:

a. Plot the data as e versus log σ'_{vc}.

b. Evaluate the overconsolidation ratio.

c. Determine the field compression index using the Schmertmann procedure.

d. If this consolidation test is representative of a 12 m thick clay layer, compute the settlement of this layer if an additional stress of 220 kPa were added.

Solution:

a. The data is plotted in Fig. Ex. 8.17.

b. The given value of σ'_{vo} is plotted on the graph, and the Casagrande construction performed to evaluate σ'_p. A value of 190 kPa is found

$$\text{OCR} = \frac{\sigma'_p}{\sigma'_{vo}} = \frac{190}{130} = 1.46$$

Thus the soil is slightly overconsolidated.

c. Using the Schmertmann procedure for overconsolidated clays, control points 1, 2, and 3 are established, as shown in Fig. Ex. 8.17. The values of C_r and C_c are evaluated directly from Fig. Ex. 8.17 over one log cycle. $C_r = 0.611 - 0.589 = 0.022$, and $C_c = 0.534 - 0.272 = 0.262$. (Note that $C_r \approx 10\%$ of C_c.)

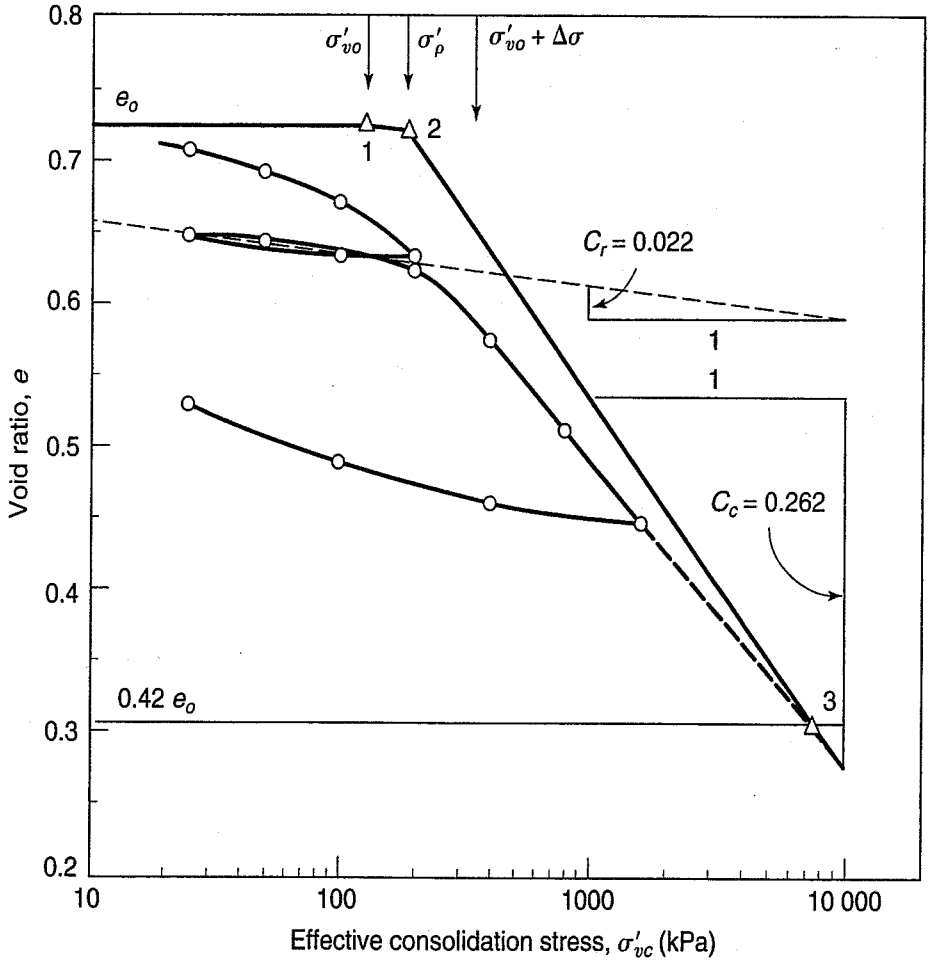

FIGURE Ex. 8.17 (Data modified slightly from Soderman and Kim, 1970.)

d. Using Eq. (8.18b), the settlement is computed:

$$s_c = \frac{C_r}{1+e_o} H_o \log \frac{\sigma'_p}{\sigma'_{vo}} + \frac{C_c}{1+e_o} H_o \log \frac{\sigma'_{vo} + \Delta\sigma}{\sigma'_p}$$

$$= \frac{0.022}{1+0.725}(12\text{ m}) \log \frac{190}{130} + \frac{0.262}{1+0.725}(12\text{ m}) \log \frac{130+220}{190}$$

$$= 0.025\text{ m} + 0.484\text{ m}$$

$$= 0.509\text{ m} \approx 0.5\text{ m}$$

Schmertmann (1955) also proposed an alternative method to obtain the in situ preconsolidation pressure from the shape of the Δe versus log σ'_{vo} curve, where Δe is the difference in the ordinate between the laboratory curve and the estimated in situ virgin compression curve. That field compression curve producing the most symmetrical Δe versus log σ' curve is considered the *correct* one. Figure 8.17(a) illustrates the concept for an overconsolidated clay. Just as in Fig. 8.16(b), we define the coordinates of point 1: σ'_{vo}, e_o.

Next, after assuming a reasonable, albeit arbitrary, value of σ'_p, we establish point 2. From point 2 we draw a line to where the laboratory curve (extension) is 0.42 × e_o, point 3. Next, we merely scale off the distance Δe for any given σ. The magnitude of Δe is the vertical distance between the lab curve and the *assumed* field virgin compression curve comprised of points 1-2-3. This procedure to find

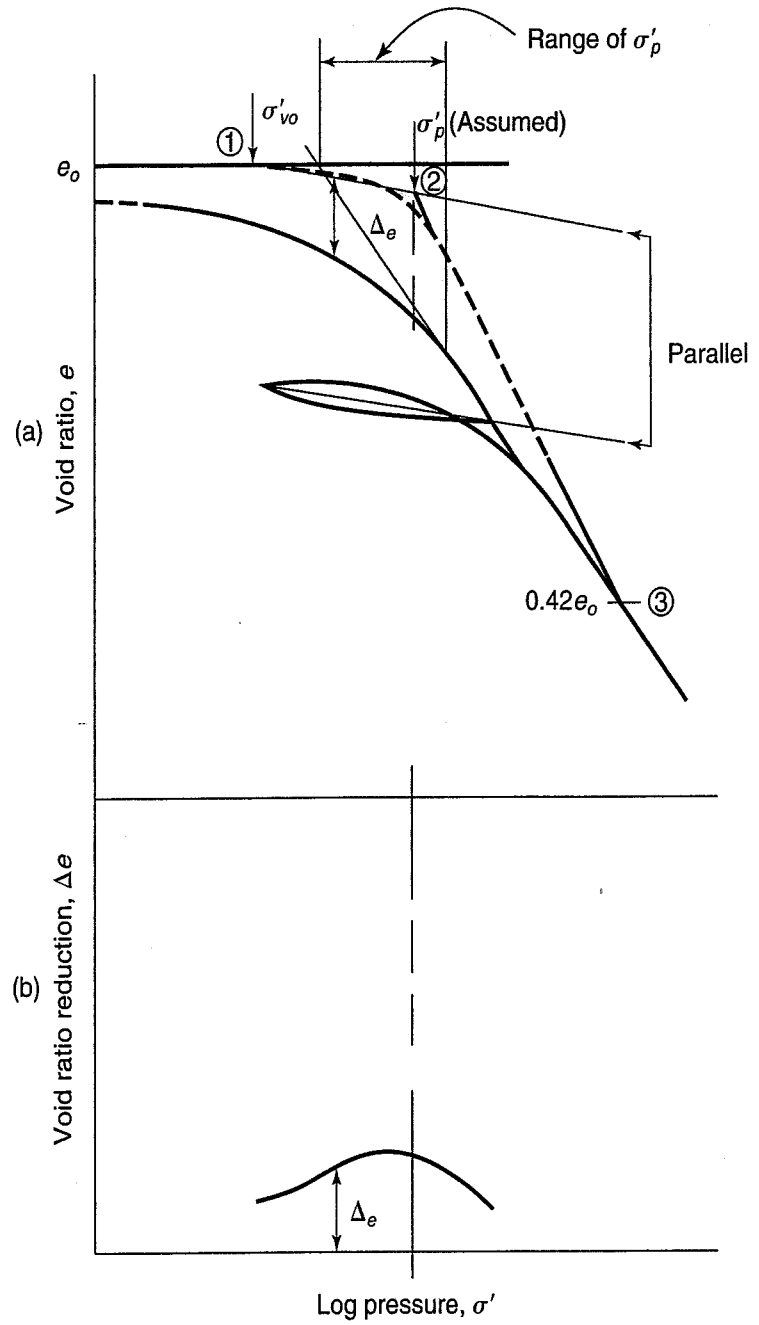

FIGURE 8.17 Schmertmann procedure for preconsolidation pressure: (a) laboratory and assumed field virgin compression curve; (b) void ratio reduction curve (after Schmertmann, 1955).

Δe is repeated at other values of σ for the first of several assumed field virgin compression curves, as shown in Fig. 8.17(b). The assumed curve that produces the highest order of symmetry defines the preconsolidation stress.

Peck (1974) presents a case history as shown in Fig. 8.18 and illustrates this procedure. In this case, the dashed line is found using Eq. (8.25), a first estimate of the field virgin compression curve. Next, Peck assumed three other possible field virgin compression curves along the line 1-2. The resulting void ratio reduction curves are shown toward the bottom right of the figure. Based upon the void ratio reduction, Peck suggested that the preconsolidation pressure was on the order of 6 tsf (575 kN/m^2), and not what was originally determined by the designers.

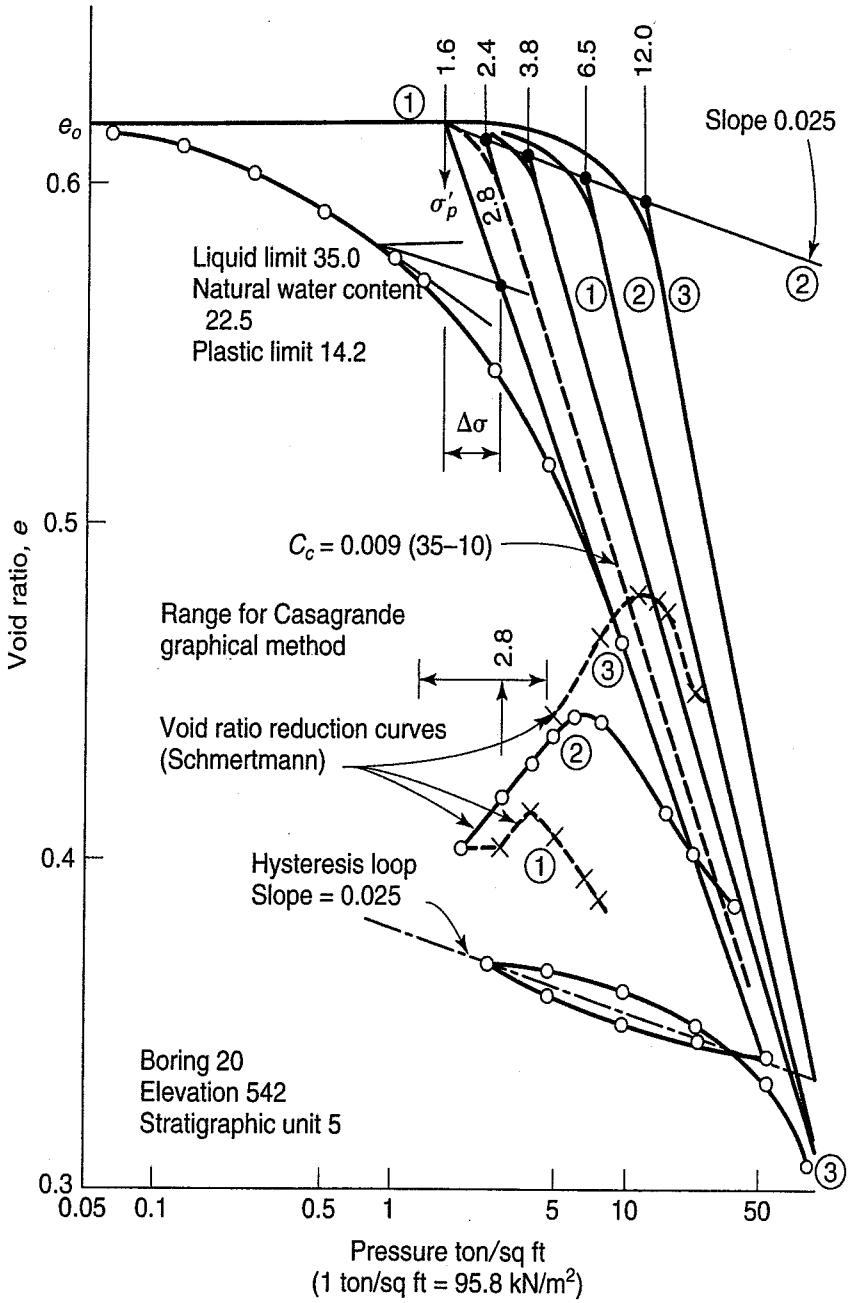

FIGURE 8.18 Example of Schmertmann procedure to obtain the in situ preconsolidation pressure (Peck, 1974).

8.11 SOIL PROFILES

In Table 8.1 we list some of the causes of preconsolidation in soil deposits. In this section, we study some typical soil profiles from various parts of the world and indicate their preconsolidation stresses as well as their effective vertical overburden stresses with depth. These overburden stress profiles were calculated just like those of Chapter 6, using the densities and thicknesses of the soil layers as well as the depths to the water table. To perform a detailed settlement analysis, typical profiles such as these are established for the proposed site and are based on subsurface investigations, undisturbed sampling, and laboratory testing. The typical soil profiles are presented in Figs. 8.19 through 8.23.

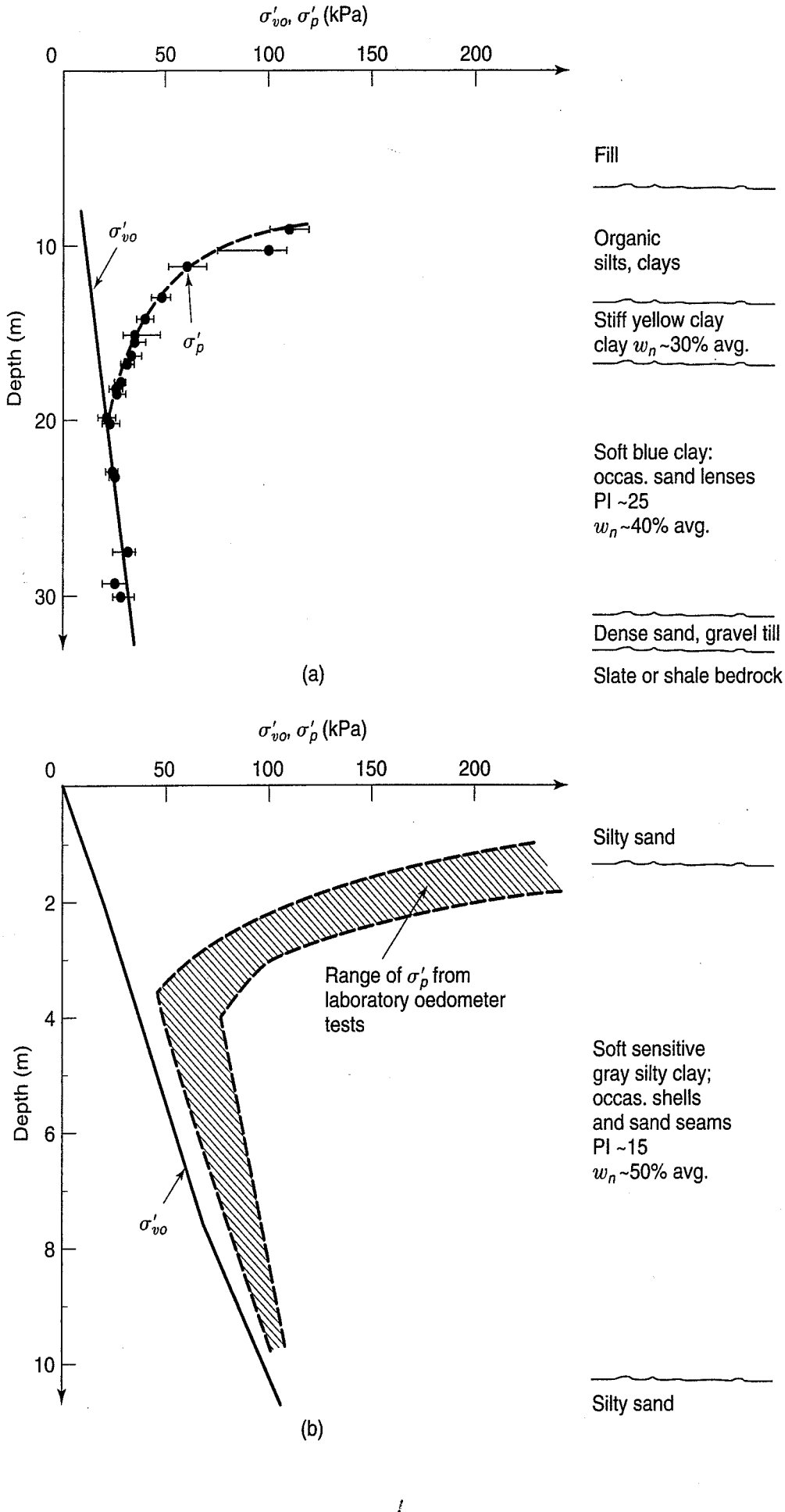

FIGURE 8.19 Overburden and preconsolidation stress profiles for marine clays of the Boston area: (a) Mystic power station (after Casagrande and Fadum, 1944); (b) I-95 test section, Portsmouth, NH (after Ladd, 1972).

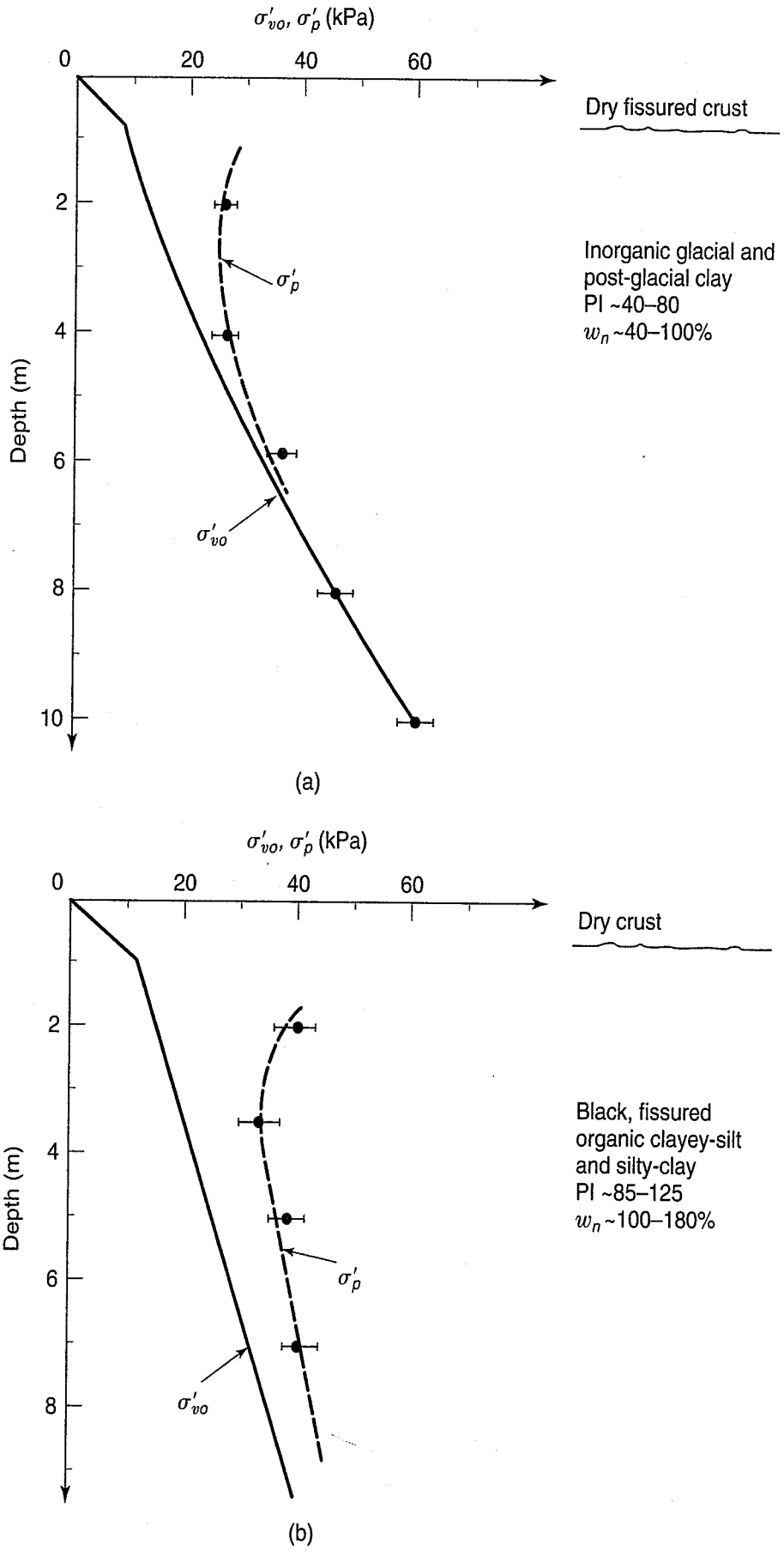

FIGURE 8.20 Overburden and preconsolidation profiles for two Swedish clays: (a) Ska-Edeby test field near Stockholm (after Holm and Holtz, 1977); (b) Kalix test site (after Holtz and Holm, 1979).

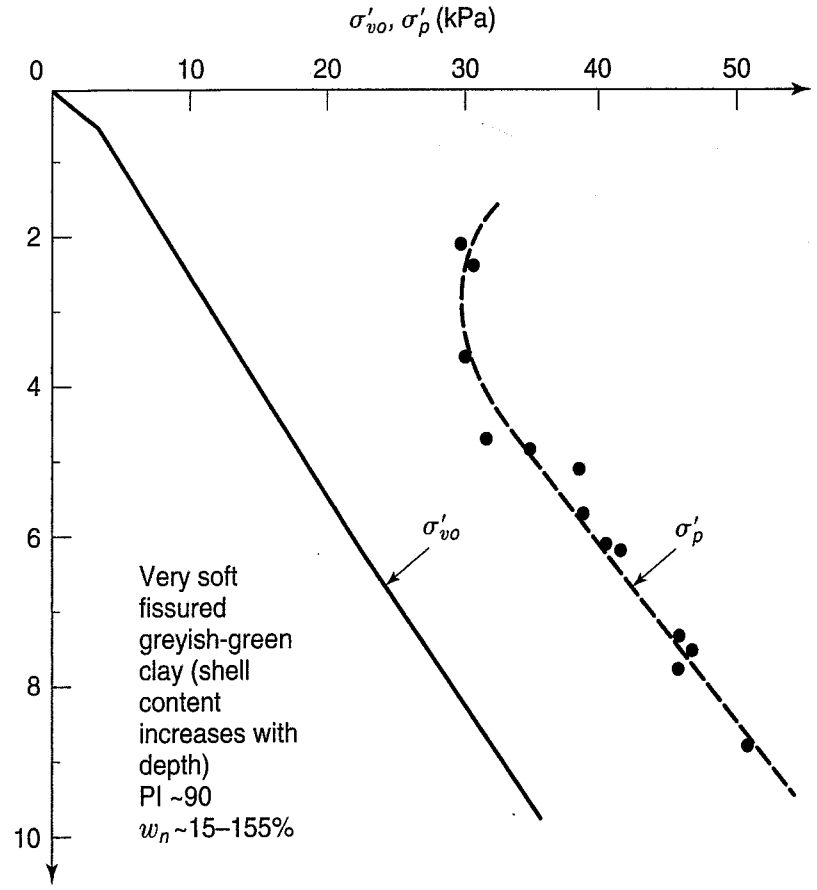

(a)

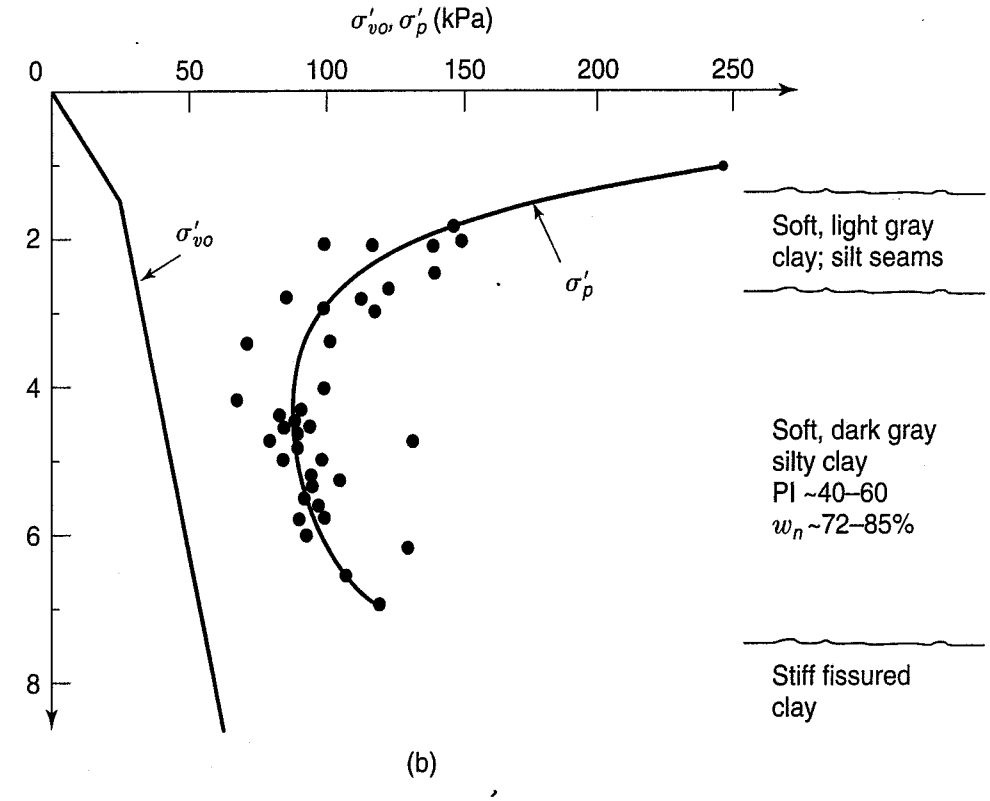

(b)

FIGURE 8.21 Overburden and preconsolidation stress profiles for marine clays near Bangkok, Thailand: (a) Bangkok-Siracha highway (after Eide and Holmberg, 1972); (b) Asian Institute of Technology (after Moh et al. 1972).

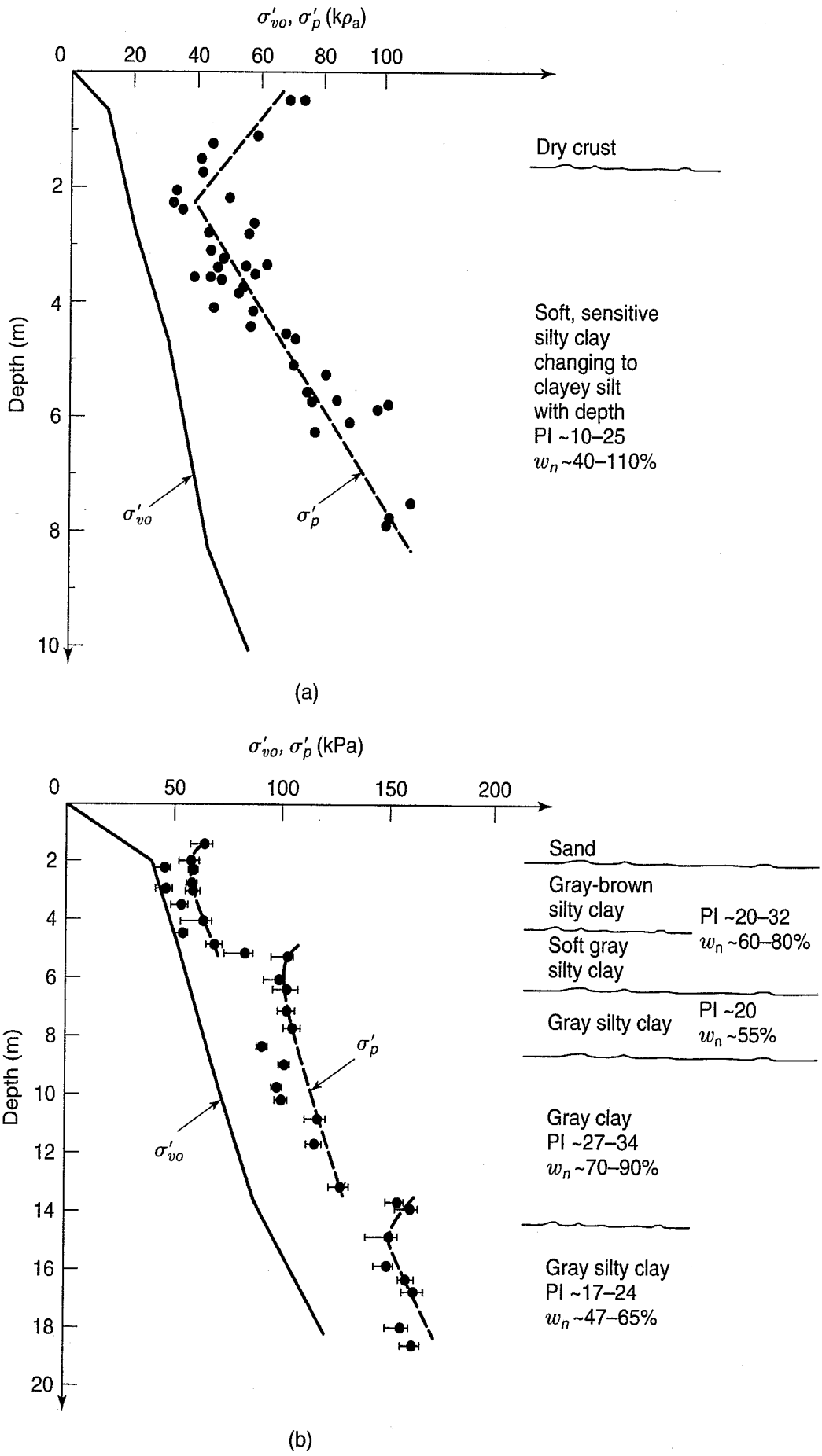

FIGURE 8.22 Overburden and preconsolidation stress profiles for Lake Champlain deposits (Laurentian or Leda clays) of Eastern Canada: (a) Saint-Alban, Québec, test fills (after Leroueil et al., 1978a); (b) C. F. S. Gloucester test (after Bozozuk and Leonards, 1972).

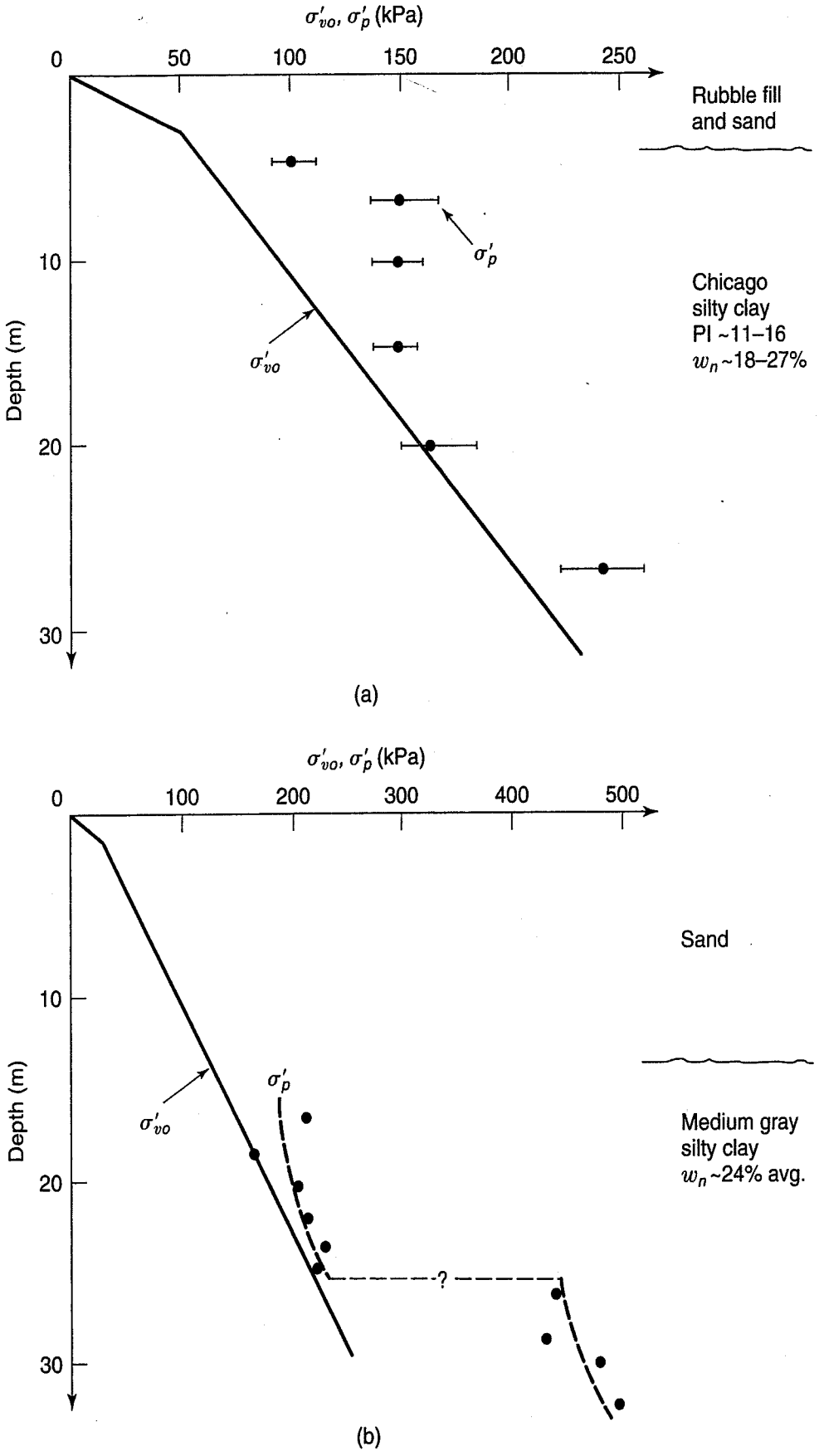

FIGURE 8.23 Overburden and preconsolidation stress profiles for glacial lake clays (reworked till?) of the Chicago area: (a) Chicago "Loop" (after data from Prof. J. O. Osterberg's graduate soil mechanics class, Northwestern University, 1966); (b) Hammond, Indiana (after Osterberg, 1963).

8.12 APPROXIMATE METHODS AND TYPICAL VALUES OF COMPRESSION INDICES

Because of the time and expense involved in consolidation testing, it is sometimes desirable to be able to relate the compression indices to the simple classification properties of soils. These relationships are also commonly used for preliminary designs and estimates and for checking the validity of test results.

Table 8.3 is a list of some published equations for the prediction of compression indices (Azzouz et al., 1976).

Terzaghi and Peck (1967) proposed the following equation, based on research on undisturbed clays of low to medium sensitivity:

$$C_c = 0.009(\text{LL} - 10) \tag{8.28}$$

which has a reliability range of about ±30%. This equation is widely used, despite its wide reliability range, to make initial consolidation settlement estimates. The equation should not be used if the sensitivity of the clay is greater than 4, the LL is greater than 100, or the clay contains a high percentage of organic matter. Some typical values of the compression index, based on our experience and the geotechnical literature, are listed in Table 8.4.

TABLE 8.3 Some Empirical Equations for C_c and $C_{c\varepsilon}$

Equation	Regions of Applicability
$C_c = 0.007(\text{LL} - 7)$	Remolded clays
$C_{c\varepsilon} = 0.208e_o + 0.0083$	Chicago clays
$C_c = 17.66 \times 10^{-5}w_n^2 + 5.93 \times 10^{-3}w_n - 1.35 \times 10^{-1}$	Chicago clays
$C_c = 1.15(e_o - 0.35)$	All clays
$C_c = 0.30(e_o - 0.27)$	Inorganic, cohesive soil; silt, some clay; silty clay; clay
$C_c = 1.15 \times 10^{-2}w_n$	Organic soils—meadow mats, peats, and organic silt and clay
$C_c = 0.75(e_o - 0.50)$	Soils of very low plasticity
$C_{c\varepsilon} = 0.156e_o + 0.0107$	All clays
$C_c = 0.01w_n$	Chicago clays

Note: w_n = natural water content.

After Azzouz et al. (1976).

TABLE 8.4 Typical Values of the Compression Index C_c

Soil	C_c
Normally consolidated medium sensitive clays	0.2 to 0.5
Chicago silty clay (CL)	0.15 to 0.3
Boston blue clay (CL)	0.3 to 0.5
Vicksburg buckshot clay (CH)	0.5 to 0.6
Swedish medium sensitive clays (CL-CH)	1 to 3
Canadian Leda clays (CL-CH)	1 to 4
Mexico City clay (MH)	7 to 10
Organic clays (OH)	4 and up
Peats (Pt)	10 to 15
Organic silt and clayey silts (ML-MH)	1.5 to 4.0
San Francisco Bay mud (CL)	0.4 to 1.2
San Francisco Old Bay clays (CH)	0.7 to 0.9
Bangkok clay (CH)	0.4

Often C_r is assumed to be 5% to 10% of C_c, but this assumption may lead to too large values of C_r. Typical values of C_r range from 0.015 to 0.035; lower values are for clays of lower plasticity and low OCR. Values of C_r outside the range of 0.005 to 0.05 should be considered questionable (Leonards, 1976). Recognize that if you use too high a value of C_r, you will overpredict the settlements. Although large overpredictions may not be dangerous, they could mean excessively expensive foundations.

Additional correlations between C_c and C_r are summarized in Kulhawy and Mayne (1990), where C_c versus LL, e_o, and w_n, and C_r versus PI, are presented. Considerable scatter is evident in these correlations.

8.13 COMPRESSIBILITY OF ROCK AND TRANSITIONAL MATERIALS

Relatively speaking, rock and rocklike materials have low compressibility when compared with soils. We like to think that we are on a "rock solid" foundation and don't really have to worry about settlement. For the most part, this is the case except for very heavy loadings or weak or badly jointed rock. Sometimes it is difficult to determine exactly where soil ends and rock begins, as discussed in Sec. 4.12. This problem becomes acute when owners and contractors disagree on excavation costs directly related to material type.

The settlement and supporting capacity of rock depends upon the rock type, amount and width of joints and their orientation, and empirically on the RQD (Rock Quality Designation–Sec. 4.13). The strain is determined once the modulus is known. The modulus may be obtained from laboratory tests or from field tests. With very specialized test equipment, *triaxial* tests (Chapter 12) are performed, while field seismic refraction tests, plate load tests, and pressuremeter tests (Baguelin et al., 1978) can be performed to obtain the modulus. For natural geotechnical materials, a relationship between the maximum Young's modulus and the compressive strength (Chapter 12) may be used to obtain the modulus. A typical value for the ratio of E_{max}/q_u for uncemented soils is 1000 and for soft and hard rocks about 500. More about the compressive strength, q_u, of soils and rocks is found in Chapter 12. For additional information on the strength and deformation of rocks, see Barton et al. (1974), Bieniawski (1976), Hoek and Brown (1980), Tatsuoka and Shibuya (1992), and Wyllie (1999).

8.14 BURLAND'S INTRINSIC COMPRESSIBILITY PROPERTIES

Burland (1990) proposed so-called "intrinsic properties" to describe compressibility and strength characteristics of reconstituted clays, and he used them as a reference for interpreting characteristics of natural sedimentary clays. He started by performing one-dimensional consolidation tests on many sedimentary clays after they had been *reconstituted*, or completely remixed to between 100% and 150% of their liquid limit without prior drying. These compression curves were also plotted in e-log σ'_v space [Fig. 8.24(a)]. The parameters e^*_{100} and e^*_{1000} are the so-called *intrinsic void ratios* for the soils tested, corresponding to their void ratios at σ'_v = 100 kPa and 1000 kPa, respectively. The compression curve is then *normalized*[1] by defining a *void index* I_v as follows:

$$I_v = \frac{e - e^*_{100}}{C^*_c} \tag{8.29}$$

where

$$C^*_c = e^*_{100} - e^*_{1000} \tag{8.30}$$

Figure 8.24(b) shows the normalized intrinsic compression curve, I_v versus log σ'_v, developed from three tests on reconstituted clays having liquid limits ranging from 35 to 128. Burland concluded

[1]Normalizing is the process of manipulating data from various sources in the same way with the goal of making the data comparable.

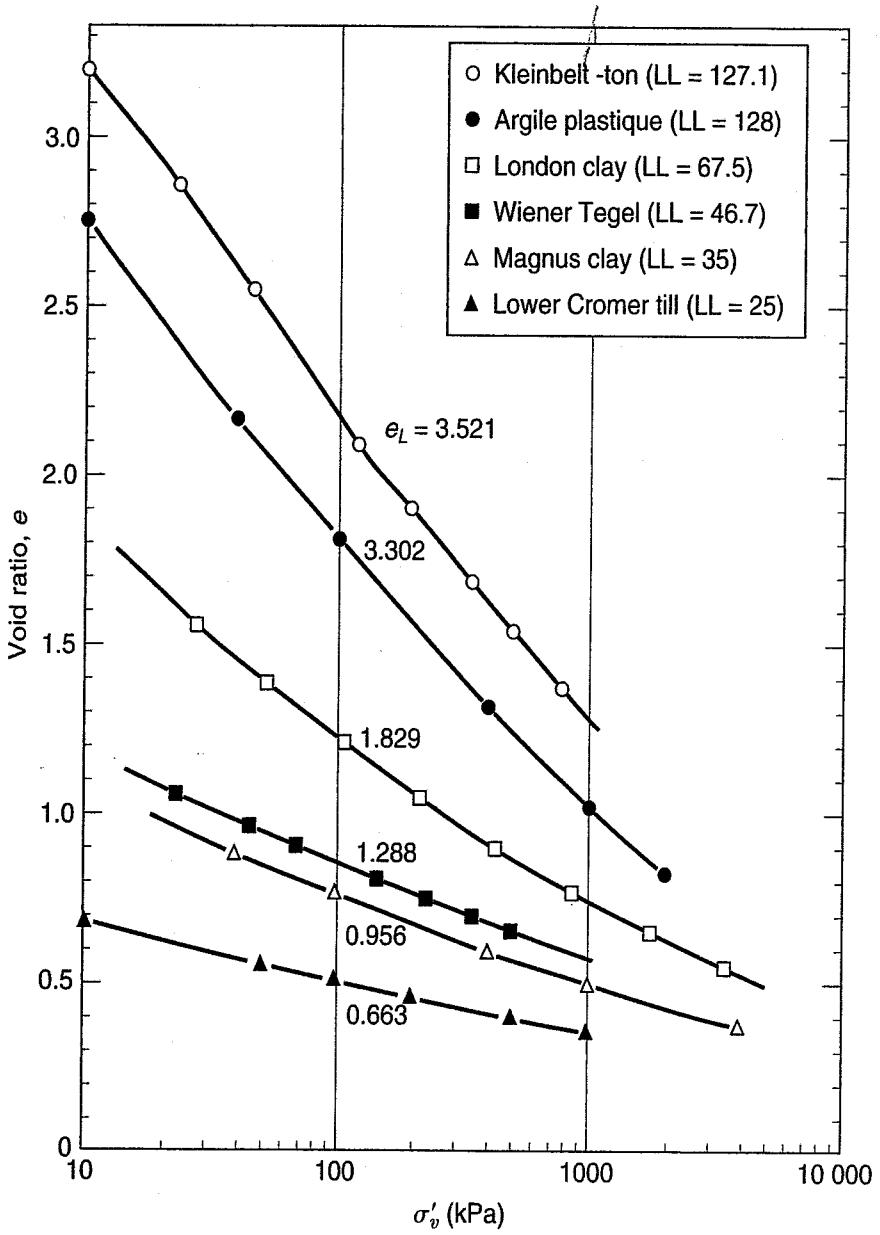

(a)

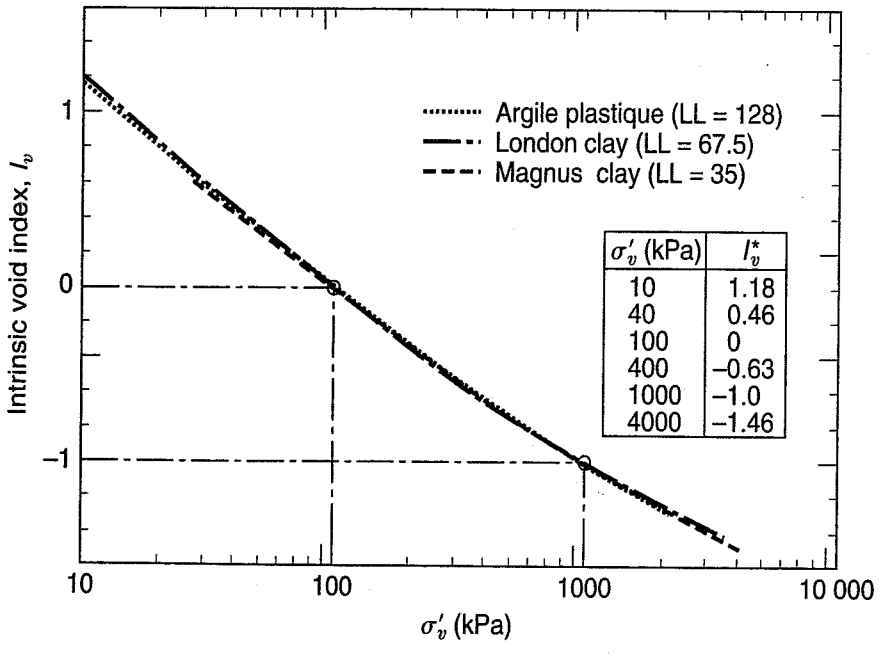

(b)

(Continued)

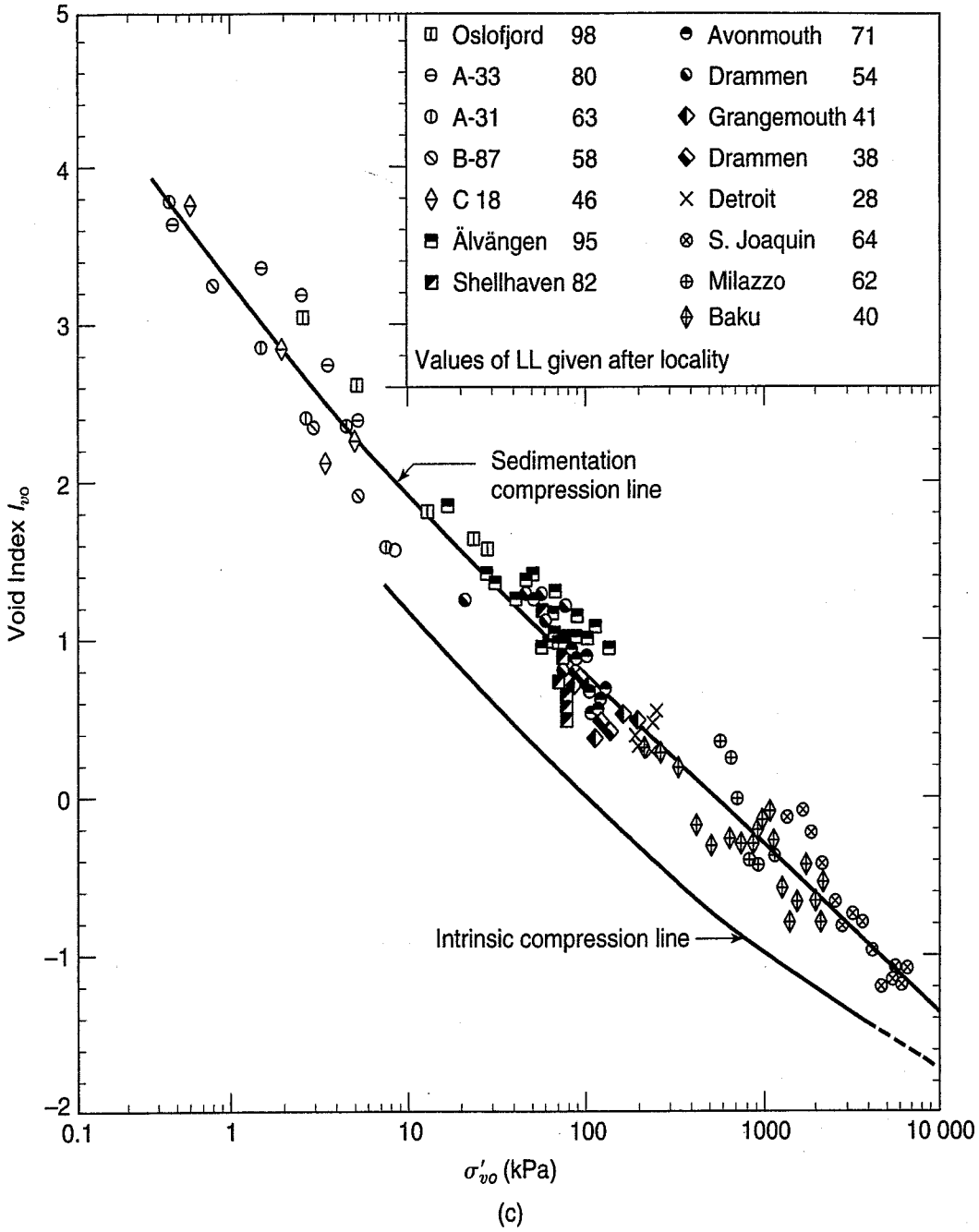

(c)

FIGURE 8.24 Development of the intrinsic compression and sedimentation compression lines: (a) one-dimensional compression curves for various reconstituted clays; (b) normalized compression curves for three reconstituted clays; and (c) intrinsic compression line from (b) plotted with sedimentation compression line for normally consolidated clays (after J.B. Burland, personal communication, 2008).

that this normalized relationship, termed the *intrinsic compression line* (*ICL*), is reasonably unique for many reconstituted soils and can be expressed as follows:

$$I_{v,\mathrm{ICL}} = 2.45 - 1.285 \log \sigma'_v + 0.015(\log \sigma'_v)^3 \tag{8.31}$$

Using the void index I_v as a unifying parameter among different deposits, Burland computed the in situ *void index* I_{vo} of a number of soils

$$I_{vo} = \frac{e_o - e^*_{100}}{C^*_c} \tag{8.32}$$

where e_o is the void ratio of normally consolidated clay under effective overburden pressure σ'_{vo}. Burland (1990) then plotted the in situ void ratio for a number of deposits versus their respective in situ σ'_v—i.e., the e-σ'_v combinations in situ for a number of deposits—thus mimicking the deposition (sedimentation) states of these soils. These void ratios were normalized in the void index space, and it was found that the various sedimentation curves can be fitted into a line termed the *sedimentation compression line* [SCL; Fig. 8.24(c)]. Within the range of σ'_v = 10 kPa to 10,000 kPa, the SCL is approximately parallel to the ICL, with following form:

$$I_{v,\,\mathrm{SCL}} = 3.2436 - 0.6239 \ln \sigma'_v + 0.0244(\ln \sigma'_v)^2 - 0.0012(\ln \sigma'_v)^3 \tag{8.33}$$

Within this stress range, for a given value of I_{vo}, the supported σ'_v of natural sediments is approximately five times that of equivalent reconstituted clay. At σ'_v values greater than 1000 kPa, the ICL and SCL tend to converge. These concepts are consistent with those of Mitchell and Soga (2005) regarding soil structure.

Figure 8.24(c) shows the relationship of ICL versus SCL in I_{vo}-log σ'_{vo} space. The ICL is reasonably unique for many sedimentary clays, allowing it to be used as a reference line for comparison with a soil's natural, in situ state. The unique SCL represents a group of normally consolidated clays with structures that can be represented by their relationship to the ICL. Thus, these two unique lines constitute the basic framework for evaluating clay structure; i.e., the distance of a soil's in situ I_{vo} to the ICL can indicate the degree to which its structure has developed when compared to the set of e-σ'_v states under intrinsic and sedimentation conditions. While the I_{vo}-log σ'_{vo} for most sedimentary clays will lie close to the SCL at various stress levels (corresponding to their depth below the surface), many soils exposed to other mechanisms that influence their structure may lie above the SCL. This would be characteristic of the structured, sensitive clays from, say, Eastern Canada or Scandinavia. Conversely, recent deltaic deposits from the Mississippi River, which have developed little structure due to rapid deposition, will have more oriented particles and natural I_{vo}-log σ'_{vo} states that lie close to the ICL.

8.15 IN SITU DETERMINATION OF COMPRESSIBILITY

Some of the most important compressibility parameters, such as the compression indices and existing void ratio, must be determined from the results of laboratory tests. As we will learn in Chapter 12, there are four field tests that may be used to estimate the preconsolidation pressure: cone penetration test (CPT), with and without a pore pressure device to measure pore pressure; flat plate dilatometer test (DMT); self boring pressuremeter test (PMT); and field vane shear test (VST). Each of these tests measures the resistance to loading in the vertical and/or horizontal, and the resulting measured parameters are compared with the preconsolidation pressure. An example of one such relationship using the VST is shown in Fig. 8.25 (Kulhawy and Mayne, 1990). [Note that the relationship between preconsolidation pressure and undrained shear strength (Chapter 12) is a log-log plot, which can hide a lot of scatter in the data.] Based upon this data, the relationship is given by

$$\sigma'_p = 3.53\,\tau_f \tag{8.34}$$

where σ'_p = preconsolidation pressure, kPa,

τ_f = undrained shear strength, kPa.

When using the above relationship and those from other in situ devices, understand that the results are only approximate and empirical.

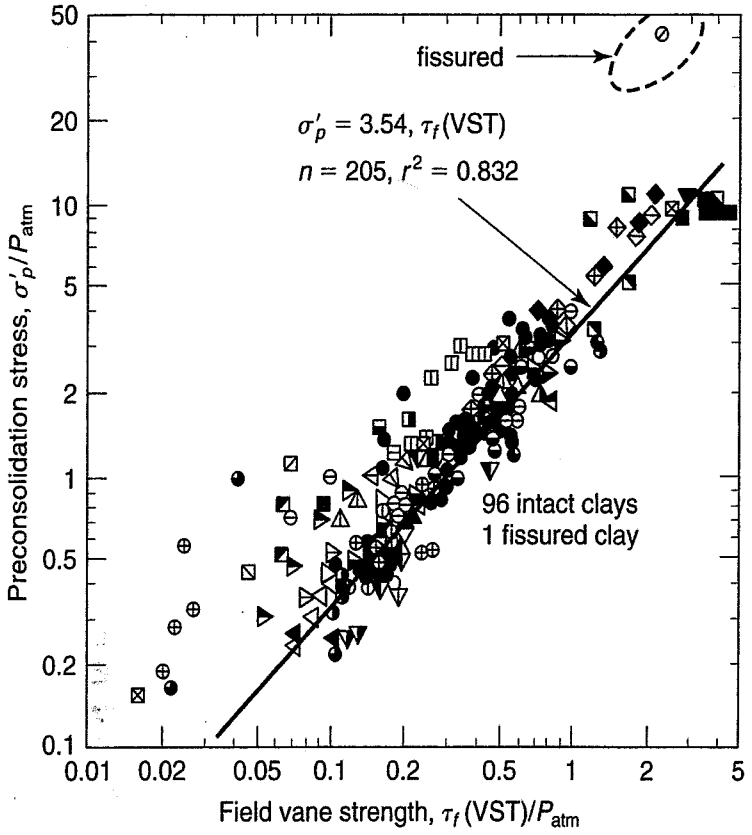

FIGURE 8.25 Correlation of σ'_p with vane shear test (VST) shear strength data normalized by atmospheric pressure (after Kulhawy and Mayne, 1990).

PROBLEMS

8.1 For the e versus log σ curves of Fig. 8.9(a), compute the compression indices. Explain why it is possible to get slightly different answers than those shown at the bottom of the figure.

8.2 Verify the values of the preconsolidation stress shown in Fig. 8.9(a).

8.3 Determine the overconsolidation ratio (OCR) for the five fine-grained soils of Fig. 8.9(a).

8.4 Verify that the values for the preconsolidation stress and the virgin compression index shown in Fig. 8.9(b) are correct.

8.5 What is the OCR of the clay till in Fig. 8.9(c)?

8.6 Estimate the preconsolidation stress for (a) the undisturbed Leda clay in Fig. 8.9(d), (b) undisturbed Mexico City clay in Fig. 8.9(e), (c) undisturbed Chicago clay in Fig. 8.9(f), and (d) the swelling clays from Texas in Fig. 8.9(g).

8.7 Determine the compression indices for the four soils of Problem 8.6.

8.8 The pressure versus void ratio data determined from a consolidation test on an undisturbed clay specimen are as follows:

Pressure (kPa)	Void Ratio	Pressure (kPa)	Void Ratio
20	0.864	1280	0.602
40	0.853	320	0.628
80	0.843	80	0.663
160	0.830	20	0.704
320	0.785	0	0.801
640	0.696		

(a) Plot the pressure versus void ratio curve on both arithmetic and semilogarithmic graphs.

(b) Determine the equations for the virgin compression curve and for the rebound curve for unloading, starting at 1280 kPa.

(c) What are the corresponding modified compression and recompression indices for this soil?

(d) Estimate the stress to which this clay has been preconsolidated. (After A. Casagrande.)

8.9 A building is to be constructed on a stratum of the clay 7 m thick for which consolidation data are given in Problem 8.8. The average existing effective overburden pressure on this clay stratum is 126 kPa. The average applied pressure on the clay after construction of the building is 285 kPa.

(a) Estimate the decrease in thickness of the clay stratum caused by full consolidation under the building load.

(b) Estimate the decrease in thickness due to the building load if the clay had never been preconsolidated under a load greater than the existing overburden.

(c) Show on the e versus log σ plot of Problem 8.8 the values of Δe used for making the estimates in parts (a) and (b). (After A. Casagrande.)

8.10 The compression curve for a certain clay is a straight line on the semilogarithmic plot, and it passes through the point $e = 1.15$, $\sigma'_v = 65$ kPa, $e = 0.76$, $\sigma'_v = 825$ kPa. Determine an equation for this relationship. (After Taylor, 1948.)

8.11 Show that Eqs. (8.9) and (8.15) are valid.

8.12 The following consolidation test data were obtained from undisturbed San Francisco Bay mud. For this clay, LL = 85, PL = 38, $\rho_s = 2.70$ Mg/m^3, and $w_n = 105.7\%$. Initially, the specimen height was 2.54 cm and its volume was 75.14 cm^3. Plot the data as percent consolidation versus log pressure. Evaluate the preconsolidation pressure and the modified virgin compression index.

Stress (kPa)	Dial Reading (mm)	Void Ratio
0	12.700	2.765
5	12.352	2.712
10	12.294	2.703
20	12.131	2.679
40	11.224	2.541
80	9.053	2.211
160	6.665	1.849
320	4.272	1.486
640	2.548	1.224
160	2.951	1.285
40	3.533	1.374
5	4.350	1.499

8.13 Plot the data of Problem 8.12, on a void ratio versus log pressure graph. Evaluate the preconsolidation pressure and the virgin compression index. Do these values agree with what you found in Problem 8.12? Comments?

8.14 The initial water content of the sample in Problem 8.12 is 105.7%, and the density of the solids, ρ_s, is 2.70 Mg/m^3. Compute the wet and dry density and degree of saturation of the consolidation test sample if the dry weight of the sample is 52.8 g. If the final water content is 59.6%, compute the degree of saturation and dry density at the end of consolidation.

8.15 A 7.8 m thick layer of soft San Francisco Bay mud is to be loaded with a granular fill 3.2 m thick, on the average. The total density of the fill is about 1.8 Mg/m^3. Assume that the test data in Problem 8.12 is typical of the clay layer, and that the layer is normally consolidated. What consolidation settlement will take place due to the weight of the fill? Make these calculations (a) using the $C_{c\varepsilon}$ determined in Problem 8.12, (b) using the C_c determined in Problem 8.13, and (c) directly from the percent consolidation-versus-log-pressure diagram you plotted in Problem 8.12.

8.16 Assume the laboratory test results in Problem 8.12 are typical of another San Francisco Bay mud site, but where the clay is slightly overconsolidated. The present vertical effective overburden stress is calculated to be about 15 kPa, and the thickness of the clay is 3.9 m. At this location, the granular fill ($\rho = 1.8$ Mg/m^3) will be only about 1.2 m thick. Estimate the consolidation settlement due to the weight of the fill.

8.17 What settlement would you expect at the overconsolidated site in Problem 8.16 if the fill to be constructed were 4 m thick? Do this problem (a) directly from the percent consolidation plot and (b) using Eq. (8.18) or (8.19). How do the results compare?

8.18 Plot the following data and determine the preconsolidation pressure and the modified compression index.

% Consolidation (Compression is +)	Pressure (kPa)	% Consolidation (Compression is +)	Pressure (kPa)
0.09	5	7.34	160
0.11	10	7.60	320
0.12	20	8.35	640
0.26	40	12.65	1280
0.98	80	17.41	2560
1.91	160	22.18	5120
4.19	320	21.65	1280
8.05	640	20.63	160
8.03	320	19.26	40
7.83	160	15.35	5
7.21	80		

Specimen height is 25.4 mm, $w_n = 32.5\%$, $\rho_d = 1.45$ Mg/m^3. Sample is from a depth of -11.5 m.

8.19 At the site where the sample of Problem 8.18 was taken, the soil profile consists of about 6.5 m of sand and rubble fill and then 9.1 m of clay. The water table is about 1.8 m below the ground surface. Average densities of the sand and rubble fill are 1.45 Mg/m^3 above the water table and 1.70 Mg/m^3 below the water table. Estimate the consolidation settlement if the average stress increase in the compressible layer is (a) 50 kPa, (b) 100 kPa, and (c) 250 kPa. Use both Eq. (8.19) [or Eq. (8.17)] and your percent compression plot from Problem 8.18, and compare the results. Comments?

8.20 Plot the following void ratio versus pressure data, and evaluate the compression index and the recompression index. Determine the preconsolidation stress.

Void Ratio, e	Pressure (kPa)	Void Ratio, e	Pressure (kPa)
1.025	0	0.837	300
1.006	10	0.780	400
0.997	20	0.655	800
0.978	40	0.504	2000
0.950	80	0.542	500
0.911	160	0.589	160
0.893	200	0.681	20

8.21 Use the consolidation data from Problem 8.20 to compute the settlement of a structure that adds 175 kPa to the already existing overburden pressure of 130 kPa at the middle of a 6 m thick layer.

8.22 What would be the settlement of the same structure in Problem 8.21 if the overconsolidation ratio of the clay were 1.0 and $\sigma'_{vo} + \Delta\sigma_v = 305$ kPa at the middepth of the clay layer? Show your work and assumptions on the e versus log σ curve of Problem 8.20.

8.23 The consolidation curve of Fig. Ex. 8.9 is typical of a compressible layer 5 m thick. If the existing overburden pressure is 50 kPa, compute the settlement due to an additional stress of 150 kPa added by a structure.

8.24 For the test data of Problem 8.12, construct the field virgin compression curve using the Schmertmann procedure for an OCR of unity.

8.25 Do Problem 8.24 for an OCR = 2.5.

8.26 At the midpoint of a 7.5 m thick soil layer, the void ratio is 1.9. Find this point on the field virgin compression curve determined in Problem 8.24. What is the corresponding pressure? If this pressure is *doubled* over the entire site, compute the consolidation settlement of the layer.

8.27 Show that the field virgin compression curve shown on Fig. 8.9(c) ($C_c = 0.19$) is correct.

8.28 Show that the point of intersection where the laboratory and field virgin compression curves meet for the percent consolidation versus log σ' graph is equal to $0.58e_o/(1 + e_o)$. This intersection is equivalent to the $0.42e_o$ point on the e versus log σ' graph.

8.29 Using the appropriate empirical relationship from Sec. 8.12, estimate the compression and recompression indices and both modified indices for as many of the clays of Fig. 8.9 as you can. How well do the empirical relationships agree with the laboratory data?

8.30 Do Problem 8.29 for the clays in Problems 8.8, 8.12, 8.18, and 8.20. Again, how good is the agreement?

8.31 Figure P8.31 shows a proposed foundation site, with 10 ft of sand overlying 15 ft of clay with consolidation properties shown. The clay is normally consolidated. Assume 1-D conditions.

(a) Compute the initial σ'_v at the middle of the clay layer prior to excavation and construction.

(b) After excavation and during construction, the foundation area will be heavily loaded with the structure and equipment so that σ'_v at the middle of the clay layer will be increased to 3900 psf. Determine the settlement that will occur under these conditions.

(c) After construction is completed, the equipment will be removed and the final σ'_v at the middle of the clay layer will be 3200 psf.

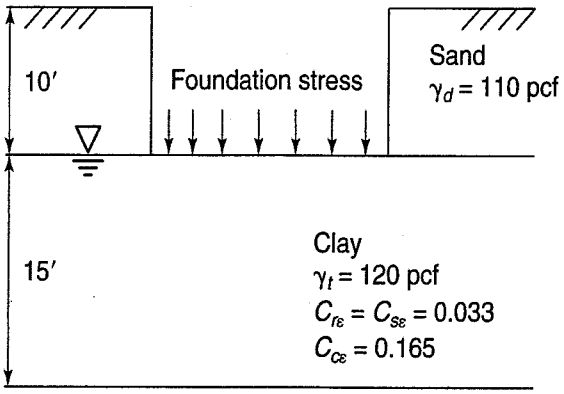

FIGURE P8.31

As part of your answer, please be sure to sketch the compression curve followed in parts (b) and (c).

8.32 As part of a construction project, a 7.5 m thick layer of clay is to be loaded with a temporary 3 m thick sand layer (refer to Fig. P8.32). The figure shows the water-table location, soil unit weights, and the compression-curve properties for the clay. Assume the sand layer remains dry.

(a) Calculate the value of σ'_v in the middle of the clay layer (at 3.75 m below the water table) before the sand layer is applied, and after consolidation is complete.

(b) Based on your answer in part (a), and the compression curve characteristics, calculate the settlement that will occur under these conditions.

(c) How much will the clay layer heave when the 3 m sand layer is removed?

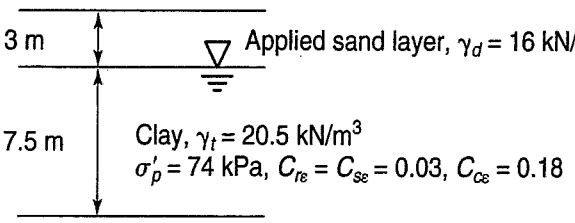

FIGURE P8.32

8.33 Refer to Fig. 8.5(a).

(a) Using log interpolation between 100 and 1000, determine the σ'_v value at a vertical strain, ε_v = 20%.

(b) If the initial void ratio, e_o = 2.6, determine C_r and C_c for this soil. For C_c, use the portion of the curve between σ'_v = 100 and 500 kPa.

(c) If the original clay layer thickness is 9.5 m, determine the settlement that occurs in the layer when it is loaded from 200 to 400 kPa. (*Note:* You don't need the results from part (b) to do this.)

8.34 A large embankment is to be built on the surface of a 15-ft clay layer. Before the embankment is built, the initial σ'_v at the middle of the clay layer is 480 psf. The results from a 1-D consolidation test on the clay from the middle of the layer are as follows:

$$\sigma'_p = 1800 \text{ psf}, \qquad C_{re} = 0.0352, \qquad C_{ce} = 0.180$$

If the final σ'_v at the middle of the layer after the embankment loading is 2100 psf, what is the settlement, in inches, of the clay layer resulting from this loading?

8.35 Figure P8.35 shows a proposed site where an excavation will be made. The 10 ft layer of sand will be removed, so that the top of the 24 ft normally consolidated clay layer will be exposed. Assume full capillarity in the clay *only*.

(a) Assume that the water-table location remains the same during excavation. Compute the σ_v, σ'_v and u values at the middle of the clay layer before and after the excavation.

(b) Assuming 1-D conditions, compute how much the clay layer will deform due to this excavation, in inches. Specify whether this is settlement or heave.

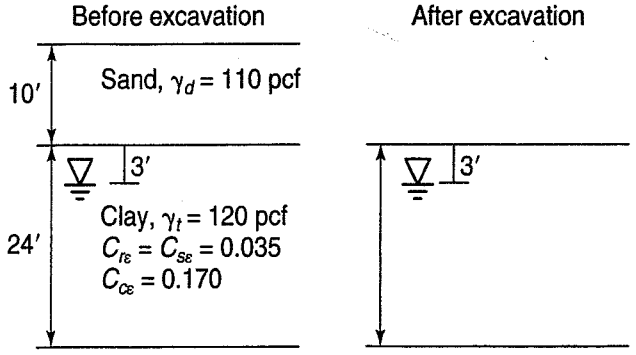

FIGURE P8.35

8.36 Figure P8.36 shows the soil profile at a site where you plan to lower the water table. You have results from two consolidation tests, one from the upper 12 ft thick overconsolidated crust, and another from the lower 32 ft thick normally consolidated zone. You plan to lower the water table from its current 12 ft depth to 20 ft below ground surface. The consolidation properties for each layer are shown. Assume full capillarity.

(a) Compute the σ'_v in the middle of each layer before and after the water table is lowered.

(b) Determine the total settlement that will result from lowering the water table.

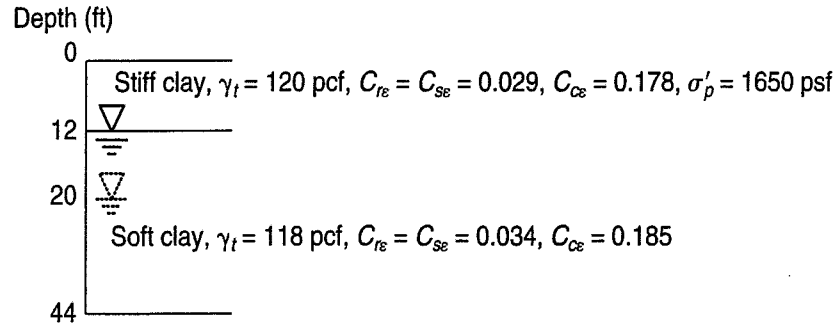

FIGURE P8.36

8.37 When a consolidation test is performed on some soils, the virgin compression region is not linear, but bilinear. Figure P8.37 shows such a compression curve from a 15 ft thick layer.

(a) What vertical strain, ε_v, occurs when the soil is loaded from an initial σ'_{v1} = 560 psf to σ'_{v2} = 3000 psf?

(b) If you load the soil further, to σ'_{v3} = 4000 psf, how much additional settlement occurs?

(c) Finally, if you unload from 4000 psf back to σ'_{v4} = 3000 psf, what additional deformation (in ft) occurs?

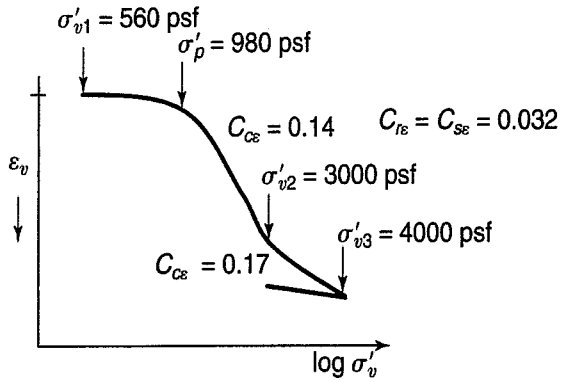

FIGURE P8.37

8.38 Refer to the compression curve marked Soil 13 in Fig. 8.9(a). Disregard the small unloading cycle in the middle of the curve. The initial void ratio for this soil is 1.17, and the preconsolidation pressure is 290 kPa. (*Note:* The right-hand vertical boundary of this graph is at σ'_{vc} = 2000 kPa.)

(a) Determine the C_r and C_c for this soil based on the compression curve.

(b) If a layer of this soil 12 m thick is loaded from 50 to 800 kPa (two of the data points shown on the curve), what settlement will result, in m?

CHAPTER 9

Time Rate of Consolidation

9.1 INTRODUCTION

In Chapter 8 we showed how to calculate the consolidation settlement of a clay layer below a structure when it reaches equilibrium with the external stress. We described how the pore water pressure in excess of hydrostatic dissipates with time (consolidation) and how the increase in the effective stress of the layer ultimately becomes equal to the applied stress. It was mentioned that the rate of consolidation would depend, among other things, on the permeability of the soil.

This process of excess pore pressure dissipation is called *primary consolidation* to distinguish it from the other time-dependent component of total settlement, *secondary compression*. Recall from Sec. 8.2 that secondary compression occurs after essentially all of the excess pore water pressure has dissipated; that is, it occurs at constant effective stress, which is why it is often referred to as drained creep (*creep* is the term used in materials engineering to describe deformation under constant applied stress). In some soils, especially inorganic clays, primary consolidation is the largest component of total settlement, whereas secondary compression can constitute a major part of the total settlement of peats and other highly organic soils. In this chapter, the theories for estimating the time rate of both primary consolidation and secondary compression of fine-grained soils are discussed.

Why is it important to know how fast a structure will settle under the applied load? For example, if the design life of a structure is 50 years, and it is estimated that it will take 500 years for all the settlement to occur, then the foundation engineer would expect only minor settlement problems during the life of the structure. On the other hand, if the settlement is expected to take about the time required to build the structure, then most if not all of it will have occurred by the time the structure is completed. If the structure is sensitive to rapid settlements (for example, reinforced concrete frames or concrete pavement), then structural damage could result. Most structures on clay foundations experience gradual settlements during their lifetimes, which may or may not impair their performance. In addition, we sometimes intentionally cause a clay layer to settle prior to construction, typically by building a temporary embankment (a process known as *preloading*). In these cases, it is important to know how long this settlement process will occur for purposes of construction scheduling. This chapter presents procedures for estimating the *rate* of foundation settlement. The engineer then can decide what effect, if any, the settlement may have on the structural integrity as well as the intended use of the structure.

The following notation is introduced in this chapter.

Symbol	Dimension	Unit	Definition
C_α	—	—	Secondary compression index - Eq. (9.27)
$C_{\alpha\varepsilon}$	—	—	Modified secondary compression index - Eq. (9.29)
c_v	L^2T^{-1}	m^2/s	Coefficient of consolidation - Eq. (9.3)
c_{vh}	L^2T^{-1}	m^2/s	Coefficient of consolidation - Eq. (9.25)
H_{dr}	L	m	Length of drainage path - Eq. (9.5)
H_s	L	m	Height of solids - Eq. (9.31)
H_v	L	m	Height of voids - Eq. (9.31)
R	L	m	Equivalent piezocone radius - Eq. (9.25)
R_e	L	m	Equivalent dilatometer blade radius - Eq. (9.26)
R_o	L	mm	Initial dial reading or converted displacement transducer reading - Eq. (9.23)
R_n	L	mm	Dial reading or converted displacement transducer reading at time t, $n = 1, 2, \ldots$
$s(t)$	L	m	Consolidation settlement at time t
T	—	—	Time factor - Eq. (9.5)
U_{avg} or U	—	(%)	Degree of consolidation
u_e	$ML^{-1}T^{-2}$	kPa	Excesss pore pressure
U_z	—	— (or %)	Consolidation ratio - Eq. (9.9)
Z	—	—	Depth factor - Eq. (9.9)
α	—	—	Factor for simplifying finite difference formulation - Eq. (9.21)

9.2 THE CONSOLIDATION PROCESS

It is useful to return to the spring analogy as presented in Chapter 8 (Fig. 8.2). Figure 9.1(a) shows a spring with a piston and a valve in a single cylinder. A pressure versus depth diagram is shown in Fig. 9.1(b). The soil, represented by the spring, is at equilibrium with an initial effective stress σ'_{vo}. For the time being, we shall assume that all of the applied stress on the piston, $\Delta\sigma$, is initially transferred to the excess pore water pressure Δu (excess above hydrostatic or initial u_o). This is the case for one-dimensional loading but (as we shall see later) not for three-dimensional loading.

With time, water is squeezed out through the valve, and the excess pore water pressure decreases. Thus, there is a gradual transfer of stress from the pore water to the soil skeleton and a concurrent increase in effective stress. Figure 9.1(c) shows the initial effective stress σ'_{vo}, the change (increase) in effective stress, $\Delta\sigma'$, and the pore pressure still to be dissipated, Δu, at $t = t_1$. The vertical dashed lines, labeled $t_1, t_2, \ldots$, represent times from the start of load application. They are called *isochrones*[1] because they are lines of equal times. Finally, at $t \rightarrow \infty$ all of the excess pore water pressure Δu will be dissipated, and the effective stress will equal the initial stress σ'_{vo} plus the applied stress increment $\Delta\sigma$. During this time, the piston will have settled an amount that is directly related to how much water is squeezed out of the cylinder.

A typical soil layer is much more complex than the simple model shown in Figs. 9.1(a)–(c). Let us increase the number of springs, pistons, and valves as shown Fig. 9.1(d). As before, we can

[1]*Isobars* are either arctic taverns or contour lines of equal pressure found on a weather map; *isopachs* are lines of equal thickness of a geologic deposit; and *isotachs* are lines of equal velocity on wind maps.

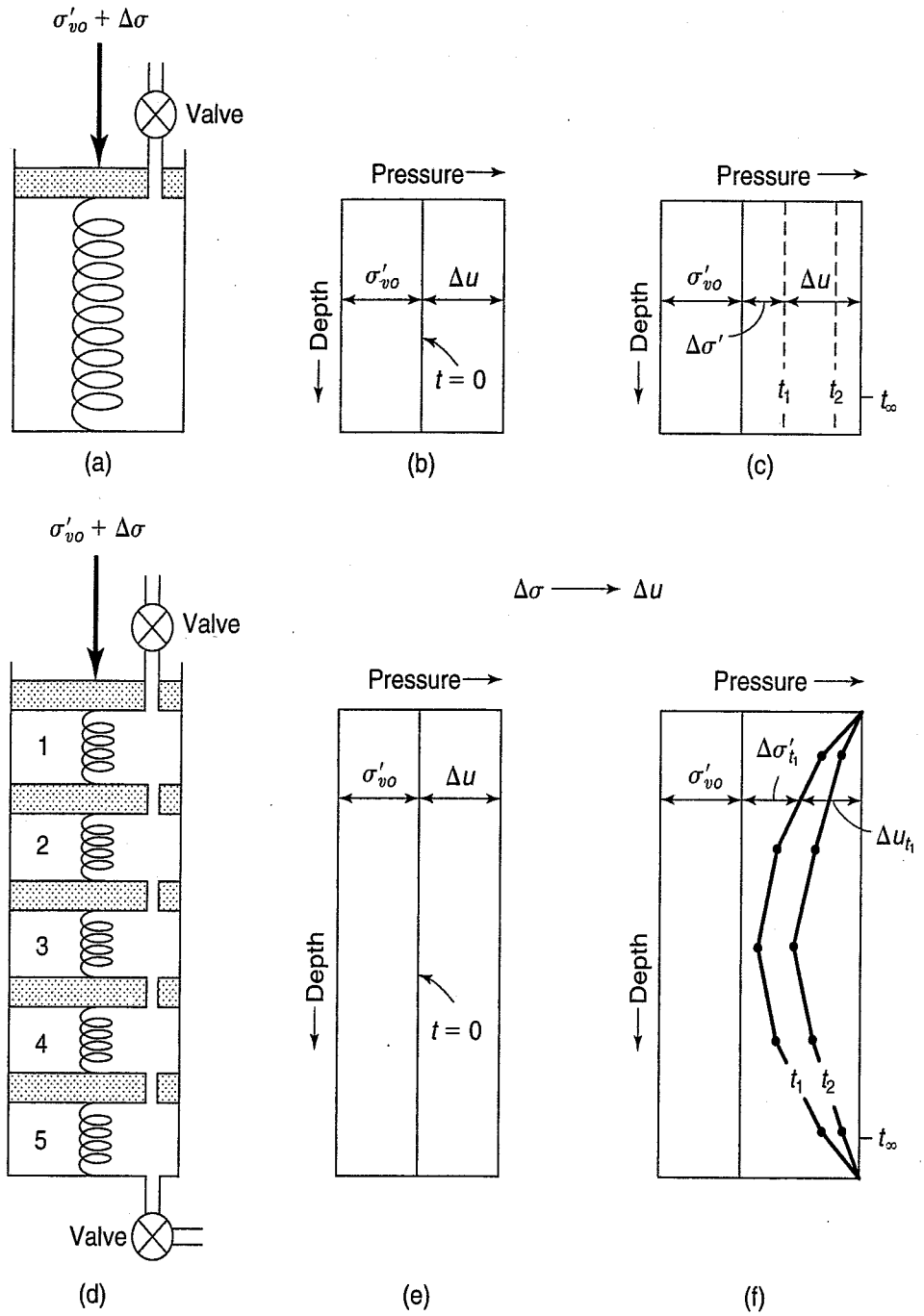

FIGURE 9.1 Spring analogy for consolidation: (a)–(c), model of a single soil layer; (d)–(f), model of multiple soil layers.

show the initial effective stress σ'_{vo} within the soil layer, and the corresponding induced pore water pressure Δu, due to the external stress on the pistons $\Delta\sigma$, in Fig. 9.1(e). Let us allow drainage to occur through each piston and valve so that we have both internal as well as top and bottom drainage. In order for the water to be squeezed out of cylinders 2, 3, and 4, some of the water in cylinders 1 and 5 must escape beforehand. Likewise, before the water can be squeezed out of the soil in cylinder 3, some of the water in cylinders 2 and 4 must be squeezed out first, and so on. Because all valves are open, upon application of the external stress $\Delta\sigma$, water will start to flow out immediately from the top and bottom cylinders. This will result in an immediate reduction of the excess pore water pressure and an increase in effective stress in cylinders 1 and 5, and so on. As shown in Fig. 9.1(f), with time the pore pressure isochrones move to the right, and they are segmented

lines because of the finite number of pistons and valves. With an infinite number of pistons, the isochrones would be smooth curves that rather accurately represent what is physically occurring with time in a consolidating soil deposit. At the center of a *doubly drained* layer, which is modeled by Figs. 9.1(d)–(f), it can be seen that the decrease in the induced pore water pressure, for example at t_1, is small compared to the change at the top and bottom of the layer. This is because the *drainage path* for the center cylinder is considerably longer than for cylinders 1 and 5. As a result it takes a longer time for the center of a doubly drained layer (or the bottom of a singly drained layer) to dissipate its excess pore pressure.

The flow of water out of the cylinders (soil voids) is physically due to the gradient i, which equals $h/l = (\Delta u/\rho_w g)/\Delta z$. The slope of the segmented isochrones in Fig. 9.1(f) is $\Delta u/\Delta z$. At the exact center of the clay layer the flow is zero, because the gradient $\Delta u/\Delta z$ is zero. At the ends, the gradient approaches infinity, and thus the flow is greatest right at the drainage surfaces.

The process just described is called *consolidation*. The amount of settlement the spring–piston system (or clay layer) experiences is directly related to how much water has squeezed out of the cylinders (or voids in the clay). How much water has squeezed out and thus the change in void ratio of the clay is in turn directly proportional to the amount of excess pore water pressure that has dissipated. Thus the *rate* of settlement is directly related to the *rate* of excess pore pressure dissipation. What we need in order to predict the rate of settlement of a foundation is an equation or theory that predicts the pore pressure and void ratio at any point in time and space in the consolidating clay layer. Then the change in thickness or settlement of the layer after any time of loading can be determined by integration of the equation over the thickness of the clay layer. The theory of consolidation most commonly used in soil mechanics is one-dimensional. It was first developed by Terzaghi in the 1920s, and its derivation and solution are summarized in the sections that follow.

9.3 TERZAGHI'S ONE-DIMENSIONAL CONSOLIDATION THEORY

In this section, we present the Terzaghi (1925) one-dimensional consolidation equation and discuss some of the assumptions necessary to derive it. A detailed derivation and the solution to the equation are given in Appendix B-2. In order to use the Terzaghi theory with some confidence, you need to understand its assumptions and therefore its limitations.

The compressible soil layer is assumed to be both homogeneous (same composition at all points) and completely saturated with water, and the mineral grains in the soil and the water in the pores are assumed to be incompressible. Darcy's law (Sec. 7.3) is considered to govern the egress of water from the soil pores, and usually both drainage and compression are assumed to be one-dimensional. Usually drainage is provided at both the top and bottom of the compressible layer, but it just as easily could be only at one surface. The Terzaghi theory is a *small strain* theory in that the applied stress increment is assumed to produce only small strains in the soil; therefore both the coefficient of compressibility a_v [Eq. (8.5)] and the Darcy coefficient of permeability, k, remain essentially constant during the consolidation process. If a_v is a constant over the increment of applied stress, then there is a *unique* relationship between the change in void ratio Δe, and the change in effective stress $\Delta\sigma'$. This implies also that there is *no secondary compression*; otherwise the relationship between Δe and $\Delta\sigma'$ would not be unique, by definition, since more than one void ratio value would be possible at a given $\Delta\sigma'$ at different times. (Recall that secondary compression is the change in void ratio that occurs with time at constant effective stress.)

The derivation of the Terzaghi equation considers the volume of water flowing out of a differential compressible soil element. From Darcy's law, we know the quantity of flow depends on the hydraulic gradient as well as on the permeability of the soil. The hydraulic gradient causing flow can be related to the excess pore water pressure in the element by $u/\rho_w g$. Since the water is assumed

incompressible, by continuity the volume change in the element must be the difference between flow in and out of the element in a differential time *dt*. This part of the equation can be written as

$$\frac{-k}{\rho_w g}\frac{\partial^2 u}{\partial z^2} dz\, dt$$

where z is the space or depth variable in the soil element. Everything else is as previously defined. Partial differentials must be used because u is a function of both the position z and time t.

The other part of the equation is obtained by relating the volume change or change in void ratio of the soil skeleton to the change in effective stress by means of the coefficient of compressibility a_v, which we determined in the consolidation test. (Thus a_v is really the stress-strain relationship or "modulus" of our soil.) From the effective stress principle, we can equate the change in effective stress to the change in pore pressure. In other words, as long as the total stress is constant, as the excess pore pressure dissipates with time, there is a concurrent increase in effective stress, or $\Delta\sigma' = -\Delta u$. As before, u is a function of both z and t. This half of the equation is usually written as

$$\frac{-a_v}{1 + e_o}\frac{\partial u}{\partial t} dt\, dz$$

Putting the two parts together, we obtain

$$\frac{-k}{\rho_w g}\frac{\partial^2 u}{\partial z^2} dz\, dt = \frac{-a_v}{1 + e_o}\frac{\partial u}{\partial t} dt\, dz \tag{9.1}$$

Rearranging, we obtain

$$c_v \frac{\partial^2 u}{\partial z^2} = \frac{\partial u}{\partial t} \tag{9.2}$$

where

$$c_v = \frac{k}{\rho_w g}\frac{1 + e_o}{a_v} \tag{9.3}$$

The coefficient c_v is called the *coefficient of consolidation*, because it contains the material properties that govern the consolidation process. If you perform a dimensional analysis of Eq. (9.3), you will find that c_v has dimensions of L^2T^{-1} or m^2/s.

Equation (9.2) is the *Terzaghi one-dimensional consolidation equation*. It could just as easily be written in three dimensions, but most of the time in engineering practice one-dimensional consolidation is assumed. Basically, the equation is a form of the diffusion equation from mathematical physics. Many physical diffusion phenomena are described by this equation—for example, heat flow in a solid body. The "diffusion constant" for the soil is the c_v. Note that we are referring to c_v as a constant. It really isn't, but we must assume that it is—i.e., that k, a_v, and e_o are constants—in order to make the equation linear and easily solvable.

So, how do we solve the Terzaghi consolidation equation? Just as we solve all other second-order partial differential equations with constant coefficients. There are a variety of ways, some mathematically exact and others only approximate. For example, Harr (1966) presents an approximate solution using the method of finite differences, as do Perloff and Baron (1976), among others. Later in this section we show you how to use finite differences to solve consolidation problems. We begin, though, with a mathematically rigorous solution developed by Terzaghi (1925a) of his own consolidation equation.

9.3.1 Classic Solution for the Terzaghi Consolidation Equation

A mathematically rigorous solution of Terzaghi (1925a) was refined and further developed by Terzaghi and Fröhlich (1936) in terms of a Fourier series expansion. Here we just give an outline of the solution, following Taylor (1948). See Appendix B.2 for the details.

First, the boundary and initial conditions for the case of one-dimensional consolidation are:

1. There is complete drainage at the top and bottom of the compressible layer.
2. The initial *excess* hydrostatic pressure $\Delta u = u_i$ is equal to the applied increment of stress at the boundary, $\Delta\sigma$.

We can write these boundary and initial conditions as follows:

$$\text{At } z = 0 \text{ and } z = 2H \rightarrow u = 0$$
$$\text{At } t = 0 \rightarrow \Delta u = u_i = \Delta\sigma = (\sigma_2' - \sigma_1')$$

We usually take the thickness of the consolidating layer to be $2H$, so that the *length of the longest drainage path* is equal to H or H_{dr}. Of course at $t = \infty$, $\Delta u = 0$, or complete dissipation of the excess pore pressure will have occurred.

Terzaghi (1925a) was obviously familiar with earlier work on heat transfer, and he adapted those closed-form solutions to the consolidation problem. The solution comes out in terms of a Fourier series expansion of the form

$$u = (\sigma_2' - \sigma_1') \sum_{n=0}^{\infty} f_1(Z) f_2(T) \tag{9.4}$$

where Z and T are dimensionless parameters (see also Taylor, 1948). The first term, Z, is a geometry parameter, and it is equal to z/H, or the actual depth below the top of the layer divided by the drainage distance. The second term, T, is known as the *time factor*, and it is related to the coefficient of consolidation c_v by

$$T = c_v \frac{t}{H_{dr}^2} \tag{9.5}$$

where t = time, and

H_{dr} = length of the longest drainage path.

We have already mentioned that c_v has dimensions of L^2T^{-1} or units of m^2/s (or equivalent).

From Eq. (9.3), the time factor can also be written as

$$T = \frac{k(1 + e_o)}{a_v \rho_w g} \frac{t}{H_{dr}^2} \tag{9.6}$$

Note that t has the same time units as k. That is, if k is in centimetres per second, then t must be in seconds. The drainage path for double drainage would be equal to half the thickness H of the clay layer, or $2H/2 = H_{dr}$. If we had only a singly drained layer, the drainage path would still be H_{dr}, but it would be equal to the entire thickness of the layer.

The progress of consolidation after some time t and at any depth z in the consolidating layer can be related to the void ratio at that time and the final change in void ratio. This relationship is called the *consolidation ratio*, expressed as

$$U_z = \frac{e_1 - e}{e_1 - e_2} \tag{9.7}$$

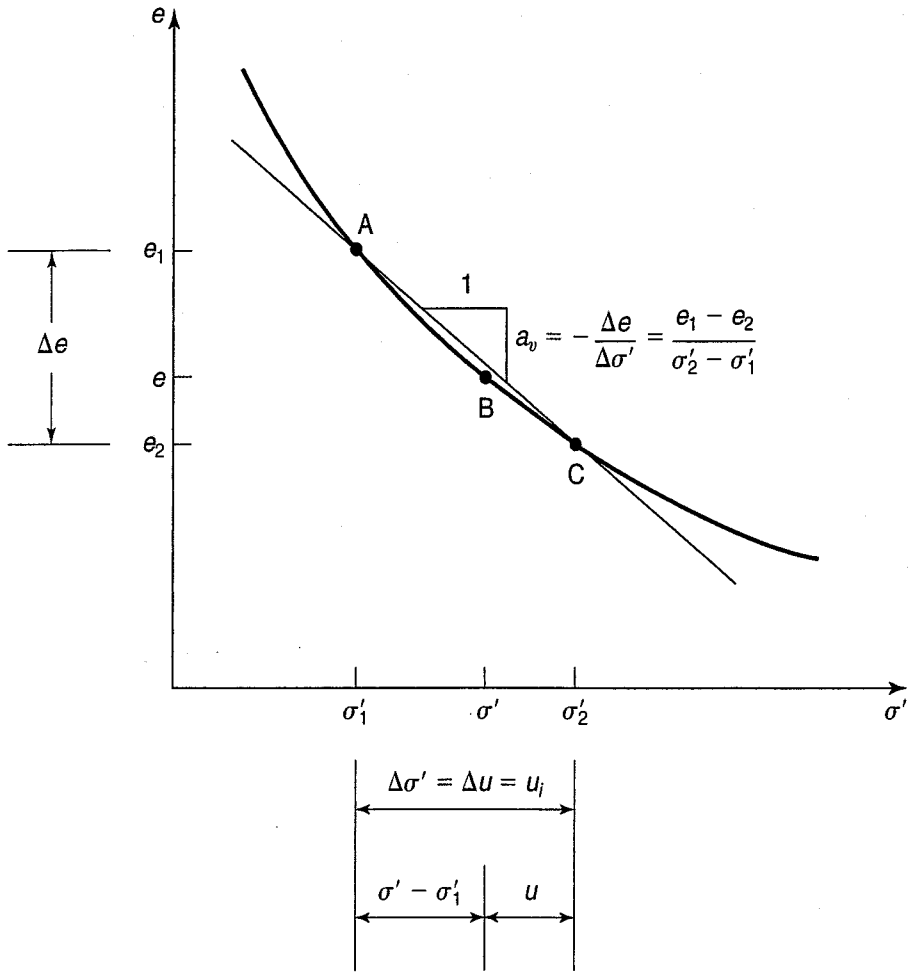

FIGURE 9.2 Laboratory compression curve.

where e is some intermediate void ratio, as shown on Fig. 9.2. Note that in Fig. 9.2, $\sigma' - \sigma'_1 = (\sigma'_2 - \sigma'_1) - u = u_i - u$. What we are looking at graphically in that figure is the ratio of ordinates corresponding to AB and AC. In terms of stresses and pore pressures, Eq. (9.7) becomes

$$U_z = \frac{\sigma' - \sigma'_1}{\sigma'_2 - \sigma'_1} = \frac{\sigma' - \sigma'_1}{\Delta\sigma'} = \frac{u_i - u}{u_i} = 1 - \frac{u}{u_i} \tag{9.8}$$

where σ' and u are intermediate values corresponding to e in Eq. (9.7), and u_i is the initial *excess* pore pressure induced by the applied stress $\Delta\sigma'$. You should satisfy yourself that these equations are correct from the relationships shown in Fig. 9.2 and from $\Delta\sigma' = -\Delta u$. (See also Appendix B.2.)

From Eqs. (9.7) and (9.8), it is evident that U_z is zero at the start of loading, and it gradually increases to 1 (or 100%) as the void ratio decreases from e_1 to e_2. At the same time, of course, as long as the total stress remains constant, the effective stress increases from σ'_1 to σ'_2 as the excess hydrostatic stress (pore water pressure) dissipates from u_i to zero. The consolidation ratio U_z is sometimes called the *degree or percent consolidation*, and it represents conditions *at a point* in the consolidating layer. We can now put our solution for u in Eq. (9.4) in terms of the consolidation ratio, Eq. (9.8), or

$$U_z = 1 - \sum_{n=0}^{\infty} f_1(Z) f_2(T) \tag{9.9}$$

The solution to this equation is shown graphically in Fig. 9.3 in terms of the dimensionless parameters already defined. The tedious calculations involved in solving Eq. (9.9) are no longer necessary.

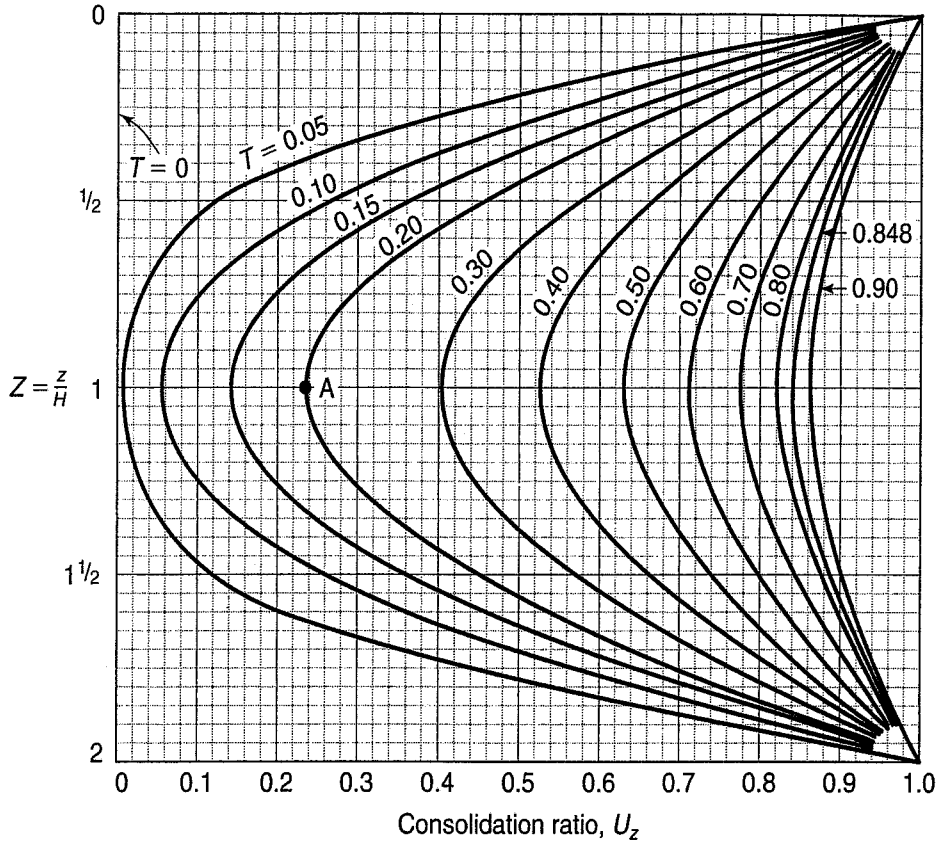

FIGURE 9.3 Consolidation for any location and time factor in a doubly drained layer (after Taylor, 1948).

From Fig. 9.3 it is possible to find the amount or degree of consolidation (and therefore u and σ') for any real time after the start of loading and at any point in the consolidating layer. All you need to know is the c_v for the particular soil deposit, the total thickness of the layer, and boundary drainage conditions. With these items, the time factor T can be calculated from Eq. (9.5). It is applicable to any one-dimensional loading situation where the soil properties can be assumed to be the same throughout the compressible layer.

Figure 9.3 also is a picture of the *progress of consolidation*. The *isochrones* (lines of constant T) in Fig. 9.3 represent the degree or percent consolidation for a given time factor throughout the compressible layer. For example, the percent consolidation at midheight of a doubly drained layer (total thickness = $2H$) for a time factor equal to 0.2 is approximately 23% (see point A in Fig. 9.3). At the same time (and time factor) at other locations within the soil layer, however, the degree of consolidation is different. At 25% of the depth, for example, $z/H = 1/2$ and $U_z = 44\%$. Similarly, near the drainage surfaces at $z/H = 0.1$, for the same time factor, because the gradients are much higher, the clay is already 86% consolidated, which means that at that depth and time, 86% of the original excess pore pressure has dissipated and the effective stress has increased by a corresponding amount.

Example 9.1

Given:

A 12 m thick layer of Chicago clay is *doubly drained.* (This means that a very pervious layer compared to the clay exists on top of and under the 12 m clay layer.) The coefficient of consolidation $c_v = 8.0 \times 10^{-8}$ m^2/s.

Required:

Find the degree or percent consolidation for the clay 5 yr after loading at depths of 3, 6, 9, and 12 m.

Solution: First, compute the time factor. From Eq. (9.5),

$$T = \frac{c_v t}{H_{dr}^2}$$
$$= \frac{8.0 \times 10^{-8}\ \text{m}^2/\text{s}(3.1536 \times 10^7\ \text{s/yr})(5\ \text{yr})}{(6)^2\ \text{m}^2} = 0.35$$

Note that $2H = 12$ m and $H_{dr} = 6$ m, since there is double drainage.

Next, from Fig. 9.3 we obtain (by interpolation) for $T = 0.35$:

At $z = 3$ m,	$z/H = 0.50$,	$U_z = 61\%$
At $z = 6$ m,	$z/H = 1.0$,	$U_z = 46\%$
At $z = 9$ m,	$z/H = 1.50$,	$U_z = 61\%$
At $z = 12$ m,	$z/H = 2.0$,	$U_z = 100\%$

Example 9.2

Given:

The soil conditions of Example 9.1.

Required:

If the structure applied an average vertical stress increase of 100 kPa to the clay layer, estimate the excess pore water pressure remaining in the clay after 5 yr for the depths in the clay layer of 3, 6, 9, and 12 m.

Solution: Assuming one-dimensional loading, the induced excess pore water pressure at the beginning of consolidation is 100 kPa. From Eq. (9.8),

$$U_z = 1 - \frac{u}{u_i}$$

or

$$u = u_i(1 - U_z)$$

From the solution in Example 9.1 we obtain:

At $z = 3$ m,	$U_z = 61\%$,	$u = 39$ kPa
At $z = 6$ m,	$U_z = 46\%$,	$u = 54$ kPa
At $z = 9$ m,	$U_z = 61\%$,	$u = 39$ kPa
At $z = 12$ m,	$U_z = 100\%$,	$u = 0$ kPa

Figure Ex. 9.2 shows these values versus depth. Note that they are *excess* pore pressures—that is, they are above the hydrostatic water pressure.

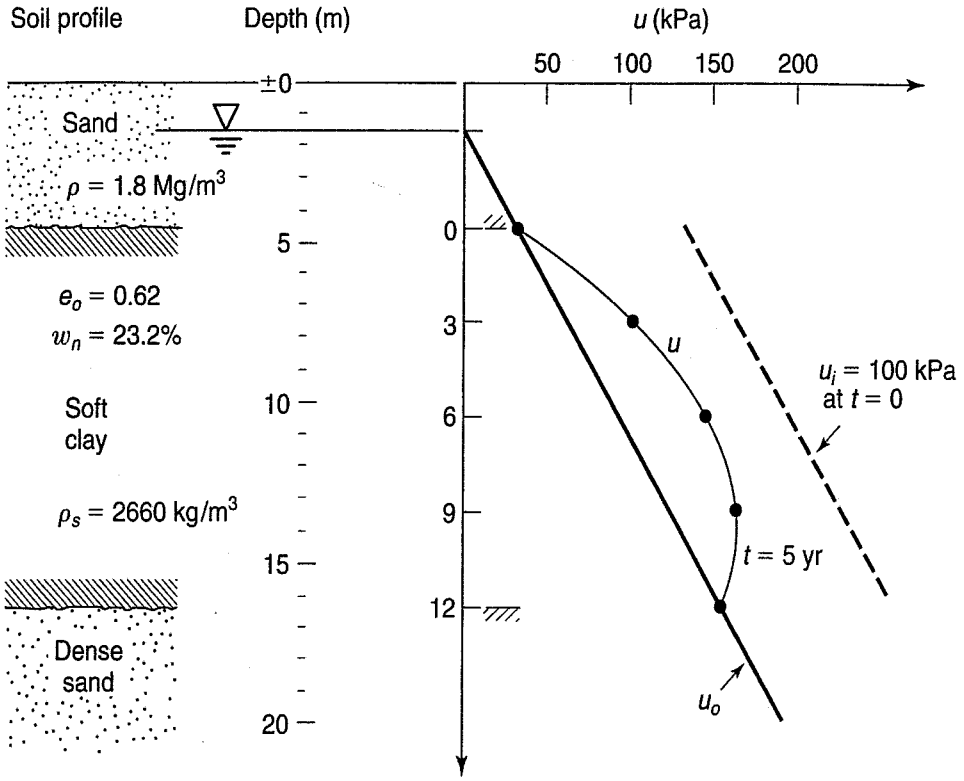

FIGURE Ex. 9.2

In most cases, we are not interested in how much consolidation has occurred at a given point in a layer. Of more practical interest is the *average degree* or *percent consolidation* of the entire layer. This value, denoted by U or U_{avg}, is a measure of how much the entire layer has consolidated, and thus it can be directly related to the *total settlement* of the layer at a given time after loading. Note that U can be expressed as either a decimal or a percentage.

To obtain the average degree of consolidation over the entire layer corresponding to a given time factor we have to find the area under the T curve of Fig. 9.3. (Actually we obtain the area outside the T curve, as shown in Fig. 9.4.) How the integration is done mathematically is shown in Appendix B.2. Table 9.1 presents the results of the integration for the case where a *linear* distribution of excess pore water pressure is assumed.

The results in Table 9.1 are shown graphically in Fig. 9.5. In Fig. 9.5(a) the relationship is shown arithmetically, whereas in Fig. 9.5(b) the relationship between U and T is shown semilogarithmically. Another form of the relationship is found in Fig. 9.5(c), where U is plotted versus $\sqrt{T}$. As discussed in the next section, Figs. 9.5(b) and 9.5(c) show certain characteristics of the theoretical U–T relationship to better advantage than Fig. 9.5(a). Note that as T becomes very large, U asymptotically approaches 100%. This means that, theoretically, consolidation never stops but continues indefinitely. It should also be pointed out that the solution for U versus T is dimensionless and applies to all types of problems where $\Delta\sigma = \Delta u$ varies *linearly* with depth.

Solutions for cases where the initial pore pressure distribution is sinusoidal, half sine, and triangular are presented by Taylor (1948) and Leonards (1962), and the results in terms of U versus T for these various initial pore pressure distributions are actually quite similar. When you consider the many assumptions in the Terzaghi theory and the real possibility of drainage that is not just one-dimensional, a uniform linear initial distribution of pore pressure is not as inaccurate as you might think. That is why it is the only one we present. Shortly, we will introduce a finite difference solution to problems with unusual initial pore pressure distributions.

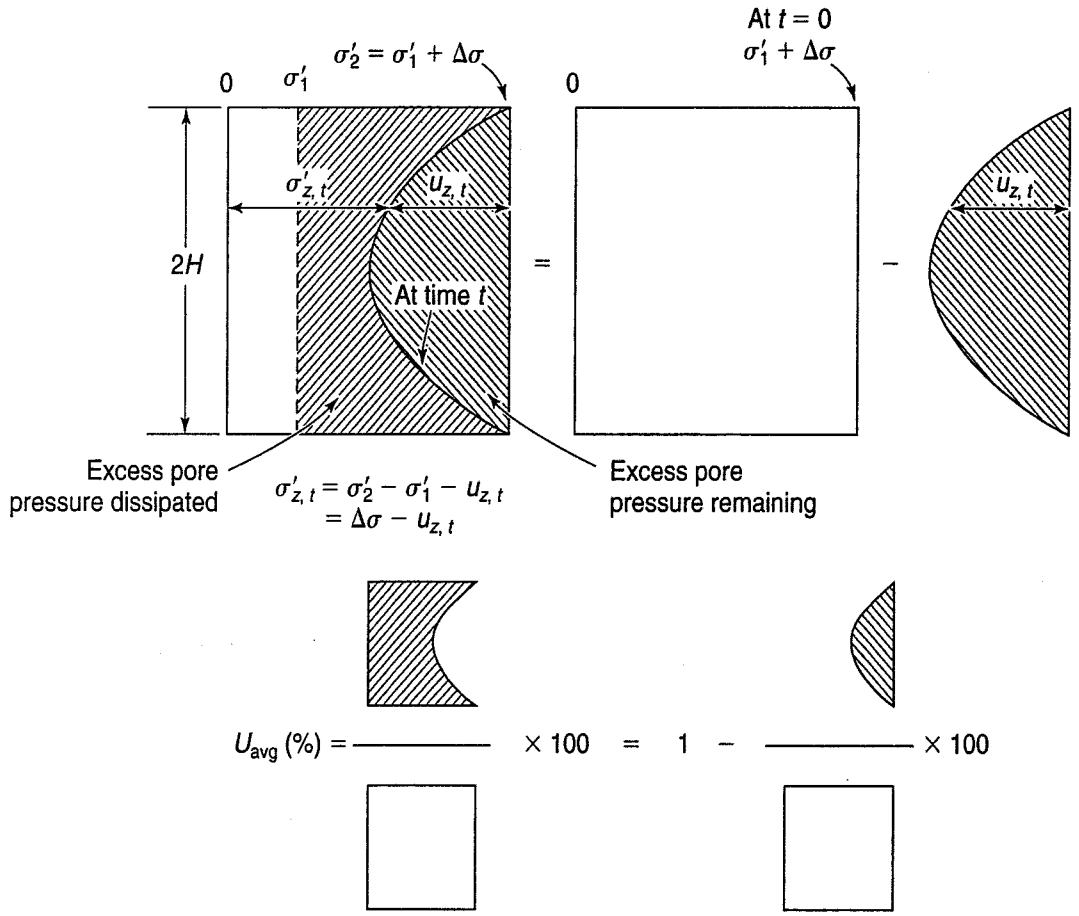

FIGURE 9.4 Average degree of consolidation, U_{avg}, defined.

TABLE 9.1 Values of U_{avg} versus T from Fig. 9.5

U_{avg}	T
0.1	0.008
0.2	0.031
0.3	0.071
0.4	0.126
0.5	0.197
0.6	0.287
0.7	0.403
0.8	0.567
0.9	0.848
0.95	1.163
1.0	∞

Casagrande (1938) and Taylor (1948) provide the following useful approximations:
For $U < 60\%$,

$$T = \frac{\pi}{4}U^2 = \frac{\pi}{4}\left(\frac{U\%}{100}\right)^2 \tag{9.10}$$

For $U > 60\%$,

$$T = 1.781 - 0.933\log(100 - U\%) \tag{9.11}$$

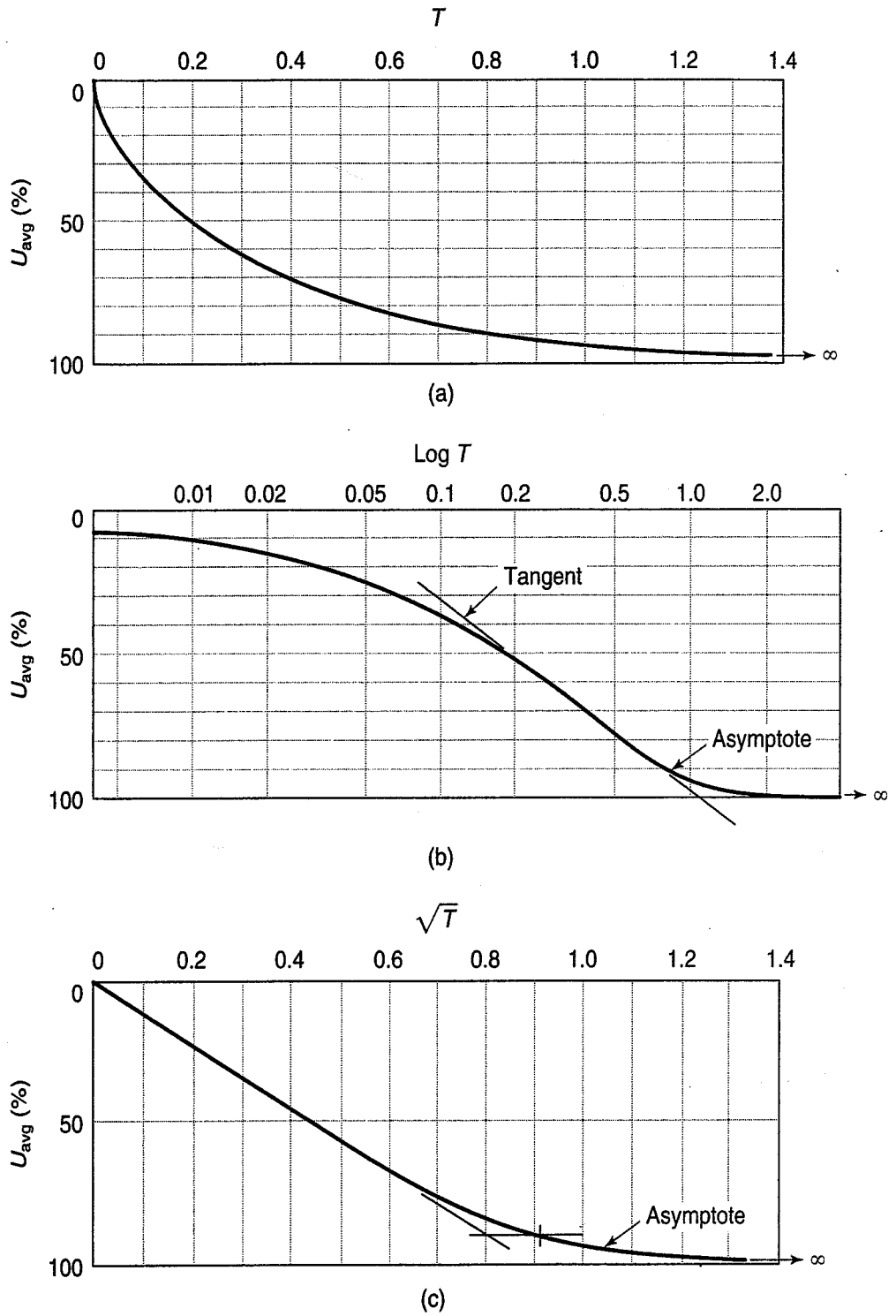

FIGURE 9.5 U_{avg} versus T: (a) arithmetic scale; (b) log scale; (c) square root scale.

Example 9.3

Given:

$T = 0.05$ for a compressible clay deposit.

Required:

Average degree of consolidation and the percent consolidation at the center and at $z/H = 0.1$.

Solution: From Table 9.1 and Fig. 9.5, $U_{avg} = 26\%$. Therefore the clay is 26% consolidated, on average. From Fig. 9.3 you can see that the center of the layer is less than 0.5% consolidated, while at the "10%" depth ($z/H = 0.1$) the clay is 73% consolidated. But, *on average* throughout the layer, the clay is 26% consolidated.

What does the average consolidation mean in terms of settlements? U_{avg} can be expressed as

$$U_{avg} = \frac{s(t)}{s_c} \tag{9.12}$$

where $s(t)$ is the settlement at any time, and s_c is the final or ultimate consolidation (primary) settlement at $t = \infty$.

Example 9.4

Given:

The data of Example 9.3.

Required:

Find the settlement when U_{avg} is 26%, if the final consolidation settlement is 1 m.

Solution: From Eq. (9.12), $s(t) = U_{avg}(s_c)$. Therefore

$$s(t) = 26\%(1\text{ m}) = 0.26\text{ m}$$

Example 9.5

Given:

The soil profile and properties of Examples 9.1 and 9.2. The stress increase in the clay layer is 100 kPa.

Required:

Compute the time required for the clay layer to settle 0.25 m.

Solution: To compute the average degree of consolidation, the final consolidation settlement s_c, must be estimated as we did in Chapter 8. From Fig. Ex. 9.2, $H_o = 12$ m and $e_o = 0.62$. For Chicago clay, the value of C_c may be found using the last relationship in Table 8.3, $C_c = 0.01 \times (w_n = 23.2\%) = 0.23$. C_c may also be found from the second expression, knowing the initial void ratio, solving for $C_{c\varepsilon}$ and dividing by $(1 + e_o)$, giving $C_c = 0.22$, or about the same. Determine ρ for the soft clay and calculate σ'_{vo} at the middepth of layer from Eqs. (6.14c) and (6.15). Assume the clay is normally consolidated. Use techniques from Chapter 2 to compute ρ_{clay}. So,

$$\sigma'_{vo} = \rho_{sand} g z_1 + (\rho_{sand} - \rho_w) g z_2 + (\rho_{clay} - \rho_w) g z_3$$

$$\sigma'_{vo} = 1.8\text{ Mg/m}^3 \times 9.8\text{ m/s}^2 \times 1.5\text{ m} + (1.8 - 1)\text{ Mg/m}^3 \times 9.8\text{ m/s}^2 \times 3\text{ m} + (2.02 - 1)\text{ Mg/m}^3 \times 9.8\text{ m/s}^2 \times 6\text{ m}$$

$$= 110\text{ kPa}$$

From Eq. (8.10),

$$s_c = 0.23\frac{12\text{ m}}{1 + 0.62}\log\frac{110\text{ kPa} + 100\text{ kPa}}{110\text{ kPa}} = 0.48\text{ m}$$

The average degree of consolidation U_{avg} when the clay layer settles 0.25 m is [Eq. (9.12)]:

$$U_{avg} = \frac{s(t)}{s_c} = \frac{0.25\text{ m}}{0.48\text{ m}} = 0.52, \text{ or } 52\%$$

To obtain T we can use either Table 9.1 or Fig. 9.5. Or, since $U_{avg} < 60\%$, we can use Eq. (9.10):

$$T = \frac{\pi}{4}(0.52)^2 = 0.212$$

From Eq. (9.5), $t = TH_{dr}^2/c_v$, where $H_{dr} = 6$ m for double drainage; or

$$t = \frac{0.212 \times (6\text{ m})^2}{8 \times 10^{-8}\text{ m}^2/\text{s} \times 3.1536 \times 10^7\text{ s/yr}}$$
$$= 3.0\text{ yr}$$

Example 9.6

Given:

The data of Examples 9.1 and 9.5.

Required:

How much time would be required for a settlement of 0.25 m to occur if the clay layer were singly drained?

Solution: Use Eq. (9.5) directly

$$c_v = 8 \times 10^{-8}\text{ m}^2/\text{s} \times 3.1536 \times 10^7\text{ s/yr} = 2.523\text{ m}^2/\text{yr}$$
$$t = \frac{TH_{dr}^2}{c_v}$$

where $H_{dr} = 12$ m for single drainage

$$t = \frac{0.212 \times (12\text{ m})^2}{2.523\text{ m}^2/\text{yr}} = 12.1\text{ yr}$$

or *four times as long* as with double drainage.

Example 9.7

Given:

A 10 m thick clay layer with *single* drainage settles 9 cm in 3.5 yr. The coefficient of consolidation for this clay was found to be 0.544×10^{-2} cm^2/s.

Required:

Compute the ultimate consolidation settlement, and find out how long it will take to settle to 90% of this amount.

Solution: From Eq. (9.5) solve for T:

$$T = \frac{tc_v}{H^2}$$

$$= \frac{3.5\text{ yr}\,(0.544 \times 10^{-2})\,\text{cm}^2}{(100\,\text{m}^2)\,\text{s}}\left(\frac{1\,\text{m}^2}{10\,000\,\text{cm}^2}\right)\left(3.1536 \times 10^7 \frac{\text{s}}{\text{yr}}\right)$$

$$= 0.6$$

From Table 9.1 we see that the average degree of consolidation is between 0.8 and 0.9. Therefore we can use either Eq. (9.11) or Fig. 9.5(a), or we can interpolate from Table 9.1. Using Eq. (9.11), we have

$$0.6 = 1.781 - 0.933 \log(100 - U\%)$$

$$1.27 = \log(100 - U\%)$$

or

$$U = 81.56\%, \text{ or } 82\%$$

Thus if 9 cm of settlement represents 82% of the total settlement, then the total consolidation settlement is [Eq. (9.12)]:

$$s_c = \frac{s(t)}{U_{\text{avg}}} = \frac{9\text{ cm}}{0.82} = 11\text{ cm}$$

For the time for 90% settlement to occur, find $T = 0.848$ for $U_{\text{avg}} = 0.9$, from Table 9.1. Using Eq. (9.5) and solving for t, we find that:

$$t = \frac{TH_{\text{dr}}^2}{c_v} = \frac{0.848\,(10\text{ m})^2}{0.544 \times 10^{-2}\,\text{cm}^2/\text{s}} \frac{10\,000\,\text{cm}^2}{\text{m}^2}$$

$$= 1.559 \times 10^8\,\text{s}\,\frac{\text{yr}}{3.1536 \times 10^7\,\text{s}}$$

$$= 4.94\text{ yr}$$

Example 9.8

Given:

The data of Example 9.7.

Required:

Find the variation in the degree of consolidation throughout the layer when $t = 3.5$ yr.

Solution: When $t = 3.5$ yr, the corresponding time factor $= 0.6$, from Example 9.7. Find the curve for $T = 0.6$ in Fig. 9.3. (For a layer with single drainage, we use the top half or bottom half, depending on where the layer is drained. Assume for this problem that the layer is drained at the *top*.) The curve

for $T = 0.6$ represents the degree of consolidation at any depth z. Using Eq. (9.5), we find that the $T = 0.6$ isochrone shows the variation of U_z for $t = 3.5$ yr. It can be seen that at the bottom of the layer, where $z/H = 1, U_z = 71\%$. At midheight of the 10 m thick layer, where $z/H = 0.5, U_z = 79.5\%$. Thus the degree of consolidation varies through the depth of the clay layer, but the *average* degree of consolidation for the entire layer is 82% (Example 9.7). Another interesting point about Fig. 9.3 is that the area to the left of the curve $T = 0.6$ represents 82% of the area of the entire graph, $2H$ versus U_z, whereas the area to the right of the curve $T = 0.6$ represents 18%, or the amount of consolidation yet to take place. (See also Fig. 9.4.)

In the event you have a problem with several compressible layers with different permeabilities and coefficients of consolidation, or if you find intermediate drainage layers in the compressible stratum, then the average degree of consolidation of the entire stratum U_T is

$$U_T = \frac{1}{s_c}(U_1 s_{c1} + U_2 s_{c2} + \cdots + U_n s_{cn}) \tag{9.13}$$

where $U_1, U_2, \ldots, U_n$ are the average degrees of consolidation of each layer, and $s_{c1}, s_{c2}, \ldots, s_{cn}$ are the consolidation settlements of each layer. The settlement s_c is, of course, the consolidation settlement of all the layers.

If two layers are next to each other, but they are both fine grained and have different permeability coefficients, the situation is called *impeded drainage*, because one layer might impede the dissipation of pore pressure of the second. The total settlement will be the same, but the time rate of consolidation will be different, and you need to calculate the time rate of consolidation using a method proposed by Gray (1945). This type of situation might fool you, for example, in cases where a *preload* is placed on the ground surface to precompress or preconsolidate a compressible layer. Upon removal of the surcharge load, some of the soil nearest the true drainage layer will have been preconsolidated to a lower void ratio. As a result, its permeability will be lower as well, hence it will impede the drainage when the building load is placed on the ground. It is a concern only in terms of how fast the structure will settle.

9.3.2 Finite Difference Solution for the Terzaghi Consolidation Equation

Finite differences is a numerical method for the solution to the Terzaghi consolidation equation (Harr, 1966). Although the solution is only approximate, it is very useful for evaluating the time rate of consolidation, because the calculations are readily performed with a spreadsheet. Here we summarize the elegant presentation by Perloff and Baron (1976). Refer to the original presentation for all the grizzly details.

To start our discussion, refer to Fig. 9.6, which illustrates the reduction of *excess* pore pressure with time along with the simultaneous increase of effective stress with time. The pore water pressure is eventually transferred to the soil skeleton. At $t = 0$, $\Delta u = \Delta\sigma$ and $\Delta\sigma' = 0$. When $t = \infty$, $\Delta u = 0$ and $\Delta\sigma' = \Delta\sigma$.

The Δu results from some loading on the soil, as shown in Fig. 9.7(a), a duplicate of Fig. 9.1(b). It is convenient for the following discussion if we modify the initial distribution of $\Delta u(z)$ to that shown in Fig. 9.7(b). Remember that Δu represents the *excess* pore water pressure that will dissipate with time. As the excess pore pressure reduces, there is a concurrent corresponding increase in effective stress. Now consider just the excess pore pressure at time $t = 0$, as shown in Fig. 9.7(c) (the figure has simply been rotated to an isometric view).

As time increases, the pore pressure will decrease with certain time increments of Δt. With time, the initial pore pressure distribution curve of Fig. 9.7(c) will create a *surface*, as shown in Fig. 9.8 in 3-D space. This surface is the solution to the one-dimensional consolidation equation [Eq. (9.2)]!

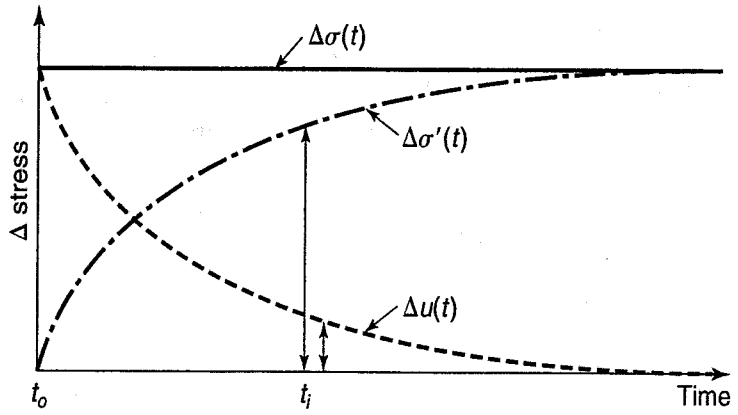

FIGURE 9.6 Stress transfer with time (C. W. Lovell, personal communication, 1988).

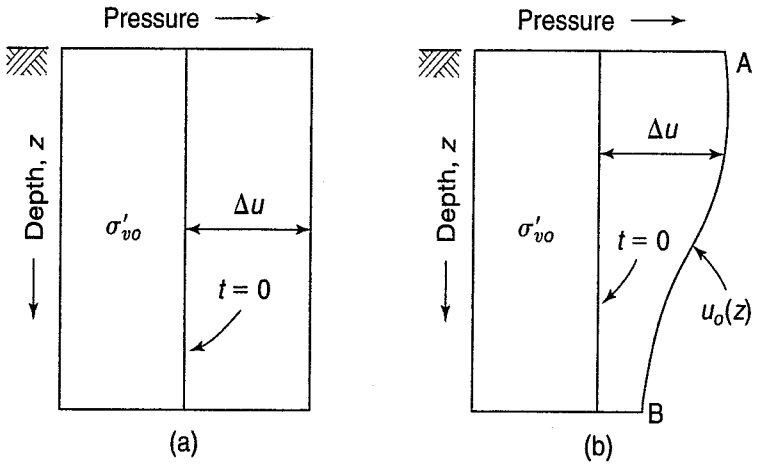

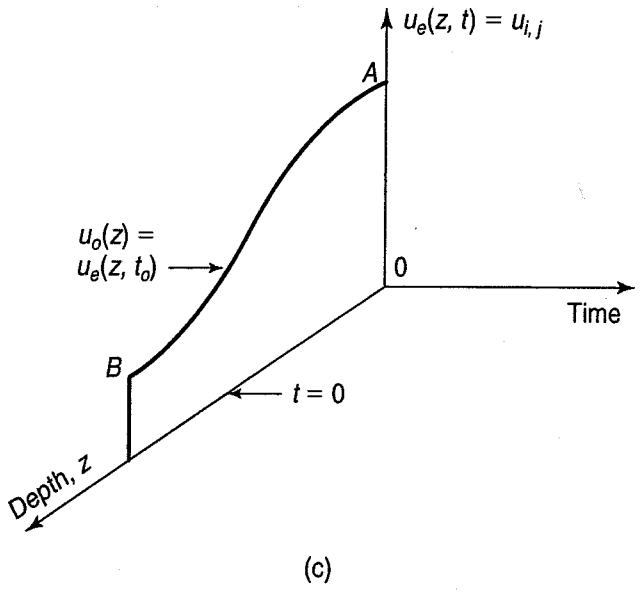

FIGURE 9.7 Development of Δu or u_e, excess pore water pressure with depth: (a) initial conditions; (b) modification of initial conditions; (c) isometric view of (b) showing excess pore pressure only.

The horizontal plane is time at some elevation in the ground. The vertical plane is depth within the compressible layer, while perpendicular to that is the excess pore pressure, $u_e(z, t)$. For any given time and depth, there is a single u_e, and when all of these values are known, the solution *surface* results. At any time, t_j, $u_e(z)$ defines the surface, which is an *isochrone*. The tangent to the isochrone is the partial derivative of $u_e(z, t)$ as shown in Fig. 9.9(a),

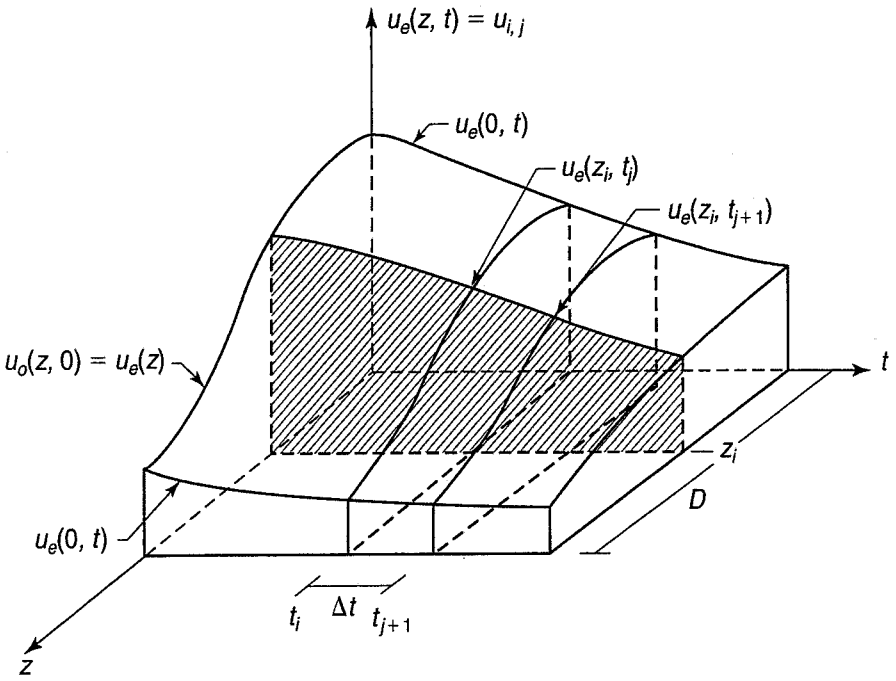

FIGURE 9.8 Surface representation of the solution for the one-dimensional consolidation equation (after Perloff and Baron, 1976).

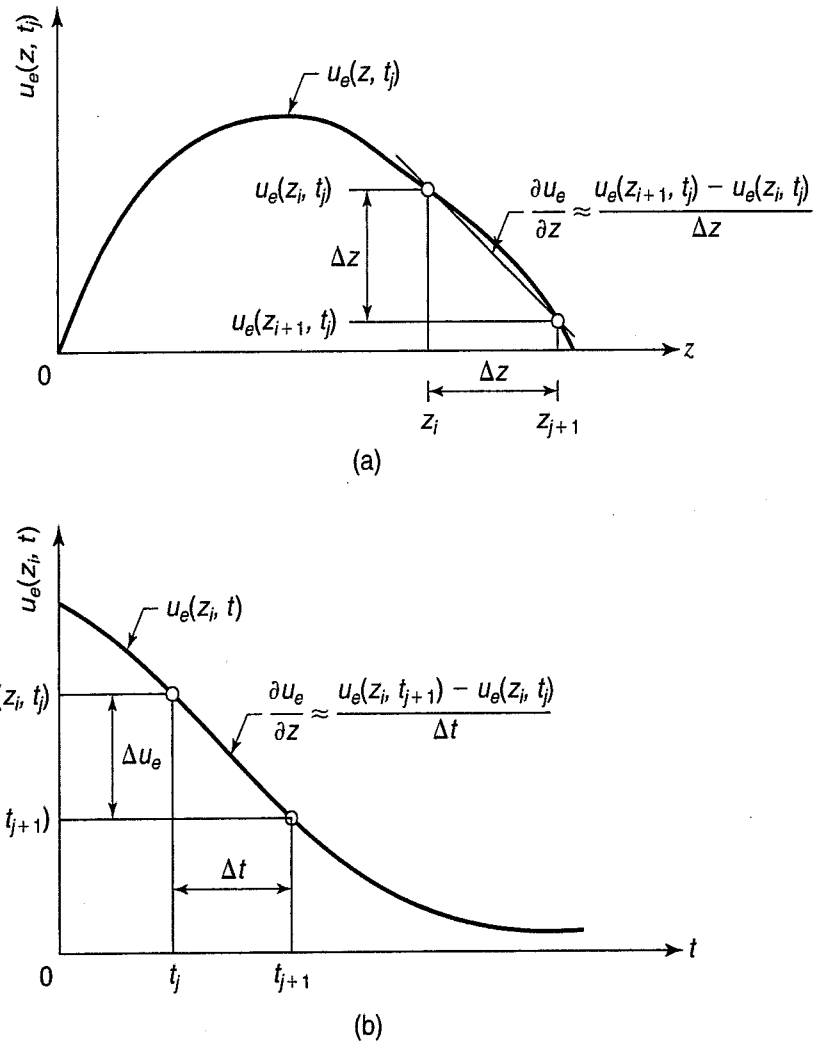

FIGURE 9.9 Definitions of partial derivatives as finite differences: (a) secant to the isochrone at time t_j; (b) secant to the excess pore pressure function at depth z_i (after Perloff and Baron, 1976).

and is given by

$$\frac{\partial u_e}{\partial z} = \lim_{\Delta z \to 0} \frac{u_e(z + \Delta z, t_j) - u_e(z, t_j)}{\Delta z} \tag{9.14}$$

Approximating the partial derivative by a secant between two points of the function, we obtain

$$\begin{aligned} \frac{\partial u_e}{\partial z} &\approx \frac{u_e(z + \Delta z, t_j) - u_e(z, t_j)}{\Delta z} \\ &= \frac{u_e(z_{i+1}, t_j) - u_e(z_i, t_j)}{\Delta z} \end{aligned} \tag{9.15}$$

Note that z_i and z_{i+1} are the two depths separated by the distance Δz. This approximation is known as a *finite difference*. We need to go one more step to obtain the left side of Eq. (9.2). We do that by noting

$$\frac{\partial^2 u_e}{\partial z^2} = \frac{\partial}{\partial z}\left(\frac{\partial u_e}{\partial z}\right) \tag{9.16}$$

Approximating the second partial derivative, we obtain

$$\frac{\partial^2 u_e}{\partial z^2} \cong \frac{u_e(z_{i+1}, t_j) - 2u_e(z_i, t_j) + u_e(z_{i-1}, t_j)}{\Delta z^2} \tag{9.17}$$

Now consider the plane of $u_e(z, t)$ as shown in Fig. 9.9(b), where the excess pore pressure at any depth z changes with time. The tangent to this surface is the partial derivative $\partial u/\partial t$ at some depth, z_i. Approximating this derivative by a secant, we obtain

$$\frac{\partial u}{\partial t} \cong \frac{u_e(z_i, t_{j+1}) - u_e(z_i, t_j)}{\Delta t} \tag{9.18}$$

Substituting Eqs. (9.17) and (9.18) into Eq. (9.2), and being more concise, we obtain

$$c_v \frac{(u_{e_{i+1,j}} - 2u_{e_{i,j}} + u_{e_{i=1,j}})}{\Delta z^2} = \frac{(u_{e_{i,j+1}} - u_{e_{i,j}})}{\Delta t} \tag{9.19}$$

Rearranging as only mathematicians can do, we uncover the *recurrence formula*,

$$u_{e_{i,j+1}} = \alpha u_{e_{i+1,j}} + (1 - 2\alpha)u_{e_{i,j}} + \alpha u_{e_{i-1,j}} \tag{9.20}$$

in which

$$\alpha = \frac{c_v \Delta t}{(\Delta z)^2} \tag{9.21}$$

Perloff and Baron (1976) then go on to describe the boundary conditions for which the recurrence formula will be stable mathematically. When $\alpha = 1/2$, the formulations are stable, and the approximate solution converges to the exact solution when Δz and Δt each approach zero. With $\alpha = 1/2$, the middle term of Eq. (9.20) drops out, and the excess pore pressure in the next time increment, $j + 1$, is merely the average of the adjacent points at time j. Review Fig. 9.10 to see this concept presented graphically.

Note that if you set $\alpha = 1/6$, a more accurate solution is obtained, one that can be readily programmed with a spreadsheet. The following example illustrates use of this method.

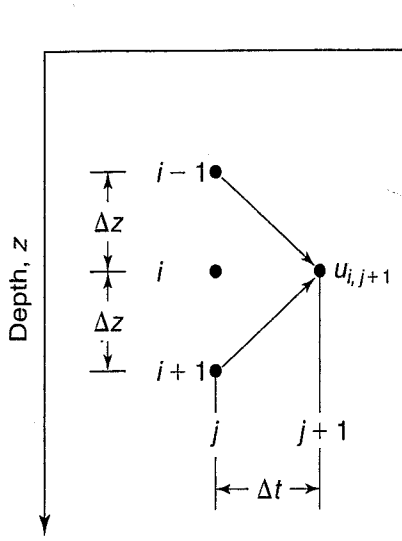

FIGURE 9.10 Graphical representation of Eq. (9.20) with $\alpha = 1/2$.

Example 9.9

Given:

Granular material 7 m thick overlies a soft compressible layer that is 14 m thick. Below the compressible material is a hard till. Figure Ex. 9.9a gives the soil profile, soil properties, and the distributions of total stress and static pore water pressure with depth. Figure Ex. 9.9b shows the effective stress with depth plus the excess pore pressure within the compressible layer due to the external loading (on top of the granular layer). The coefficient of consolidation (c_v) is 9.3 m^2/min, obtained from a consolidation test on the soft material.

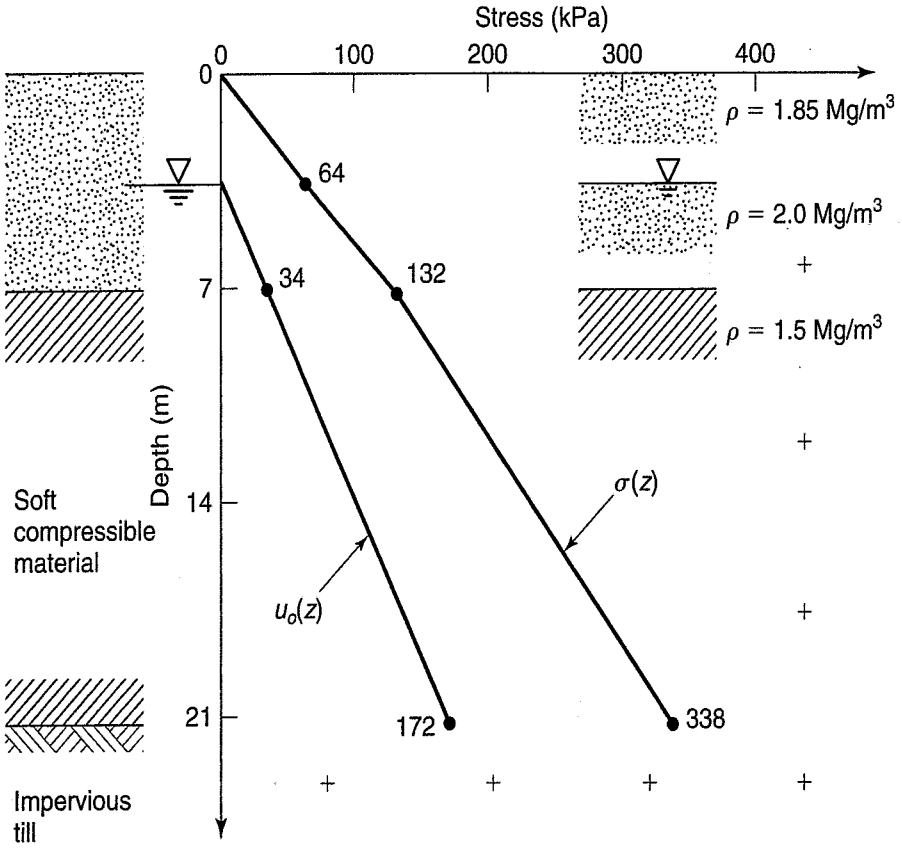

FIGURE Ex. 9.9a

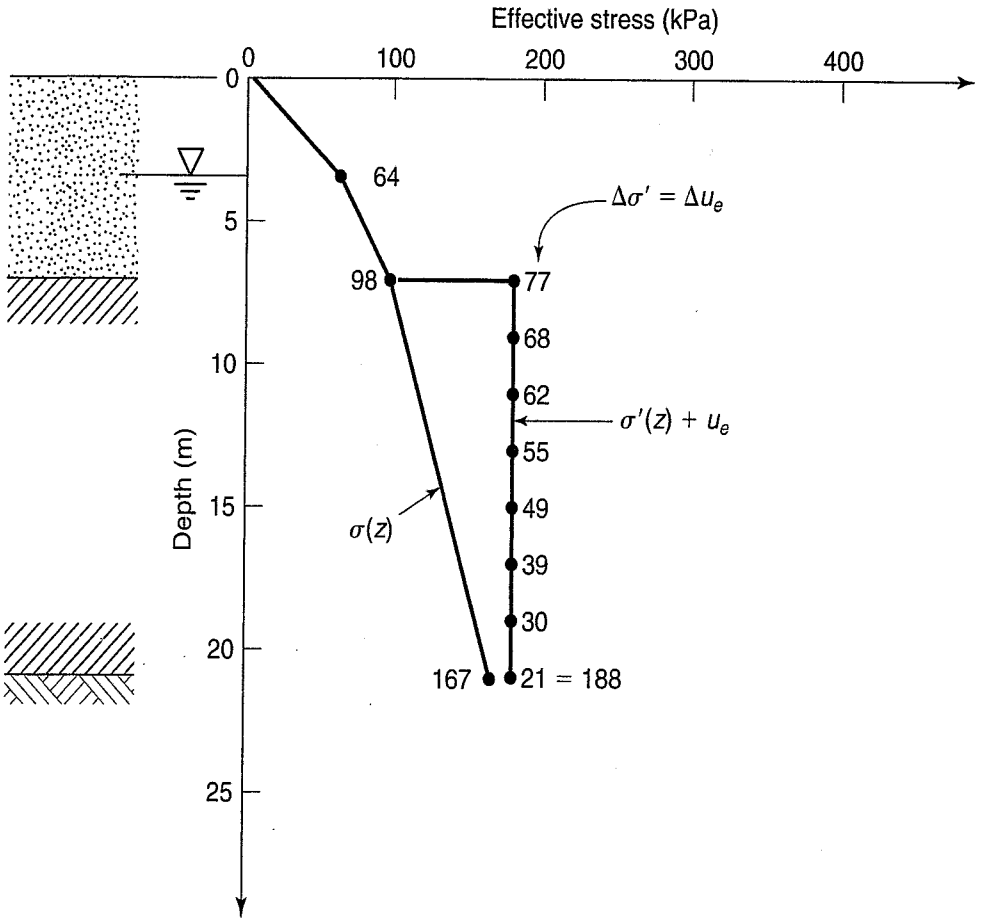

FIGURE Ex. 9.9b

Required:

Evaluate the pore pressure dissipation with time until about 5 yr have passed. Plot the isochrones with depth.

Solution: We start our solution by making an assumption for the number of layers or increments. We choose seven layers of compressible soil, or $\Delta z = 2$ m per layer. Next, set $\alpha = {}^1/_2$ and solve for Δt using Eq. (9.21) with 2 m per increment of Δz. Solving for Δt,

$$\Delta t = \frac{\alpha(\Delta z)^2}{c_v}$$

$$= \frac{0.5(2\text{ m})^2}{9.3 \times \frac{\text{m}^2}{\text{min}} \times 60\frac{\text{min}}{\text{hr}} \times 24\frac{\text{hr}}{\text{da}}}$$

$$= 149.3\text{ da} \approx 150\text{ da}$$

We use Table Ex. 9.9 for our computations. First, the depth increment number i is given in row A at the top. Next, row B gives the depth z_i below the top of the compressible layer. The time increment number j is located in the left two columns below row B. Time increases downward in the table of Table Ex. 9.9. The initial conditions, from Fig. Ex. 9.9b, are shown in row E, with depth to the right, horizontal plane. (These initial values of Δu were obtained from the theoretical stress distributions in the compressible layer based on the surface loading. We will discuss how to do this in Chapter 10.)

TABLE Ex 9.9

A		$i \rightarrow$	0	1	2	3	4	5	6	7	
B	z_i (m)		0	2	4	6	8	10	12	14	
C	Time										
D	t (da)	t (yr)	Excess Pore Pressure $u_e(z,t)$ (kPa)								
			Initial Conditions								
E	0^-	0^-	77	68	62	55	49	39	30	21	Mirror
$j = 1$	0	0	38.5	68.0	62.0	55.0	49.0	39.0	30.0	21.0	30.0
2	150	0.4	0.0	50.3	61.5	55.5	47.0	39.5	30.0	30.0	30.0
3	300	0.8	0.0	30.8	52.9	54.3	47.5	38.5	34.8	30.0	34.8
4	450	1.2	0.0	26.4	42.5	50.2	46.4	41.1	34.3	34.8	34.3
5	600	1.6	0.0	21.3	38.3	44.4	45.7	40.3	37.9	34.3	37.9
6	750	2.1	0.0	19.2	32.8	42.0	42.4	41.8	37.3	37.9	37.3
7	900	2.5	0.0	16.4	30.6	37.6	41.9	39.8	39.9	37.3	39.9
8	1050	2.9	0.0	15.3	27.0	36.2	38.7	40.9	38.6	39.9	38.6
9	1200	3.3	0.0	13.5	25.8	32.9	38.6	38.6	40.4	38.6	40.4
10	1350	3.7	0.0	12.9	23.2	32.2	35.8	39.5	38.6	40.4	38.6
11	1500	4.1	0.0	11.6	22.5	29.5	35.8	37.2	39.9	38.6	39.9
12	1650	4.5	0.0	11.3	20.5	29.2	33.3	37.9	37.9	39.9	37.9
13	1800	4.9	0.0	10.3	20.2	26.9	33.5	35.6	38.9	37.9	38.9
14	1950	5.3	0.0	10.1	18.6	26.9	31.3	36.2	36.7	38.9	36.7
15	2100	5.8	0.0	9.3	18.5	24.9	31.5	34.0	37.5	36.7	37.5
16	2250	6.2	0.0	9.2	17.1	25.0	29.5	34.5	35.4	37.5	35.4
17	2400	6.6	0.0	8.6	17.1	23.3	29.8	32.4	36.0	35.4	36.0
18	2550	7.0	0.0	8.6	15.9	23.4	27.9	32.9	33.9	36.0	33.9
19	2700	7.4	0.0	8.0	16.0	21.9	28.2	30.9	34.5	33.9	34.5
20	2850	7.8	0.0	8.0	14.9	22.1	26.4	31.3	32.4	34.5	32.4
21	3000	8.2	0.0	7.5	15.0	20.7	26.7	29.4	32.9	32.4	32.9
22	3150	8.6	0.0	7.5	14.1	20.9	25.0	29.8	30.9	32.9	30.9
23	3300	9.0	0.0	7.0	14.2	19.5	25.3	28.0	31.4	30.9	31.4
24	3450	9.5	0.0	7.1	13.3	19.8	23.7	28.3	29.4	31.4	29.4
25	3600	9.9	0.0	6.6	13.4	18.5	24.1	26.6	29.9	29.4	29.9
26	3750	10.3	0.0	6.7	12.6	18.7	22.5	27.0	28.0	29.9	28.0
27	3900	10.7	0.0	6.3	12.7	17.6	22.9	25.3	28.4	28.0	28.4
28	4050	11.1	0.0	6.4	11.9	17.8	21.4	25.6	26.6	28.4	26.6
29	4200	11.5	0.0	6.0	12.1	16.7	21.7	24.0	27.0	26.6	27.0
30	4350	11.9	0.0	6.0	11.3	16.9	20.4	24.4	25.3	27.0	25.3
31	4500	12.3	0.0	5.7	11.5	15.8	20.6	22.8	25.7	25.3	25.7
32	4650	12.7	0.0	5.7	10.7	16.0	19.3	23.2	24.1	25.7	24.1
33	4800	13.2	0.0	5.4	10.9	15.0	19.6	21.7	24.4	24.1	24.4
34	4950	13.6	0.0	5.4	10.2	15.2	18.4	22.0	22.9	24.4	22.9

Making the assumption that $\Delta u_e = \Delta\sigma$, we put the initial Δu in the table of Table Ex. 9.9 under the words "Initial Conditions" at time $t = 0^-$ (row E). Next, we remind you that there is free drainage at the top of the compressible layer but not at the bottom of the layer. However, in the next line ($j = 1$), we show a difference in the initial conditions and the boundary conditions. This condition is taken care of by computing the average of the initial- and boundary-condition pore pressures to begin the

recurrence formulation. (We do this because in the finite increments, there would be no gradient at the boundaries at $t = 0$ if the initial conditions were not modified as mentioned. The small error introduced is minimal after a few increments of time.) A look at Table Ex. 9.9 at $t = 0$ shows that the initial Δu is $^1/_2$ of 77 or 38.5 kPa.

As an example to see how the computations progress, set $z = 6$ m ($i = 3$) and $t = 450$ da or 1.2 yr ($j = 3$). The resulting Δu is given by inserting $\alpha = {}^1/_2$ into Eq. (9.20) to obtain

$$u_{e_{i,j+1}} = 0.5(u_{e_{i-1,j}} + u_{e_{i+1,j}}) \tag{9.22}$$

Inserting the numerical values for this point

$$\Delta u_{3,3} = 0.5(52.9 + 47.5)\ \text{kPa}$$
$$= 50.2\ \text{kPa}$$

Because the layer is only singly drained (at the top), the lower boundary requires a "mirror" of Δu in order for us to proceed. Note that the mirror has a fictitious i parameter = 8. Then for $i = 7$, use Eq. (9.22) to calculate the next j down. Having the mirror results in Δu's initially higher than the original value, but with time, the values will revert to reality. Figure Ex. 9.9c provides a plot of how the pore water pressure decreases with time as a function of depth. Each of the curves is an *isochrone*.

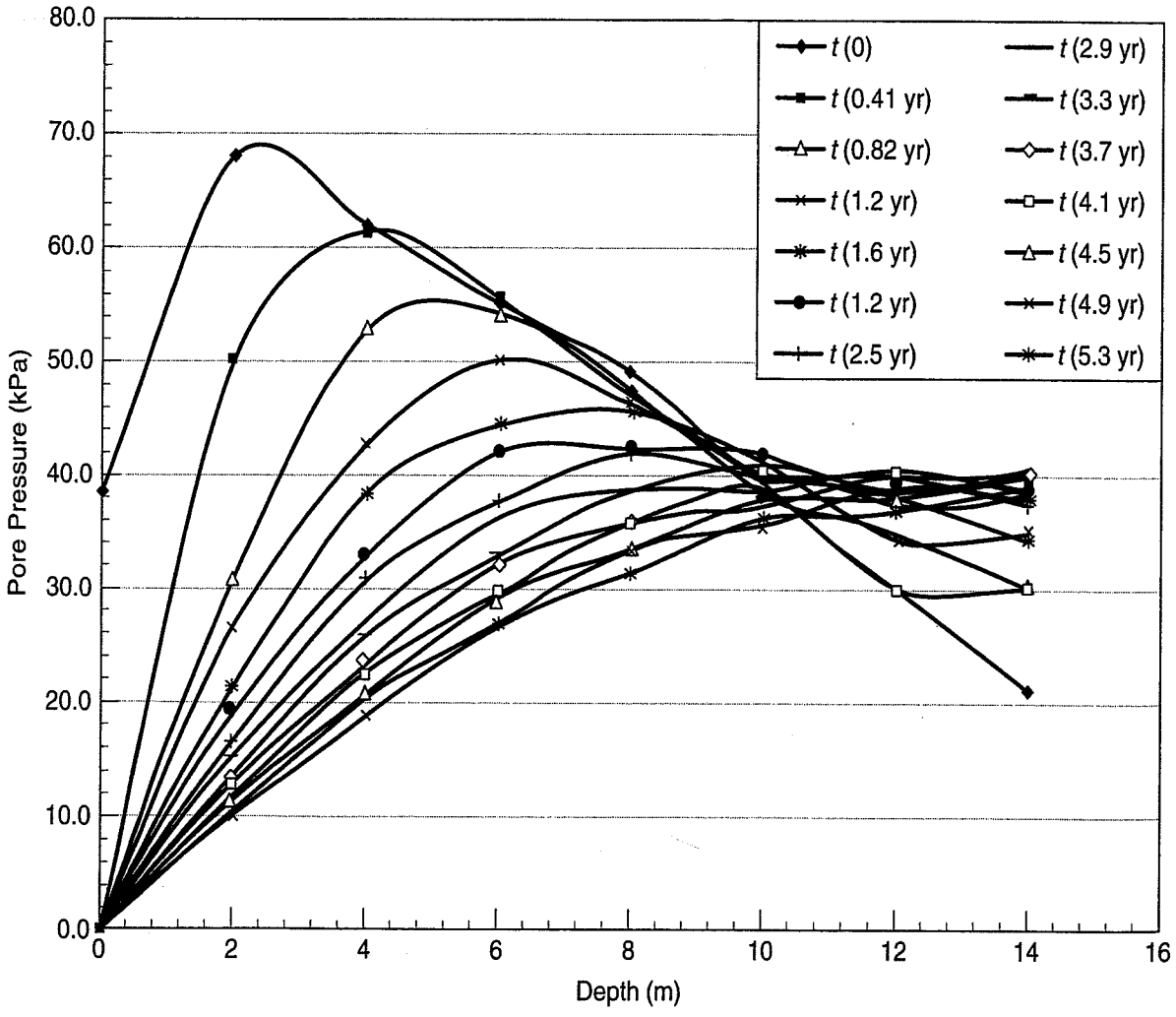

FIGURE Ex. 9.9c

With the above information, you should be able to solve a problem with any initial pore water pressure distribution. Note that you can use superposition with any results you obtain from using the finite difference method. For any given time, you may add or subtract resulting pressure distributions. It is a useful tool, especially if you set a problem up using a spreadsheet.

9.4 DETERMINATION OF THE COEFFICIENT OF CONSOLIDATION c_v

How do we obtain the coefficient of consolidation c_v? This coefficient is the only part of the solution to the consolidation equation that takes into account the soil properties which govern the rate of consolidation. In Chapter 8 we described the procedure for performing incremental load consolidation tests to obtain the compressibility of the soil. We mentioned that each load increment usually remains on the test specimen an arbitrary length of time, until (we hope) essentially all of the excess pore pressure has dissipated. Deformation dial readings or converted transducer readings are obtained during this process, and the coefficient of consolidation c_v is determined from the time versus deformation data.

The curves of actual deformation readings versus real time for a given load increment often have shapes very similar to the theoretical *U–T* curves shown in Fig. 9.5. We shall take advantage of this observation to determine the c_v by so-called *curve-fitting methods* developed by Casagrande and Taylor. These empirical procedures were developed to fit approximately the observed laboratory test data to the Terzaghi theory of consolidation. Many factors such as sample disturbance, load increment ratio (LIR), duration, temperature, and a host of test details have been found to strongly affect the value of c_v obtained by the curve-fitting procedures (Leonards and Ramiah, 1959; Leonards, 1962). But research by Leonards and Girault (1961) has shown that the Terzaghi theory is applicable to the laboratory test if large LIRs [Eq. (8.27)], usually around unity, are used.

The curve-fitting procedures outlined in this section will enable you to determine values of the coefficient of consolidation c_v from laboratory test data. They also will allow you to separate the secondary compression from the primary consolidation.

Probably the easiest way to illustrate the curve-fitting methods is to work with time-deformation data from an actual consolidation test. We will use the data for the load increment from 100 to 200 kPa for the test shown in Fig. 8.5. This data is shown in Table 9.2 and plotted in Figs. 9.11(a), (b), and (c). Note how similar the shapes of these curves are to the theoretical curves of Figs. 9.5(a), (b), and (c).

TABLE 9.2 Time-Deformation Data for Load Increment 100 to 200 kPa (Fig. 8.5)

Elapsed Time (min)	$\sqrt{t}$ ($\sqrt{\text{min}}$)	Dial or converted transducer reading, R (mm)	Displacement (mm)
0	0	6.627	0
0.1	0.316	6.528	0.099
0.25	0.5	6.480	0.147
0.5	0.707	6.421	0.206
1	1.0	6.337	0.290
2	1.41	6.218	0.409
4	2.0	6.040	0.587
8	2.83	5.812	0.815
15	3.87	5.489	1.138
30	5.48	5.108	1.519
60	7.75	4.775	1.852
120	10.95	4.534	2.093
240	15.5	4.356	2.271
480	21.9	4.209	2.418
1382	37.2	4.041	2.586

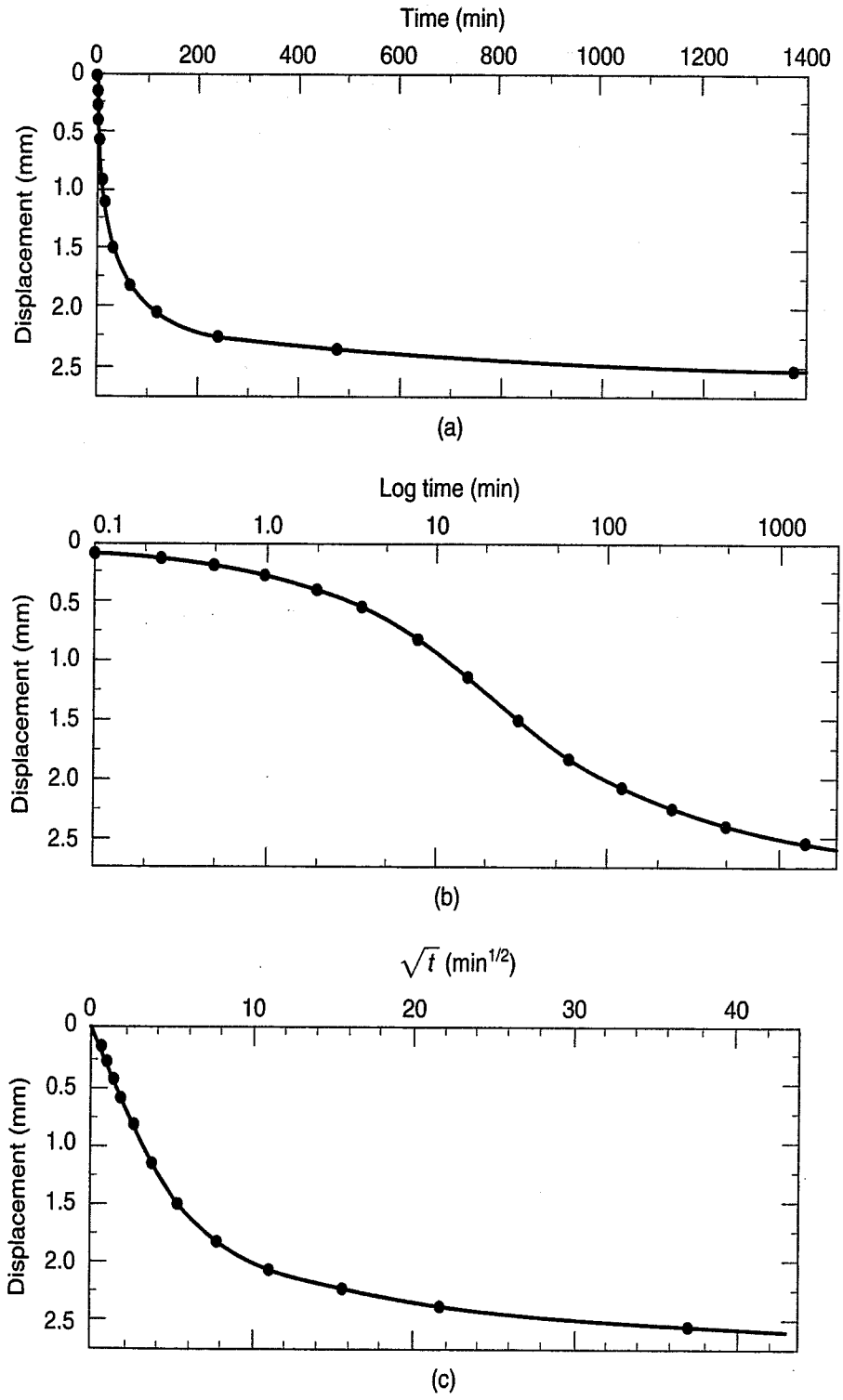

FIGURE 9.11 Deformation-time curves for data from Table 9.2: (a) arithmetic scale; (b) log time scale; (c) square root of time scale.

9.4.1 Casagrande's Logarithm of Time-Fitting Method

In this method, the deformation dial (or converted transducer) readings are plotted versus the *logarithm of time*, as shown in Fig. 9.11(b) and to larger scale in Fig. 9.12. The idea is to find R_{50} and thus t_{50}, the time for 50% consolidation, by approximating R_{100}, the deformation reading corresponding to the time for 100% primary consolidation, t_{100} or t_p. Refer to Fig. 9.5(b), the theoretical U–T curve,

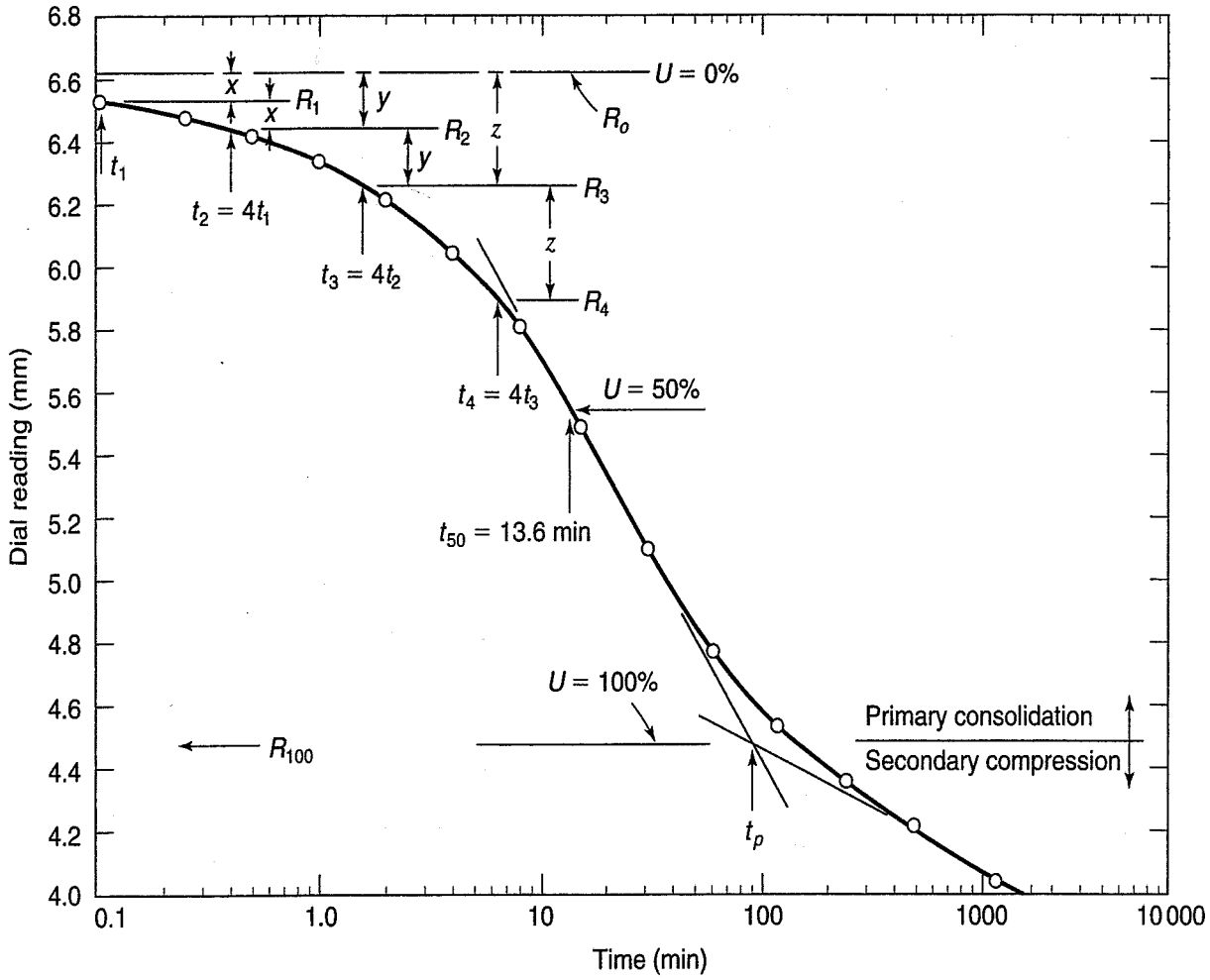

FIGURE 9.12 Determination of t_{50} by the Casagrande method; data from Table 9.2.

curve for a moment. Note that the intersection of the tangent and the asymptote to the theoretical curve defines $U_{avg} = 100\%$. The time for 100% consolidation, of course, occurs at $t = \infty$. Casagrande (1938) suggested that R_{100} could be approximated rather arbitrarily by the intersection of the two corresponding tangents to the laboratory consolidation curve (Fig. 9.12). Later research (for example, Leonards and Girault, 1961) showed that this procedure defines to a good approximation the deformation reading at which the excess pore water pressure approaches zero, especially when the LIR is large and the preconsolidation stress is exceeded by the applied load increment. After R_{100} is defined, the next step is to find R_o, the initial dial or converted transducer reading.

How do we determine R_o, the reading corresponding to *zero* percent consolidation, on a semilog plot? Since T is proportional to U_{avg}^2 up to $U = 60\%$ [Eq. (9.10)], the first part of the consolidation curve must be a parabola. To find R_o, choose any two times, t_1 and t_2, in the ratio of 4 to 1, and note their corresponding deformation readings. Then mark off a distance above R_1 equal to the difference $R_2 - R_1$; this defines the corrected zero point R_o. In equation form,

$$R_o = R_1 - (R_2 - R_1) \tag{9.23a}$$

Several trials are usually advisable to obtain a good average value of R_o, or

$$R_o = R_2 - (R_3 - R_2) \tag{9.23b}$$

and

$$R_o = R_3 - (R_4 - R_3) \tag{9.23c}$$

In Fig. 9.12, three different trials are shown for determining R_o from R_1, R_2, R_3, and R_4. The distances x, y, and z are marked off above the ordinates corresponding to times t_2, t_3, and t_4, respectively. You should satisfy yourself that use of both the graphical procedure and Eqs. (9.23a)–(c) indicate about the same value for R_o (6.62 mm in this case).

After the initial and 100% primary consolidation points have been determined, find t_{50} by subdividing the vertical distance between R_o and R_{100} [or $R_{50} = \frac{1}{2}(R_o + R_{100})$]. Then t_{50} is simply the time corresponding to the deformation reading R_{50}. In Fig. 9.12, $t_{50} = 13.6$ min. To evaluate c_v, we use Eq. (9.5) with $T_{50} = 0.197$ (Table 9.1). We also need the average height of the specimen during the load increment. At the beginning of this increment, H_o was 21.87 mm. From the data of Table 9.2,

$$H_f = H_o - \Delta H = 21.87 - 2.59 = 19.28 \text{ mm}$$

Thus the average height of specimen during the increment is 20.58 mm (2.06 cm). Remember that in the standard consolidation test the specimen is doubly drained, so use $H_{dr} = 2.06/2$ in Eq. (9.5). Thus we have

$$c_v = \frac{TH_{dr}^2}{t} = \frac{T_{50}H_{dr}^2}{t_{50}}$$

$$= \frac{0.197\left(\frac{2.06}{2}\right)^2 \text{cm}^2}{13.6 \text{ min}\left(60\frac{\text{s}}{\text{min}}\right)}$$

$$= 2.56 \times 10^{-4}\frac{\text{cm}^2}{\text{s}}\left(3.1536 \times 10^7 \frac{\text{s}}{\text{yr}}\right)\left(\frac{\text{m}^2}{10^4 \text{ cm}^2}\right)$$

$$= 0.81 \text{ m}^2/\text{yr}$$

Recall that the Casagrande fitting procedure found R_{50} and thus t_{50} by approximating R_{100}. This procedure did not find t_{100} since the time for any other degree of consolidation must be obtained from the classical consolidation theory in which $t_{100} = \infty$. But the procedure does define a t called t_p (for "primary"), which is a practical time required to obtain a good, usable value of R_{100}. Often, in practice, t_p is called t_{100}. The deviation of the experimental curve from the theoretical curve is shown in Fig. 9.13.

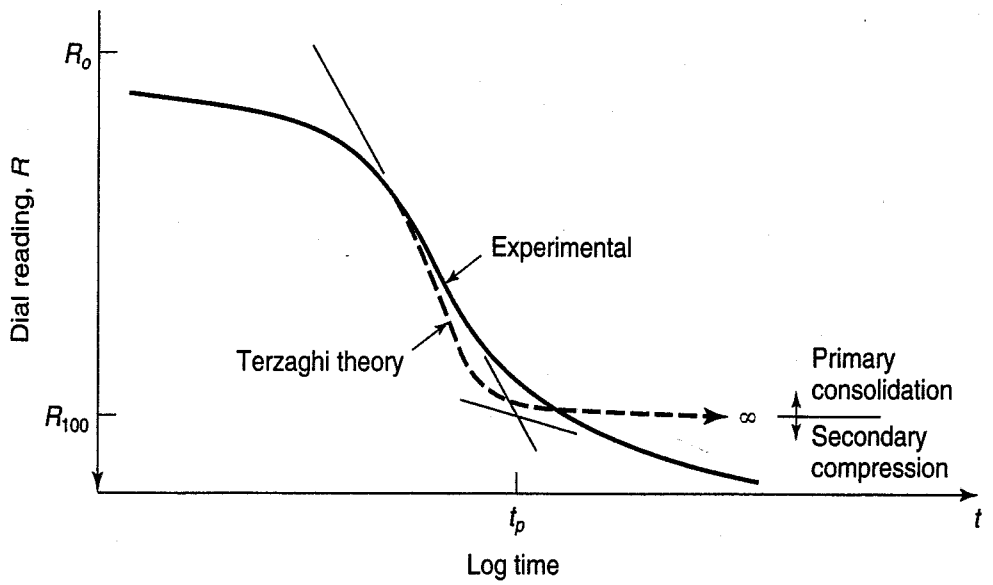

FIGURE 9.13 Terzaghi consolidation theory and a typical experimental curve used to define t_p.

Differences in the curves are the result of secondary compression and other effects, such as the rate of effective stress increase (Leonards, 1977), not considered by the Terzaghi theory.

9.4.2 Taylor's Square Root of Time Fitting Method

Taylor (1948) also developed a procedure for evaluating c_v, using the square root of time. Like Casagrande's curve fitting method, Taylor's procedure is based on the similarity between the shapes of the theoretical and experimental curves when plotted versus the square root of T and t. Refer to Fig. 9.5(c) and compare it with Fig. 9.11(c). Note that in Fig. 9.5(c) the theoretical curve is a straight line to at least $U \cong 60\%$ or greater. Taylor observed that the abscissa of the curve at 90% consolidation was about 1.15 times the abscissa of the extension of the straight line [Fig. 9.5(c)]. He thus could determine the point of 90% consolidation on the laboratory time curve.

We will use the same data as before (Table 9.2) to illustrate the $\sqrt{t}$ fitting method. These data are plotted in Fig. 9.14. Usually a straight line can be drawn through the data points in the initial part of the compression curve. The line is projected backward to zero time to define R_o. The common point at R_o may be slightly lower than the initial deformation reading (at zero time) observed in the laboratory due

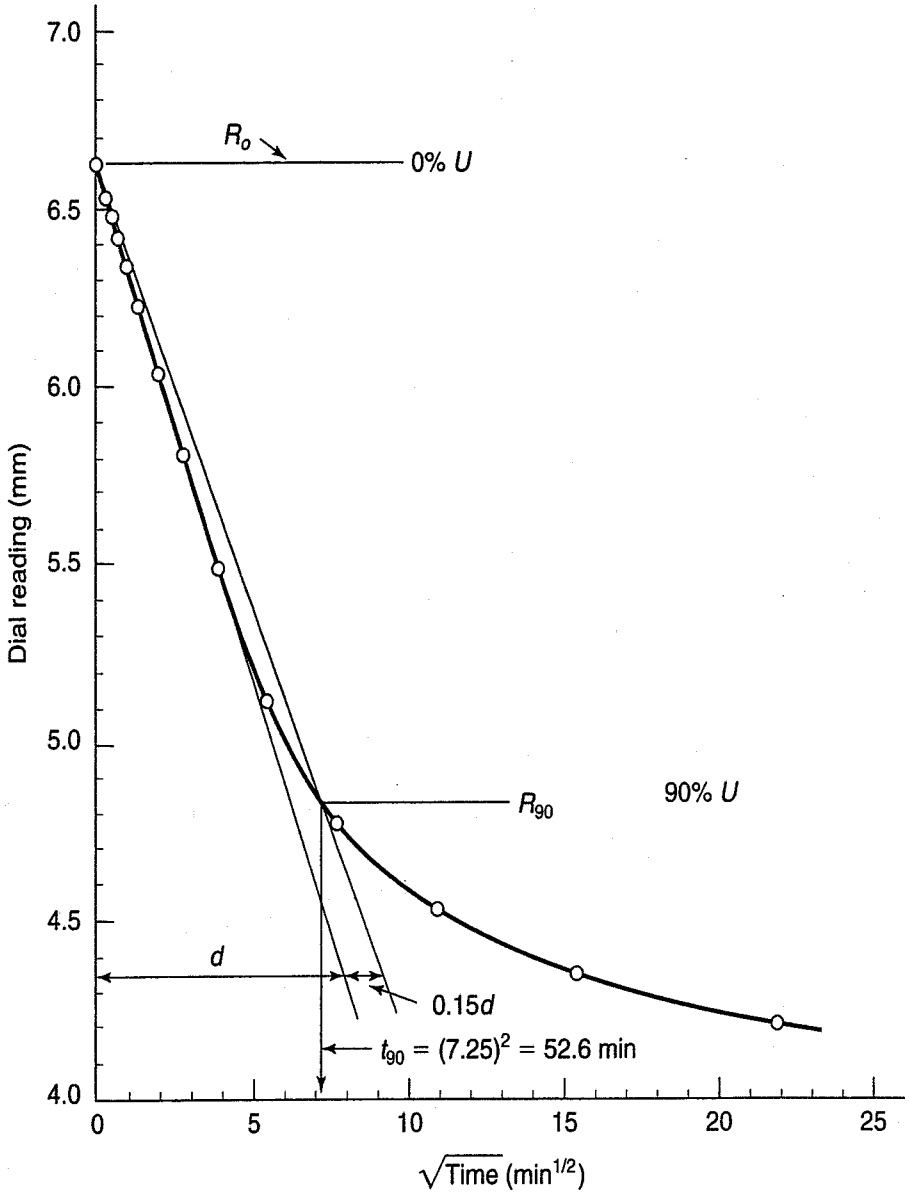

FIGURE 9.14 Determination of c_v, using Taylor's square root of time method; data from Table 9.2.

to immediate compression of the specimen and apparatus. Draw a second line from R_o with all abscissas 1.15 times as large as corresponding values on the first line. The intersection of this second line and the laboratory curve defines R_{90} and is the point of 90% consolidation. Its time is, of course, t_{90}.

The coefficient of consolidation is, as before, determined by using Eq. (9.5). From Table 9.1, $T_{90} = 0.848$. The average height of specimen is also used, as before. Therefore

$$c_v = \frac{0.848(2.06/2)^2 \text{ cm}^2}{52.6 \text{ min}(60 \text{ s/min})}$$
$$= 2.85 \times 10^{-4} \text{ cm}^2/\text{s or } 0.90 \text{ m}^2/\text{yr}$$

This value is reasonably close to the one obtained using the Casagrande method. Because both fitting methods are approximations of theory, you should not expect them to agree exactly. Often c_v as determined by the $\sqrt{t}$ method is slightly greater than c_v by the log t fitting method, by as much as a factor of 1.5 to 2.

You should also note that c_v is not a constant for a test on a given soil, but it depends greatly on the load increment ratio and whether the preconsolidation stress has been exceeded (Leonards and Girault, 1961). For load increments less than the preconsolidation stress, consolidation occurs quite rapidly, and c_v values can be rather high. However, determinations of t_p for these increments are often difficult because the time-settlement curves do not have the "classical" shapes of Figs. 9.12 and 9.14. For undisturbed clays c_v is usually a minimum for increments near the preconsolidation pressure (Taylor, 1948). For design, this minimum value is often used. However, for some situations it may be more appropriate to use the c_v for the anticipated load increment in the field.

An important advantage of the $\sqrt{t}$ fitting method for incremental load tests is that you can determine t_{90} without having to maintain the current load much beyond t_p. If displacement readings are plotted as you go during the test, then the next increment of load can be added as soon as t_{90} is reached. Not only is the time for testing significantly less than when the conventional 24-h increments are used, but the contribution of secondary compression to the e versus log σ' curve can be effectively minimized (see Leonards, 1976).

By now you should have noticed that the data do not exactly coincide with the initial starting point in either of Figs. 9.12 or 9.14; that is, R_o does not equal exactly the initial reading of Table 9.2. The difference between the initial laboratory deformation reading and R_o, the "corrected deformation reading" corresponding to 0% consolidation is due to several factors that may exist during laboratory consolidation testing. These may include:

1. Vertical elastic compression of the soil specimen, porous stones, and apparatus.
2. Lateral expansion of the soil specimen if it is not trimmed exactly to the diameter of the ring.
3. Deformation associated with lateral expansion of the consolidometer ring.

You will have the opportunity to use the two curve-fitting methods to determine c_v in the problems at the end of this chapter.

9.5 DETERMINATION OF THE COEFFICIENT OF PERMEABILITY

You may recall from Sec. 7.6 that the coefficient of permeability or hydraulic conductivity, k, of the soil may also be obtained indirectly from the consolidation test. If you take Eq. (9.3) and solve for k, you obtain

$$k = \frac{c_v \rho_w g a_v}{1 + e_o} \tag{9.24}$$

The value of e_o is the void ratio at the start of the time-rate readings for a given load increment.

Example 9.10

Given:

The time-deformation data for the load increment 100 to 200 kPa of the test in Fig. 8.4. From Table 9.2 and Fig. 9.12, a c_v value of 0.81 m^2/yr (2.56×10^{-4} cm^2/s) can be determined.

Required:

Compute the coefficient of permeability, assuming the temperature of the water is 20°C.

Solution: It is first necessary to compute the coefficient of compressibility from Eq. (8.5) and using Fig. 8.4(b):

$$a_v = \frac{e_1 - e_2}{\sigma_2' - \sigma_1'} = \frac{2.12 - 1.76}{(200 - 100)\ \text{kPa}}$$

$$= 0.0036/\text{kPa} = 3.6 \times 10^{-6}\ \frac{\text{m}^2}{\text{N}}$$

From Eq. (9.24),

$$k = \frac{c_v \rho_w g a_v}{1 + e_o}$$

$$= \frac{2.56 \times 10^{-4}\ \frac{\text{cm}^2}{\text{s}} \times 1000\ \frac{\text{kg}}{\text{m}^3} \times 9.81\ \frac{\text{m}}{\text{s}^2} \times 3.6 \times 10^{-6} \frac{\text{m}^2}{\text{N}}\ \frac{1\ \text{m}}{100\ \text{cm}}}{1 + 2.12}$$

$$k = 2.9 \times 10^{-8}\ \frac{\text{cm}}{\text{s}} = 2.9 \times 10^{-10}\ \frac{\text{m}}{\text{s}}$$

Note that the e used in the equation is the void ratio at the start of the load increment rather than the original or in situ void ratio.

9.6 TYPICAL VALUES OF THE COEFFICIENT OF CONSOLIDATION c_v

Typical values of the coefficient of consolidation c_v for a variety of soils are listed in Table 9.3. Approximate correlations of c_v with the liquid limit are presented in Fig. 9.15.

TABLE 9.3 Typical Values of the Coefficient of Consolidation c_v

Soil	c_v	
	cm^2/s $\times 10^{-4}$	m^2/yr
Boston blue clay (CL) (Ladd and Luscher, 1965)	40 ± 20	12 ± 6
Organic silt (OH) (Lowe, Zaccheo and Feldman, 1964)	2–10	0.6–3
Glacial lake clays (CL) (Wallace and Otto, 1964)	6.5–8.7	2.0–2.7
Chicago silty clay (CL) (Terzaghi and Peck, 1967)	8.5	2.7
Swedish medium sensitive clays (CL–CH) (Holtz and Broms, 1972)		
1. laboratory	0.4–0.7	0.1–0.2
2. field	0.7–3.0	0.2–1.0
San Francisco Bay mud (CL)	2–4	0.6–1.2
Mexico City clay (MH) (Leonards and Girault, 1961)	0.9–1.5	0.3–0.5

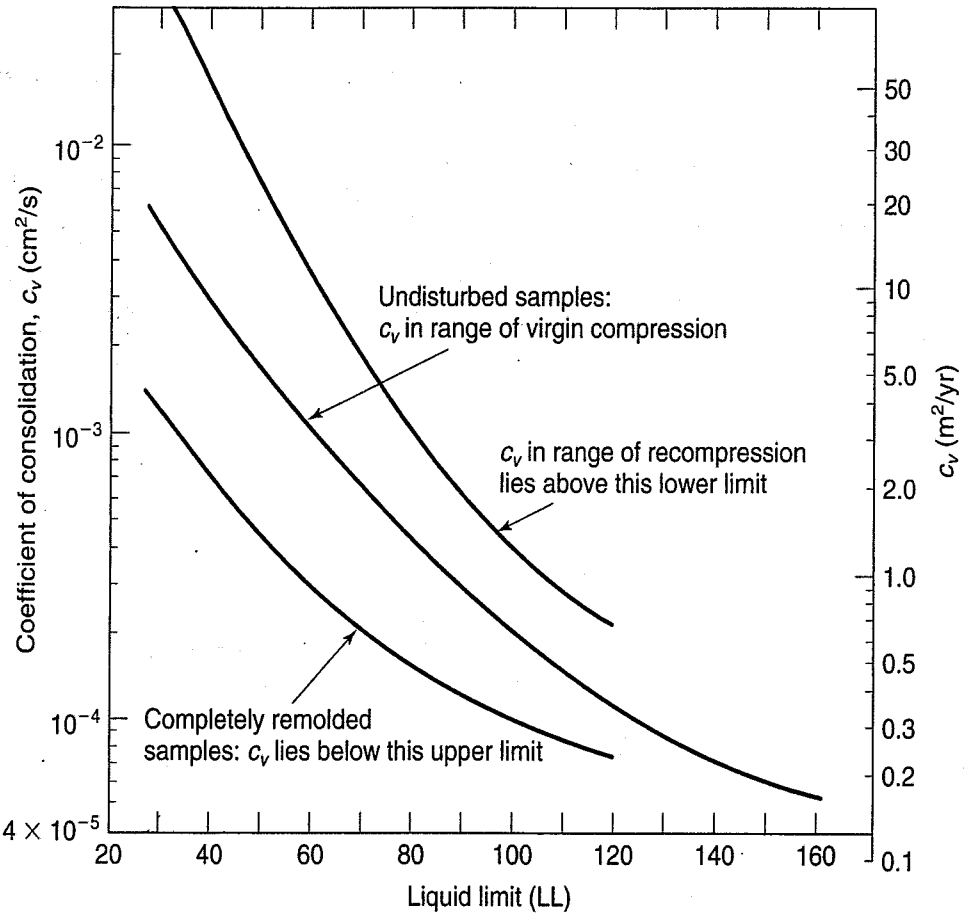

FIGURE 9.15 Approximate correlations of the coefficient of consolidation c_v with the liquid limit (after U.S. Navy, 1986).

9.7 IN SITU DETERMINATION OF CONSOLIDATION PROPERTIES

It is possible to obtain the horizontal coefficient of consolidation (and the coefficient of permeability also) by means of field testing with the piezocone and the dilatometer (see Table 11.1). Realize that water-deposited soil layers are quite variable, with seams, varves, and lenses, for example; laboratory evaluations may be quite different than field determinations.

For the piezocone test, the horizontal coefficient of consolidation, c_{vh} is given by

$$c_{vh} = \frac{TR^2}{t} \tag{9.25}$$

where c_{vh} = coefficient of horizontal consolidation,

T = time factor,

R = equivalent piezocone cavity radius,

t = time it takes to achieve appropriate degree of consolidation.

See Jamiolkowski et al. (1985) for further information on the use of cavity expansion theory and the rigidity index to obtain c_{vh}. For test details, equipment, procedures, and typical results, see ASTM (2010) D 5778.

Robertson et al. (1988) devised a procedure to do the same thing using the Marchetti dilatometer. The equation for the horizontal coefficient of consolidation is

$$c_{vh} = \frac{TR_e^2}{t} \tag{9.26}$$

where R_e = equivalent radius of the dilatometer blade.

Further information on the dilatometer test may be obtained from Marchetti (1980) and ASTM (2010) D 6635.

Schmertmann (1993) presents a field test procedure that simulates full-scale prototype loading by means of a conical pile of soil fill. This type of small-scale load test is both economical and easy to perform, and from the measurements, the magnitude and rate of consolidation are rapidly determined. The consolidation parameters of the subsoil are back-calculated from the measurements and settlement pattern.

The conical test load (CTL) is performed by first placing a settlement plate at the center of the loaded area. Next a conical pile of soil is heaped at its angle of repose by a front-end loader. The pile can be up to 7 m high. After the soil pile is completed (usually within a day), settlement readings are taken with time. Depending upon the thickness of the compressible deposit under consideration, prediction of the prototype settlement and its time rate of consolidation is possible. Applying the CTL for a long enough period of time will permit the evaluation of secondary compression as well. Schmertmann (1993 and 1994) gives the details of this method, including equations, examples, and the effects of multiple layers.

9.8 EVALUATION OF SECONDARY SETTLEMENT

Thus far we have discussed how to compute the consolidation or primary settlement s_c, and how it varies with time. The other two components of total settlement in Eq. (8.1) were the immediate settlement s_i and *secondary compression* (settlement) s_s. Immediate settlement is discussed in Sec. 10.4.

Secondary compression is a continuation of the volume change that started during primary consolidation, only it usually occurs at a much slower rate. Secondary compression is different from primary consolidation in that it takes place at a *constant effective stress*—that is, after essentially all the excess pore pressure has dissipated. This component of settlement seems to result from compression of the bonds between individual clay particles and domains, as well as other effects on the microscale that are not yet clearly understood. Another complicating factor is that in the field it is often difficult to separate secondary compression from primary consolidation settlement. Both types of settlements contribute to the total surface settlement, and separating the effects in order to predict the final surface settlement is not a simple matter, especially in thicker or stratified deposits with variable properties. Also, conventional consolidation testing normally does not provide much information about secondary compression. In this section we present a practical working hypothesis, acceptable for engineering practice, for estimating secondary compression, and we shall show you how to make estimates of secondary settlement for some simple cases.

There is, unfortunately, a lot of confusion in the geotechnical literature as to the best way to describe the magnitudes and rates of secondary compression. In this section, we shall follow Raymond and Wahls (1976), Mesri and Godlewski (1977), and Terzaghi et al. (1996) who define the *secondary compression index* C_α as

$$C_\alpha = \frac{\Delta e}{\Delta \log t} \tag{9.27}$$

where Δe = the change in *void ratio* along a part of the void ratio versus the *logarithm* of time curve between times t and t_p, and

$\Delta \log t = \log t - \log t_p$.

This definition is analogous, of course, to the primary compression index C_c [Eq. (8.7)]. To determine the magnitude of secondary settlement under the final vertical effective stress σ'_{vf}, we use an equation patterned after Eq. (8.10), or

$$s_s = \frac{C_\alpha}{1 + e_o} H_o \log \frac{t}{t_p} \tag{9.28}$$

Thus, the secondary settlement depends on C_α as well as on the ratio t/t_p. Equation (9.28) also assumes that C_α is approximately constant over the time interval $t - t_p$.

We can also define the *modified secondary compression index* $C_{\alpha\varepsilon}$, analogous to Eq. (8.9), as

$$C_{\alpha\varepsilon} = \frac{C_\alpha}{1 + e_o} \tag{9.29}$$

where C_α = the secondary compression index, Eq. (9.27),
e_o = the initial void ratio.

Sometimes $C_{\alpha\varepsilon}$ is called the *secondary compression strain index*, the *secondary compression ratio*, or the *rate of secondary consolidation*. As Ladd et al. (1977) note, $C_{\alpha\varepsilon} = \Delta\varepsilon/\Delta \log t$. The equation for secondary settlement then becomes

$$s_s = C_{\alpha\varepsilon} H_o \log \frac{t}{t_p} \tag{9.30}$$

This equation is, of course, analogous to Eq. (8.12) for primary settlement.

The secondary compression index C_α, and the modified secondary compression index $C_{\alpha\varepsilon}$, can be determined from the slope of the straight line portion of the deformation (ΔR) versus log time curve, which occurs after primary consolidation is complete or after t_p (see, for example, Fig. 9.12). Usually the ΔR is determined over one log cycle of time. The corresponding change in void ratio is calculated from the settlement equation [Eq. (8.3)], since you know e_o and the height of specimen for that increment.

To provide a working hypothesis for estimating secondary settlements, we shall make the following assumptions about the behavior of fine-grained soils in secondary compression [based on the work of Ladd (1971a) and others and summarized by Raymond and Wahls (1976)]:

1. C_α is independent of time (at least during the time span of interest).
2. C_α is independent of the thickness of the soil layer.
3. C_α is independent of the LIR, as long as some primary consolidation occurs.
4. The ratio C_α/C_c is approximately constant for many geo-materials over the normal range of engineering stresses.

The working hypothesis is useful as a first approximation for estimating secondary settlements. However, you should expect some aberrations in the actual long-term settlement response of the foundation, because the assumptions are admittedly an oversimplification of real behavior. Typical deformation versus log time behavior curves illustrating these assumptions for a normally consolidated clay are shown in Fig. 9.16.

Although we assumed in No. 1 that C_α is a constant, there is considerable evidence both in the laboratory (Mesri and Godlewski, 1977; Terzaghi et al., 1996) and in the field (Leonards, 1973) that it may change with time, especially if the time after the end of primary is long. Also, the duration and

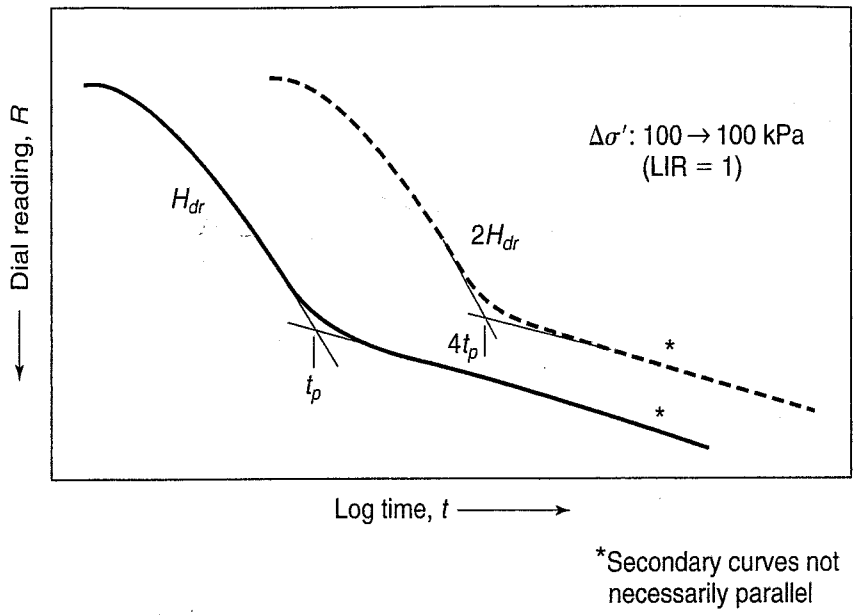

(a)

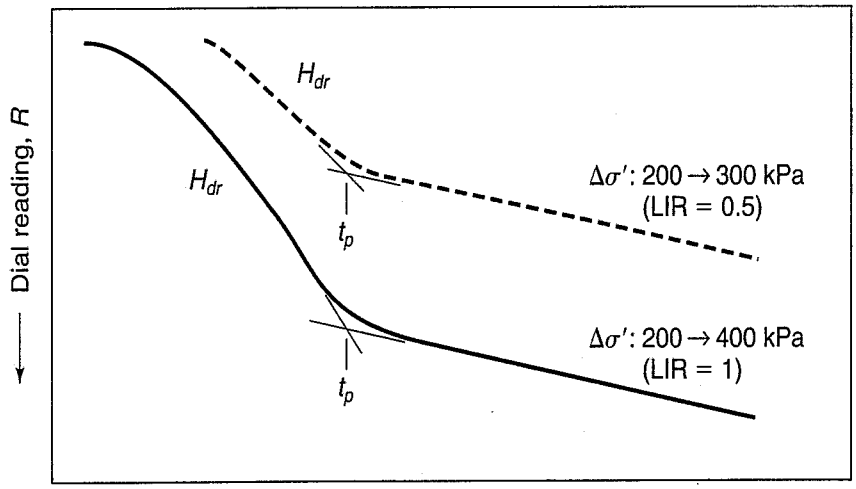

(b)

FIGURE 9.16 Typical secondary compression behavior from the working hypothesis by Raymond and Wahls (1976): (a) effect of drainage distance and (b) effect of load increment ratio and consolidation stress.

therefore the magnitude of secondary settlement is a function of the time required for completion of primary consolidation (t_p), and from earlier work in this chapter you know that the thicker the consolidating layer, the longer is the time required for primary consolidation. On the other hand, because in practical problems the range of t/t_p is small, often less than 100, you usually can assume ratio C_α is constant for settlement analyses. More about this point later in this section.

Assumption 2 seems to be valid, as shown in Fig. 9.16(a), because the strain at the end of primary consolidation for both thin and thick layers is about the same. Assumption 3, that C_α is independent of the LIR, is approximately correct, as verified by Leonards and Girault (1961) and Mesri and Godlewski (1977). Note that the load increment must go well beyond the preconsolidation stress.

The fourth assumption, that the ratio C_α/C_c is approximately a constant, has also been verified for a wide variety of natural soils by Prof. Mesri and his students, starting with Mesri and Godlewski

TABLE 9.4 Values of C_α/C_c for Natural Geotechnical Materials

Material	C_α/C_c
Granular soils including rockfill	0.02 ± 0.01
Shale and mudstone	0.03 ± 0.01
Inorganic clays and silts	0.04 ± 0.01
Organic clays and silts	0.05 ± 0.01
Peat and muskeg	0.06 ± 0.01

After Terzaghi et al. (1996).

(1977). This work is summarized in Table 9.4. For most geo-materials, the ratio C_α/C_c is between 0.01 and 0.07, and the midpoint of the range is 0.04. This is also the most common value for inorganic silts and clays. Organic materials are slightly higher and granular soils somewhat lower. This ratio also is valid for any time, effective stress, and void ratio during secondary compression. The only exception, as shown by Leonards and Girault (1961, Fig. 3) seems to be the load increment that straddles the preconsolidation stress, σ'_p. However, Mesri and Castro (1987) show that this discrepancy results from using an average C_c over an increment, rather than an instantaneous C_c, to determine the $C_{\alpha\varepsilon}/C_c$ ratio.

If you do not want to or cannot determine C_α from laboratory test data, you can use the C_α/C_c data of Table 9.4 for similar soils, or simply use an average C_α/C_c value of 0.04 to 0.05, which is acceptable for preliminary estimates of secondary settlement. Mesri (1973) has provided another method to obtain the secondary compression index, actually the modified secondary compression index, and it is shown in Fig. 9.17 Here the $C_{\alpha\varepsilon}$ is plotted versus natural water content of the soil.

We will illustrate how to estimate secondary settlement in Examples 9.11 and 9.12.

We mentioned earlier that t/t_p is rarely greater than 100. This is because the typical useful design life of most civil construction is 80–120 yr, and the t_p in the field is months to a very few years. On the other hand, in laboratory tests t/t_p can be rather long, because with the typical laboratory sample heights, t_p is usually quite short. Thus prediction of secondary properties from laboratory tests is somewhat problematic. There are exceptions, of course, as noted by Terzaghi et al. (1996): clays with intermediate permeable layers, peats, certain residual soils with high initial permeability, and sites where vertical drains have been used to accelerate the primary consolidation. In these cases, t/t_p can be long because t_p is usually quite short.

From a practical point of view, how do you judge when s_s is important (Holtz, 1991)? You need to be concerned when (1) the ratio of $s_s/s_c > 1$, and (2) in the field, the t_p is short, and therefore the site will experience rapid s_c (within a few weeks or months). One or both of these conditions may be present at sites with peats, organic silts and clays, or stratified or varved clays. Accurate predictions of secondary settlement at these sites require more than simple estimates.

Another factor to consider is that although t/t_p may be less than 100, secondary settlements occur over a very long time, and this fact may mean long-term maintenance of some facilities—for example, highway embankments on peat bogs. Because of the high permeability of the peat, primary settlement occurs very quickly, and thus the embankment is soon undergoing secondary compression. This means continual settlements that distort the roadway pavement or rail bed. Maintenance crews frequently resurface the roadway to keep it as close to grade as possible. In some older roads, the thickness of the gravel and asphalt under the embankments can be as much as 80% of the thickness of the peat deposit.

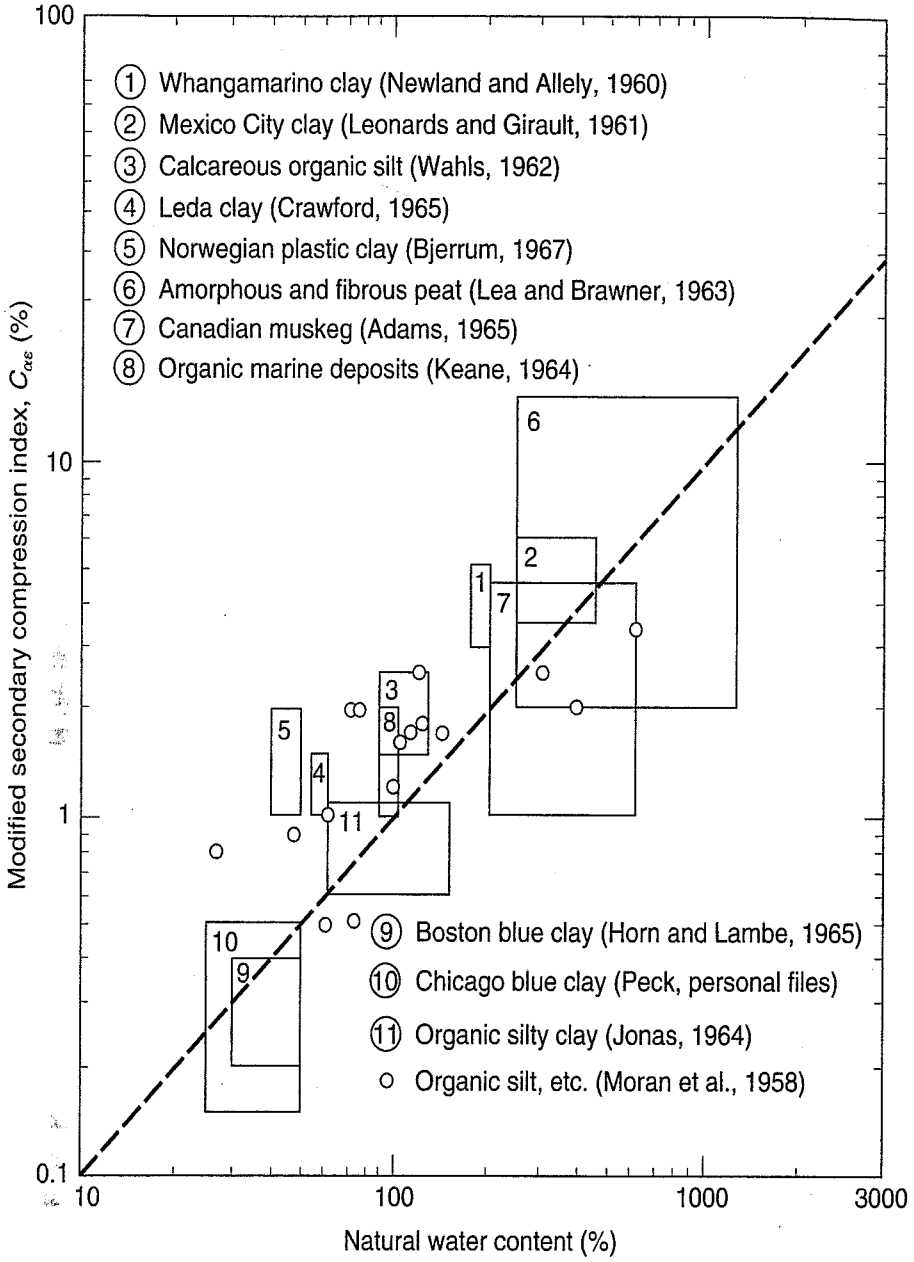

FIGURE 9.17 Modified secondary compression index versus natural water content (after Mesri, 1973).

Example 9.11

Given:

A consolidometer test on a specimen of San Francisco Bay mud gave the following time rate of consolidation data for the load increment of 400 to 800 kPa. This load increment represents the anticipated load in the field. Laboratory tests on trimmings adjacent to the specimen indicated that the natural water content w_n = 105.7%, initial void ratio e_o = 2.855, LL = 88, PL = 43, and ρ_s = 2.7 Mg/m^3. The initial height of the test specimen was 25.4 mm, and the initial deformation reading was 12.700 mm.

(1) Deformation Reading (mm)	(2) Elapsed Time (min)	(3) Void Ratio
11.224	0	2.631
11.151	0.1	2.620
11.123	0.25	2.616
11.082	0.5	2.609
11.019	1.0	2.600
10.942	1.8	2.588
10.859	3.0	2.576
10.711	6	2.553
10.566	10	2.531
10.401	16	2.506
10.180	30	2.473
9.919	60	2.433
9.769	100	2.410
9.614	180	2.387
9.489	300	2.368
9.373	520	2.350
9.223	1350	2.327
9.172	1800	2.320
9.116	2850	2.311
9.053	4290	2.301

Assume that the consolidation settlement s_c is 30 cm and that it occurs after 25 yr. The thickness of the compressible layer is 10 m.

Required:

Compute the amount of secondary compression that would occur from 25 to 50 yr after construction.

Solution: Assume that the time rate of deformation for the load range in the test approximates that occurring in the field.

The solution to this problem requires an evaluation of C_α [Eq. (9.27)]. So a void ratio versus log t curve must be plotted from the given data. We can readily calculate the void ratio at any height or thickness of the specimen during the consolidation test by using the following method. By definition, $e = V_v/V_s$ and, for a constant specimen area, $e = H_v/H_s$, which is the ratio of height of voids to the height of solids. Then, from the phase diagram (Fig. Ex. 9.11a), the void ratio at any deformation reading R may be obtained from

$$e = \frac{H_v}{H_s} = \frac{H_o - H_s}{H_s} = \frac{H_o - (R_o - R) - H_s}{H_s}$$
$$= \frac{(H_o - H_s) - (R_o - R)}{H_s} \tag{9.31}$$

where H_v = the height of voids at time t,
H_s = the height of solids,
H_o = the original height of specimen,
R_o = the initial deformation reading, and
R = deformation reading at time t.

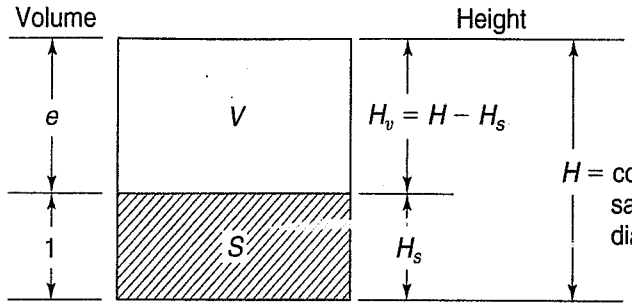

FIGURE Ex. 9.11a For initial conditions, $e = e_o$, $H = H_o$, and $R = R_o$.

From the phase diagram and the initial conditions of this problem,

$$H_s = \frac{H_o}{1 + e_o} = \frac{25.4}{1 + 2.855} = 6.589 \text{ mm}$$

For the load increment 400 to 800 kPa, the initial deformation reading is 11.224 mm; the deformation reading R_o at the beginning of the test (corresponding to specimen height H_o) is 12.700 mm. Thus, for the beginning of this load increment, e from Eq. (9.31) is

$$e = \frac{(25.4 - 6.589) - (12.700 - 11.224)}{6.589} = 2.631$$

This value of e at $R = 11.224$ is shown in Column (3) of the given data. The remainder of Column (3) can be calculated by substituting the other values of R into Eq. (9.31).

Next, plot the void ratio, Column (3), and the elapsed time, Column (2), on semilog paper or on a spreadsheet with the time axis on a log (base 10) scale, as shown in Fig. Ex. 9.11b. C_α is then found to be 0.052. Note that $C_\alpha = \Delta e$ when $\Delta \log t$ covers one full log cycle. The corresponding modified secondary compression index $C_{\alpha\varepsilon}$ [Eq. (9.29)] is $0.052/(1 + e_o) = 0.052/(1 + 2.855) = 0.0135$.

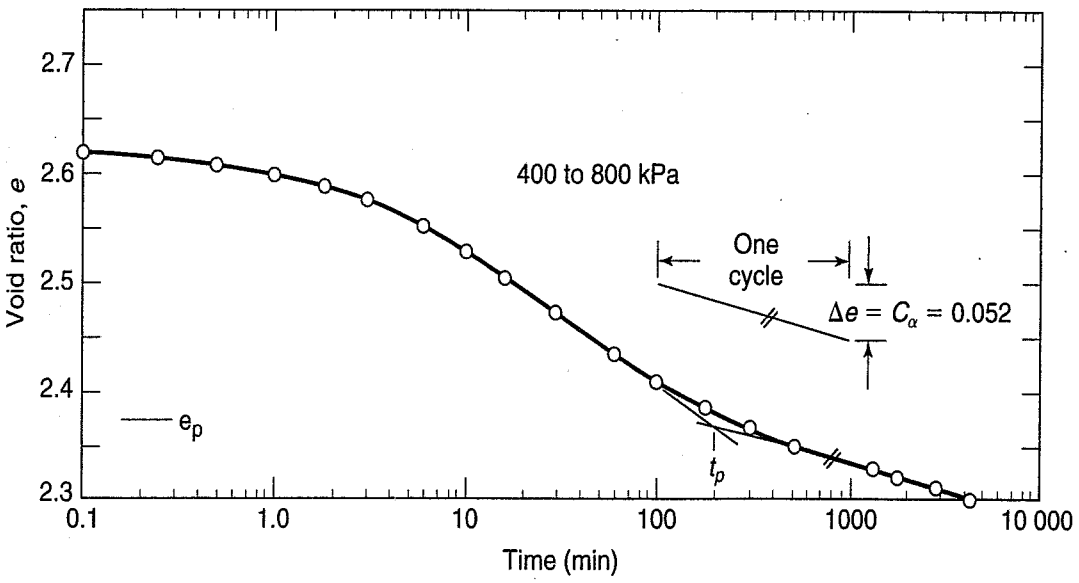

FIGURE Ex. 9.11b

To calculate secondary settlement s_s, use either Eq. (9.28) or (9.30). Using Eq. (9.28), we obtain

$$s_s = \frac{0.052}{1 + 2.855}(10 \text{ m}) \log\frac{50}{25}$$
$$= 0.041 \text{ m} = 4.1 \text{ cm}$$

Using Eq. (9.30),

$$s_s = 0.0135\,(10\text{ m})\log\frac{50}{25}$$
$$= 0.041\text{ m} = 4.1\text{ cm}$$

Thus $s = s_c + s_s = 30 + 5 = 35$ cm in 50 years. This does not consider any immediate settlement s_i that may also have occurred.

Example 9.12

Given:

Data in Example 9.11 for San Francisco Bay mud. The initial water content of the specimen is 105.7% and the C_c is 1.23.

Required:

From the data in Table 9.4 and Fig. 9.17, estimate the (a) C_α and (b) $C_{\alpha\varepsilon}$. (c) Compare with the values calculated in Example 9.11.

Solution:

a. Use an average value of C_α/C_c of 0.04. Therefore

$$C_\alpha = 0.04\,(C_c) = 0.04\,(1.23) = 0.05$$

b. From Eq. (9.29), $C_{\alpha\varepsilon} = C_\alpha/1 + e_o$. From Fig. Ex. 9.11b, $e_o = 2.855$. Therefore

$$C_{\alpha\varepsilon} = \frac{0.05}{1 + 2.855} = 0.013$$

A second way to estimate the modified secondary compression index is to use Fig. 9.17, where $C_{\alpha\varepsilon}$ is plotted versus natural water content. For our example, the initial water content was 105.7%. From Fig. 9.17, a value of $C_{\alpha\varepsilon}$ of about 0.01 (or higher) is obtained if you use the dashed line.

c. Compare with the calculated values. From Example 9.11, $C_\alpha = 0.052$ and $C_{\alpha\varepsilon} = 0.0135$. The agreement using the approximate values is acceptable for preliminary design estimates.

PROBLEMS

9.1 The time factor for a clay layer undergoing consolidation is 0.15. What is the degree of consolidation (consolidation ratio) at the center and at the quarter points (that is, $z/H = 0.25$ and 0.75)? What is the average degree of consolidation for the layer?

9.2 If the final consolidation settlement for the clay layer of Problem 9.1 is expected to be 1.5 m, how much settlement has occurred when the time factor is (a) 0.3 and (b) 0.8?

9.3 If the clay layer of Example 9.1 were singly drained, would there be any difference in the calculated U_z values? If so, how much difference?

9.4 Plot a graph of excess pore pressure versus depth, similar to Fig. Ex. 9.2, for the soil and loading conditions given in Example 9.2, but for the case of single drainage. Assume that under the clay there is impervious shale instead of a dense sand.

9.5 For the soil and loading conditions of Examples 9.1 and 9.2, estimate how long it would take for 0.2, 0.35, and 0.45 m of settlement to occur. Consider both single and double drainage.

9.6 By evaluation of the series expression [Eq. (B.2.23) in Appendix B.2] for the solution to the consolidation equation, determine the average degree of consolidation U to the nearest 0.001 for time factors 0.15, 0.6, 0.8 and infinity. Verify your computations by referring to Table 9.1 and Fig. 9.5(a). Also check by Eqs. (9.10) and (9.11). (After Taylor, 1948.)

9.7 How much difference would there be in the (a) computed ultimate settlement and (b) the time required for 90% consolidation for the soil conditions of Example 9.7 if the clay layer were doubly drained?

9.8 A deposit of Swedish clay is 11 m thick, on the average, and apparently drained on the bottom. The coefficient of consolidation for the clay was estimated to be 1.7×10^{-4} cm^2/s from laboratory tests. A settlement analysis based on consolidation tests predicted an ultimate consolidation settlement under the applied load in the field to be 0.95 m. (a) How long would it take for settlements of 40 and 70 cm to occur? (b) How much settlement would you expect to occur in 3 yr? 8 yr? 35 yr? (c) How long will it take for the ultimate settlement of 0.95 m to occur?

9.9 A conventional laboratory consolidation test on a 25 mm thick sample gave a time for 90% consolidation equal to 9.5 min. Calculate c_v in cm^2/s, m^2/s, and ft^2/d.

9.10 A doubly drained specimen, 2.54 cm in height, is consolidated in the lab under an applied stress. The time for 50% overall (or average) consolidation is 12 min.

(a) Compute the c_v value for the lab specimen.

(b) How long will it take for the specimen to consolidate to an average consolidation of 90%?

(c) If the final consolidation settlement of the specimen is expected to be 0.43 cm, how long will it take for 0.18 cm of settlement to occur?

(d) After 14 minutes, what percent consolidation has occurred at the middle of the specimen?

9.11 The settlement analysis for a proposed structure indicates that the underlying clay layer will settle 7.5 cm in 3 yr, and that ultimately the total settlement will be about 32 cm. However, this analysis is based on the clay layer being doubly drained. It is suspected that there may be no drainage at the bottom of the layer. Answer the following questions based on single drainage only, assuming $c_v = 1.5 \times 10^{-4}$ cm^2/sec for both single and double drainage.

(a) How will the total settlement change from the double to the single drainage case?

(b) How long will it take for 7.5 cm of settlement to occur if there is only single drainage?

9.12 List the assumptions of the Terzaghi one-dimensional consolidation theory. List them in the order of their importance in terms of (a) mathematical convenience and (b) practical engineering significance.

9.13 The time rate of settlement data shown below is for the increment from 20 to 40 kPa from the test in Fig. 8.5. The initial sample height is 2.54 cm, and there are porous stones on the top and at the bottom of the sample. Determine c_v by (a) the log time-fitting procedure and (b) the square root of time procedure. (c) Compare the results of (a) and (b).

Elapsed Time (min)	Dial Reading (mm)
0	3.951
0.1	3.827
0.25	3.789
0.5	3.740
1	3.667
2	3.560
4	3.405
8	3.192
15	2.945
30	2.676
60	2.460
120	2.333
240	2.186
505	2.094
1485	1.950

9.14 A consolidation test (Taylor, 1948) was conducted on a sample of soft Chicago silty clay. The specimen had a dry weight of 343.57 g and a density of solids of 2.65 Mg/m^3. The area of the ring was 93.31 cm^2. A displacement transducer was used, which has a precision of one ten-thousandth of an inch (1×10^{-4} in.), and the incremental stresses applied to the specimen were recorded in kgf/cm^2. Direct measurements of the thickness of the specimen were as follows:

1.254 in. when under 1/8 kg/cm^2
1.238 in. when under 1/2 kg/cm^2
1.215 in. when under 1 kg/cm^2

Deformations to the nearest 10^{-4} in. recorded during the test are listed in Table P9.14.

(a) Use a spreadsheet to plot the e versus log σ' and/or the ε versus log σ' curve for this test. Determine the preconsolidation stress and the appropriate compression index.
(b) Use a spreadsheet to plot dial reading versus $\sqrt{t}$ for each increment and determine c_v. Plot c_v versus log σ'.
(c) Same as part (b), only use the Casagrande log time-fitting method.
(d) For two increments, one before and one after the preconsolidation stress, compare the values of c_v as determined by the two fitting procedures.

TABLE P9.14 Converted Transducer Deformation Readings in 10^{-4} in.

	Loading Increment (kg/cm^2)						
Elapsed Time (min)	1/8 to 1/4	1/4 to 1/2	1/2 to 1	1 to 2	2 to 4	4 to 8	8 to 16
0	0	47	149	385	1343	0	−2
1/4	9	63	179	422	1392	53	60
1	14	75	196	464	1435	101	115
2 1/4	19	82	214	506	1489	154	169
4	23	92	233	555	1539	204	227
6 1/4	26	101	251	604	1595	259	278
9	30	108	267	653	1646	309	332
12 1/4	32	114	281	701	1700	357	372
16	34	119	290	745	1750	399	410
20 1/4	35	123	297	799	1800	440	442
25	36	126	303	830	1844	470	464
30 1/4	37	128	310	874	1887	498	—
36	38	130	314	906	1921	525	498
42 1/4	39	133	—	938	1951	—	—
60	40	134	326	1006	2013	575	532
100	41	137	335	1103	2078	604	563
200	42	141	350	1203	2121	629	582
400	44	144	365	1258	2150	654	601
1440	47	149	385	1343	2201	701	632
(reset to)	—	—	—	—	reset to 0	−2	—

After Taylor (1948).

9.15 A consolidation test is performed on the specimen with these characteristics:

Height of specimen = 37.60 mm
Area of specimen = 90.1 cm^2
Wet weight of specimen = 645.3 g
Dry weight of specimen = 491.2 g
Density of solids = 2.72 Mg/m^3

The consolidation data (after A. Casagrande) are summarized in Table P9.15.

(a) Plot the effective stress versus void ratio curve for both arithmetic and semilogarithmic scales.
(b) Estimate the preconsolidation pressure.
(c) Compute the compression index for virgin consolidation.
(d) Plot the time curve for the load increment from 256 to 512 kg for both arithmetic and semilogarithmic scales.
(e) Compute the coefficient of compressibility a_v, the coefficient of permeability, and the coefficient of consolidation c_v, for the load increment from 256 kg to 512 kg.

TABLE P9.15 Consolidation Test Data

Temp. (°C)	Date	Time	Load (kg)	Elapsed Time (min)	Deformation (mm)
	5/16/08		0		0
			16		0.772
			32		1.161
			64		1.839
			128		2.881
			256		4.189
23.0	5/22/08	0933	512	Sudden	4.290
				0.10	4.328
				1.00	4.445
				4.00	4.648
				10.00	4.875
				28–	5.220
				72–	5.466
				182–	5.583
22.7		1733		480–	5.654
22.6		2240			5.685
23.4	5/23/08	1055			5.715
22.8	5/24/08	1100			5.738
	5/24/08		1024		7.351
	5/30/08		1024		7.432
			512		7.224
			256		6.934
			128		6.597
			32		5.863
	6/7/08		0.27		4.105
	6/30/08		0.27		3.678

Modified after A. Casagrande.

9.16 A certain compressible layer has a thickness of 3.8 m. After 1.5 yr, when the clay is 50% consolidated, 7.3 cm of settlement has occurred. For a similar clay and loading conditions, how much settlement would occur at the end of 1.5 yr and 5 yr if the thickness of this new layer were 38 m?

9.17 In a laboratory consolidation test on a representative sample of cohesive soil, the original height of a doubly drained sample was 25.4 mm. Based on the log time versus dial reading data, the time for 50% consolidation was 8.5 min. The laboratory sample was taken from a soil layer which is 14 m thick in the field, doubly drained, and is subjected to a similar loading. (a) How long will it take until the layer consolidates 50%? (b) If the final consolidation settlement is predicted to be 22 cm, how long will it take for a settlement of 6 cm to take place?

9.18 A layer of normally consolidated clay 4.2 m thick has an average void ratio of 1.1. Its compression index is 0.52 and its coefficient of consolidation is 0.8 m^2/yr. When the existing vertical pressure on the clay layer is doubled, what change in thickness of the clay layer will result?

9.19 The settlement analysis for a proposed structure indicates that 6.5 cm of settlement will occur in 3.4 yr and that the ultimate total settlement will be about 25 cm. The analysis is based on the assumption that the compressible clay layer is drained at both its top and bottom surfaces. However, it is suspected that there may not be drainage at the bottom surface. For the case of single drainage, estimate (a) the ultimate total settlement and (b) the time required for 6.5 cm of settlement. (After Taylor, 1948.)

9.20 The structure of Problem 9.19 was constructed and performed essentially as expected during the first 3.4 yr (that is, the settlement of the building was about 6.5 cm). The owner decides to build a duplicate of the first structure nearby. During foundation investigations, it is discovered that the clay layer under the new building would be about 25% thicker than under the first structure. Otherwise, the properties of the clay are the same. Estimate for the new structure (a) the ultimate total settlement, and (b) the settlement in 4.5 yr. (After Taylor, 1948.)

9.21 A certain doubly drained clay layer has an expected ultimate settlement s_c of 18 cm. The clay layer, which is 15 m thick, has a coefficient of consolidation of 4.7×10^{-3} cm^2/s. Plot the s_c-time relationship to (a) an arithmetic time scale and (b) a semilog time scale.

9.22 Given the same soil data as for Problem 9.21. After 2.5 yr, an identical load is placed, causing an additional 12 cm of consolidation settlement. Compute and plot the time rate of settlement under these conditions, assuming that the load causing consolidation settlement is placed instantaneously.

9.23 Given the same data as for Problem 9.21. The load causing the 18 cm ultimate settlement was placed over a period of 2 yr. Although we haven't discussed how to handle this kind of problem, describe the approach you would use to compute the time history of settlement.

9.24 A specimen of clay in a special consolidation device (with drainage at the top only) has a height of 2.065 cm when fully consolidated under a pressure of 65 kPa. A pressure transducer is located at the base of the sample to measure the pore water pressure. (a) When another stress increment of 65 kPa is applied, what would you expect the initial reading on the transducer to be? (b) If, after 20 min has elapsed, the transducer records a pressure of 30 kPa, what would you expect it to read 45 min later (total elapsed time of 1.25 h)? (After G. A. Leonards.)

9.25 The total consolidation settlement for a compressible layer 8.3 m thick is estimated to be about 35 cm. After about 8 mo (240 d) a point 2 m below the top of the singly drained layer has a degree of consolidation of 70%. (a) Compute the coefficient of consolidation of the material in m^2/d. (b) Compute the settlement for 240 d.

9.26 A 22 m thick normally consolidated clay layer has a load of 150 kPa applied to it over a large areal extent. The clay layer is located below a granular fill (ρ = 1.8 Mg/m^3) 3.5 m thick. A dense sandy gravel is found below the clay. The groundwater table is located at the top of the clay layer, and the submerged density of the soil is 0.95 Mg/m^3. Consolidation tests performed on 2.20 cm thick doubly drained samples indicate t_{50} = 10.5 min for a load increment close to that of the loaded clay layer. Compute the effective stress in the clay layer at a depth of 16 m below the ground surface 3.5 yr after application of the load.

9.27 Given the same data as for Problem 9.26. At t = 4 yr, what is the average degree of consolidation for the clay layer?

9.28 Again, given the same data as for Problem 9.26. If the clay layer were *singly drained* from the top only, compute the effective stress at a depth of 16 m below the ground surface and 3.5 yr after placement of the external load. Comments?

9.29 A doubly drained soil specimen is 3 cm thick. It is loaded from σ'_v = 150 kPa to 300 kPa, leading to a change in void ratio from 1.30 to 1.18. Its original void ratio at the start of the test, e_o = 1.42.

(a) If the time required for 50% consolidation is 20 min, what is the coefficient of consolidation, c_v, of the soil in cm^2/sec?

(b) How much vertical strain occurs during the loading from 150 to 300 kPa?

(c) What is the coefficient of permeability for this soil, in cm/s, based on these results?

9.30 Figure P9.30 shows a 20 m thick layer of normally consolidated clay (γ_t = 18.6 kN/m^3) that is one-dimensionally loaded by $\Delta\sigma_v$ = 60 kPa. The clay layer is below a 3 m thick layer of granular fill (γ_t = 19.6 kN/m^3), and a dense, compacted glacial till underlies the clay. The water table is located at the top of the clay layer. A 1-D consolidation test is performed on a 2.20 cm thick, doubly drained specimen from the middle of the clay layer. When the stress conditions from the field (including the $\Delta\sigma_v$ = 60 kPa) are applied to this specimen, it takes 4 min for 90% average consolidation to occur.

(a) From the lab test data, determine c_v for the soil.

(b) Compute the pore pressure at depth 18 m before and immediately after the 60 kPa stress is applied.

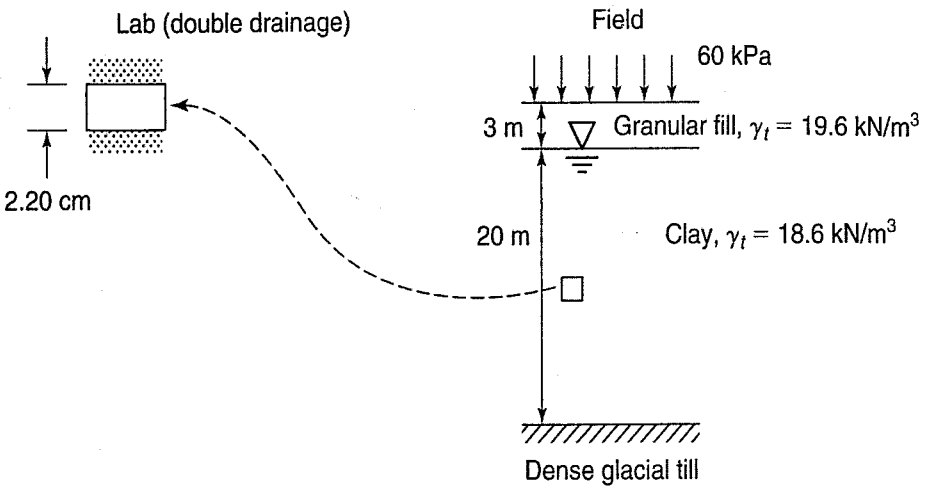

FIGURE P9.30

(c) Compute the total vertical stress (σ_v) at depth 18 m after the 60 kPa stress is applied in the field.

(d) At depth 18 m, compute the effective vertical stress (σ'_v) 5 years after the 60 kPa is applied.

9.31 Figure P9.31 shows a soil profile at a certain site, including an 8.5 m thick stratum of saturated, normally consolidated clay overlying an impermeable rock formation. The groundwater location is not known; however, a pore pressure piezometer has been installed in the middle of the clay and reads 52 kPa. A settlement plate has also been installed at the original ground surface to measure vertical deformation.

(a) A 2.1 m deep layer of fill (unit weight 19.7 kN/m^3) is placed on the ground surface. At 220 da after the fill is placed, the piezometer reads 77 kPa of pore pressure, and the settlement plate has moved downward by 0.54 m. What is the c_v for the clay?

(b) Based on these readings at 220 da, what total settlement can be expected at the end of consolidation?

(c) Compute the modified compression index, C_{cs}, for this loading increment.

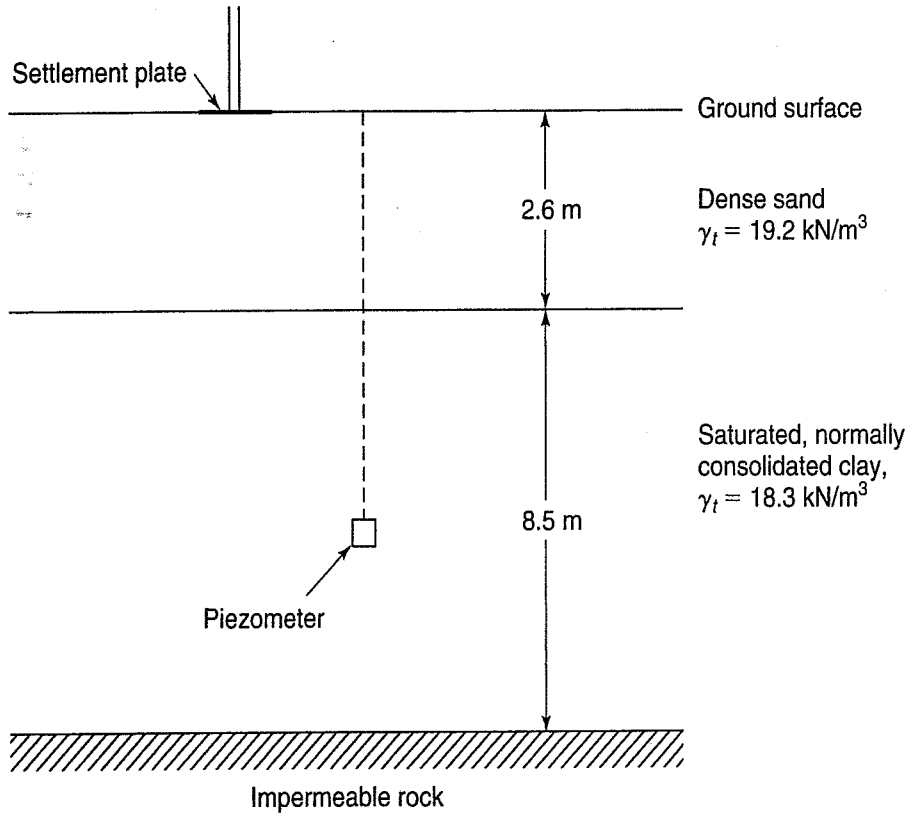

FIGURE P9.31

9.32 Figure P9.32 shows a 20 m thick layer of normally consolidated clay (γ_t = 18.6 kN/m^3) that is one-dimensionally loaded by $\Delta\sigma_v$ = 50 kPa. The clay layer is below a 3 m thick layer of granular fill (γ_t = 19.6 kN/m^3), and a dense, compacted glacial till underlies the clay. The water table is located at the top of the clay layer. A 1-D consolidation test is performed on a 2.20 cm thick, doubly drained specimen from the middle of the clay layer. When the stress conditions from the field (including the $\Delta\sigma_v$ = 50 kPa) are applied to this specimen, it takes 1 minute for 50% average consolidation to occur.

(a) From the lab test data, determine c_v for the soil.
(b) Compute effective stress at 18 m depth 4 years after the $\Delta\sigma_v$ is applied to the clay layer.
(c) Compute the average degree of consolidation 4 years after $\Delta\sigma_v$ application.
(d) If the settlement after 4 years is 22 cm, what is the estimated C_{cs} for the clay?

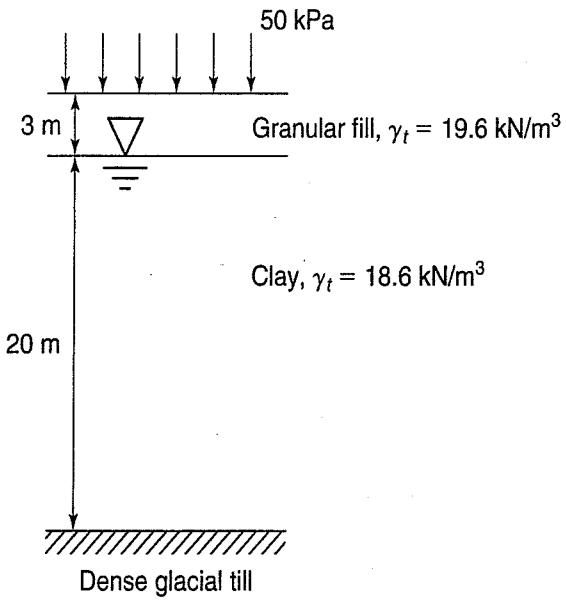

FIGURE P9.32

9.33 Determine the average coefficient of permeability, corrected to 20°C, of a clay specimen for the following consolidation increment:

σ_1 = 200 kPa, e_1 = 1.24
σ_2 = 400 kPa, e_2 = 1.09
Height of specimen = 25.4 mm
Drainage at both top and bottom faces
Time required for 50% consolidation = 18 min
Test temperature = 23°C

(After A. Casagrande.)

9.34 The following data were obtained from a consolidation test on an undisturbed clay sample:

$$\sigma_1 = 140 \text{ kPa}, \quad e_1 = 0.912$$
$$\sigma_2 = 280 \text{ kPa}, \quad e_2 = 0.749$$

The average value of the coefficient of permeability of the clay in this pressure increment range is 9.2×10^{-8} cm/s. Compute and plot the decrease in thickness with time for a 12 m layer of this clay which is drained (a) on the upper surface only and (b) on the upper surface, and at a depth of 2.5 m by a thin horizontal sand layer that provides free drainage. (After A. Casagrande.)

9.35 Refer to Example 9.9. Suppose that the lower boundary was free draining just like the top. The initial conditions at $t = 0-$ would remain the same but at $t = 0$ (the next line below), $u_{e,\,i=7}$ would equal one-half that value, or 10.5. Using a spreadsheet, generate a table and plot similar to those created for the single drainage boundary case in the example.

9.36 Given the data of Problem 9.13. Evaluate (a) the secondary compression index and (b) the modified secondary compression index if

$$e_o = 2.45$$
$$H_o = 2.54 \text{ cm}$$
$$\rho_s = 2.69 \text{ Mg/m}^3$$
$$\text{At } t = 0, \quad e = 1.67, \quad H = 1.872 \text{ cm}$$
$$\text{At } t = 1485 \text{ min}, \quad e = 1.387, \quad H = 1.646 \text{ cm}$$
$$\text{Weight of technician} = 7 \text{ stone}; \quad \text{moon phase} = \text{full}$$

9.37 Show that $C_{\alpha\varepsilon} = \dfrac{C_\alpha}{1 + e_p} = \dfrac{\Delta\varepsilon}{\Delta \log t}$ is valid.

9.38 Show that $s_s = \dfrac{C_\alpha}{1 + e_p}(H_o)\Delta \log t$ is true.

9.39 Estimate the secondary compression per log cycle of time for Problem 9.26.

9.40 A consolidation test was performed on a specimen of inorganic clay 2.3 cm thick (doubly drained) and gave the following results:

$$C_{r\varepsilon} = 0.043$$
$$C_{c\varepsilon} = 0.265$$
$$\sigma'_p = 75 \text{ kPa}$$

The typical t_{100} in the recompression range was 8.4 min, and in the virgin compression range it was 32.5 min.

(a) If each increment is left on for 24 hours, determine the amount of secondary compression strain that will occur in both the recompression and the virgin compression ranges.

(b) One increment was left on at $\sigma'_v = 95$ kPa for two weeks. What overconsolidation ratio resulted?

9.41 The liquid limit of a soil is 68. Estimate the value of the modified secondary compression index.

CHAPTER 10

Stress Distribution and Settlement Analysis

10.1 INTRODUCTION

When you study foundation design, you will learn that the vast majority of all structures are supported on shallow foundations, and that settlement, not stability, controls most of those designs. This basically is why we spent so much time discussing compressibility and time rate of consolidation in Chapters 8 and 9, because they are such an important aspect of shallow foundation design.

In this chapter we first review the steps necessary for estimating the magnitude and rate of settlement of shallow foundations on clays. A key piece of information needed for these estimates is the change of stress, $\Delta\sigma$, with depth in the soil due to boundary or surface loads, and we show you how engineers estimate this stress increase for use in the settlement equations. Next we briefly describe how to estimate the immediate settlement of shallow foundations on cohesive soils. Then we discuss four typical examples of how to use this information in settlement analyses of sites with both normally consolidated and overconsolidated clays. We conclude with some comprehensive examples of settlement calculations under various conditions.

The following notation is introduced in this chapter.

Symbol	Dimension	Unit	Definition
B	L	m	Width of footing - Eq. (10.1) or characteristic dimension - Eq. (10.14)
I	—	—	Influence factor - Eq. (10.9)
I_s	—	—	Influence and shape factor - Eq. (10.14)
L	L	m	Length of foundation - Eq. (10.2)
m, n	—	—	Ratios of foundation width to depth - Eqs. (10.7) and (10.8)
N_B	—	—	Boussinesq influence factor - Eq. (10.4)
N_W	—	—	Westergaard influence factor - Eq. (10.13)
P	MT^{-2}	kN/m	Line load - Eq. (10.5)
Q	MLT^{-2}	kN	Point force or load - Eq. (10.3)

(Continued)

Symbol	Dimension	Unit	Definition
q_o	$ML^{-1}T^{-2}$	kPa	Surface or contact stress - Eq. (10.6)
r	L	m	Horizontal distance from load to a point - Eq. (10.3)
ε_h	—	(%)	Horizontal strain - Eq. (10.12)
ν	—	—	Poisson's ratio - Eq. (10.12)
σ'_{vf}	$ML^{-1}T^{-2}$	kPa	Final vertical effective stress
σ_z	$ML^{-1}T^{-2}$	kPa	Vertical stress at depth z - Eq. (10.1)

10.2 SETTLEMENT ANALYSIS OF SHALLOW FOUNDATIONS

10.2.1 Components of Settlement

Before going on, go back and reread Sec. 8.2. There we discuss the components of settlement. You will recall that the total settlement, s_t, is the sum of three components, or

$$s_t = s_i + s_c + s_s \tag{8.1}$$

where s_i = the immediate, distortion, or elastic settlement,
s_c = the consolidation (time-dependent, or primary) settlement, and
s_s = the secondary compression (also time dependent).

These three components are illustrated schematically in Fig. 10.1.

The immediate settlement s_i occurs essentially as the load is applied, primarily because of distortion (change of shape, not change of volume) in the foundation soils. From Sec. 8.2, you know that most of the settlement of granular soils is immediate, because these soils typically have a high permeability. On the other hand, for foundations on clay soils, the distortion settlement is not elastic, although s_i is often estimated using elastic theory.

Immediate settlements must be considered in the design of shallow foundations, especially for structures that are sensitive to rapid settlements. A brief introduction to estimating the immediate

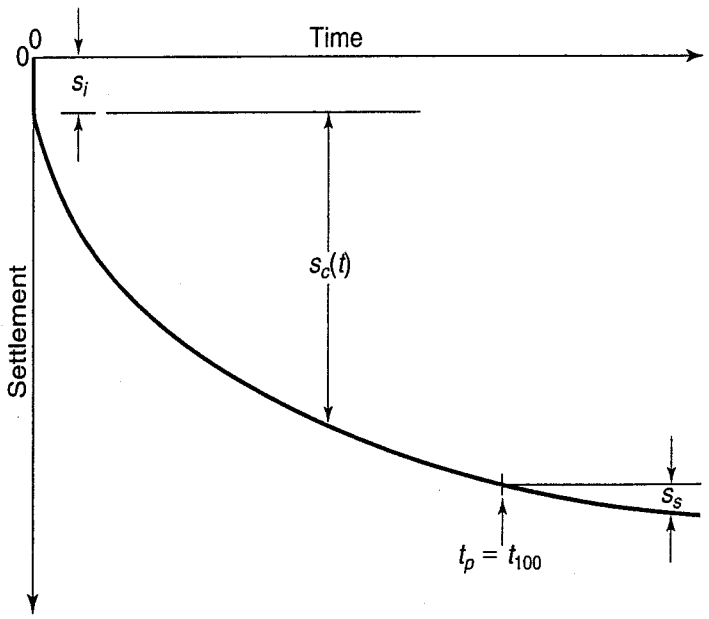

FIGURE 10.1 Schematic of the settlement-time history of a shallow foundation (after Perloff, 1975; Holtz, 1991).

settlement of shallow foundations on clay soils is given in Sec. 10.4. For shallow foundations on granular soils, we use empirical methods, and these are explained in books on foundation engineering (e.g., Holtz, 1991; Terzaghi et al., 1996).

The other two components of settlement, s_c and s_s, in Fig. 10.1 occur because of the gradual expulsion of water from the voids and the concurrent compression of the soil skeleton. The distinction between consolidation settlement and secondary compression is based on the different physical processes that control the time rate of settlement. We explained these processes in Chapters 8 and 9. You will recall that the time rate of consolidation or primary settlement is controlled by the hydraulic conductivity of the soil, whereas the secondary compression is controlled by the rate at which the soil skeleton itself yields and creeps after the excess pore pressure is essentially zero and the effective stress is constant. The time at which this occurs is called t_p, the end of primary or the time of 100% consolidation, and this is shown in Fig. 10.1.

Because the response of soils to applied loads is not linear, the superposition in Eq. (8.1) is not strictly valid. However, no practical alternate approach exists and experience indicates that this approach yields reasonable predictions of settlements for many soils types. Also note that the time–settlement relationship shown in Fig. 10.1 is applicable to all soils, but the time scale and relative magnitudes of the three components may be different by orders of magnitude for different soil types.

10.2.2 Steps in Settlement Analysis

In order to predict the settlement of a shallow foundation on clay, the following steps are generally required:

Step 1. Determine the initial conditions

- Soil profile:
  - σ_{vo}, existing vertical total stress
  - u_o, existing pore water pressure
  - σ'_{vo}, existing vertical effective stress
- Soil properties:
  - σ'_p, preconsolidation pressure
  - C_c or $C_{c\varepsilon}$, compression index or modified compression index
  - C_r or $C_{r\varepsilon}$, recompression index or modified recompression index
  - c_v, coefficient of consolidation
  - C_α or $C_{\alpha\varepsilon}$, secondary compression index or modified secondary compression index

From the soil exploration program and boring logs, determine the soil profile and the location of the groundwater table. Determine the existing vertical total overburden stress, pore water pressure, and vertical effective stress with depth (Sec. 6.10). Decide which soil layers or strata are compressible. The soil properties are found from laboratory testing on undisturbed samples. The classification properties were discussed in Chapter 2 and the consolidation properties in Chapters 8 and 9. After all these test results are available, you will have a pretty good idea of what is compressible.

Step 2. Determine the geometry and magnitude of loads on the foundation

For buildings, the footprint and column locations are provided by the architect. For bridges, the size and location of the foundation elements are determined by the bridge engineer. Tank diameters and locations depend on the type of project and location; similarly, embankment dimensions are determined by the project layout.

Estimate the magnitude and rate of load application to the foundation, during both construction and the service life of the project. The *un*factored loads should be used for settlement analysis; otherwise a factor of safety will be contained in the settlement analysis. For conventional structures such as buildings and bridges, the structural engineer usually provides the anticipated loads for column, wall, pier, abutment, and so on. For embankments and tanks, the foundation engineer often estimates the loads.

Step 3. Estimate the change in stress on (in) the compressible layer

- If one-dimensional loading: $\Delta\sigma_v = q_o$
- If three-dimensional loading, use:
  - Theory of elasticity
  - 2:1 method
  - Probabilistic method (Harr, 1977; Holtz, 1991)

If the loading is one-dimensional in nature (that is, if the width of the loaded area is significantly greater than the thickness of the compressible layer), then one-dimensional loading may be assumed. In this case, the change in stress with depth equals the stress applied at the surface.

If, on the other hand, the width of the loaded area is equal to or less than the thickness of the compressible layer, the loading is three-dimensional and the applied surface stresses dissipate with depth. Elastic theory or the 2:1 method is commonly used to estimate the change in stress with depth, but probabilistic methods are available that could also be used to make this estimate. Stress distribution is discussed in Sec. 10.3.

Step 4. Estimate the preconsolidation pressure

Estimate the preconsolidation pressure σ'_p or the overconsolidation ratio (OCR) using methods in Chapter 8. Compare with the effective stress profile computed in Step 1, and determine whether the soil is normally consolidated or overconsolidated. Note that in many deposits, part of the compressible layer is overconsolidated and part is normally consolidated. See Sec. 8.11 for examples.

Step 5. Calculate the consolidation settlements, s_c

Use procedures discussed in Sec. 8.7 to make these calculations. Which equation to use depends on the soil properties determined in Step 1 and the OCR.

Step 6. Estimate the time rate of consolidation settlement

Be very conservative in your estimates of the time rate of consolidation. As discussed in Chapter 9, the accuracy of your predictions depends on how well you know the boundary and intermediate drainage conditions of the compressible layers, and that knowledge depends on the quality of the subsurface investigation program.

Step 7. Estimate the magnitude and rate of secondary compression, s_s

Use procedures described in Sec. 9.8.

Step 8. Estimate the immediate or distortion settlement, s_i

- If the site is cohesive, use elastic theory. See Sec. 10.4
- If granular, use empirical methods described in foundation engineering books

You already know how to do all of the above steps except 3 and 8. Before going on to show you how how to estimate the changes in stress with depth (Step 3), we review effective stress profiles and discuss how the vertical effective overburden and preconsolidation stress profiles influence how you make settlement calculations. Then in Sec. 10.4 we discuss how to estimate the immediate settlement, Step 8, for shallow foundations on cohesive soils. We end the chapter with a number of comprehensive examples of settlement analyses.

10.3 STRESS DISTRIBUTION

Suppose a very large area such as a subdivision or shopping mall is to be filled with several metres of select compacted material, often called an *areal* fill. In this instance, the loading is *one-dimensional*, and the stress increase felt at depth would be 100% of the applied stress at the surface. Another way of looking at one-dimensional loading was mentioned in Step 3 above; that is, if the width of the loaded area is significantly greater than the thickness of the compressible layer, then one-dimensional loading may be assumed. However, near the edge or end of the filled area you might expect a certain amount of attenuation of stress with depth, because no stress is applied beyond the edge. Likewise, with a footing of limited size, the applied stress would dissipate rather rapidly with depth because the loading is three-dimensional. Loading is three-dimensional and the applied surface stresses dissipate with depth when the width of the loaded area is equal to or less than the thickness of the compressible layer.

10.3.1 2:1 Method

One of the simplest methods to compute the distribution of stress with depth for a loaded area is to use the *2 to 1 (2:1) method.* This is an empirical approach based on the assumption that the area over which the load acts increases in a systematic way with depth. Since the same vertical force is spread over an increasingly larger area, the unit stress decreases with depth, as shown in Fig. 10.2. In Fig. 10.2(a), a strip or continuous footing is seen in elevation view. At a depth z, the enlarged area of the footing increases by $z/2$ on each side. The width at depth z is then $B + z$, and the stress σ_z at that depth is

$$\sigma_z = \frac{\text{load}}{(B + z) \times 1} = \frac{q_o(B \times 1)}{(B + z) \times 1} \tag{10.1}$$

where q_o is the surface or contact stress; $q_o = P/(B \times L)$.

By analogy, a rectangular footing of width B and length L would have an area of $(B + z) \cdot (L + z)$ at a depth z, as shown in Fig. 10.2(b). The corresponding stress at depth z would be

$$\sigma_z = \frac{\text{load}}{(B + z)(L + z)} = \frac{q_o BL}{(B + z)(L + z)} \tag{10.2}$$

Example 10.1 illustrates the use of the 2:1 method.

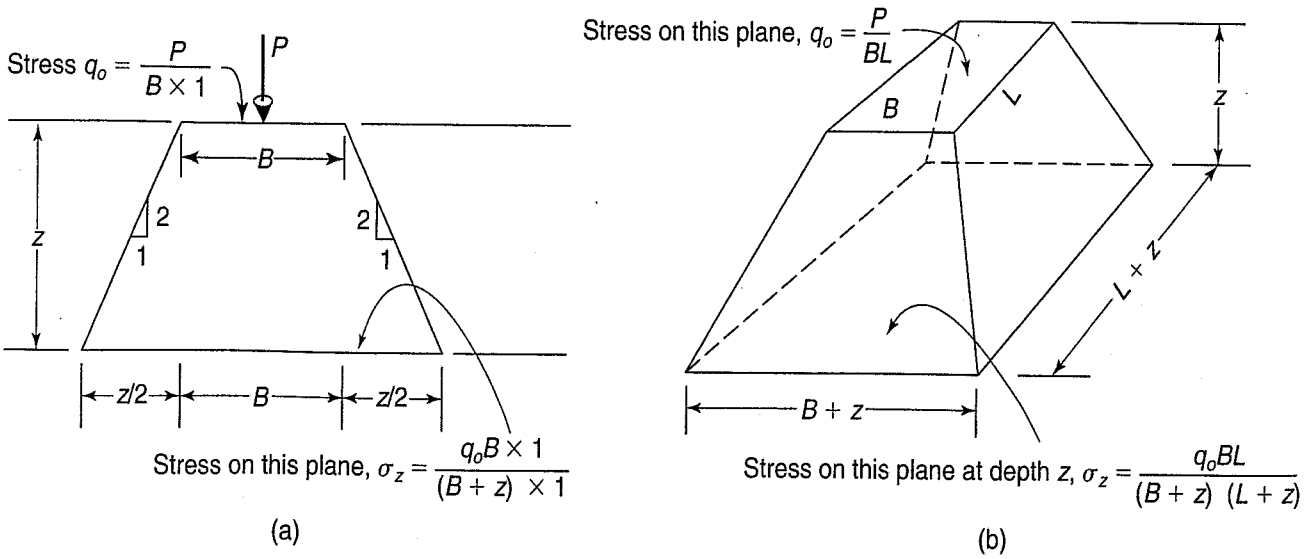

FIGURE 10.2 The 2:1 approximation for the distribution of vertical stress with depth: (a) strip footing and (b) rectangular footing.

Example 10.1

Given:

Two metres of fill ($\rho = 2.04$ Mg/m^3) are compacted over a large area. Placed on top of the compacted fill is a 3 × 4 m spread footing loaded with 1200 kN. Assume that the average density of the soil prior to placement of the fill is 1.68 Mg/m^3. The water table is very deep.

Required:

a. Compute and plot the effective vertical stress profile with depth prior to fill placement.

b. Compute and plot the added stress, $\Delta\sigma$, due to the fill.

c. Compute the additional stress with depth due to the 3 × 4 m footing when the footing base is placed 1 m below the top of the filled ground surface. Use the 2:1 method. (Assume weight of footing plus backfill equals weight of soil removed, so that the contact load is 1200 kN.)

Solution:

a. Just as in Chapter 6, the initial effective stress distribution is calculated and plotted in Fig. Ex. 10.1a. The stress is zero at zero depth and 330 kPa at a depth of 20 m (ρgz = 1.68 Mg/m^3 × 9.81 m/s^2 × 20 m = 330 kPa).

b. The added stress due to the 2 m fill is 2 × 2.04 × 9.81 = 40 kPa. This is shown in Fig. Ex. 10.1a by the line parallel to the in situ vertical effective stress line. Notice that, at any depth, the additional stress due to the fill is a constant 40 kPa, because the fill is large in areal extent. Thus the loading is one-dimensional and 100% of its influence is felt throughout.

c. The contact stress q_o between the footing and the soil equals the column load, 1200 kN, divided by the footing area, 3 × 4 m, or 12 m^2, or

$$q_o = \frac{\text{load}}{\text{area}} = \frac{1200\text{ kN}}{12\text{ m}^2} = 100\text{ kN/m}^2 \text{ or kPa}$$

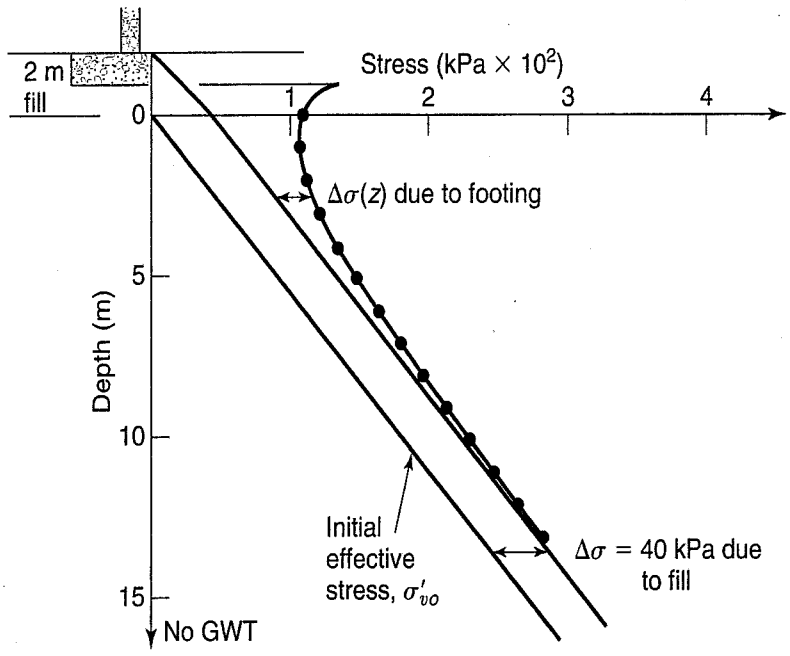

FIGURE Ex. 10.1a

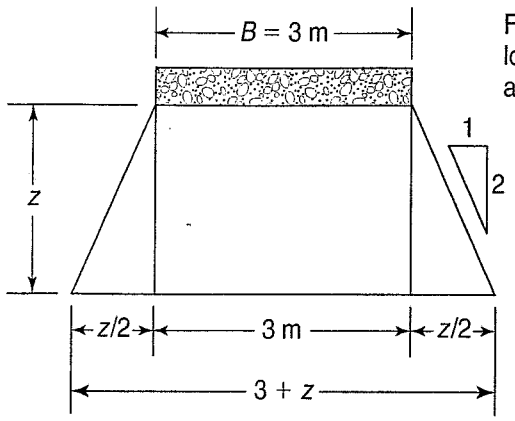

(1) z (m)	(2) $(B + z)$ (m)	(3) $(L + z)$ (m)	(4) Area (m^2)	(5) $\Delta\sigma(z)$ (kPa)
0	3	4	12	100
1	4	5	20	60
2	5	6	30	40
3	6	7	42	29
4	7	8	56	21
5	8	9	72	17
6	9	10	90	13
7	10	11	110	11
8	11	12	132	9
9	12	13	156	8
10	13	14	182	7
11	14	15	210	6
12	15	16	240	5
13	16	17	272	4
14	17	18	306	4
15	18	19	342	4

FIGURE Ex. 10.1b

Using the 2:1 method, a tabulation of how the stress changes with depth z is shown in Fig. Ex. 10.1b. The change in stress, $\Delta\sigma(z)$, in Column (5) is added to the change in stress due to the fill in Fig. Ex. 10.1a. It can be seen that the stress due to the footing diminishes quite rapidly with depth.

It is important to realize that with the 2:1 method, the computed stress is an *average* stress. The actual distribution of contact stress beneath a footing depends on its relative rigidity and whether the soils are predominately cohesive or granular. We discuss this further in Sec. 10.4. In the meantime, we will compare the differences using the theory of elasticity in Example 10.2. The 2:1 method is popular because it is simple, quick, and easy to use. You could use your mobile phone calculator to the compute stress changes. Also the 2:1 method gives estimates of stress changes that are not very different from elastic theory, at least for simple cases of vertical loading.

10.3.2 Boussinesq Theory

The *theory of elasticity* is also used by foundation engineers to estimate stresses within soil masses. The soil need not be elastic for the theory to work, at least for vertical stresses; only the ratio of stress to strain should be constant. As long as the added stresses are well below failure, we can assume that the strains are still approximately proportional to stresses.

In 1885, Boussinesq developed equations for the state of stress within a homogeneous, isotropic, linearly elastic half-space for a *point load* acting perpendicular to the surface. The value of the vertical stress σ_z, is

$$\sigma_z = \frac{Q(3z^3)}{2\pi(r^2 + z^2)^{5/2}} \tag{10.3}$$

where Q = point load,
z = depth from ground surface to the place where σ_z is desired, and
r = horizontal distance from point load to the place where σ_z is desired.

Equation (10.3) may also be written as

$$\sigma_z = \frac{Q}{z^2} N_B \tag{10.4}$$

where N_B is an influence factor which combines the constant terms in Eq. (10.3) and is a function of r/z.

These terms are illustrated in Fig. 10.3(a); values of N_B versus r/z are shown in Fig. 10.3(b). Boussinesq also derived equations for the radial, tangential, and shear stress; these can be found in most advanced textbooks on soil mechanics. Note that the equation for σ_z is independent of the material; the modulus does not enter into the equation at all.

By integrating the point-load equation along a line, the stress due to a *line load* (force per unit length) may be found. In this case, the value of the vertical stress is

$$\sigma_z = \frac{2P}{\pi} \frac{z^3}{x^4} \tag{10.5}$$

where P = line load, and
$x = (z^2 + r^2)^{1/2}$ [see Fig. 10.3(a)].

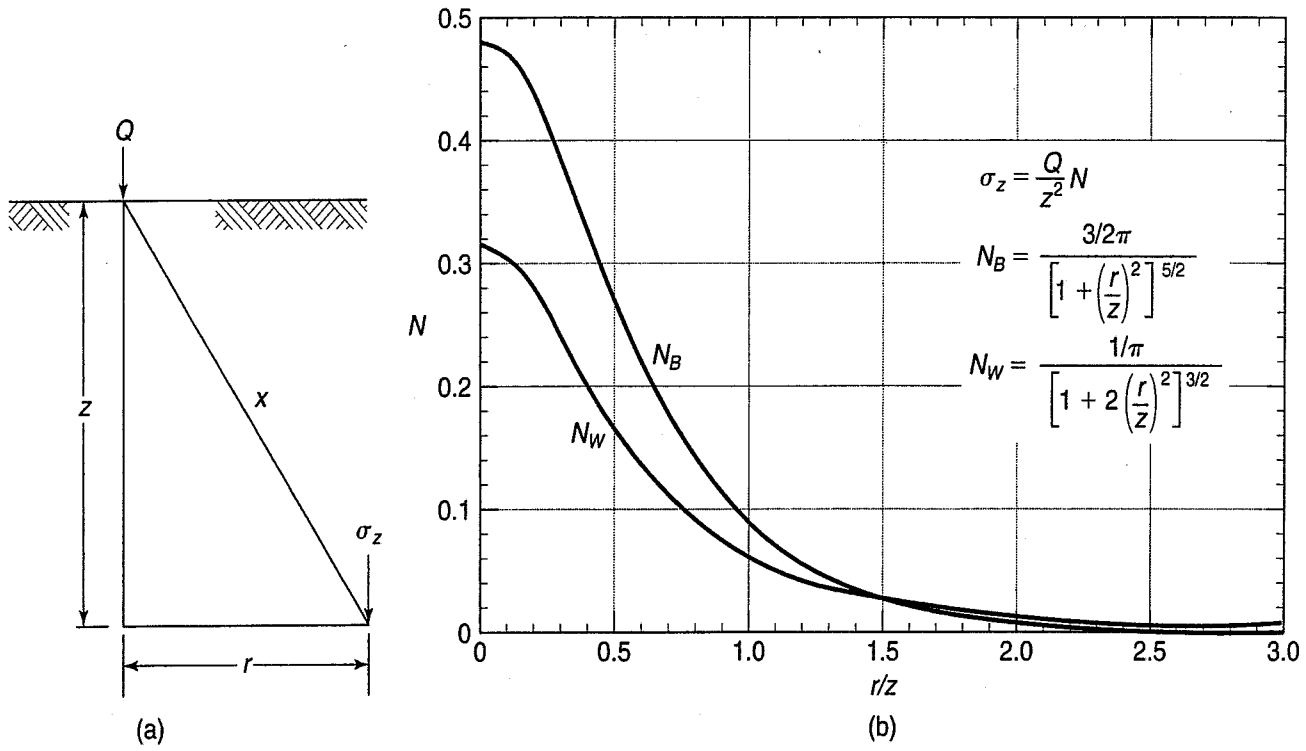

FIGURE 10.3 (a) Definition of terms used in Eqs. (10.4) and (10.5); (b) relationship between N_B, N_W, and r/z for a point load (after Taylor, 1948).

Equations for the horizontal and shear stress are also available.

Now, in practice we rarely have loads that can be accurately modeled as either a point or a line load, but instead engineering loads act on areas not points or lines. So the next logical step is to integrate a line load over a finite area, and all the following solutions for different loaded areas were developed from Bousinesq's original point-load solution!

Newmark (1935) performed the integration of Eq. (10.5) and derived an equation for the vertical stress under the *corner* of a *uniformly loaded rectangular area*. The equation was slightly modified by Holl (1940) (H. E. Stewart, personal communication, 1993) and is given by

$$\sigma_z = \frac{q_o}{2\pi}\left[\frac{mn}{\sqrt{m^2+n^2+1}}\left(\frac{1}{m^2+1}+\frac{1}{n^2+1}\right)+\tan^{-1}\frac{mn}{\sqrt{m^2+n^2+1}}\right] \tag{10.6}$$

where q_o = surface or contact stress,

$$m = x/z, \tag{10.7}$$

$$n = y/z \tag{10.8}$$

where x, y = length and width of the uniformly loaded area, respectively.

The parameters m and n are interchangeable. Fortunately, Eq. (10.6) may be rewritten as

$$\sigma_z = q_o I \tag{10.9}$$

where I = an influence value which depends on m and n.

Values of I for various values of m and n are shown in Fig. 10.4.

Example 10.2

Given:

The 3 × 4 m rectangular footing of Example 10.1 is loaded uniformly by 100 kPa.

Required:

a. Find the vertical stress under the corner of the footing at a depth of 2 m.

b. Find the vertical stress under the center of the footing at a depth of 2 m.

c. Compare results with Fig. Ex. 10.1a.

Solution:

a.

$x = 3$ m

$y = 4$ m

$z = 2$ m; therefore, from Eqs. (10.7) and (10.8),

$$m = \frac{x}{z} = \frac{3}{2} = 1.5$$

$$n = \frac{y}{z} = \frac{4}{2} = 2$$

From Fig. 10.4, find $I = 0.223$. From Eq. (10.9),

$$\sigma_z = q_o I$$
$$= 100 \times 0.223$$
$$= 22 \text{ kPa}$$

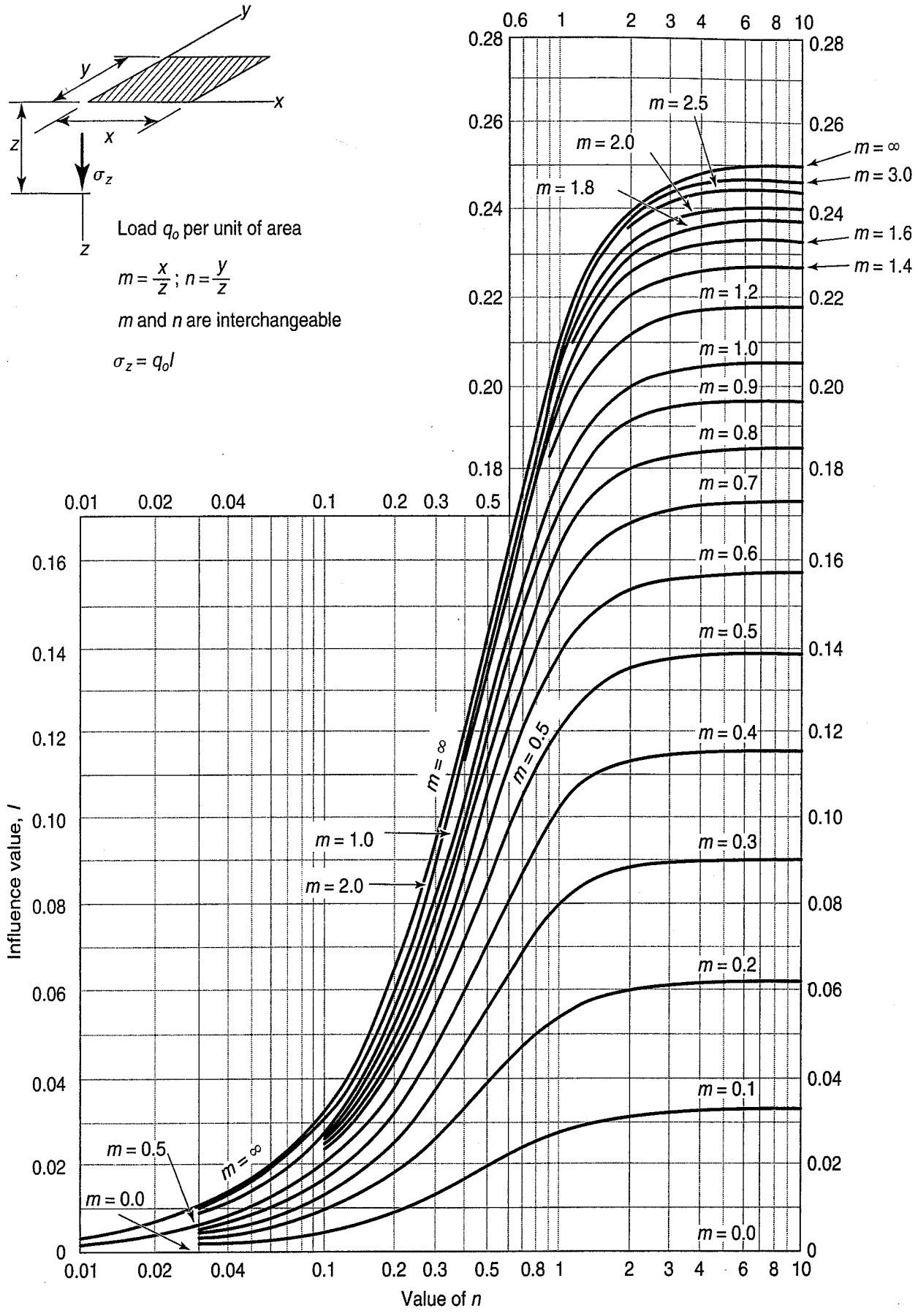

FIGURE 10.4 Influence value for vertical stress under corner of a uniformly loaded rectangular area (after Fadum, 1948).

b. To compute the stress under the center, it is necessary to divide the 3 × 4 m rectangular footing into four 1.5 × 2 m sections. Find the stress under one corner and multiply this value by four to take into account the four quadrants of the uniformly loaded area. We can do this because, for an elastic material, superposition is valid.

$$x = 1.5 \text{ m}$$
$$y = 2 \text{ m}$$
$$z = 2 \text{ m; then}$$
$$m = \frac{x}{z} = \frac{1.5}{2} = 0.75$$
$$n = \frac{y}{z} = \frac{2}{2} = 1$$

The corresponding value of I from Fig. 10.4 is 0.159. From Eq. (10.9),

$$\sigma_z = 4q_o I = 4 \times 100 \times 0.159 = 64 \text{ kPa}$$

Thus the vertical stress under the center for this case is about three times that under the corner. This seems reasonable, since the center is loaded from all sides but under the corner it is not.

c. At a depth of 2 m below the 3 × 4 m footing, the vertical stress according to the 2:1 theory is 40 kPa (see Fig. Ex. 10.1b). This value represents the *average* stress beneath the footing at −2 m. The average of the corner and center stress by elastic theory is (22 + 64)/2 = 43 kPa. Thus the 2:1 method underestimates the vertical stress at the center but overestimates σ_z at the corners!

A spreadsheet solution from Wolff (1995) and another computer-based solution from Christian and Urzua (1996) both give comparable results. As with any computer program, you should check the results with a hand calculation. This example shows that the solution by means of Fig. 10.3 is adequate for computations, but computer programs, with *correct* data entry, usually don't make mistakes and are very fast!

Suppose we want to find the vertical stress at some depth z *outside* the loaded area. Under these conditions we merely fabricate other uniformly loaded rectangles, all with corners above the point where the vertical stress is desired, and subtract and add their stress contributions as necessary. We illustrate this procedure in Example 10.3.

Example 10.3

Given:

A 5 × 10 m area uniformly loaded with an applied stress of 100 kPa.

Required:

a. Find the stress at a depth of 5 m under point A in Fig. Ex. 10.3.

b. Find what the stress would be at point A if the right half of the 5 × 10 m area were loaded with an additional 1 MPa.

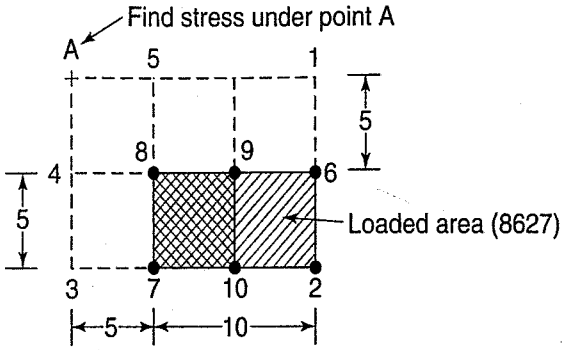

FIGURE Ex. 10.3

Solution:

a. Refer to Fig. Ex. 10.3 and the numbered points as shown. Add the rectangles in the following manner (+ for loaded areas, − for unloaded areas, and A plus the numbers denote the boundary points for each shape): +A123 − A164 − A573 + A584 result in the loaded rectangle we want, 8627. Find four separate influence values from Fig. 10.4 for each rectangle at a depth of 5 m, then add and subtract the computed stresses. Note that it is necessary to add rectangle A584 because it was subtracted twice as part of rectangles A164 and A573.

The computations are shown in the following table.

	Area			
Item	+A123	−A164	−A573	+A584
x	15	15	10	5
y	10	5	5	5
z	5	5	5	5
$m = x/z$	3	3	2	1
$n = y/z$	2	1	1	1
I	0.238	0.209	0.206	0.180
σ_z	23.8	−20.9	−20.6	+18.0

Total $\sigma_z = 23.8 - 20.9 - 20.6 + 18.0 = 0.3$ kPa

A computer solution by Christian and Urzua (1996) gives an answer of about 1 kPa. Our answer is somewhat lower, but both are quite small stress increases under point A. This shows that even a rather crude chart will give a reasonable solution from an engineering point of view.

b. When rectangle $789\overline{10}$ is loaded with 0.1 MPa and rectangle $962\overline{10}$ is loaded with 200 kPa, repeat part **a** above to obtain the stress under point A at 5 m depth for the entire rectangle 8627 loaded with 100 kPa. Next, a second set of four rectangles would have to be calculated just as for part **a**, but only rectangle $962\overline{10}$ would be loaded with +100 kPa; the others would be −100 kPa. The total $\sigma_z = 0.3$ kPa from part **a** plus $23.8 - 21.0 - 23.2 + 20.6 = 0.5$ kPa.

Thus it is possible to find the stress at any depth z, in or around a uniformly loaded area, or even under a step-loaded area, by using the procedures outlined in Examples 10.2 and 10.3. Remember that a new set of calculations is required for each depth where σ_z is desired.

Similar procedures are available for vertical stresses under uniformly loaded circular areas. Use Fig. 10.5 to obtain influence values in terms of x/r and z/r, where z = depth, r = radius of uniformly loaded area, x = horizontal distance from the center of the circular area, and q_o = surface contact pressure, in kPa.

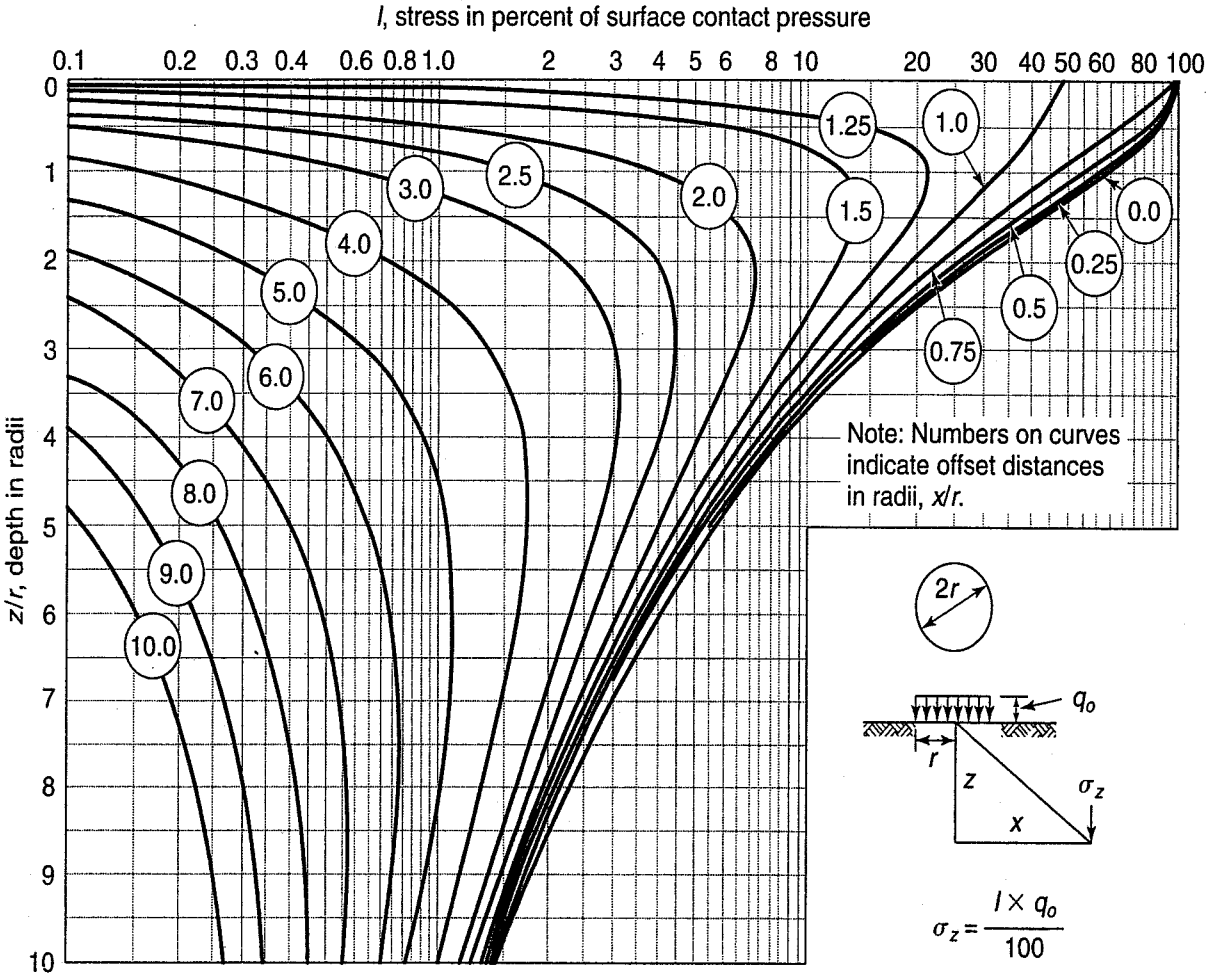

FIGURE 10.5 Influence values, expressed in percentage of surface contact pressure q_o, for vertical stress under uniformly loaded circular area (after Foster and Alvin, 1954, and U.S. Navy, 1986).

Example 10.4

Given:

A circular tank 3.91 m in diameter is uniformly loaded with 100 kPa.

Required:

a. Compute the stress under the center of the tank at a depth of 2 m below the tank.

b. Compute the stress under the edge of the tank, also a depth of 2 m.

Solution:

a. Refer to Fig. 10.5.

$$z = 2 \text{ m}$$
$$r = 3.91/2 = 1.95 \text{ m}$$
$$x = 0; \text{ then}$$
$$z/r = 2/1.95 = 1.02$$
$$x/r = 0/1.95 = 0$$

Find $I = 0.63$. Using Eq. (10.9), we obtain,

$$\sigma_z = q_o I = 100 \times 0.63 = 63 \text{ kPa}$$

(This compares almost exactly with $\sigma_z = 64$ kPa at the center for a 3 × 4 m rectangular area in Example 10.2. In both cases, the area is 12 m^2.)

b. Again, refer to Fig. 10.5. For the edge of the circular loaded area:

$$z = 2 \text{ m}$$
$$r = 1.95 \text{ m}$$
$$x = r = 1.95 \text{ m}$$
$$z/r = 2/1.95 = 1.02$$
$$x/r = 1.0$$

Find $I = 0.33$; then, using Eq. (10.9),

$$\sigma_z = q_o I = 100 \times 0.33 = 33 \text{ kPa}$$

(This compares with $\sigma_z = 26$ kPa at a corner for a 3 × 4 m uniformly loaded rectangular area. In each case, the area loaded is the same.) Spreadsheet answers are 74 and 38. Notice we dropped the decimal places. Remember, we are using the *theory* of elasticity, which only approximates reality.

Another useful integration of the Boussinesq equations is the trapezoidal loading shown in Fig. 10.6, which models the loading caused by a *long embankment.* Influence values are in terms of the dimensions a and b, as shown in the figure. If the embankment is not infinitely long, then use Fig. 10.7 together with Fig. 10.4 to represent different load configurations.

Example 10.5

Given:

A highway embankment, as shown in Fig. Ex. 10.5. Assume the average density of the material in the embankment is 2.0 Mg/m^3.

Required:

Compute the vertical stress under the centerline at depths of 3 and 6 m.

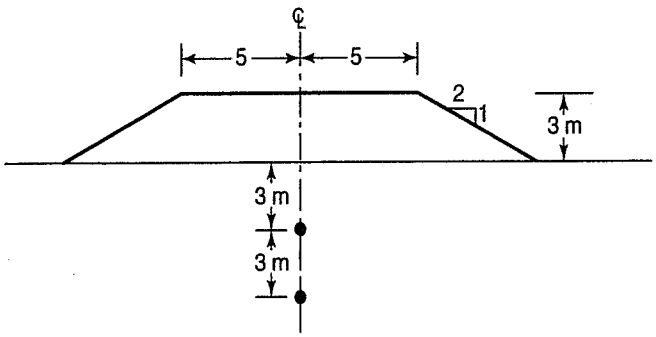

FIGURE Ex. 10.5

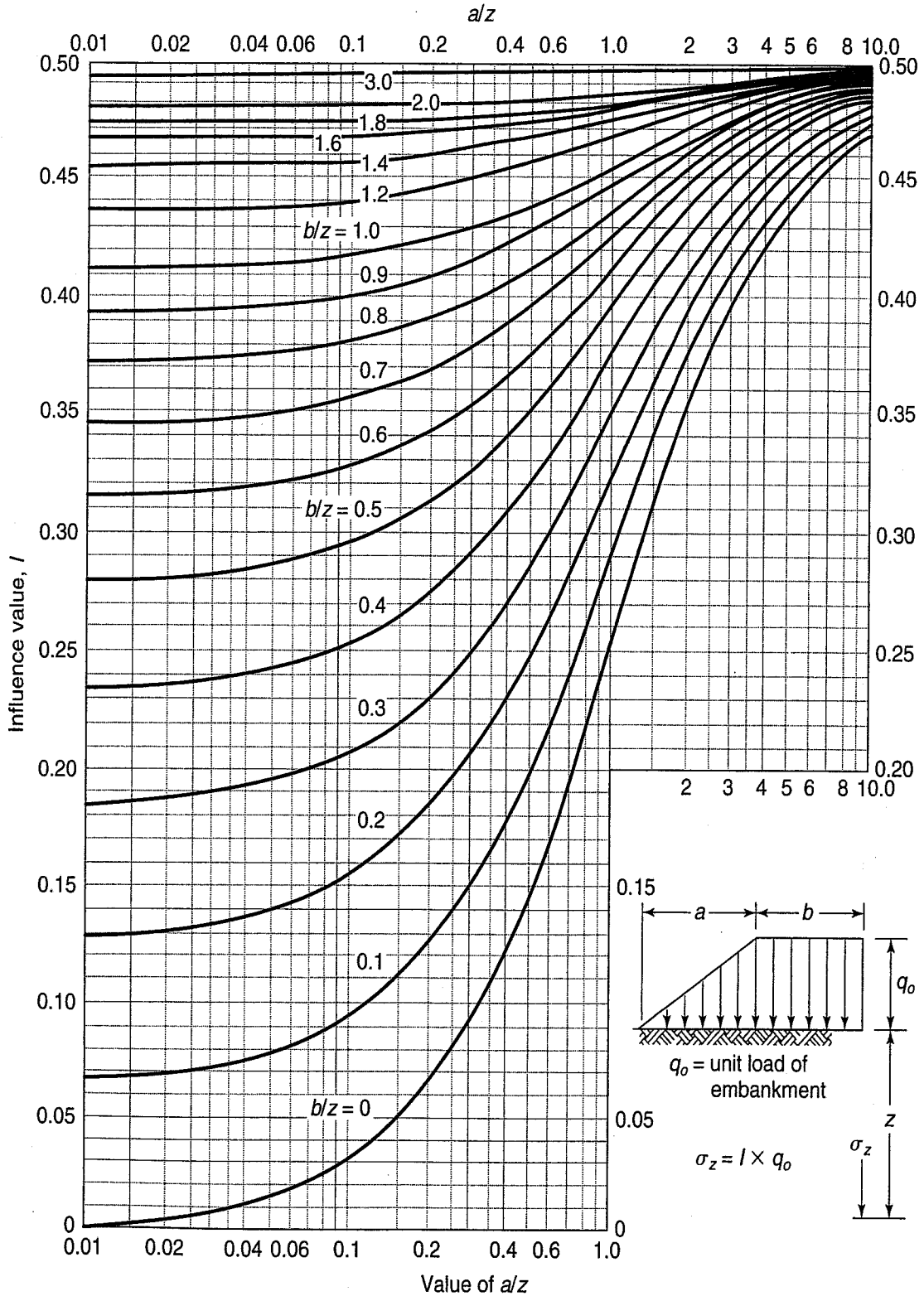

FIGURE 10.6 Influence values for vertical stress under a very long embankment; length = ∞ (from U.S. Navy, 1986, after Osterberg, 1957).

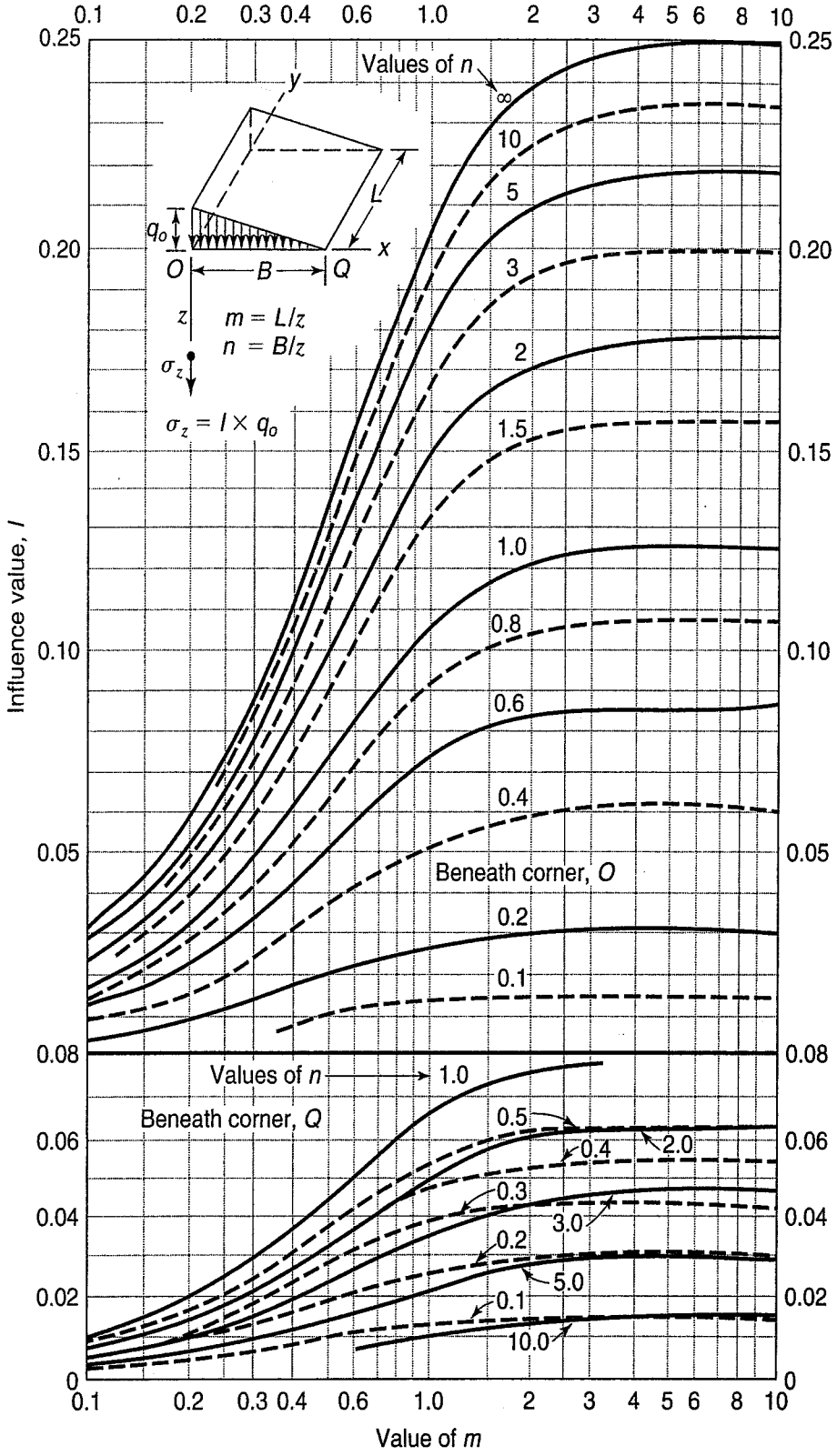

FIGURE 10.7 Influence values for vertical stress under the corners of a triangular load of limited length (after U.S. Navy, 1986).

Solution: First, calculate the applied surface stress q_o and the dimensions of the embankment in terms of a and b.

$$q_o = \rho g h = 2.0\ \text{Mg/m}^3 \times 9.81\ \text{m/s}^2 \times 3\ \text{m} = 59\ \text{kPa}$$

From Fig. 10.6, and Fig. Ex. 10.5,

$$b = 5\ \text{m}$$
$$a = 2 \times 3\ \text{m} = 6\ \text{m}$$

Next, calculate the vertical stress for $z = 3$ m.

$$a/z = 6/3 = 2$$
$$b/z = 5/3 = 1.67$$

From Fig. 10.6, $I = 0.49$,

$$\sigma_z = q_o I = 59\ \text{kPa} \times 0.49 = 29\ \text{kPa}$$

for one-half of the embankment, or 58 kPa for the entire embankment. Thus, at this shallow depth σ_z is almost the same as the contact stress.

Finally, calculate the vertical stress for $z = 6$ m.

$$a/z = 6/6 = 1$$
$$b/z = 5/6 = 0.83$$

From Fig. 10.6, $I = 0.44$,

$$\sigma_z = q_o I = 59\ \text{kPa} \times 0.44 \times 2 = 52\ \text{kPa}$$

Now and then it becomes necessary to compute the vertical stress due to an irregularly shaped loaded area at various points inside and/or outside an area. To facilitate computations, Newmark (1942) developed *influence charts* from which the vertical stress (and even the horizontal and shear stresses) may be computed. These influence charts are based on Boussinesq's theory, although similar charts have been prepared for the Westergaard theory, to be discussed shortly. Examples of influence charts may be found in foundation engineering textbooks—for example, Leonards (1962), Peck et al. (1974) and Poulos and Davis (1974). Figure 10.8 shows the Newmark influence chart for the computation of vertical stresses due to a loaded area. Think of the chart as a contour map that shows a volcanic cone, the top of which is located at the center (O) of the influence chart. If it were possible to look normal to a three-dimensional surface of the chart, you would see that each of the "areas" or "blocks" has the *same surface area.* We see only the projection on the contour map; the blocks grow smaller as the center is approached.

The charts are scaled with respect to depth so that they may be used for a structure of any size, in the following manner. On the chart is the line OQ. This line represents the distance below the ground surface z for which the vertical stress σ_v is desired, and this distance is used as the scale for a drawing of the loaded area. The point at which the vertical stress is desired is placed *over the center* of the chart. The vertical stress at that point is computed by merely counting the number of areas or blocks on the chart, *within* the boundary of the loaded area that is drawn to the proper scale on the chart. That number multiplied by an influence value I, specified on the chart, and by the contact pressure is used to obtain the vertical stress at the desired depth. Example 10.6 illustrates the use of the Newmark influence chart.

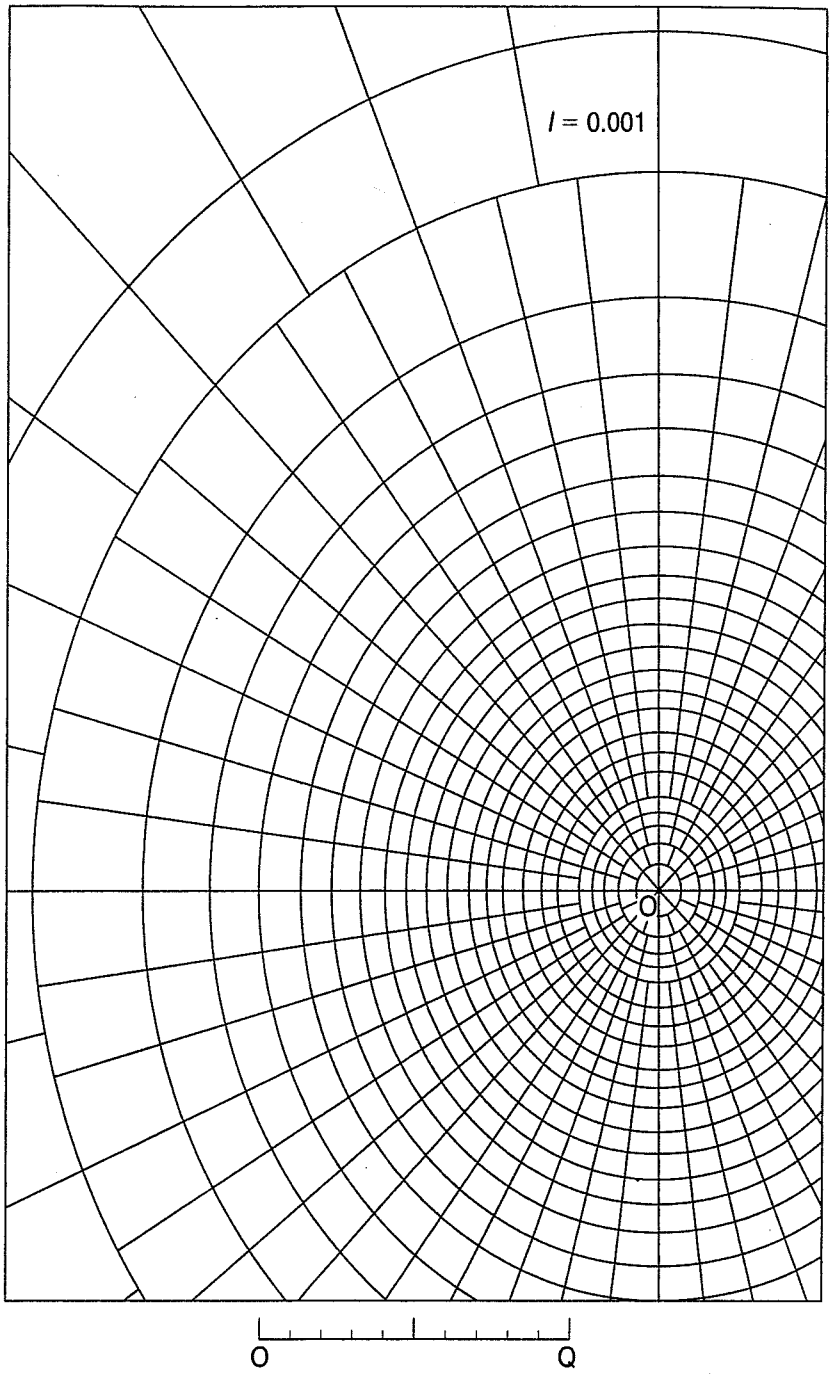

FIGURE 10.8 Influence chart for vertical stress on horizontal planes (after Newmark, 1942).

Example 10.6

Given:

A uniform stress of 250 kPa is applied to the loaded area shown in Fig. Ex. 10.6a.

Required:

Compute the stress at a depth of 80 m below the ground surface due to the loaded area under point O′.

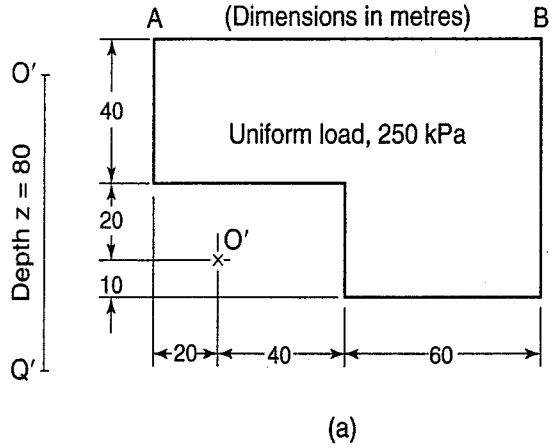

(a)

FIGURE Ex. 10.6a After Newmark (1942).

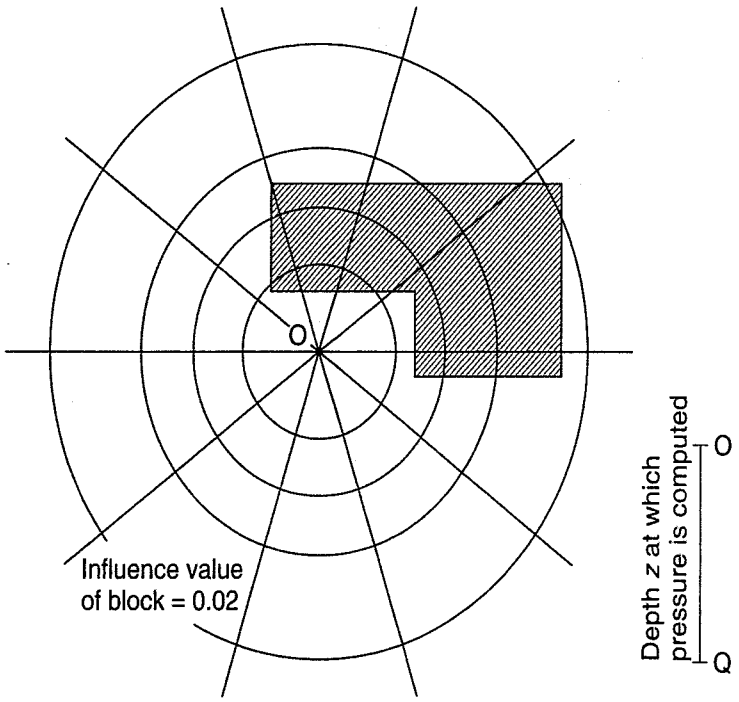

(b)

FIGURE Ex. 10.6b After Newmark (1942).

Solution: Draw the loaded area such that the length of the line $\overline{OQ}$ is scaled to 80 m. For example, the distance $\overline{AB}$ in Fig. Ex. 10.6a is 1.5 times the distance $\overline{OQ} \cdot \overline{OQ}$ = 80 m and $\overline{AB}$ = 120 m. Next, place point O′, the point where the stress is required, over the center of the influence chart (as shown in Fig. Ex. 10.6b to a slightly smaller scale). The number of blocks (and partial blocks) are counted under the loaded area. In this case, about eight blocks are found. The vertical stress at 80 m is then indicated by

$$\sigma_v = q_o I \times \text{number of blocks} \tag{10.10}$$

where q_o = surface or contact stress, and

I = influence value per block (0.02 in Fig. Ex. 10.6b).

Therefore,

$$\sigma_v = 250 \text{ kPa} \times 0.02 \times 8 \text{ blocks} = 40 \text{ kPa}$$

To compute the stress at other depths, the process is repeated by making other drawings for the different depths, changing the scale *each time* to correspond to the distance on the influence chart, Fig. Ex. 10.6b.

The Newmark chart was developed for the case of uniform surface loading and any arbitrary surface geometry. If you have an arbitrary load intensity as well as an arbitrary surface geometry, you can use one of the finite element stress distribution programs (e.g., Christian and Urzua, 1996) or a method proposed by Thompson et al. (1987).

10.3.3 Westergaard Method

All of the preceding stress distribution solutions were integrations of the original Boussinesq equations for vertical stress in a homogeneous isotropic linearly elastic half-space. Natural soil deposits do not approach these ideal material conditions. In fact, many important sedimentary soil deposits were

formed by the aggradation of alternate horizontal layers of silts and clays. These deposits are called *varved clays* (Secs. 3.3.4 and 3.3.5), and the solution for stresses at a point developed by Westergaard (1938) may be more applicable. In this theory, an elastic soil is interspersed with infinitely thin but perfectly rigid layers that allow only vertical movement but no lateral movement. Westergaard's solution for the vertical stress for a *point load* (for Poisson's ratio $\nu = 0$) is

$$\sigma_z = \frac{Q}{z^2\pi} \frac{1}{\left[1 + 2\left(\frac{r}{z}\right)^2\right]^{3/2}} \tag{10.11}$$

where the terms were defined in Fig. 10.2 and Eq. (10.3). *Poisson's ratio*, ν, is defined as the ratio of the horizontal strain, ε_h, to the vertical strain, ε_v, or

$$\nu = \frac{\varepsilon_h}{\varepsilon_v} \tag{10.12}$$

Typical values of ν for silts and sands range from 0.2 for loose materials to 0.4 for dense materials. Values for saturated clays vary from about 0.4 to 0.5. The theoretical maximum for a saturated clay undergoing no volume change when stressed (a so-called "undrained" condition; e.g., Sec. 11.5) is 0.5.

Equation (10.11) may be written as

$$\sigma_z = \frac{Q}{z^2} N_W \tag{10.13}$$

where N_W is an influence factor combining terms in Eq. (10.11) and is a function of r/z. Values of N_W are plotted in Fig. 10.3(b).

The Boussinesq and Westergaard theories are compared in Fig. 10.3(b). For r/z less than 1.5, Boussinesq indicates values larger than Westergaard. When $r/z \geq 1.5$, both theories provide about the same results. Which theory should you use? From a philosophical point of view, both theories are based on assumptions which are far from reality. It often boils down to a matter of personal preference, even though the assumptions of the Westergaard theory probably are closer to reality for a layered soil deposit. The 2:1 method, crude as it may be, is probably used about as often in practice as the solutions from the theory of elasticity for estimating vertical stresses.

A graph similar to Fig. 10.4 for influence values for vertical stress under a corner of a *uniformly loaded rectangular area* has been prepared for the Westergaard case (for Poisson's ratio, $\nu = 0$) and is shown as Fig. 10.9. You use it as you would use Fig. 10.4.

Tables 10.1 through 10.3 present the influence values for vertical stress under the center of a *square load*, under the center of an infinitely long *strip load*, and under the corner of a *uniformly loaded rectangular area*, respectively. These tables present influence coefficients for both the Boussinesq and Westergaard assumptions. You may find these charts useful in engineering practice.

It must be pointed out that once you have found the vertical stresses from the equations and charts provided in this section, they must be *added* to the existing in situ overburden effective stress, as was done in Example 10.1. This procedure is necessary because the elastic solutions consider the half-space to be weightless, and only the stress due to an external loading is considered. Further, for sites where a layered subsoil exists—that is, where there are large variations in the modulus of elasticity—other solutions must be used to take into account the relative stiffnesses of the layers. Solutions to these kinds of stress distributions may be found in Harr (1966) and Poulos and Davis (1974). These references also supply equations and charts for estimating the horizontal and shear stresses in elastic media.

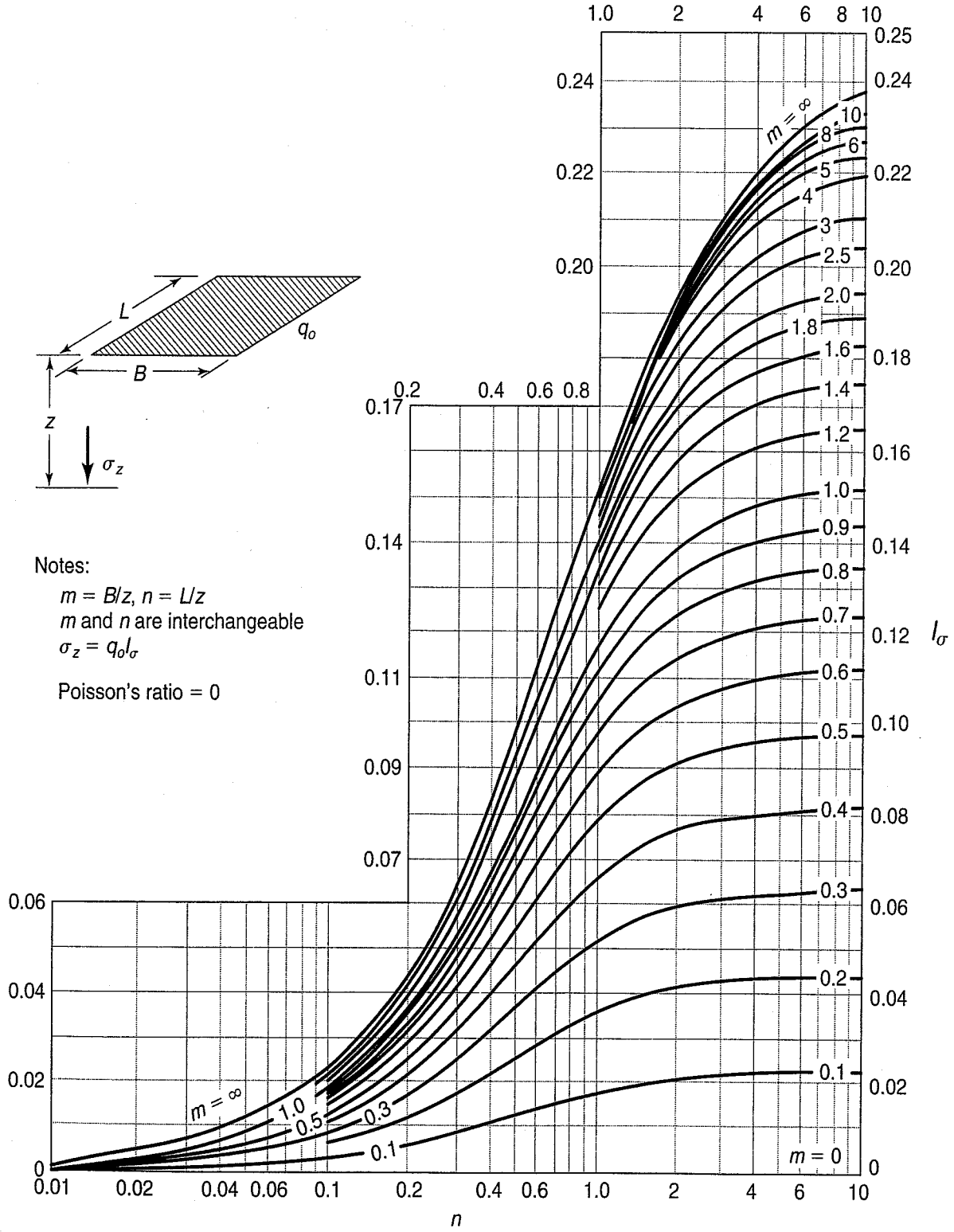

FIGURE 10.9 Influence values for vertical stress under corners of a uniformly loaded rectangular area for the Westergaard theory (after Duncan and Buchignani, 1976).

TABLE 10.1 Influence Values for Vertical Stress Under the Center of a Square Uniformly Loaded Area (Poisson's Ratio, $\nu = 0.0$)

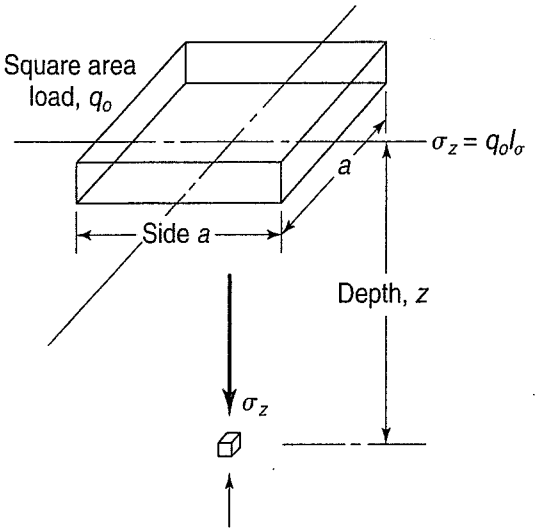

	I_σ	I_σ
a/z	Boussinesq	Westergaard
∞	1.0000	1.0000
20	0.9992	0.9365
16	0.9984	0.9199
12	0.9968	0.8944
10	0.9944	0.8734
8	0.9892	0.8435
6	0.9756	0.7926
5	0.9604	0.7525
4	0.9300	0.6971
3.6	0.9096	0.6659
3.2	0.8812	0.6309
2.8	0.8408	0.5863
2.4	0.7832	0.5328
2.0	0.7008	0.4647
1.8	0.6476	0.4246
1.6	0.5844	0.3794
1.4	0.5108	0.3291
1.2	0.4276	0.2858
1.0	0.3360	0.2165
0.8	0.2410	0.1560
0.6	0.1494	0.0999
0.4	0.0716	0.0477
0.2	0.0188	0.0127
0	0.0000	0.0000

After Duncan and Buchignani (1976).

TABLE 10.2 Influence Values for Vertical Stress Under the Center of an Infinitely Long Strip Load

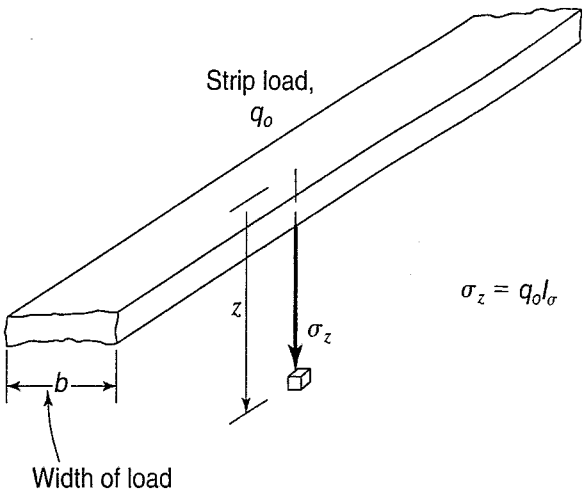

	I_σ	I_σ
b/z	Boussinesq	Westergaard
∞	1.000	1.000
100	1.000	0.990
10	0.997	0.910
9	0.996	0.901
8	0.994	0.888
7	0.991	0.874
6.5	0.989	0.864
6.0	0.986	0.853
5.5	0.983	0.835
5.0	0.977	0.824
4.5	0.970	0.807
4.0	0.960	0.784
3.5	0.943	0.756
3.0	0.920	0.719
2.5	0.889	0.672
2.0	0.817	0.608
1.5	0.716	0.519
1.2	0.624	0.448
1.0	0.550	0.392
0.8	0.462	0.328
0.5	0.306	0.216
0.2	0.127	0.089
0.1	0.064	0.045
0	0.000	0.000

After Duncan and Buchignani (1976).

TABLE 10.3 Influence Values for Vertical Stress Under Corner of a Uniformly Loaded Rectangular Area

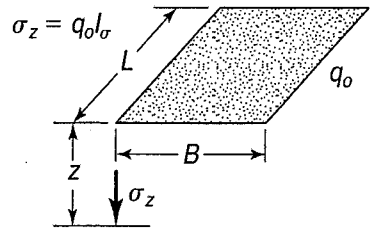

Boussinesq Case

	L/z							
B/z	0.1	0.2	0.4	0.6	0.8	1.0	2.0	∞
0.1	0.005	0.009	0.017	0.022	0.026	0.028	0.031	0.032
0.2	0.009	0.018	0.033	0.043	0.050	0.055	0.061	0.062
0.4	0.017	0.033	0.060	0.080	0.093	0.101	0.113	0.115
0.6	0.022	0.043	0.080	0.107	0.125	0.136	0.153	0.156
0.8	0.026	0.050	0.093	0.125	0.146	0.160	0.181	0.185
1.0	0.028	0.055	0.101	0.136	0.160	0.175	0.200	0.205
2.0	0.031	0.061	0.113	0.153	0.181	0.200	0.232	0.240
∞	0.032	0.062	0.115	0.156	0.185	0.205	0.240	0.250

Westergaard Case

	L/z							
B/z	0.1	0.2	0.4	0.6	0.8	1.0	2.0	∞
0.1	0.003	0.006	0.011	0.014	0.017	0.018	0.021	0.022
0.2	0.006	0.012	0.021	0.028	0.033	0.036	0.041	0.044
0.4	0.011	0.021	0.039	0.052	0.060	0.066	0.077	0.082
0.6	0.014	0.028	0.052	0.069	0.081	0.089	0.104	0.112
0.8	0.017	0.033	0.060	0.081	0.095	0.105	0.125	0.135
1.0	0.018	0.036	0.066	0.089	0.105	0.116	0.140	0.152
2.0	0.021	0.041	0.077	0.104	0.125	0.140	0.174	0.196
∞	0.022	0.044	0.082	0.112	0.135	0.152	0.196	0.250

After Duncan and Buchignani (1976).

10.4 IMMEDIATE SETTLEMENT

When we discussed the components of settlement in Sec. 10.2.1, we mentioned that the immediate settlement s_i occurs essentially as the load is applied, primarily because of distortion (change of shape, not change of volume) in the foundation soils. We mentioned that most of the settlement of granular soils is immediate because these soils typically have a high permeability. On the other hand, for foundations on clay soils, the distortion settlement is not elastic, although s_i is often estimated using elastic theory. Immediate settlements must be considered in the design of shallow foundations, especially for structures that are sensitive to rapid settlements.

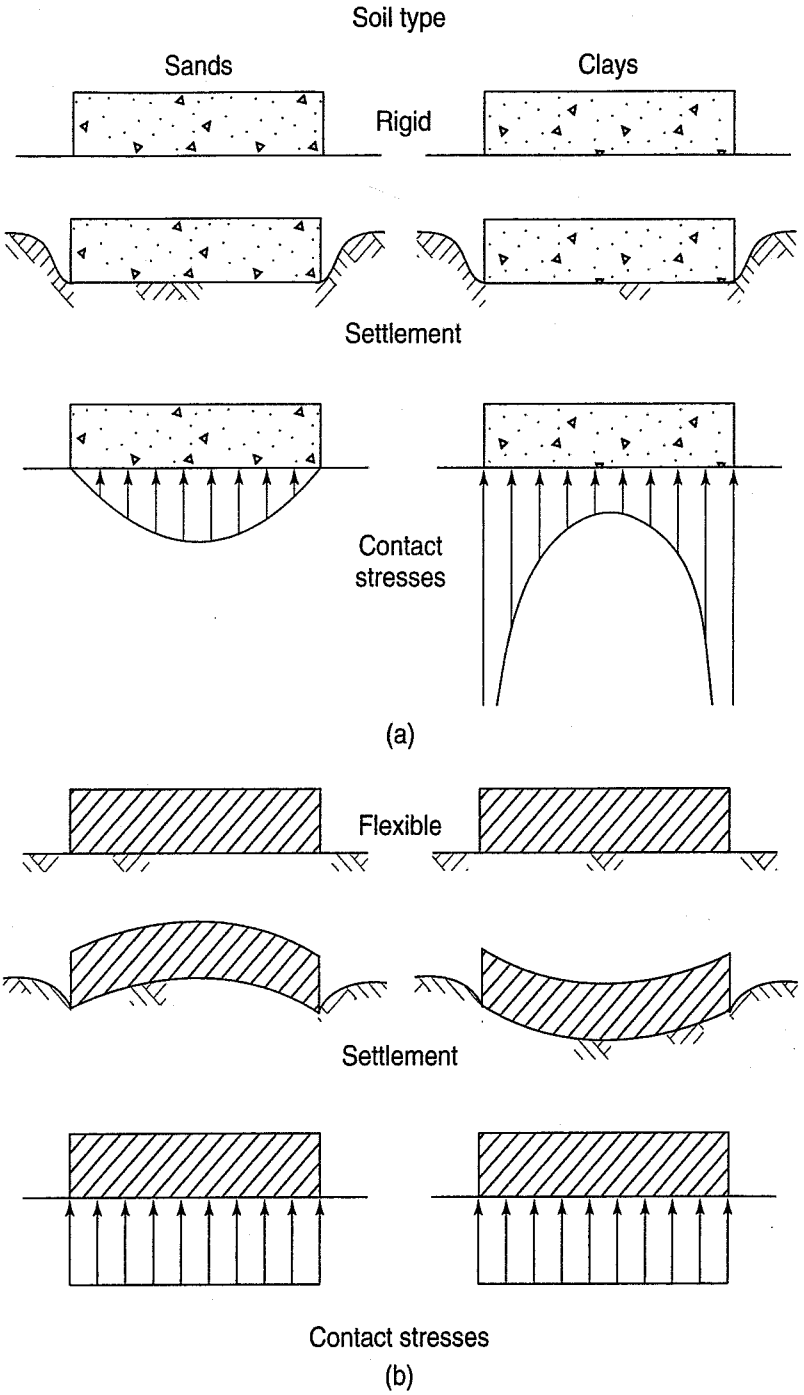

FIGURE 10.10 Distribution of settlement and contact stresses for (a) rigid, and (b) flexible loaded areas on cohesive and granular soils.

The change in shape of the loaded area depends on whether the foundation is relatively rigid or flexible and whether the foundation soil is cohesive or granular. Figure 10.10 shows the possibilities. The stress distribution under a *rigid* footing on cohesive soil is theoretically infinite at the edges and much lower in the interior of the footing. Of course, in real soils the contact stress is much less than infinity at the edges, and in fact is limited by the shear strength of the soil τ_f (Chapters 11, 12, and 13), as shown in Fig. 10.10(a). Naturally, with a rigid footing, the settlement pattern is uniform. On the other hand, with a flexible foundation, the contact stress is uniform but the displacement under the footing is least at the edges and a maximum at the center of the footing.

When it comes to granular soils, the stress distribution under a rigid footing is a maximum at the center and much lower at the edges [Fig. 10.10(a)]. Why is it much lower near the edges of the footing? The reason is the lack of confinement at the edges; in fact, the contact stress is zero at the edge (no footing, no stress). The resulting settlement pattern is, of course, uniform. However, with a flexible footing on granular material, the contact stress is uniform, but the settlement pattern is concave upward [Fig. 10.10(b)] with the maximum settlement at the edges and not in the center as in cohesive soils. The reason, of course, is that there is more confinement in the center of the footing than at the edges. For estimating immediate settlements on granular soils, linear elastic theory doesn't work, and we don't have any other good theory to use, so we rely on empirical methods using in situ test results to estimate settlements (e.g., Holtz, 1991; Terzaghi et al., 1996).

If you can assume that elastic theory is appropriate for your project, then the basic equation for elastic settlement s_i due to a uniform applied stress q_o is given by

$$s_i = \frac{q_o B}{E_u}(1 - \nu^2) I_s \tag{10.14}$$

where B = characteristic dimension of the loaded area (Fig. 10.11),
ν = Poisson's ratio [Eq. (10.12)],
E_u = undrained Young's modulus (Chapter 13),
I_s = a shape and rigidity factor.

The coefficient I_s accounts for the shape and rigidity of the loaded area and depends on the location of the influence point for which the immediate settlement is desired. Values of I_s are given in Table 10.4. Two cases are tabulated: (a) infinite depth, and (b) limited depth over a rigid base. Actual soil profiles are neither, and you have to choose the case that most closely approximates your situation. Soil properties needed are Poisson's ratio ν and undrained Young's modulus E_u. Poisson's ratio is usually assumed to be 0.5 for saturated cohesive soil sites, because no volume change (consolidation) occurs during immediate settlement. A smaller value, probably 0.25 or 0.33, is appropriate for unsaturated sites. Much more difficult to determine accurately is the undrained Young's modulus. Ideally, you could use the initial slope or tangent modulus of the stress-strain curve from triaxial or unconfined compression tests on undisturbed soil specimens. Unfortunately, sample disturbance greatly reduces the Young's modulus, and therefore the calculated immediate settlement will be way too large. In situ tests such as plate load tests may be used to estimate the undrained modulus, but most of the time, geotechnical engineers use simple correlations with the undrained shear strength, as described in Chapter 13. See Holtz (1991) for additional information about determining immediate settlement and its importance in foundation design.

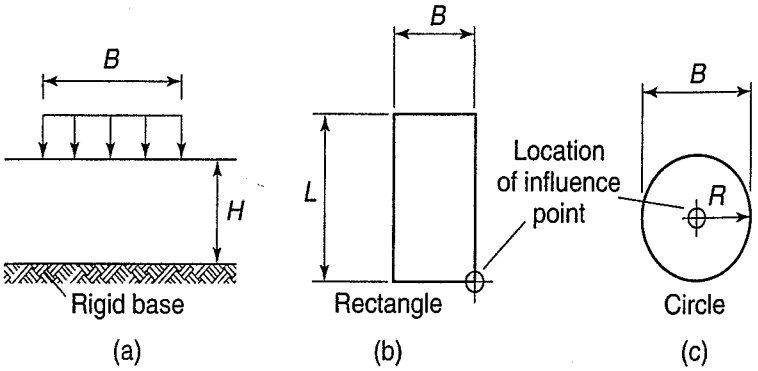

FIGURE 10.11 Notation for dimensions of loaded areas: (a) profile view; (b) rectangular loaded area in plan; and (c) circular loaded area in plan (after U.S. Navy, 1986).

TABLE 10.4 Shape and Rigidity Factors, I_s, for Calculating Settlements of Points on Loaded Areas at the Surface of an Elastic Half-Space

a. Loaded Areas on Surface of Infinite Depth

Shape and Rigidity	Center	Corner	Edge/Middle of Long Side	Average
Circle (flexible)	1.0		0.64	0.85
Circle (rigid)	0.79		0.79	0.79
Square (flexible)	1.12	0.56	0.76	0.95
Square (rigid)	0.82	0.82	0.82	0.82
Rectangle (flexible)				
length/width				
2	1.53	0.76	1.12	1.30
5	2.10	1.05	1.68	1.82
10	2.56	1.28	2.10	2.24
Rectangle (rigid)				
length/width				
2	1.12	1.12	1.12	1.12
5	1.6	1.6	1.6	1.6
10	2.0	2.0	2.0	2.0

b. Loaded Areas on Surface over a Rigid Base (see figure below)

	Center of Rigid Circular Area, Diameter = B	Corner of Flexible Rectangular Area				
		$L/B = 1$	$L/B = 2$	$L/B = 5$	$L/B = 10$	$L/B = \infty$
H/B		For Poisson's ratio $\nu = 0.5$				
0	0.00	0.00	0.00	0.00	0.00	0.00
0.5	0.14	0.05	0.04	0.04	0.04	0.04
1	0.35	0.15	0.12	0.10	0.10	0.10
1.5	0.48	0.23	0.22	0.18	0.18	0.18
2.0	0.54	0.29	0.29	0.27	0.26	0.26
3.0	0.62	0.36	0.40	0.39	0.38	0.37
5.0	0.69	0.44	0.52	0.55	0.54	0.52
10	0.74	0.48	0.64	0.76	0.77	0.73
H/B		For Poisson's ratio $\nu = 0.33$				
0	0.00	0.00	0.00	0.00	0.00	0.00
0.5	0.20	0.09	0.08	0.08	0.08	0.08
1.0	0.40	0.19	0.18	0.16	0.18	0.16
1.5	0.51	0.27	0.28	0.25	0.25	0.25
2.0	0.57	0.32	0.34	0.34	0.34	0.34
3.0	0.64	0.38	0.44	0.46	0.45	0.45
5.0	0.70	0.48	0.56	0.60	0.61	0.61
10	0.74	0.49	0.66	0.80	0.82	0.81

After U.S. Navy (1986).

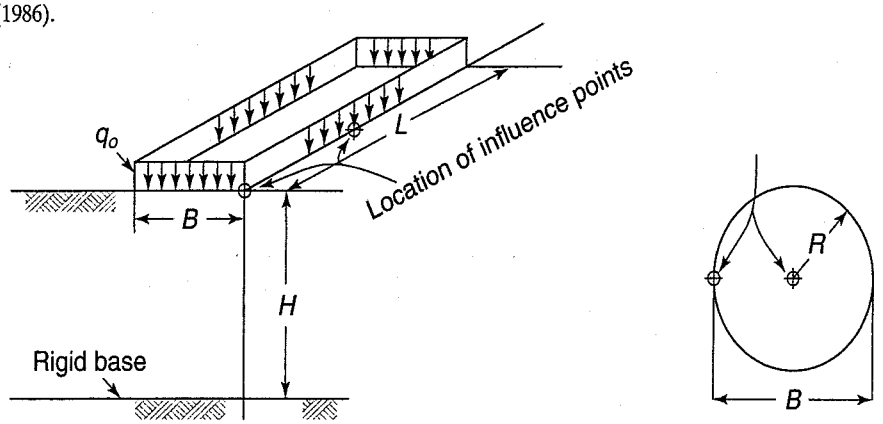

Example 10.7

Given:

A rectangular footing with a width of 2 m and a length of 3 m carries a column load of 1800 kN on a very deep deposit of saturated clay. It is estimated that the undrained Young's modulus of the underlying clay is 36 MPa.

Required:

Compute the immediate settlement for the center and the corner of the footing.

Solution: A column load of 1800 kN on a footing of 6 m^2 gives a contact stress of 300 kPa. Because the foundation clays are saturated, we can assume that the Poisson's ratio is 0.5. Next determine the shape and rigidity factor, I_s.

The length to width ratio of the footing = 3/2 = 1.5, or halfway between two given values on Table 10.4**a**, so you need to interpolate. From Table 10.4**a**, find I_s = 0.82 and 1.12 for L/B = 1 and 2, respectively. Or, I_s for this case is 0.97. We have assumed the footing is rigid, because it is carrying a column load, and to prevent shear in the reinforced concrete footing, it will have to be relatively thick. Thus the settlements at the center and corner will be the same.

Using Eq. (10.14), we compute

$$s_i = \frac{q_o B}{E_u}(1 - \nu^2)I_s$$

$$= \frac{300 \text{ kPa } (2 \text{ m})}{36 \text{ MPa}}(1 - 0.25)(0.97)$$

$$= 0.012 \text{ m or } 12 \text{ mm}$$

If the footing were flexible, then from Table 10.4, the two I_s values for L/B = 1 and 2 are 1.12 and 1.53, respectively. So for L/B = 1.5, I_s = 1.33, and the center s_i would be 16.6 or 17 mm. The corner settlements should be about half of this value, and it is; I_s = 0.66, so s_i = 8 mm.

If this footing were on a soil layer with limited depth, then Table 10.4**b** would be used for a given H/B ratio. Remember that Table 10.4**b** gives only the settlement under the corner. If you wanted the settlement under the center, you would have to solve for the settlement under the corner of four quarter footings or quadrants, and then multiply the result by 4. Superposition holds!

The above procedure is for a loaded area on the surface of an elastic foundation. What if the foundation is buried—for example, to get to firmer soils, or to avoid frost action or swelling clays? In fact, footings for buildings are almost never located directly on the ground surface, but other structures such as tanks and embankments often are. For loaded areas founded at depth, the chart developed by Janbu et al. (1956), modified by Christian and Carrier (1978) using finite element calculations, as well as the work of other researchers, is often found in foundation engineering textbooks—for example, Coduto (2001) and U.S. Army Corps of Engineers (1994). This chart is shown in Fig. 10.12. The settlement equation is basically Eq. (10.14) for a saturated clay (Poisson's ratio = 0.5) with coefficients μ_0 for depth of the excavation, and μ_1 for the distance below the footing to the rigid base.

Mayne and Poulos (1999) provide a comprehensive discussion of estimating the elastic settlement of footings and mat foundations that includes consideration of the flexibility, shape, and depth of the foundation, layer thickness, whether the soil profile is homogeneous or the modulus is increasing with depth ("Gibson modulus profile"), etc. See also their closure to the discussion by Fowler et al. (2001).

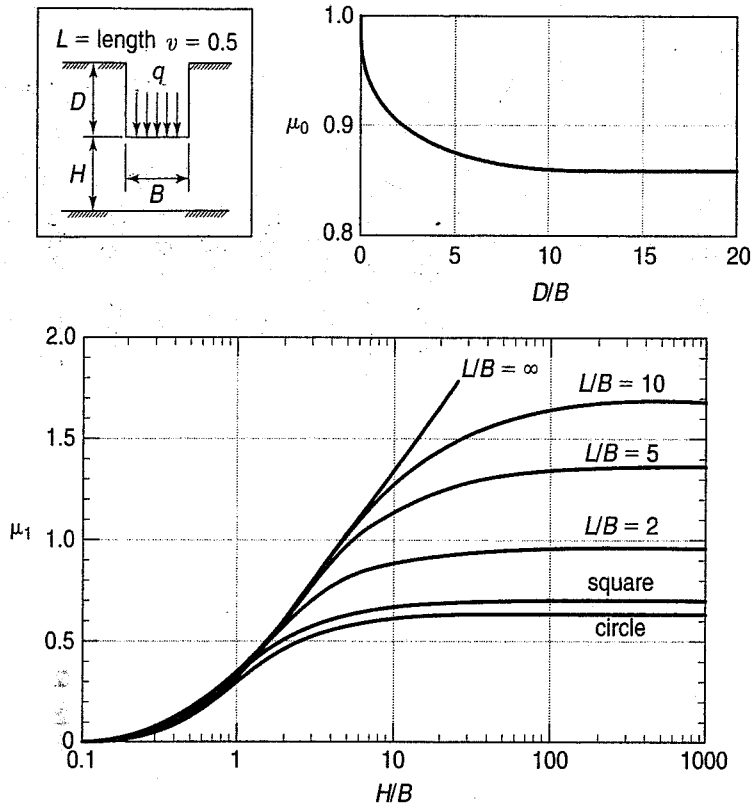

FIGURE 10.12 Chart for estimating the elastic settlement under a loaded area in saturated clay (Carrier and Christian, 1978).

10.5 VERTICAL EFFECTIVE OVERBURDEN AND PRECONSOLIDATION STRESS PROFILES

Go back and review Sec. 6.10 on vertical stress profiles. There we illustrated how to calculate the vertical effective overburden stress with depth for various soil profiles and different depths of the groundwater table. We mentioned that in foundation engineering, plots of the total stress, pore pressure, and effective stress with depth at a site are often needed for an evaluation of the settlement of shallow foundations.

In this section we review four typical soil profiles that illustrate different field conditions frequently encountered in practice. You may want to also take a quick look at Sec. 8.11 for some soil profiles for natural soil deposits. We mentioned in Sec. 10.2.2 that this information is ordinarily obtained from a site investigation, soil sampling, and laboratory testing program. From consolidation tests the preconsolidation pressure is determined and plotted at the depth corresponding to the depth of the samples on the same diagram as the vertical effective overburden stress versus depth. Note that the preconsolidation pressure is always plotted from the *zero stress line*, not the vertical overburden stress line. On the other hand, the $\Delta\sigma$ determined from the stress distribution under the foundation (Sec. 10.3) is always added directly to the vertical effective overburden stress at any given depth (muy importante).

In Fig. 10.13 we show four possible cases of a simple soil profile with the compressible stratum and the groundwater table starting at the ground surface. Plotted on each graph are the vertical effective overburden stress σ'_{vo}, the preconsolidation pressure σ'_p, and the change in stress $\Delta\sigma$ due to the foundation load. For each case we show how to calculate the settlement for that layer using Eq. (8.18a).

Case 1: Normally Consolidated Soil, One-Dimensional Loading Figure 10.13(a) shows a typical diagram of stress versus depth. Notice that the soil is *normally consolidated*, because from consolidation tests performed on several specimens, the preconsolidation pressure σ'_p is found to be equal to the existing vertical overburden pressure σ'_{vo}. In Fig. 10.13(a), both the σ'_{vo} and σ'_p profiles are identical. The line labeled $\sigma'_{vo} + \Delta\sigma$ is parallel to the σ'_{vo} and σ'_p line because the $\Delta\sigma$ is one-dimensional (e.g., when the external stress is applied over a large area). Because the soil is normally consolidated, we don't use the

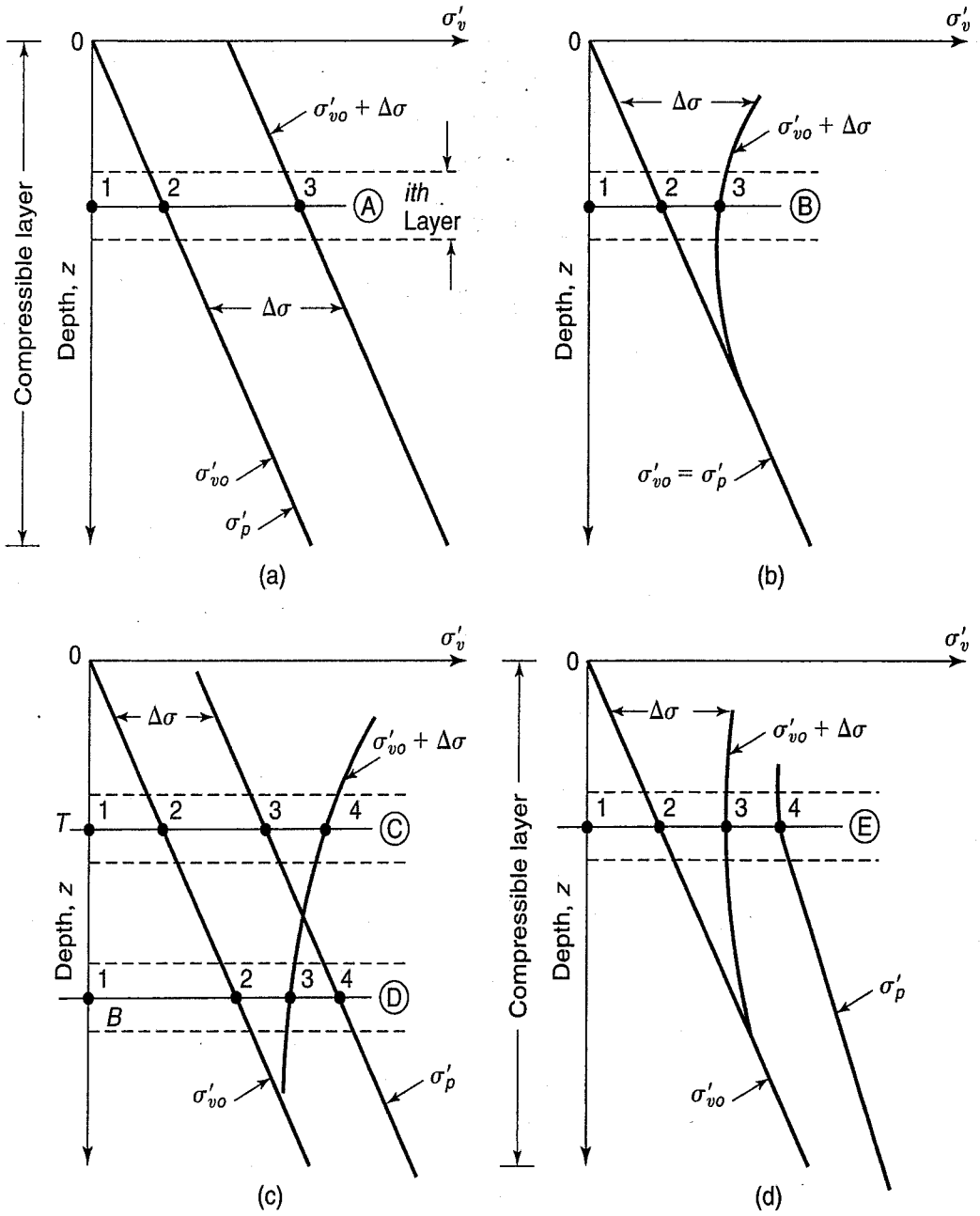

FIGURE 10.13 Four profiles of σ'_{vo}, $\Delta\sigma$, and σ'_p with depth: (a) Case 1, normally consolidated, one-dimensional loading; (b) Case 2, normally consolidated, three-dimensional loading; (c) Case 3, lightly overconsolidated, three-dimensional loading; and (d) Case 4, heavily overconsolidated, three-dimensional loading. *Note:* Not drawn to the same scale.

left side of Eq. (8.18a); we just use the right hand term, which is the same as Eq. (8.11). If there are several strata with different compressibilities, then we use Eq. (8.14). Sometimes, if the compressible stratum is very thick, engineers divide it into a number of sublayers. Six to 10 layers should be sufficient. Then we find the average stress within each sublayer to use in the settlement equation, which is a combination of Eqs. (8.11) and (8.14). For Case 1, the equation looks like this:

$$s_c = \frac{C_c}{1 + e_o} \sum_{i=1}^{n} H_i \log \frac{\sigma_i + \Delta\sigma_i}{\sigma_i} \tag{10.15}$$

As you can see, there are three constants plus the log term. The center of the ith layer in Fig. 10.13(a) is shown as line A. If all the stresses are accurately plotted, then scaling off the distance 1–3 and dividing

it by the scaled distance 1–2 gives the ratio of the log term. Multiply this out and you have the settlement of the ith layer! Sum them all up and you have the settlement for the entire compressible stratum.

Case 2: Normally Consolidated Soil, Three-Dimensional Loading This case illustrates three-dimensional loading, or, as shown in Fig. 10.13(b), $\Delta\sigma$ decreases with depth. The resulting equation for the consolidation settlement is identical to Case 1. Similar to Case 1, line B is the center of the ith layer.

Case 3: A Lightly Overconsolidated Soil, Three-Dimensional Loading In this case, the σ'_{vo} curve is somewhat parallel to the preconsolidation pressure σ'_p curve as shown in Fig. 10.13(c). In some parts of the profile, the $\sigma'_{vo} + \Delta\sigma$ is both greater and less than the preconsolidation pressure; this is called *compound compressibility*. Now you use both parts of Eq. (8.18a) or (8.18b). Let's consider the middle of a layer as the line C. Here $\sigma'_{vo} + \Delta\sigma > \sigma'_p$, so the corresponding equation would look like a combination of Eqs. (8.18) and (8.14).

$$\cdots \frac{H_i}{1 + e_o}\left[C_r \sum \log \frac{\sigma_3}{\sigma_2} + C_c \sum \log \frac{\sigma_4}{\sigma_3}\right]$$

We left out the bunch of constants, but from points 2–3 the soil is preconsolidated, so we use C_r [see Fig. 8.12(a)]; from points 3–4 the soil is normally consolidated, and we use C_c [see Fig. 8.12(b)]. For the line D in Fig. 10.13(c), we see that $\sigma'_{vo} + \Delta\sigma$ is within the overconsolidation zone. As a result, only C_r is used; the equation is

$$\cdots \frac{H_i}{1 + e_o}\left[C_r \sum \log \frac{\sigma_3}{\sigma_2}\right]$$

Case 4: Heavily Overconsolidated Soil, Three-Dimensional Loading In Case 4, the soils are so heavily overconsolidated that overburden stress σ'_{vo} plus the applied stress $\Delta\sigma$ is always less than the preconsolidation stress σ'_p. This is shown in Fig. 10.13(d). In this case we use only the left term of the consolidation equation, Eq. (8.18a), and use C_r only, and we don't need the term with C_c. This the equation would look like

$$s_c = \frac{H_i}{1 + e_o}\left[C_r \sum \log\left(\frac{\sigma_3}{\sigma_2}\right)_i\right]$$

10.6 SETTLEMENT ANALYSIS EXAMPLES

During the site investigation, the geotechnical engineer or engineering geologist logging the borehole will already be thinking about what type of foundation will be most suitable for the structure and soil conditions. He or she should always be thinking of what soil parameters will be needed for future analysis for this project. If, for example, compressible soils are discovered under the site, the engineer or geologist should be asking, "Where should I be taking undisturbed samples for consolidation tests?" By the time the site investigation is completed and samples are in the laboratory, he or she should have a good idea of the preliminary foundation design and what laboratory or perhaps additional field testing will be necessary to obtain the appropriate soil parameters for settlement analyses. So when we give all those soil properties in an example problem, you now have an idea of how those properties were obtained and what went into the project up to that point.

The following four example problems are quite comprehensive, and they are typical of settlement analyses geotechnical engineers must do as an important part of any shallow foundation project. These examples also provide a number of implications and practical lessons for geotechnical engineers.

Example 10.8

Given:

A brown silty sand fill 5 m thick was placed over a 15 m thick layer of compressible gray silty clay. Underlying the clay layer is brown sandy gravel. The soil profile is shown in Fig. Ex. 10.8a. Assume for this problem that the settlement of the fill and the sandy gravel is small compared to the settlement of the silty clay layer. Properties of the normally consolidated silty clay layer are:

Initial void ratio, $e_o = 1.1$.

Compression index, $C_c = 0.36$.

Secondary compression index, $C_\alpha = 0.06$.

Saturated density, $\rho_{sat} = 1.52\ \text{Mg/m}^3$.

Coefficient of consolidation, $c_v = 0.86\ \text{m}^2/\text{yr}$.

The density of the silty sand fill ρ is $2.0\ \text{Mg/m}^3$, and the groundwater table is at the interface of the fill and clay, or at -5 m.

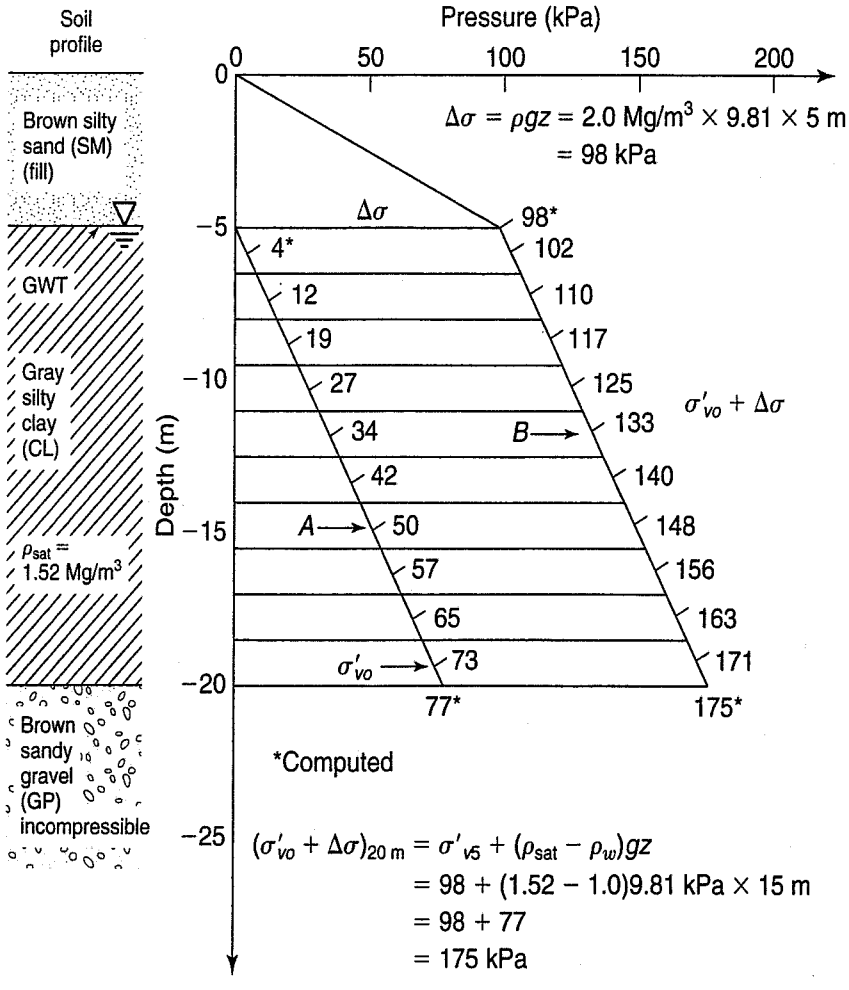

FIGURE Ex. 10.8a Soil profile and effective stress versus depth.

Required:

Part I. Compute the consolidation settlement of the silty clay layer due to the weight of the 5 m of new fill.

Part II. Compute the time rate of settlement.

Part III. Compute and plot $\sigma'(z)$ when $U = 50\%$.

Part IV. Compute the secondary settlement.

Solution: Part I: The procedure for this part is to (1) compute the initial effective overburden pressures of soil layers, (2) compute the increase in vertical stress due to external load, (3) compute the final effective vertical stress, and (4) compute settlement

(1) Initial effective stress: $\sigma'_{vo} = \rho' gz$, prior to fill placement

$$\sigma'_{vo}(0\text{ m}) = 0$$
$$\sigma'_{vo}(\text{at } -15\text{ m}) = (1.52 - 1.0)\text{ Mg/m}^3 \times 9.81\text{ m/s}^2 \times 15\text{ m} = 77\text{ kPa}$$

(2) Increase in σ due to fill $= \rho g h_{\text{fill}}$

$$\Delta\sigma_{\text{fill}} = 2.0\text{ Mg/m}^3 \times 9.81\text{ m/s}^2 \times 5\text{ m} = 98\text{ kPa}$$

(3) Final effective stress = initial effective stress + $\Delta\sigma_{\text{fill}}$

$$\sigma'_v(\text{top of silty clay}) = 0 + \Delta\sigma = 98\text{ kPa}$$
$$\sigma'_v(\text{bottom of silty clay}) = 77 + 98 = 175\text{ kPa}$$

The above stresses are plotted in Fig. Ex. 10.8a. Curve A represents the initial vertical effective overburden stresses σ'_{vo} prior to the placement of the 5 m of silty sand fill. Curve B represents the final vertical effective overburden stress due to the fill after complete consolidation of the silty clay layer has taken place. Curve B equals $\sigma'_{vo} + \Delta\sigma$, where $\Delta\sigma$ is the increase in pressure due to the fill. We assume that $\Delta u = \Delta\sigma$ (one-dimensional compression) and that the load is placed all at once. (Actually 5 m of fill may take days to weeks to place and compact, but, for purposes of our example, let us assume it was placed instantaneously in one load increment.)

(4) Recall that the silty clay is normally consolidated. Thus the consolidation settlement of the layer is given by Eq. (8.11)

$$s_c = C_c \frac{H_o}{1 + e_o} \log \frac{\sigma'_{vo} + \Delta\sigma_v}{\sigma'_{vo}} \tag{8.11}$$

For the mid depth of the layer, $\sigma'_{vo} = 38$ kPa and $\sigma'_{vo} + \Delta\sigma_v = 136$ kPa.
Thus

$$s_c = 0.36 \frac{15\text{ m}}{1 + 1.1} \log \frac{136}{38} = 1.42\text{ m}$$

Since the silty clay layer is 15 m thick, it is prudent to divide the total thickness into thinner layers to improve the accuracy of results. A 1.5 m thick layer is chosen. The settlement of each of these layers is summed up to obtain the total consolidation settlement of the silty clay layer. To assist in the computations, Table Ex. 10.8a is employed, and the corresponding pressures σ'_{vo} and $\sigma'_{vo} + \Delta\sigma$ are indicated at the *mid depth* of each layer. For example, the average depth of the sixth layer is -13.25 m; $\sigma'_{vo} = 42$ kPa while $\sigma'_{vo} + \Delta\sigma = 140$ kPa. These values are simply scaled off from Fig. Ex. 10.8a. Inserting the appropriate values into Eq. (8.11), we obtain

$$s_c\,(12.5 - 14\text{ m}) = 0.36 \frac{1.5\text{ m}}{1 + 1.1} \log \frac{140}{42} = 0.134\text{ m}$$

TABLE Ex. 10.8a Settlement Computations

(1) Depth Below Ground Surface (m)	(2) Average Depth Below Ground Surface (m)	(3) Soil Type	(4) σ'_{vo} (kPa)	(5) $\Delta\sigma$ (kPa)	(6) $\frac{\sigma'_{vo} + \Delta\sigma}{\sigma'_{vo}}$	(7) Log Col. (6)	(8) C_c	(9) $\frac{C_c}{1 + e_o}$	(10) Thickness of Depth Increment (m)	(11) Settlement (m)	
5	5.75	(CL)	4	98	$\frac{101.9}{3.8}$	1.43	0.36	$\frac{0.36}{1 + 1.1}$	1.5	0.367	
6.5	7.25	↓	12	↓	$\frac{109.6}{11.5}$	0.979	↓	↓	↓	0.252	
8	8.75		19		$\frac{117.2}{19.1}$	0.788				0.203	
9.5	10.25		27		$\frac{124.9}{26.8}$	0.668				0.172	
11	11.75		34		$\frac{132.5}{34.4}$	0.586				0.151	
12.5	13.25		42		$\frac{140.2}{42.1}$	0.522				0.134	← 6th
14	14.75		50		$\frac{147.8}{49.7}$	0.473				0.122	
15.5	16.25		57		$\frac{155.5}{57.4}$	0.433				0.111	
17	17.75		65		$\frac{163.1}{65.0}$	0.400				0.103	
18.5	19.25	↓	73	↓	$\frac{170.8}{72.7}$	0.371	↓	↓	↓	0.095	
20					—			—	$s_c = \Sigma \Delta H = 1.71$ m		
					—			—	$\epsilon_v = 11\%$		
					—			—			
					—			—			

The computations for each layer are listed in Table Ex. 10.8a. The total consolidation settlement of the 15 m thick layer is 1.71 m, or about 11% strain. This value of s_c is about 20% larger than the settlement calculated above for a single 15 m thick layer. All things considered, it probably is a more accurate prediction. Although the answer is given to two decimal places, there is seldom justification for such precision in settlement computations. An estimate of "approximately 1.7 m" would usually be accurate enough. Research (for example, Holtz and Broms, 1972; Leonards, 1977) has shown that consolidation settlements can be predicted within about ±20%.

Note that a settlement of 1.7 m means that 1.7 m of the fill would settle below the groundwater table, which is at the original ground surface, and a decrease in the density of the fill due to buoyancy would result. Thus the actual settlement would be somewhat less than 1.7 m. This condition has been ignored in this example. Otherwise the solution is one of *trial and error*.

In Part II of this example you are asked to compute the time rate of settlement. We can construct Table Ex. 10.8b incorporating U_{avg}, T, s_c, and t by using Eqs. (9.5) and (9.12) and Table 9.1. We usually

assume H remains constant at 15 m (see Sec. 9.3 and Appendix B.2). Since the clay layer has double drainage, the value of H_{dr} in Eq. (9.5) is 15 m/2, or 7.5 m. The value of c_v is given as 0.86 m^2/yr.

Values of T for given values of U_{avg} from Table 9.1 are substituted into this equation and solved for t, Column (4) in Table Ex. 10.8b. The settlement in Column (3) is obtained from Eq. (9.12) by multiplying the total consolidation settlement for this example, 1.71 m, by Column (1). The data in Columns (3) and (4) are plotted [similar to Fig. 9.5(a)] in Fig. Ex. 10.8b.

In engineering practice, because of the great dependence that the rate of settlement has on the drainage path, only *estimates* of the time rate of settlement can be made. If there were *continuous* layers of permeable soil—for example, thin sand seams—interbedded in the 15 m clay layer, then the rate of settlement would be significantly greater (see, for instance, Example 9.6). Another factor is our inability to accurately predict the coefficient of consolidation c_v. If possible, estimates should be field checked, especially for important jobs.

In Part III of this example you are asked to determine the effective stress with depth when $U_{avg} = 50\%$. The computations start with the evaluation of U_z from Fig. 9.3 and the construction of Table Ex. 10.8c.

The depths in Column (1) of Table Ex. 10.8c represent evenly spaced elevations within the 15 m thick clay layer. Column (2) is the ratio of the depth to layer thickness. The time factor for U_{avg} of 50% is found from Table 9.1 to be 0.197 (use 0.2 for convenience). Using Fig. 9.3 along the time factor curve for $T = 0.2$ and the various ratios of z/H in Column (2) of Table Ex. 10.8c, find the values of the degree of consolidation U_z at these ratios. For example, at $z/H = 0$ (and 2.0), the value of U_z is 1.0, or 100% consolidation at the top and bottom of the clay layer. At a ratio of 0.25 z/H (and 1.75 z/H) the degree of consolidation is 70%, etc. These values are placed in Column (3). The effective stress is found by multiplying U_z in Column (3) by $\Delta\sigma$, the weight of added fill, or 98 kPa. A plot of the isochrone for $U_{avg} = 50\%$ is shown in Fig. Ex. 10.8c. You should compare this figure with Fig. Ex. 10.8a. From Table Ex. 10.8b, you can see that it takes about 13 yr to develop this isochrone. The isochrone represents the dividing line between the portion of $\Delta\sigma$ that has gone into effective stress and the amount of pore pressure in the clay layer that remains to be dissipated. If the clay layer were sampled and a consolidation test were performed at a depth of −12.5 m (the middle of the clay layer), the value of the preconsolidation pressure, σ'_p, would be 61 kPa ($\sigma'_{vo} + \Delta\sigma$, 38 + 23 kPa). This value is obtained from Fig. Ex. 10.8c.

There are practical implications to be derived from Part III. If a foundation engineer wanted to reduce the consolidation settlement of a structure, the site could be *preloaded* with a surcharge fill,

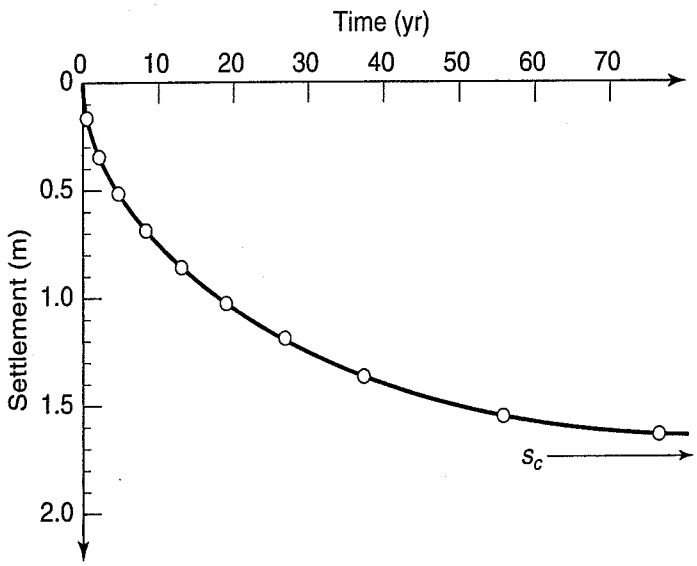

FIGURE Ex. 10.8b Data from Table Ex. 10.8b.

TABLE Ex. 10.8b Time Rate of Settlement

(1) U_{avg}	(2) T	(3) s_c (m)	(4) t (yr)
0.1	0.008	0.17	0.52
0.2	0.031	0.34	2.03
0.3	0.071	0.51	4.65
0.4	0.126	0.68	8.26
0.5	0.197	0.86	12.92
0.6	0.287	1.03	18.82
0.7	0.403	1.20	26.42
0.8	0.567	1.37	37.17
0.9	0.848	1.54	55.59
0.95	1.163	1.62	76.25
1.00	∞	1.71	∞

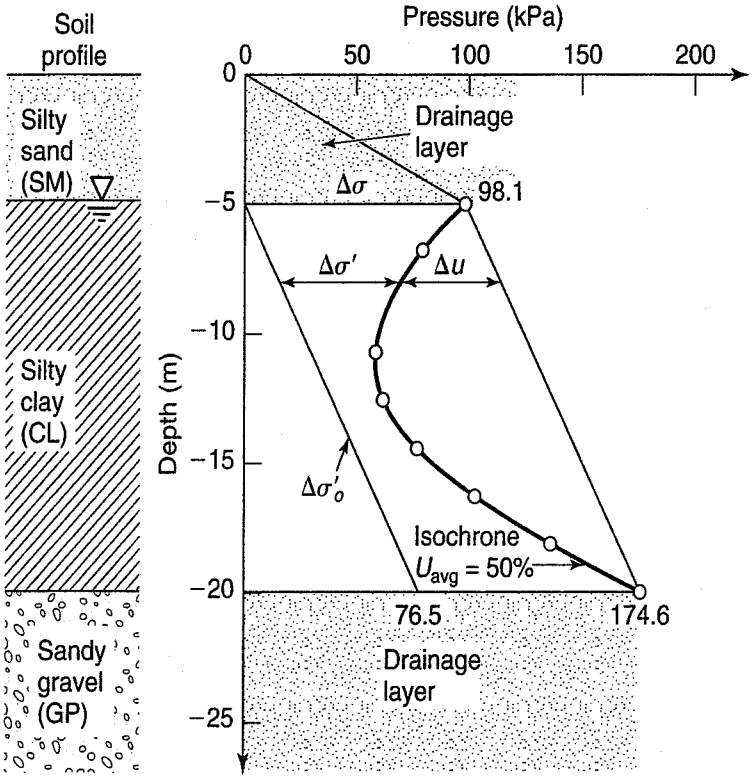

At t = 12.92 yr, U_{avg} = 50% Isochrone represents amount of $\Delta\sigma$ converted into $\Delta\sigma'$ and shows remaining Δu to be dissipated.

FIGURE Ex. 10.8c Data from Fig. Ex. 10.8a and Table Ex. 10.8c.

TABLE Ex. 10.8c Isochrone Data for U_{avg} = 50%

(1) Depth (m)	(2) z/H	(3) U_z	(4) $\Delta\sigma'_z$ (kPa)
−5	0	1.00	98
−6.88	0.25	0.70	69
−8.75	0.5	0.455	45
−10.63	0.75	0.285	28
−12.5	1.0	0.23	23
−14.38	1.25	0.285	28
−16.25	1.5	0.455	45
−18.13	1.75	0.70	69
−20	2.0	1.00	98

which is later removed. The time the preload should be applied may be calculated as in this example. If the stress distribution of the new structure is about the same as or less than the 50% isochrone shown in Fig. Ex. 10.8c, then the consolidation settlement would be calculated by using the recompression index C_r, and the settlements would be substantially less (Sec. 8.7.2).

Part IV, the final part, illustrates the computation for time rate of secondary compression. First plot the consolidation settlement data in Table Ex. 10.8b, s_c versus log time, shown in Fig. Ex. 10.8d.

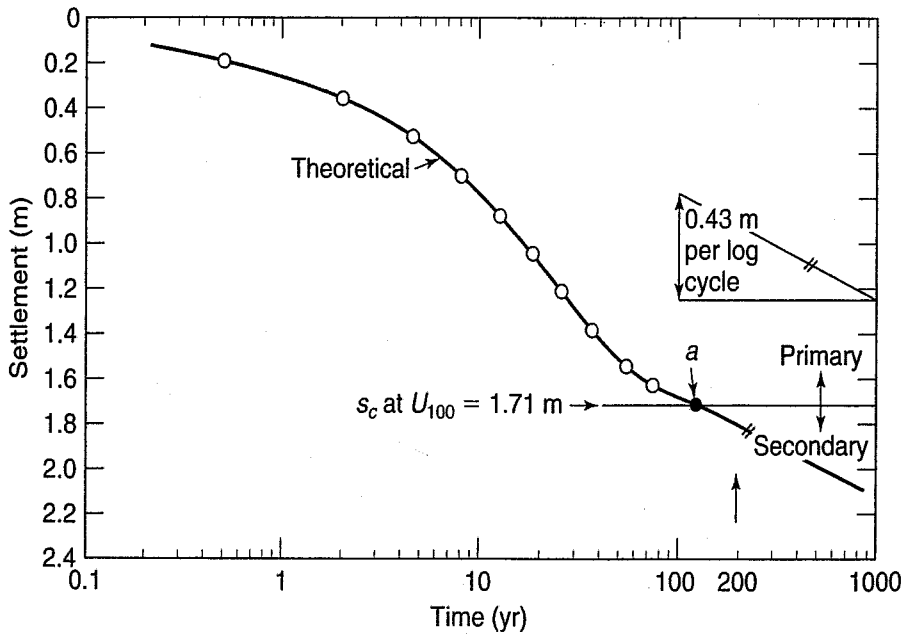

FIGURE Ex. 10.8d Data from Table Ex. 10.8b.

Note that this is a theoretical settlement-log time relationship. Solving for the secondary settlement Eq. (9.28) for one log cycle, we obtain

$$s_c = \frac{C_\alpha}{1 + e_o}(H_o)(\Delta \log t)$$
$$= \frac{0.06}{1 + 1.1}(15\text{ m})(1)$$
$$= 0.43\text{ m/log cycle of time}$$

This slope is shown in Fig. Ex. 10.8d. This same rate of secondary compression starts at point a on the theoretical settlement-time curve. Point a corresponds to the settlement at 100% primary consolidation (s_c = 1.71 m). Note that the primary consolidation curve has been extrapolated slightly to point *a*. Thus, from Fig. Ex. 10.8d, the total settlement at the end of, say, 200 years is expected to be about 1.8 m. To be more precise than this in predicting settlements is beyond our ability to accurately evaluate soil properties and field drainage conditions.

The preceding example illustrates some of the computational details of a time rate of settlement analysis for the simple case of one-dimensional loading and for a normally consolidated clay. If the loaded area were of limited extent, then you would have to take into account the stress distribution with depth at key points under the loaded area. You would use the techniques discussed in Sec. 10.3 to establish curve B ($\Delta\sigma$) in a diagram, similar to Fig. Ex. 10.8a. You might even have to do this for several sections under the foundation—for example, in the center, at the edge, and under the corner of the loaded area.

Because the clay in Example 10.8 was normally consolidated, computation of the consolidation settlement (Part I) was relatively straightforward. If the clay had been overconsolidated—that is, if $\sigma'_{vo} < \sigma'_p$—then you would use Eq. (8.16) or (8.17) and the concepts discussed in Sec. 10.5.

Sometimes the upper part of the layer is overconsolidated and the lower part normally consolidated, and you have to take this into account in your computations. Another frequent complication is that the soil and consolidation properties (C_c, e_o) vary throughout the soil profile. In that case, when you break up the profile into smaller layers, as we do in the next example, the layers may not necessarily be evenly spaced. In this situation, tables, such as in Table Ex. 10.8a, are very helpful for making the actual computations.

Procedures for handling complex settlement problems in engineering practice are treated in depth in foundation engineering textbooks. When soil permeability and therefore c_v varies within the compressible layer, or when boundary layers impede drainage, the problem of time rate of consolidation becomes very complex, and numerical techniques such as found in Scott (1963) and Harr (1966) are called for. Often these involve finite difference type solutions (Sec. 9.3.2).

Example 10.9

Given:

Soil profile, soil properties, and $\sigma'_{vo}(z)$, $\sigma'_p(z)$, and $\sigma'_{vo} + \Delta\sigma(z)$, as shown in Fig. Ex. 10.9. The foundation rests at an elevation of −2 m.

Required:

Compute the settlement.

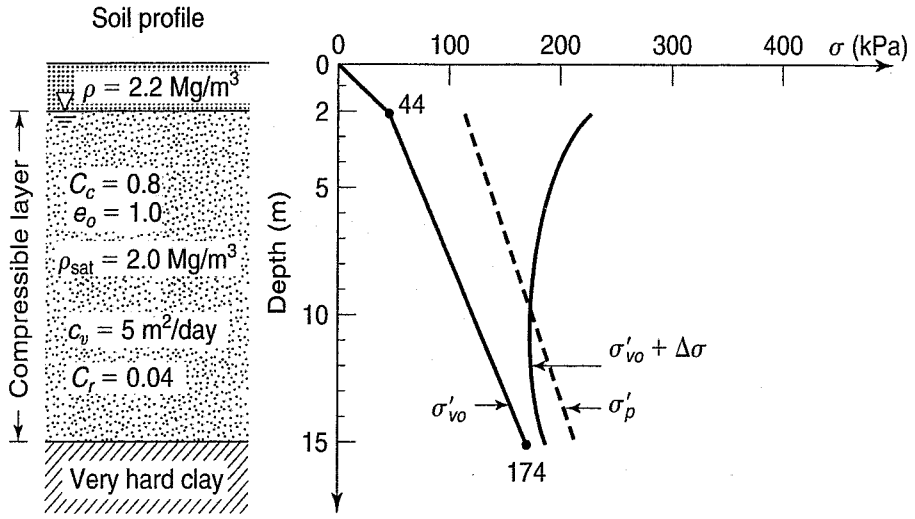

FIGURE Ex. 10.9

Solution: Figure Ex. 10.9 shows that the soil is overconsolidated and that down to a depth of 10 m, the addition of $\Delta\sigma$ leads to a final vertical effective stress that exceeds the preconsolidation pressure. Further, the groundwater table is at the top of the compressible layer and the external loading is shown as the resulting $\Delta\sigma(z)$ curve.

Break the compressible layer up into seven layers; the top layer has a thickness of 1 m and the rest of the layers are 2 m thick. Prepare a table to facilitate computations. For each layer, record the stresses at the mid depth of each layer to represent the "average" conditions. (This problem is similar to the compound compressibility Case 3 in Sec. 10.5.) We have filled in the top portion of Table Ex. 10.9 with the layers above a depth of 10 m as they all have terms using C_c. At the average depth of 2.5 m for the first layer, determine from the graph $\sigma'_{vo}(= 48\text{ kPa})$, $\sigma'_{vo} + \Delta\sigma_v(= 217\text{ kPa})$ and $\sigma'_p(= 117\text{ kPa})$. These numbers are used in Columns (6) $[C_r \log(\sigma'_p/\sigma'_{vo})]$ and (7) to determine the recompression and virgin compression portions of the change in void ratio, respectively, which are then summed and divided by $(1 + e_o)$ in Column (8) to get the vertical strain. This is multiplied

TABLE Ex. 10.9

(1) Depth, z (m)	(2) Mid-layer depth (m)	(3) σ'_{vo} (kPa)	(4) σ'_p (kPa)	(5) $\sigma'_{vf} = \sigma'_{vo} + \Delta\sigma_v$ (kPa)	(6) $C_r \log(\sigma'_p/\sigma'_{vo})$ or $C_r \log(\sigma'_{vf}/\sigma'_{vo})$	(7) $C_c \log(\sigma'_{vf}/\sigma'_p)$	(8) Vertical strain, ε_v	(9) H_i (m)	(10) ΔH_i (m)
2									
	2.5	48	117	217	0.0155	0.215	0.115	1	0.115
3									
	4	63	129	200	0.0125	0.152	0.0824	2	0.165
5									
	6	82	146	185	0.0100	0.0823	0.046	2	0.0923
7									
	8	102	160	177	0.0078	0.0351	0.021	2	0.043
9									
	10	122	175	175	0.0063	—	0.003	2	0.006
11									
	12	141	192	175	0.0038	—	0.0019	2	0.004
13									
	14	161	208	181	0.002	—	0.001	2	0.002
15							Total settlement (m)		0.427

by the layer thickness in Column (9) to obtain that layer's contribution to the total settlement in Column (10). This is essentially a layer-by-layer use of Eq. (8.18a).

For the layers below a depth of 10 m in this problem, the influence of the foundation stress is so small that the final effective stress, $\sigma'_{vo} + \Delta\sigma_v$, does not reach the preconsolidation pressure, so that all settlement is from recompression strains only. In this case, rather than using the ratio $C_r \log(\sigma'_p/\sigma'_{vo})$, we use $C_r \log(\sigma'_{vf}/\sigma'_{vo})$ to compute the change in void ratio, and that is the only contribution to settlement. When all layer contributions to settlement are summed, we obtain the total settlement of 0.43 m.

Here is a very important statement of philosophy: When settlement is reported to a client in a report, you should say "the settlement is estimated to be about 0.5 m." To report the settlement as "0.490 m" implies that geotechnical engineers can predict settlement with that amount of precision. In fact, we can predict with an accuracy of only about ±20 percent. To be overly precise will only get you into trouble.

Example 10.10

Given:

A circular water tank, 8 m high and 27 m in diameter, (q_0 = 80 kPa) is supported on a flexible mat foundation on a sand layer 9 m thick that overlies a 30 m thick layer of San Francisco Bay mud. Below the clay is another layer of granular material (assumed incompressible). Consolidation test data is shown in Fig. 8.5. The groundwater table is 2 m below the ground surface. For simplicity, we assume that the tank is on the ground surface, but ordinarily the bottom of the foundation is placed below the frost penetration depth. The average soil parameters and profile are shown in Fig. Ex. 10.10a.

Required:

a. Compute the change in stress with depth due to the foundation load at the center and edge of the tank.

b. Compute the settlement of the tank at the center and at the edge.

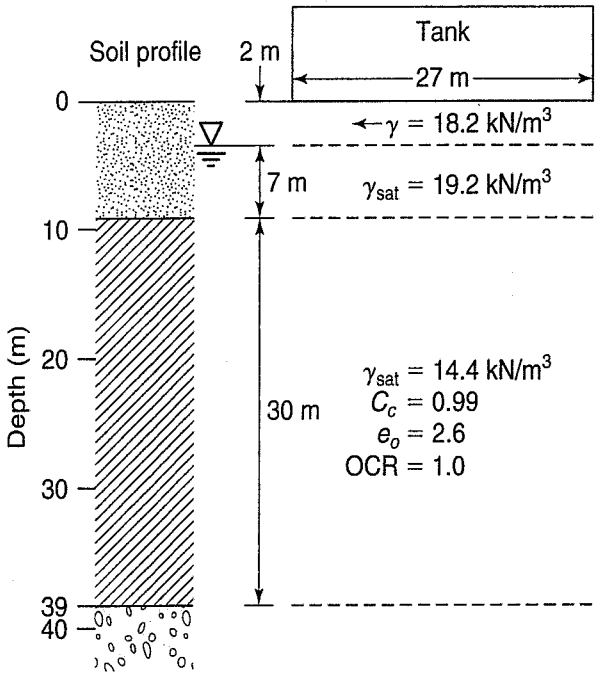

FIGURE Ex. 10.10a Soil profile and tank dimensions.

Solution:

a. We solve this part by first computing the existing vertical effective overburden stress with depth. Next, we compute the change in stress $\Delta\sigma\ (z)$ due to the tank loading. [We will assume that the compressible layer is infinite in depth and compute $\Delta\sigma$. Actually, the existence of a relatively rigid layer (compared to the clay) below the compressible layer will change the true stress distribution. We will give that solution as well, later.]

As explained in Example 10.8, the accuracy of the settlement calculations can be improved by breaking the 30 m thick clay layer into sublayers. In this case, we select 10 sublayers of 3 m each. Then find the stress in the *middle* of each sublayer for both overburden stress and $\Delta\sigma$. For example, the average stress (σ'_{vo}) at the center of sublayer 7 at 19.5 m below the top of the clay layer (or 28.5 m below the ground surface) is

$$\begin{aligned}\sigma_{vo} &= (\rho g z)_1 + (\rho' g z)_2 + (\rho' g z)_3 \\ &= 18.2\frac{\text{kN}}{\text{m}^3}\cdot 2\,\text{m} + (19.2 - 9.8)\cdot 7 + (14.4 - 9.8)\cdot 19.5 \\ &= 36\,\text{kPa} + 66 + 90 = 192\,\text{kPa}\end{aligned}$$

The rest are shown on Fig. Ex. 10.10b, where we have plotted σ'_{vo} versus depth.

The value of $\sigma_z(z)$ has been calculated for both the center and edge of the circular tank using Fig. 10.4 and the calculated values for z/r and x/r. As an example, the stress change at the center of the tank $(x/r = 0)$ for a depth of 9 m $(z/r = 9/13.5 = 0.67)$ gives an influence value of 80; multiplying 80 by $q_o = 80$ kPa gives 64 kPa. This value and subsequent numbers for the center of the tank are shown in Column (2) of Table Ex. 10.10a. Column (5) gives the $\Delta\sigma$ for the edge of the tank.

The corresponding values using the computer program by Christian and Urzua (1996) are given in Columns (3) and (6). Notice that both methods give about the same number. Both of these first two approaches assumed an infinite depth of the clay layer. Actually, this is not correct, because there is an incompressible pervious layer below the clay that alters the stress distribution. We used the chart in Poulos and Davis (1974), based on Milovic (1970), to take into account the rigid base. Still, we had to make an assumption that the upper granular

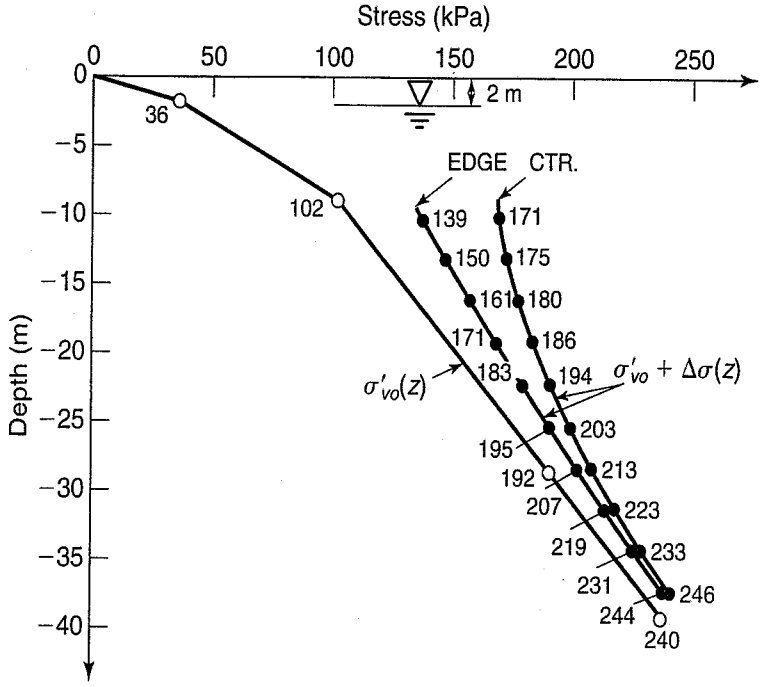

FIGURE Ex. 10.10b Vertical stress profiles.

TABLE Ex. 10.10a Evaluation of $\Delta\sigma(z)$ Using Three Different Methods of Calculation: (a) Fig. 10.5; (b) Christian and Urzua (1996); and (c) Poulos and Davis (1974)[a]

Depth (m)	(1)	(2)	(3)	(4)	(5)	(6)
	Center			Edge		
−9	64	66	64	38	31	30
−15	48	47		26	25	
−20	37	34	38	21	21	24
−25	26	25		18	16	
−30	19	19	26	14	14	18
−35	14	15		11	11	
−39	13	12	19	10	10	16

[a]Stresses in Columns (1)–(6) are in units of kPa.

layer has the same modulus as the clay layer. Obviously, it does not. The answers, however, appear to be about the same. Recognize that when we use elastic theory it is only a way to estimate the stress changes with depth (Sec. 10.3).

b. With the stresses now known, we use Table Ex. 10.10b to compute the settlement of the tank center and the edge. The table is set up to solve the consolidation settlement Eq. (8.18a) for a normally consolidated soil. Data are entered for the soil sublayers of 3 metres. Column (2) shows the average depth within a layer. Column (3) gives the soil type. In our case, there is one soil type (denoted in the computer program as c-3). In Column (4), we compute the vertical effective overburden stress, σ'_{vo}, at the average depths of the ten sublayers. From our stress-distribution computations, we add $\Delta\sigma$ that we obtained from Table Ex. 10.9a, using using Columns (2) and (5) for the center and edge values, respectively. Next, we take $\sigma'_{vo} + \Delta\sigma$ and divide by σ'_{vo} [Column (4) + Column (5) divided by Column (5)]. Column (7) is the log of Column (6). We skipped Column (8) and took care of it in Column (9) by

TABLE Ex. 10.10b Computations for Tank Center Settlement

(1) Depth, z (m)	(2) Mid-layer depth (m)	(3) Soil type	(4) σ'_{vo} (kPa)	(5) $\Delta\sigma'_v$ (kPa)	(6) $\frac{\sigma'_{vo} + \Delta\sigma'_v}{\sigma'_{vo}}$	(7) log Col. (6)	(8) C_c	(9) $C_c/1 + e_o$	(10) H_i (m)	(11) ΔH_i (m)
9	10.5	c-3	109	62	1.57	0.195		0.274	3	0.161
12	13.5	↓	123	52	1.42	0.153		↓	↓	0.126
15	16.5		137	43	1.31	0.119				0.098
18	19.5		151	35.5	1.24	0.092				0.076
21	22.5		164	30	1.18	0.073				0.060
24	25.5		178	25	1.14	0.057				0.047
27	28.5		192	21	1.11	0.045				0.037
30	31.5		206	18	1.09	0.036				0.030
33	34.5		220	15	1.07	0.029				0.024
36	37.5	↓	233	13	1.06	0.024		↓	↓	0.019
39								Total Settlement		0.677

TABLE Ex. 10.10c Computations for Tank Edge Settlement

(1) Depth, z (m)	(2) Mid-layer depth (m)	(3) Soil type	(4) σ'_{vo} (kPa)	(5) $\Delta\sigma'_v$ (kPa)	(6) $\frac{\sigma'_{vo} + \Delta\sigma'_v}{\sigma'_{vo}}$	(7) log Col. (6)	(8) C_c	(9) $C_c/1 + e_o$	(10) H_i (m)	(11) ΔH_i (m)
9	10.5	c-3	109	30	1.27	0.106		0.274	3	0.087
12	13.5	↓	123	27	1.22	0.086		↓	↓	0.071
15	16.5		137	24	1.18	0.070				0.058
18	19.5		151	21	1.14	0.057				0.047
21	22.5		164	19	1.12	0.048				0.039
24	25.5		178	17	1.10	0.040				0.033
27	28.5		192	15	1.08	0.033				0.027
30	31.5		206	13	1.06	0.027				0.022
33	34.5		220	12	1.05	0.023				0.019
36	37.5	↓	233	11	1.05	0.020		↓	↓	0.016
39								Total Settlement		0.418

computing the ratio of $C_c/(1 + e_o)$. Column (10) is the thickness of the sublayer, in our case 3 m each. The settlement computation for each sublayer is given in Column (11), where we multiplied Columns (7) × (9) × (10), and the total settlement is given by summing up the settlement of each sublayer in Column (11). The settlement for the center of the tank is 0.68 m (0.675 m using the computer program), and the edge settlement is 0.42 m (0.413 m using the computer program).

In our report to the client, we would state that the settlement in the center of the tank would be about 0.7 m and about 0.5 m at the edge. Incidentally, on difficult and/or important jobs, it is good practice to measure and plot the actual settlement versus time (as we did in Chapter 9) and then compare the measurements with our predictions. This way geotechnical engineers can become better calibrated and perhaps adjust some of the parameters such as the coefficient of consolidation to obtain the best fit between actual and predicted settlement. This information will lead to improved designs and less expensive foundations in future projects on the same soil deposit.

Example 10.11

Given:

Data from Fig. Ex. 10.10a. The value of c_v, the coefficient of consolidation, is 1 m^2/yr.

Required:

Compute and plot the time rate of consolidation settlement.

Solution: From Fig. Ex. 10.10b you probably noticed that the increase in $\Delta\sigma$ from the loaded tank on the surface is almost linear. Such a linear variation of $\Delta u = \Delta\sigma$ allows us to use Eqs. (9.5), (10.9) and (9.12) to prepare our plot.

A look at Fig. Ex. 10.10a will show that both the top *and* bottom layers are pervious and will drain the compressible clay layer during consolidation. Therefore, we have a case of double drainage, and $2H = 30$ m, where H = the drainage distance.

Using Eq. (9.5), we find

$$T = c_v \frac{t}{H_{dr}^2} = 1\frac{\text{m}^2}{\text{yr}} \frac{t}{(15\text{ m})^2}$$

Solving for the real time, t,

$$t = \frac{T(15\text{ m})^2}{c_v} = T\frac{225\text{ m}^2}{1\frac{\text{m}^2}{\text{yr}}} = T \times 225\text{ yr}$$

Now, make a copy of Table 9.1 and add two more columns—one for Δh and the other for time t. For a given value of U_{avg}, multiply the corresponding value of T in Column (2) of Table Ex. 10.11 in the above equation and solve for t (or, $225 \times 0.008 = 1.8$ yr) and this goes in Column (3). Fill in the rest of Column (3) the same way.

The fourth column is nothing more than $U_{avg} \times s_c$; for $U_{avg} = 0.1$, the Δh is 0.1×68 cm $= 6.8$ cm. Fill in the rest of Column (4).

A plot of expected settlement versus time that would be sent to the client is shown in Fig. Ex. 10.11. If the life of the expected structure is only 50 yr, then the most settlement that would occur by that time would be only about 40 cm. Note that the *rate* of settlement depends on many factors. Just as in Example 10.10, for important structures, geotechnical engineers would try to take settlement measurements with time and compare them with the predicted values. If the field data deviates, then one could back-calculate the coefficient of consolidation, c_v, for example, and recalculate the time-settlement. After all, you have a full-scale field loading test with the prototype structure!

TABLE Ex. 10.11 Time History of Consolidation Settlement

(1) U_{avg} (%)	(2) T	(3) t (yr)	(4) Δh (cm)
0.1	0.008	1.8	6.8
0.2	0.031	7	13.6
0.3	0.071	16	20.4
0.4	0.126	28	27.2
0.5	0.197	44	34
0.6	0.287	65	40.8
0.7	0.403	91	47.6
0.8	0.567	128	54.4
0.9	0.848	190	61.2
0.95	1.163	262	64.6
1.0	∞	∞	68

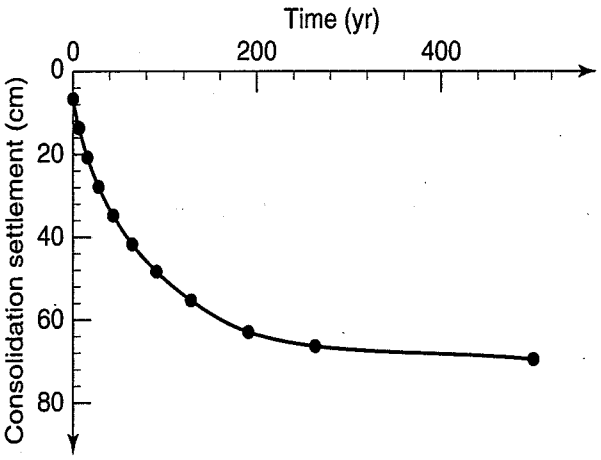

FIGURE Ex. 10.11 Consolidation settlement versus time.

If there were a continuous pervious seam (even 1 cm thick) in the middle of the 30 m clay layer, what effect would that have on the time rate of consolidation? It would reduce the overall time by one quarter. Check Eq. (9.5) and confirm this. Suppose that the continuous seam was at 10 m from the top boundary. What then? You would have a case of double drainage with two layers. The drainage path of the top layer would be 5 m, while that for the 20 m thick layer would be 10 m. In this case, you would have to make two tables of time rate of settlement, as the layers would dissipate Δu at different rates. Then you would have to superimpose the combined settlements.

PROBLEMS

10.1 Compare the stress distribution with depth for (a) a point load of 1200 kN and (b) a 1200 kN load applied over an area of 3 × 3 m. Plot the results.

10.2 If you used the Boussinesq (or Westergaard) theory for Problem 10.1, do the problem again but use the Westergaard (or Boussinesq) theory instead. Comment on the differences between the two theories.

10.3 Compute the data and draw a curve of σ_z/Q versus depth for points directly below a point load Q. On the same plot draw curves of σ_z/Q versus depth for points directly below the center of square footings with breadths of 6.5 m and 20 m, respectively, each carrying a uniformly distributed load Q. On the basis of this plot, make a statement relative to the range within which loaded areas may be considered to act as point loads. (After Taylor, 1948.)

10.4 The center of a rectangular area at ground surface has Cartesian coordinates (0, 0), and the corners have coordinates (7, 18). All dimensions are in metres. The area carries a uniform pressure of 150 kPa. Estimate the stresses at a depth of 20 m below ground surface at each of the following locations: (0, 0), (0, 18), (7, 0), (7, 18), and (12, 28); obtain values by both Boussinesq and Westergaard methods, and also determine the ratio of the stresses as indicated by the two methods. (After Taylor, 1948.)

10.5 Compare the results of Problem 10.4 with those of the 2:1 method. Comments?

10.6 Calculate the stress distribution with depth at a point 3.5 m from the corner (along the longest side) of a rectangularly loaded area 15 by 35 m with a uniform load of 75 kPa. Do by (a) the Boussinesq theory, (b) the Westergaard theory, and (c) the 2:1 method.

10.7 How far apart must two 18 m diameter tanks be placed such that their stress overlap is not greater than 10% of the contact stress at depths of 10, 20, and 30 m?

10.8 Compute the stresses for the data of Example 10.5 parts (a) and (b), using the Newmark chart, Fig. 10.8.

10.9 Work Example 10.5, using superposition of the results of Figs. 10.7 and 10.4. How does your answer compare with the solution for Example 10.5?

10.10 Given the data of Example 10.6. Instead of a load on the surface, compute the depth of an excavation to cause a reduction in stress at the bottom of the excavation of 200 kPa if $\rho = 2.1$ Mg/m^3. The excavation plan area is shown in Fig. Ex. 10.6a.

10.11 For the excavation of Problem 10.10, *estimate* the stress change at a depth of 50 m below the bottom of the excavation at point O′.

10.12 Is the 2:1 method usable for excavations? Why?

10.13 A strip footing 2.5 m wide is loaded on the ground surface with a pressure equal to 175 kPa. Calculate the stress distribution at depths of 2.5, 5 and 10 m under the center of the footing. If the footing rested on a normally consolidated cohesive layer whose LL was 78 and whose PL was 47, estimate the settlement of the footing.

10.14 How would the estimated settlement under the center of a 4 × 4 m square footing compare with the settlement of the 4 m wide strip footing in the previous problem, assuming soil conditions were the same? Assume the footing is flexible enough to provide uniform contact pressure to the soil.

10.15 How much difference in the computed settlements is there in Problem 10.14 if the Westergaard theory is used instead of Boussinesq theory?

10.16 A large oil storage tank 90 m in diameter is to be constructed on the soil profile shown in Fig. P10.16. Average depth of the oil in the tank is 18 m, and the specific gravity of the oil is 0.92. Consolidation tests from the clay layer are similar to those given in Problem 8.18. Estimate the maximum total and differential consolidation settlement of the tank. Neglect any settlements in the sand. Work this problem (a) assuming conditions at the middepth of the clay are typical of the entire clay layer, and (b) dividing the clay layer into four or five thinner layers, computing the settlement of each thin layer and summing up by Eq. (8.14). (*Hint:* See Example 10.8.)

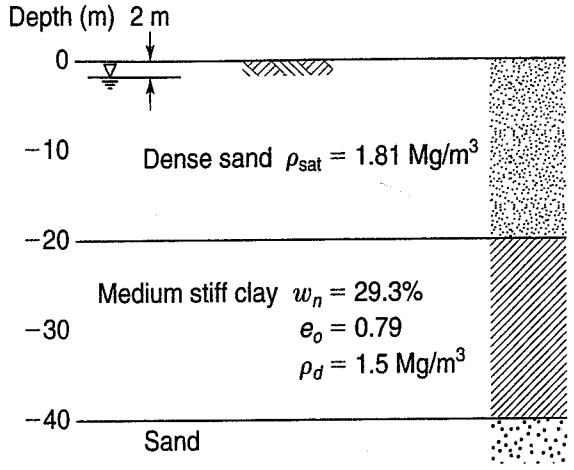

FIGURE P10.16

10.17 Estimate the ultimate consolidation settlement under the centerline of a 17 × 17 m mat foundation. The mat is 1.2 m thick reinforced concrete, and the average stress on the surface of the slab is 80 kPa. The soil profile is shown in Fig. P10.17. Oedometer tests on samples of the clay provide these average values:

$$\sigma'_p = 130 \text{ kPa}, \quad C_c = 0.40, \quad C_r = 0.03$$

Neglect any settlements due to the sand layer.

10.18 Three uniformly distributed loads of 100 kPa each are applied to 10 × 10 m square areas on the soil profile shown in Fig. P10.18. Undisturbed samples of the clay were taken prior to construction, and consolidation tests indicated that the average preconsolidation stress is about 110 kPa, the average compression index is 0.50, and the average recompression index is 0.02. Estimate the total consolidation settlement for the clay layer only under the center of the middle loaded area.

10.19 A series of oil storage tanks are to be constructed near Mystic River power station in Boston, MA. The typical tank is 22 m in diameter, and it exerts an average foundation stress of about 125 kPa. The soil profile at the site is very similar to that shown in Fig. 8.19(a). Estimate both the total and differential consolidation settlement under the average tank. (*Hint:* See Example 10.8.)

10.20 A new highway to Siracha, Thailand, is to be constructed east of Bangkok, across a region of deep deposits of very soft marine clay. A typical soil profile is shown in Fig. 8.21(a). The average C_{cr} = 0.8 below the drying crust. The proposed embankment is 17 m wide at the top, has three horizontal to one vertical side slope, and is 2.5 m high. Estimate the ultimate consolidation settlement of the centerline of the embankment.

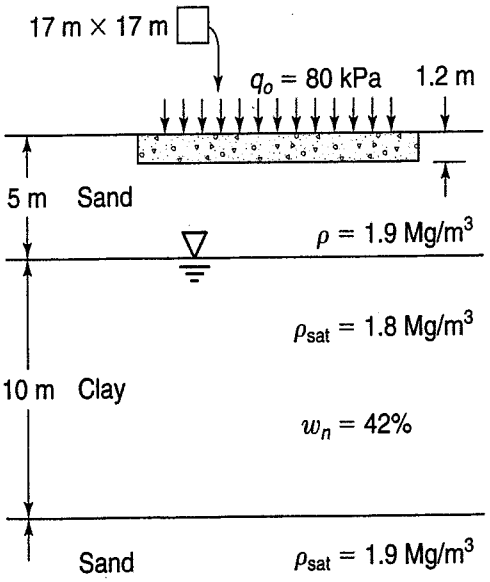

FIGURE P10.17

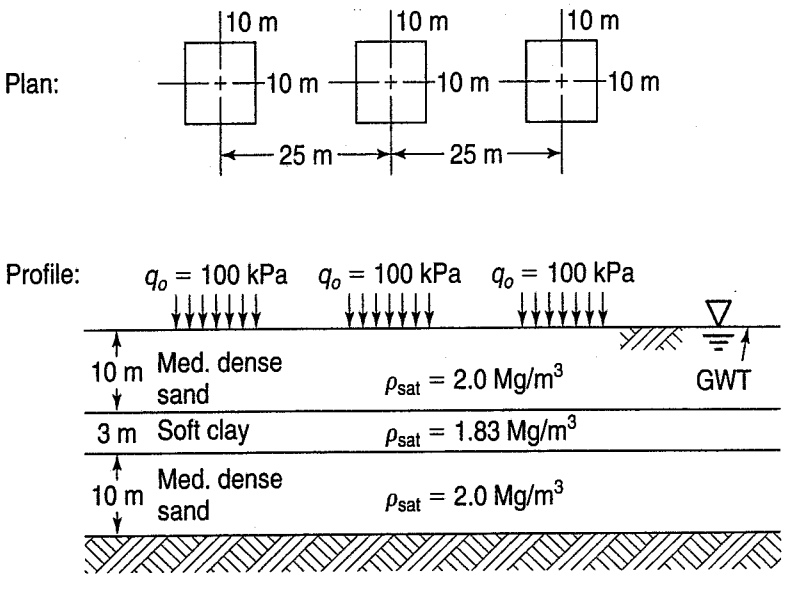

FIGURE P10.18

10.21 Figure P10.21 shows a proposed foundation site, with 10 ft of sand overlying 15 ft of clay with consolidation properties shown. The clay is normally consolidated. Assume 1-D conditions.

(a) Compute the initial σ'_v at the middle of the clay layer prior to excavation and construction.

(b) After excavation and during construction, the foundation area will be heavily loaded with the structure and equipment so that σ'_v at the middle of the clay layer will be increased to 3900 psf. Determine the settlement that will occur under these conditions.

(c) After construction is completed, the equipment will be removed, and the final σ'_v at the middle of the clay layer will be 3200 psf.

As part of your answer, please be sure to sketch the compression curve followed in parts (b) and (c).

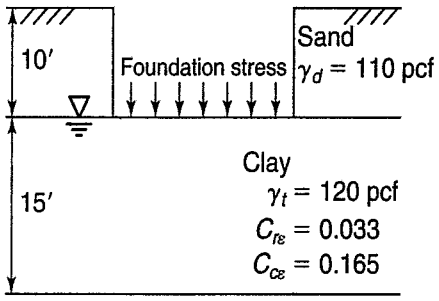

FIGURE P10.21

10.22 As part of a construction project, a 7.5 m thick layer of clay is to be loaded with a temporary 3 m thick sand layer (refer to Fig. P10.22). The figure shows the water table location, soil unit weights, and the compression curve properties for the clay. Assume the sand layer remains dry.

(a) Calculate the value of σ'_v in the middle of the clay layer (at 3.75 m below the water table) before the sand layer is applied, and after consolidation is complete.

(b) Based on your answer in part (a) and the compression curve characteristics, calculate the settlement that will occur under these conditions.

(c) How much will the clay layer heave when the 3 m sand layer is removed?

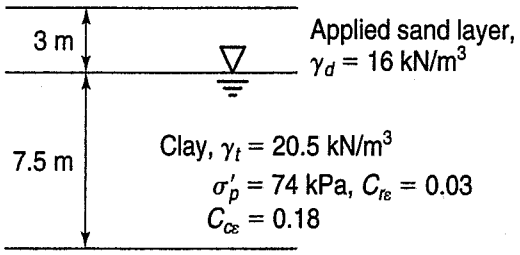

FIGURE P10.22

10.23 Figure P10.23 shows the 1-D compression curve for a clay.

(a) Using log interpolation between 100 and 1000, determine the σ'_v value at a vertical strain, ε_v = 20%.

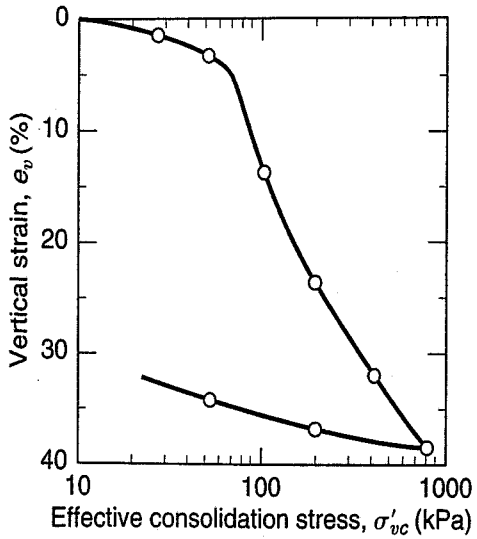

FIGURE P10.23

(b) If the initial void ratio, $e_o = 0.846$, determine C_r and C_c for this soil. For C_c, use the portion of the curve between $\sigma'_v = 200$ and 800 kPa.

(c) If the original clay layer thickness is 9.5 m, determine the settlement that occurs in the layer when it is loaded from 70 to 200 kPa. (*Note:* You don't need the results from part (b) to do this.)

10.24 A large embankment is to be built on the surface of a 15 ft clay layer. Before the embankment is built, the initial σ'_v at the middle of the clay layer is 480 psf. The results from a 1-D consolidation test on the the clay from the middle of the layer are as follows: $\sigma'_p = 1800$ psf, $C_{r\varepsilon} = 0.0352$, $C_{c\varepsilon} = 0.180$. If the final σ'_v at the middle of the layer after the embankment loading is 2100 psf, what is the settlement, in inches, of the clay layer resulting from this loading?

10.25 Figure P10.25 shows a proposed site where an excavation will be made. The 10 ft layer of sand will be removed, so that the top of the 24 ft normally consolidated clay layer will be exposed. Assume full capillarity in the clay *only*.

(a) Assume that the water table location remains the same during excavation. Compute the σ_v, σ'_v and u values at the middle of the clay layer before and after the excavation.

(b) Assuming 1-D conditions, compute how much the clay layer will deform due to this excavation, in inches. Specify whether this is settlement or heave.

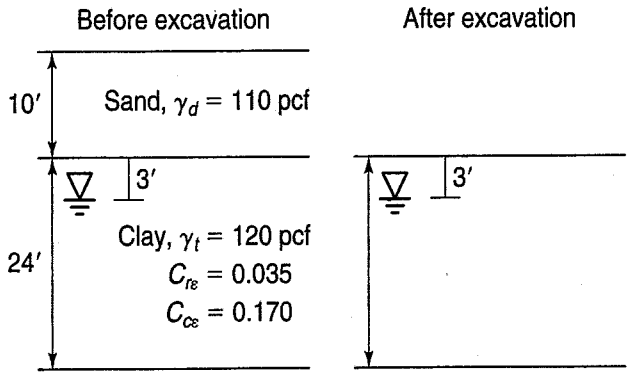

FIGURE P10.25

10.26 Figure P10.26 shows the soil profile at a site where you plan to lower the water table. You have results from two consolidation tests, one from the upper 12 ft thick overconsolidated crust, and another from the lower 32 ft thick normally consolidated zone. You plan to lower the water table from its current 12 ft depth to 20 ft below ground surface. The consolidation properties for each layer are shown. Assume full capillarity.

(a) Compute the σ'_v in the middle of each layer before and after the water table is lowered.

(b) Determine the total settlement that will result from lowering the water table.

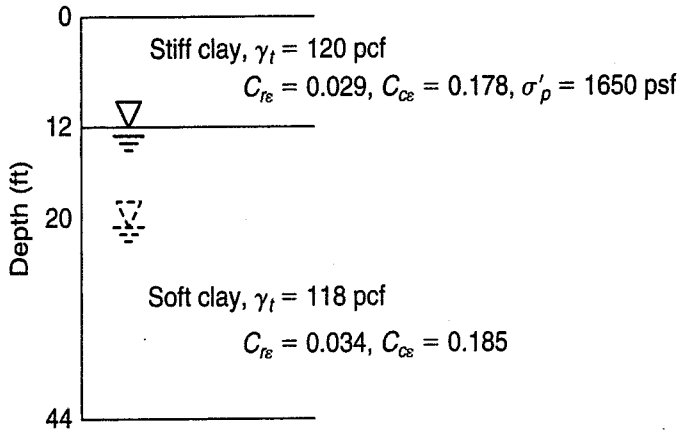

FIGURE P10.26

10.27 When a consolidation test is performed on some soils, the virgin compression region is not linear, but bilinear. Figure P10.27 shows such a compression curve from a 15 ft thick layer.

(a) What vertical strain, ε_v, occurs when the soil is loaded from an initial $\sigma'_{v1} = 560$ psf to $\sigma'_{v2} = 3000$ psf?

(b) If you load the soil further, to $\sigma'_{v3} = 4000$ psf, how much additional settlement occurs?

(c) Finally, if you unload from 4000 psf back to $\sigma'_{v4} = 3000$ psf, what additional deformation (in feet) occurs?

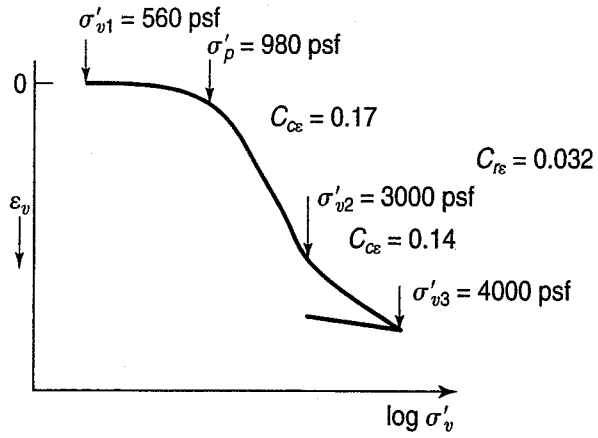

FIGURE P10.27

10.28 Figure P10.28 shows a soil profile where a clay layer will consolidate under an embankment loading of 150 kPa. There is no capillarity. Your firm performed two consolidation tests:

one test indicated that the soil is overconsolidated, with σ'_p = 110 kPa.

one test indicated that the soil is normally consolidated.

Both tests gave the same $C_{r\varepsilon}$ and $C_{c\varepsilon}$ values, shown in the figure.

(a) Determine the initial σ'_v at the middle of the clay layer (i.e., at depth 5.5 m).

(b) Compute the settlement due to the embankment loading, assuming that the overconsolidated assumption is correct (σ'_p = 110 kPa).

(c) Compute the settlement again, this time assuming that the soil is normally consolidated.

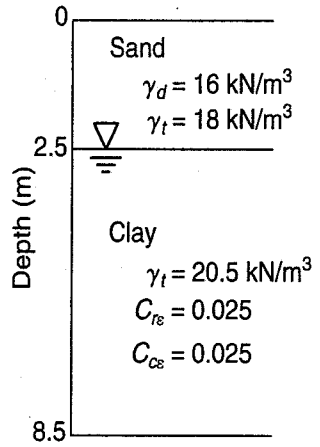

FIGURE P10.28

CHAPTER 11

The Mohr Circle, Failure Theories, and Strength Testing of Soil and Rocks

11.1 INTRODUCTION

In order to discuss the stress-deformation and shear strength properties of soils, we need to introduce some new definitions and concepts about stress and failure. From Chapters 8 through 10, you know something about the load-settlement-time characteristics of cohesive soils due to one-dimensional loading. But to understand the response of sands and nonplastic silts, clays and plastic silts, and rocks to types of loading other than one-dimensional, we need to give you some background information on how we describe stresses in geotechnical engineering, failure theories, and tests commonly used on soils and rocks.

If the load or stress in a foundation or on a slope is increased until the deformations become unacceptably large, we say that the soil in the foundation or slope has "failed." In this case we are referring to the *strength* of the material, which is really the maximum or ultimate stress the material can sustain. In geotechnical engineering, we are generally concerned with the *shear strength* of soils and rocks, because, in most of our problems in foundations and slope stability, failure results from excessive applied shear stresses.

The following notation is introduced in this chapter.

Symbol	Dimension	Unit	Definition
c	$ML^{-1}T^{-2}$	kPa	Intercept of the Mohr failure envelope - Eq. (11.8)
f_s	$ML^{-1}T^{-2}$	kPa	Friction on the friction sleeve of a Dutch cone penetrometer
h	L	mm	Penetration of Swedish fall-cone
p_l	$ML^{-1}T^{-2}$	kPa	Limit pressure in the pressuremeter test
q_c	$ML^{-1}T^{-2}$	kPa	Point resistance of a Dutch cone penetrometer

(Continued)

Symbol	Dimension	Unit	Definition
D	L	mm	Diameter of vane
H	L	mm	Height of vane
N	—	—	Blow count in the Standard Penetration Test
N_c	—	—	CPT correlation or bearing capacity factor
T	$MLT^{-2} \cdot L$	N · m	Torque in vane shear test
CD	—	—	Consolidated drained (triaxial test)
CU	—	—	Consolidated undrained (triaxial test)
UU	—	—	Unconsolidated undrained (triaxial test)
α_f	—	(degree)	Angle of the failure plane in the Mohr–Coulomb failure criteria - Eq. (11.10)
γ	—	(%)	Shear strain (angle of rotation in DSS test)
δ	L	m	Horizontal displacement
θ	—	(degree)	Angle of inclination of resultant shear and normal stress, or angle of principal stress rotation
σ	$ML^{-1}T^{-2}$	kPa	Normal stress
σ_1	$ML^{-1}T^{-2}$	kPa	Major principal stress
σ_2	$ML^{-1}T^{-2}$	kPa	Intermediate principal stress
σ_3	$ML^{-1}T^{-2}$	kPa	Minor principal stress
σ_{ff}	$ML^{-1}T^{-2}$	kPa	Normal stress on the failure plane at failure - Eq. (11.7)
σ_n	$ML^{-1}T^{-2}$	kPa	Normal stress
τ	$ML^{-1}T^{-2}$	kPa	Shear stress
τ_f	$ML^{-1}T^{-2}$	kPa	Undrained shear strength
τ_{ff}	$ML^{-1}T^{-2}$	kPa	Shear stress on the failure plane at failure - Eq. (11.7)
τ_{hv}	$ML^{-1}T^{-2}$	kPa	Shear stress on the horizontal plane during direct simple shear test
ϕ	—	(degree)	Slope of the Mohr failure envelope (sometimes called the *angle of internal friction*) - Eq. (11.8)

Note: A prime on an angle or stress denotes *effective stress*.

11.2 STRESS AT A POINT

As we mentioned when we discussed effective stresses in Chapter 6, the concept of stress at a point in a soil is really fictitious. The point of application of a force within a soil mass could be on a particle or in a void. Clearly, a void cannot support any force, but if the force were applied to a particle, the stress could be extremely large. Thus, when we speak about stress in the context of soil materials, we are really speaking about a force per unit area, in which the area under consideration is the gross cross-sectional or engineering area. This area contains grain-to-grain contacts as well as voids. The concept is similar to the "engineering area" used in seepage and flow problems (Chapter 7).

Consider a soil mass that is acted upon by a set of forces $F_1, F_2, \ldots, F_n$, as shown in Fig. 11.1. For the time being, lettuce assume that these forces act in a two-dimensional plane. We could resolve these forces

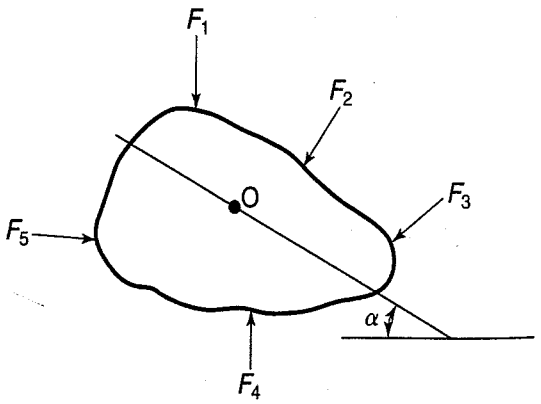

FIGURE 11.1 A soil mass acted upon by several forces.

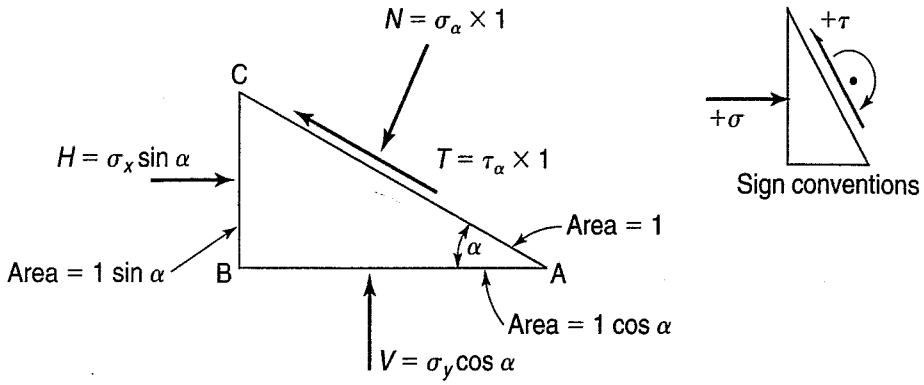

FIGURE 11.2 Resolution of the forces of Fig. 11.1 into components on a small element at point O. Sign conventions are shown in the small inset figure.

into components on a small element at any point within the soil mass, such as point O in that figure. The resolution of these forces into normal and shear components acting, for example, on a plane passing through point O at an angle α from the horizontal is shown in Fig. 11.2, which is an expanded view of a small element at point O. Note that for convenience our sign convention has *compressive forces and stresses positive* because most normal stresses in geotechnical engineering are compressive. This convention, then, requires that *positive* shear stresses produce *counterclockwise* couples on our element (Perloff and Baron, 1976). Put another way: *positive* shears produce *clockwise* moments about a point just *outside* the element, as shown by the insert in Fig. 11.2. *Clockwise* angles also are taken to be *positive*. These conventions are the *opposite* of those normally assumed in structural mechanics.

To begin, assume that the distance AC along the inclined plane in Fig. 11.2 has unit length, and that the figure has a unit depth perpendicular to the plane of the paper. Thus the vertical plane BC has the dimension of $1 \cdot \sin\alpha$, and the horizontal dimension AB has a dimension equal to $1 \cdot \cos\alpha$. At equilibrium, the sum of the forces in any direction must be zero. So, summing in the horizontal and vertical directions, we obtain

$$\sum F_h = H - T\cos\alpha - N\sin\alpha = 0 \tag{11.1a}$$

$$\sum F_v = V + T\sin\alpha - N\cos\alpha = 0 \tag{11.1b}$$

Dividing the forces in Eq. (11.1) by the areas upon which they act, we obtain the normal and shear stresses. (We shall denote the horizontal normal stress by σ_x and the vertical normal stress by σ_y; the stresses on the α-plane are the normal stress σ_α and the shear stress τ_α.)

$$\sigma_x \sin\alpha - \tau_\alpha \cos\alpha - \sigma_\alpha \sin\alpha = 0 \tag{11.2a}$$

$$\sigma_y \cos\alpha - \tau_\alpha \sin\alpha - \sigma_\alpha \cos\alpha = 0 \tag{11.2b}$$

Solving Eqs. (11.2a) and (11.2b) simultaneously for σ_α and τ_α, we obtain

$$\sigma_\alpha = \sigma_x \sin^2\alpha + \sigma_y \cos^2\alpha = \frac{\sigma_x + \sigma_y}{2} + \frac{\sigma_x - \sigma_y}{2}\cos 2\alpha \tag{11.3}$$

$$\tau_\alpha = (\sigma_x - \sigma_y)\sin\alpha\cos\alpha = \frac{\sigma_x - \sigma_y}{2}\sin 2\alpha \tag{11.4}$$

If you square and add these equations, you will obtain the equation for a *circle* with a radius of $(\sigma_x - \sigma_y)/2$ and its center at $[(\sigma_x + \sigma_y)/2, 0]$. When this circle is plotted in τ–σ space, as shown in Fig. 11.3(b) for the element in Fig. 11.3(a), it is known as the *Mohr circle of stress* (Mohr, 1887). It represents the state of stress *at a point at equilibrium*, and it applies to any material, not just soil. Note that the scales for τ and σ have to be the same to obtain a circle from these equations.

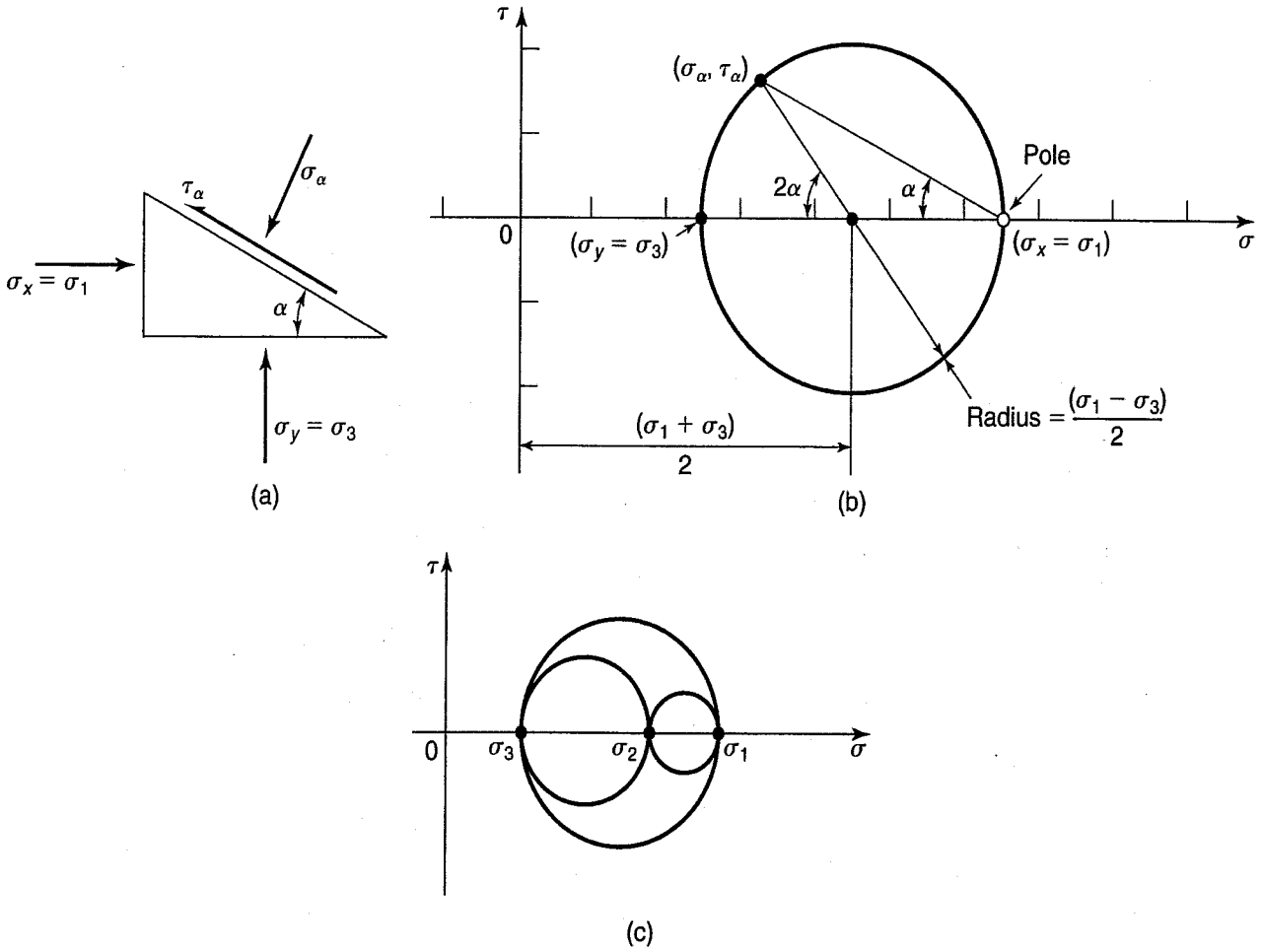

FIGURE 11.3 The Mohr circle of stress: (a) element at equilibrium; (b) the Mohr circle; (c) Mohr circles including σ_2.

Since the vertical and horizontal planes in Fig. 11.2 and Fig. 11.3(a) have no shearing stresses acting on them, they are by definition *principal planes*. Thus the stresses σ_x and σ_y are really *principal stresses*. You may recall from your study of mechanics of materials that principal stresses act on planes where $\tau = 0$. The stress with the largest algebraic magnitude is called the *major principal stress* and denoted by the symbol σ_1. The smallest principal stress is called the *minor principal stress*, σ_3, and the stress in the third dimension is the *intermediate principal stress*, σ_2. In Fig. 11.3(b), σ_2 is neglected, since our derivation was for two-dimensional (plane stress) conditions. We could, however, construct two additional Mohr circles, one for σ_1 and σ_2, and one for σ_2 and σ_3, to make a complete Mohr diagram, as shown in Fig. 11.3(c).

Now we can write Eqs. (11.3) and (11.4) in terms of principal stresses

$$\sigma_\alpha = \frac{\sigma_1 + \sigma_3}{2} + \frac{\sigma_1 - \sigma_3}{2}\cos 2\alpha \tag{11.5}$$

$$\tau_\alpha = \frac{\sigma_1 - \sigma_3}{2}\sin 2\alpha \tag{11.6}$$

Here we have arbitrarily assumed that $\sigma_x = \sigma_1$ and $\sigma_y = \sigma_3$. You should verify that the coordinates of $(\sigma_\alpha, \tau_\alpha)$ in Fig. 11.3(b) can be determined by Eqs. (11.5) and (11.6). From these equations, also verify that the coordinates of the center of the circle are $[(\sigma_1 + \sigma_3)/2, 0]$, and that the radius is $(\sigma_1 - \sigma_3)/2$.

It is now possible to calculate the normal stress σ_α and shear stress τ_α on any plane α, as long as we know the principal stresses. In fact, we could almost as easily derive equations for the general case where σ_x and σ_y are not principal planes. These equations, known as the *double angle equations*, are those

generally presented in mechanics of materials textbooks. The analytical procedure is sometimes awkward to use in practice because of the double angles; we prefer to use a graphical procedure based on a unique point on the Mohr circle called the *pole* or the *origin of planes*. This point has a very useful property: *any straight line drawn through the pole will intersect the Mohr circle at a point which represents the state of stress on a plane inclined at the same orientation in space as the line.* This concept means that if you know the state of stress, σ and τ, on some plane in space, you can draw a line parallel to that plane through the *coordinates* of σ and τ on the Mohr circle. The pole then is the point where that line intersects the Mohr circle. Once the pole is known, the stresses on *any plane* can readily be found by simply drawing a line from the pole parallel to that plane; the coordinates of the point of intersection with the Mohr circle determine the stresses on that plane. A few examples will illustrate how the pole method works.

Example 11.1

Given:

Stresses on an element as shown in Fig. Ex. 11.1a.

Required:

The normal stress σ_α and the shear stress τ on the plane inclined at $\alpha = 35°$ from the horizontal reference plane.

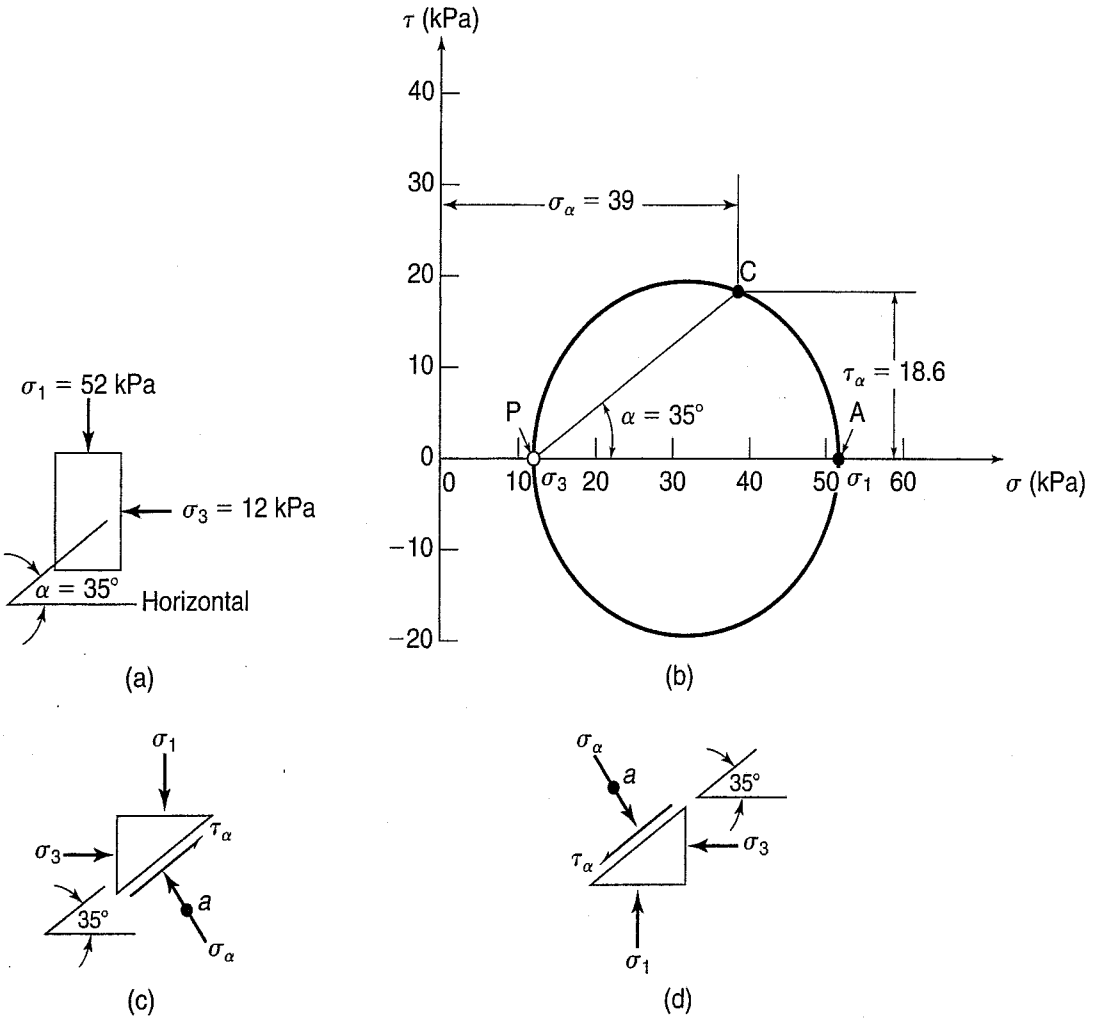

FIGURE Ex. 11.1

Solution:

1. Plot the Mohr circle to some convenient scale (see Fig. Ex. 11.1b).

$$\text{center of circle} = \frac{\sigma_1 + \sigma_3}{2} = \frac{52 + 12}{2} = 32 \text{ kPa}$$

$$\text{radius of circle} = \frac{\sigma_1 - \sigma_3}{2} = \frac{52 - 12}{2} = 20 \text{ kPa}$$

2. Establish the origin of planes or the pole. It is probably easier to use the horizontal plane upon which σ_1 acts. The state of stress on this plane is indicated by point A in Fig. Ex. 11.1b. Draw a line parallel to the plane upon which this state of stress $(\sigma_1, 0)$ acts (the horizontal plane) through the point representing σ_1 and 0. By definition, the pole P is where this line intersects the Mohr circle. [By coincidence, it intersects at $(\sigma_3, 0)$.] A line through the pole inclined at an angle $\alpha = 35°$ from the horizontal plane would be parallel to the plane on the element in Fig. Ex. 11.1a, and this is the plane on which we require the normal and shear stress. The intersection is at point C in Fig. Ex. 11.1b, and we find that $\sigma_\alpha = 39$ kPa and $\tau_\alpha = 18.6$ kPa.

You should verify these results by using Eqs. (11.5) and (11.6). Note that τ_α is positive, since point C occurs above the abscissa. Thus the sense of τ_α on the 35° plane is determined as indicated in Fig. Ex. 11.1c and d, which represent the top and bottom parts of the given element. For both parts, the direction or sense of the shear stress τ_α is equal and opposite (as it should be). However, they are both positive shear stresses, which is consistent with our sign convention (Fig. 11.2).

Example 11.2

Given:

The same element and stresses as in Fig. Ex. 11.1a, except that the element is rotated 20° from the horizontal, as shown in Fig. Ex. 11.2a.

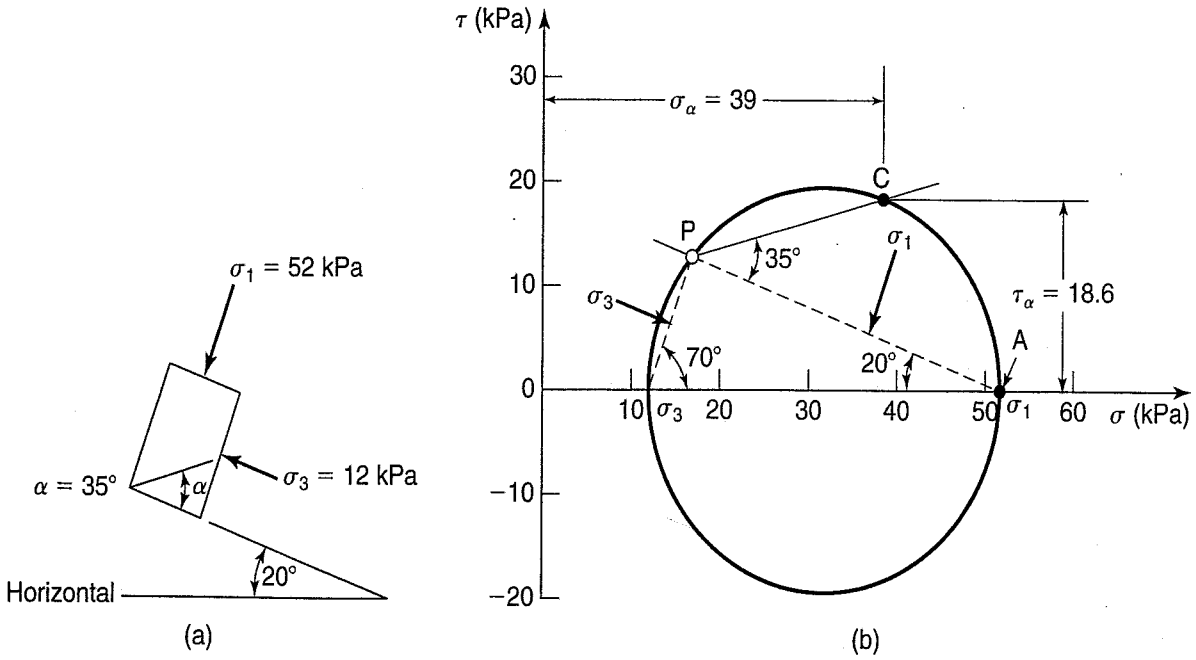

FIGURE Ex. 11.2

Required:

As in Example 11.1, find the normal stress σ_α and the shear stress τ_α on the plane inclined at $\alpha = 35°$ from the base of the element.

Solution:

1. Plot the Mohr circle (Fig. Ex. 11.2b). Since the principal stresses are the same, the Mohr circle will be the same as in Example 11.1.
2. Find the pole of the circle. As in the previous example, draw a line parallel to a plane on which you know the stresses. If we again begin with the major principal plane, this plane is inclined at an angle of 20° to the horizontal. Start at point A, and where this line intersects the Mohr circle defines the pole P of this circle.
3. Now find the stresses on the σ-plane, which as before is inclined at 35° to the base of the element. From line AP, turn an angle in the same direction as in the element, 35°, and the stresses on that plane are defined by the point of intersection of the line with the Mohr circle (in this case at point C). Scale off the coordinates of point C to determine σ_α and τ_α. Note that these stresses are the same as in Example 11.1. Why? Because nothing has changed except the orientation in space of the element.

For step 2, we could just as well have used the minor principal plane as our starting point. In this case a line from $(\sigma_3, 0)$ could be drawn at 70° from the horizontal (parallel to the σ_3-plane), and it would intersect the Mohr circle at the same point as before, point P. We now have a check on the step—if we have done everything correctly, we should obtain the same pole. Since line AP is parallel to the major principal plane, we can show the direction of σ_1 right on this line in Fig. Ex. 11.2; similarly, the dashed line from the pole to σ_3 is parallel to the σ_3-plane.

Now you can probably begin to see what is really happening with the pole. It is just a way of relating the Mohr circle of stress to the geometry or orientation of our element in the real world. We could just as well rotate the τ-σ axes to coincide with the directions of the principal stresses in space, but traditionally τ versus σ is plotted with the axes horizontal and vertical.

Example 11.3

Given:

The stress shown on the element in Fig. Ex. 11.3a.

Required:

a. Evaluate σ_α and τ_α when $\alpha = 30°$.
b. Evaluate σ_1 and σ_3 when $\alpha = 30°$.
c. Determine the orientation of the major and minor principal planes.
d. Find the maximum shear stress and the orientation of the plane on which it acts.

Solution: Construct the Mohr circle, as shown in Fig. Ex. 11.3, according to the following steps:

1. Plot the state of stress on the horizontal plane (6, 2) (Fig. Ex. 11.3b) at point A. Note that the shear stress makes a counterclockwise moment about point a and therefore is positive.

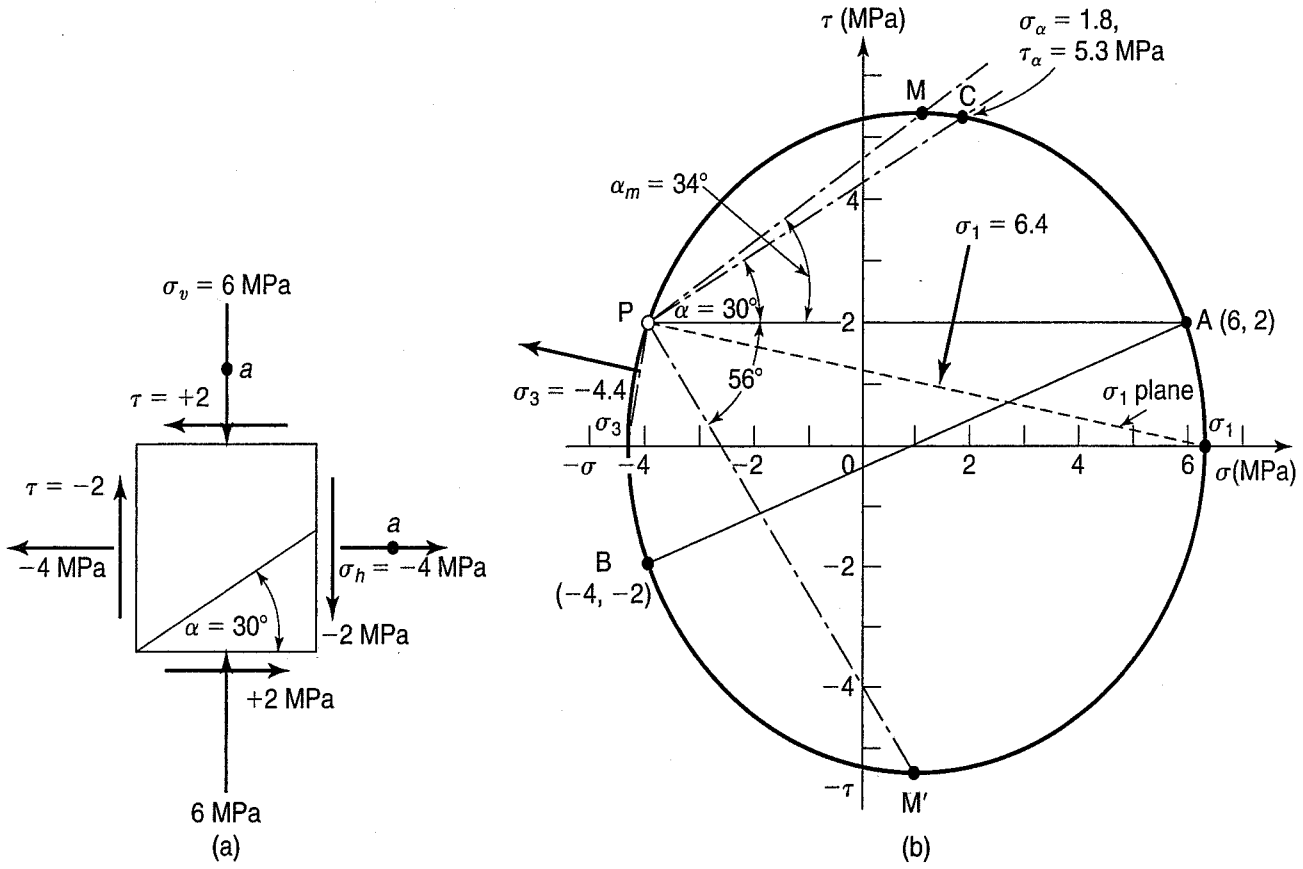

FIGURE Ex. 11.3

2. In a similar manner, plot point B (−4, −2). The shear stress on the vertical plane is negative, since it makes a clockwise moment.
3. Points A and B are two points on a circle (a diameter in this case, since their planes are 90° apart); the center of the circle has coordinates of $[(\sigma_x + \sigma_y)/2, 0]$. Construct the Mohr circle with center at (1, 0).
4. To find the pole, remember that a line drawn parallel to the plane (horizontal in this example) upon which a known state of stress acts, point A, intersects the Mohr circle at the pole P. As a check, you could also draw a line in the vertical direction from point B (−4, −2) and find the same pole.
5. To find the state of stress on the plane inclined at angle $\alpha = 30°$ from the horizontal, draw the line PC at an angle 30° from the horizontal (see Fig. Ex. 11.3b). The state of stress on this plane is given by the coordinates at point C (1.8, 5.3) MPa.
6. Lines drawn from P to σ_1 and σ_3 establish the orientation of the major and minor principal planes. The values of σ_1 and σ_3 are determined automatically once the circle is drawn; here they are 6.4 and −4.4 MPa, respectively. Of course σ_1 and σ_3 are perpendicular to their respective planes, which are oriented at 11° and 101° to the horizontal, respectively.
7. The maximum shear stress can be calculated by Eq. (11.6) when $2\sigma = 90°$. This is $(\sigma_1 - \sigma_3)/2$ or ± 5.4 MPa (see points M or M′). You can also simply scale off the maximum value of τ from the Mohr diagram. The orientation of τ_{max} is the line PM or PM′, depending on which mutually perpendicular plane you desire. (Actually $\tau = -5.4$ MPa is the minimum shear stress.)

Example 11.4

Given:

Two planes, a and b, are separated by an unknown angle θ. On plane a, $\sigma_a = 10$ kPa and $\tau_a = +2$ kPa. Plane a lies 15° from the horizontal, as shown in Fig. Ex. 11.4a. The stresses on plane b are $\sigma_b = 9$ kPa and $\tau_b = -3$ kPa.

Required:

a. Find the major and minor principal stresses and their orientation.

b. Find the stresses on the horizontal plane.

c. Find the angle between planes a and b.

Solution:

1. Plot the coordinates of the stresses on planes a and b. If you assume the body or element is in equilibrium, then these coordinates are *on* the circumference of the Mohr circle. To find the center, construct a perpendicular to the line AB, which joins the two points. The intersection of the horizontal σ-axis and the perpendicular bisector to AB is the center of the circle C.
2. Establish the pole by drawing a line from point A parallel to the plane (15° from the horizontal) upon which the stresses at point A act to where it intersects the Mohr circle. The intersection of this line and the Mohr circle is the pole P.

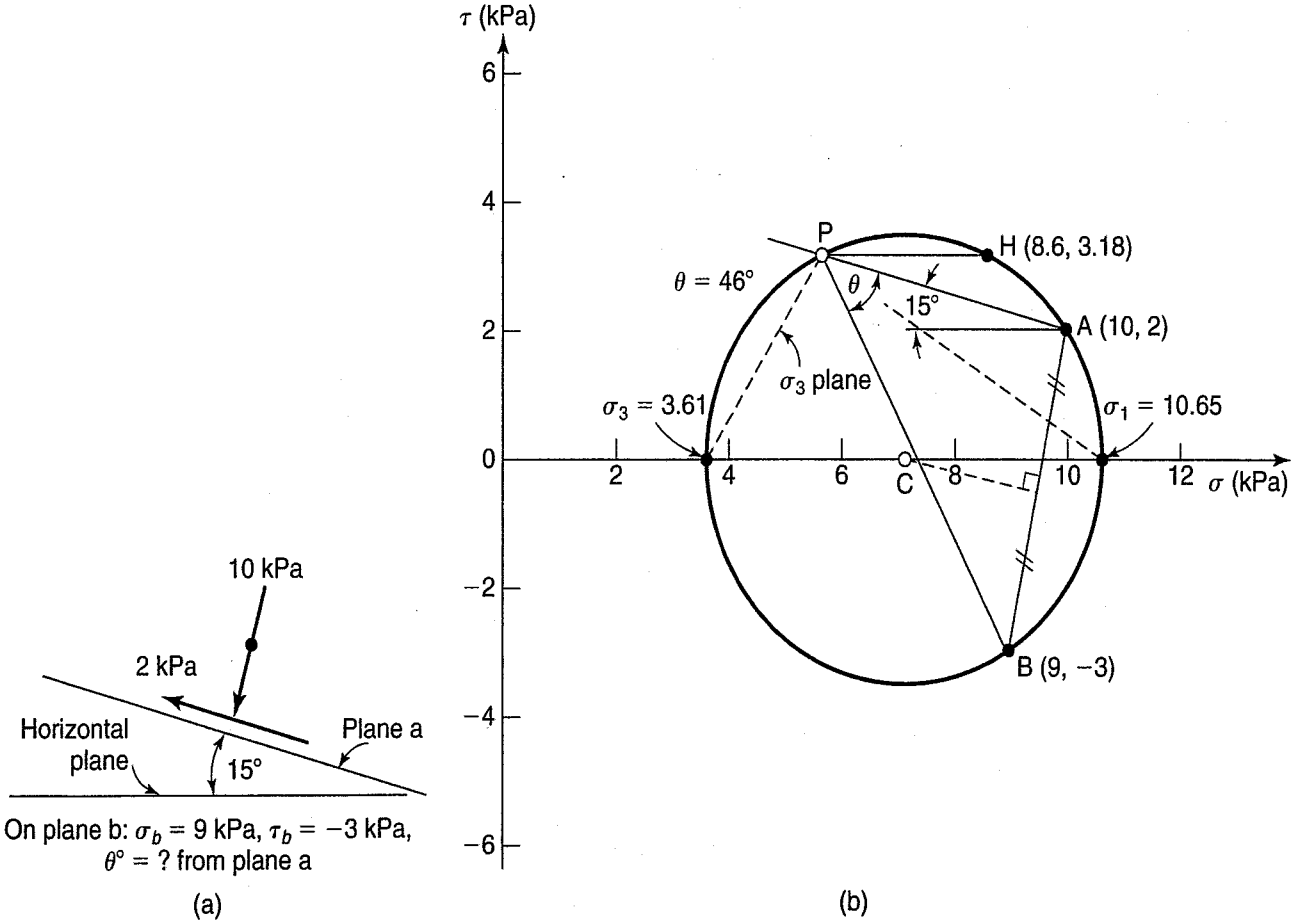

FIGURE Ex. 11.4

3. Lines from the pole P to σ_1 and σ_3 indicate the orientation of the major and minor principal planes. The principal stresses act perpendicular to these planes. The scaled-off value of σ_1 is equal to 10.65 kPa, and σ_3 is found to be 3.61 kPa.
4. The stresses on the horizontal plane are found by drawing a horizontal line from the pole until it intersects the Mohr circle at point H; the stresses on this plane are (8.6, 3.18) kPa.
5. To find the angle between the two planes a and b, draw the line PB from the pole to B. This line is the actual orientation in space of plane B. The angle θ then represents the true angle between planes A and B, or $\theta = 46°$.

Example 11.5

Given:

The stress on an element shown in Fig. Ex. 11.5a.

Required:

Find the magnitude and direction of the major and minor principal stresses.

Solution: Refer to Fig. Ex. 11.5b for the following steps:

1. Plot the two points X and Y from the given stress coordinates. These two points lie on the circumference of the circle. Where the line XY intersects the σ-axis establishes the center of the Mohr circle at (6, 0).
2. Locate the pole by drawing a line from point Y parallel to the plane on which the stress at Y acts. This line is at 45° from the horizontal, and it intersects the Mohr circle at the pole P, which is the same point as point X.

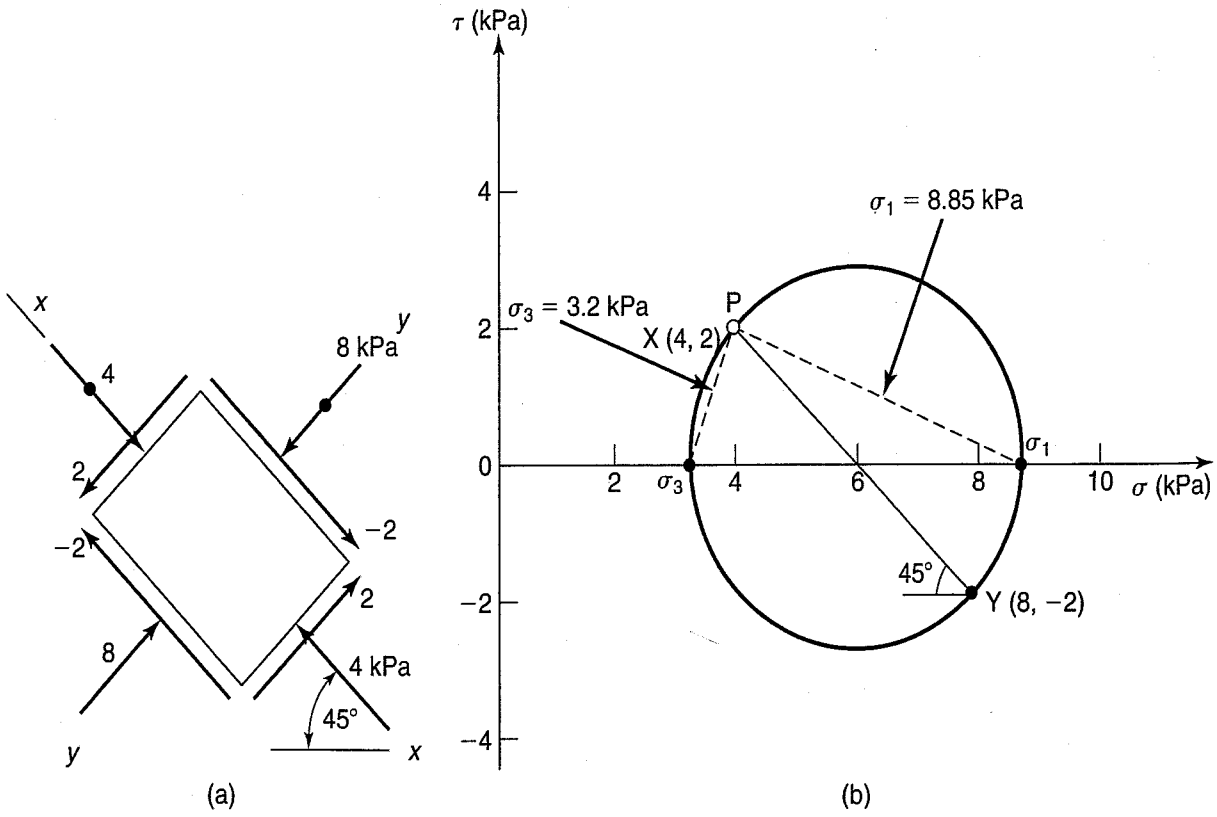

FIGURE Ex. 11.5

3. To find the direction of the principal stresses, draw a line from the pole to σ_1 and σ_3; these lines are shown dashed on Fig. Ex. 11.5b. The direction (arrows) of σ_1 and σ_3 are shown in the figure. The values of σ_1 and σ_3 are scaled off the figure and found to be 8.85 kPa and 3.2 kPa, respectively.

By now you can see that the Mohr circle of stress represents the complete two-dimensional state of stress *at equilibrium* in an element or at a point. The pole simply couples the Mohr circle to the orientation of the element in the real world. The Mohr circle and the concept of the pole are very useful in geotechnical engineering; we shall use them throughout the rest of this text.

11.3 STRESS-STRAIN RELATIONSHIPS AND FAILURE CRITERIA

Earlier, in the introduction to Chapter 8, we briefly mentioned some stress-strain relationships. Now we want to elaborate on, as well as illustrate, some of those ideas. The stress-strain curve for mild steel is shown in Fig. 11.4(a). The initial portion up to the proportional limit or yield point is *linearly elastic*. This means that the material will return to its original shape when the stress is released, as long as the applied stress is below the yield point. It is possible, however, for a material to have a *nonlinear* stress-strain curve and still be elastic, as shown in Fig. 11.4(b). Note that both these stress-strain relationships are independent of time. If time is a variable, then the material is called *visco-elastic*. Some real materials such as most soils and polymers are visco-elastic. Why, then, don't we use a visco-elastic theory to describe the behavior of soils? The problem is that soils have a highly nonlinear stress-strain-time behavior, and unfortunately only a mathematically well-developed linear theory of visco-elasticity is available.

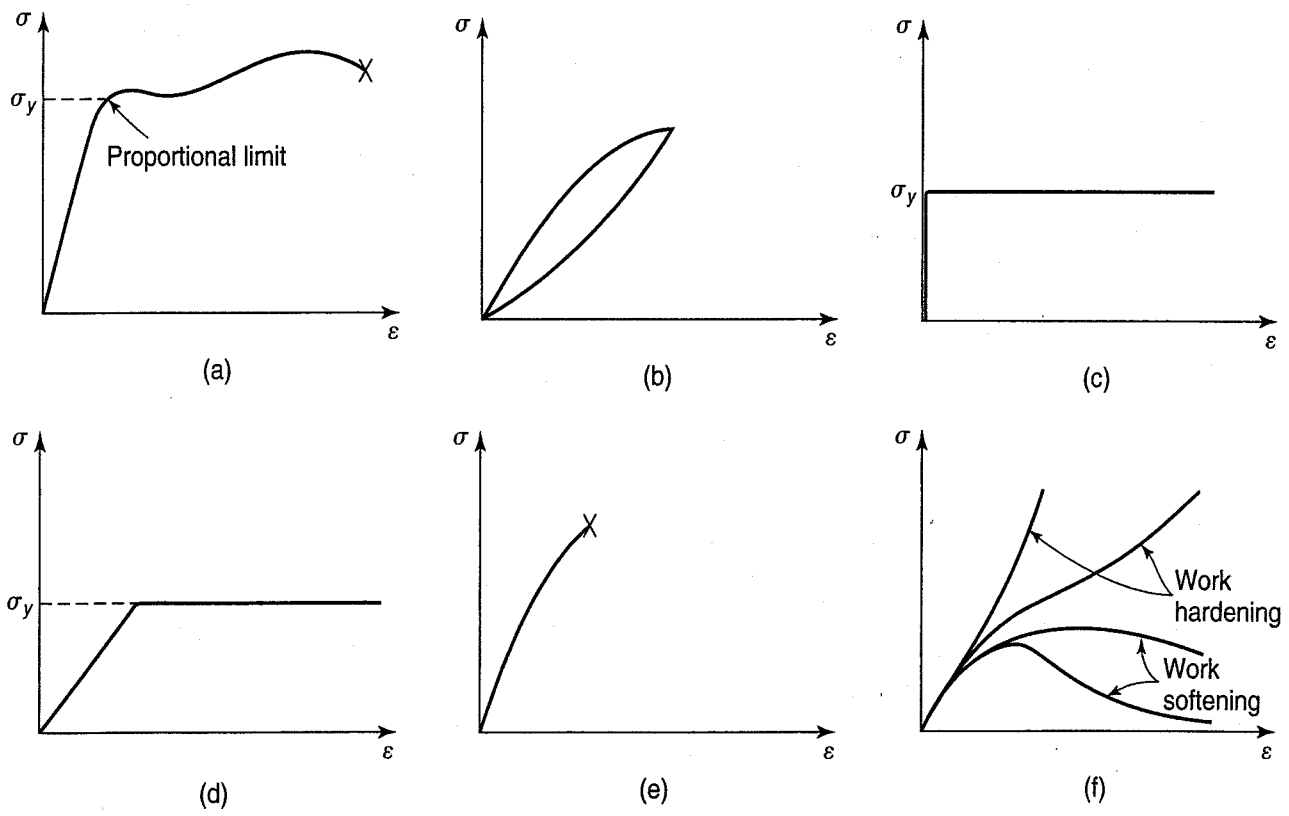

FIGURE 11.4 Examples of stress-strain relationships for ideal and real materials: (a) mild steel; (b) nonlinear elastic; (c) perfectly plastic; (d) elasto-plastic; (e) brittle; and (f) work-hardening and work-softening.

Note that so far we've said nothing about failure or yield. Even linearly elastic materials yield, as indicated in Fig. 11.4(a), if sufficient stress is applied. At the proportional limit, the material is said to become *plastic* or to *yield plastically*. The behavior of real materials can be idealized by several plastic stress-strain relationships, as shown in Figs. 11.4(c), (d), and (f). *Perfectly plastic* materials [Fig. 11.4(c)], sometimes called *rigid-plastic*, can be treated relatively easily mathematically, and thus are popular subjects of study by mechanicians and mathematicians. A more realistic stress-strain relationship is *elasto-plastic* [Fig. 11.4(d)]. The material is linearly elastic up to the yield point σ_y; then it becomes perfectly plastic. Note that both perfectly plastic and elasto-plastic materials continue to strain even without any additional stress applied. The stress-strain curve for mild steel can be approximated by an elasto-plastic stress-strain curve, and this theory is very useful in, for example, working, punching, and machining of metals.

Sometimes materials such as cast iron, concrete, and a lot of rocks are *brittle*, in that they exhibit very little strain as the stress increases. Then, at some point, the material suddenly collapses or crushes [Fig. 11.4(e)]. More complex but also realistic for many materials are the stress-strain relations shown in Fig. 11.4(f). *Work-hardening* materials, as the name implies, become stiffer (higher modulus) as they are strained or "worked." The little hump in the stress-strain curve for mild steel after yield [Fig. 11.4(a)] is an example of work-hardening. Many soils are also work-hardening—for example, compacted clays and loose sands. *Work-softening* materials [Fig. 11.4(f)] show a decrease in stress as they are strained beyond a peak stress. Sensitive clay soils and dense sands are examples of work-softening materials.

At what point on the stress-strain curve do we have failure? We could call the yield point "failure" if we wanted to. In some situations, if a material is stressed to its yield point, the strains or deflections are so large that for all practical purposes the material has failed. This means that the material cannot satisfactorily continue to carry the applied loads. The stress at "failure" is often very arbitrary, especially for nonlinear materials. With brittle-type materials, however, there is no question when failure occurs—it's obvious. Even with work-softening materials [Fig. 11.4(f)], the peak of the curve or the maximum stress is usually defined as failure. On the other hand, with some plastic materials it may not be obvious. Where would you define failure if you had a work-hardening stress-strain curve [Fig. 11.4(f)]? With materials such as these, we usually define failure at some arbitrary percent strain—for example, 15% or 20%—or at a strain or deformation at which the function of the structure might be impaired.

Now we can also define the *strength* of a material. It is the maximum or yield stress, or the stress at some strain which we have defined as "failure."

As suggested by the above discussion, there are many ways of defining failure in real materials—or, put another way, there are many *failure criteria*. Most of them don't work for soils, and in fact the one we do use, which is the subject of the next section, doesn't always work so well either. Even so, the most common failure criterion applied to soils is the *Mohr–Coulomb failure criterion*.

11.4 THE MOHR–COULOMB FAILURE CRITERION

11.4.1 Mohr Failure Theory

Mohr is the same Otto Mohr of Mohr circle fame. Coulomb you know from coulombic friction and electrostatic attraction and repulsion, among other things. Around the turn of the twentieth century, Mohr (1900) hypothesized a criterion of failure for real materials in which he stated that materials fail when the *shear stress on the failure plane at failure reaches some unique function of the normal stress on that plane*, or

$$\tau_{ff} = f(\sigma_{ff}) \tag{11.7}$$

where τ is the shear stress and σ is the normal stress. The first subscript f refers to the plane on which the stress acts (in this case the *failure plane*) and the second f means "at failure."

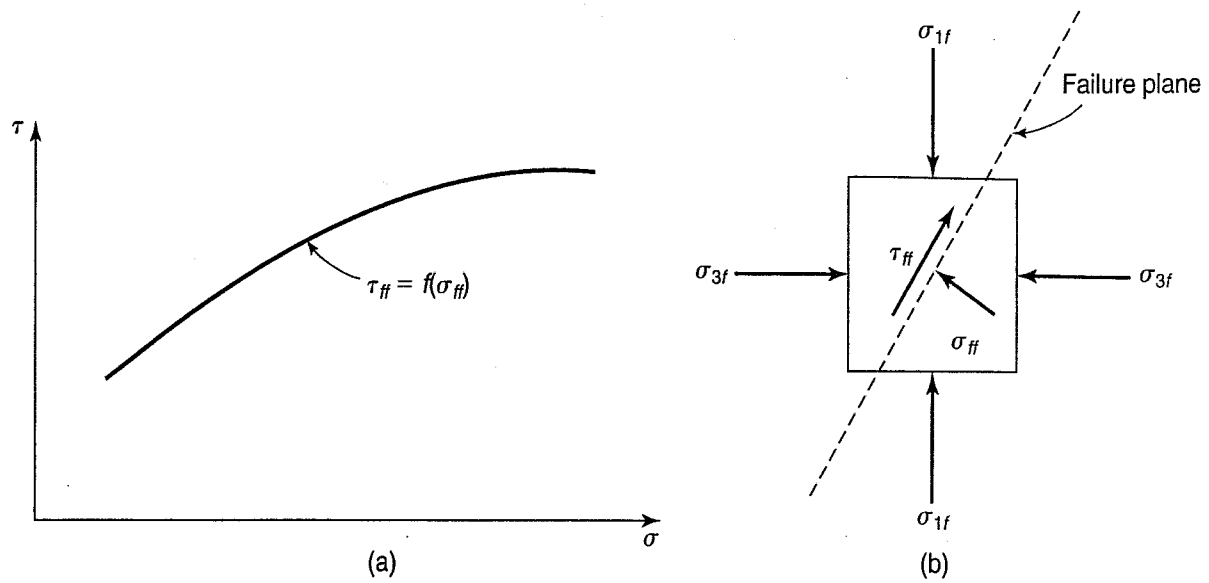

FIGURE 11.5 (a) Mohr failure criterion; (b) element at failure, showing the principal stresses and the stresses on the failure plane.

τ_{ff} is called the *shear strength* of the material, and the relationship expressed by Eq. (11.7) is shown in Fig. 11.5(a). Figure 11.5(b) shows an element at failure with the principal stresses that caused failure and the resulting normal and shear stresses on the failure plane.

For the present, we will assume that a failure plane exists, which is not a bad assumption for soils, rocks, and many other materials. Also, we won't worry now about how the principal stresses at failure are applied to the element (test specimen or representative element in the field) or how they are measured.

Anyway, if we know the principal stresses at failure, we can draw or sketch a Mohr circle to represent this state of stress for this particular element. Similarly, we could conduct several tests to failure, or we could measure the stresses in several elements at failure and construct Mohr circles for each test or element at failure. Such a series is plotted in Fig. 11.6. Note that only the top half of each Mohr circle is drawn, which is conventionally done in soil mechanics for convenience only. Since the Mohr circles are determined at failure, it is possible to construct the limiting or failure envelope of the shear stress. This envelope, called the *Mohr failure envelope*, expresses the functional relationship between the shear stress τ_{ff} and the normal stress σ_{ff} at failure [Eq. (11.7)].

Note that any Mohr circle lying below the Mohr failure envelope (such as circle A in Fig. 11.6) represents a stable condition. Failure occurs only when the combination of shear and normal stress is such that the Mohr circle is *tangent* to the Mohr failure envelope. Note also that circles lying above the Mohr failure envelope (such as circle B in Fig. 11.6) cannot exist. The material would fail before reaching these states of stress. If this envelope is unique for a given material, then the point of tangency of the Mohr failure envelope gives the stress conditions on the failure plane at failure. Using the pole

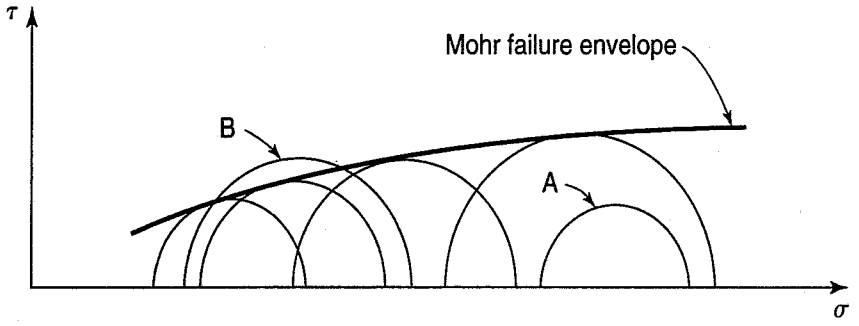

FIGURE 11.6 The Mohr circles at failure define the Mohr failure envelope.

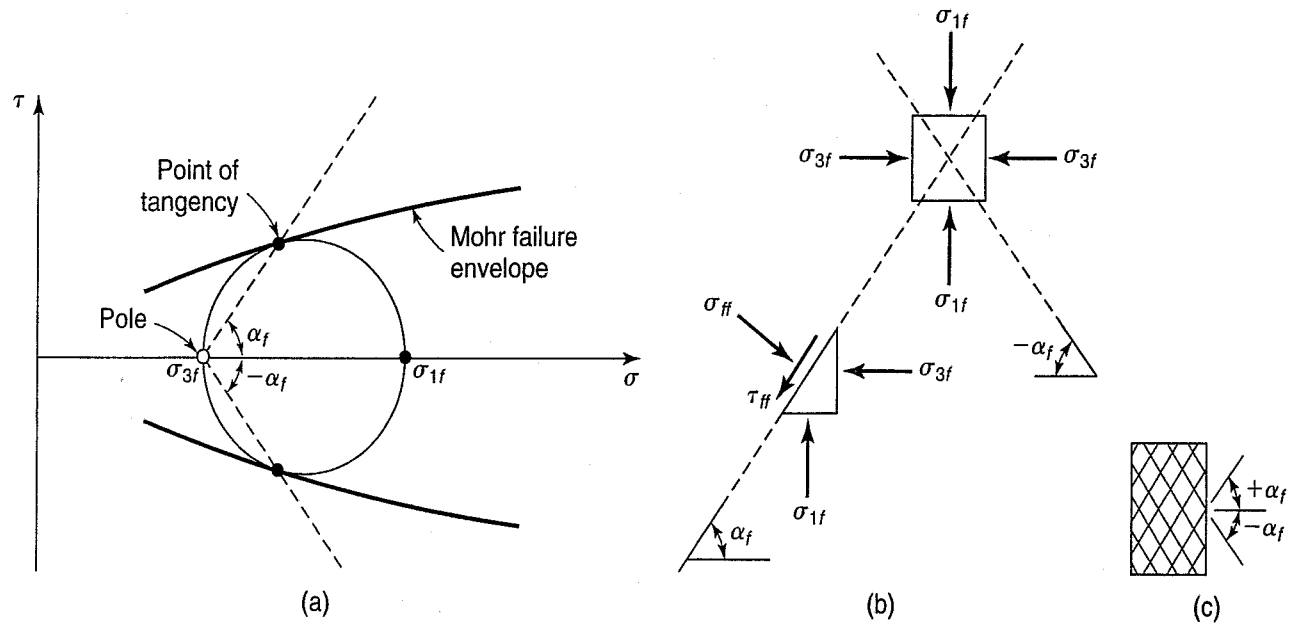

FIGURE 11.7 (a) Mohr failure hypothesis for determining the angle of the failure plane in the (b) element; (c) conjugate failure planes.

method, we can therefore determine the angle of the failure plane from the point of tangency of the Mohr circle and the Mohr failure envelope. The hypothesis, that the point of tangency defines the angle of the failure plane in the element or test specimen, is the *Mohr failure hypothesis*. You should distinguish this hypothesis from the Mohr failure theory. The Mohr failure hypothesis is illustrated in Fig. 11.7(a) for the element at failure shown in Fig. 11.7(b). Stated another way: the Mohr failure hypothesis says that the point of tangency of the Mohr failure envelope with the Mohr circle at failure determines the inclination of the failure plane.

Another thing you should note from Fig. 11.7(a) is that, even though in soil mechanics we commonly draw only the top half of the Mohr circle, there is a bottom half, and also a bottom-half Mohr failure envelope. This also means, if the Mohr failure hypothesis is valid, that it is equally likely that a failure plane will form at an angle of $-\alpha_f$, as shown in Fig. 11.7(a). In fact, it is the nonuniform stress conditions on the ends of a test specimen and small inhomogeneities within the specimen itself that we think cause a single failure plane often to form in a test specimen. Ever wonder why a cone forms at failure in the top and bottom of a concrete cylinder when it is failed in compression? Shear stresses between the testing machine and specimen caps cause nonuniform stresses to develop within the specimen. If everything is homogeneous and uniform stress conditions are applied to a specimen, then multiple failure planes form at conjugate angles, $\pm\ \alpha_f$, as shown in Fig. 11.7(c).

11.4.2 Mohr–Coulomb Failure Criterion

Now we are going to involve Monsieur Dr. Coulomb in our story. In addition to his famous experiments with cats' fur and ebony rods, M. Coulomb (1776) was also concerned with military defense works such as revetments and fortress walls. At that time, these constructions were built by rule of thumb, and unfortunately for the French military defenses many of these works failed. Coulomb became interested in the problem of the lateral pressures exerted against retaining walls, and he devised a system for analysis of earth pressures against retaining structures that is still used today. One of the things he needed for design was the shearing strength of the soil. Since he was also interested in the sliding friction characteristics of different materials, he set up a device for determining the shear resistance of soils. He observed that there was a stress-independent component of shear strength and a stress-dependent component. The stress-dependent component is similar to sliding friction in solids,

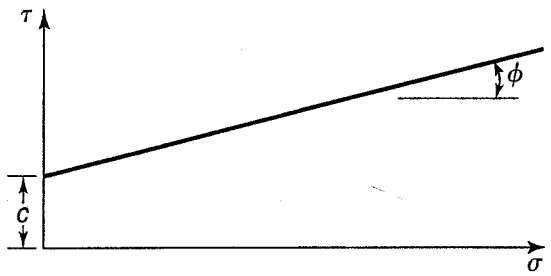

FIGURE 11.8 The Coulomb strength equation presented graphically.

so he called this component the *angle of internal friction*, denoting it by the symbol ϕ. The other component seemed to be related to the intrinsic *cohesion* of the material and it is commonly given the symbol c. Coulomb's equation is, then,

$$\tau_f = \sigma \tan \phi + c \tag{11.8}$$

where τ_f is the shear strength of the soil, σ is the applied normal stress, and ϕ and c are called the *strength parameters* of the soil, as defined above. This relationship gives a straight line and is, therefore, easy to work with. As is explained in the next chapter, neither ϕ nor c is an inherent property of the material; on the contrary, they are dependent on the conditions operative in the test. We could, much as M. Coulomb probably did, plot the results of a shear test on soil to obtain the strength parameters ϕ and c (Fig. 11.8). Note that either strength parameter could be zero for any particular stress condition; that is, $\tau = c$ when $\phi = 0$, or $\tau = \sigma \tan \phi$ when $c = 0$. As we shall see in Chapter 12, these relationships are valid for certain specific test conditions for some soils.

Although who first did so is unknown, it would seem reasonable to combine the Coulomb equation, Eq. (11.8), with the Mohr failure criterion, Eq. (11.7). Engineers traditionally prefer to work with straight lines, since anything higher than a first-order equation (straight line) is more complicated. So the natural thing to do was to straighten out that curved Mohr failure envelope, or at least approximate the curve by a straight line over some given stress range; then the equation for that line in terms of the Coulomb strength parameters could be written. Thus was born the *Mohr–Coulomb strength criterion*, which is by far the most popular strength criterion applied to soils. The Mohr–Coulomb criterion can be written as

$$\tau_{ff} = \sigma_{ff} \tan \phi + c \tag{11.9}$$

These terms have been defined previously. This simple, easy-to-use criterion has many distinct advantages over other failure criteria. It is the only one that predicts the stresses on the failure plane at failure, and since soil masses have been observed to fail on rather distinct surfaces, we would like to be able to estimate the state of stress at failure on potential sliding surfaces. So the Mohr–Coulomb criterion is very useful for analyses of the stability of earth slopes and foundations.

Before we discuss the kinds of tests used to determine the Mohr–Coulomb strength parameters, we should look a little more carefully at some Mohr circles, both before failure and at failure. They have several interesting characteristics that will be useful later on.

First, if we know the angle of inclination of the Mohr failure envelope or have determined it from laboratory tests, then it is possible to write the angle of the failure plane α_f in terms of the slope ϕ of the Mohr failure envelope. To do this, we have to invoke the Mohr failure hypothesis. Then the failure angle measured relative to the plane of the major principal stress is

$$\alpha_f = 45° + \frac{\phi}{2} \tag{11.10}$$

A proof of this equation is requested in one of the problems at the end of the chapter.

Second, let's look at a soil element subjected to principal stresses that are *less* than the stresses required to cause failure. Such a state of stress might be represented by the Mohr circle shown in Fig. 11.9(a). In this case τ_f is the *mobilized* shear resistance on the *potential* failure plane, and τ_{ff} is the shear strength available (shear stress on the failure plane at failure). Since we haven't reached

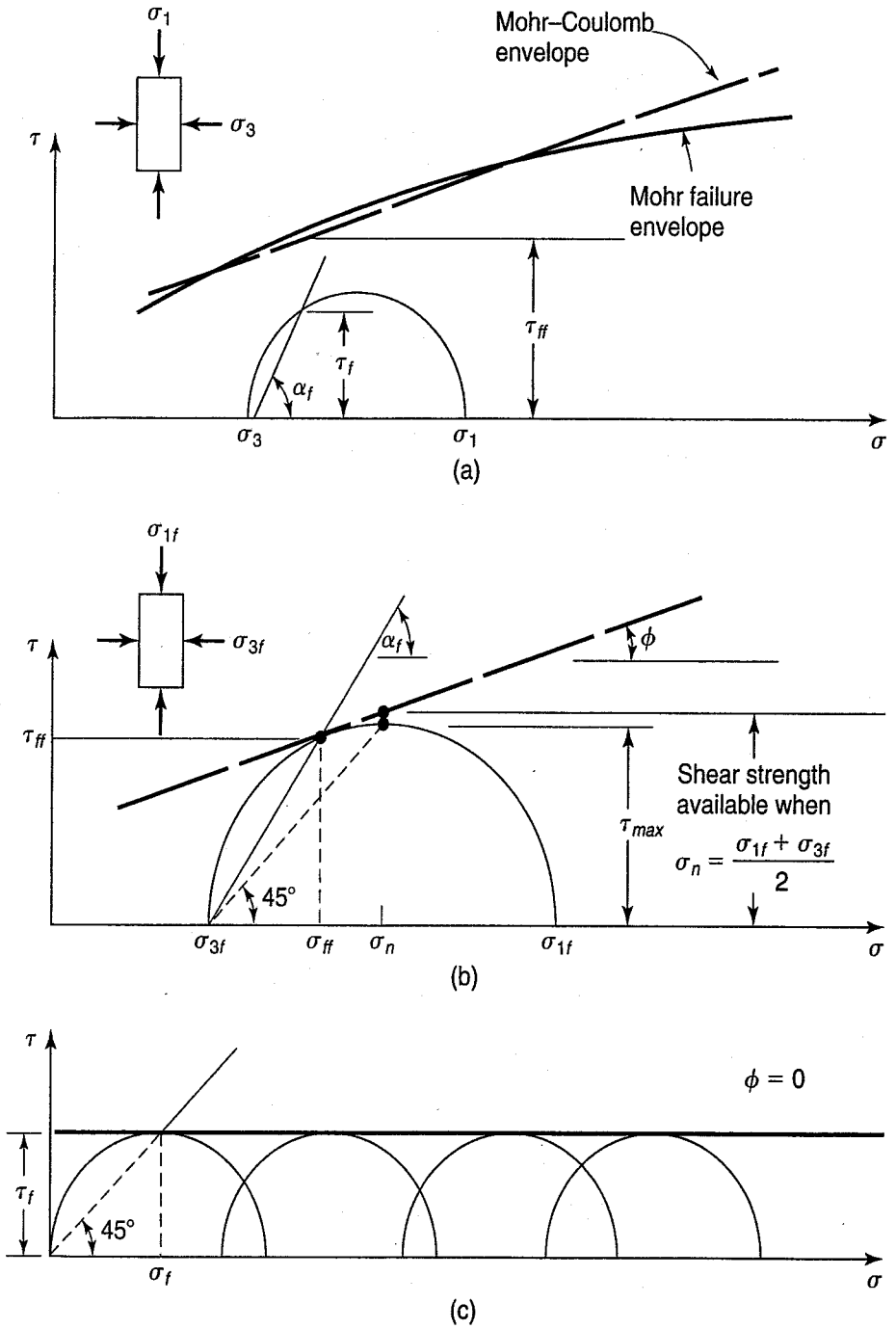

FIGURE 11.9 (a) Stress conditions before failure; (b) stress conditions at failure; (c) Mohr failure envelope for a purely cohesive material (after Hirschfeld, 1963).

failure yet, some reserve strength remains, and this in a way is a definition of the *factor of safety* in the material. Or,

$$\text{factor of safety (F.S.)} = \frac{\tau_{ff}\,(\text{available})}{\tau_f\,(\text{applied})} \tag{11.11}$$

Now, if the stresses increase so that failure occurs, then the Mohr circle becomes tangent to the Mohr failure envelope. According to the Mohr failure hypothesis, failure occurs on the plane inclined

at α_f and with shear stress on that plane of τ_{ff}. Note that this is not the largest or maximum shear stress in the element! The maximum shear stress acts on the plane inclined at 45° and is equal to

$$\tau_{\max} = \frac{\sigma_{1f} - \sigma_{3f}}{2} > \tau_{ff} \tag{11.12}$$

Why, then doesn't failure occur on the 45° plane? Well, it cannot, because on that plane the shear strength available is greater than $\tau_{\max}$. This condition is represented by the distance from the maximum point on the Mohr circle up to the Mohr failure envelope in Fig. 11.9(b). That would be the shear strength available when the normal stress σ_n on the 45° plane was $(\sigma_{1f} + \sigma_{3f})/2$.

The only exception to the above discussion would be when the shear strength is independent of the normal stress; that is, when the Mohr failure envelope is horizontal and $\phi = 0$. This situation, shown in Fig. 11.9(c), is valid for special conditions, which are discussed in Chapter 12. Such materials are often called *purely cohesive* for obvious reasons. For the case shown in Fig. 11.9(c), failure *theoretically* occurs on the 45° plane (it doesn't really, as is explained in Chapter 12). The shear strength is τ_f, and the normal stress on the theoretical failure plane at failure is $(\sigma_{1f} + \sigma_{3f})/2$.

11.4.3 Obliquity Relations

Another useful thing we should do before going on is to write the Mohr–Coulomb failure criterion in terms of principal stresses at failure, rather than as in Eq. (11.9) in terms of τ_{ff} and σ_{ff}. Look at Fig. 11.10 and note that $\sin\phi = R/D$, or

$$\sin\phi = \frac{\dfrac{\sigma_{1f} - \sigma_{3f}}{2}}{\dfrac{\sigma_{1f} + \sigma_{3f}}{2} + c\cot\phi}$$

or $(\sigma_{1f} - \sigma_{3f}) = (\sigma_{1f} + \sigma_{3f})\sin\phi + 2c\cos\phi$. If $c = 0$, then $(\sigma_{1f} - \sigma_{3f}) = (\sigma_{1f} + \sigma_{3f})\sin\phi$, which can be written as

$$\sin\phi = \frac{(\sigma_{1f} - \sigma_{3f})}{(\sigma_{1f} + \sigma_{3f})} \tag{11.13}$$

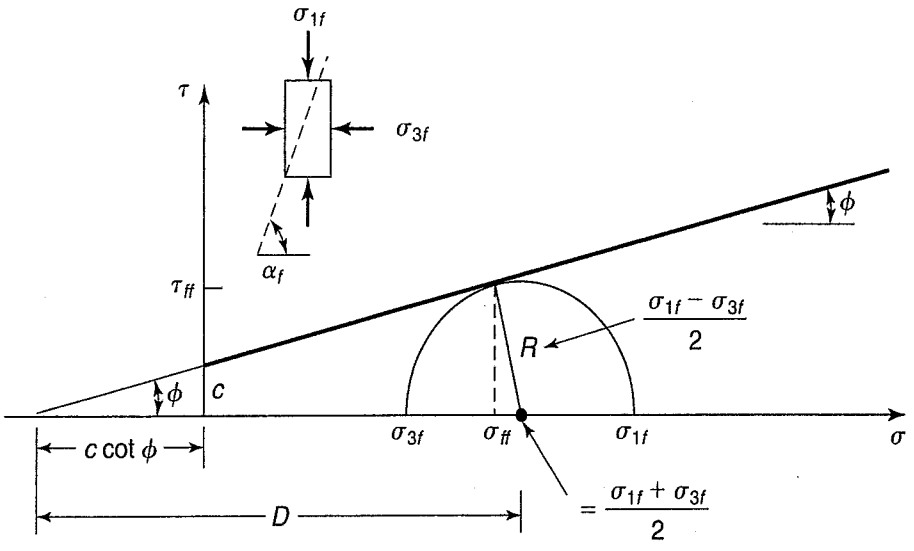

FIGURE 11.10 Mohr–Coulomb strength envelope with one Mohr circle at failure.

Rearranging, we have

$$\frac{\sigma_1}{\sigma_3} = \frac{1 + \sin\phi}{1 - \sin\phi} \tag{11.14}$$

or the reciprocal is

$$\frac{\sigma_3}{\sigma_1} = \frac{1 - \sin\phi}{1 + \sin\phi} \tag{11.15}$$

Using some trigonometric identities, we can express Eqs. (11.14) and (11.15) as

$$\frac{\sigma_1}{\sigma_3} = \tan^2\left(45° + \frac{\phi}{2}\right) \tag{11.16}$$

$$\frac{\sigma_3}{\sigma_1} = \tan^2\left(45° - \frac{\phi}{2}\right) \tag{11.17}$$

Equations (11.14) through (11.17) are called the *obliquity relationships*, because they relate the major and minor principal stresses at failure when the angle of obliquity is a maximum. Obliquity in soils can be explained by analogy with the sliding friction behavior of a block on a rigid surface subject to normal and shear forces, or we can use a more realistic case of a foundation block resting on the ground surface. As shown in Fig. 11.11(a), the foundation block has only a normal stress σ acting on it.

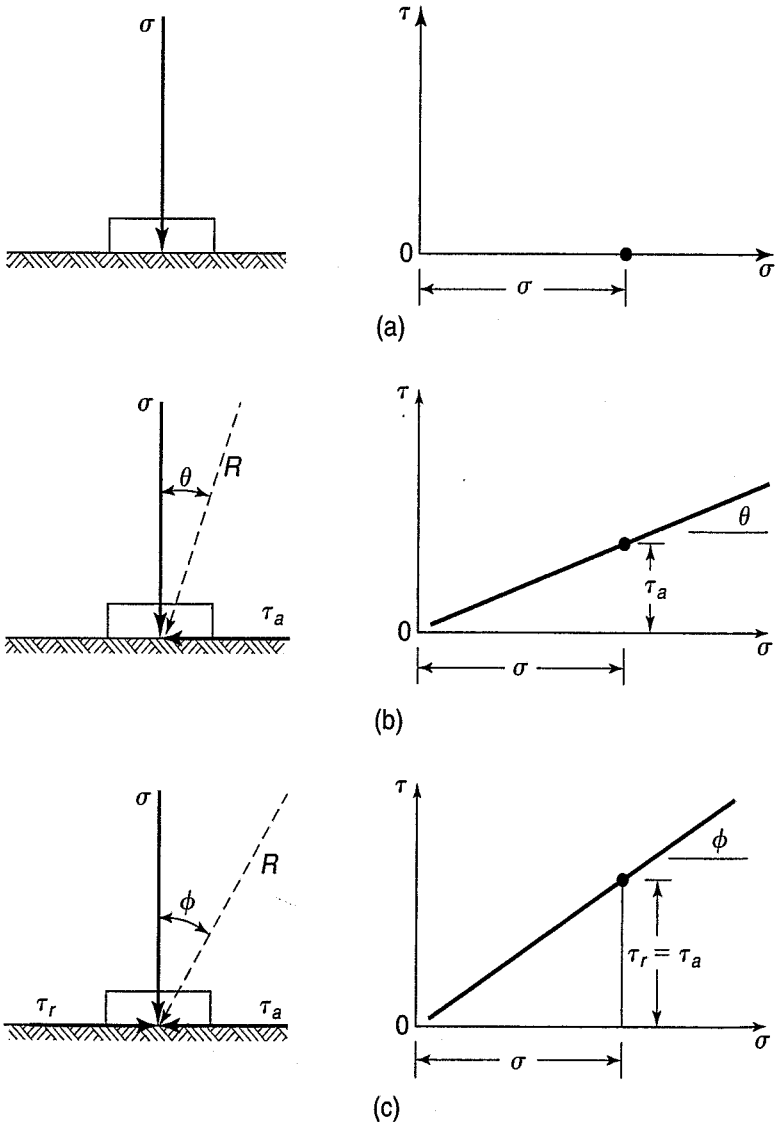

FIGURE 11.11 Foundation block under normal and shear stresses: (a) application of normal stress only; (b) addition of shear stress to block in (a); (c) increase of applied stress to point of sliding (incipient failure) and $\theta = \phi$, angle of maximum obliquity.

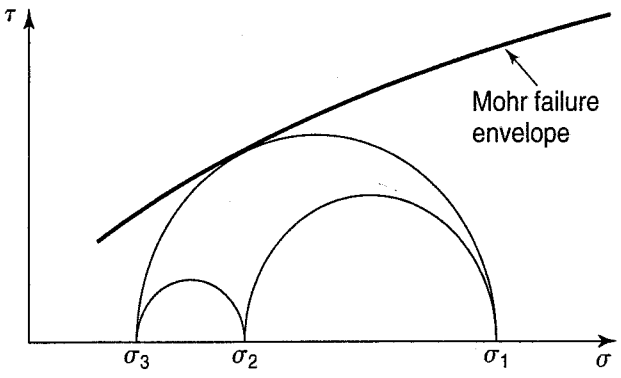

FIGURE 11.12 Mohr circles for a three-dimensional state of stress.

The Mohr diagram for this condition is on the right side of Fig. 11.11(a). In Fig. 11.11(b), a shear stress τ_a is applied to the base of the block, and the movement of the block to the left is resisted by the frictional resistance τ_r. The resultant R acts at an angle θ from the vertical, and the tangent of θ is, of course, τ_a/σ, as shown in the Mohr diagram to the right for this stable condition ($\tau_r > \tau_a$). Finally, in Fig. 11.11(c), the applied shear stress just equals the maximum frictional resistance ($\tau_a = \tau_r = \sigma \tan \varphi$) and the block is at incipient failure, or just starts to slide. The angle θ then becomes equal to coefficient of friction between the block and the ground surface, and the static friction becomes the sliding friction. The Mohr plot is shown at the right, at the failure condition, and the *angle of maximum obliquity*, θ_{max}, is equal to the angle of internal friction ϕ. The obliquity relationships are useful for evaluating laboratory test data and in foundation design and analysis.

The last factor we should consider is the effect of the intermediate principal stress σ_2 on conditions at failure. Since by definition σ_2 lies somewhere between the major and minor principal stresses, the Mohr circles for the three principal stresses look like those shown in Fig. 11.3(c) and again in Fig. 11.12. It is obvious that σ_2 can have no influence on the conditions at failure for the Mohr failure criterion, no matter what magnitude it has. The intermediate principal stress σ_2 probably does have some influence in real soils, but the Mohr–Coulomb failure theory does not consider it.

11.4.4 Failure Criteria for Rock

When tested in compression, most rocks except those that are very soft, will have a very brittle type failure. Their stress-strain response is similar to that shown in Fig. 11.4(e). Probably the best known theory to predict brittle failures and the development of tensile cracks in rocks and other brittle materials is the Griffith crack theory. Although it predicts tensile behavior of rock rather well, it is quite complicated (Jaeger et al., 2007) and not very practical to use. The Mohr–Coulomb theory, on the other hand, is simple and practical, and although far from perfect, it is probably the most commonly used failure theory in rock mechanics (Goodman, 1989). Because intact rock usually has an appreciable unconfined compressive strength at zero confining stress, the Mohr failure envelope has a significant intercept, because unconfined compressive strength, as we shall see in Chapter 12, is twice the undrained shear strength τ_f. (The unconfined compression test on rock is discussed in Sec. 11.5.4 below.) Mohr–Coulomb is applied to rocks by extrapolating the failure envelope to the left of the τ-axis, through this intercept on the zero-confining stress axis, and into the tensile side of the normal stress axis, as shown in Fig. 11.13. Because rocks can fail in tension, there is a tensile stress cutoff to the Mohr failure envelope on the tensile side of the Mohr diagram. As noted by Goodman (1989), the minor principal stress can never be less than the tensile strength of the rock.

Another popular failure criterion for rock is the Hoek and Brown (1980; 1988) criterion for fractured rock (see also Wyllie, 1999, and Jaeger et al., 2007). The Hoek–Brown criterion is a very practical empirical criterion based on years of experience observing the behavior of rock masses in tunnel and slope construction, supplemented by laboratory tests on fractured rock and model studies of jointed rock. We discuss the Hoek–Brown criterion in some detail in Sec. 13.16, after we know more about laboratory testing of both soils and rock.

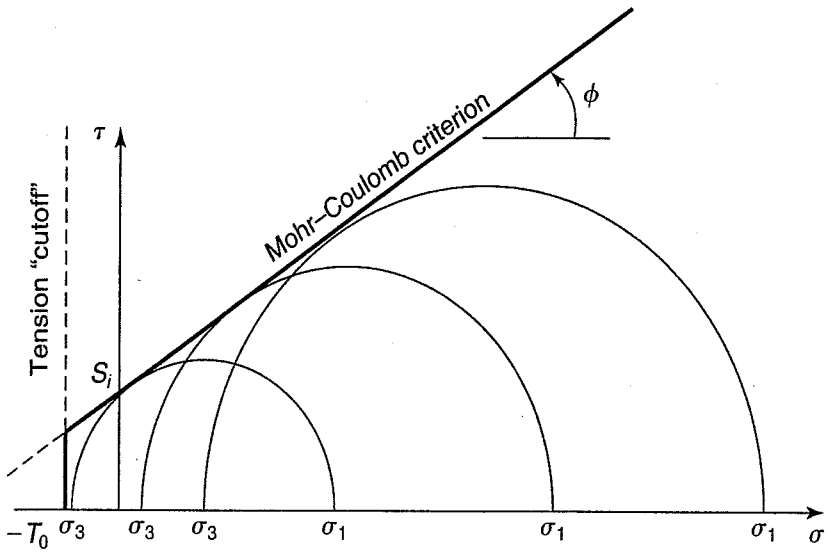

FIGURE 11.13 Mohr–Coulomb failure criterion showing a tension cut-off (Goodman, 1989).

11.5 LABORATORY TESTS FOR THE SHEAR STRENGTH OF SOILS AND ROCKS

In this section we briefly describe some of the more common laboratory tests for determining the shearing strength of soils and rocks. Some of the tests are rather complicated, and for details you should consult manuals and books on laboratory testing of soils—for example, U.S. Army Corps of Engineers (1986), U.S. Dept. of the Interior (1990), Bardet (1997), and Head (1996 and 1998). For testing rock, see Goodman (1989), Wyllie (1999), Jaeger et al. (2007), and The International Society for Rock Mechanics (ISRM) Blue Book of ISRM suggested test methods (Ulusay and Hudson, 2007). Many routine tests for both soils and rocks are now standard ASTM (2010) tests.

11.5.1 Direct Shear Test

The direct shear test is probably the oldest strength test for soils. Coulomb used a type of shear box test more than 230 years ago to determine the necessary parameters for his strength equation. The test in principle is quite simple. Basically, there is a specimen container, or "shear box," which is separated horizontally into halves. One-half is fixed; with respect to that half, the other half is either pushed or pulled horizontally. A normal load is applied to the soil specimen in the shear box by a rigid loading cap. The shear load, horizontal deformation, and vertical deformation are measured during the test. Dividing the shear force and the normal force by the *nominal* area of the specimen, we obtain the shear stress as well as the normal stress on the failure plane. Remember that the failure plane is *forced* to be horizontal with this apparatus.

A cross-sectional diagram of the essential features of the apparatus is shown in Fig. 11.14(a), while Fig. 11.14(b) shows some typical test results. The Mohr–Coulomb diagram for conditions at failure appears in Fig. 11.14(c). As an example, if we were to test three samples of a sand at the same relative density just before shearing, then as the normal stress σ_n was increased, we would expect from our knowledge of sliding friction a concurrent increase in the shear stress on the failure plane at failure (the shear strength). This condition is shown in the typical shear stress versus deformation curves for a dense sand in Fig. 11.14(b) for $\sigma_{n1} < \sigma_{n2} < \sigma_{n3}$. When these results are plotted on a Mohr diagram, Fig. 11.14(c), the angle of internal friction ϕ can be obtained.

Typical results of vertical deformation ΔH for a dense sand are shown in the lower portion of Fig. 11.14(b). At first there is a slight reduction in height or volume of the soil specimen, followed by a dilation or increase in height or volume. As the normal stress σ_n increases, it becomes more difficult for the soil to dilate during shear, which seems reasonable.

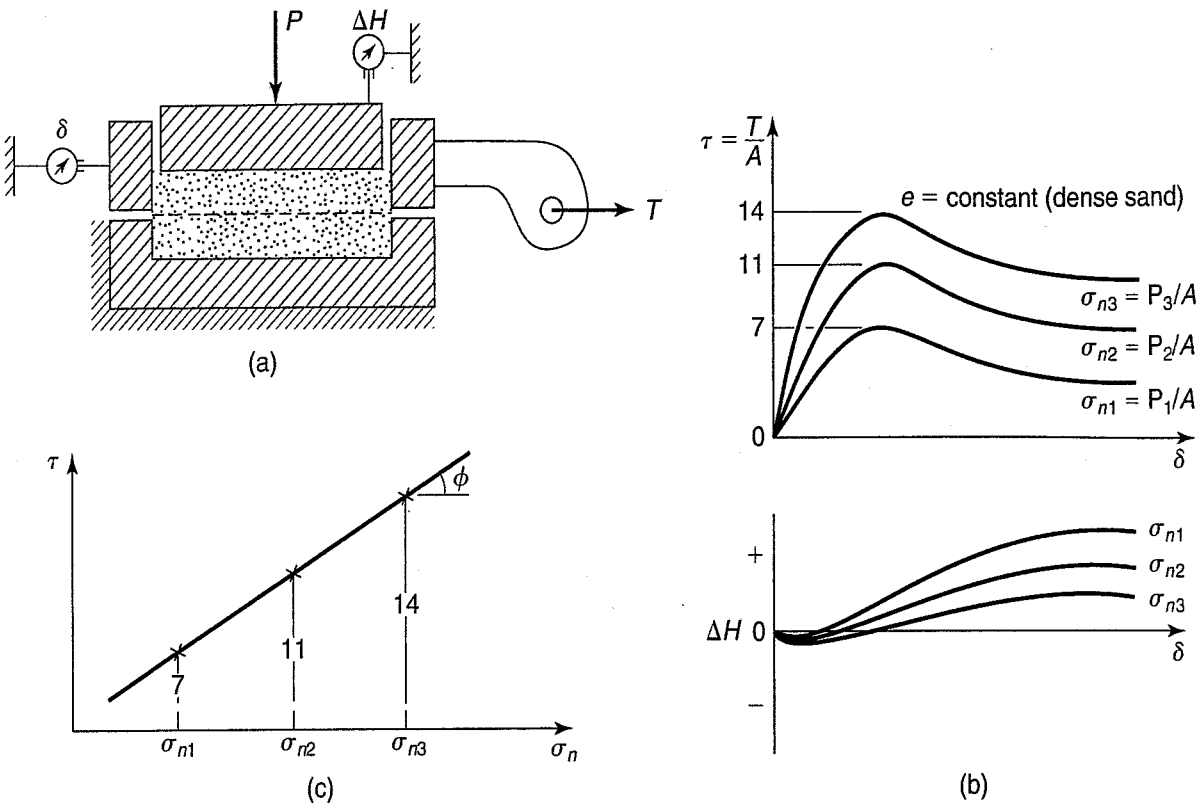

FIGURE 11.14 (a) Cross-sectional schematic diagram of direct shear apparatus; (b) typical test results (dense sand); and (c) Mohr diagram for specimens at the same relative density.

We do not obtain the principal stresses directly in the direct shear test. Instead, if they are needed, they may be inferred if the Mohr–Coulomb failure envelope is known. Then, as shown in Example 11.6, the angle of rotation of the principal stresses may be determined. Why is there rotation of the principal planes? Initially, the horizontal plane (potential failure plane) is a principal plane (no shear stress), but after the shearing stress is applied and at failure, by definition, it cannot be a principal plane. Therefore, the principal planes must rotate in the direct shear test. How much do they rotate? It depends on the slope of the Mohr failure envelope, but it is fairly easy to determine, as is shown in Example 11.6, if you make some simple assumptions.

Example 11.6

Given:

The initial and failure conditions in a direct shear test, as shown in Fig. Ex. 11.6.

Required:

Plot the Mohr circles for both initial conditions and at failure, assuming ϕ is known. Find the principal stresses at failure and their angles of rotation at failure.

Solution: The Mohr circles both for initial conditions and at failure are shown on the right side of Fig. Ex. 11.6. At failure, you know that the normal stress on the failure plane, σ_{ff}, is the same as the initial normal stress, σ_n. Since ϕ is known (assume c is small or zero), from the Mohr failure

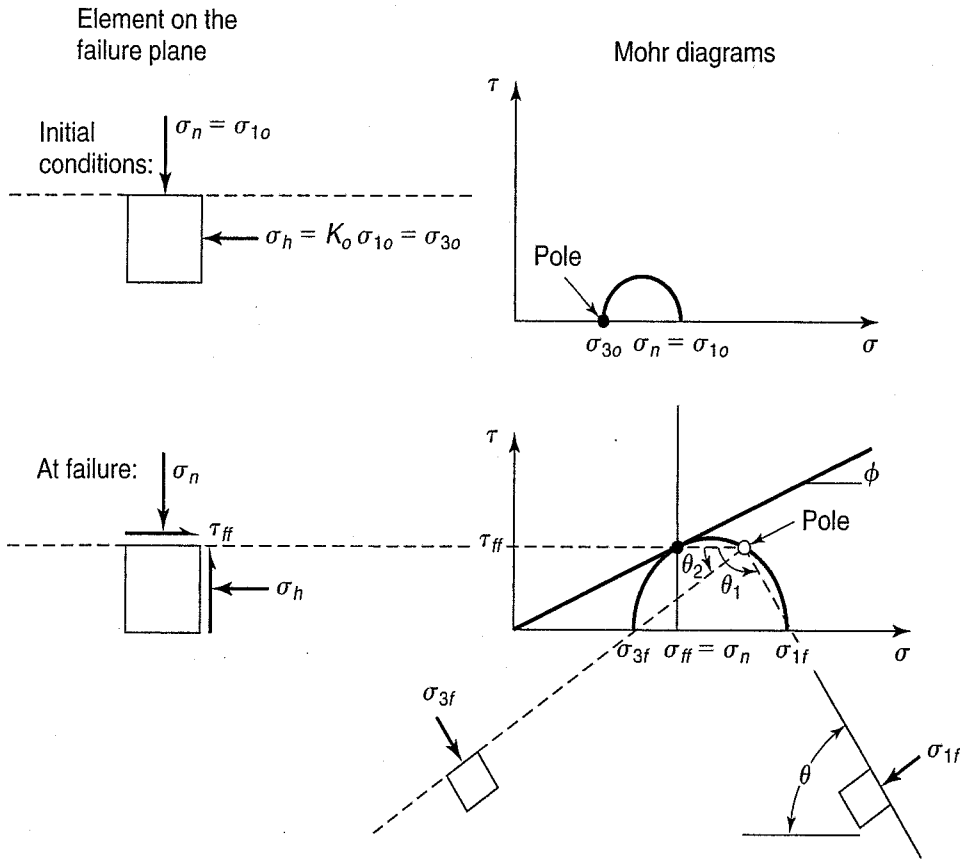

FIGURE Ex. 11.6

hypothesis (Fig. 11.7) the shear stress on the failure plane at failure is determined by the point of tangency of the Mohr circle at failure. The center of the failure circle can be found by drawing a perpendicular to the Mohr failure envelope from the point of tangency. The radial distance is, of course, equal to $[(\sigma_1 - \sigma_3)/2]_f$.

Another way to find the Mohr circle at failure is graphically by trial and error. Find the only circle that is tangent at (σ_{ff}, τ_{ff}) and whose diameter lies on the σ-axis. Once the failure circle is drawn, the values of σ_{1f} and σ_{3f} can be scaled off. From the pole method, the angles of rotation of these stresses are readily found, as shown in Fig. Ex. 11.6.

There are, of course, several advantages and disadvantages of the direct shear test. Primarily, the test is inexpensive, fast, and simple, especially for granular materials. We do observe shear planes and thin failure zones in nature, so it seems all right to actually shear a specimen of soil along some plane to see what the stresses are on that plane. Disadvantages include the problem of controlling drainage—it is very difficult if not impossible, especially for fine-grained soils. Consequently, the test is not so suitable for other than completely drained conditions. When we force the failure plane to occur, how can we be sure that it is the weakest direction or even at the same critical direction as occurs in the field? We don't know. Another flaw in the direct shear test is that there are rather serious stress concentrations at the sample boundaries, which lead to highly nonuniform stress conditions within the test specimen itself. And finally, as shown by Example 11.6, an uncontrolled rotation of principal planes and stresses occurs between the start of the test and failure. To accurately model the in situ loading conditions, the amount of this rotation should be known and accounted for, but it isn't. The Mohr circles for the direct shear test are further illustrated by Example 11.7.

Example 11.7

Given:

A direct shear test is run on a medium dense sandy silt, with the normal stress $\sigma_n = 65$ kPa. $K_o = 0.5$. At failure, the normal stress is still 65 kPa and the shear stress is 41 kPa.

Required:

Draw the Mohr circles for the initial conditions and at failure and determine:

a. The principal stresses at failure.
b. The orientation of the failure plane.
c. The orientation of the major principal plane at failure.
d. The orientation of the plane of maximum shear stress at failure.

Solution:

a. The initial conditions are shown in Fig. Ex. 11.7 by circle i. Since $K_o = 0.5$, the initial horizontal stress is 32.5 kPa. The normal stress on the specimen is held constant at 65 kPa during the test, so σ_{1i} is also σ_{ff}. Since the shear stress at failure is 41 kPa, the failure point [as in Fig. 11.13(c)] is plotted as point F. The ϕ is determined to be 32°. What happens between the initial Mohr circle i and at failure f is unknown. The construction of circle f was described in Example 11.6. The center of circle f is found to be at (91 kPa, 0). So, $\sigma_{1f} = 139$ kPa and $\sigma_{3f} = 43$ kPa.

b. The state of stress at failure point F is (65, 41) kPa, and the failure plane is assumed to be horizontal—a good assumption for the direct shear test.

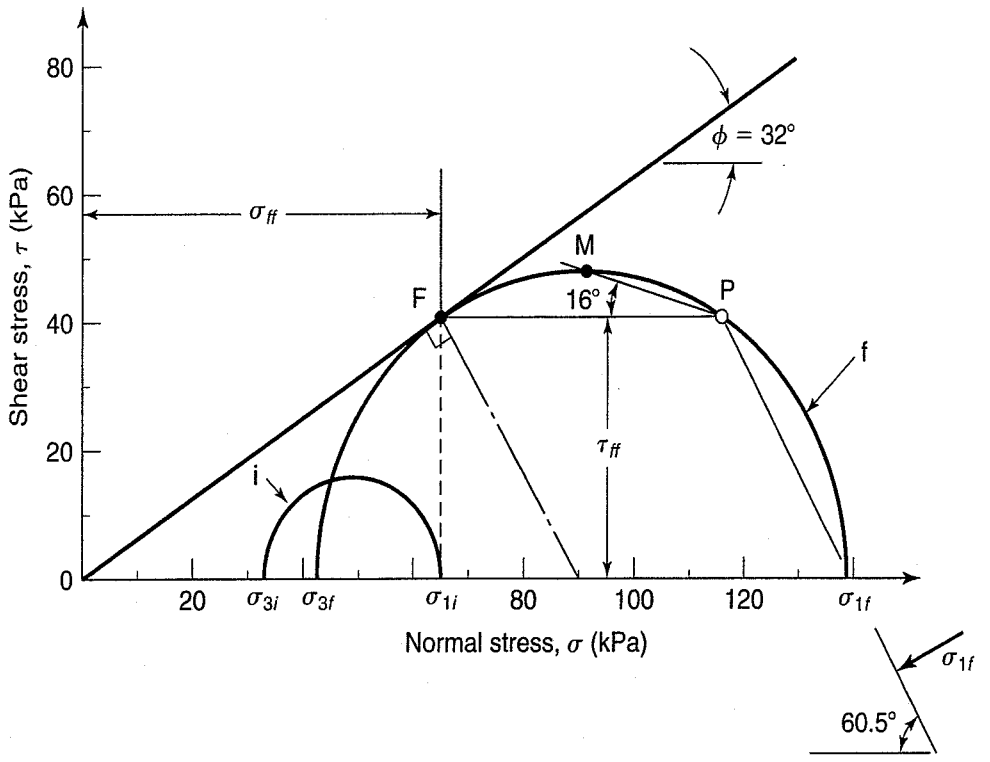

FIGURE Ex. 11.7

c. A line drawn horizontally from the known state of stress at point F intersects the Mohr circle at P, the pole. Line $\overline{P\sigma_{1f}}$ indicates the orientation of the major principal plane. It makes an angle of about 60.5° with the horizontal.

d. Line $\overline{PM}$ is the orientation of the plane of maximum shear stress; it is about 16° from the horizontal. Note that, in this example, if we didn't assume that the Mohr failure envelope passed through the origin of the Mohr diagram, more than one test at different σ_{1i}'s would be required to establish the Mohr envelope.

11.5.2 Triaxial Test

During the early history of soil mechanics, the direct shear test was one of the most common tests for measuring soil shear strength. Then, about 1930, A. Casagrande while at M.I.T. began research on the development of a cylindrical compression test in an attempt to overcome some of the serious disadvantages of the direct shear test. Now this test, commonly called the *triaxial test*, is by far the more popular of the two. It is much more complicated than the direct shear but also much more versatile. We can control drainage quite well, and there is no rotation of σ_1 and σ_3. Stress concentrations still exist, but they are significantly less than in the direct shear test. Also, the failure plane can occur anywhere. An added advantage: we can control the stress paths to failure reasonably well, which means that complex stress paths in the field can more effectively be modeled in the laboratory with the triaxial test. Stress paths are explained in Chapter 13.

The principle of the triaxial test is shown in Fig. 11.15(a). The soil specimen is usually encased in a rubber membrane to prevent the pressurized cell fluid (usually water) from penetrating the pores of the soil. Axial load is applied through a piston, and often the volume change of the specimen during a drained test or the induced pore water pressure during an undrained test is measured. As mentioned above, we can control the drainage to and from the specimen, and it is possible, with some assumptions, to control the stress paths applied to the specimen. Basically, we assume the stresses on the boundary of the specimen are principal stresses [Fig. 11.15(b)]. This is not really true because of some small shear

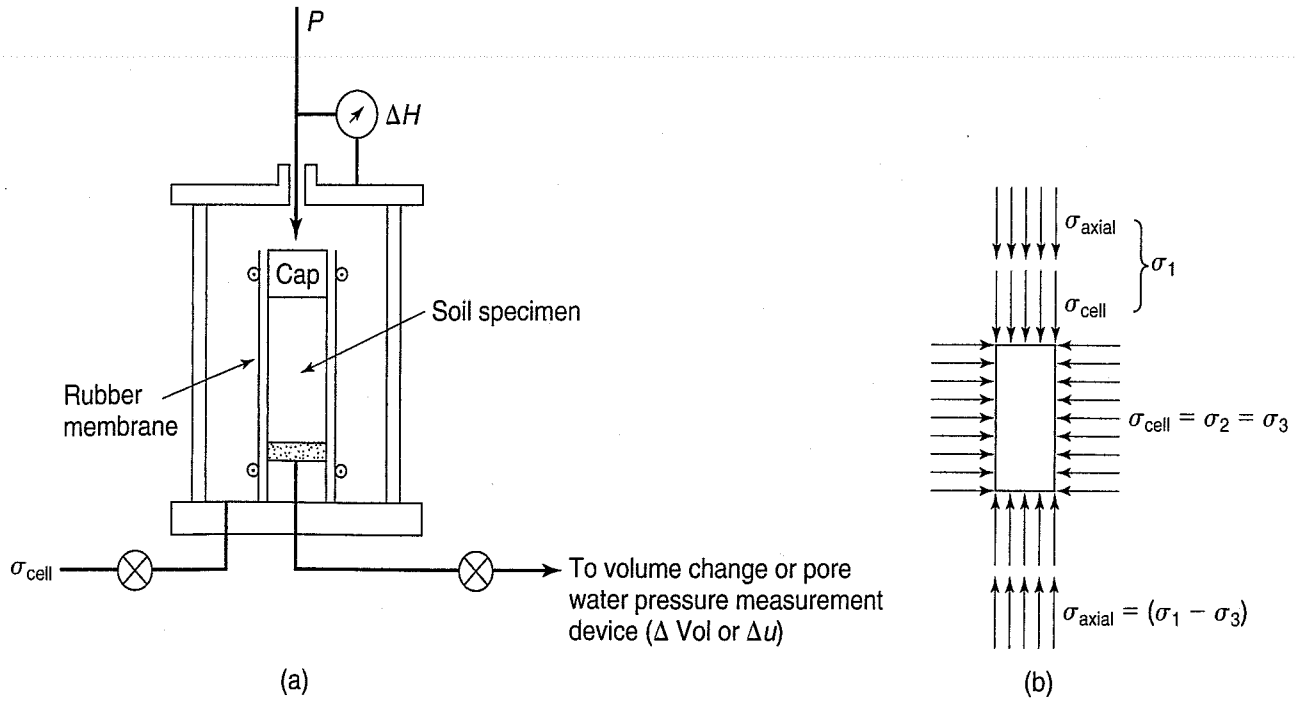

FIGURE 11.15 (a) Schematic diagram of the triaxial apparatus; (b) assumed stress conditions on the triaxial specimen.

stresses acting on the ends of the specimen. Also, as mentioned before, the failure plane is not forced—the specimen is free to fail on any weak plane or, as sometimes occurs, to simply bulge.

You will note that the σ_{axial} in Fig. 11.15(b) is the difference between the major and minor principal stresses; it is called the *principal stress difference* (or sometimes, incorrectly, the deviator stress). Note also that for the conditions shown in the figure, $\sigma_2 = \sigma_3 = \sigma_{cell}$. Sometimes we will assume that $\sigma_{cell} = \sigma_1 = \sigma_2$ for special types of stress path tests.

As mentioned, the triaxial test is far more complex than the direct shear test; entire books have been written on test details and interpretation of the results (see, for example, Bishop and Henkel, 1962). Most of the data and test results described in Chapter 12 were derived from triaxial tests.

Drainage conditions in the triaxial test are models of specific critical design situations required for the analysis of stability in geotechnical engineering practice. These are commonly designated by a two-letter symbol. The first letter refers to what happens *before shear*—that is, whether the specimen is consolidated. The second letter refers to the drainage conditions *during shear*. The three permissible drainage paths in the triaxial test are as follows:

Drainage Path Before Shear–During Shear	Symbol
Unconsolidated–Undrained	UU
Consolidated–Undrained	CU
Consolidated–Drained	CD

For reasons explained in Chapter 12, the unconsolidated–drained test defies interpretation and is therefore meaningless. Triaxial test results for the three drainage paths are described in detail in Chapter 12.

Example 11.8

Given:

A conventional consolidated–drained (CD) triaxial test is conducted on a sand. The cell pressure is 100 kPa, and the applied axial stress at failure is 200 kPa.

Required:

a. Plot the Mohr circles for both the (1) initial and (2) failure stress conditions.

b. Determine ϕ (assume $c = 0$).

c. Determine (3) the shear stress on the failure plane at failure τ_{ff}, and find (4) the theoretical angle of the failure plane in the specimen. Also (5) determine the angle of maximum obliquity.

d. Determine (6) the maximum shear stress at failure τ_{max} and (7) the angle of the plane on which it acts; calculate (8) the available shear strength on this plane and (9) the factor of safety on this plane.

Solution:

a. Refer to Fig. 11.14(b) and Fig. Ex. 11.8. (1) The initial conditions are shown at the top of Fig. Ex. 11.8 for the conventional triaxial test. The initial stress is equal to the cell pressure σ_{cell}, and it is equal in all directions (hydrostatic). Therefore the Mohr circle for the initial stress conditions is a *point* at 100 kPa, as shown in the Mohr diagram of Fig. Ex. 11.8.

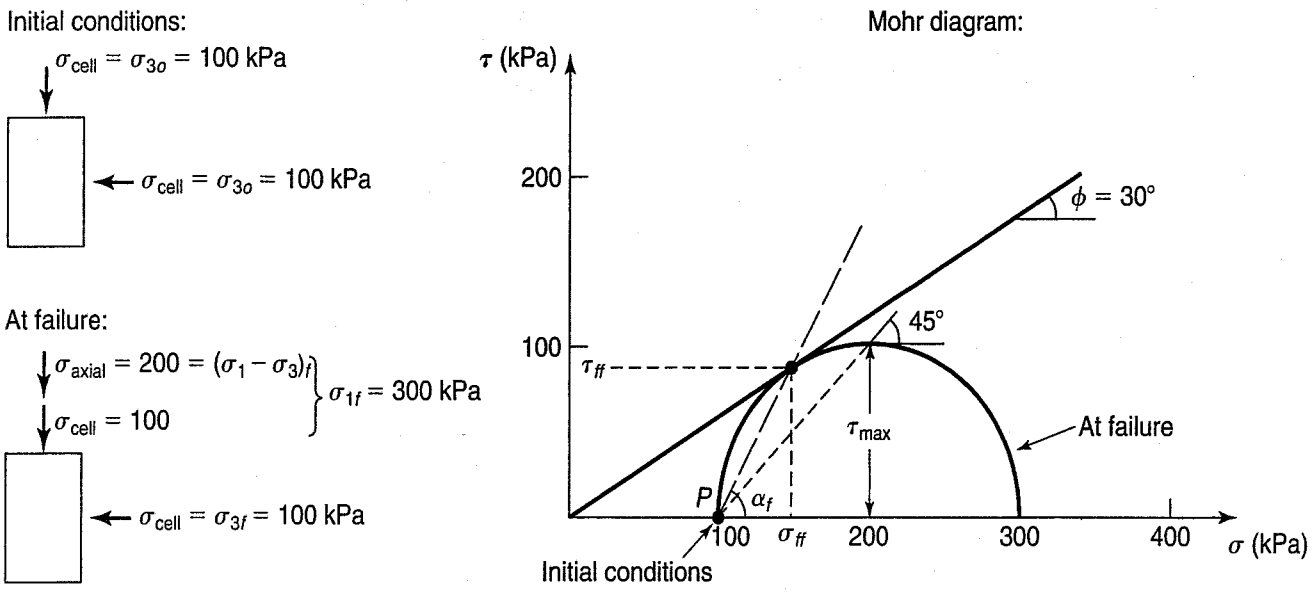

FIGURE Ex. 11.8

(2) At failure, the $\sigma_{axial} = (\sigma_1 - \sigma_3)_f = 200$ kPa, and the cell pressure $\sigma_{cell} = 100$ kPa is held constant during the conventional test. So

$$\sigma_{1f} = (\sigma_1 - \sigma_3)_f + \sigma_{3f} = 200 + 100 = 300 \text{ kPa}$$

Now we can plot the Mohr circle at failure; $\sigma_{1f} = 300$ and $\sigma_{3f} = 100$. The center is at $(\sigma_1 + \sigma_3)/2 = 200$, and the radius is $(\sigma_1 - \sigma_3)/2 = 100$. The circle at failure is shown in Fig. Ex. 11.8.

b. We find ϕ graphically to be 30°. We can also use Eq. (11.13) if we prefer an analytical solution. Thus

$$\phi = \arcsin\frac{\sigma_{1f} - \sigma_{3f}}{\sigma_{1f} + \sigma_{3f}} = \arcsin\frac{200}{400} = 30°$$

c. (3) From the Mohr failure hypothesis, the coordinates of the point of tangency of the Mohr failure envelope and the Mohr circle at failure are (σ_{ff}, τ_{ff}). From Eq. (11.9), we know that $\tau_{ff} = \sigma_{ff} \tan\phi$, but unlike the direct shear test we don't know σ_{ff} in the triaxial test. Look carefully at Fig. 11.10. The small angle near the top of the Mohr circle is ϕ (by a theorem from high school geometry). Therefore, since $c = 0$, and solving for σ_{ff}, we obtain

$$\sigma_{ff} = \frac{\sigma_{1f} + \sigma_{3f}}{2} - \frac{\sigma_{1f} - \sigma_{3f}}{2}\sin\phi$$
$$= 200 - 100\sin 30° = 150 \text{ kPa}$$
$$\tau_{ff} = \sigma_{ff}\tan\phi = 150\tan 30° = 87 \text{ kPa}$$

(4) The theoretical angle of inclination of the failure plane can be found *graphically* by the pole method or analytically. From the stress conditions at failure shown in Fig. Ex. 11.8, the pole is at (100, 0), and α_f can be measured to be 60°.

For the *analytical* solution, use Eq. (11.10)

$$\alpha_f = 45° + \frac{\phi}{2} = 60°$$

(5) The inclination of the Mohr failure envelope is 30° and the point of tangency determines the condition of maximum obliquity. In other words, the ratio τ_{ff}/σ_{ff} is a maximum at this point on the Mohr circle and thus the maximum obliquity angle $\theta_{max} = \phi$.

d. (6) $\tau_{max} = \dfrac{\sigma_{1f} - \sigma_{3f}}{2} = 100\ \text{kPa}.$

(7) From the pole, the plane of τ_{max} is inclined at 45° from the horizontal.

(8) The available τ [see Fig. 11.9(b)] can be determined from

$$\tau_{available} = \sigma_n \tan\phi = \frac{\sigma_{1f} + \sigma_{3f}}{2}\tan\phi$$
$$= 200 \tan 30° = 115.5\ \text{kPa}$$

which is greater than $\tau_{max} = 100$ kPa. Therefore the factor of safety on the 45° plane [Eq. (11.11)] is

$$\text{F.S.} = \frac{\tau_{available}}{\tau_{max}} = \frac{115.5}{100} = 1.16$$

(9) Note that the factor of safety on the $\alpha_f = 60°$ plane is

$$\text{F.S.} = \frac{\tau_{available}}{\tau_{ff}} = \frac{86.6}{86.6} = 1$$

A factor of safety of one makes sense in this latter case because the specimen is at failure.

11.5.3 Special Laboratory Soils Tests

Other types of laboratory strength tests that you may hear about include *hollow cylinder tests*, *plane strain tests*, and so-called *true triaxial* or *cuboidal shear tests*. These tests are schematically illustrated in Fig. 11.16. In the common triaxial test, the intermediate principal stress can be equal only to either the major or minor principal stress—nothing in between. With these other tests it is possible to vary σ_2,

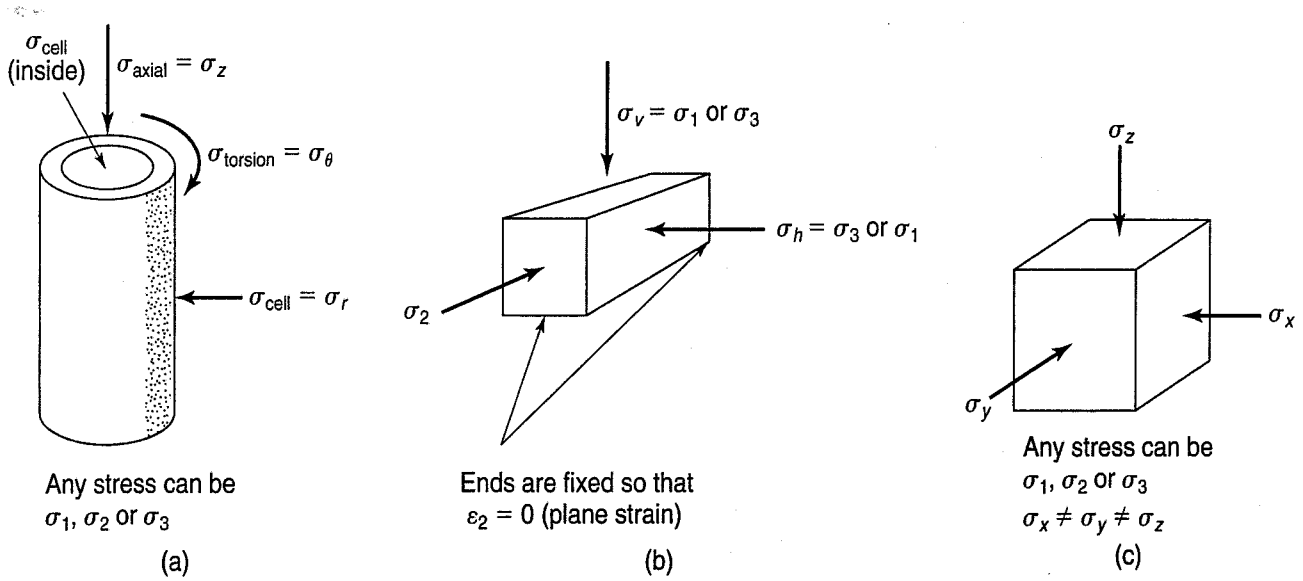

FIGURE 11.16 Schematic diagrams for the: (a) hollow cylinder test; (b) plane strain test; and (c) true triaxial or cuboidal shear test.

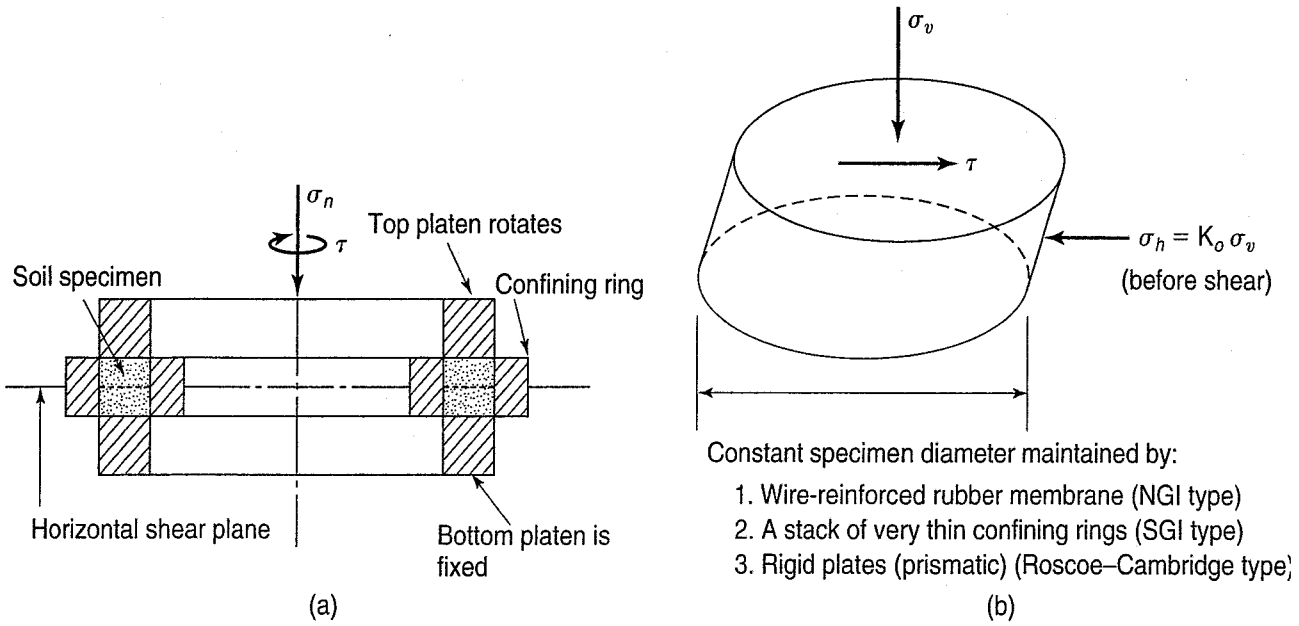

FIGURE 11.17 Schematic diagrams of: (a) torsional or ring shear; (b) direct simple shear apparatus.

which probably models the stress conditions in real problems more accurately. These tests are primarily used for research rather than for practical engineering applications.

A couple of other tests of the direct shear type should also be mentioned. *Torsional* or *ring shear* tests [Fig. 11.17(a)] have been developed so that the test specimen may be sheared to very large deformations. This is sometimes necessary to obtain the *residual* or *ultimate shear strength* of certain materials, and it is easier to do with a ring shear device than by repeatedly reversing a direct shear box. A more common test used in Scandinavia, Japan, and North America for static and dynamic testing is the *direct simple shear* (DSS) test [Fig. 11.17(b)]. In this test, a fairly homogeneous state of shear stress is applied, thereby avoiding the stress concentrations that exist in the ordinary direct shear apparatus. Since stress conditions in the DSS test are not the same as those shown in Examples 11.6 and 11.7 for the direct shear box, they are described in Example 11.9.

Example 11.9

Given:

The DSS test.

Required:

Illustrate the stress conditions in the test, and draw the Mohr circles for both initial and failure conditions.

Solution: The initial conditions for the DSS test shown in Fig. Ex. 11.9a are the same as those for the direct shear box test shown in Fig. Ex. 11.7. The sides of the soil sample are forced to rotate through an angle γ by the application of a horizontal shear stress, τ_{hv}. These stress conditions are shown in Fig. Ex. 11.9b. Note the absence of complementary shear stresses on the *outside* of the soil sample; this is necessary for simple shear. *Inside* the sample, however, the applied stress system is assumed to be *pure* shear, and complementary stresses are necessary for equilibrium. With the application of τ_{hv}, and with σ_v and σ_h constant, the Mohr circle enlarges about the same center as the initial Mohr

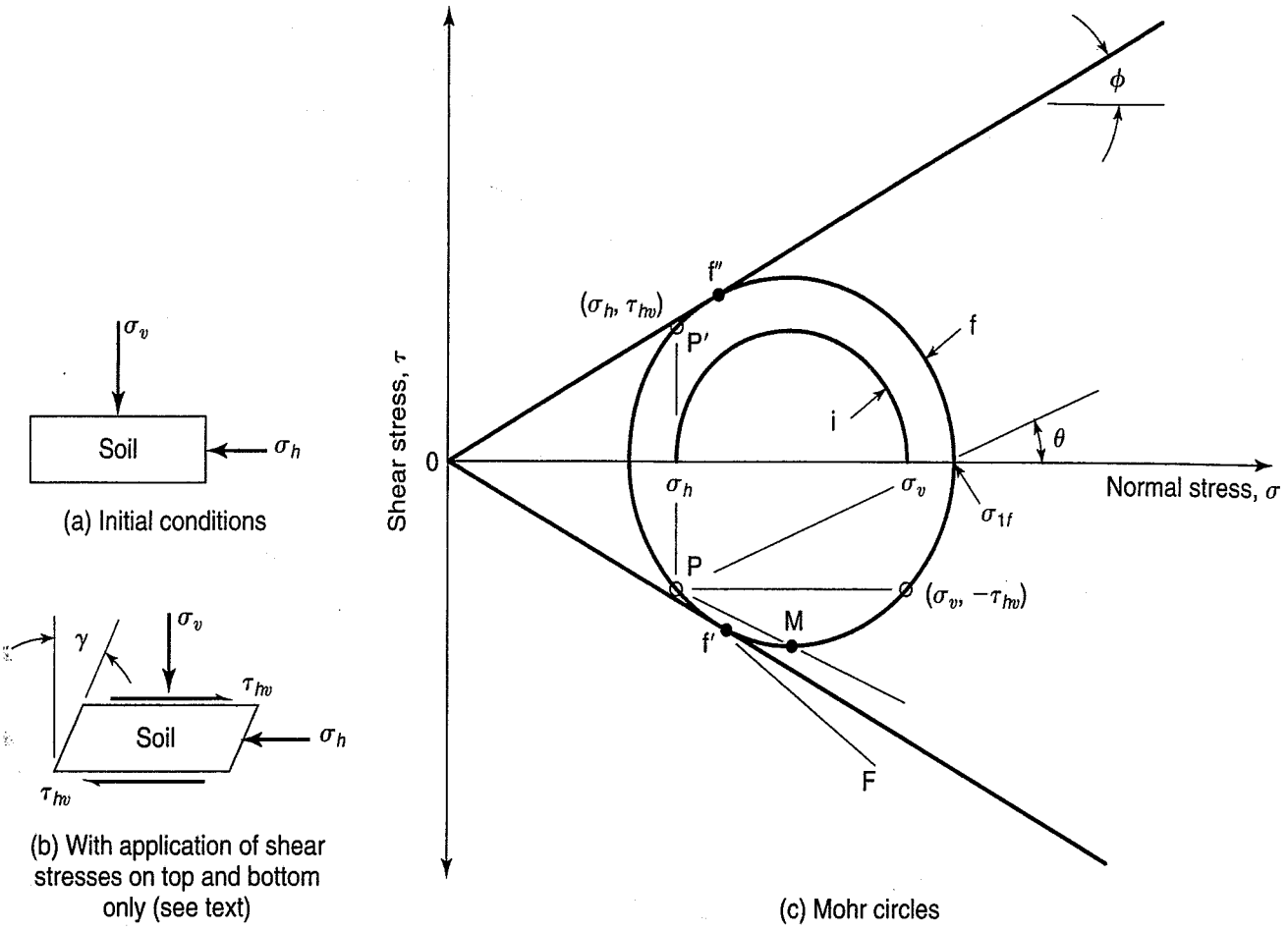

FIGURE Ex. 11.9

circle i. At failure, the Mohr circle is just tangent to the Mohr failure envelope, and the Mohr circle looks like circle f of Fig. Ex. 11.9c.

For this condition at failure, the pole P is found by extending a line from $(\sigma_v, -\tau_{hv})$ horizontally (the plane on which these stresses act) to where it intersects the Mohr circle. Lines drawn from the pole represent the orientations of different states of stress within the soil sample. The line PM corresponds to the plane of maximum (absolute value) shear stress; the line PF represents the orientation of the failure plane—it is *not* horizontal as in the direct shear test. The line $\overline{P\sigma_{1f}}$ denotes the orientation of the σ_1 planes when τ_{hv} is negative on the horizontal surface. When (and if) the sign of τ_{hv} becomes positive on the horizontal plane, as in a *cyclic simple shear* test, then the pole is located at P′ for that part of the circle. The line $\overline{P\sigma_{1f}}$ becomes the new orientation of the principal plane with a negative θ, the angle of principal stress rotation.

11.5.4 Laboratory Tests for Rock Strength

In Chapter 3 we described how, in rock mechanics and rock engineering, it is the defects (joints, fractures, faults, bedding planes, etc.) in the rock that control its behavior. Even if the intact rock between the defects is very strong and impermeable, the defects usually make a rock mass weaker and more permeable. Nonetheless, we are still interested in the strength and other mechanical properties of intact rock specimens. As with natural soil deposits, rock masses often have highly variable properties, and knowing only the type of rock gives just a very general idea of its engineering properties. Laboratory tests on rock specimens help engineers characterize the rock mass variability and also provide design information.

In this section, we discuss some of the more common laboratory tests for the rock strength and related mechanical properties. In situ tests for rock are mentioned in the next section. For a good description of the equipment and procedures for rock core drilling and sampling, see ASTM (2010) D 2113.

Laboratory tests are performed mostly on rock cores of various sizes obtained from the core barrels of rock drills. Test specimens are selected from cores in core boxes similar to what we showed in Sec. 4.13. The test specimens must be properly prepared so that the results are meaningful and repeatable (Goodman, 1989; ASTM, 2010, D 4543).

Probably the oldest and perhaps the most common rock test is the *uniaxial* or *unconfined compression test*. The configuration is very similar to tests on concrete cylinders, and many of the same consideration as to end conditions and rate of loading apply. The ends of the core must be cut parallel, then polished and capped to minimize end effects. See ASTM (2010) D 7012, Method C, and ISRM Method No. 14 (Ulusay and Hudson, 2007) for detailed test procedures. Because the strains at failure are very small, flexing of the testing machine can adversely influence the test results; thus these tests must be performed using a very stiff compression testing machine.

A stiff testing machine is also required for *triaxial compression* tests performed on rock cores. The equipment and interpretation are basically the same as for triaxial tests on soils described in Sec. 11.5.2. The main difference is that the equipment for testing rock has a much greater lateral pressure and axial load capacity than normally used for soils. For detailed test procedures, see ASTM (2010) D 7012, Method A, and ISRM Method No. 20 (Ulusay and Hudson, 2007).

Because unconfined and triaxial tests on rock cores are expensive and time consuming, sometimes an index of the compressive strength of the rock will provide sufficient information for a preliminary assessment of strength. In this case, the point load test will provide an index of the strength of the rock, and ASTM (2010) D 5731 is the appropriate standard. Rock cores can be tested on their diameter (*diametral test*) or axially (*axial test*) similar to soils. The test can also be performed on specimens of different shapes, such as the *block test* and the *irregular lump test*, to provide an index of the rock strength.

The shear strength of rock may be tested in a *direct shear* device similar to that used for testing of soils, but much stronger and heavier. Minimum cross sectional area should be 1900 mm^2 (about 3 $in.^2$). The test procedure is outlined in ASTM (2010) D 5607 and ISRM Method 15 (Ulusay and Hudson, 2007).

The tensile strength of intact rock is also of interest to rock engineers, because, depending on the loading conditions in the field, it may govern design. The tensile strength can be determined directly or by index tests. The test procedure for the *direct tensile strength* of rock cores is in ASTM (2010) D 2936. Another tensile strength test performed on rock cores is the splitting tension test, sometimes called the Brazilian test; the procedure is in ASTM (2010) D 3967. See also ISRM Method No. 21 (Ulusay and Hudson, 2007).

The elastic properties of rock cores may be obtained from the results of *ultrasonic* testing. By applying either a steady state compression or a high frequency shear pulse to the end of a rock specimen, the measured travel times and specimen dimensions determine the pulse velocity, and from elastic theory, the ultrasonic elastic constants such as the Young's modulus, shear modulus, and Poisson's ratio may be determined. For details see ASTM (2010) D 2845 and ISRM Method No. 19 (Ulusay and Hudson, 2007).

For further information on laboratory testing of rocks and especially the interpretation of the test results, see Goodman (1989), Wyllie (1999), and Jaeger et al. (2007).

11.6 IN SITU TESTS FOR THE SHEAR STRENGTH OF SOILS AND ROCKS

Obtaining high quality undisturbed samples of the subsurface soils and rocks is expensive and often difficult, and some deposits such as stiff fissured clays, loose sands, and highly fractured rock are almost impossible to sample. Another consideration is that poor quality soil and rock sampling is,

unfortunately, often the case rather than the exception in the United States. We have already discussed the effect of sample disturbance on the consolidation properties of clays (Sec. 8.5.3); similarly, sample disturbance can significantly and negatively affect the measured shear strength in laboratory tests. Rock cores made by single-core barrel drilling are often badly broken and disturbed by the drilling process, and thus the strength properties measured in subsequent laboratory tests on these samples are seriously compromised. Also, in the case of rock, it may be impossible to obtain samples for laboratory testing of, for example, discontinuities in rock masses or soft, weak, or, as mentioned above, highly fractured rock. Often, in situ tests are performed on the rock—for example, in the walls of a tunnel or other underground excavation.

Because of all these considerations, in recent years there has been increasing interest in determining the strength of soil and rock in situ. In soils, this is accomplished by various probes and instruments that are inserted relatively easily and quickly into the subsurface. The major disadvantage of in situ tests is that the properties are obtained only indirectly through correlations with laboratory tests or by back calculation from theory or actual failures. On the other hand, there are significant statistical advantages to having lots of even indirect subsurface information obtained rapidly and at relatively low cost compared with a few, expensive laboratory tests on samples of what may not even be the weakest or the most critical strata at the site. Finally, some properties, such as K_o, deformation modulus, and shear strength of discontinuities in rock, can be determined reliably only in the field.

11.6.1 In Situ Tests for Shear Strength of Soils

Table 11.1 lists the common tests for determining in situ the shear strength and related properties of soils. This will give you a general idea of what techniques are available as well as some of their limitations. References are also listed in the table if you need additional details about these tests and their interpretation.

TABLE 11.1 Field Methods for Determining Shear Strength In Situ

Test	Remarks	Fig. No.	Best For	Limitations	References
Standard penetration test (SPT)	A standard "split-spoon" sampler is driven by a 63.5 kg hammer falling 0.76 m. The number of blows required to drive the sampler 0.3 m is called the *standard penetration resistance* or *blow count*, *N*. Disturbed sample obtained.	11.18	Sandy soils	Good estimates of density and strength of sands. Very rough correlation with τ_f for stiff clays. Unreliable in soft, sensitive clays. Gravel and cobbles can cause problems. Results are sensitive to test details and borehole stability. Several corrections required.	ASTM (2010) D 1586; de Mello (1971); Schmertmann (1975); Kovacs et al. (1977); Sabatini et al. (2002)
Vane shear test (VST)	Four bladed vane rotated; maximum torque measured; τ_f from theoretical formula or empirical correlations.	11.19	Soft to medium clays	Unreliable if sand layers, varves, gravel, etc., or if vane rotated too rapidly. Corrections may be required unless calibrated to local soils.	ASTM (2010) D 2573; Cadling and Odenstad (1950); Bjerrum (1972); Schmertmann (1975); Ladd et al. (1977); Jamiolkowski et al. (1985); Richards (1988)

(Continued)

TABLE 11.1 (Continued)

Test	Remarks	Fig. No.	Best For	Limitations	References
Dutch cone penetrometer (CPT)	A 60° cone (projected area 10 cm^2) pushed at 1 to 2 m/min. Point resistance q_c and friction on the friction sleeve f_s measured either electrically or mechanically at 5–20 cm intervals.	11.20	All soil types except very coarse granular soils	Gravel causes problems. Requires local correlation for soft clays.	ASTM (2010) D 3441 and D 5778; Sanglerat (1972); ESOPT (1974); Schmertmann (1975, 1978); Ladd et al. (1977); Meigh (1987); Lunne et al. (1997); Mayne (2007)
Piezocone penetrometer (CPTu)	A Dutch cone penetrometer with a piezometer included at the point.	11.20(d)	Same as CPT; very effective with stratified cohesive deposits	Same as for CPT	ASTM (2010) D 5778; Lunne et al. (1997); Mayne (2007)
Pressuremeter (PMT)	A cylindrical probe is inserted in a drill hole (may be self-boring). Lateral pressure is applied incrementally to side of hole.	11.21	All soil types, provided that a stable and constant diameter borehole can be excavated	Requires a correlation between P_l and τ_f.	ASTM (2010) D 4719; Ménard (1956, 1975); Schmertmann (1975); Ladd et al. (1977); Baguelin et al. (1978); Mair and Wood (1987); Briaud (1992); Clarke (1995)
Flat Plate dilatometer test (DMT)	A flat 96 × 15 mm blade, sharpened at the end, with an inflatable 60 mm diameter steel disc on one face.	11.22	All soil types without gravel particles	Theoretical basis in elastic theory; soil properties from empirical correlations, not all equally reliable.	ASTM (2010) D 6635; Marchetti (1980); Schmertmann (1986); Briaud and Miran (1992); Sabatini et al. (2002)
Screw plate compressometer (SPC)	The plate is screwed down to the desired testing depth; hydraulic pressure is applied incrementally and the settlement is observed; continue loading until the bearing capacity of the soil is reached.	11.23	All soil types except very coarse granular soils	Mostly used to study the compressibility of granular soils. Schwab (1976) found good agreement with the screw plate and the VST in plastic Swedish clays.	Janbu and Senneset (1973); Mitchell and Gardner (1975); Schwab (1976); Schmertmann (1970)
Iowa borehole shear test (BST)	Device is lowered into a borehole and expanded against the side walls (σ_n). Then entire mechanism is pulled from ground surface and maximum shear load measured. Stage test results are used to plot Mohr diagram to get ϕ'. Range of σ_n is from about 30 to 100 kPa.	11.24	Loessial (silty) soils	Cannot be used with soils with 10% or more gravel or caving sands. Rate effects and uncertain drainage conditions during shear make the test difficult to interpret. (Is it CD or CU or somewhere in between? What is the effect of rate of shear?)	Wineland (1975); Schmertmann (1975); Handy (1986)

Because shear strength is determined indirectly, in situ tests give only an *index* of the actual shear strength of the soil. On the other hand, when correctly performed in the appropriate soil conditions, the results can be very useful to geotechnical engineers. For information on how to interpret in situ test results and select design parameters in geotechnical engineering practice, see Ladd et al. (1977), Jamiolkowski et al. (1985), Sabatini et al. (2002), and Canadian Geotechnical Society (2006), as well as the references in Table 11.1.

The *standard penetration test* (SPT) (Fig. 11.18) has been around for more than a century and is probably the most common in situ test in the world. The equipment is relatively simple, and the test can be performed with a conventional geotechnical drill rig in most soil types. However, it is best suited for testing sandy soils, because the SPT blow count N correlates well with density and, as we shall see in Chapter 12, indirectly with the friction angle of the sand. The SPT is sometimes used for cohesive soils, but it is much less accurate, and in fact the results are meaningless in soft, sensitive clays. Another big advantage of the SPT is that a sample is obtained, and although the sample is badly disturbed, it can be used for visual classification and index test. The SPT results are very dependent on the equipment details and even the person performing the test (Kovacs et al., 1977), so to get reasonably repeatable results, the measured N must be corrected for applied energy, rod length, and borehole diameter (Sabatini et al., 2002). Another important consideration is the liners that should be used inside the sampling spoon, and are often left out by the driller, which leads to underestimates of the blow count by about 20%.

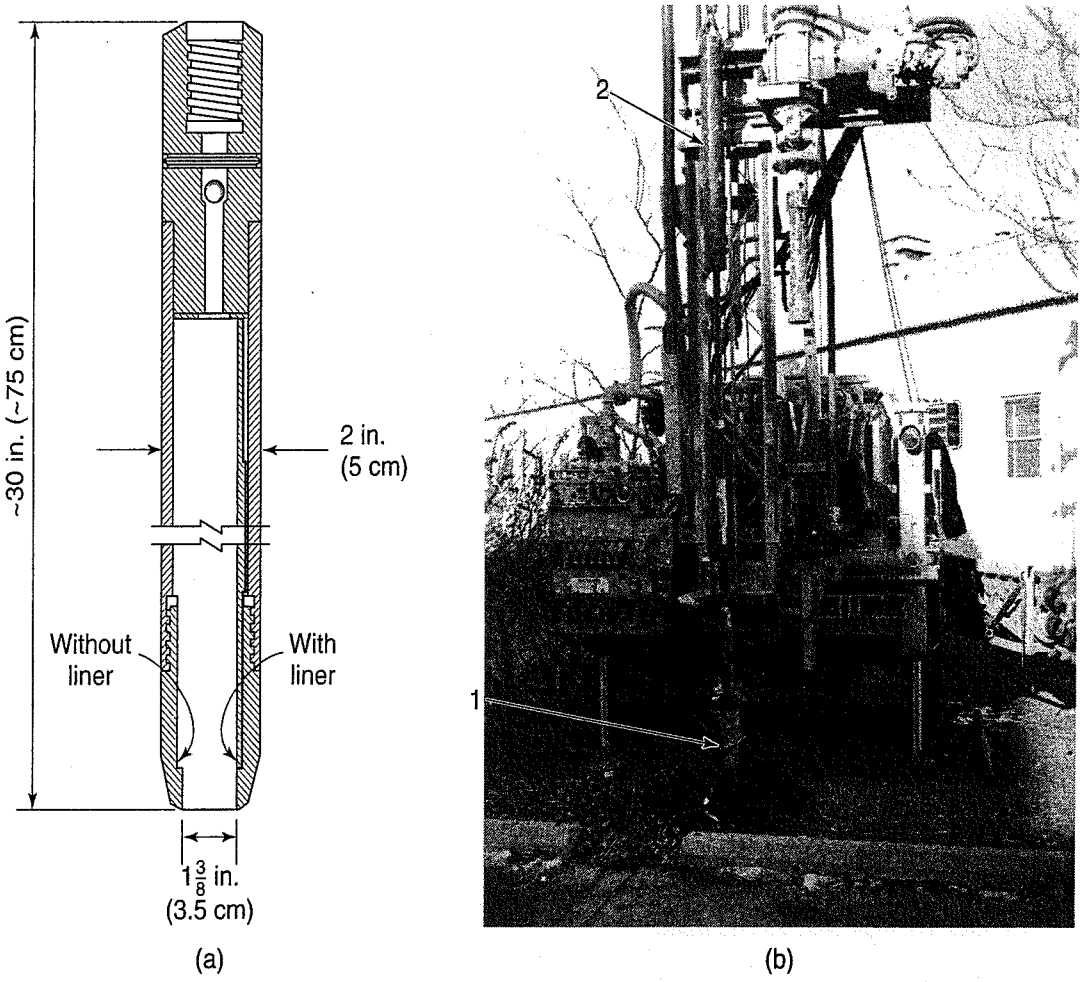

FIGURE 11.18 Standard penetration test (SPT): (a) "split-spoon" sampler; (b) drill rig with sampler being inserted inside hollow stem auger at 1. The sleeve encloses the 63.5 kg hammer. Hammer in the raised position is shown at 2. (Drawing courtesy of Mobile Drilling Co., Indianapolis, Indiana. Photograph by W. D. Kovacs.)

One of the best in situ tests for soft to medium clays is the *vane shear test* (VST; Table 11.1). As shown in Fig. 11.19(a), torque is applied to the vane rods and after some rotation of the vane, the soil shears along a cylindrical rupture surface [Fig. 11.19(b)]. Most field vanes have a height-to-diameter (H/D) ratio of 2; common sizes are 76 × 38 mm, 100 × 50 mm and 130 × 65 mm [the standard Swedish Geotechnical Institute (SGI) vane]. The shear strength is obtained from either empirical correlations or from theoretical formulas [Fig. 11.19(c)] relating the torque to an assumed shear stress distribution on the sides of the blades. Both approaches may be unreliable unless calibrated for local conditions. Cadling and Odenstad (1950) describe the calibration process for the SGI VST. Another possibility is to apply a correction factor for very soft clays based on embankment failures (see Sec. 12.11.4).

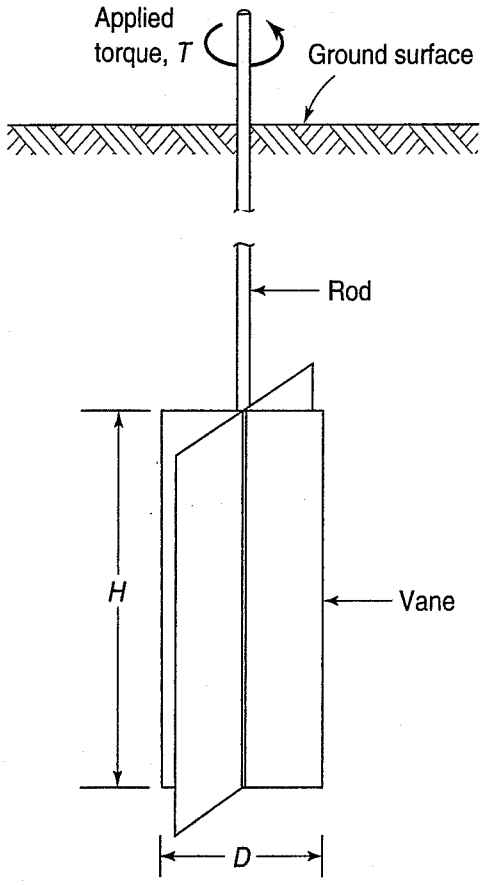

(c) Theorectical formulas:

$$\frac{H}{D} = 1: \quad \tau_f = \frac{3}{2}\frac{T_{max}}{\pi D^3}$$

$$\frac{H}{D} = 2: \quad \tau_f = \frac{6}{7}\frac{T_{max}}{\pi D^3}$$

FIGURE 11.19 (a) Principle of the vane shear test; (b) end view of the vane, showing the probable zone of disturbance and the rupture surface (after Cadling and Odenstad, 1950); (c) theoretical formulas for τ_f, assuming a uniform stress distribution.

As indicated in Table 11.1, the Dutch *cone penetrometer test* (CPT) can be used in sand soils as well as at sites with soft to stiff clays, as long as neither one has much gravel and larger particles. Because it is a quasi-static test, the CPT is especially effective in loose sands. The test was originally developed in the 1930s in Holland, thus its name. There are two types of Dutch cone penetrometers, mechanical and electrical. With the mechanical CPT [Fig. 11.20(a)], the cone and friction sleeve are pushed by a system of hydraulic jacks, and the point resistance q_c and sleeve friction f_s are measured by calibrated hydraulic load cells. The modern electrical cone uses strain gage load cells to make the same measurements [Fig. 11.20(b)]. An even more modern development is the *piezocone* penetrometer, which is basically a conventional electrical cone with peizometric ports. Two different peizocone configurations are shown in Fig. 11.20(c) along with the standard cone dimensions. In addition to the conventional measurements, the piezocone measures the induced pore water pressure during penetration, and if the test is stopped periodically, the dissipation of that pore pressure can be used to determine consolidation properties (Sec. 9.7). Figure 11.20(d) shows some typical CPT results; the soil profile is obtained either from correlations with q_c and f_s or from a nearby soil boring, because no samples of the subsurface are obtained with the CPT.

The principal features of the pressuremeter test (PMT) are shown in Fig. 11.21. The original Ménard pressuremeter has three cells, as shown in Fig. 11.21(b); the measuring cell is between the two outside guard cells. The OYO pressuremeter (lateral load tester, LLT) from Japan uses a single long cell that apparently gives similar results. After the borehole is excavated, the probe is lowered to

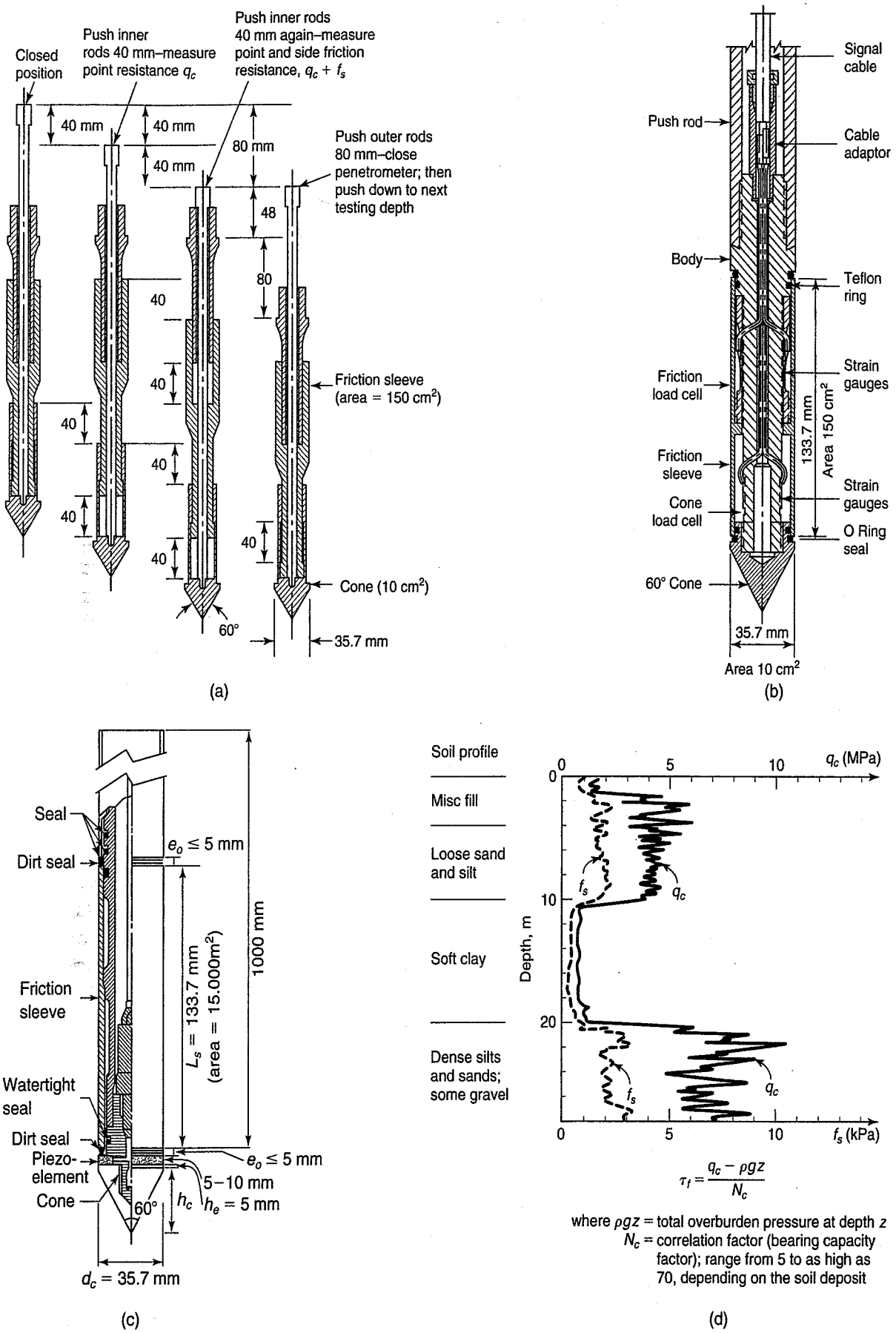

FIGURE 11.20 Dutch cone penetrometer (CPT): (a) Begemann (1953) mechanical cone with friction sleeve; (b) cross section of a modern electrical penetrometer with strain-gage load cells to measure both the point resistance and the sleeve friction (after Holden, 1974); (c) Dutch cone and piezocone configurations (after ASTM, 2010); (d) typical cone penetrometer test results correlated with the soil profile, and formula for calculating τ_f from cone penetrometer results.

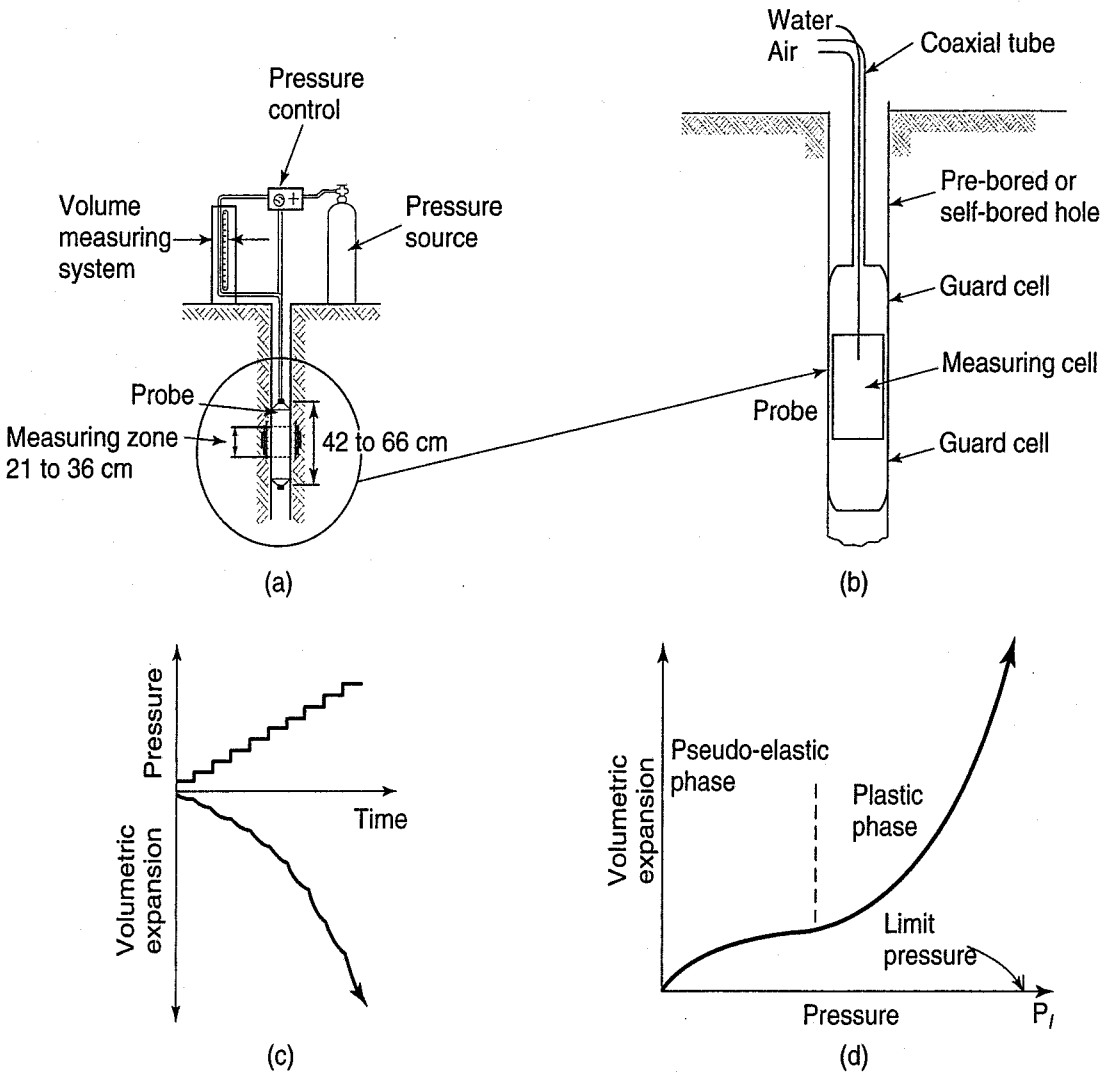

FIGURE 11.21 Pressuremeter test (PMT): (a) Schematic diagram of probe and measuring system (after Mitchell and Gardner, 1975); (b) detail of probe. Typical test results: (c) pressure and volumetric expansion versus time, and (d) volumetric expansion versus pressure (after Ménard, 1975).

the desired testing depth and inflated with equal increments of pressure [Fig. 11.21(c)] or volume and held for 60 s. The process is continued until the borehole yields or the maximum pressure or volume of the device is reached. Results are plotted as shown in Fig. 11.21(d). Although the limit pressure p_l depends on the shearing resistance of the soil in the borehole, it tends to greatly overpredict the undrained shear strength as determined on laboratory samples by other in situ tests. Thus, some type of local correlation is advisable (see the references in Table 11.1). There are problems in many soil deposits with the stability of the borehole, and a *self-boring pressuremeter* (SBPMT) helps to overcome some of these difficulties. However, the SBPMT is rather complex and requires considerable experience to obtain good results (refer to Jamiolkowski et al., 1985, for further details regarding this device).

The *dilatometer test* (DMT) was developed in Italy by Marchetti about 1980, and since then, because of considerable research and development, it has become rather popular, especially on the east coast of the United States and in Florida. The DMT equipment is shown in Fig. 11.22. The blade is pushed into the ground to the desired testing depth at a rate of 1.2 m/min. Then the membrane is gradually inflated and the pressures required to just move the membrane about 0.05 mm and to move it 1 mm are recorded. Sometimes the pressure during deflation is recorded at the point when the membrane deflection is again 0.05 mm. Marchetti used these readings and the theory of elasticity to develop the material and lateral stress indices as well as the dilatometer modulus. A number of other soil properties including

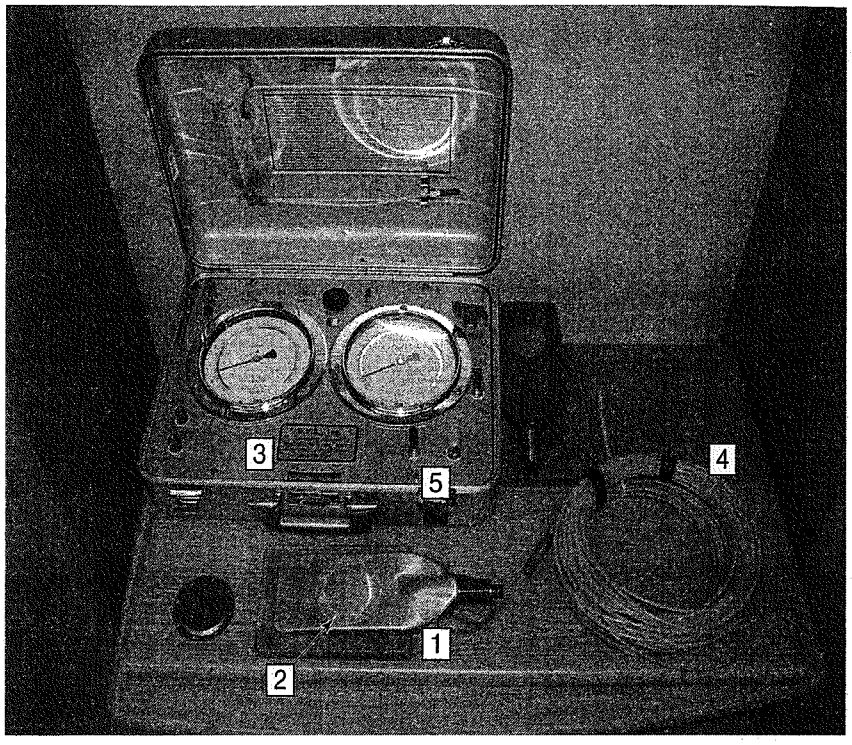

FIGURE 11.22 Flat plate dilatometer test (DMT) equipment: (1) blade; (2) expandable steel membrane; (3) control unit showing low- and high-pressure gages; (4) tubing and cabling for downhole control; and (5) valves for controlling and venting gas (photo courtesy of Prof. Paul Mayne).

the friction angle for sands and silts and the undrained shear strength of clays can be determined by empirical correlations.

The *screw plate compressometer* (SPC) was developed in Norway in the early 1970s. The principle and field test setup are shown in Fig. 11.23(a) and (b). Two sizes of plates, 160 mm and 300 mm, are commonly used, although smaller diameters may be better for very stiff clays. The plate and hydraulic loading system are screwed down to the desired testing depth, the pressure applied in increments typically held for 5 min, and the plate settlement recorded. Two ways of plotting the test data are shown in Fig. 11.23(c) and (d). One big advantage of the screw plate compressometer over the pressuremeter and dilatometer tests is that it loads the soil in the same direction as common foundation loading.

The *Iowa borehole shear test* was developed for use in loess soils in Iowa. The equipment is shown in Fig 11.24, and the procedure and limitations are briefly described in Table 11.1.

Other in situ tests you may encounter in practice include geophysical methods, the seismic cone test (SCPT) test, and the Becker penetration test (BPT). Geophysical methods such as seismic refraction and electrical resistivity have been used for many years, but not very commonly, for site characterization. In recent years, however, techniques such as ground-penetrating radar, SASW (spectral analysis of surface waves), geotomography, and several borehole logging techniques have been developed to where they are practical and economic. Many of these developments are described in the papers in Woods (1994). The SCPT gives information on subsurface shear wave velocity and damping, properties useful for geotechnical earthquake engineering. The Becker penetration test was developed in the late 1950s in Alberta for oil exploration in predominantly gravel sites (CGS, 2006). The BPT uses a double acting Diesel pile driving hammer (rated energy 11 kJ) to drive a double wall closed-ended casing up to 3 m in length and 230 mm in diameter rapidly through gravelly deposits. The driving resistance or blow counts of the BPT are roughly correlated with the SPT N (Harder and Seed, 1986) and Canadian Geotechnical Society (2006).

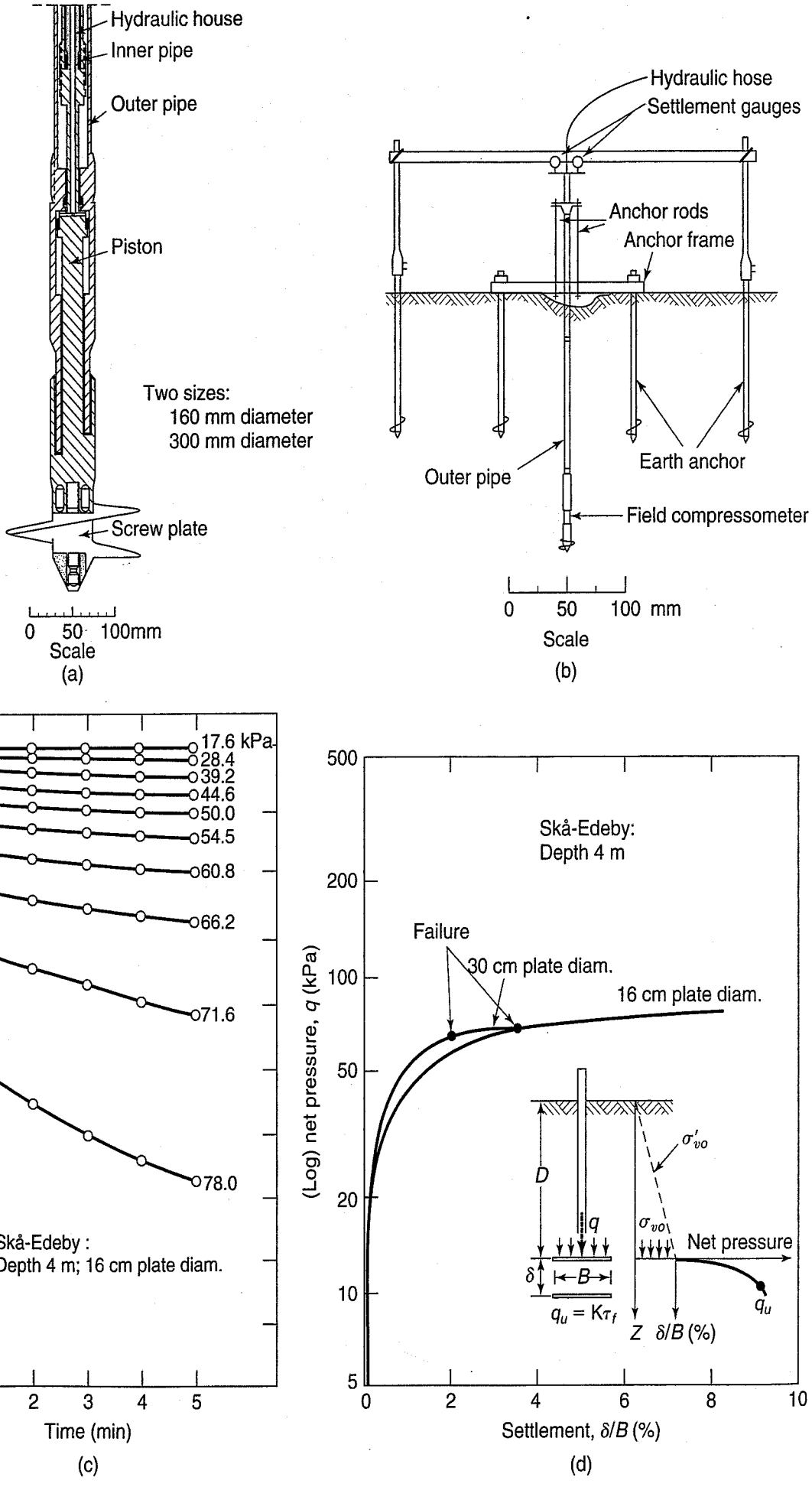

FIGURE 11.23 Screw plate compressometer (SPC): (a) principle; (b) field setup (after Janbu and Senneset, 1973); (c) settlement-time and (d) pressure-settlement data for Skå-Edeby clay, Sweden (after Schwab, 1976).

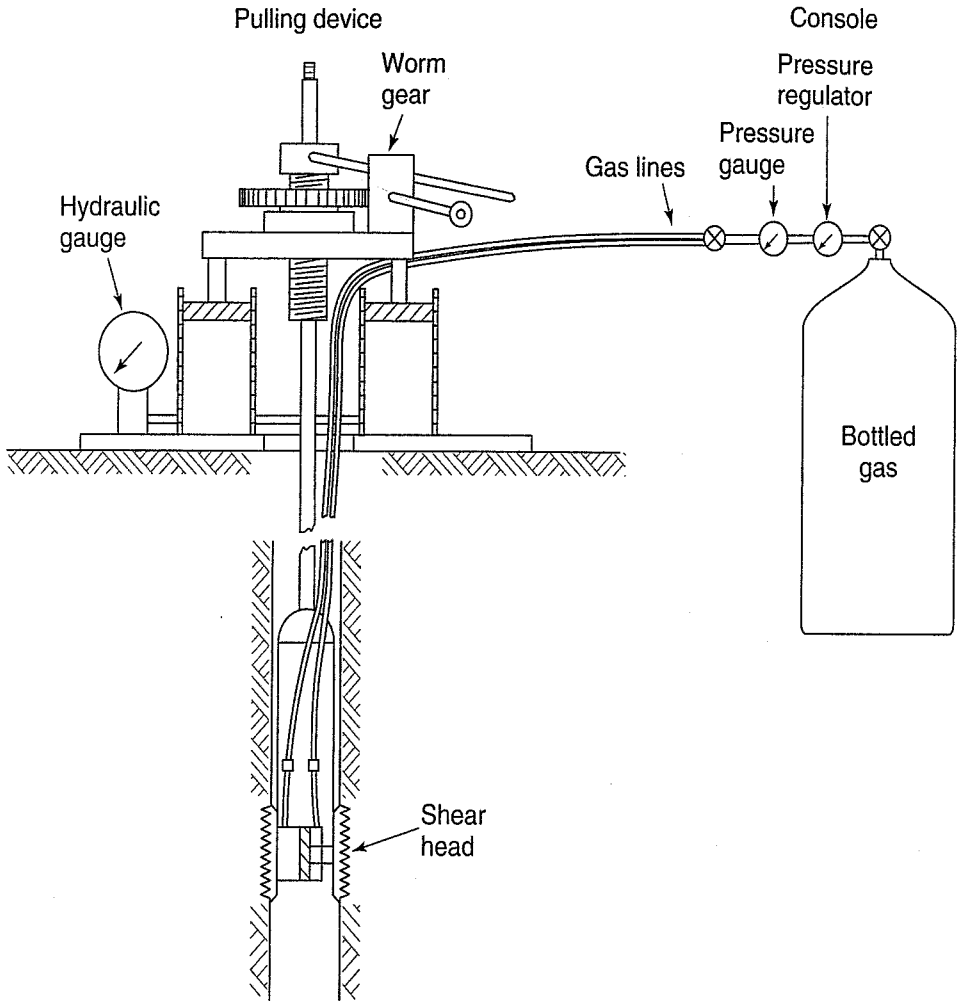

FIGURE 11.24 The Iowa borehole shear (BST) device, showing the pressure source and instrumentation console, the pulling device, and the expanded shear head on the sides of a borehole (after Wineland, 1975).

11.6.2 Field Tests for Modulus and Strength of Rocks

Depending on the type and size of the construction, it may be necessary to test the rocks at a site in situ rather than in the laboratory. The rocks at a site may be so fractured or weak that core drilling and undisturbed sampling are impossible. Sometimes size of the construction involves large loaded areas—for example, dams and bridges—and if the joints are closely spaced or infilled with highly weathered rock, undesirable settlements of the structure could occur. In such cases, to provide realistic design information, it would be necessary to test large specimens of the rock, which is impractical and too costly.

Field testing is especially needed to evaluate the strength across discontinuities that may negatively influence stability. The equipment is massive, because a large chunk of undisturbed rock is being tested. Large jacks are employed to provide the normal and the shear forces. See Wyllie (1999) and ASTM (2010) D 4554 for additional information and test details.

For weaker rock (RQD < 50%), an in situ *uniaxial compression test* may be performed by forming a square specimen from natural material in a tunnel, for example. The rock is loaded by a suitable jack using the surrounding rock as a reaction. See ASTM (2010) D 4555 for details.

Because compressibility is so important in many design situations, ASTM and ISRM have developed test procedures to provide information on the in situ modulus of rock.

Flatjack tests are performed in natural rock masses usually parallel to the long axis to a small tunnel or adit in order to provide information about the in situ state of stresses (normal to the flatjack)

in the rock and to obtain the modulus of deformation as a by-product. The flatjack consists of two steel plates welded together, having a surface area of about 600 cm^2. Measuring points are constructed on the rock face. A slot is drilled into the rock face by means of overlapping holes, and the flatjack is inserted and grouted in place. A hydraulic pressure is applied to the inside of the jack to overcome the deformation cause by creating the slot, and this gives the initial in situ stresses. Using elastic theory, the modulus of deformation is also found. Refer to Goodman (1989), ASTM (2010) D 4729 and ISRM Method No. 33 (Ulusay and Hudson, 2007) for further details.

The *borehole jack* (or the Goodman jack) is inserted into a borehole in rock and expanded diametrically, sometimes in various orientations (to obtain an estimate of anisotropy). Applied pressure and borehole diameter are observed and the modulus of deformation calculated. Sometimes the borehole jack is called a stiff dilatometer. Additional details and test procedure are found in ASTM D 4971 and ISRM Method No. 38 (Ulusay and Hudson, 2007).

ISRM Method No. 35 (Ulusay and Hudson, 2007) is a procedure for determining the deformability of rock using a flexible dilatometer test. Other in situ tests for rock modulus include various types of plate load tests and radial jacking tests; see Wyllie (1999) for additional information.

Finally, geophysical methods such as seismic refraction, electrical resistivity, and ground penetrating radar have been successfully used to supplement information provided by good old-fashioned geologic mapping for geotechnical site investigations (refer to Mayne et al., 2001, for a survey of these methods).

PROBLEMS

11.1 Given an element with stresses as indicated in Fig. P11.1. Find:

(a) The major and minor principal stresses and the planes on which they act.
(b) The stresses on a plane inclined at 30° from the horizontal.
(c) The maximum shear stress and the inclination of the plane on which it acts.

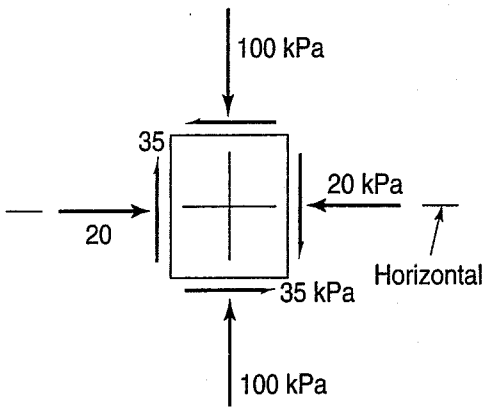

FIGURE P11.1

11.2 Work Problem 11.1 with the element rotated 30° clockwise from the horizontal.

11.3 With the element of Problem 11.2 rotated 40°, find the magnitude and direction of the stresses on the *vertical* plane.

11.4 Work Example 11.3 with the element rotated 30° clockwise from the horizontal. In addition, find the stresses (magnitude and direction) on the horizontal plane.

11.5 Equations (11.5) and (11.6) were derived from Fig. 11.2, with σ_x and σ_y as principal stresses. Derive the more general equations for the Mohr circle when σ_x and σ_y are *not* acting on principal planes.

11.6 The state of plane stress in a body is described by the following stresses: $\sigma_1 = 8500$ kN/m^2 compression, $\sigma_3 = 1500$ kN/m^2 tension. Determine by means of the Mohr circle the normal stress and shear stress on a plane inclined at 20° to the plane on which the minor principal stress acts. Check the results analytically. (After A. Casagrande.)

11.7 At a certain critical point in a steel beam, on a vertical plane the compressive stress is 115 MPa and the shearing stress is 31.5 MPa. There is no normal stress on the longitudinal (horizontal) plane. Find the stresses acting on the principal planes and the orientation of principal planes with the horizontal. (After Taylor, 1948.)

11.8 A soil sample is under a biaxial state of stress. On plane 1, the stresses are (13, 4), while on plane 2, the stresses are (5.8, −2). Find the major and minor principal stresses.

11.9 For the element shown in Fig. P11.9: (a) Find the magnitude of the unknown stresses σ_h and τ_h on the horizontal plane. (b) Find the orientation of the principal stresses; clearly indicate their orientation in a small sketch. (c) Show the orientation of the planes of maximum as well as minimum shear.

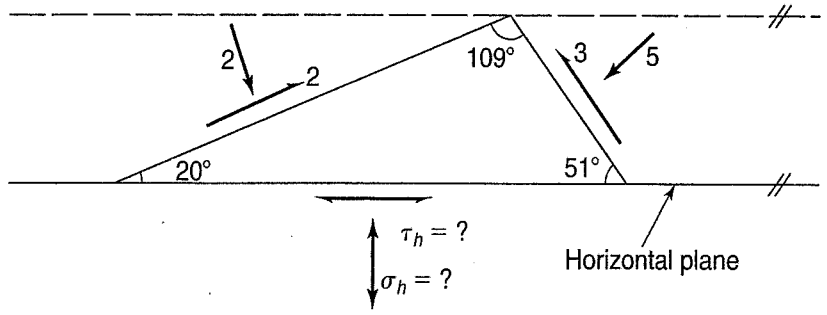

FIGURE P11.9

11.10 Given the element with stresses as shown in Fig. P11.10: (a) Find the magnitude and direction of σ_H and τ_H. (b) Find the magnitude and direction of σ_1 and σ_3. Be sure to clearly indicate these stresses and their directions on a separate sketch.

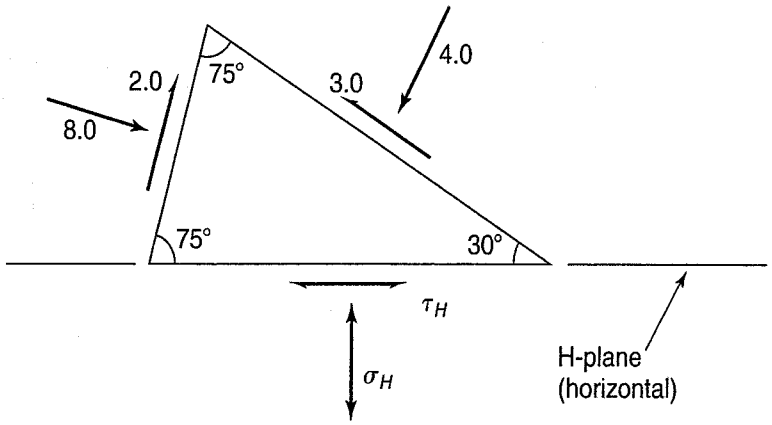

FIGURE P11.10

11.11 Given the data of Example 11.5. (a) Find the magnitude and direction of the stresses on the horizontal plane. (b) Find the maximum shear stress, and determine the angle between the plane on which it acts and the major principal plane.

11.12 The state of stress on a small element is σ_v = 21 kPa, σ_h = 10 kPa, and the shear stress on the horizontal plane is +3 kPa. (a) Find the magnitude and directions of the major and minor principal stresses. (b) If the material is a loose sand, can you say whether the element is in a state of failure? If it isn't, how close is it? Why? State your assumptions clearly. (Assume ϕ = 28° for the loose sand.)

11.13 Given the vertical and horizontal normal stresses of Problem 11.12. Find the maximum values of shear stress on the horizontal and vertical planes to cause failure in a medium dense sand. Assume the angle of internal friction for the sand is 32°.

11.14 The state plane stress in a mass of dense cohesionless sand is described by the following stresses:

Normal stress on horizontal plane = 296 kPa

Normal stress on vertical plane = 160 kPa

Shear stress on horizontal and vertical planes = ± 64 kPa

Determine by means of the Mohr circle the magnitude and direction of the principal stresses. Is this state of stress safe against failure? (After A. Casagrande.)

11.15 At a given point within a sand deposit the major, intermediate, and minor principal stresses are 10, 6, and 4 MN/m^2, respectively. Construct the Mohr diagram, and from it scale the normal and shearing stresses and the obliquity angles on planes at 35°, 50°, 65°, and 80° from the major principal plane. (After Taylor, 1948.)

11.16 A 1-m cube within a mass of stressed soil has a stress of 200 kPa on its top and bottom faces, 100 kPa on one pair of vertical faces, and 60 kPa on the other pair of vertical faces. There is no shear stress on any face. Fill in the numerical values for each stress and angle in the following table. (After Taylor, 1948.)

	σ (kPa)	τ (kPa)	α
Major principal plane:			
Intermediate principal plane:			
Minor principal plane:			
Plane of maximum shearing stress:			
Plane of maximum obliquity:			

Note: α is the angle of orientation of the required plane with respect to the horizontal plane.

11.17 In Problem 11.16 what is ϕ, assuming $c = 0$?

11.18 Show that on a plane inclined at 45° with respect to the principal planes, the ratio of τ_{max} to $(\sigma_1 + \sigma_3)/2$ is in fact less than τ_{ff}/σ_{ff}. (*Hint:* Assume a ϕ, σ_1, and σ_3.)

11.19 Figure P11.19 shows stresses at a point.

(a) Draw the Mohr circle for this point, showing the pole location.

(b) What are the stresses acting on a horizontal plane passing through this point?

(c) The cohesion intercept for this soil is c = 5 psi, and the friction angle is $\phi = 30°$. If the major principal stress remains the same, what would the minor principal stress have to be to cause failure?

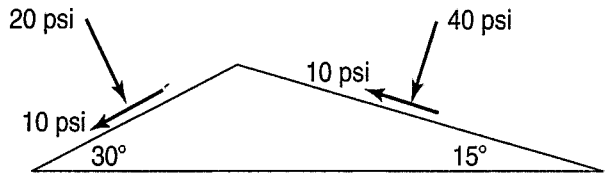

FIGURE P11.19

11.20 Figure P11.20 shows an element of soil at the interface between two dry sand layers on a 28° slope. The interface is 10 ft below the ground surface, and for both sand layers the friction angle is 34° and $K_o = 0.44$. Assume that the shear stress is zero on both the vertical and horizontal planes.

(a) Draw the Mohr circle for this point, and determine the pole location.

(b) Determine the normal and shear stresses on the soil interface (i.e., on the 28° plane).

(c) For the same normal stress, σ, found in part (b), what would be the shear stress at failure on the failure plane?

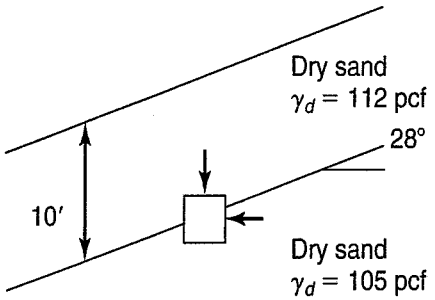

FIGURE P11.20

11.21 Prove that Eq. (11.10) is true, assuming that the Mohr–Coulomb failure criterion is valid. Does it matter if $c = 0$? (*Hint:* Derive the equation first with $c = 0$, then with $c \neq 0$.)

11.22 Show that Eq. (11.13) is identical to Eq. (11.14).

11.23 Equation (11.14) is true if $c = 0$. Derive the expression for the principal stress ratio, including the strength parameter c.

11.24 Show that Eq. (11.17) is true from Eq. (11.16).

11.25 Show that Eqs. (11.16) and (11.17) are identical to Eqs. (11.14) and (11.15). (This is a good review of trigonometric identities!)

11.26 In a direct shear test on a specimen of cohesionless sand, the vertical normal stress on the specimen is 240 kN/m^2 and the horizontal shear stress at failure is 160 kN/m^2. (a) Assuming uniform stress distribution within the failure zone and a straight line failure envelope which goes through the origin, determine by means of the Mohr circle the magnitude and direction of the principal stresses at failure. (b) Explain why it is not possible to determine the principal stresses in a direct shear specimen for an applied horizontal shear stress which is not large enough to cause failure. (After A. Casagrande.)

11.27 A specimen of sand is tested in direct simple shear. The stress conditions in the test are as shown in Fig. Ex. 11.9.

Initial conditions:

$$\sigma_v = 3.12 \text{ kg/cm}^2, \quad K_o = 0.5$$

At failure:

$$\sigma_v = 3.12 \text{ kg/cm}^2, \quad \tau_{hv} = 1.80 \text{ kg/cm}^2$$

(a) Draw the Mohr circles for both initial and final stress conditions.
(b) Show clearly the locations of the poles of these circles.
(c) Determine the magnitude and orientation of the principal stresses at failure.
(d) What is the orientation of the failure plane?
(e) If the shear strain at failure is 10° as shown in the figure, what are the stresses σ_s and τ_s on the sides of the specimen at failure?

(*Note:* $\tau_s \neq \tau_{hv}$.)

11.28 Two conventional CD triaxial compression tests were conducted on a dense angular dry sand at the same void ratio. Test A had a confining pressure of 150 kPa, while in test B the confining pressure was 600 kPa; these stresses were held constant throughout the test. At failure, tests A and B had maximum principal stress differences of 600 and 2550 kPa, respectively.

(a) Plot the Mohr circles for both tests at initial conditions and at failure.
(b) Assuming $c = 0$, determine ψ.
(c) What is the shear stress on the failure plane at failure for both tests?
(d) Determine the theoretical orientation of the failure plane in each specimen.
(e) What is the orientation of the plane of maximum obliquity?

11.29 Two consolidated–drained triaxial tests were performed on specimens of the same clay, with the following results at failure:

Test no.	σ_3' (psi)	σ_1' (psi)
1	26.6	73.4
2	12.0	48.0

Determine the effective Mohr–Coulomb failure envelope (c' and ϕ') based on these test results.

11.30 A triaxial specimen of loose sand is first consolidated nonhydrostatically, with $\sigma_1 = 15$ kPa and $\sigma_3 = 10$ kPa. The sample is then failed by holding the vertical stress constant and decreasing the horizontal stress (this is a lateral extension test). The angle of internal friction is 30° ($c = 0$). (a) Draw the Mohr circles for both initial and "at failure" conditions. (b) What will be the major and minor principal stresses at failure?

11.31 Another sample of the same sand tested in Problem 11.30 is tested by holding the vertical stress constant and increasing the horizontal stress (this is a lateral compression test). Complete parts (a) and (b) requested in Problem 11.30 for this test.

CHAPTER 12

An Introduction to Shear Strength of Soils and Rock

12.1 INTRODUCTION

The shear strength of soils and rock is a most important aspect of geotechnical engineering. The bearing capacity of shallow or deep foundations, slope stability, retaining wall design and, indirectly, pavement design are all affected by the shear strength of the soil in a slope, behind a retaining wall, or supporting a foundation or pavement. Structures and slopes must be stable and secure against total collapse when subjected to maximum anticipated applied loads. The collapse or failure state is called the ultimate or *limit state*, and *limiting equilibrium* methods of analysis are conventionally used for the design of foundations and slopes. These methods require determination of the ultimate or limiting shear resistance (shear strength) of the soil and rock.

In Chapter 11, we defined the shear strength of a soil as the ultimate or maximum shear stress the soil can withstand. We mentioned that sometimes the limiting value of shear stress is based on a maximum allowable strain or deformation. Very often, this allowable deformation actually controls the design of a structure, because, with the large safety factors we use, the actual shear stresses in the soil produced by the applied loads are much less than the stresses causing collapse or failure.

The shear strength can be determined in several different ways; we described some of the more common laboratory and field tests in Secs. 11.5 and 11.6. We mentioned that laboratory tests give the shear strength directly, while in situ methods such as the vane shear test or penetrometers avoid some of the problems of disturbance associated with the extraction of soil samples from the ground. However, in situ tests determine the shear strength only indirectly through correlations with laboratory results or back calculated from actual failures. In addition, laboratory tests provide valuable information about the stress-strain behavior and the development of pore pressures during shear. In this chapter, we illustrate the fundamental stress-deformation and shear strength response of soils using the results of laboratory tests for typical soils. In this way, we hope you can gain some understanding of how soils actually behave when sheared. Chapter 13 presents more advanced topics in shear strength, including specialized test methods, more complex soil behavior and stress paths, dynamic behavior, advanced analytical methods, and applications to engineering practice.

In this chapter we draw heavily on the work of our teachers and colleagues. We gratefully acknowledge the important contributions by A. Casagrande, R. C. Hirschfeld, C. C. Ladd, K. L. Lee, G. A. Leonards, J. O. Osterberg, H. G. Poulos, and H. B. Seed. Other pioneers in the field of geotechnical engineering are also cited in both this chapter and Chapter 13, including L. Bjerrum, T. W. Lambe, J. K. Mitchell, R. B. Peck, and A. W. Skempton. Our discussion of shear strength of soils starts with sands and is followed by the strength properties of cohesive soils.

The following notation is introduced in this chapter.

Symbol	Dimension	Unit	Definition
A	–	–	Particle angularity
$A, \bar{A}, B$	–	–	Skempton's pore pressure parameters
A_o, A_s	L^2	m^2	Initial specimen area and area at some strain, respectively - Eq. (12.11)
C_v, C_{sk}, C_w	$M^{-1}LT^2$	1/kPa	Compressibility of the soil skeleton, pore fluid, and water, respectively - Eq. (12.15)
c, c', c_T	$ML^{-1}T^{-2}$	kPa	Intercept on τ axis when $\sigma = 0$
e_c	–	(decimal)	Void ratio after consolidation
e_{crit}	–	(decimal)	Critical void ratio
e_{cd}	–	(decimal)	e_{crit}-dense
e_{cl}	–	(decimal)	e_{crit}-loose
e_d	–	(decimal)	e-dense
e_l	–	(decimal)	e-loose
h	–	–	An empirical exponent - Eq. (12.9)
K_D	–	–	Horizontal stress index for flat-plate dilatometer - Eq. (12.7)
K_{o-oc}, K_{o-nc}	–	–	Coefficient of lateral earth pressure at rest, overconsolidated and normally consolidated soil, respectively - Eq. (12.9)
q_c	$ML^{-1}T^{-2}$	kPa	Cone tip resistance - Eq. (12.6)
q_u	$ML^{-1}T^{-2}$	kPa	Unconfined compressive strength
R	–	–	Particle surface roughness
S	L	m	Particle size
S_t	–	–	Shear strength sensitivity - Eq. (12.12)
u_o	$ML^{-1}T^{-2}$	kPa	Initial pore water pressure; back pressure
u_r	$ML^{-1}T^{-2}$	kPa	Residual (capillary) pore water pressure after sampling
V_o	L^3	m^3	Initial volume - Eq. (12.4)
ΔV	L^3	m^3	Change in volume - Eq. (12.4)
ε_v	–	(%)	Vertical or axial strain
μ	–		Correction factor to vane shear strength
σ_{hc}	$ML^{-1}T^{-2}$	kPa	Total horizontal consolidation stress
σ_{vc}	$ML^{-1}T^{-2}$	kPa	Total vertical consolidation stress
σ'_{3c}	$ML^{-1}T^{-2}$	kPa	Effective consolidation pressure
$\sigma'_{3\,crit}$	$ML^{-1}T^{-2}$	kPa	Critical effective confining pressure
σ'_{3f}	$ML^{-1}T^{-2}$	kPa	Effective confining pressure at failure
σ'_1/σ'_3			Principal effective stress ratio - Eq. (12.1)
$(\sigma_1 - \sigma_3)$	$ML^{-1}T^{-2}$	kPa	Principal stress difference - Eq. (12.2)
τ_f	$ML^{-1}T^{-2}$	kPa	Undrained shear strength
ϕ'_d		(degree)	Angle of internal friction from CD tests
ϕ', ϕ_T		(degree)	Angle of internal friction in terms of effective stress and total stress, respectively

Note: A prime mark on an angle or stress indicates *effective stresses*. Subscripts o, c, and f indicate initial, consolidation, and failure conditions, respectively.

12.2 ANGLE OF REPOSE OF SANDS

If we were to deposit a granular soil by pouring it from a single point above the ground, it would form a conical pile. As more and more granular material was deposited on the pile, the slope for a short period of time might appear to be steeper, but then the soil particles would slip and slide down the slope to the *angle of repose* (Fig. 12.1). This angle of the slope with respect to the horizontal plane would remain constant at some *minimum* value. Since this angle is the steepest *stable* slope for very loosely packed sand, the angle of repose represents the angle of internal friction of the granular material at its *loosest* state.

Sand dunes are an example from nature of the angle of repose. You may recall from Sec. 3.3.6 that sand dunes are landforms resulting from wind as a geologic process. Figure 12.2 shows how both a stationary dune (SD) and a migrating dune (MD) are formed. On the leeward side (LS), the slope of the dune will have an angle (of repose) which varies from 30° to 35°, depending on factors discussed later in this chapter. If the slope on the leeward side becomes steeper than 30° to 35°, then the slope is unstable and sand grains will roll down the slope until the angle of repose is reached. An unstable condition is shown on the slope at the far right-hand side of Fig. 12.2; eventually a smooth slope at the angle of repose will form.

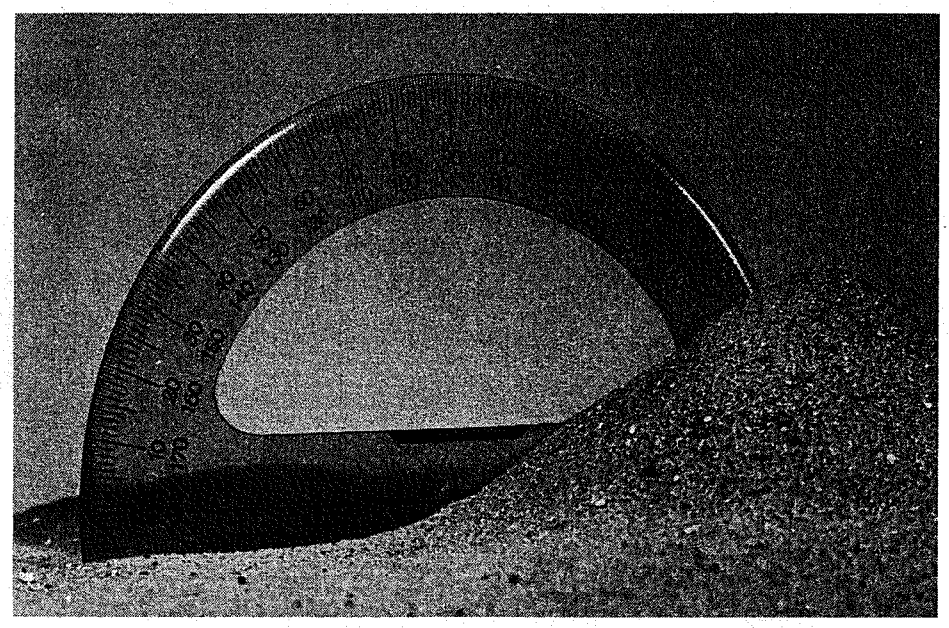

FIGURE 12.1 Illustration of the angle of repose (photograph by M. Surrendra).

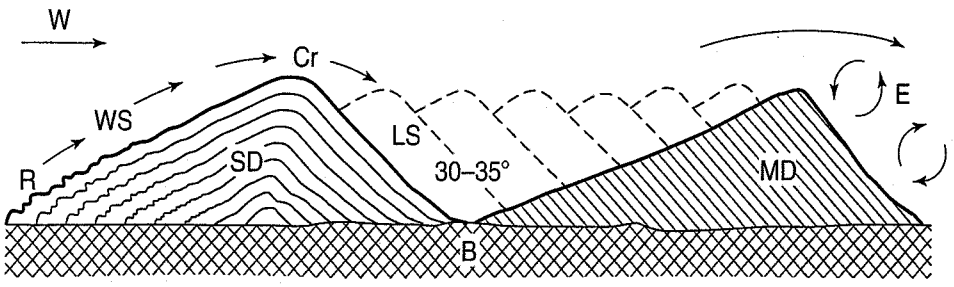

FIGURE 12.2 Formation of sand dunes and illustration of the angle of repose (after von Bandat, 1962). Deposition of sand by wind. Ideal structure of stationary or fixed dunes (SD) and migrating live dunes (MD). The arrows indicate the direction of air currents (W). E shows eddies. WS is the windward slope of the dune, LS the leeward, or down-wind slope. R mark ripples, and Cr is the crest of the dune. Dashed lines show the former positions of live dune MD. B is the base rock (after A. Holmes).

The angle of repose depends on the type of materials and other factors, and it represents the angle of internal friction or shearing resistance ϕ at its loosest state. Recall that the terms *loose* or *dense* are only relative terms (see Sec. 4.9), especially with respect to their behavior in shear. As we shall soon see, the stress-strain and volume change response depends on the confining pressure as well as on the index density. Note that in Section 5.5.1 we defined the relative density, D_r, sometimes referred to as the index density.

12.3 BEHAVIOR OF SATURATED SANDS DURING DRAINED SHEAR

To illustrate the behavior of sands during shear, let's start by taking two specimens of sand—one at a very high void ratio, the "loose" sand, and the other at a very low void ratio, the "dense" sand. We could perform direct shear tests [Fig. 11.14(a)], but to better measure the volume changes we shall use the triaxial apparatus, as shown in Figs. 11.15(a) and 12.3. We will run the two tests under consolidated drained (CD) conditions, which means we will allow water to freely enter or leave the specimen during shear without interference. If we have a saturated specimen, we can easily monitor the amount of water that enters or leaves it and equate this to the volume change and thus the void ratio change in the specimen. Water leaving the specimen during shear indicates a volume decrease, and vice versa. In both our tests the confining pressure, σ_c equals σ_3, is held constant and the axial stress is increased until failure occurs. Failure may be defined as:

1. Maximum principal stress difference, $(\sigma_1 - \sigma_3)_{max}$.
2. Maximum principal effective stress ratio, $(\sigma_1'/\sigma_3')_{max}$.
3. $\tau = [(\sigma_1 - \sigma_3)/2]$ at a prescribed strain.

Most of the time, we will define failure as the *maximum principal stress difference*, which is the same as the *compressive strength* of the specimen. Typical stress-strain curves for loose and dense sand are shown in Fig. 12.4(a), while the corresponding stress versus void ratio curves are presented in Fig. 12.4(b).

When the loose sand is sheared, the principal stress difference gradually increases to a maximum or ultimate value $(\sigma_1 - \sigma_3)_{ult}$. Concurrently, as the stress is increased, the void ratio *decreases*

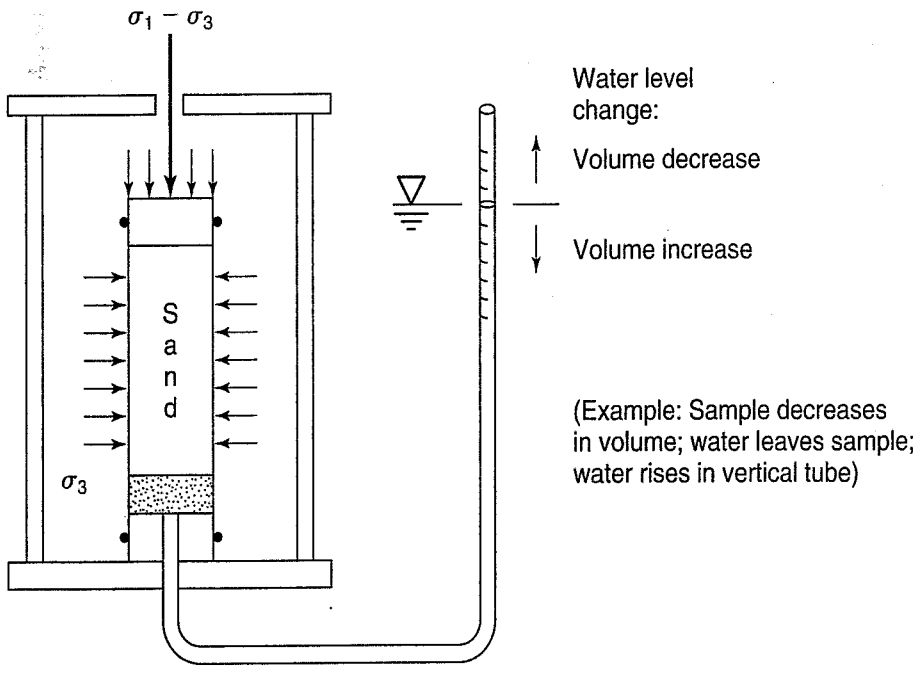

FIGURE 12.3 Consolidated-drained triaxial test with volume change measurements.

from e_l (e-loose) down to e_{cl} (e_c-loose), which is very close to the *critical void ratio*, e_{crit}, which Casagrande (1936a) defined as the ultimate void ratio at which continuous deformation occurs with no change in principal stress difference.

When the dense specimen is sheared, the principal stress difference reaches a peak or maximum, after which it decreases to a value very close to $(\sigma_1 - \sigma_3)_{ult}$ for the loose sand. The void ratio-stress curve shows that the dense sand decreases in volume slightly at first, then *expands* or *dilates* up to e_{cd} (e_c-dense). Notice that the void ratio at failure e_{cd} is very close to e_{cl}. Theoretically, they both should be equal to the *critical void ratio* e_{crit}. Similarly, the values of $(\sigma_1 - \sigma_3)_{ult}$ for both tests should be the same. The differences are usually attributed to difficulties in precise measurement of ultimate void ratios as well as nonuniform stress distributions in the test specimens (Hirschfeld, 1963). Evidence of this latter phenomenon is illustrated by the different ways in which the specimens usually fail. The loose specimen just *bulges*, while the dense specimen often fails along a distinct plane oriented approximately $45° + \phi'/2$ from the horizontal (ϕ' is, of course, the *effective* angle of shearing resistance of the dense sand). Note that it is at least theoretically possible to set up a sample at an initial void ratio such that the volume change at failure would be zero. This void ratio would, of course, be the critical void ratio e_{crit}.

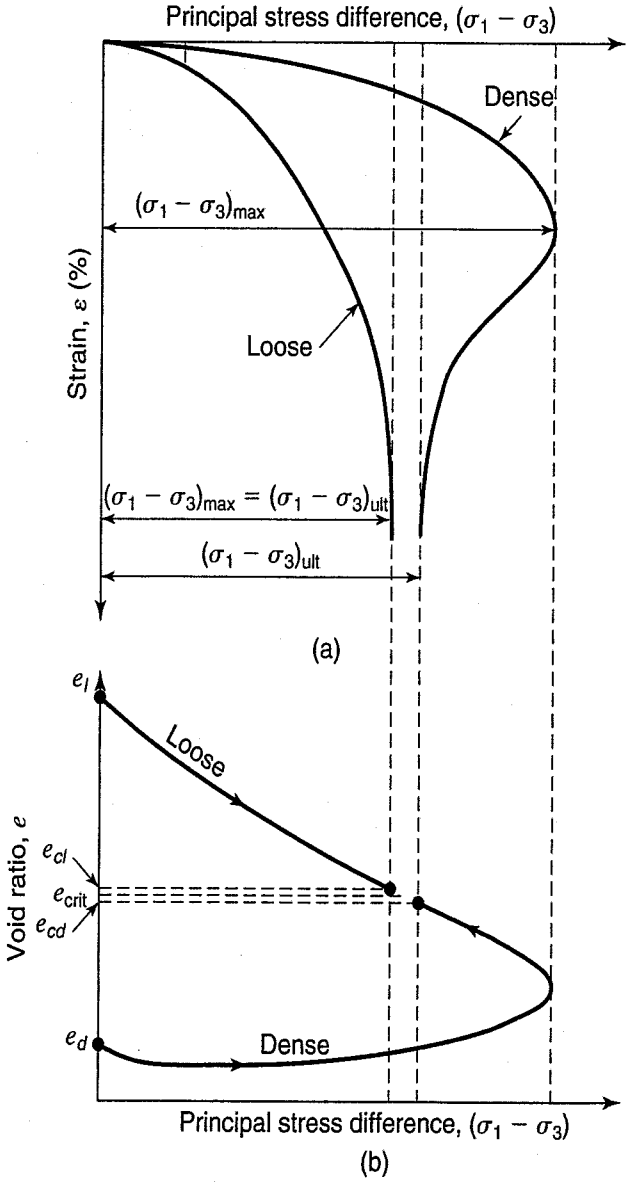

FIGURE 12.4 Triaxial tests on "loose" and "dense" specimens of a typical sand: (a) stress-strain curves; (b) void ratio changes during shear (after Hirschfeld, 1963).

Example 12.1

Given:

An apparatus shown in Fig. Ex. 12.1 consists of a rubber squeeze bulb filled with *dense* sand connected to a glass tube. The bulb and sand are completely saturated with water.

Required:

If the bulb is squeezed, describe what happens to the water level in the glass tube. Will it go up, down, or remain the same?

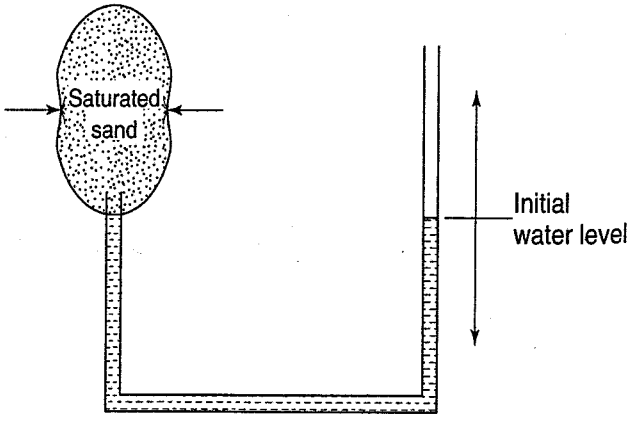

FIGURE Ex. 12.1

Solution: Because the sand is dense, it tends to dilate or expand when sheared. This action creates a slightly negative pressure in the water, which draws water into the voids and causes the level in the glass tube to move downward.

Example 12.2

Given:

The same apparatus as for Example 12.1, only now the bulb is filled with *loose* sand.

Required:

Predict the behavior of the water level in the glass tube when the bulb is squeezed (Fig. Ex. 12.1).

Solution: When loose sand is sheared, the soil tends to decrease in volume. This action creates a positive pressure in the water, which squeezes water out of the voids. Thus the water level in the tube will move upward.

It follows that if the sand in the bulb is at its critical void ratio, then upon squeezing (shearing) the bulb, the water level may at first decrease slightly, but with continued squeezing it will return to its original level; that is, no net volume change will occur when the sand is at e_{crit}.

12.4 EFFECT OF VOID RATIO AND CONFINING PRESSURE ON VOLUME CHANGE

Thus far, in describing the behavior of the two drained triaxial tests on loose and dense sands shown in Fig. 12.4, we have mentioned the following parameters:

- principal stress difference
- strain
- volume change
- critical void ratio e_{crit} and indirectly,
- relative or index density [Eqs. (5.4) and (5.5)]

We have purposely avoided defining the terms *loose* and *dense* because the volume change behavior during shear depends not only on the initial void ratio and relative density but also on the confining pressure. In this section we consider the effect of confining pressure on the stress-strain and volume change characteristics of sands in drained shear.

We can assess the effects of σ_3 (and, remember, in a drained test $\sigma_3 = \sigma'_3$, as the excess pore water pressure is always zero) by preparing several samples at the same void ratio and testing them at different confining pressures. We will find that the shear strength increases with σ_3. A convenient way to plot the principal stress difference versus strain data is to *normalize* it by plotting the *principal stress ratio* σ_1/σ_3 versus strain. For a drained test, of course, $\sigma_1/\sigma_3 = \sigma'_1/\sigma'_3$. At failure, the ratio is $(\sigma'_1/\sigma'_3)_{max}$. From Eqs. (11.14) and (11.16),

$$\left(\frac{\sigma'_1}{\sigma'_3}\right)_{max} = \frac{1 + \sin\phi'}{1 - \sin\phi'} = \tan^2\left(45 + \frac{\phi'}{2}\right) \tag{12.1}$$

where ϕ' is the *effective* angle of internal friction. The principal stress difference is related to the principal stress ratio by

$$\sigma_1 - \sigma_3 = \sigma'_3\left(\frac{\sigma'_1}{\sigma'_3} - 1\right) \tag{12.2}$$

At failure, the relationship is

$$(\sigma_1 - \sigma_3)_f = \sigma'_{3f}\left[\left(\frac{\sigma'_1}{\sigma'_3}\right)_{\max} - 1\right] \tag{12.3}$$

Let's look first at the behavior of loose sand. Typical drained triaxial test results are shown for loose Sacramento River sand in Fig. 12.5(a). The principal stress ratio is plotted versus axial strain for different effective consolidation pressures σ'_{3c}. Note that none of the curves has a distinct peak, and they have a shape similar to the loose curve shown in Fig. 12.4(a). The volume change data is also normalized by dividing the volume change ΔV by the original volume V_o to obtain the volumetric strain, or

$$\text{volumetric strain, \%} = \frac{\Delta V}{V_o} \times 100 \tag{12.4}$$

To better appreciate what is going on in Fig. 12.5(a), let us compute the principal stress difference $(\sigma_1 - \sigma_3)$ at a strain of 5% for $\sigma'_{3c} = 3.9$ MPa and $\sigma'_{3c} = 0.1$ MPa. The principal stress ratios for these

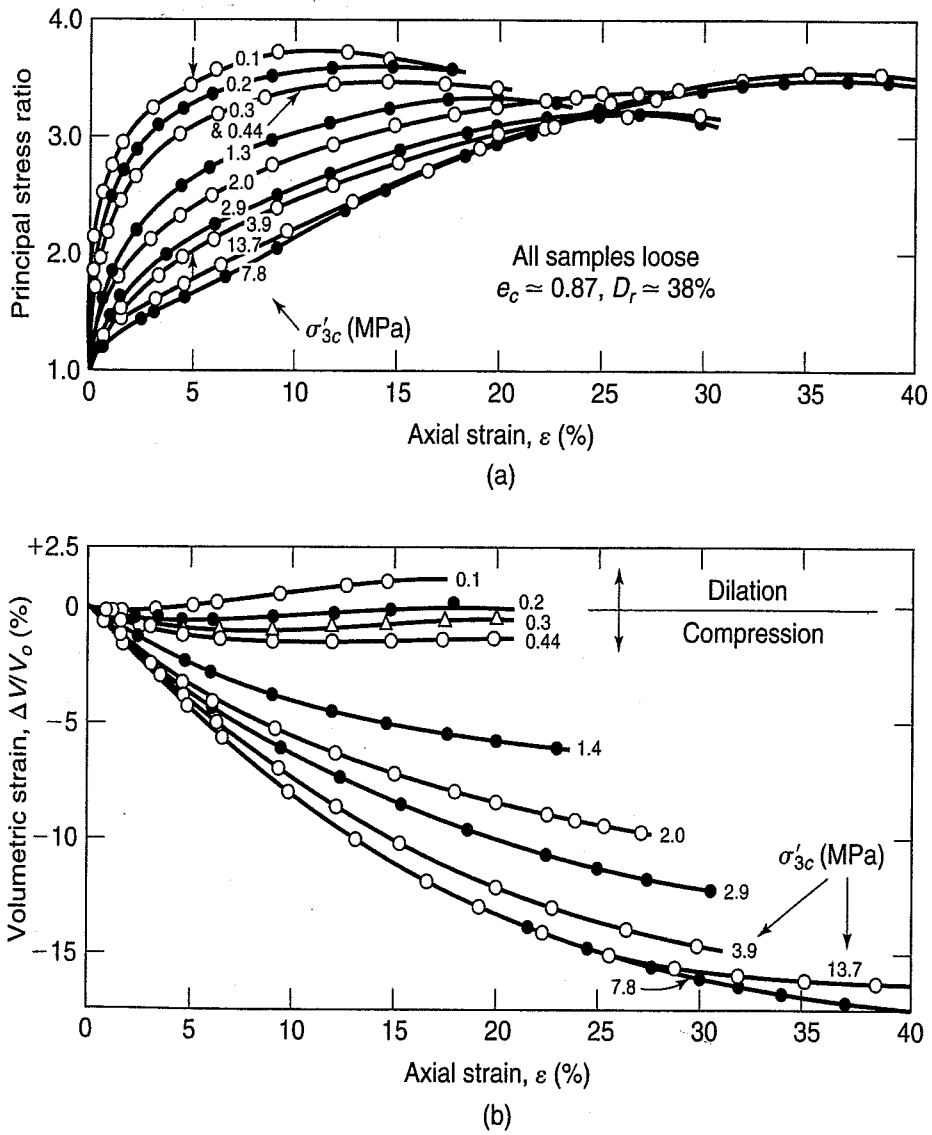

FIGURE 12.5 Typical drained triaxial test results on loose Sacramento River sand: (a) principal stress ratio versus axial strain; (b) volumetric strain versus axial strain (after Lee, 1965).

conditions are 2.0 and 3.5, respectively, as indicated by the arrows in Fig. 12.5(a). Utilizing Eq. (12.2), we obtain the following results:

σ'_{3c} (MPa)	σ'_1/σ'_3 —	$(\sigma_1 - \sigma_3)$ (MPa)	σ'_1 (MPa)
0.1	3.5	0.25	0.35
3.9	2.0	3.9	7.8

It is interesting to look at the shapes of the volumetric strain versus axial strain curves in Fig. 12.5(b). As the strain increases, the volumetric strain for the most part decreases. This is consistent with the behavior of a loose sand, as shown in Fig. 12.4(b). However at low confining pressures (for example, 0.1 and 0.2 MPa), the volumetric strain is positive, or *dilation* is taking place! Thus even an initially loose sand behaves like a dense sand; that is, it dilates if σ'_{3c} is low enough!

Now, let's look at the behavior of dense sand. The results of several drained triaxial tests on dense Sacramento River sand are presented in Fig. 12.6. Although the results look like those in Fig. 12.5, there

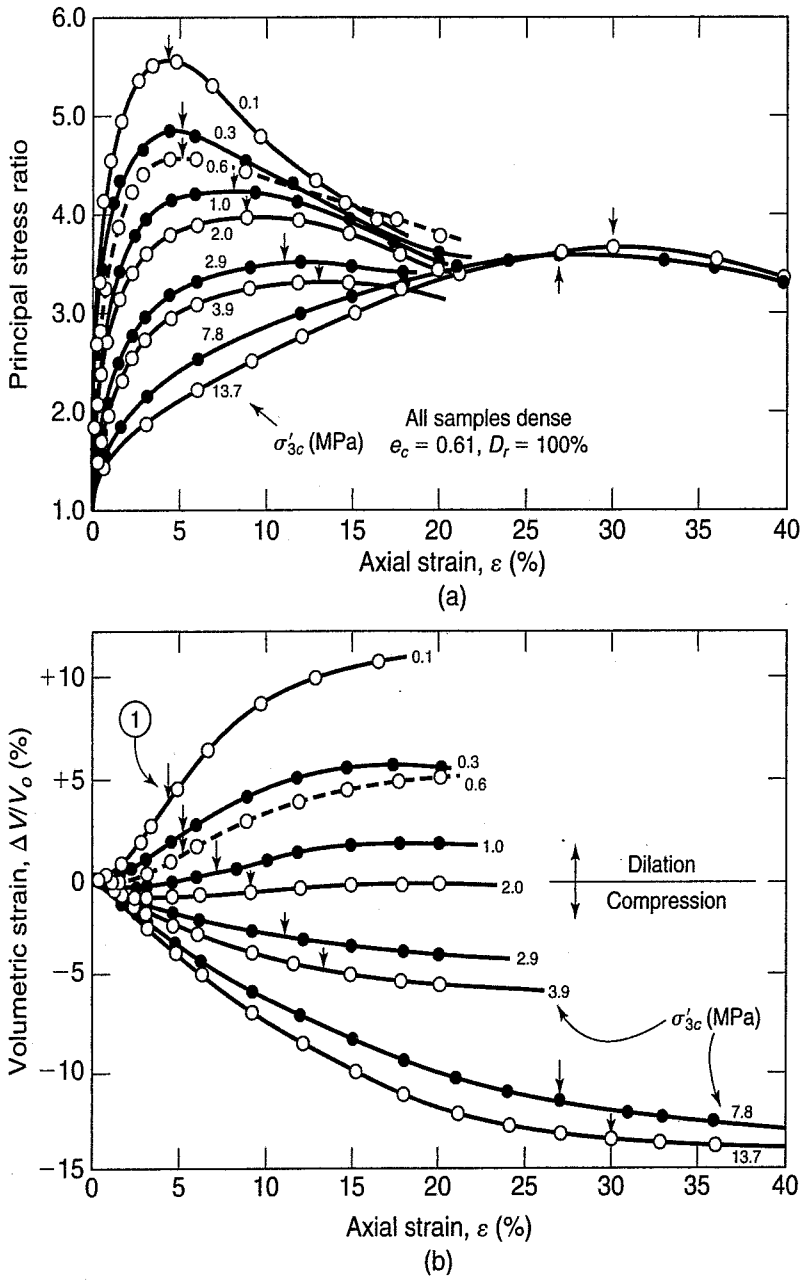

FIGURE 12.6 Typical drained triaxial test results on dense Sacramento River sand: (a) principal stress ratio versus axial strain; (b) volumetric strain versus axial strain (after Lee, 1965).

are some significant differences. First, definite peaks are seen in the (σ_1'/σ_3')-strain curves, which are typical of dense sands [compare with Fig. 12.4(a)]. Second, large *increases* of volumetric strain (dilation) are observed. However, at higher confining pressures, dense sand exhibits the behavior of loose sand by showing a *decrease* in volume or compression with strain.

By testing specimens of the same sand at the same void ratios or densities but with different effective consolidation pressures, we can determine the relationship between volumetric strain at failure and void ratio or relative density. We could define failure as either the maximum $(\sigma_1 - \sigma_3)$ or maximum σ_1'/σ_3'. For drained tests, failure occurs at the same strain according to both criteria. Points at failure are shown as small arrows in Fig. 12.6. Volumetric strain at failure versus void ratio at the end of consolidation, from the data in Figs. 12.5(b) and 12.6(b) for various confining pressures (other data have been added as well), are shown in Fig. 12.7. For example, point 1 in Fig. 12.6(b) is plotted as point 1 in Fig. 12.7. It can be seen that for a given confining pressure the volumetric strain decreases (becomes more negative) as the density decreases (void ratio increases). By definition, the critical void ratio is the void ratio *at failure* when the volumetric strain is zero. Thus for the various values of σ_{3c}' in Fig. 12.7, e_{crit} is the void ratio when $\Delta V/V_o = 0$. For example, e_{crit} for $\sigma_{3c}' = 2.0$ MPa is 0.555.

We can see how e_{crit} varies with confining pressure by taking the critical void ratios of Fig. 12.7 and plotting them versus σ_{3c}', as in Fig. 12.8. Here we have called σ_{3c}' the *critical* confining pressure σ_{3crit}', because this is the effective confining pressure at which zero volumetric strain occurs at failure for a given void ratio.

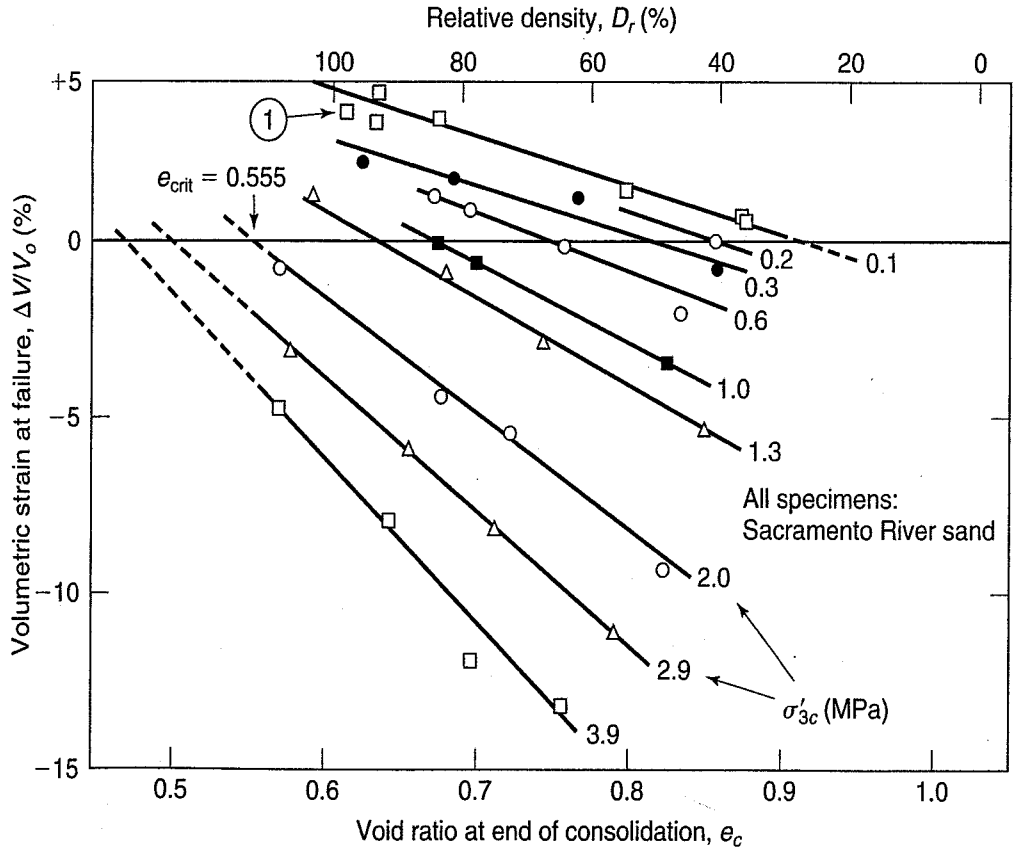

FIGURE 12.7 Volumetric strain at failure versus void ratio at end of consolidation for drained triaxial tests at various confining pressures (after Lee, 1965).

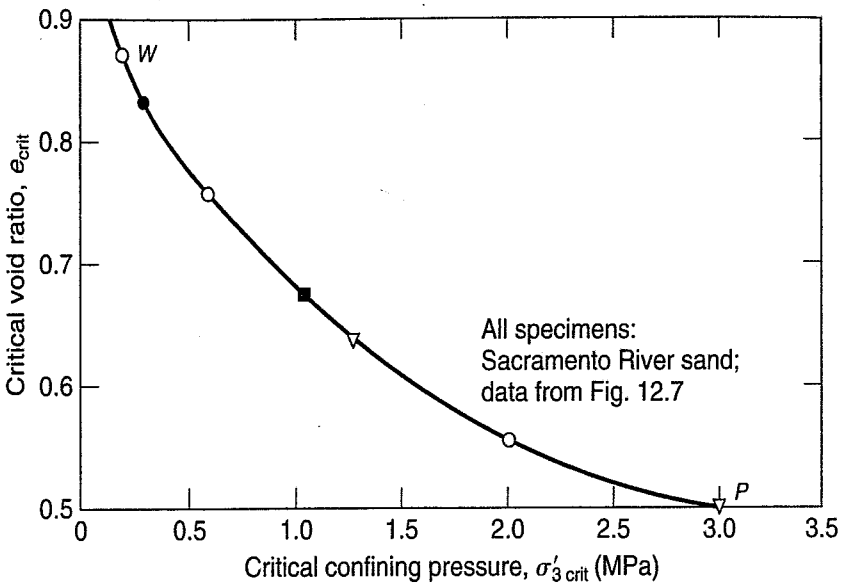

FIGURE 12.8 Critical void ratio versus pressure conditions from drained triaxial tests. Data from Fig. 12.7 (after Lee, 1965).

Example 12.3

Given:

A CD triaxial test is conducted on a granular soil. At failure, $\sigma'_1/\sigma'_3 = 4.0$. The effective minor principal stress at failure is 100 kPa.

Required:

a. Compute ϕ'.

b. Determine the principal stress difference at failure.

c. Plot the Mohr circle and the Mohr failure envelope.

Solution:

a. From Eqs. (11.14), (11.16), or (12.1), we know that

$$\frac{\sigma'_{1f}}{\sigma'_{3f}} = \frac{1 + \sin\phi'}{1 - \sin\phi'} = \tan^2\left(45° + \frac{\phi'}{2}\right) = 4.0$$

Solving for ϕ', we obtain $\phi' = 37°$.

b. From Eq. (12.3),

$$(\sigma_1 - \sigma_3)_f = \sigma'_3\left(\frac{\sigma'_{1f}}{\sigma'_{3f}} - 1\right)$$

$$= 100 \text{ kPa } (4 - 1)$$

$$= 300 \text{ kPa}$$

c. See Fig. Ex. 12.3.

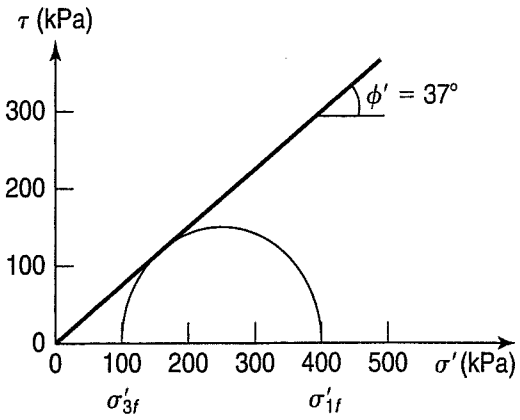

FIGURE Ex. 12.3

Example 12.4

Given:

Figure 12.7.

Required:

What is the critical void ratio for Sacramento River sand when the confining pressure is 1.5 MPa?

Solution: From Fig. 12.7, interpolating between the curves for $\sigma'_3 = 1.3$ and 2.0 MPa, we find that e_c (for $\sigma'_3 = 1.5$) is about 0.61 for Sacramento River sand.

A second and equally interesting approach to looking at volume changes during shear is to use the data shown in Figs. 12.5(b) and 12.6(b) (plus other data at intermediate void ratios) and plot the relationship between volumetric strain at failure and confining pressure for various values of void ratio after consolidation. Such a graph is shown in Fig. 12.9, although the void ratios indicated are initial void ratios and not those after consolidation. Note that the value of σ'_{3c} at $\Delta V/V_o = 0$ is the critical confining pressure, $\sigma'_{3\,\text{crit}}$. Since they are drained tests, $\sigma'_{3c} = \sigma'_{3f}$. This relationship could also be obtained from Fig. 12.7 by noting the values of volumetric strain at constant void ratios and plotting $\Delta V/V_o$ versus σ'_{3c}. We show the relationships of Figs. 12.7 and 12.9 idealized with straight lines in Fig. 12.10.

Since both Figs. 12.7 and 12.9 have a common axis, it is possible to combine them in a single three-dimensional graph known as the *Peacock diagram* (after William Hubert Peacock, who first constructed such a diagram in 1967), as shown in Fig. 12.11.

With the Peacock diagram, we are able to predict the behavior of sand at any void ratio after consolidation e_c and at any confining pressure σ'_3. For example, if the effective confining pressure is given at point C in Fig. 12.11, which is higher than $\sigma'_{3\,\text{crit}}$ for this given void ratio e_c, then we would expect a decrease in the volume or a negative $\Delta V/V_o$, which is equal to the ordinate BS. On the other hand, if σ'_3 is less than $\sigma'_{3\,\text{crit}}$, such as point A for the given value of e_c, then a dilation or positive volume change will take place equal to the ordinate RD. As the void ratio after consolidation varies along the

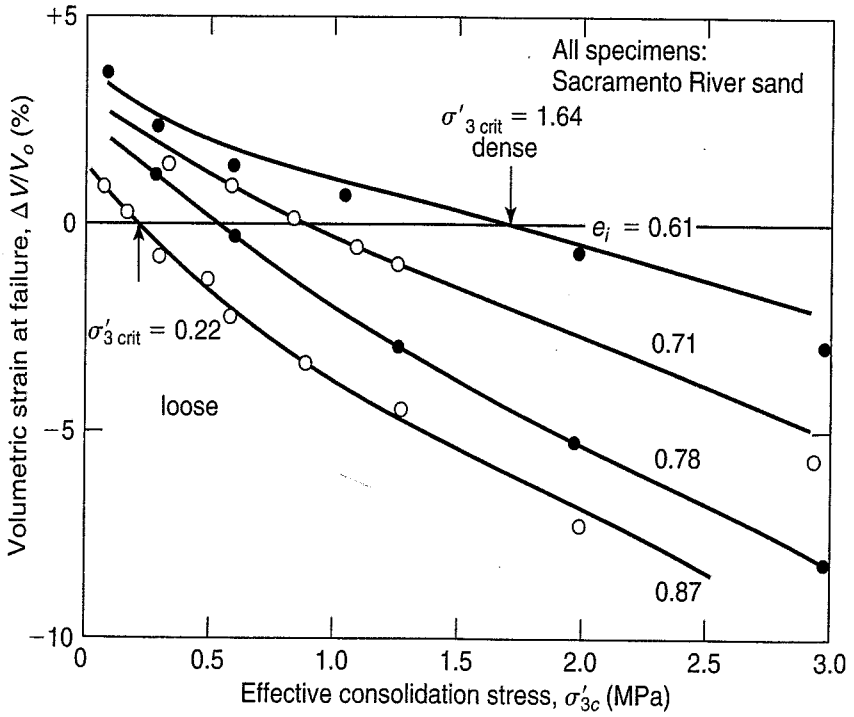

FIGURE 12.9 Volumetric strain at failure versus effective consolidation stress for different initial void ratios (after Lee, 1965).

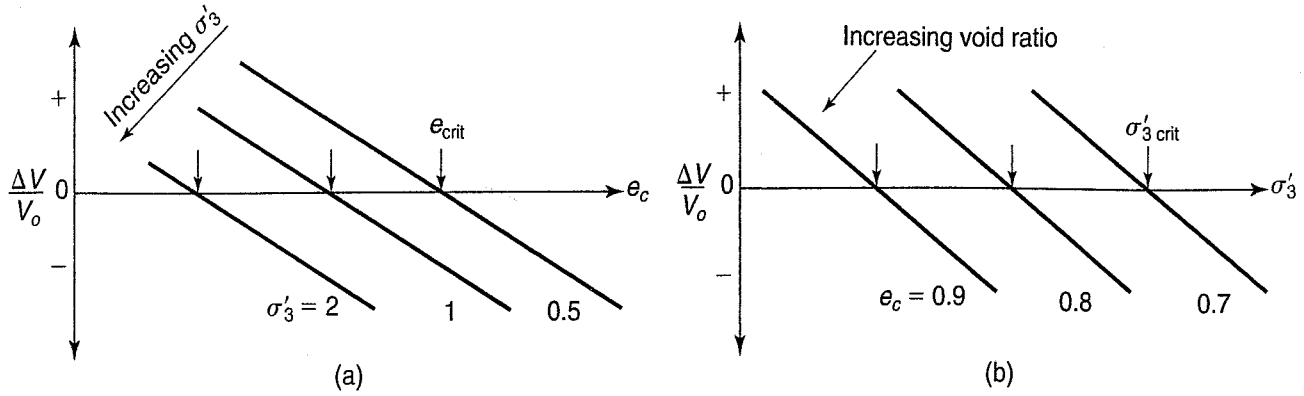

FIGURE 12.10 Idealized volumetric strain data from drained triaxial tests: (a) $\Delta V/V_o$ versus e_c; (b) $\Delta V/V_o$ versus σ'_3.

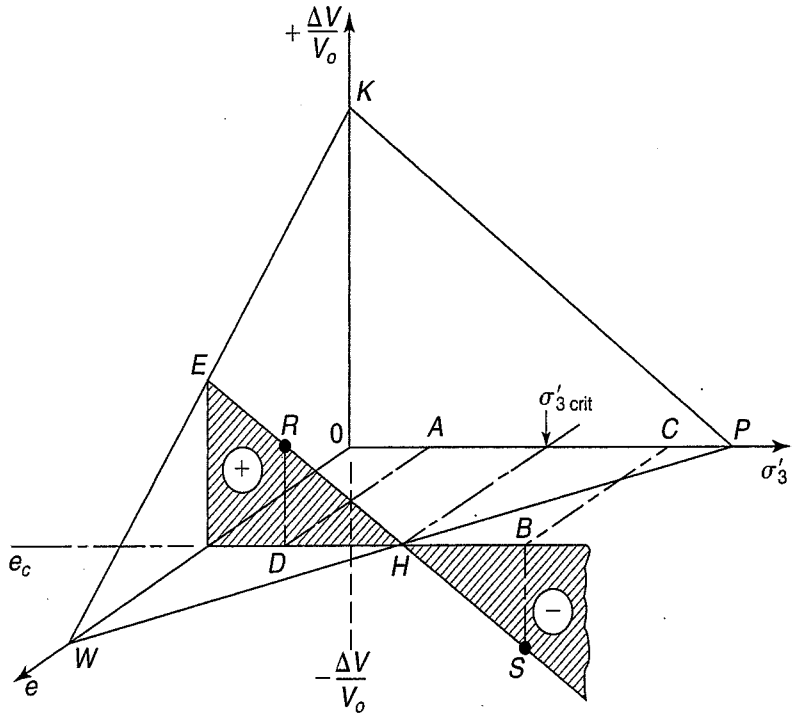

FIGURE 12.11 Peacock diagram, which combines Figs. 12.10(a) and (b) in an idealized graph to show the behavior of drained triaxial tests on sand.

void ratio axis, $\sigma'_{3\,crit}$ varies, and so will the volume changes at failure. For a real sand, the Peacock diagram has curved surfaces. For example, the line *KP* in Fig. 12.11 should look like one of the curves in Fig. 12.9. The line *PW* in Fig. 12.11 is also curved. See line *PW* in Fig. 12.8; here you are looking at a plane on the Peacock diagram where $\Delta V/V_o = 0$.

Example 12.5

Given:

Figure 12.9.

Required:

What is the critical confining pressure for Sacramento River sand if the void ratio equals 0.75?

Solution: From Fig. 12.9, we can interpolate between the curves for $e_i = 0.71$ and 0.78 for the value of σ'_3 when $\Delta V/V_o$ is zero. We obtain a σ'_3 of about 0.7 MPa.

Example 12.6

Given:

Figure 12.11, but scaled to the idealized behavior of Sacramento River sand (a combination of Figs. 12.7 and 12.9); $\sigma'_{3\,\text{crit}} = 0.4$ MPa and $e_c = e_{\text{crit}} = 0.8$.

Required:

Describe the drained behavior of this sand if the test void ratios after consolidation at $\sigma'_{3c} = 0.4$ MPa are (a) 0.85 and (b) 0.75.

Solution: Since σ'_{3c} and e_c are at critical, there is by definition no volume change during shear. Thus our test plots at point H in Fig. 12.11, with the values of $\sigma'_{3\,\text{crit}}$ and e_c as given. (You can verify these values in Figs. 12.7 and 12.9.)

a. When $e_c > e_{\text{crit}}$ $(0.85 > 0.8)$, then at $\sigma'_{3c} = 0.4$ MPa the coordinates of our test would have to plot *below* the *WOP* plane, which means $\Delta V/V_o$ is negative. During *drained* shear, σ'_3 is constant (no excess pore pressure develops), and the specimen would consolidate and decrease in volume during shear. Its coordinates would be on the extension of plane *WKP*.

b. When $e_c < e_{\text{crit}}$ $(0.75 < 0.80)$ the opposite of (a) happens. During drained shear, σ'_3 is again constant and equal to 0.4 MPa, so, for the coordinates of our test to remain on plane *WKP*, the $\Delta V/V_o$ must increase.

Example 12.7

Given:

Figure 12.11 is scaled to the behavior of Sacramento River sand (Figs. 12.7 and 12.9), with $e_{\text{crit}} = 0.6$ and $\sigma'_{3\,\text{crit}} = 1.6$ MPa.

Required:

Describe the behavior in drained shear if we maintain this void ratio of 0.6 but test the specimen with σ'_{3c} of (a) 1.5 MPa and (b) 1.7 MPa.

Solution:

a. When $\sigma'_{3c} < \sigma'_{3\,\text{crit}}$, the specimen will dilate and a positive $\Delta V/V_o$ will occur. This behavior is similar to what happens to point A in Fig. 12.11. The dilation is measured by the ordinate RD, so that the coordinates of our test remain on plane *WKP*.

b. When $\sigma'_{3c} > \sigma'_{3\,\text{crit}}$, the behavior would be similar to path BS in Fig. 12.11 in drained shear.

Example 12.8

Given:

A drained triaxial test on sand with $\sigma'_3 = 150$ kPa and $(\sigma'_1/\sigma'_3)_{\text{max}} = 3.7$.

Required:

a. σ'_{1f}
b. $(\sigma_1 - \sigma_3)_f$
c. ϕ'

Solution:

a. Since we know σ'_3 and $(\sigma'_1/\sigma'_3)_f = 3.7$, we can solve for $\sigma'_{1f} \cdot \sigma'_{1f} = 3.7(150) = 555$ kPa.
b. $(\sigma_1 - \sigma_3)_f = (\sigma'_1 - \sigma'_3)_f = 555 - 150 = 405$ kPa.
c. Assume for sand that $c' = 0$. So, from Eq. (11.13),

$$\phi' = \arcsin\left(\frac{\sigma'_{1f} - \sigma'_{3f}}{\sigma'_{1f} + \sigma'_{3f}}\right) = \arcsin\frac{405}{705} = 35°$$

Note: We could also determine ϕ' graphically from the Mohr circle plotted for failure conditions, as shown in Fig. Ex. 12.8.

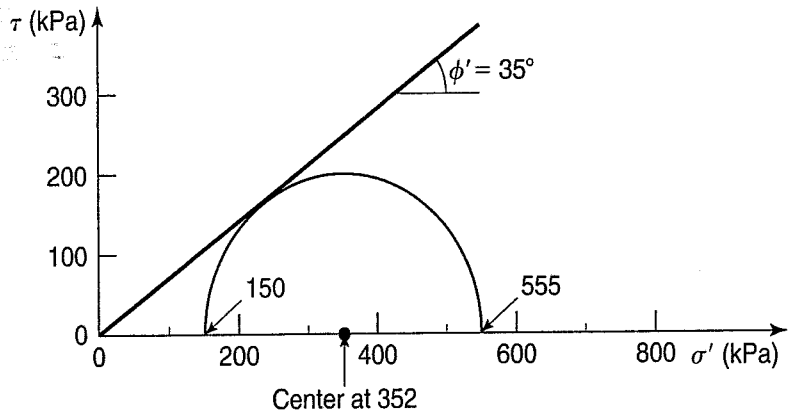

FIGURE Ex. 12.8

12.5 FACTORS THAT AFFECT THE SHEAR STRENGTH OF SANDS

Since sand is a "frictional" material, we would expect those factors that increase the frictional resistance of sand to lead to increases in the angle of internal friction. First, let us summarize the factors that influence ϕ.

1. Void ratio or relative density.
2. Particle shape.
3. Grain size distribution.
4. Particle surface roughness.
5. Water.
6. Intermediate principal stress.
7. Particle size.
8. Overconsolidation or prestress.

Void ratio, related to the density of the sand, is perhaps the most important single parameter that affects the strength of sands. Generally speaking, for drained tests either in the direct shear or triaxial test apparatus, the lower the void ratio (higher density or higher index, or relative, density), the higher the shear strength. The Mohr circles for the triaxial test data presented earlier are shown in Fig. 12.12

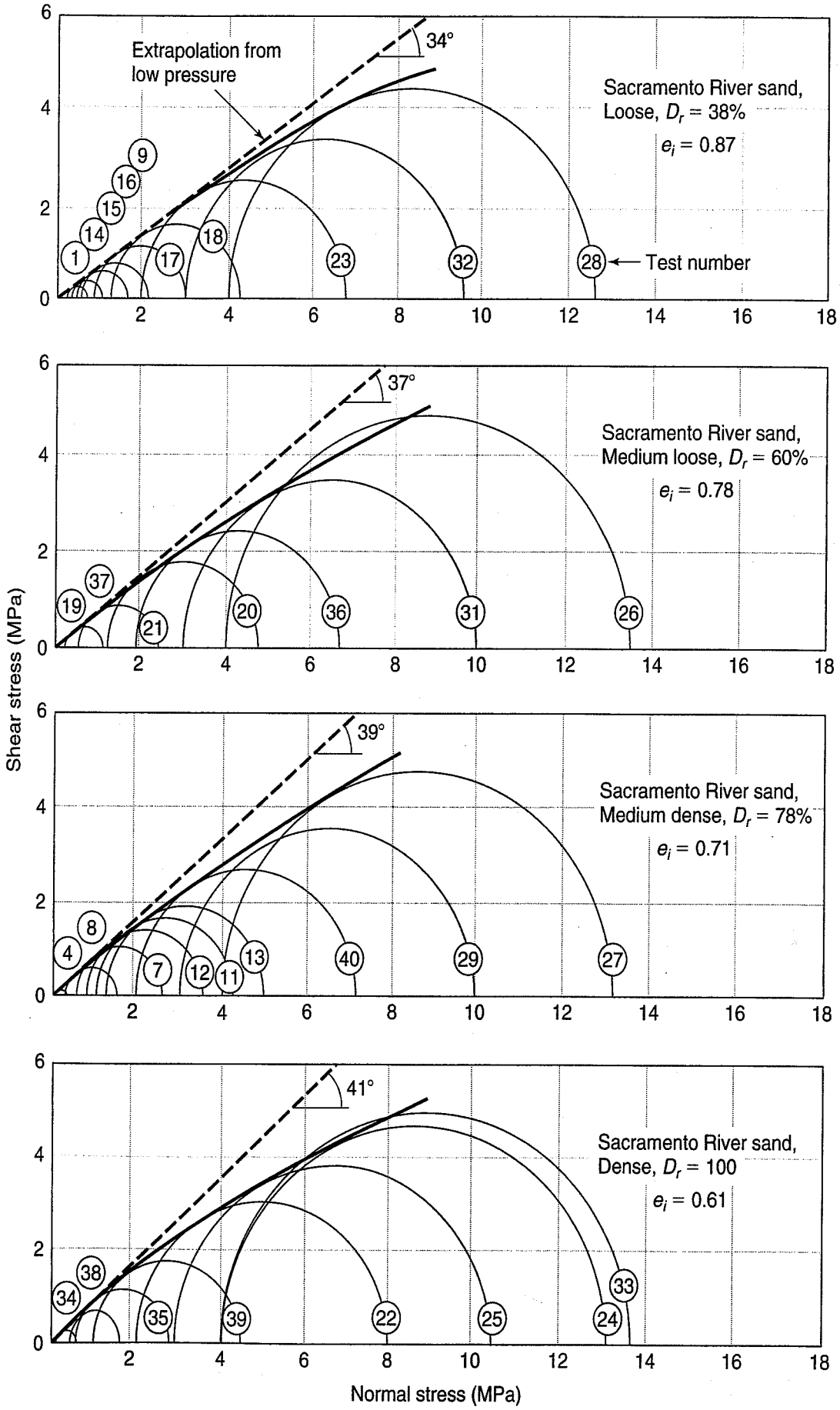

FIGURE 12.12 Mohr circles and failure envelopes from drained triaxial tests, illustrating the effects of void ratio or relative density on shear strength (after Lee, 1965; also after Lee and Seed, 1967).

for various confining pressures and four initial void ratios. You can see that, as the void ratio decreases, or the density increases, the angle of internal friction or angle of shearing resistance ϕ increases.

Another thing you should notice is that the Mohr failure envelopes in Fig. 12.12 are curved; that is, ϕ' is not a constant if the range in confining pressure is large. We usually speak of ϕ' as if it were a constant, but we understand that the Mohr failure envelope really is curved (Sec. 13.9.2). In practice, we approximate the curved envelope by a straight line and thus a constant ϕ' over the range of *working* stresses anticipated in the field.

The effects of relative density or void ratio, grain shape, grain size distribution, and particle size on ϕ are summarized by Casagrande in Table 12.1. Values were determined by triaxial tests on saturated specimens at moderate confining pressures. Generally speaking, with all else constant, ϕ increases with increasing angularity (Fig. 2.7). If two sands have the same relative density, the soil that is better graded (for example, an SW soil as opposed to an SP soil) has a larger ϕ. (As a reminder, two sands at the same void ratio may not necessarily have the same relative density.) Particle size, at constant void ratio, does *not* seem to influence ϕ significantly. Thus, a fine sand and a coarse sand at the same void ratio will probably have about the same ϕ. Casagrande also published a very useful graph of the effective angle of friction versus the void ratio in Fig. 12.13, as cited by Means and Parcher (1963). Notice the limits for *natural* granular soils indicated on the figure. As expected, the data given in Table 12.1 fit nicely in the figure.

Figure 12.14 shows the correlation between the effective friction angle from triaxial compression test results and the dry density, relative density, and Unified Soil classification. The scales for porosity, void ratio, and dry density are based on a specific gravity of 2.68. (Note that the three scales also act as a nomograph for these three interrelated parameters.)

TABLE 12.1 Angle of Internal Friction of Cohesionless Soils

					Loose		Dense	
No.	General Description	Grain Shape	D_{10} (mm)	C_u	e	ϕ (deg)	e	ϕ (deg)
1	Ottawa standard sand	Well rounded	0.56	1.2	0.70	28	0.53	35
2	Sand from St. Peter sandstone	Rounded	0.16	1.7	0.69	31	0.47	37[a]
3	Beach sand from Plymouth, MA	Rounded	0.18	1.5	0.89	29	—	—
4	Silty sand from Franklin Falls Dam site, NH	Subrounded	0.03	2.1	0.85	33	0.65	37
5	Silty sand from vicinity of John Martin Dam, CO	Subangular to subrounded	0.04	4.1	0.65	36	0.45	40
6	Slightly silty sand from the shoulders of Ft. Peck Dam, MT	Subangular to subrounded	0.13	1.8	0.84	34	0.54	42
7	Screened glacial sand, Manchester, NH	Subangular	0.22	1.4	0.85	33	0.60	43
8	Sand from beach of hydraulic fill dam, Quabbin Project, MA	Subangular	0.07	2.7	0.81	35	0.54	46[b]
9	Artificial, well-graded mixture of gravel with sands No. 7 and No. 3	Subrounded to subangular	0.16	68	0.41	42	0.12	57
10	Sand for Great Salt Lake fill (dust gritty)	Angular	0.07	4.5	0.82	38	0.53	47
11	Well-graded, compacted crushed rock	Angular	—	—	—	—	0.18	60

[a]The angle of internal friction of the undisturbed St. Peter sandstone is larger than 60°, and its cohesion is so small that slight finger pressure or rubbing, or even stiff blowing at a specimen by mouth, will destroy it.

[b]Angle of internal friction measured by direct shear test for No. 8, by triaxial tests for all others.

After A. Casagrande (Hirschfeld, 1963).

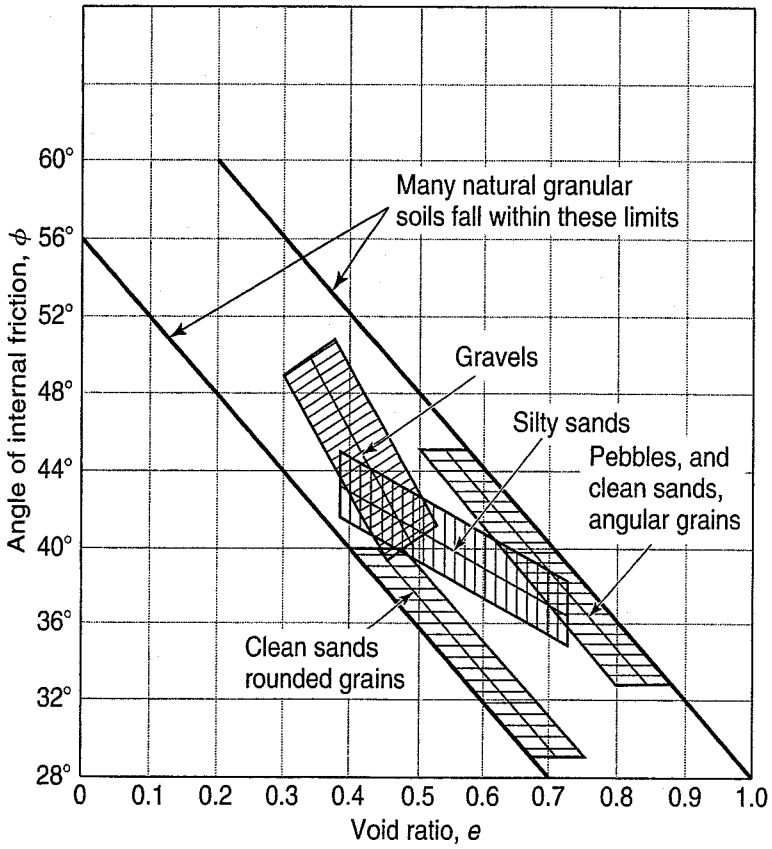

FIGURE 12.13 Range of angle of internal friction of natural, granular soils as a function of the void ratio (after Casagrande as cited by Means and Parcher, 1963).

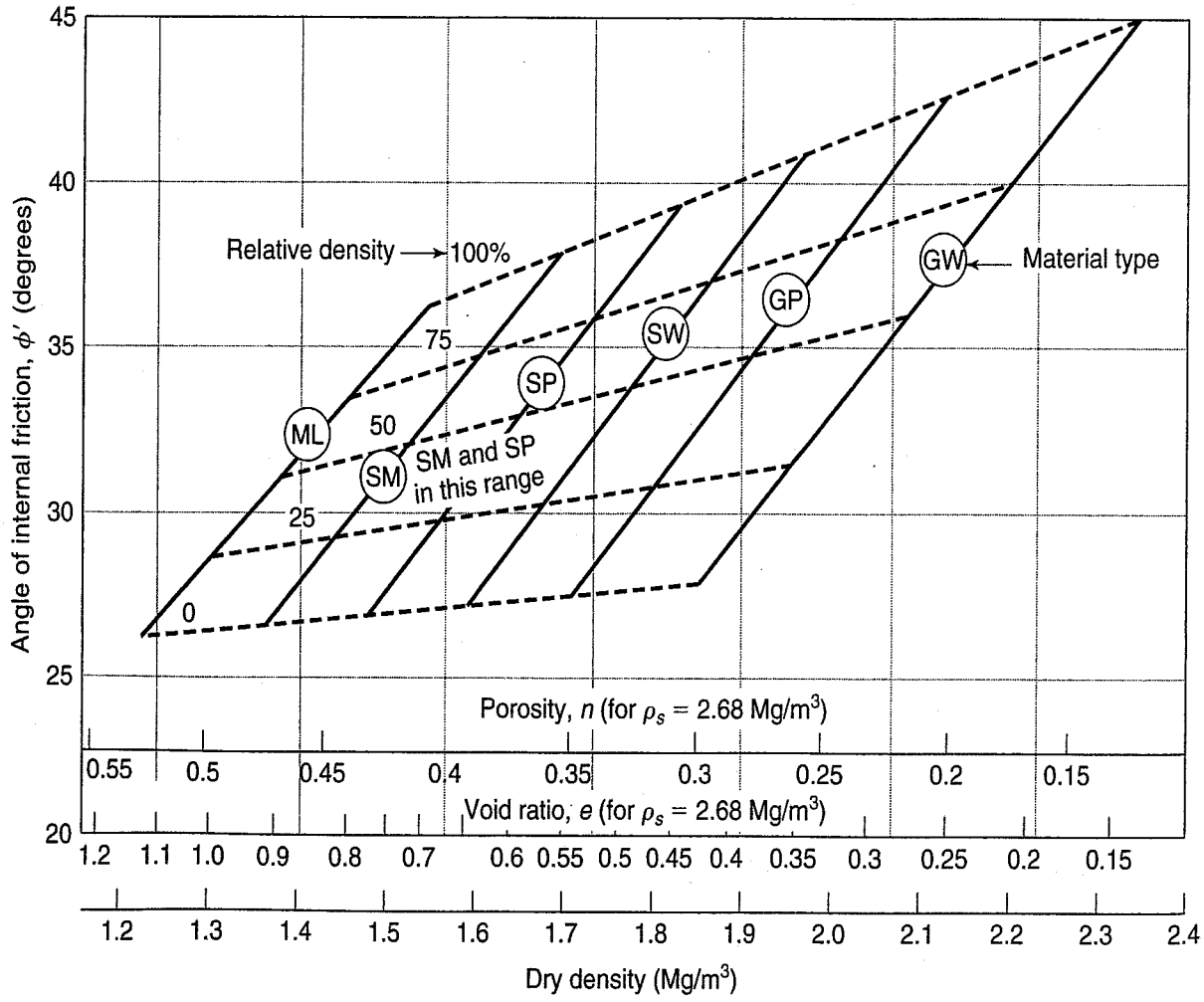

FIGURE 12.14 Correlations between the effective friction angle in triaxial compression and the dry density, relative density, and soil classification. Approximate correlation is for cohesionless materials without plastic fines (after U.S. Dept. of the Navy, 1986).

We have combined Figs. 12.13 and 12.14, as they are related by the angle of internal friction and void ratio. This combined new figure looks different, because Fig. 12.13 is now reversed, as the void ratio scale is different between the two original graphs. Figure 12.13 was replotted using the void ratio scale on Fig. 12.14 into the new Fig. 12.15.

In this figure it is interesting to note that the right half of Fig. 12.14 does not contain any void ratio e data less than about 0.4 from the Casagrande plot as shown in Fig. 12.13. There are two reasons for this absence. One may be that the Casagrande plot deals with "many natural (soil) grains" and the second is that we usually don't find many soils in nature with void ratios less than 0.4. Further, many *dumped* granular soils have relative densities ~80%, and it is unusual for soils in situ to have *dry* densities greater than 125 lbf/ft^3 (or ~2 Mg/m^3). (With dry density that high, it will be difficult, for example, to drive a pile into this soil formation.) A quick glance at Fig. 5.2 will show you that the void ratio at that dry density will be about 0.35. Tough stuff!

Another parameter, not included in Table 12.1, is surface roughness, which is very difficult to measure. It will, however, have an effect on ϕ. Generally, the greater the surface roughness, the greater will be ϕ. It has also been found that wet soils show a ϕ value 1° to 2° *lower* than if the sands were dry.

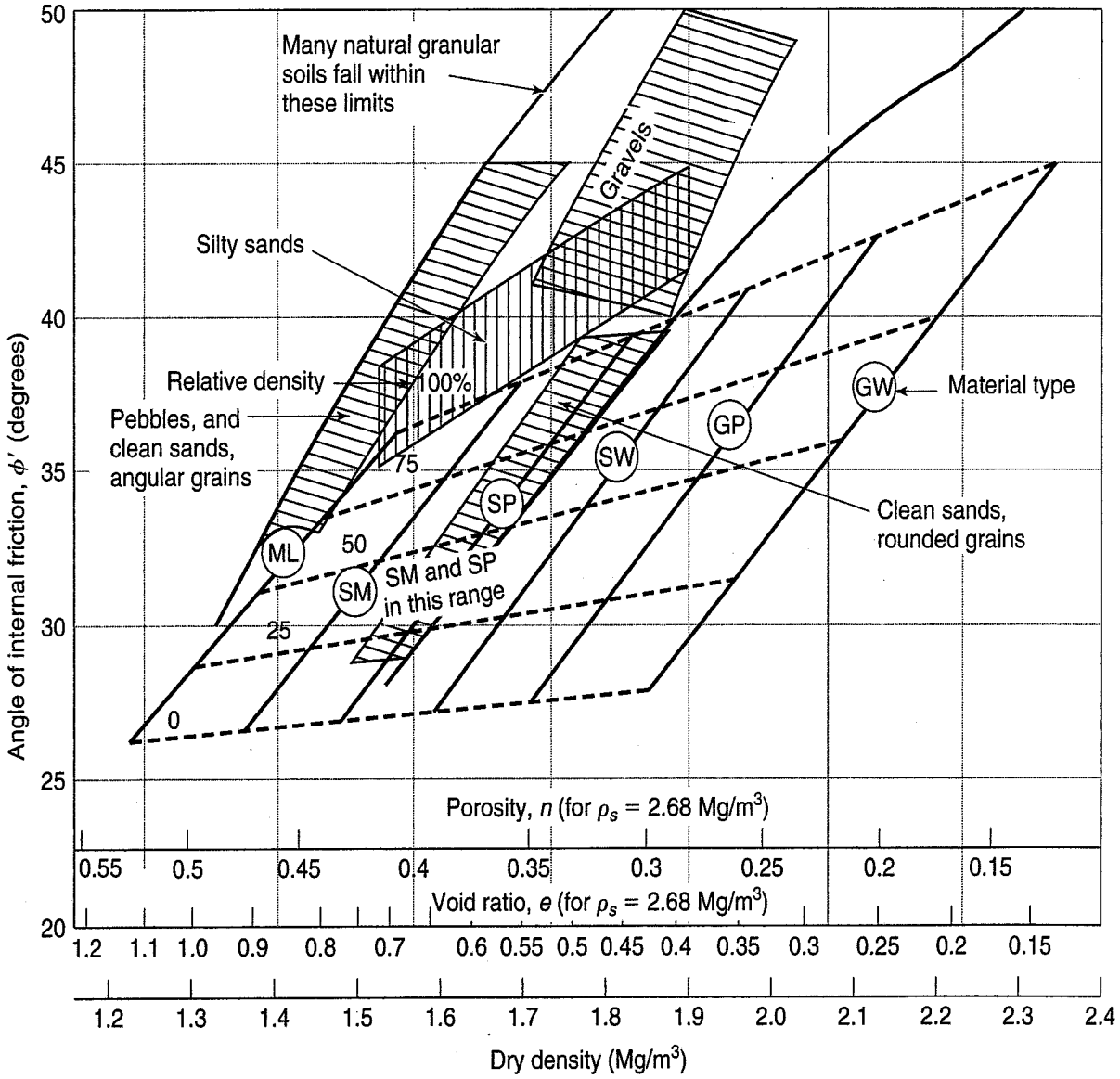

FIGURE 12.15 Correlations between the effective friction angle in triaxial compression and the dry density and soil classification (after U.S. Navy, 1971, 1986) with the reversed Fig. 12.13 superimposed. Note the scale change due to the nonlinear relationship between dry density and void ratio.

TABLE 12.2 Summary of Factors Affecting ϕ

Factor	Effect
Void ratio, e	$e\uparrow$, $\phi\downarrow$
Angularity, A	$A\uparrow$, $\phi\uparrow$
Grain-size distribution	$C_u\uparrow$, $\phi\uparrow$
Surface roughness, R	$R\uparrow$, $\phi\uparrow$
Water content, w	$w\uparrow$, $\phi\downarrow$ slightly
Intermediate principal stress	$\phi_{ps} \geq \phi_{tx}$ (see Sec. 13.11)
Particle size, S	No effect (with constant e)
Overconsolidation or prestress	Little effect

All the factors mentioned above are summarized in Table 12.2. Some correlations between ϕ' and dry density, relative density, and soil classification are shown in Fig. 12.13. This figure and Table 12.1 are very useful for estimating the frictional characteristics of granular materials. If you have a complete visual classification of the materials at your site, together with some idea of the in situ relative density, you already have a pretty good idea about the shear strength behavior of the soils in advance of a laboratory testing program. For small projects, such estimates may be all you need for design.

12.6 SHEAR STRENGTH OF SANDS USING IN SITU TESTS

Our discussion so far on the shear strength of sands has been largely based on their behavior as observed in triaxial tests. You may recall from our discussion of in situ tests in Sec. 11.6.1 that the Standard Penetration Test (SPT), Dutch cone penetrometer test (CPT), and flat plate dilatometer test (DMT) can be used to obtain the drained friction angle ϕ' of sandy soils. Empirical correlations have been developed for ϕ' with the SPT blow count (N), CPT cone tip resistance q_c, and horizontal stress index K_D determined by the DMT. This section gives some of these correlations.

12.6.1 SPT

The SPT blow count N correlates rather well with relative density and friction angle, as long as proper corrections are made for applied energy, rod length, and borehole diameter (Sabatini et al., 2002). One common relationship is shown in Table 12.3 for clean sands. For clayey sands the ϕ' in the table should be reduced by about 5°, and for gravelly sands, increased by 5°. If the SPT N-value is determined in very fine or silty sands below the groundwater table and if it is greater than about $N = 15$, then the measured

TABLE 12.3 Correlation between Relative Density, SPT N, and Friction Angle

Relative Density Descriptors	Relative Density (%)	SPT N (blows/300 mm)	Friction Angle, ϕ' (deg)
Very loose	<20	<4	<30
Loose	20–40	4–10	30–35
Medium	40–60	10–30	35–40
Dense	60–80	30–50	40–45
Very dense	>80	>50	>45

After Meyerhoff (1956) and Sabatini et al. (2002).

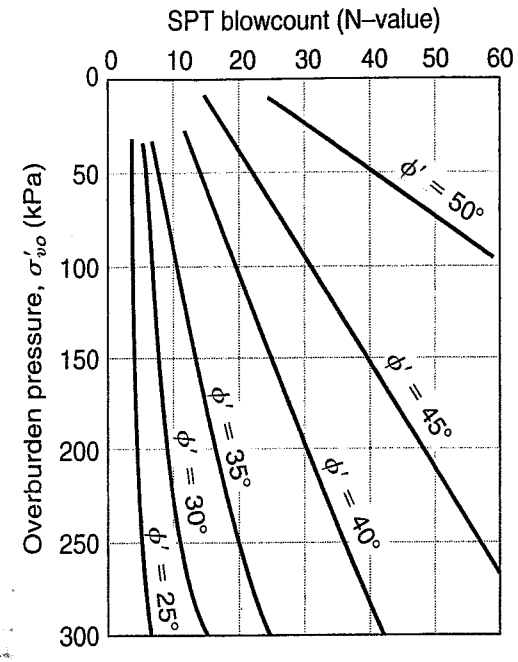

FIGURE 12.16 Correlation between ϕ' and N corrected for effective overburden stress (after Schmertmann, 1975).

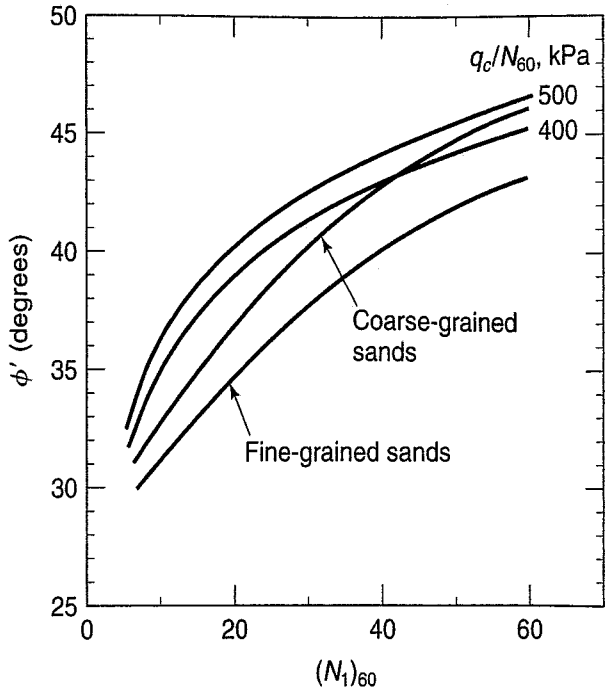

FIGURE 12.17 Correlation between ϕ' and corrected N value (Terzaghi et al., 1996).

N value must be corrected for dilatancy. One approach is to use $N = 15 + (N' - 15)/2$ where the measured $N' > 15$.

Because the N value depends on overburden stress, Schmertmann (1975) proposed the correlation shown in Fig. 12.16, based on calibration chamber tests. According to Kulhawy and Mayne (1990), this correlation can be approximated by

$$\phi' \approx \tan^{-1}\left[\frac{N}{\left(12.2 + 20.3\dfrac{\sigma'_{vo}}{p_a}\right)}\right]^{0.34} \tag{12.5}$$

where p_a = reference pressure (atmospheric, ≈ 100 kPa).

Terzaghi et al. (1996) state that this figure underestimates the ϕ' for calcareous sands (Sec. 4.11.2) with crushable particles and overconsolidated sands. Figure 12.17 shows an improved correlation between ϕ' and the blowcount, $(N_1)_{60}$, which is the N-value corrected for applied energy, rod length, and borehole diameter (Sabatini et al., 2002).

12.6.2 CPT

Because the CPT is a quasi-static test, it is especially effective in loose sands without much gravel. Probably the best known correlation between cone tip resistance q_c and the drained friction angle ϕ' is shown in Fig. 12.18 for normally consolidated uncemented clean quartz sands. According to Sabatini et al. (2002) the correlations in Fig. 12.18 can be approximated by

$$\phi' \approx \tan^{-1}\left[0.1 + 0.38 \log\left(\frac{q_c}{\sigma'_{vo}}\right)\right] \tag{12.6}$$

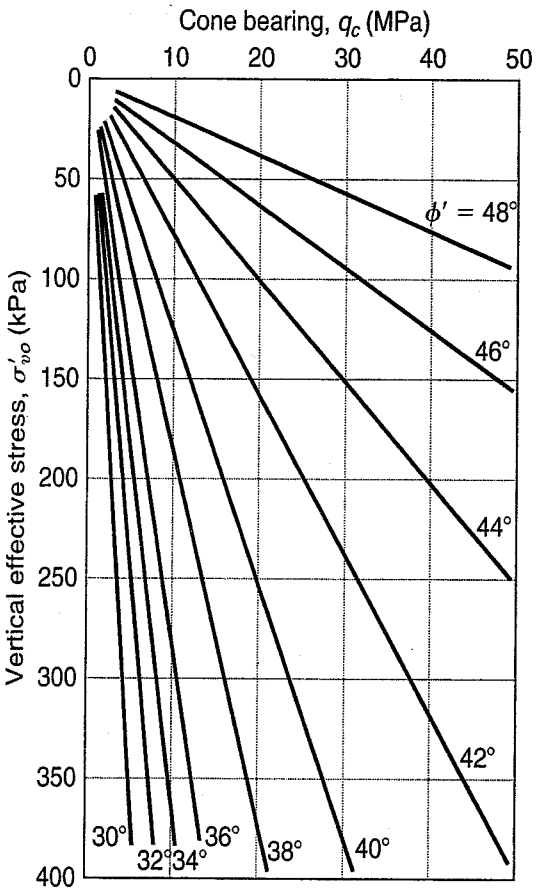

FIGURE 12.18 Drained friction angle ϕ' as a function of cone tip resistance q_c and effective vertical overburden stress (Robertson and Campanella, 1983).

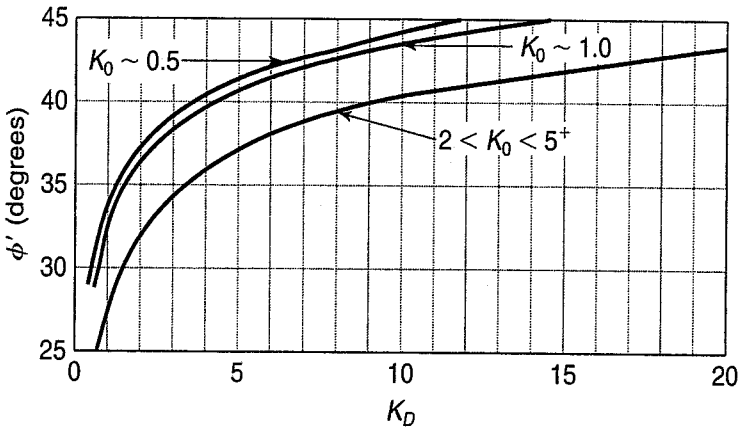

FIGURE 12.19 Correlation of ϕ' with the horizontal stress index K_D for clean sands (after Campanella and Robertson, 1991; Marchetti, 1997; and Sabatini et al., 2002).

12.6.3 DMT

DMT results are used to develop material and lateral stress indices that have been correlated to various soil properties including the friction angle for sands and silts. One correlation for clean sand is through the horizontal stress index K_D proposed by Campanella and Robertson (1991), and modified by Marchetti (1997). According to Sabatini et al. (2002), Eq. (12.7) is the lower bound proposed by Marchetti (1997). It is plotted in Fig. 12.19 and according to the correlation by Campanella and Robertson (1991) appears to be for overconsolidated sands.

$$\phi' = 28° + 14.6 \log K_D - 2.1 \log^2 K_D \tag{12.7}$$

12.7 THE COEFFICIENT OF EARTH PRESSURE AT REST FOR SANDS

In Sec. 6.11 we defined the coefficient of earth pressure at rest as

$$K_o = \frac{\sigma'_{ho}}{\sigma'_{vo}} \tag{6.19}$$

where σ'_{ho} = the horizontal effective stress in situ, and
σ'_{vo} = the vertical effective stress in situ.

We mentioned that a knowledge of K_o is very important for the design of earth-retaining structures and many foundations; it also influences liquefaction potential, as we shall see in Chapter 13. Thus, if your assessment of the initial in situ stresses in the soil is inaccurate, you can be way off in your prediction of the performance of such structures.

You already know from Sec. 6.9 how to estimate σ'_{vo} from the densities of the overlying materials, the thicknesses of the various layers, and the location of the groundwater table. Accurate measurements of σ'_{ho} are not easy, especially in sands. It is virtually impossible to install an earth pressure cell in situ, for example, without causing some disturbance and densification of the sands around the cell, and this changes the stress field at the very point of measurement. Consequently, the approach usually taken is to estimate K_o from theory or laboratory tests, and then calculate σ'_{ho} from σ'_{vo} from Eq. (6.19).

The best known equation for estimating K_o, derived by Jáky (1944, 1948), is a theoretical relationship between K_o and the angle of internal friction ϕ', or

$$K_o = 1 - \sin \phi' \tag{12.8}$$

This relationship, as shown in Fig. 12.20, seems to be an adequate predictor of K_o for normally consolidated sands. Since most of the points lie between 0.35 and 0.5 for these sands, K_o of 0.4 to 0.45 would be a reasonable average value to use for preliminary design purposes.

If the sand has been preloaded, then K_o is somewhat greater. Schmidt (1966, 1967) and Alpan (1967) suggested that the increase in K_o could be related to the overconsolidation ratio (OCR) by

$$K_{o-oc} = K_{o-nc}\,(\text{OCR})^h \tag{12.9}$$

where $K_{o-oc} = K_o$ for the overconsolidated soil,
$K_{o-nc} = K_o$ for the normally consolidated soil, and
h = an empirical exponent.

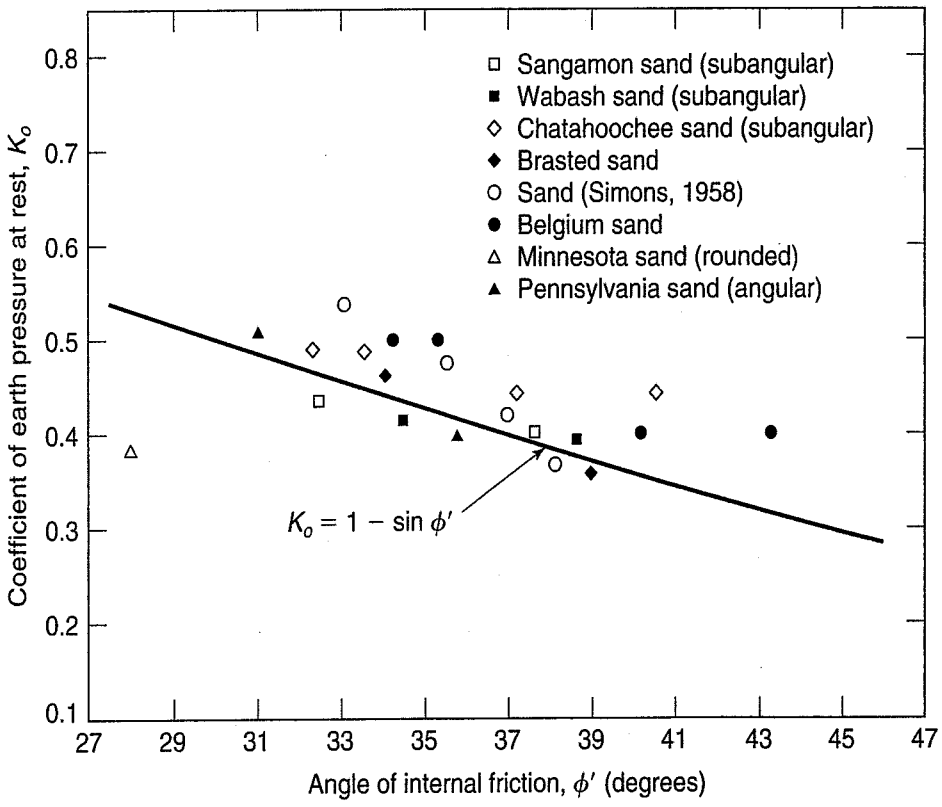

FIGURE 12.20 Relationship between K_o and ϕ' for normally consolidated sands (after Al-Hussaini and Townsend, 1975).

Values of h range between 0.4 and 0.5 (Alpan, 1967; Schmertmann, 1975) and even as high as 0.6 for very dense sands (Al-Hussaini and Townsend, 1975). Schmidt (1966) suggested that $h = \sin\phi'$. Ladd et al. (1977) pointed out that this exponent itself varies with OCR, and it seems to depend on the direction of the applied stresses. For example, Al-Hussaini and Townsend (1975) found a significantly lower K_o during reloading than during unloading in laboratory tests on a uniform medium sand. Thus K_o appears to be very sensitive to the precise stress history of the deposit.

Kulhawy et al. (1989) provide a tentative evaluation of cone penetration tests in a calibration chamber where the relative density is known. Figure 12.21 shows how the cone tip resistance q_c varies with horizontal effective stress σ'_{ho} for a given relative density. Notice that both σ'_{ho} and q_c (also a stress) are normalized with respect to atmospheric pressure p_a so as to give dimensionless parameters. The value of p_a in SI units is 101.3 kPa, but using 100 kPa is sufficiently accurate. Knowing the normalized tip resistance and the relative density, we find the normalized effective stress. The value of K_o is computed according to Eq. (6.19). Equation (12.10) gives the interrelationship in the figure

$$\frac{\sigma'_{ho}}{p_a} = \frac{(q_c/p_a)^{1.25}}{35e^{(D_r/20)}} \tag{12.10}$$

where σ'_{ho} = horizontal effective stress,
q_c = cone tip resistance,
p_a = reference pressure (atmospheric, ≈100 kPa).

We will have more to say about this subject when we discuss K_o for clays in Sec. 12.13.

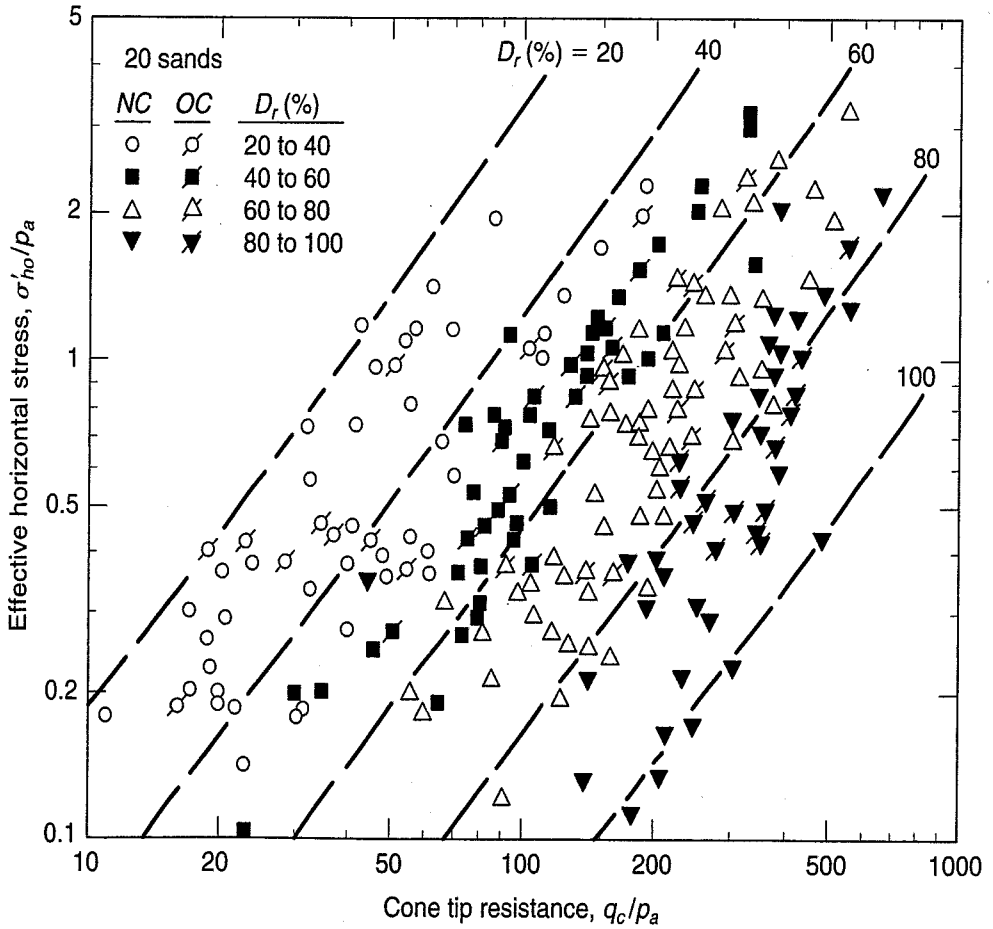

FIGURE 12.21 Normalized cone tip resistance versus normalized horizontal effective stress as a function of relative density (after Kulhawy et al., 1989).

12.8 BEHAVIOR OF SATURATED COHESIVE SOILS DURING SHEAR

What happens when shear stresses are applied to saturated cohesive soils? Most of the remainder of this chapter addresses this question. But first, let's briefly review what happens when saturated sands are sheared.

From our previous discussion, you know that volume changes occur in a drained test, and that the direction of the volume changes, whether dilation or compression, depends on the relative density as well as the confining pressure. If shear takes place undrained, then the mechanisms that produce volume change under drained conditions tend to produce corresponding changes in pore pressures in the sand. When sands are loaded statically, because they have such a high permeability as compared to silts and clays, sands drain as fast as the load is applied, so undrained loading under static conditions happens only in the laboratory. Dynamic loading is another matter. The behavior of saturated sands under dynamic loads, for example, due to blasting, pile driving, or earthquakes, can be quite dramatic under certain conditions, as we explain in Chapter 13.

In the laboratory triaxial test, by simply closing the drainage values (Figs. 11.15 and 12.3) during axial loading, no volume change is allowed and the sand is sheared undrained. However, unless the confining pressure just happens to be at $\sigma'_{3\,\text{crit}}$, the sand will *tend to change volume* during loading. A loose sand specimen would *tend* to decrease in volume, but it cannot, so as a result, a *positive* pore pressure is induced, which causes a *reduction* in the effective stress. The opposite happens with dense specimens. They tend to dilate, so a *negative* pore pressure is induced, which causes an *increase* in the effective stress.

Basically, the same things happen when clay soils are sheared. In drained shear, whether the volume changes are dilation or compression depends not only on the density and the confining pressure but also on the stress history of the soil. Similarly, in undrained shear the pore pressures developed depend greatly on whether the soil is normally consolidated or overconsolidated.

Typically, engineering loads are applied much faster than the water can escape from the pores of a clay soil, and consequently excess pore pressures are produced. If the loading is such that failure does not occur, then the pore pressures dissipate and volume changes develop by the process we call *consolidation* (Chapters 8 and 9). The primary difference in behavior between sands and clays, as mentioned when we discussed the compressibility of soils (Chapter 8), is in the *time* it takes for these volume changes to occur. The time aspect strictly depends on, or is a function of, the difference in permeability between sands and clays. Since cohesive soils have a much lower permeability than sands and gravels, it takes much longer for the water to flow in or out of a cohesive soil mass.

Now, what happens when the loading is such that a shear failure is imminent? Since (by definition) the pore water cannot carry any static shear stress, all the applied shear stress must be resisted by the soil structure. Put another way, the shear strength of the soil depends *only on the effective stresses* and not on the pore water pressures. This does not mean that the pore pressures induced in the soil are unimportant. On the contrary, as the total stresses are changed because of some engineering loading, the pore water pressures also change, and until equilibrium of effective stresses occurs, instability is possible. These observations lead to two fundamentally different approaches to the solution of stability problems in geotechnical engineering: (1) the *total stress approach* and (2) the *effective stress approach.*

In the total stress approach, we allow no drainage to occur during the shear test, and we make the assumption, admittedly a big one, that the pore water pressure and therefore the effective stresses in the test specimen are identical to those in the field. The method of stability analysis is called the *total stress analysis*, and it utilizes the *total* or the *undrained shear strength* τ_f, of the soil. The undrained shear strength can be determined by either laboratory or field tests. If field tests such as the vane shear, Dutch cone penetrometer, or pressuremeter test are used, then they must be conducted rapidly enough so that undrained conditions prevail in situ.

The second approach to calculate the stability of foundations, embankments, slopes, etc., uses the shear strength in terms of *effective stresses*. In this approach, we have to measure or estimate the pore pressures, both in the laboratory and in the field. Then, if we know or can estimate the initial and

applied total stresses, we can calculate the effective stresses acting in the soil. Since we believe that shear strength and stress-deformation behavior of soils is really controlled or determined by the effective stresses, this second approach is philosophically more satisfying. But it does have its practical problems. For example, estimating the field pore pressures during design and before construction is not easy. This method of stability analysis is called the *effective stress analysis*, and it utilizes the *drained shear strength* or the shear strength in terms of effective stresses. The drained shear strength is ordinarily determined only by laboratory tests.

You probably recall, from our description of triaxial tests in Sec. 11.5, that there are limiting conditions of drainage in the tests that model real field situations. We mentioned that you could have consolidated-drained (CD) conditions, consolidated-undrained (CU) conditions, or unconsolidated-undrained (UU) conditions. It is also convenient to describe the behavior of cohesive soils at these limiting drainage conditions. It is not difficult to translate these test conditions into specific field situations with similar drainage conditions.

We mentioned in Sec. 11.5 that the unconsolidated-drained test (UD) is not a meaningful test. First, it models no real engineering design situation. Second, the test cannot be interpreted, because drainage occurs during shear, and you cannot separate the effects of the confining pressure and the shear stress.

As we did with sands, we shall discuss the shear behavior of cohesive soils with reference to their behavior during triaxial shear tests. You can think of the specimen in the triaxial cell as representing a typical soil element in the field under different drainage conditions and undergoing different loading or stress paths. In this manner, we hope you will gain some insight into how cohesive soils behave in shear, both in the laboratory and in the field. Keep in mind that the following discussion is somewhat simplified, and that real soil behavior is much more complicated. In Chapter 13, we shall explore some of these complexities. Our primary references are Leonards (1962), Hirschfeld (1963), and Ladd (1964 and 1971b), as well as the lectures of Professors B. B. Broms, H. B. Seed and S. J. Poulos.

12.9 CONSOLIDATED-DRAINED STRESS-DEFORMATION AND STRENGTH CHARACTERISTICS

12.9.1 Consolidated-Drained (CD) Test Behavior

We described the CD test when we discussed the strength of sands earlier in this chapter. Briefly, the procedure is to consolidate the test specimen under some state of stress appropriate to the field or design situation. The consolidation stresses can either be *hydrostatic* (equal in all directions, sometimes called *isotropic*) or *nonhydrostatic* (different in different directions, sometimes called *anisotropic*). Another way of looking at this second case is that a stress difference or (from the Mohr circles) a shear stress is applied to the soil. When consolidation is over, the "C" part of the CD test is complete.

During the "D" part, the drainage valves remain *open* and the stress difference is applied very slowly, so that essentially *no* excess pore water pressure develops during the test. Professor A. Casagrande termed this test the *S-test* (for "slow" test).

Figure 12.22 shows the total, pore pressure, and effective stress conditions in an axial compression CD test at the end of consolidation, during application of axial load, and at failure. The subscripts v and h refer to vertical and horizontal, respectively; c means consolidation. For conventional axial compression tests, the initial consolidation stresses are hydrostatic. Thus $\sigma_v = \sigma_h = \sigma'_{3c}$ (cell pressure), which is usually held constant during the application of the axial stress $\Delta\sigma$. In the axial compression test, $\Delta\sigma = \sigma_1 - \sigma_3$, and at failure $\Delta\sigma_f = (\sigma_1 - \sigma_3)_f$. The axial stress can be applied either by increasing the load on the piston incrementally (*stress-controlled* loading) or through a system that deforms the specimen at a constant rate (called a *constant rate of strain* or deformation test).

Note that at all the times during the CD test the pore water pressure is essentially zero. This means that the total stresses in the drained test are *always* equal to the effective stresses. Thus

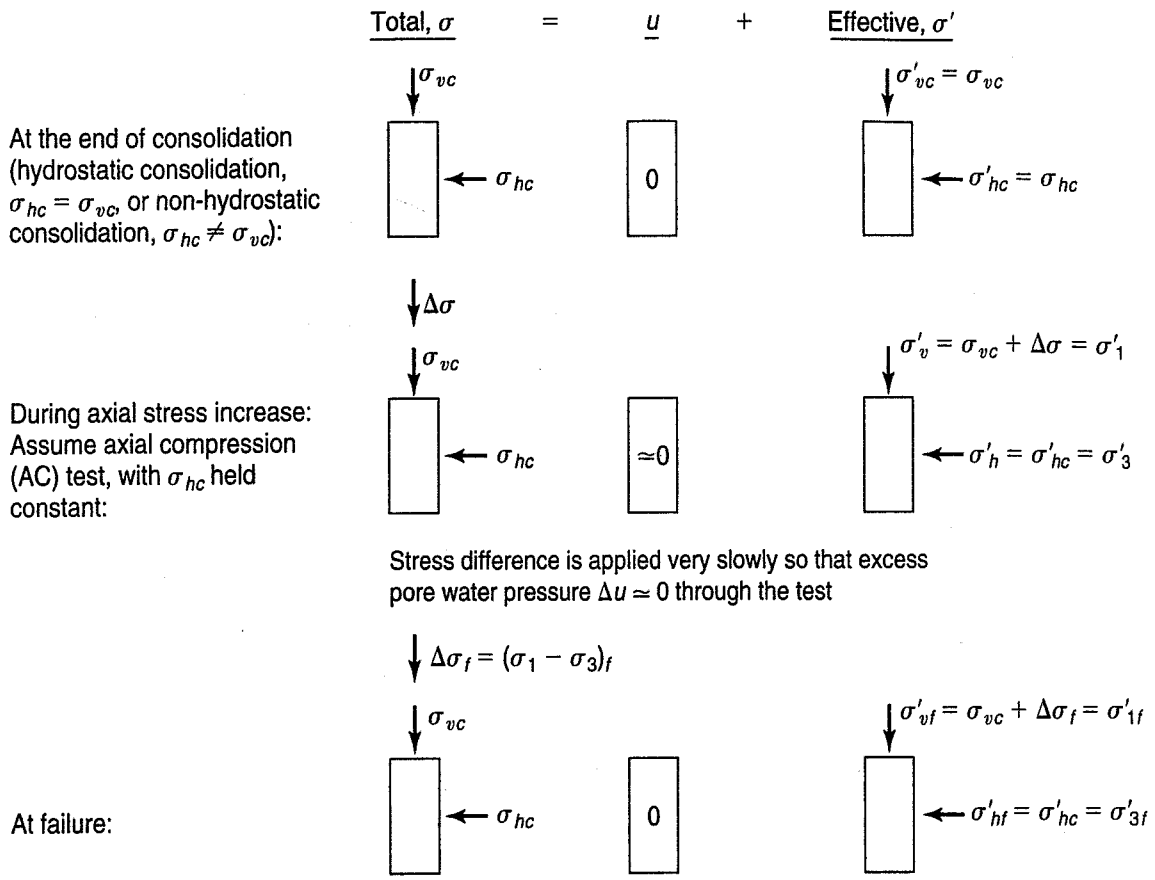

FIGURE 12.22 Stress conditions in the consolidated-drained (CD) axial compression triaxial test.

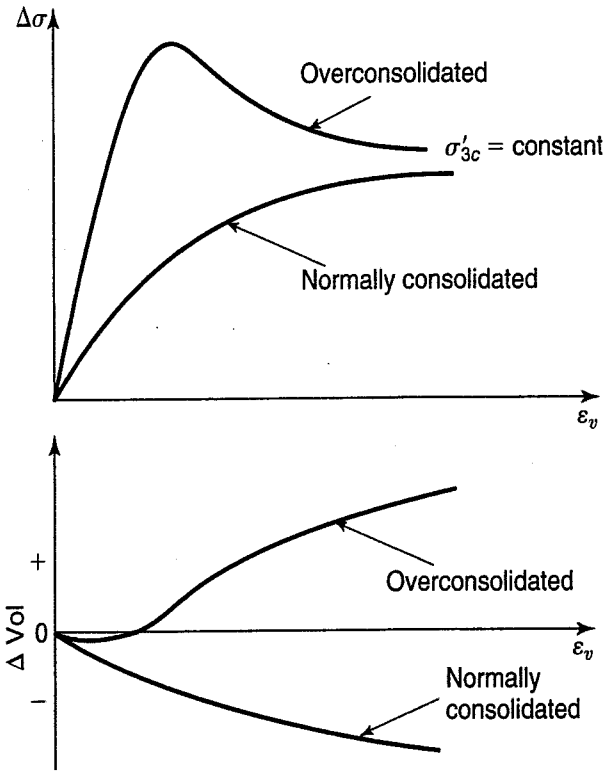

FIGURE 12.23 Typical stress-strain and volume-change-versus-strain curves for CD axial compression tests on compacted clay at the same effective confining stress.

$\sigma_{3c} = \sigma'_{3c} = \sigma_{3f} = \sigma'_{3f}$, and $\sigma_{1f} = \sigma'_{1f} = \sigma'_{3c} + \Delta\sigma_f$. If nonhydrostatic consolidation stresses were applied to the specimen, then $\sigma_{1f} = \sigma'_{1f}$ would be equal to $\sigma'_{1c} + \Delta\sigma_f$.

Typical stress-strain curves and volume change versus strain curves for a remolded or compacted clay are shown in Fig. 12.23. Even though the two specimens were tested at the same confining pressure, the overconsolidated specimen has a greater strength than the normally consolidated clay. Note also that it has a higher modulus and that failure [the maximum $\Delta\sigma$, which for the triaxial test is equal to $(\sigma_1 - \sigma_3)_f$] occurs at a much lower strain than for the normally consolidated specimen. Note, too, the analogy to drained behavior of sands. The overconsolidated clay *expands* during shear, while the normally consolidated clay *compresses* or consolidates during shear. Thus, normally consolidated clays behave similarly to loose sands, whereas overconsolidated clays behave like dense sands.

Dilation and expansion of normally and overconsolidated clays in drained shear is shown

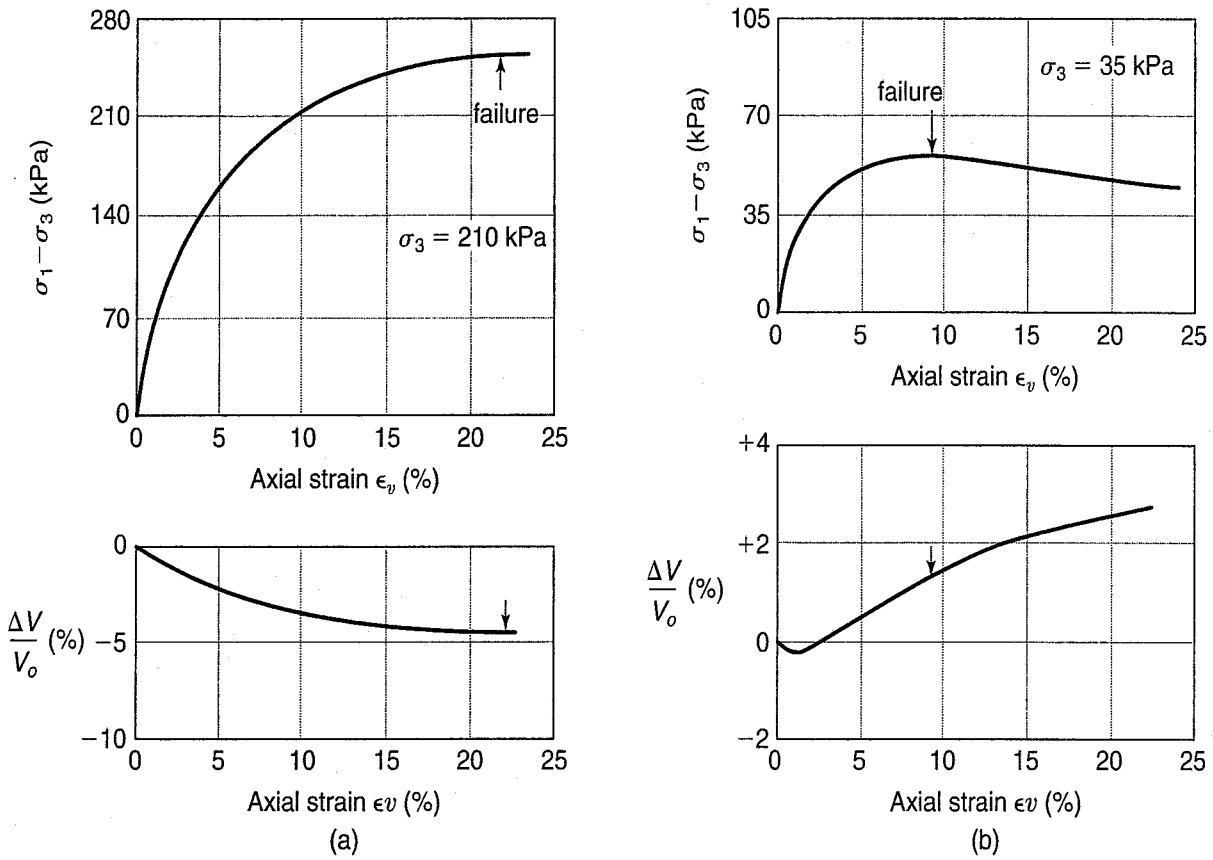

FIGURE 12.24 Consolidated-drained triaxial tests at a constant rate of strain on (a) normally consolidated, and (b) overconsolidated (OCR = 24) remolded and resedimented samples of Weald clay (after Henkel, 1956).

in Fig. 12.24 for tests on remolded and resedimented specimens of Weald clay (Henkel, 1956). The normally consolidated specimen was consolidated to 210 kPa and sheared with the drainage valves open. The other specimen was first consolidated to 840 kPa, then rebounded and tested at a cell pressure of 35 kPa (OCR = 24). Note the strongly dilative behavior in the overconsolidated specimen and the different shapes of the stress-strain curves. Also note that when failure occurs in the overconsolidated specimen [shown by the small arrows in Fig. 12.24(b)], defined as the peak of the stress-strain curve or the maximum $(\sigma_1 - \sigma_3)$, this point coincides with the inflection point in the volume-change curve. Although we don't show any small arrows in Fig. 12.23, you can see that the same thing occurs in the stress-strain and volume change-strain curves for the overconsolidated specimen.

The Mohr failure envelope for a CD test on a normally consolidated clay soil is shown in Fig. 12.25. Even though only one Mohr circle (representing the stress conditions at failure in Fig. 12.22) is shown, the results of three or more CD tests on identical specimens at different consolidation pressures would ordinarily be required to plot the complete Mohr failure envelope. If the consolidation stress range is large or the specimens do not have exactly the same initial water content, density, and stress history, then the three failure circles will not

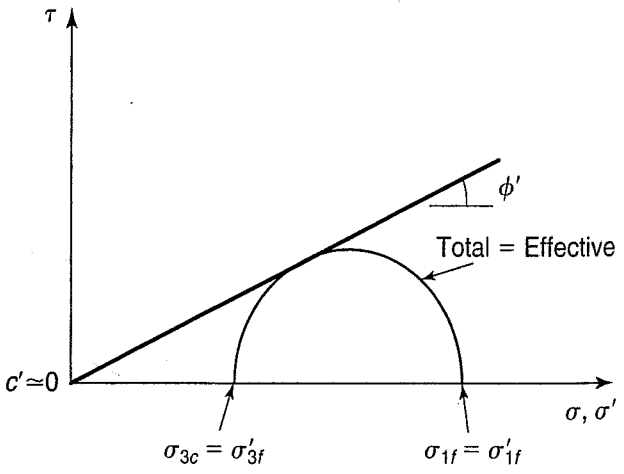

FIGURE 12.25 Mohr failure envelope for a normally consolidated clay in drained shear.

exactly define a straight line, and an average best-fit line by eye is drawn. The slope of the line determines the Mohr–Coulomb strength parameter ϕ', of course, in terms of effective stresses. When the failure envelope is extrapolated to the shear axis, it will show a surprisingly small intercept. Thus it is usually assumed that the c' parameter for normally consolidated non-cemented clays is essentially zero for all practical purposes.

The behavior of overconsolidated clays is a little more complicated, as illustrated in Fig. 12.26(b). To make things easier to see, we show the Mohr failure envelope without the Mohr circles. The c' parameter is greater than zero, because the overconsolidated portion of the strength envelope (DEC) lies *above* the normally consolidated envelope (ABCF). This portion (DEC) of the Mohr failure envelope is sometimes called the *preconsolidation hump*. The explanation for this behavior is shown in the e versus σ' curve of Fig. 12.26(a). (Recall from Fig. 8.4 that the virgin compression curve, when plotted arithmetically, is concave upward.) To understand the entire behavior shown in Fig. 11.24, assume that we begin consolidation of a sedimentary clay at a very high water content and high void ratio. As we continue to increase the vertical stress, when we reach point A on the virgin compression curve, we conduct a CD triaxial test. (We could, of course, do the same thing with a CD direct shear test.) The strength of the specimen consolidated to point A on the virgin curve corresponds to point A on the normally consolidated Mohr failure envelope in Fig. 12.26(b). If we consolidate and test another otherwise identical specimen that is loaded to point B, then we obtain the strength, again normally consolidated, at point B on the failure envelope in Fig. 12.26(b).

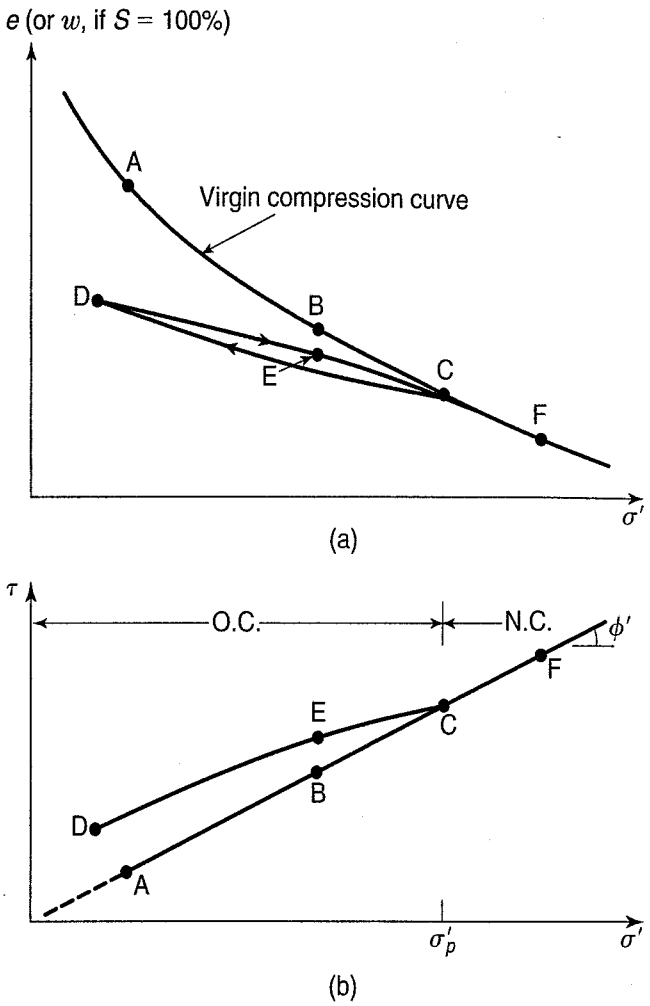

FIGURE 12.26 (a) Compression curve; (b) Mohr failure envelope (DEC) for an overconsolidated clay.

If we repeat the same process to point C (σ'_p, the preconsolidation stress), then rebound the specimen to D and shear it, we obtain the strength shown at point D in the lower figure. If we repeat the process to point C, rebound to D, and reload to E and shear, we obtain the strength shown at point E in the lower figure. Note that the shear strengths of specimens D and E are greater than their corresponding normally consolidated strengths, even though they are tested at the same effective consolidation stresses. The reason for the greater strength of, for example, E than B is that E is at a lower water content, has a lower void ratio, and thus is denser than B, as shown in Fig. 12.26(a). If another specimen were loaded to C, rebounded to D, reloaded back past E and C and on up to F, it would have the strength shown in the figure at point F. Note that at this point it is now back on the virgin compression curve and the normally consolidated failure envelope. The effects of the rebounding and reconsolidation have been in effect *erased* by the increased loading to point F. Once the soil has been loaded well past the preconsolidation pressure σ'_p, it no longer "remembers" its stress history.

12.9.2 Typical Values of Drained Strength Parameters for Saturated Cohesive Soils

For the Mohr failure envelopes of Figs. 12.25 and 12.26, we did not indicate any numerical values for the effective stress strength parameters ϕ'. Average values of ϕ' for undisturbed clays typically range from around 20° for normally consolidated highly plastic clays up to 30° or more for silty and sandy clays. The value of ϕ' for compacted clays is typically 25° or 30° and occasionally as high as 35°. As mentioned earlier, the value of c' for normally consolidated non-cemented clays is very small and can be neglected for practical work. If the soil is overconsolidated, then ϕ' will be less, and the c' intercept greater, than for the normally consolidated part of the failure envelope [see Fig. 12.26(b) again]. According to Ladd (1971b), for natural, overconsolidated, non-cemented clays with a preconsolidation stress of less than 500 to 1000 kPa, c' will probably be less than 5 to 10 kPa at low stresses. For compacted clays at low stresses, c' will be much greater due to the prestress caused by compaction. For stability analyses, the Mohr–Coulomb effective stress parameters ϕ' and c' are determined over the range of effective normal stresses likely to be encountered in the field.

It has been observed (for example, Kenney, 1959) that there is not much difference between ϕ' determined on undisturbed or remolded specimens at the same water content. Apparently, the development of the maximum value of ϕ' requires so much strain that the soil structure is broken down and almost remolded in the region of the failure plane.

Empirical correlations between ϕ' and the plasticity index for normally consolidated clays are shown in Fig. 12.27. This correlation is based on work by Kenney (1959), Bjerrum and Simons (1960), U.S. Dept. of the Navy (1986), and Ladd et al. (1977). Since there is considerable scatter around the "average line," you should use this correlation with considerable caution. However Fig. 12.27 is useful for preliminary estimates and for checking laboratory results.

12.9.3 Use of CD Strength in Engineering Practice

Where do we use the strengths determined from the CD test? As mentioned previously, the limiting drainage conditions modeled in the triaxial test refer to real field situations. CD conditions are the most critical for the long-term steady seepage case for embankment dams and the long-term stability of excavations or slopes in soft and stiff clays. CD conditions are very critical in clays with higher overconsolidation ratios, typically OCR > 4. This is because overconsolidated stiff clays tend to expand and take in water over time, thus reducing their shear strength. Examples of CD analyses are shown in Fig. 12.28. Explanations of how you actually go about making these analyses for stability can be found in textbooks on foundation and embankment dam engineering.

You should be aware that, practically speaking, it is not easy to actually conduct a CD triaxial test on a clay in the laboratory. To ensure that no pore pressure is really induced in the specimen during shear for materials with very low permeabilities, the rate of loading must be very slow. The time required to fail the specimen ranges from days to several weeks (Bishop and Henkel, 1962). Such a long time leads to practical problems in the laboratory such as leakage of valves, seals, and the membrane that surrounds the specimen. Consequently, since it is possible to measure the induced pore pressures in a consolidated-undrained (CU) test and thereby calculate the effective stresses in the specimen, and because CU tests with pore pressures measured can be conducted more rapidly than CD tests and still give reasonable results, they are more practical for obtaining the effective stress strength parameters. Therefore, CD triaxial tests on clay soils are very rarely, if ever, performed in practice.

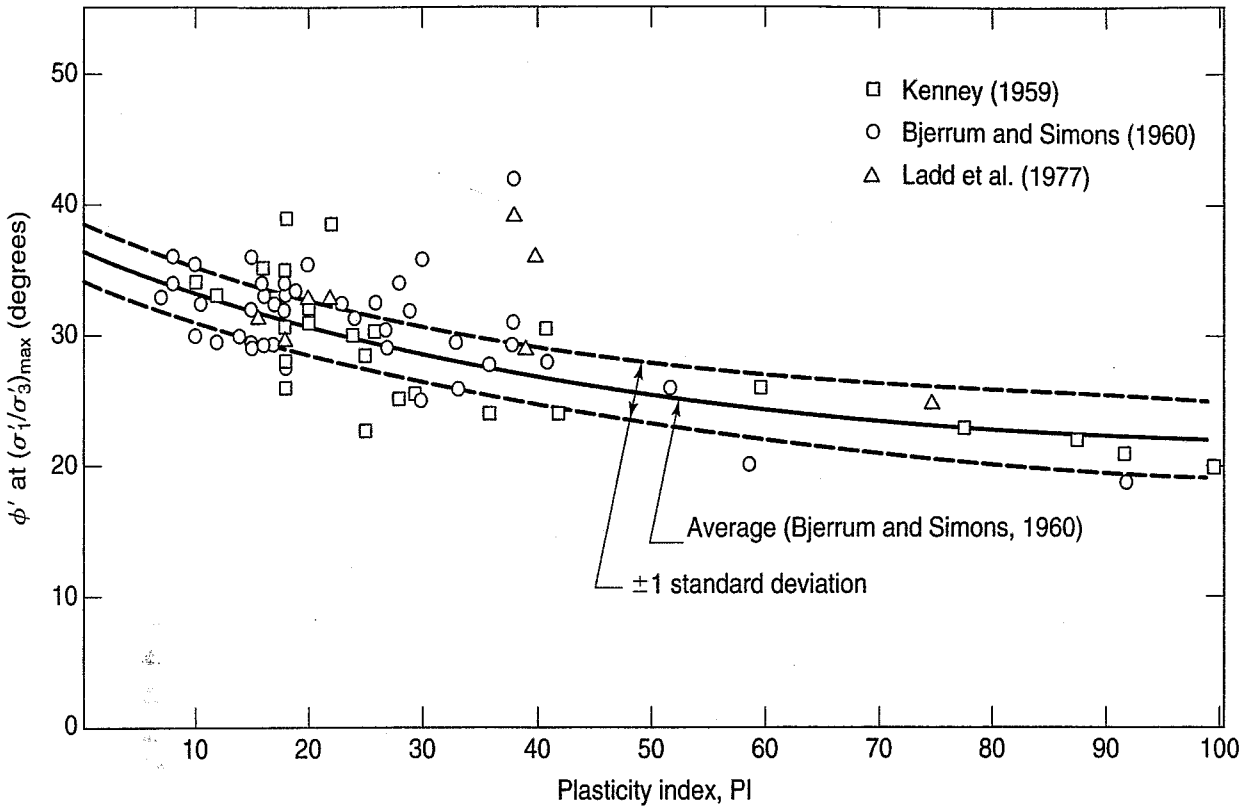

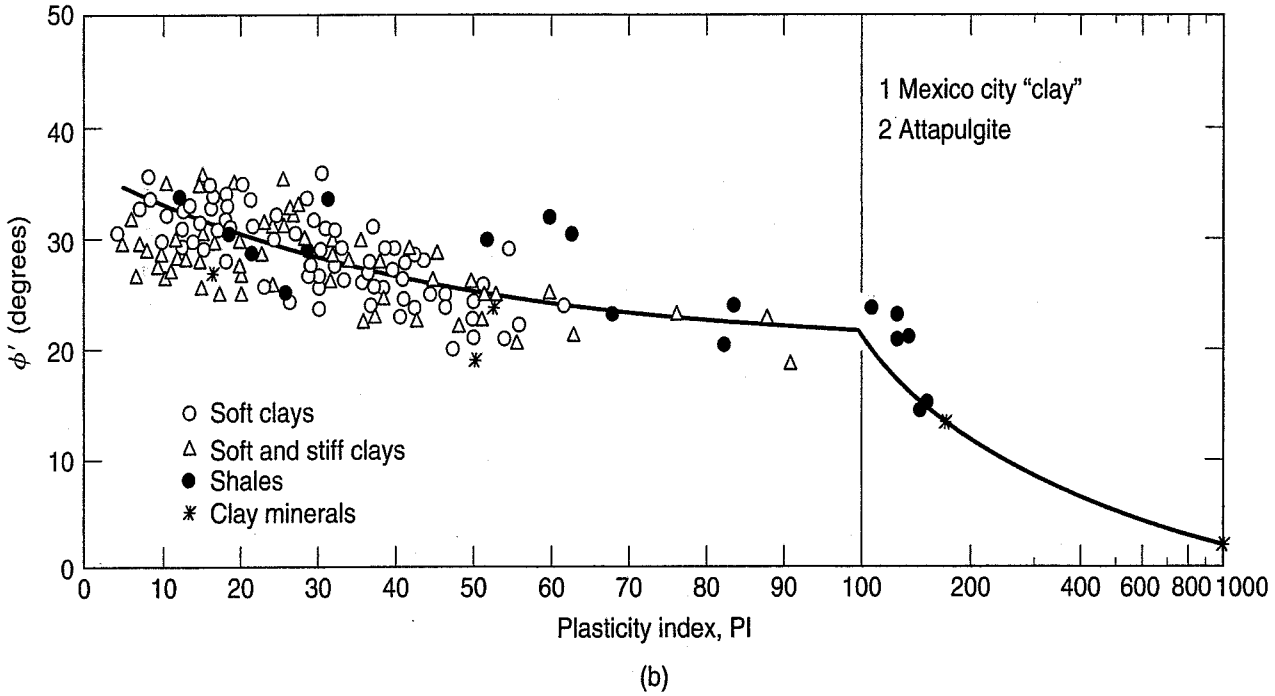

FIGURE 12.27 Empirical correlation between ϕ' and PI: (a) from triaxial compression tests on normally consolidated undisturbed clays (after U.S. Dept. of the Navy, 1986, and Ladd et al., 1977); (b) for a wide range of clay minerals and different soils (after Terzaghi et al., 1996).

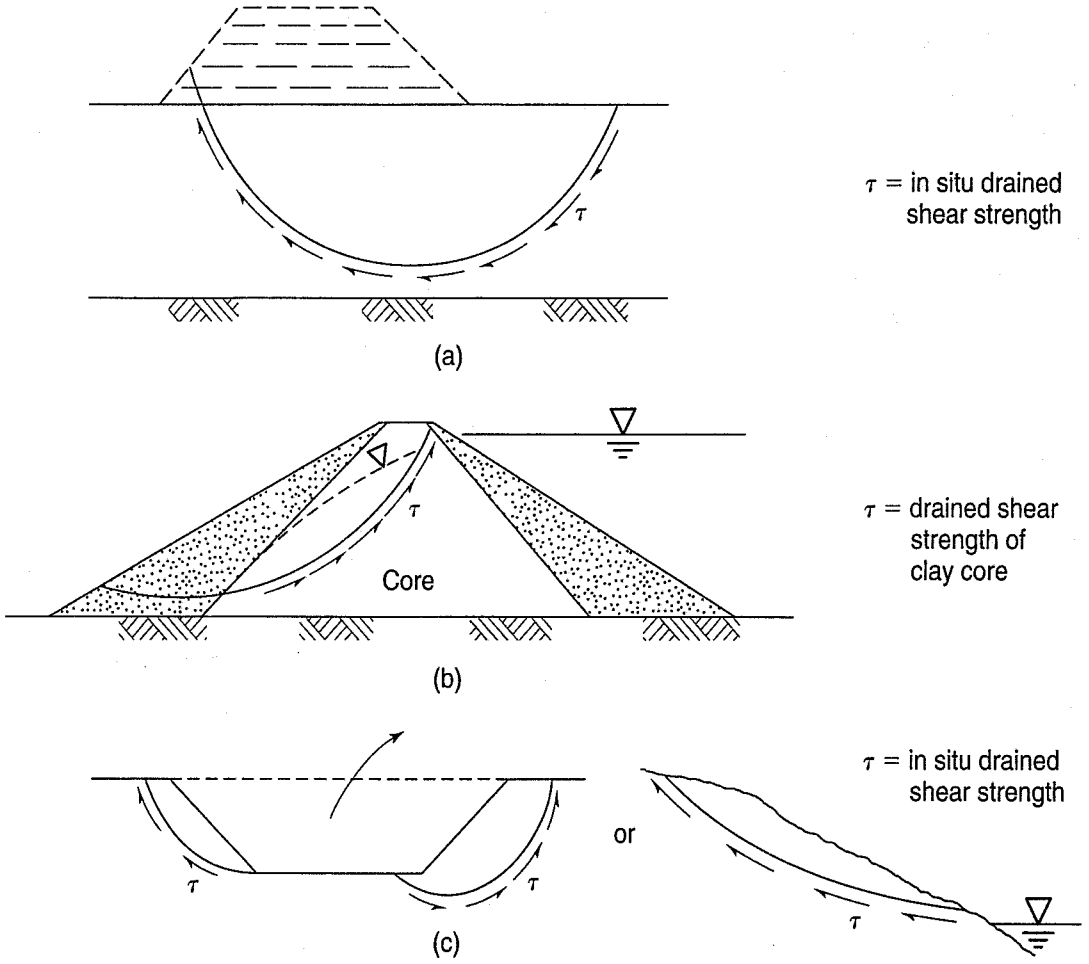

FIGURE 12.28 Some examples of CD stability analyses for clays (after Ladd, 1971b): (a) embankment constructed very slowly, in layers, over a soft clay deposit; (b) earth dam with steady-state seepage; (c) excavation or natural slope in clay.

12.10 CONSOLIDATED-UNDRAINED STRESS-DEFORMATION AND STRENGTH CHARACTERISTICS

12.10.1 Consolidated-Undrained (CU) Test Behavior

As the name implies, a consolidated-undrained (CU) triaxial test specimen is first consolidated (drainage valves open, obviously) under the desired consolidation stresses. As before, these stresses can either be hydrostatic or nonhydrostatic. After consolidation is complete, the drainage valves are closed, and the specimen is loaded to failure in undrained shear. Often, the pore water pressures developed during shear are measured, and both the total and effective stresses may be calculated during shear and at failure. Thus this test can either be a total *or* an effective stress test. This test is sometimes called the *R-test* (for "rapid" test), but only if total stresses are measured.

Total, pore pressure, and effective stress conditions in the specimen during the several phases of the CU test are shown in Fig. 12.29. The symbols are the same as we used before in Fig. 12.22. The general case of unequal consolidation is shown, but typically for routine triaxial testing the specimen is consolidated hydrostatically under a cell pressure which remains constant during shear. Thus,

$$\sigma_{\text{cell}} = \sigma_{vc} = \sigma_{hc} = \sigma'_{1c} = \sigma'_{3c} = \sigma_{3f} \neq \sigma'_{3f}$$

$$\Delta\sigma_f = (\sigma_1 - \sigma_3)_f$$

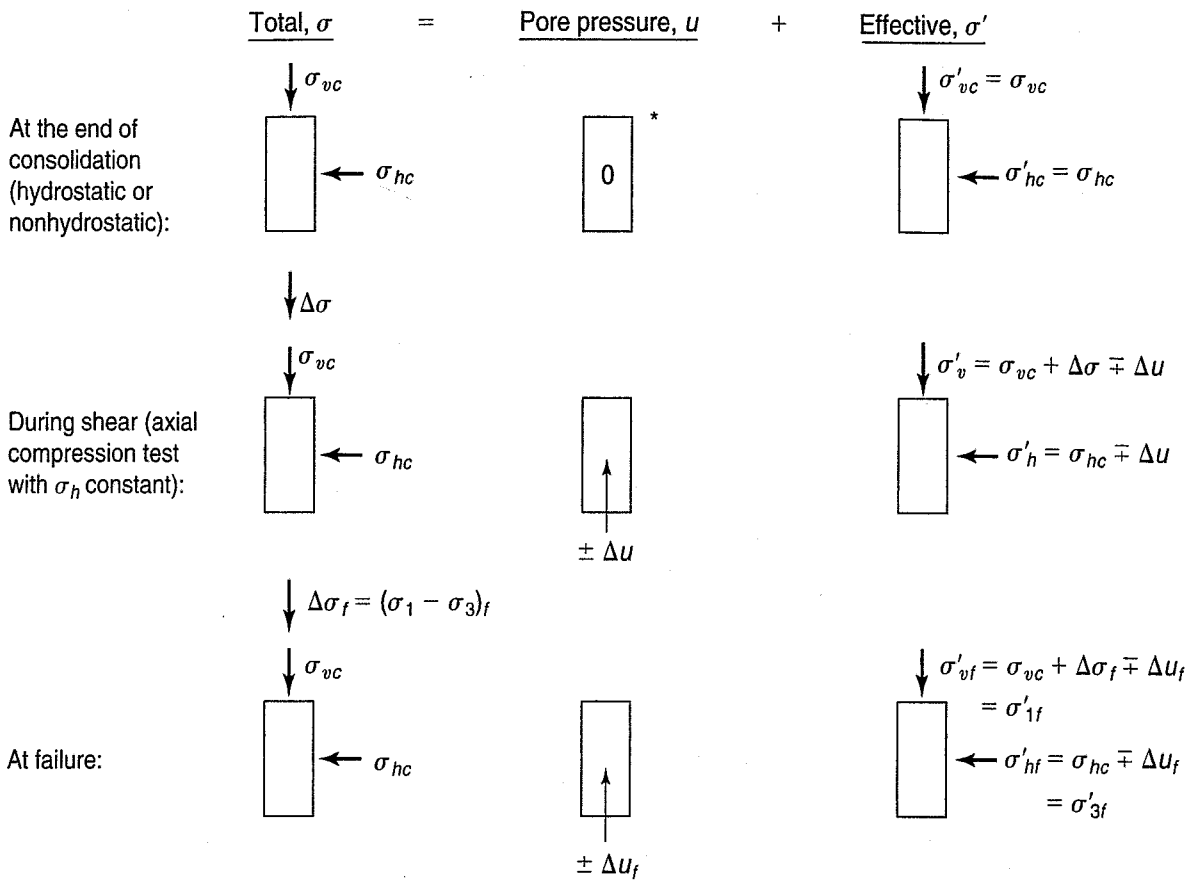

*In practice, to ensure 100% saturation, which is necessary for good measurement of the pore water pressure, *a back pressure* is applied to the pore water. To keep the effective consolidation stresses constant, the total stresses during consolidation are accordingly increased by an amount exactly equal to the applied back pressure, which is the same as raising atmospheric pressure by a constant amount–the effective stresses on the clay do not change.

Example: Initial conditions with back pressure:

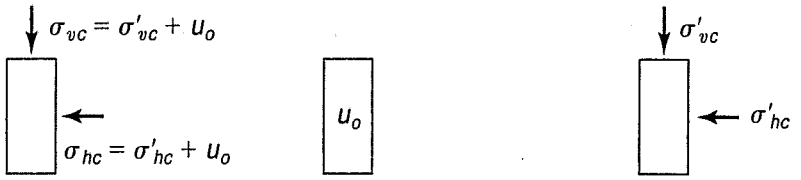

FIGURE 12.29 Conditions in specimen during a consolidated-undrained axial compression (CU) test.

Like the CD test, the axial stress can be increased incrementally or at a constant rate of strain. At failure, then, the test illustrated in Fig. 12.29 is a conventional axial compression test in that the axial stress is increased to failure.

Note that the excess pore water pressure Δu developed in the specimen during shear can be either positive (that is, increase) or negative (that is, decrease). This happens because the specimen tries to either contract or expand during shear. Remember, we are not allowing any volume change (an undrained test), and therefore no water can flow in or out of the specimen during shear. Because volume changes are prevented, the *tendency* toward volume change induces a pressure in the pore water. If the specimen *tends* to contract or consolidate during shear, then the induced pore water pressure is *positive*. It wants to contract and squeeze water out of the pores, but cannot; thus the induced pore water pressure is positive. Positive pore pressures occur in normally consolidated clays. If the specimen *tends* to expand or swell during shear, the induced pore water pressure is *negative*. It wants to expand and draw water into the pores, but cannot; thus the pore water pressure decreases and may even go negative (that is, below zero gage pressure, or below atmospheric pressure). Negative pore pressures

occur in overconsolidated clays. Thus, as noted in Fig. 12.29, the *direction* ($\pm$) of the induced pore water pressure Δu is important, since it directly affects the magnitudes of the effective stresses.

You might note also that in actual testing the initial pore water pressure typically is greater than zero. In order to ensure full saturation, a *back pressure* u_o is usually applied to the test specimen. Back pressure not only compresses the air in the soil voids but also causes the air to go into solution in the pore water, so that the space previously occupied by air bubbles is filled with water. As explained in the footnote in Fig. 12.29, when a back pressure is applied to a specimen, the cell pressure must also be increased by an amount equal to the back pressure, so that the effective consolidation stresses remain the same. Since the effective stress in the specimen does not change, the strength of the specimen is not supposed to be changed by the use of back pressure. In practice this may not be exactly true, but the advantage of having 100% saturation for accurate measurement of induced pore water pressures far outweighs any disadvantages of using back pressure.

Typical stress-strain, Δu, and σ_1'/σ_3' curves for CU tests on compacted clays are shown in Fig. 12.30 for both normally and overconsolidated clays. Also shown for comparison is a stress-strain curve for an overconsolidated clay at low effective consolidation stress. Note the peak, then the drop-off of stress as strain increases (work-softening material, Fig. 11.4). The pore pressure versus strain curves illustrate what happens to the pore pressures during shear. The normally consolidated specimen develops positive pore pressure. In the overconsolidated specimen, after a slight initial increase, the pore pressure goes "negative"—in this case, negative with respect to the back pressure u_o. Another quantity useful for analyzing test results is the principal (effective) stress ratio, σ_1'/σ_3'. Note how this ratio peaks early, just like the stress difference curve, for the overconsolidated clay. Similar test specimens having similar behavior on an effective stress basis will have similarly shaped σ_1'/σ_3' curves. They are simply a way of normalizing the stress behavior with respect to the effective minor principal stress during the test. Sometimes, too, the maximum of this ratio is used as a criterion of failure. However, we will continue to define failure as the maximum principal stress difference. Note that this value is also the *compressive strength* of the test specimen.

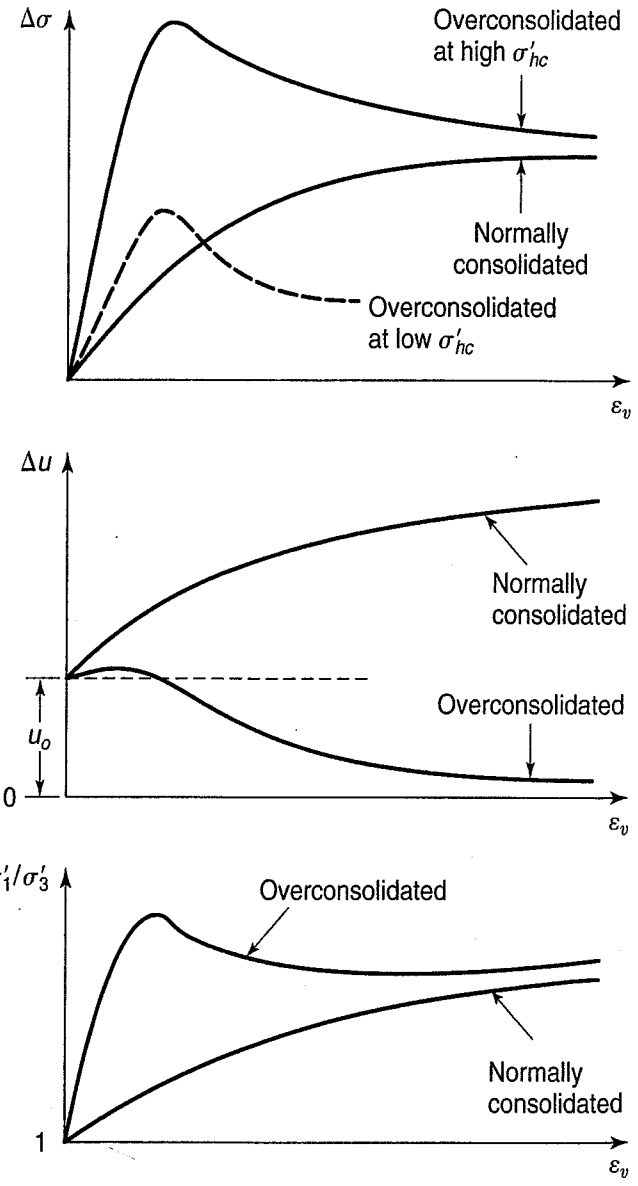

Note: For hydrostatic consolidation, $\sigma_1'/\sigma_3' = 1$ at the start of the test; for nonhydrostatic consolidation, $\sigma_1'/\sigma_3' > 1$.

FIGURE 12.30 Typical ε, Δu, and σ_1'/σ_3' curves for normally and overconsolidated compacted clays in undrained shear (CU test).

Figure 12.31 shows results from consolidated-undrained tests on remolded and resedimented specimens of Weald clay (Henkel, 1956). These data are from companion tests on the same soil as the CD

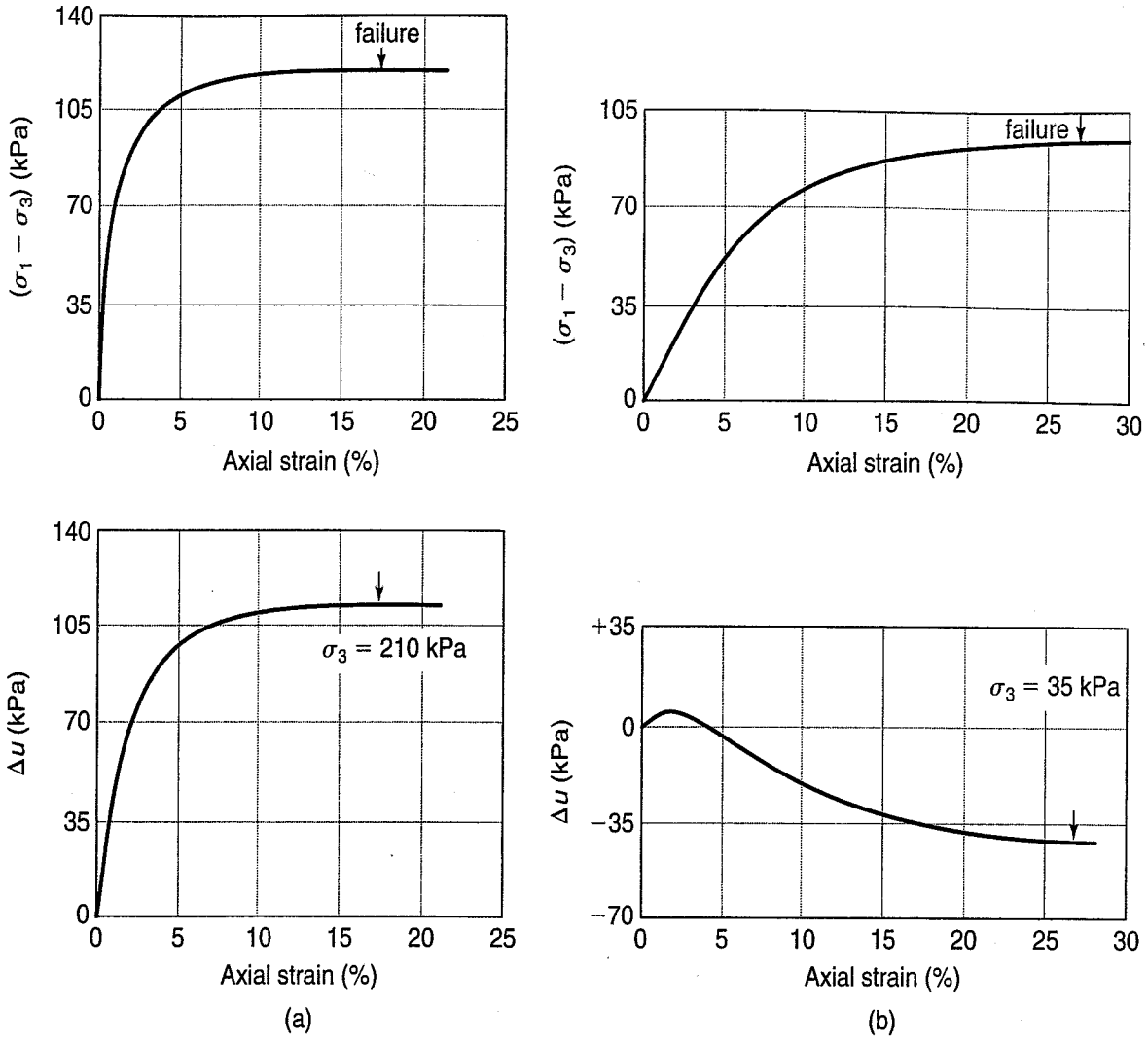

FIGURE 12.31 Consolidated undrained triaxial tests at a constant rate of strain on remolded and resedimented samples of Weald clay: (a) normally consolidated; and (b) overconsolidated, OCR = 24 (after Henkel, 1956).

tests in Fig. 12.24. Test specimens were prepared in exactly the same way as those tests, with one specimen normally consolidated and the other heavily overconsolidated. Then the CU tests were, of course, sheared undrained with pore pressures measured. You can see the similarities with the curves in Fig. 12.32. Another thing to note is that the shapes of the stress-strain curves may be very different, depending on the soil structure and whether the test specimens were compacted or undisturbed natural clays. CU stress-strain behavior can be complicated, and we discuss this further in Chapter 13.

What do the Mohr failure envelopes look like for CU tests? Since we can get both the total and effective stress circles at failure for a CU test when we measure the induced pore water pressures, it is possible to define the Mohr failure envelopes in terms of both total and effective stresses. This is illustrated in Fig. 12.32 for a normally consolidated clay. For clarity, only one set of Mohr circles is shown. These circles are simply plotted from the stress conditions at failure in Fig. 12.29. Note that the effective stress circle is displaced to the left, toward the origin, for the normally consolidated case. This is because the specimens develop positive pore pressure during shear and $\sigma' = \sigma - \Delta u$. Note that both circles have the *same diameter* because of our definition of failure at maximum $(\sigma_1 - \sigma_3) = (\sigma'_1 - \sigma'_3)$. You should verify that this equation is true.

At least three triaxial tests are usually conducted on identical specimens over a range of stresses in order to define the Mohr failure envelopes. From these envelopes the Mohr–Coulomb strength

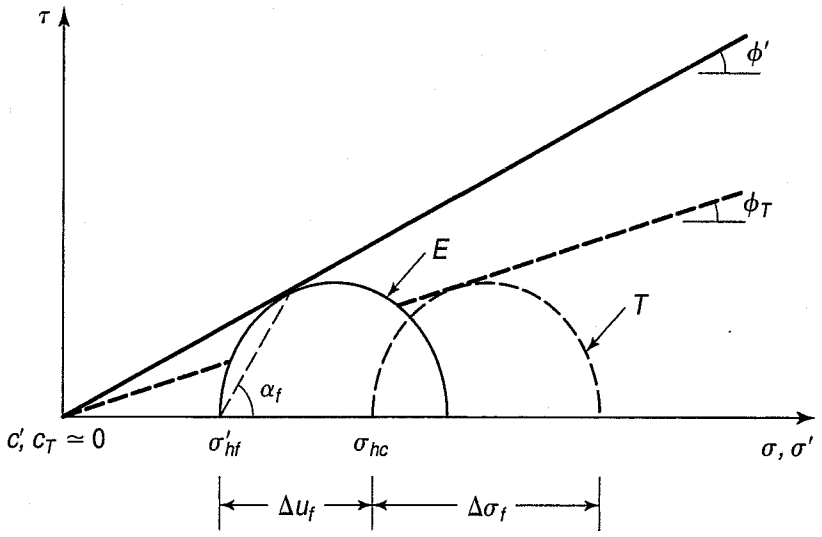

FIGURE 12.32 Mohr circles at failure and Mohr failure envelopes for total (T) and effective (E) stresses for a normally consolidated clay.

parameters are readily determined in terms of both total (c, ϕ or sometimes c_T, ϕ_T) and effective stresses (c', ϕ'). Again, as with the CD test, the envelope for normally consolidated clay passes essentially through the origin, and thus for practical purposes c' can be taken to be zero. The total stress c parameter is also rather small for a normally consolidated clay. Note that ϕ_T is less than ϕ', and often it is about one-half of ϕ'. Also, when you plot the total stress circle, you must be sure to subtract the back pressure from the measured total stresses. In other words, this "T" circle in Fig. 12.32 is really the $(T - u_o)$ circle.

Things are different if the clay is overconsolidated. Since an overconsolidated specimen tends to expand during shear, the pore water pressure decreases or even goes negative, as shown in Fig. 12.33. Because $\sigma'_{3f} = \sigma_{3f} - (-\Delta u_f)$ and $\sigma'_{1f} = \sigma_{1f} - (-\Delta u_f)$, the effective stresses are *greater* than the total stresses, and the effective stress circle at failure is shifted to the *right* of the total stress circle, as shown in Fig. 12.33. The shift of the effective stress circle at failure to the right sometimes means that the ϕ' is less than ϕ_T. Also note that in this case both the c' and c parameters are not small. As mentioned above, the complete Mohr failure envelopes are determined by tests on three or more specimens consolidated over the working stress range of the field problem.

Figure 12.34 shows the Mohr failure envelopes over a wide range of stresses spanning the preconsolidation stress. Thus some of the specimens are overconsolidated and others are normally consolidated. Notice that the "break" in the *total* stress envelope (point z) occurs at about twice the σ'_p for typical clays (Hirschfeld, 1963). The two sets of Mohr circles at failure shown in Fig. 12.34 correspond to the two tests shown in Fig. 12.30 for the "normally consolidated" specimen and the specimen marked "overconsolidated at low σ'_{hc}."

You may have noticed that an angle α_f was indicated on the effective stress Mohr circles of Figs. 12.32, 12.33, and 12.34. Do you recall the Mohr failure hypothesis, wherein the point of tangency of the Mohr failure envelope with the Mohr circle at failure defined the angle of the failure plane in the specimen? If not, reread Sec. 11.4. Since we believe that the shear strength is controlled by the effective stresses in the specimen at failure, the Mohr failure hypothesis is valid in terms of *effective stresses only*.

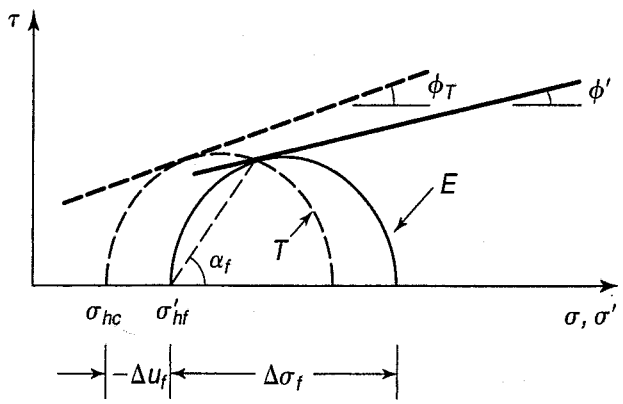

FIGURE 12.33 Mohr circles at failure and Mohr failure envelopes for both total (T) and effective (E) stresses for an overconsolidated clay.

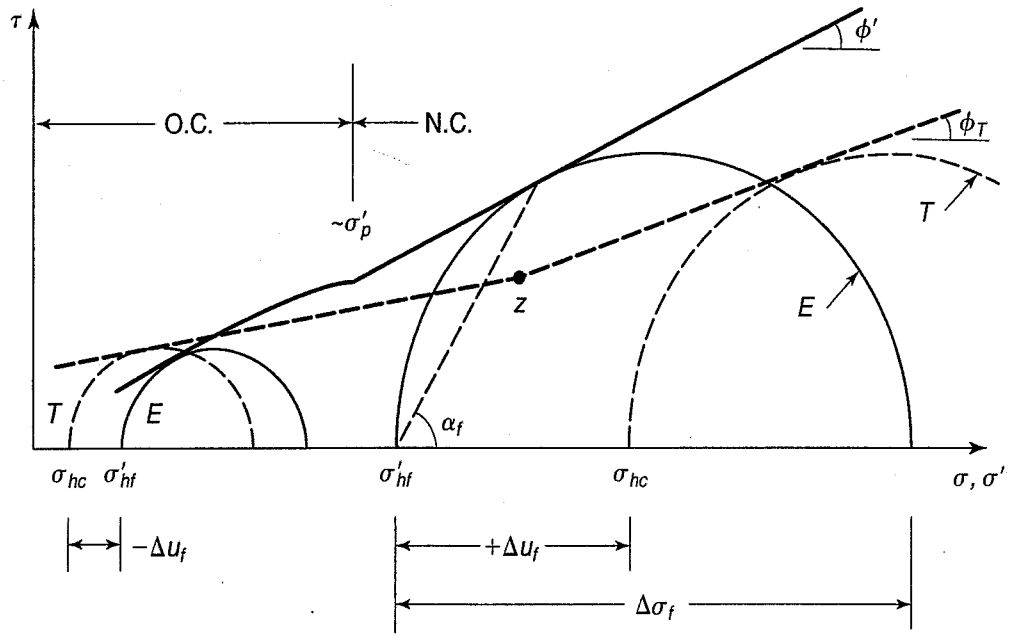

FIGURE 12.34 Mohr failure envelopes over a range of stresses spanning the preconsolidation stress σ'_p.

12.10.2 Typical Values of the Undrained Strength Parameters

In Sec. 12.9.2, we gave some typical values for c' and ϕ' determined by CD triaxial tests. The range of values indicated is also typical for effective stress strengths determined in CU tests with pore pressure measurements, with the following reservation. In our discussion so far, we have tacitly assumed that the Mohr–Coulomb strength parameters in terms of effective stresses determined by CU tests with pore pressure measurements would be the same as those determined by CD tests. We used the same symbols, c' and ϕ', for the parameters determined both ways. Although this assumption makes sense from a theoretical point of view, it may not be strictly correct—for a number of reasons. First, as we mentioned in Sec. 12.9.3, it is very difficult to run a CD test on a saturated clay. Second, companion CD and CU tests on the same soil not only are very rare but also are always suspect because of small differences in soil structure, possible sample disturbance, and differences in testing procedures. The problem is complicated by alternative definitions of failure and yielding in undrained triaxial tests. These factors are discussed in more detail in Sec. 13.8.2.

Figure 12.27 showed empirical correlations for ϕ' and PI for many different soils, most normally consolidated. In fact most of the tests used to develop this figure were CU tests with pore pressures measured. Figure 12.27 still can be used for preliminary estimates and for checking laboratory test results, because the differences in ϕ', depending on how failure is defined, etc., are less than the scatter in the figures.

For the Mohr–Coulomb strength parameters in terms of total stresses, the problem of defining failure doesn't come up. Failure is defined at the maximum compressive strength $(\sigma_1 - \sigma_3)_{max}$. For normally consolidated clays, ϕ seems to be about half of ϕ'; thus, values of 10° to 15° or more are typical, and the total stress c is very close to zero. For overconsolidated and compacted clays, ϕ may decrease and c will often be much greater than zero. When the failure envelope straddles the preconsolidation stress, interpretation of the strength parameters in terms of total stresses is difficult. This is especially true for undisturbed samples that may have some variation in water content and void ratio, even within the same geologic stratum.

12.10.3 Use of CU Strength in Engineering Practice

Where do we use the CU strength in engineering practice? As mentioned earlier, this test, with pore pressures measured, is commonly used to determine the shear-strength parameters in terms of both total and effective stresses. CU strengths are used for stability problems where the soils have first become fully consolidated and are at equilibrium with the existing stress system. Then, for some reason, *additional* stresses are applied quickly, with no drainage occurring. Practical examples include rapid drawdown of embankment dams and the slopes of reservoirs and canals. Also, in terms of effective stresses, CU test results are applied to the field situations mentioned in the earlier discussion of CD tests. Some of these practical examples are illustrated in Fig. 12.35.

As you might expect, there are some problems with CU tests on clay. For proper measurement of the pore pressures induced during shear, special care must be taken to see that the specimen is fully saturated, that no leaks occur during testing, and that the rate of loading (or rate of strain) is sufficiently slow so that the pore pressures measured at the ends of the specimen are the same as those occurring in the vicinity of the failure plane. As we mentioned, the use of back pressure is common to assure 100% saturation. The effects of the other two factors can be minimized by proper testing techniques, which are described in detail by Bishop and Henkel (1962).

Another problem, not often mentioned, results from trying to determine the long-term or effective stress strength parameters and the short-term or CU-total stress strength parameters from the same test series. The rates of loading or strain required for correct effective stress strength determination may

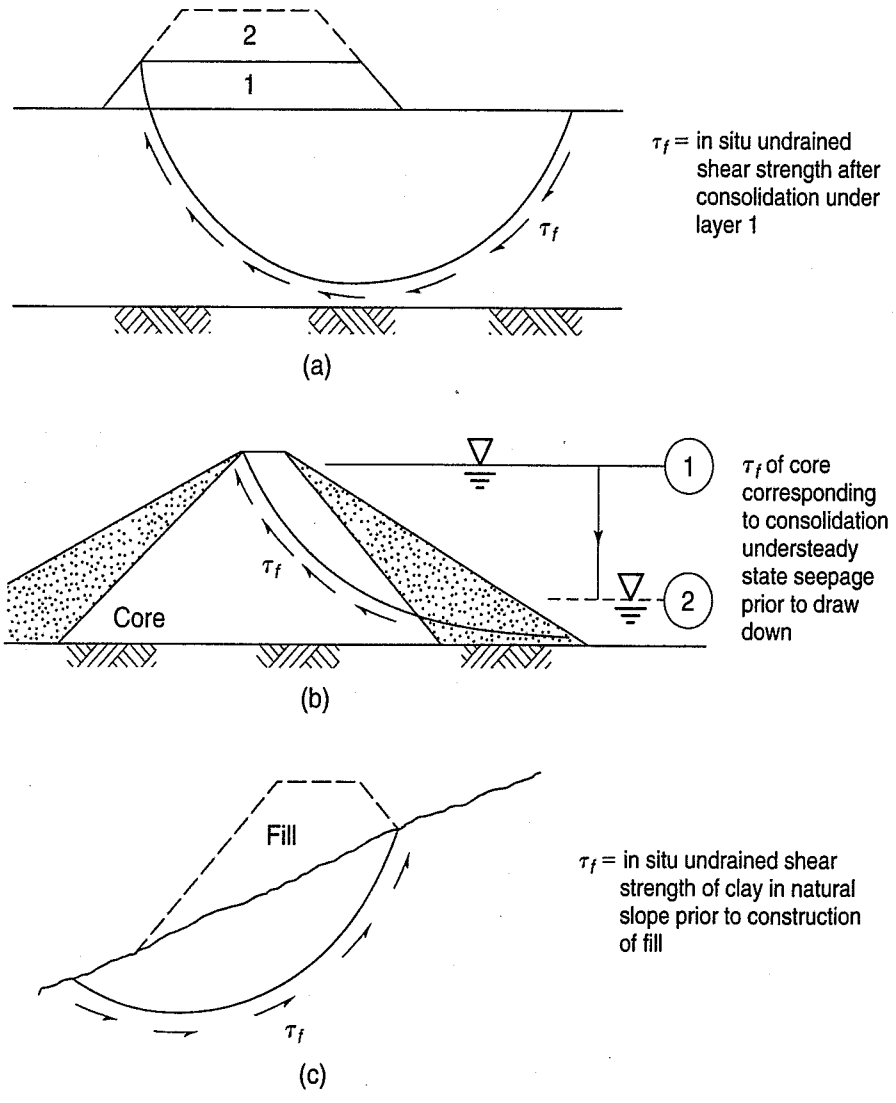

FIGURE 12.35 Some examples of CU stability analyses for clays (after Ladd, 1971b): (a) embankment raised (2) subsequent to consolidation under its original height, (1); (b) rapid drawdown behind an earth dam. No drainage of the core. Reservoir level falls from ① → ②; (c) rapid construction of an embankment on a natural slope.

not be appropriate for the short-term or undrained loading situation. As discussed in Sec. 13.14.7, the stress-deformation and strength response of clay soils is rate dependent; that is, usually the faster you load a clay, the stronger it becomes. In the short-term case, the rate of loading in the field may be quite rapid, and therefore for correct modeling of the field situation, the rates of loading in the laboratory specimen should be comparable. Thus the two objectives of the CU-effective stress test are really incompatible. The best thing to do, though rarely done in practice, would be to have two sets of tests, one set tested under CD conditions modeling the long-term situation and the other CU set modeling the short-term undrained loading.

Example 12.9

Given:

A normally consolidated clay is consolidated under a stress of 150 kPa, then sheared undrained in axial compression. The principal stress difference at failure is 100 kPa and the induced pore pressure at failure is 88 kPa.

Required:

Determine the Mohr–Coulomb strength parameters in terms of both total and effective stresses (a) analytically and (b) graphically. Plot the total and effective Mohr circles and failure envelopes. (c) Compute $(\sigma'_1/\sigma'_3)_f$ and $(\sigma_1/\sigma_3)_f$. (d) Determine the theoretical angle of the failure plane in the specimen.

Solution: To solve this problem we need to assume that both c' and c_T are negligible for a normally consolidated clay. Then we can use the obliquity relationships [Eqs. (11.14) through (11.17)] to solve for ϕ' and ϕ_T.

a. To use these equations, we need σ_{1f}, σ'_{1f}, σ_{3f}, and σ'_{3f}. We know $\sigma_{3f} = 150$ kPa and $(\sigma_1 - \sigma_3)_f = 100$ kPa. Therefore

$$\sigma_{1f} = (\sigma_1 - \sigma_3)_f + \sigma_{3f} = 100 + 150 = 250 \text{ kPa}$$
$$\sigma'_{1f} = \sigma_{1f} - u_f = 250 - 88 = 162 \text{ kPa}$$
$$\sigma'_{3f} = \sigma_{3f} - u_f = 150 - 88 = 62 \text{ kPa}$$

From Eq. (11.13),

$$\phi' = \arcsin\frac{100}{224} = 26.5°$$
$$\phi_T = \arcsin\frac{100}{400} = 14.5°$$

b. For the graphical solution, we need to plot the total and effective Mohr circles, and to do this we need to calculate σ_{1f}, σ'_{1f}, and σ'_{3f}. The centers of the circles are at (200, 0) for total stresses and at (112, 0) for effective stresses. The graphical solution including the failure envelopes is shown in Fig. Ex. 12.9.

c. The stress ratios at failure are

$$\frac{\sigma'_1}{\sigma'_3} = \frac{162}{62} = 2.61$$
$$\frac{\sigma_1}{\sigma_3} = \frac{250}{150} = 1.67$$

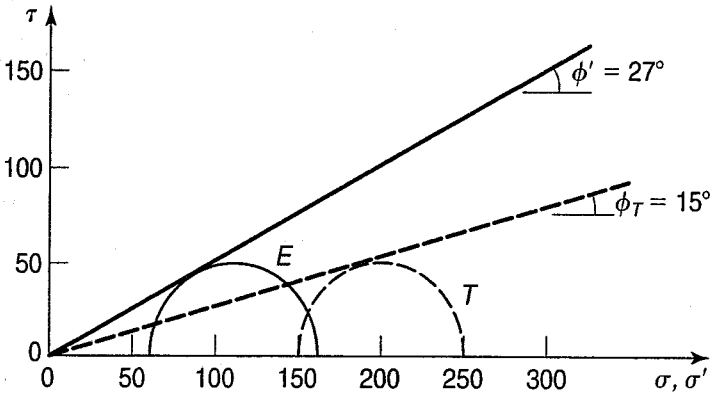

FIGURE Ex. 12.9

Another way to get these values would be to use Eq. (11.14).

$$\frac{\sigma_1'}{\sigma_3'} = \frac{1 + \sin 26.5°}{1 - \sin 26.5°} = \frac{1.45}{0.55} = 2.61$$

$$\frac{\sigma_1}{\sigma_3} = \frac{1 + \sin 14.5°}{1 - \sin 14.5°} = \frac{1.25}{0.75} = 1.67$$

d. Use Eq. (11.10), in terms of *effective* stresses:

$$\alpha_f = 45° + \frac{\phi'}{2} = 58° \text{ from the horizontal}$$

12.11 UNCONSOLIDATED-UNDRAINED STRESS-DEFORMATION AND STRENGTH CHARACTERISTICS

12.11.1 Unconsolidated-Undrained (UU) Test Behavior

In the unconsolidated-undrained (UU) test, the specimen is placed in the triaxial cell with the drainage valves closed from the beginning. Thus, even when a confining pressure is applied, no consolidation can occur if the specimen is 100% saturated. Then, as with the CU test, the specimen is sheared undrained. The specimen is loaded to failure in about 10 to 20 min; usually pore water pressures are not measured in this test. This is a *total stress test* and it yields the strength in terms of total stresses. A. Casagrande first called this test the *Q-test* (for "quick"), since the specimen was loaded to failure much more quickly than in the S-test.

Total, neutral, and effective stress conditions in the specimen during the several phases of the UU test are shown in Fig. 12.36. The symbols are as used before in Figs. 12.22 and 12.29. The test illustrated in Fig. 12.36 is quite conventional in that hydrostatic cell pressure is usually applied, and the specimen is failed by increasing the axial load, usually at a constant rate of strain. As with the other tests, the principal stress difference at failure is $(\sigma_1 - \sigma_3)_{max}$.

Note that initially, for undisturbed samples, the pore pressure is negative, and it is called the *residual pore pressure*, u_r, which results from stress release during sampling. Since the effective stresses initially must be greater than zero (otherwise the specimen would simply disintegrate) and the total stresses are zero (atmospheric pressure = zero gage pressure), the pore pressure must be negative. (See Sec. 13.13.4 for insight into the sampling process.) When the cell pressure is applied with the drainage valves closed, a positive pore pressure Δu is induced in the specimen, which is exactly equal to the applied cell pressure σ_c. All the increase in hydrostatic stress is carried by the pore water,

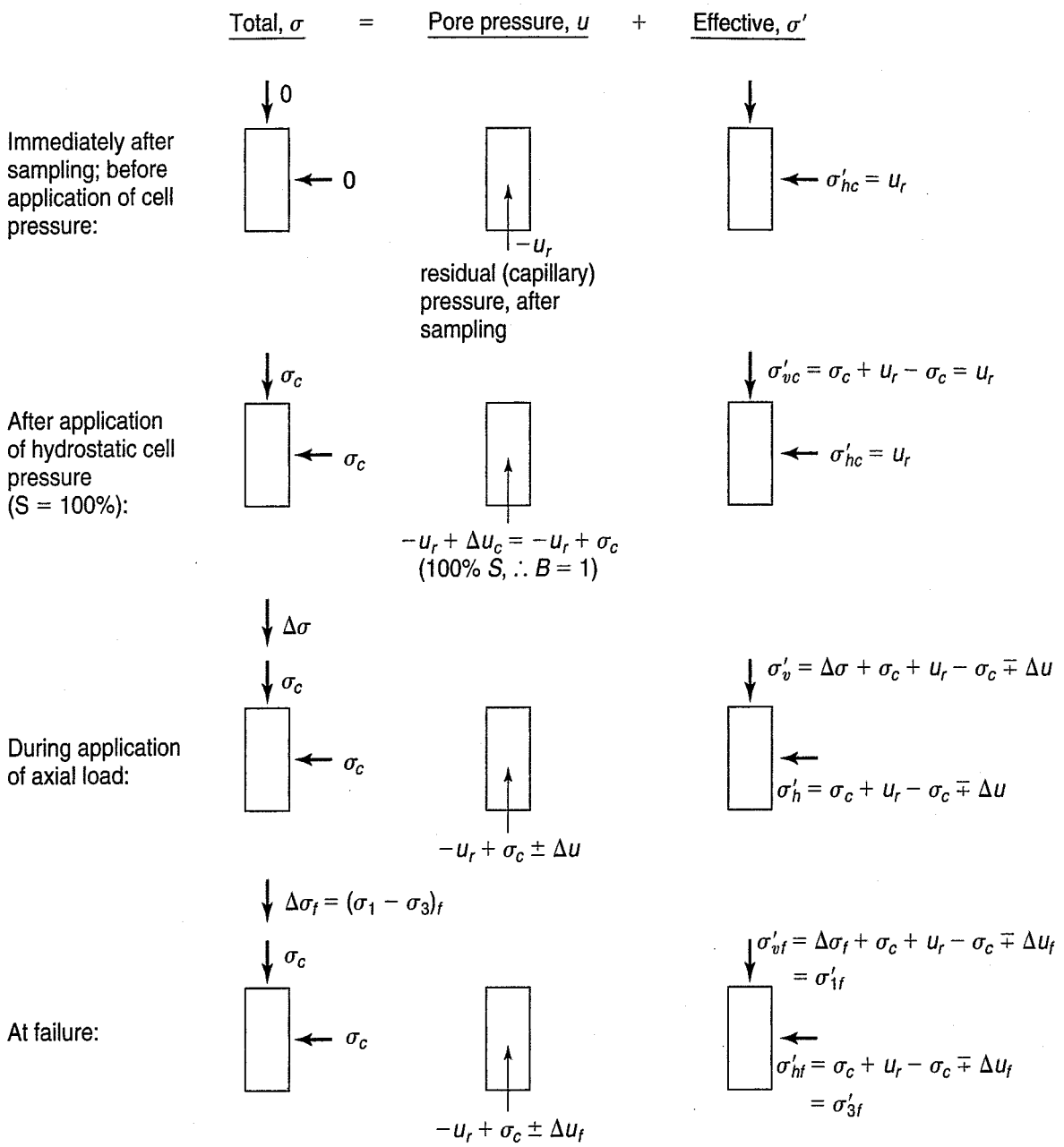

FIGURE 12.36 Conditions in the specimen during the unconsolidated-undrained (UU) axial compression test.

because (1) the soil is 100% saturated, (2) the compressibility of the water and individual soil grains is small compared to the compressibility of the soil structure, and (3) there is a unique relationship between the effective hydrostatic stress and the void ratio (Hirschfeld, 1963). Number (1) is obvious. Number (2) means that no volume change can occur unless water is allowed to flow out of (or into) the specimen, and we are preventing that from occurring. Number (3) means basically that no secondary compression (volume change at constant effective stress) takes place. You may recall from the discussion of the assumptions of the Terzaghi theory of consolidation (Chapter 9) that the same assumption was required—that is, that the void ratio and effective stress were uniquely related. Thus, there can be no change in void ratio without a change in effective stress. Since we prevent any change in water content, the void ratio and effective stress remain the same.

Stress conditions during axial loading and at failure are similar to those for the CU test (Fig. 12.29). They may appear to be complex, but if you study Fig. 12.36 you will see that the UU case is as readily understandable as the CU case.

Typically, stress-strain curves for UU tests are not particularly different from CU or CD stress-strain curves for the same soils. For undisturbed samples, the initial portions of the curve (initial tangent modulus) in particular depend strongly on the *quality* of the undisturbed samples. Also, the sensitivity (Secs. 2.7.3 and 12.12) affects the shape of these curves; highly sensitive clays have sharply peaked stress-strain curves. The maximum stress difference often occurs at very low strains, usually less than 0.5%. Some typical UU stress-strain curves are shown in Fig. 12.37.

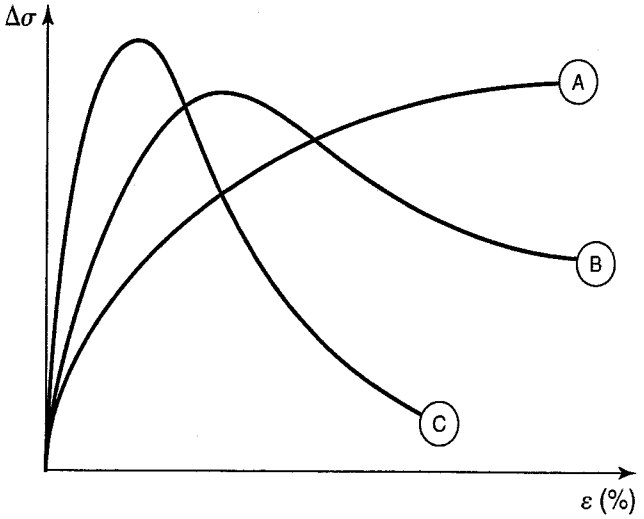

FIGURE 12.37 Typical UU stress-strain curves for (A) remolded and some compacted clays; (B) medium sensitive undisturbed clay; and (C) highly sensitive undisturbed clay.

The Mohr failure envelopes for UU tests are shown in Fig. 12.38(a) for 100% saturated clays. All test specimens for fully saturated clays are presumably at the same water content (and void ratio), so they will have the same shear strength, since no consolidation is allowed. Therefore all Mohr circles at failure will have the *same* diameter, and the Mohr failure envelope will be a horizontal straight line [see Fig. 11.9(c)]. This is a very important point. If you don't understand it, refer again to Fig. 12.36 to see that in the UU test the effective consolidation stress is the same throughout the test. If all the specimens are at the same water content and density (void ratio), then they will have the same strength. The UU test, as previously mentioned, gives the shear strength in terms of total stresses, and the slope ϕ_T of the UU Mohr failure envelope is *equal to zero*. The intercept of this envelope on the τ-axis defines the total stress strength parameter c, or $\tau_f = c$, where τ_f is undrained shear strength.

For unsaturated soils, a series of UU tests will define an initially curved failure envelope [Fig. 12.38(b)] until the clay becomes essentially 100% saturated due simply to the cell pressure alone.

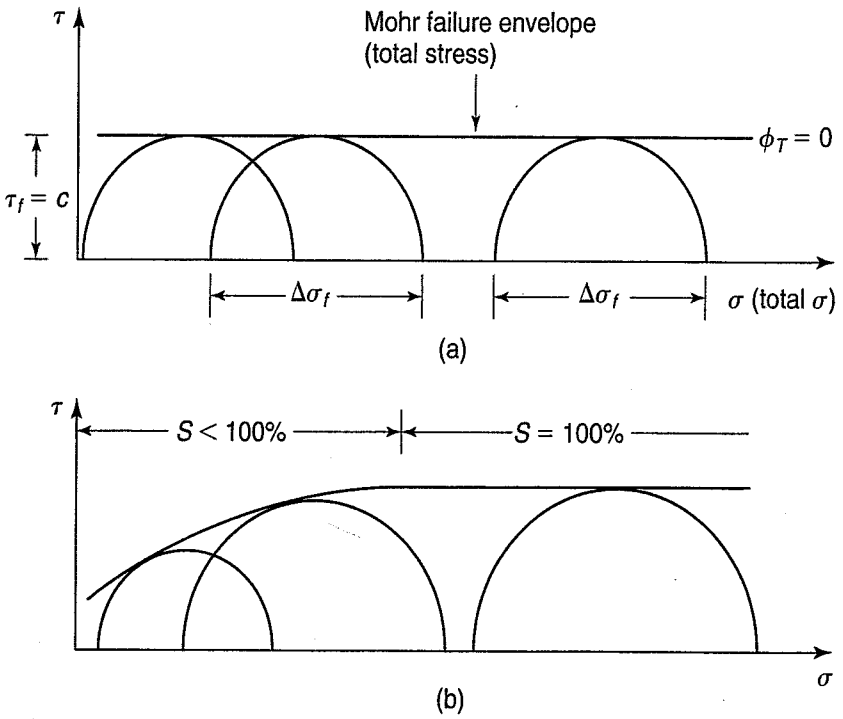

FIGURE 12.38 Mohr failure envelopes for UU tests: (a) 100% saturated clay; (b) unsaturated clay.

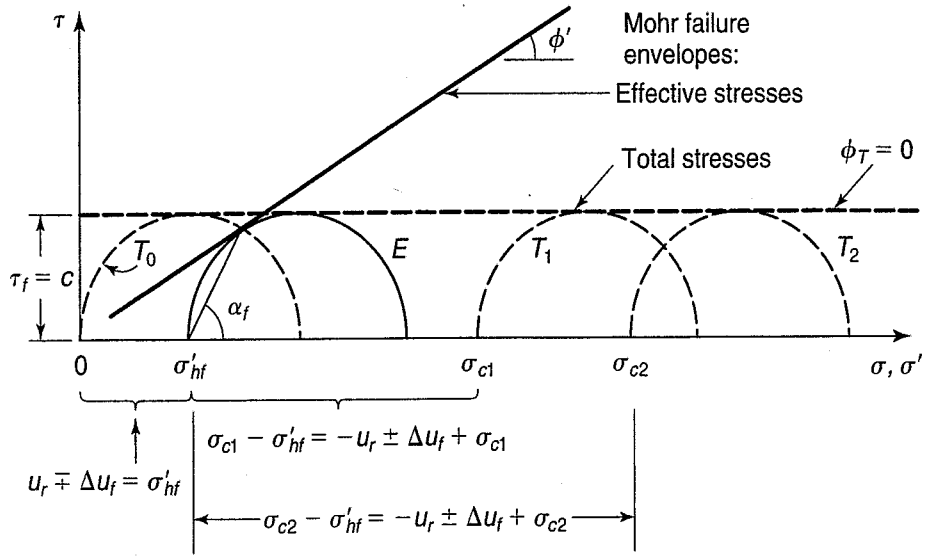

Note: σ'_{hf} is the same for all three total stress circles!

FIGURE 12.39 UU test results, illustrating the unique effective stress Mohr circle at failure.

Even though the drainage valves are closed, the confining pressure will compress the air in the voids and decrease the void ratio. As the cell pressure is increased, more and more compression occurs. Eventually, when sufficient pressure is applied, essentially 100% saturation is achieved. Then, as for initially 100% saturated clays, the Mohr failure envelope becomes horizontal, as shown on the right side of Fig. 12.38(b). The strength of unsaturated soils is very complex, and we briefly discuss this topic in Sec. 13.14. See Fredlund and Radharjo (1993) for a comprehensive treatment of this subject.

In principle, it is possible to measure the induced pore water pressures in a series of UU tests although it is not commonly done, because it is very difficult to do. Since the effective stresses at failure are *independent* of the total cell pressures applied to the several specimens of a test series, there is only *one* UU effective stress Mohr circle at failure. This point is illustrated in Fig. 12.39. Note that no matter what the confining pressure (for example, σ_{c1}, σ_{c2}, etc.), there is only one effective stress Mohr circle at failure. The minor effective principal stress at failure (σ'_{hf}) is the same for *all* total stress circles shown in the figure. Since we have only one effective circle at failure, strictly speaking, we need to know both ϕ' and c' in advance in order to draw the Mohr failure envelope in terms of effective stresses for the UU test. We could perhaps measure the angle of the failure plane in the failed UU specimens and invoke the Mohr failure hypothesis, but, as discussed in Sec. 11.4, there are practical problems with this approach. It should also be noted that the angle of inclination of the failure plane α_f shown in Fig. 12.39 is defined by the effective stress envelope. Otherwise, as indicated in Fig. 11.9(c) and Eq. (11.10), theory would predict α_f to be 45°. Since the strength ultimately is controlled or governed by the effective stresses, we believe that the physical conditions controlling the formation of a failure plane in the test specimen must in some fashion be controlled by the effective stresses acting in the specimen at failure. Thus, Eq. (11.10) should be in terms of ϕ' instead of ϕ_T, or $\alpha_f = 45° + \phi'/2$.

12.11.2 Unconfined Compression Test

The *unconfined compression test* is a special case of the UU test, but with the confining or cell pressure equal to zero (atmospheric pressure). The stress conditions in the unconfined compression test specimen are similar to those of Fig. 12.36 for the UU test, except that σ_c is equal to zero, as shown in Fig. 12.40. If you compare these two figures, you will see that the effective stress conditions at failure are *identical* for both tests. And if the effective stress conditions are the same in both tests, then the strengths will be the same!

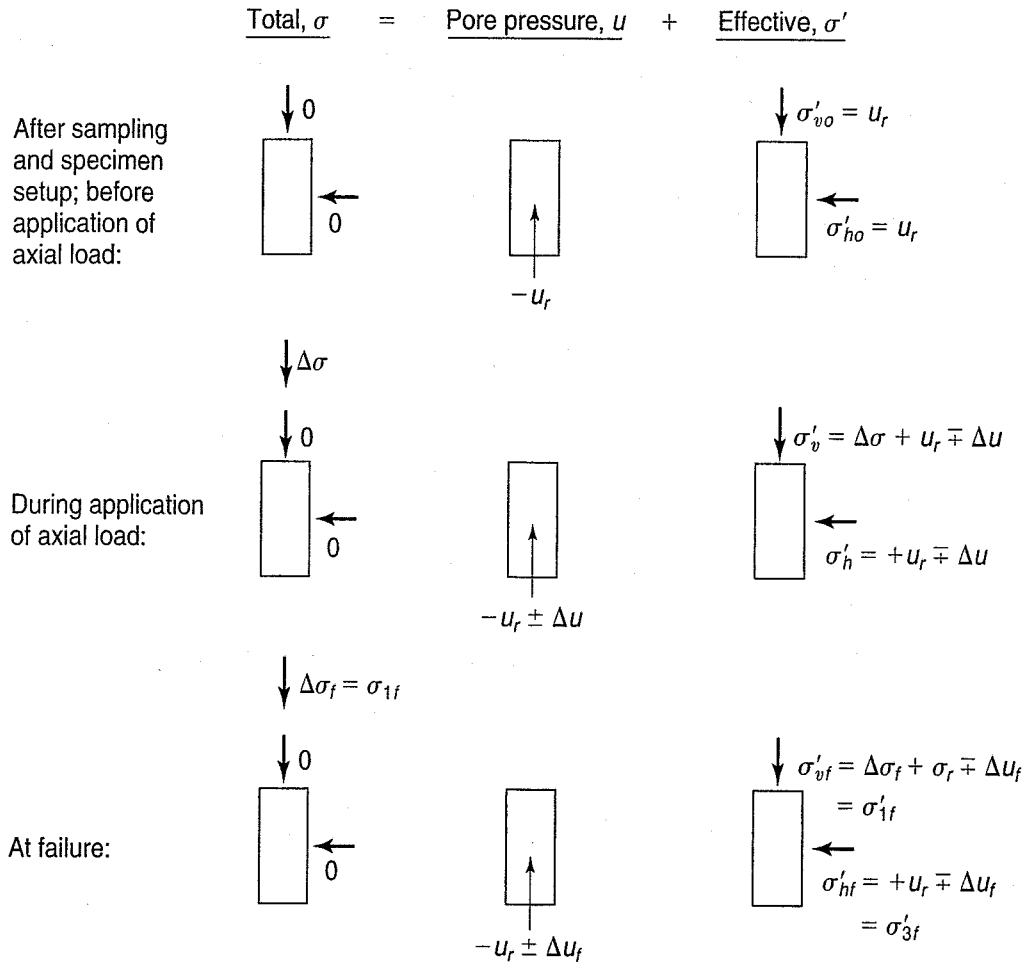

FIGURE 12.40 Stress conditions for the unconfined compression test.

Practically speaking, for the unconfined compression test to yield the same strength as the UU test, several assumptions must be satisfied. These are as follows:

1. The specimen must be 100% saturated; otherwise compression of the air in the voids will occur and cause a decrease in void ratio and an *increase* in strength.
2. The specimen must not contain any fissures, silt seams, varves, or other defects; this means that the specimen must be *intact*, homogeneous clay. Rarely are natural overconsolidated clays intact, and often even normally consolidated clays have some fissures and other defects.
3. The soil must be very fine grained; the initial effective confining stress as indicated in Fig. 12.40 is the residual capillary stress, which is a function of the residual pore pressure, u_r; this usually means that *only clay soils* are suitable for testing in unconfined compression.
4. The specimen must be sheared rapidly to failure; it is a total stress test and the conditions must be undrained throughout the test. If the time to failure is too long, evaporation and surface drying will increase the confining pressure, and too high a strength will result. Typical time to failure is 5 to 15 min.

Be sure to distinguish between unconfined *compressive* strength $(\sigma_1 - \sigma_3)_f$ and the undrained *shear* strength, which is $\tau_f = \frac{1}{2}(\sigma_1 - \sigma_3)_f$. You can see this in Fig. 12.32, where the far left total stress circle starts at the origin, which means that it is an unconfined compression test.

Example 12.10

Given:

An unconfined compression test is conducted on a soft clay. The specimen is trimmed from the undisturbed tube sample and is 35 mm in diameter and 80 mm high. The load on the force transducer at failure is 14.3 N and the axial deformation is 11 mm.

Required:

Calculate the unconfined compressive strength and the shear strength of the specimen.

Solution: To calculate the stress at failure, we have to know the area of the specimen A_s at failure. However, A_s at failure is *not* equal to the original area A_o, but is somewhat greater because in compression, the specimen decreases in height and increases in diameter as long as Poisson's ratio [Eq. (10.12)] is greater than zero. For soft clays in undrained shear, Posson's ratio = 0.5, because there is no volume change, and since the volume is unchanged, we assume that the specimen deforms as a right circular cylinder. Thus A_s at any strain ε is

$$A_s = \frac{A_o}{1 - \varepsilon} \tag{12.11}$$

Now we can calculate the area of the specimen A_s. The strain at failure is $\Delta L/L_o$ = 11 mm/80 mm = 0.1375, or 13.8%. Thus A_s = 1115 mm^2. Now the compressive stress at failure is 14.3 N/1115 mm^2 = 12.8 kN/m^2 (kPa). If we had simply divided by the original area of the specimen, we would have obtained 14.9 kN/m^2, a significant error.

The shear strength for the unconfined compression test is one-half the compressive strength, or 6.4 kPa.

It should be noted that the actual shear stress on the failure plane at failure τ_{ff} is somewhat less than the undrained shear strength, $\tau_f = c$, because τ_{ff} occurs on a failure plane whose inclination is determined by the effective stresses, as explained previously for the UU test. The conditions and the approximate magnitude of associated error are indicated in Fig. 12.41(a) for the specimen at failure in Fig. 12.41(b). The magnitude of the error depends on ϕ', as indicated by the calculations in Example 12.1.

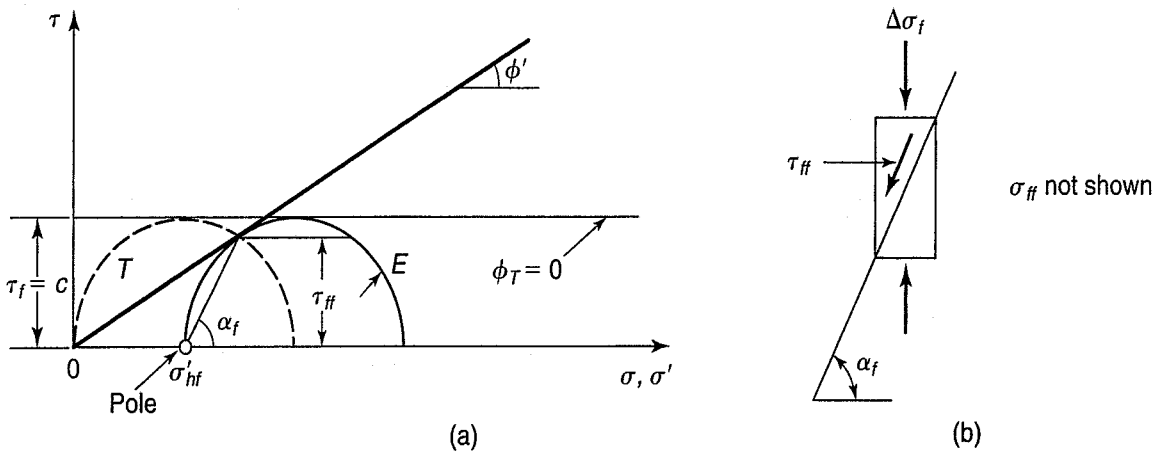

FIGURE 12.41 (a) Difference between τ_{ff} and $\tau_f = c$ in (b) an unconfined compression-test specimen (after Hirschfeld, 1963).

Example 12.11

Given:

The stress conditions for the unconfined compression test shown in Figs. 12.41(a) and (b).

Required:

Find the error in assuming the undrained shear strength $\tau_f = c = {}^1/_2 \Delta\sigma_f$, rather than τ_{ff} for a normally consolidated clay where $\phi' = 30°$.

Solution: From Eq. (11.6),

$$\tau_{ff} = \frac{\sigma_1 - \sigma_3}{2} \sin 2\alpha_f$$

$$= \frac{\Delta\sigma_f}{2} \sin 2\alpha_f$$

From Eq. (11.10), $\alpha_f = 45° + \phi'/2$. So, $\alpha_f = 60°$. Therefore

$$\tau_{ff} = \frac{\Delta\sigma_f}{2} \sin 120° = 0.433\,\Delta\sigma_f$$

But $\tau_f = c = 0.5\,\Delta\sigma_f$.

Conclusion: $\tau_f = c$ (strength) is about 15% greater than τ_{ff} for $\phi' = 30°$. Thus the actual shear strength on the failure plane is *overestimated* by using one-half the unconfined compressive strength. Note that the error is less for smaller ϕ' angles. Also note that

$$\tau_f = c = \frac{\Delta\sigma_f}{2} = \frac{(\sigma_1 - \sigma_3)_f}{2} = \tau_{\max}$$

For most of the twentieth century, the unconfined compression test was probably the most common laboratory strength test used in the United States for the design of shallow and deep foundations in clay, as well as other soft ground engineering problems. Remember the four conditions given in the previous section that must be satisfied for the UCC test to yield the same strength as the UU test? Many times in geotechnical practice those conditions are not met, because clays above the groundwater table are unsaturated. Also, clay deposits are rarely homogeneous, intact, and without fissure or defects. In many cases, however, the UCC test seemed to give good results, probably because of *compensating errors*. Sample disturbance especially tends to reduce the undrained shear strength. Anisotropy also is a factor, as is the assumption of plane strain conditions for most design analyses, whereas the real stress conditions are more three-dimensional. These factors tend to reduce the undrained shear strength so that the difference between $\tau_f = c$ and τ_{ff} becomes negligible in engineering practice. Several of these points are discussed by Ladd et al. (1977) and in Chapter 13.

12.11.3 Typical Values of UU and UCC Strengths

The undrained strength of clays varies widely. Of course, ϕ_T is zero, but the magnitude of τ_f can vary from almost zero for extremely soft sediments to several MPa for very hard soils and soft rocks. Often, we normalize the undrained shear strengths measured at a site with respect to the vertical effective overburden stress σ'_{vo} at each sampling point. Then the τ_f/σ'_{vo} ratios are analyzed and compared with other data. This point is covered in more detail in Sec. 12.11.5 below and in Chapter 13.

TABLE 12.4 Consistency or Strength Terms for Cohesive Soils

Consistency Term	Standard Penetration Resistance,[a] N_{SPT} (blows/ft)	Unconfined Compressive Strength,[b] q_u (kPa)	Field Identification	
			Undisturbed Soil	Visual-Manual
Very soft	<2	<25	Easily penetrated several inches by the fist	Extruded between fingers when squeezed
Soft	2 to 4	25 to 50	Easily penetrated several inches by the thumb	Molded by light finger pressure
Medium	4 to 8	50 to 100	Can be penetrated several inches by the thumb with moderate effort	Molded by strong finger pressure
Stiff (or firm)	8 to 15	100 to 200	Readily indented by thumb but penetrated only with great effort	
Very stiff	15 to 30	200 to 400	Readily indented by thumbnail	
Hard	>30	>400	Indented by thumbnail with difficulty	

[a]The SPT is very unreliable in soft, sensitive clays and is not recommended.
[b]Unconfined compressive strength $q_u = (\sigma_1 - \sigma_3)_f = 2\tau_f$.

After U.S. Dept. of the Interior (1998); U.S. Dept. of the Navy (1986).

When we described the visual-manual classification of soils in Sec. 2.9.1, we mentioned that *consistency* of fine-grained soils in the natural state was usually evaluated by noting the ease with which the deposit could be penetrated by one's fingers, etc. Such terms as *very soft*, *soft*, *medium*, *stiff* (or *firm*), *very stiff*, and *hard* were employed to describe consistency. Table 12.4 presents the relationship between consistency, standard penetration resistance (blow count), unconfined compressive strength, and a field identification test that is often used in practice. Notice that the terms "stiff" and "firm" are used interchangeably.

12.11.4 Other Ways to Determine the Undrained Shear Strength

We mentioned above that drainage conditions in the triaxial test are models of specific critical design situations for stability in geotechnical practice. For example, for the design of foundations on clay soils the critical drainage condition is the *unconsolidated-undrained* (UU) condition. Besides the UU triaxial test and its variant the unconfined compression test (Sec. 12.11.2), the undrained shear strength τ_f of cohesive soils can be estimated by some very simple laboratory tests on undisturbed samples. Some of these tests can also be used in the field in test pits and on field samples. Because the test occurs very quickly, we assume that undrained conditions exist in the soil being tested. The explanation for how this shear strength τ_f is equivalent to the UU strength is given in Sec. 12.11.

Table 12.5 summarizes the four tests and provides limitations and references. The results of these simple tests have been correlated with the undrained shear strength τ_f, as indicated in the table.

Although not as popular in North America as it is in Northern Europe, the *Swedish fall-cone* test is very useful for determining the undrained shear strength of soft and sensitive clays, sludge deposits, and soft oozes from the ocean bottom. The fall-cone test is very quick and simple to perform. A schematic of the test is shown in Fig. 12.42 along with the shear strength ranges for the four standard Swedish cones. The cone mass and angle are selected according to an estimate of the magnitude of the shear strength. The cone is positioned just touching the top of the soil specimen and then released. The amount of penetration is measured and correlated with the shear strength of the soil, which is proportional to the mass of the cone and inversely proportional to the penetration squared. Hansbo's (1957) calibration for Swedish

TABLE 12.5 Simple Laboratory and Field Tests for the UU Strength of Clays

Test	Use	Remarks	Best For	Limitations	References
Swedish fall-cone	Lab	Quick; used on tube samples; requires calibration; τ_f depends on cone angle and mass; specimen observable.	Very soft to soft clays	Cohesive soils without pebbles, fissures, etc. Tests only a small amount of soil near the surface; good correlation with τ_f on soft, sensitive clays.	Hansbo (1957)
Pocket penetrometer	Lab, field	Hand held; piston and calibrated spring in compression; results in unconfined compressive strength ($= 2\tau_f$); quick; used on tube samples or sides of exploratory trenches, etc.; specimen observable.	Very soft to stiff clays	Same as above, except very rough calibration with τ_f.	
Torvane	Lab, field	Hand held; calibrated spring in torsion; quick; used on tube samples or the sides of exploratory trenches, etc.; specimen observable.	Very soft to stiff clays	Same as above; slightly better correlation with τ_f on soft clays.	
Vane shear test	Lab	Torsion from calibrated spring; most common vane sizes are 12 × 12 and 25 × 12 mm; specimen observable.	Soft to stiff clays	Unreliable if vane encounters sand layers, varves, stones, etc., or if vane rotated too rapidly.	ASTM (2010) D 4648

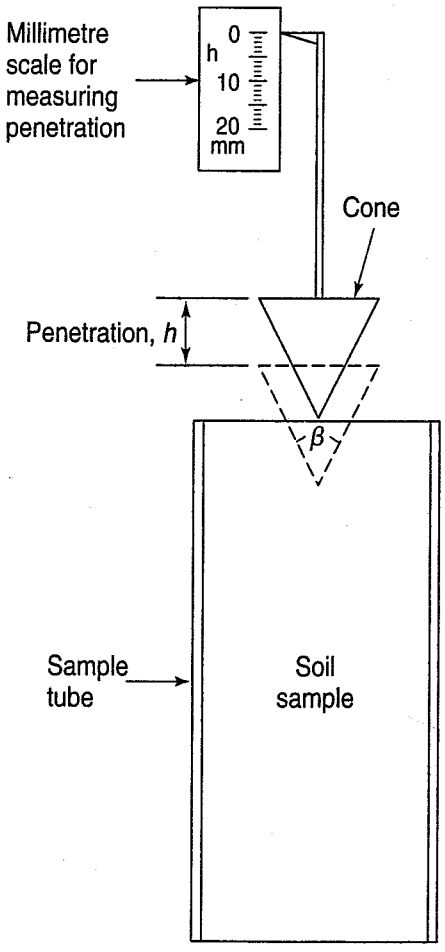

Mass (g)	Cone angle β (degrees)	Range of τ_f (kPa)
400	30	10–250
100	30	25–63
60	60	0.5–11
10	60	0.08–2

FIGURE 12.42 Schematic of the Swedish fall-cone test and the shear strength ranges for the four standard Swedish cones.

glacial and postglacial clays is commonly used even for other soils. The test is also useful to obtain the *sensitivity* of the soil (Sec. 12.12). There is a good correlation with the strength obtained with the field vane shear test discussed in Sec. 11.6.1.

The three other simple strength tests listed in Table 12.5 are the *pocket penetrometer*, *Torvane*, and (*laboratory*) *vane shear test* (Figs. 12.43, 12.44, and 11.19, respectively). The first two tests may be used in the laboratory on undisturbed (or remolded) specimens as well as performed in test pits and on samples in the field. The lab vane shear test, as the name implies, is only a laboratory test. The pocket penetrometer (Fig. 12.43) has a small piston about 6 mm in diameter that reacts against a calibrated spring when pushed about 6 mm into the soil surface. The readings on the scale are in unconfined compressive strength, which is twice the undrained shear strength τ_f. Both the Torvane (Fig. 12.44) and lab vane (Fig. 11.19) are rotated against a torsional spring, and the angle of the rotation at failure is correlated with the torque in the spring. In the Torvane, the scale on the torque head is multiplied or divided appropriately, depending on the diameter of the vanes, as shown in Fig. 12.44. In the lab vane, the torque on the spring at failure is used in one of the theoretical equations shown in

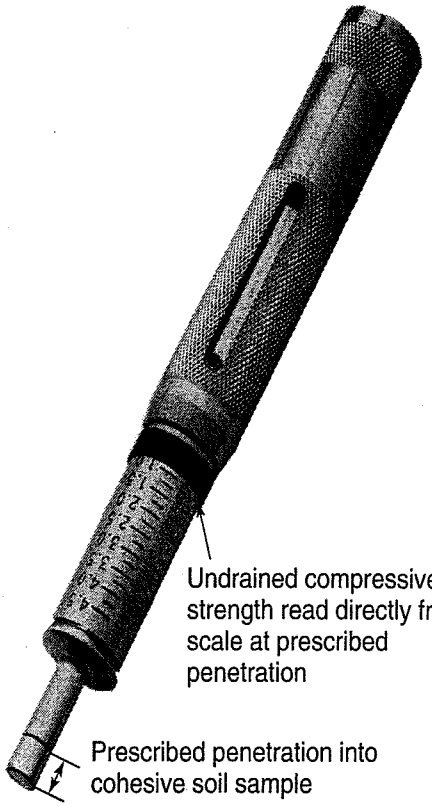

FIGURE 12.43 Pocket penetrometer, a hand-held device which indicates unconfined compressive strength (photograph courtesy of Soiltest, Inc., Evanston, Illinois).

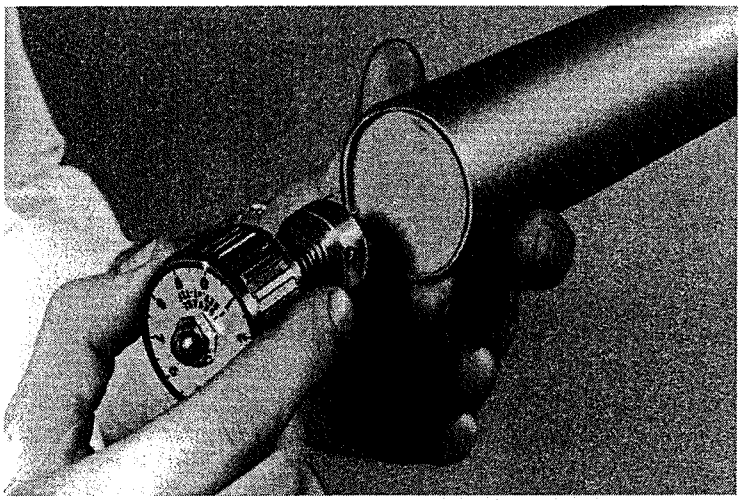

(a)

Diameter (mm)	Height of vanes (mm)	Maximum τ_f (kPa)
19	3	250
25	5	100 (standard)
48	5	20

(b)

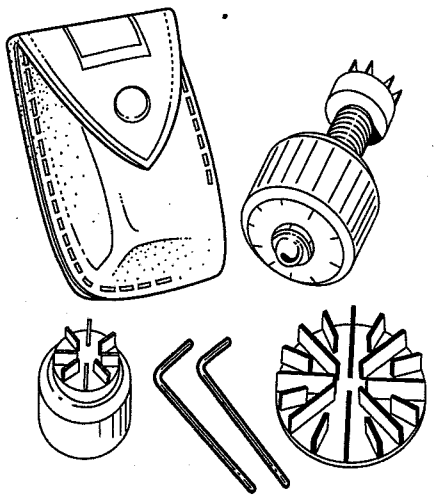

FIGURE 12.44 Torvane, a hand-held device which indicates undrained shear strength: (a) standard model shown on its side. The other two vanes, which can be attached to the standard Torvane, are for very soft or very stiff clays; (b) specifications for the three vanes (photograph courtesy of Soiltest, Inc., Evanston, Illinois).

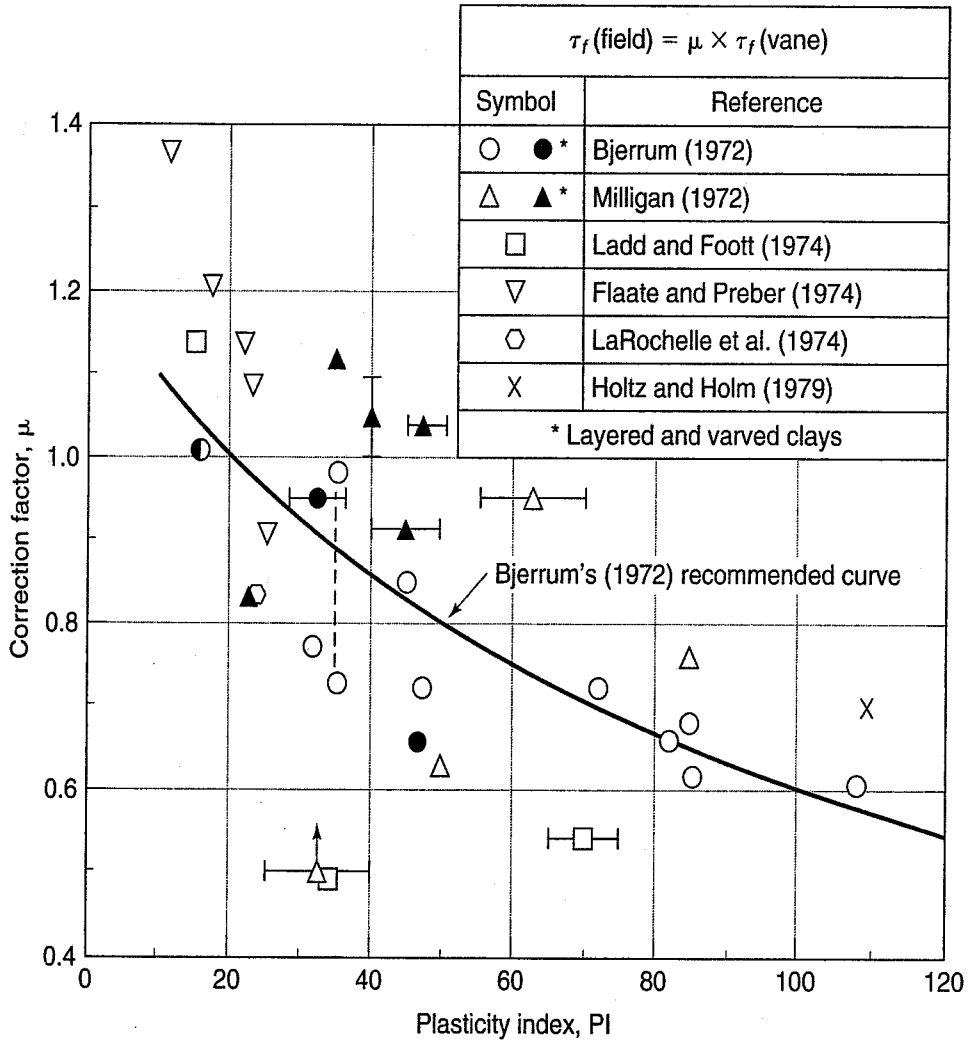

FIGURE 12.45 Correction factor for the field vane test (VST) as a function of PI, based on embankment failures (after Ladd, 1975, and Ladd et al., 1977).

Fig. 11.19(c) to give the undrained shear strength. The beauty of all these tests is that they may be performed within a few centimetres of each other so as to obtain a statistical representation or a continuous profile of shear strength with position or depth.

Several other in situ tests have been used to determine the UU shear strength through correlations, and these were described in Sec. 11.6.1. One of the best for soft clays (Table 11.1) is the field vane shear test (VST). Properly calibrated by correlations based on back-analyses of failure and field tests (e.g., Cadling and Odenstad, 1950), the VST can give a good estimate of the undrained shear strength of these materials. Theoretical formulas [Fig. 11.19(c)] are less reliable. Another possibility is to apply an empirical correction factor for very soft clays based on back-calculation from embankment failures (Bjerrum, 1972). An example of this is shown in Fig. 12.45.

The Dutch cone penetrometer test (CPT) and its close relative the piezocone penetrometer test (CPTu) can also be used at sites with soft to stiff clays. Through correlations, both can provide very useful information about the variability of the soil profile, the UU shear strength, and other useful properties of soft clay sites.

Although the pressuremeter test (PMT) has been used in soft clays, it is probably more suitable for stiffer clay sites. It can provide good estimates of the in situ soil modulus, but it tends to greatly overpredict the undrained shear strength in comparison with the results of laboratory strength tests and other in situ tests. Similarly, the dilatometer test (DMT) is less successful at soft clay sites, but it appears to provide a good estimate of the modulus, especially in stiffer soils.

The screw plate compressometer (SPC) can be used in both soft and stiff clays to give the shear strength and compressibility properties at several test points throughout the soil profile. As mentioned in Sec. 11.6.1, one big advantage of the screw plate compressometer over the pressuremeter and dilatometer tests is that it loads the soil in the same direction as common foundation loading.

12.11.5 Use of UU Strength in Engineering Practice

Like the CD and CU tests, the undrained or UU strength is applicable to certain critical design situations in engineering practice. In these situations the engineering loading is assumed to take place so rapidly that there is no time for the induced excess pore water pressure to dissipate or for consolidation to occur during the loading period. We also assume that the change in total stress during construction does not affect the in situ undrained shear strength (Ladd, 1971b). Examples shown in Fig. 12.46 include foundations for embankments, compacted clay cores of embankment dams, and footings on soft clays. Another example (not shown in the figure) is the stability or bearing capacity of deep foundations such as piles in soft clays. For all these cases, often the most critical design condition is *immediately after* the application of the load (at the *end of construction*), when the induced pore pressure is the greatest but

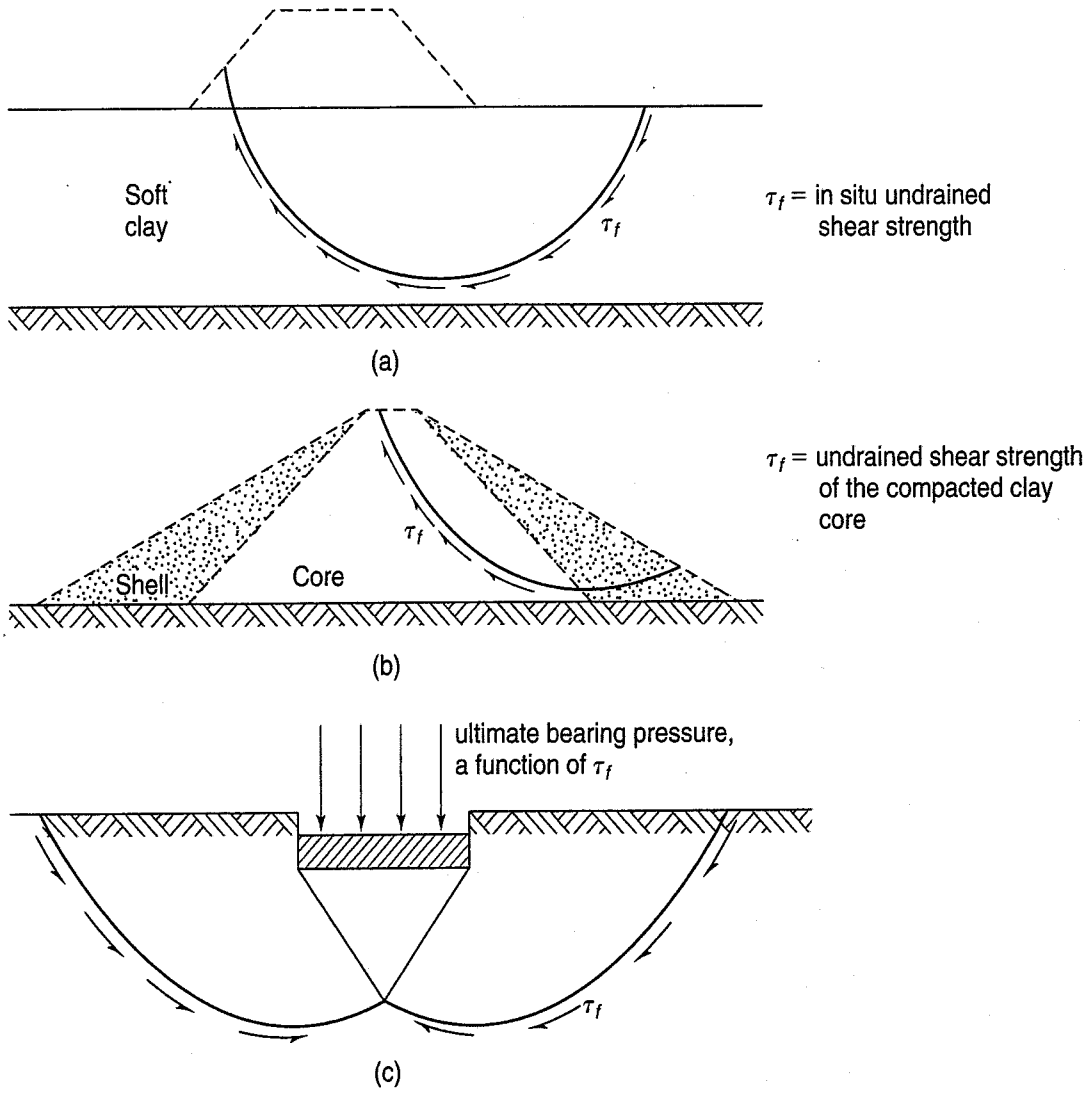

FIGURE 12.46 Some examples of UU analyses for clay: (a) embankment constructed rapidly over a soft clay deposit; (b) large earth dam constructed rapidly with no change in water content of clay core; (c) footing placed rapidly on clay deposit (after Ladd, 1971b).

before consolidation has had time to take place. Once consolidation begins, the void ratio and the water content naturally decrease and the strength increases. So the embankment or foundation should become increasingly *safer* with time due to consolidation.

In Sec. 12.8 we briefly described the two different approaches to the solution of stability problems in geotechnical engineering: (1) the *total stress approach* and (2) the *effective stress approach*. We mentioned that the appropriate shear strength for these cases is, respectively, in terms of total and effective stresses. For the cases in Fig. 12.46, because no drainage and therefore no consolidation is assumed to occur during construction, a total stress analysis using shear strength in terms of total stresses is carried out, and the undrained shear strength τ_f normally is used.

There are, however, some of exceptions that you should be aware of. The first involves foundation loading [Fig. 12.46(a)] of lightly overconsolidated clays. They may exhibit dilatant behavior when sheared, and this has been observed both in laboratory tests and in the field, for example in offshore structures in the Canadian Beaufort Sea (Crooks and Becker, 1988). This case is described in detail in Chapter 13 as part of our discussion of stress paths and their use in geotechnical practice.

The other exception is the example of an earth dam [Fig. 12.46(b)] constructed of a well-compacted silty clay as described by Humphrey and Leonards (1986). They investigated the failure of the steep upstream face of an embankment dam constructed without the granular shells shown in Fig. 12.46(b). They found that a total stress analysis was unreliable because the calculated factor of safety using the UU strength was on the unsafe side. While the case history is interesting from a number of viewpoints, it is the shear behavior of the material that is relevant here. Well compacted silty clay tends to dilate when sheared, and this causes negative pore water pressures during shear. Thus the shear strength in the embankment increases, but it is temporary. Conditions in the dam do not remain undrained for long, and the effective normal stress active on a potential failure surface will decrease, because the pore pressures become less negative rather quickly. And this means that the effective stresses correspondingly decrease rather quickly.

What happens in the UU laboratory test on compacted silty clay? The shear stress is usually applied rapidly, often reaching failure within 20–30 min. If the pore pressures were measured, they would decrease after the strains exceed a few percent, and lower pore pressures mean higher effective stresses and thus higher undrained shear strengths. This effect is shown in Fig. 12.47. Therefore a total stress analysis of a dam of compacted silty clay using UU strengths is not reliable and may be unsafe. Humphrey and Leonards (1986) recommend instead using an effective stress analysis. The effective stress strength parameters c' and ϕ' used in the stability

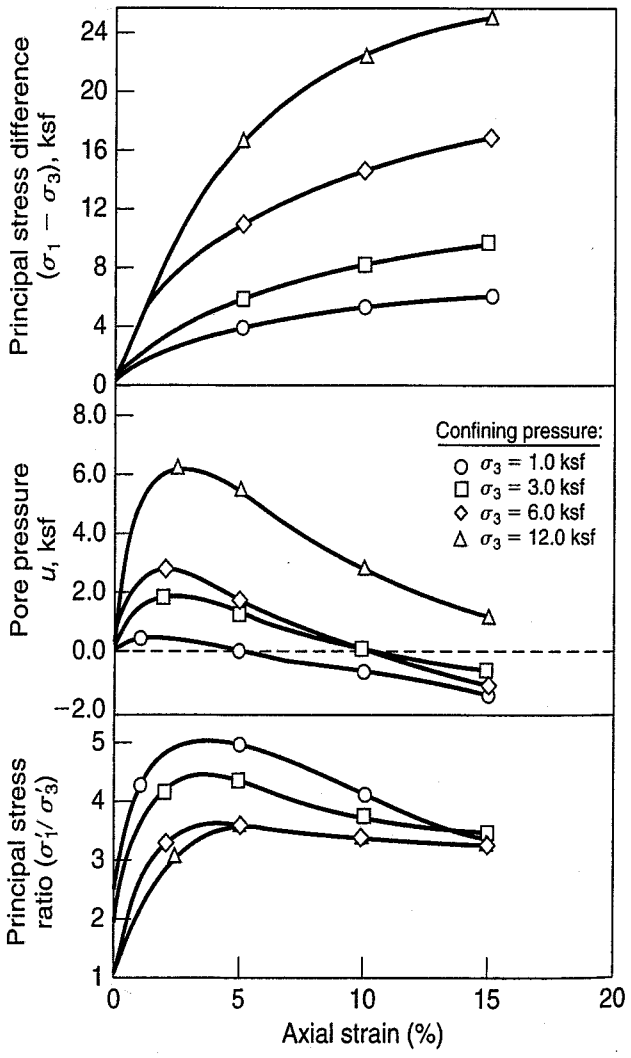

FIGURE 12.47 Typical stress-strain and pore pressure-strain behavior for a UU test on compacted silty clay (LL = 19; PI = 7) (after Humphrey and Leonards, 1986).

analysis should be evaluated at large strains and at slow strain rates. For compacted clays of low to medium plasticity, use a CD test—either a direct shear or a CD triaxial test—conducted slowly enough that $\Delta u \approx 0$.

One of the more useful ways to express the undrained shear strength is in terms of the τ_f/σ'_{vo} ratio for normally consolidated clays. In natural deposits of sedimentary clays, the undrained shear strength has been found to increase with depth, and thus it is proportional to the increase in effective overburden stress with depth. The background and use of this ratio are discussed in detail in Chapter 13.

12.12 SENSITIVITY

Earlier, in Sec. 2.7.3, we mentioned very generally the concept of clay sensitivity. We were vague because we had not yet discussed shear strength. Now we can define sensitivity more precisely, at least within the precision limits of the strength measurements themselves. Usually, sensitivity is based on some measure of the undrained shear strength τ_f as determined in the laboratory or the field. *Sensitivity* S_t is therefore

$$S_t = \frac{\tau_f \text{ (undisturbed)}}{\tau_f \text{ (remolded)}} \tag{12.12}$$

It should be noted that the remolded strength determination must be at the *same* water content—the natural water content w_n—as the water content of the undisturbed specimen. Table 12.6 indicates the range of sensitivity values commonly used in the United States, where highly sensitive clays are not as common as they are in eastern Canada and Scandinavia. Other sensitivity scales are available besides those listed in Table 12.5 (for example, Skempton and Northey, 1952; Bjerrum, 1954b).

Figure 2.11 showed what happened to a sample of Leda clay from eastern Canada before and after remolding. Leda clays are often very stiff in their natural state. Their unconfined compressive strengths may be greater than 100 kPa, but their liquidity indices [Eq. (2.39)], are often 2 or more. No wonder that their strengths are so low when they are thoroughly remolded! The sample shown in Fig. 2.11 had a sensitivity of about 1500 (Penner, 1963), which definitely qualifies it as quick according to Table 12.5. Note that with such clays you have to use either a very sensitive laboratory vane or fall-cone test to obtain the remolded τ_f (Eden and Kubota, 1962).

Correlations between sensitivity and liquidity index have been made by several researchers, as shown in Fig. 12.48.

TABLE 12.6 Typical Values of Sensitivity

	Range of S_t		
Condition	U.S.	Canada	Sweden
Low sensitive	2–4	<2	<10
Medium sensitive	4–8	2–4	10–30
Highly sensitive	8–16	4–8	>30
Extra sensitive	16	8–16	>50
Quick	—	>16	>100
Greased lightning	—	>>16	

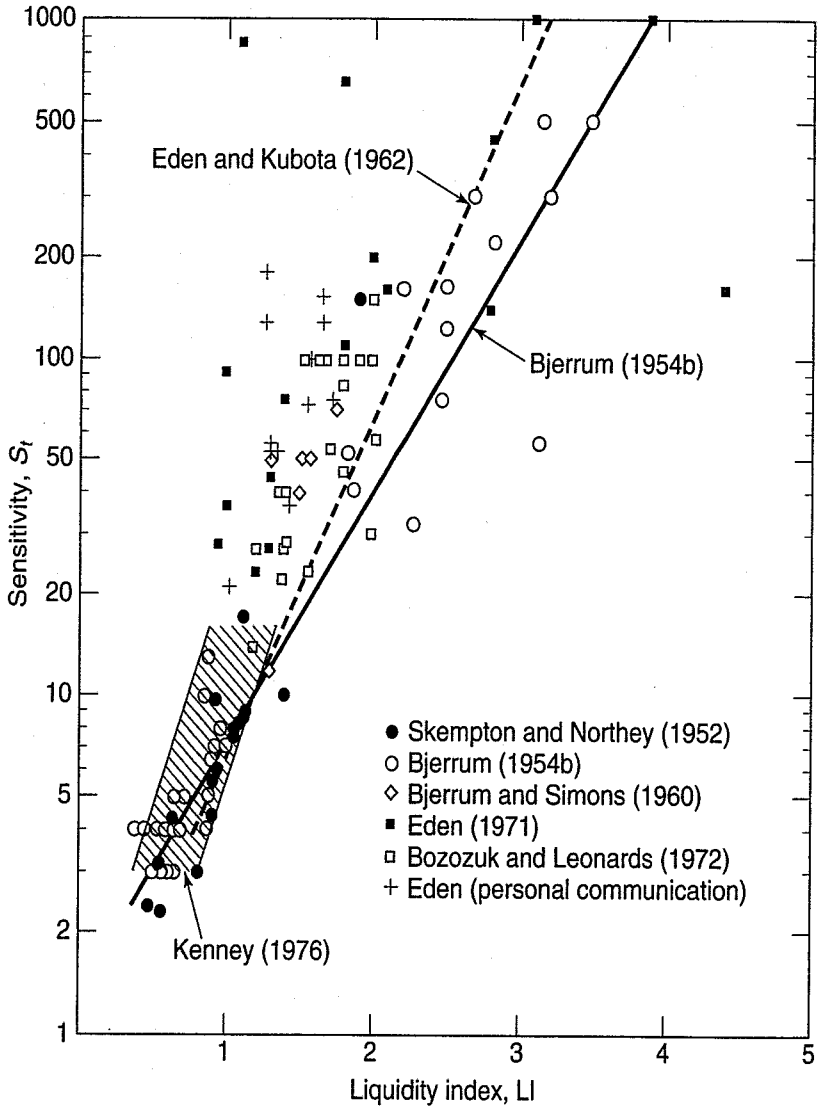

FIGURE 12.48 The relationship between sensitivity and liquidity index for Scandinavian, British, Canadian, and some U.S. clays.

12.13 THE COEFFICIENT OF EARTH PRESSURE AT REST FOR CLAYS

As is true for sands, a knowledge of the coefficient of earth pressure at rest, K_o, for a clay deposit is often very important for the design of earth-retaining structures, excavations, and some foundations. In Sec. 12.7 we gave some typical values of K_o for sands. We said that K_o was empirically related to ϕ' [Eq. (12.8) and Fig. 12.20], and we also mentioned that the coefficient for overconsolidated sand deposits is greater than for normally consolidated sands [Eq. (12.9)].

Correlations between K_o and ϕ' have been made for clays by Brooker and Ireland (1965) and others. Their data for normally consolidated clays are shown in Fig. 12.49. Brooker and Ireland (1965) also found a tendency for the normally consolidated K_o to increase with plasticity index. Massarsch (1979) collected the results from 12 investigations, including the compilation by Ladd et al. (1977), and they are shown in Fig. 12.50. The equation of the best fit line is

$$K_o = 0.44 + 0.42(\text{PI}/100) \tag{12.13}$$

Note that the intercept of the best-fit line, or 0.44, is very close to the average of K_o for normally consolidated sands, as shown in Fig. 12.20.

The effect of increasing the overburden stress and subsequent unloading on σ'_h and K_o is shown in Figs. 12.51(a) and (b), respectively. During sedimentation, the effective horizontal stress σ'_h increases in proportion to the increase in effective vertical stress, so K_o is constant. If unloading occurs—for

Remolded	Undisturbed	Reference
○		Brooker and Ireland (1965)
□		R. Ladd (1965)
⊙	●	Bishop (1958)
	◆	Simons (1958)
	▲	Campanella and Vaid (1972)
◎		Compiled by Worth (1972)
*		Abdelhamid and Krizek (1976)

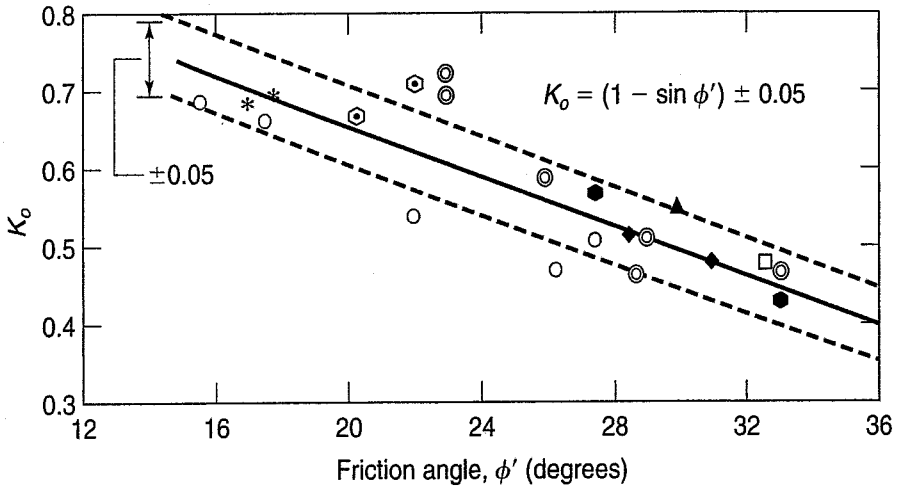

FIGURE 12.49 K_o versus ϕ' for normally consolidated clays (after Ladd et al., 1977).

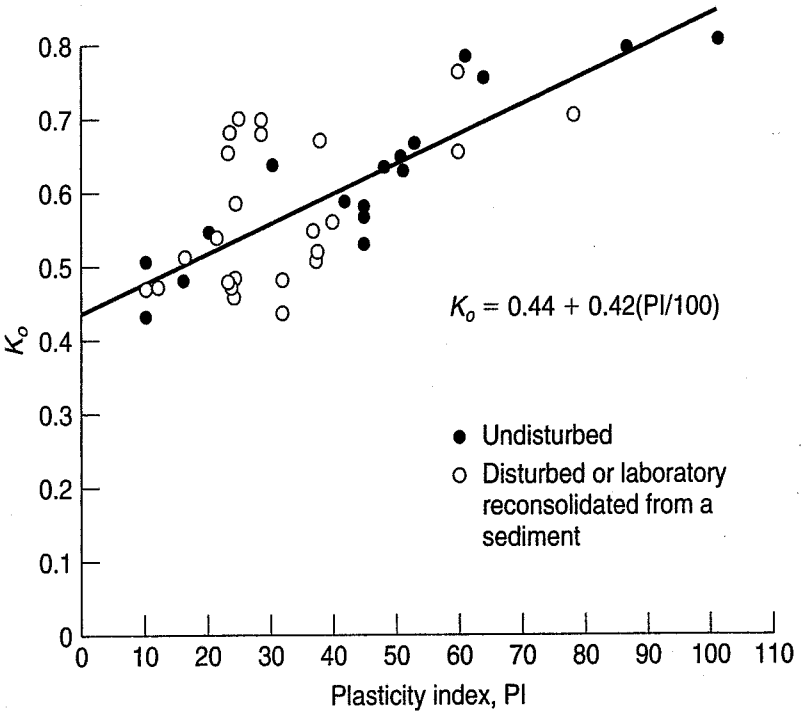

FIGURE 12.50 Correlation between K_o from laboratory tests and plasticity index PI (after Massarsch, 1979).

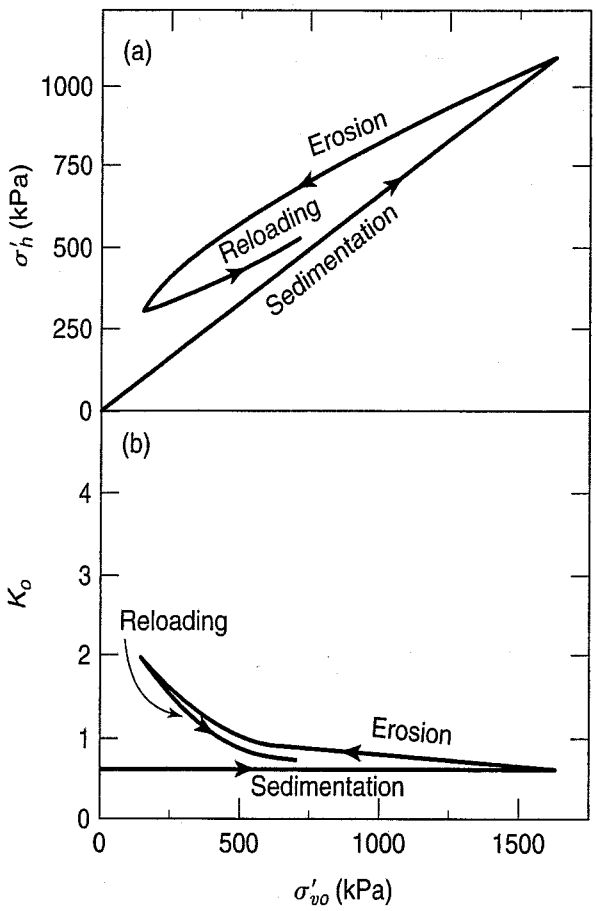

FIGURE 12.51 Relationships showing the effect of a changing overburden stress during sedimentation, erosion, and reloading on (a) horizontal stress σ'_h and (b) coefficient of earth pressure at rest K_o (after Morgenstern and Eisenstein, 1970).

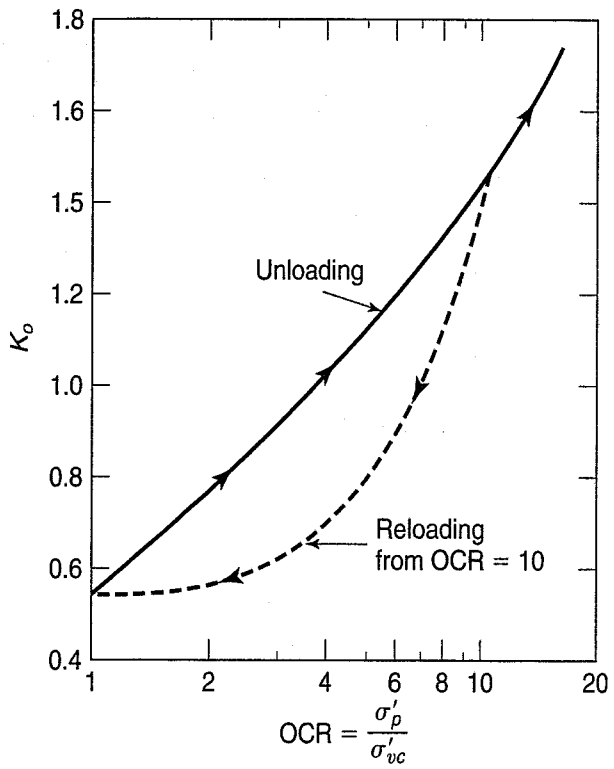

FIGURE 12.52 Effect of overconsolidation on K_o of a sensitive clay during unloading and reloading. The data by Campanella and Vaid (1972) was replotted by Ladd et al. (1977).

example, because of erosion—then there is a hysteresis effect, and the value of K_o increases. Depending on how much unloading actually takes place, it is possible for the lateral stresses relative to σ'_v to *approach* a state of failure;[1] that is, the ratio σ'_h/σ'_{vo} could be 3.0 or 3.5, which corresponds to $\phi' = 30°$ or 35° [Eq. (11.14)]. If there is subsequent reloading, then the K_o tends to decrease, as shown in Fig. 12.51(b). The effect of overconsolidation on the K_o of a sensitive clay is shown in Fig. 12.52. Again, there is some hysteresis when the clay is rebounded from a high OCR.

Brooker and Ireland (1965) suggested that the relationship between K_o and OCR depended on the plasticity of the clay, and this was confirmed to some extent by Ladd (1971a), as shown in Fig. 12.53. But when Kulhawy and Mayne (1990) plotted data on 135 clays in Fig. 12.54, there was no apparent trend.

The relationship between K_o and OCR may be better estimated using ϕ' from laboratory triaxial compression tests rather than PI. This was shown by Mayne and Kulhawy (1982) from data on 48 clays as reproduced in Fig. 12.55. Their relationship is given by

$$K_o = (1 - \sin\phi')\,\mathrm{OCR}^{\sin\phi'} \tag{12.14}$$

where K_o = coefficient of lateral earth pressure at rest,
OCR = over consolidation ratio.

[1]In terms of lateral earth pressures, this is called a *passive state of failure*. The stress ratio K_p is called the *coefficient of passive earth pressure*, and $K_p = \sigma'_{hf}/\sigma'_{vf}$ (and not related to the military term).

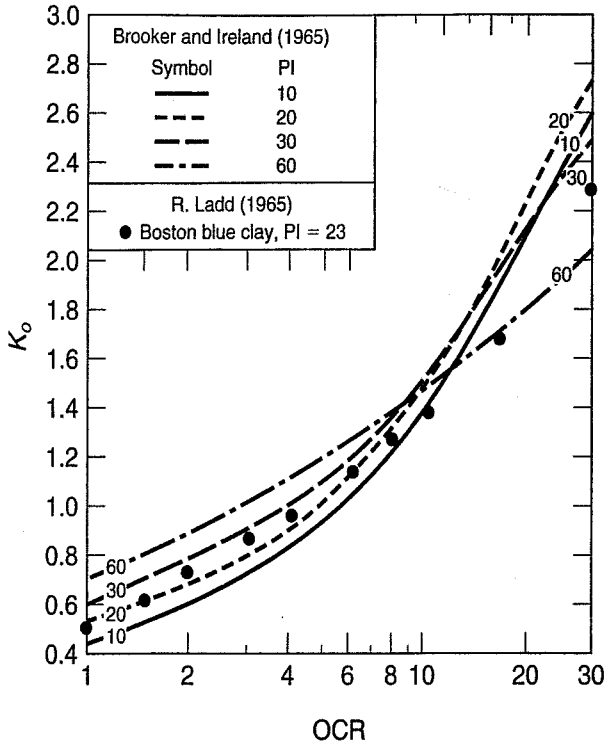

FIGURE 12.53 K_o versus OCR for soils of different plasticities. The data by Brooker and Ireland (1965) on five clays and one sand was replotted by Ladd (1971a).

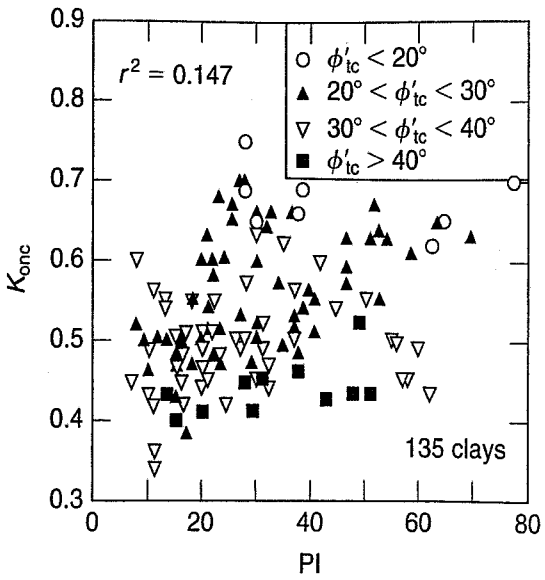

FIGURE 12.54 K_{onc} versus PI on 135 clays (tc = triaxial compression) (Kulhawy and Mayne, 1990; Kulhawy, 2005).

Equation (12.14) is basically a combination of Eqs. (12.8) and (12.9) with the exponent $h = \sin\phi'$. Ladd et al. (1977) also determined the exponent h in Eq. (12.9) for several clays during unloading and recompression. For clays with a PI of about 20, a value of $h = 0.4$ is reasonable. Then h decreases slightly as PI increases, with the lowest value of $h = 0.32$ at PI = 80. These values of h are somewhat lower than those for sands (Sec. 12.6). Keep in mind, too, that all these data are for laboratory consolidated specimens.

Field behavior is much more erratic than laboratory data, as shown by Massarsch et al. (1975) and Tavenas et al. (1975). These authors and Wroth (1975) describe techniques for estimating the in situ K_o in deposits of soft clays. Wroth (1975) also discusses the effects of erosion and a fluctuating groundwater table on the variation of K_o with depth. Generally, the upper few metres of a soft clay deposit are overconsolidated (the *drying crust*), and K_o can be quite high. Then it will decrease with depth as the OCR decreases, until it is equal to the normally consolidated value when OCR = 1.

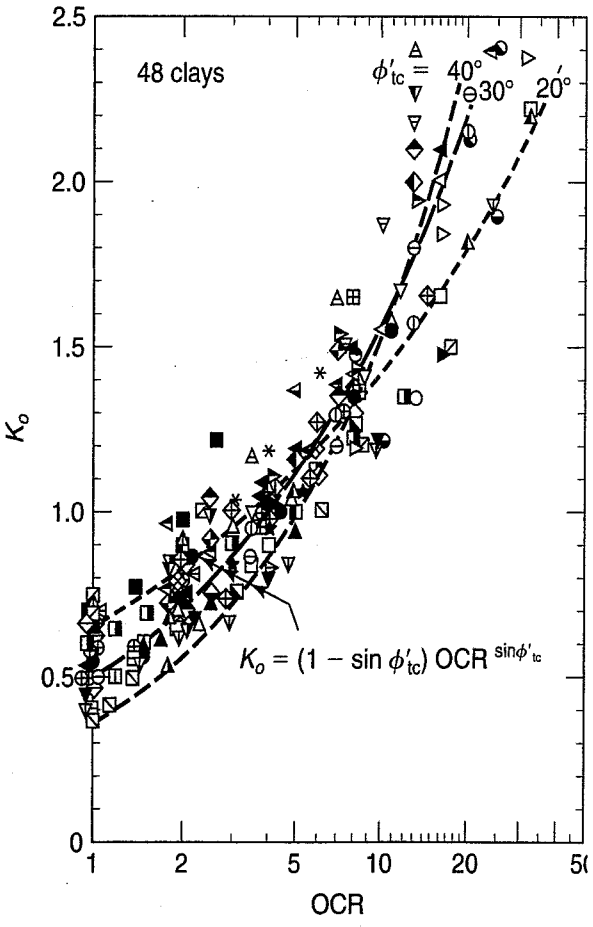

FIGURE 12.55 K_o versus OCR for 48 clays compiled by Mayne and Kulhawy (1982) and plotted by Kulhawy and Mayne (1990) and Kulhawy (2005).

In summary, the coefficient of earth pressure at rest K_o is very dependent on the stress history of the deposit, and especially for overconsolidated clays with complex stress histories it can be very difficult to accurately measure in the field or estimate based on laboratory tests. Simple correlations based on PI and the results of in situ tests are often the only feasible approach, but they seem to work best in recent deposits with overconsolidation caused by one unload-reload cycle (Kulhawy and Mayne, 1990; Kulhawy, 2005).

12.14 STRENGTH OF COMPACTED CLAYS

We discussed compaction in some detail in Chapter 5 but did not say much about the specific properties of compacted soils. That discussion was left to the individual chapters on soil properties. From our earlier discussions of shrinkage and swelling characteristics, hydraulic conductivity, and compressibility of compacted clays, you probably have the idea that compacted clays are not simple materials. The strength of compacted clays is no exception, and their behavior is rather complex both in the field and in the laboratory. In general, samples compacted dry of optimum have higher strengths than those compacted wet of optimum. The wet of optimum strengths also depend somewhat on the type of compaction because of differences in soil structure induced by different compaction methods. If the samples are soaked, the picture changes due to swelling, especially if they were initially dry of optimum. Because the structure of compacted clays so strongly affects their soil properties including their strength, a quick review of Sec. 5.4 on the structure of fine-grained soils will help you understand the present section. Note particularly Fig. 5.5, showing the effect of compaction on soil structure.

Figure 12.56 is an example of the influence of molding water content on the soil structure and on the stress-strain behavior of kaolinite. Samples were compacted at different water contents but at the same compactive effort, and the resulting compaction curve is shown in Fig. 12.56(c). As the compaction water content increases, the degree of particle orientation increases [Fig. 12.56(b)]. The stress-strain curves [Fig. 12.56(a)] determined by UU triaxial tests show a great difference in stress-strain response, depending on whether compacted wet or dry of optimum. The difference is due to the differences in soil structure between the wet and dry samples. Samples 1 and 2, compacted dry of optimum, are more flocculated in comparison with those compacted wet (samples 4 to 6). The dry samples are stronger, have a higher modulus, and develop their maximum strengths at lower strains than the wet samples. The two samples 5 and 6 compacted very wet have very flat stress-strain curves, and their strengths continue to increase even at high strains.

A common misconception is that increased density at the same water content must result in greater shear strength. However, this is not necessarily true, as shown by the undrained test results in Fig. 12.57 on a silty clay compacted by kneading compaction at three different compactive efforts. In Fig. 12.57(a), the stress required to cause 25% strain is plotted versus molding water content, while Fig. 12.57(b) shows the stress required to cause just 5% strain for the three compactive efforts. Note that the "strengths" are about the same for specimens compacted wet of optimum but increase significantly on the dry side of optimum. Note, too, that at a given water content wet of optimum, the stress at 5% strain is actually less for the higher compaction energies.

In Sec. 5.7.5 we discussed *overcompaction*, the condition when lower shear strengths are obtained at higher water contents, e.g., wet of optimum, even with higher compaction energies. A good example is shown in Fig. 12.58, where strength is measured by the CBR (California bearing ratio) test. In this test, the resistance to penetration of a 3 in.^{2} piston developed in a compacted specimen is compared to that developed by a standard sample of densely compacted crushed rock. The CBR is a common pavement design test. In Fig. 12.58 a greater compactive effort produces a greater CBR dry of optimum, as you would expect. But notice how the CBR is actually less wet of optimum for the higher compaction energies. As we explained in Chapter 5, this fact is important in the proper design and construction of a compacted earth fill.

A comparison of the effects of four different methods of compaction on relative strength of a silty clay is shown in Fig. 12.59. As expected, the method of compaction has little effect on the strength of

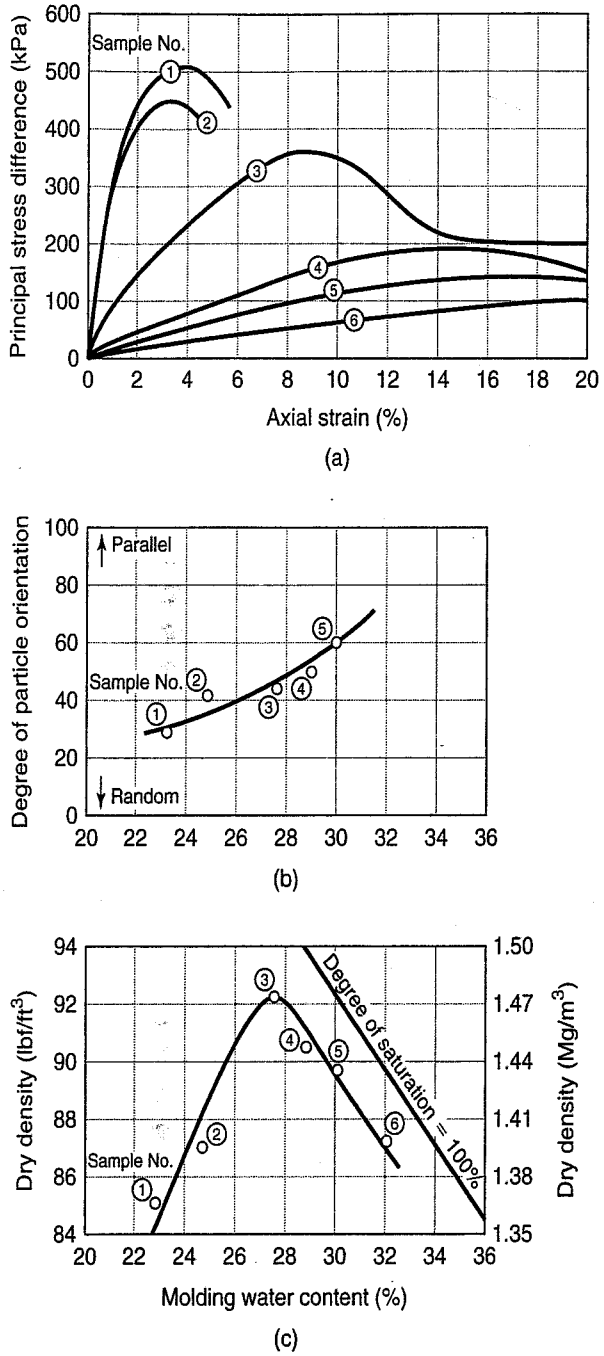

FIGURE 12.56 Influence of molding water content on the structure and stress-strain of kaolinite at the same compactive effort: (a) stress versus strain from UU triaxial tests; (b) degree of particle orientation versus water content; (c) dry density versus water content (after Seed and Chan, 1959).

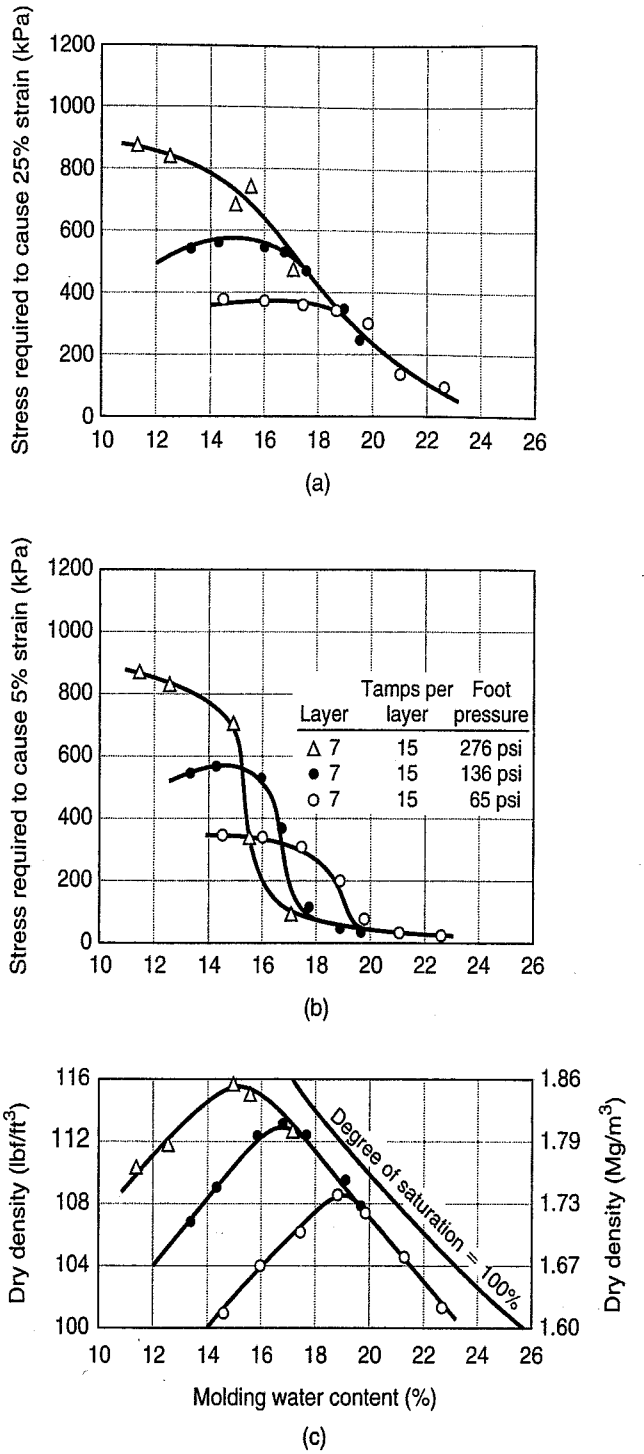

FIGURE 12.57 Relationship between dry density, water content, and stress required to cause (a) 25% strain and (b) 5% strain, as a function of compactive effort and molding water content; (c) dry density versus water content. Data are from unconsolidated-undrained tests with confining pressure = 100 kPa (after Seed and Chan, 1959).

samples compacted dry of optimum. However, for specimens compacted wet of optimum, the method of compaction has considerable influence on the strength, especially at large strains [Fig. 12.59(a)]. The reason for this is the effect of soil structure induced by the compaction method. Methods such as kneading and impact produce a more oriented soil structure than vibratory and static compaction because of the shear deformations induced during compaction. Specimens dry of optimum experience small shear

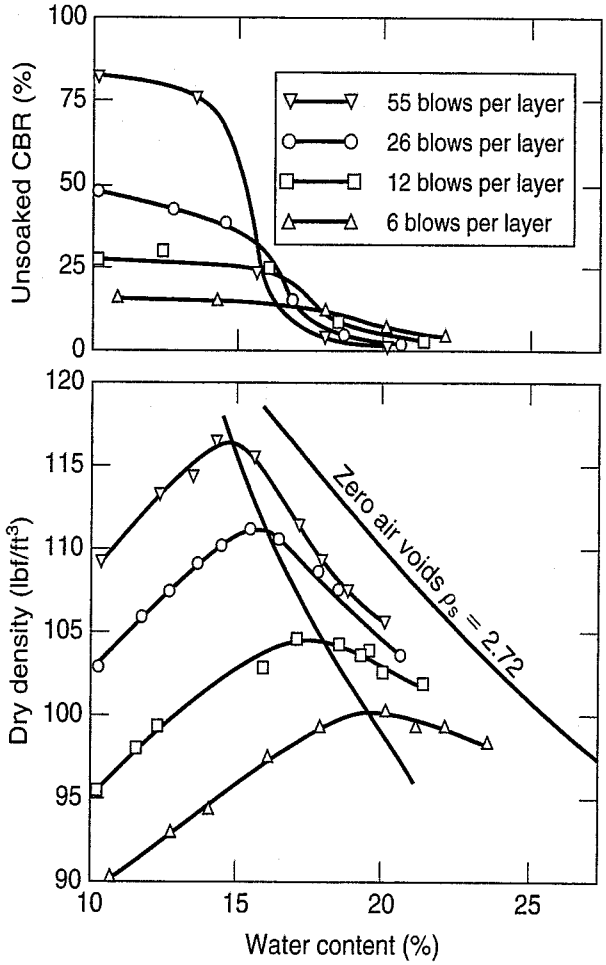

Note: 10 lb hammer, 18 in. drop (modified Proctor)

FIGURE 12.58 Strength as measured by the CBR and the dry density versus water content for laboratory impact compaction (after Turnbull and Foster, 1956).

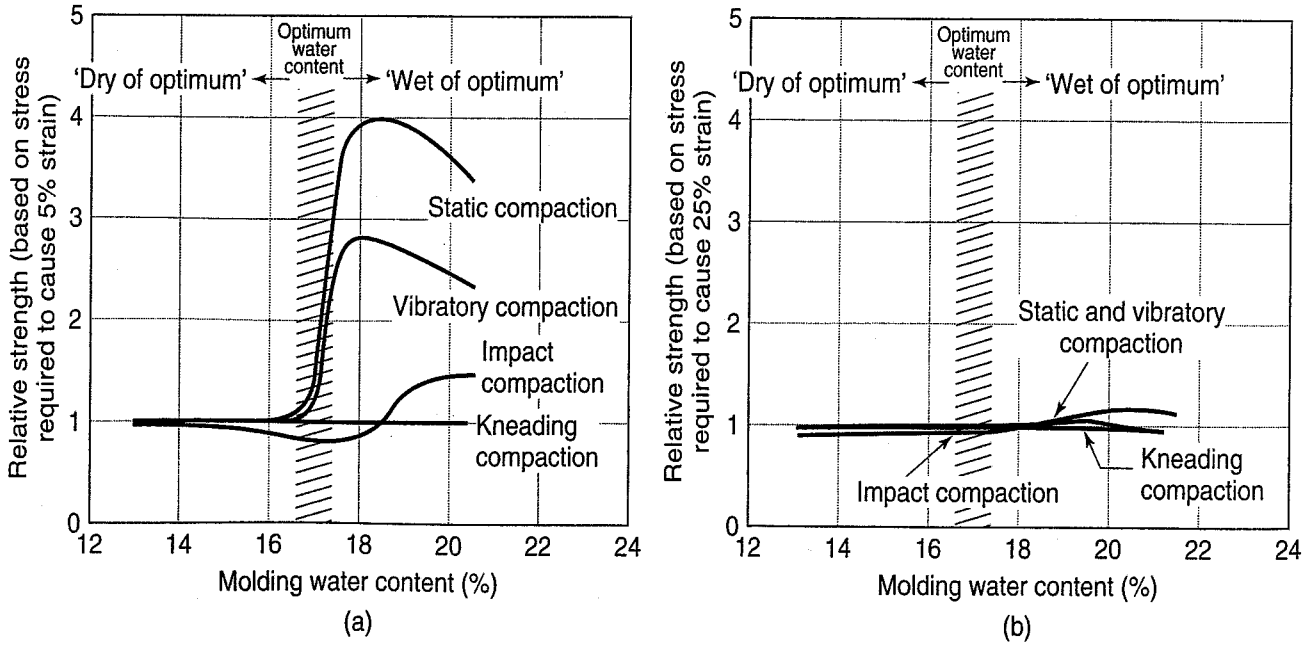

FIGURE 12.59 Influence of method of compaction on the relative strength of a silty clay: (a) stress required to cause 5% strain; (b) stress required to cause 25% strain (after Seed and Chan, 1959).

strains during compaction, so the specimens have a flocculated soil structure. This is not the case for specimens compacted wet of optimum, in which the compaction methods such as kneading and impact induce shear deformations during compaction that results in a more oriented soil structure. Specimens compacted statically are still flocculated even wet of optimum, so are relatively stronger, especially at small strains [Fig. 12.59(a)]. But at large strains, the differences are small, as shown in Fig. 12.59(b), because the structures of all specimens become more oriented at large shear strains.

Now let's look at the influence of the compaction method on different soil types. Figure 12.60 shows the relative "strengths" of samples of three soils prepared by static and kneading compaction. As before, the "strength" is relative to the stress required to cause low (5%) and high (20%) strains. Note that the effect of the method of compaction can vary significantly depending on soil type, whether the specimens are wet or dry of optimum, and the strain at which "strength" is defined. Some differences are huge, as much as 400%, due to the differences in soil structure produced by the compaction method.

An interesting design problem related to compacted clay properties is that of clay liners required for municipal solid waste landfills. These are compacted soil layers used on the slopes and base of the "bowl" created to store such waste and to prevent the leachate caused by the decomposition of the waste from getting into the groundwater. These liners are at least 0.9 to 1.2 m thick, and they must have hydraulic conductivity of less than 10^{-9} m/s. As shown in Fig. 7.8, compacted clay permeability reaches a minimum close to w_{opt}, and remains close to that minimum even at water contents higher than w_{opt}. So, from a hydraulic barrier point of view, it is best to compact at or slightly above optimum. However, this also leads to lower shear strengths, an important property for slope stability. This paradox requires careful slope stability analyses to be performed, as there have been several failures of liners due to low shear strengths on the slopes.

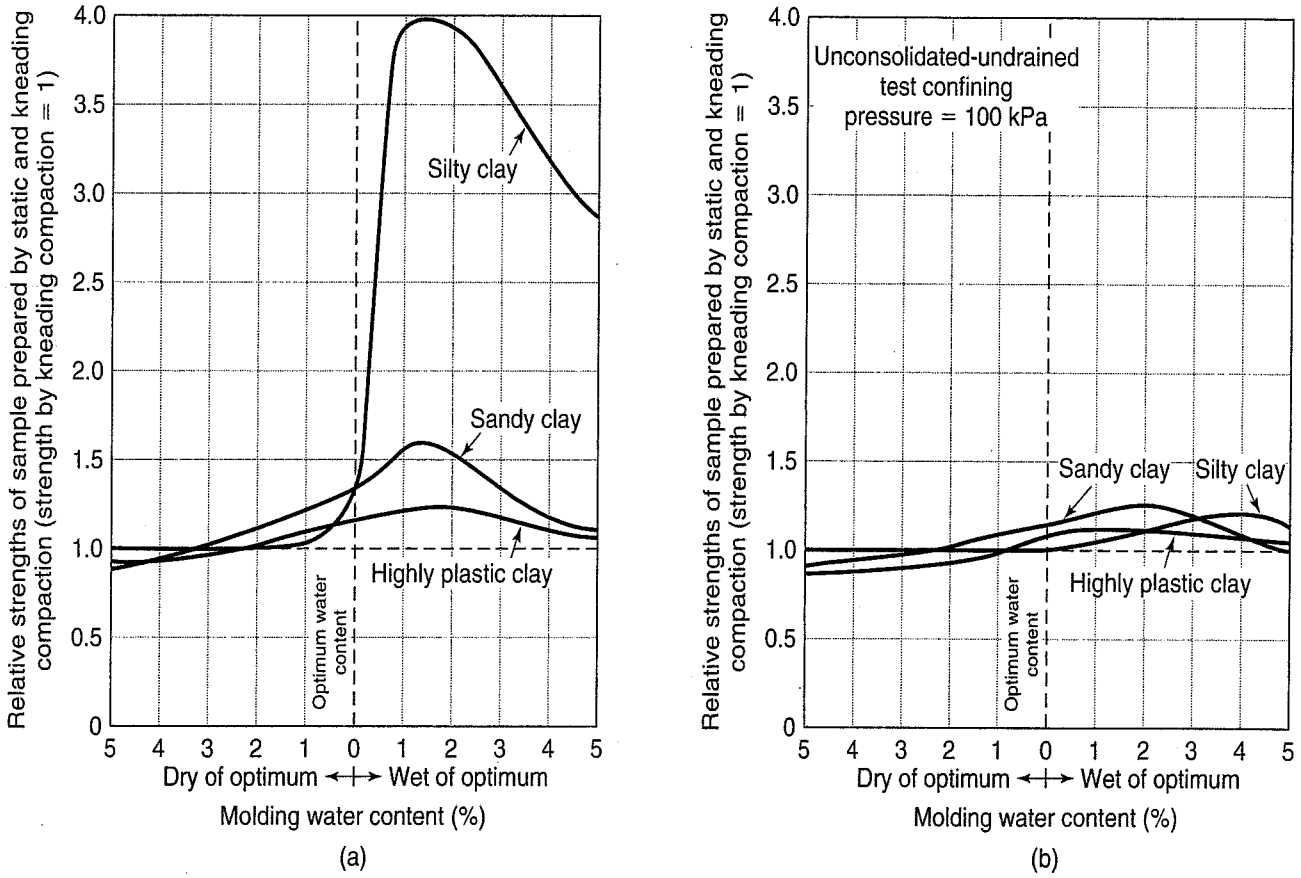

FIGURE 12.60 Relative strengths of samples of three soils prepared by static and kneading compaction and tested UU at a confining stress of 100 kPa: (a) stress required to cause 5% strain; (b) stress required to cause 20% strain (after Seed and Chan, 1959).

12.15 STRENGTH OF ROCKS AND TRANSITIONAL MATERIALS

When referring to rock strength and other mechanical properties (e.g., stiffness), it is important to distinguish between *intact* rock and the rock mass. In Chapters 3, 4, and 11, we mentioned that rock defects such as fractures, joints, bedding planes, and minor faults are common in rock masses. Both the intact rock and these discontinuities are much more difficult to characterize due to the large potential variability in conditions and subsequent properties. Section 4.14.3 described the various descriptive rock mass classification systems, the most common of which is the Rock Quality Designation (RQD), which essentially quantifies the proportion of the rock core that is intact.

In Sec. 11.5.5 we described the various tests for determining the engineering properties of intact rock. Probably the most common is the uniaxial compression test, which is fundamentally an unconfined compression test, and ASTM (2010) D 7012 gives the details of the testing procedure. In addition to the unconfined compressive strength q_u, other measured parameters include elastic modulus and Poisson's ratio. While the procedures for this test are simple in principle, Goodman (1989) points out that it is difficult to perform properly, with results varying by a factor of two as procedures are varied. Other methods for determining rock strength include the split tensile test, point load strength test, direct shear test, and so-called *slake* test to determine the durability of shales and weak rocks under wetting and drying cycles; these were briefly described in Sec. 11.5.4.

Table 12.7 gives the uniaxial compressive strength of representative rocks. The variation in q_u among what would seem to be rocks of the same type is extraordinary, reflecting the wide ranges in the

TABLE 12.7 Unconfined Compressive Strength of Representative Intact Rocks

Description	Unconfined Compressive Strength (q_u)	
	MPa	psi
Berea sandstone, Amherst, Ohio	73.8	10 700
Navajo sandstone, Glen Canyon Dam, Arizona	214.0	31 030
Tensleep sandstone, Casper, Wyoming	72.4	10 500
Hackensack siltstone, New Jersey	122.7	17 800
Monticello Dam siltstone/greywacke, California	79.3	11 500
Solenhofen limestone, Bavaria	245.0	35 500
Bedford limestone, Indiana	51.0	7400
Tavernalle limestone, Carthage, Missouri	97.9	14 200
Oneota dolomite, Kasota, Minnesota	86.9	12 600
Lockport dolomite, Niagara Falls, New York	90.3	13 100
Flaming Gorge shale, Utah	35.2	5100
Micaceous shale, Ohio	75.2	10 900
Dworshak Dam gneiss, 45° to foliation, Idaho	162.0	23 500
Quartz mica, $\perp$ to schistocity	55.2	8000
Baraboo quartzite, Wisconsin	320.0	46 400
Taconic marble, Rutland, Vermont	62.0	8990
Cherokee marble, Tate, Georgia	66.9	9700
Nevada Test Site granite	141.1	20 500
Pikes Peak granite, Colorado Springs, Colorado	226.0	32 800
Cedar City tonalite, Utah	101.5	14 700
Palisades diabase, West Nyack, New York	241.0	34 950
Nevada Test Site basalt	148.0	21 500
John Day basalt, Arlington, Oregon	355.0	51 500
Nevada Test Site tuff	11.3	1650

After Goodman (1989).

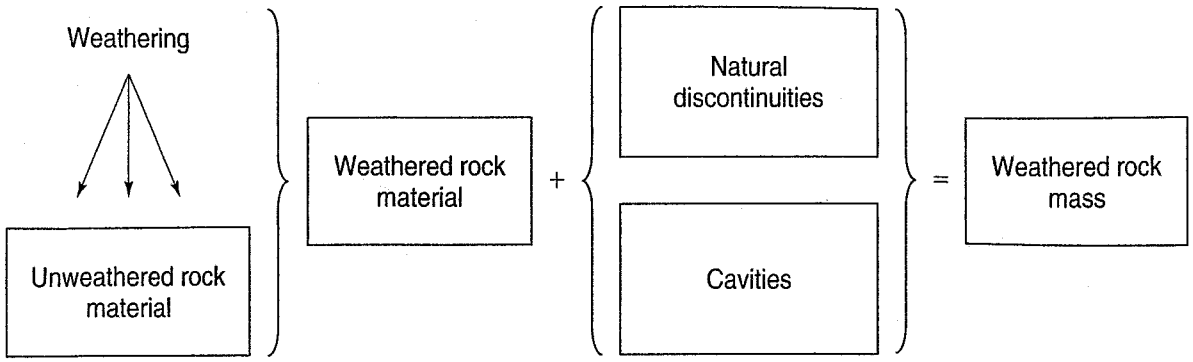

FIGURE 12.61 General progression of rock weathering (after Kulhawy et al., 1991).

degrees of cementation and consolidation that are important determinants of intact rock strength. Also, as mentioned above, some of the variability must be due to difference in testing procedures.

The strength of a rock mass is much more complicated and obviously more variable, since it includes discontinuities. There are a number of correlations between rock mass strength and RQD, joint number and characteristics, stress level and groundwater conditions, among other factors. Some of these correlations were described in Sec. 4.13.3 under rock mass classification. A number of empirical relationships for computing rock mass modulus are summarized in NCHRP (2006), Table 12.

If rock mass strength is complicated, then the strength of transitional or weathered rock mass materials is even more problematic. This stems from the fact that transitional materials are highly variable and, as their name implies, are at some stage of transition from rock to soil along the weathering spectrum. Figure 12.61 shows the general progression of unweathered rock material as it transitions to weathered rock mass, beyond which it further weathers to either a mixture of soil and rock or, in some environments, to a residual soil that often has the appearance of rock but lacks rock's cohesiveness and strength (Sec. 4.2).

The fundamental test for determining the degree of weathering and strength degradation from rock to soil is the material's reaction to water—i.e, the degree of disaggregation of the mass in the presence of water. Welsh et al. (1991) describe two such tests, the jar slake or soak test, and the free swell index test. In the slake test, descriptive observations are made of the disaggregation and a qualitative scale used to classify the degree of slaking. In the free swell test, dilantancy in the presence of water is measured quantitatively, so that it may be less prone to operator error than the slake test. Another test for the durability of shales and similar rocks is the slake durability test, ASTM (2010) D 4644.

Weathered rock and its ultimate end product, either residual soil or soil with rock fragments, presents a significant engineering challenge and requires knowledge of the local geology and geohydrologic influences.

12.16 MULTISTAGE TESTING

Several times in our discussions of direct shear and triaxial testing (see Secs. 11.5, 12.5, 12.9.1, and 12.10.1) we mentioned that we usually test at least three or more identical specimens at different confining pressures to determine the complete Mohr failure envelope for a given soil. This is true for CD and CU tests on all types of soils and soft rocks. Another important consideration is that, as we mentioned in Sec. 11.6 on in situ testing, obtaining high quality undisturbed samples of the subsurface soils and rocks is expensive and often problematic, especially in highly stratified or interbedded geologic deposits. (Subsurface investigation and undisturbed soil sampling are usually discussed in courses and books on foundation engineering, but a brief description is given in Sec. 13.13.4.)

Multistage testing on only one specimen is sometimes used in practice to overcome the problem of lack of identical test specimens, and it saves time and money. Ideally, the specimens should be saturated, and both direct shear and triaxial CD tests may be performed multistage. Sometimes it is used for testing

remolded compacted specimens of fine grained soils that are unsaturated. These tests should be UU triaxial tests (Sec. 12.11.1), but because the Mohr failure envelope is curved [Fig. 12.38(b)], interpretation of the results requires experience. Multistage testing should be used only for soils and soft rocks that are not structured, sensitive, cemented, or brittle.

How is multistage testing actually done? As with all strength testing, the testing pressures, loading rates, and other test details appropriate for the project should be specified by an experienced geotechnical design engineer in collaboration with laboratory technicians. After the specimen is set up in the test apparatus, the first phase confining pressure is applied and the specimen allowed to consolidate under this first stage effective confining stress. Then the axial load is applied at a controlled strain rate or using small increments of constant stress until the specimen starts to yield as the peak stress or first stage "failure" point is approached. An experienced laboratory technician (assisted by automatic data acquisition and plotting) will know when to stop loading and immediately increase the second stage confining pressure. Some time may be required for second stage consolidation, depending on the type of soil and test. The process is repeated for the third stage of the tests.

Judgment based on the shape of the stress-strain curve as well as the amount of strain that has occurred is necessary to decide where the "failure" points are. For example, some laboratories test a first specimen to a strain well above the failure strain. This is done to get a good idea of the minimum strain to achieve prior to running the second stage in another specimen. This is a conservative and reasonable approach. When all the stress-strain curves are plotted, the second one will start where the first one ended, and so on.

A three stage test is illustrated in Fig. 12.62 by the typical stress-strain curves from a CD triaxial test on a loose silty sand. The resulting Mohr circles and Mohr failure envelope are shown in Fig. 12.63. Is the resulting angle of internal friction shown in Fig. 12.63 typical for a fine to medium sand?

If there is any question about the use of a multistage test for a particular deposit, one could run tests on individual specimens at different confining pressures and compare the results with the multistage results. A geotechnical engineer familiar with the soils in his or her geographic area will know when it is appropriate to run multistage tests.

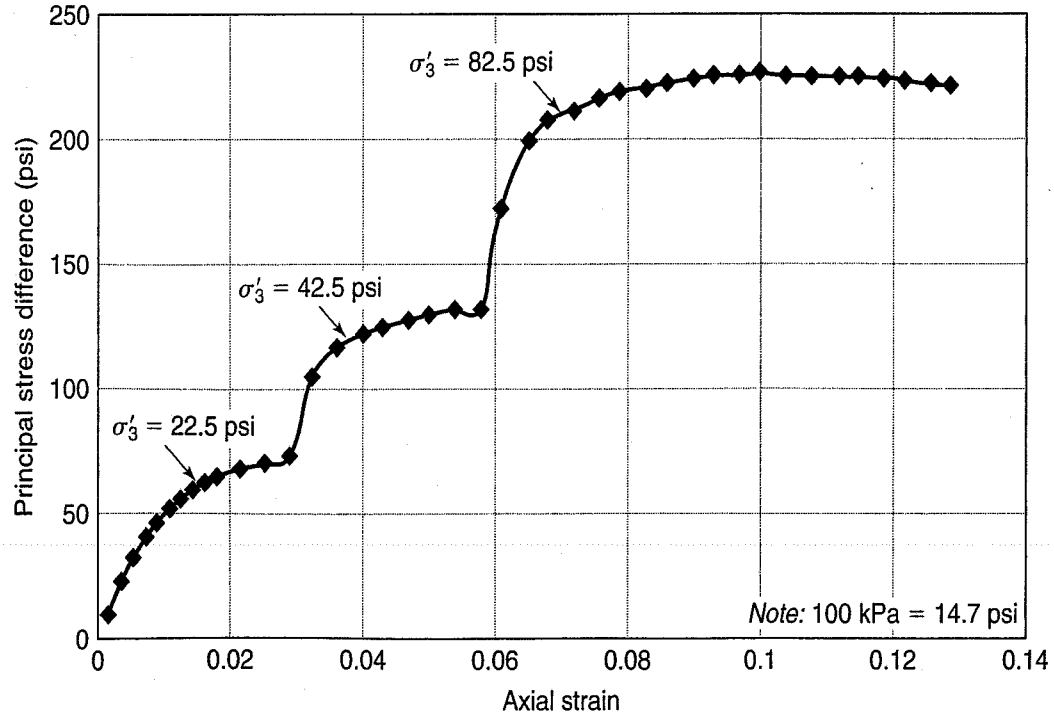

FIGURE 12.62 Stress-strain curves for a multistage CD triaxial test on a fine silty sand ($e = 0.75$) (data courtesy of Shannon and Wilson, Inc., Seattle, WA).

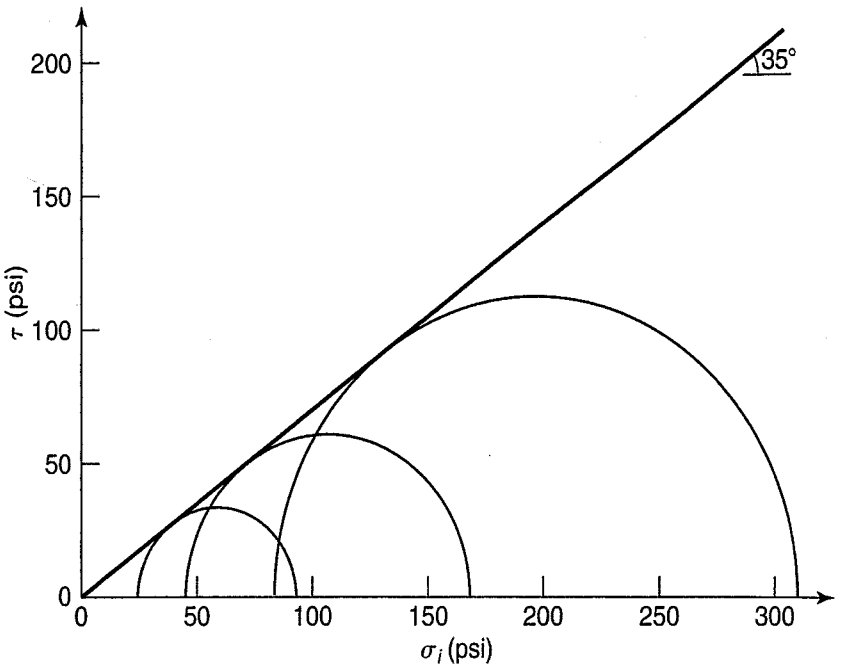

FIGURE 12.63 Mohr circles from data in Fig. 12.62 from a multistage CD triaxial test on sand (data courtesy of Shannon and Wilson, Inc., Seattle, WA).

Note: 100 kPa = 14.7 psi

Example 12.12

Given:

Data (courtesy Shannon & Wilson, Inc., Seattle) from multistage CU triaxial tests on Lake Bonneville lacustrine deposits. The soil is a moist gray silty clay (CL) with traces of fine gravel, sand, and organics. Two specimens were tested. The first specimen, Test 1, was consolidated to the in situ effective vertical overburden stress, then axially loaded in the undrained state to failure at a strain rate of about 0.006 in./min. The test data is given in Table Ex. 12.12a and plotted in Fig. Ex. 12.12a.

TABLE EX. 12.12a Data from Test 1

Item	Symbol	Test 1
Natural water content, %	w_n	41.9
Dry unit weight, pcf	γ_d	91.6
Liquid limit	LL	35
Plasticity index	PI	12
In situ overconsolidation ratio	OCR	~1.5–1.7
Effective consolidation stress, psf	σ'_3	2506
Total cell pressure, psf	$\sigma_{3\,\text{cell}}$	6819
Initial back pressure, psf	u_o	4313
Principal stress difference at failure, psf	$(\sigma_1 - \sigma_3)_f$	2523
Pore water pressure at failure, psf	Δu_f	1592
Axial strain at failure, %	ε_f	3.34
Effective major principal stress at failure, psf	σ'_{1f}	3363
Effective minor principal stress at failure, psf	σ'_{3f}	852
Effective principal stress ratio at failure	$\sigma'_{1f}/\sigma'_{3f}$	3.94

Note: 48 kPa = 1000 psf.

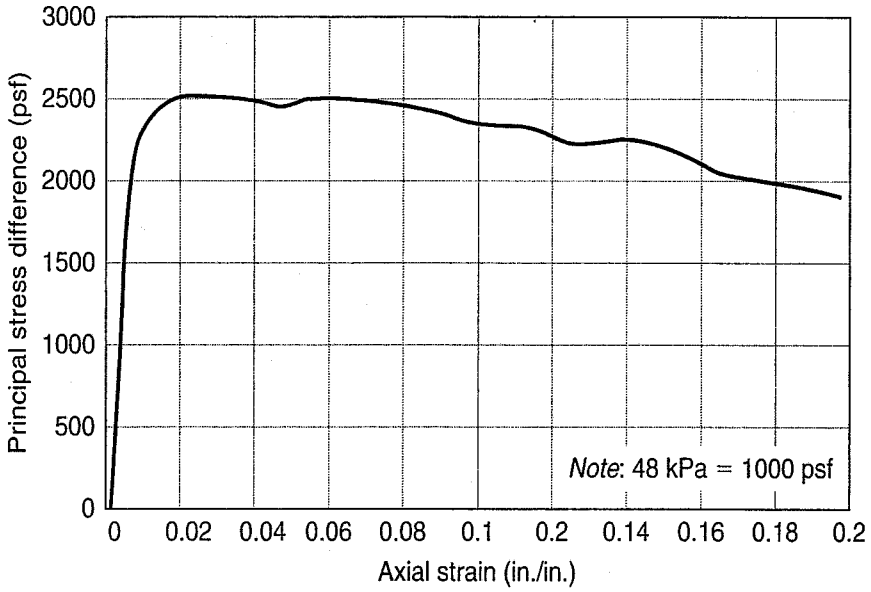

FIGURE Ex. 12.12a Stress-strain data from Test 1.

The second specimen was obtained from the same sample tube and tested in two stages at effective consolidation pressures of 4464 and 5904 psf, respectively. Data from these two tests, Tests 2A and 2B, are shown below.

Required:

a. Use the results of Test 1 to predict the starting point for the next subsequent phases from the stress-strain data. Discuss the basis of your prediction.

b. From the sample description, classification, and natural water content and dry density, are the triaxial test results reasonable, based on the all the information that you have learned thus far?

Solution:

a. From Fig. Ex. 12.12a, the maximum principal stress difference is 2523 psf, and this point occurs at an axial strain of 2.67%. Because the stress-strain curve is essentially flat after that point, we could go up to about 4% for the next phase if we wanted to. However, the test phase is usually stopped as soon as possible, so as to leave additional axial strain for the remaining phases.

Now, using the results from the multistage CU tests, let's discuss the process that the Shannon & Wilson laboratory followed. The first stage, Test 2A, is conducted at an effective confining pressure of 4464 psf, and Fig. Ex. 12.12b illustrates the stress strain curve for the second stage, which is terminated at about a strain of 3.5%. As this strain reaches about 3.5%, the stress-strain curve flattens out, as would be expected from the first phase results. Then the cell pressure is increased so that the effective confining pressure is 5904 psf. After consolidation, the drainage valve is closed. The resulting stress-strain curve is shown in Fig. Ex. 12.12c.

Why didn't we use the first specimen to provide the second stage? Well, in that test, the applied axial strain was carried out to 20%, and at that axial strain, starting another stage would be problematic because the structure of the specimen would be so drastically changed. (Note that this test was carried to an axial strain greater than the maximum of 15% recommended by ASTM D 4767.)

Table Ex. 12.12b summarizes all the stress conditions at the beginning and end of the two stages. Now we can plot the Mohr circles in terms of both effective and total stresses and evaluate the total and effective angles of internal friction. This is done in Fig. Ex. 12.12d. The total stress strength parameters are $\phi = 18°$ and $c = 100$ psf, and the parameters in terms of

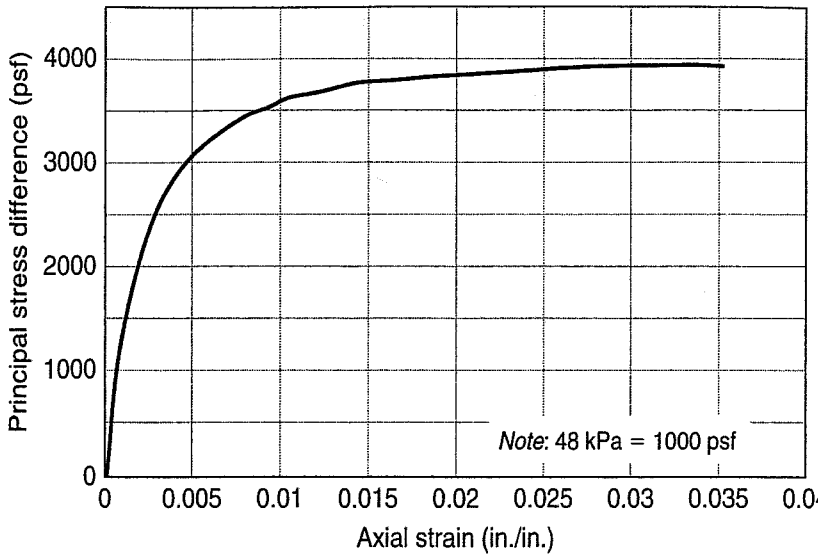

FIGURE Ex. 12.12b Stress-strain data from Test 2A.

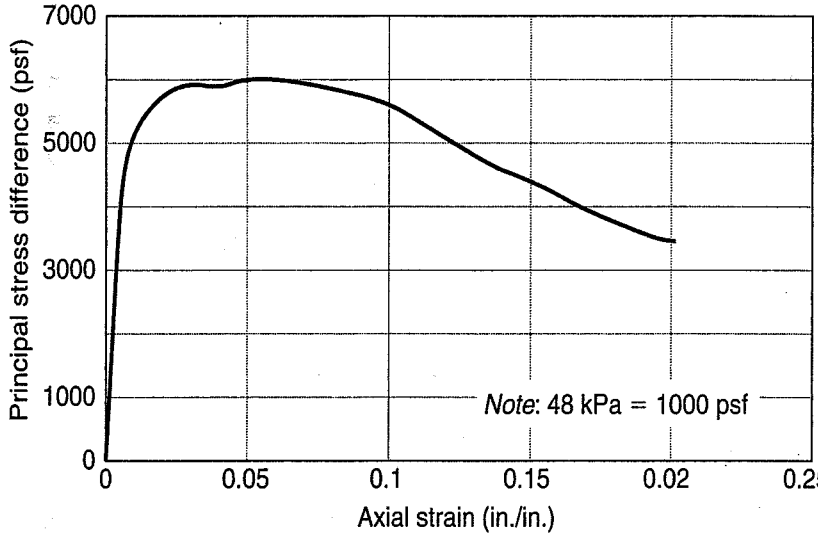

FIGURE Ex. 12.12c Stress-strain data from Test 2B.

TABLE EX. 12.12b Tabulation of Triaxial Compression-Test Data

Item	Symbol	Test 2A	Test 2B
Natural water content, %	w_n	36.6	34.5
Dry unit weight, pcf	γ_d	84	87.8
Liquid limit	LL	36	36
Plasticity index	PI	14	14
In situ overconsolidation ratio	OCR	~1.5–1.7	~1.5–1.7
Effective consolidation stress, psf	σ'_3	4464	5904
Total cell pressure, psf	$\sigma_{3\,\text{cell}}$	8784	10 224
Initial back pressure, psf	u_o	4331	4336
Principal stress difference at failure, psf	$(\sigma_1 - \sigma_3)_f$	3939	5959
Pore water pressure at failure, psf	Δu_f	2915	3749
Axial strain at failure, %	ε_f	3.54	6.70
Effective major principal stress at failure, psf	σ'_{1f}	5488	8113
Effective minor principal stress at failure, psf	σ'_{3f}	1549	2155
Effective principal stress ratio at failure	$\sigma'_{1f}/\sigma'_{3f}$	3.54	3.76

Note: 1000 psf = 48 kPa.

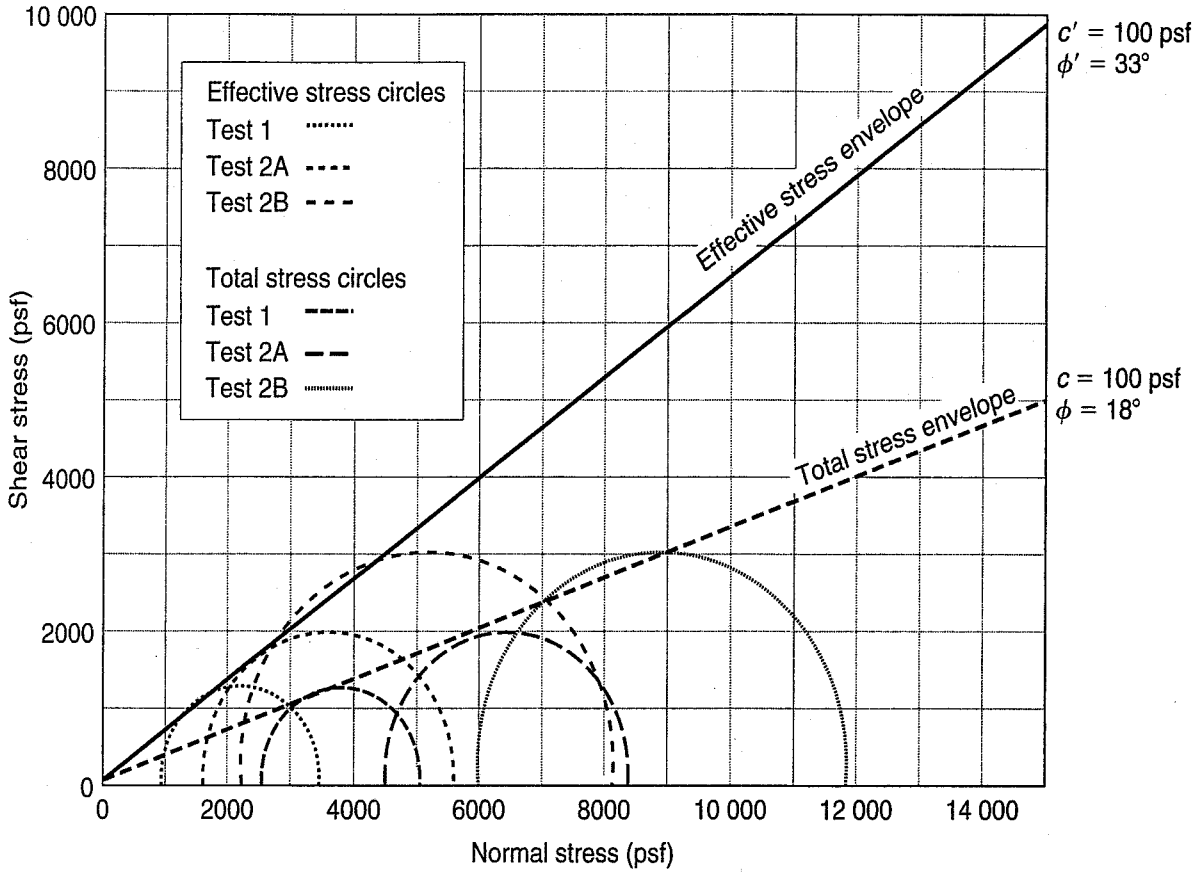

Notes:
1. Mohr's circle plotted here are based upon effective stresses computed from consolidated-undrained triaxial testing.
2. Mohr's circle in this plot are based upon the maximum principal stress difference observed during loading.

FIGURE Ex. 12.12d Total and effective stress Mohr envelopes and circles from the results of multistage tests.

effective stresses are $\phi' = 33°$ and $c' = 100$ psf. Note that the Mohr failure envelopes are a best fit by eye, and you might get slightly different values of the strength parameters. There will always be slight variations in laboratory test results of natural materials; all is not perfect in the ground or in the laboratory.

b. Are the triaxial test results reasonable? The answer is yes, they seem reasonable, based on the sample description, classification, natural water content, and dry density, as well as the information in Chapters 11 and 12.

The stress paths for this example are presented in Sec. 13.2.

12.17 INTRODUCTION TO PORE PRESSURE PARAMETERS

It should now be apparent that when saturated soils are loaded, pore water pressures will develop. In the case of one-dimensional loadings (Chapter 8), the induced pore water pressure is initially *equal* to the magnitude of the applied vertical stress. In three-dimensional or triaxial-type loadings, pore water pressures are also induced, but the actual magnitude will depend on the soil type and its stress history. Of course, the rate of loading as well as the soil type determines whether we have drained or undrained loading.

It is often necessary in engineering practice to be able to estimate just how much excess pore water pressure develops in undrained loading due to a given set of stress changes. Note that these stress changes are in terms of *total stresses*, and they can be either hydrostatic (equal all-around) or

nonhydrostatic (shear). Because we are interested in how the pore water pressure Δu responds to these changes in total stress, $\Delta\sigma_1$, $\Delta\sigma_2$, and $\Delta\sigma_3$, it is convenient to express these changes in terms of *pore pressure coefficients* or *parameters*, which were first introduced in 1954 by Prof. A. W. Skempton of Imperial College in England.

In general, we can visualize the soil mass as a compressible soil skeleton with air and water in the voids. If we increase the principal stresses acting on a soil element, as in the triaxial test, for example, then we will obtain a decrease in volume of the element and an increase in pore pressure. Refer again to Fig. 12.36, which represents the stress conditions in the UU test. Consider what happens when we apply the hydrostatic cell pressure σ_c and prevent any drainage from occurring. If the soil is 100% saturated, then we will obtain a change in pore pressure Δu ($= \Delta u_c$ in Fig. 12.36), numerically equal to the change in cell pressure $\Delta\sigma_c$ ($= \sigma_c$ in Fig. 12.36) we just applied. In other words, the ratio $\Delta u/\Delta\sigma_c$ equals 1. If the soil were less than 100% saturated, then the ratio of the induced Δu due to the increase in cell pressure $\Delta\sigma_c$ would be less than 1. It can be shown (see Appendix B.3 for details) that this ratio for the ordinary triaxial test is

$$\frac{\Delta u}{\Delta\sigma_3} = \frac{1}{1 + \dfrac{nC_v}{C_{sk}}} = B \tag{12.15}$$

where $\Delta\sigma_3 = \Delta\sigma_c$,
n = porosity,
C_v = compressibility of the voids, and
C_{sk} = compressibility of the soil skeleton.

For convenience, Professor Skempton called this ratio B. The pore pressure parameter B expresses the increase in pore pressure in undrained loading due to the increase in hydrostatic or cell pressure.

If the soil is completely saturated with water, then $C_v = C_w$, and for most soils $C_w/C_{sk} \to 0$, since the compressibility of water C_w is so small compared with the compressibility of the soil skeleton. Therefore, for saturated soils, $B = 1$. If the soil is dry, then the ratio of C_v/C_{sk} approaches infinity, since the compressibility of air is vastly greater than the soil structure; hence $B = 0$ for dry soils. Partially saturated soils have values of B ranging between 0 and 1. Because in general both C_v and C_{sk} are nonlinear for soils, the relationship between B and the degree of saturation S is also nonlinear, as shown in Fig. 12.64. This relationship will depend on the soil type and stress level, and the exact relationship will have to be determined experimentally.

Equation (12.15) is very useful in the triaxial testing to determine if the test specimen is saturated. The pore pressure response to a small change in cell pressure is measured, and B is calculated. If $B = 1$ or nearly so, then for soft clays the test specimen is saturated. However, if the soil skeleton is relatively stiff, then it is possible to have B less than 1 and still have $S = 100\%$ (see Table 12.8). This condition is possible because as C_{sk} gets smaller (a more rigid soil skeleton), the ratio C_w/C_{sk} becomes larger; thus B decreases. Wissa (1969) and Black and Lee (1973) suggest procedures to increase saturation and thereby increase the reliability of pore pressure measurements in undrained tests.

Now let's apply a stress difference or a shear stress to our soil sample (see Fig. 12.36 again for the UU test). In this case, a pore pressure Δu is induced in the specimen due to the change in stress difference $\Delta\sigma = \Delta\sigma_1 - \Delta\sigma_3$, or we can write, as Prof. Skempton did for triaxial compression conditions ($\Delta\sigma_2 = \Delta\sigma_3$),

$$\Delta u = B\frac{1}{3}(\Delta\sigma_1 - \Delta\sigma_3) \tag{12.16}$$

if the soil skeleton is *elastic*. Since soils in general are not elastic materials, the coefficient for the principal stress difference term is not $^1/_3$. So Skempton used instead the symbol A for this coefficient.

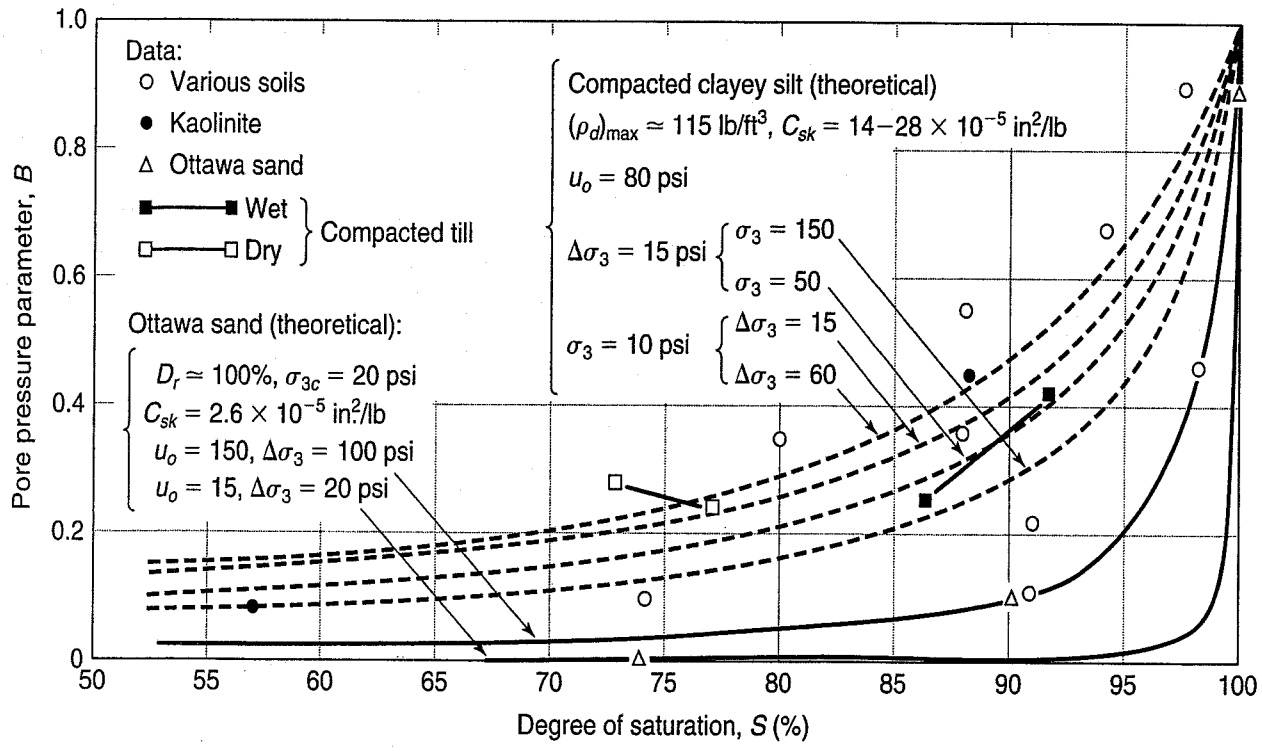

FIGURE 12.64 The pore pressure parameter B as a function of the degree of saturation for several soils (after Black and Lee, 1973).

TABLE 12.8 Theoretical B-Values for Different Soils at Complete or Nearly Complete Saturation

Soil Type	$S = 100\%$	$S = 99\%$
Soft, normally consolidated clays	0.9998	0.986
Compacted silts and clays; lightly overconsolidated clays	0.9988	0.930
Overconsolidated stiff clays; sands at most densities	0.9877	0.51
Very dense sands; very stiff clays at high confining pressures	0.9130	0.10

After Black and Lee (1973).

Now we can combine Eqs. (12.15) and (12.16) to take into account the two components of pore pressure: (1) that due to change in average or mean stress and (2) that due to change in shear stress, or

$$\Delta u = B[\Delta\sigma_3 + A(\Delta\sigma_1 - \Delta\sigma_3)] \tag{12.17}$$

Equation (12.17) is the well-known Skempton equation for relating the induced pore pressure to the changes in *total* stress in undrained loading. If $B = 1$ and $S = 100\%$, then we normally write Eq. (12.17) as

$$\Delta u = \Delta\sigma_3 + A(\Delta\sigma_1 - \Delta\sigma_3) \tag{12.18}$$

Sometimes it is convenient to write Eq. (12.18) as

$$\Delta u = B\Delta\sigma_3 + \overline{A}(\Delta\sigma_1 - \Delta\sigma_3) \tag{12.19}$$

where $\overline{A} = BA$.

Equations (12.17) through (12.19) are derived in detail in Appendix B.3. There we show that these equations are true for both triaxial compression ($\Delta\sigma_2 = \Delta\sigma_3$) and triaxial extension ($\Delta\sigma_2 = \Delta\sigma_1$) conditions, although the specific value of A is dependent on the stress path, as discussed in Sec. 13.3.

Like the parameter B, the parameter A also is not a constant; it must be determined for each soil and stress path. The parameter A is very dependent on the strain, the magnitude of σ_2, the overconsolidation

TABLE 12.9 Values of A_f for Various Soil Types

Type of Clay	A_f
Highly sensitive clays	$+3/4$ to $+1\,1/2$
Normally consolidated clays	$+1/2$ to $+1$
Compacted sandy clays	$+1/4$ to $+3/4$
Lightly overconsolidated clays	0 to $+1/2$
Compacted clay-gravels	$-1/4$ to $+1/4$
Heavily overconsolidated clays	$-1/2$ to 0

After Skempton (1954).

ratio, anisotropy, and—for natural clays tested in the laboratory—on sample disturbance. Table 12.9 relates the type of clay to different values of the A parameter at failure, A_f in triaxial compression. Of course, A can be calculated for the stress conditions at any strain up to failure, as well as at failure.

The Skempton pore pressure coefficients are most useful in engineering practice, since they enable us to predict the induced pore pressure if we know or can estimate the change in the total stresses. In the field, the Skempton equations are used, for example, when we want to estimate the pore pressure response during undrained loadings that might be applied by a highway embankment constructed on a very soft clay foundation. Typically, the embankment is constructed more rapidly than the excess pore water pressure can dissipate, and thus we assume that undrained conditions apply. The increase in excess pore pressure can result in instability if the pore pressure gets too high. Consequently, it is important to be able to estimate just how high the pore pressures are likely to get and thereby obtain some idea of how close to failure the embankment might be. If it is too high, stage construction might be utilized; then field monitoring of the pore pressures would be advisable. Skempton's parameters have also been used for the design and construction control of compacted earthfill dams.

Example 12.13

Given:

The CU test of Example 12.9.

Required:

A_f.

Solution: Use Eq. (12.17). Since pore pressures were measured, the specimen must have been saturated. Thus assume $B = 1$. So A at failure is

$$A_f = \frac{\Delta u_f - \Delta\sigma_{3f}}{\Delta\sigma_{1f} - \Delta\sigma_{3f}}$$

In an ordinary triaxial compression test, $\Delta\sigma_3 = 0$ since the cell pressure is held constant throughout the test. From Example 12.9, $\Delta\sigma_{1f} = (\sigma_1 - \sigma_3)_f = 100$ kPa and $\Delta u_f = 88$ kPa. Therefore

$$A_f = \frac{88}{100} = 0.88$$

From Table 12.9 you can see that the clay was probably somewhat sensitive.

PROBLEMS

12.1 A granular material is observed being dumped from a conveyor belt. It forms a conical pile with about the same slope angle, 1.8 horizontal to 1 vertical. What is the angle of internal friction of this material?

12.2 The bulb in the device shown in Fig. Ex. 12.1 is filled with a medium rounded sand in the densest state possible. Every effort is made to keep the sand saturated. A transparent tube allows observation of the water level in the battery filler. What will happen to the water level, if anything, as the bulb is squeezed very hard? Why? Would it matter if the sand were loose? Explain.

12.3 Derive Eq. (12.3). Start by using Eq. (12.1), and then draw the Mohr circle and Mohr–Coulomb envelope at failure for a sand.

12.4 A direct shear test was conducted on a fairly dense sample of Franklin Falls sand from New Hampshire. The initial void ratio was 0.668. The shear box was 76 mm square, and initially the height of the specimen was 11 mm. The following data were collected during shear. Compute the data needed and plot the usual curves for this type of test.

Time Elapsed (min)	Vertical Load (kN)	Horizontal Displacement (mm)	Thickness Change (mm)	Horizontal Load (N)
0	2.25	0.00	0.00	0
0.5	(constant)	0.07	−0.02	356
1		0.26	−0.04	721
2		0.45	−0.05	1014
3		0.97	−0.03	1428
4		1.71	0.03	1655
5		2.51	0.07	1770
6		3.40	0.09	1744

After Taylor (1948).

12.5 A conventional triaxial compression test was conducted on a sample of dense sand from Ft. Peck Dam, Montana. The initial area of the test specimen was 10 cm^2 and its initial height was 70 mm. Initial void ratio was 0.605. The following data were observed during shear. First, calculate the average area of the specimen, assuming it is a right circular cylinder at all times during the test. Then make the calculations necessary to plot the axial stress versus axial strain and volumetric-strain-versus-axial-strain curves for this test. Assuming $c' = 0$, what is ϕ'?

Time Elapsed	Chamber Pressure	Strain Dial (giving ΔH)		Buret (giving ΔV)	Axial Load	
sec	kPa (psi)	mm	(10^{-3} in.)	cc	N	(lbf)
0	206.8	5.08	(200)	2.00	0	(0)
	(30)	5.21	(205)	1.91	182	(41)
		5.33	(210)	1.86	374	(84)
45		5.69	(224)	1.92	641	(144)
		6.10	(240)	2.13	787	(177)
90		7.06	(278)	2.80	921	(207)
		8.10	(319)	3.66	970	(218)
		9.12	(359)	4.56	983	(221)
240		10.21	(402)	5.40	970	(218)
		12.90	(508)	7.30	898	(202)
460		15.32	(603)	8.09	814	(183)

After Taylor (1948).

12.6 The results of two CD triaxial tests at different confining pressures on a medium dense, cohesionless sand are summarized in the table below. The void ratios of both specimens were approximately the same at the start of the test. Plot on one set of axes the principal stress difference versus axial strain and volumetric strain [Eq. (12.4)] versus axial strain for both tests. Estimate the initial tangent modulus of deformation, the "50%" secant modulus, and the strain at failure for each of these tests.

Test No. 1 (σ_c = 100 kPa)			Test No. 2 (σ_c = 3000 kPa)		
Axial Strain (%)	$(\sigma_1 - \sigma_3)$ (kPa)	Volumetric Strain (%)	Axial Strain (%)	$(\sigma_1 - \sigma_3)$ (kPa)	Volumetric Strain (%)
0	0	0	0	0	0
1.71	325	−0.10	0.82	2090	−0.68
3.22	414	+0.60	2.50	4290	−1.80
4.76	441	+1.66	4.24	5810	−2.71
6.51	439	+2.94	6.00	6950	−3.36
8.44	405	+4.10	7.76	7760	−3.88
10.4	370	+5.10	9.56	8350	−4.27
12.3	344	+5.77	11.4	8710	−4.53
14.3	333	+6.33	13.2	8980	−4.71
16.3	319	+6.70	14.9	9120	−4.84
18.3	318	+7.04	16.8	9140	−4.92
20.4	308	+7.34	18.6	9100	−4.96
			20.5	9090	−5.01

After A. Casagrande.

12.7 For the two tests of Problem 12.6, determine the angle of internal friction of the sand at (a) peak compressive strength, (b) at ultimate compressive strength, and (c) at 5.5% axial strain. Comments?

12.8 A sand is hydrostatically consolidated in a triaxial test apparatus to 450 kPa and then sheared with the drainage valves open. At failure, $(\sigma_1 - \sigma_3)$ is 1121 kPa. Determine the major and minor principal stresses at failure and the angle of shearing resistance. Plot the Mohr diagram. (This problem should be followed by the next one.)

12.9 The same sand as in Problem 12.8 is tested in a direct shear apparatus under a normal pressure of 390 kPa. The specimen fails when a shear stress of 260 kPa is reached. Determine the major and minor principal stresses at failure and the angle of shearing resistance. Plot the Mohr diagram. Explain the differences, if any, of these values with those obtained in the preceding problem.

12.10 Indicate the orientations of the major principal stress, the minor principal stress, and the failure plane of the tests in Problems 12.8 and 12.9.

12.11 A granular soil is tested in direct shear under a normal stress of 350 kPa. The size of the specimen is 7.62 cm in diameter. If the soil to be tested is a dense sand with an angle of internal friction of 38°, determine the size of the force transducer required to measure the shear force with a factor of safety of 2 (that is, the capacity of the transducer should be twice that required to shear the sand).

12.12 The stresses induced by a surface load on a *loose* horizontal sand layer were found to be σ_v = 5.13 kPa, τ_v = 1.47 kPa, σ_h = 3.22 kPa, τ_h = −1.47 kPa. By means of Mohr circles, determine if such a state of stress is safe. Use Eq. (11.11) for the definition of factor of safety.

12.13 If the same stress conditions as in Problem 12.12 act on a very dense gravelly sand, is such a state safe against failure?

12.14 The effective normal stresses acting on the horizontal and vertical planes in a silty gravel soil are 1.77 MPa and 2.95 MPa, respectively. The shear stress on these planes is ±0.59 MPa. For these conditions, what are the magnitude and direction of the principal stresses? Is this a state of failure?

12.15 A specimen of dense sand tested in a triaxial CD test failed along a well-defined failure plane at an angle of 62° with the horizontal. Find the effective confining pressure of the test if the principal stress difference at failure was 115 kPa.

12.16 A dry loose sand is tested in a vacuum triaxial test in which the pore air pressure of the specimen is lowered below gage pressure to within about 95% of −1 atm. Estimate the principal stress difference and the major principal stress ratio at failure.

12.17 For the data shown in Fig. 12.5(a), what is (a) the principal stress difference and (b) the principal stress ratio at an axial strain of 12% for an effective confining pressure of 1.3 MPa?

12.18 For the conditions given in Problem 12.17, plot the Mohr circle.

12.19 Do Problems 12.17 and 12.18 for the data shown in Fig. 12.6(a).

12.20 A specimen of Sacramento River sand has a critical confining pressure of 1000 kPa. If the specimen is tested at an effective confining pressure of 600 kPa, describe its behavior in drained shear. Show results in the form of unscaled Mohr circles.

12.21 For the sand of Problem 12.20, describe the behavior in drained shear in a triaxial test if the effective confining pressure is 1300 kPa.

12.22 A drained triaxial test is performed on a sand with $\sigma'_{3c} = \sigma'_{3f} = 450$ kPa. At failure, $\tau_{max} = 594$ kPa. Find σ'_{1f}, $(\sigma_1 - \sigma_3)_f$, and ϕ'.

12.23 Assume the sand of Problem 12.22 is Sacramento River sand at a void ratio of 0.6. If the initial volume of the specimen was 62 cm^3, what change in volume would you expect during shear?

12.24 A silty sand is tested consolidated-drained in a triaxial cell where both principal stresses at the start of the test were 625 kPa. If the total axial stress at failure is 2.04 MPa while the horizontal pressure remains constant, compute the angle of shearing resistance and the theoretical orientation of the failure plane with respect to the horizontal.

12.25 A specimen of sand failed when $(\sigma_1 - \sigma_3)$ was 750 kPa. If the hydrostatic consolidation stress was 250 kPa, compute the angle of shearing resistance of the sand. What else can you say about the sand?

12.26 A specimen of sand at the field density is known to have a $(\sigma_1/\sigma_3)_{max}$ of 3.8. If such a specimen is hydrostatically consolidated to 1180 kPa in a triaxial test apparatus, at what effective confining pressure σ'_{3f} will the specimen fail if the vertical stress is held constant? (This is a lateral extension test.)

12.27 Two CD triaxial tests are conducted on identical specimens of the same sand. Both specimens are initially consolidated hydrostatically to 50 kPa; then each specimen is loaded as shown in Fig. P12.27. Specimen A failed when the applied $\Delta\sigma_1$ was 180 kPa. Make the necessary calculations to (a) plot the Mohr circles at failure for both tests, and (b) determine ϕ' for the sand. (After C.W. Lovell.)

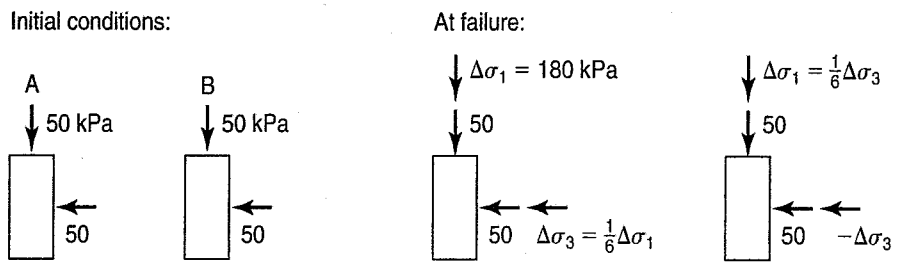

FIGURE P12.27

12.28 Plot a graph of σ'_1/σ'_3, versus ϕ'. (Aren't you sorry you didn't do this sooner? It would have been helpful for solving some of these problems.) What range of values of ϕ' should be used?

12.29 Estimate the shear strength parameters of a fine (beach) sand (SP). Estimate the minimum and maximum void ratios.

12.30 A subrounded to subangular sand has a D_{10} of about 0.1 mm and a uniformity coefficient of 3. The angle of shearing resistance measured in the direct shear test was 47°. Is this reasonable? Why or why not?

12.31 Estimate the ϕ' values for (a) a well-graded sandy gravel (GW) at a density of 1.9 Mg/m^3; (b) a poorly graded silty sand with a field density of 1.70 Mg/m^3; (c) an SW material at 100% relative density; and (d) a poorly graded gravel with an in situ void ratio of 0.5.

12.32 The results of a series of CD triaxial tests on a medium dense, cohesionless sand are summarized in the table below. The void ratios for all the test specimens were approximately the same at the start of the test. Plot the strength circles and draw the Mohr failure envelope for this series of tests. What angle of internal friction should be used in solving stability problems in which the range of normal stresses is (a) 0–500 kPa; (b) 1000–1500 kPa; (c) 3–6 MPa; and (d) 0–6 MPa?

Test No.	Confining Pressure (kPa)	Compressive Strength (kPa)
1	120	576
2	480	2240
3	1196	4896
4	2256	8460
5	3588	12 240
6	3568	15 228

After A. Casagrande.

12.33 Estimate the values of the coefficient of earth pressure at rest, K_o, for the four soils of Problem 12.31.

12.34 If the sands of Problem 12.33 had been preloaded, would your estimate of K_o be any different? If so, would it be higher or lower? Why?

12.35 Estimate K_o for sands 1, 4, 5, 6, 8, and 10 in Table 12.1 for relative densities of 40% and 85%.

12.36 For future reference, place a scale of K_o on the ordinate of Fig. 12.14(b). You should probably also indicate a range of values of K_o.

12.37 We stated in Secs. 11.5 and 12.11.1 that the unconsolidated-drained test was meaningless because it could not be properly interpreted. Why is this so? Discuss in terms of laboratory tests as well as possible practical applications.

12.38 A CD axial compression triaxial test on a normally consolidated clay failed along a clearly defined failure plane of 54°. The cell pressure during the test was 220 kPa. Estimate ϕ', the maximum σ_1'/σ_3', and the principal stress difference at failure.

12.39 An unconfined compression test is performed on a dense silt. Previous drained triaxial tests on similar samples of the silt gave $\phi' = 32°$. If the unconfined compressive strength was 420 kPa, estimate the height of capillary rise in this soil above the ground water table. (*Hint:* Find the effective confining pressure acting on the specimen. Draw elements similar to Fig. 12.40.)

12.40 Estimate the in situ value of K_o of the silt of Problem 12.50. Is this value reasonable in terms of the correlation shown in Fig. 11.57?

12.41 Another specimen of the dense silt of Problem 12.39 is tested in unconfined compression. Assume the average pore size of the silt is 2 μm and estimate the compressive strength of the sample.

12.42 What would happen if the specimen of Problem 12.39 were prepared in a loose state, then sheared? What would be its unconfined compressive strength?

12.43 The results of unconfined compression tests on a sample of clay in both the undisturbed and remolded states are summarized below. Determine the compressive strength, the initial tangent modulus of deformation, and the secant modulus of deformation at 50% of the compressive strength for both the undisturbed and remolded specimens. Determine the sensitivity of the clay. For the solution of a practical stability problem involving this clay in the undisturbed state, what shear strength would you use if no change in water content occurs during construction? (After A. Casagrande.)

Undisturbed State		Remolded State	
Axial Strain (%)	$\Delta\sigma$ (kPa)	Axial Strain (%)	$\Delta\sigma$ (kPa)
0	0	0	0
1	31	1	7
2	58	2	10
4	104	4	22
6	126	6	30
8	142	8	38
12	152	12	45
16	153	16	47
20	153	20	48

12.44 (a) Show that Eq. (12.11) (in Example 12.10) is correct for *undrained* triaxial or unconfined compression tests. (b) Derive a similar expression for the area of the specimen in a *drained* triaxial test. [*Hint:* $A_s = f(A_o, H_o, \varepsilon, \Delta V)$.]

12.45 For the data shown in Fig. 8.5, estimate the unconfined compressive strength and the sensitivity of this soil. Typical values for the clay are LL = 88, PL = 43, and PI = 45.

CHAPTER 13

Advanced Topics in Shear Strength of Soils and Rocks

13.1 INTRODUCTION

In this chapter we build on shear strength basics introduced in Chapters 11 and 12, presenting additional information and advanced topics on the stress-deformation and shear strength properties of soils and rocks. We begin with a detailed discussion of stress paths and their use in engineering practice. Then we present a brief introduction to critical state soil mechanics and discuss other aspects of the constitutive (stress-strain) behavior and modulus of soils. Next we look at the fundamentals of the drained, undrained, and the plane strain behavior of saturated sands. As a transition into fine grained soils, the dynamic behavior, including strain rate effects, as well as the residual shear strength of both sands and clays are summarized. Next we discuss some special topics on the stress-deformation and shear strength of cohesive soils, including Hvorslev strength parameters, the τ_f/σ'_{vo} ratio, Jürgenson-Rutledge hypothesis, consolidation methods to overcome sampling disturbance, strength anisotropy, and the plane strain strength of clays. We conclude with an introduction to the strength of unsaturated soils and failure theories for rocks.

The following notation is used in this chapter.

Symbol	Dimension	Unit	Definition
a	—	—	Henkel's pore pressure parameter - Eq. (13.15)
a	$ML^{-1}T^{-2}$	kPa	Cohesion intercept in stress path space - Eq. (13.6)
c'_e	$ML^{-1}T^{-2}$	kPa	Hvorslev effective "cohesion" parameter
E_d	$ML^{-1}T^{-2}$	kPa	Drained modulus
E_i or E_t	$ML^{-1}T^{-2}$	kPa	Initial or initial tangent modulus
E_u	$ML^{-1}T^{-2}$	kPa	Undrained modulus
E_{ur}	$ML^{-1}T^{-2}$	kPa	Unload-reload modulus - Eq. (13.27)
ESP	—	—	Effective stress path
G_{max}	$ML^{-1}T^{-2}$	kPa	Maximum (small-strain) shear modulus - Eq. (13.24)
K_b	$ML^{-1}T^{-2}$	kPa	Bulk modulus - Eq. (13.28)
K_f	—	—	Stress ratio at failure - Eq. (13.3)
K_{ur}	$ML^{-1}T^{-2}$	kPa	Unload-reload modulus - Eq. (13.27)
m	—	—	Empirical constant - Eqs. (13.28) and (13.77)

(Continued)

Symbol	Dimension	Unit	Definition
n	—	—	Dimensionless constant - (Eq. 13.27)
N	MLT^{-2}	N	Normal force - Eq. (13.30)
p	$ML^{-1}T^{-2}$	kPa	$(\sigma_v + \sigma_v)/2$ - Eq. (13.2)
q	$ML^{-1}T^{-2}$	kPa	$(\sigma_v - \sigma_v)/2$ - Eq. (13.1)
R_f	—	—	Model parameter failure ratio - Eq. (13.29)
s	—	—	Empirical constant - Eq. (13.77)
S	—	—	Undrained strength ratio, τ_f/σ'_v, for normally consolidated clay - Eq. (13.53)
S_{res}	—	%	Residual degree of saturation
SR_o	T^{-1}	(%/hr)	Reference axial strain rate
T	MLT^{-2}	—	Shear force - Eq. (13.30) or surface tension - Eq. (13.61)
TSP	$ML^{-1}T^{-2}$	—	Total stress path
u_a	$ML^{-1}T^{-2}$	kPa	Air pressure
V_s	LT^{-1}	m/s	Shear wave velocity - Eq. (13.24)
V	—	—	Specific volume
W	$ML^{-1}T^{-2}$	kPa	Strain energy dissipated during one cycle of loading - Eq. (13.66)
α			
β	—	—	Slope of line of constant stress ratio K for $K < K_f$ - Eq. (13.4)
ΔH	L	m	Vertical expansion
δ	—	(degree)	Angle between direction of deposition and major principal stress loading
$\varepsilon_1, \varepsilon_2, \varepsilon_3$	—	(%)	Major, intermediate, and minor principal strains
η	—	—	Deviatoric component
λ	—	—	Damping ratio
ν	—	(degree)	Dilation angle
ρ_{SRo}			Change in undrained strength per log cycle change in strain rate - Eq. (13.60)
σ_c	$ML^{-1}T^{-2}$	kPa	Uniaxial compressive strength of rock - Eq. (13.77)
σ_{oct}	$ML^{-1}T^{-2}$	kPa	Octahedral normal stress - Eq. (13.16)
σ_t	$ML^{-1}T^{-2}$	kPa	Tensile strength - Eq. (13.76)
σ'_m	$ML^{-1}T^{-2}$	kPa	Mean principal effective stress - Eq. (13.72)
σ'_{ps}	$ML^{-1}T^{-2}$	kPa	Perfect sampling effective stress - Eq. (13.23)
σ'_r	$ML^{-1}T^{-2}$	kPa	Residual effective stress
$(\sigma'_Y)_{hydrostatic}$	$ML^{-1}T^{-2}$	kPa	Yield stress for hydrostatically consolidated specimens
τ_e	$ML^{-1}T^{-2}$	kPa	Expansion shear stress
τ_{oct}	$ML^{-1}T^{-2}$	kPa	Octahedral shear stress - Eq. (13.17)
τ_R			
ϕ^b		(degree)	Angle representing increase in shear strength due to suction - Eq. (13.63)
ϕ'_e		(degree)	Hvorslev effective friction parameter
ϕ'_i		(degree)	Instantaneous friction angle - Eq. (13.80)
ϕ_{ps}, ϕ_{tx}		(degree)	Angle of internal friction from plane strain tests and triaxial tests, respectively - Eq. (13.37)
ϕ_μ		(degree)	Friction angle between mineral surfaces (Table 13.5)
ϕ'_R		(degree)	
ξ			Hydrostatic component
ψ		(degree)	Slope of K_f line - Eq. (13.6)
χ	—	—	Matric suction parameter - Eq. (13.62)

13.2 STRESS PATHS

As you know from Chapter 11, states of stress at a point in equilibrium can be represented by a Mohr circle in a τ–σ coordinate system. Sometimes it is convenient to represent that state of stress by a *stress point*, which has the coordinates $(\sigma_1 - \sigma_3)/2$ and $(\sigma_1 + \sigma_3)/2$, as shown in Fig. 13.1. For many situations in geotechnical engineering, we assume σ_1 and σ_3 act on vertical and horizontal planes, so the coordinates of the stress point become $(\sigma_v - \sigma_h)/2$ and $(\sigma_v + \sigma_h)/2$, or simply q and p, respectively; or

$$q = \frac{\sigma_v - \sigma_h}{2} \tag{13.1}$$

$$p = \frac{\sigma_v + \sigma_h}{2} \tag{13.2}$$

Both q and p could, of course, be defined in terms of the principal stresses. By convention, q is considered positive when $\sigma_v > \sigma_h$; otherwise it is negative.

We often want to show successive states of stress that a test specimen or a typical element in the field undergoes during loading or unloading. A diagram showing the successive states with a series of Mohr circles could be used [Fig. 13.2(a)], but it might be confusing, especially if the stress path were complicated. It is simpler to show only the *locus* of the stress points. This locus, called the *stress path*, is plotted on what we call a *p–q diagram* [Fig. 13.2(b)]. Note that both p and q could be defined in terms of either total stresses or effective stresses. As before, a prime mark is used to indicate effective stresses. So from Eqs. (13.1) and (13.2) and the effective stress equation [Eq. (6.8)] we know that $q' = q$ while $p' = p - u$, where u is the excess hydrostatic or pore water pressure.

Although the concept of a stress path has been around for a long time, Prof. T. W. Lambe of M.I.T. demonstrated its usefulness as a teaching device (Lambe and Whitman, 1969) and developed the method into a practical engineering tool for the solution of stability and deformation problems (Lambe, 1964 and 1967; Lambe and Marr, 1979). Very often in geotechnical engineering practice, if you understand the complete stress path of your problem, you are well along the way toward the solution.

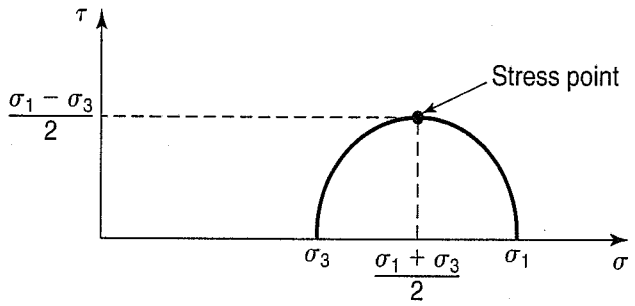

FIGURE 13.1 A Mohr circle of stress and corresponding stress point.

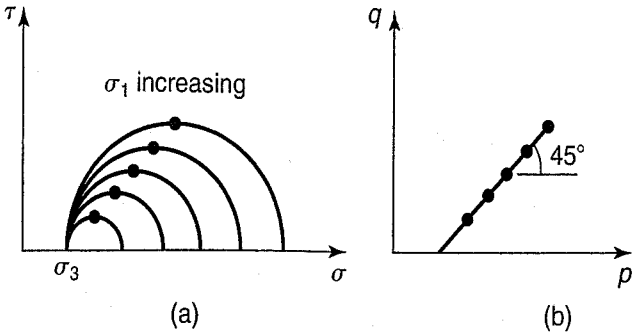

FIGURE 13.2 (a) Successive Mohr circles; (b) stress path for constant σ_3 and increasing σ_1 (after Lambe and Whitman, 1969).

A simple case to illustrate stress paths is the common triaxial test in which σ_3 remains fixed as we increase σ_1. Some Mohr circles for this test are shown in Fig. 13.2(a) along with their stress points. The corresponding stress path shown in Fig. 13.2(b) is a straight line at an angle of 45° from the horizontal, because the stress point represents the state of stress on the plane oriented 45° from the principal planes. (Note that this is the plane of maximum shear stress.)

Some examples of stress paths are shown in Figs. 13.3 and 13.4. In Fig. 13.3 the initial conditions are $\sigma_v = \sigma_h$, an equal-all-around or hydrostatic state of stress. Those in Fig. 13.4, where the initial vertical stress is not the same as the initial horizontal stress, represent a nonhydrostatic state of stress. You should verify that each stress path in Figs. 13.3 and 13.4 has in fact the direction as indicated in the figures. We will show you how to do this in Example 13.1.

1. Initial conditions:
$\sigma_v = \sigma_h$ (hydrostatic compression)

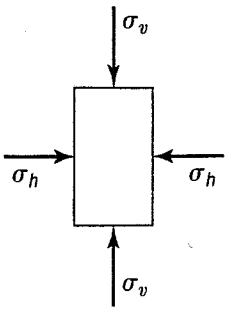

2. During loading (or unloading)

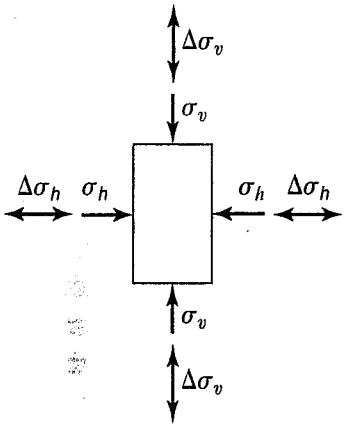

3. Stress paths

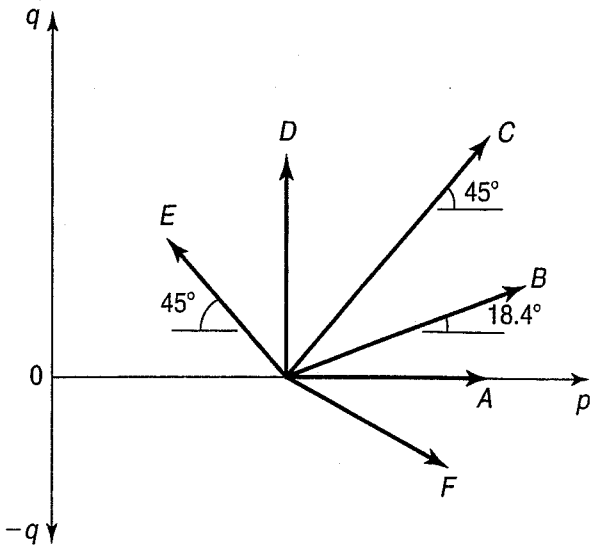

Path *A*: $\Delta\sigma_h = \Delta\sigma_v$

B: $\Delta\sigma_h = \frac{1}{2}\Delta\sigma_v$

C: $\Delta\sigma_h = 0$, $\Delta\sigma_v$ increases

D: $\Delta\sigma_h = -\Delta\sigma_v$

E: $\Delta\sigma_h$ decreases, $\Delta\sigma_v = 0$

F: $\Delta\sigma_h$ increases, $\Delta\sigma_v$ decreases

FIGURE 13.3 Different stress paths for initially hydrostatic stress conditions (after Lambe and Whitman, 1969).

1. Initial conditions:
$\sigma_v \neq \sigma_h \neq 0$ (nonhydrostatic compression)

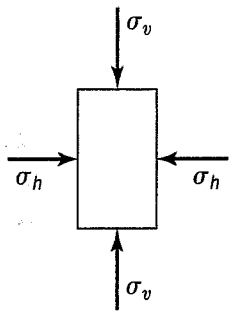

2. During loading (or unloading)

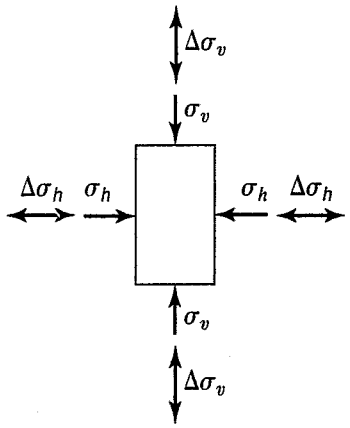

3. Stress paths

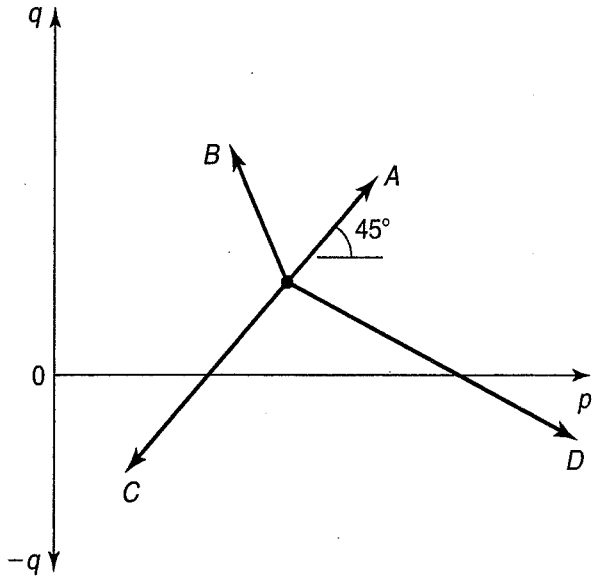

Path *A*: $\Delta\sigma_v$ increases, $\Delta\sigma_h = 0$

B: $\Delta\sigma_v$ increases, $\Delta\sigma_h$ decreases

C: $\Delta\sigma_v$ decreases, $\Delta\sigma_h = 0$

D: $\Delta\sigma_v$ decreases, $\Delta\sigma_h$ increases

FIGURE 13.4 Different stress paths for initially nonhydrostatic stress conditions (after Lambe and Whitman, 1969).

Example 13.1

Given:

Figures 13.3 and 13.4.

Required:

Verify that stress paths A, B, and C of Fig. 13.3 and A and D of Fig. 13.4 are correct as shown.

Solution: The initial conditions for all stress paths in Fig. 13.3 are $p_o = (\sigma_v + \sigma_h)/2 = \sigma_v = \sigma_h$ and $q_o = 0$. Final conditions are [Eqs. (13.1) and (13.2)].

$$q_f = \frac{(\sigma_v + \Delta\sigma_v) - (\sigma_h + \Delta\sigma_h)}{2}$$

$$p_f = \frac{(\sigma_v + \Delta\sigma_v) + (\sigma_h + \Delta\sigma_h)}{2}$$

For stress path A, $\Delta\sigma_v = \Delta\sigma_v$; so

$$q_f = \frac{\sigma_v + \Delta\sigma_v - \sigma_v - \Delta\sigma_v}{2} = 0$$

$$p_f = \frac{\sigma_v + \Delta\sigma_v + \sigma_v + \Delta\sigma_v}{2} = \sigma_v + \Delta\sigma_v$$

Thus the stress path A moves out on the p-axis by an amount $\Delta\sigma_v = \Delta\sigma_h$.

For stress path B, $\Delta\sigma_h = \frac{1}{2}\Delta\sigma_v$; so

$$q_f = \frac{\sigma_v + \Delta\sigma_v - \sigma_v - \frac{1}{2}\Delta\sigma_v}{2} = \frac{1}{4}\Delta\sigma_v$$

$$p_f = \frac{\sigma_v + \Delta\sigma_v + \sigma_v + \frac{1}{2}\Delta\sigma_v}{2} = \sigma_v + \frac{3}{4}\Delta\sigma_v$$

These values are the (p, q) coordinates of the end of stress path B. Thus the q and p both increase by an amount $\Delta q = \frac{3}{4}\Delta\sigma_v$ and $\Delta p = \frac{3}{4}\Delta\sigma_v$, which means that the stress path has a slope of $\frac{1}{3}$ or is inclined at 18.4°, as shown in Fig. 13.3.

For stress path C, $\Delta\sigma_h = 0$ and $\Delta\sigma_v$ increases by some amount.

$$q_f = \frac{\sigma_v + \Delta\sigma_v - \sigma_v}{2} = \frac{1}{2}\Delta\sigma_v$$

$$p_f = \frac{\sigma_v + \Delta\sigma_v + \sigma_v}{2} = \sigma_v + \frac{1}{2}\Delta\sigma_v$$

So $\Delta q = \frac{1}{2}\Delta\sigma_v$ and $\Delta p = \frac{1}{2}\Delta\sigma_v$. Therefore the slope of the stress path must be 1 or inclined at 45°. This solution holds also for stress path A in Fig. 13.4. Here initial conditions are nonhydrostatic, so

$$q_o = \frac{\sigma_v - \sigma_h}{2}$$

$$p_o = \frac{\sigma_v + \sigma_h}{2}$$

The final coordinates for path A are

$$q_f = \frac{\sigma_v + \Delta\sigma_v - \sigma_h}{2}$$

$$p_f = \frac{\sigma_v + \Delta\sigma_v + \sigma_h}{2}$$

So $\Delta q = \frac{1}{2}\Delta\sigma_v$ and $\Delta p = \frac{1}{2}\Delta\sigma_v$, which is the same as for stress path C in Fig. 13.3.

For stress path D in Fig. 13.4, $\Delta\sigma_v$ decreases while $\Delta\sigma_h$ increases. Initial (p_o, q_o) are the same as path A in this figure, while the final values of (p_f, q_f) are

$$q_f = \frac{(\sigma_v - \Delta\sigma_v) - (\sigma_h + \Delta\sigma_h)}{2}$$

$$p_f = \frac{(\sigma_v - \Delta\sigma_v) + (\sigma_h + \Delta\sigma_h)}{2}$$

So

$$\Delta q = -\frac{1}{2}\Delta\sigma_v - \frac{1}{2}\Delta\sigma_h \quad \text{and} \quad \Delta p = -\frac{1}{2}\Delta\sigma_v + \frac{1}{2}\Delta\sigma_h$$

The actual slope of the stress path depends on the relative magnitudes of $\Delta\sigma_v$ and $\Delta\sigma_h$, but in general it trends down and out, as shown in Fig. 13.4.

It is often convenient to consider *stress ratios*. In Chapter 6 we defined a lateral stress ratio K, which is the ratio of horizontal to vertical stress,

$$K = \frac{\sigma_h}{\sigma_v} \tag{6.18}$$

In terms of *effective* stresses, this ratio is

$$K_o = \frac{\sigma'_h}{\sigma'_v} \tag{6.19}$$

where K_o is called the coefficient of lateral earth pressure at rest for conditions of no lateral strain. Finally, we can define a ratio K_f for the stress ratio at failure:

$$K_f = \frac{\sigma'_{hf}}{\sigma'_{vf}} \tag{13.3}$$

where σ'_{hf} = the horizontal effective stress at failure, and

σ'_{vf} = the vertical effective stress at failure.

Usually K_f is defined in terms of effective stresses, but it could also be expressed in terms of total stresses. Constant stress ratios appear as straight lines on a p–q diagram (Fig. 13.5). These lines could also be stress paths for initial conditions of $\sigma_v = \sigma_h = 0$ with loadings of K equal to a constant (that is, constant σ_h/σ_v). Other initial conditions are, of course, possible, such as those shown in Figs. 13.3 and 13.4.

Note that

$$\frac{q}{p} = \tan\beta = \frac{1 - K}{1 + K} \tag{13.4}$$

or in terms of K

$$K = \frac{1 - \tan\beta}{1 + \tan\beta} \tag{13.5}$$

where β is the slope of the line of constant K when $K < K_f$. At failure, the slope of the K_f line is indicated by the symbol ψ. Note also that for any point where you know p and q (for example, point A in Fig. 13.5), σ_h and σ_v can readily be found graphically; that is, lines at 45° from the stress point intersect the σ-axis at σ_h and σ_v. Finally, there is no reason why σ_v must always be greater than σ_h. It usually is, but in many important situations in geotechnical engineering $\sigma_h > \sigma_v$. In these cases, by convention q is negative and $K > 1$, as shown in Fig. 13.5.

Now we describe some stress paths that are important in geotechnical engineering. When soils are deposited in a sedimentary environment like a lake or the sea, there is a gradual buildup of overburden stress as additional material is deposited from above. As this stress increases, the sediments consolidate and decrease in volume (Chapters 8 and 9). If the area of deposition is relatively large compared with the thickness of the deposit, then it seems reasonable that the compression is essentially one-dimensional. In this case the stress ratio would be constant and equal to K_o, and the stress path during sedimentation and

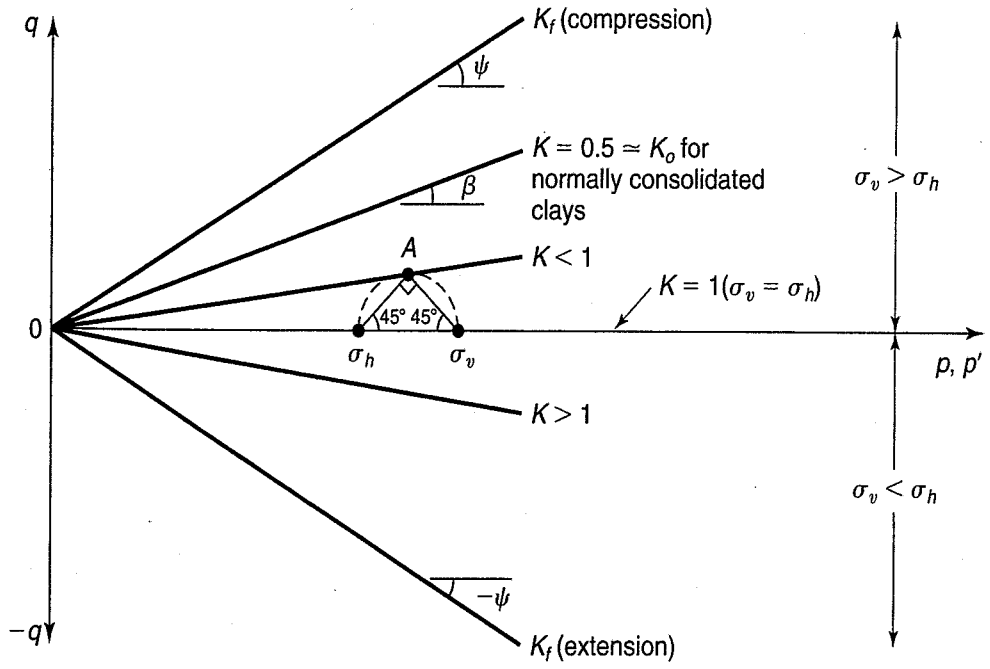

FIGURE 13.5 Different constant stress ratios and examples of stress paths, starting from $\sigma_v = \sigma_h = 0$ (after Lambe and Whitman, 1969).

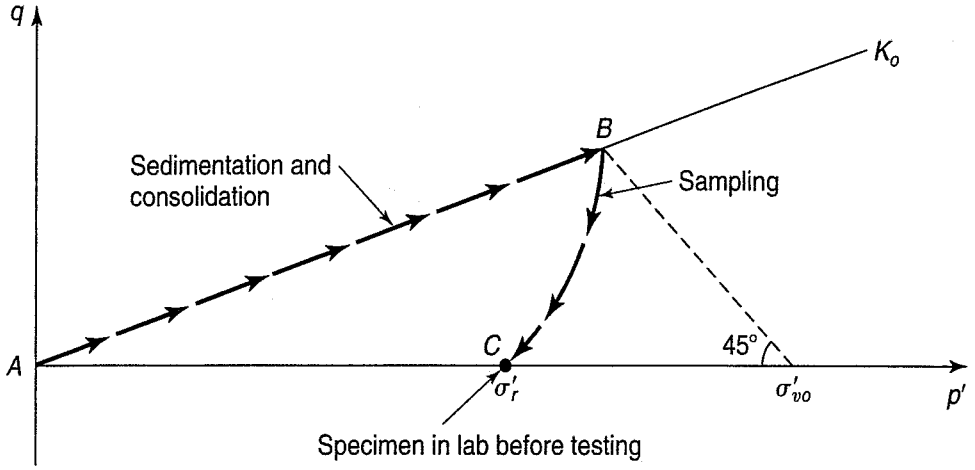

FIGURE 13.6 Stress paths during sedimentation and sampling of normally consolidated clay, where $K_o < 1$.

consolidation would be similar to path AB in Fig. 13.6. Typical values of K_o for granular materials range from about 0.4 to 0.6, whereas for normally consolidated clays K_o can be a little less than 0.5 to perhaps as high as 0.8. A good average value is about 0.5. (See Secs. 12.7 and 12.13.) When a sample of the soil is taken, stress decrease occurs, because the overburden stress σ_{vo} has to be removed to get at the sample. The stress path follows approximately line BC in Fig. 13.6, and the soil specimen ends up someplace on the hydrostatic ($\sigma_h = \sigma_v$) or $K = 1$ axis. This stress path and its relation to the strength of clays is discussed in Sec. 13.6 and more extensively in Ladd and DeGroot (2003).

If, instead of by sampling, the overburden stress were decreased by erosion or some other geologic process, an unloading stress path similar to BC in Fig. 13.6 would be followed. If the vertical stress continued to be removed, the path could extend to a point well below the p-axis. The soil would then be overconsolidated, and K_o would be greater than 1.0.

Sometimes in engineering practice a test specimen is reconsolidated in the laboratory under K_o conditions so as to reinstate the estimated in situ stresses. Such conditions are shown in Fig. 13.4 and at point A in Fig. 13.7. After consolidation, the loading (or unloading) path followed to failure depends on the field loading conditions one wishes to model. Four common field conditions and the laboratory stress paths that model them are shown in Fig. 13.7. Note that these stress paths are for *drained* loading (discussed in the previous chapter), in which there is *no* excess pore water pressure; therefore total stresses equal effective stresses and the total stress path (TSP) for a given loading is identical to the effective stress path (ESP).

As suggested by Eq. (13.3), we are often interested in conditions at failure, and it is useful to know the relationship between the K_f line and the Mohr–Coulomb failure envelope. Consider the two Mohr circles shown in Fig. 13.8. The circle on the left, drawn for illustrative purposes only, represents failure in terms of the p–q diagram. The identical circle on the right is the same failure circle on the Mohr τ–σ diagram. To establish the slopes of the two lines and their intercepts, several Mohr circles and stress paths, determined over a range of stresses, were used. The equation of the K_f line is

$$q_f = a + p_f \tan \psi \tag{13.6}$$

where a = the intercept on the q-axis, in stress units, and

ψ = the angle of the K_f line with respect to the horizontal, in degrees.

The equation of the Mohr–Coulomb failure envelope is

$$\tau_{ff} = \sigma_{ff} \tan \phi + c \tag{11.9}$$

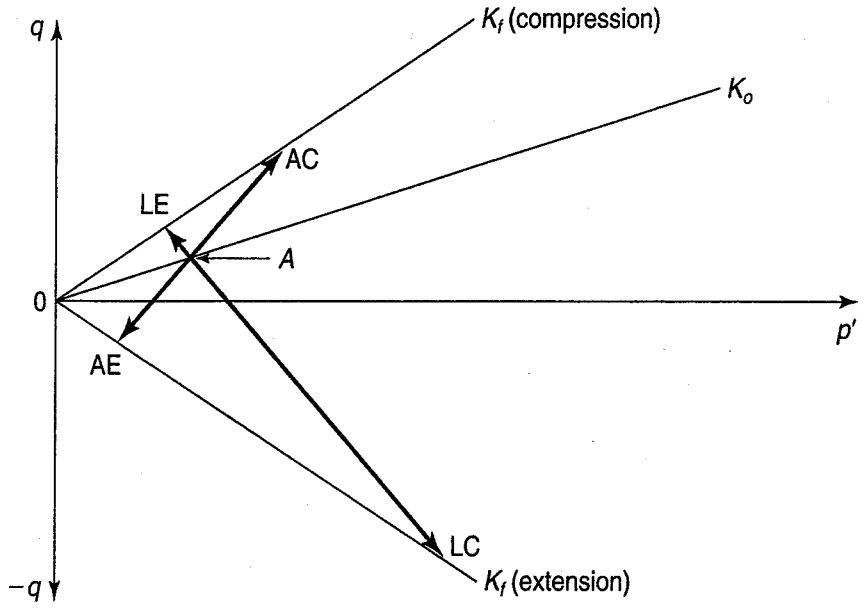

Symbol	Geotechnical engineering example
AC: Axial compression	Foundation loading – increase σ_v, σ_h constant
LE: Lateral extension	Active earth pressure – decrease σ_h, σ_v constant
AE: Axial extension	Unloading (excavation) – decrease σ_v, σ_h constant
LC: Lateral compression	Passive earth pressure – increase σ_h, σ_v constant

FIGURE 13.7 Stress paths during drained loadings on normally consolidated clays and sand (after Lambe, 1967).

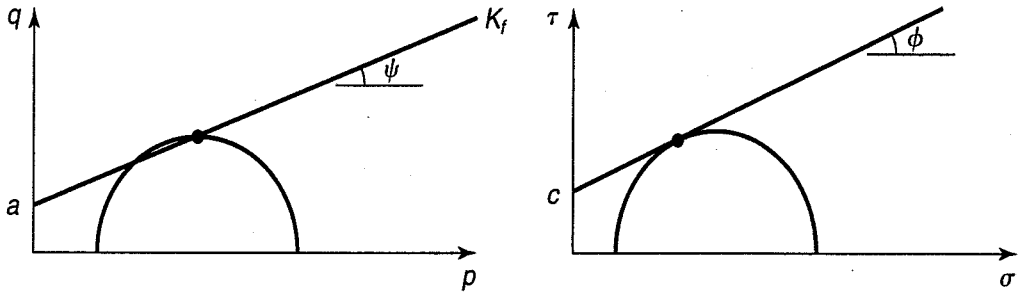

FIGURE 13.8 Relationship between the K_f line and the Mohr–Coulomb failure envelope.

From the geometries of the two circles, it can be shown that

$$\sin \phi = \tan \psi \tag{13.7}$$

and

$$c = \frac{a}{\cos \phi} \tag{13.8}$$

So, from a p–q diagram the shear-strength parameters ϕ and c may readily be computed.

Another useful aspect of the p–q diagram is that it may be used to show both total and effective stress paths on the same diagram. We said earlier that for drained loading, the total stress path (TSP) and the effective stress path (ESP) are identical (excluding any back pressure used to saturate the soil specimen; see Sec. 12.10). This is because the pore water pressure induced by loading was approximately equal to zero at all times during shear. However, in general, during *undrained* loading the TSP is not

equal to the ESP, because excess pore water pressure develops. For axial compression (AC) loading of a normally consolidated clay ($K_o < 1$), a *positive* excess pore water pressure Δu develops. Therefore the ESP lies to the *left* of the TSP because $\sigma' = \sigma - \Delta u$. At any point during the loading, the pore water pressure Δu may be scaled off any horizontal line between the TSP and ESP, as shown in Fig. 13.9.

The stress paths for the multi-stage consolidated undrained triaxial tests results presented in Example 12.12 are shown in Fig. 13.10. As in Fig. 13.9, the shapes of the effective stress paths indicate that these specimens were normally or only lightly overconsolidated.

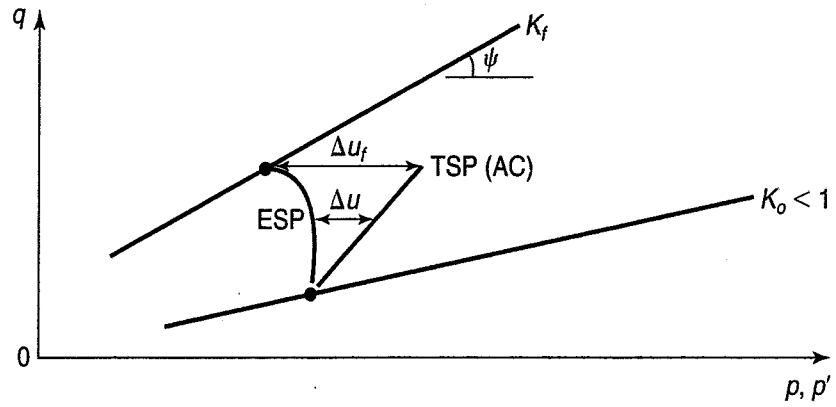

FIGURE 13.9 Stress paths during undrained axial compression loading of a normally consolidated clay.

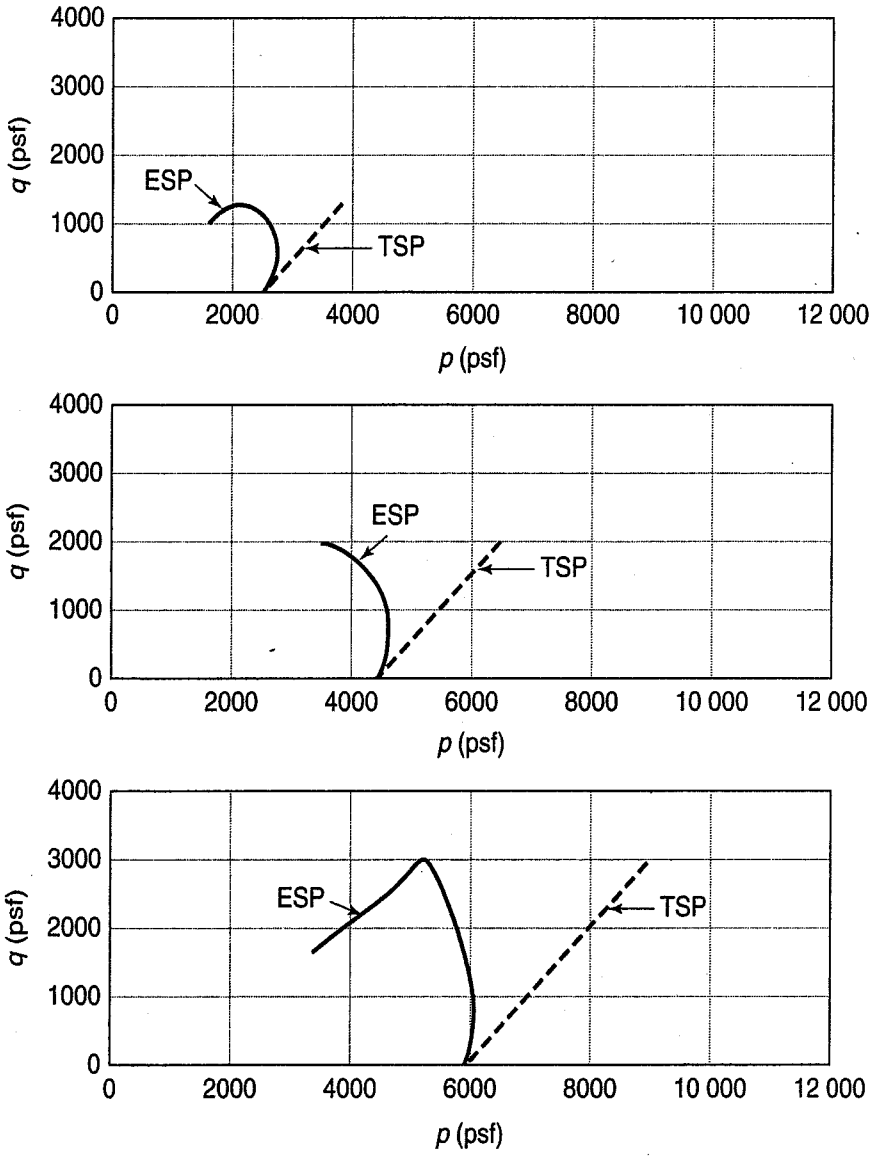

FIGURE 13.10 Stress paths from the multi-stage test results presented in Example 12.12 (courtesy Shannon & Wilson, Inc., Seattle).

Example 13.2

Given:

The results in Fig. 13.10.

Required:

Using the stress paths in Fig. 13.10, verify that the total and effective strength parameters shown in Fig. Ex. 12.12(d).

Solution: From the slope and intercept of the best-fit-by-eye K_f-lines for the effective and total stress paths, determine the parameters ψ', a', ψ and a using Eqs. (13.7) and (13.8). The results are given in Table Ex. 13.1 along with the corresponding Mohr–Coulomb strength parameters.

TABLE Ex. 13.1 Effective and Total Stress Strength Parameters

Stress Paths				Mohr–Coulomb			
ψ'(deg)	a' (psf)	ψ (deg)	a (psf)	ϕ' (deg)	c' (psf)	ϕ (deg)	c (psf)
29	88	17	100	33	100	18	100

If a clay is overconsolidated ($K_o > 1$), then *negative* pore water pressure ($-\Delta u$) develops because the clay *tends* to expand during shear, but it can't. (Remember: we are talking about undrained loading in which no volume change is allowed.) For AC loading on an overconsolidated clay, stress paths like those shown in Fig. 13.11 will develop. Similarly, we can plot total and effective stress paths for other types of loadings and unloadings, for both normally and overconsolidated soils, and we shall show some of these in Sec. 13.6.

In most practical situations in geotechnical engineering, there exists a static groundwater table; thus an initial pore water pressure u_o, is acting on the element in question. So there are really three stress paths we should consider: the ESP, the TSP, and the $(T - u_o)$SP. These three paths are shown in Fig. 13.12 for a normally consolidated clay with an initial pore water pressure u_o undergoing AC loading. Note that as long as the groundwater table remains at the same elevation, u_o does not affect either the ESP or the conditions at failure.

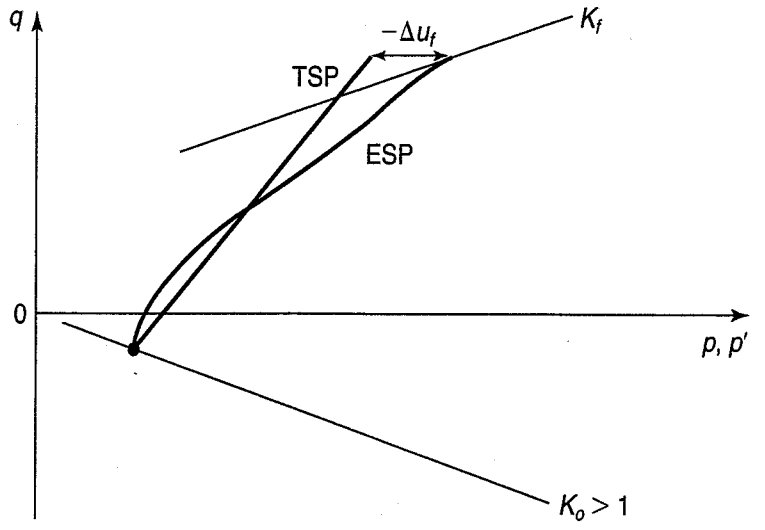

FIGURE 13.11 Stress paths during axial compression of a heavily over-consolidated clay.

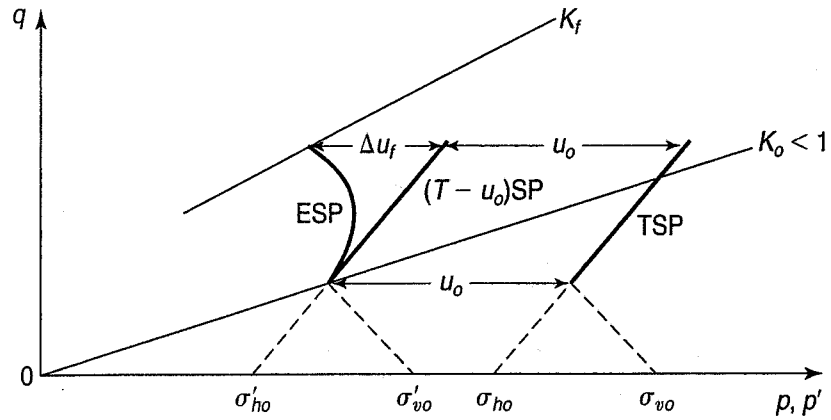

FIGURE 13.12 ESP, TSP, and $(T - u_o)$SP for a normally consolidated clay (after Lambe, 1967).

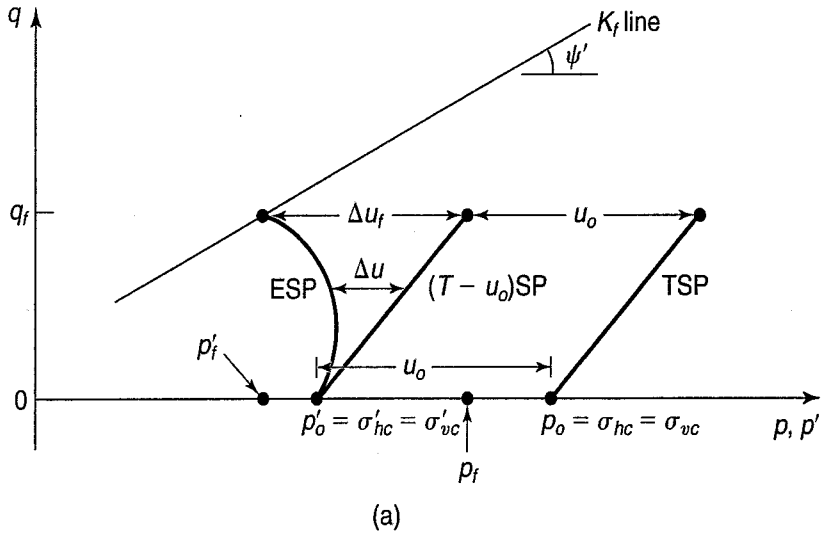

(a)

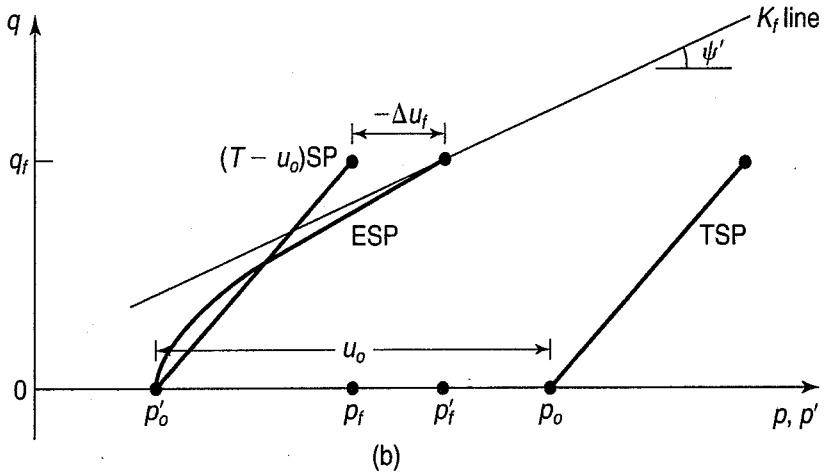

(b)

FIGURE 13.13 Stress paths for the hydrostatically consolidated axial compression tests on (a) normally consolidated clays; (b) overconsolidated clays.

In the CD triaxial test the stress paths are straight lines, since we usually keep one of the stresses constant and simply vary the other. Typical drained stress paths are shown in Fig. 13.7 for four common engineering situations that can be modeled in the triaxial test. The stress path for the axial compression test illustrated in Fig. 12.22 is the straight line *AC* in Fig. 13.7.

Stress paths for the two CU tests of Fig. 12.32 are shown in Fig. 13.13. The tests are quite conventional, hydrostatically consolidated, axial compression tests. Let's look first at Fig. 13.13(a), the stress paths for the test on normally consolidated clay. Three stress paths are shown: the effective stress path (ESP), the total stress path (TSP), and the total-u_o stress path, $(T - u_o)$SP. Because the test is

hydrostatically consolidated, the paths begin on the hydrostatic axis at values of p equal to the total and effective consolidation pressures, respectively. Note that $p = p' + u_o$. The total stress path for axial compression and constant cell pressure is the straight line inclined at 45° as shown. Since positive pore pressures develop in the normally consolidated clay, the ESP lies to the *left* of the TSP, because $\sigma' = \sigma - \Delta u$. The situation is directly analogous to that shown in Fig. 13.9. Note that q_f is the same for all three stress paths, because we define the failure at the maximum $(\sigma_1 - \sigma_3)$. Figure 13.13(a) is similar to Fig. 13.9, except the initial consolidation in that case was nonhydrostatic $(K_o < 1)$.

Since the overconsolidated clay was tested in axial compression with a constant hydrostatic cell pressure, the two total stress paths of Fig. 13.13(b) are exactly like those of Fig. 13.13(a)—straight lines inclined at 45° to the hydrostatic axis. But the shape of the ESP is significantly different. Look back at the development of pore pressure with axial strain for this test in Fig. 12.28. See how it starts out slightly positive, then goes way negative (actually, less than u_o, as explained previously). The same thing happens to the ESP in Fig. 13.13(b). It goes slightly to the left $(+\Delta u)$ of the $(T - u_o)$SP at first; then, as the pore pressure becomes increasingly negative, the ESP crosses the $(T - u_o)$SP until maximum q or q_f is reached. Again, because of the way we define failure, q_f is the same for all three stress paths. You may recall that the ESP in Fig. 13.13(b) for the overconsolidated clay has a shape similar to that shown in Fig. 13.11, except that the latter sample was consolidated with $K_o < 1$.

Stress paths for the UU tests of Fig. 12.39 are shown in Fig. 13.14. Behavior is for a normally consolidated clay, and the values of p and q for all three tests are listed in the table below the figure. Refer

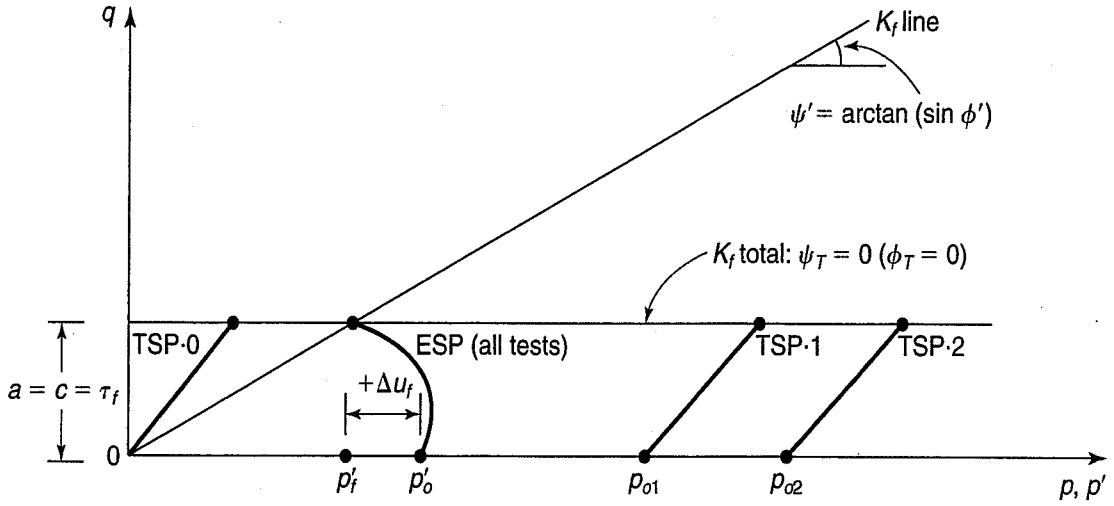

		Initial conditions		At failure	
	Test	p_o	q_o	p_f	q_f
Total stresses	0	0	0	$\frac{\Delta\sigma_f}{2}$	$\frac{\Delta\sigma_f}{2}$
	1	σ_{c1}	0	$\frac{\Delta\sigma_f + 2\sigma_{c1}}{2}$	$\frac{\Delta\sigma_f}{2}$
	2	σ_{c2}	0	$\frac{\Delta\sigma_f + 2\sigma_{c2}}{2}$	$\frac{\Delta\sigma_f}{2}$
Effective stresses		p'_o	q_o	p'_f	q_f
	All	u_r	0	$\frac{\Delta\sigma_f + 2u_r - 2\Delta u_f}{2}$	$\frac{\Delta\sigma_f}{2}$

FIGURE 13.14 Stress paths for UU tests on a normally consolidated clay. Same tests as in Fig. 12.39.

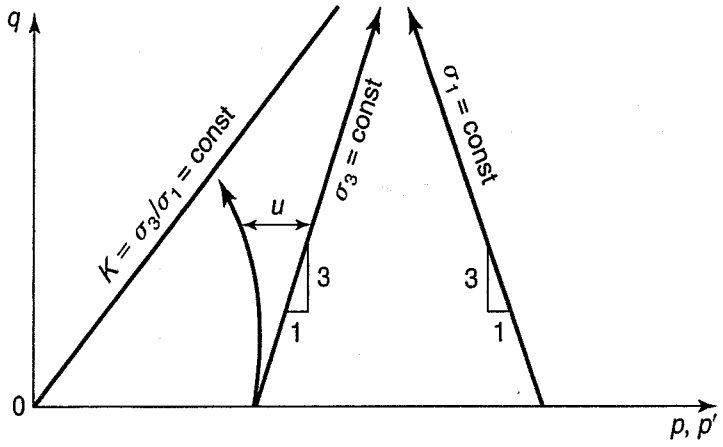

FIGURE 13.15 Cambridge stress paths for (1) a conventional CU triaxial test with the cell pressure σ_3 constant and (2) LE CD test with σ_1 constant.

to Fig. 12.39 if necessary to verify these values. If the clay were overconsolidated, then from your knowledge of CU behavior you would expect the ESP to have a shape similar to those of Fig. 13.12(b).

At the beginning of this section we mentioned that there are several ways of representing stress paths in geotechnical engineering. *Vector curves* were developed at Harvard by Prof. Casagrande and his associates (e.g., Hirschfeld, 1963). They defined the vector curve as the state of stress on the potential failure plane, but this was not very practical unless you already knew the friction angle of the soil (see Sec. 11.4.2). Later, for convenience they plotted vector curves assuming the angle of the failure plane α_f was 60°, which automatically assumed a friction angle of 30° [Eq. (11.10)]. Although Lambe's stress point and stress paths are a simplification of the vector curve concept, *MIT stress paths* with $p' = \frac{1}{2}(\sigma'_v + \sigma'_h)$ are very useful in practice, as we will see in the next few sections.

Another stress path common in critical-state soil mechanics (Sec. 13.7) is the *Cambridge stress path*. The differences are that: q is the principal stress difference, or $q = (\sigma_1 - \sigma_3)$, instead of $\frac{1}{2}(\sigma_1 - \sigma_3)$ as in the MIT system; and the Cambridge stress path has a 3-D definition of the mean effective stress, or $p' = (\sigma'_1 + 2\sigma'_3)/3$. The Cambridge stress paths will have a different shape than the MIT paths, as shown in Fig. 13.15. For example, the total stress path (TSP) for a conventional CU triaxial test with the cell pressure σ_3 constant has a slope of 3V:1H instead of 1:1 as in the conventional MIT case. The ESP is typical for a NC clay, although it is not as curved as a MIT stress path plot. Also shown in Fig. 13.15 is the stress path for an LE CD test with σ_1 constant. Instead of a 1:1 slope, it has a negative inclination of 3V:1H.

13.3 PORE PRESSURE PARAMETERS FOR DIFFERENT STRESS PATHS

In Sec. 12.17, we introduced the Skempton pore pressure parameters A and B and described how they are used in laboratory testing and in geotechnical practice. We also mentioned that the common Skempton equation

$$\Delta u = B[\Delta\sigma_3 + A(\Delta\sigma_1 - \Delta\sigma_3)] \tag{12.18}$$

was derived for conventional triaxial compression conditions. But, as in shown in Appendix B.3, it is also true for triaxial extension. You recall that in triaxial extension the principal stresses have rotated 90°, because now $\sigma_1 = \sigma_2$. The following discussion explains the reason that, although the definition is the same for both triaxial compression and extension conditions, the specific value of A is different and dependent on the stress path. The common triaxial stress paths are shown in Fig. 13.7 and discussed in detail in Secs. 13.4 and 13.5.

As shown by Law and Holtz (1978) and in Appendix B.3, where rotation of principal stresses occurs, it is better to define the pore pressure parameter A in terms of principal stress increments which are independent of the initial stress system. If this is done, then the equations for A for each of the common triaxial stress paths are

$$A_{ac} = \frac{\Delta u}{\Delta \sigma_v} \tag{13.9}$$

$$A_{le} = 1 - \frac{\Delta u}{\Delta \sigma_h} \tag{13.10}$$

$$A_{ae} = 1 - \frac{\Delta u}{\Delta \sigma_v} \tag{13.11}$$

$$A_{lc} = \frac{\Delta u}{\Delta \sigma_h} \tag{13.12}$$

It is also shown in Appendix B.3 that

$$A_{ac} = A_{le} \tag{13.13}$$

and

$$A_{ae} = A_{lc} \tag{13.14}$$

You will find these equations useful in understanding stress paths during undrained loading (Secs. 13.4 and 13.5) and for the problems at the end of this chapter.

A more general pore pressure equation was proposed by Henkel (1960) to take into account the effect of the intermediate principal stress. It is

$$\Delta u = B(\Delta \sigma_{oct} + a \Delta \tau_{oct}) \tag{13.15}$$

where

$$\sigma_{oct} = \tfrac{1}{3}(\sigma_1 + \sigma_2 + \sigma_3) \tag{13.16}$$

$$\tau_{oct} = \tfrac{1}{3}\sqrt{(\sigma_1 - \sigma_2)^2 + (\sigma_2 - \sigma_3)^2 + (\sigma_3 - \sigma_1)^2} \tag{13.17}$$

and a is the *Henkel pore pressure parameter*. Sometimes the Henkel parameter is denoted by the symbol α, and sometimes $a = 3\,\alpha$. Equation (13.15) is derived in Appendix B.3. As pointed out by Perloff and Baron (1976), because τ_{oct} is not linearly related to stress, you cannot in general calculate $\Delta \tau_{oct}$ directly from the principal stress increments. Instead, you have to determine the initial and final stresses, substitute them into Eq. (13.17) to get the initial and final values of τ_{oct}, and then calculate $\Delta \tau_{oct}$.

The equations for getting the equivalent Skempton A from Henkel's a parameter for triaxial compression and extension conditions are developed in Appendix B.3. These relationships are for triaxial compression (AC and LE) conditions

$$A = \frac{1}{3} + a\frac{\sqrt{2}}{3} \tag{13.18}$$

For triaxial extension (AE and LC) conditions

$$A = \frac{2}{3} + a\frac{\sqrt{2}}{3} \tag{13.19}$$

These equations mean, of course, that $a = 0$ for elastic materials (since $A = 1/3$ in triaxial compression and $2/3$ in triaxial extension).

If you have some idea of what the intermediate principal stress is in the field, then you probably should use Eqs. (13.15) through (13.17) to estimate the in situ pore pressures. It is not easy to predict the field pore pressures from laboratory test results, primarily because the pore pressure parameters are very sensitive to sample disturbance. Höeg et al. (1969), D'Appolonia et al. (1971), and Leroueil et al. (1978a and b) provide methods for estimating pore pressures under embankments on soft clays.

13.4 STRESS PATHS DURING UNDRAINED LOADING—NORMALLY AND LIGHTLY OVERCONSOLIDATED CLAYS

We show examples of stress paths for undrained loading of normally consolidated clays in Figs. 13.9, 13.12, 13.13(a), and 13.14. These stress paths also apply to clay soils that are lightly overconsolidated, probably with an OCR < 2 or so. When the OCR in a natural deposit is greater than 3 or 4, it starts to behave more like an overconsolidated clay. Natural clay deposits, unless they are very recent, are rarely truly normally consolidated, and in this chapter, when we discuss normally consolidated properties and behavior, we include lightly overconsolidated deposits in that category.

Undrained stress paths for overconsolidated clays are shown in Figs. 13.11 and 13.13(b). From our comments concerning those figures you should now understand why these stress paths have the shapes they do. The stress paths we showed for undrained shear were for the most common type of triaxial test used in engineering practice, the axial compression (AC) test. Most of the time, the initial consolidation stresses are *hydrostatic* ($K_o = 1$) because laboratory procedures are simpler. However, a better model for in situ stress conditions would be *nonhydrostatic* consolidation; that is, the axial stress would be different than the cell pressure ($K_o \neq 1$). As we mentioned in Sec. 13.2, there are stress paths other than axial compression that model real engineering design situations. Some of these are shown in Fig. 13.16, along with their laboratory model. Axial compression (AC) models foundation loading such as from an embankment or footing. Lateral extension (LE) models the active earth pressure conditions behind retaining walls. Axial extension (AE) models unloading situations like excavations, and lateral compression (LC) models passive earth pressure conditions such as might occur around an earth anchor or in pipe-jacking applications.

If you think about it, the ordinary triaxial test is not the best model for the design conditions illustrated in Fig. 13.16. It would be all right for cases (a) and (c) if the foundation or excavation were circular (for example, an oil tank, underground shaft, or nuclear reactor pit). The more usual case is where one dimension (perpendicular to the page in Fig. 13.16) is very long compared to the others. This is the case for *plane strain*. Examples are long embankments, strip footings, and long retaining walls. In these cases, strictly speaking, the shear strengths should be determined by using plane strain tests [Fig. 13.16(b)]. The laboratory models on the right side of Fig. 13.16 can also apply to stress conditions in this test just as well as in the triaxial test. Since the plane strain test is more complicated in several respects than the triaxial test, it is rarely used in engineering practice. Triaxial strengths are still commonly obtained for design problems that are obviously plane strain.

It is important that you know how to make the computations necessary to plot undrained stress paths; the procedures for doing so are illustrated by the following examples.

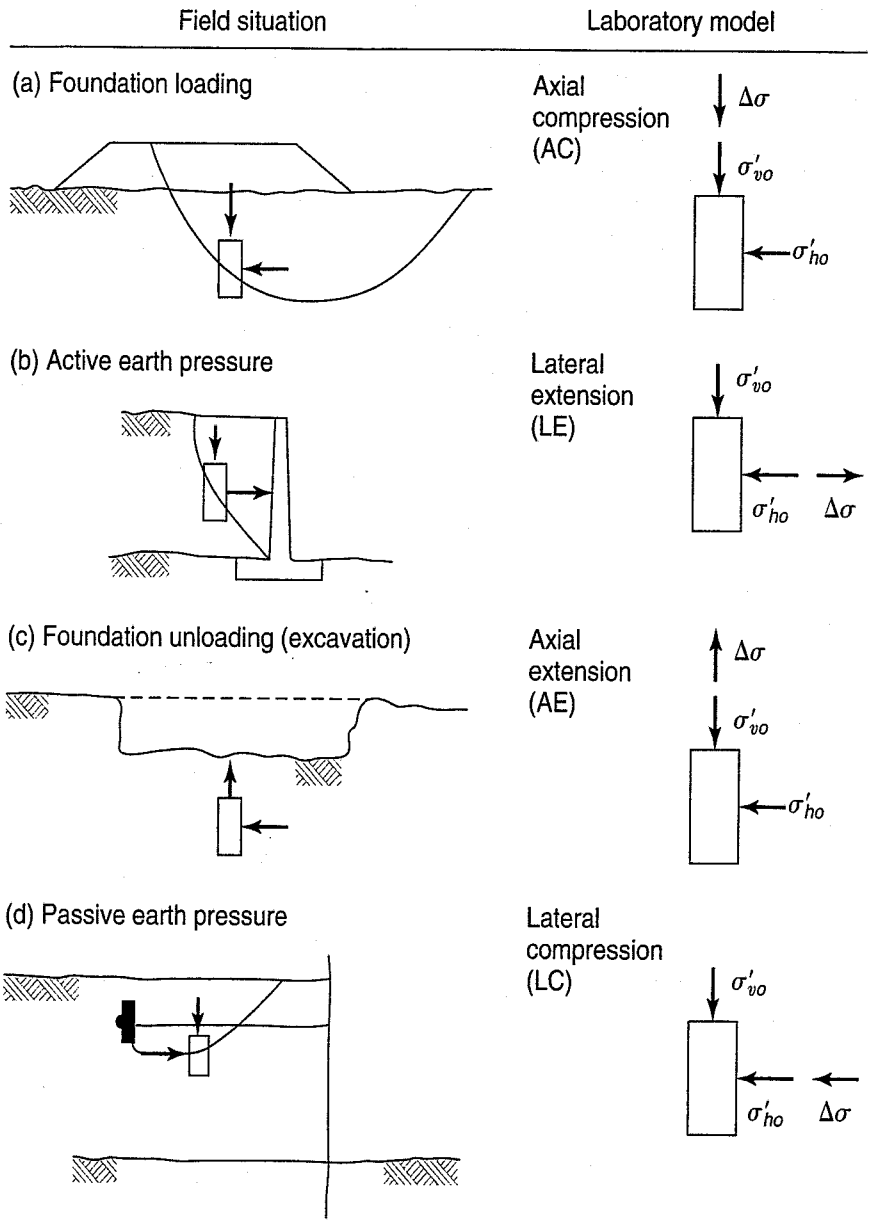

FIGURE 13.16 Some common field stability situations along with their laboratory model.

Example 13.3

Given:

The $\sigma-\varepsilon$ and $u-\varepsilon$ data of Fig. Ex. 13.3a were recorded when the normally consolidated clay of Example 12.9 was tested in axial compression.

Required:

Draw the total and effective stress paths for this test. Determine the Mohr–Coulomb strength parameters.

Solution: Using Eqs. (13.1) and (13.2), we have to determine p, p' and q for several strains in order to plot the stress paths. Usually five or six points are sufficient. Sometimes, to keep things in order, a

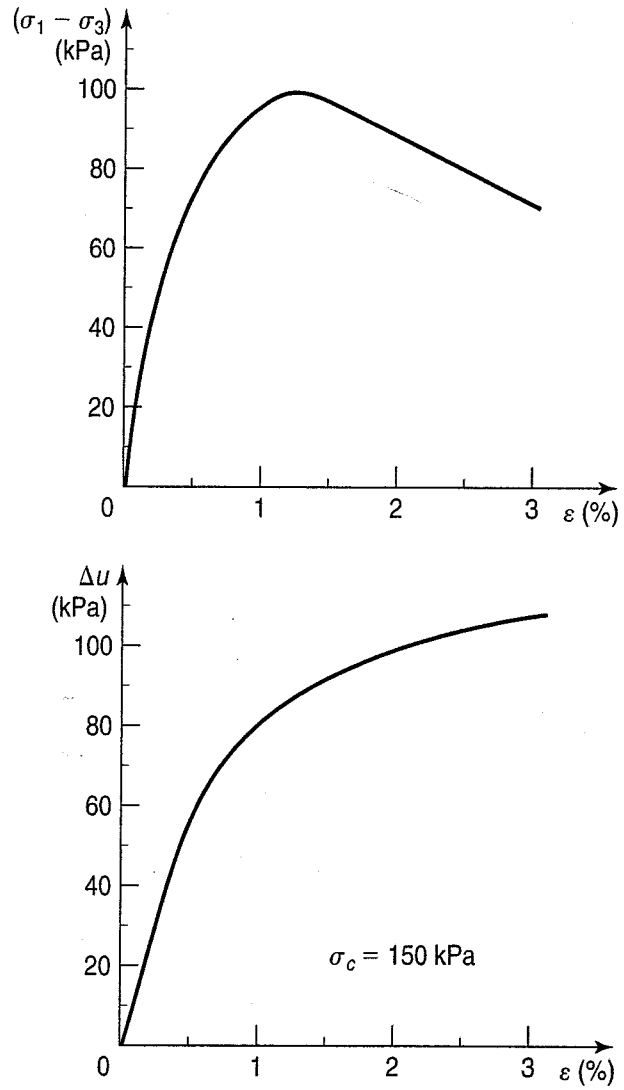

FIGURE Ex. 13.3a

table is helpful. Then just fill in the appropriate columns. It may also be helpful to know that

$$\sigma_1 + \sigma_3 = (\sigma_1 - \sigma_3) + 2\sigma_3 \qquad (13.20)$$

and

$$\frac{\sigma_1 + \sigma_3}{2} = \frac{\sigma_1 - \sigma_3}{2} + \sigma_3 \qquad (13.21)$$

Also, since $\sigma' = \sigma - u$, $p' = p - u$. And finally,

$$\frac{\sigma_1' + \sigma_3'}{2} = \frac{\sigma_1 - \sigma_3}{2} + \sigma_3' \qquad (13.22)$$

because $(\sigma_1' - \sigma_3') = (\sigma_1 - \sigma_3)$.

Now just choose the values of $(\sigma_1 - \sigma_3)$ and Δu at several convenient strains, and fill in the table (Table Ex. 13.3) by using the above equations. Note that σ_3 in Example 12.9 was 150 kPa.

Total and effective stress paths are shown in Fig. Ex. 13.3b. The failure lines are also drawn, assuming $a' = a = 0$.

From Eq. (13.7)

$$\psi' = 24.1°, \quad \text{then } \phi' = 26.6°$$

and

$$\psi_T = 14.1°, \quad \text{so } \phi_T = 14.5°$$

Note that the problem could be solved graphically by plotting the TSP first, then scaling off the corresponding Δu values horizontally to the *left* of the TSP; one point done this way is shown in Fig. Ex. 13.3b.

TABLE Ex. 13.3

	ε (%)	$\sigma_1 - \sigma_3$ (kPa)	Δu (kPa)	σ_3' (kPa)	$q = \frac{\sigma_1 - \sigma_3}{2}$ (kPa)	$p = \frac{\sigma_1 + \sigma_3}{2}$ (kPa)	$p' = \frac{\sigma_1' + \sigma_3'}{2}$ (kPa)
	0.25	49	35	115	25	175	140
	0.50	73	57	93	37	187	130
	0.75	86	72	78	43	193	121
	1	94	80	68	47	197	115
Failure	1 1/4	100	88	62	50	200	112
	1 1/2	96	92	58	48	198	106
	2	89	99	51	45	195	96

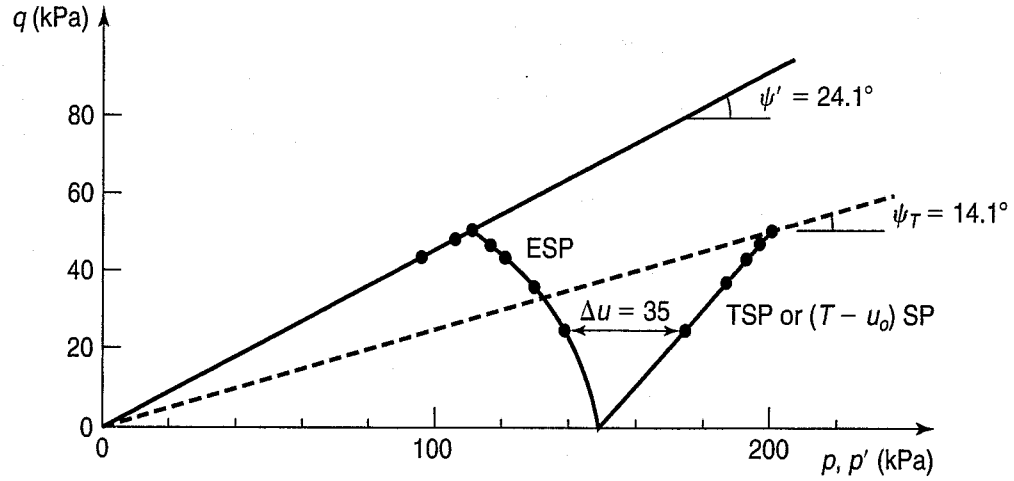

FIGURE Ex. 13.3b

Example 13.4

Given:

A long embankment shown in Fig. Ex. 13.4a is to be constructed rapidly on a deposit of soft organic silty clay in northern Sweden. The soil profile and properties are also shown in Fig. Ex. 13.4a. Assume $K_o = 0.6$. Also assume A before failure is about 0.35; at failure, $A_f = 0.5$ (after Holtz and Holm, 1979).

Required:

Determine the TSP, (T − u_o)SP, and ESP for a typical element 5 m below the centerline of the embankment.

Solution: First, calculate the initial stress conditions for the element. Use Eqs. (6.13), (6.14), and (6.15).

$$\sigma_{vo} = 1.24(9.81)(1) + 1.30(9.81)(4) = 63 \text{ kPa}$$
$$u_o = 1.0(9.81)(4) = 39 \text{ kPa}$$

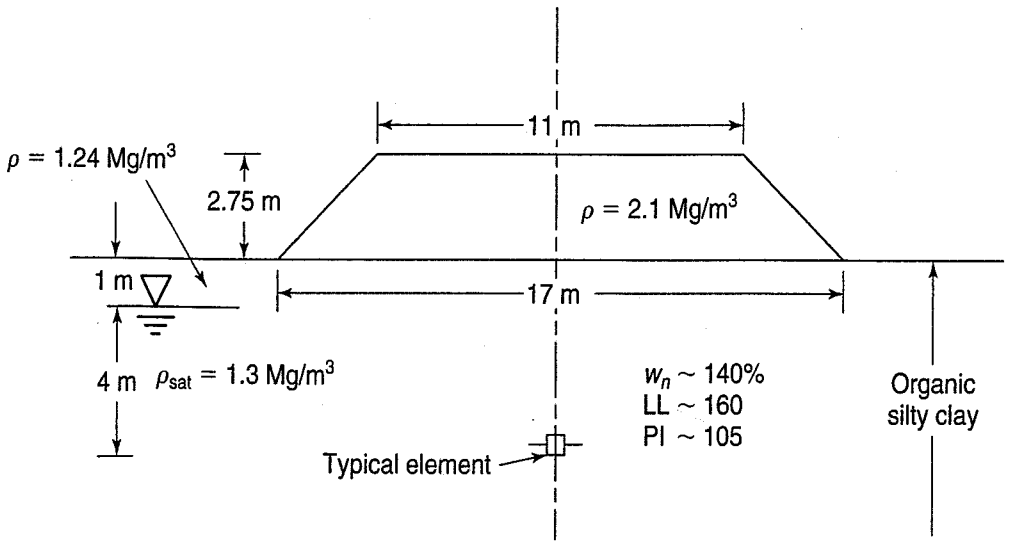

FIGURE Ex. 13.4a

$$\sigma'_{vo} = \sigma_{vo} - u_o \qquad = 24 \text{ kPa}$$
$$\sigma'_{ho} = 0.6\sigma'_{vo} (K = 0.6) = 14 \text{ kPa}$$
$$\sigma_{ho} = \sigma'_{ho} + u_o \qquad = 53 \text{ kPa}$$

Second, calculate the $\Delta\sigma$ due to the embankment.

$$\Delta\sigma \text{ at the surface} = 2.1(9.81)(2.75) = 57 \text{ kPa}$$

σ_z at −5 m; use Fig. 10.6,

$$I = 0.45 \times 2 = 0.9$$
$$\sigma_z = 0.9 \times 57 = 51 \text{ kPa}$$

This is $\Delta\sigma_v$ on the typical element.

To determine the increase in horizontal stress $\Delta\sigma_h$, equations and some charts are available for a limited number of geometries (see, for example, Poulos and Davis, 1974). For this example, let's assume the increase in horizontal stress is one-third of the increase in vertical stress.

$$\Delta\sigma_h = 0.33(51) = 17 \text{ kPa}$$

Next, use Eqs. (13.1) and (13.2) to determine q, p, and p' for both initial and final conditions. Don't forget the conditions for the $(T - u_o)SP$. To get the final effective stresses, we need to estimate the induced pore pressures. Use the pore pressure parameter information given. Assume initially that the soil is not stressed to failure, so $A = 0.35$. $B = 1$ below the water table. Use Eq. (12.19).

$$\Delta u = \Delta\sigma_3 + A(\Delta\sigma_1 - \Delta\sigma_3) = 17 + 0.35(51 - 17) = 29 \text{ kPa}$$

If the embankment were overstressing the underlying soil, then the induced Δu would be 34 kPa (because $A_f = 0.5$).

It is sometimes helpful when calculating stress paths to draw elements with the appropriate total, total $- u_o$, pore pressure, and effective stresses indicated (similar to Fig. 12.27). This technique is shown in Fig. Ex. 13.4b both for initial conditions and after loading. Note that stresses on the elements for initial

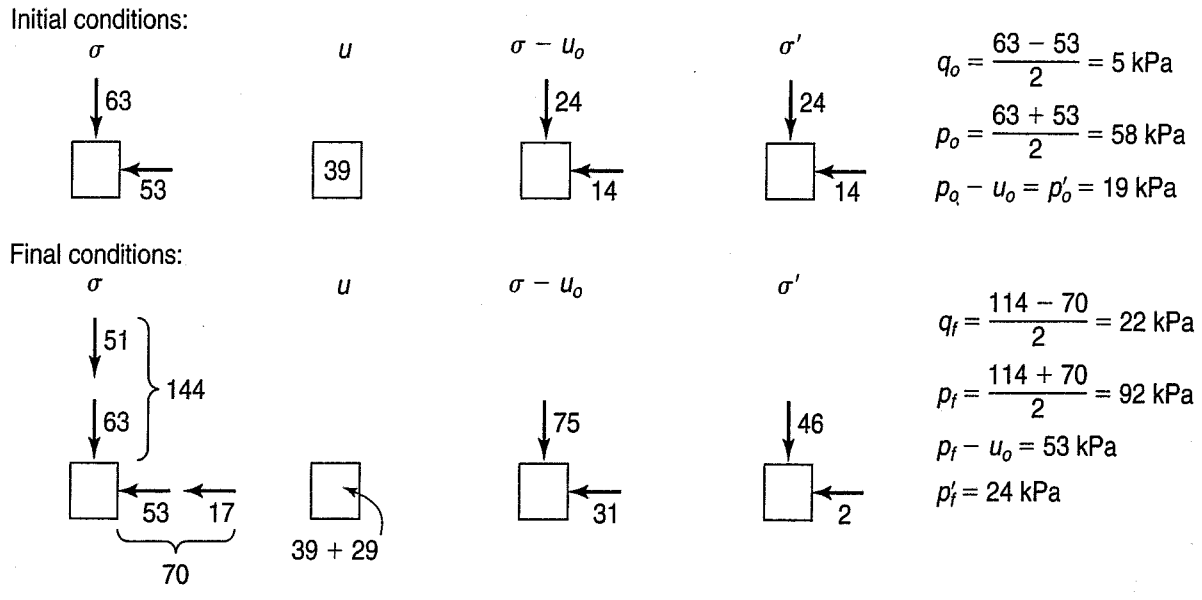

FIGURE Ex. 13.4b

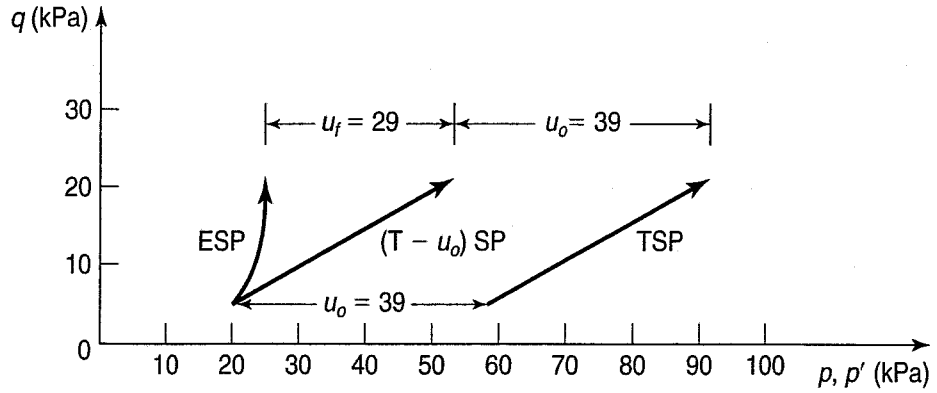

FIGURE Ex. 13.4c

conditions are those we calculated at the beginning of this example. For final stresses, the vertical total stress increased by 51 kPa and the horizontal total stress increased by 17 kPa, as we determined previously from elastic theory. The induced pore pressures shown are those we found from the pore pressure equation. The calculations for p, p', and q for both initial and final conditions are shown below the elements.

Finally, plot the stress paths on the p–q diagram, as shown in Fig. Ex. 13.4c. Sketch the ESP so it has a shape similar to those shown previously [for example, Figs. 13.13 and 13.14(a)] for normally consolidated clays.

Example 13.5

Given:

The initial stress conditions and stress changes from Example 13.4.

Required:

Estimate the induced pore water pressure using the Henkel pore pressure parameters.

Solution: Recall from Sec. 13.3 that the Henkel pore pressure equation is

$$\Delta u = B(\Delta\sigma_{oct} + a\,\Delta\tau_{oct}) \tag{13.15}$$

where σ_{oct} and τ_{oct} were defined in Eqs. (13.16) and (13.17). To obtain $\Delta\sigma_{oct}$ and $\Delta\tau_{oct}$, we need the three initial and three final stresses so we can determine the initial and final values of σ_{oct} and τ_{oct}. One way to do this is to use Fig. Ex. 13.4b and simply assume that $\sigma_h = \sigma_2 = \sigma_3$. Determining $\Delta\sigma_{oct}$ is easy, because $\Delta\sigma_{oct} = (\sigma_{oct})_{initial} - (\sigma_{oct})_{final} = \frac{1}{3}(\Delta\sigma_1 + \Delta\sigma_2 + \Delta\sigma_3)$, but as we mentioned in Sec. 13.3, you cannot do the same thing with $\Delta\tau_{oct}$. To get $\Delta\tau_{oct}$ you have to use the initial and final stresses, substitute them into Eq. (13.17) to get the initial and final values of τ_{oct}, and then calculate $\Delta\tau_{oct}$.

From Fig. Ex. 13.4b, $\Delta\sigma_{oct} = (\sigma_{oct})_{final} - (\sigma_{oct})_{initial} = \frac{1}{3}(114 + 70 + 70) - \frac{1}{3}(63 + 53 + 53) = 28$ kPa.

For $\Delta\tau_{oct} = (\tau_{oct})_{final} - (\tau_{oct})_{initial}$

$$(\tau_{oct})_{final} = \frac{1}{3}\sqrt{(114 - 70)^2 + (70 - 70)^2 + (70 - 114)^2} = 21$$

$$(\tau_{oct})_{initial} = \frac{1}{3}\sqrt{(63 - 53)^2 + (53 - 53)^2 + (53 - 63)^2} = 5$$

So $\Delta\tau_{oct} = 16$ kPa.

Next we need to find the Henkel parameter a. From Eq. (13.18),

$$A = \frac{1}{3} + a\frac{\sqrt{2}}{3}$$

Since $A = 0.35$ before failure, Henkel's $a = 0.035$. So $\Delta u = [(28\text{ kPa} + 0.035(16\text{ kPa})] = 29\text{ kPa}$.

It is interesting that in this example, if you substitute the individual stress increments into Eq. (13.17), you also get the same numerical value of $\Delta\tau_{oct} = 16$ kPa. This is because in this example we assumed $\sigma_h = \sigma_2 = \sigma_3$. In general, $\sigma_2 \neq \sigma_3$, and you must calculate the final and initial values separately and then subtract to obtain a correct value of $\Delta\tau_{oct}$.

The next example is a little more complicated. First, we shall construct the stress paths and determine the strength parameters for an axial compression test; then we use the AC test and our knowledge of stress paths to determine the pore pressure response of a lateral extension test. We will see that the effective stress paths for both tests are identical, even though the total stress paths are very different.

Example 13.6

Given:

Two identical specimens (same w, e, etc.) of a normally consolidated saturated clay were hydrostatically consolidated ($K_o = 1$) and then sheared undrained. In test A, the axial compression (AC) test, the cell pressure was held constant while the axial stress was increased until failure. Specimen B was failed by lateral extension (LE) in which the vertical stress was held constant while the cell pressure was decreased until failure occurred. Stress-strain and pore pressure data for test A are shown in Table Ex. 13.6a.

Required:

a. Compute and plot the stress-strain and pore pressure-strain curves for test A.
b. Plot the TSP and ESP for both tests.
c. Determine ϕ' and ϕ_T for both tests.
d. Show that the stress-strain curve for test A (AC) is identical to that for test B (LE).
e. Evaluate the pore pressure-strain data for test B from the LE stress paths.
f. Compute the pore pressure parameter $\overline{A}$ for both tests.

TABLE Ex. 13.6a Test A (AC Test Data)

ε (%)	$\Delta\sigma/\sigma_c'$	$\Delta u/\sigma_c'$
0	0	0
1	0.35	0.19
2	0.45	0.29
4	0.52	0.41
6	0.54	0.47
8	0.56	0.51
10	0.57	0.53
12	0.58	0.55

After Ladd (1964).

Solution:

a. Plot $\sigma-\varepsilon$ and $\Delta u-\varepsilon$ curves for test A (AC), as shown in Fig. Ex. 13.6a. Note that the data in Table Ex. 13.6a is normalized with respect to the effective consolidation stress σ_c' in the test. We could assume a σ_c' (in whatever units the test was conducted), or we can work everything out in terms of the normalized stresses.

b. As for the previous example, it is helpful to sketch elements showing the total, pore pressure, and effective stresses for the initial consolidation conditions, during shear, and at failure, as is done in Fig. Ex. 13.6b. Use these stresses to compute the TSP for both tests and the ESP for the AC test. Since at this time we don't know anything about the pore pressures developed in the LE test, we cannot plot its ESP.

Calculations for p, p', and q for test A (AC):

Initial conditions:

$$p_o = p_o' = \frac{1+1}{2} = 1 \quad \text{and} \quad q_o = \frac{1-1}{2} = 0$$

At failure:

$$p_f = \frac{1.58+1}{2} = 1.29 \quad \text{and} \quad p_f' = p_f - \Delta u = 0.74$$

$$\left(\text{Check: } p_f' = \frac{1.03+0.45}{2} = 0.74\right)$$

$$q_f = \frac{1.58-1}{2} = 0.29$$

$$\left(\text{Check: } \frac{1.03-0.45}{2} = 0.29\right)$$

For Test B (LE):

$$p_o = p_o' = \frac{1+1}{2} = 1 \quad \text{and} \quad q_o = \frac{1-1}{2} = 0$$

$$p_f = \frac{1+0.42}{2} = 0.71 \quad \text{and} \quad q_f = \frac{1-0.42}{2} = 0.29$$

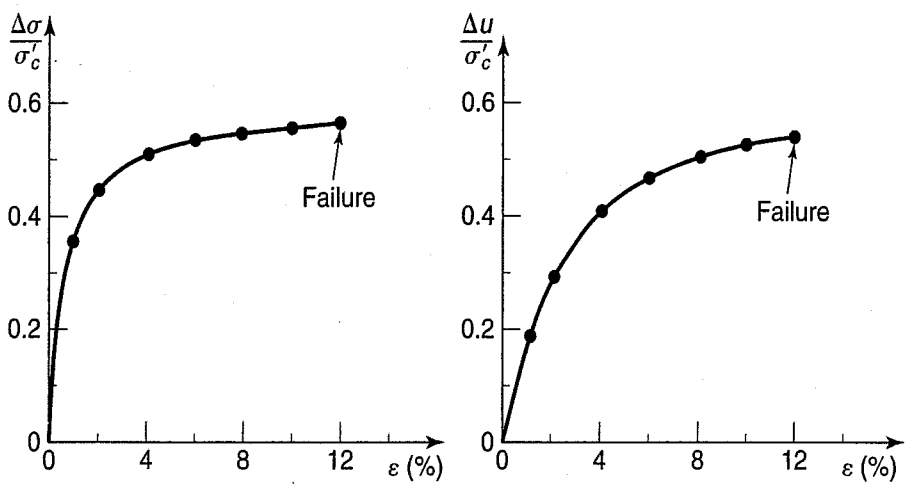

FIGURE Ex. 13.6a Stress-strain and pore pressure-strain curves for the AC test.

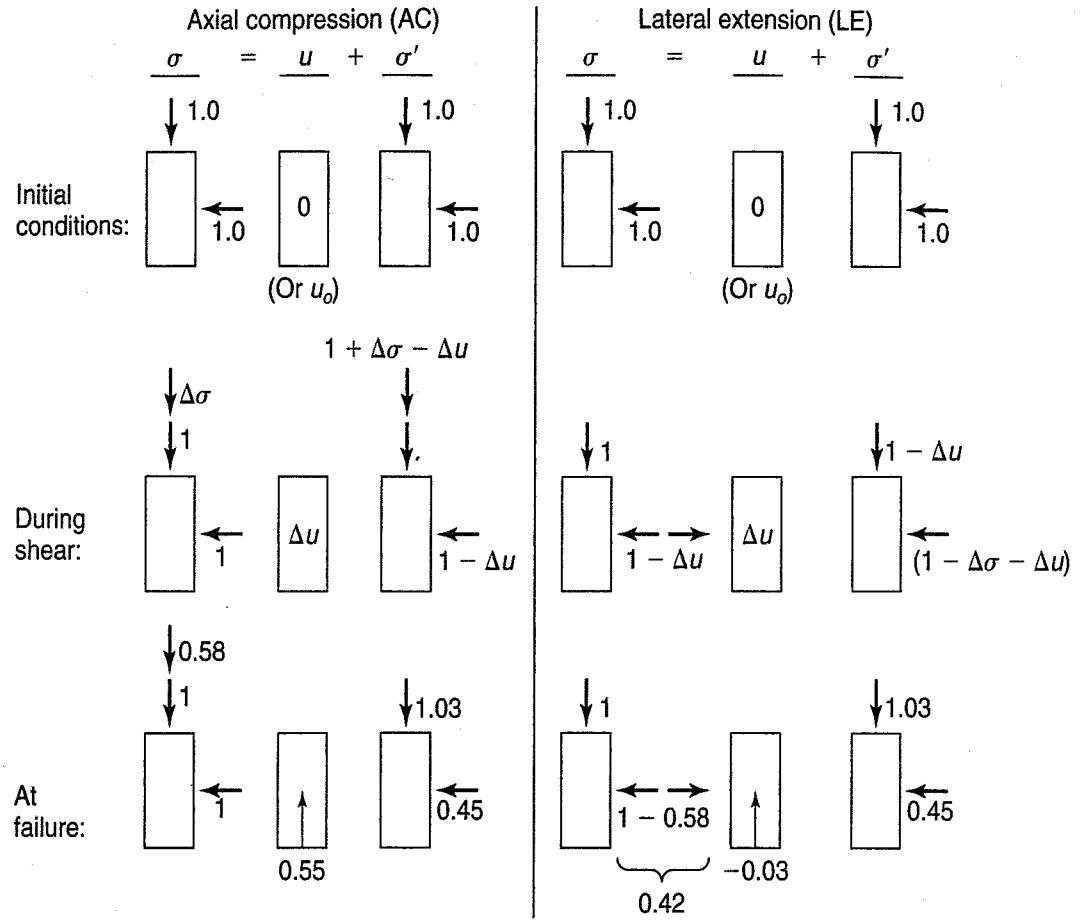

FIGURE Ex. 13.6b Total, pore pressure, and effective stress conditions for the AC and LE tests.

Now plot the TSP's for both test A (AC) and test B (LE). We know that the TSP's will be straight lines inclined at 45° from the stress conditions in both tests, since one of the principal stresses remains constant during the test. Therefore we need only calculate and plot the end points q_o, p_o, and q_f on Fig. Ex. 13.6c, and connect these points with straight lines.

Intermediate points for both the TSP and ESP may be calculated from the stress-strain and pore pressure-strain information of Table Ex. 13.6a and Fig. Ex. 13.6a. This process is exactly like

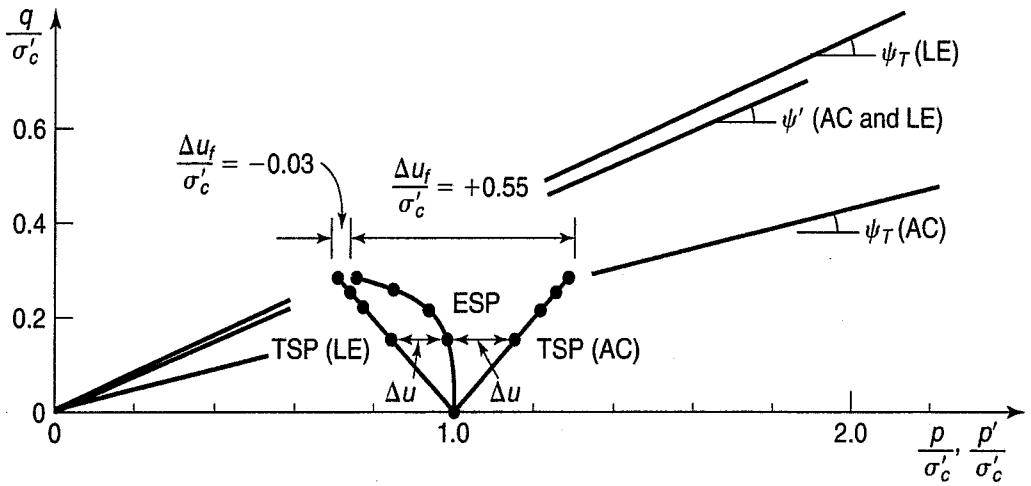

FIGURE Ex. 13.6c Stress paths for the AC and LE tests.

that shown in Example 13.3. Usually it is easier to do the problem graphically by simply plotting the intermediate q values on the TSP ($q = \Delta\sigma/2$) at several conveniently spaced strains. This determines the intermediate p values. Then, scale off the Δu values horizontally to determine the intermediate p' values at these same strains. This process, shown in Fig. Ex. 13.3b and Fig. Ex. 13.6c, determines the corresponding ESP.

Note that only one ESP is shown for *both* tests. This is because the effective stress conditions in both tests are the same. Why? Note that during shear the stress difference $\Delta\sigma$, which is equal to $(\sigma_1 - \sigma_3)$, is the same for both tests. Looking at it another way:

For the AC test,

$$\Delta\sigma_{AC} = 1 + \Delta\sigma - 1 = \Delta\sigma$$

For the LE test,

$$\Delta\sigma_{LE} = 1 - 1 + \Delta\sigma = \Delta\sigma$$

Therefore at every strain (including at failure) $\Delta\sigma_{AC} = \Delta\sigma_{LE}$. Thus the stress-strain curves for both tests must be the *same*. So, if we plotted the LE stress-strain curve, it would look exactly like the AC curve shown in Fig. Ex. 13.6a. (By the way, this is the answer to part **d.**)

If the two specimens have exactly the same stress-strain curve and identical strengths, then the effective stress conditions in the specimens must be identical, both at failure and during loading. This means that the ESP's must also be the same.

Another way of looking at this is that in the LE test, the change in stress difference $\Delta\sigma$ is produced by a change, a decrease, in cell or hydrostatic pressure. When the hydrostatic pressure changes in an undrained test, only a change in pore pressure results, not a change in effective stresses. If there is no change in effective stresses, then the stress-strain and strength behavior must be the same (Hirschfeld, 1963). The only difference at failure between the tests must be in the amount of pore pressure Δu that develops. If this is true at failure, then it is also true throughout the test. Therefore we can construct the pore pressure-strain curve [part **e** of this example] for the test B (LE) from the stress path plots.

As with test A (AC) the amount of pore pressure developed in test B (LE) is simply the horizontal distance between the TSP and the ESP for that test. Note that for the LE test all values of Δu are *negative*. The constructed pore pressure-strain curve for the LE test is shown in Fig. Ex. 13.6d along with the stress-strain curve for both tests and the pore pressure-strain curve for the AC test. For easy comparison, numerical values of the pore pressure are listed in Table Ex. 13.5b. Figure Ex. 13.6d and Table Ex. 13.6b are solutions to part **e**.

TABLE Ex. 13.6b Test B (LE Test Data)

ε (%)	$\Delta\sigma/\sigma'_c$	$\Delta u/\sigma'_c$
0	0	0
1	0.35	−0.16
2	0.45	−0.16
4	0.52	−0.11
6	0.54	−0.07
8	0.56	−0.05
10	0.57	−0.04
12	0.58	−0.03

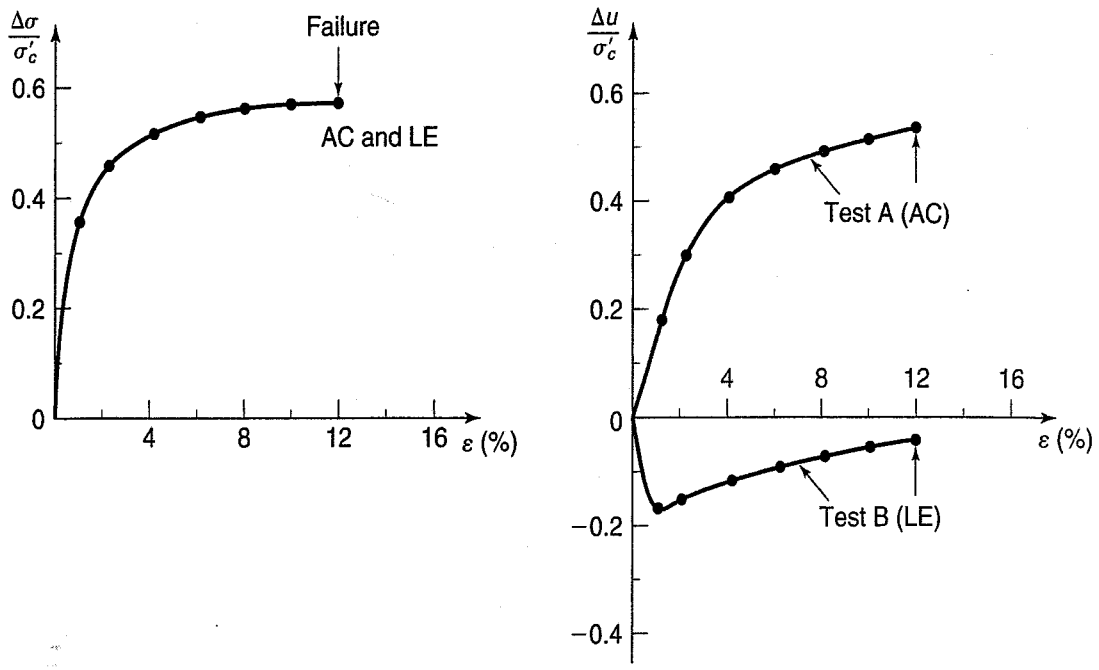

FIGURE Ex. 13.6d Stress-strain and pore pressure-strain data for both tests.

Now you can see where the effective stress values for the LE test in Fig. Ex. 13.6b came from. Another curious fact about the AC and LE test is that the numerical difference between the two pore pressure curves at a given strain is exactly equal to the principal stress difference at that strain. You can check this statement by using the values of Tables Ex. 13.6a and b or scaling off $\Delta\sigma$ values between the two Δu curves of Fig. Ex. 13.6d. Also the horizontal distance between the two TSP's in Fig. Ex. 13.6c is equal to $\Delta\sigma$ at a given strain.

Now that we know the TSP's and ESP's for both tests, we can compute ϕ' and ϕ_T for the two tests [part **c**]. From Fig. Ex. 13.6c we can measure the angles ψ', $\psi_{T\,(AC)}$, and $\psi_{T\,(LE)}$ with a protractor, or we can use Eq. (13.4). Since the clay is normally consolidated, we can assume that $c' \simeq 0$, and this is why we drew the intercepts a and a' on the p–q diagram to be essentially zero. From Eqs. (13.7) and (13.8) we may readily compute ϕ', $\phi_{T\,(AC)}$, and $\phi_{T\,(LE)}$. These values are shown in Table Ex. 13.6c.

TABLE Ex. 13.6c Strength Parameters from Fig. Ex. 13.6c (in degrees)

Angle	Test A (AC)	Test B (LE)
ψ_T	12.5	22
ϕ_T	12.8	23.8
ψ'	21	21
ϕ'	22.6	22.6

f. Let us now compute the pore pressure parameter $\overline{A}$ for both tests. By Eq. (12.19),

$$\overline{A}_f = \frac{\Delta u - \Delta\sigma_3}{\Delta\sigma_1 - \Delta\sigma_3}$$

To obtain the stress changes during the test, it is usually easier to refer to the elements of Fig. Ex. 13.6b and select the changes in total stress from the initial conditions to the conditions at failure.

For the test A (AC), $\Delta\sigma_3 = 0$ and $\Delta\sigma_1 = \sigma_{1f} - \sigma_{1o} = 1.58 - 1.0 = 0.58$; $\Delta u_f = 0.55$. So,

$$\overline{A}_f = \frac{0.55 - 0}{0.58 - 0} = 0.95$$

For the test B (LE), $\Delta\sigma_1 = 0$ and $\Delta\sigma_3 = \sigma_{3f} - \sigma_{3o} = 0.42 - 1.0 = -0.58$; $\Delta u_f = -0.03$. So,

$$\overline{A}_f = \frac{-0.03 - (-0.58)}{0 - (-0.58)} = \frac{0.55}{0.58} = 0.95$$

If this is confusing, it might be easier to use Eq. (13.10) for the LE test:

$$\overline{A}_{le} = 1 - \frac{\Delta u}{\Delta\sigma_h} = 1 - \frac{\Delta u}{\Delta\sigma_3} = 1 - \frac{-0.03}{-0.58} = 0.95$$

(Of course we knew from Eq. (13.13) that $\overline{A}_{le}$ should equal $\overline{A}_{ac}$.) The term $\Delta\sigma_h$ is negative because it is decreased during the LE test (refer again to Fig. Ex. 13.6b).

What conclusions can we draw from Example 13.6? First, both the axial compression and lateral extension tests have identical stress-strain curves and their compressive strengths $\Delta\sigma_f$ are the same. If the stress-strain curves are the same, then they have the same E modulus. They also have the same ESP. However they have markedly different TSPs and markedly different pore pressure responses, but A_f (and thus $\overline{A}_f$) is the same for both tests. We can summarize these observations as follows:

Same $\Delta\sigma$ and $\Delta\sigma_f$
Same σ–ε curves and E modulus
Same ESP
Same ϕ'
Same A_f (and $\overline{A}_f$)
Different TSP
Different ϕ_T
Different Δu

In Example 13.6 we showed the stress conditions and plotted the stress paths for the AC and LE tests, where you will note that the principal stresses at failure had the same orientation as they did at the beginning of the test. For the axial extension (AE) and lateral compression (LC) tests (see Figs. 13.7 and 13.16 for a review of these tests), the principal stresses *rotate* during shear, and the stress paths go *below* the horizontal axis. In this case, q becomes negative. If we went through on exercise similar to what we did in Example 13.6, we would reach the same conclusions as for the AC and LE tests: they have the same strength, ESP, $\overline{A}_f$, and ϕ', but different TSP and Δu. The stress conditions for the AE and LC tests are shown in Fig. 13.17; you might compare these stresses with those shown in Fig. Ex. 13.6b and see what is meant by the rotation of principal stresses. Figure 13.18 then shows typical test results from AE and LC tests. The stress paths for both tests are shown in Fig. 13.19.

The difference between the AC–LE and the AE–LC tests really depends on the intermediate principal stress σ_2. Note that for the first two types of tests we assume that $\sigma_2 = \sigma_3$, and there is no rotation of principal stresses from the beginning of the test until failure. On the other hand, for the AE–LC tests $\sigma_2 = \sigma_1$, and a rotation of principal stresses occurs. This rotation would be even more

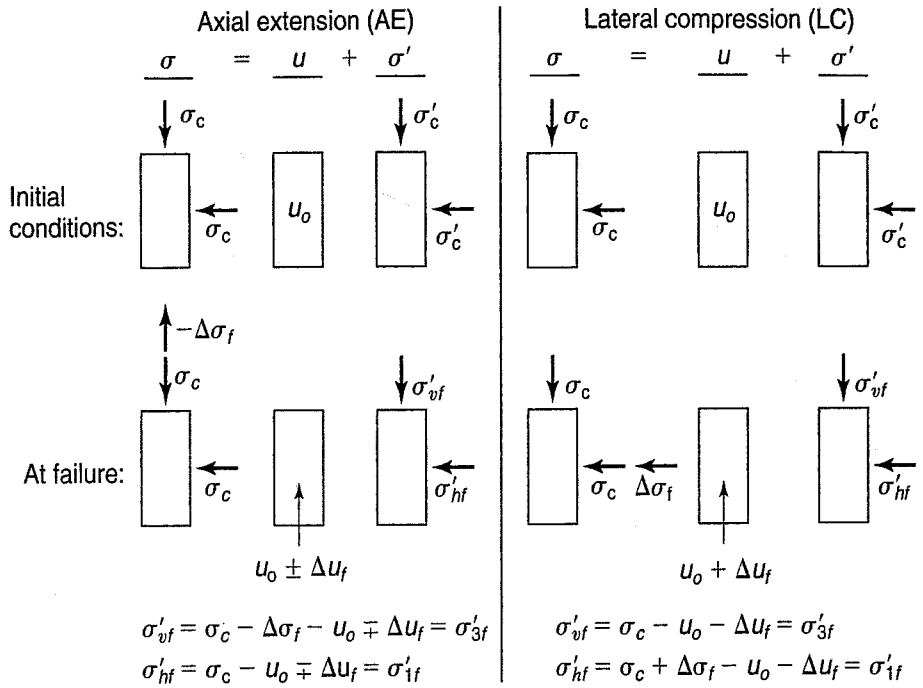

FIGURE 13.17 Stress conditions for the axial extension (AE) and lateral compression (LC) tests. Note that the major principal stress is now horizontal for both these tests at failure.

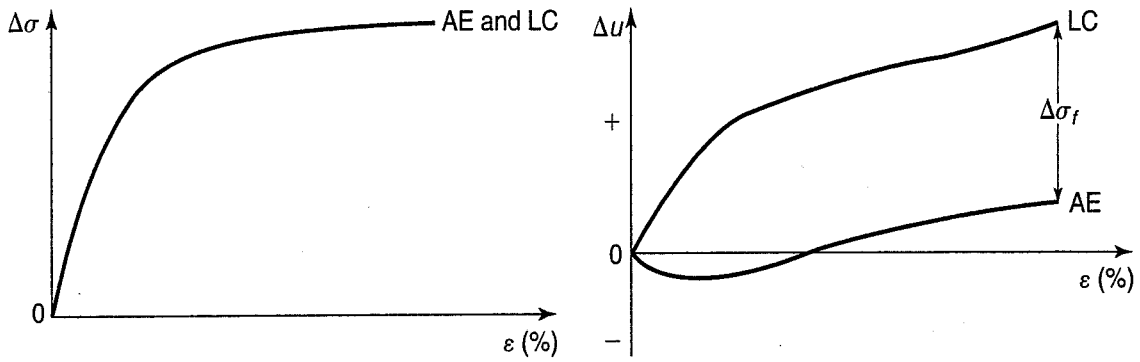

FIGURE 13.18 Stress-strain and pore pressure-strain curves for AE and LC tests on a normally consolidated clay (after Hirschfeld, 1963).

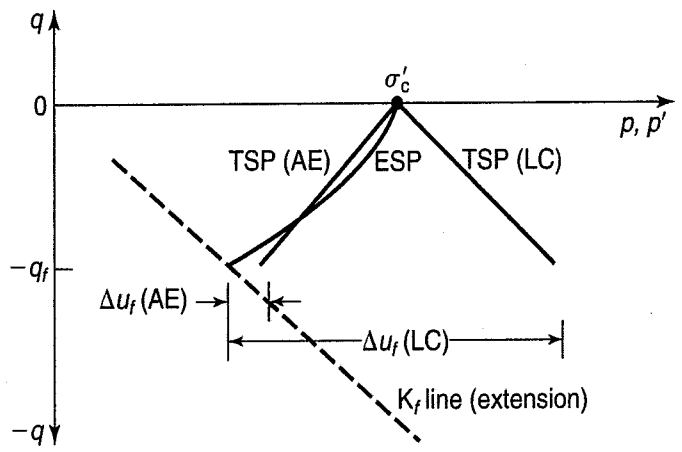

FIGURE 13.19 Stress paths for the AE and LC tests—normally consolidated clay.

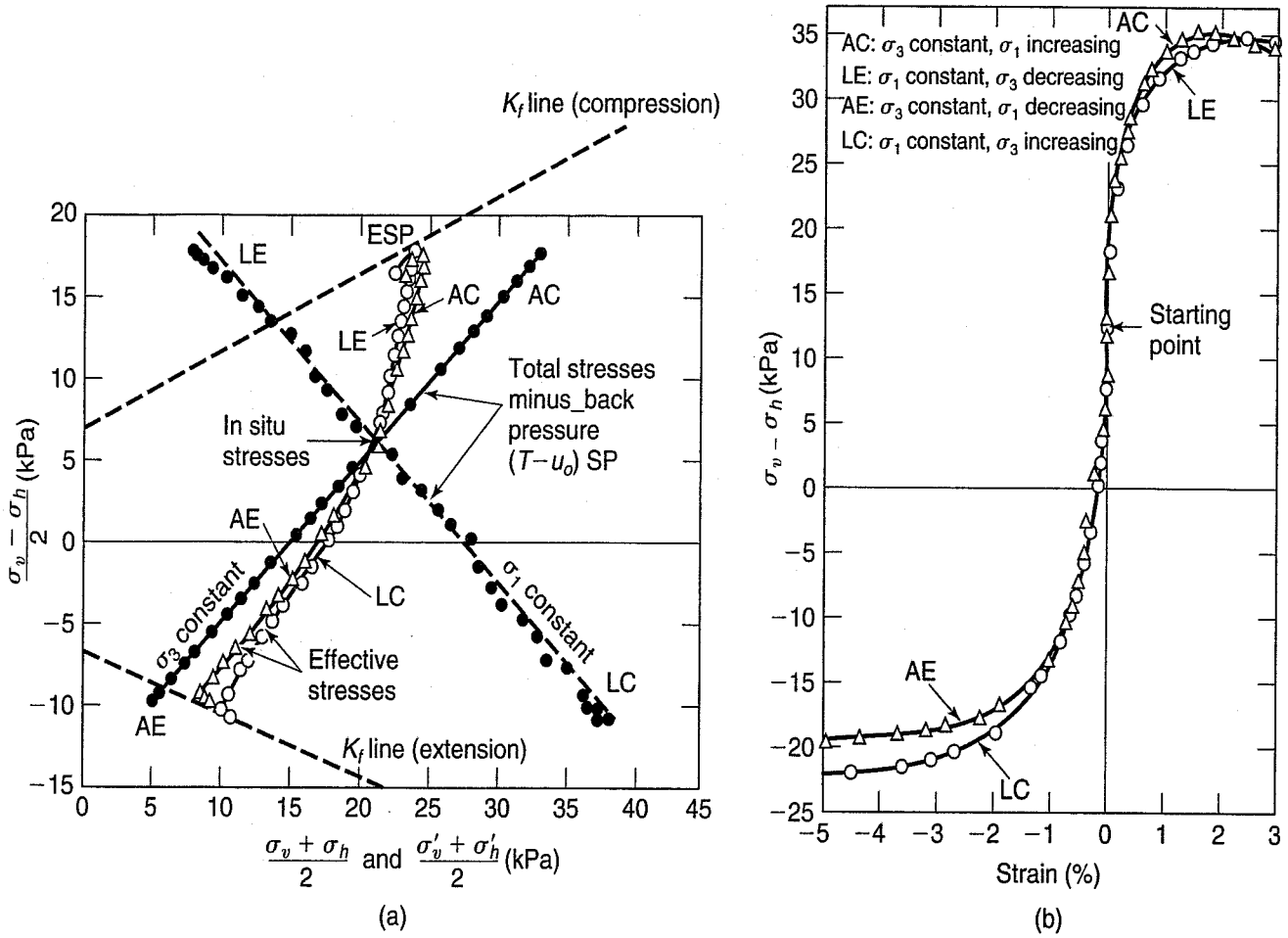

FIGURE 13.20 (a) Total and effective stress paths and (b) stress-strain curves for K_o-consolidated undrained triaxial tests on a normally consolidated clay (after Bishop and Wesley, 1975).

dramatic if, for initial conditions, we had different vertical stresses than horizontal stresses: that is, if $\sigma_{vo} \neq \sigma_{ho} = \sigma_{\text{cell}}$. For this initial condition, $\sigma_{vo} = \sigma_{1o}$ and $\sigma_{ho} = \sigma_{3o} = \sigma_{\text{cell}}$. For both the AE and LC tests, the horizontal stress at failure becomes the major principal stress, as shown in Fig. 13.17.

Some actual test data on natural clays is shown in Figs. 13.20 and 13.21. These results verify the assertions made above that the ESP, $\sigma-\varepsilon$, and A_f responses of AC and LE, and AE and LC, tests are essentially the same for saturated soils. The effective stress and $\sigma-\varepsilon$ behavior is determined *only* by the sign and magnitude of the principal stress difference, $\Delta\sigma = \sigma_v - \sigma_h$, and is independent of the particular shape of the total stress path (Bishop and Wesley, 1975).

Note that the ESP for the AE and LC tests in Figs. 13.20 and 13.21 did not cross the AE–TSP as it did in Fig. 13.19. This means that the induced pore pressure in these tests did not go slightly negative, in contrast to the behavior shown in Fig. 13.19. The specific ESP characteristics for any given soil must be determined by laboratory tests.

The angle of inclination of the failure planes determined according to the Mohr failure hypothesis (discussed in Sec. 11.4) is different for the AE and LC tests because of the rotation of principal stresses. We may determine this angle by using the pole method. This procedure is shown in Fig. 13.22 for the AC and AE tests; similar results would be found for the LE and LC tests. In summary, then:

For AC and LE, no rotation of σ_1 and σ_3: $\alpha_f = 45° + \phi'/2$

For AE and LC, with rotation of σ_1 and σ_3: $\alpha_f = 45° - \phi'/2$

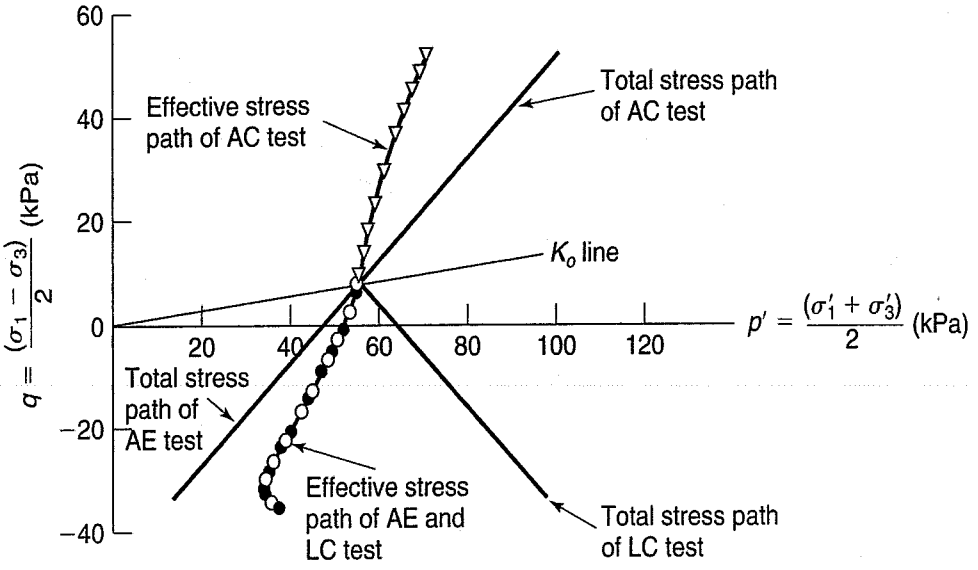

(a)

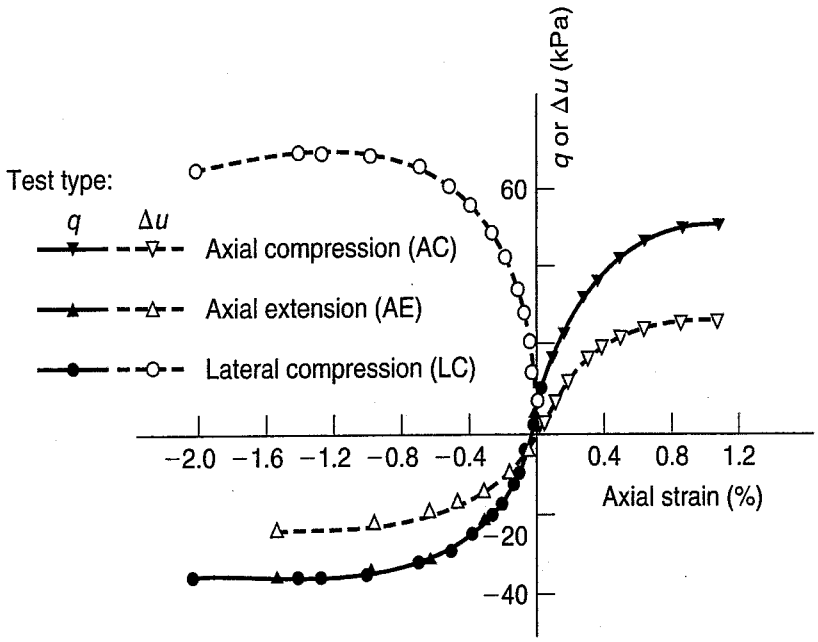

(b)

Specimen	K_o	Test type	w_n (%)	w_f (%)	$\left(\frac{\sigma_1 - \sigma_3}{2}\right)_{max}$ (kPa)	A_f^*
Kars clay:						
195-22-5	0.75	AC	71.5	70.4	51.2	0.32
195-22-7	0.75	LC	73.5	72.0	34.9	0.73
195-22-3	0.75	AE	71.5	70.3	34.5	0.73

A_f^* is the pore pressure parameter at failure based on expression in Table B.3.2

FIGURE 13.21 (a) Total and effective stress paths and (b) stress-strain and pore pressure-strain response of K_o-consolidated undrained triaxial tests on undisturbed samples of Leda clay from Kars, Ontario (after Law and Holtz, 1978).

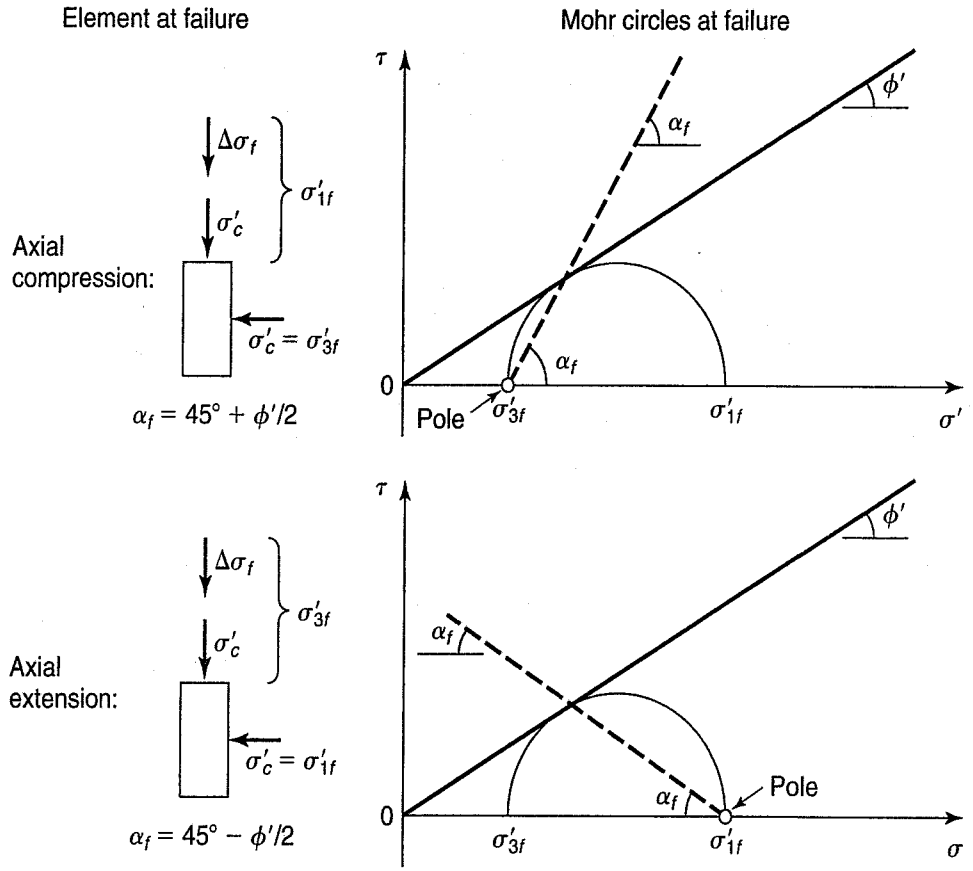

FIGURE 13.22 Angle of inclination of the failure plane for AC and AE tests.

13.5 STRESS PATHS DURING UNDRAINED LOADING—HEAVILY OVERCONSOLIDATED CLAYS

All of the previous section on undrained stress paths concerned the behavior of normally consolidated clays. For overconsolidated clays, the principles are the same, but the shapes of the stress paths are different because the developed pore pressures are different. Examples of stress paths for axial compression tests on overconsolidated clays are shown in Figs. 13.11 and 13.13(b). Knowing how the excess pore water pressures develop along with the shapes of the total stress paths for the various types of tests, you can readily construct the ESP's for overconsolidated clays.

As discussed in Sec. 12.13, overconsolidated clays may have a K_o greater than one. Therefore the stress paths for overconsolidated clays in situ (or for samples reconsolidated to in situ stresses in the laboratory) may start from below the hydrostatic ($K_o = 1$) axis, as shown in Fig. 13.11. Figure 13.23 shows how the stress paths for AE and LC tests on an overconsolidated clay might appear.

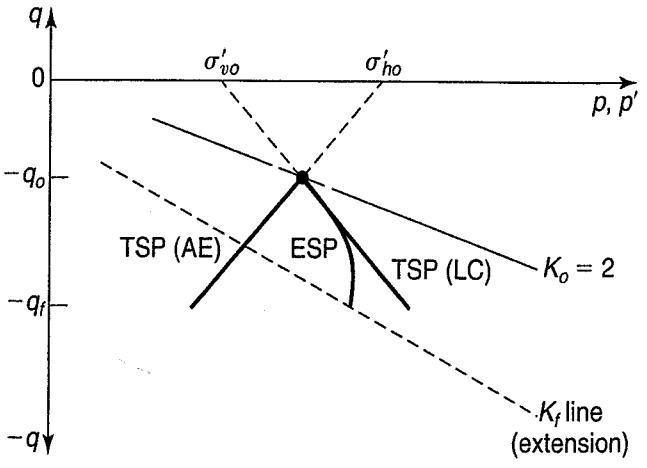

FIGURE 13.23 AE and LC stress paths for an overconsolidated clay.

Example 13.7

(After C. W. Lovell.)

Given:

Consolidated undrained triaxial compression tests are conducted on an overconsolidated clay with preconsolidation stress σ'_p of 800 kPa, which is equivalent to an OCR of 10. The results are shown in Fig. Ex. 13.7a. Another CU test is conducted on the same clay at the same OCR and thus the same σ'_c. In the latter test, the lateral stress is not held constant but is increased at the same time as the axial stress is increased, so that $\Delta\sigma_3 = 0.2\,\Delta\sigma_1$. (See Fig. Ex. 13.7b.) Assume that the test results on this clay shown in Fig. Ex. 13.7a are valid for all ways of changing the boundary stresses in compression—that is, both σ_1 and σ_3 increasing during the test.

Required:

Predict the behavior of the second CU test.

a. Calculate the quantities and fill in the columns of Table Ex. 13.7 for 0%, 0.5%, 2.5%, 5%, and 7.5% strain.

b. Draw the TSP and the ESP for this test.

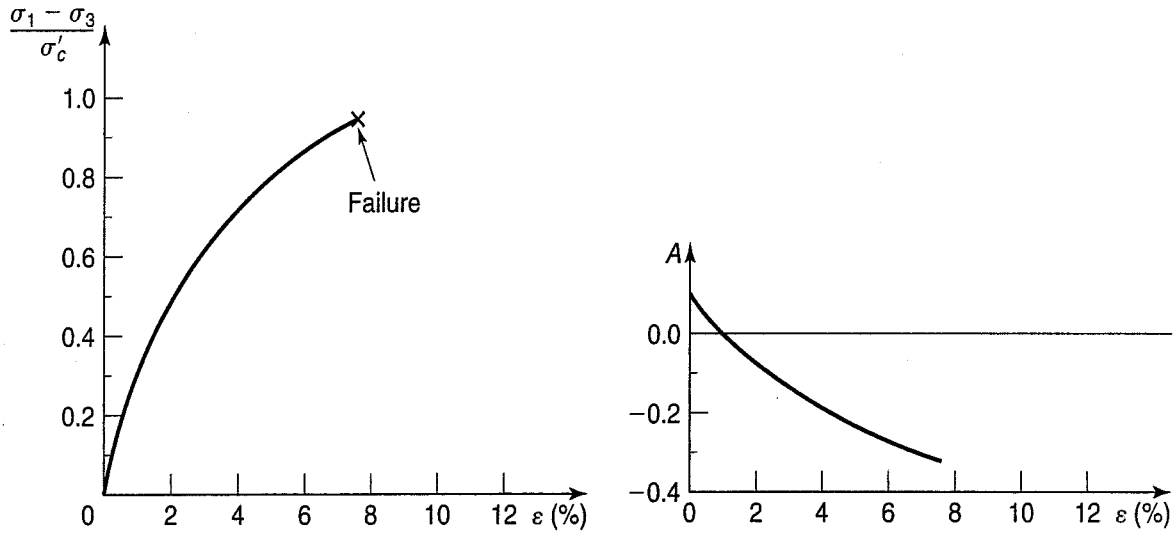

FIGURE Ex. 13.7a

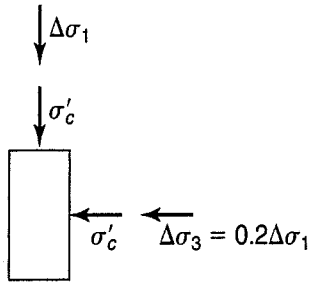

FIGURE Ex. 13.7b

TABLE Ex. 13.7[a]

ε (%)	$\Delta\sigma_1$	$\Delta\sigma_3$	σ_1	σ_3	A	Δu
0	0	0	80	80	+0.1	0
0.5	16	3	96	83	+0.05	4
2.5	58	12	138	92	−0.11	7
5.0	80	16	160	96	−0.23	1
7.5	94	19	174	99	−0.32	−5

[a] All stresses in kPa.

Solution:

a. Table Ex. 13.7, filled in.

b. Fig. Ex. 13.7c. Note that $\sigma_c' = \sigma_p'/(\text{OCR})$ from Eq. (8.2). Thus

$$\sigma_c' = \frac{800}{10} = 80 \text{ kPa}$$

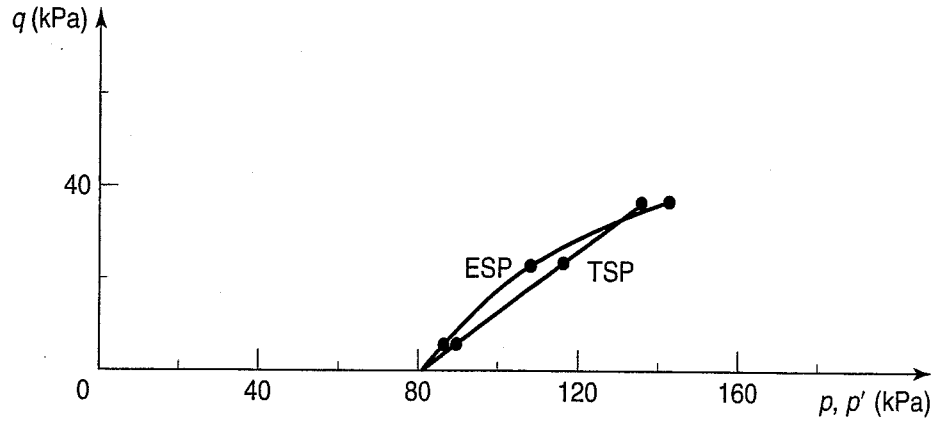

FIGURE Ex. 13.7c

Also

$$\sigma_1 = \sigma_c' + \Delta\sigma_1$$

$$\sigma_3 = \sigma_c' + \Delta\sigma_3 = \sigma_c' + 0.2\,\Delta\sigma_1$$

$$(\sigma_1 - \sigma_3) = \Delta\sigma_1 - 0.2\,\Delta\sigma_1 = 0.8\,\Delta\sigma_1$$

$$\frac{(\sigma_1 - \sigma_3)}{\sigma_c'} = \frac{0.8\,\Delta\sigma_1}{\sigma_c'}$$

But $\sigma_c' = 80$ kPa, so

$$\Delta\sigma_1 = 100\left(\frac{\sigma_1 - \sigma_3}{\sigma_c'}\right)$$

The quantity in parentheses is what is plotted in Fig. Ex. 13.7a. Now the values for $\Delta\sigma_1$ and $\Delta\sigma_3$ ($= 0.2\,\Delta\sigma_1$) can be determined from the figure and inserted appropriately in Table Ex. 13.7. Once the initial values are known, σ_1 and σ_3 at each strain are also readily obtained.

For calculation of Δu, use Eq. (12.19) (assumes $S = 100\%$ for a triaxial test with pore pressures measured) or

$$\Delta u = \Delta\sigma_3 + A(\Delta\sigma_1 - \Delta\sigma_3)$$

$$= 0.2\,\Delta\sigma_1 + A(\Delta\sigma_1 - 0.2\,\Delta\sigma_1)$$

$$= (0.2 + 0.8A)\,\Delta\sigma_1$$

Thus values of Δu in Table Ex. 13.6 are readily determined.

Stress paths are either calculated from Eqs. (13.1) and (13.2) or constructed graphically (Fig. Ex. 13.7c).

Example 13.7 illustrates two important points. First, the ESP has the typical shape of an overconsolidated clay [compare with Figs. 13.11 and 13.13(b)]. Second, you can use the principles developed previously for simple ordinary triaxial tests (constant cell pressure) to plot the results of more complex stress path tests.

13.6 APPLICATIONS OF STRESS PATHS TO ENGINEERING PRACTICE

In this section we offer some examples of how a knowledge of the stress paths helps to explain what is happening to the stresses in the ground during a given engineering loading or unloading situation. If you can draw the complete stress path for some critical elements in your engineering problem, then you will have a much better understanding of the entire problem. This knowledge will enable you to design an appropriate laboratory test program, to estimate the in situ load-deformation response of the soil and structure, and finally to plan a suitable observation and instrumentation program for monitoring the construction operations and final performance of the structure.

Let's look first at what happens when we take a sample of normally consolidated clay from a deposit of soft clay. We showed the stress path during sedimentation and consolidation, from A to B, in Fig. 13.6, and point B corresponds to point 1 in Fig. 13.24. Figure 13.24 is a more complete picture of all the operations necessary before a tube specimen is ready for laboratory testing. As we shall see, it is not surprising that if the samples are disturbed—and they always are to some extent—the measured undrained shear strengths are often much less than in situ strengths.

Ladd and DeGroot (2003) explain the various paths and events in Fig. 13.24, and they give detailed recommendations for minimizing the effects of sample disturbance that often occurs during each of the six events. These recommendations are not especially costly or complicated, but when implemented, they can result in much more reliable estimates of the in situ shear strength on especially soft and sensitive soils.

When the in situ soils at point 1 are loaded by a foundation, the stress path in situ follows the dashed curve up to the failure line. This also would be the undrained stress path followed in an ideal laboratory test on an ideal test specimen. However, even *perfect sampling* results in a loss of shear strength of up to 10% (Skempton and Sowa, 1963; Ladd and Lambe, 1963; and Noorany and Seed, 1965), and we

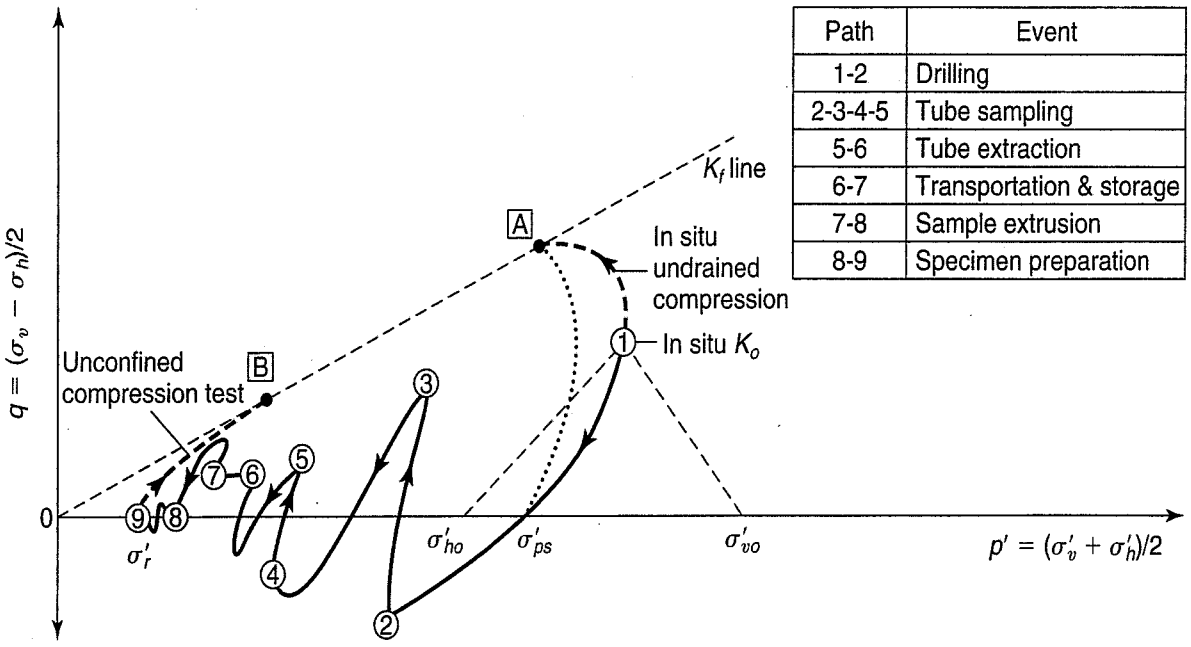

Path	Event
1-2	Drilling
2-3-4-5	Tube sampling
5-6	Tube extraction
6-7	Transportation & storage
7-8	Sample extrusion
8-9	Specimen preparation

FIGURE 13.24 Hypothetical stress path during tube sampling and specimen preparation of a soft, nearly normally consolidated clay (from Ladd and DeGroot, 2003).

can see why in Fig. 13.24. Perfect sampling is sampling with no additional mechanical disturbance, and with the specimen in the test apparatus ready to be sheared. If you go back and look at Fig. 12.34, you will see the conditions in the test specimen immediately after sampling but before application of cell pressure and axial load. In this case, we called the pore pressure "residual (capillary) pressure, after sampling," $-u_r$, (Sec. 12.11.1), and the corresponding effective stress is σ'_r. For perfect sampling, the effective stress conditions would be σ'_{ps}, and this is the σ'_{ps} shown in Fig. 13.24. Now if you were to load the perfect sample at that point, its ESP would be similar in shape to the stress paths for NC soils in Figs. 13.9 and 13.12 and as shown with the dotted curve in Fig. 13.24. Thus the loss in shear strength even with perfect sampling is significant.

Using the stress conditions in Fig. 12.34, the definitions of the stress increments described in Sec. 13.3 and Appendix B, it is possible to derive the equation for σ'_{ps}, or for $K_o < 1$

$$\sigma'_{ps} = \sigma'_{vo}[K_o + A_u(1 - K_o)] \tag{13.23}$$

Because even with the best equipment and techniques we cannot obtain perfect samples, in reality the loss in strength due to all the additional steps shown in Fig. 13.24 is much greater than 10%. Look at the unconfined compression test stress path from point 9 up to the failure line. You can see that the measured shear strength is much less than the in situ strength. Calculations of the stability of a foundation based on the measured shear strength from disturbed samples will result in excessively expensive foundations and overly conservative designs. Procedures for evaluating sample disturbance and correcting the measured shear strengths are suggested by Ladd and Lambe (1963), Ladd et al. (1977), and Ladd and DeGroot (2003).

Next, let's take a close look at what happens to the in situ stress path for foundation loading, from point 1 in Fig. 13.24 up to the failure line. Consider the case of, for example, a highway embankment constructed on a soft clay foundation in which the clay is 100% saturated and essentially normally consolidated. This case, shown in Fig. 13.25(a), may be modeled by axial compression stress conditions. Strictly speaking, as mentioned previously, the loading should be plane strain ($\varepsilon_2 = 0$) for a long embankment, but we shall use the common triaxial test, with which you are familiar, for illustrative purposes. The stress paths for this case are shown in Fig. 13.25(a) (compare with Fig. 13.12).

Let's look a little more closely at these stress paths and their engineering implications. For this normally consolidated clay, the K_o is less than 1 (about 0.6), so that the initial stress conditions in the ground are plotted as point A on the figure. In foundation *loading*, the horizontal stresses probably increase slightly, as was done in Example 13.6, but for this case we will assume that they are essentially constant. Then the $(T - u_o)$SP is the straight line AC. The total stresses represented by point C are applied at the end of construction. The induced pore pressures are positive, of course, for a normally consolidated clay, and so we will have the typically shaped ESP hooking off to the left, as is illustrated by curve AB in Fig. 13.25(a). The distance BC, then, is numerically equal to the excess pore pressure induced by the embankment loading. Note that the shear stress on a typical element under the embankment increases from its initial value of q_o to q_1. Had loading continued to the level of q_f, the ESP would have intersected the K_f line and failure would have occurred.

For this example, let's assume that we are good designers, that we correctly estimated the in situ shear strength of the soil, and that no failure occurred. Then we are at point B on the ESP at the *end of construction*, the most critical design condition for foundation loadings on normally consolidated clays. Why is this the "most critical"? Well, look at what happens after we reach point B. The applied loading is constant thereafter (assuming no additional construction loading occurs), the clay starts to consolidate, and the excess pore water pressure caused by the load dissipates. This excess pore pressure is represented by the distance BC. Thus the ESP proceeds along line BC. Ultimately at $U = 100\%$, all the excess pore pressure will be dissipated and our element will be at point C in equilibrium under the embankment load. It will still have a shear stress q_1 acting on it, and $p = p' = p_1$. Since there is no

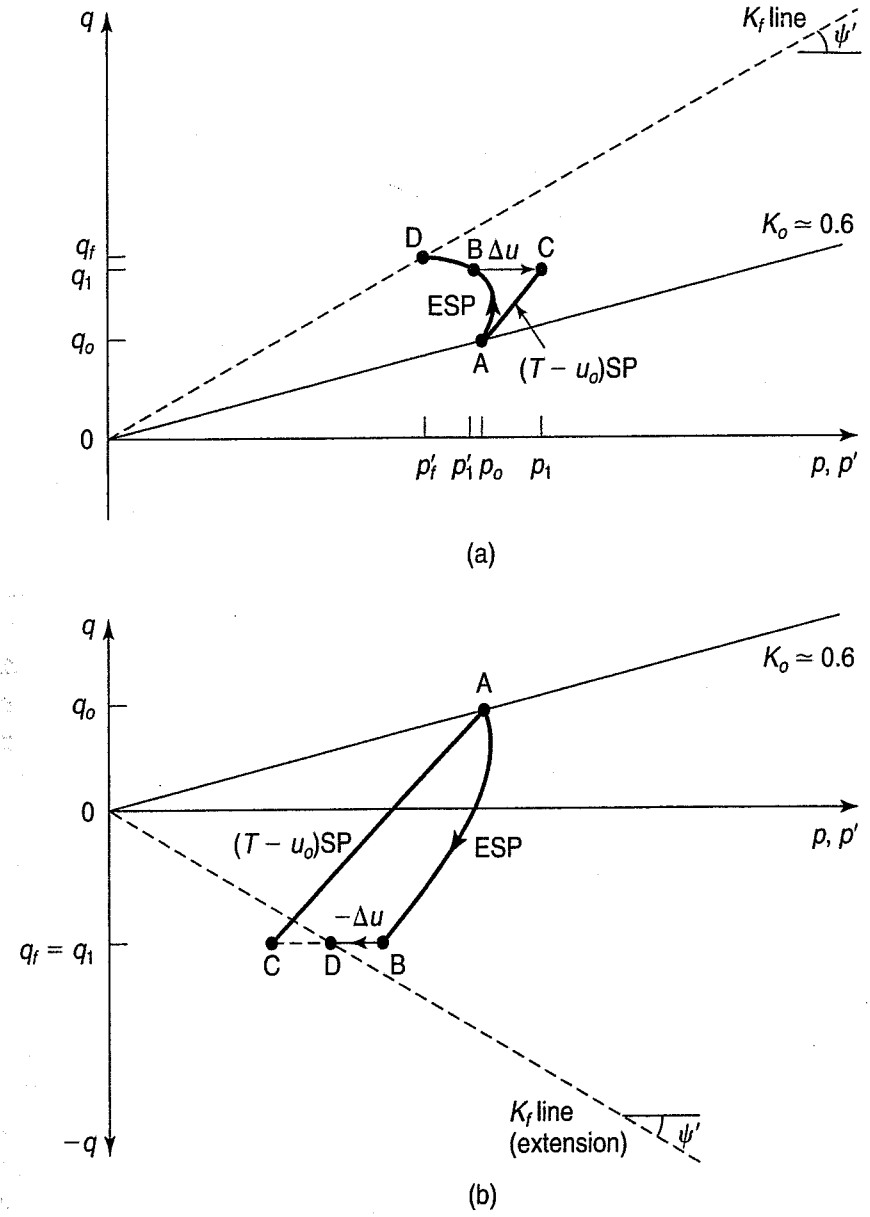

FIGURE 13.25 Stress paths for (a) foundation loading and (b) foundation excavation of normally consolidated clay.

excess pore water pressure remaining in the element, the total stresses will equal the effective stresses at point C. Now you can see why point B at the end of construction is the most critical for this case. Point B is the closest point to the failure line K_f. After that, because of consolidation, the foundation soil becomes stronger with time (safer) until at point C we are at the farthest point from the K_f line for this particular loading situation. That is why the end of construction is the most critical for foundation loading of normally consolidated clays. The engineering lesson here is that if you make it through the end of the construction period for this type of loading, then conditions become *safer* with time.

For the foundation loading of an overconsolidated clay, the TSP and ESP would look something like the paths shown in Figs. 13.11 and 13.13(b). As the negative excess pore pressure dissipates, the stresses on the element move closer to the K_f line, which means that the long-term conditions are actually the *least* safe after dissipation of the pore pressure has occurred. But in most cases for foundation loading on overconsolidated clays, we are so far from the K_f line anyway that long-term conditions are usually not critical.

Example 13.8

Given:

The embankment of Example 13.4. Triaxial compression tests indicate $\phi' = 23°$ and $c' = 7$ kPa.

Required:

Construct the K_f line and determine whether the embankment will be stable.

Solution: From Eqs. (13.7) and (13.8), $\psi' = 21.3°$ and $a' = 6.4$ kPa. Draw the K_f line on the p–q diagram (Fig. Ex. 13.8). Since the ESP would intersect the K_f line before the final design loads could be applied, failure would occur. At that time, q would be approximately 15 kPa.

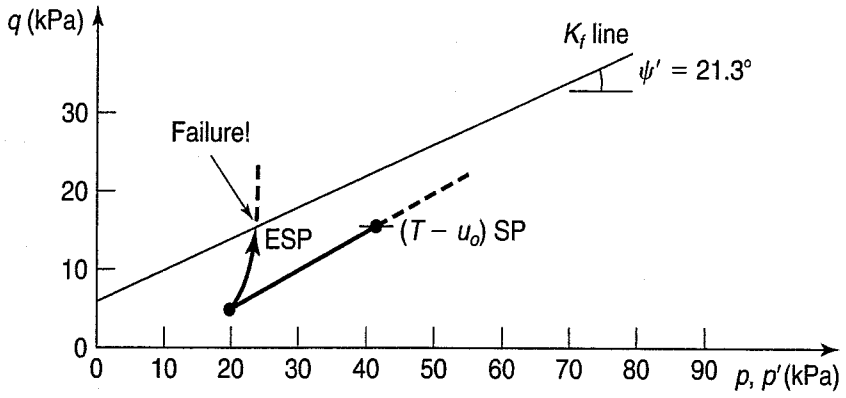

FIGURE Ex. 13.8

In Sec. 12.11.5 on the use of UU strength in practice, we mentioned the case of foundation loading of lightly overconsolidated clays that exhibit dilatant behavior when sheared. This behavior has been observed both in laboratory tests and in the field under offshore structures in the Canadian Beaufort Sea. Crooks and Becker (1988) estimated total stress changes from elastic theory at the location of a piezometer under an offshore island and constructed the field $(T - u_o)$SP caused by the island's construction [Fig. 13.26(b)]. Then the measured excess pore pressures at various stages during construction were subtracted from the computed total stresses to construct the ESP at the piezometer location, also shown in Fig. 13.26(b). The shape of this ESP indicated dilatant behavior [compare with Figs. 13.11 and 13.13(b)], which was also observed in lab shear tests on the same material in Fig. 13.26(a).

The stress paths also indicated that when the shear stresses reached point A on the $(T - u_o)$SP, corresponding to the shear strength of the material at point A′ on the ESP, no further increase in shear stress was possible. In order to maintain the imposed shear stress at a constant value, the horizontal stress in the foundation clay had to increase. Because at points A and A′ the foundation clay was in a state of failure, significant plastic deformations developed under the island. However, because of the island's large diameter and flat side slopes, the overstress zone was confined. It also helped that the soft layer was thin compared with the diameter of the island. This example shows how valuable stress paths can be in practice.

Another important engineering situation concerns an excavation for a foundation in normally consolidated clay. This situation is illustrated in Fig. 13.16 as an example of axial extension. We already know from Fig. 13.19 what the TSP and ESP look like for this case; they are also in Fig. 13.25(b). Since the vertical stress decreases during an excavation, the total stress path goes from the initial conditions at point A to point C. As with the case of foundation loading, the horizontal stresses may also decrease slightly, but for illustration purposes we shall assume that they remain essentially unchanged. Since negative pore pressures occur due to unloading, the ESP must lie to the right of the $(T - u_o)$SP. For the case shown with unloading from q_o down to q_1, the ESP then follows curve AB, and point B represents conditions

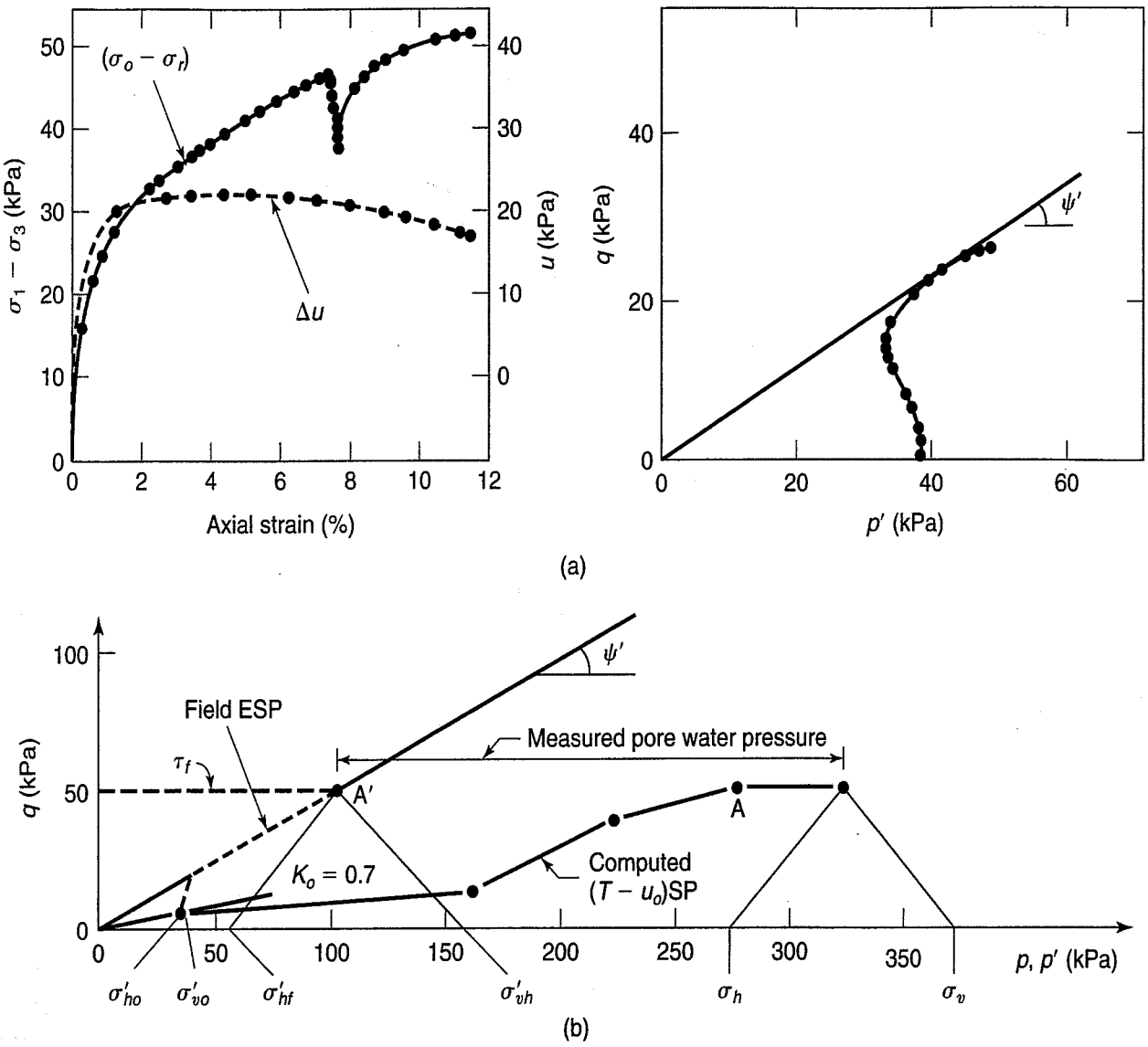

FIGURE 13.26 (a) Stress-strain and pore pressure-strain response and effective stress path of a CU triaxial test on Tarslut Clay; (b) stress paths in clay under Tarslut Island, Beaufort Sea (after Crooks and Becker, 1988).

at the end of construction. For this case, failure did not occur, and we are safe at the end of construction. Now, the excess pore pressure starts to dissipate—it is negative in this case, and now it starts to become more and more positive, following line BDC. At point C, of course, all the excess negative pore pressure would be dissipated and the total stresses would equal the effective stresses. This would never occur, however, because when the ESP reached point D, it would intersect the K_f line in extension and failure would occur. Therefore the long-term conditions are the more critical for the case of an excavation in normally consolidated clays. In contrast to the case of foundation loading, just because you get through construction without a failure doesn't mean that you are free of a possible failure. No, the excavation (unloading) will become less and less safe with time. Field measurements (for example, Lambe and Whitman, 1969) have shown that the rate of dissipation of this negative pore pressure occurs relatively fast, much faster than in the case of foundation loading. Therefore the engineering implication for this case is to get that excavation filled and the clay reloaded as fast as possible. Otherwise you risk a failure occurring at some time, perhaps only a few weeks after completion of the excavation. This is another example of the long-term conditions being more critical than the end of construction conditions.

The above examples illustrate the value of the stress path method. You can construct similar TSP and ESP diagrams for the other cases shown in Fig. 13.16, for both normally (and lightly overconsolidated

TABLE 13.1 Critical Conditions for the Stability of Saturated Clays

Foundation Loading	Soft (NC and Slightly OC) Clay	Stiff (Heavily OC) Clay
Critical condition	UU (no drainage).	Probably UU but check CD (drainage with equilibrium pore pressures).
Remarks	Use $\phi = 0, c = \tau_f$ with appropriate corrections for sample disturbance, strain rate, anisotropy, age, etc.	Stability usually not a major problem.
Excavation or Natural Slope	**Soft (NC) Clay**	**Stiff (Highly OC) Clay**
Critical condition	Could be either UU or CD.	CD (complete drainage).
Remarks	If soil is very sensitive, it may change from drained to undrained conditions.	Use effective stress analysis with equilibrium pore pressures. If clay is fissured, c' (and perhaps ϕ') will likely decrease with time.

After Ladd (1971b).

clays) and heavily overconsolidated clays, and see what the critical design situations are. Some of the critical conditions for stability are summarized in Table 13.1 (Ladd, 1971b).

13.7 CRITICAL STATE SOIL MECHANICS

We have already seen that simplified, conceptual frameworks of soil behavior, like the Peacock diagram for sand shear behavior (Sec. 12.4, Fig. 12.11), can provide a means for understanding how soil under a certain preshear state will behave when sheared to failure. One of the most important conceptual and theoretical frameworks in all of soil mechanics is known as *critical state soil mechanics* (*CSSM*). Developed at Cambridge University, this framework was originally presented by Schofield and Wroth (1968). It brought together previous well-known concepts such as the Mohr–Coulomb failure criterion and Hvorslev parameters (Sec. 13.13.2). However, it also provided new levels of sophistication in terms of our ability to model soil behavior by including prefailure behavior [albeit using a simple elastic-plastic model, Fig. 11.4(d)], the effect of stress history on generalized soil yielding, and drained versus undrained behavior in clays. The development of this framework served as the foundation for today's more sophisticated soil constitutive models, which in turn are used in numerical analyses for simulating highly complex geotechnical problems. These constitutive models include Modified Cam clay (Roscoe and Burland, 1968), cap models (e.g., Drucker et al., 1957), nested models (e.g., Prevost, 1977), and bounding surface models (e.g., Dafalias, 1986; Whittle, 1987; and Pestana, 1994), among others. Constitutive models are reviewed in Sec. 13.8.

It is important to mention that the CSSM framework was originally developed for saturated, reconstituted clay—that is, clays completely remolded and then reconsolidated to a normally consolidated state. This reconsolidation can be followed by mechanical overconsolidation to some overconsolidation ratio (OCR). Stated in its most fundamental form, the CSSM framework links a pair of well-known, two-dimensional (2-D) soil mechanical "spaces," void ratio–effective stress and shear stress–effective stress spaces. It combines these 2-D spaces into a three-dimensional (3-D) space that describes how a clay with a particular stress history will behave when sheared to failure, including volume change if it is a drained test, and shear-induced pore pressure if it is an undrained test.

Let's first reintroduce the 2-D spaces with which you are already familiar. Figure 13.27(a) shows a typical plot of void ratio (e) versus the logarithm (base 10) of vertical effective stress (σ'_v) such as that

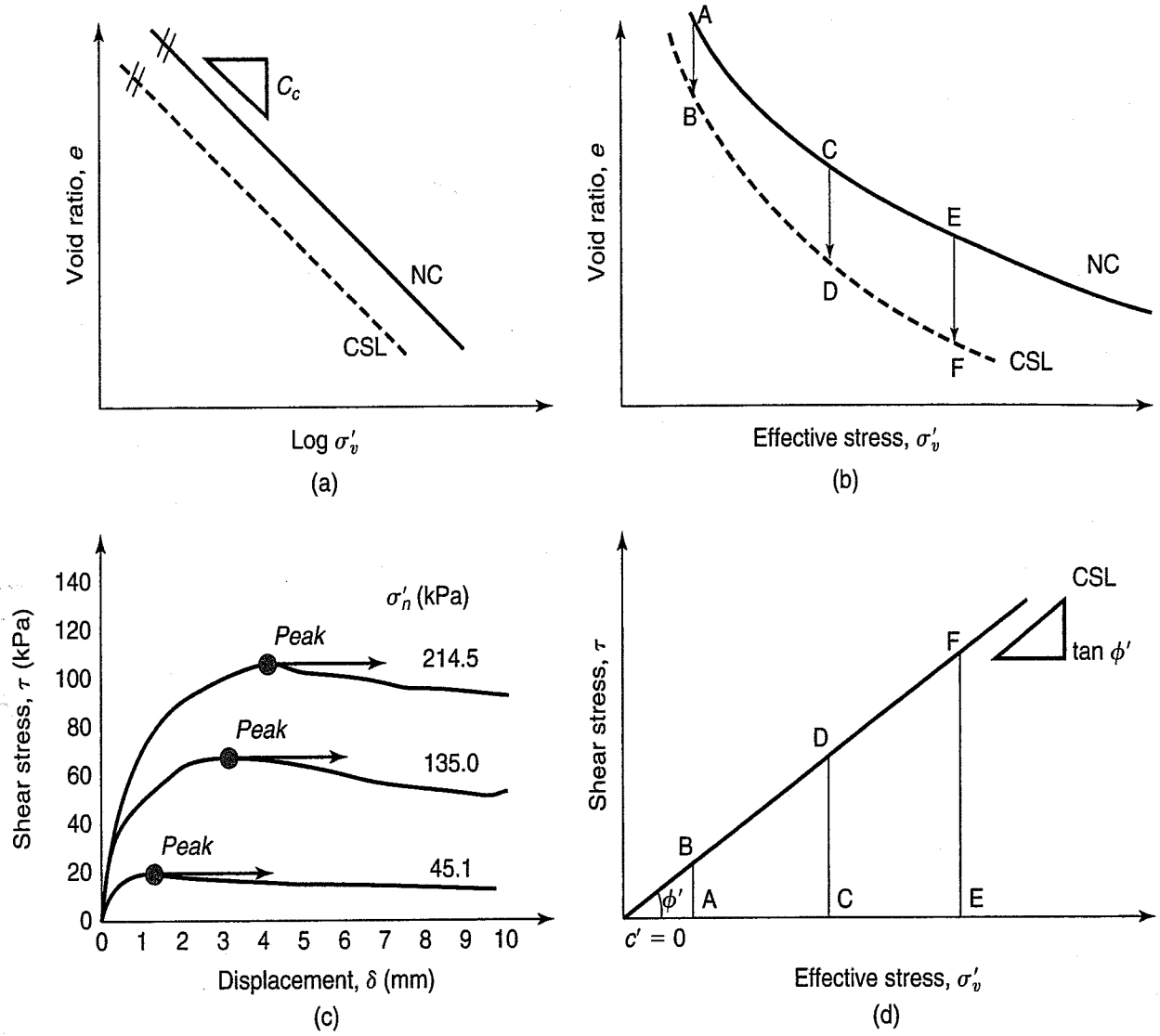

FIGURE 13.27 Simplified critical state framework for direct shear tests that are one-dimensionally consolidated, then sheared to failure: (a) e–log σ'_v relationships for consolidation and critical states; (b) e–σ'_v relationships for consolidation and critical states; (c) shear stress versus displacement for direct shear tests at three σ'_v values; and (d) shear stress versus σ'_v for the three direct shear tests (after Mayne, 2006).

presented in Chapter 8.[1] In this case, the slope in the normally consolidated range is the compression index, C_c [Eq. (8.7)]. Figure 13.27(b) shows this same plot, except that σ'_v is plotted on a linear scale, resulting in the curved shape of the consolidation relationship.

Next, as shown in Fig. 13.27(c), we perform CD direct shear tests on three clay specimens consolidated to three different σ'_v values. While CSSM can depict test results from other, more complex tests such as the triaxial test (discussed later), use of direct shear results provides a simple way to understand CSSM principles. The preshear e–log σ'_v states are shown on the compression curves of Fig. 13.27(a) and (b), and the peaks are plotted in shear stress τ versus normal stress σ'_v space in Fig. 13.27(c). These failure τ–σ'_v states form the familiar Mohr–Coulomb failure envelope defined by

[1]Schofield and Wroth (1968) originally used *specific volume* (v) instead of void ratio, where $v = 1 + e$, i.e., v is the volume of soil for which there is a unit volume of solids. They also used the natural logarithm (base e) instead of log base10, and they used the 3-D definition of the mean effective stress, or $p' = (\sigma'_1 + 2\sigma'_3)/3$, we mentioned earlier. To illustrate CSSM principles in familiar terms, we will use e and log σ'_v and then later use our familiar definition of $p' = \frac{1}{2}(\sigma'_v + \sigma'_h)$ to illustrate the usefulness of the critical state concept.

the effective friction angle ϕ', in Fig. 13.27(d). In the CSSM framework, this envelope, which always has an intercept $c' = 0$, is known as the critical state line (CSL). The CSL represents the state of stress at failure for all soils, regardless of their stress history.

In order to link the e–log σ'_v and τ–σ'_v spaces together, we return to Fig. 13.27(a) and plot the e–log σ'_v states at failure for the three direct shear tests that were performed. Since these were drained tests on normally consolidated specimens under constant σ'_v, we know from Sec. 12.9 that the specimens contract during shear, and that the preshear $\sigma'_v = \sigma'_v$ at failure. This leads to failure states that lie directly under the preshear states, and the formation of a new line in Fig. 13.27(a) that is the CSL, only now it is in e–log σ'_v space (perhaps you can now start to visualize the 3-D CSL, which for these tests would be the combination of e–τ–σ'_v).

For each of the drained, direct shear tests at different σ'_v values, the paths followed during shear to failure on the CSL can be drawn first on the e–log σ'_v plot [Fig. 13.27(b)]; these are the paths labeled AB, CD, and EF. The same tests can be depicted on the τ–σ'_v plot in Fig. 13.27(d)—they are also vertical for the same reason, that σ'_v is constant during these tests. If the paths AB, CD, and EF were plotted in 3-D space (e–τ–σ'_v), we would refer to them as their *state paths*, since they track both the stresses and physical states (as represented by the void ratio) of the specimen during shear.

You can begin to see that, like other soil behavior models that we've discussed, once the compression curve and CSL are established for a particular set of tests, they can be used for simple predictions of failure stresses and void ratio changes for given values of preshear σ'_v. To expand the CSSM framework to undrained shear, Fig. 13.28 shows the same compression relationships, e–log σ'_v and e–σ'_v, and the τ–σ'_v space shown in Fig. 13.27. This time, the direct shear test is performed undrained after consolidation to σ'_{vo} at point A, so that the void ratio is unchanged as it moves to the CSL. The

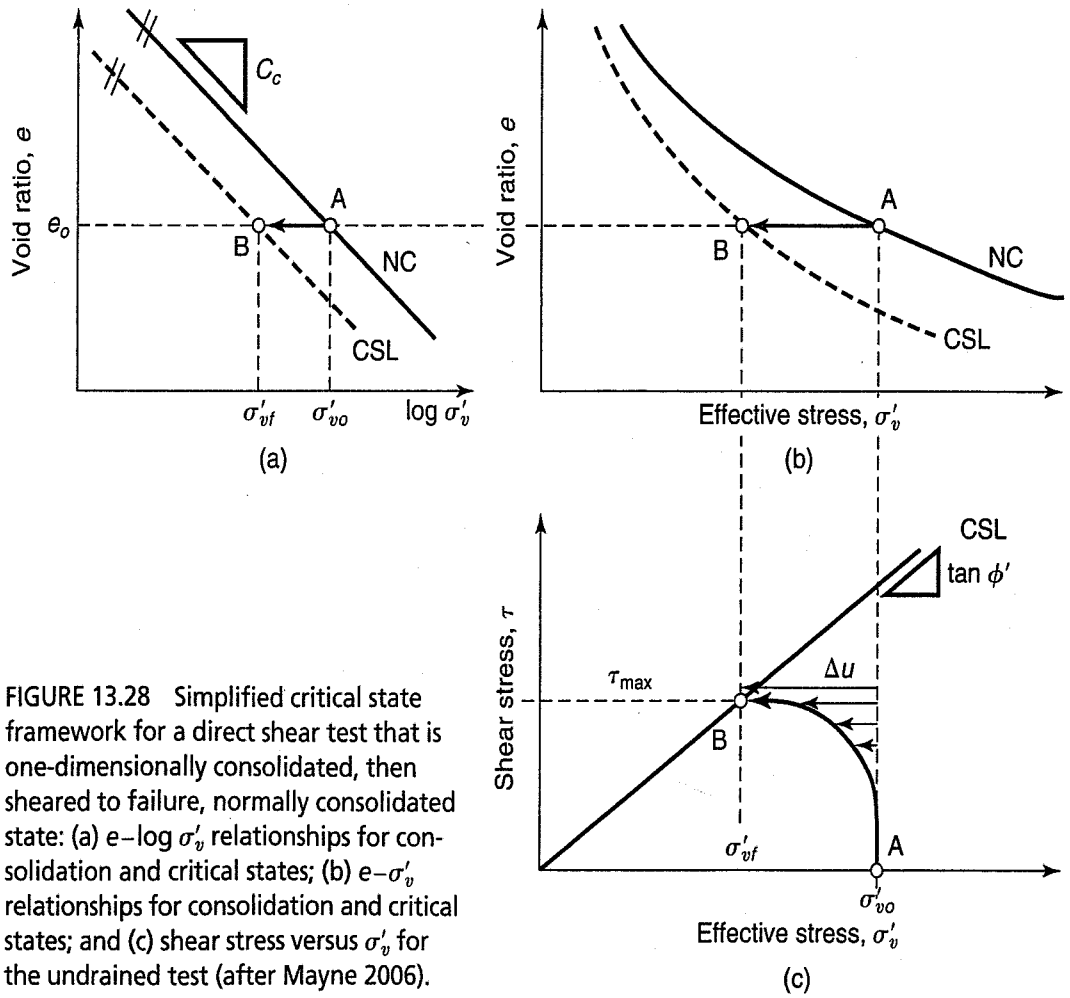

FIGURE 13.28 Simplified critical state framework for a direct shear test that is one-dimensionally consolidated, then sheared to failure, normally consolidated state: (a) e–log σ'_v relationships for consolidation and critical states; (b) e–σ'_v relationships for consolidation and critical states; and (c) shear stress versus σ'_v for the undrained test (after Mayne 2006).

result is that the σ'_v at failure (point B) is lower than the preshear σ'_v, the result of positive excess pore pressure, Δu, being generated during shear. In fact, $\Delta u = \sigma'_{v\,(\text{preshear})} - \sigma'_{v\,(\text{failure})}$.

We mentioned that CSSM can also be used to model behavior of mechanically overconsolidated soils—i.e., those that were loaded to some maximum stress (σ'_{vm}), then unloaded to a final stress (σ'_{vf}), which produces an OCR = $\sigma'_{vm}/\sigma'_{vf}$. In Fig. 13.29, a swelling line with slope C_s has been added to the compression curves, e–log σ'_v and e–σ'_v, and the CSL remains the same in all three spaces as it was for the normally consolidated specimens. The slope of this unloading or swelling part of the e–log σ'_v path is C_s, which is defined by the same equation as the compression index, C_c [Eq. (8.7)]. The framework can once again be used for predicting both drained and undrained test results, as indicated by paths AB and AC, respectively. The undrained path AC indicates that since $\sigma'_{v\,(\text{preshear})}$ is less than $\sigma'_{v\,(\text{failure})}$, the specimen experienced excess pore pressure during shear, $\Delta u < 0$, resulting in a τ–σ'_v path that curls up and to the right to land on the CSL in Fig. 13.29(c). One question to ask is this: in an undrained test, is there a preshear σ'_v value that would lead to a vertical τ–σ'_v path during shear (in other words, $\Delta u = 0$ during shear)? This would be the case when $\sigma'_{v\,(\text{preshear})}$ is where the swelling line crosses the CSL in Fig. 13.29(a) and (b), point D. Thus, the CSL in these two figures can be treated as a dividing line of sorts: when $\sigma'_{v\,(\text{preshear})}$ is to the right of this crossing point, the clay is normally or lightly overconsolidated and will contract during drained shear, or develop $\Delta u > 0$ during undrained shear. When $\sigma'_{v\,(\text{preshear})}$ is to the left of this crossing point, the clay is heavily overconsolidated and will dilate or produce $\Delta u < 0$.

Our use of direct shear tests in the above discussion allowed us to learn some basics of the critical state framework, namely the relationship between preshear states on the compression curve and failure states on the CSL. However, this by itself would not have made it that much more advantageous than the Mohr–Coulomb failure criterion. The other significant piece of the critical state framework is the

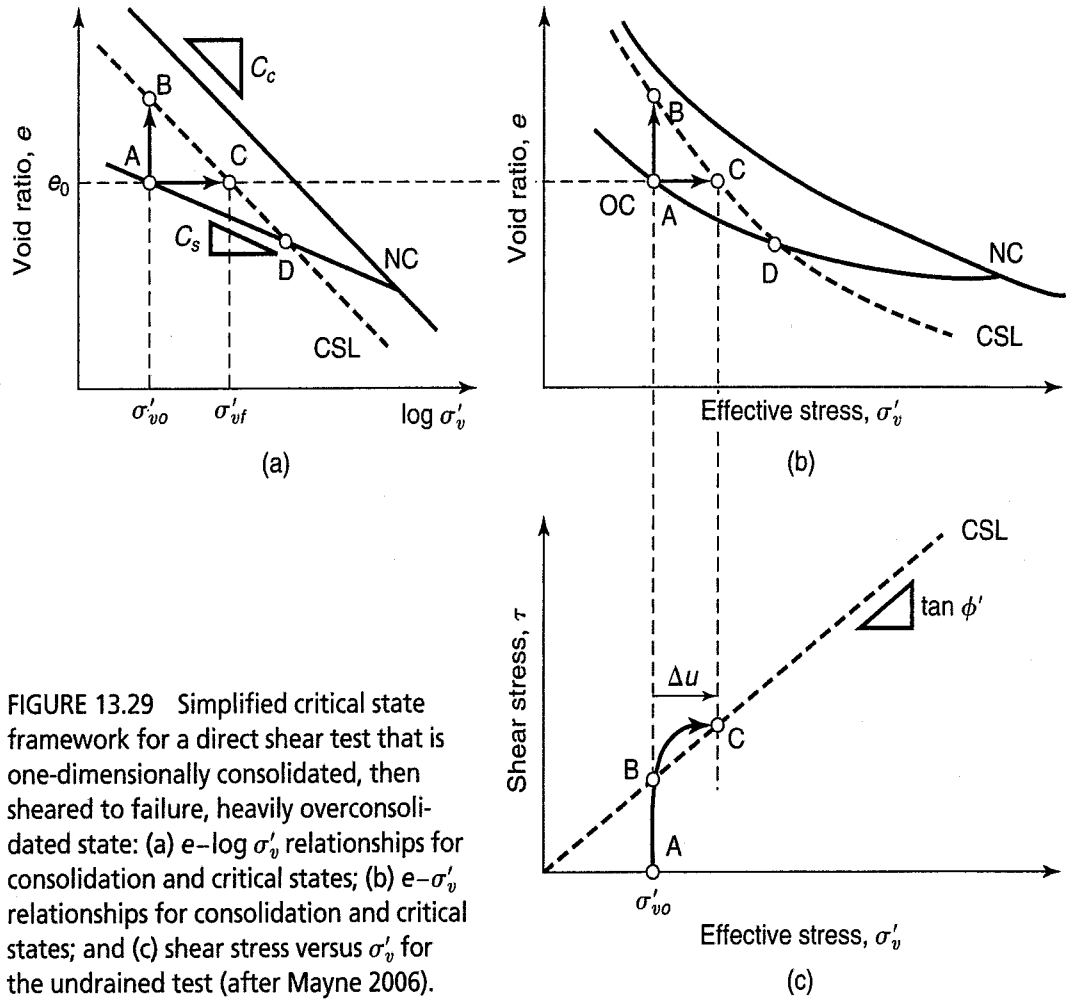

FIGURE 13.29 Simplified critical state framework for a direct shear test that is one-dimensionally consolidated, then sheared to failure, heavily overconsolidated state: (a) e–log σ'_v relationships for consolidation and critical states; (b) e–σ'_v relationships for consolidation and critical states; and (c) shear stress versus σ'_v for the undrained test (after Mayne 2006).

concept of the *yield surface*. To understand what this surface represents, we will now look at the q versus p' stress space of a triaxial soil specimen that is hydrostatically consolidated. As Fig. 13.30 shows, there is still a compression curve for this situation, except that we now plot it as e–log p' and e–p', instead of using σ'_v, which was for one-dimensional conditions used in the direct shear test. There is still a CSL plotted in these two spaces as well as in q–p' space [Fig. 13.30(c)]. *The yield surface in q–p' space is the dividing line between elastic behavior and plastic or inelastic behavior*, and its size is determined by the maximum value of p' to which the soil is consolidated. Figures 13.30(a) and (b) show three normally consolidated p' levels for the soil, A, B and C. As p' increases, the size of the yield surface in Fig. 13.30(c) also increases, defined by the intersections of the surfaces with the p'-axis at points A, B and C.

A very simple case using the yield surface is during hydrostatic consolidation. In Figs. 13.30(a) and (b), the soil is mechanically overconsolidated to point D; this is also shown on the p'-axis in Fig. 13.30(c). When the soil is reconsolidated to point B, the recompression portion D-B is elastic, since it lies inside the yield surface, and the portion beyond this (path B-C) is plastic, which also increases the size of the yield surface due to consolidation.

Let's consider a hydrostatically consolidated, drained triaxial test on a lightly overconsolidated soil. As shown in Figs. 13.31(a) and (b), the soil has been consolidated from point A to point B and unloaded to point C. These consolidation points are also shown in the stress path space of Fig. 13.31(c). During the drained shear portion of the test, as shown by path CD in Fig. 13.31(c), the initial part of this loading, inside the existing yield surface, will be elastic. The soil then yields and begins deforming plastically, expanding the yield surface until it fails on the CSL at point D. You can see the subsequent decrease in void ratio on the compression curve. For a hydrostatically consolidated, drained triaxial test on a normally consolidated soil, the stress path would start where the yield surface crosses the p' axis, and the yield surface would progressively expand to failure.

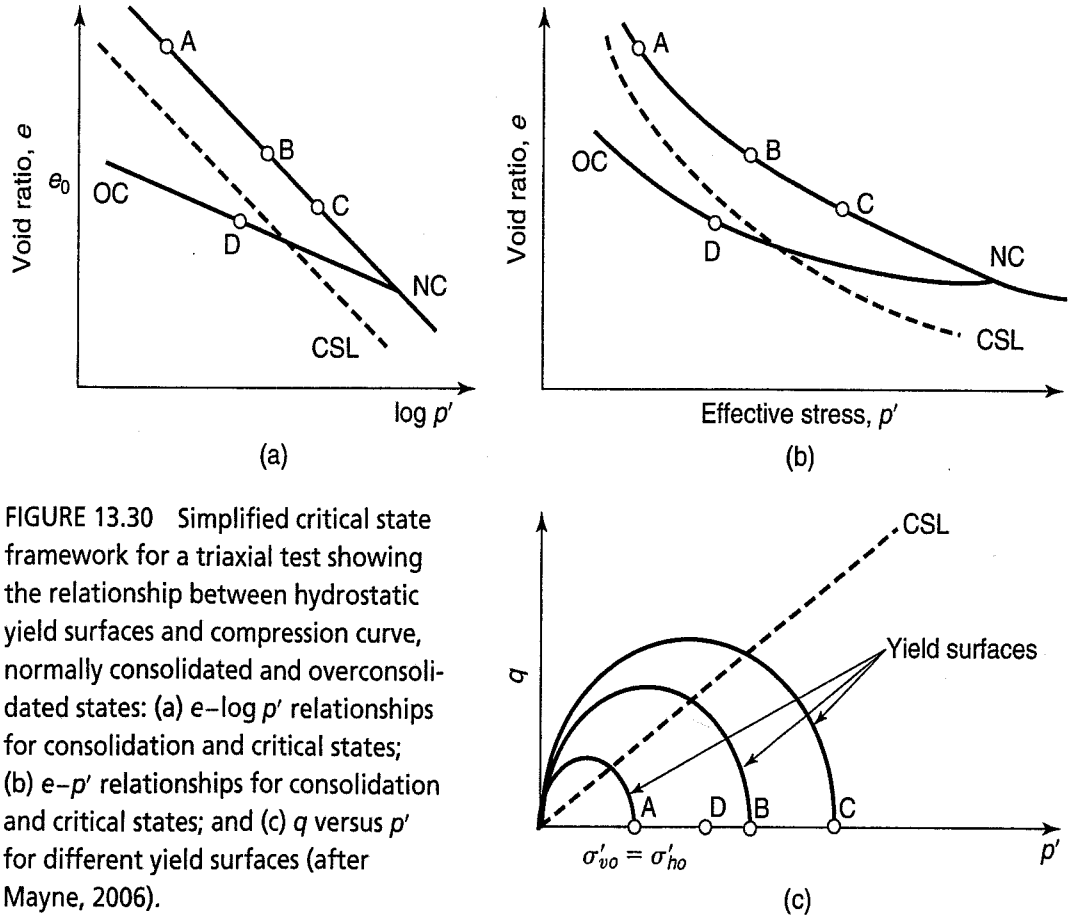

FIGURE 13.30 Simplified critical state framework for a triaxial test showing the relationship between hydrostatic yield surfaces and compression curve, normally consolidated and overconsolidated states: (a) e–log p' relationships for consolidation and critical states; (b) e–p' relationships for consolidation and critical states; and (c) q versus p' for different yield surfaces (after Mayne, 2006).

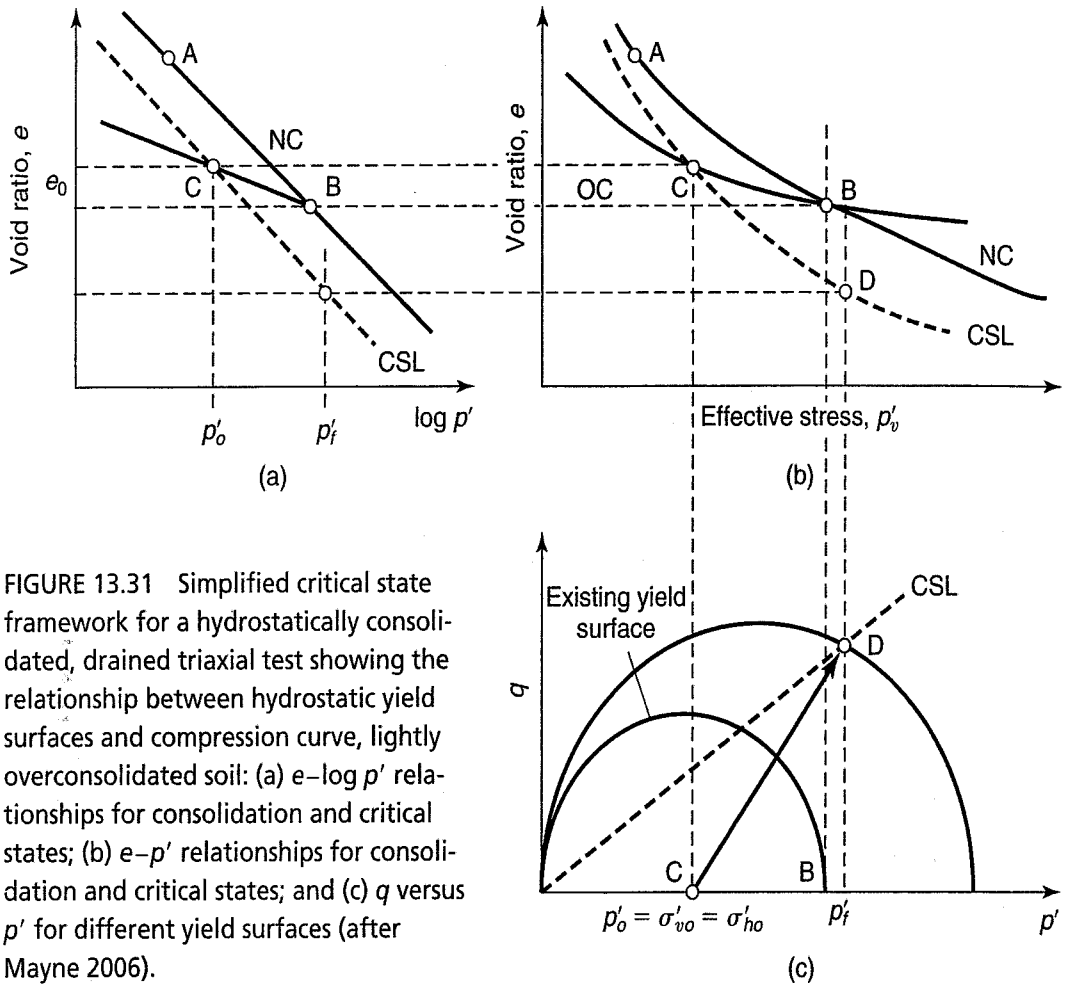

FIGURE 13.31 Simplified critical state framework for a hydrostatically consolidated, drained triaxial test showing the relationship between hydrostatic yield surfaces and compression curve, lightly overconsolidated soil: (a) e–log p' relationships for consolidation and critical states; (b) e–p' relationships for consolidation and critical states; and (c) q versus p' for different yield surfaces (after Mayne 2006).

Undrained tests will obviously behave very differently, since their yield surfaces are fixed by their preshear p'. Consider two hydrostatically consolidated, undrained triaxial tests, one normally consolidated and one heavily overconsolidated, shown in Fig. 13.32. The normally consolidated soil starts at a preshear state, point A. Since all of its deformation will be plastic, it will follow the yield surface up and to the left to point B on the CSL; this is consistent with the idea that normally consolidated soils contract or produce $\Delta u > 0$ during shear, and this is also seen in the e–log p' and e–p' spaces. In addition, a normally consolidated clay tends to strain harden, monotonically rising to failure as it climbs up the yield surface. For the heavily overconsolidated clay starting at point C in Fig. 13.32, the soil would climb up through the yield surface with resulting elastic strains and then fall to the CSL, where it would fail at point D. This is consistent with expected $\Delta u < 0$ during shear, and strain softening behavior after peak shear stress is reached.

So, how do we determine the yield surfaces (or yield curves in 2-D) for a particular soil? We can run tests following different stress paths, as shown in Fig. 13.33(a) or, as shown in Fig. 13.33(b), we can use different stress ratios. Both approaches will result in the same yield curve—i.e., the yield curve is independent of the stress path used to establish it (Leroueil et al., 1990).

An example of the second approach [Fig. 13.33(b)] is illustrated by some data obtained by Tavenas, Leroueil, and their coworkers at Université Laval using triaxial tests on samples of Laurentian clays from Saint-Alban, Quebec. Stress-strain and pore pressure-strain data at three different consolidation pressures on overconsolidated specimens from 3 m depth is shown in Fig. 13.34. Note that the strain at failure (at the maximum principal stress difference) is only about 1%, suggesting that this soil is highly structured, which is typical for Laurentian clays from Quebec.

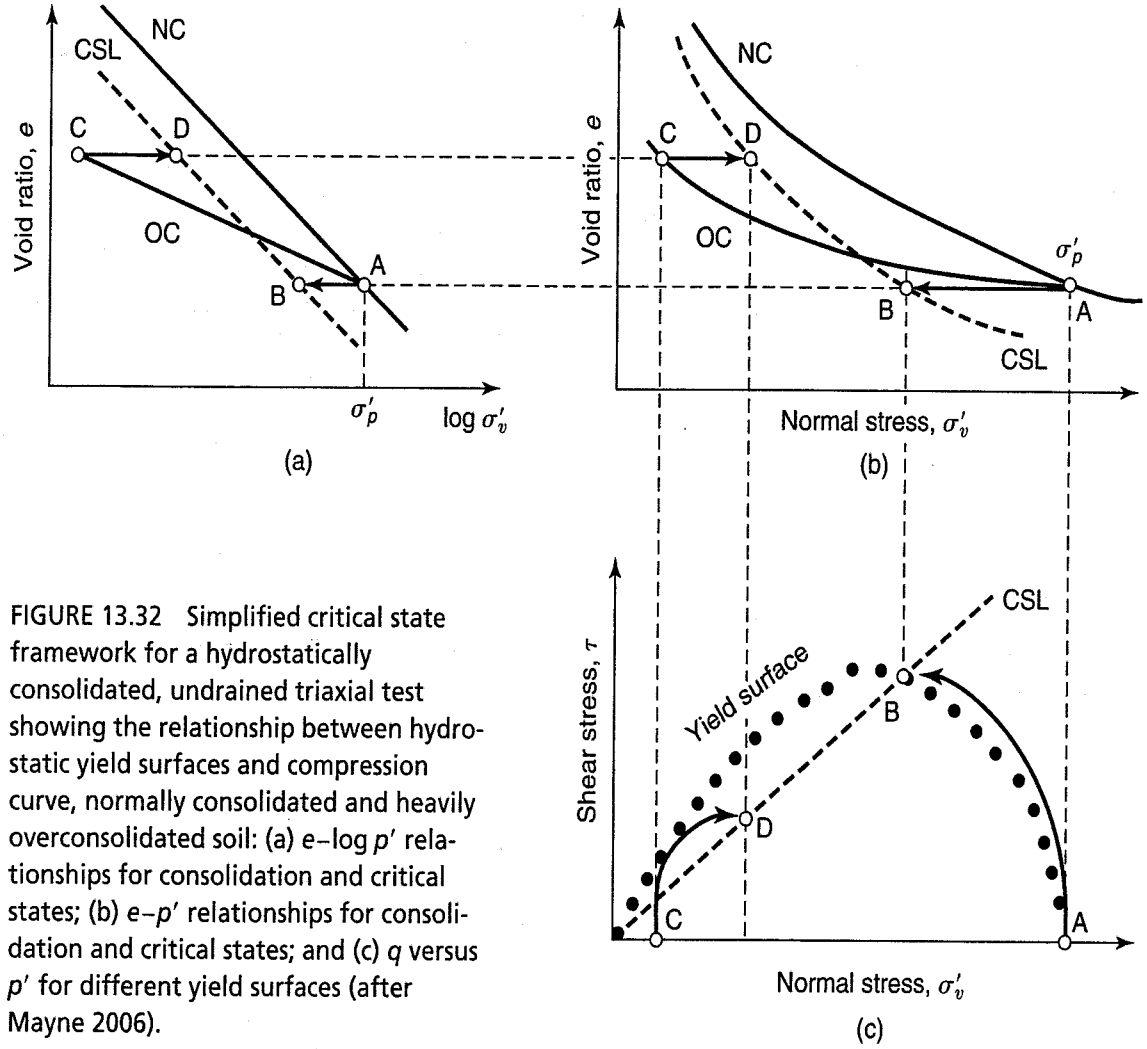

FIGURE 13.32 Simplified critical state framework for a hydrostatically consolidated, undrained triaxial test showing the relationship between hydrostatic yield surfaces and compression curve, normally consolidated and heavily overconsolidated soil: (a) e–log p' relationships for consolidation and critical states; (b) e–p' relationships for consolidation and critical states; and (c) q versus p' for different yield surfaces (after Mayne 2006).

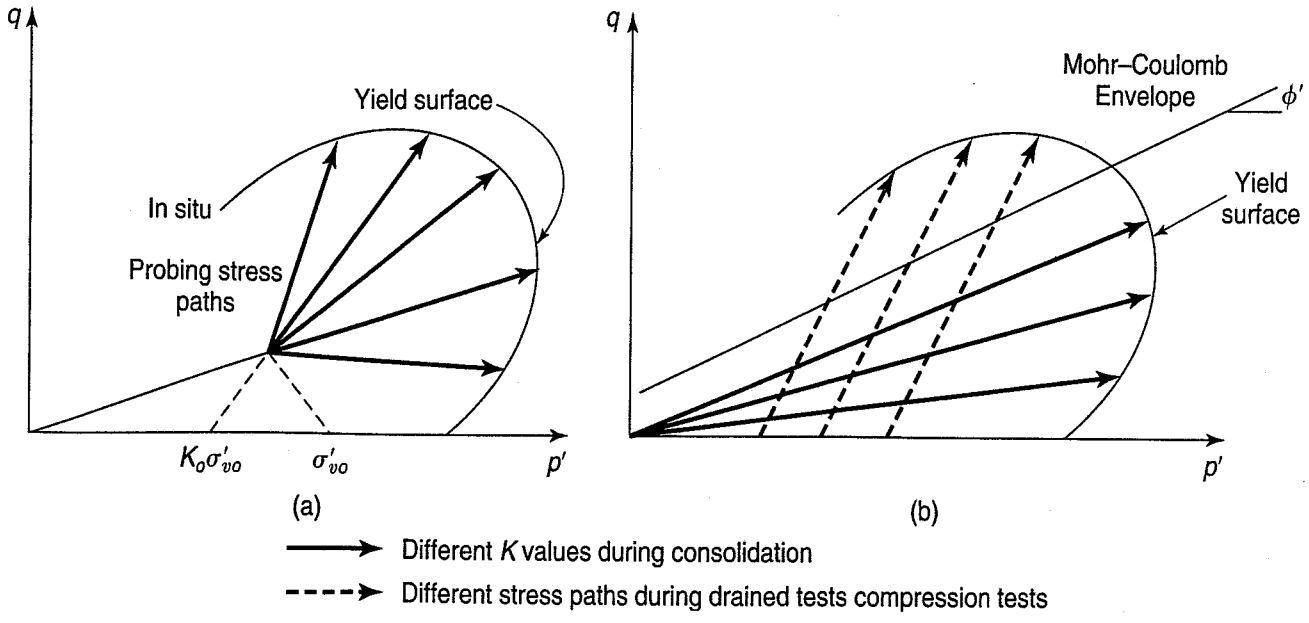

FIGURE 13.33 Determining the yield curves by (a) different stress paths, or (b) different stress ratios (Leroueil et al., 1990).

Stress paths for the three triaxial tests in Fig. 13.34 are shown in Fig. 13.35. The data are plotted with the MIT definition of p' (Sec. 13.2). Tests 1, 2, and 3 were conventional CU triaxial tests consolidated hydrostatically—that is, with the confining pressure held constant. From the shapes of the stress paths, you know that the clay was overconsolidated.

The yield curve in Fig. 13.35 was determined from peaks of the three stress-strain curves in Fig. 13.34 and from the yield points of four nonhydrostatic consolidation tests—that is, with the ratio $K = \sigma_3'/\sigma_1'$ held constant during consolidation, as shown in Fig. 13.36. The yield surface appears to be centered about the $K_{o\text{-}nc}$-line, with $K_o \approx 1 - \sin\phi'$ [Eq. (11.8)], rather than about the CSL line as would be predicted by the Cam clay model shown in Fig. 13.32. Note that at point A, the major principal effective stress $\sigma_1' \approx \sigma_p'$, as determined from 1-D consolidation tests. This suggests that a good estimate of the yield curve can be made from ordinary 1-D consolidation tests performed on high-quality samples.

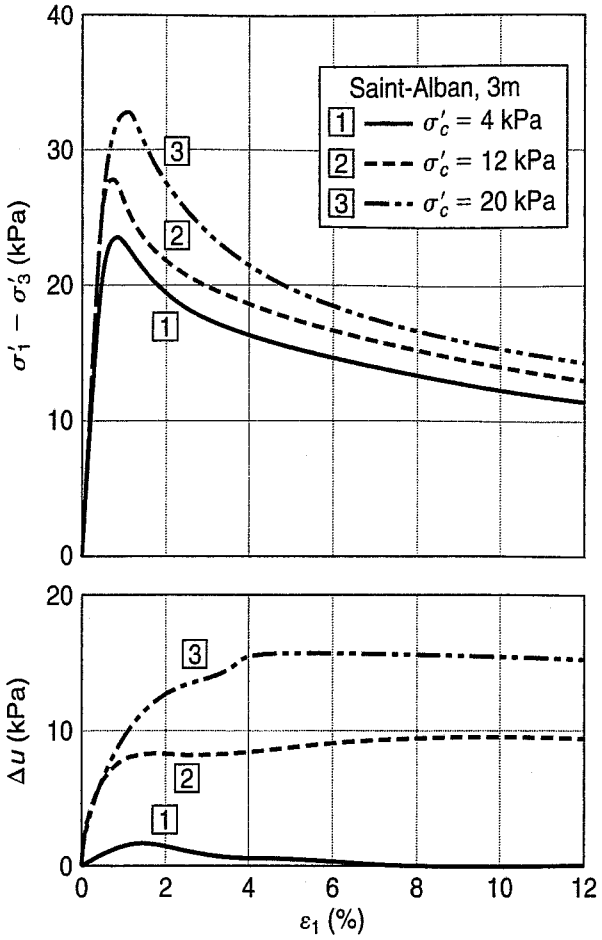

FIGURE 13.34 Stress-strain and pore pressure-strain curves (after Tavenas and Leroueil, 1977).

Yield curves obtained from specimens from three different depths of the Saint-Alban clay shown in Fig. 13.37 have a similar shape, so it may be possible to normalize the test results from the same deposit with respect to the preconsolidation pressure σ_p'. In fact, as shown by Leroueil et al. (1990), samples taken from different depths and consolidated under a cell pressure σ_c', such that the ratio σ_c'/σ_p' is constant, will have essentially the same $(\sigma_1' - \sigma_3')/\sigma_p'$ and $\Delta u/\sigma_p'$ versus axial strain relationships.

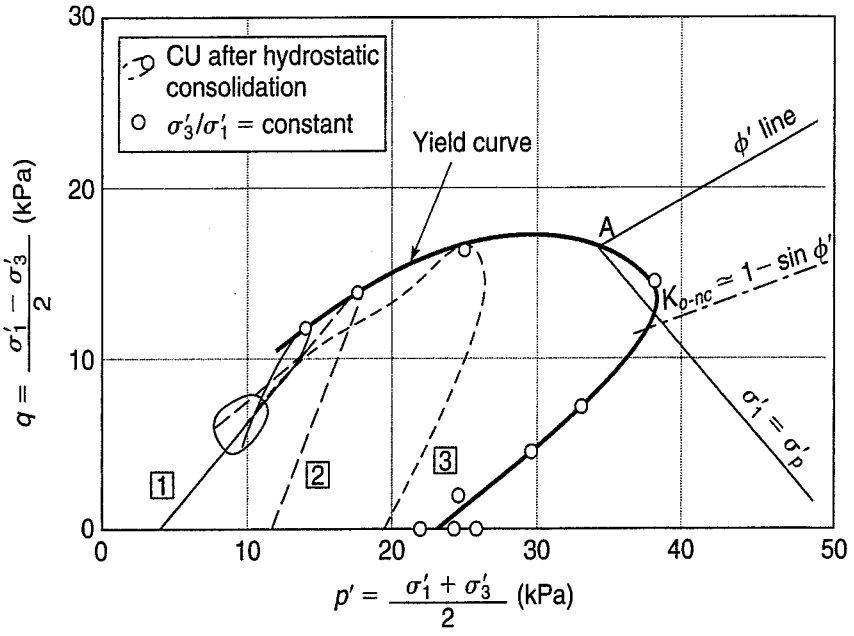

FIGURE 13.35 Yield curve for Saint Alban clay at 3 m; see text for description of the types of tests (after Tavenas and Leroueil, 1977).

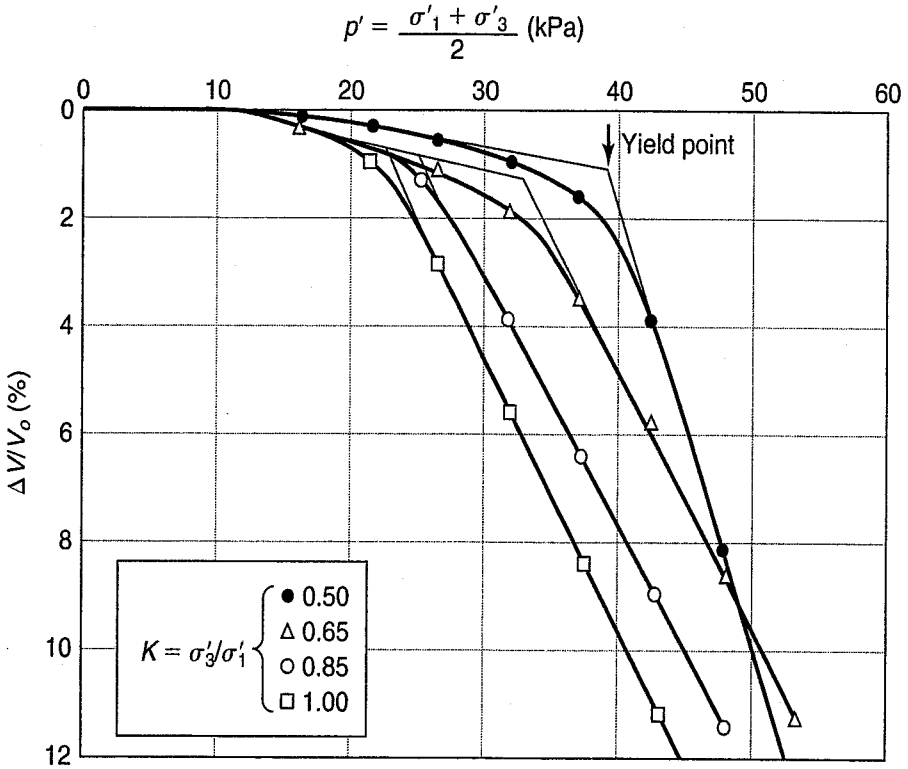

FIGURE 13.36 Volumetric strains from nonhydrostatic CU triaxial tests on St. Alban clay (after Tavenas and Leroueil, 1977).

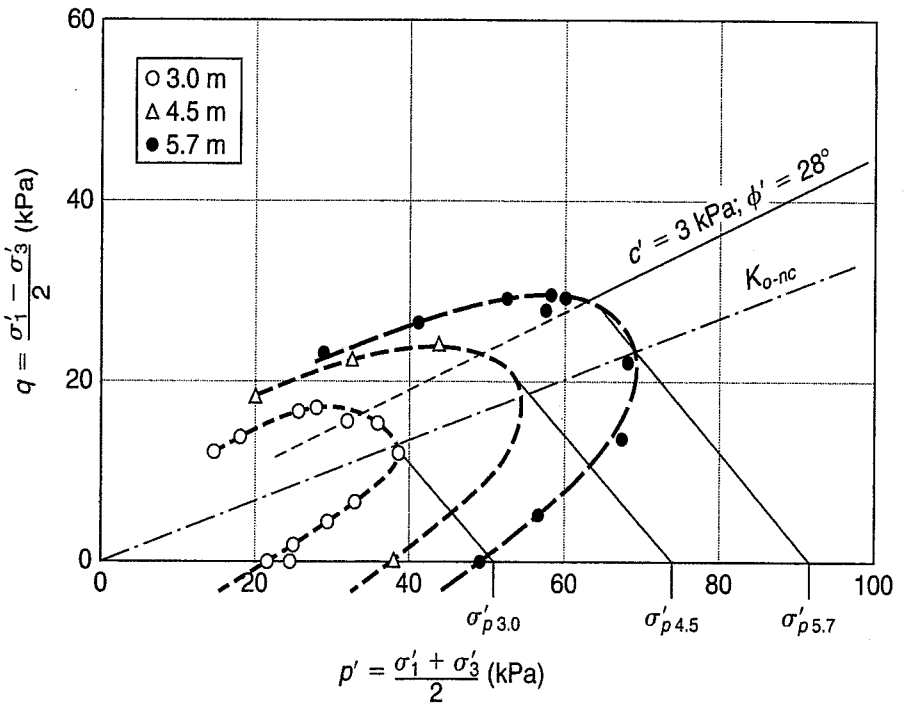

FIGURE 13.37 Yield curves for specimens of Saint-Alban clay obtained at different depths (after Tavenas and Leroueil, 1979).

Diaz-Rodríguez et al. (1992) presented normalized yield curves from tests on 17 natural soft clays of very different geologic origins, all normalized with respect to σ'_p, as shown in Fig. 13.38. The sources and geotechnical characteristics of these clays are given in Table 13.2. All yield curves had the same general shape as the yield surfaces of the Saint-Alban clay from Canada in Fig. 13.37, and they appeared to be centered about the $K_{o\text{-}nc}$-line, rather than about the CSL line as predicted by Cam clay.

When the specimens were hydrostatically consolidated, their yield stress $(\sigma'_Y)_{\text{hydrostatic}}$ depended on the preoconsolidation pressure. The ratio $(\sigma'_Y)_{\text{hydrostatic}}/\sigma'_p$ varied between 0.44 and 0.73 with an average

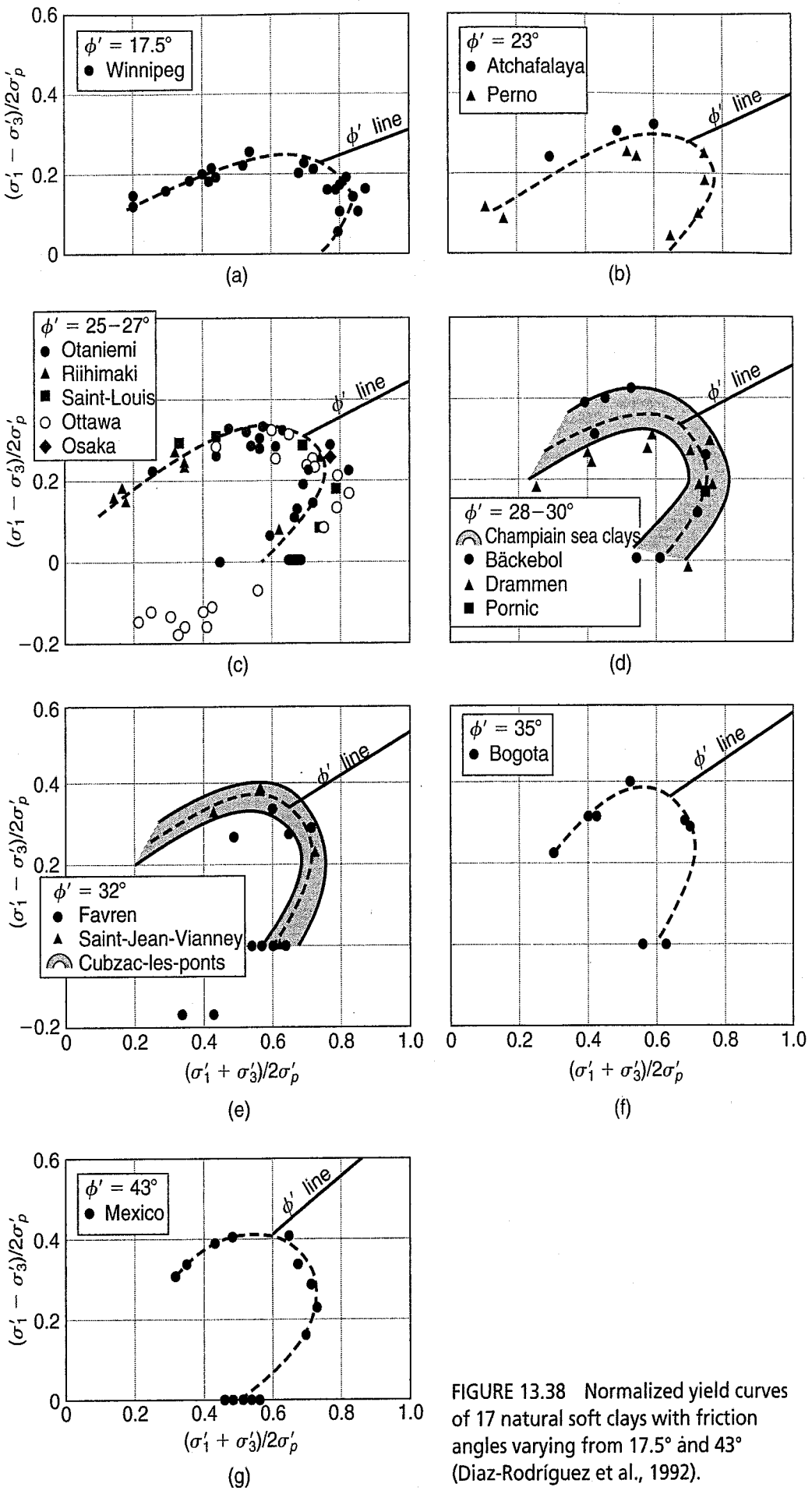

FIGURE 13.38 Normalized yield curves of 17 natural soft clays with friction angles varying from 17.5° and 43° (Diaz-Rodríguez et al., 1992).

TABLE 13.2 Geotechnical characteristics for the natural clays in Fig. 13.38 (Diaz-Rodriguez et al., 1992)

Site	Depth (m)	w (%)	PI	σ'_p (kPa)	ϕ'_{NC} (°)	Reference
Atchafalaya, Louisiana	21.3	58	44	150	23	Tavenas and Leroueil (1985)
Bäckebol, Sweden	3.4	87	42	57	30	Brousseau (1983), Tavenas and Leroueil (1985)
Bogotá, Colombia	7–12	90–160	100–170	150–255	35	Maya and Rodriguez (1987)
Champlain Sea clays, Quebec	—	58–90	17–45	50–290	27–30	Brousseau (1983)
Cubzac-les-Ponts, France	4.5–5.5	60–80	40	46–75	32	Magnan et al. (1982)
Drammen, Norway	—	52	29	—	30	Berre (1972), after Larsson (1977)
Favren, Sweden	—	60	—	70	32	Larsson (1977)
Mexico City, Mexico	1.7	460	493	71	43	Diaz-Rodriguez et al. (1992)
Osaka, Japan	30.0	63	—	330	25	Oka et al. (1988)
Otaniemi, Finland	2.0	130	63	20	25	Lojander (1988)
Ottawa, Ontario	—	65	36	150	27	Wong and Mitchell (1975)
Perno, Finland	4.2	100	39	22	23	Korhonen and Lojander (1987)
Pornic, France	1.2–2.0	75–88	40	35–45	29	Moulin (1988, 1989)
Riihimaki, Finland	4	55	25	90	27	Lojander (1988)
St. Jean-Vianney, Quebec	3.7	41	9	1150	32	Brousseau (1983)
St. Louis, Quebec	—	67	23	190	25	La Rochelle et al. (1981)
Winnepeg, Manitoba	8–12	54–63	35–60	190–380	17.5	Graham et al. (1983)

value of about 0.6. The ratio also tended to decrease as ϕ' increased. The position of the yield curve above the ϕ'_{nc}-line changes with the value of the friction angle and with the structure of the clay. The further the upper part of the yield curve tends to be above that line, the more highly structured it is. Also the height of this "hump" above the ϕ'_{nc}-line decreases with increasing sample disturbance. You will recall a similar "hump" in the Mohr failure envelopes for OC clays in both drained and undrained shear (see, e.g., Figs. 12.26 and 12.34). An extreme example of disturbance is complete remolding or *destructuring* of the clay. The effect on the shapes of the stress-strain curves is dramatic, as shown in Fig. 13.39, and of course the change is equally dramatic in the shapes of the yield curves, as shown by Tavenas and Leroueil (1985).

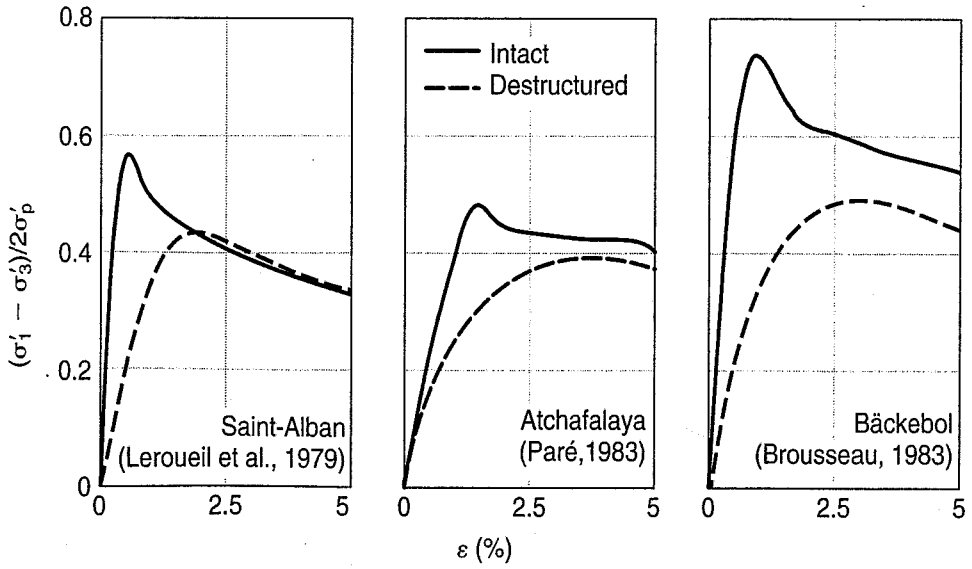

FIGURE 13.39 Stress-strain curves from hydrostatically consolidated CU tests on intact and destructured soft clays (Tavenas and Leroueil, 1985).

From this brief introduction, you can see that critical state soil mechanics is a powerful framework for describing soil behavior and predicting soil response under a variety of preshear and failure states. However, a number of textbooks, mostly by British authors, have appeared in recent years that provide additional information and applications of critical state soil mechanics to geotechnical problems. Recommended are Atkinson and Bransby (1978), Bolton (1979), Muir Wood (1990), Aziz (2000), Powrie (2004), Atkinson (2007), and Budhu (2007).

13.8 MODULUS AND CONSTITUTIVE MODELS FOR SOILS

Several times in Chapters 8, 10, 11, and 12 we mentioned that soils and rocks were often simply assumed to be elastic, and that this assumption was important for settlement analyses (stress distributions and immediate settlement in Chapter 10) and in our discussion of the stress-deformation characteristics of geo-materials (Chapters 11 and 12). We also occasionally mentioned the modulus of a soil, either a compression modulus or a Young's modulus. You may recall from your courses in strength of materials that the modulus is the slope of the stress-strain curve. Sometimes the modulus of a material is called its stiffness. We showed several different types of stress-strain curves in Fig. 11.4. If the stress-strain curve is linear, obtaining the modulus or stiffness is easy, but how is the modulus determined on a nonlinear curve?

We begin with a detailed discussion of soil modulus, its definitions, and how it is measured or estimated. Soil modulus is part of what are known as constitutive relations in solid mechanics. Constitutive modeling of soils and rocks has become increasingly important in recent years, because many geotechnical projects require deformation predictions in addition to conventional analyses of potential failure and factors of safety. Well-calibrated soil constitutive models are required to make reliable predictions of deformations. We end this section with a brief description of the hyperbolic (Duncan–Chang) nonlinear soil model, because it is commonly used in geotechnical practice.

13.8.1 Modulus of Soils

Although there are a number of ways to describe the modulus of a material, all are basically the ratio of stress increment to strain increment (or the slope) over a particular range of the stress-strain relationship for that material. Figure 13.40 shows some definitions of modulus that include:

- *Tangent modulus*: slope of the tangent to the stress-strain curve at any point; an important modulus shown in Fig. 13.40(a) is the *initial tangent modulus* (E_i or E_t).
- *Secant modulus*: slope of a straight line drawn from the origin to some predetermined stress level, such as 50% of the maximum stress; a chord modulus is the slope of a straight line between any two points on the curve. Figure 13.40(a) shows examples of both tangent and secant moduli.
- *Cyclic loading-related moduli*: when there is an unload-reload cycle, the modulus may be defined by drawing a tangent from the lower bound stress on either the unload or reload portion, or by connecting the end points of the hysteresis loop, as shown in Fig. 13.40(b). The hysteresis loop modulus is sometime called the *unload-reload modulus* E_{ur}.

Besides the loading condition, other factors that influence modulus include (1) for granular materials, particle packing (as measured by the dry density, void ratio, and/or relative density, and may include the influence of compaction), and (2) for cohesive soils, water content, plasticity index, stress history, and cementation (Briaud, 2001). It is sometimes difficult to generalize about the effect each of these factors has on modulus. For example, while dry density tells us something about the packing of the particles, it cannot be assumed that soils with the same dry density will have the same modulus. The two soils may have very different structures or fabrics (e.g., flocculated versus dispersed—Chapter 4) and thus they will have very different modulus values. Another example is the effect of water content. While higher water content tends to indicate a lower modulus, this assumption would be invalid for some compacted soils as well as high water content clays that are cemented or highly structured.

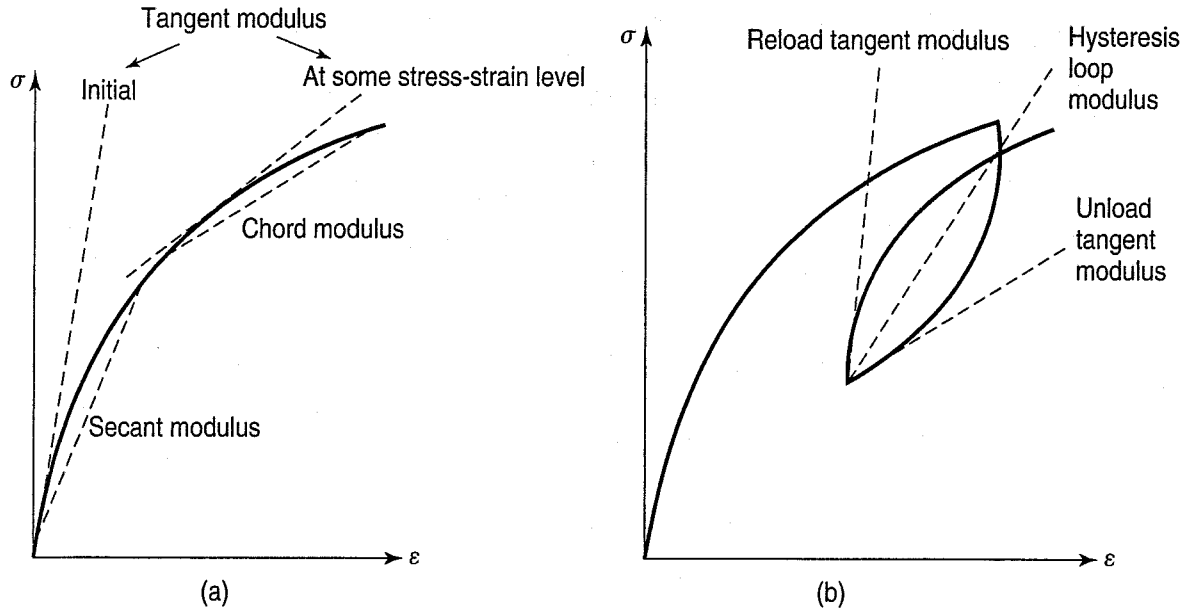

FIGURE 13.40 Definitions of soil modulus for various loading and unloading conditions: (a) tangent, secant, and chord modulus; (b) cyclic loading moduli (after Briaud, 2001).

Note also that all of the moduli shown in Fig. 13.40 can be either drained or undrained, depending on the drainage aconditions in the field or in the laboratory. When specifying or reporting modulus values in practice, it is important to clearly state what drainage conditions apply. For example, when using elastic theory to estimate the immediate settlement (Sec. 10.4) of fine-grained soils, because the immediate settlement takes place before any consolidation can occur, the appropriate modulus is the *undrained modulus* E_u. For granular soils, the appropriate modulus for settlement analyses is of course a *drained modulus* E_d.

Measurement of Modulus You might think that a particular modulus can be easily determined from the stress-strain curve obtained by a triaxial or other type of shear test. However, as mentioned in Sec. 11.6, obtaining undisturbed samples of granular soils is not easy or inexpensive. Consequently, granular soil moduli are most commonly determined from empirical correlations with in situ test results.

As for cohesive soils, many researchers have shown that the undrained modulus is significantly affected by sample disturbance. Mostly the disturbance tends to reduce the undrained modulus E_u, and thus you would tend to overpredict the immediate settlements in the field. Because other factors also affect the undrained modulus in laboratory tests (D'Appolonia et al., 1971b; Simons, 1974), field loading tests are sometimes used for important projects. From settlement measurements, the modulus is back calculated using elastic theory (Chapter 10). Load tests have shown that stress level is a very important factor that strongly affects E_u. For example, large-scale loading tests carried out in Norway, Canada, and Sweden (Höeg et al., 1969; Tavenas et al., 1974; and Holtz and Holm, 1979) showed very little settlement, because the load was applied rapidly. However, when about one-half the failure load was reached, the settlements started to rapidly accelerate as the load was increased. Thus the back-calculated E_u values were very dependent on the level of the shear stress applied by the surface load.

Because of the difficulties mentioned above, other techniques and procedures have been developed for estimating the modulus of soils.

Small Strain Stiffness Burland (1989) showed that under service loading conditions, the strains experienced by the foundation material can be very small. Measurements on full-scale foundations have indicated that strains are less than 0.01%, and the stress-strain behavior is remarkably linear and

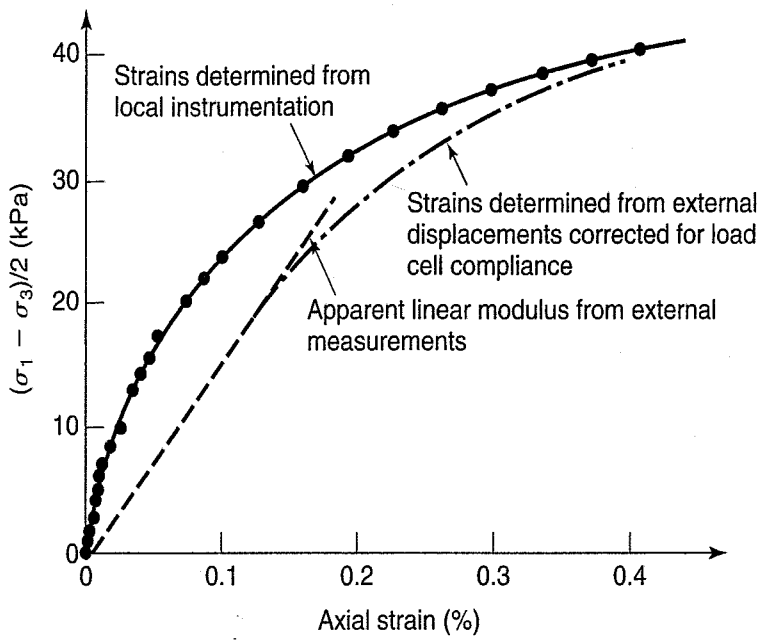

FIGURE 13.41 Initial stress-strain behavior from unconsolidated undrained triaxial test on London Clay—internal versus external strain measurements (Jardine et al., 1985).

recoverable (i.e., elastic) with only a small amount of hysteresis. Unfortunately, measurement of small strains and therefore soil stiffness in laboratory specimens is impossible in conventional triaxial tests with axial strain measurements (dial indicators or linear variable differential transducers—LVDTs) that determine the overall deformation of the specimen. Figure 13.41 shows the dramatic differences in stress-strain behavior between strain measurements from instruments mounted internally on the soil specimen and those from external displacement sensors in the same triaxial test. The strains have to be measured locally, and ignoring the errors caused by external strain measurement can lead to significant under-estimation of modulus and soil stiffness.

Local strain measurement techniques on triaxial and hollow cylinder tests include the use of miniature LVDTs, noncontact proximity transducers, Hall-effect sensors, and flexible beams with strain gages (Scholey et al., 1995). Santagata et al. (2005) attached miniature displacement transducers to the specimen, while O'Kelly and Naughton (2008) used noncontact proximity sensors that sense the position of targets on the specimen. Hall-effect transducers that measure magnetic field changes were used by Clayton and Khatrush (1986), and Rechenmacher and Finno (2004) successfully used image analysis techniques for local strain measurements.

Regardless of the method used, the local strain sensing device has to be mounted directly on the soil specimen inside the triaxial cell, but submerged electrical devices and risk of leakage pose major technical challenges. However, with special techniques and precision testing equipment, it is possible to make extremely small and precise strain measurements. For example, Fig. 13.42 shows the time history of the stress, strain, and excess pore pressure variation from a strain-controlled cyclic triaxial test on Ottawa sand with a strain amplitude of less than 0.001%. The tests were performed in a device developed by Huang et al. (1994) that has an extremely high resolution stepper motor and preloaded ball screw to provide the driving force, and uses noncontact proximity transducers for local strain measurements.

Because of the strong international interest in small strain stiffness, five international conferences on prefailure deformation of geomaterials have taken place since 1994 (for example, Burns et al., 2008). Their emphasis has been on small-strain laboratory and field modulus measurements, and their use in analytical methods.

One method for making small-strain laboratory modulus measurements that has gained popularity in recent years is the use of *bender elements*. Bender elements are polarized, piezoceramic elements that are essentially cantilevers used in pairs. One element is used for transmitting a mechanical shear wave through the soil by electrical charge excitation, and the other one receives the resulting wave at

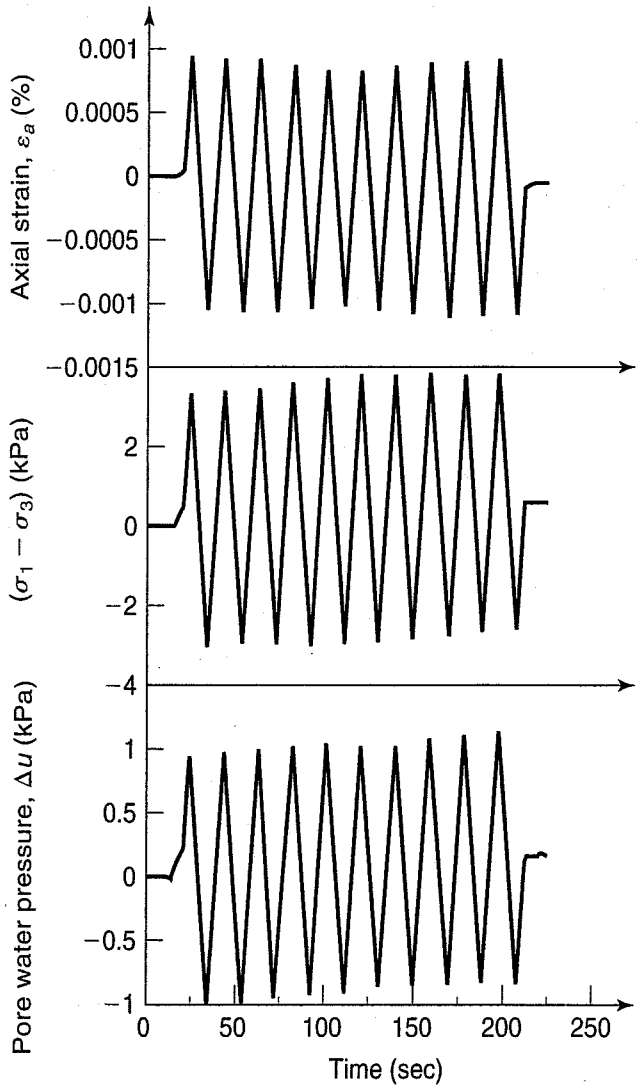

FIGURE 13.42 A time history of stress, strain and excess pore pressure from a cyclic triaxial test on Ottawa sand (A. B. Huang, personal communication, 2008).

some distance from the transmitting element and converts it into an output electrical signal. This allows the shear wave velocity V_s to be computed, which can be used to compute the small strain shear modulus G_{max}, or

$$G_{max} = \rho_t V_s^2 \qquad (13.24)$$

where ρ_t = the total density of the soil through which the shear wave is transmitted.

In the field, the most common tool for determining shear modulus is the seismic cone penetration test (Lunne et al., 1997). After the cone is penetrated to the desired testing depth, the arrival time of a surface-generated shear wave is detected at that depth. This information can be used to compute the V_s and G_{max}. Shear wave velocity and shear modulus are discussed in more detail in Sec. 13.15.

Estimates of Modulus Based on Other Properties Because of all the problems with laboratory and in situ modulus measurements, correlations of the modulus with a classification or other property that is more easily measured have been developed for cohesive as well as granular soils.

1. *Cohesive soils*: It is quite common in practice to assume that E_u is somehow related to the undrained shear strength. For example, Bjerrum (1972) said that the ratio E_u/τ_f ranges from 500 to 1500, with τ_f determined by the field vane shear test. The lowest value is for highly plastic clays, while the highest is for clays of lower plasticity. D'Appolonia et al. (1971b) reported an average E_u/τ_f of 1200 for load tests at 10 sites, but for the clays of higher plasticity the range was 80 to 400. Simons (1974) found published values ranged from 40 to as high as 3000! These cases plus a few others we have taken from the literature are plotted versus PI in Fig. 13.43 for softer clays—stiff fissured soils and glacial tills are not included. There is much scatter for PI < 50 and not much data for PI > 50. It seems reasonable to simply use Bjerrum's recommendation (E_u/τ_f = 500 to 1500) especially for preliminary estimates of E_u. See also Sec. 10.4. If you need a good estimate of the undrained modulus, see D'Appolonia et al. (1971b) and Holtz (1991).

Ladd et al. (1977) also showed how E_u/τ_f varies with OCR, but the relationship is not so simple because, as we mentioned earlier, E_u/τ_f depends so strongly on the level of shear stress. In general, however, it decreases with increasing OCR for a given stress level (Fig. 13.44).

Kulhawy and Mayne (1990) recommended a hyperbolic stress-strain model (Sec. 13.8.5) for foundation design and for estimating tangent modulus values for cohesive soils. They provided a range of undrained modulus values for clay, as shown in Table 13.3, normalized by atmospheric pressure (i.e., multiply these dimensionless values by 14.7 psi or 101.3 kPa).

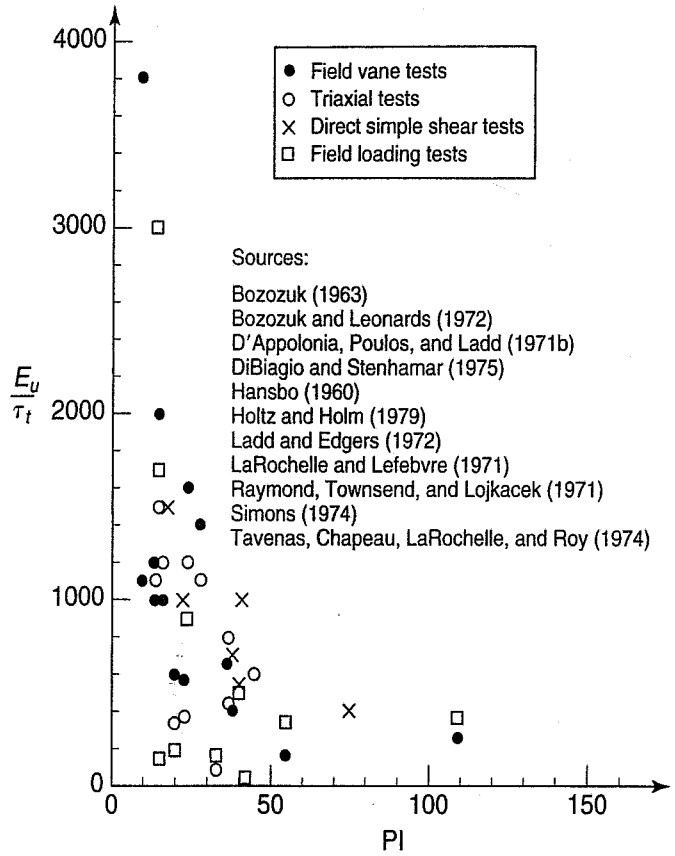

FIGURE 13.43 The ratio E_u/τ_f versus plasticity index, as reported by several authors.

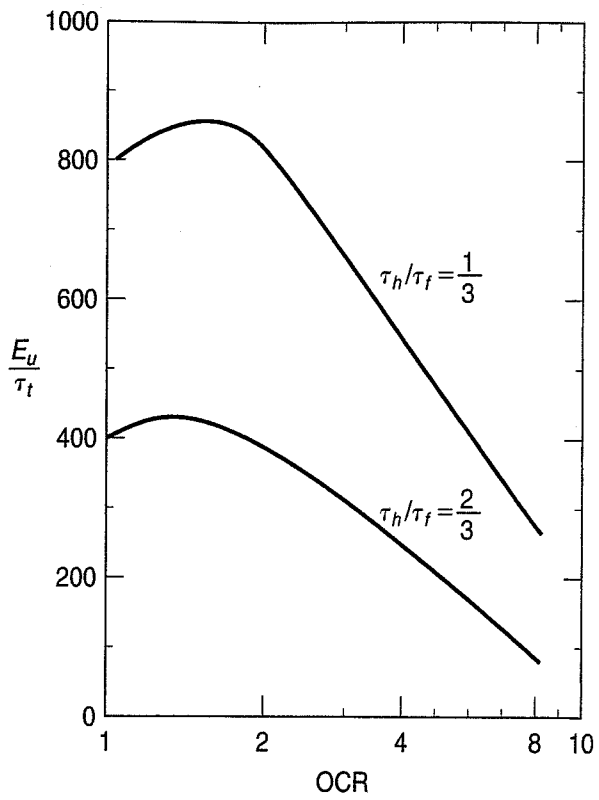

FIGURE 13.44 Effect of OCR on E_u/τ_f from direct simple shear tests on Bangkok clay (after Ladd and Edgers, 1972, and Ladd et al., 1977).

TABLE 13.3 Typical Ranges of Undrained Modulus for Clay

Consistency	Normalized Undrained Modulus, E_u/p_a
Soft	15 to 40
Medium	40 to 80
Stiff	80 to 200

After Kulhawy and Mayne (1990).

Ladd et al. (1977) showed E_u values from direct simple shear tests for cohesive soils with varying plasticity indices (PI) at different shear stress levels (τ_h) relative to undrained shear strength, τ_f [Fig. 13.45(a)], and relative to overconsolidation ratio (OCR) as given in Fig. 13.45(b) and (c). Duncan and Buchignani (1976) suggested the plot shown in Fig. 13.46 to unify E_u/τ_f, PI, and OCR in a generalized plot.

2. *Granular materials*: Since undrained conditions exist only for very short periods in granular deposits, the drained modulus (E_d) is appropriate. Table 13.4 shows the relationship between density classification and range of E_d, again normalized by atmospheric pressure.

As noted in Secs. 11.6 and 12.11.4, in situ tests are probably best for sandy deposits, although they provide only an indirect measurement of modulus. Probably the most common methods to determine E_d in the field are the SPT and CPT, although, as concluded by Kulhawy and Mayne (1990), correlations between the blowcount N and E_d show "considerable scatter."

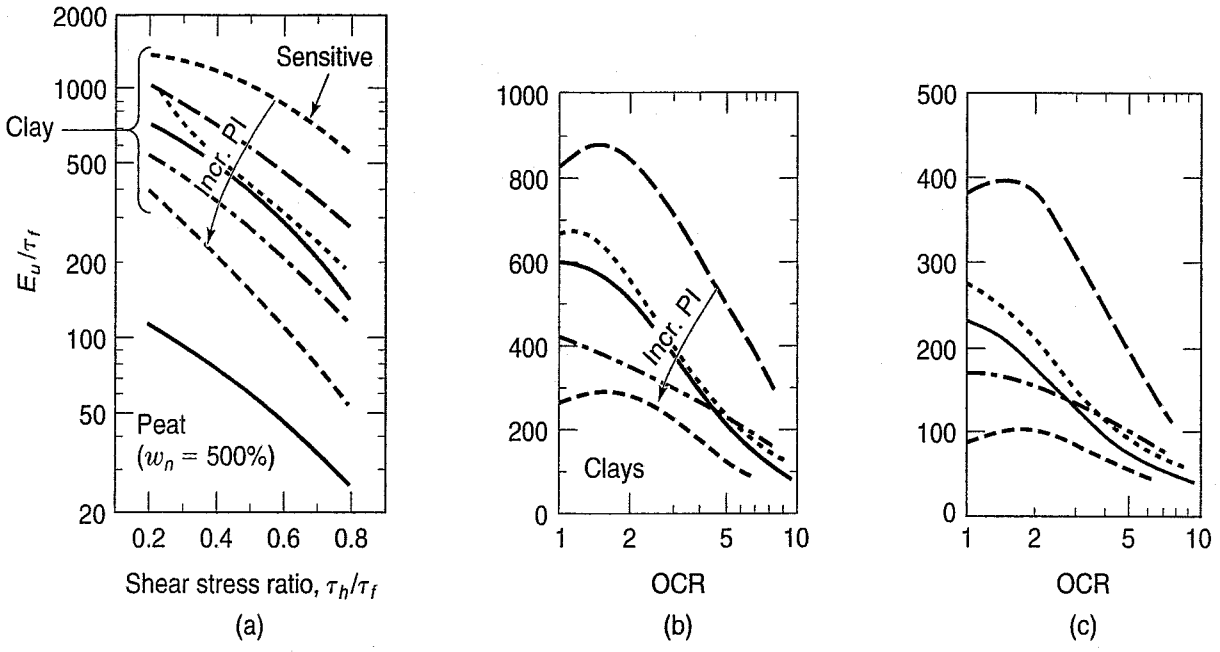

FIGURE 13.45 Relationships among normalized modulus (E_u/τ_f), PI and OCR from direct simple shear tests (from Ladd et al., 1977): (a) E_u/τ_f versus applied shear stress level (τ_h/τ_f) for soils of various PIs; (b) E_u/τ_f versus OCR at τ_h/τ_f = 1/3, various PIs; (c) E_u/τ_f versus OCR at τ_h/τ_f = 2/3, various PIs (after Kulhawy and Mayne, 1990).

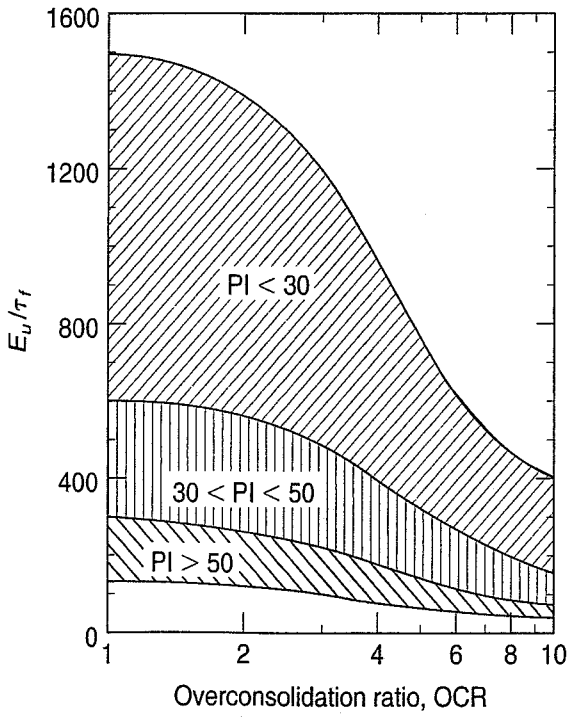

FIGURE 13.46 Generalized relationship among normalized modulus (E_u/τ_f), PI, and OCR (after Duncan and Buchignani, 1976).

TABLE 13.4 Typical Ranges of Drained Modulus for Sand

Density Classification	Normalized Drained Modulus, E_d/p_a
Loose	100 to 200
Medium	200 to 500
Dense	500 to 1000

After Kulhawy and Mayne (1990).

13.8.2 Constitutive Relations

Although the process is not usually mentioned in undergraduate mechanics courses, basically all problems in solid or continuum mechanics are solved by starting with the body forces (usually gravity) and surface forces and tractions acting on the body, which are connected by the equations of equilibrium. Next we consider the displacements and strains in the body. They are connected by geometric or

compatibility relationships that insure that the body remains continuous. All of this is valid for all materials, whether elastic or plastic including soils, as long as they behave as a continuum. In Sec. 6.9 on effective stress, we mentioned that even though they are particulate media, finer grained soils especially are often assumed to be a continuum and thus can be treated as a solid body.

In order to predict strains (and thus deformations) from the applied stresses (and forces), we need some sort of connection or association between them that represents the mechanical behavior of the material. Because the constituents of the material affect its behavior, the mathematical equations expressing the connection between stress and strain are called *constitutive relations*.

How do we determine the constitutive relations for real materials? As you can guess, the real behavior is very complex, and it is almost impossible to consider all factors that might influence their mechanical behavior. We can imagine that the response of a material to applied stresses depends on their magnitude, time over which they act, temperature of the body, stress and strain history, and maybe even the material's response to different electrical fields or chemical environments. Attempts to determine the constitutive relationships of a material based on the statistical mechanics of its elementary particles or the micromechanics of the constituent components have not yet been successful.

So, we are left with determining these relations experimentally, and then developing simple but reasonable mathematical models of mechanical behavior that can be used to solve engineering problems. This type of constitutive model is a called a *phenomenological* model. Phenomenological models are consistent with fundamentals of solid mechanics and soil behavior, but they lie somewhere between the theoretical and empirical. They are the most common type of constitutive model, although they must be calibrated and adjusted by curve-fitting experimentally observed behavior. *Constitutive modeling* refers to the mathematical expression of the assumed or calibrated stress-strain relationship used to describe the behavior of soils.

13.8.3 Soil Constitutive Modeling

The complexity of real material behavior means that we must use approximations or idealizations in order to formulate the mathematical expressions for constitutive relations. We mentioned several times in Chapters 8, 10, 11, and 12 that soils and rocks are often simply assumed to be linearly elastic, even though we know they truly are neither linear nor elastic. Other examples of ideal material behavior include nonlinear elasticity, linear visco-elasticity, elasto-plasticity, and other composite material models.

As noted by Muir Wood (2004), the key to successful constitutive modeling is to identify the important characteristics of soil behavior for a particular application. If the model is too simple, it will miss the important behavior characteristics, but if it is too complex with many parameters, then it requires too many laboratory or in situ tests to define those material parameters. For virtually all useful soil constitutive models, closed-form solutions for strains and deformations are impossible except for very simple loading and boundary conditions. Therefore for the vast majority of geotechnical problems, numerical analysis such as the finite element method is required to obtain approximately correct solutions.

The critical state soil mechanics (CSSM) framework presented in Sec. 13.7 was a very important development in soil modeling, since it described the relationship between void ratio (e), shear stress (q), and effective normal stress (p') for a number of loading paths, including drained (varying e) and undrained (constant e) conditions. We can trace CSSM's ideas to common conceptual roots with the more simplistic, but practical Peacock diagram described in Sec. 12.4 (Fig. 12.11) and Sec. 13.10. CSSM initiated some 30 years of constitutive model development for soils, including the Cam clay model and its offspring, modified Cam clay (in which the bullet-shaped yield surface of Cam clay was replaced by an elliptical yield surface; Roscoe and Burland, 1968), which moved soil modeling beyond relatively simple failure criteria and linearly elastic stress-strain behavior. However, since CSSM models are

elasto-plastic, they still lack many of the crucial shear stress-strain-strength characteristics of real soils, as we showed with the real soil data at the end of Sec. 13.7.

Since the early 1970s, soil constitutive models have been developed that have become increasingly more sophisticated and complex. Along with the concurrent dramatic increases in readily available computing power, they were increasingly incorporated in numerical analyses of large-scale geotechnical problems. Perhaps the most important development in some of the newer models is their ability to integrate more subtle transitions from elastic to plastic soil behavior, as well as viscous (i.e., time-dependent) components of that behavior. Some models also included common soil behavior characteristics such as anisotropy and loading direction, which in turn allowed their use in modeling behavior measured in more advanced testing devices and more complex field situations. However, considering more complex behavioral characteristics requires more materials properties to be determined by laboratory or in situ tests, and these are quite costly. Thus in practice, when more advanced soil modeling techniques are employed, parametric analyses are commonly performed using a wide range of material properties determined from correlations with classification and in situ test data rather than from expensive sampling and laboratory tests.

For further information on constitutive modeling, see Perloff and Baron (1976) for a simple introduction to linear elasticity and linear visco-elasticity models, while Muir Wood (2004) presents an introduction to constitutive modeling with a description of elastic, elastic-perfectly plastic, and elastic-hardening plasticity models that include extended Mohr–Coulomb and Cam clay. See Aziz (2000) for details about Cam clay and modified Cam clay; he also provides a brief but useful analysis of the shortcomings of these popular soil models.

Other useful references include Fung (1965), Yong and Ko (1980), Chen and Saleeb (1982), Chen and Baladi (1985), and Chen (1994).

This section will first explore the different failure criteria for soils, one of which you are already very familiar with, the *Mohr–Coulomb criterion*. After this, different classes of models will be described to give an idea of how this area has evolved since CSSM arrived on the scene.

13.8.4 Failure Criteria for Soils

A common requirement for all soil models is the existence of a failure criterion. Such criteria are generally divided into one- and two-parameter types, depending on the number of parameters used in their definition. For the simplest assumption of an isotropic soil with only principal stresses acting on the soil element, these criteria are typically defined for a three-dimensional state of stress consisting of the major, intermediate, and minor principal stresses on the soil (σ_1, σ_2, and σ_3, respectively). Failure occurs when, for a given normal stress, the deviator or shear stress on a soil element increases to some state defined as failure for that element. It turns out that failure criteria for soils, including the Mohr–Coulomb (Secs. 11.4 and 13.14), can be defined in terms of their *octahedral normal stress* (the average or mean hydrostatic stress)

$$\sigma_{oct} = \tfrac{1}{3}(\sigma_1 + \sigma_2 + \sigma_3) \tag{13.16}$$

and the *octahedral shear stress* (an average of the possible shear stresses on the element)

$$\tau_{oct} = \tfrac{1}{3}[(\sigma_1 - \sigma_2)^2 + (\sigma_2 - \sigma_3)^2 + (\sigma_3 - \sigma_1)^2]^{1/2} \tag{13.17}$$

As Fig. 13.47 shows, the stress state $P(\sigma_1, \sigma_2, \sigma_3)$ for a soil element with only principal stresses acting on it (as is the case for, say, the triaxial test), can be depicted using a vector representation that brings this stress state into a two-dimensional representation with a position vector OP that has a hydrostatic component $\xi = \sqrt{3}\,\sigma_{oct}$ and a deviatoric component normal to the hydrostatic axis, $\eta = \sqrt{3}\,\tau_{oct}$ (McCarron and Chen, 1994).

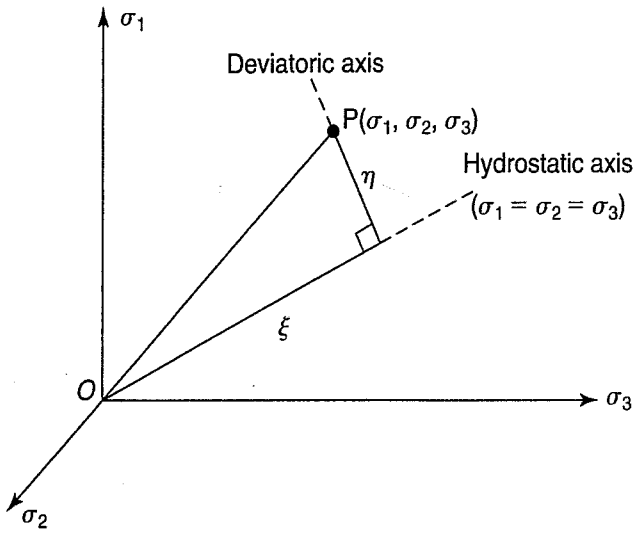

FIGURE 13.47 Three-dimensional representation of the stress state in principal stress space (after McCarron and Chen, 1994).

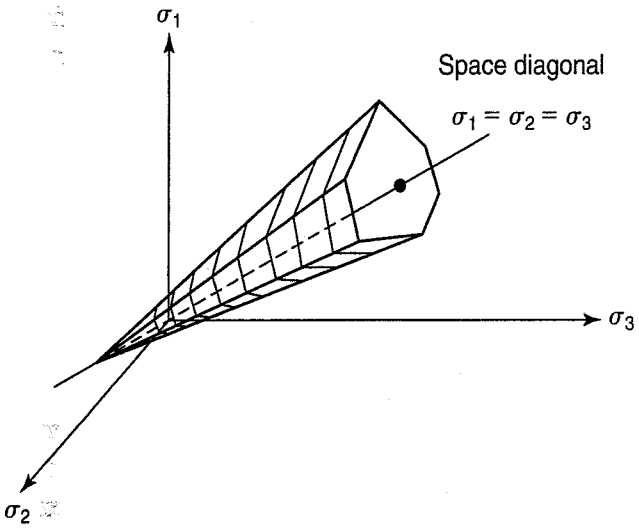

FIGURE 13.48 Mohr–Coulomb criterion in three-dimensional principal stress space (McCarron and Chen, 1994).

The one-parameter failure criteria include maximum shear stress models, the Tresca criterion and von Mises criterion, which are independent of hydrostatic stress and therefore are symmetric about the hydrostatic axis. The Tresca failure envelope is a six-sided prism, while the von Mises envelope is a cylinder. You know that soil shear strength is strongly dependent on applied normal stress, so these failure criteria are not particularly useful for soils, but they introduce us to the idea of three-dimensional failure criteria. The other one-parameter failure criterion is the Lade–Duncan model (Lade and Duncan, 1975), which has been used to describe the strength of cohesionless soils ($c = 0$). Because the strength is defined using a linear dependence on η (McCarron and Chen, 1994), it is useful for depicting sand behavior that is dependent on friction angle, ϕ'.

Two-parameter failure criteria are more common for a general representation of shear strength in geologic materials, and the most common among these is the Mohr–Coulomb criterion. We have shown this thus far only in two-dimensional, τ–σ space. A more generic, three-dimensional view is given in Fig. 13.48, which shows that the actual Mohr–Coulomb surface is a six-sided conical prism that expands with increasing hydrostatic stress. The prism reaches an apex either at the origin (in the case of cohesionless materials) or at some point along the hydrostatic axis where ($\sigma_1 = \sigma_2 = \sigma_3 < 0$) for cohesive soils. The Drucker–Prager criterion, also known as the extended von Mises criterion, has a true conical shape; i.e., if you slice this surface normal to the hydrostatic axis at a given η value [refer to Fig. 13.49(a) for the 3-D representation, and Fig. 13.49(b) for the 2-D representation], a circular shape is obtained.

A third, common, two-parameter criterion used for geologic materials is the Lade two-parameter criterion (Lade, 1977). This was fundamentally an extension of the Lade–Duncan one-parameter criterion, used primarily for sands, but introduced a curvature to the failure surface as hydrostatic stress increases, accounting for the nonlinear relationship between normal and shear stress at higher stress levels in cohesionless soils.

One other failure criterion is the Matsuoka–Nakai criterion (Matsuoka and Nakai, 1977). This is a perfectly plastic model, so that the fixed yield surface is the same as the failure surface. It corresponds to the Mohr–Coulomb model for axisymmetric stresses, and in 3-D problems has a smooth surface, which is advantageous from a computational point of view.

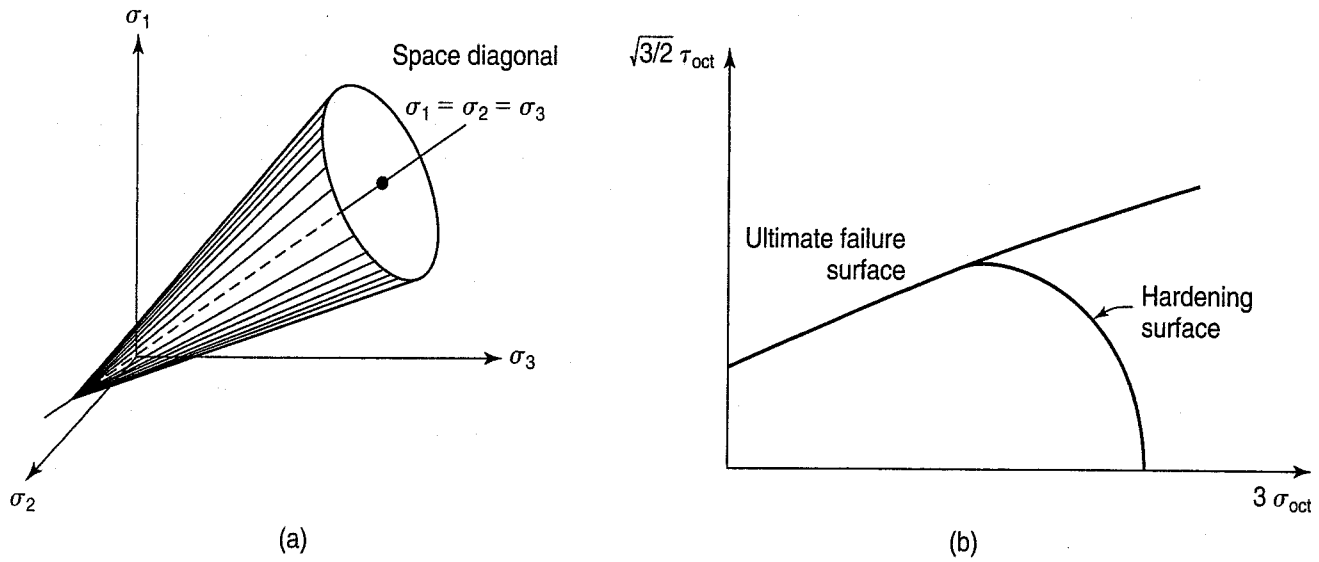

FIGURE 13.49 (a) Three-dimensional representation of Drucker–Prager failure criterion (Chen and Saleeb, 1994); (b) Two-dimensional depiction of Drucker–Prager cap model (McCarron and Chen, 1994).

13.8.5 Classes of Constitutive Models for Soils

There are three general classes of constitutive models for soils: cap models, nested models, and bounding surface models. We have already seen the classic cap model for soils in Sec. 13.8.2, when we described the principles of critical state soil mechanics and the modified Cam clay model. As defined by McCarron and Chen (1994), the cap models consist of a fixed failure criterion (e.g., Mohr–Coulomb) that describes the point where the soil becomes perfectly plastic [shear stress remains constant with additional shear strain—see Figs. 11.4(c) and (d)], and a subfailure surface that allows the soil to "work harden" or undergo an increase in plastic yield stress due to changes in volume.

A simple example of the cap model behavior is the one-dimensional (K_o) case, in which the consolidation stress shifts the plastic yield stress outward in the form of an increasing preconsolidation stress, σ'_p. Figure 13.50 shows, in q–p' space [Eqs. (13.1) and (13.2), respectively] how this loading expands the cap while the perfectly plastic failure surface remains the same. The computational method or rule by which the cap expands is clearly important, and you are referred to Aziz (2000) for further information on such flow rules.

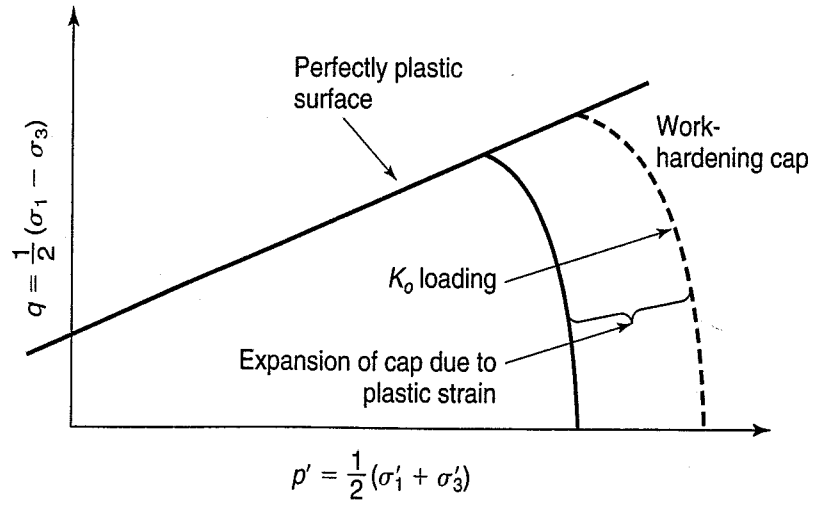

FIGURE 13.50 Simple example of work-hardening cap model during one-dimensional (K_o) consolidation (after McCarron and Chen, 1994).

The second major class of constitutive models for soils is the nested model (Mroz, 1967; Iwan, 1967; Prevost 1977; Lacy and Prevost, 1987; Prevost and Popescu, 1996), which became very useful both for characterizing soil anisotropy and for modeling cyclic loading. These models are based on either cylindrical or conical yield surfaces in our three-dimensional stress space of Fig. 13.47, and they can both shift and expand/contract with loading and unloading. While they were innovative in their approach to modeling more complex aspects of soil behavior under nonmonotonic loadings, as McCarron and Chen (1994) suggest, the potentially large number of input parameters is a significant obstacle to their implementation.

Because they are defined by surfaces that explicitly separate elastic and plastic behavior, both cap and nested models have an inherent and important disadvantage in the modeling of geologic materials. As we shall see in Sec. 13.16, the stress range over which soils and rock behave in a purely elastic mode is extremely small, and plastic strains begin to emerge at very low stress/strain levels. The third major class of constitutive models are the bounding surface models (e.g., Dafalias and Popov, 1975, Dafalias and Herrmann 1982, Kaliakin and Dafalias 1990a) that allow plastic strains to occur inside a new yield surface known as the bounding surface, with the plastic strain magnitude determined by the proximity of the stress state to the surface (McCarron and Chen, 1994). This is arguably a more sophisticated method for achieving the nested model goal, but without having the many parameters required in the nested model to maintain multiple surface shapes and locations. This class of models has been especially useful for cohesive soils under cyclic loading (e.g., Whittle, 1987), and has been extended to use in modeling cohesionless soils as well (e.g., Bardet, 1986; Pestana, 1994). A final aspect of these models is their ability to incorporate viscous (or rate-dependent) effects based on the original work by Perzyna (1963) and later implementation and verification by Kaliakin and Dafalias [1990(a, b)]. Sheahan and Kaliakin (1996) provide a number of additional papers on the topic of modeling rate-dependent soil behavior.

In order for constitutive models to accurately predict stresses and deformations, they must be properly calibrated. The material properties should be determined on high-quality soil samples using the best testing equipment and techniques, and the characterization should also consider the effect of loading and unloading, dilatancy, and fabric anisotropy. Model limitations, simplifications, and capabilities should be well understood. Experience has shown that accurate predictions are possible with well-calibrated constitutive models and valid input parameters.

13.8.6 The Hyperbolic (Duncan–Chang) Model

We mentioned in Sec. 13.8.2 that most geotechnical problems involving constitutive modeling require numerical analysis such as the finite element method to obtain a solution. One of the most common soil models used for finite element analyses in practice is a simple incremental nonlinear elastic stress-strain model popularly known as the Duncan–Chang hyperbolic model (Duncan and Chang, 1970). It is based on the transformation of a hyperbola into a straight line, as shown in Fig. 13.51.

Kondner (1963) recognized that the shape of the stress-strain curves for many soils could be approximated by a hyperbola. The equation for a hyperbola is $x^2 - y^2 = 1$, and it can be transformed into a straight line by plotting y/x versus x. As shown in Fig. 13.51(a), the equation for a hyperbolic-shaped stress-strain curve is:

$$(\sigma_1 - \sigma_3) = \frac{\varepsilon}{\dfrac{1}{E_i} + \dfrac{\varepsilon}{(\sigma_1 - \sigma_3)_{\text{ult}}}} \tag{13.25}$$

where E_i = initial tangent modulus, and

$(\sigma_1 - \sigma_3)_{\text{ult}}$ = asymptote to the ultimate or peak principal stress difference.

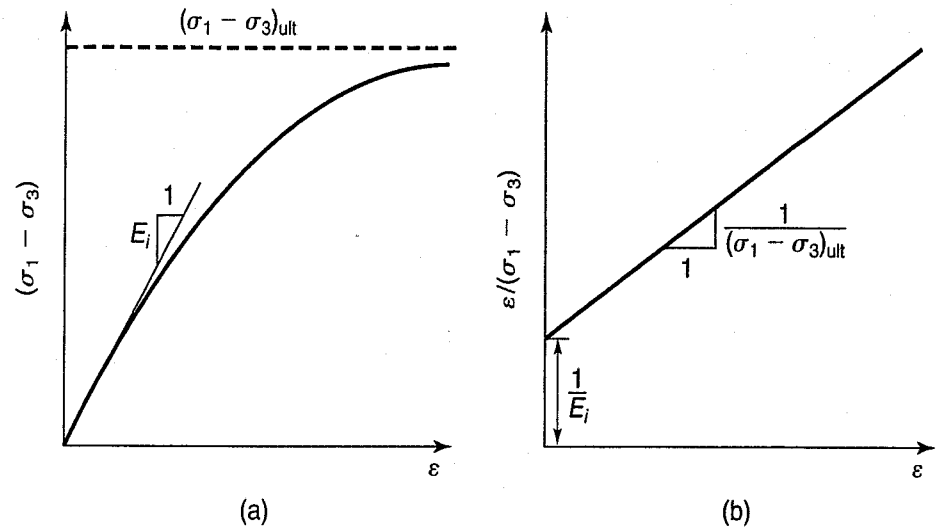

FIGURE 13.51 Hyperbolic representation of a stress-strain curve: (a) actual soil, and (b) transformed (Duncan et al., 1980).

Equation (13.25) can be transformed into a straight line:

$$\frac{\varepsilon}{(\sigma_1 - \sigma_3)} = \frac{1}{E_i} + \frac{\varepsilon}{(\sigma_1 - \sigma_3)_{ult}} \tag{13.26}$$

As shown in Fig. 13.51(b), the slope of the line is $1/(\sigma_1 - \sigma_3)_{ult}$ and the intercept is $1/E_i$. As explained in Sec. 13.8.1, determining the initial tangent modulus E_i is often problematic for especially non-linear σ–ε relationships. So this transformation can provide a good estimate of E_i.

For many geo-materials, stiffness and modulus increase with increasing confining pressure. Thus a power relationship similar to Eq. (8.21) is appropriate for both the unload-reload modulus E_{ur} and the bulk modulus B. For the E_{ur}

$$E_{ur} = K_{ur} p_a \left(\frac{\sigma_3}{p_a}\right)^n \tag{13.27}$$

where K_{ur} = the unload-reload modulus number, a dimensionless constant. The other variables were defined in Eq. (8.21). For the bulk modulus, the relationship is

$$B = K_b p_a \left(\frac{\sigma_3}{p_a}\right)^m \tag{13.28}$$

where K_b = bulk modulus number, and

m = dimensionless bulk modulus exponent; $0 < m < 1.0$.

When the Mohr–Coulomb failure criterion is included in the hyperbolic model, the mathematical expression for the tangent modulus E_t is (Duncan et al., 1980):

$$E_t = \left[1 - \frac{R_f(1 - \sin\phi)(\sigma_1 - \sigma_3)}{2c\cos\phi + 2\sigma_3 \sin\phi}\right]^2 K p_a \left(\frac{\sigma_3}{p_a}\right)^n \tag{13.29}$$

where R_f, K, and n are model parameters; the other parameters were defined previously. The model parameter R_f is the failure ratio, or $(\sigma_1 - \sigma_3) = R_f\,(\sigma_1 - \sigma_3)_{ult}$. The modulus number K determines

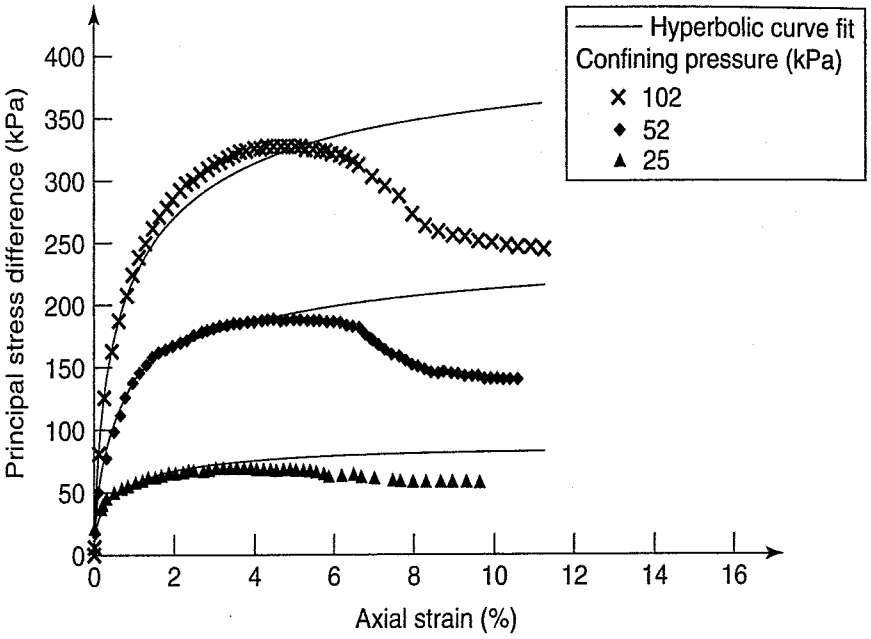

FIGURE 13.52 Hyperbolic curve fitting of triaxial test data on a poorly graded subangular RMC sand; $K = 850$, $R_f = 0.73$, $n = 0.5$ (Lee, 2000).

the scale of the soil modulus, and the modulus exponent n defines the hyperbolic relationship between the soil modulus and confining pressure. The values of R_f, K, and n can be determined from your own tests or from the data base in Duncan et al. (1980).

For plane strain loading conditions, the stress-strain relationships are different than for triaxial conditions (Sec. 13.11). Therefore, different hyperbolic model parameters are required. Lee (2000) adjusted the model parameters from triaxial tests to plane strain loading conditions, and some of his results are shown in Figure 13.52.

The Duncan–Chang hyperbolic parameters are not fundamental but are empirical coefficients that represent the behavior of soil under a limited range of conditions. The values of the parameters depend on the density of the soil, the water content, range of testing pressures, and the drainage conditions. The laboratory test conditions should be representative of the soil behavior in the field.

A big advantage of the Duncan–Chang hyperbolic model is its versatility and generality. It can be used for all soils—sands, clays, gravels, rockfills, saturated and unsaturated soils, and compacted or natural. But it does have some limitations. Post-peak behavior is not modeled, as shown in Fig. 13.52. As Duncan (1980) noted, it does not account for volume changes or dilatancy, so its accuracy for predicting deformations in in dense sands under low confining pressures is limited.

In spite of its limitations, the Duncan–Chang hyperbolic model is one of the most practical and successful of the available constitutive models (Yong and Ko, 1980).

13.9 FUNDAMENTAL BASIS OF THE DRAINED STRENGTH OF SANDS

In Chapter 12, we described the stress-strain and volume change behavior of sands during drained shear. We also discussed the effect of void ratio and confining pressure, as well as the various factors that affect the CD strength of sands. In this section, we take a more fundamental look at the frictional strength of granular soils, as well as the important characteristic of dilatancy of dense sands. We end this section with a discussion of curved Mohr envelopes, because, although they are usually assumed to be straight, they are actually curved, especially over a wide range of confining stresses.

13.9.1 Basics of Frictional Shear Strength

In Sec. 11.4.2, when we discussed the Mohr–Coulomb failure criterion, we arbitrarily assumed that the analogy between sliding friction of solids and the internal friction in soils was valid. Undoubtedly,

Coulomb was aware of *Amontons' laws*, the two basic laws of friction, which were well stated by Lambe and Whitman (1969) as follows:

1. The shear resistance between two bodies is proportional to the normal force acting between the two bodies.
2. The shear resistance between two bodies is independent of the dimensions of the two bodies.

According to Lambe and Whitman (1969) these laws were originally stated by Leonardo da Vinci about 1500 and then rediscovered about 200 yr later by the French engineer Guillaume Amontons.

Equation (13.30) is an expression of the First Law, the ratio of the shear force T to the normal force N acting on the plane surface between the two solid bodies. This ratio is, of course, the coefficient of friction, μ, or in equation form

$$\mu = \frac{T}{N} \tag{13.30}$$

The coefficient of friction μ can also be expressed as the tangent of the angle ϕ_μ between the N force vector and the resultant of the N and the T vectors just as the block starts to slide. When that happens, $T = T_{max}$. Thus $\mu = \tan \phi_\mu$. Go back and look at Fig. 11.11 for an explanation of sliding friction and what happens to that angle prior to slippage.

The next important developments in our understanding of frictional resistance between solids are attributed to Terzaghi (1920 and 1925, pp. 50–52), who postulated that solid friction was caused by small imperfections or asperities in even smooth solid surfaces. The contact area at these asperities changes due to plastic flow that occurs due to normal and shear stresses. As noted by Mitchell and Soga (2005), these concepts were further developed by Bowden and Tabor (1950, 1964), and the Terzaghi–Boden and Tabor hypothesis is now known as the adhesion theory of friction. This theory suggests that two important features of the contact surface affect frictional resistance: surface roughness and surface adsorption. The influences of both features are described in some detail by Mitchell and Soga (2005). When we think of soils, both surface roughness and the presence of contaminants or even water on the mineral surfaces can influence their frictional resistance.

The frictional resistance between mineral surfaces for some common minerals found in soils has been tabulated by Mitchell and Soga (2005) under a variety of tests and conditions. It is interesting that water has been found to increase the friction angle, especially for very smooth surfaces, but this effect decreases as the surface roughness increases. Because all naturally occuring soil mineral surfaces are undoubtedly rough and not chemically clean, we report only those values of friction angle that seem practically relevant or are available in Table 13.5. An exception is the sheet minerals (layer silicates—Chapter 4) such as mica and chlorite that have a natural cleavage; for these minerals water apparently acts as a lubricant to reduce friction.

Other Models of Granular Soil Behavior Other approaches to explain the behavior of granular soils have been described by Scott (1963). His analysis began with simplified models of cohesionless soils, the application of failure theory, the influence of intermediate principal stress on failure, the effects of stress history and strain rate on failure, and finally pore water considerations and drainage effects.

Mitchell and Soga (2005) provide considerable detail about physical interactions among granular particles. They discuss the effects of buckling, sliding, and rolling of particles, fabric anisotropy, changes in number of contacts with shear, and the effects of particle shape and angularity.

Finally, Harr (1977) takes a different approach to the mechanics of particulate media using the methods of statistics and probability theory.

TABLE 13.5 Values of Friction Angle (ϕ_μ) Between Mineral Surfaces

Mineral	Type of Test	Conditions	ϕ_μ (degrees)
Quartz	Particle to particle	Saturated	26
Feldspar	Particle to plane	Saturated	29
Calcite	Block on block	Saturated	34
Mica—Muscovite	Along cleavage faces	Dry	23
		Saturated	13
Mica—Biotite	Along cleavage faces	Dry	17
		Saturated	7
Chlorite	Along cleavage faces	Dry	28
		Saturated	12

After Mitchell and Soga (2005).

13.9.2 Stress-Dilatancy and Energy Corrections

It has long been recognized that dense sands expand when sheared. Osborne Reynolds of Reynolds Number fame tried to explain the phenomenon and first called it *dilatancy* (Reynolds, 1885). Although it is often assumed that the behavior of granular material is relatively simple in comparison with that of fine-grained soils, in reality this is not necessarily the case, as we show in this section.

Figure 13.53 shows schematically what happens to a volume of dense and loose granular soils when they are sheared. Both volumes are subjected to the same normal stress σ_n [Fig. 13.53(a) and (c)]. Then the shear stress τ is applied, as shown in Fig. 13.53(b) and (d); in this figure, the volume change is indicated by the symbol ΔH. The dense sand expands and ΔH is positive; the loose sand contracts, so ΔH is negative.

We begin this section with attempts to explain dilation by the mechanical energy required to overcome the shear resistance during direct and triaxial tests on sand. While simple, these analyses considered only the external energy required for shear. To account for the internal energy expended during shear, we need Rowe's elegant stress-dilatancy theory. We then show how the components of dilation or contraction, grain crushing, and grain-to-grain mineral friction all contributed to the Mohr failure envelope (MFE) of sands. Next we describe the important contributions of Bolton (1979 and 1986) on dilation, contractions, and critical states. Finally, we give some data on the magnitude of the dilation angles at high and low confining stess.

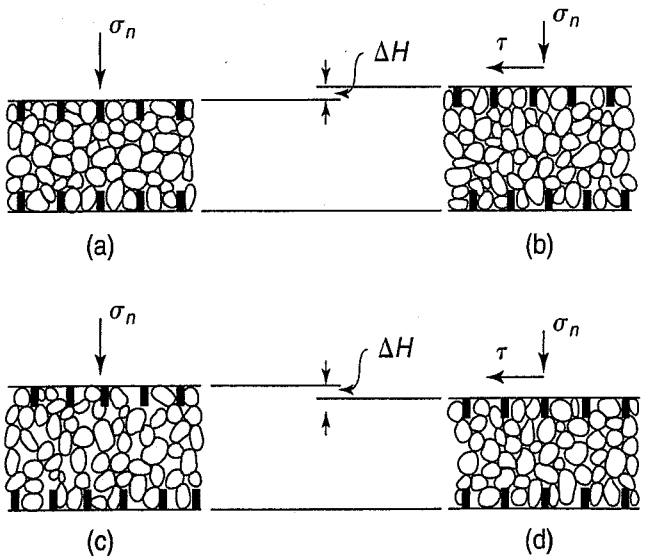

FIGURE 13.53 Effects of shearing on a volumes of dense and loose granular soils: (a) dense before shear; (b) dense after shear; (c) loose before shear; and (d) loose after shear (Leonards, 1962).

Energy Corrections Taylor (1948, pp. 345–6) explained the expansion or dilation due to the interlocking of the grains in a dense sand by the mechanical energy expended in a direct shear test. Figure 13.54 shows typical direct shear results for a dense sand and a loose sand. During shear of the dense specimen, at ΔH, τ_{max} is still increasing and doing work against the normal stress σ_N acting on the shear plane.

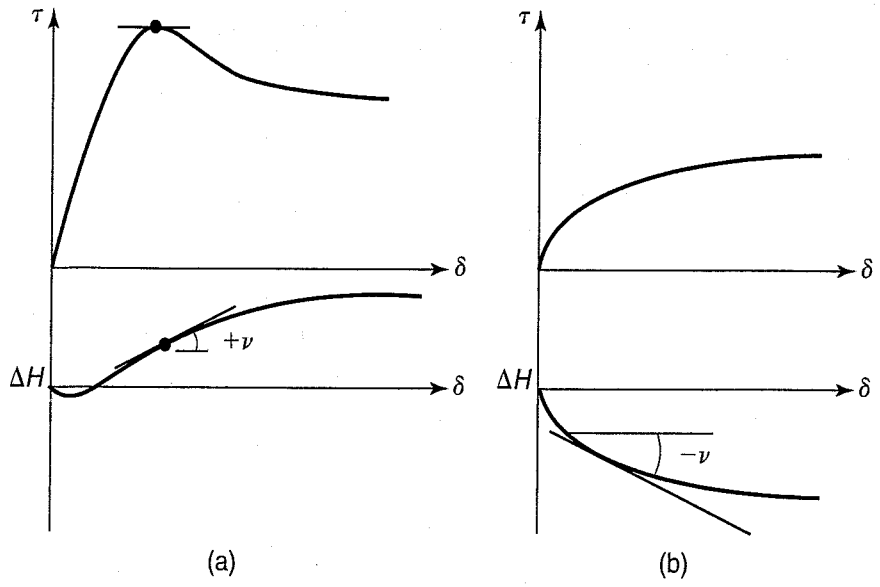

FIGURE 13.54 Shear and volume change behavior in a direct shear test on (a) dense sand and (b) loose sand.

To find the part of the total shear energy τ required for expansion τ_e, we equate the expansion shear energy $\tau_e A\delta$ to the vertical expansion energy $\sigma_N A\,\Delta H$, or

$$\tau_e A\delta = \sigma_N A\,\Delta H$$

$$\tau_e = \sigma_N\left(\frac{\Delta H}{\delta}\right)$$

where the quantity $(\Delta H/\delta)$ equals the slope of the ΔH-versus-δ curve. This slope is defined as the *dilation angle* ν. For a dense sand, we have friction plus interlock, whereas for a loose sand, we have friction only (with no or negative ΔH). The dilation angle ν can be found geometrically as shown in Fig. 13.54(a). A positive dilation angle, $+\nu$, indicates expansion or dilation whereas a negative dilation angle, $-\nu$, indicates contraction, as shown in Fig. 13.54(b).

Bishop (1954) performed a similar analysis for an ordinary triaxial compression test. We don't include it here, because, as Rowe (1962) and Rowe et al. (1964) showed, both the previous analyses are technically incorrect, since they consider only the external work caused by dilation and neglect the additional internal work required by dilation. Rowe's (1962) *stress-dilatancy theory* correctly accounts for this internal work, and the basic stress-dilatancy equation is:

$$\frac{\sigma_1'}{\sigma_3'} = \left(1 + \frac{dv}{d\varepsilon_1}\right)\tan^2\left(\frac{\pi}{4} + \frac{\phi_\mu}{2}\right) \tag{13.31}$$

where $v = dV/V_o$ = differentialvolumetric strain,

$\varepsilon = \Delta H/H_o$

$\dfrac{dv}{d\varepsilon_1}$ = slope of dV/V_o-versus-ε_1 curve,and

ϕ_μ = basic mineral friction—for example, as given in Table 13.5.

Figure 13.55 shows the various component of the total friction angle in drained shear, ϕ_d. According to Rowe (1962), there are three components of the total friction angle: (1) mineral friction, (2) particle reorientation, and (3) expansion (dilation).

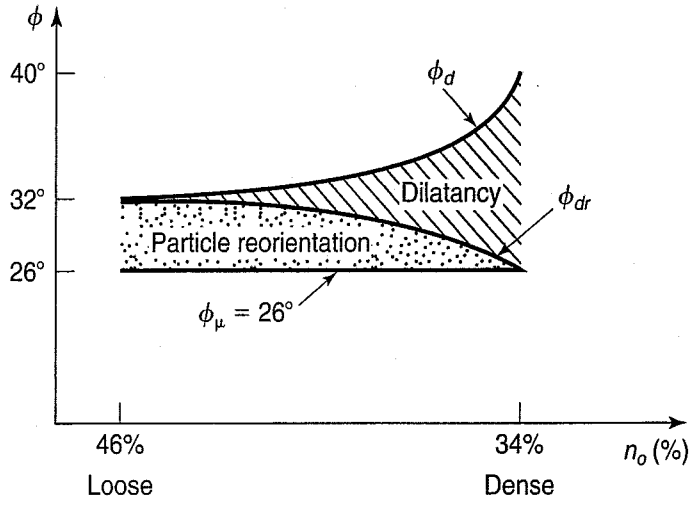

FIGURE 13.55 Components of the friction angle as a function of porosity; n_o = initial porosity, ϕ_μ = mineral friction already defined, ϕ_d = the measured CD friction angle, and $\phi_{dr} = \phi_d$ − dilatancy effect.

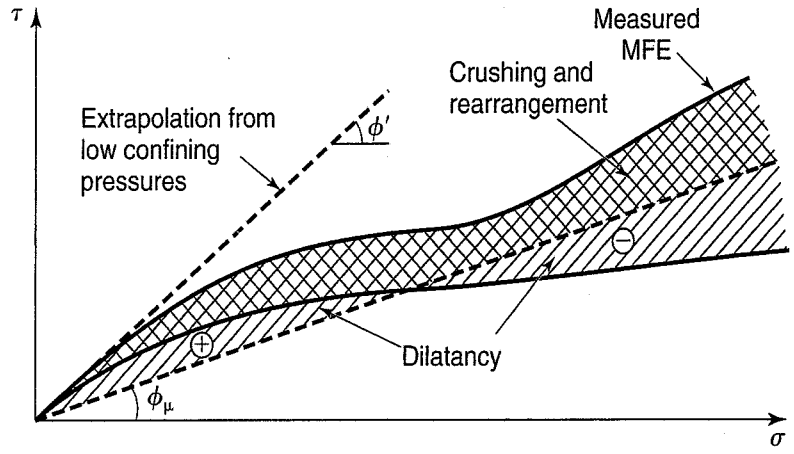

FIGURE 13.56 Components of the Mohr failure envelope for a granular soil over a wide range of confining pressures (after Lee and Seed, 1967).

At high confining pressures, we have a fourth component, particle crushing, reflecting the fact that, after an initial decrease or flattening of the MFE slope, the slope tends to increase as pressure increases. Note that crushing requires considerable energy. As pointed out by Lee and Seed (1967), the measured strength = sliding friction ± dilatancy + particle rearranging + particle crushing, as shown in Fig. 13.56.

Dilation, Contraction, and Critical States We can summarize behavior of CD DS tests on sands as follows (Bolton, 1979, 1986):

1. A given sand has an approximately unique ϕ'_{ult}, that is, it is independent of the initial void ratio and density (e_o and ρ_o). Also ϕ'_{ult} is essentially independent of the effective normal stress σ'_n in a DS test (and the effective confining pressure σ'_c in a CD triaxial test).
2. For dense sands, ϕ'_{peak} and $\tau_{peak} \gg \phi'_{ult}$ and τ_{ult}.
   - Beyond the peak, thin rupture zones or dislocations develop, and sometimes as shearing continues, these dislocations split into branches called *bifurcations*.
   - The initial void ratio and initial density approach the critical void ratio e_{crit} or the critical density ρ_{crit} due to dilation; as the volume increases, the density decreases.
3. Loose sands strain to reach ultimate or maximum strength, and there is no peak in the curve. This phenomenon is shown in Fig. 13.54(b) above. In this case, as the volume decreases, the void ratio decreases and density increases until the critical void ratio e_{crit} and critical density ρ_{crit} are reached.
4. Magnitude of the peak shear stress is a function of the rate of dilation.

In order to understand the frictional behavior of sands, the concept of the *critical state* is important. When a sand is sheared, it eventually reaches a critical state which has a unique ratio of $\tau/\sigma' = \tan \phi'_{crit}$ on the shear planes. According to Bolton (1979) at the critical state in the zones of shear, the critical void ratio e_{crit} is a logarithmic function of the stresses. Figure 13.42 shows the critical state lines in two-dimensional $\tau-\sigma'$ and $e-\sigma'$ space. Figure 13.42(c) indicates that $e-\ln \sigma'$ data is usually linear over the stress range of interest. If you read Sec. 13.7 on CSSM, then Fig. 13.57 should look familiar. Figure 13.57(b) is the same as Fig. 12.8. We could also depict these concepts is in a three-dimensional $\tau-\sigma'-e$ plot, similar to the Peacock diagram (Fig. 12.11).

You can also see from Fig. 13.57 that the magnitude of τ_{ult} or τ_{crit} is independent of e_o for either e_{loose} or e_{dense}. If the specimen is initially loose, it contracts until it reaches the CSL at e_c and σ'_c. Similarly, if the specimen is initially dense, it expands or dilates until it reaches the CSL at e_c and σ'_c. Although the critical state model is useful, it does not explain the peak strength of dense sands. For this we need a stress-dilatancy model, for example the Rowe (1962) theory described above.

Because it dilates, the dense sand mobilizes a greater angle of internal friction than ϕ'_{crit}, or

$$\phi' = \phi_{max} = \phi_{crit} + \nu \geq \phi'_{crit} \tag{13.32}$$

As shown in Fig. 13.54(a), the peak of the stress-deformation response corresponds to the maximum dilation angle $+\nu$, and its magnitude depends on the amount of expansion and on the characteristics of the sand grains such as particle shape, particle roughness, and grain size distribution. Beyond the peak, the dilation angle decreases and $\phi' \rightarrow \phi'_{crit}$ at the ultimate or critical state where the dilation angle is zero and the measured friction angle $\phi' = \phi'_{crit}$. This is called the *fully softened critical state strength.* The loose specimen [Fig. 13.54(b)] of course does not reach maximum shear stress until the critical state, where the dilation angle is negative or $-\nu$.

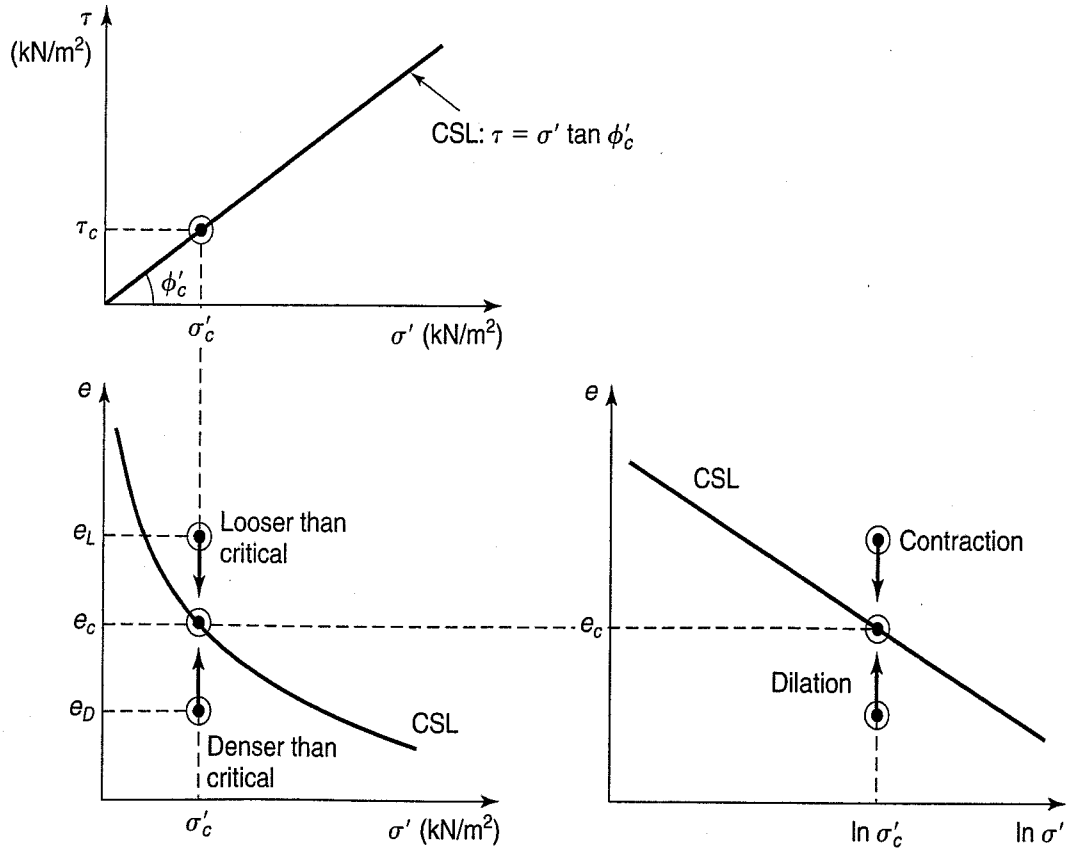

FIGURE 13.57 Critical state lines (CSL) in $\tau-\sigma'-e$ space: (a) τ versus σ'; (b) e versus σ'; and (c) e versus ln σ' (after Bolton, 1979).

In Sec. 12.3, we mentioned that CD triaxial specimens of dense sand usually fail along distinct planes. This is because when a dense sand is sheared past the peak, strain tends to concentrate in a thin rupture zone called a *strain localization*. Sometime the localization *bifurcates* into two or more branches. Localization and bifurcations are characteristics of dense sand at large strains. This is not true for loose sands, which experience a more general distortion and shear strains all the way to ultimate shear stress at the critical state.

Magnitude of the Dilation Angle According to Bolton (1979 and 1986), typical values of dilation angles are 10 to 20 deg for granular soils tested at confining pressures higher than 100 kPa. What happens if the confining pressures are less—a situation quite common in practice? Lee (2000) found much greater dilation angles, some as high as 25 to 40 deg, in both triaxial and plane-strain tests performed on dense sands ($I_D \approx 90\%$) at confining pressures between 25 and 100 kPa. Even for materials prepared in a loose state ($I_D \approx 50\%$), the measured dilation angle was 26 deg at those same confining pressures. In some numerical modeling work (e.g., Lee, 2000), the dilation angle has an enormous effect on the predicted deformations. So, if you are working at lower confining stresses and predicting deformations is important to your problem, then you need to accurately measure the dilation angle in the appropriate soils tests.

13.9.3 Curvature of the Mohr Failure Envelope

In Sec. 11.4.2, we gave the following equation for the Mohr–Columb failure theory:

$$\tau_{ff} = \sigma_{ff} \tan \phi + c \tag{11.9}$$

We mentioned that this equation is a straight-line approximation of a curved Mohr failure envelope over a given stress range, usually that anticipated in the field.

Later, in Sec. 12.5, when we introduced the shear strength properties of sands, we mentioned that the Mohr–Coulomb failure envelopes were curved, especially over a wide range of confining stresses. This is also shown in Fig. 12.12. The source of the curvature is thought to be due to particle rearrangement and crushing, as shown in Fig. 13.56. Even with a modest curvature of the envelope, a straight line approximation will often show an intercept on the τ-axis at $\sigma = 0$. This intercept is an artifact of the envelope geometry, and the shear strength of the soil at zero confining stress is zero. A curved failure envelope starting at the origin of a Mohr diagram also means that at small confining stresses, the secant Mohr failure envelope is very steep, and thus the angle of internal friction can be quite large (see, e.g., Fannin et al., 2005).

Of course, with a curved MFE, its slope is constantly reducing from a very steep initial tangent value to what might be a rather modest slope if the confining pressure were large. Therefore we need some expression that takes into account this reduction in friction angle as the confining pressure increases. Probably the simplest way to do this is to use the expression developed by Duncan and Wright (2005). Consider first the slope of the *secant* friction angle that is defined by the slope of a straight line drawn from the origin and just tangent to the Mohr's circle at failure. Duncan and Wright (2005) use this expression to reduce the secant friction angle:

$$\phi'_{\text{sec}} = \phi_o - \Delta\phi \log \frac{\sigma'_3}{p_a} \tag{13.33}$$

where ϕ'_{sec} = secant angle of internal friction,

ϕ_o = value of ϕ when σ'_3 = 1 atm $\approx$ or 100 kPa,

$\Delta\phi$ = the reduction in ϕ' for a 10-fold increase in confining pressure,

σ'_3 = the confining pressure, and

p_a = atmospheric pressure, 1 atm $\approx$ 100 kPa.

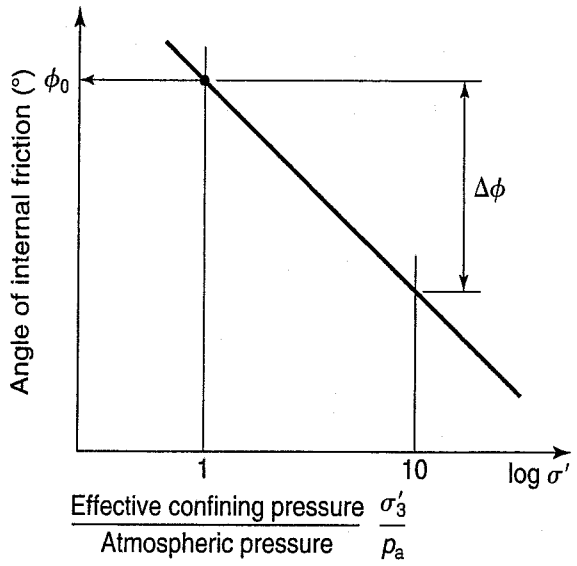

FIGURE 13.58 Relationship between ϕ' and σ'_3 (Duncan and Wright, 2005).

Figure 13.58 shows the relationship between ϕ' and σ'_3, which is a plot of the secant friction angle for a series of triaxial tests versus the effective confining pressure of each test. The slope of the line indicates the reduction in friction angle $\Delta\phi$ with confining pressure for that test series.

Baligh (1976) developed a somewhat more complex expression for the reduction in secant friction angle due to the curvature of the Mohr failure envelope, which is

$$\tau = \sigma\left[\tan\phi_{ref} + \tan\alpha\left(\frac{1}{2.3} - \log\frac{\sigma}{\sigma_{ref}}\right)\right] \quad (13.34)$$

where ϕ_{ref} and α are constant angles defining the MFE ($\alpha \geq 0$ and $\phi_{ref} > 0$), and σ_{ref} is an arbitrary reference stress. Note that when $\alpha = 0$, ϕ_{ref} = the secant angle of friction ϕ_{sec}.

13.10 BEHAVIOR OF SATURATED SANDS IN UNDRAINED SHEAR

In the introduction to Sec. 12.8, we mentioned that when sands are loaded statically, because they have such a high hydraulic conductivity as compared to silts and clays, they drain as fast as the load is applied. Thus undrained loading of sands under static conditions happens only in the laboratory, and it is largely of academic interest. Dynamic loading is, of course, another matter, and we discuss the behavior of saturated sands under dynamic loads—for example, due to blasting, pile driving, or earthquakes—later in this chapter.

In this section, we describe and explain the results of both CU and UU tests on sands. This section ends with a brief discussion of strain rate effects in sands, because the rate of application of the shear stress determines whether drainage is likely to occur during shear.

13.10.1 Consolidated-Undrained Behavior

The main difference between drained and undrained triaxial shear is that in an undrained test no volume change is allowed during axial loading, therefore e_c is the same at the end of the test as it was at the beginning. However, unless the confining pressure just happens to be at $\sigma'_{3\,crit}$, the soil will *tend to change volume* during loading. To understand what happens with undrained loading, we can refer again to the Peacock diagram in Fig. 12.11. Because with undrained loading, there is no volume change, all of the action takes place on the plane WOP.

First, let's look at a soil specimen set up at a void ratio e_c and tested *undrained* at a confining pressure σ'_3. This test corresponds to point C in the Peacock diagram. Because $\sigma'_{3c} > \sigma'_{3\,crit}$, as explained in Sec. 12.4, the sand specimen would behave as if it were loose. Thus it *tends* to decrease in volume, but it can't. As a result, a *positive* pore pressure is induced, which causes a *reduction* in the effective stress. The limiting or minimum effective pressure at failure is $\sigma'_{3\,crit}$, because at this pressure $\Delta V/V_o$ is zero. If no tendency toward volume change takes place, then no excess pore pressure is induced. So the maximum possible pore pressure in this example is equal to $\sigma'_{3c} - \sigma'_{3\,crit}$, or the distance $\overline{BH}$ in Fig. 12.11.

The Mohr circles at failure for this case are shown in Fig. 13.59. The solid circles E represent the effective stress conditions, whereas the dashed circle T is in terms of total stresses. Since the effective stress equation [Eq. (6.8)] always holds, the two circles are separated by the value of Δu induced at any

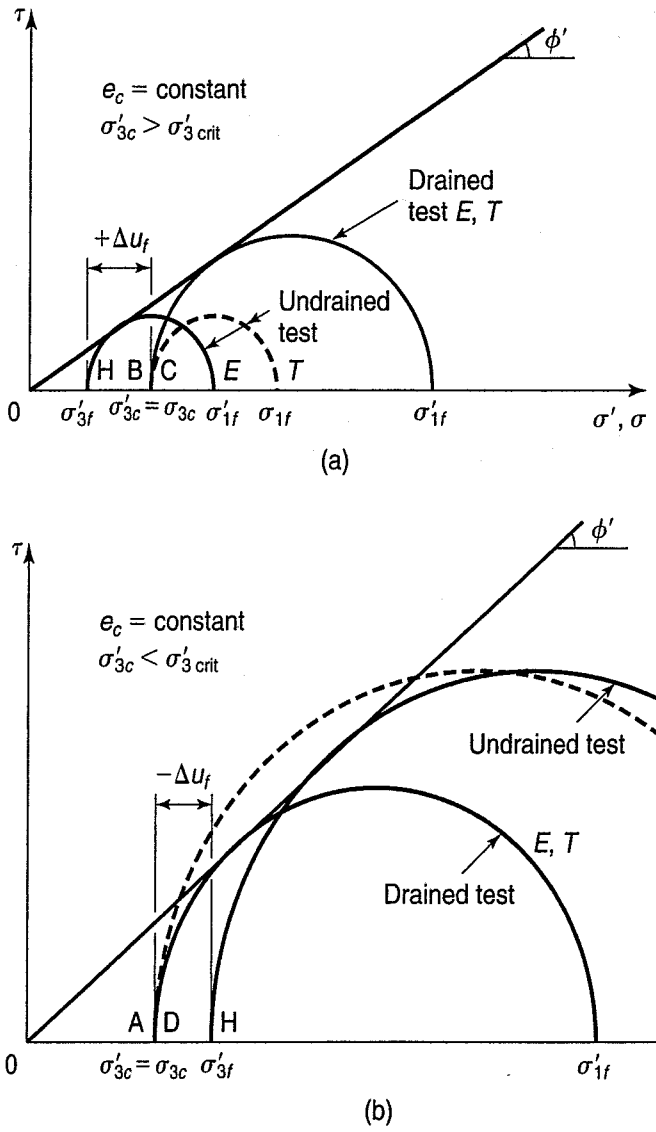

FIGURE 13.59 The Mohr circles for undrained and drained triaxial compression tests: (a) case where $\sigma'_{3c} > \sigma'_{3\,crit}$ or "loose" behavior; (b) case where $\sigma'_{3c} < \sigma'_{3\,crit}$ or "dense" behavior.

time during the test. Since the volume change *tendency* is to reduce, a positive change (increase) in pore pressure is caused, which in turn results in a *reduction* in the effective stress. Thus, for this example at failure, $\Delta u_f = \text{B} - \text{H} = \sigma'_{3c} - \sigma'_{3f} = \sigma'_{3c} - \sigma'_{3\,crit}$. The $(\sigma_1 - \sigma_3)_f$ is given by Eq. (12.3) when the confining pressure at failure is $\sigma'_{3\,crit}$.

$$(\sigma_1 - \sigma_3)_f = \sigma'_{3\,crit}\left[\left(\frac{\sigma'_1}{\sigma'_3}\right)_f - 1\right]$$

Also, if we were to run a *drained* test with the confining pressure equal to σ'_{3c} at point C, the drained strength would be much larger than the undrained strength since its Mohr circle must be tangent to the effective Mohr failure envelope. Just look at the relative sizes of the two effective Mohr circles in Fig. 13.59.

A different response occurs when we run a test with the effective confining pressure less than $\sigma'_{3\,crit}$ such as point A in Fig. 12.11. From the Peacock diagram, we would expect the sample to *tend* to dilate (ordinate RD). Since the specimen is prevented from actually expanding, a *negative* pore pressure is developed that *increases* the effective stress from D (A) toward H ($\sigma'_{3\,crit}$). Thus, as in the previous example, the limiting effective stress is the critical confining pressure $\sigma'_{3\,crit}$. (The situation may arise where the negative pore water pressure approaches −100 kPa or −1 atmosphere, and unless back

pressure is used, cavitation occurs). The whole point of this exercise is that we are able to predict the *undrained* behavior of sands from the *drained* behavior when we know the volume change *tendencies* as idealized in the Peacock diagram. We will do this in the next section.

The Mohr circle representation for the case where $\sigma'_{3c} < \sigma'_{3\,\text{crit}}$ is presented in Fig. 13.59(b). The undrained test starts out at σ'_{3c}, point A, and since the induced pore water pressure is negative, the effective confining pressure increases until failure is reached at point H. Note that the effective stress Mohr circles E at failure in Figs. 13.59(a) and (b) are the same size because, for this void ratio e_c, the effective stress at failure is the same, $\sigma'_{3\,\text{crit}}$. If the effective stress and void ratio are the same, then the specimens would have the same compressive strength, $\sigma'_{1f} - \sigma'_{3f}$, thus the circles have the same diameter. Note that the total stress circle T, at failure, is also the same size as the effective stress circle because $(\sigma_1 - \sigma_3)_f$ is the same for both T and E; also T lies to the *left* of E. This case is the opposite of Fig. 13.59(a). (The total stress Mohr failure envelopes have been omitted from both figures for clarity.) Note also that the *drained* Mohr circle for this second case is substantially *smaller* than the effective stress circle for the undrained case. As before, the circle starts at σ'_{3c}, and it must be tangent to the effective Mohr failure envelope. Since the void ratio after consolidation e_c is a constant for all the tests shown in Fig. 13.65, all the effective Mohr circles must be tangent to the effective stress failure envelope.

A summary of the main points discussed above is presented in Table 13.6.

The stress-strain and pore pressure-strain curves for CU and CD tests, both "loose" and "dense," are shown in Fig. 13.60(a) and (b). Also shown are the results for the volumetric strain versus axial strain. These results correspond to the behavior in Fig. 13.59. We mentioned above that the limiting effective stress in any specimen of sand undergoing undrained shear is the critical confining pressure $\sigma'_{3\,\text{crit}}$. In a dense sand, the limitation on how negative the pore water pressure can be is the vapor pressure of water, −1 atm or about −100 kPa (Sec. 6.2). At that point, cavitation will occur unless back pressure is used [Fig. 13.60(b)]. If cavitation occurs, the volume of the specimen increases, the effective confining stress decreases, and the strength of the specimen will not be as great. However, if back pressure is used, then the pore pressure can continue to go negative as long as the total cell pressure is less than $(\sigma'_{3\,\text{crit}} - 1\ \text{atm})$. Thus means that the strength of the specimen is basically controlled by how much back pressure is used and the maximum pressure capacity of the triaxial cell.

For a more comprehensive treatment of the undrained strength characteristics of sands, see Seed and Lee (1967).

TABLE 13.6 A Summary of Concepts Shown in Fig. 13.59

Effective Consolidation Pressure	Mohr Circles		
	Drained, Effective = Total	Undrained, Effective	Undrained, Total
$\sigma'_{3c} > \sigma'_{3\,\text{crit}}$	Larger than undrained	Smaller than drained: Left of total stress circle $\sigma'_{3f} < \sigma'_{3c}$	Smaller than drained: Right of effective stress circle
$\sigma'_{3c} < \sigma'_{3\,\text{crit}}$	Smaller than undrained	Larger than drained: Right of total stress circle $\sigma'_{3f} > \sigma'_{3c}$	Larger than drained: Left of effective stress circle
$\sigma'_{3f} \equiv \sigma'_{3\,\text{crit}}$	All circles would be the same; because no volume change tendencies exist, $\Delta u = 0$ during the test		

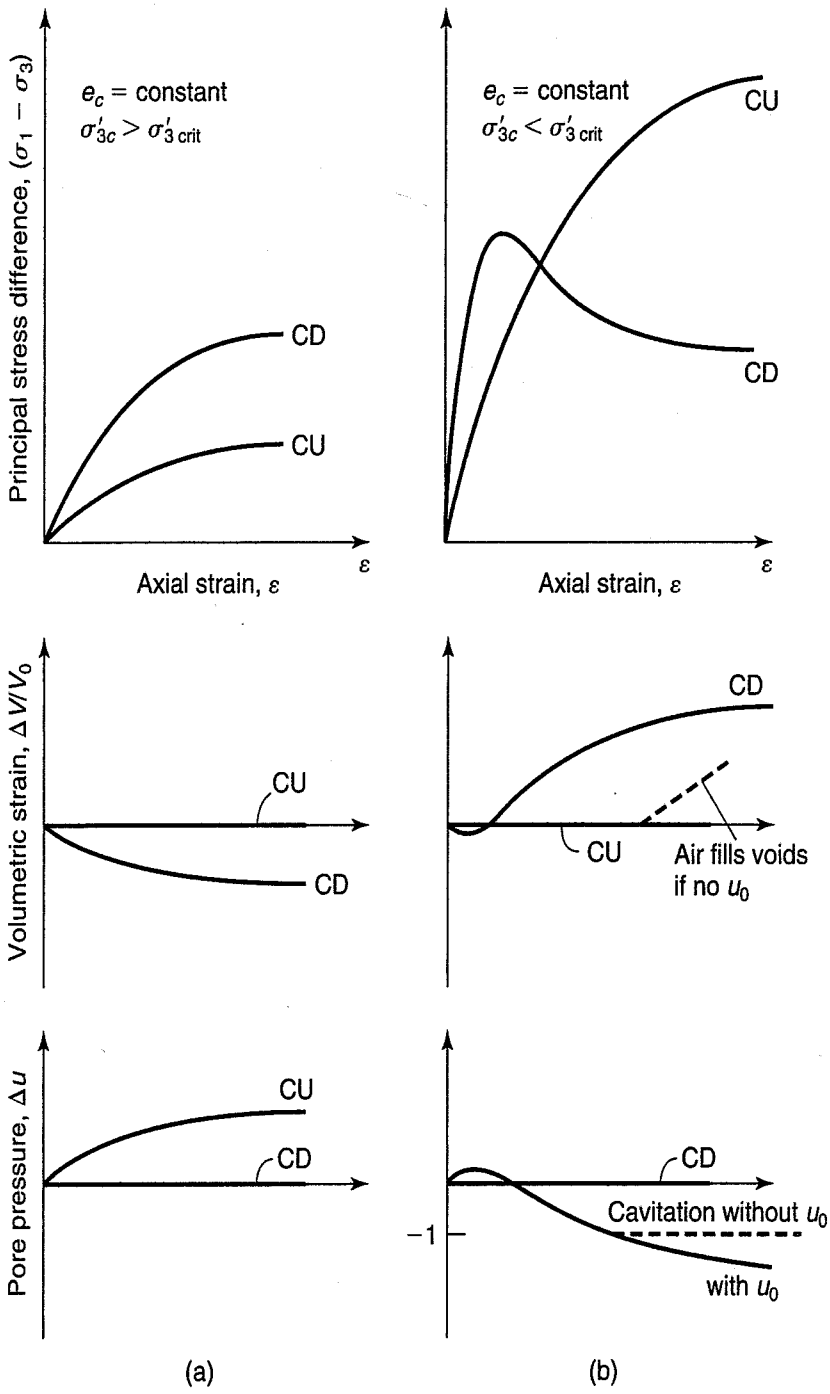

FIGURE 13.60 The stress-strain, volumetric strain versus axial strain, and pore pressure-strain curves for CU and CD tests on sands: (a) case where $\sigma'_{3c} > \sigma'_{3\,crit}$ or "loose" behavior; (b) case where $\sigma'_{3c} < \sigma'_{3\,crit}$ or "dense" behavior.

Example 13.9

Given:

Figure 12.11, but scaled to the idealized behavior of Sacramento River sand (a combination of Figs. 12.7 and 12.9); $\sigma'_{3\,crit} = 0.4$ MPa and $e_c = e_{crit} = 0.8$.

Required:

Describe the undrained behavior of this sand if the test void ratios after consolidation at $\sigma'_{3c} = 0.4$ MPa are (a) 0.85 and (b) 0.75.

Solution: Since σ'_{3c} and e_c are at critical, there is by definition no volume change during shear. Thus our test plots at point H in Fig. 12.11, with the values of $\sigma'_{3\,\text{crit}}$ and e_c as given. (You can verify these values in Figs. 11.6 and 11.8.)

a. When sheared the specimen would *tend* to decrease in volume, but since it is undrained it cannot. Therefore the specimen would develop positive pore water pressure along with a concurrent decrease in σ'_3. In Fig. 12.11, the test coordinates must remain on the $e = 0.85$ line *and* in the plane WOP. The only way this can happen is for σ'_3 to decrease, which makes sense in view of the increase in pore water pressure.

b. In undrained shear, the *tendency* towards volume increase would cause the pore water pressure to decrease and the σ'_3 to increase. This is what happens when our test coordinates remain on plane WOP; that is, σ'_3 increases.

Example 13.10

Given:

Figure 12.11 is scaled to the behavior of Sacramento River sand (Figs. 12.7 and 12.9), with $e_{\text{crit}} = 0.6$ and $\sigma'_{3\,\text{crit}} = 1.6$ MPa.

Required:

Describe the behavior in undrained shear if we maintain this void ratio of 0.6 and test the specimen with σ'_{3c} of (a) 1.5 MPa and (b) 1.7 MPa.

Solution:

a. In undrained shear, the *tendency* will be for dilation, which is prevented; we must remain at $e_c = 0.6$ and on plane WOP. Therefore σ'_3 must increase, which makes sense physically since the induced pore water pressure tends to decrease.

b. In undrained shear, the tendency towards compression would result in positive excess pore pressure and a decrease in σ'_3.

Example 13.11

Given:

The test specimen of Example 12.8 was sheared *undrained* at the same total cell pressure (150 kPa). The induced excess pore water pressure at failure Δu_f is equal to 70 kPa.

Required:

Evaluate the the following parameters:

a. σ'_{1f},

b. $(\sigma_1 - \sigma_3)_f$,

c. ϕ in terms of *total* stress, and

d. the angle of the failure plane α_f.

Solution: **a** and **b.** Since the void ratio after consolidation would be the same for this test as for Example 12.8, assume ϕ' is the same. You can do this problem either (1) analytically or (2) graphically.

1. *Analytically*: We know from Eq. (12.3) that

$$(\sigma_1 - \sigma_3)_f = \sigma'_{3f}\left[\left(\frac{\sigma'_1}{\sigma'_3}\right)_{\max} - 1\right]$$

$$\sigma'_{3f} = \sigma_{3f} - \Delta u_f = 150 - 70 = 80\ \text{kPa}$$

So

$$(\sigma_1 - \sigma_3)_f = 80(3.7 - 1) = 216\ \text{kPa}$$

$$\sigma'_{1f} = (\sigma_1 - \sigma_3)_f + \sigma'_{3f} = 216 + 80 = 296\ \text{kPa}$$

These are the answers to parts **a** and **b.**

c. We can write Eqs. (11.13) and (12.1) in terms of total stresses. Using Eq. (11.13),

$$\sin \phi_{\text{total}} = \frac{\sigma_1 - \sigma_3}{\sigma_1 + \sigma_3} = \frac{216}{(296 + 70) + 150} = 0.42$$

$$\phi_{\text{total}} = 24.8°$$

Using Eq. (12.1),

$$\frac{\sigma_{1f}}{\sigma_{3f}}(\text{no primes}) = \frac{(296 + 70)}{150} = 2.44 = \tan^2\left(45° + \frac{\phi}{2}\right)$$

2. *Graphically*: Plot the Mohr failure envelope with $\phi' = 35°$ on a Mohr diagram (Fig. Ex. 13.3). There is only *one* circle that is tangent to the envelope and with $\sigma'_{3f} = 80$ kPa (150 − 70). Once the circle is drawn (trial and error), σ'_{1f} is automatically determined ($\sigma'_{1f} = 296$ kPa) as is $(\sigma_1 - \sigma_3)_f$, the diameter of the failure circle (= 216 kPa).

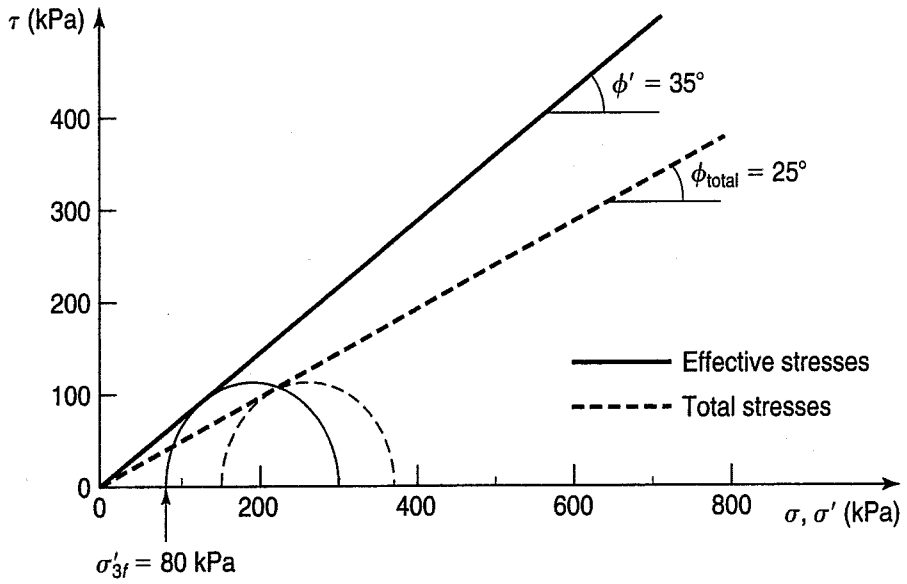

FIGURE Ex. 13.11

The Mohr circle at failure in terms of total stresses has the same diameter since $(\sigma_1 - \sigma_3) = (\sigma'_1 - \sigma'_3)$. You can plot the total stress circle starting at $\sigma_{3f} = 150$, the total cell pressure, and determine ϕ_{total}. Compare Figs. Ex. 13.2 and 13.3 with Fig. 13.59(a).

d. From Eq. (11.10), $\alpha_f = 45° + \phi'/2 = 62.5°$.

Example 13.12

Given:

The same sand as for Example 13.11 except that the cell pressure is 300 kPa.

Required:

Δu_f.

Solution: There are several approaches to this problem. Graphically, we could construct a total stress circle tangent to the total failure envelope shown in Fig. Ex. 13.11 but starting at $\sigma'_{3c} = \sigma_{3f} = 300$ kPa. Then shift your compass (or circle template or AutoCAD circle maker) to the left until the circle is just tangent to the effective Mohr failure envelope.

$$\Delta u_f = \sigma_{3f} - \sigma'_{3f} = 300\,\text{kPa} - 160 = 140\,\text{kPa}$$

Analytically, use Eq. (12.1) and $(\sigma_1/\sigma_3)_{\text{total}}$ from Ex. 13.11

$$\sigma_{1f} = \sigma_{3f}\left(\frac{\sigma_1}{\sigma_3}\right)_{\text{total}} = 300(2.44) = 732\,\text{kPa}$$

$$\sigma_{1f} - \sigma_{3f} = 732 - 300 = 432\,\text{kPa}$$

From Eq. (12.3) and $(\sigma'_1/\sigma'_3)_f = 3.7$ (Example 12.8),

$$\sigma'_{3f} = \frac{(\sigma_1 - \sigma_3)_f}{(\sigma'_1/\sigma'_3) - 1} = \frac{423}{3.7 - 1} = 160\,\text{kPa}$$

$$\Delta u_f = \sigma_{3f} - \sigma'_{3f} = 300 - 160 = 140\,\text{kPa}$$

Check: $\Delta u_f = \sigma_{1f} - \sigma'_{1f} = 732 - 3.7(160) = 140\,\text{kPa}$

13.10.2 Using CD Tests to Predict CU Results

We suggest you do a quick review of the *drained* shear strength tests in Chapter 12. There we saw that the stress-strain and volumetric strain $(\Delta V/V_o)$ data plots may be used to determine the volume change at failure for different void ratios and effective confining pressures, using the idealized figures in Fig. 12.10(a) and (b). Also, in our previous discussion of the shear strength of sands in Chapter 12, we defined the critical void ratio, e_{crit} as the void ratio at failure for a given effective confining pressure in a drained test where the volumetric strain is equal to zero. Further, we defined the critical effective confining pressure, $\sigma'_{3\,\text{crit}}$ as the effective confining pressure at failure when the volumetric strain is zero. See Fig. 12.4.

Using a section of the Peacock diagram (Fig 12.11) where the void ratio after consolidation is e_c, an effective confining pressure σ_c' to represent the conditions at the time of the consolidation phase of an undrained test. If the effective confining pressure is located at point A, we see that the positive volume change *tendency* at point D results in a negative pore pressure during an undrained test. On the other hand, if the effective confining pressure is at point C, we observe that the negative volume change tendency at point B results in a positive pore pressure resulting for an undrained test. These changes in pore water pressure affect the strength of the soil under undrained testing. As we shall see shortly, the rule is: with positive volume change *tendency*, a negative pore pressure results; likewise with a negative volume change *tendency*, a positive pore pressure results.

Let's assume that the void ratio at the time of consolidation is e_c and is a constant. (Of course whenever we consolidate a granular material with an in situ void ratio of e_o, at different confining pressures in the triaxial test, for example, the void ratio *after* consolidation will be different with each confining pressure. The higher the confining pressure, the lower the void ratio after consolidation. We will ignore this fact for our present discussion.)

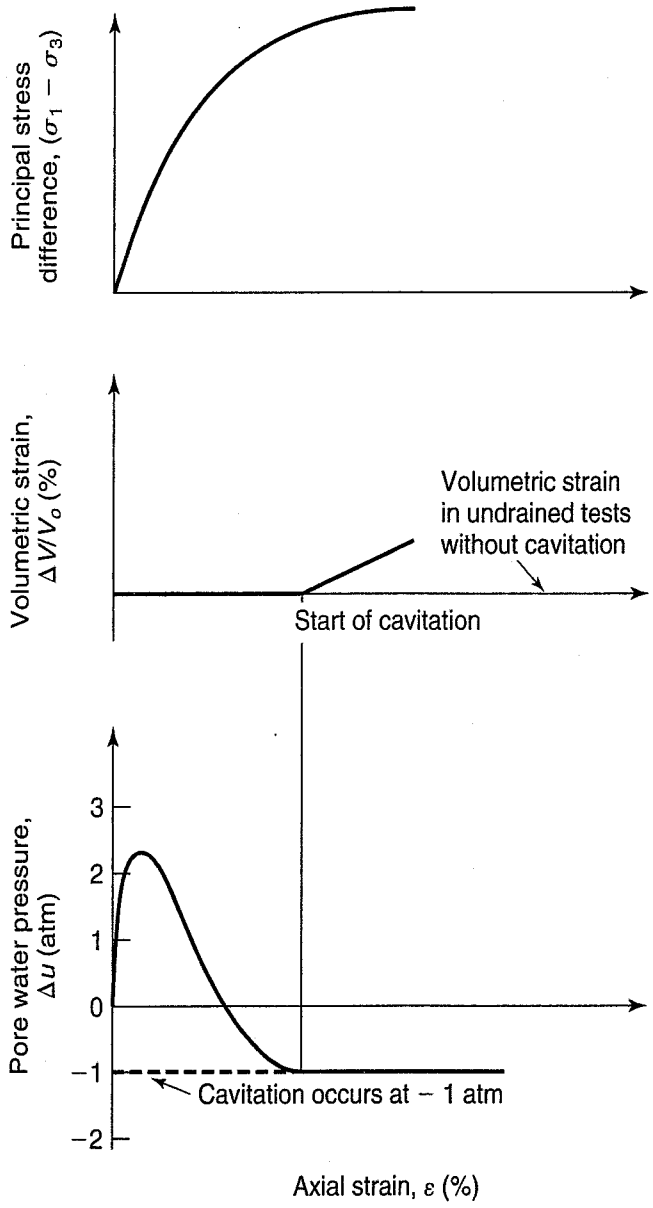

FIGURE 13.61 Typical stress, volumetric strain, and axial strain for a medium dense sand during undrained loading.

A lot depends on the void ratio. For soils that are loose to medium dense, the pore water pressure will be positive. On the other hand, soils that are medium to dense will tend to dilate with a resulting negative pore pressure. Another look at the Peacock Diagram will show this for conditions (e_c and σ_c') to the left of the critical state line, WHP (where for any void ratio, the resulting volume change for drained tests would be positive). For those soils in the undrained states with positive volume change tendencies, the resulting induced pore pressures will be negative. So, for soil conditions of this type, the pore water pressure would slightly rise initially and then become negative. At the point when the negative pore pressure reaches −1 atm, the specimen cavitates (water vaporizes and bubbles form) and the volumetric strain increases, as shown in Fig. 13.61! (Compare this figure with the CU part of Fig. 13.60.)

Review Fig. 12.29 for information on the use of *back pressure* when conducting consolidated undrained tests (CU) on soils. Back pressure is the use of an artificial positive pore pressure u_o, to ensure that the soil is saturated prior to the consolidation and shear phases. Increasing the back pressure while at the same time increasing the cell pressure σ_3 by the same amount, maintains the desired effective confining pressure.

We will consider five possible cases (summarized in Fig. 13.62) of how the

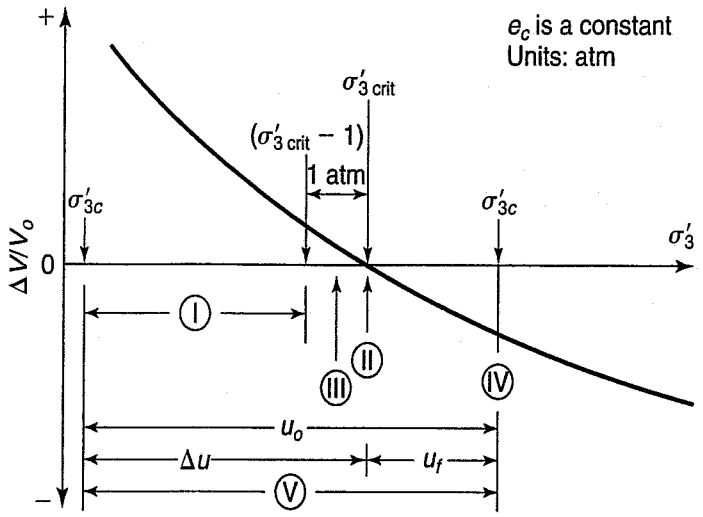

Case	σ	u_o	Failure
I	$\sigma'_{3c} << \sigma'_{3\,crit}$	$u_o = 0$	Cavitation
II	$\sigma'_{3c} = \sigma'_{3\,crit}$	$u_o = 0$	$\sigma'_{3\,crit}$
III	$(\sigma'_{3\,crit} - 1) < \sigma'_{3c} < \sigma'_{3\,crit}$	$u_o = 0$	$\sigma'_{3\,crit}$
IV	$\sigma'_{3c} > \sigma'_{3crit}$	$u_o = 0$	$\sigma'_{3\,crit}$
V	$\sigma'_{3c} < \sigma'_{3\,crit} < \sigma_{3\,cell}$	u_o large	$\sigma'_{3\,crit}$

FIGURE 13.62 The five cases are summarized on a between the volumetric strain and effective confining pressure showing their range of stress conditions. *Note:* e_c is a constant.

undrained shear strength will vary depending on the void ratio after consolidation, the consolidation pressure σ'_{3c} and the critical confining pressure. In each case, we will be using a "slice" of the Peacock diagram (Fig. 12.11), specifically volumetric strain versus effective confining pressure, to illustrate the effect on undrained strength. After these cases are described, we show a numerical example for one of these cases.

In **Case I**, σ'_{3c} is much less than $\sigma'_{3\,crit}$ and the pore pressure becomes negative until cavitation occurs (in this case with zero back pressure). As a result, the strength of the specimen is controlled by cavitation with $u_f = -1$ atm. Thus, the range of this type of failure is governed by

$$0 < \sigma'_{3\,cell} = \sigma'_{3c} < (\sigma'_{3\,crit} - 1)$$

Case II, again with back pressure = 0, is very simple. Because the effective stress during consolidation is the same as the critical confining pressure, there is no volume change tendency and therefore no pore pressure development. The effective confining pressure at failure equals the critical confining pressure, or

$$\sigma'_{3f} = \sigma'_{3\,crit}$$

Case III involves a situation where the cell pressure is between $(\sigma'_{3\,crit} - 1)$ and $\sigma'_{3\,crit}$. As we expect for any sand with a confining pressure less than the critical confining pressure, the volume change tendency results in a negative pore pressure and an increase in effective stress. In this case, the effective confining stress equals the critical confining pressure $(\sigma'_{3\,crit})$ before the specimen cavitates. The range of confining stresses for this case is

$$(\sigma'_{3\,crit} - 1) < \sigma'_{3c} < \sigma'_{3\,crit} \quad (u_o = 0)$$

In **Case IV**, when a sand specimen is consolidated with zero back pressure at a greater pressure than the critical confining pressure, the resulting pore pressure is positive causing a gradual decrease in effective stress. When the effective stress lowers to the critical confining pressure, volume change tendency becomes zero and the confining pressure at failure σ'_{3f} is equal to the critical confining pressure. The limits for this case are

$$\sigma'_{3\,crit} < \sigma'_{3c} < \infty \quad (u_o = 0)$$

Case V is the first case we discuss with a back pressure greater than zero. Such a case represents most field conditions with a ground water table. The critical confining pressure controls the undrained shear strength. As stress is applied to the specimen, the negative volume change tendency causes an increase in pore pressure, and this reduces the effective confining pressure until the critical confining pressure is reached. No additional volume change tendency occurs, and the test stops at the critical confining pressure. The limits for this case are

$$\sigma'_{3c} < \sigma'_{3\,\text{crit}} < \sigma'_{3\,\text{cell}};\quad u_o > \sigma'_{3\,\text{crit}}$$

Example 13.13

Given:

The initial stress conditions for Case I. Let $\sigma_{3\,\text{crit}} = 10$ atm, point H, and $\sigma'_{3c} = 4$ atm, point D on Fig. 12.11.

Required:

Evaluate the total, pore water, and effective stresses at the end of consolidation, during shear, and at failure for an undrained compression test. Show these stresses on the specimen for the vertical and horizontal planes for these stages.

Solution: Fig. Ex. 13.13a shows the initial and final conditions. The test starts at point D and as the principal stress difference is applied, the positive volume change tendency causes a negative pore pressure. The pore pressure in Case I continues to go negative until cavitation occurs at -1 atm. Failure occurs at Point D′ when $u_f = -1$ atm and $\sigma_{3f} = \sigma_{3c} - (-1) = \sigma_{3c} + 1 = 5$ atm. The initial and final conditions are shown in Fig. Ex. 13.13b. In order to plot the Mohr circles for the case, the principal stress ratio $(\sigma'_1/\sigma'_3)_f = K_f$ would have to be known for the void ratio after consolidation. Note that $\Delta\sigma_f = (\sigma_1 - \sigma_3)_p = \sigma'_{3f}(K_f - 1)$; $\sigma'_{3\text{crit}} = 10$ atm.

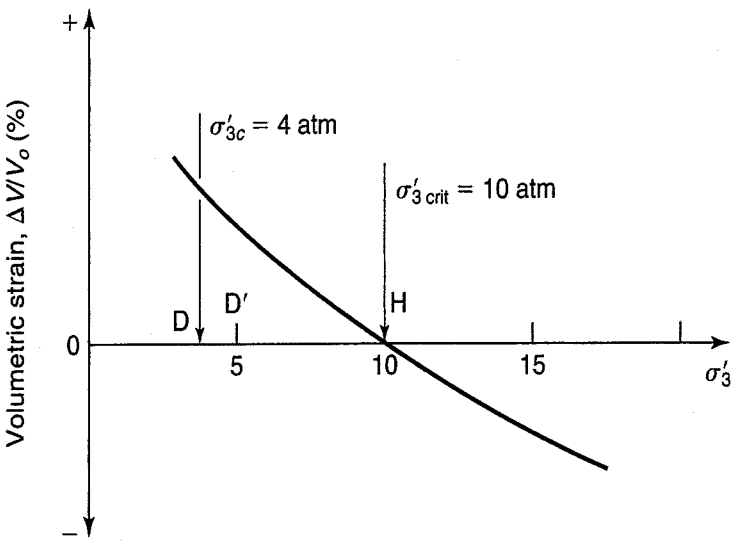

FIGURE Ex. 13.13a Case I. Volumetric strain versus effective confining pressure for a consolidation pressure of σ'_{3c} and constant e_c. The test starts out with $\sigma'_{3c} = 4$ atm (Point D) and ends at σ'_{3f} at 5 atm at Point D′.

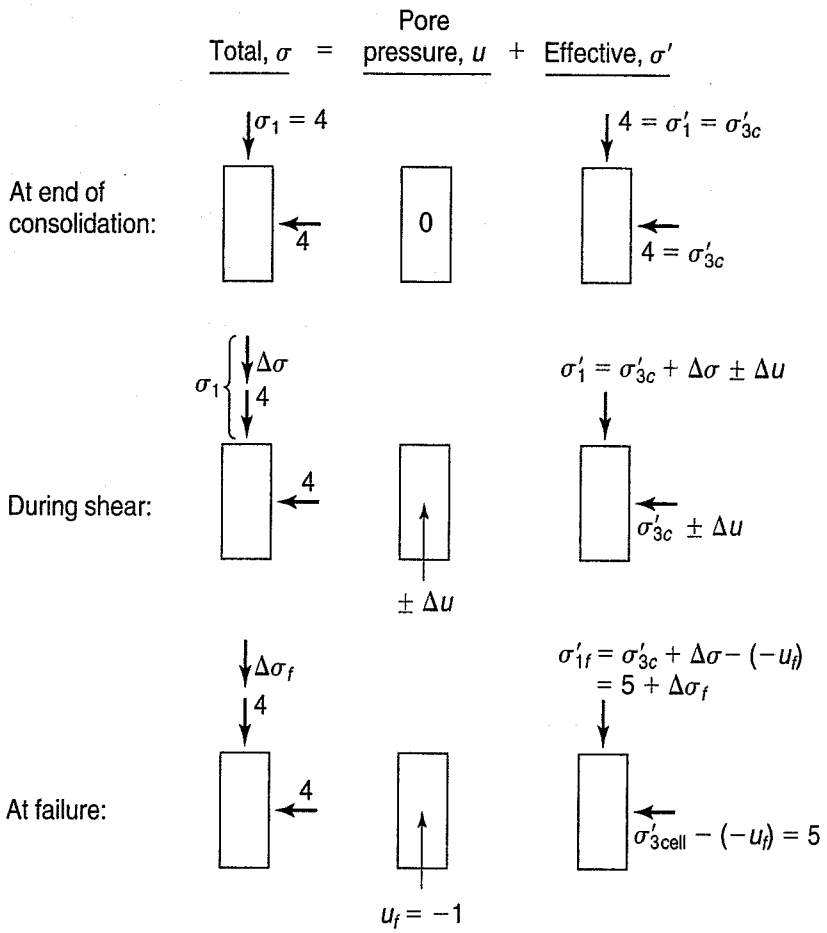

FIGURE Ex. 13.13b Case I. Conditions in specimen during a consolidated-undrained triaxial compression (CU) test. Void ratio after consolidation = e_c = a constant.

One last point. There are two different ways to test soils in the laboratory triaxial device. The usual way is to set up specimens with the same initial void ratio at increasing confining pressures. The second way is to compact at some initial void ratio and then consolidate to some pressure to obtain the same void ratio after consolidation. This approach is very time-consuming and therefore very costly. We end up reconstituting sand specimens at the estimated in situ void ratio and subjecting them to increasing consolidation pressures. Two things occur. The first is that the shear strength will be higher due to the increased consolidation stress above the critical confining pressure. The second thing that occurs is that during consolidation, the void ratio *decreases*. We also know that when the void ratio changes, the critical confining pressure also changes. With a decrease in e_c, the $\sigma'_{3\,crit}$ increases. Just look at Fig. 13.63, in which there is an exaggerated change in $\sigma'_{3\,crit}$. The higher consolidation pressure results in a decrease in e_c, which results in an increase in $\sigma'_{3\,crit}$. The end result is an increase in the undrained shear strength with increasing consolidation pressure.

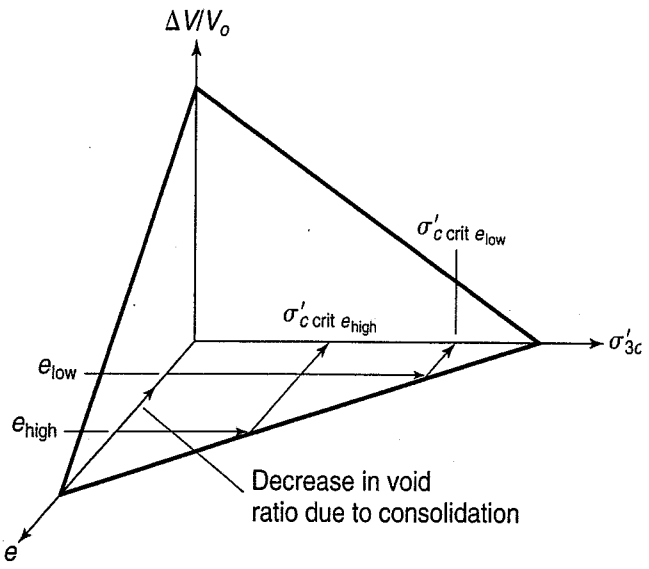

FIGURE 13.63 The Peacock Diagram showing an exaggerated change in the critical confining pressure and a decrease in void ratio after consolidation.

13.10.3 Unconsolidated-Undrained Behavior

Seed and Lee (1967) explained what happens during UU tests on saturated sand. They considered two cases. For Case I, the cell pressure σ_c is less than the critical confining pressure $\sigma'_{3\,\text{crit}}$ minus the atmospheric pressure, or

$$\sigma_c < \sigma'_{3\,\text{crit}} - 1\ \text{atm} \tag{13.35}$$

In Case II, the confining pressure is greater than the critical confining pressure $\sigma'_{3\,\text{crit}}$ minus the atmospheric pressure, or

$$\sigma_c > \sigma'_{3\,\text{crit}} - 1\ \text{atm} \tag{13.36}$$

Figure 13.64 shows what happens to the total, pore pressure, and effective stress conditions at all stages in the test for Case I. In order to give the specimen some initial effective stress σ'_{co}, we apply a hydrostatic cell pressure of σ_{co} with the drainage valves open. Now we close the drainage valves, and increase the cell pressure σ_{c1}. Because no drainage is permitted, all this increase in cell pressure goes into the pore pressure Δu, which is now equal to $\sigma_{c1} - \sigma_{co}$. Note that the effective stress in the specimen remains the same as before, or $\sigma'_{co} = \sigma_{co}$.

Now when the axial stress $\Delta\sigma$ is applied to the specimen, the specimen tends to dilate because the total cell pressure σ_c is less than the critical confining pressure $\sigma'_{3\text{crit}} - 1$ atm. Concurrently, the pore pressure decreases, but it cannot go lower than about 1 atm because at that pressure, the pore water cavitates. Thus at failure for Case I, $\Delta u_f = -1$ atm, $\sigma'_{1f} = \Delta\sigma_f + \sigma_{c1} + 1$, and $\Delta\sigma'_{3f} = \sigma_{c1} + 1$.

For Case II where the confining pressure is greater than $\sigma'_{3\,\text{crit}} - 1$ atm, the initial conditions are the same as in Case I, that is $\sigma_{co} < \sigma'_{3\,\text{crit}}$ (see Fig. 13.65). When the cell pressure is increased to $\sigma_{c2} > \sigma_{co}$ with the drainage valves closed, all the increase in cell pressure goes into the pore pressure

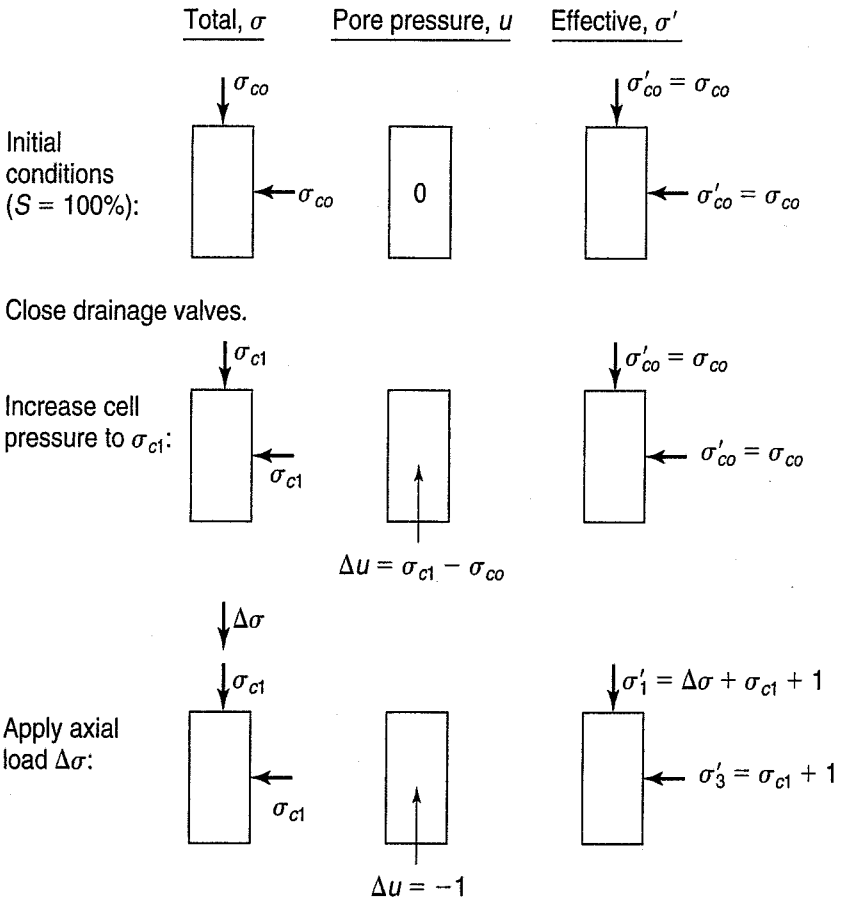

FIGURE 13.64 Total, pore pressure, and effective stress conditions in a UU specimen of saturated sand; Case I with $\sigma_c < \sigma'_{3\,\text{crit}} - 1$.

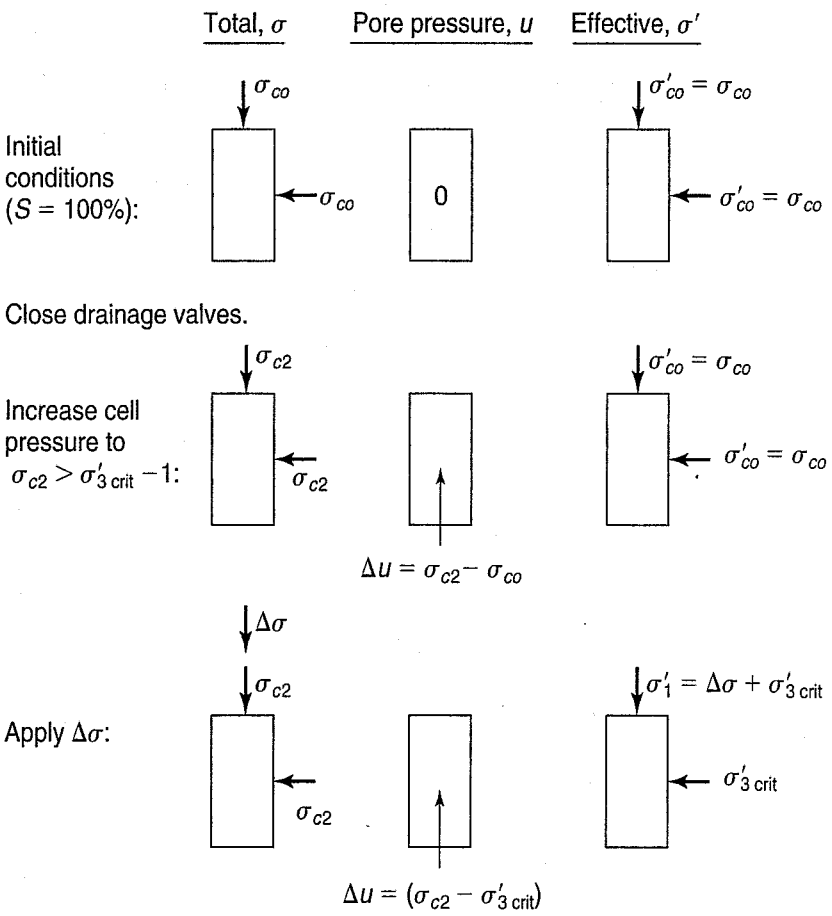

FIGURE 13.65 Total, pore pressure, and effective stress conditions in a UU specimen of sand; Case II with $\sigma_c > \sigma'_{3\,\text{crit}} - 1$ atm.

Δu, and $\Delta u = \sigma_{c2} - \sigma_{co}$. As in Case I, the effective stress in the specimen remains the same as before, or $\sigma'_{co} = \sigma_{co}$. Now when the axial stress $\Delta\sigma$ is applied to the specimen, the specimen still tends to dilate because $\sigma'_{co} < \sigma'_{3\,\text{crit}}$ and Δu tends to decrease. But before the pore pressure can reach -1 atm, the effective confining stress σ'_c increases from σ'_{co} to σ'_{c2} to $\sigma'_{3\,\text{crit}}$. Of course, at $\sigma'_{3\,\text{crit}}$, $e = e_{\text{crit}}$ and no further tendency towards volume change will occur. Thus at "failure" or maximum principal stress difference, $\sigma'_{3f} = \sigma'_{3\,\text{crit}}$, and $\sigma'_{1f} = \Delta\sigma_f + \sigma'_{3\,\text{crit}}$.

The Mohr's circles and Mohr failure envelopes for both cases are shown in Fig. 13.64. For Case I when $\sigma_c < \sigma'_{3\,\text{crit}} - 1$ atm, the pore water pressure at failure is -1 atm (Fig. 13.64), so the total stress circle plots to the left of the effective stress circle. Both failure envelopes begin at the origin, so the total stress envelope must be curved as shown in Fig. 13.66(a). Note that the effective stress UU friction angle, $\phi'_{\text{UU}} \approx \phi'_{\text{CD}}$.

For Case II when $\sigma_c > \sigma'_{3\,\text{crit}} - 1$, the pore pressure at failure is $\Delta u_f = \sigma_{c2} - \sigma'_{3\,\text{crit}}$, and the effective stresses on the specimen are $\sigma'_{3\,\text{crit}}$ and $\sigma'_{1f} = \Delta\sigma_f + \sigma'_{3\,\text{crit}}$. Thus the total stress circle will plot to the right of the effective stress Mohr's circle, and this will be the case for all total stress circles with cell pressures greater than $\sigma'_{3\,\text{crit}} - 1$. Thus the total stress failure envelope will be horizontal, as shown in Fig. 13.66(b) for all confining pressures greater than this value. Note that there is only one effective stress Mohr circle when $\sigma'_3 > \sigma'_{3\,\text{crit}}$. Case II is of course analogous to the UU test results on cohesive soils shown in Fig. 12.39: the total stress envelope is horizontal and there is only one effective stress Mohr circle.

Just as with the CU test, the behavior in the UU tests is strongly dependent on the back pressure. Back pressure prevents cavitation, so that the induced pore water pressure can go much more negative than -1 atm. This means that the effective confining stress can increase much more than without back pressure, and that the specimen can be much stronger than without back pressure.

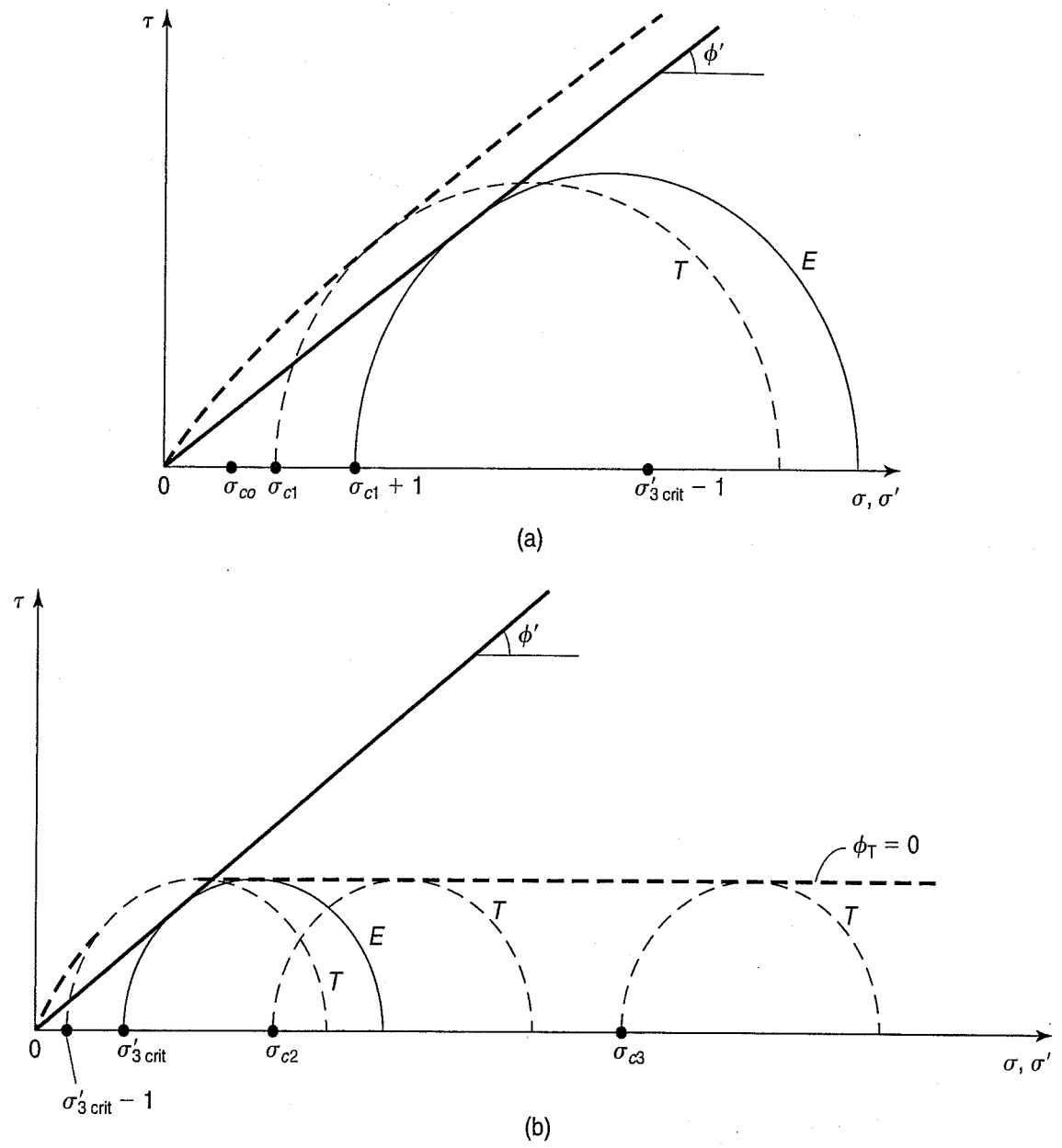

FIGURE 13.66 Mohr failure envelopes for UU tests on saturated sands: (a) Case I, $\sigma_c < \sigma'_{3\,crit} - 1$ atm; and (b) Case II, $\sigma_c > \sigma'_{3\,crit} - 1$ atm. Case I is an enlarged view of Case II near the origin.

13.10.4 Strain-Rate Effects in Sands

For sands, the effects of rate of shearing on stress-strain-strength properties do not become significant until extremely high rates are imposed—for example, by earthquakes, vehicle wheel loadings, blasting, pile driving, and projectile and other rapidly penetrating objects. Of these, only the example of rapidly penetrating objects and projectiles is monotonic; all the other examples are of cyclic and mostly aperiodic and random loading. In this section, we describe the results of research on high rates of monotonic loading. The properties of soils subjected to vibratory and cyclic loading are discussed in Sec. 13.12.

The rates used in undrained triaxial compression experiments reported by Whitman and Healy (1962) resulted in times to failure from 5 min (approximately 0.03% strain per sec) to 5 msec (approximately 2650% strain per sec), and they found no dependence of friction on strain rate. The other component contributing to shear strength is excess pore pressure development, and this was found to be independent of strain rate in dry sands (obviously, since there is no pore pressure) and dense saturated

sands (which have negative excess pore pressures leading to cavitation). For tests on loose Ottawa sand, the rate dependence of excess pore pressure led to a 40% increase in strength when the time to failure went from 5 sec to 0.025 sec, and a 100% increase in strength for Camp Cooke sand for times to failure ranging from 3 min to 0.2 sec.

However, as Whitman and Healy (1962) pointed out, such tests are fraught with potential errors, including membrane penetration effects leading to localized volume changes, inertial effects as the specimen expands radially, and the influence of nonuniform strain conditions within the specimen resulting from end restraint. Yamamuro and Abrantes (2005) addressed these issues in drained triaxial compression tests on crushed coral (D_r = 58%). By maintaining a 98 kPa (1 atm) vacuum in the pore water system, no excess pore pressures could be sustained even at the highest strain rate used, 1764% strain per sec. The drained conditions eliminated the membrane penetration problems, and the researchers used high-speed photography and digital image analysis to examine deformation patterns through the specimen height. Thus any nonuniform deformation observed could be characterized, although lubricated end platens were used to reduce nonuniformity. Finally, their results showed that inertial effects were not significant beyond relatively small strains. At the lower confining stress tested (98 kPa), the shear strength increased about 25% from a strain rate of 0.23 to 1764% strain per sec, with a corresponding decrease in strain to failure. At the higher confining stress of 350 kPa, the strength increased about 50% when the strain rate increased from 0.23 to 1495% strain per sec.

When compared with strain rate effects in clays (Sec. 13.13.7), a significant strain rate effect on sand shear strength requires much higher rates of loading for a large change in shear strength.

13.11 PLANE STRAIN BEHAVIOR OF SANDS

In Sec. 11.5.2 we described that what we commonly call triaxial tests are really cylindrical compression tests, in which the test and stress conditions were shown in Fig. 11.15. We call these stress conditions *axi-symmetric*, because the stresses acting in the horizontal direction (the cell pressure) are equal in all directions. We have also mentioned before (Secs. 11.5.2 and 12.8) that laboratory strength tests are attempts to model the drainage conditions that we think exist in the field, and that also applies to field stress conditions. What about axi-symmetric stress conditions? Do they exist in the field? Yes, and some examples are circular footings, tanks on shallow foundations, piles and drilled shafts, and cylindrical excavations.

On the other hand, for many important geotechnical applications, two-dimensional or *plane-strain* conditions more reliably model field stress conditions. These applications include strip foundations, highway and railroad embankments, many earth dams, slopes, retaining walls, and some excavations—all of which have in common that they are long relative to their width or breadth. Plane strain conditions mean that the strain in the long direction of the foundation, earth structure, slope, or excavation is very small compared to the other directions. So we can assume in our strength test that $\varepsilon_2 = 0$. Even then, the intermediate principal stress σ_2 is undoubtedly greater than zero, especially in field situations.

To investigate the influence of the intermediate principal stress, special tests such as plane strain or cuboidal shear tests must be used. We showed schematic diagrams of these tests in Fig. 11.16. In plane strain compression tests, for example, the principal stresses are $\sigma_1 > \sigma_2 > \sigma_3$. If plane strain is more indicative of certain field conditions, why are plane strain tests not used more often in practice? For one thing, vey few plane strain devices have been built, and most of those are at university research laboratories. The equipment is considerably more expensive to develop and more expertise is required operate it than for traixial and direct tests.

In this section, we summarize the results of some plane strain tests on different sands so you can get an idea of the difference in friction angle and modulus compared with conventional triaxial test results on the same sands. We use the symbol PS for plain strain and TC for triaxial compression.

Cornforth (1964) conducted a comprehensive testing program of PS and TC tests on Brasted sand, a rather uniform (C_u = 2.1) medium (D_{50} = 0.25 mm) sand over a wide range of densities. Results are shown in Figs. 13.67 and 13.68. The angle of internal friction in plane strain is somewhat higher than in triaxial compression, especially at higher densities (lower void ratios and porosities). That the axial strain at failure is significantly lower in plane strain (Fig. 13.67) indicates that the PS modulus is probably much greater than the TC modulus, and this is indeed the case, as indicated by the test results shown in Fig. 13.68. In addition, the peak strengths are markedly greater, especially at higher densities. Estimates of the peak secant moduli scaled from the figures Fig. 13.68 indicated that the ratios of this modulus in plane strain to the corresponding triaxial modulus was between 3 and 4.6; the lower values were for the higher densities.

Sultan and Seed (1967), in a study of the stability of sloping core earth dams, reported results of PS and TC compression tests on medium to coarse uniform Monterey sand (C_u = 1.25 and C_c = 1.0) and Ottawa sand over a range of void ratios, as shown in Fig. 13.69.

Marachi et al. (1981) conducted a comprehensive series of experiments, also on Monterey sand, to examine the effects of a number of soil and test specimen variables on PS test results. Of interest to us are the results shown in Fig. 13.70, which are very similar in appearance to those of Cornforth (1964) shown in Fig. 13.68. Both the peak strength and initial tangent moduli are greater in plane strain. Peak secant moduli were scaled from these figures, and the ratios of PS to TC moduli ranged from 3.7 to 1.9. In this case, however, the denser specimens apparently had the greater modulus ratios—opposite of what Cornforth's (1964) data showed.

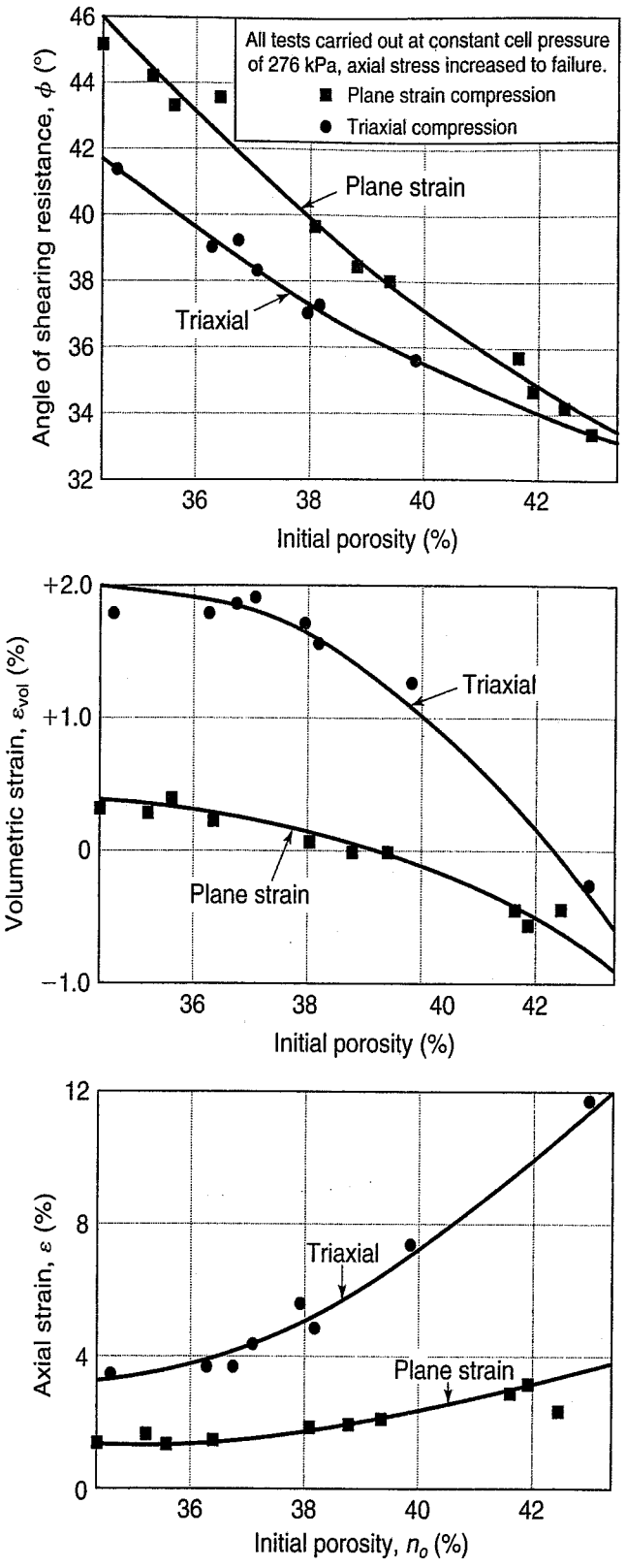

FIGURE 13.67 Comparison of plane strain and triaxial-compression tests on Brasted sand at failure (Cornforth, 1964).

Marachi et al. (1981) verified that the PS friction angle is greater than the TC friction angle, especially for denser sands. These results are given in Fig. 13.71 in terms of initial void ratio, and in Fig. 13.72 versus confining pressure.

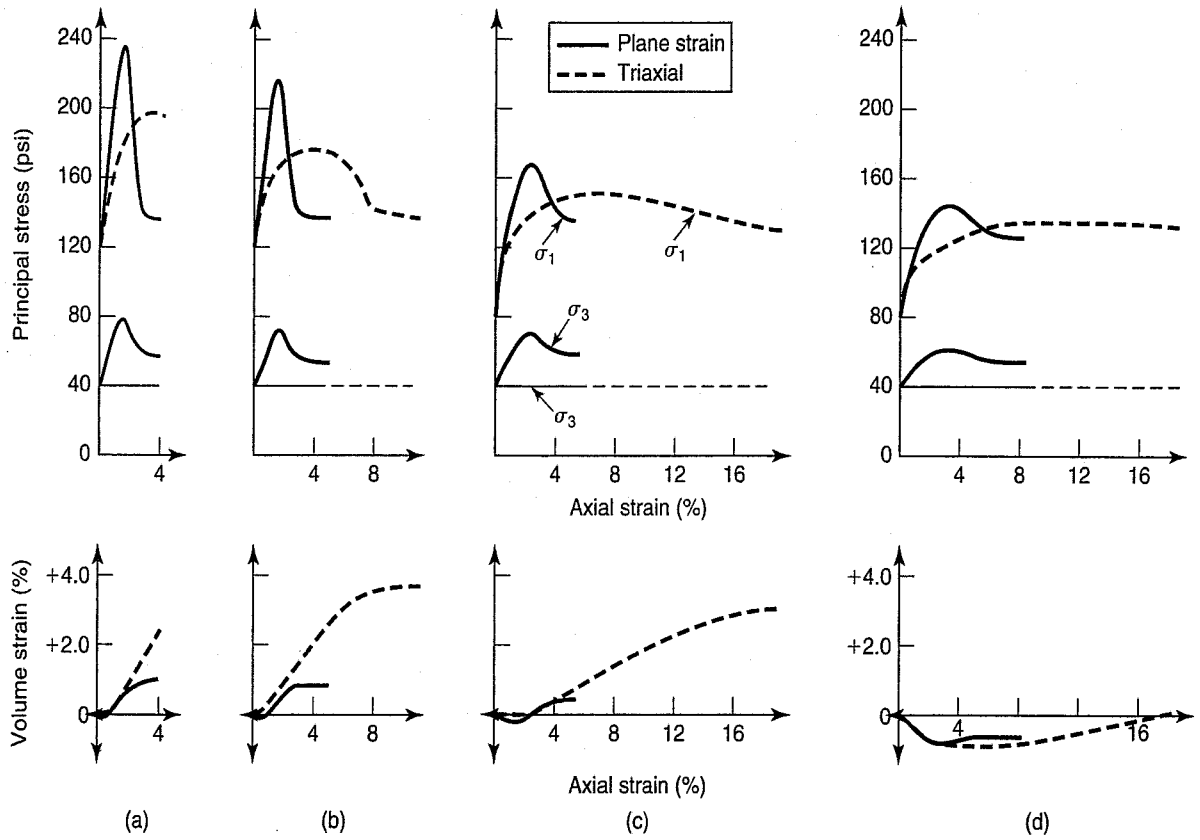

FIGURE 13.68 Comparison of plane-strain and triaxial-compression tests at different densities: (a) dense, $D_r = 80\%$; (b) medium dense, $D_r = 65\%$; (c) loose, $D_r = 40\%$; and (d) very loose, $D_r = 15\%$ (Cornforth, 1964).

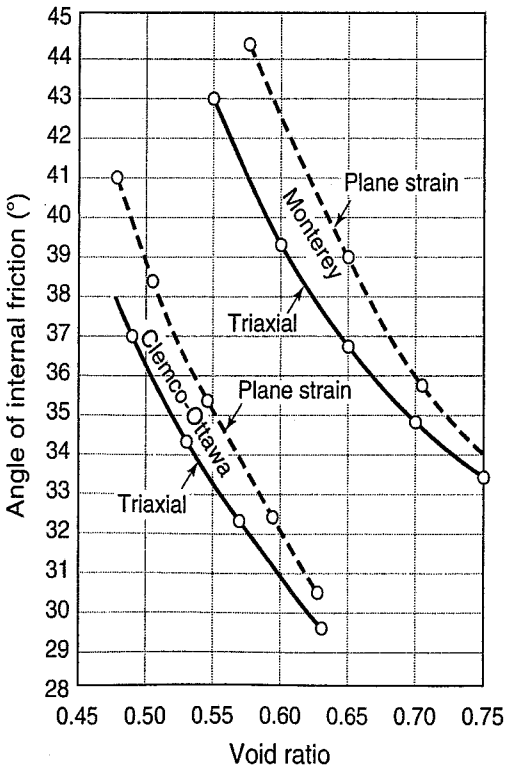

FIGURE 13.69 Angle of internal friction for Monterey and Ottawa sands as determined by PS and TC tests (Sultan and Seed, 1967).

Boyle (1995) conducted a few PS and TC tests on very dense ($D_r = 96\%-101\%$) specimens of uniform ($C_u = 1.7$) and round-grained Ottawa sand and a slightly better graded ($C_u = 2.9$), coarser, and very angular Rainier sand. The TC tests were conventional strain-rate controlled, while the PS tests were conducted in a special PS device that used incremental (stress-controlled) loading. The test results for the two sands are shown in Figs. 13.73 and 13.74. The ratio of the PS to TC secant modulus ranged from 0.9 to 2.1 for the Ottawa sand and from 2.9 to 4.2 for the Rainier sand.

A summary of the test results for both sands is shown in Fig. 13.75. The difference in PS versus TC friction angle is significant for the angular Rainier sand, especially at low confining pressures.

In summary, based on considerable experimental evidence, it is generally accepted that the PS friction angle is significantly greater than the friction angle measured in TC tests, especially for denser sands and sands with friction angles greater than about 35°. The tests on uniform sands with rounded grains such as Ottawa sand indicated that the PS friction angles were only slightly higher than triaxial friction angles at low

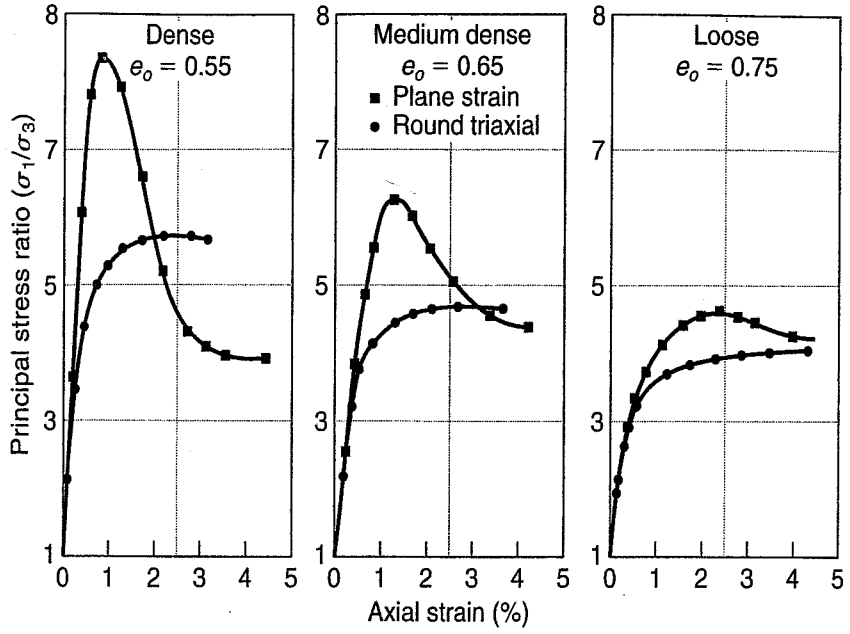

FIGURE 13.70 Stress-strain relationships for PS and TC tests on Monterey sand at three densities; all tests conducted at σ_3 = 70 kPa (Marachi et al., 1981).

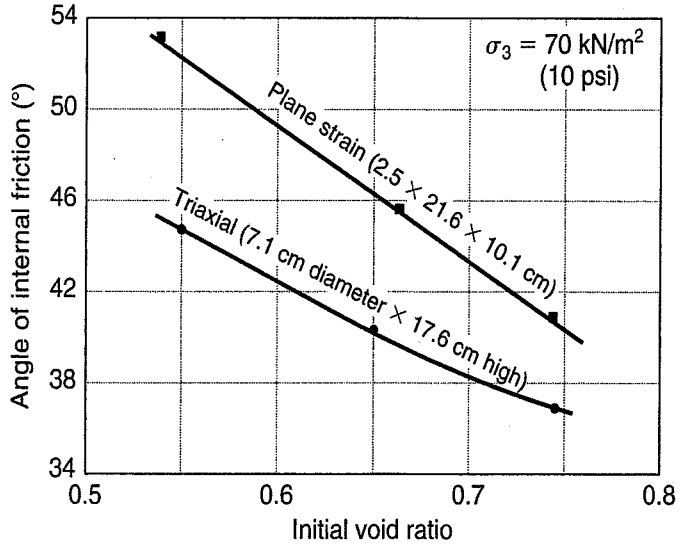

FIGURE 13.71 Angle of internal friction versus void ratio for PS and TC tests on Monterey sand; all tests conducted at σ_3 = 70 kPa (Marachi et al., 1981).

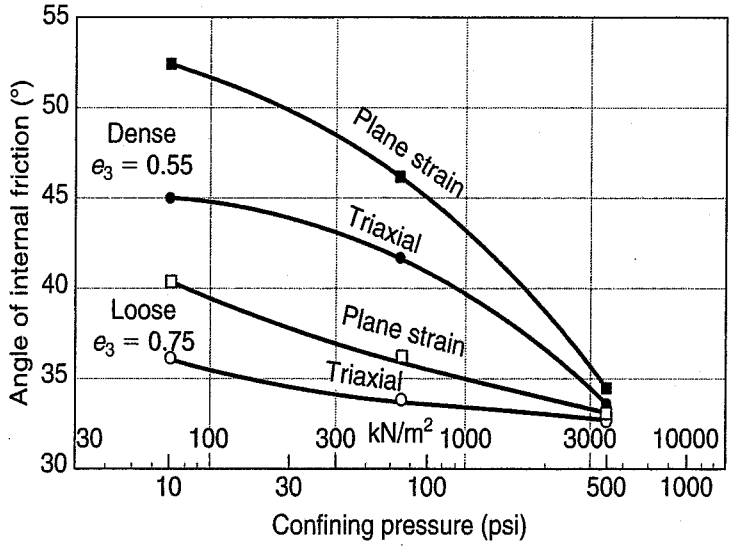

FIGURE 13.72 Relation between friction angle and confining pressure for PS and TC tests on loose and dense Monterey sand (Marachi et al., 1981).

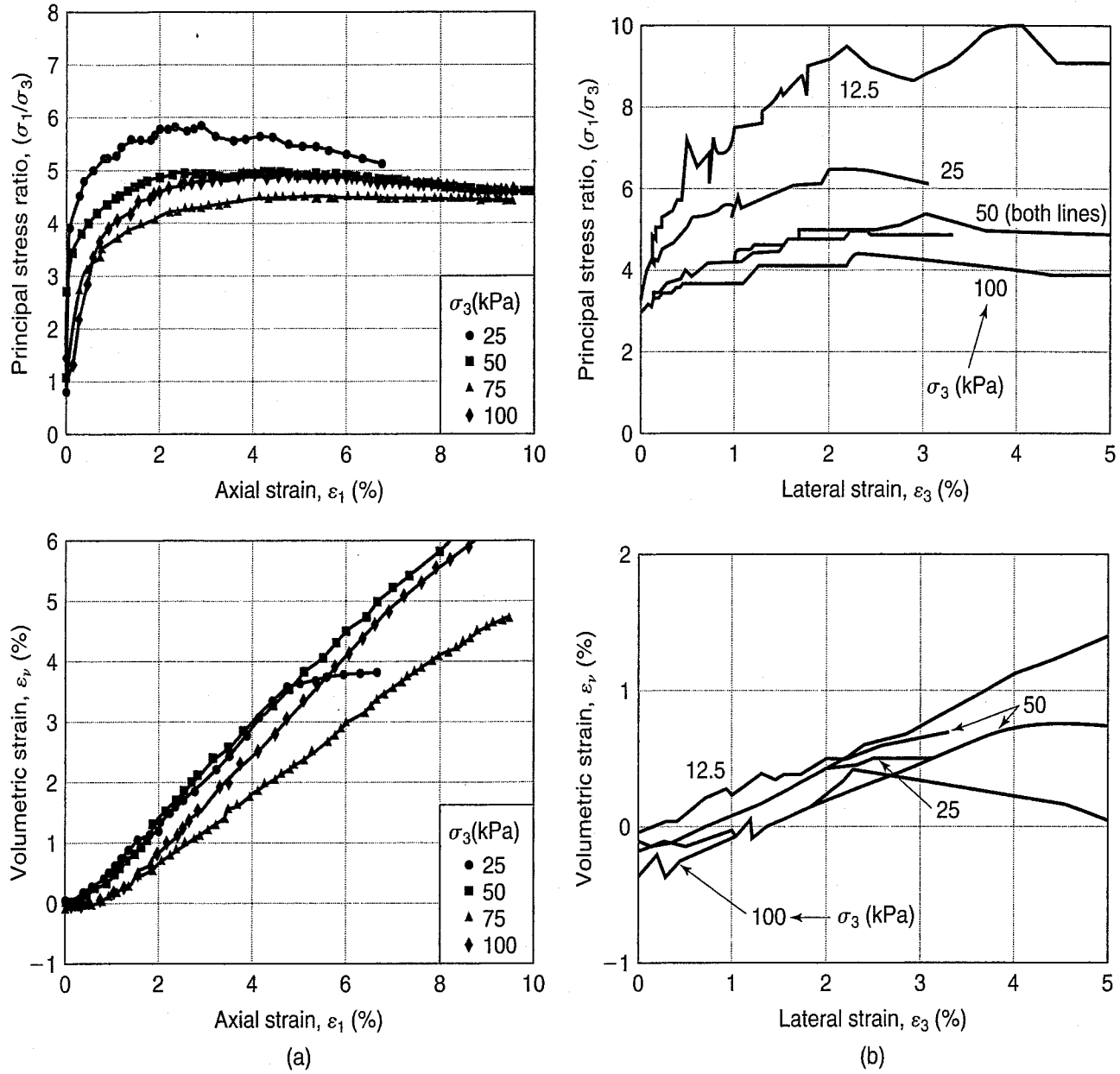

FIGURE 13.73 Test results for Ottawa sand: (a) triaxial, and (b) plane strain (Boyle, 1995).

confining pressures. Research summarized by Ladd et al. (1977) indicated that the PS ϕ is larger than the TC ϕ by 4° to 9° in dense sands and 2° to 4° in loose sands. This effect is even greater at very low confining pressures (see, e.g., Lee, 2000, and Fannin et al., 2005).

Lade and Lee (1976) proposed the following empirical equations to convert triaxial friction angles ϕ_{tx} to plane-strain friction angles ϕ_{ps}, or

$$\phi_{ps} = 1.5\phi_{tx} - 17° \qquad (\phi_{tx} > 34°) \tag{13.37a}$$

$$\phi_{ps} = \phi_{tx} \qquad (\phi_{tx} \leq 34°) \tag{13.37b}$$

Lee (2000) found that these equations were able to predict the PS soil friction angles within a degree or two for sands with angular grains at low confining pressures, but they significantly overpredicted the PS friction angles of rounded grain Ottawa sand at low confining pressures. So, use Eqs. (13.37a) and (13.37b) with some caution.

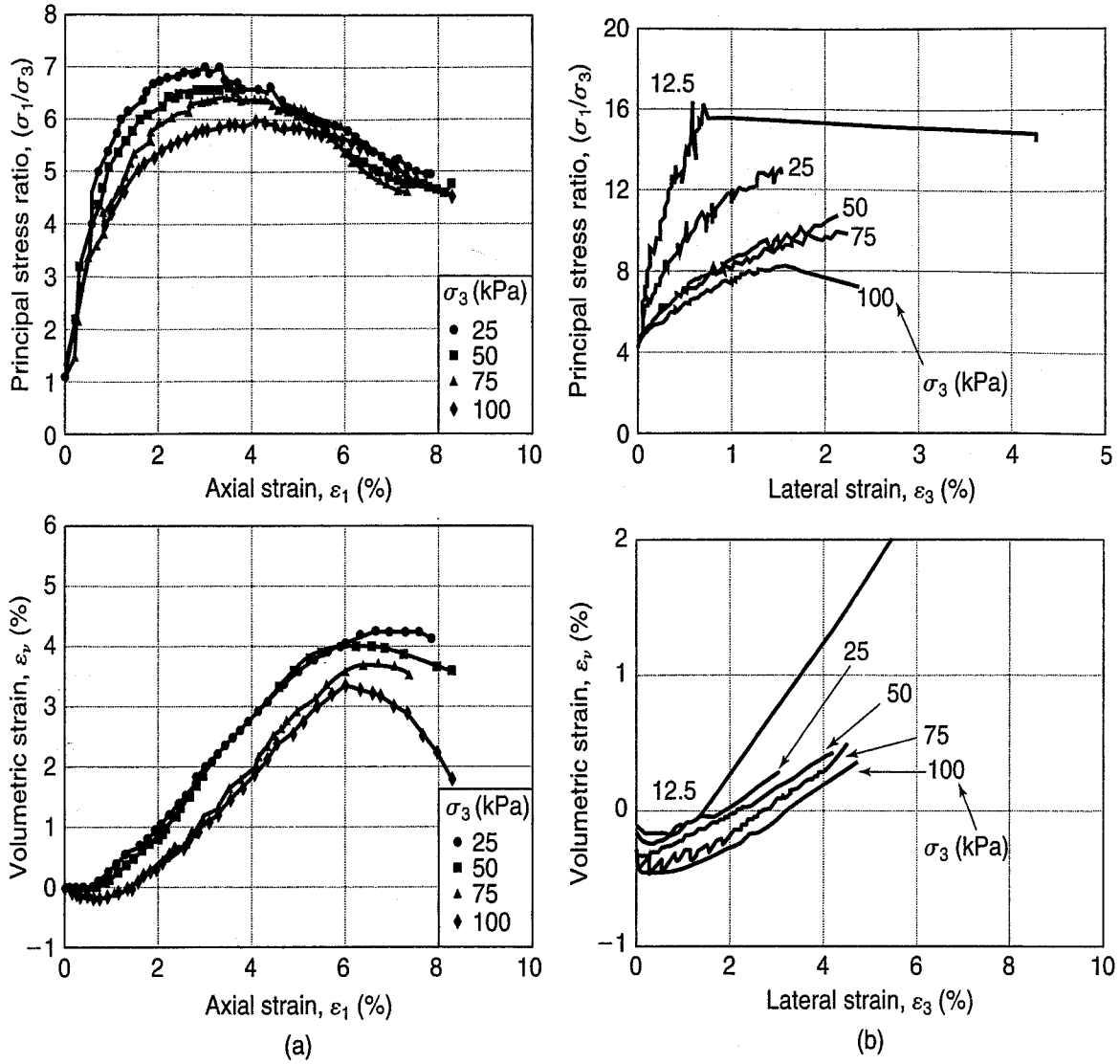

FIGURE 13.74 Test results for Rainier sand: (a) triaxial, and (b) plane strain (Boyle, 1995).

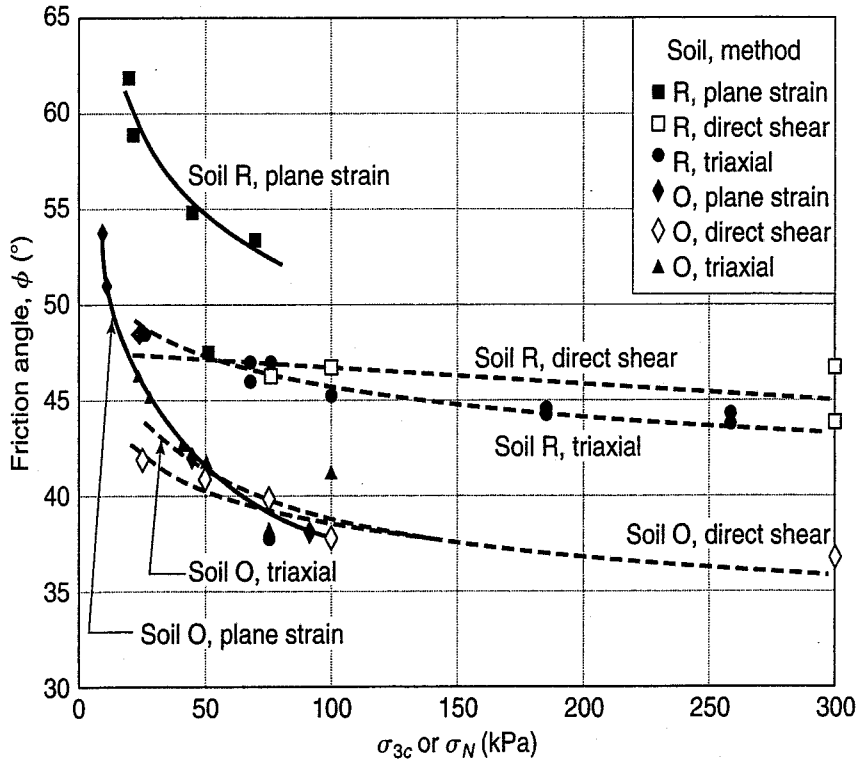

FIGURE 13.75 Summary of all plane-strain, triaxial, and direct-shear test results conducted by Boyle (1995) on Ottawa (O) and Rainier (R) sands.

Although published test results are somewhat inconsistent, it appears that the PS modulus at higher densities is between two and four times the TC modulus for most medium to coarse uniform sands. There is some evidence (Lee, 2000) that the initial tangent moduli are even greater, by as much as a factor of seven, than those values, especially for dense angular sands, but only about twice as great for loose angular materials. The differences in secant moduli can be somewhat less, depending on the percent strain used to determine it.

13.12 RESIDUAL STRENGTH OF SOILS

So far in this chapter and in Chapter 12, the primary focus has been on a soil's peak shear strength, since that is typically used for design purposes, usually after applying an appropriate factor of safety or another type of resistance factor. However, in some important applications, the soil's shear resistance after it has undergone significant deformation beyond that at peak shear strength is needed. A soil's minimum shear strength reached at large deformations or strains is referred to as its *residual strength.* In particular, this is used to analyze the stability of slopes that have experienced prior movement, and in the case of sands, for postliquefaction analyses of earth dams and embankments. As in many areas of geotechnical engineering, the approaches for analyzing the two classes of soils are very different, and there has been considerable progress in understanding these concepts over the past 30 years or so.

13.12.1 Drained Residual Shear Strength of Clays

The primary application for residual shear strength in clays is the analysis of slopes that have previously experienced significant movement due to landslides, interbedding slippage, or slippage in joints or faults. If such preexisting movements exist at a site, the slip surface may represent the critical surface along which future movements may occur. Overconsolidated clays are particularly susceptible to residual strength failures, since these clays tend to soften dramatically with additional deformation after peak shear strength, which is related to their dilation and subsequent increase in water content. Normally consolidated clays tend to experience much less softening, in some cases having a residual strength quite close to their peak strength values.

As a result of these softening behavior characteristics, the residual strength of clays has been analyzed using drained tests to account for the more critical case of overconsolidated clays. The torsional or ring shear test [Fig. 11.17(a)] is used to measure the drained, large strain strength of clays. Soil is trimmed into an annular specimen, a normal stress is applied to the flat surface, and a torque applied to shear the top portion of the soil over the stationary lower portion. The rotation essentially allows unlimited deformation to be applied to the soil.

After performing ring shear tests, Lupini et al. (1981) examined the specimen soil fabrics using polarized light on thin sections and electron microscope images. They identified three modes of residual shear behavior in clays. Turbulent mode occurs in soils with round particles (e.g., clays with significant sand content), or those with platy particles that have high interparticle friction (they specifically looked at halloysite and allophane from Java). Because these soils don't tend to develop any preferred particle orientation, their residual strength (τ_R) and residual friction angle (ϕ'_R) remains relatively high. Sliding mode occurs in clays with platy, low-friction particles (the majority of clays), with a strongly oriented structure developing at larger deformations, leading to low τ_R and ϕ'_R values. In between these two extremes is what they termed transitional mode, for soils that do not have a predominant particle shape; ϕ'_R values for these soils are highly dependent on soil gradation. Figure 13.76 shows $\phi'_R = \tan^{-1}(\tau_R/\sigma'_n)$, where σ'_n is the applied normal stress, versus clay fraction (percent less than 2-μm particle size) for the ring shear tests performed, where the individual numbers refer to specific soils tested, given in Table 13.7. With the exception of the soils numbered 48,

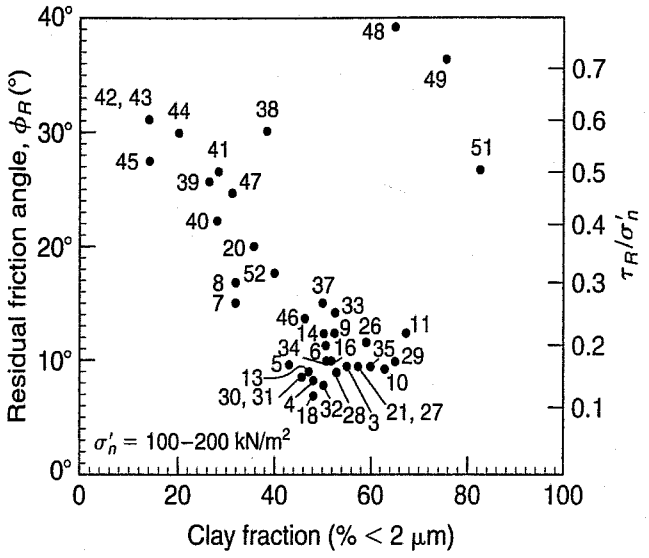

FIGURE 13.76 Residual friction angle versus clay fraction (after Lupini et al., 1981).

TABLE 13.7 Ring Shear Test Results for Various Clays Shown in Fig. 13.76

No.	Site and Soil Type	Liquid limit, LL	Plasticity index, PI	Clay fraction, % < 2 μm	Best-fit envelope	
					c'_R, kPa	ϕ', °
3	Bury Hill-Etruria marl	71	43	55	3.4	7.1
5	Mam Tor-Carboniferous clay	59	31	43	1.9	8.1
6	Holme Hse. W.-Carboniferous clay	57	33	50	2.9	9.4
7	Taren slip-Carboniferous clay	26	6	32	8.1	10.1
8	Taren slip-Carboniferous clay	31	12	32	7.4	12.1
9	Arlington-Weald clay	65	33	51	6.1	8.7
11	Barnsdale-Lias clay	82	49	67–74	3.6	11.1
14	Empinham-Lias clay	59	29	50	5.2	9.2
15	Empinham-Lias clay	59	31	—	5.4	8.6
16	Wansford-Lias clay	63	37	51	3.8	7.3
26	Herne Bay-London clay	95	61	59	3.1	9.4
27	Hadleigh-London clay (brown)	82	54	57	1.2	8.4
28	Walthamstow-London clay (brown)	66	42	53	1.4	8.0
30	Swindon-Gault clay	62	36	46	1.4	8.2
31	Swindon-Gault clay	62	36	46	1.2	7.8
32	Folkestone-Gault clay (montmorillonitic)	85	58	50	1.4	6.6
33	Folkestone-Gault clay (kaolinitic)	58	32	52	6.2	10.7
34	Amuay-Venezuela clay	59	36	51	4.9	7.1
35	Cotsgrave-Rhaetic clay	93	61	60	4.0	7.0
37	Kent alluvium	94	60	50	2.7	12.6
38	Oslo-Studenterlunden clay	41	20	38	3.3	28.7
39	Bingley till	29	13	26	1.5	25.3
41	Cowden till	34	18	28	5.8	23.8
45	Penwortham till	42	23	14	3.9	24.4
48	Java-allophane	165	46	65	0.0	39.0
49	Java-halloysite	95	30	76	3.9	35.0
51	Java-halloysite	101	57	83	4.9	24.5

49, and 51 (the aforementioned clays from Java), it is clear that as clay fraction increases, sliding behavior predominates and ϕ'_R falls below 10°. Table 13.7 gives the best fit linear regression results (residual intercept c'_R and friction angle ϕ'_R) for the soils shown in Fig. 13.76 that were reported with a full record of results (it is assumed that other soils shown in Fig. 13.76 must have had their values inferred).

While the values of ϕ'_R reported are based on the assumption of a linear failure envelope (with either an assumed $c'_R = 0$ or an intercept from linear regression), it has been found that residual strengths tend to lie on a nonlinear envelope, so that the relationship between τ_R and σ'_n will depend on the soil and the σ'_n level.

13.12.2 Residual Shear Strength of Sands

Steady state behavior of sands is when a specimen continues to deform at some constant effective stress and constant void ratio (Poulos, 1981). These were previously referred to as the critical confining stress, $\sigma'_{3\,\text{crit}}$, and critical void ratio, e_{crit}, respectively, and the framework of the Peacock diagram (Fig. 12.11) was presented to summarize the behavior under any combination of σ'_3 and e conditions. So, for all practical purposes, the shear strength at steady state and the residual strength for sands are essentially the same thing (Sladen et al., 1986). The primary application of sand residual strength is for the analysis of embankments, slopes, and earth dams that have significant sand percentage as part of their composition. Unlike clays, the most critical case for sands is the undrained case, and CU tests have been performed to evaluate the residual strength under these conditions. In addition, standard penetration test (SPT) results have been correlated to CU residual strength tests by Seed (1987), and this is shown in Fig. 13.77, where $(N_1)_{60}$ is the SPT blow count normalized for an effective vertical stress of 1 ton/ft^2 and 60% of the theoretical energy applied to the hammer. Like many such correlations in geotechnical engineering, it can be argued that the correlation is somewhat speculative; however, it provides some guidance on deducing strengths needed for stability analyses from a common field test that can be performed at relatively close spacing over a field site.

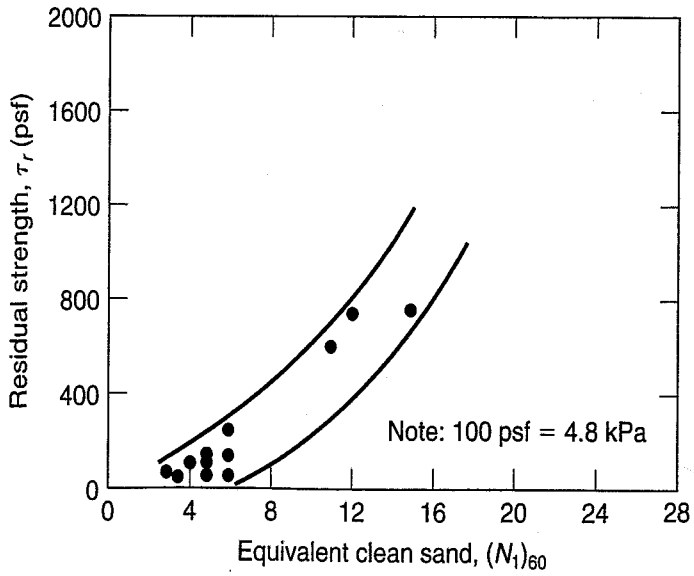

FIGURE 13.77 Tentative relationship between residual sand strength and SPT N-values for sands (from Seed, 1987).

13.13 STRESS-DEFORMATION AND SHEAR STRENGTH OF CLAYS: SPECIAL TOPICS

In this section we discuss some special topics on the stress-deformation and shear-strength properties of clay soils. We begin with a brief discussion of the different definitions of failure in CU tests. Then we discuss the Hvorslev strength parameters that were considered for many years the "true" strength parameters. Hvorslev's work was the basis for Critical State Soil Mechanics (Sec. 13.7). Next we discuss the τ_f/σ'_{vo} ratio, a very useful practical relationship, in some detail. Included are effect of stress history on shear strength, and the Jürgenson–Rutledge hypothesis, another practical application of the τ_f/σ'_{vo} ratio.

Because undisturbed sampling is so important to good estimates of the shear strength of cohesive soil deposits, we describe two approaches to overcoming sampling disturbance. Finally, the section ends with a discussion of anisotropy and the plane-strain strength of clays.

13.13.1 Definition of Failure in CU Effective Stress Tests

In Chapter 12, we gave some typical values for c' and ϕ' determined by CD triaxial tests. The range of values indicated is typical for effective stress strengths determined in CU tests with pore pressure measurements, with the following reservation. In our discussion so far, we have tacitly assumed that the Mohr–Coulomb strength parameters in terms of effective stresses determined by CU tests with pore pressure measurements would be the same as those determined by CD tests. We used the same symbols, c' and ϕ', for the parameters determined both ways. This assumption is not strictly correct. The problem is complicated by alternative definitions of failure. We have used the maximum principal stress difference $(\sigma_1 - \sigma_3)_{max}$ to define failure throughout this chapter, but often in the literature and sometimes in practice you will find failure defined in terms of the maximum principal effective stress ratio $(\sigma'_1/\sigma'_3)_{max}$, which is the same as the maximum obliquity [Eqs. (11.14) through (11.17)]. Depending on how the stress difference and the pore water pressures actually develop with strain, these two definitions may indicate different c's and ϕ's. This is especially true for sensitive clays, as shown in Fig. 13.78.

Bjerrum and Simons (1960) studied this problem in some detail, and their results are summarized in Fig. 13.79. Here, ϕ' as defined at $(\sigma'_1/\sigma'_3)_{max}$ and $(\sigma_1 - \sigma_3)_{max}$ are plotted versus ϕ'_d, the effective stress parameter determined in drained tests. Note that ϕ' from the maximum principal effective stress ratio (the dots) is from 0° to 3° greater than ϕ'_d. Also note that ϕ' at maximum principal stress difference (the squares) is less than both ϕ'_d and ϕ' at the maximum principal effective stress ratio. In one case the difference is about 7°.

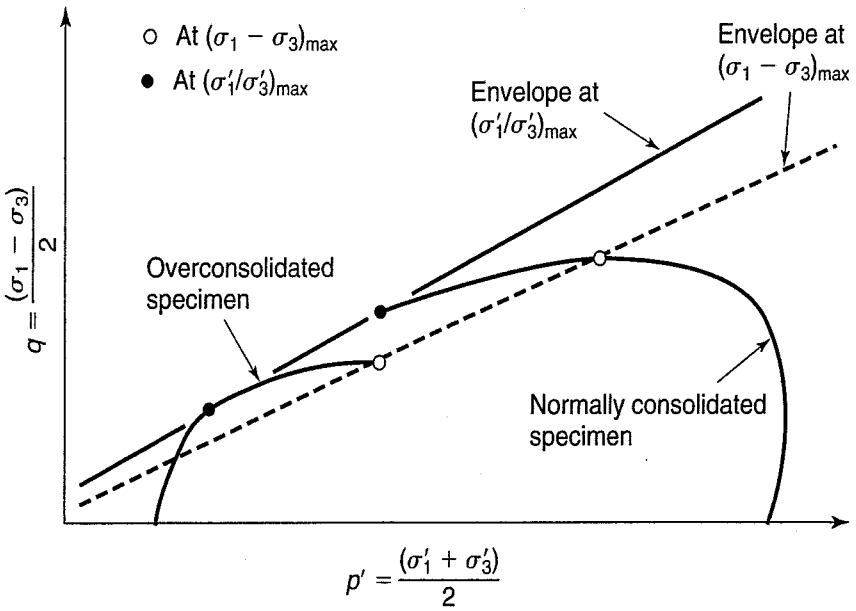

FIGURE 13.78 Typical failure envelopes for CU tests on a sensitive clay, illustrating the effect of different failure criteria on the slope and intercept of the Mohr–Coulomb failure envelope (after Ladd, 1971b).

Another factor to be considered in trying to determine the shear strength parameters is the influence of soil structure and yielding of especially sensitive clays on the shear strength parameters c' and ϕ'. In view of our earlier discussion of critical state soil mechanics (Sec. 13.7), different values of these parameters are obtained, depending on which yield surface is used to define them. For many clay deposits that are nearly normally or only lightly overconsolidated, the c' and ϕ' at yield are larger than these parameters at the critical state or large strain state. Another consideration is how to express the undrained shear strength—for example, as determined by the field vane shear test (Sec. 12.11.4)—in terms of effective stresses, something you might want to do for a stability analysis in terms of effective stresses. Terzaghi et al. (1996) give an excellent discussion of all these factors and their practical engineering implications.

In any event, you should be very careful when studying published data or engineering test reports to determine exactly how the strength tests were conducted, how failure was defined, and how any reported Mohr–Coulomb parameters were determined. The misinterpretation of strength tests and the incorrect use of the shear strength parameters have occasionally resulted in stability failures and costly lawsuits.

13.13.2 Hvorslev Strength Parameters

Because of their variability and heterogeneity, it is virtually impossible to perform a sufficient number of strength tests and with controlled variables on specimens of natural clay deposits. Consequently, much of our basic understanding of the shear behavior of saturated cohesive soils was developed from tests on sufficiently homogeneous remolded clays.

This was the case for Hvorlsev (1937), who worked in the soils laboratory at Technische Hochschule in Vienna with Prof. Terzaghi. Because this work was published in German and the Second World War intervened, Hvorslev's pioneering work on shear strength was, with few exceptions, ignored until he summarized his thesis research in English (Hvorslev, 1960). According to Bjerrum (1954a), Hvorslev can be credited for confirming that Coulomb's friction law is valid for soils.

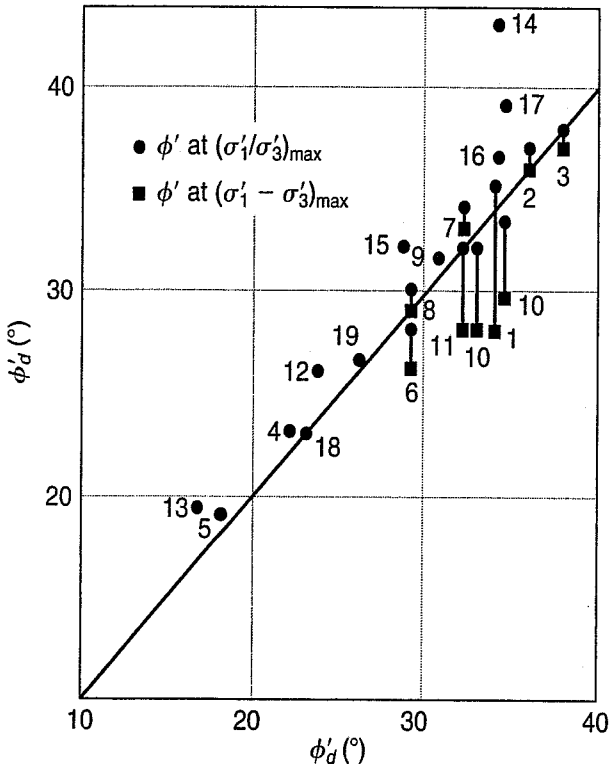

Clay	State	Reference
1 Cornwall	U	Kenney
2 Cornwall	R	"
3 Bersimis	R	"
4 Weald	R	Henkel
5 London	R	"
6 Oslo	U	N.G.I.
7 Fredrikstad	U	"
8 Lodalen	U	"
9 Fornebu	U	"
10 Drammen	U	"
11 Ökernbråten	U	"
12 Seven Sisters	U	Casagrande and Rivard
13 North Ridge	U	" "
14 Organic	U	Casagrande
15 Boston blue	U	"
16 Weymouth	U	Hirschfeld
17 New Haven	U	"
18 Haslemere	R	Skempton and Bishop
19 Wiener Tegel	R	Hvorslev

U = undisturbed
R = remolded

FIGURE 13.79 Relationship between ϕ_d' determined from CD tests and ϕ' determined from CU tests with pore pressure measured. Two failure criteria are indicated for the undrained tests (after Bjerrum and Simons, 1960).

We have already seen that neither the effective consolidation stress nor the void ratio or water content at failure is sufficient to determine the undrained shear strength. You'll see this is the case if you go back and look at Fig. 12.26. Specimens B and E are at the same effective normal stress, but they have different shear strengths. Similarly, if you draw a horizontal line at any convenient water content or void ratio between D and E, you'll see that the shear strength of the NC specimen on the virgin compression curve (VCC) will have different shear strength than the OC specimen at the same w or e.

These observations were the basis for the shear strength theory developed by Hvorslev (1937). He showed the how the measured shear strength could be separated into two components, one dependent on water content at failure and one dependent on the effective normal stress at failure (Lambe and Whitman, 1969), or

$$\tau_{ff} = \mathrm{f}(w_f) + \mathrm{f}(\sigma'_{ff}) \tag{13.38}$$

where w_f = water content at failure, and

σ'_{ff} = average normal stress at failure.

The following is only a brief summary of Hvorslev's important contributions.

First we define the equivalent consolidation pressure, σ'_e. See Fig. 13.80. It is the effective pressure that corresponds to the void ratio e on the virgin consolidation curve, or the VCC. This is important for normalizing the results of tests on overconsolidated specimens.

Because the triaxial test was invented only in the early 1930s and not universally available, Hvorslev used direct shear tests and conducted them slowly enough to consider the tests fully drained. The results of a series of CD direct shear tests on clays remolded near their LL and then consolidated are shown schematically in Fig. 13.81. Note that this figure is similar to Fig. 12.26.

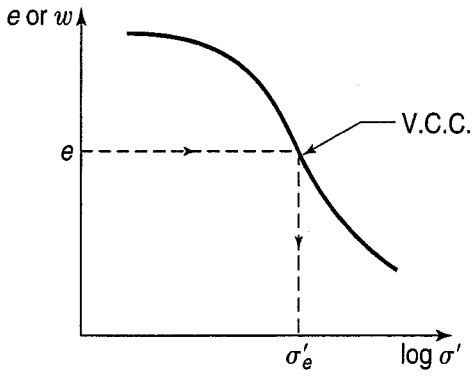

FIGURE 13.80 Definition of equivalent consolidation pressure, σ'_e.

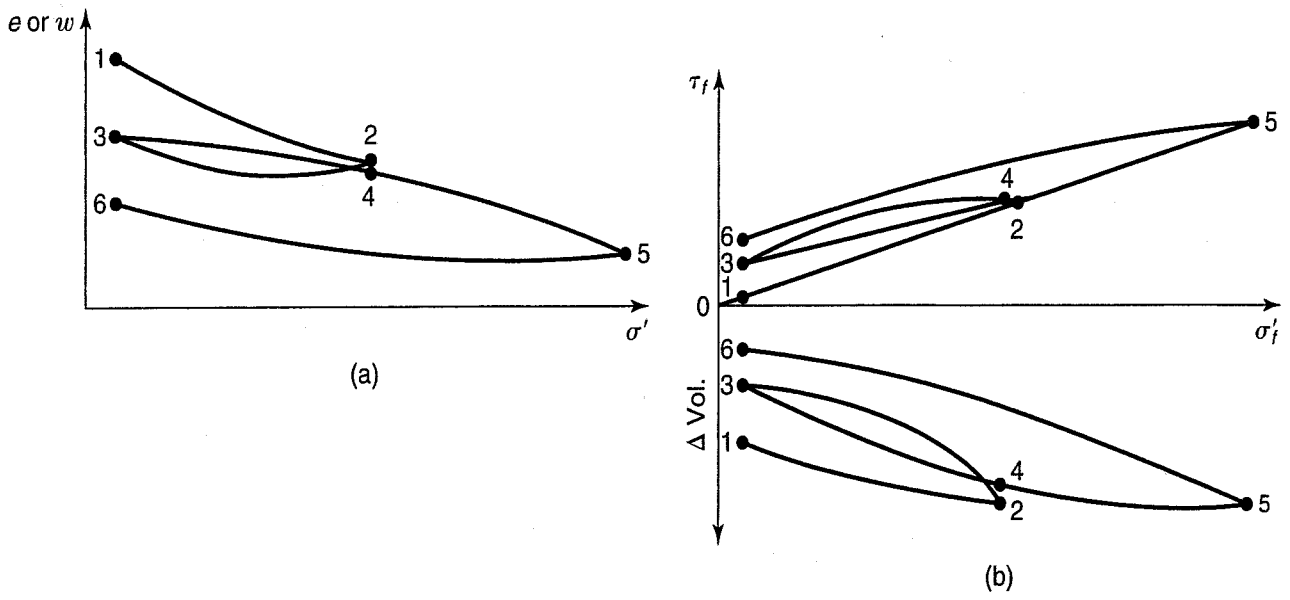

FIGURE 13.81 Results of a series of CD direct shear tests on remolded saturated clays: (a) void ratio or water content at the end of consolidation; and (b) shear stress and volume change at failure in shear.

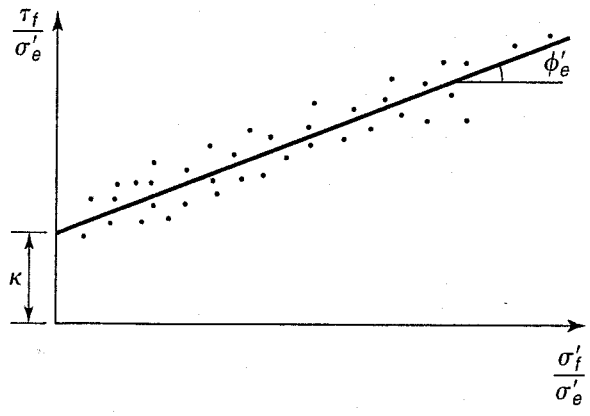

FIGURE 13.82 Results of many CD direct shear tests normalized with their equivalent consolidation pressure.

From these results, Hvorslev showed that the shear strength on the failure plane at failure was a function of the effective normal stress and the void ratio, both at failure, or, $\tau_{ff} = f(\sigma'_f, e_f)$. This function is almost unique and independent of stress history. When Hvorslev plotted the results of many tests and normalized them with the equivalent consolidation pressure for their void ratios, he got results similar to those shown in Fig. 13.82.

Because the straight line through all the data points in Fig. 13.82 reminded Hvorslev of the typical Mohr–Coulomb relationship, he then derived an expression for the shear strength on the failure plane at failure as a function of the intercept κ and the slope angle ϕ'_e (Hvorslev, 1960); or

$$\tau_{ff} = f(\phi'_e, c_e) \tag{13.39}$$

where ϕ'_e = Hvorslev effective friction parameter, and

c_e = Hvorslev effective "cohesion" parameter = $\kappa\sigma'_e$

Terzaghi (1938) showed that it is possible to get the Hvorslev strength parameters, ϕ'_e and c_e, directly from the results of CD direct shear tests, as shown in Fig. 13.83. The basic assumption is that

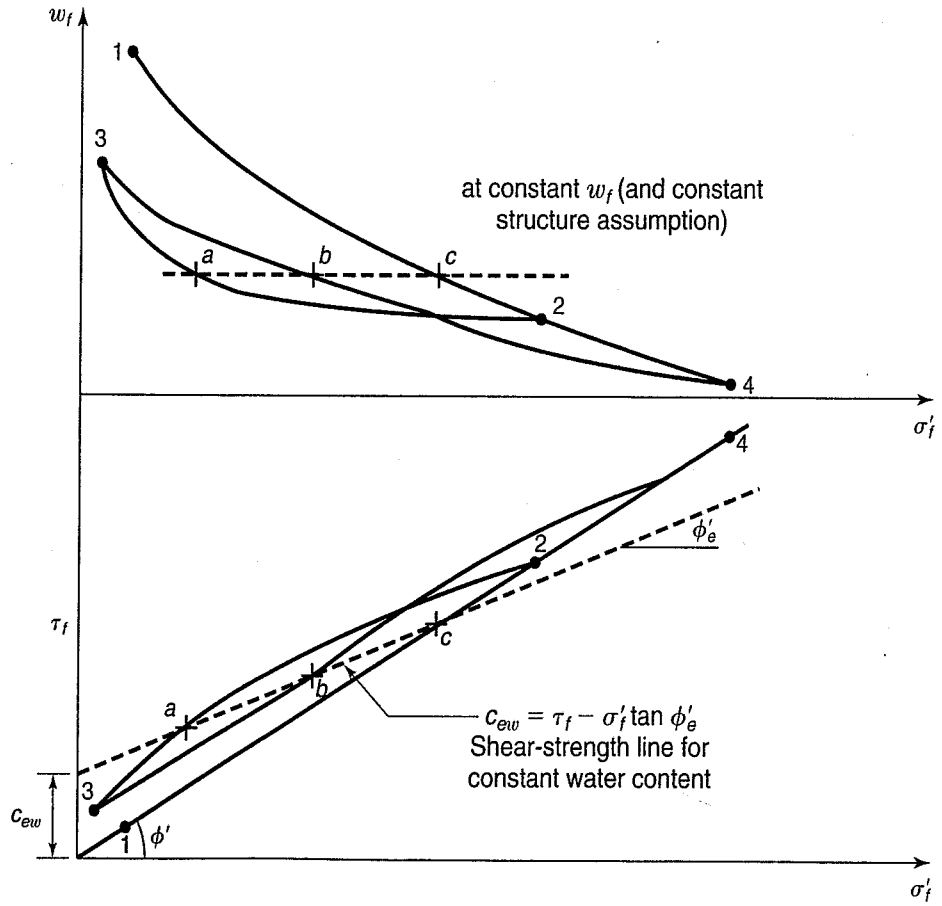

FIGURE 13.83 Determination of the Hvorslev shear-strength parameters from CD direct shear test results on a saturated remolded clay at a constant water content.

for a constant water content, the c_{ew}, void ratio, and soil structure are constant. Of course, it is doubtful that the soil structure is constant, but for remolded specimens, the assumption is approximately OK.

Bishop and Henkel (1962) suggested two ways to obtain ϕ'_e and c_e from CD triaxial tests. One way is to conduct a series of triaxial tests in a similar manner to the direct shear tests shown above. Another way is to use the following equation:

$$\frac{(\sigma'_1 - \sigma'_3)_f}{2\sigma'_e} = \frac{c'_e}{\sigma'_e}\frac{\cos\phi'_e}{(1 - \sin\phi'_e)} + \frac{c'_{3f}}{\sigma'_e}\left(\frac{\sin\phi'_e}{1 + \sin\phi'_e}\right) \tag{13.40}$$

If we plot $\dfrac{(\sigma'_1 - \sigma'_3)}{2\sigma'_e}$ versus $\dfrac{\sigma'_3}{\sigma'_e}$ as shown in Fig. 13.84, we get almost a straight line. Then the Hvorslev parameters, ϕ'_e and c_e, are determined from

$$\sin\phi'_e = \frac{\tan\beta_3}{1 + \tan\beta_3}, \text{ and} \tag{13.41}$$

$$c'_e = \sigma'_e\frac{c_3(1 - \sin\phi'_e)}{\cos\phi'_e} \tag{13.42}$$

Lambe and Whitman (1969) replotted some test data on NC and OC specimens of Weald clay, probably from Henkel (1958), in conventional stress path (q–p') space (Fig. 13.85). The dashed lines in the figure were determined from data similar to the top part of Fig. 13.83 and indicate constant water content values w_f. These lines are called Hvorslev failure lines, and only p'_f varies along these lines; everything else is constant. They all have different intercepts, but the slope or friction angle is the same. The Hvorslev failure lines (the short dashed lines in Fig. 13.85) define the Hvorslev shear strength parameters c'_e and ϕ'_e, or

$$q_f = c'_e + p'_f \tan\phi'_e \tag{13.43}$$

For example, look at the short dashed line for $w_f = 23.5\%$ and the two data points represented by solid dots. Because they are at the same water content, void ratio, and density, the only difference in strength for the one with $p' \approx 9$ psi ($q_f \approx 4$ psi) and the other one at ≈ 20 psi ($q_f \approx 7.5$ psi) must be

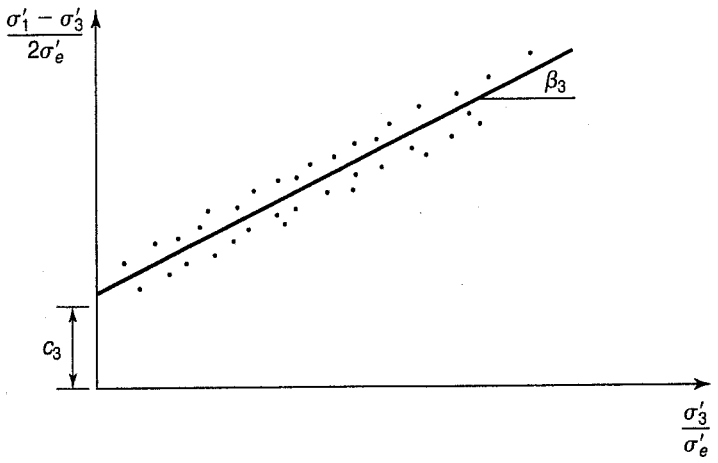

FIGURE 13.84 Plot of CD triaxial test results as suggested by Bishop and Henkel (1962).

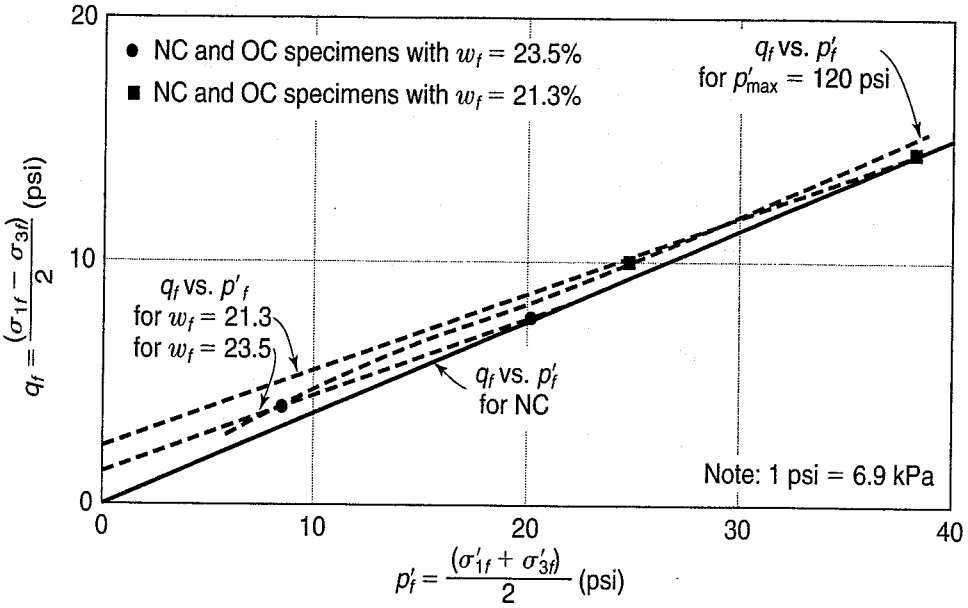

FIGURE 13.85 Construction to obtain Hvorslev parameters for Weald clay (after Lambe and Whitman, 1969).

due to different degrees of internal friction mobilized at the different values of p'. It cannot be due to any volume changes or differences in void ratio or density. The Hvorslev friction parameter ϕ'_e is 18° for both water contents shown in Fig. 13.85.

Others as well as Hvorslev have found that for many clay soils, ϕ'_e is essentially independent of water content; also c_e versus log w_f is a straight line. Considerations such as these have led researchers consider the Hvorslev strength parameters more fundamental than the traditional Mohr–Coulomb parameters. Thus the ϕ'_e represents the actual interparticle friction, dependent only on effective normal stress between particles, and "cohesion" of the clay being primarily dependent upon void ratio or water content.

Validity of the Hvorslev Parameters—For much of the middle of the last century, the Hvorslev strength parameters were called the "true" shear strength parameters. Because most of the verification tests were performed on remolded, saturated homogeneous clays, results tended to confirm that supposition. However, when researchers tried to determine the Hvorslev parameters on undisturbed natural clays, especially if they were sensitive, structured, or heavily overconsolidated, the results were less encouraging. Similar conclusions were found for tests performed on clays at natural water contents near the PL—i.e., stiff clays with LI $\approx$ 0. See, for example, Brink (1967), Chandler, (1967), and Karlsson and Pusch (1967).

In conclusion, the shear strength is not a function of σ'_f and e_f only. Natural soils especially are very complex, and void ratio is not a sufficient measure of soil structure and fabric. The Hvorslev parameters are not the "true" shear strength parameters. We really do not know what the "true" parameters are, but we do know they are parameters of shear strength and not fundamental properties. This point was also made in the previous section.

While the practical use of Hvorslev's parameters is limited, they led to further developments regarding the interrelationship between void ratio, effective stress, and shear strength. It is fair to say that Hvorslev's work ultimately formed the basis for critical state soil mechanics (Sec. 13.7) and the development of other constitutive models for soils (Sec. 13.8).

13.13.3 The τ_f/σ'_{vo} Ratio, Stress History, and Jürgenson–Rutledge Hypothesis

In this section, we discuss a very useful practical relationship, the τ_f/σ'_{vo} ratio, and how it might be obtained theoretically as a function of the basic soil properties K_o, A_f, and ϕ'. Then we consider the effect of stress history on shear strength, and the Jürgenson–Rutledge hypothesis, another practical application of the τ_f/σ'_{vo} ratio.

The τ_f/σ'_{vo} Ratio—One of the more useful ways to express the undrained shear strength is to normalize it by the vertical effective overburden pressure σ'_{vo}. Sometimes this ratio is called the *c/p ratio*. In natural deposits of sedimentary clays the undrained shear strength has been found to increase with depth, and thus it is proportional to the increase in effective overburden stress with depth.

It was first observed by Skempton and Henkel (1953) and confirmed by Bjerrum (1954b) that the τ_f/σ'_{vo} ratio tended to increase with increasing plasticity index. Bjerrum's (1954b) results are shown in Fig. 13.86 along with those of several other researchers, as well as several best-fit correlations. There is a lot of scatter, so Fig. 13.86 should only be used with caution. However, as with Fig. 12.25, such correlations are useful for preliminary estimates and for checking laboratory data.

Kenney (1959) and Bjerrum and Simons (1960) presented some theoretical τ_f/σ'_{vo} ratios versus PI based on the correlations of Fig. 12.27, K_o, and the Skempton pore pressure parameter A (Sec. 12.14). These theoretical relationships tended to decrease rather than increase with PI, but the agreement was satisfactory for PI > 30. Kenney (1959) concluded that τ_f/σ'_{vo} was essentially independent of PI after all; rather, it probably depended more on the geologic history of the clay than on its plasticity.

Bjerrum and Simons (1960) also presented the relationship between τ_f/σ'_{vo} and liquidity index (LI) for some Norwegian marine clays, as shown in Fig. 13.87. As you know from Fig. 12.48, the quick clays are those with very high LI's. Therefore it appears that Norwegian quick clays have a τ_f/σ'_{vo} ratio of about 0.1 to 0.15.

You should be aware that the τ_f/σ'_{vo} ratio depends strongly on the total stress path. This point is discussed by Bjerrum (1972) and Ladd et al. (1977), among others. In other words, you probably will

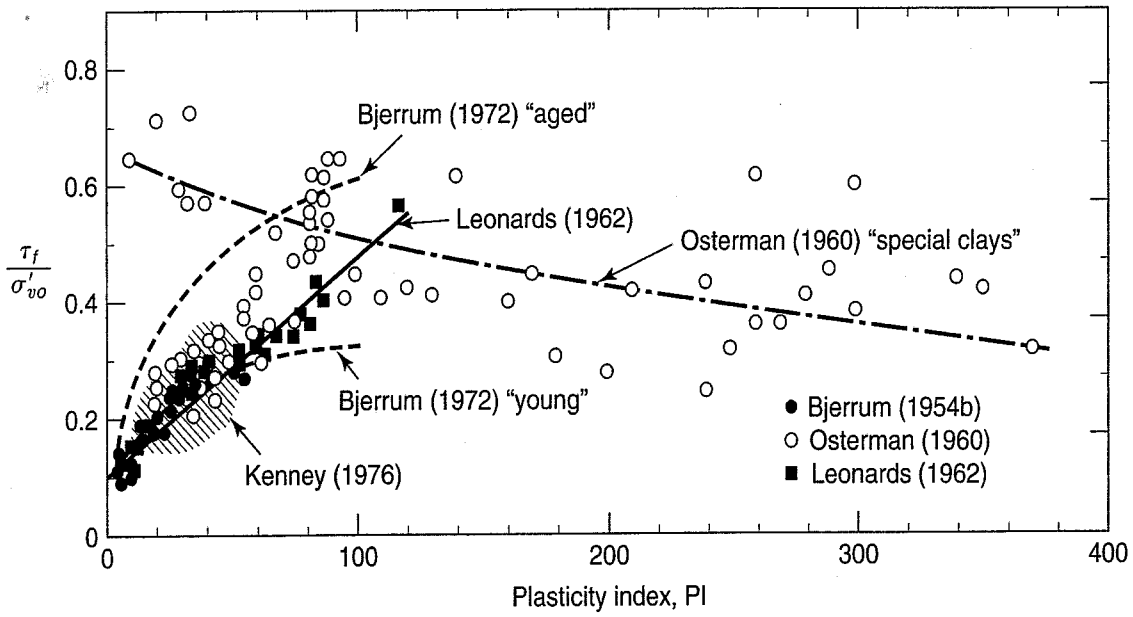

FIGURE 13.86 Relationship between the ratio τ_f/σ'_{vo} and plasticity index for normally consolidated clays.

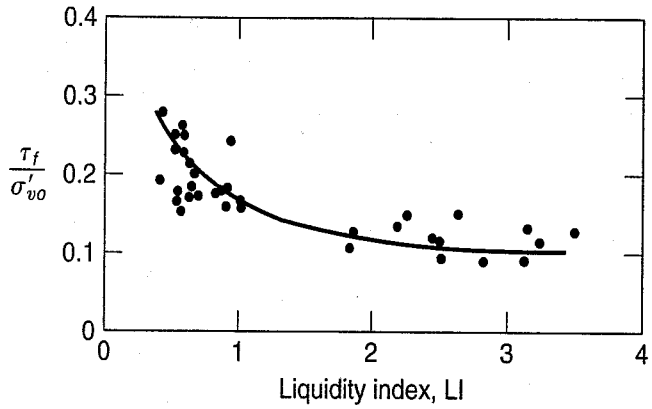

FIGURE 13.87 Relationship between τ_f/σ'_{vo} and liquidity index for Norwegian clays (after Bjerrum and Simons, 1960).

obtain different values of τ_f/σ'_{vo}, depending on whether you run field vane tests, axial compression or axial extension triaxial tests, or direct simple shear tests.

It is possible to derive a theoretical equation for τ_f/σ'_{vo} in terms of K_o, A_f, and ϕ' (Leonards, 1962). First, consider the Mohr–Coulomb obliquity relations (Sec. 11.4.3 and Fig. 11.10) in terms of effective stresses:

$$\sin\phi' = \frac{\dfrac{\sigma'_{1f} - \sigma'_{3f}}{2}}{\dfrac{\sigma'_{1f} + \sigma'_{3f}}{2} + c\dfrac{\cos\phi'}{\sin\phi'}} \tag{13.44}$$

By assuming that $\tau_f = \dfrac{(\sigma'_1 - \sigma'_3)_f}{2}$, you can see how this equation is obtained from the Mohr circle in terms of effective stress shown in Fig. 13.88.

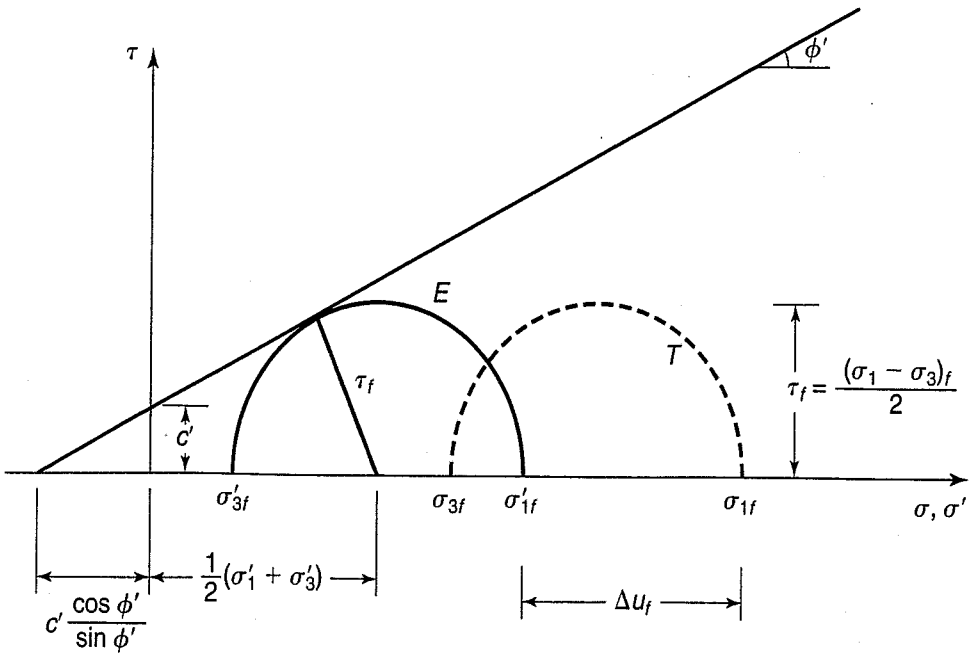

FIGURE 13.88 Mohr circles at failure for a normally consolidated clay.

Rearranging Eq. (13.44),

$$\tau_f = \frac{\sigma_1' + \sigma_3'}{2}\sin\phi' + c'\cos\phi'$$
$$= \frac{\sigma_1' - \sigma_3'}{2}\sin\phi' + \sigma_3'\sin\phi' + c'\cos\phi'$$
$$= \tau_f \sin\phi' + (\sigma_3 - u)\sin\phi' + c'\cos\phi'$$

Thus

$$\tau_f = \frac{c'\cos\phi' + (\sigma_3 - u)\sin\phi'}{1 - \sin\phi'} \tag{13.45}$$

From the initial and at-failure stress conditions in situ shown Fig. 13.89, similar to those shown in Fig. 12.29, we obtain

$$\sigma_3 - u = K_o\sigma_{vo}' + \Delta\sigma_3 - u_f$$
$$= K_o\sigma_{vo}' + \Delta\sigma_3 - [\Delta\sigma_3 + A_f(\Delta\sigma_1 - \Delta\sigma_3)]$$
$$= K_o\sigma_{vo}' - A_f(\Delta\sigma_1 - \Delta\sigma_3) \tag{13.46}$$

We also know from Fig. 13.89 that

$$\tau_f = \tfrac{1}{2}(\sigma_1 - \sigma_3)_f = \tfrac{1}{2}(\Delta\sigma_1 - \Delta\sigma_3) + \tfrac{1}{2}(1 - K_o)\sigma_{vo}'$$

so

$$\Delta\sigma_1 - \Delta\sigma_3 = 2\tau_f - (1 - K_o)\sigma_{vo}' \tag{13.47}$$

Combining Eqs. (13.46) and (13.47), we obtain

$$\sigma_3 - u = \sigma_{vo}'[K_o + A_f(1 - K_o)] - 2A_f\tau_f$$

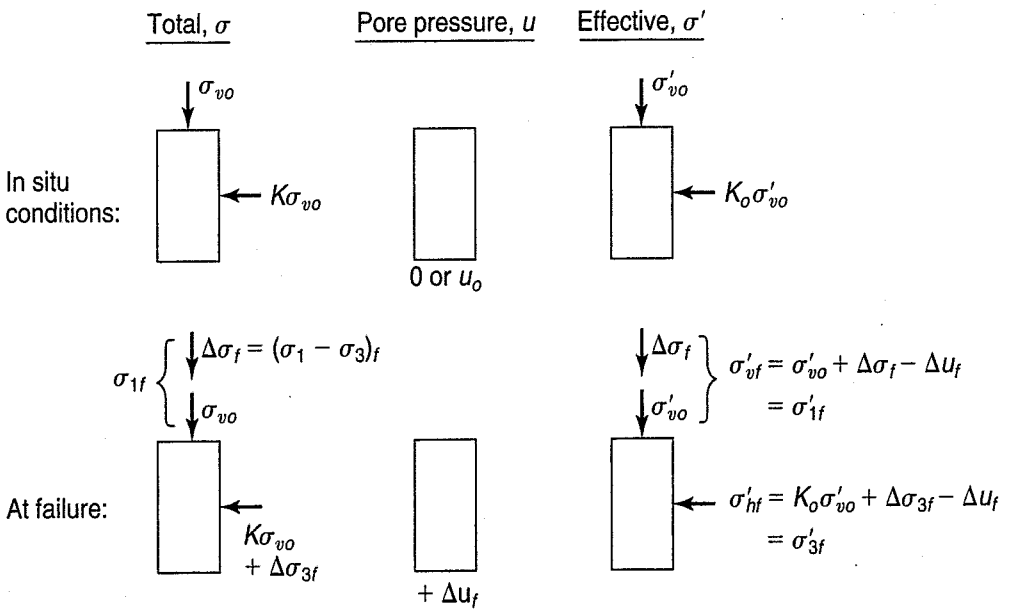

FIGURE 13.89 Initial and final stress conditions in situ for a normally consolidated clay.

Now we can put this expression into Eq. (13.45), or

$$\tau_f = \frac{c' \cos\phi' + \sigma'_{vo} \sin\phi'[K_o + A_f(1 - K_o)}{1 - (2A_f - 1)\sin\phi'} \tag{13.48}$$

For normally consolidated clays, we usually assume that $c' \approx 0$, thus Eq. (13.48) becomes

$$\frac{\tau_f}{\sigma'_{vo}} = \frac{\sin\phi'[K_o + A_f(1 - K_o)]}{1 + (2A_f - 1)\sin\phi'} \tag{13.49}$$

From this equation, we see that the τ_f/σ'_{vo} ratio is a constant. Recognize that this is for normally or near normally consolidated clays with $K_o < 1$ and a negligible c'. So, it is theoretically possible to determine the τ_f/σ'_{vo} ratio in the field with a knowledge of the ϕ', K_o, and A_f of the clay deposit. But how easy is it to obtain reasonable estimates of these properties from laboratory or field tests? Except for ϕ', not so easy. We mentioned the difficulties of obtaining a good estimate on K_o in Sec. 12.13, even in relatively homogeneous natural deposits of soft clays. Thus reliance on simple correlations with classification properties such as the PI is the only feasible approach, and we have already mentioned the scatter in that data. Finally, obtaining good estimates of the Skempton parameter A_f is often difficult, because it is very sensitive to sample disturbance. Furthermore, you must use the correct definition of A_f for your stress path in the field (see Law and Holtz, 1978, and Appendix B.3).

What do you do about overconsolidated soils when $K_o > 1$ and $c' \neq 0$? What does Eq. (13.49) look like for OC clays? To obtain this equation for overconsolidated clays requires a good understanding of the fundamentals of the shear strength properties of clay soils, and it is one of the homework problems at the of the chapter.

In laboratory studies of clays, researchers often normalize the undrained shear strength with respect to the effective *consolidation* pressure σ'_{vc}. Thus the ratio becomes τ_f/σ'_{vc}. We did this in Examples 13.6 and 13.7. But what do you do when testing specimens of overconsolidated natural clays? In this case, it is better to normalize the undrained shear strength with respect to the preconsolidation stress σ'_p, rather than use the effective overburden stress. For these test specimens, the undrained strength is really controlled by the effective consolidation pressure (or stress history) rather than the existing effective overburden stress. Thus the ratio becomes τ_f/σ'_p.

Bjerrum (1972), in a study of failures of embankments constructed on soft foundation soils, hypothesized that the ratio between σ'_p and σ'_{vo} would vary with PI, as shown in Fig. 13.90(a). So-called "young" clays are normally consolidated recent sediments, and thus they haven't had time to be overconsolidated by any of the factors listed in Table 8.1. On the other hand, "aged" clays are slightly overconsolidated, and Bjerrum found that the amount of overconsolidation increased somewhat with the PI [Fig. 13.90(b)]. The resulting effect on the strength was indicated by the dashed curves labeled "Bjerrum (1972)" in Fig. 13.86.

Bjerrum (1972), in a study of failures of embankments constructed on soft foundation soils, found that the field vane shear test (VST) in many cases tended to seriously overpredict the back-calculated undrained shear strength at failure. (See Secs. 11.6.1 and 12.11.4 for a discussion of the VST.) The degree of overprediction appeared to be greater with higher-plasticity clays. Bjerrum's empirical correction factor μ as a function of PI was shown in Fig. 11.19 and should be applied to the undrained shear strength as determined by the VST. For convenience, this figure is reproduced without all the data points as Fig. 13.90(c).

Mesri (1975) discovered a very interesting relationship between all these observations. Combining Figs. 13.90(a) and 13.90(b), Mesri obtained Fig. 13.90(d), τ_f/σ'_p versus PI, which shows essentially the same behavior for "aged" and "young" clays. Now apply Bjerrum's correction factor μ for the field

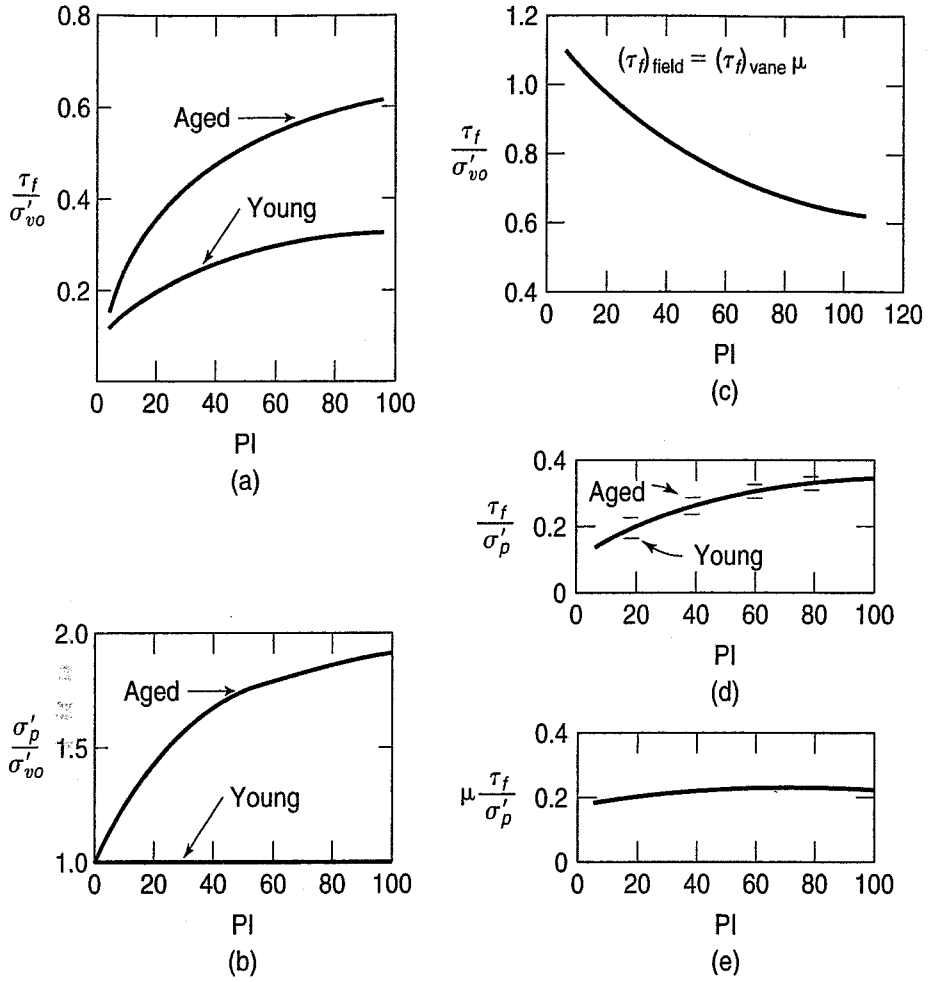

FIGURE 13.90 (a) τ_f/σ'_{vo} and (b) σ'_p/σ'_{vo} for normally consolidated late glacial clays (after Bjerrum, 1972); (c) Bjerrum's (1972) correction factor for the vane shear test (Fig. 11.19); (d) τ_f/σ'_p from (a) and (b); (e) $\mu(\tau_f/\sigma'_p)$ (after Mesri, 1975).

vane shear test to obtain the in situ strengths; the result is Fig. 13.90(e). In other words, $(\tau_f/\sigma'_{vc})_{field}$ is almost a constant equal to 0.22 and independent of PI!

$$\frac{\tau_f}{\sigma'_p} = 0.22\sigma'_p \tag{13.50}$$

There is great uncertainty in such a conclusion because of the scatter in the empirical relationships upon which it is based, and the relationships shown in Fig. 13.90(d) and Fig. 13.90(e) may be only a coincidence. However, the possibility that the in situ τ_f/σ'_p may well exist within a rather narrow range for soft sedimentary clays has tremendous practical implications (Ladd et al., 1977).

Stress History—Another factor which strongly affects the undrained shear strength of clays is stress history. We mentioned this factor when we pointed out the difference in behavior between normally consolidated and overconsolidated clays (see, for example, Figs. 12.30, 12.31, and 12.34). Let's first consider some data showing how the normalized undrained strength τ_f/σ'_{vc} varies with the overconsolidation ratio (OCR). These data are shown for six clays in Fig. 13.91. If you take the *ratio* of the τ_f/σ'_{vc} ratios, as shown in Fig. 13.92, all these soils fall into a rather narrow band, with only the varved clay

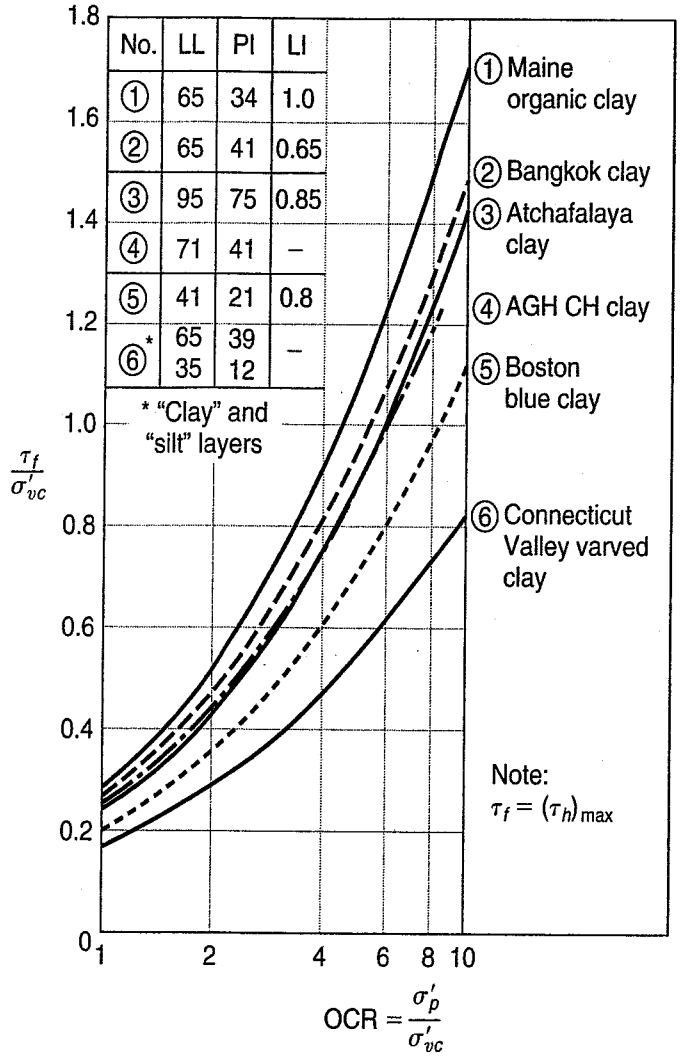

FIGURE 13.91 Undrained strength ratio versus overconsolidation ratio from direct simple shear tests on six clays (after Ladd and Edgers, 1972, and Ladd et al., 1977).

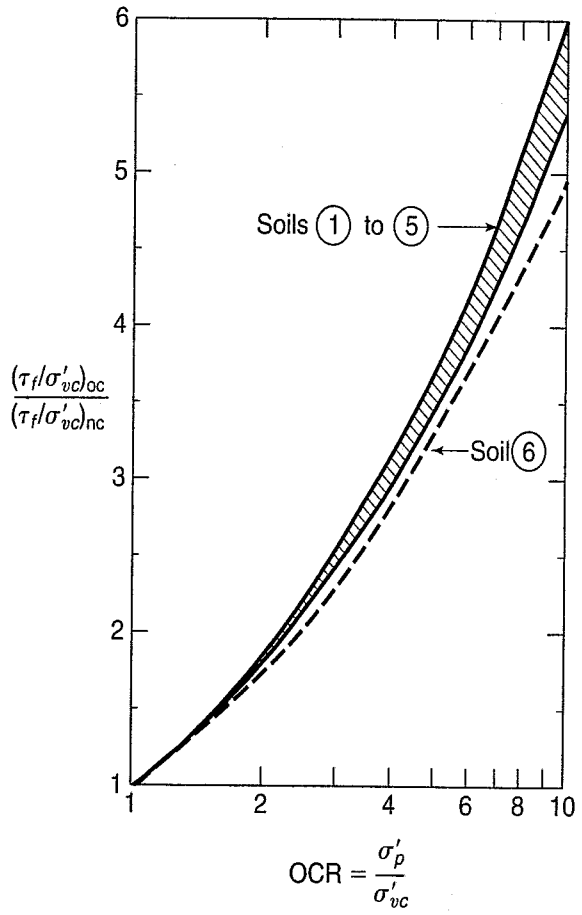

FIGURE 13.92 Relative increase in undrained strength ratio with OCR from direct simple shear tests (soils 1 through 6 are identified in Fig. 13.91) (after Ladd et al., 1977).

somewhat lower. Ladd et al. (1977) showed that this ratio of ratios is approximately equal to the OCR to the 0.8 power, or

$$\frac{(\tau_f/\sigma'_{vc})_o}{(\tau_f/\sigma'_{vc})_{nc}} \approx (\text{OCR})^{0.8} \tag{13.51}$$

Relationships such as this can be useful for comparing strength data from different sites or even from the same site.

Jürgenson–Rutledge Hypothesis—Rendulic (1936; 1937) first postulated that, for normally consolidated saturated clay, the water content (and therefore the void ratio) during shear was a unique function of the principal stresses σ'_1, σ'_2, and σ'_3. Henkel (1958) verified this uniqueness hypothesis with his triaxial tests on saturated remolded Weald clay (see Leonards, 1962, and Lambe and Whitman, 1969). However, Skempton and Sowa (1963) showed that the relationship was not strictly unique but depended somewhat on the stress path.

Rutledge[1] (1947) reviewed the results of the Cooperative Triaxial Shear Research Program of the U.S. Army Corps of Engineers. The U.S. Army Waterways Experiment Station, MIT, and Harvard had performed several hundred triaxial tests on many clays, and all these results were available in about 17 data reports. Rutledge's job was to summarize all these results and data and to draw some final conclusions from all this research. Among his several conclusions were the three following observations, based on Fig. 13.93, which became known as the *Rutledge hypothesis*:

1. There is a unique curve (A) of σ'_{vc} (or σ'_{1c}) versus e_f (or w_f).
2. There is a unique curve (B) of $(\sigma_1 - \sigma_3)_f$ versus e_f (or w_f).
3. Curves (A) and (B) are essentially parallel in the virgin compression region.

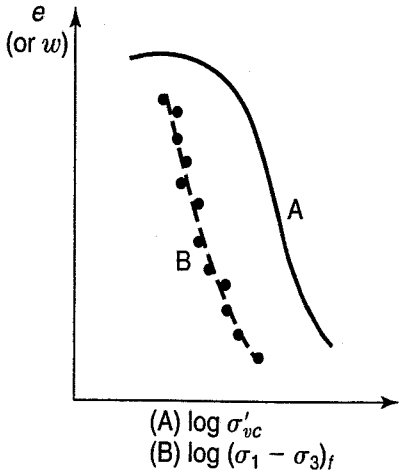

FIGURE 13.93 Illustration of the Rutledge hypothesis for clay soils.

Important implications of the Rutledge hypothesis are:

1. Consolidation, either 1-D compression or 3-D triaxial consolidation, yields the same result—independent of σ_2, σ_3, and the stress path.
2. The compressive (and thus the shear) strength $(\sigma_1 - \sigma_3)_f \equiv (\sigma'_1 - \sigma'_3)_f = f(e_f)$ and therefore of σ'_{vc} only. This implies that stress path, stress history, etc. are not important factors affecting the shear strength.
3. Approximately parallel curves are an empirical observation of the results of many tests, as shown in Rutledge (1947).
4. From parallel lines, it can be shown that

$$\frac{\tau_f}{\sigma'_{vc}} = \frac{\tau_f}{\sigma'_{1c}} = \text{const.} \tag{13.52}$$

The relationship in Eq. (13.52) was first noticed by Jürgenson (1934). Therefore a better name for this hypothesis is the *Jürgenson–Rutledge hypothesis*.

How valid are these three observations?

1. Number 1 is not strictly true; σ'_{vc} is also a function of σ'_{hc} (or σ'_{2c} and σ'_{3c}), but it is reasonable for NC and slightly OC clays.
2. From Rutledge's review of lots of test results, Curve B seemed to be independent of how one gets to failure; therefore he concluded that the shear strength was a function of e_f only and was not path dependent. Again, however, this is not strictly true, as the shear strength may also involve some effect of the intermediate principal stress σ'_{2c}, stress history, and the soil structure. But it is approximately reasonable for NC and slightly OC clays.
3. Satisfactory by empirical observation, although there is some scatter.

Three examples of data provided by Osterberg (1967) from the Cooperative Triaxial Shear Research Program performed at Harvard and Northwestern are shown in Figs. 13.94, 13.95 and 13.96.

[1]Historical note: P. C. Rutledge obtained his Ph.D. from Harvard University in 1936 as Prof. Arthur Casagrande's first Ph.D. student. He taught soil mechanics at Purdue University from 1937 to 1943, when he became Chair of the Department of Civil Engineering at Northwestern University. In 1952 he went into full-time consulting practice with Mueser–Rutledge in New York. He was the Fifth Terzaghi Lecturer in 1969. He retired in 1977 and died in 1986.

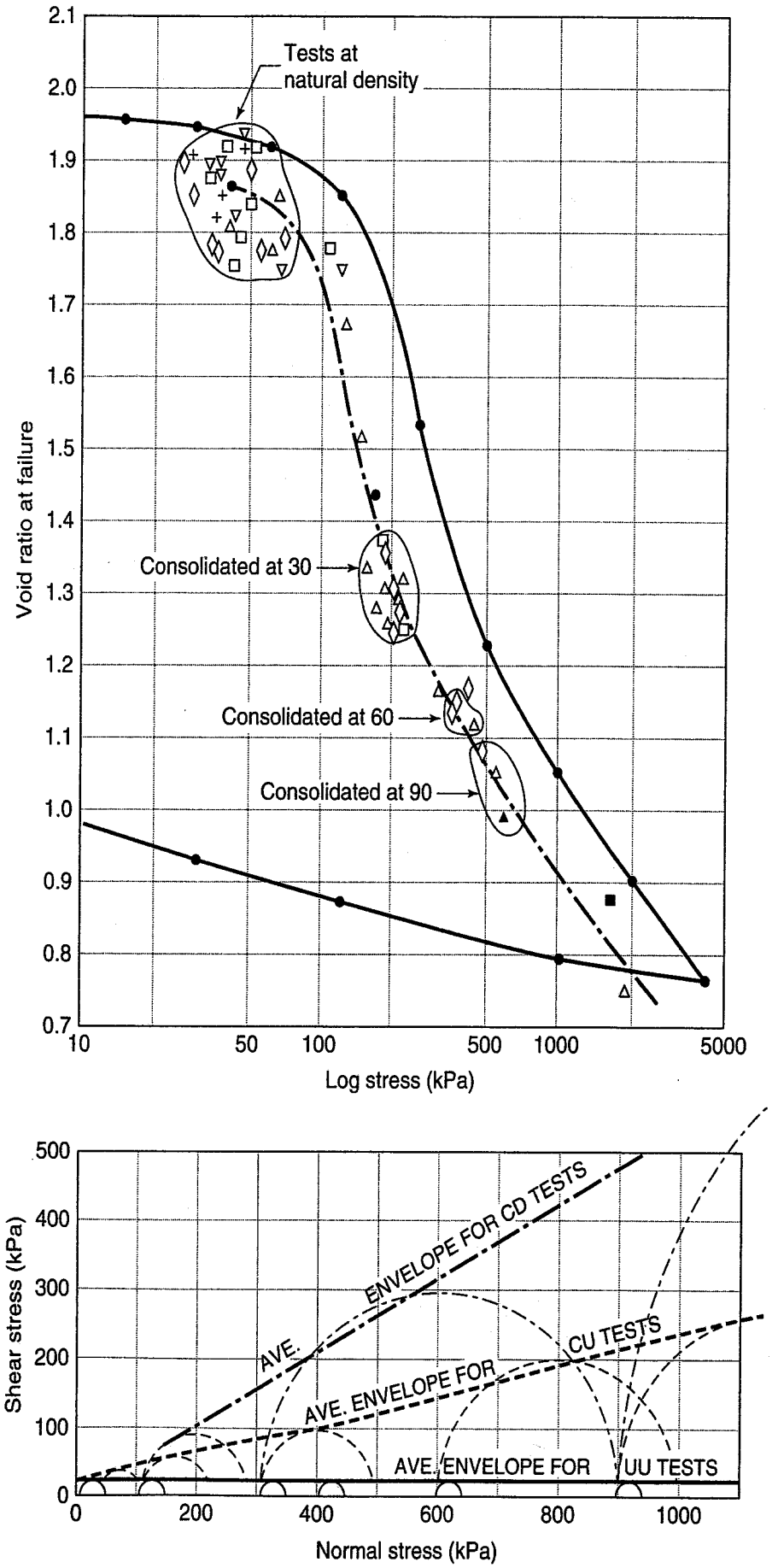

FIGURE 13.94 Results from consolidation and CD, CU, and UU triaxial tests on clay from Massena, NY, performed at Harvard (Osterberg, 1967).

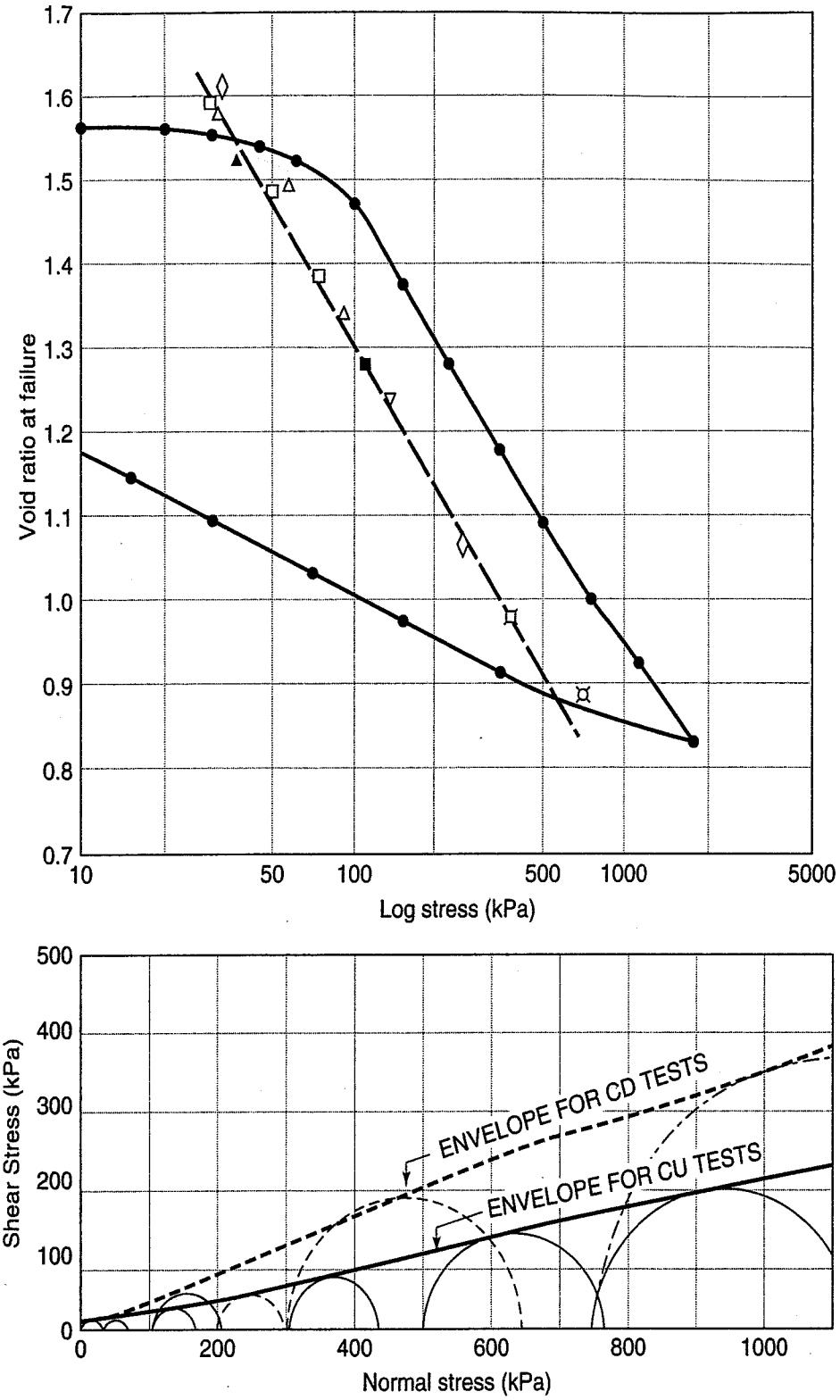

FIGURE 13.95 Results from consolidation and CD and CU triaxial tests on Chicago clay performed at Harvard (Osterberg, 1967).

The Massena (NY) clay is from the St. Lawrence Valley and is representative of the sensitive Laurentian or Leda clays of Ontario and Quebec. Soft Chicago clay is thought to be a glacially reworked lacustrine clay that is quite silty. Glacial Lake Agassiz clay is typical of the clays from the Red River of the North valley of Northern Minnesota, Eastern North Dakota, and Southern Manitoba. All three tests tend to verify the Rutledge hypothesis.

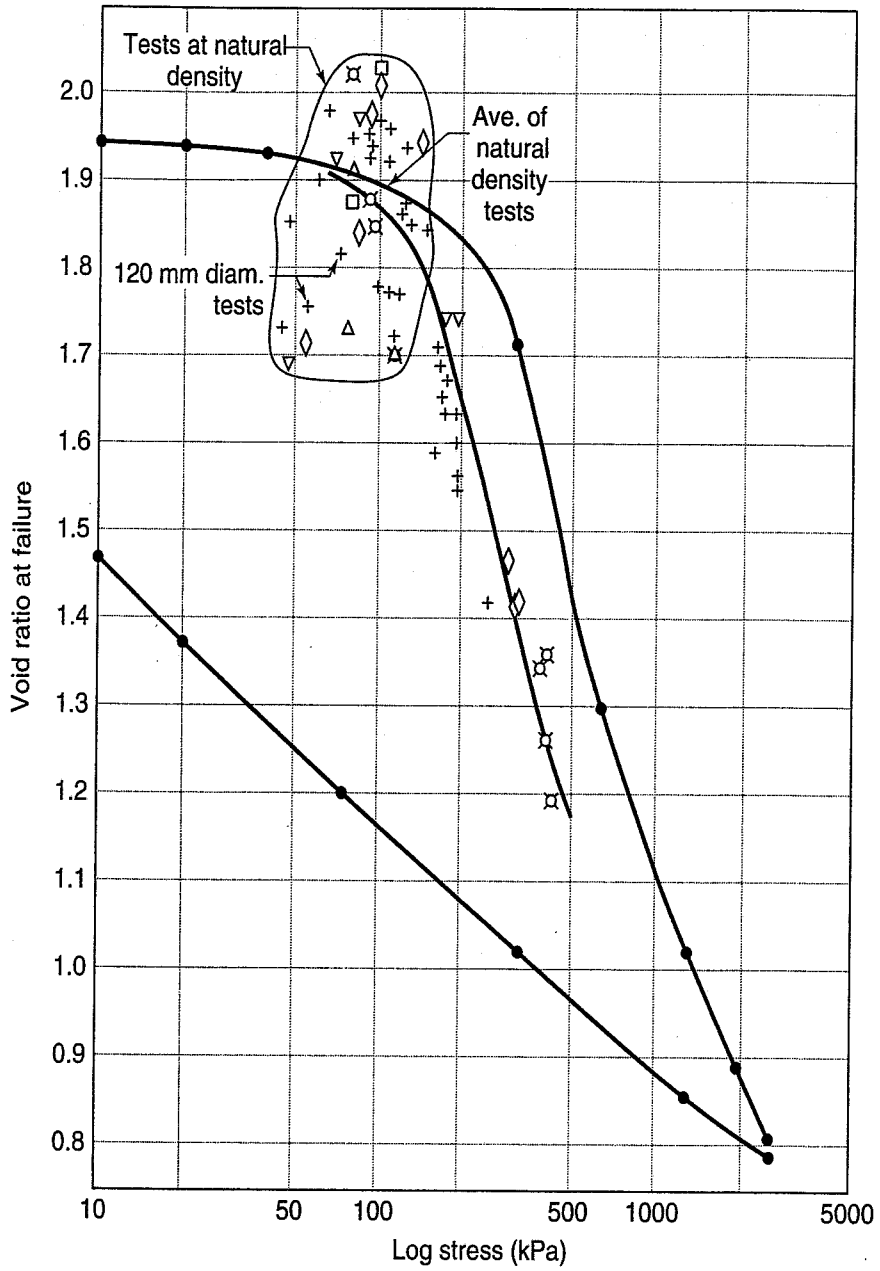

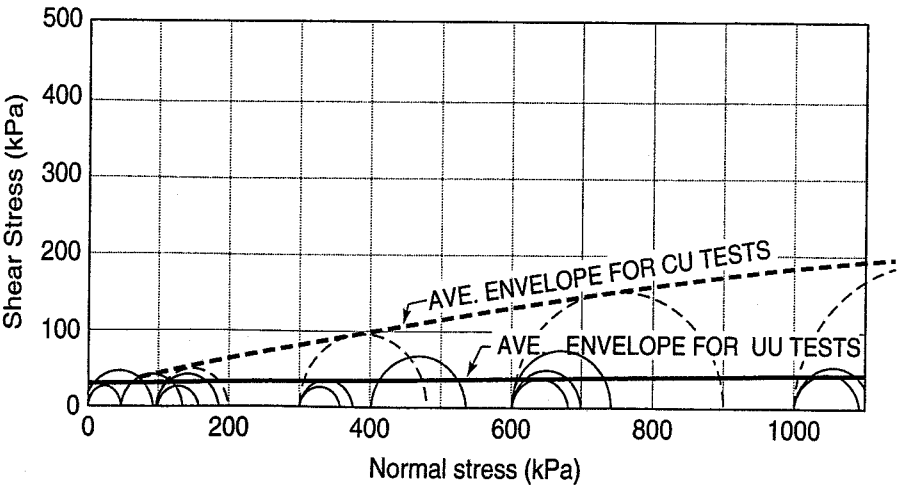

FIGURE 13.96 Results from consolidation and CU and UU triaxial tests on Glacial Lake Agassiz clay performed at Northwestern (Osterberg, 1967).

Another important feature of the Jürgenson–Rutledge hypothesis is that if you have the results of a consolidation test and you know the relationship between the compressive strength and the void ratio (or water content), then you can theoretically obtain the results of both CD and CU triaxial tests on that same soil (Fig. 13.97).

1. For a CD test on NC clay:

   Start at a given value of σ'_{1c} as indicated in Fig. 13.97. Because it is a drained test, the specimen will consolidate during shear and end up at σ'_{1f}. Note that $\sigma'_{1f} - (\sigma_1 - \sigma_3)_f = \sigma'_{3f}$. Therefore the distance $\Delta = \sigma'_{3f}$. Since it is a semilog plot, there is only one value of w_f (and e_f) where the difference Δ between the curves is $\sigma'_3 = \sigma_3$. In a CD test they are, of course, equal. It is a trial and error solution. By using different hypothetical values of the effective consolidation pressure σ'_3 one can construct the Mohr failure envelope and determine the ϕ' for a hypothetical CD test on the clay.

2. For a CU test on NC clay (Fig. 13.98):

   This is a traditional hydrostatically consolidated CU total stress test conducted at a constant cell pressure $\sigma'_{3c} = \sigma'_{3c} = \sigma'_{1c}$. As shown in Fig. 13.98, these pressures correspond to the consolidation water content w_c. Because the hypothetical specimen is sheared undrained, both the water content and void ratio at the end of consolidation and at the end of shear are the same; e.g., $w_c = w_f$ = constant and $e_c = e_f$ = constant. Also the constant cell pressure is $\sigma_{3c} = \sigma'_{3c} = \sigma_{3f}$, and the distance $\Delta = \sigma_{3f} - (\sigma_1 - \sigma_3)_f$. For this cell pressure, the compressive strength at failure is $(\sigma_1 - \sigma_3)_f$ at w_f and σ_{3f}. Again, because the plot is semilog, this value of Δ is not a constant—it changes throughout the stress range. If we repeat the process at different water contents or different cell pressures, we can construct the hypothetical Mohr failure envelope in terms of total stresses and thereby determine the hypothetical ϕ_T.

   Now we have both ϕ' and ϕ_T without conducting any triaxial tests!

Finally, in spite of the assumptions and uncertainty associated with the Jürgenson–Rutledge hypothesis, there are some practical applications that you may find useful.

1. The Jürgenson–Rutledge relationship can be used with the results of in situ tests such as the VST to estimate the C_c, ϕ', ϕ_T, and other properties, as shown in Fig. 13.99. This information would be useful for preliminary work on a project at a new site.
2. Different soils will have different Jürgenson–Rutledge relationships—e.g., as shown in Fig. 13.100.

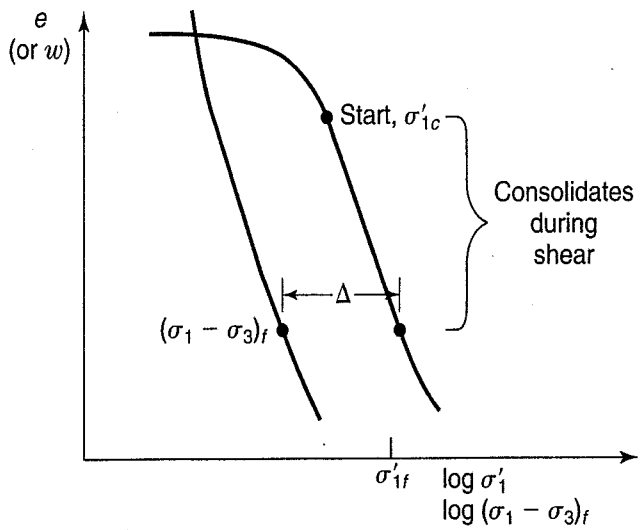

FIGURE 13.97 Using the Jürgenson–Rutledge hypothesis to determine the results of a CD triaxial test.

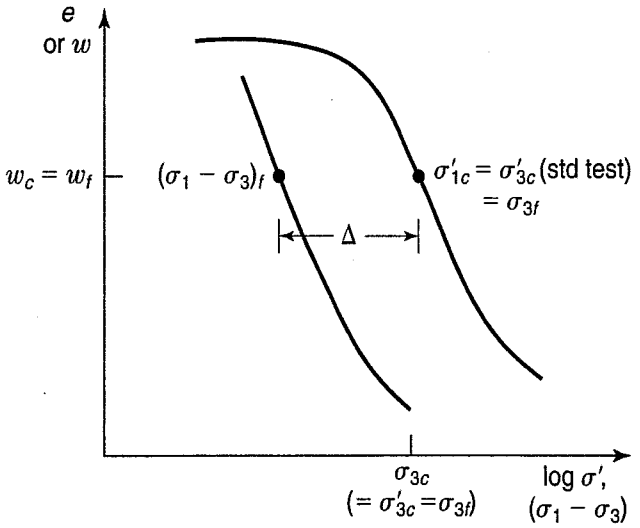

FIGURE 13.98 Using the Jürgenson–Rutledge hypothesis to determine the results of a CU triaxial test.

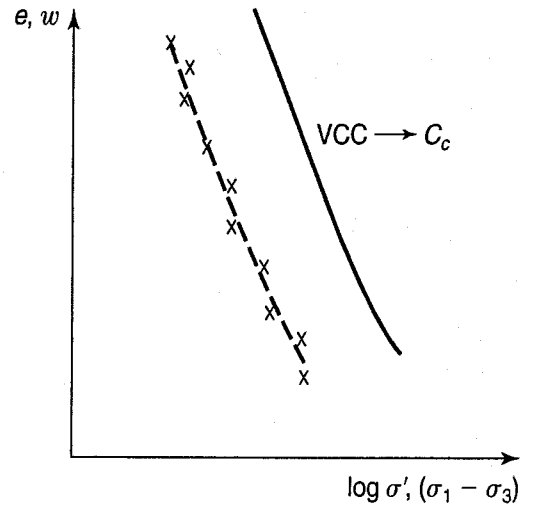

FIGURE 13.99 Using the VST or other estimates of the in situ undrained shear strength and the VCC to establish the Jürgenson–Rutledge relationship for a clay deposit.

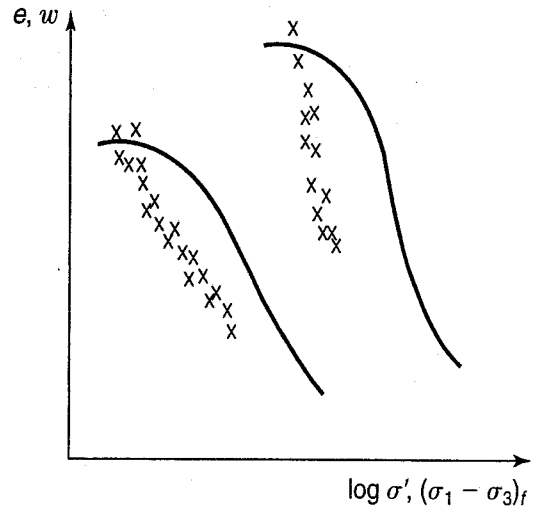

FIGURE 13.100 Different Jürgenson–Rutledge relationships for different soil deposits.

3. If the deposit is silty, there is often a large scatter in $(\sigma_1 - \sigma_3)_f$ results; i.e., they do not follow the Jürgenson–Rutledge hypothesis (developed for clay soils). This means that basically they behave as granular soils, and, for example, a stability analysis in terms of total stresses would not be appropriate for this site.

Remember that you still have sample quality and disturbance issues, especially in deposits of soft sensitive clays, but for these sites, the assumptions of Jürgenson–Rutledge are basically no worse than we usually make for strength and consolidation testing in geotechnical practice.

13.13.4 Consolidation Methods to Overcome Sample Disturbance

Several times before, we have mentioned that soil samples are taken from the subsurface for subsequent testing in the laboratory in order to obtain their engineering properties. Because those properties in situ are so dependent on everything from their water content and density to the soil structure and stress history of the deposit, we usually attempt to take soil samples that are as undisturbed as possible. Subsurface investigation and undisturbed soil sampling are usually discussed in courses and books on foundation engineering; see also, for example, Hvorslev (1949), Lowe and Zaccheo (1991), and Becker (2001). We also recommend an educational video on drilling and sampling by DeJong and Boulanger (2000) that is available online.

The three primary factors that cause the measured shear strength to be less than in situ are: strain rate effects (described in Secs. 13.10.4 and 13.13.7); anisotropy (different behavior in different directions and measured under different stress systems—discussed in Sec. 13.13.5); and sample disturbance. Sample disturbance results from shear distortion, changes in water content and density, and other effects on the soil as it is extracted from the ground.

Soil samples are most commonly obtained in thin-walled steel (Shelby) tubes or some other type of cylindrical container. The samples are extruded from the tubes, and individual specimens are trimmed appropriately and placed in the testing apparatus. This entire sampling and testing process has several opportunities for mechanical disturbance and changes in water content and void ratio that will cause the measured behavior to be very different than the behavior that will occur in the field. In Sec. 13.6, we briefly described the stress path when we take samples of normally consolidated clay from

a soft clay deposit; they are always disturbed to some extent. We mentioned that the measured undrained shear strength will be lower than in situ, even with perfect sampling.

In Sec. 8.5, the effects of sampling disturbance on the one-dimensional (1-D) compression curve were described. Figure 13.101 shows how the laboratory reconsolidation curve on a disturbed sample differs from the in situ compression curve. Such disturbance can also have a profound effect on the measured shear strength of the soil and thus contribute to the misrepresentation of field behavior in conventional laboratory strength tests. The test designation UUC represents a unconfined compression test, and CK_0U indicates a triaxial test that is one-dimensionally consolidated (CK_0) prior to being sheared undrained (U).

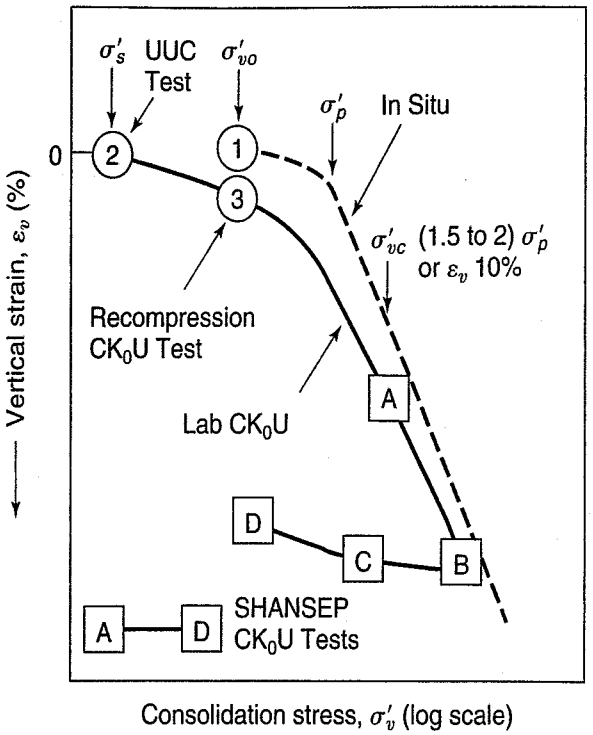

FIGURE 13.101 Schematic of laboratory reconsolidation procedures to overcome sampling disturbance effects (after Ladd and DeGroot, 2003).

In order to minimize the effects of sampling disturbance on measured shear behavior, two methods have been developed in which the test specimens are reconsolidated prior to applying the shear stresses to failure. These are the (1) *Recompression* and (2) *SHANSEP* techniques (SHANSEP stands for Stress History and Normalized Soil Engineering Properties). While both of these methods involve reconsolidation, the principles are fundamentally quite different.

In the Recompression method, developed at the Norwegian Geotechnical Institute (NGI) by Bjerrum (1973) and coworkers, the in situ σ'_{vo} and σ'_{ho} are reapplied in order to recover strains imposed on the soil during sampling and to expel any water that may have been absorbed due to sampling-induced swelling of the soil. The Recompression method reapplies stresses from the sampling effective stress (σ'_s at Point 1 in Fig. 13.101) to the σ'_{vo} and σ'_{ho} at point 2. Once this stress state is achieved, the usual shear testing of the soil occurs.

The SHANSEP method (Ladd and Foott, 1974) assumes that for many clays, the behavior in a given mode of shear (e.g., compression or extension) is determined by the clay's overconsolidation ratio (OCR). Specimens of clay can either be loaded in 1-D compression beyond their preconsolidation pressure (σ'_p) to a normally consolidated state (points A and B in Fig. 13.101) or unloaded to a particular OCR that corresponds to that in the field (points C and D in Fig. 13.101). By normalizing the measured stresses during shear (typically dividing by the final consolidation pressure σ'_{vc}), one can then estimate behavior at the same OCR, but at different consolidation σ'_{vc} values (for example, at the in situ σ'_{vo} in Fig. 13.101). In fact, a generalized equation can be developed to predict the undrained shear strength τ_f for any OCR for a particular soil sheared in a given mode:

$$\frac{\tau_f}{\sigma'_{vc}} = S(\text{OCR})^m \tag{13.53}$$

where S = the value of τ_f/σ'_{vo} for OCR = 1, and

m = a constant determined from the test data.

So, which method is better or more valid? The Recompression method was originally developed for more structured and sensitive clays, and because this method reconsolidates to σ'_{vo}, which is less than σ'_p, it does not destructure the clay prior to shear. However, the method requires high quality samples so that points 1 and 3 in Fig. 13.101 are not significantly different. If these points have significantly different strain levels or void ratios (due to sampling disturbance), deceptively different laboratory behavior can result. In comparison, the SHANSEP method, by consolidating clays well beyond σ'_p, significantly destructures the soil in order to impose a new stress history to it. As a result, SHANSEP tends to be better suited for soft or even stiff clays that have been mechanically overconsolidated (versus those that have been affected by salt or other cementation effects), and it provides a conservative estimate of strength for more structured soils.

13.13.5 Anisotropy

You probably recall from your basic mechanics courses that an *isotropic* material has the same mechanical properties in all directions, while the properties of an *anisotropic* material are directionally dependent. We commonly assume that clay deposits are isotropic, but actually the mechanical behavior of most clays is directionally dependent—that is, the shear strength and compressibility depend on the direction of loading versus the direction of deposition (typically assumed to be vertical). This characteristic is fundamentally the result of so-called *inherent* or *intrinsic anisotropy* resulting from the preferred particle orientation that developed during deposition and any subsequent stress history. Both the microfabric and macrofabric features such as varves and seams (see Secs. 4.8.1 and 4.8.2) contribute the inherent anisotropy of the clay deposit.

Inherent anisotropy leads to variations in undrained shear strength, modulus, pore pressure response during undrained loading, and Mohr–Coulomb parameters c' and ϕ' (for example, Hvorslev, 1960; Saada and Bianchini, 1975; Ladd et al., 1977). For shear strength, the angle (δ) between the major principal stress (σ_1) direction and the vertical is used to denote the direction of loading. Thus, for traditional compression tests, $\delta = 0°$, and for extension tests, $\delta = 90°$. Direct shear and direct simple shear tests impose δ angles at failure that are somewhere in between this range, although where is not known exactly.

The measurement of anisotropy in clays is confusing because of another type of anisotropy, called by various authors *stress system*, *induced*, *apparent*, or *evolving anisotropy*. It occurs when a soil is consolidated under K_o-conditions, and then sheared in such a way that the principal stresses rotate and the angle δ changes during shearing. For example, a specimen K_o-consolidated in a triaxial cell to a normally consolidated state ($\sigma'_{3c}/\sigma'_{1c}$ and $K_o < 1$), then sheared in axial extension, starts at a $\delta = 0°$ state (σ'_{1c} is vertical during consolidation), and then the principal stresses rotate as the stress path moves into the extension shear stress range. Then $\delta = 90°$ and $q = \frac{1}{2}(\sigma_v - \sigma_h) < 0$ (see Fig. 13.23). This 90° rotation in the direction of σ_1 results in a significant change in the soil's apparent anisotropy. If the loading in extension were stopped prior to failure and then axial compressive stresses were applied, a much lower compressive strength would result than if the principal stress rotation had not occurred in the first place. Thus, axial extension shearing changes the preferred anisotropy of the soil from its original compression orientation to a more neutral state, leading to lower compressive strength. A similar kind of experiment could be done on a soil that is K_o-consolidated, unloaded to a heavily overconsolidated state ($K_o > 1$), and then sheared in axial compression.

To study both types of anisotropy, specialized testing devices such as the directional shear cells (Arthur et al., 1980), cuboidal or true triaxial cells, and torsional shear hollow cylinder devices (Sec. 11.5.3) are used. As noted by Ladd et al. (1977), often for practical purposes it is sufficient to characterize the combined effect from inherent and induced anisotropy, and this is best done using tests in which specimens are K_o-consolidated to their in situ stress state prior to shear.

Anisotropy is important in practice because it affects such factors as the modulus and the yield surface and thus the shear strength of clays, as we have just explained. An important illustration of the importance of anisotropy is in the choice of shear strength for stability analyses. For example, consider the embankment on a soft soil shown in Fig. 13.102. The variation of shear strength along a potential sliding surface can vary significantly, and to measure the correct shear strength, a different type of test would be appropriate for different portions of the potential sliding surface.

Bjerrum (1972, 1973) suggested that the best way to estimate the stability of embankments on soft clays was to use AC triaxial tests, direct simple shear (DSS), and AE triaxial tests, all reconsolidated to their in situ state of stress (the Recompression method described above in Sec. 13.13.4), as shown in Fig. 13.102. Different shear strengths would be appropriate for different segments of the slip surface, typically $^1/_3$–$^1/_3$–$^1/_3$ each, for the embankment case.

A summary of τ_f/σ'_{vo} data measured in K_o-consolidated AC triaxial tests (TC), direct simple shear (DSS), and AE triaxial tests (TE) on several NC clays is shown in Fig. 13.103. You can see that the undrained strength can vary significantly depending on the type of test. Jamiolkowski et al. (1985) concluded that: (1) less plastic and more sensitive clays have more anisotropy as compared with high plastic clays; and (2) the use of only hydrostatically consolidated undrained triaxial compression tests or even

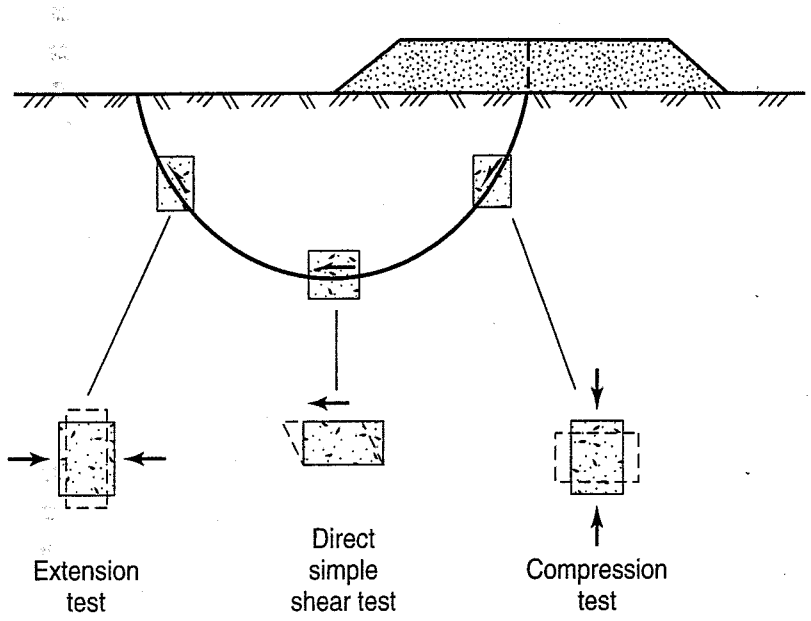

FIGURE 13.102 Relevance of laboratory shear tests to the shear strength required for stability analyses (Bjerrum, 1972; 1973).

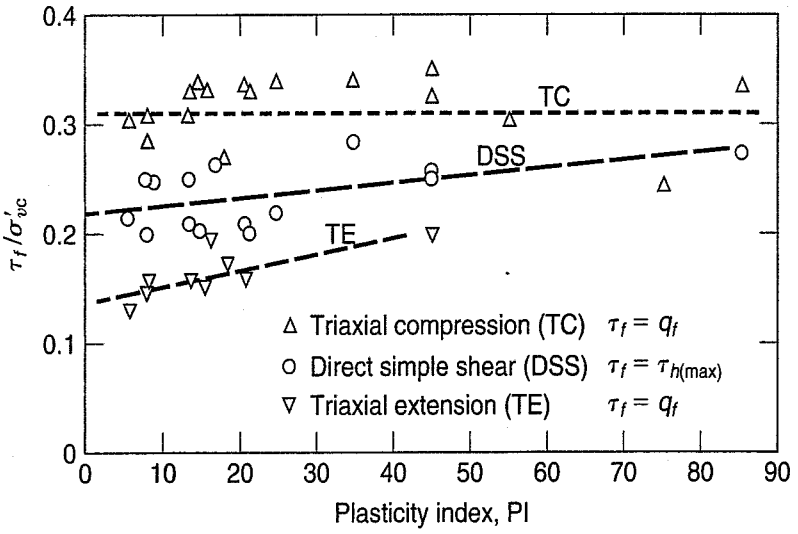

FIGURE 13.103 Undrained shear strength anisotropy from K_o-consolidated undrained triaxial tests on NC clays, with data from from the University of British Columbia, Sherbrooke and Laval Universities in Canada, MIT in the United States, and the Norwegian Geotechnical Institute (after Jamiolkowski et al., 1985).

K_o-consolidated undrained triaxial compression tests to obtain the undrained shear strength τ_f for stability analysis is generally unsafe for clays of low to moderate OCR. This is because the shear strength measured in triaxial compression is greater than measured by the other two types of tests. Using only the AC strength would seriously overestimate the calculated safety factor, and an unsafe design could result.

So what should you do? Similar to Bjerrum (1972 and 1973), Jamiolkowski et al. (1985) recommend, if at all possible, conducting DSS tests, triaxial extension, and triaxial compression tests on high quality undisturbed specimens. If such a test program is not possible, then perform consolidation tests on high quality samples (e.g., Holtz et al., 1986) to obtain the σ'_p and OCR; then use Eq. (13.54) to estimate τ_f/σ'_{vo}:

$$\frac{\tau_f}{\sigma'_{vc}} = (0.23 \pm 0.04)(\text{OCR})^{0.8} \tag{13.54}$$

They strongly suggest that using this empirical equation will be more reliable than conducting only hydrostatically consolidated undrained triaxial compression tests to determine the undrained shear strength for stability analysis!

In Sec. 13.13.3, when we discussed the τ_f/σ'_{vo} ratio, we mentioned the interesting discovery by Mesri (1975) that the mobilized undrained shear strength in the field was almost equal to 0.22 σ'_p and independent of plasticity of a soft clay [Fig. 13.90(e) and Eq. (13.55)]:

$$\frac{\tau_f}{\sigma'_p} = 0.22\sigma'_p \tag{13.55}$$

Mesri (1989) in a reevaluation showed that essentially the same relationship can be obtained from laboratory shear tests, provided that the anisotropy and strain rate are correctly accounted for. We have discussed the vane shear tests in Secs. 11.6.1 and 12.11.4, when we mentioned that the VST is a common in situ test for determining the undrained shear strength of soft clays. The Bjerrum's correction factor μ (Figs. 12.45 and 13.90) was probably due to anisotropy and strain rate effects not accounted for by the VST. Although, as we mentioned, Bjerrum (1973) recommended the use of recompressed AC, DSS, and AE triaxial tests, he recognized that such an approach may not be practical for most projects. Therefore he suggested that the corrected undrained VST strength could be used instead. In other words, $\tau_{f(\text{mob})}$ determined from a program of high quality and expensive laboratory strength tests may not be significantly different from corrected τ_f determined by the VST.

To the lab test results shown in Fig. 13.103, Mesri added some VST data (FV curve = "field vane"), as shown in Fig. 13.104 and then assumed that $\tau_f/\sigma'_p \approx \tau_f/\sigma'_{vc}$.

In spite of the scatter, the results were encouraging. Next, Mesri applied the correction factor μ for VST [Figs. 12.45 and 13.90(c)], as well as corrections for strain rate summarized from several studies by Chandler (1987). These results are shown in Fig. 13.105. The two curves are (1) $\mu_{R\,100}$ for t_f = 100 min, a typical time to failure for laboratory strength tests, and (2) $\mu_{R\,10000}$ for t_f = 10000 min or about 1 wk, a typical time to failure for an embankment. Also shown in this figure are the correction factors μ and μ_R; the first is from Figs. 12.45 and 13.90(c) and the second is from Bjerrum's (1973) modification for strain rate effects. It is remarkable that it matches Chandler's $\mu_{R\,10000}$ data so well.

Mesri then applied the ratio of $\mu_{R\,10000}$ and $\mu_{R\,100}$ to the τ_f/σ'_p from the AC, DSS, and AE tests to one-third of the failure surface in Fig. 13.103 to get the ratio $\tau_{f(\text{mob})}/\sigma'_p$, or

$$\frac{\tau_{f(\text{mob})}}{\sigma'_p} = \frac{1}{3}\left[\left(\frac{\tau_f}{\sigma'_p}\right)_{TC} + \left(\frac{\tau_f}{\sigma'_p}\right)_{DSS} + \left(\frac{\tau_f}{\sigma'_p}\right)_{TE}\right]\frac{\mu_{R\,10000}}{\mu_{R\,100}} \tag{13.56}$$

When this is plotted in Fig. 13.106, we see that the $\tau_{f(\text{mob})}/\sigma'_p$ is indeed independent of PI; or

$$\tau_{f(\text{mob})} = 0.22\sigma'_p \tag{13.57}$$

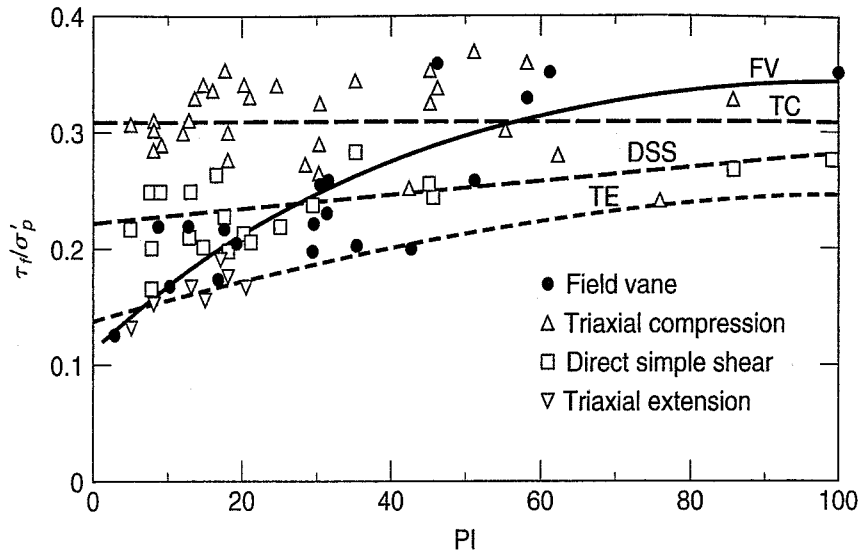

FIGURE 13.104 Values of τ_f/σ'_p from Jamiolkowski et al. (1985) and Chandler (1987), as compiled by Mesri (1989).

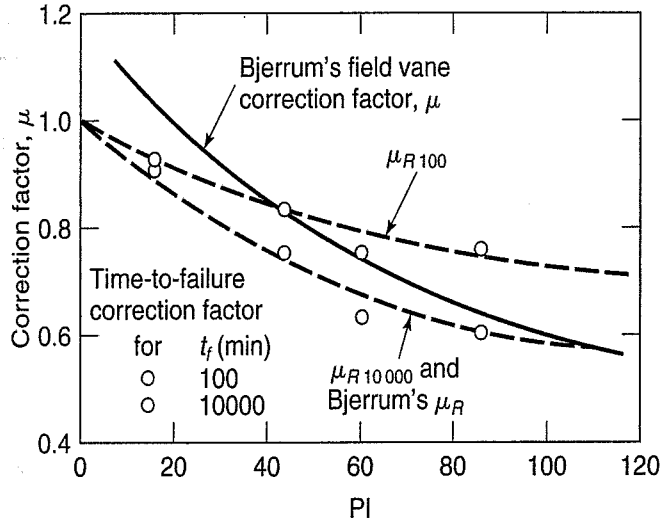

FIGURE 13.105 Correction factors for VST test (Bjerrum, 1973; Chandler, 1987).

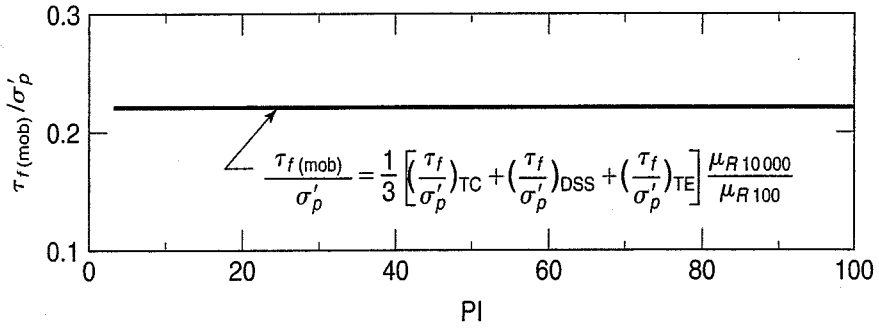

FIGURE 13.106 Mobilized field undrained shear strength from laboratory tests (Mesri, 1989).

Example 13.17

Given:

The data in Fig. 13.105.

Required:

If the PI is 40, show that Eq. (13.57) is satisfactory.

Solution: From Figs. 13.104 and 13.105, and using Eq. (13.56), we obtain

$$\frac{\tau_f}{\sigma'_p} = \tfrac{1}{3}[TC + DSS + TE]\frac{\mu_{R\,10000}}{\mu_{R\,100}} = \tfrac{1}{3}[0.310 + 0.245 + 0.195]\frac{0.76}{0.85} = 0.244$$

Therefore, Eq. (13.57) is quite satisfactory.

As Mesri (1989) notes, because Eqs. (13.50) and (13.57) were obtained from such different analysis sets of field and laboratory data, it is amazing that they agree so well, in spite of the scatter of the data and the simplifying assumptions used in the 1989 analysis. The practical conclusion, as noted above, is that use of the more time-consuming and thus more expensive sampling and laboratory testing program provides, at best, results comparable to those from corrected VST testing for undrained stability analyses of soft clays.

13.13.6 Plane Strain Strength of Clays

In Sec. 13.4, we described field situations in which plane strain conditions exist and are therefore more appropriately modeled using plane strain laboratory testing, in which strains in one axis are prevented [Fig. 11.16(b)]. Plane strain conditions can exist for all types of geotechnical materials. We discussed the plane strain properties of sands in Sec. 13.11, but in contrast, there have been few studies of the plane strain properties of fine grained and cohesive soils. Perhaps the most complete data set was presented by Vaid and Campanella (1974), who compared plane strain test results with those from triaxial tests on undisturbed specimens of normally consolidated Haney clay (LL = 44, PI = 18, and sensitivity 6–10). Specimens were K_o consolidated prior to shear, then loaded in AC and AE stress conditions, both undrained and drained.

Results are shown in Table 13.8 in terms of both maximum principal stress difference and maximum obliquity. Also given are axial strain, volumetric strain (for drained tests), the undrained strength τ_f normalized by σ'_1 (for undrained tests), the obliquity value, σ'_1/σ'_3, and effective friction angle ϕ'. The drained test specimens did not strain-soften during testing, so their failure states are defined by the condition at $(\sigma'_1/\sigma'_3)_{max}$. From these results, the following conclusions can be drawn:

- In comparison to triaxial test results, plane strain tests gave undrained strengths that were about 10% higher in compression, and about 25% higher in extension; the increases in maximum ϕ' values were 2° and 0.5°, respectively. Shear-induced pore pressures were approximately the same for compression and slightly higher in the plane strain extension tests than those for triaxial extension.
- For the drained tests, both compression and extension plane strain tests gave higher values of $(\sigma'_1/\sigma'_3)_{max}$. Increases in ϕ' were only 0.4° to 0.8° for unloading tests (compression and extension), but this difference was 3.2° for AC tests.

Ladd et al. (1977) incorporated these results from Haney clay with those from other clays and found that for the undrained strength of clay for compression (based on six clays including Haney clay)

$$\tau_{f(\text{plane strain})}/\tau_{f(\text{triaxial})} = 1.03 \text{ to } 1.15 \tag{13.58}$$

and for extension (based on three clays including Haney clay)

$$\tau_{f(\text{plane strain})}/\tau_{f(\text{triaxial})} = 1.19 \text{ to } 1.25 \tag{13.59}$$

TABLE 13.8 Comparison of Triaxial and Plane Strain Results on Normally Consolidated Haney Clay*

	At maximum principal stress difference, $(\sigma_1 - \sigma_3)_{max}$					At maximum obliquity, $(\sigma'_1/\sigma'_3)_{max}$			
Test conditions	Axial strain (%)	Volumetric strain (%)	τ_f/σ'_1	σ'_1/σ'_3	ϕ' (°)	Axial strain (%)	Volumetric strain (%)	σ'_1/σ'_3	ϕ' (°)
Undrained compression									
Plane strain	0.4	—	0.296	2.48	25.2	4.5	—	3.20	31.6
Triaxial	0.35	—	0.268	2.15	21.4	12	—	2.98	29.8
Undrained extension									
Plane strain	−10.5	—	0.211	3.57	34.3	−10.5	—	3.57	34.3
Triaxial	−13	—	0.168	3.49	33.8	−13	—	3.49	33.8
Drained loading compression									
Plane strain	4.5	0.9	—	2.93	29.4	4.5	0.9	2.93	29.4
Triaxial	15	3.2	—	2.84	28.6	15	3.2	2.84	28.6
Drained unloading compression									
Plane strain	−9	−0.8	—	3.65	34.7	−9	−0.8	3.65	34.7
Triaxial	−14	0.7	—	3.60	34.3	−14	0.7	3.60	34.3

*All samples initially K_o consolidated.

From Vaid and Campanella (1974).

13.13.7 Strain Rate Effects

We discussed strain rate effects in sands in Sec. 13.10.4, concluding that the effects are most important at relatively high rates of deformation. Because of clays' viscous nature, their mechanical behavior tends to be highly dependent on the time scale over which they are loaded, and over a much wider range of strain rates than sands. Two aspects of this dependency affect engineering practice. We discussed in Sec. 9.8 the first one, the long-term settlement due to secondary compression in. The second is the effect of strain rate on undrained strength. To some extent, all clays exhibit strain rate dependence of their undrained strength, and usually the faster you load a clay soil, the stronger it becomes.

We mentioned in Sec. 13.13.5 that strain rate effects were part of Bjerrum's correction factor for the VST conducted on deposits of soft clay. Taylor (1948) showed that the undrained strength of a remolded Boston blue clay increased about 10% per log cycle of time increase in speed of shear [Fig. 13.107(a)]. Bjerrum (1972) showed about the same increase in CU tests on a Norwegian plastic clay [Fig. 13.107(b)]. Differences between the rate of loading in the laboratory and in the field can significantly affect the undrained shear strength. Ladd et al. (1977) also discussed this point.

One way to express the dependency of the undrained strength on strain rate, SR, is by rate effect strength parameter,

$$\rho_{SRo} = (\Delta\tau_f/\tau_{fo})/\Delta \log SR \tag{13.60}$$

where τ_{fo} is the undrained strength at some reference axial strain rate SR_o. The parameter ρ_{SRo} is usually expressed as a percentage, and it represents the change in τ_f over one logarithmic cycle change in strain rate.

Sheahan et al. (1996) present data from a comprehensive set of K_o-consolidated CU tests on specimens of resedimented Boston blue clay (LL = 45; PI = 24) consolidated to OCRs of 1, 2, 4, and 8, then

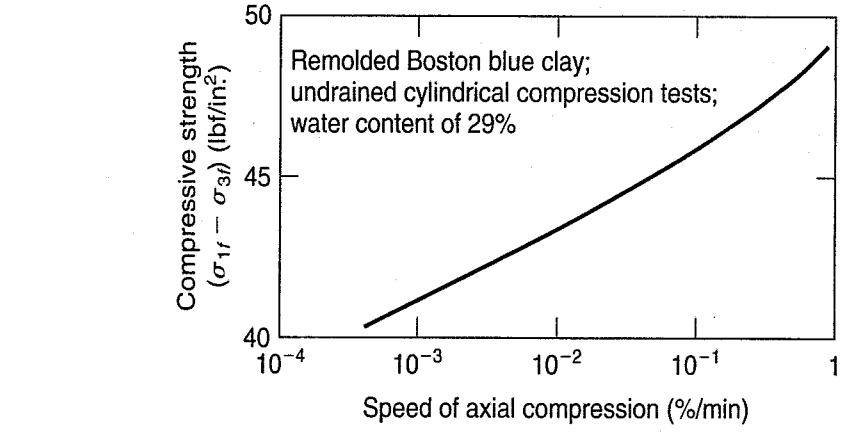

(a)

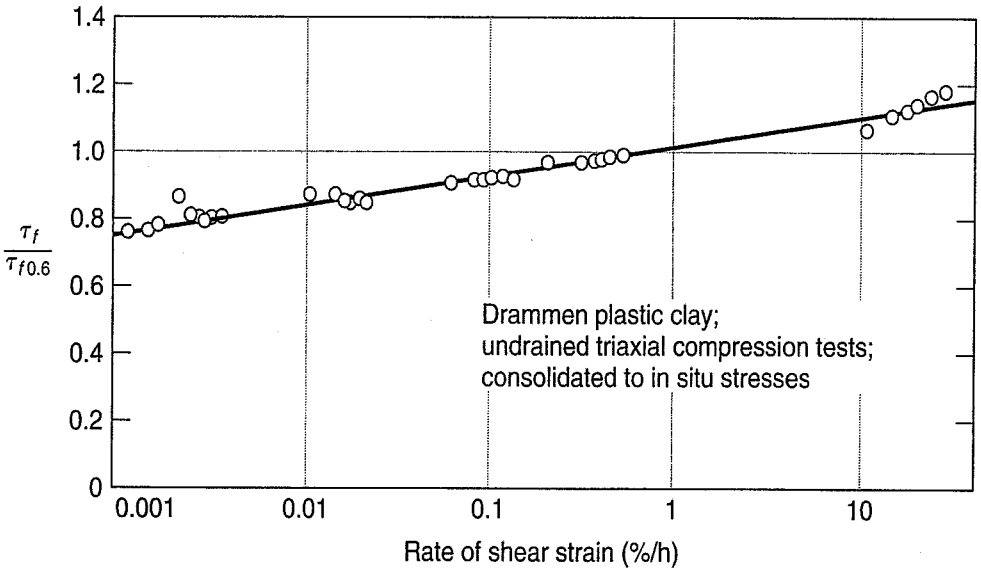

(b)

FIGURE 13.107 Effect of rate of loading on the undrained strength of (a) Boston blue clay (after Taylor, 1948); and (b) Drammen, Norway, plastic clay. The strength ratio in these latter tests is with respect to the strength at the NGI standard rate of 0.6%/hr (after Bjerrum, 1972).

sheared at strain rates varying from 0.05 to 50%/hr. Figure 13.108 shows the summary of τ_f normalized by the maximum vertical effective stress σ'_{vm} versus strain rate. The value of ρ_{SRo} is relatively independent of OCR, averaging about 9.5%, across the faster rates from 5% to 50%/hr, but at lower strain rates the rate dependence decreases with increasing OCR. Soils more structured than resedimented Boston blue clay can be expected to exhibit even more rate dependence, regardless of stress history.

The rate dependence of undrained behavior, if not properly accounted for, can lead to overestimates of undrained strength that may result in unsafe designs. Ladd and DeGroot (2003) estimate that when compared to τ_f values from laboratory K_o-consolidated CU tests (typically performed at 0.5% to 1.0%/hr), uncorrected τ_f values derived from cone penetration tests are 50% higher, τ_f from lab unconfined compression tests are 15% higher, and field strengths may be 10% lower.

Another problem, not often mentioned, results from trying to determine the long-term or effective stress strength parameters and the short-term or CU-total stress strength parameters from the same test series of CU triaxial tests. It is common practice when testing compacted specimens of core materials for the design of embankments to determine both the effective and total stress strength parameters

from the same test series. The rates of loading or strain required for correct determination of the effective stress strength parameters may not be appropriate for the short-term or undrained loading situation, because, as mentioned above, the stress-deformation and strength response of clay soils is rate-dependent. Long-term or drained loading in the field may take many days or even weeks and months, so the effective stress parameters should be determined on a test conducted at a very slow rate of strain. On the other hand, for the short-term or undrained case, the rate of loading in the field may be quite rapid, and therefore for correct modeling of the field situation, the rates of loading in the laboratory sample should be comparable. Thus the two objectives of the CU-effective stress test are really incompatible. The best thing to do, though it is rarely done in practice, would be to have two sets of tests, one set CD modeling the long-term situation and the other set CU modeling the short-term undrained loading.

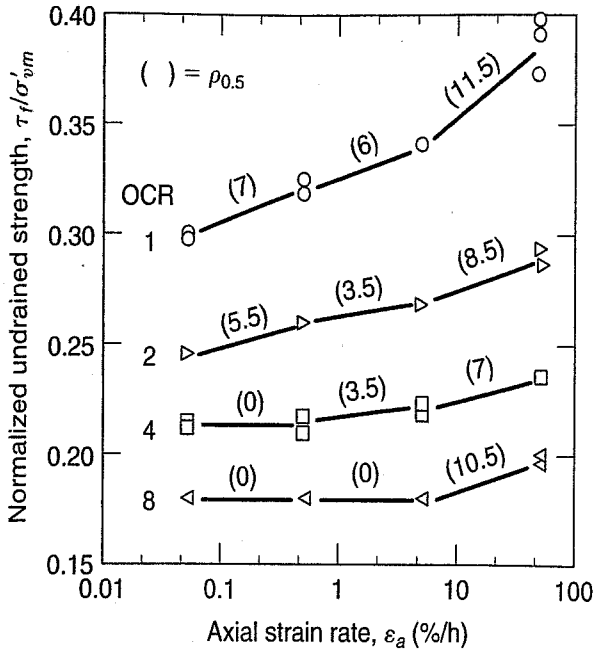

FIGURE 13.108 Effect of axial strain rate on normalized undrained shear strength of resedimented Boston blue clay at different OCRs (from Ladd and DeGroot, 2003, after Sheahan et al., 1996).

13.14 STRENGTH OF UNSATURATED SOILS

Virtually all of the presentation of soil shear strength in this book has assumed that the soil is either completely dry or completed saturated (S = 100%). This stems from the origins of modern soil mechanics and represents simplifying assumptions, despite the well-known fact that many important geotechnical applications involve saturation conditions somewhere between these two extreme states. These include seepage problems, compacted soils for a multitude of applications (waste and contaminant isolation, constructed embankments, highway and building foundation soils, and so on) and soils prone to severe expansion and contraction associated with groundwater fluctuation (Fredlund, 1997). In addition, any shear strength applications for soils above the groundwater table should ideally include consideration of unsaturated soil mechanics. Much of this section is based on Fredlund and Rahardjo (1993) and Lu and Likos (2004), and you can refer to those books to further understand all of the complexities involved in unsaturated soil mechanics.

13.14.1 Matric Suction in Unsaturated Soils

The most important differentiating aspect of unsaturated soil effective stress and corresponding shear strength is the existence of soil suction, usually termed *matric suction*. We have already seen a simple example of matric suction in our discussion of capillary effects (Chapter 6). While other factors such as soil-water electrical interactions, particle-to-particle van der Waals attractive forces, and dissolved pore water solutes can contribute to soil suction (Lu and Likos, 2004), we will consider only capillary effects to understand fundamentals of unsaturated soil behavior.

Recall from Chapter 6 that for a capillary tube (Fig. 6.2), the surface tension is related to the curvature of the capillary meniscus, the height of the capillary rise, and the capillary pressure in the pore water. As a soil goes from a saturated to a unsaturated state, the water in the pores is no longer

continuous but starts to form these menisci, leading to changes in the effective stress state. In fact, a more generic version of Eq. (6.6a) includes consideration of the air pressure (u_a) at the meniscus interface:

$$u_a - u_w = -2T/r_m \tag{13.61}$$

where T is the surface tension and r_m is the radius of curvature of the meniscus. This difference, $u_a - u_w$, is the matric suction.

Just as in laboratory testing of saturated soils it is desirable to control the pore water pressure, in unsaturated soil testing it is necessary to control both the air and water pressures. In all cases, $u_a > u_w$, since that is the condition under which unsaturated soils exist. This is done using what is known as a *high air entry* (HAE) porous stone (or, more likely, ceramic). To understand how the HAE ceramic disk functions, a simple experiment can be performed using the setup shown in Figure 13.109, in which u_a and u_w can be separately controlled, with air and water phases separated by an HAE ceramic interface. The HAE ceramic is specified by its air entry value, u_{wa}, the maximum pressure differential that can be sustained across the ceramic material, which essentially functions as a membrane between the air and water. So a porous material with a "high air entry value" leads to some confusion: it does not mean that it allows a lot of air to enter or pass through it; it means that water saturating it forms a membrane that can maintain a high level of soil or matric suction without air entering the water-pressure measurement system. The matric suction rating for a porous material is thus inversely proportional to the pore diameter, with 15 bars (15 atmospheres of suction or −1500 kPa) being the highest rating cited.

Again referring to Fig. 13.109, as long as the u_{wa} value of the HAE ceramic is higher than the u_a being applied, the HAE ceramic will be able to keep the air and water separated due to the surface tension at the ceramic–air–water interface.

This simple experiment can now be extended to a *controlled stress variable* test setup that can apply a hydrostatic total stress to a soil specimen while controlling the pore air and water pressures, as shown in Fig. 13.110. It is easy to see that such a setup could be adapted to the triaxial, direct shear, and one-dimensional consolidation test devices. Just as in the simple experiment shown in Fig. 13.109, the HAE ceramic disk keeps air from entering the pore water pressure control system, and a *low air entry* disk (a coarse porous stone) allows the free exchange of air.

It is important to remember that in such tests, a stress hierarchy must be maintained such that the total stress, $\sigma > u_a > u_w$. When the magnitudes of these stress components are changed in equal increments and in the same direction (either all increased or all decreased), the matric suction and the *net normal stress*, $\sigma - u_a$, remain constant. This is referred to as *null testing* (Fredlund, 1973).

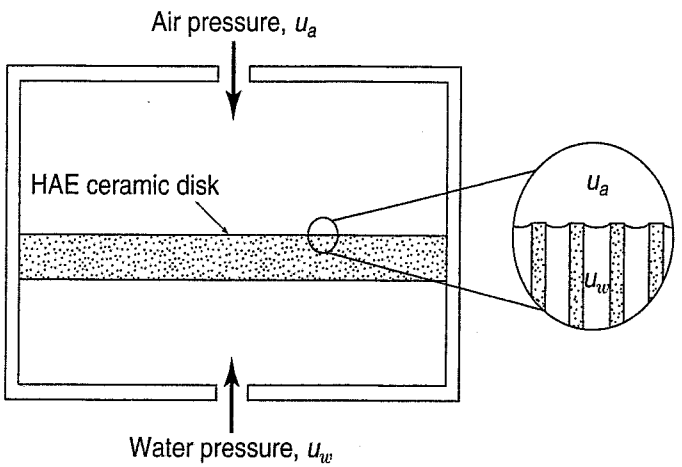

FIGURE 13.109 Equilibrium position for air–water–HAE ceramic interface (after Lu and Likos, 2004).

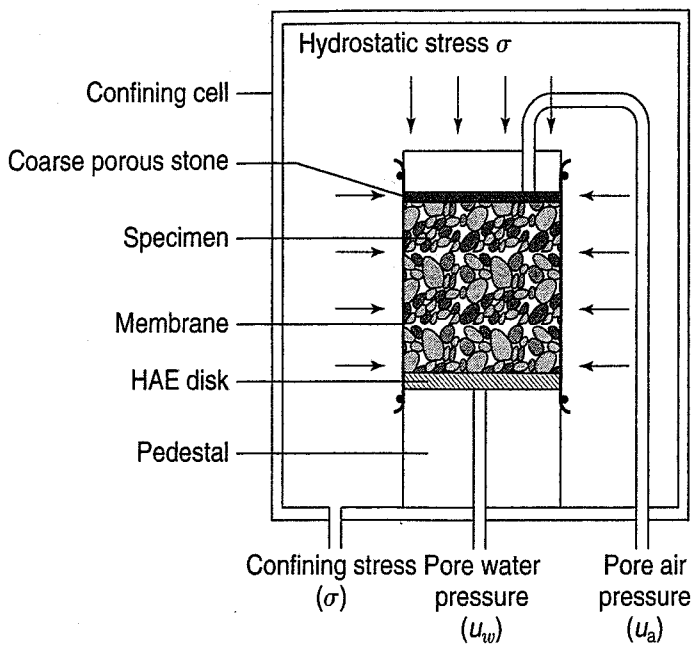

FIGURE 13.110 Example of controlled stress variable testing using a hydrostatic stress cell (after Lu and Likos, 2004).

13.14.2 The Soil–Water Characteristic Curve

From Sec. 6.8, you know that the soil–water characteristic curve (SWCC) relates the soil's degree of saturation to its matric suction and is fundamental to the state of stress and the corresponding shear behavior. Figure 13.111 shows the typical shape of this relationship. It is noteworthy that the air entry value of soil occurs at a relatively high degree of saturation, typically greater than 90%. This is because the capillary action that determines the air entry behavior requires more or less continuous water "columns" through the soil void space. As the saturation level decreases along the flat portion of the SWCC, the pore water regime remains continuous, until the residual saturation level is reached, when water forms distinct interparticle menisci.

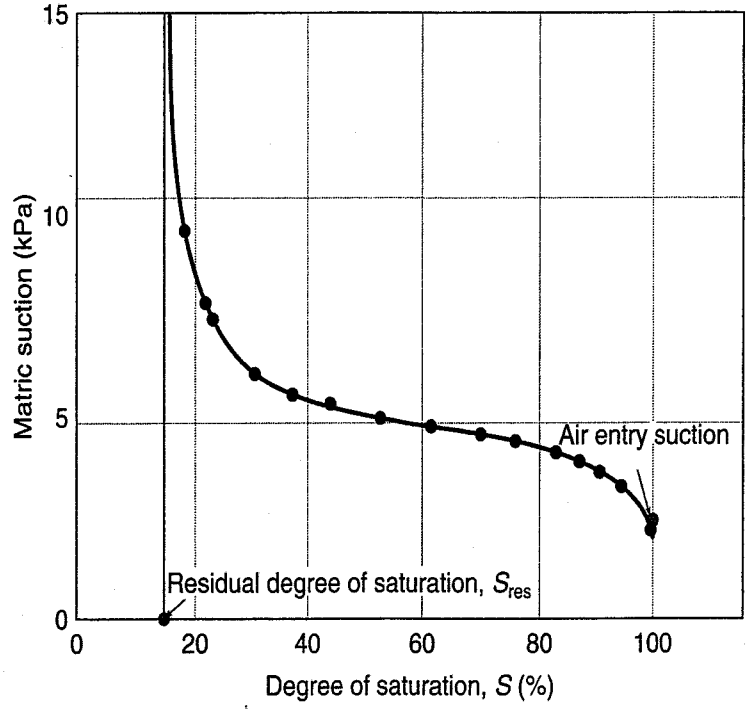

FIGURE 13.111 Soil–water characteristic curve (SWCC) for a typical soil.

The SWCC, while a relatively simple relationship, is important as a framework for understanding how the soil's physical state (degree of saturation) directly impacts a primary factor in its mechanical behavior (via matric suction).

13.14.3 The Mohr–Coulomb Failure Envelope for Unsaturated Soils

Bishop et al. (1960) conducted an extensive experimental program on unsaturated soils and introduced the parameter χ to characterize the contribution of matric suction to effective stress. The resulting equation for an unsaturated soil was as follows:

$$\sigma' = (\sigma - u_a) + \chi(u_a - u_w) \tag{13.62}$$

Until the mid-1970s, however, there was no systematic framework for considering the shear strength of unsaturated soils. Fredlund and Morgenstern (1977) presented a mechanistic framework for describing the shear strength that was based on a stress state principle and a modified Mohr–Coulomb criterion that considers both the pore water pressure, u_w, and pore air pressure, u_a. The stress state on any normal plane for unsaturated soil is given by a combination of $(\sigma - u_a)$ and $(u_a - u_w)$, where σ is the normal stress on that plane. When u_w and u_a are equal to one another (soil suction goes to zero), the second part of this stress state is eliminated, and we are left with the original effective stress principle, $\sigma' = (\sigma - u_w)$.

From this stress state concept, a modified Mohr–Coulomb equation was developed, where the shear strength, τ_{ff}, is given by

$$\tau_{ff} = c' + (\sigma_f - u_a)_f \tan\phi' + (u_a - u_w)_f \tan\phi^b \tag{13.63}$$

where ϕ^b = the angle representing the increase in shear strength with respect to a change in soil suction.

As we saw in Section 11.4, the Mohr–Coulomb envelope for a saturated (or dry) soil can be obtained by plotting the effective stress Mohr circles at failure, in τ versus $(\sigma - u_w)$ space, and drawing a common tangent line to those circles, defining c' and ϕ'. For unsaturated soils, the Mohr circles are plotted in τ versus net normal stress, $(\sigma - u_a)$, space to determine c' and ϕ', but a third dimension is added to the plot, the matric suction, $(u_a - u_w)$, to determine the angle ϕ^b. Referring to Fig. 13.112,

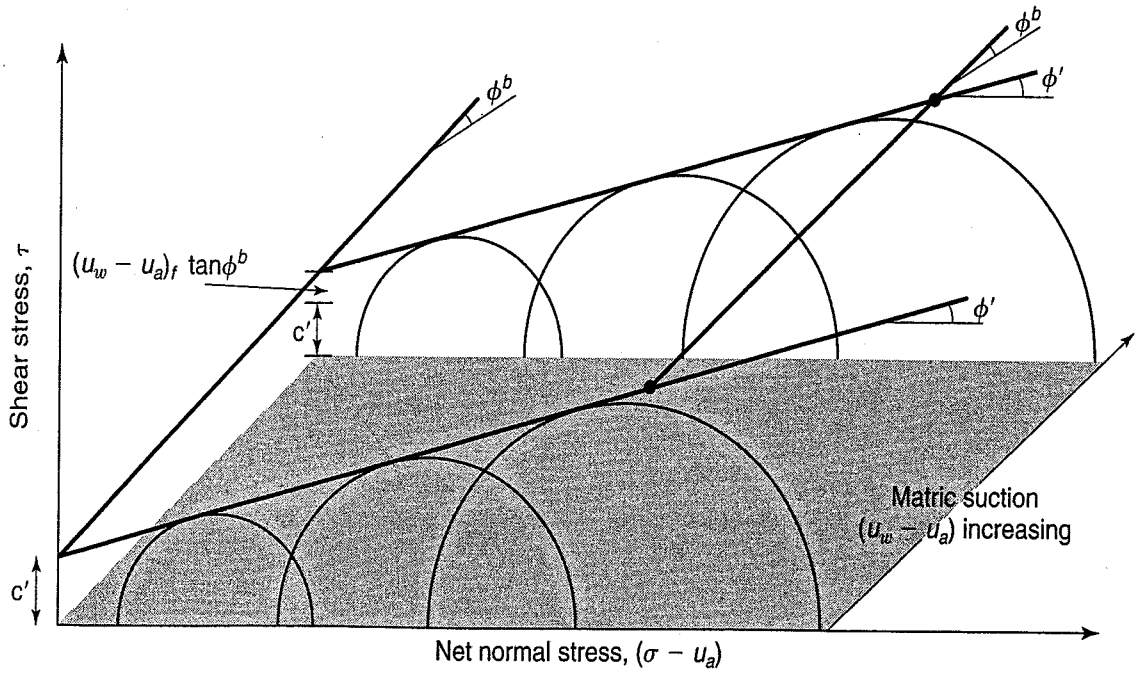

FIGURE 13.112 Mohr–Coulomb failure envelope concept extended for unsaturated soils (after Fredlund and Rajardjo, 1993).

one set of three tests at different effective confining pressures is shown for a saturated soil ($u_a - u_w = 0$), and a second set is shown for three tests at some nonzero matric suction. This results in a set of larger Mohr circles (because the matric suction contributes to higher shear strengths at a given $\sigma - u_a$) that are offset by the matric suction, and are still connected by a common tangent line at the same ϕ', but with a higher cohesion intercept. The slope of the line connecting the respective envelopes is ϕ^b, the increase in shear strength due to the matric suction. Referring to the SWCC in Fig. 13.111, at higher saturation levels corresponding to matric suction below the air entry value, the Mohr–Coulomb envelope remains linear, ϕ^b is close to ϕ', and so the conventional Mohr–Coulomb relationship can be used. For matric suction values beyond the air entry value, the relationship between shear strength and the matric suction has been shown to become much more nonlinear, indicative of the more complex moisture regime that is introduced as saturation decreases (Fig. 13.113). In other words, at lower saturation levels, ϕ^b is consistently lower than ϕ', and the mechanisms for strength development in this range are still not well understood.

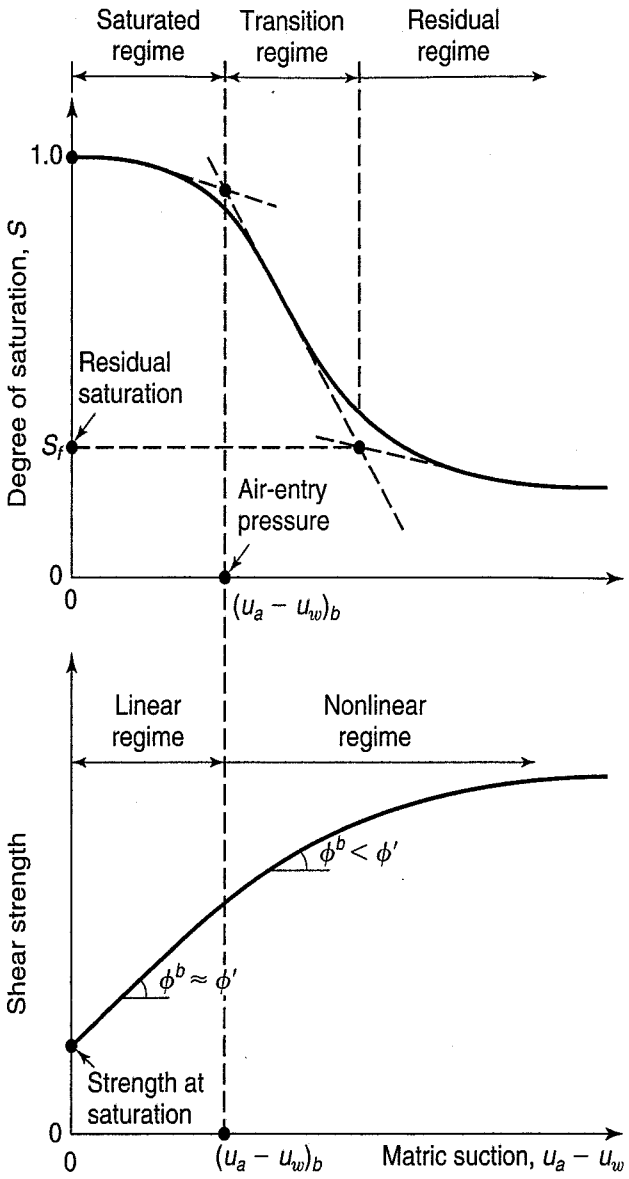

FIGURE 13.113 Conceptual relationship between soil–water characteristic curve and unsaturated shear-strength envelope (after Lu and Likos, 2004).

13.14.4 Shear Strength Measurement in Unsaturated Soils

As noted in Sec. 13.14.1, conducting shear strength tests for unsaturated soils is more complicated than for saturated or dry soils, since the matric suction must also be controlled and/or measured in order to obtain an accurate understanding of the soil behavior. This is because, as Eq. (13.63) indicates and Fig. 13.112 shows, not one, but two, friction angles must be determined: the friction angle, ϕ', related to the net normal stress variable, $(\sigma_f - u_a)_f$; and the angle, ϕ^b, associated with the increase in shear strength due to matric suction, $(u_a - u_w)_f$.

Triaxial tests on unsaturated soils use many of the same test designations as in saturated soil testing to describe the test conditions—e.g., consolidated-drained (CD), consolidated-undrained (CU), unconsolidated-undrained (UU), and unconfined compression (UCC). The pore air pressure is typically controlled/measured through a coarse porous disc at one end of the specimen, and the pore water pressure controlled/measured using a high-air-entry porous disc at the other end. A test that is unique to unsaturated soils is the *constant water content test* (CW), in which the specimen is consolidated and then sheared in such a way that the pore air pressure is maintained constant, but the pore water line is kept closed as in an undrained test. For a CD test, both the net confining stress $(\sigma_3 - u_a)$ and matric

suction $(u_a - u_w)$ remain constant during shear. In a CU, UU and UCC test, both air and water are prevented from leaving or entering the specimen during shear. It is noteworthy that for undrained tests on specimens with a given initial degree of saturation, the higher the total confining stress, the higher the saturation level becomes, leading to conditions that approach 100% saturation. This results in a flatter total stress Mohr–Coulomb envelope at higher confining stresses, consistent with total stress envelopes for undrained tests on saturated soils (Fig. 12.38).

For direct shear tests on unsaturated soils, the same pore water and pore air control/measurement capabilities must be in place as for the triaxial test on these soils. Typical values for c', ϕ', and ϕ^b for a number of unsaturated soils from both triaxial and direct shear tests are given in Table 13.9.

For unsaturated soils, a series of UU tests will define an initially curved failure envelope [Fig. 12.38(b)] until the clay becomes essentially 100% saturated due simply to the cell pressure alone. Even though the drainage valves are closed, the confining pressure will compress the air in the voids and decrease the void ratio. As the cell pressure is increased, more and more compression occurs, and eventually, when sufficient pressure is applied, essentially 100% saturation is achieved. Then, as with the case for initially 100% saturated clays, the Mohr failure envelope becomes horizontal, as shown on the right side of Fig. 12.38(b).

Another way of looking at the compression of unsaturated clays is shown in Fig. 13.114. As the cell pressure is increased incrementally, the measured increment of pore pressure increases gradually, until at some point, for every increment of cell pressure added, an equal increment of pore water pressure is observed. At this point, the soil is 100% saturated and the solid (experimental) curve becomes parallel to the 45° line shown in the figure.

TABLE 13.9 Experimental Values of Mohr–Coulomb Envelope Parameters for Unsaturated Soils

Soil Type	Water Content (%)	Dry Density (kg/m^3)	c' (kPa)	ϕ' (deg)	ϕ^b (deg)	Test Procedure	Reference
Compacted shale	18.6	–	15.8	24.8	18.1	Undrained triaxial	Bishop et al. (1960)
Boulder clay	11.6	–	9.6	27.3	21.7	Undrained triaxial	Bishop et al. (1960)
Dhanauri clay	22.2	1580	37.3	28.5	16.2	CD triaxial	Satija (1978)
Dhanauri clay	22.2	1478	20.3	29.0	12.6	CW triaxial	Satija (1978)
Dhanauri clay	22.2	1580	15.5	28.5	22.6	CW triaxial	Satija (1978)
Dhanauri clay	22.2	1478	11.3	29.0	16.5	Undrained triaxial	Satija (1978)
Madrid grey clay	29	–	23.7	22.5[a]	16.1	CD direct shear	Escario (1980)
Undisturbed, decomposed granite, Hong Kong	–	–	28.9	33.4	15.3	CD multistage triaxial	Ho and Fredlund (1982)
Undisturbed, decomposed rhyolite, Hong Kong	–	–	7.4	35.3	13.8	CD multistage triaxial	Ho and Fredlund (1982)
Tappen-Notch Hill silt	21.5	1590	0.0	35.0	16.0	CD multistage triaxial	Krahn et al. (1989)
Compacted glacial till	12.2	1810	10	25.3	7–25.5	CD multistage direct shear	Gan et al. (1988)

[a]Average value.

After Fredlund and Rahardjo (1993).

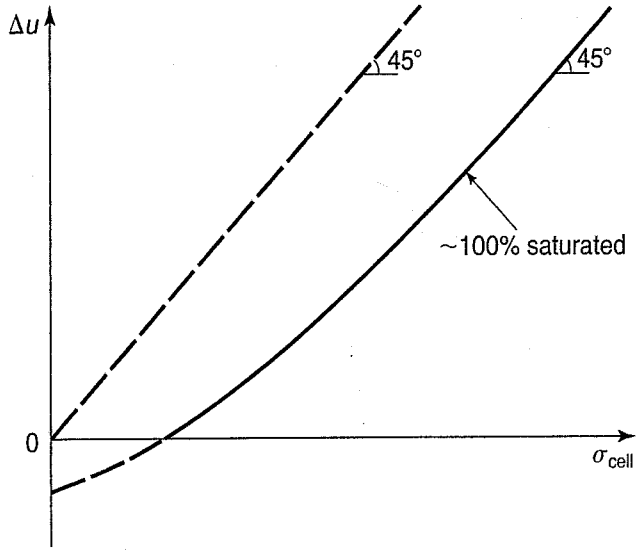

FIGURE 13.114 Results obtained from a PH test on an unsaturated compacted clay (after Skempton, 1954, and Hirschfeld, 1963).

13.15 PROPERTIES OF SOILS UNDER DYNAMIC LOADING

Most of the discussion of soils and rocks in this book has dealt with their static properties, because for many important geotechnical problems the loading or shearing of the geomaterials occurs so slowly that rate of loading does not influence their behavior. On the other hand, the rate of strain does influence some soil properties, as described in Sec. 13.10.4 for sands and 13.13.7 for fine grained soils. We also mentioned the dramatic example of the liquefaction of loose saturated sands (see Sec. 7.6.3). In this section we describe the properties of soils when they are subjected to *dynamic*, *vibratory*, or *cyclical* loading conditions.

Conditions causing dynamic loading include wind forces, wave action, pile driving, earthquakes, blasting, and steady state and transient vibrations due to traffic, compaction equipment, and rotating machinery. Vibrations can be of low or high frequency, periodic (cyclic) or aperiodic. The waveforms from these dynamic loadings may be steady state (periodic; sinusoidal), random, or transient; Fig. 13.115 shows some typical waveforms.

Because vibratory and dynamic loads can cause excessive deformations or even failure of foundations, earth slopes, and other structures, specialized design procedures have been developed for the analysis and design of foundations subjected to vibrations (McNeill, 1969; Richart et al., 1970), blasting and construction vibrations (Dowding, 1985; 1996), and geotechnical earthquake engineering (Kramer, 1996). The Dept. of Defense Handbook (1997) is a very useful and practical summary of the geotechnical problems due to dynamic loads, including machine foundations, impact loading, and the effect of earthquake ground motions on slope stability, sheet pile walls, and pile foundations.

13.15.1 Stress-Strain Response of Cyclically Loaded Soils

The theory of particle mechanics, mechanical vibrations and vibratory motion, dynamics of discrete systems, and wave propagation in solids is well developed and is the basis for both the design references given above and our understanding of the dynamic behavior of geomaterials. From this theoretical background as well as the results of laboratory experiments, we know that the characteristics of a soil that most strongly influence its dynamic behavior are its shear modulus or stiffness, damping, Poisson's ratio, and density. Of these four, the most important are the *shear modulus* G and *damping ratio* λ. Both G and λ vary with shear strain.

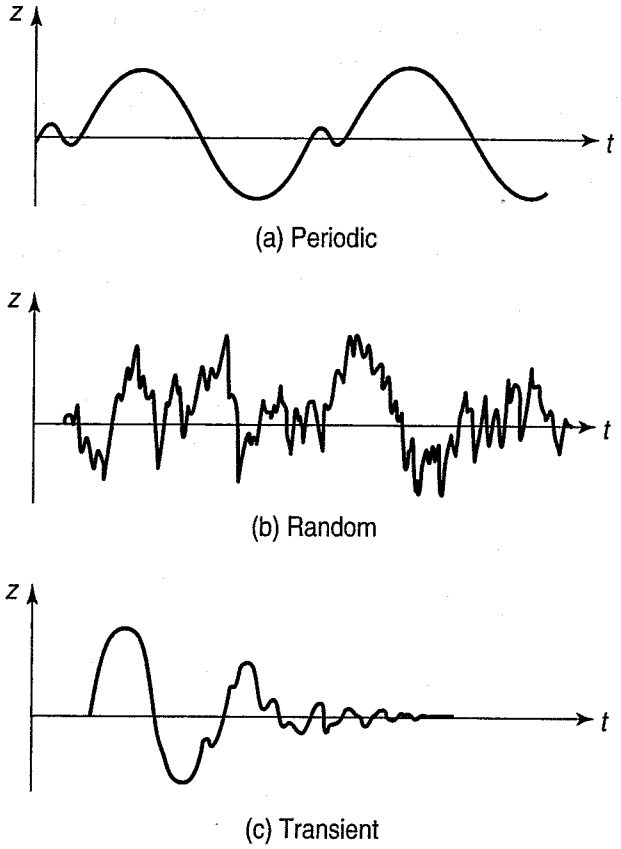

FIGURE 13.115 Typical wave forms: (a) periodic; (b) random; and (c) transient motions (after Richart et al., 1970).

In Sec. 13.8.1 we discussed the small strain stiffness of soils. We mentioned that the small-strain shear modulus G or G_{max} is given by

$$G_{max} = \rho_t V_s^2 \tag{13.24}$$

where ρ_t = total density, and
V_s = shearwave velocity.

Why shear wave velocity? Because when waves propagate through geomaterials, it is the distortion or shear waves and not the compression waves that cause the most deformation of the foundation or structure. This is why we use the shear modulus and not the Young's modulus (Sec. 13.8.) in soil dynamics. From the theory of elasticity, the shear modulus can be related to the Young's modulus E by

$$G = \frac{E}{2(1 + \nu)} \tag{13.64}$$

where ν = Poisson's ratio. Note that both G and E are strain dependent.

When a symmetrical cyclic loading is applied to a soil, its shear stress-shear strain relationship typically has a hysteresis loop similar to that that shown in Fig. 13.116. The loop has an inclination that depends on the stiffness or modulus of the soil. As shown in Fig. 13.116, the modulus can be a *tangent* shear modulus G_{tan} that varies continuously, or a *secant* shear modulus G_{sec} that is the average slope of the entire hysteresis loop.

$$G_{sec} = \frac{\tau_c}{\gamma_c} \tag{13.65}$$

The loop in Fig. 13.116 indicates that energy is being dissipated during cyclic loading. The peak energy during one cycle W is the area of the triangle OAB in the figure, or $W = \frac{1}{2}\tau_c\gamma_c = \frac{1}{2}G_{sec}\gamma_c^2$.

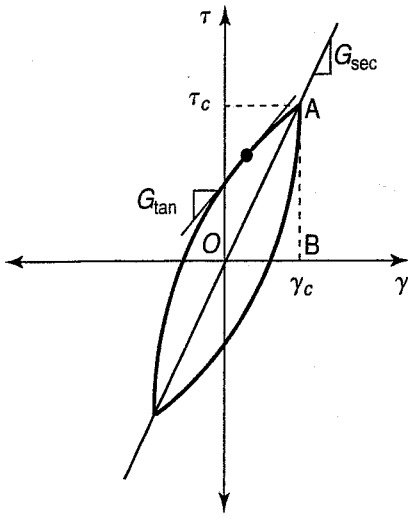

FIGURE 13.116 Shear stress/shear strain response of a cyclically loaded soil showing a hysteresis loop and definitions of tangent and secant shear moduli (after Kramer, 1996).

The energy dissipated during one cycle is ΔW, and it is shown by the area inside the hysteresis loop A_{loop}. It is convenient to relate energy loss to the damping ratio λ, usually defined as

$$\lambda = \frac{1}{4\pi}\frac{\Delta W}{W} = \frac{1}{2\pi}\frac{A_{loop}}{G_{sec}\gamma_c^2} \tag{13.66}$$

As noted by Kramer (1996), the parameters G_{sec} and λ are often called *equivalent linear* material parameters when they are used for ground response analyses in geotechnical earthquake engineering. However, the equivalent linear parameters are only an approximation of the actual nonlinear soil behavior, and thus predictions of soil deformations with linear parameters may not be very accurate.

The secant shear modulus G_{sec} is strongly affected by the cyclic strain amplitude, mean principal stress, the void ratio (and thus the density), the PI if a fine grained soil, and the OCR. The shear modulus also varies with the number of loading cycles, which means that at low strain amplitudes, the modulus is high, but it decreases as the number of loading cycles increases. If we plot the locus of the tips of the hysteresis loops with the cyclic shear strain, the resulting curve is called a *backbone curve*, as shown in Fig. 13.117(a). This curve also shows that the shear modulus at zero strain is G_{max} and that the G_{sec} decreases as the strain amplitude increases.

The decrease in shear modulus with increase in strain is shown in Fig. 13.117(b), where the *modulus ratio* G/G_{max} is plotted against log of shear strain γ. The G/G_{max} is 1.0 at zero strain and decreases as the strain increases; also shown is the corresponding ratio at γ_c. When the modulus ratio is mentioned in geotechnical practice, the G in the ratio is usually understood to mean G_{sec}.

The reason that Eq. (13.24) was defined for G_{max} is because when G is determined using geophysical tests that apply shear waves, the strains are extremely small, usually less than 0.001%. This is why the modulus reduction curve in Fig. 13.117(b) is initially flat before it starts to decrease with increasing shear strain. The point when the linear curve starts to become nonlinear is called the linear cyclic threshold shear strain γ_{tl} (Kramer, 1996).

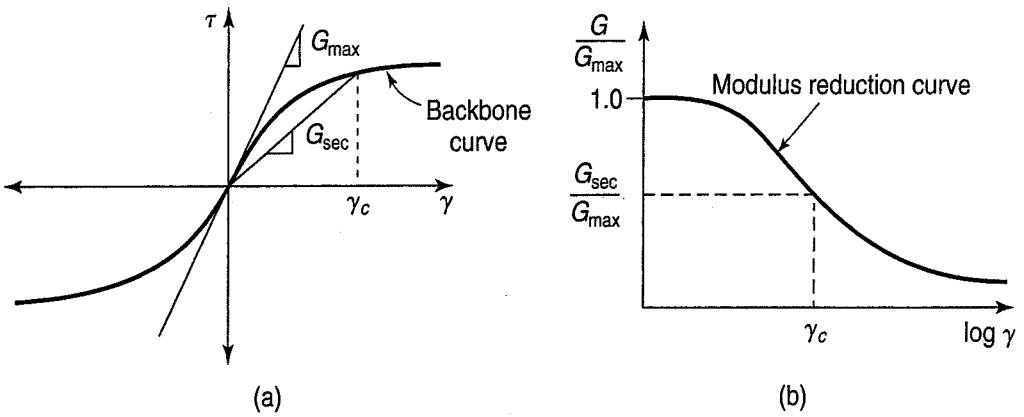

FIGURE 13.117 (a) Backbone curve showing the reduction in G_{max} with shear strain; (b) modulus reduction curve with shear strain (Kramer, 1996).

13.15.2 Measurement of Dynamic Soil Properties

Dynamic soil properties can be measured either in the laboratory or in the field. Laboratory tests are conducted on undisturbed or reconstituted specimens and may be either low strain or high strain. Low strain laboratory tests include resonant column (ASTM D 4015), ultrasonic pulse, and bender element tests. High strain laboratory tests include cyclic triaxial (D 3999 and D 5311), cyclic direct simple shear, and cyclic torsional shear tests.

In situ or field tests also can be classified as low strain or high strain. Low strain tests include several geophysics-type tests such as seismic reflection, seismic refraction (ASTM D 5777), suspension logging, spectral analysis of surface waves (SASW), seismic cross-hole (ASTM D 4428), seismic down-hole (ASTM D 7400), and seismic cone (CPT) tests. High strain tests are basically conventional in situ tests (Chapter 11) with correlations for dynamic properties. The SPT and its cousins the BPT, CPT, DMT, and PMT are in this category.

Collection of Dynamic Data—The basic way in which dynamic data is collected is shown in Fig. 13.118. Illustrated is the time history during a cyclic direct simple shear test with shear stress and shear strain under a sinusoidal displacement (calibrated in terms of shear strain) at a frequency of 1 Hz. For every 0.05 sec, the graph would be read and the corresponding shear stress and shear strain plotted in Fig. 13.119 to form a hysteresis loop. The shear modulus would be found as the slope of the line CA, shown dashed. The chord modulus (which is the G_{sec}) for this test is 2000 psf. The percent of critical (hysteretic) damping is given by Eq. (13.69) expressed as a percentage. For Fig. 13.119, the resulting value of λ_h is 8.8%. The subscript h denotes hysteretic damping.

In addition to obtaining data from cyclic tests, the moduli and damping may also be obtained from *free vibration tests*. Basically, you "pluck the violin string"—i.e., displace the soil sample (or other

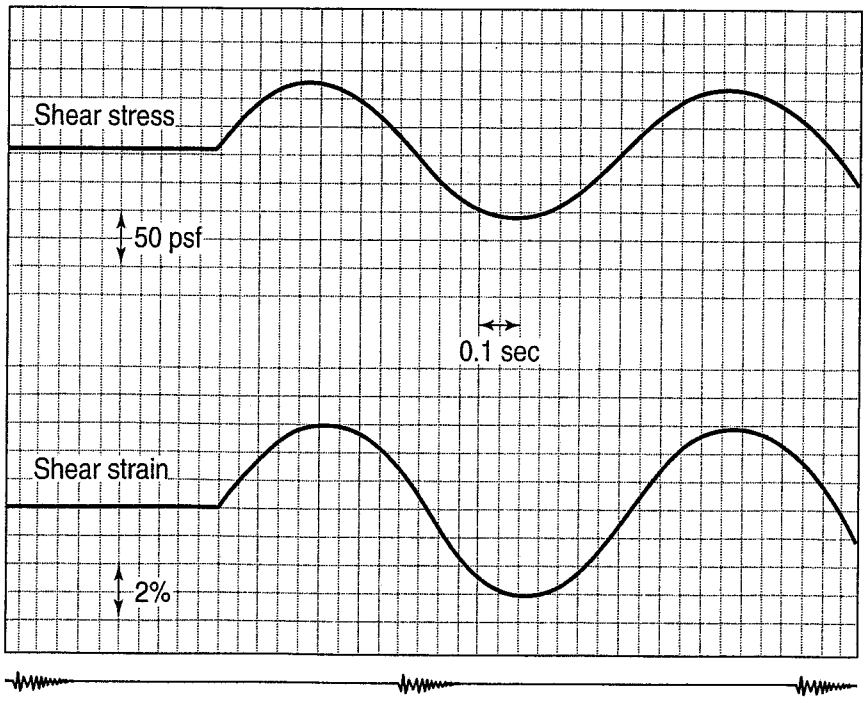

FIGURE 13.118 Typical cyclic simple shear test data on remolded soft clay, w = 88%.

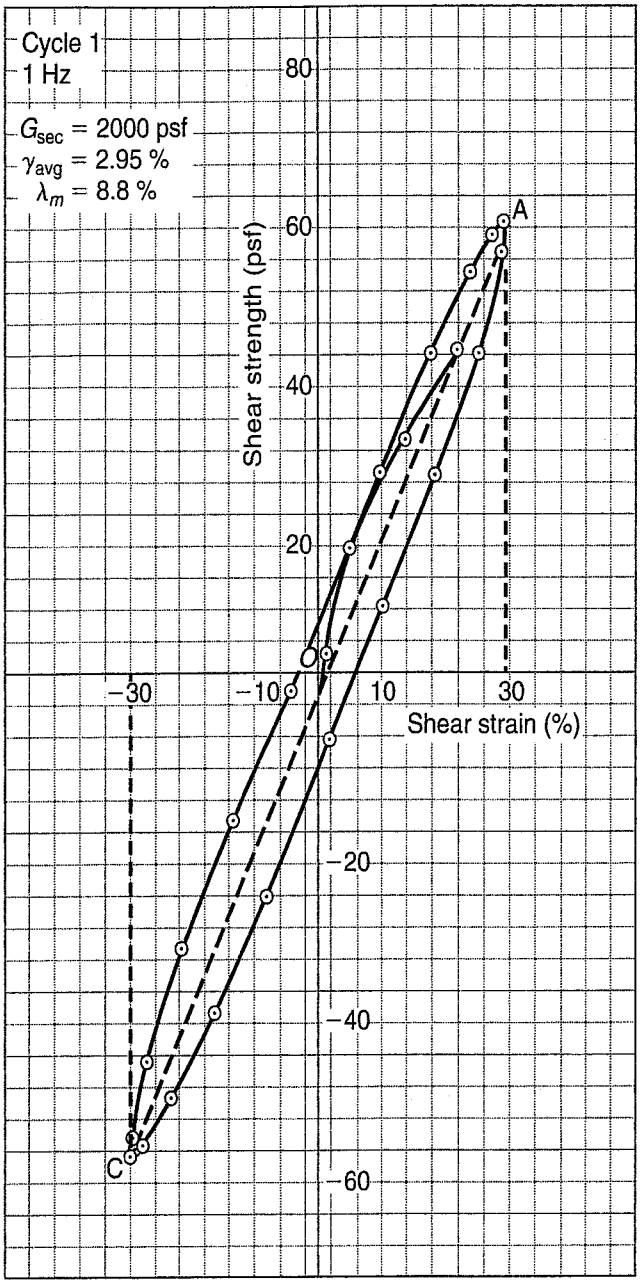

FIGURE 13.119 Typical shear stress–shear strain hysteresis curve from data in Fig. 13.118 (units: psf = lbf/ft^2).

structure) and let go before the specimen can react. Figure 13.120 shows the results of a free vibration test on an undisturbed block sample. At t_1, the sample is loaded (pushed) horizontally and then immediately let go and allowed to vibrate at its own natural frequency. For small values of damping, it can be shown that

$$\lambda_T = \frac{1}{2\pi} \ln \frac{x_n}{x_{n+1}} \qquad (13.67)$$

where λ_T = percent of critical *total* damping,
x_n = the ordinate of the nth cycle,
x_{n+1} = the ordinate of the $(n + 1)$th cycle.

In the example shown in Fig. 13.120, $\lambda_T = 6.25\%$ and the average period of free vibration is 0.080 sec. (For these physical conditions, 0.080 sec is the *natural period of vibration.*) We used the subscript T to indicate that this damping is not the result from a steady state or cyclic loading but from a free vibration test. Kovacs et al. (1971) have shown that for a given shear strain, the damping from a free vibration test is larger than from a cyclic shear test.

In dynamic foundation and blast design, the designer makes sure that the foundation being designed is never excited by a frequency at or near its natural period of vibration. See Richart et al. (1970) and Dowding (1996) for information on foundation and blasting design.

Also, for free vibrations, the shear modulus G may be found, for the first mode, by

$$G = \frac{24\gamma H^2}{gT^2} \qquad (13.68)$$

where γ = unit weight of the soil (lbf/ft^2),
H = height of the soil layer (ft),
g = gravitational constant (32.2 ft-sec^{-2}),
T = period of free vibration (sec).

We showed some results of static tests with bender elements in Sec. 13.8.1. How are they used for dynamic measurements? Recall that bender elements measure the shear wave velocity, thus they

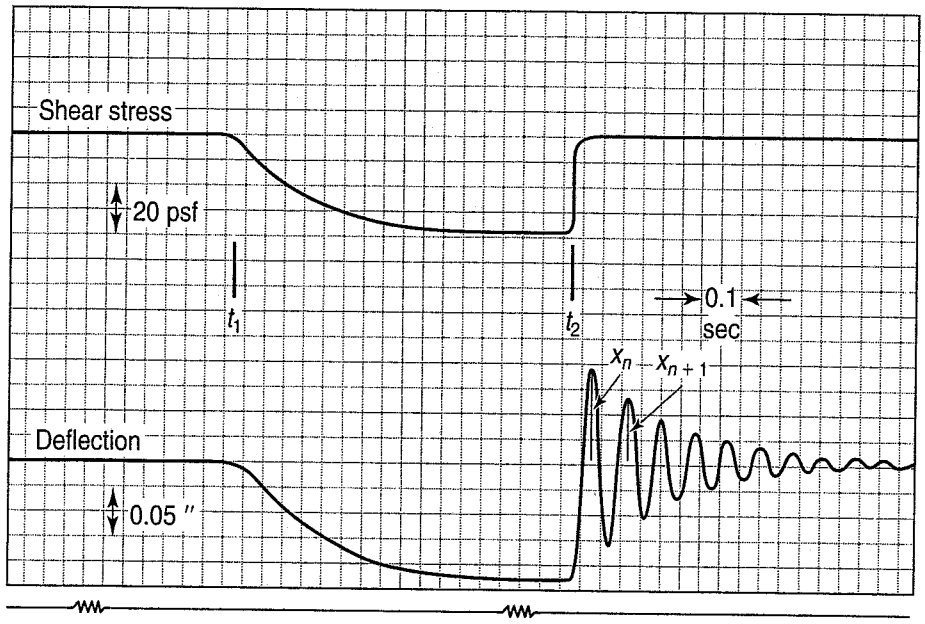

FIGURE 13.120 Typical free vibration test data from a simple shear specimen $w = 110\%$.

provide a quick and economical determination of the G_{max} of soil specimens (Dyvik and Madshus, 1985). Because of the very small strains, the shear wave velocity V_s is related to G_{max} by Eq. (13.24). Figure 13.121 shows a time history of output voltage from the receiver in a bender element test on Mai Liao sand (Huang et al., 2004). Point C in Fig. 13.121 is taken as the time of shear wave arrival according to Kawaguchi et al. (2001). Then the velocity of the shear wave is determined from this time and the distance between transmitter and receiver.

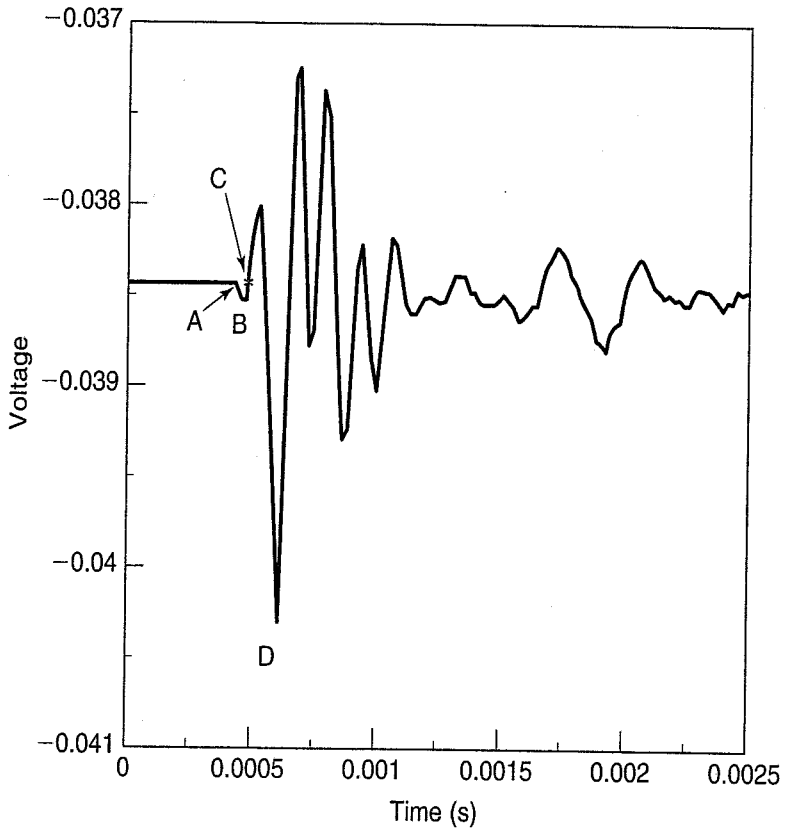

FIGURE 13.121 Time history of output voltage from the bender element receiver (Huang et al., 2004).

13.15.3 Empirical Estimates of G_{max}, Modulus Reduction, and Damping

In addition to direct measurements of shear modulus and damping, empirical relationships are also commonly used for preliminary design and for checking laboratory and field results. Hardin and Drnevich (1970a, b) proposed an equation for the maximum shear modulus G_{max} as

$$G_{max}(\text{psf}) = 14{,}760\frac{(2.973 - e)^2}{1 + e}(\text{OCR})^a(\sigma'_m(\text{psf}))^{0.5} \tag{13.69}$$

where σ'_m = mean principal effective stress (psf), and
a = OCR exponent that depends on the PI (Fig. 13.122).

This equation was developed in British engineering units (psf is short for lbf/ft^2), and it is applicable for all soils at a very low shear strains.

Hardin and Drnevich (1970a, b) also gave a relationship for the damping ratio λ at some strain level γ by

$$\lambda = \frac{\lambda_{max}\frac{\gamma}{\gamma_r}}{1 + \frac{\gamma}{\gamma_r}} \tag{13.70}$$

where λ_{max} = the maximum damping ratio at very large shear strains, and γ_r = a reference shear strain. The maximum value of the damping ratio for sands is given by

$$\lambda_{max} = D - 1.5 \log N \tag{13.71}$$

where D = 33% for clean dry sands,
D = 28% for clean saturated sands,
N = the number of cycles.

The maximum damping ratio for saturated clays is more complicated and involves the frequency of oscillation, effective stress, and the number of cycles, or

$$\lambda_{max} = 31 - (3 - 0.03f)(\sigma'_m)^{0.5} + 1.5f^{0.5} - 1.5 \log N \tag{13.72}$$

where f = frequency in Hz,
σ'_m = the mean principal effective stress in kg/cm^2,
N = the number of cycles.

Hardin (1978) updated Eq. (13.70) as

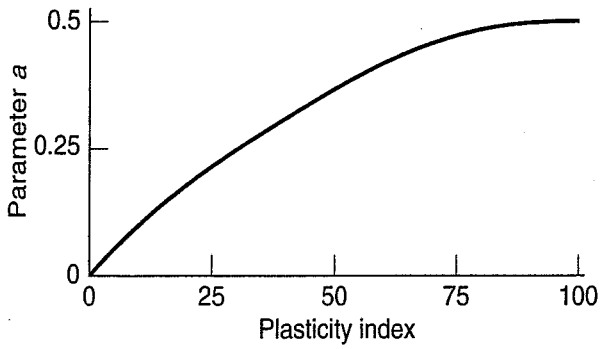

FIGURE 13.122 Parameter a versus PI (after Hardin and Drnevich, 1970b).

$$\frac{G_{max}}{p_a} = \frac{625}{0.3 + 0.7e^2}(\text{OCR})^a\left(\frac{\sigma'_m}{p_a}\right)^{0.5} \tag{13.73}$$

This equation has been normalized with respect to the atmospheric pressure p_a. The OCR exponent a depends on the PI, as shown in Fig 13.122. Note that the expression containing the void ratio e in this equation is different than in Eq. (13.70), and it results in a smaller multiplier for all values of e.

Seed and Idriss (1970) took the equations developed by Hardin and Drnevich (1970a, b)

and showed the results graphically using typical values of soil properties. Their equation for the shear modulus of sands is

$$G_{\max} = 1000K_2(\sigma'_m)^{0.5} \tag{13.74}$$

where K_2 = function of the void ratio, relative density, and shear strain amplitude.

Figure 13.123 shows the effects of the angle of internal friction, confining pressure, void ratio, and K_o on the magnitude of K_2 for a given shear strain. At any given shear strain (we'll use 10^{-2} percent, for example), the value of K_2 is *higher* for a higher ϕ', a higher confining pressure, and a higher K_o. All four graphs in Fig.13.123 have the same initial conditions.

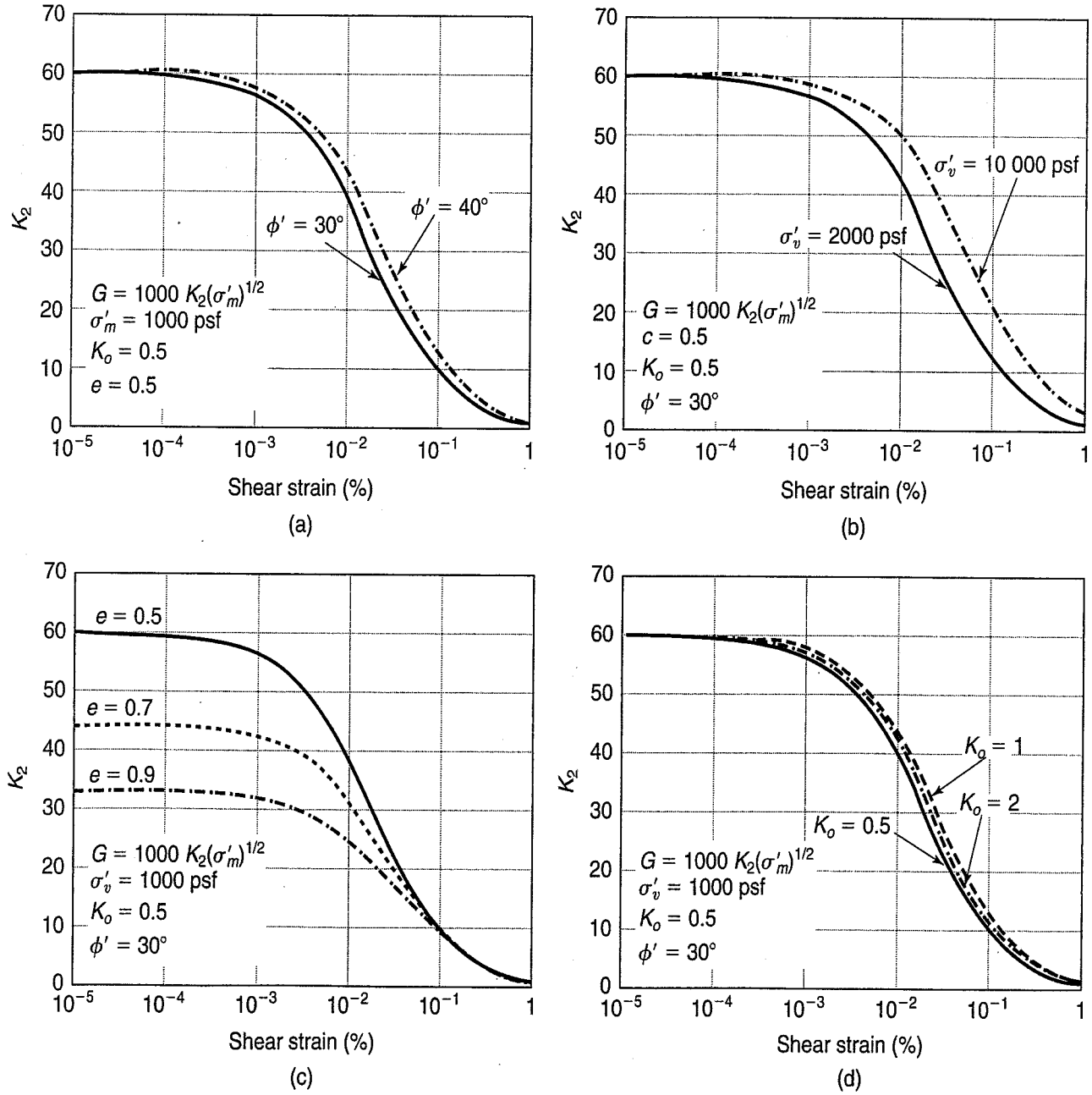

FIGURE 13.123 Influence of various factors for the shear moduli of sands, based on Hardin and Drnevich expressions (after Seed and Idriss, 1970): (a) effect of angle of friction, ϕ': (b) effect of effective vertical strain, σ'_v; (c) effect of void ratio e; (d) effect of K_o.

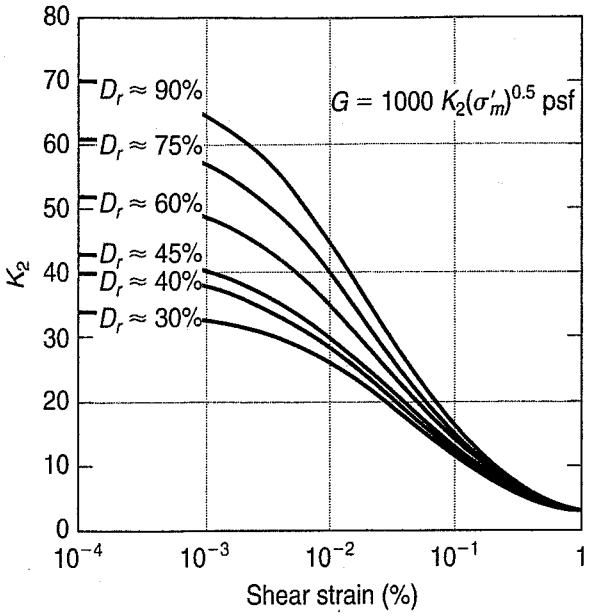

FIGURE 13.124 Shear modulus of sands at different relative densities, based on Hardin and Drnevich expressions (after Seed and Idriss, 1970).

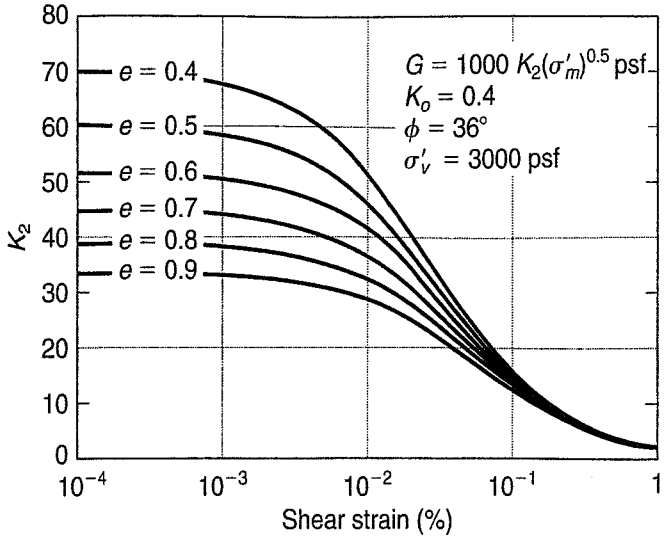

FIGURE 13.125 Shear moduli of sands at different void ratios, based on Hardin and Drnevich expressions (after Seed and Idriss, 1970).

The values of K_2 depend on the relative density or density index, the void ratio, and the shear strain, as shown in Figs. 13.124 and 13.125 for sands and in Fig. 13.126 for gravelly soils. Recall that the void ratio and relative density go together. We discussed relative density and relative compaction of granular soils in Chapter 5.

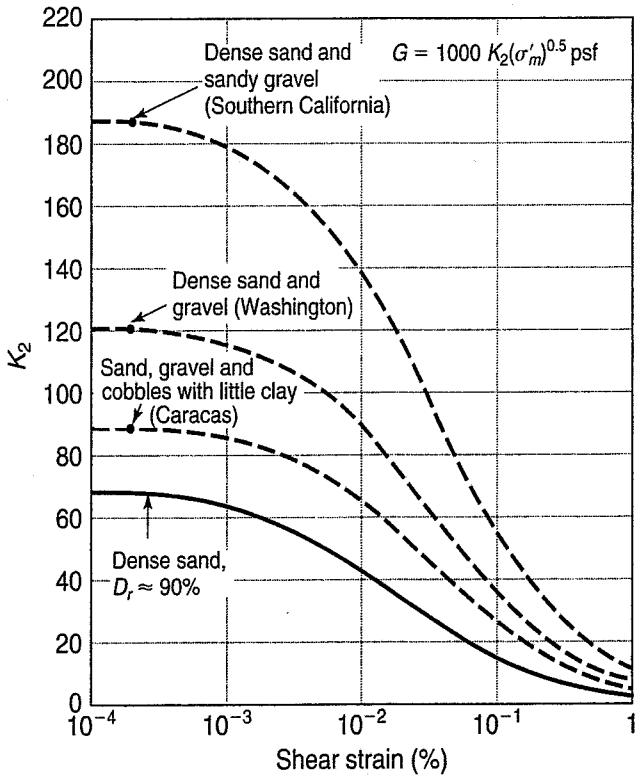

FIGURE 13.126 Moduli determination for gravelly soils (after Seed and Idriss, 1970).

Silver and Seed (1971) showed that for a given cyclic shear strain and at a given vertical stress, the shear modulus of sands *increases* with increasing cycle number. For a given cycle number, they also showed that at a given shear strain, the modulus increased as the confining pressure increased. And, for a given confining pressure, the modulus increased at a given shear strain as the relative density increased—all of the above as expected.

Table 13.10 gives a summary of empirical relationships for G_{max} as determined from in situ test parameters for the SPT, CPT, DMT, and PMT tests. Recall from our description of these tests in Sec. 11.6 that they are all large-strain tests, and thus their correlation with the small-strain G_{max} is purely empirical and should be used for preliminary estimates only.

The reduction in shear modulus and modulus ratio G/G_{max} with increasing shear

TABLE 13.10 Empirical Relationships between G_{max} and In Situ Test Parameters

In Situ Test	Relationship	Soil Type	Reference(s)	Comments
SPT	$G_{max} = 20{,}000[(N_1)_{60}]^{0.333}(\sigma'_m)^{0.5}$	Sand	Ohta and Goto (1976) Seed et al. (1986)	G_{max} and σ'_m in lb/ft^2
	$G_{max} = 325(N_{60})^{0.68}$	Sand	Imai and Tonouchi (1982)	G_{max} in kips/ft^2
CPT	$G_{max} = 1634(q_c)^{0.250}(\sigma'_v)^{0.375}$	Quartz sand	Rix and Stokoe (1991)	G_{max}, q_c, and σ'_v in kPa; based on field tests in Italy and on calibration chamber tests
	Fig. 13.129	Silica sand	Baldi et al. (1986)	G_{max}, q_c, and σ'_v in kPa; based on field tests in Italy
	$G_{max} = 406(q_c)^{0.695}e^{-1.130}$	Clay	Mayne and Rix (1993)	G_{max}, q_c, and σ'_v in kPa; based on field tests at worldwide sites
DMT	$G_{max}/E_d = 2.72 \pm 0.59$	Sand	Baldi et al. (1986)	Based on calibration chamber tests
	$G_{max}/E_d = 2.2 \pm 0.7$	Sand	Bellotti et al. (1986)	Based on field tests
	$G_{max} = \frac{530}{(\sigma'_v/p_a)^{0.25}} \frac{\gamma_D/\gamma_w - 1}{2.7 - \gamma_D/\gamma_w} K_D^{0.25}(p_a\sigma'_v)^{0.5}$	Sand, silt, clay	Hryciw (1990)	G_{max}, p_a, σ'_v in same units; γ_D is dilatometer-based unit weight of soil; based on field tests
PMT	$3.6 \le G_{max}/G_{ur,c} \le 4.8$	Sand	Bellotti et al. (1986)	$G_{ur,c}$ is corrected unloading-reloading modulus from cyclic PMT
	$G_{max} = (1.68/\alpha_p)G_{ur}$	Sand	Byrne et al. (1991)	G_{ur} is secant modulus of unloading-reloading portion of PMT; α_p is factor that depends on unloading-reloading stress conditions; based on theory and field test data

After Kramer (1996).

strain [Fig. 13.117(b)] is shown for granular soils in Fig. 13.126 and for normally and moderately overconsolidated fine grained soils in Fig. 13.127(a). Note that the curve for PI = 0 in Fig. 13.127(a) is similar to that for granular materials. Also, the linear threshold shear strain γ_{tl}, defined in Sec. 13.15.1, increases with increasing PI. Figure 13.128 shows the effect of confining stress on the modulus reduction of both granular and high-PI soils.

Damping ratios are shown in Fig. 13.130 for granular soils and for fine grained soils in Figs. 13.127(b) and 13.131. At a given shear strain, the magnitude of damping *decreases* with the number of cycles. Seed et al. (1986) found that the values for gravels and gravelly soils fit well inside the limits of the plot for sands, as shown in Fig. 13.130.

Borden et al. (1996) performed resonant column and torsional shear tests on Piedmont residual soils classified as MH, ML, SM-ML, and SM. Their relationships between the normalized shear modulus (G/G_{max}) and damping ratio λ are related to the shear strain relationships so they developed the relationships as shown in Fig. 13.132(a). Note that the Borden et al. (1996) relationships fit in between

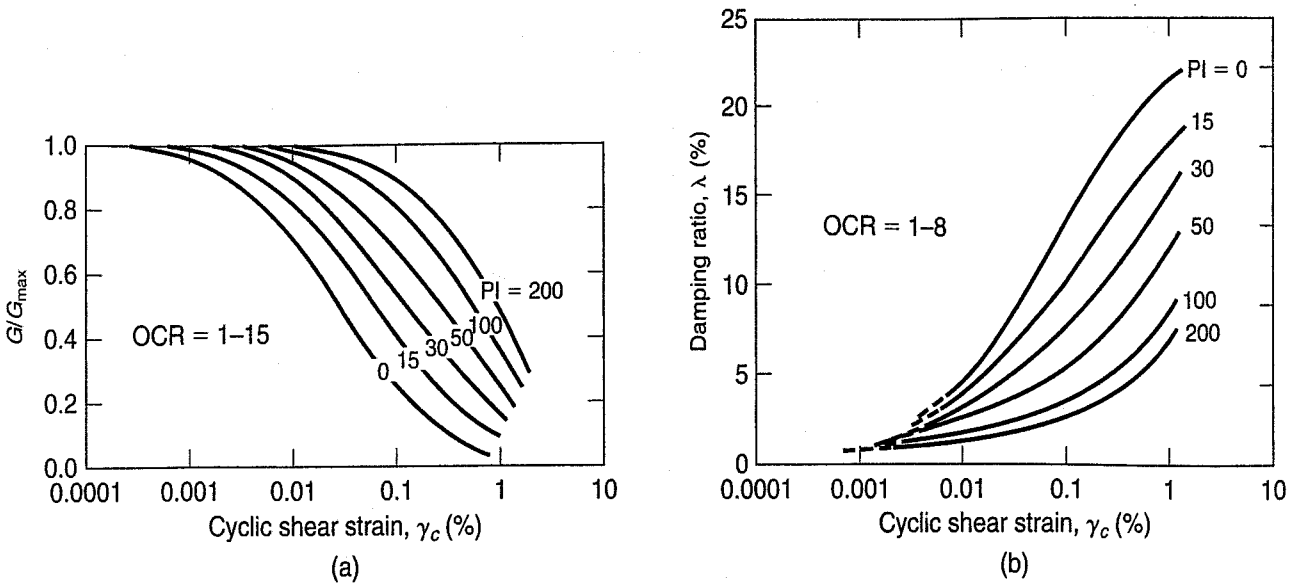

FIGURE 13.127 Variation of (a) normalized shear modulus and (b) damping ratio, both as a function of cyclic shear strain for normally and moderately overconsolidated fine grained soils (Vucetic and Dobry, 1991).

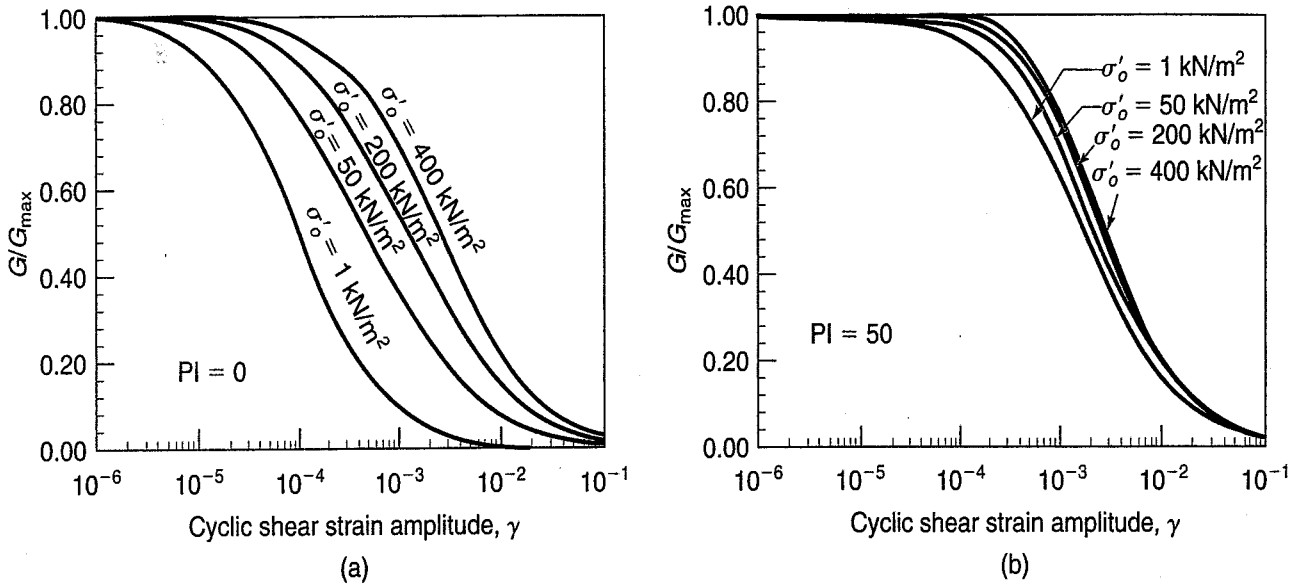

FIGURE 13.128 Modulus reduction as a function of confining stress for (a) a nonplastic soil and (b) a highly plastic soil (Ishibashi, 1992).

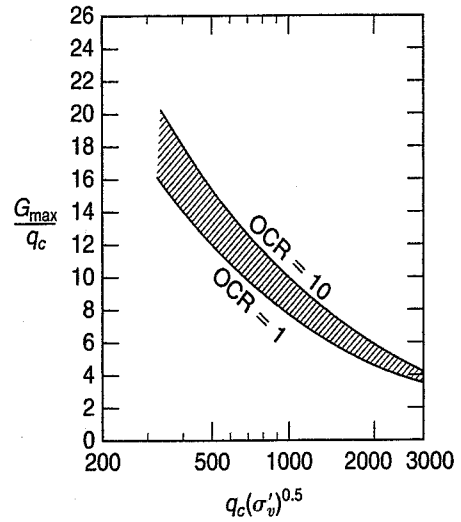

FIGURE 13.129 Evaluation of the small strain shear modulus G_{max} from the CPT cone tip resistance q_c, for uncemented silica sands (Baldi et al., 1989).

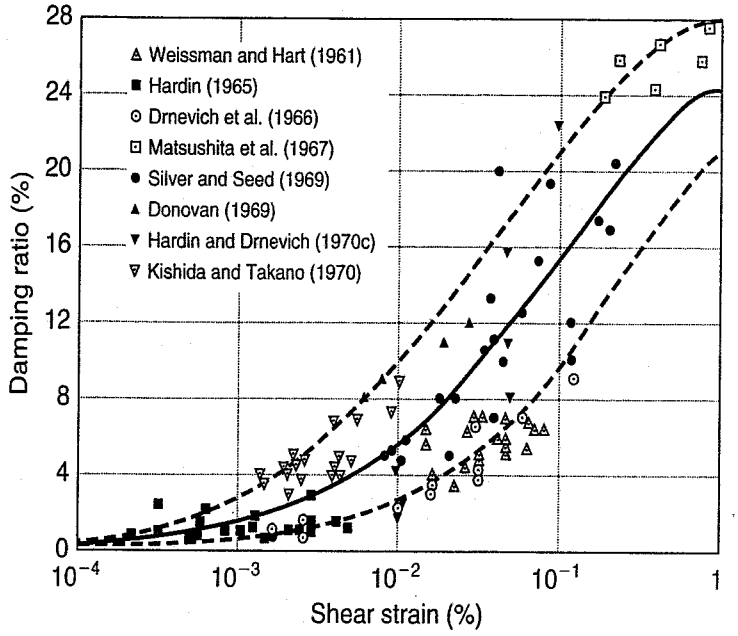

FIGURE 13.130 Damping ratios versus shear strain (%) for granular materials (after Seed & Idriss, 1970).

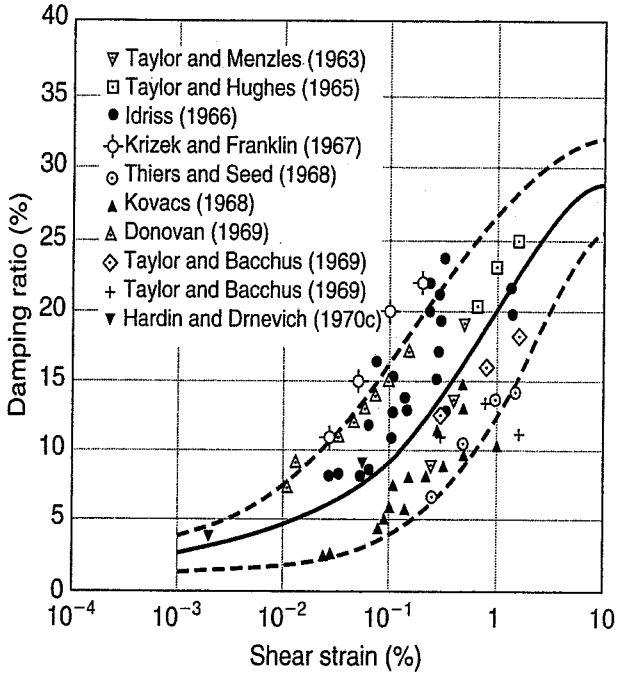

FIGURE 13.131 Damping ratios for saturated clays (after Seed and Idriss, 1970).

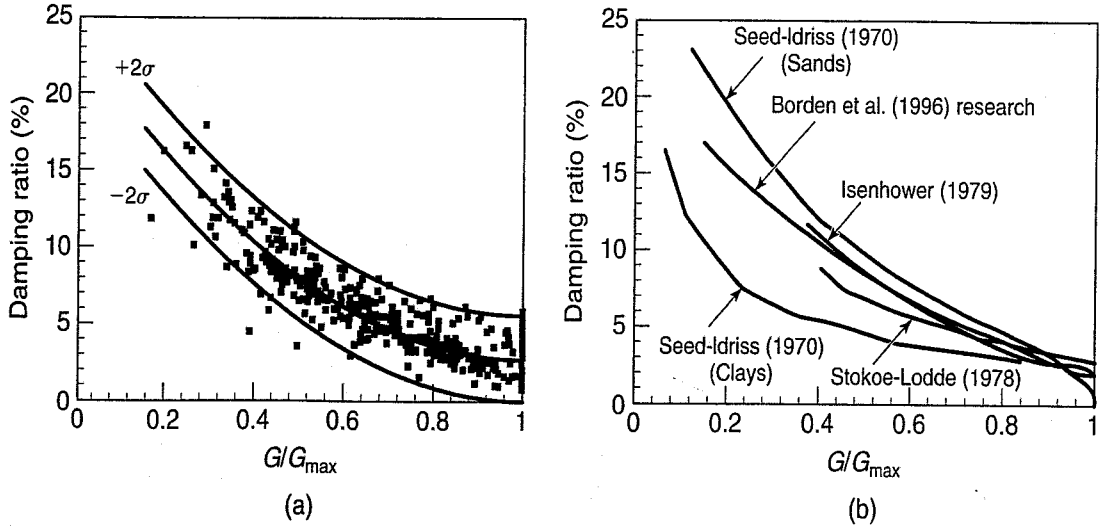

FIGURE 13.132 (a) Damping ratio as a function of the normalized shear modulus for silty soils; and (b) comparison of NCSU data with other experimental results in the literature (after Borden et al., 1996).

those of sands and clays, as shown in Fig. 13.132(b). Based on their study, they formulated an equation of the relationship as

$$\lambda(\%) = 20.4\left(\frac{G}{G_{\max}} - 1\right)^2 + 3.1 \tag{13.75}$$

Since the early work by Hardin and Drnevich (1970) and Seed and Idriss (1970), perhaps the best reference summarizing recent research is a state of the art paper by Stokoe et al. (1999) that describes the results of both laboratory and field studies for dynamic soil properties. Laboratory experiments used combined resonant column and torsional shear tests, and the field studies used seismic downhole, surface wave, and suspension-logging tests to measure the shear wave velocity profiles. This paper is a good summary of Sec. 13.15.3.

13.15.4 Strength of Dynamically Loaded Soils

Kramer (1996) presents an excellent discussion of the strength of cyclically loaded soils. The stability of slopes, foundations, and retaining structures during earthquakes, for example, is strongly influenced by their cyclic shear strength. We discussed some of the definitions of failure used by geotechnical engineers earlier in this chapter and in Chapter 12, and just as with static loading, failure due to dynamic or cyclic loading can be defined in different ways.

When we think about the dynamic behavior of granular materials, it is the deposits of loose sands below the groundwater table that are subject to liquefaction, a phenomenon mentioned briefly in Chapter 7 that is very important in geotechnical earthquake engineering (see, e.g., Kramer, 1996, Chapter 9, and Idriss and Boulanger, 2008). The behavior of fine grained soils is a bit different, and strength is usually discussed in terms of their *cyclic shear strength* or their *monotonic shear strength.* Cyclic strength is usually based on a limiting value of *cyclic strain* during cyclic loading, while monotonic strength typically is the "ultimate static strength that can be mobilized *after cyclic loading has ended*" (Kramer, 1996, p 244).

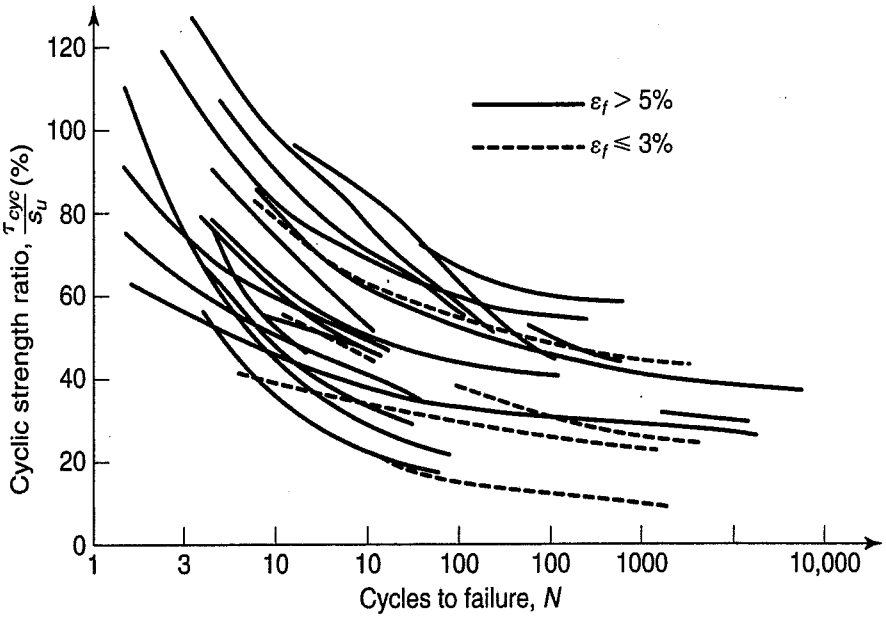

FIGURE 13.133 Variation of cyclic strength ratio versus the number of cycles to obtain failure (determined as <3% failure strain and >5% failure strain) with number of cycles for various soil types (after Lee and Focht, 1976, as cited by Kramer, 1996).

13.16 FAILURE THEORIES FOR ROCK

In our brief discussion of failure criteria for rock in Sec. 11.4.4, we mentioned three failure theories: the Griffith crack theory, Mohr–Coulomb, and the Hoek–Brown failure criterion. The Mohr–Coulomb failure criterion with the tension cut-off was shown in Fig. 11.13. Because of our extensive discussion of the Mohr–Coulomb failure theory for soils in Chapter 11, you should be quite familiar with it. See Goodman (1989) for more on the Mohr–Coulomb failure theory applied to rock,

According to Lo and Hefny (2001), the Griffith (1924) theory of fracture was originally developed to explain why the measured tensile strength was less than the theoretical bond strength of brittle materials such as glass. Griffith postulated that this difference was due to microcracks or flaws in what might otherwise appear to be intact and solid material. Figure 13.134 shows the Griffith (1924) failure criterion in (a) σ_1–σ_3 space and (b) τ_n–σ space. In τ_n–σ space, the Griffith criterion is

$$\tau^2 + 4\sigma_t\sigma'_n = 4\sigma_t^2 \tag{13.76}$$

where σ_t = tensile strength, and
σ_n = effective normal stress.

Note that at $\sigma_3 = 0$, σ_1 is the uniaxial compressive strength σ_c. Thus the ratio of σ_1 to σ_t is a constant equal to eight. In reality, this ratio ranges between 6 and 12, far off of field measurements (Lo and Hefny, 2001). This theory was not really developed as a failure criterion but was an attempt to predict the state of stress required for the propagation of cracks in brittle materials under tensile stresses. However, in brittle materials, the stresses required to initiate cracks are very close the failure stresses, and the Griffith theory with some empirical modifications for compressive stresses was a useful starting point for other failure theories such as the Hoek and Brown criterion.

Besides the Mohr–Coulomb theory, probably the most commonly used failure theory in rock engineering practice is the Hoek–Brown (1980) failure criterion. It was originally developed for the design of underground excavations, such as tunnels and shafts, and it has been updated several times (e.g., Hoek and Brown, 1988; Hoek et al., 1995). For a history of the original development of the criterion, see Hoek (1983).

In terms of principal stresses, the Hoek–Brown criterion is

$$\sigma'_1 = \sigma'_3 + (m\sigma_c\sigma'_3 + s\sigma_c^2)^{1/2} \tag{13.77}$$

where σ'_1 and σ'_3 = major and minor principal effective stresses, respectively,
m and s = dimensionless empirical constants, and
σ_c = uniaxial compressive strength of the rock.

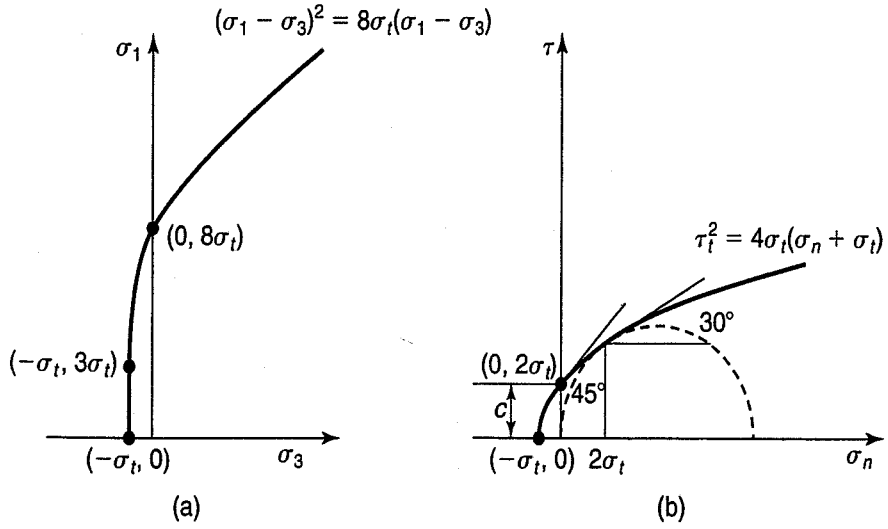

FIGURE 13.134 Griffith failure criterion in (a) σ_1–σ_3 space, and (b) τ_n–σ space (after Lo and Hefny, 2001).

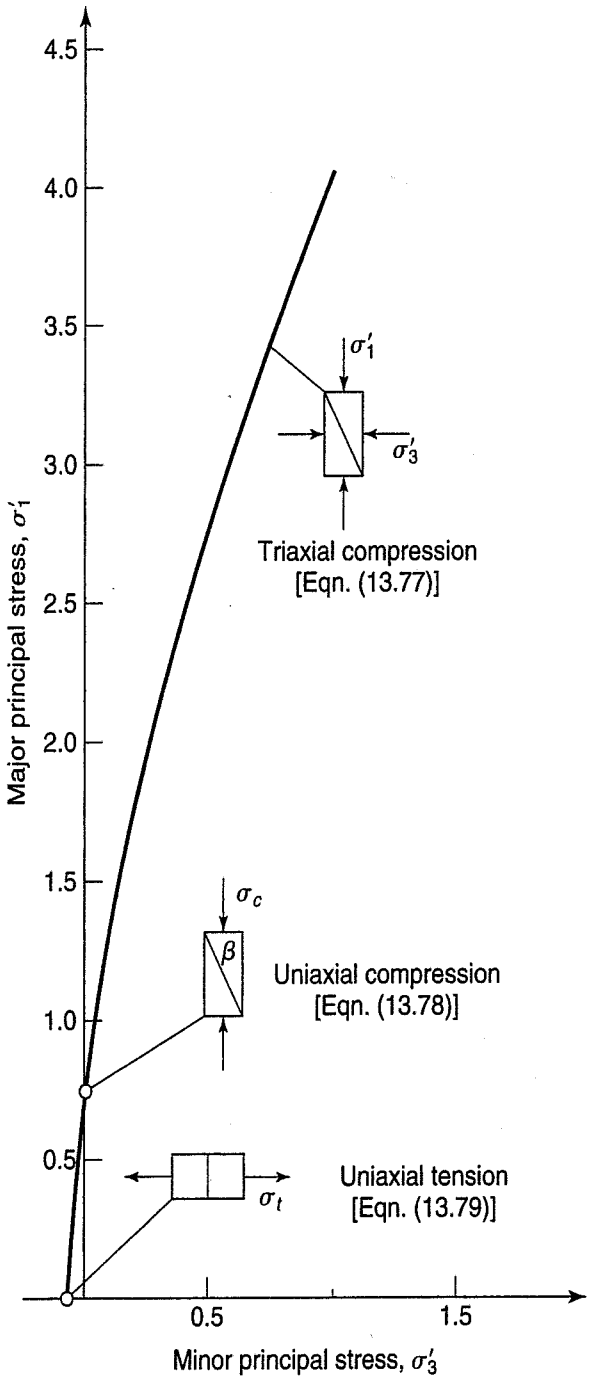

FIGURE 13.135 Strength of fracture rock according to the Hoek–Brown criterion; equations are given for three different test configurations, triaxial compression, uniaxial compression, and uniaxial tension (after Hoek, 1983).

When the Hoek–Brown criterion is stated in terms of principal stresses, it is most useful for the design of tunnels and other underground excavations. Note that when σ_3' is zero, according to Eq. (13.77), the unconfined compressive strength of a rock mass is

$$\sigma_1' = \sigma_c' = (s\sigma_c^2)^{1/2} \tag{13.78}$$

Substituting $\sigma_1' = 0$ in Eq. (13.77) results in a quadratic equation, and when it is solved for σ_3', gives the uniaxial tensile strength of the rock σ_t, or

$$\sigma_3' = \sigma_t = \frac{1}{2}\sigma_c(m - (m^2 + 4s)^{1/2}) \tag{13.79}$$

One way to understand the physical significance of Eqs. (13.77), (13.78) and (13.79) is to plot σ_1' versus σ_3', as shown in Fig. 13.135. This figure shows the Hoek–Brown criterion for the three different test configurations, triaxial compression, uniaxial compression, and uniaxial tension. For descriptions of these tests refer to Sec. 11.5.4.

For slope stability calculations, we need the shear strength at a specific effective normal stress on a given failure surface. So let us put the Hoek–Brown criterion in terms of a shear stress-normal stress Mohr diagram, as shown in Fig. 13.136.

The equation for the curved Mohr failure envelope is

$$\tau = (\cot\phi_i' - \cos\phi_i')\frac{m\sigma_c}{8} \tag{13.80}$$

where τ = the shear stress at failure, and

ϕ_i' = the "instantaneous" friction angle.

Note that the "instantaneous" friction angle is the slope of the tangent to the failure envelop at a specific value of σ' and τ, as shown in Fig. 13.136. The instantaneous or tangent friction angle ϕ_i' at τ and σ' is

$$\phi_i' = \arctan\left\{4h\cos^2\left[30 + \frac{1}{3}\arcsin(h^{-3/2})\right] - 1\right\}^{-1/2} \tag{13.81}$$

where $h = 1 + \dfrac{16(m\sigma' + s\sigma_c)}{3m^2\sigma_c}$, and

σ' = effective normal stress.

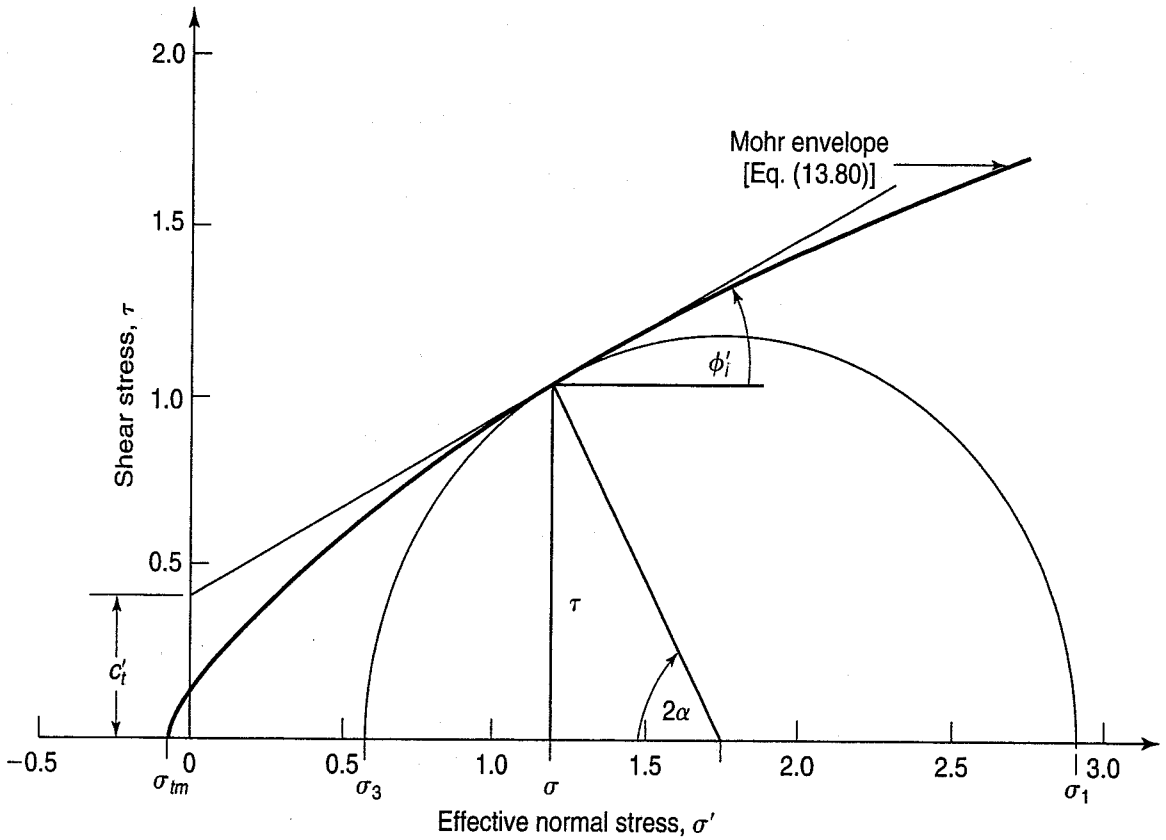

FIGURE 13.136 Mohr envelope according to the Hoek and Brown failure theory for rock masses (after Hoek, 1983).

The "instantaneous" c-intercept is c_i', and it is the intercept of the tangent line extended to the shear stress axis; its value is

$$c' = \tau - \sigma' \tan \phi_i'$$

From the Mohr circle, as shown in Fig. 13.136, the slope of the failure plane is

$$\alpha_f = 45^o + \frac{\phi}{2} \tag{11.10}$$

In terms of principal stresses, σ_1' and σ_3',

$$\alpha_f = \frac{1}{2}\arcsin\frac{\tau_m}{\tau_m + m\sigma_c/8}(1 + m\sigma_c/4\tau_m)^{1/2} \tag{13.82}$$

where $\tau_m = \frac{1}{2}(\sigma_1' - \sigma_3')$.

The Hoek–Brown dimensionless constants m and s depend on the rock type and the discontinuities or degree of fracturing of the rock mass, as defined in Table 13.11. The RMR and Q ratings systems were briefly mentioned in Sec. 4.13. There are six categories of rock mass quality ranging from intact to very poor, and the constants m and s are given for five different rock types described on the top of the table. Note that these values of m and s are for rock that has been disturbed by blasting and loosening that occurs during excavations.

TABLE 13.11 Estimated/approximate values of Hoek-Brown dimensionless constants m and s for different rock types and conditions of the rock mass (from Hoek and Brown, 1988, and Wyllie, 1999)

Empirical failure criterion:

$\sigma'_1 = \sigma'_3 + \sqrt{m\sigma_{u(r)}\sigma'_3 + s\sigma^2_{u(r)}}$

σ'_1 = major principal effective stress

σ'_3 = minor principal effective stress

$\sigma_{u(r)}$ = uniaxial compressive strength of intact rock, and

m and s are empirical constants.

		CARBONATE ROCKS WITH WELL DEVELOPED CRYSTAL CLEAVAGE *dolomite, limestone an marble*	LITHIFIED ARGILLACEOUS ROCKS *mudstone, siltstone, shale and slate (normal to cleavage)*	ARENACEOUS ROCKS WITH STRONG CRYSTALS AND POORLY DEVELOPED CRYSTAL CLEAVAGE *sandstone and quartzite*	FINE GRAINED POLYMINERALLIC IGNEOUS CRYSTALLINE ROCKS *andesite, dolerite, diabase and rhyolite*	COARSE GRAINED POLYMINERALLIC IGNEOUS & METAMORPHIC CRYSTALLINE ROCKS *amphibolite, gabbro gnesis, granite, norite, quartz-diorite*
INTACT ROCK SAMPLES	m	7.00	10.00	15.00	17.00	25.00
Laboratory size specimens free from discontinuties	s	1.00	1.00	1.00	1.00	1.00
*CSIR rating: RMR = 100						
† NGI rating: Q = 500						
VERY GOOD QUALITY ROCK MASS	m	2.40	3.43	5.14	5.82	8.56
Tightly interlocking undisturbed rock with unweathered joints at 1–3 m	s	0.082	0.082	0.082	0.082	0.082
CSIR rating: RMR = 85						
NGI rating: Q = 100						
GOOD QUALITY ROCK MASS	m	0.575	0.821	1.231	1.395	2.052
Fresh to slightly weathered rock, slightly disturbed with joints at 1–3 m	s	0.00293	0.00293	0.00293	0.00293	0.00293
CSIR rating: RMR = 65						
NGI rating: Q = 10						
FAIR QUALITY ROCK MASS	m	0.128	0.183	0.275	0.311	0.458
Several sets of moderately weathered joints spaced at 0.3–1 m	s	0.00009	0.00009	0.00009	0.00009	0.00009
CSIR rating: RMR = 44						
NGI rating: Q = 1						
POOR QUALITY ROCK MASS	m	0.029	0.041	0.061	0.069	0.102
Numerous weathered joints at 30–500 mm, some gouge. Clean compacted waste rock	s	0.000003	0.000003	0.000003	0.000003	0.000003
CSIR rating: RMR = 23						
NGI rating: Q = 0.1						
VERY POOR QUALITY ROCK MASS	m	0.007	0.010	0.015	0.017	0.025
Numerous heavily weathered joints spaced > 50 mm with gouge. Waste rock with fines	s	0.0000001	0.0000001	0.0000001	0.0000001	0.0000001
CSIR rating: RMR = 3						
NGI rating: Q = 0.01						

*CSIR Council of Scientific and Industrial Research (Bieniawski, 1974).

† NGI Norwegian Geotechnical Institute (Barton et al., 1974).

PROBLEMS

13.1 Evaluate the K_o and β for the conditions shown in Fig. 13.6. Are these values reasonable? Why?

13.2 If the initial stress conditions in a soil sample are $\sigma_v = 10$ MPa and $\sigma_h = 5$ MPa, draw the stress paths for σ_v being held constant while (a) σ_h increases to 10 MPa and (b) σ_h decreases to 0 MPa.

13.3 Show that stress paths D, E, and F in Fig. 13.3 are correct.

13.4 Show that stress paths B and C in Fig. 13.4 are correct.

13.5 Prove that Eqs. (13.4) and (13.5) are valid.

13.6 A soil sample is subjected to an initial equal-all-around hydrostatic state of stress of 50 kPa. Sketch the stress paths for the loading conditions when (a) σ_h remains constant and σ_v increases to 100 kPa; (b) σ_v is held constant while σ_h increases to 100 kPa; (c) both σ_h and σ_v are increased to 100 kPa; (d) σ_v remains constant while σ_h decreases to 10 kPa; and (e) σ_v is increased by 25 kPa at the same time that σ_h is decreased by 25 kPa.

13.7 Given the same initial conditions as for Problem 13.6, draw the stress paths for loading when (a) $\Delta\sigma_h = \Delta\sigma_v/3$ and (b) $\Delta\sigma_h = \Delta\sigma_v/4$.

13.8 A triaxial sample of loose sand is tested in lateral extension (LE) (see Fig. 13.7). The sample is first consolidated nonhydrostatically, with $\sigma_1 = 15$ kPa and $\sigma_3 = 10$ kPa. The sample is then failed in LE, and the angle of internal friction is 30° ($c = 0$). (a) Draw the Mohr circles for both initial and "at failure" conditions. (b) What will be the major and minor principal stresses at failure?

13.9 Another sample of the same sand tested in Problem 13.8 is tested in lateral compression (LC). Complete parts (a) and (b) requested in Problem 13.8 for this test.

13.10 Repeat Problem 12.20, but for undrained shear. A sample of Sacramento River sand has a critical confining pressure of 1000 kPa. If the sample is tested at an effective confining pressure of 1500 kPa, describe its behavior in undrained shear. Show results in the form of unscaled Mohr circles.

13.11 For the sand of Problem 12.20, describe the behavior in undrained shear in a triaxial test if the effective confining pressure is 750 kPa.

13.12 If the test of Problem 12.22 had been conducted undrained, determine $(\sigma_1 - \sigma_3)_f$, ϕ', ϕ_{total}, and the angle of the failure plane in the specimen. $\Delta u_f = 100$ kPa.

13.13 If the test of Problem 13.12 were conducted at an initial confining pressure of 1000 kPa, estimate the principal stress difference and the induced pore water pressure at failure.

13.14 A silty sand is tested consolidated-drained in a triaxial cell where both principal stresses at the start of the test were 500 kPa. If the total axial stress at failure is 1.63 MPa while the horizontal pressure remains constant, compute the angle of shearing resistance and the theoretical orientation of the failure plane with respect to the horizontal. The silty sand of Problem 11.29 was inadvertently tested consolidated-undrained, but the laboratory technician noticed that the pore pressure at failure was 290 kPa. What was the principal stress difference at failure?

13.15 If the consolidation pressure in the CU test of Problem 13.14 were 1000 kPa instead of 500 kPa, estimate the pore pressure at failure.

13.16 If the sample of Problem 13.15 were sheared undrained and the induced pore pressure at failure were 200 kPa, estimate the principal stress difference at failure. What would be the angle of shearing resistance in terms of total stresses?

13.17 Explain the difference between liquefaction and cyclic mobility.

13.18 The Peacock diagram (Fig. 12.11) has been used to predict the pore pressure response of undrained tests on sands, based on the volume changes observed at failure in drained tests. At a given void ratio a sample consolidated at an effective confining pressure less than $\sigma'_{3\,\text{crit}}$ would be expected to offer *more* resistance to liquefaction (since it should have a dilative tendency and therefore develop negative pore water pressure) than a sample consolidated at a confining pressure higher than $\sigma'_{3\,\text{crit}}$ (as this one should tend to decrease in volume during shear). This is contrary to what has been found in the laboratory in cyclic triaxial tests. Explain the apparent contradiction.

13.19 The data presented in Fig. 8.20(b) are for a black fissured organic silty clay or clayey silt. At a depth of 6 m, estimate the expected value or range of values of the undrained modulus.

13.20 The medium gray silty clay of Fig. 8.23(b) at a depth of 20 m had an LL of 38 and a PL of 23. Estimate the following parameters for this soil: (a) coefficient of earth pressure at rest; (b) effective angle of internal friction;

(c) ratio of τ_f/σ'_{vo}; (d) activity; (e) sensitivity; and (f) the undrained Young's modulus. Are there any inconsistencies in the values you obtained? If so, discuss the possible reasons.

13.21 During an undrained cyclic triaxial test on a loose sand, at the tenth cycle, the change in pore water pressure is about 66 kPa just at the beginning of the application of the principal stress difference. Yet, a quarter of a cycle later (as well as slightly before) the pore water pressure is just about equal to the effective confining pressure. At this time the principal stress difference is *zero!* Explain this observation. (It will help if you understand the answer to Problem 13.18.)

13.22 A large power plant is to be constructed at a site immediately adjacent to the Ohio River. The soils at the site consist of 50 m of loose to medium dense granular materials, and the groundwater table is near the ground surface. Since there are several potential earthquake source areas that could influence the site, list some measures that could be taken to protect the foundation of this important structure from liquefaction and/or cyclic mobility.

13.23 Suppose an identical specimen of the same clay as in Problem 12.38 was sheared undrained, and the induced pore pressure at failure was 85 kPa. Determine the principal stress difference, total and effective principal stress ratios, ϕ', ϕ_{total}, A_f, and α_f for this test.

13.24 A series of *drained* direct shear tests were performed on a saturated clay. The results, when plotted on a Mohr diagram, gave $c' = 10$ kPa and $\tan \phi' = 0.5$. Another specimen of this clay was consolidated to an effective pressure of 100 kPa. An *undrained* direct shear test was performed, and the measured value of τ_{ff} was 60 kPa. What was the pore water pressure at failure? Was the specimen normally consolidated? Why?

13.25 The following information was obtained from laboratory tests on specimens from a completely saturated sample of clay:

(a) The sample had in the past been precompressed to at least 200 kPa.

(b) A specimen tested in direct shear under a normal stress of 600 kPa, with complete drainage allowed, showed a shearing strength of 350 kPa.

(c) A specimen which was first consolidated to 600 kPa, and then subjected to a direct shear test in which no drainage occurred, showed a shearing strength of 175 kPa.

Compute ϕ' and ϕ_T for the undrained case. Sketch the Mohr envelopes which you would expect to obtain from a series of undrained and drained tests on this clay. (After Taylor, 1948.)

13.26 Triaxial tests were performed on undisturbed samples from the same depth of organic clay whose preconsolidation load, determined from consolidation tests, was in the range 90 to 160 kPa. The principal stresses at failure of two CD tests were

Test No. 1:	$\sigma_3 = 200$ kPa,	$\sigma_1 = 704$ kPa
Test No. 2:	$\sigma_3 = 278$ kPa,	$\sigma_1 = 979$ kPa

Data from one CU test on the same clay are shown below. The effective consolidation pressure was 330 kPa and the specimen was loaded in axial compression.

Stress Difference (kPa)	Strain (%)	Pore Pressure (kPa)
0	0	0
30	0.06	15
60	0.15	32
90	0.30	49
120	0.53	73
150	0.90	105
180	1.68	144
210	4.40	187
240	15.50	238

(a) Plot the Mohr circles at failure and determine ϕ' from the CD tests for the normally consolidated portion of the failure envelope.

(b) For the CU test, plot curves of principal stress difference and pore pressure versus strain.

(c) Assuming that the single CU test for which data are given is representative for CU tests run at pressures well above the preconsolidation stress: (a) What is ϕ in terms of total stresses above the effects of preconsolidation? (b) What is ϕ' determined by the CU test above the effects of preconsolidation?

(After A. Casagrande.)

13.27 An undrained triaxial compression test was performed on a saturated sample of normally consolidated clay. The consolidation pressure was 100 kPa. The specimen failed when the principal stress difference was 85 kPa and the induced pore water pressure was 67 kPa. A companion undrained test was performed on an identical sample of the same clay, but at a consolidation pressure of 250 kPa. What maximum principal stress difference would you expect at failure for this second test specimen? What are ϕ' and ϕ_{total}? Predict the angle of the failure planes for the two undrained tests.

13.28 Triaxial compression tests were run on specimens from a large undisturbed block sample of clay. Data are given below. Tests 1 through 4 were run so slowly that complete drainage may be assumed. In tests 5 through 8, no drainage was permitted. Plot the Mohr failure envelopes for this soil. Determine the Mohr–Coulomb strength parameters in terms of both total and effective stresses. (After Taylor, 1948.)

Test No.:	1	2	3	4	5	6	7	8
$(\sigma_1 - \sigma_3)_f$, kPa	447	167	95	37	331	155	133	119
σ'_{3f}, kPa	246	89	36	6				
σ_c, kPa					481	231	131	53

What can you say about the probable in situ OCR and K_o of this clay? Is it possible to estimate the E_u and τ_f of this soil?

13.29 A CU triaxial test is performed on a cohesive soil. The effective consolidation stress was 750 kPa. At failure, the principal stress difference was 1250 kPa, and the major effective principal stress was 1800 kPa. Compute Skempton's pore pressure coefficient A at failure.

13.30 Suppose another specimen of the soil in the preceding problem developed a major effective principal stress of 2200 kPa at failure. What would Skempton's pore pressure coefficient A at failure be, if $\sigma'_c = 900$ kPa?

13.31 Two samples of a slightly overconsolidated clay were tested in triaxial compression, and the following data at failure were obtained. The preconsolidation stress for the clay was estimated from oedometer tests to be about 400 kPa.

Specimen	X (kPa)	Y (kPa)
σ'_c	75	750
$(\sigma_1 - \sigma_3)_f$	265	620
Δu_f	−5	+450

(a) Determine the Skempton pore pressure parameter A at failure for both tests.

(b) Plot the Mohr circles at failure for both total and effective stresses.

(c) Estimate ϕ' in the normally consolidated range, and c' and ϕ' for the overconsolidated range of stresses.

13.32 Two identical specimens of soft saturated normally consolidated clay were consolidated to 150 kPa in a triaxial apparatus. One specimen was sheared drained, and the principal stress difference at failure was 300 kPa. The other specimen was sheared undrained, and the principal stress difference at failure was 200 kPa. Determine (a) ϕ' and ϕ_{total}; (b) u_f in the undrained specimen; (c) A_f in the undrained specimen; and (d) the theoretical angle of failure planes for both specimens.

13.33 A clay sample is hydrostatically consolidated to 1.0 MPa and then sheared undrained. The $(\sigma_1 - \sigma_3)$ at failure was also equal to 1 MPa. If drained tests on identical samples gave $\phi' = 22°$, evaluate the pore pressure at failure in the undrained test and compute Skempton's A parameter.

13.34 The following data were obtained from a CU test with pore pressures measured on an undisturbed specimen of sandy silt. The consolidation pressure was 850 kPa and the specimen was sheared in axial compression.

Principal Stress Difference (kPa)	Strain (%)	Induced Pore Pressure (kPa)
0	0	0
226	0.11	81
415	0.25	187
697	0.54	323
968	0.99	400
1470	2.20	360
2060	3.74	219
2820	5.78	−009
3590	8.41	−281
4160	11.18	−530
4430	13.93	−703
4310	16.82	−767
4210	19.71	−789

(a) Plot curves of principal stress difference and pore pressures versus strain. Plot on one sheet.
(b) Plot the stress paths on a p–q diagram.
(c) What is the maximum effective principal stress ratio developed in this test? Is it the same as the maximum obliquity for this specimen?
(d) Is there any difference in ϕ' as determined when the principal stress difference or the principal effective stress ratio is a maximum?

(After A. Casagrande.)

13.35 Typical consolidated-drained behavior of saturated normally consolidated samples of Ladd's (1964) simple clay are shown in Fig. P13.35. You are to conduct another axial compression CD triaxial test on the same clay with the effective consolidation stress equal to 100 kPa. For this test estimate (a) the water content and (b) the principal stress difference at an axial strain of 5%. (After C. W. Lovell.)

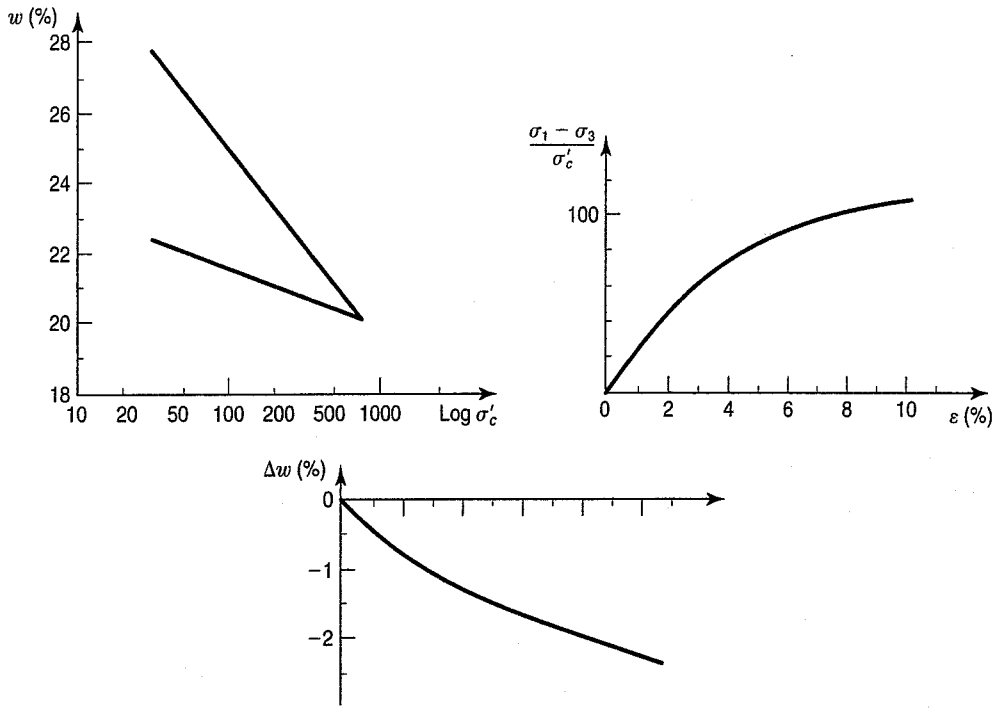

FIGURE P13.35

13.36 The consolidation behavior of the simple clay of Problem 13.35 is shown in Fig. P13.35. Estimate the water content of a sample of this clay at an OCR of 10, if the maximum consolidation stress is 500 kPa instead of 800 kPa. (After C. W. Lovell.)

13.37 Strength tests conducted on samples of a stiff overconsolidated clay gave lower strengths for CD tests than for CU tests. Is this reasonable? Why? (After Taylor, 1948.)

13.38 An undisturbed sample of clay has a preconsolidation load of 500 kPa. In which of the following triaxial tests would you expect the compressive strength to be larger? Why?

(a) A CD test performed at a chamber pressure of 10 kPa.

(b) A CU test performed at a chamber pressure of 10 kPa.

(After A. Casagrande.)

13.39 In each of the following cases state which test, X or Y, should show the greater shearing strength. Except for the difference stated below, the two tests are the same type in each case (triaxial, direct shear, etc.) and for identical clay samples.

(a) The tests are run with no drainage allowed, and test Y is run much faster than test X.

(b) Sample Y is preconsolidated to a larger pressure than sample X; the pressures during the tests are alike for the two cases.

(c) Neither sample is preconsolidated; test X is allowed to drain during shear and test Y is not allowed to drain.

(d) Both samples are highly overconsolidated; test X is not allowed to drain and test Y is allowed to drain.

(e) Test Y is on a sample that is essentially in the undisturbed state, and test X is on a specimen with appreciably disturbed structure but with the same void ratio as Y.

(After Taylor, 1948.)

13.40 List the advantages and disadvantages of each of the field tests listed in Tables 11.1 and 12.5 for determining the undrained shear strength of cohesive soils.

13.41 Which of the tests in Tables 11.1 and 12.5 are appropriate to measure the undrained shear strength for (a) a building foundation and (b) a cut slope for a highway in each of the following five cases:

(i) Sensitive Scandinavian clay.

(ii) Organic marine clay from the U.S. Gulf Coast.

(iii) Stiff fissured clay till from the midwest United States.

(iv) Canadian fibrous peat.

(v) Heavily overconsolidated swelling clay from New Mexico.

13.42 Estimate the maximum expected value of the pore pressure parameter B for the following soils:

(a) Compacted glacial till at $S = 90\%$.

(b) Soft saturated normally consolidated Boston blue clay.

(c) Soil (a) at $S = 100\%$

(d) Stiff overconsolidated clay at $S = 99\%$.

(e) Loose Ottawa sand at $S = 95\%$ and 100%.

(f) Compacted clayey silt at $S = 90\%$ and subjected to high confining pressures.

(g) Dense Ottawa sand at $S = 99\%$ and 100%.

13.43 A 2-m-thick fill is constructed at the surface of the soil profile of Example 6.8. If the clay is slightly overconsolidated, estimate the change in pore pressure at point A of Fig. Ex. 6.8.

13.44 A soil sample is taken from the midpoint of the clay layer of Example 6.8—that is, from a depth of 6 m. If the pore pressure parameter A_u for unloading is 0.90, estimate the effective vertical and horizontal stresses acting on the sample just before testing in the laboratory. Assume ϕ' for the clay is 25°. (*Hint:* Draw elements with stresses similar to Fig. 12.36, and use the definition of stress *increments* in Appendix B.3.) (After G. A. Leonards.)

13.45 What would your answer to Problem 13.44 be if you used Eq. (13.15) instead of (12.17)?

13.46 A sample of normally consolidated clay is removed from −10 m below the ground surface. The effective vertical overburden stress is 250 kPa, and K_o is 0.8. If the pore pressure parameter due to sampling is 0.7, estimate the change in pore pressure in the sample when it is removed from the clay layer. What effective stresses act on the specimen after extrusion from the sample tube? Assume the groundwater table is at the surface.

13.47 Show that Δu in Example 13.4 is about 32 kPa, as predicted by Eqs. (13.15) and (13.18).

13.48 A normally consolidated clay has a ϕ' of 30°. Two identical specimens of this clay are consolidated to 200 kPa in a triaxial cell. Predict the maximum and minimum possible axial stresses in the specimens for a constant cell pressure. (*Hint:* The first test is an axial compression test, the second test is an axial extension test.) What assumptions are necessary to solve this problem?

13.49 The effective stresses at failure for three identical triaxial specimens of an overconsolidated clay are shown in Fig. P13.49. Plot the Mohr circles at failure and determine ϕ' and c'. Determine the theoretical angle of inclination of the failure planes in each test specimen, and show these on a small sketch. Also sketch the effective stress paths for the three tests. (After C. W. Lovell.)

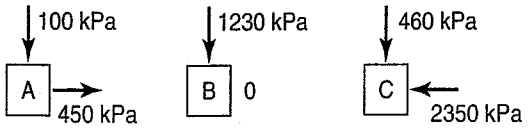

FIGURE P13.49

13.50 Three identical specimens (same e, w) of a clay are normally consolidated and sheared consolidated-drained (CD) in both compression and extension. The stresses at failure for the three specimens are as shown in Fig. P13.50.

(a) Plot the Mohr circles at failure, and determine ϕ' and ϕ_{total}.

(b) Determine the inclination of the predicted failure planes (from the Mohr failure hypothesis). Sketch the failed specimens, showing their failure planes.

(c) Sketch the three stress paths.

(After C. W. Lovell.)

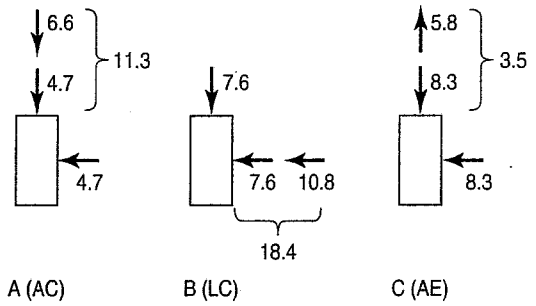

FIGURE P13.50

13.51 A series of conventional triaxial compression tests were conducted on three identical specimens of a saturated clay soil. Test results are tabulated below.

Specimen	σ_c (kPa)	$(\sigma_1 - \sigma_3)_f$ (kPa)	Δu_f (kPa)
A	100	170	40
B	200	260	95
C	300	360	135

(a) Sketch the total and effective stress paths for each test, and determine the Mohr–Coulomb strength parameters in terms of both total and effective stresses. (b) Estimate the theoretical angle of the failure planes for each specimen. (c) Do you believe this clay is normally or overconsolidated? Why?

13.52 Assume that the induced pore pressures at failure for Problem 13.51 were: specimen *A*, −15 kPa; specimen *B*, −40 kPa; and specimen *C*, −80 kPa; and that everything else was the same. Now do parts (a) and (b) above, and then answer part (c).

13.53 An axial compression CU test has been performed on an undisturbed specimen of 100% saturated organic clay. The data for the test is given in Problem 13.26. A lateral extension test is to be performed on an identical specimen at the same consolidation pressure and with the same time of consolidation and time of loading as in the axial compression test.

(a) Plot the total and effective stress paths. Determine the curve of pore pressure versus (1) principal stress difference and (2) axial strain that you would predict theoretically for the lateral extension test.

(b) On the p-q diagram, draw the line corresponding to zero induced pore pressure and the line along which the magnitude of the induced negative pore pressure is equal to the principal stress difference.

(c) What is A_f for both the AC and LE test?

(After A. Casagrande and R. C. Hirschfeld.)

13.54 The following data were obtained from a conventional triaxial compression test on a saturated ($B = 1$), normally consolidated simple clay (Ladd, 1964). The cell pressure was held constant at 10 kPa, while the axial stress was *increased* to failure (axial compression test).

ε_{axial} (%)	$\Delta\sigma_{axial}$ (kPa)	Δu (kPa)
0	0	0
1	3.5	1.9
2	4.5	2.8
4	5.2	3.5
6	5.4	3.9
8	5.6	4.1
10	5.7	4.3
12	5.8 failure	4.4

(a) Plot the $\Delta\sigma$ and Δu versus axial strain curves. Determine A_f.
(b) Plot the total and effective stress paths for the AC test.
(c) What is ϕ'? (Assume $c' = 0$ for normally consolidated clay.)

A lateral extension (LE) test was conducted on an identical sample of the same clay (same e, w). In this test, the axial or vertical stress was held constant at 10 kPa, while the cell pressure was *decreased* to 4.2 kPa, at which time the specimen failed.

(d) Plot both the total and effective stress paths for the LE test.
(e) Determine u_f, σ'_{1f}, σ'_{3f}, and A_f for this tests.
(f) Find ϕ_{total} for both the AC and the LE tests.
(g) Find the theoretical inclinations (from the Mohr failure hypothesis) of the failure planes in each test. Sketch the specimen at failure, indicating the effective stresses at failure and the failure plane inclination.

13.55 A conventional triaxial compression (AC) test was conducted on a saturated sample of overconsolidated clay, and the following data, normalized with respect to the effective confining pressure, were obtained.

ε_{axial} (%)	$\Delta\sigma/\sigma'_c$	$\Delta u/\sigma'_c$
0	0	0
0.5	0.57	+0.07
1	0.92	+0.05
2	1.36	−0.03
4	1.77	−0.22
6	1.97	−0.35
8	2.10	−0.46
10	2.17	−0.52
12	2.23	−0.58
14	2.28	−0.62
16	2.33 failure	−0.67

A lateral extension (LE) test was conducted on an identical specimen of the same clay. While the vertical stress was maintained constant, the cell pressure was decreased until failure occurred at the same principal stress difference as the AC specimen ($\Delta\sigma/\sigma'_c = 2.33$). From your knowledge of stress paths and soil behavior, determine (a) the effective and total stress paths for both tests and (b) the pore pressure versus strain response of the LE test. (c) Can the Mohr–Coulomb strength parameters be determined? Why? (After C. W. Lovell.)

13.56 A K_0 consolidated-undrained triaxial compression (σ_{cell} = constant) test was conducted on an undisturbed specimen of sensitive Swedish clay. The initial conditions were as shown in Fig. P13.56a. The stress-strain and pore pressure responses of the specimen are shown in Fig. P13.56b.

(a) Find the stress conditions at failure and symbolically show the total, neutral, and effective stresses (like the "initial conditions" shown above).
(b) Sketch the total and effective stress paths.
(c) Plot A versus ε. What is A_f? What are ϕ' and ϕ_T?

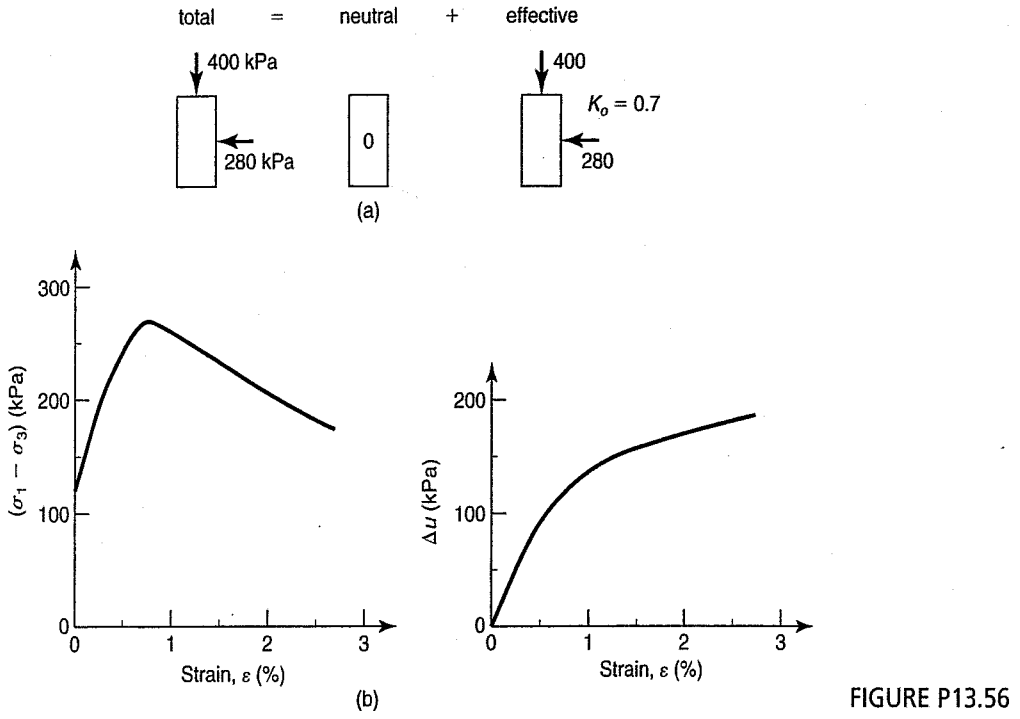

FIGURE P13.56

13.57 If an LE test were conducted on a sample of Swedish clay identical to that tested in Problem 13.56, predict the pore pressure versus strain response of the clay. What are u_f and $\overline{A}_f$? What is ϕ_T?

13.58 The data shown in Fig. P13.58 are obtained from several CU tests on a saturated clay which has an OCR of 10 and a preconsolidation stress of 800 kPa. It is assumed that these results are valid for all compression stress paths on this clay. You are going to run a special stress path test on this clay. After consolidation at σ'_{vo}, the cell pressure will be increased in such a way that $\Delta\sigma_3 = 0.2\,\Delta\sigma_1$ until failure occurs. For this special stress path test, fill in the table below and plot the total and effective stress paths. (After C. W. Lovell.)

ε (%)	$\Delta\sigma_1$ (kPa)	$\Delta\sigma_3$ (kPa)	σ_1 (kPa)	σ_3 (kPa)	Δu (kPa)	A
0						
0.5						
2.5						
5.0						
7.5						

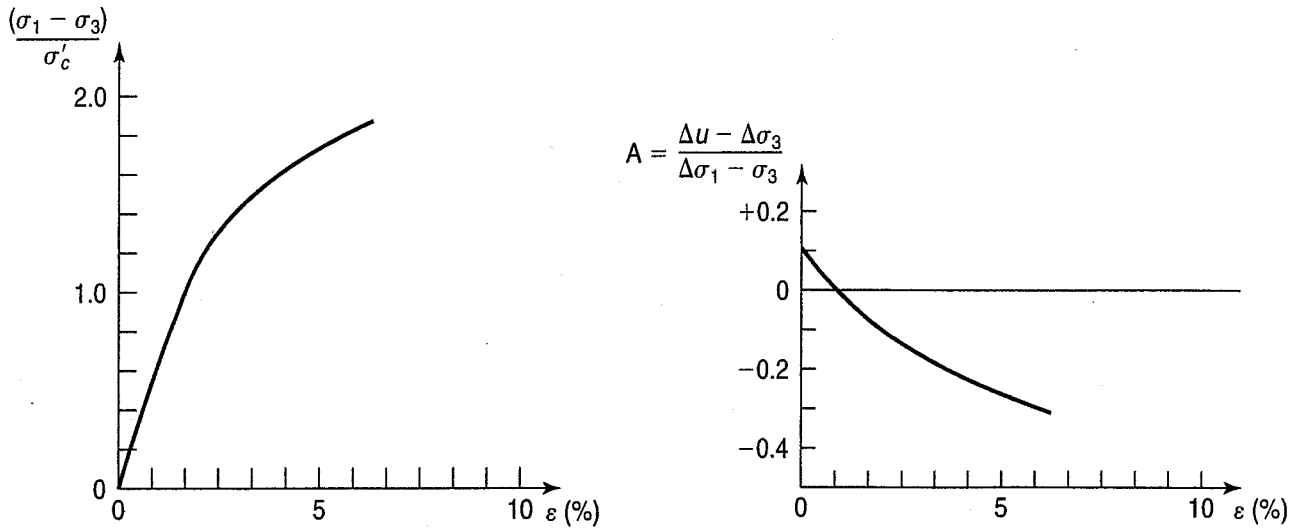

FIGURE P13.58

13.59 A series of CU compression tests on a simple clay (Ladd, 1964) provided the following test results:

ε_{axial} (%)	$2\tau_f/\sigma'_c$	A
0	0	—
1	0.35	0.53
2	0.45	0.64
3	0.50	0.72
4	0.52	0.76
6	0.54	0.88
8	0.56	0.92
10	0.57	0.93
12 failure	0.58	0.945

(a) In an axial compression test, if $\sigma'_c = 200$ kPa, determine q_f, p_f, and p'_f. (b) Find ϕ' and c'. A special lateral extension stress path test was conducted on this clay in which the decrease in lateral stress was exactly equal to the increase in axial stress; that is, $-\Delta\sigma_3 = \Delta\sigma_1$. For this case, if $\sigma'_c = 400$ kPa, determine $\Delta\sigma_1$, q, p, p', and Δu (c) when the axial strain is 4% and (d) at failure. (After C. W. Lovell.)

13.60 Figure P13.60 shows normalized data from an axial compression (AC) triaxial test and a lateral compression (LC) triaxial test on saturated simple clay (Ladd, 1964). Make the appropriate calculations, and plot the complete total and effective stress paths for both tests. What are the Mohr–Coulomb strength parameters? Determine A_f for each test.

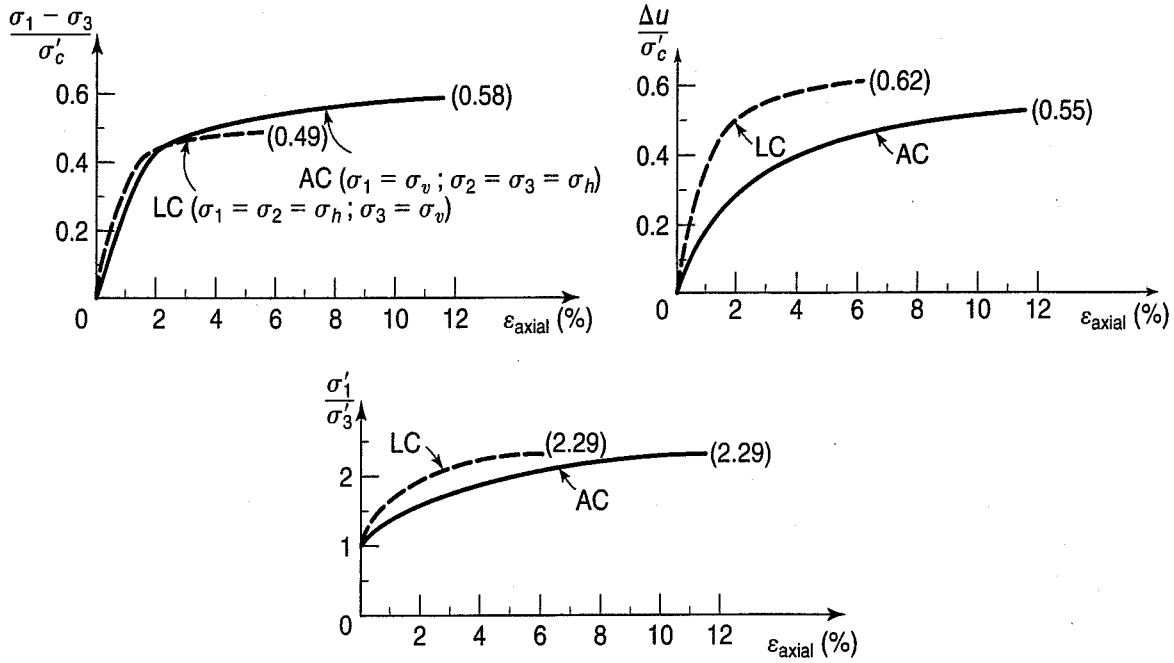

FIGURE P13.60

13.61 Two specimens of a soft clay from the Skå-Edeby test field in Sweden were reconsolidated to their initial in situ effective stress conditions and then sheared to failure. One specimen was loaded in axial compression (AC), while the other was failed by axial extension (AE). The normalized stress-strain and pore pressure strain data for both tests is shown in Fig. P13.61 (after Zimmie, 1973). Pertinent specimen data is given in the accompanying table. (a) On a p–q diagram, sketch the total, total $-u_o$, and effective stress paths for both tests. (b) Determine ϕ' and ϕ_{total} in both compression and extension. (c) Calculate the Skempton pore pressure parameter A at failure for both tests. (d) Show in a sketch the predicted theoretical angles of the failure planes for the two specimens.

Test	Type	Depth (m)	σ'_{vo} (kPa)	LL	PL	w_n (%)	$K_o{}^a$	OCR
3A1	AC	4.87	30.2	93	29	103.0	0.65	1.07
3A2	AE	5.02	31.0	87	29	84.2	0.65	1.07

[a]Assumed.

Note: Tests were conducted with a back pressure of 20 kPa. In situ pore water pressure is approximately 40 kPa.

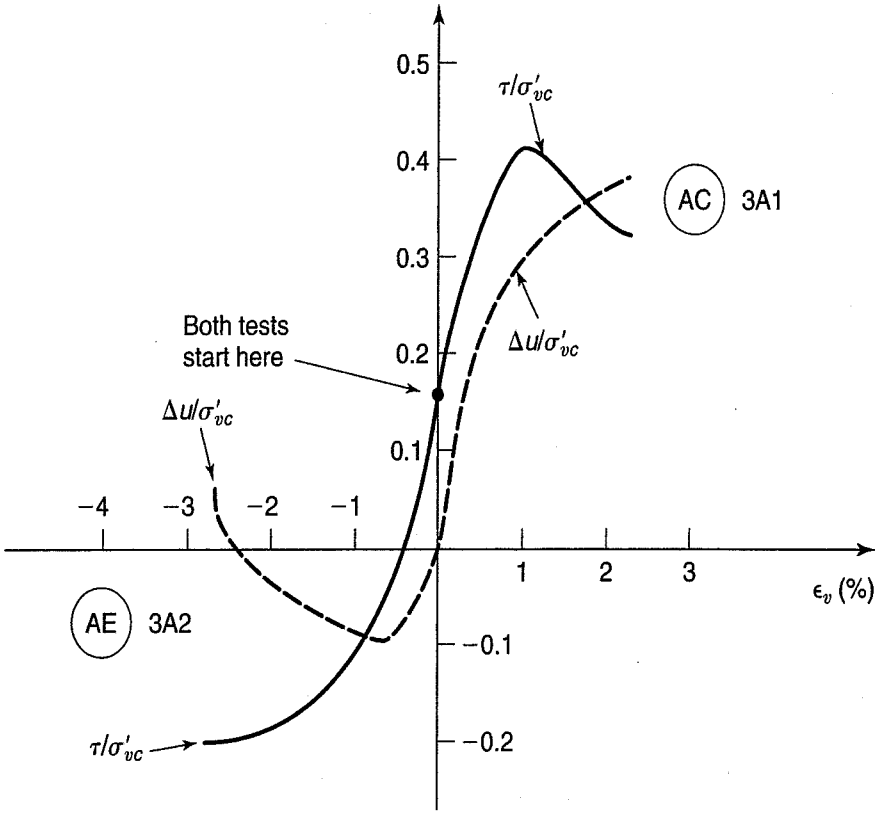

FIGURE P13.61

13.62 Are the values given and calculated for K_o, τ_f/σ'_{vo}, ϕ', and so on for the Skå-Edeby clay of Problem 13.61 reasonable in terms of the simple correlations with PI, LI, etc., given in this chapter?

13.63 For the oil tank problem in Chapter 10 (Problem 10.16), plot the complete total, total $-u_o$, and effective stress paths due to construction and filling of the tank for an element under the centerline of the tank and at the midpoint of the clay layer. Assume that K_o at the site is 0.7 and that the average value of the A parameter before failure is 0.4; assume $A_f = 0.5$. Make reasonable estimates of the strength parameters, and estimate the factor of safety against failure.

13.64 What is the maximum safe height of the embankment for Examples 13.4 and 13.8? Plot a graph of factor of safety versus height of the embankment.

13.65 How would you recommend the shear strength be determined for the following design situations? Your answer can include both laboratory and field tests or, in some cases, no tests but some other design approach that may be appropriate. Be as specific as you can.

(a) Long-term stability of a compacted clay earth dam.
(b) Stability of a hydraulic fill sand dam under seismic loading.
(c) End of construction of a compacted clay earthfill dam.
(d) Foundation on a soft saturated normally consolidated clay.
(e) Shallow foundation on a loose dry sand.
(f) End of construction of an excavation in soft normally consolidated clay.
(g) Cut slope in an overconsolidated stiff fissured clay.
(h) Highway embankment on a stiff fissured clay.

13.66 Two tests are conducted on specimens of a stiff, overconsolidated clay, one a CD test and one a CU test, both of which are sheared in axial compression. The drained test resulted in a lower strength than the undrained test. Explain how this could occur, including a sketch of the stress paths for the 2 tests.

13.67 A CU extension test was performed on a normally consolidated specimen using axial extension. The strength ratio was −0.280, and the effective failure angle, $\alpha' = 26.5°$. Find A_f.

13.68 The following data was obtained from CD direct shear tests on NC and OC specimens of a low plasticity clay. The OC specimens were originally consolidated to 600 kPa, then rebounded to obtain the OCRs shown below.

Normally Consolidated			Overconsolidated		
Consolidation Stress, σ'_c (kPa)	Shear Stress at Failure, τ_f (kPa)	Void Ratio at Failure, e_f	OCR	Shear Stress at Failure, τ_f (kPa)	Void Ratio at Failure, e_f
200	100	1.07	3	165	0.923
400	200	0.935	6	115	0.965
600	300	0.855	2	200	0.900

Determine the Hvorslev shear strength parameters ϕ'_e, c_e, and the Hvorslev coefficient κ. (After Perloff and Baron, 1976.)

13.69 Derive an expression similar to Eq. (13.49) for overconsolidated clays with $K_o > 1$ and $c' \neq 0$. (*Hint:* First assume that $\Delta\sigma_3 = 0$, then do the more general case of $\Delta\sigma_3 \neq 0$.)

13.70 Undisturbed piston samples of grey silty Chicago clay were obtained from a depth of −9 m, as shown in the soil profile in Fig. P13.70a, for laboratory testing. Different types of strength tests as well as a consolidation test were conducted, and the results of the consolidation test are shown in Fig. P13.70b. Unconfined compression (UCC) tests on adjacent specimens from that depth had an average unconfined compressive strength of about 100 kPa.

(a) An additional specimen was trimmed and consolidated hydrostatically in a triaxial cell to 300 kPa; then it was sheared *undrained* (CU test). Estimate the compressive strength of this specimen.

(b) A companion specimen of the same clay was also consolidated to 300 kPa, but then it was sheared *drained* (CD test). Estimate the compressive strength of this specimen.

(c) Estimate the water content at failure for both the CD and CU triaxial specimens.

(d) Estimate ϕ' and ϕ_T for the two specimens.

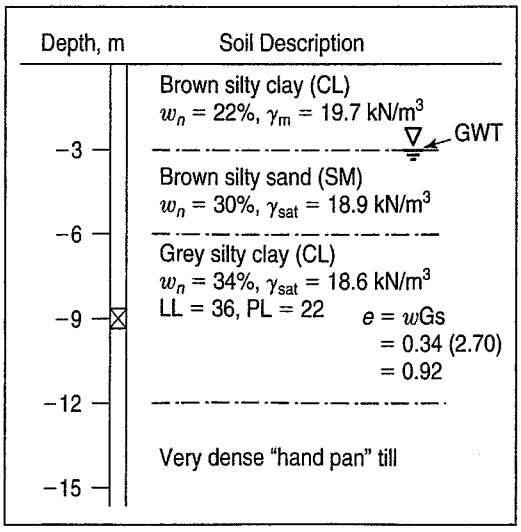

FIGURE P13.70a

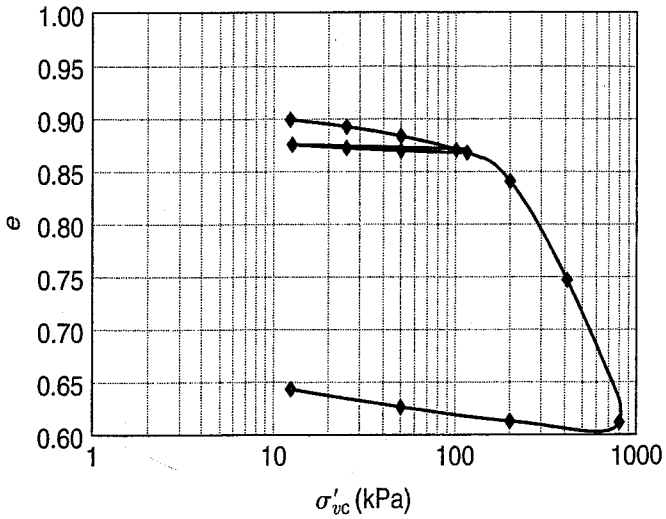

FIGURE P13.70b

13.71 Assuming that the Jürgenson–Rutledge hypothesis is correct, show that τ_f/σ'_{vc} = constant.

APPENDIX A

Application of the SI System of Units to Geotechnical Engineering[1]

A.1 INTRODUCTION

Within the scientific and engineering community, there has always been some confusion about the proper system of units for physical measurements and quantities. Many systems have been advanced, and some, including the Imperial or British engineering system, the so-called "metric system," and a few hybrids, have achieved popular usage. With the growth of international cooperation and trade, it has become increasingly apparent that a single, commonly accepted system of units would be not only convenient but also of tremendous practical value.

Although the field of geotechnical engineering may not claim the greatest confusion in the use of units, it undoubtedly ranks near the top of all fields in the number of different systems in common usage. Laboratory engineers, following their counterparts in the physical sciences, have attempted to use some sort of metric system, usually the cgs (centimetre-gram-second) system, for simple laboratory tests. With ease, they apply the mks (metre-kilogram-second) system to measurements of pressure and stress in consolidation and triaxial tests, and, with some impunity, they use British engineering units for compaction tests. As any teacher of soil mechanics can testify, the confusion to the uninitiated is tremendous. At least practicing geotechnical engineers in North America have been somewhat consistent in the use of the British engineering system for laboratory and field densities, stress measurements, etc., although they commonly alternate between pounds per square foot, kips per square foot, tons per square foot, and pounds per square inch, depending on how they or their clients feel about the subject. Fortunately, 1 ton-force/ft^2 is within 3% of 1 kg-force/cm^2, a common laboratory unit for stress and pressure, and the foundation engineer utilizing consolidation test data can convert directly with small error. Strictly speaking, using force as a basic unit is incorrect; mass should be the basic unit, with force derived according to

[1]This appendix has been adapted from an unpublished paper by R. D. Holtz at Northwestern University, November 1969. See also Holtz (1980).

Newton's second law of motion. Use of the kilogram as a unit of force is one of the difficulties with the so-called "metric system," a modified version of the mks system, which was common among continental European engineers. At least they tried to keep the distinction between mass and force by calling the kilogram-force a *kilopond* (kp).

A modernized version of the metric system known as *SI*, which stands for "Le Système International d'Unités" ("The International System of Units"), was formally adopted by the General Conference on Weights and Measures (CGPM) about 1960. It is described in detail in IEEE/ASTM (2002), and an SI Quick Reference Guide given in the back of every current *Annual Book of ASTM Standards*. The United States is just about the only country in the world still using the Imperial or British engineering system. Even Great Britain itself converted completely to SI in 1972, and Australia, New Zealand and Canada followed shortly thereafter.

A.2 THE SI METRIC SYSTEM

The SI metric system is fully coherent and rational. It is founded on seven basic units for *length* (metre or meter), *mass* (kilogram), *time* (second), *electric current* (ampere), *thermodynamic temperature* (kelvin), *luminous intensity* (candela), and *amount of substance* (mole). All these basic units have precise definitions, names, and symbols, and in terms of these units, we can derive units for all other physical quantities. Sometimes the derived quantities are given specific names, such as the *newton* for force and the *watt* for power. The derived unit of force replaces the kilogram-force (kgf) of the mks system, so that the name of the unit indicates it is a unit of force, not mass. A great advantage is that *one and only one unit exists of each physical quantity*, and all other mechanical quantities such as velocity, force, and work can be derived from the basic units. In addition, the SI units for force, energy, and power are *independent* of the nature of the physical process, whether mechanical, electrical, or chemical.

As previously mentioned, a major advantage of SI is that it is a fully coherent system, which means that a product or quotient of any two unit quantities is a unit of the resulting quantity. For example, unit length squared should be unit area, and unit force should be unit mass times unit acceleration. Obviously, many of the engineering units in common use (for example, acre, lb-force, kg-force) are not coherent units. Also, units that might be related to basic units by powers of 10 are *not* consistent within the SI system. A good example is the litre, or liter, which is a cubic decimetre. The equivalent volume of the litre has been defined as exactly 10^{-3} m^3 (1000 cm^3). Additional advantages of SI include the use of unique and well-defined symbols and abbreviations and the convenient decimal relation between multiples and submultiples of the basic units.

In the next two sections of this appendix we describe in detail the SI units of particular interest in geotechnical engineering and present appropriate conversion factors for some of the common mks and British engineering units. Since you are likely to encounter just about anything in your engineering practice, it is important that you know how to convert between these systems and SI, and that you have some feel for physical quantities in both sets of units.

A.3 BASIC AND DERIVED SI METRIC UNITS

The three *base units* of interest to geotechnical engineers are *length*, *mass*, and *time*. The SI units for these quantities are the *metre*, m, the *kilogram*, kg, and the *second*, s. Temperature, which might also be of interest, is expressed in *kelvins* (K), although the system does allow for use of the degree Celsius (°C), which has the same interval. Electric current is expressed in *amperes* (A), amount of a substance in *moles* (mol), and luminous intensity in *candelas* (cd).

As mentioned, these basic SI units have precise physical definitions. For example, contrary to a popular misconception, the metre is *not* the distance between two bars in Paris, but rather it has been

defined as exactly equal to a certain number of wavelengths of radiation corresponding to a specific transition level of krypton 86. The standard kilogram is equal to the mass of the international prototype kilogram, a cylinder of platinum-iridium alloy preserved in a vault at Le Bureau International des Poids et Mesures at Sèvres, France. Similar standard kilograms can also be found at the National Bureau of Standards near Washington, D.C. The second has been defined as the duration of a certain number of periods of the radiation corresponding to a specific transition state of cesium 133.

Derived units geotechnical engineers use include those listed in Table A.1.

Prefixes are used to indicate multiples and submultiples of the basic and derived units. SI prefixes are listed in Table A.2. Although units larger or smaller than 10^{+3} or 10^{-3} are in multiples of three, this custom is not universal. In India, for example, it is common to use multiples of two for larger numbers. Thus a *lakh* is equivalent to 10^{+5}, a *crore* equals 10^{+7}, an *arab* is 10^{+9}, a *kharab* is 10^{+11}, and so on.

The prefixes should be applied to indicate orders of magnitude of the basic or derived units and to reduce redundant zeros so that numerical values lie between 0.1 and 1000. They should *not* be applied to the *denominator* of compound units (kilogram is an exception, since kg is a basic unit in the SI system). Note that *spaces*, not commas, should be used to separate groups of zeros (a concession to the Europeans to persuade them to stop using a comma as a decimal point!).

To maintain the coherence of the system, it is recommended that *only basic units be used to form derived units*. For example, the unit of force, the newton, is derived according to Newton's second law, $F = Ma$, where the mass M is in kilograms and the acceleration a is in m/s^2, all basic units. For derived combinational units such as pressure or stress (pascals or newtons per square metre), multiples and submultiples of the basic metric units (in this case metres) should be avoided. For example, N/cm^2 and N/mm^2 are wrong; the appropriate prefix should be used with the numerator to indicate larger or smaller quantities—for example, kN/m^2 or MN/m^2 (for kilonewtons per square metre or meganewtons per square metre).

TABLE A.1

Quantity	Unit	SI Symbol	Formula
acceleration	metre per second squared	m/s^2	—
angle, plane	radian	rad	—
area	square metre	m^2	—
area	hectare	ha	$hm^2 = 10^4\ m^2$
density	kilogram per cubic metre	kg/m^3	—
force	newton	N	$kg \cdot m/s^2$
frequency	hertz	Hz	1/s
moment or torque	newton metre	$N \cdot m$	$kg \cdot m^2/s^2$
power	watt	W	J/s
pressure	pascal	Pa	N/m^2
stress	pascal	Pa	N/m^2
surface tension	newton per metre	N/m	$kg \cdot s^2$
unit weight	newton per cubic metre	N/m^3	$kg \cdot m^{-2}/s^2$
velocity	metre per second	m/s	—
voltage	volt	V	W/A
volume	cubic metre	m^3	—
volume	litre	L	$dm^3 = 10^{-3}\ m^3$
work (energy)	joule	J	$N \cdot m$

TABLE A.2

Factor	Prefix	Symbol
10^{24}	yotta	Y
10^{21}	zetta	Z
10^{18}	exa	E
10^{15}	peta	P
10^{12}	tera	T
10^{9}	giga	G
10^{6}	mega	M
10^{3}	kilo	k
10^{2}	hecto	h
10^{1}	deka	da
10^{-1}	deci	d
10^{-2}	centi	c
10^{-3}	milli	m
10^{-6}	micro	μ
10^{-9}	nano	n
10^{-12}	pico	p
10^{-15}	femto	f
10^{-18}	atto	a
10^{-21}	zepto	z
10^{-24}	yocto	y

A.4 SI UNITS OF INTEREST TO GEOTECHNICAL ENGINEERS AND THEIR CONVERSION FACTORS

Length You should already be familiar with the SI unit for length (the metre, m). Useful SI length multiples and submultiples are the kilometre (km), millimetre (mm), micrometre (μm), and nanometre (nm). Conversion factors for the common British engineering and mks systems are:

$$\begin{aligned}
1 \text{ inch, in.} &= 25.4 \text{ mm} = 0.0254 \text{ m} \\
1 \text{ foot, ft} &= 0.3048 \text{ m} \\
1 \text{ yard, yd} &= 0.9144 \text{ m} \\
1 \text{ mile (U.S. statute)} &= 1.609 \times 10^{3} \text{ m} = 1.609 \text{ km} \\
1 \text{ mile (nautical)} &= 1.852 \times 10^{3} \text{ m} = 1.852 \text{ km} \\
1 \text{ angstrom, Å} &= 1 \times 10^{-10} \text{ m} = 0.1 \text{ nm} \\
1 \text{ mil} &= 2.54 \times 10^{-5} \text{ m} = 0.0254 \text{ mm} = 25.4 \text{ μm}
\end{aligned}$$

Good SI practice suggests that multiple and submultiple metric units be used in increments of 1000—for example, mm, m, km. The centimetre, especially for lengths under 300 mm, should be avoided.

Mass You may recall from physics that the inertia or mass (SI unit: kilogram, kg) of a physical object is a measure of the property that controls the response of that object to an applied force. It is convenient to measure the mass in terms of the acceleration of an object produced by a unit force, as related

by Newton's second law of motion. Thus a unit force causes 1 kg mass to accelerate 1 m/s^2. The mass, then, is an appropriate measure of the amount of matter an object contains. The mass remains the same even if the object's temperature, shape, or other physical attributes change. Unlike weight, which is discussed later, the mass of an object does not depend on the local gravitational attraction, and thus it is also independent of the object's location in the universe.

Among all the SI units, the kilogram is the only one whose name, for historical reasons, contains a prefix. The names of multiples and submultiples of the kilogram are formed by attaching prefixes to the word *gram* rather than to *kilogram*. In other words, 10^{-6} kg is not a micro-kilogram, but a milligram = 10^{-3} g. Similarly, 1000 kg is not 1 kilo-kilogram but is equivalent to 1 megagram (Mg), the only large mass unit permitted by SI. The British long ton (2240 lb), short ton (2000 lb), and the metric ton (1000 kg) and sometimes spelled *tonne*) are best left to commercial usage and avoided in engineering practice. Practical units of mass in engineering practice are the megagram (Mg), the kilogram (kg), and the gram (g), the latter two units being primarily used in laboratory work.

Some useful relationships and conversion factors are:

$$\begin{aligned}
1 \text{ pound mass, lbm (avoirdupois)} &= 0.4536 \text{ kg} \\
1 \text{ British (short) ton} &= 2000 \text{ lbm} = 907.2 \text{ kg} \\
1 \text{ gram, g} &= 10^{-3} \text{ kg} \\
1 \text{ metric ton, t} &= 10^3 \text{ kg} = 10^6 \text{ g} = 1 \text{ Mg} \\
1 \text{ slug (1 lb-force/ft/s}^2\text{)} &= 14.59 \text{ kg}
\end{aligned}$$

Time Although the second (s) is the basic SI time unit, minutes (min), hours (h), days (d), etc., may be used where convenient, even though they are not decimally related. (Maybe some day we will even have a decimal time system; see Carrigan, 1978.)

Force As mentioned, the SI unit of force is derived from $F = Ma$, and it is termed the *newton* (N), which is equal to 1 kg · m/s^2. Conversion factors for common engineering force units are:

$$\begin{aligned}
1 \text{ lb-force} &= 4.448 \text{ N} \\
1 \text{ British short ton-force} &= 8.896 \times 10^3 \text{ N} = 8.896 \text{ kN} \\
1 \text{ kg-force} &= 1 \text{ kp} = 9.807 \text{ N} \\
1 \text{ kip} &= 1000 \text{ lb-force} = 4.448 \times 10^3 \text{ N} = 4.448 \text{ kN} \\
1 \text{ metric ton-force} &= 1000 \text{ kg-force} = 9.807 \times 10^3 \text{ N} = 9.807 \text{ kN} \\
1 \text{ dyne (g · cm/s}^2\text{)} &= 10^{-5} \text{ N} = 10 \ \mu\text{N}
\end{aligned}$$

It is obvious that the numbers in newtons for such items as column loads would be very large indeed and consequently somewhat awkward. Therefore, consistent with the rules for application of prefixes, it is simple to adjust these rather large numbers to more manageable quantities for engineering work. The common prefixes would be kilo (10^3), mega (10^6), and giga (10^9), so that engineering forces would be kilonewtons, kN, meganewtons, MN, and giganewtons, GN. (The symbol for mega is M, to avoid confusion with the symbol for milli, m.) Thus, since 1 ton-force is 8.9 kN, 1000 tons would be 8.9 MN.

Some useful relationships of these prefixes are:

$$\begin{aligned}
1 \text{ kilonewton, kN} &= 10^3 \text{ newton} = 1000 \text{ N} \\
1 \text{ meganewton, MN} &= 10^6 \text{ newton} = 10^3 \text{ kN} = 1000 \text{ kN} \\
1 \text{ figanewton, FN} &= 10^8 \text{ newton} = 10^5 \text{ kN} = 10^2 \text{ MN} = 100 \text{ MN}
\end{aligned}$$

1 giganewton, GN = 10^9 newton = 10^6 kN = 10^3 MN = 1000 MN
3 giganewtons = 30 figanewtons = 1 boxafiganewtons[2]
14.4 giganewtons = 1 grossafiganewtons

The correct unit to express the *weight* of an object is the newton, since the weight is the gravitational force that causes a downward acceleration of the object. Or, weight W equals Mg, where M is the mass of the object and g is the acceleration due to gravity. You will recall that the acceleration due to gravity varies with latitude and elevation and, in fact, SI recommends that weight be avoided and that mass be used instead. If weight must be used, it is suggested that the location and gravitational acceleration also be stated. However, for most ordinary engineering purposes, the difference in acceleration (about 0.5%) can be neglected, and as long as we express the weight in newtons, the units will be consistent.

Another problem with weight is that it is commonly used when we really mean the mass of an object. For example, in the laboratory when we "weigh" an object on a laboratory balance, we really are comparing two masses, the mass of the unknown object with objects of known mass. Even scales or balances that displace linear springs are calibrated by using objects of known mass.

Further ambiguity occurs, of course, because common units of mass such as the pound or kilogram are often used in engineering practice as units of force. If pound is used as a unit of force, then depending on the resulting accelerations, different mass units are defined. For example, if a 1 lb-force causes an acceleration of 1 ft/s^2, then the mass is 1 lb-force · s^2/ft, which is called a *slug*. In other words, 1 lb-force = 1 slug × 1 ft/s^2. Using slugs as units of mass avoids the confusion with pounds-mass, and this unit has been commonly used in aerodynamics and fluid mechanics.

If we wanted to use instead a pound-mass system, we could define a unit of force called the *poundal*, where 1 poundal = 1 lbm × 1 ft/s^2. Poundals are apparently used only in physics books.

Example A.1

Given:

A force of 1 lb acts on an object weighing 1 lb.

Required:

Find the resulting acceleration.

Solution: From Newton's second law,

$$F = Ma = \left(\frac{W}{g}\right)a$$

or

$$a = \frac{Fg}{W} = \frac{(1\text{ lbf})(32.17\text{ ft/s}^2)}{1\text{ lbf}} = 32.17\text{ ft/s}^2$$

---

[2]This unit is a constant only prior to opening the box.

Example A.2

Given:

The object in Example A.1, which weights 1 lbf.

Required:

Find its mass when a 1 lbf causes an acceleration of 1 ft/s^2.

Solution:

$$F = Ma = \left(\frac{W}{g}\right)a$$

or

$$M = \frac{W}{g} = \frac{1\text{ lbf}}{32.17\text{ ft/s}^2} = 0.031\frac{\text{lbf}\cdot\text{s}^2}{\text{ft}} = 0.031\text{ slug}$$

Example A.3

Given:

The Mars rover vehicle weighs 400 lbs on earth.

Required:

How much does it weigh on the surface of Mars?

Solution: First, we have to calculate the rover's mass on earth. Unless it lost equipment en route, its mass will be the same on Mars.

$$M = \frac{W}{g} = \frac{400\text{ lbf}}{32.17\text{ ft/s}^2} = 12.43\frac{\text{lbf}\cdot\text{s}^2}{\text{ft}}\text{, or, } 12.43\text{ slugs}$$

Since 1 slug = 14.59 kg, its mass is 181.41 kg. Another way to calculate its mass is to convert its weight to newtons, then divide by g.

$$W = 400\text{ lbf}\left(\frac{4.448\text{ N}}{1\text{ lbf}}\right) = 1779.20\text{ N or } 1779.2\frac{\text{kg}\cdot\text{m}}{\text{s}^2}$$

$$M = \frac{W}{g} = \frac{1779.2\text{ kg}\cdot\text{m/s}^2}{9.807\text{ m/s}^2} = 181.41\text{ kg}$$

Next, we have to either ask an astronomer or look up in the *Handbook of Chemistry and Physics* (2008) or some other reference the gravitational acceleration on the surface of Mars. We find that $g_{\text{Mars}} = 3.728\text{ m/s}^2$.

Thus,

$$W_{\text{Mars}} = Mg_{\text{Mars}} = 181.41\text{ kg}\,(3.728\text{ m/s}^2) = 676.30\text{ N}$$

Or, since 4.448 N = 1 lbf,

$$W_{\text{Mars}} = 676.30\ \text{N} = \left(\frac{1\ \text{lbf}}{4.448\ \text{N}}\right) = 150.05\ \text{lbf}$$

Check: On earth, $1779\ \text{N}\left(\frac{3.728}{9.81}\right) = 676.30\ \text{N}$ on Mars.

See how confusing the old British engineering system can be? However, if you think this is bad, wait until you try to convert densities and unit weights!

Stress and Pressure The SI unit for stress and pressure is the *pascal* (Pa), which is exactly equal to 1 newton per square metre (N/m^2).

There has been some objection, especially in Europe, to the use of the pascal as the basic unit of stress and pressure because it is so small. The Germans and French, for example, often use the *bar*, which is exactly 10^5 Pa. However, the pascal is more logical, since it is a coherent unit; that is, equations involving the pascal with other SI units can be written without coefficients of proportionality being required.

Conversion factors for some common engineering units are:

$$\begin{aligned}
1\ \text{psi (lb-force/in.}^2) &= 6.895 \times 10^3\ \text{Pa or } 6.895\ \text{kPa}\\
1\ \text{atm at STP}^3 &= 1.013 \times 10^5\ \text{Pa or } 101.3\ \text{kPa}\\
1\ \text{kg-force/cm}^2 &= 9.807 \times 10^4\ \text{Pa or } 98.07\ \text{kPa}\\
1\ \text{metric ton-force/m}^2 &= 9.807 \times 10^3\ \text{Pa or } 9.807\ \text{kPa}\\
1\ \text{bar} &= 1 \times 10^5\ \text{Pa or } 100\ \text{kPa}\\
1\ \text{ksi (kip/in.}^2) &= 6.895 \times 10^6\ \text{Pa or } 6.895\ \text{MPa}\\
1\ \text{British ton-force/ft}^2 &= 95.76 \times 10^3\ \text{Pa or } 95.76\ \text{kPa}\\
1\ \text{lb-force/ft}^2 &= 47.88\ \text{Pa}
\end{aligned}$$

It is obvious that the pascal is a small unit, but as with SI force units, it is easy to add prefixes to make the large numbers more manageable. Thus, 1 psi in the above table is more conveniently expressed as 6.9 kPa (kN/m^2) than as 6.9×10^3 Pa. For ordinary triaxial testing of soils, for example, hydrostatic cell pressures rarely exceed 200 or 300 psi (1379 or 2068 kPa). Or, if all the pressures in a test series are in this range, it might be convenient to use 1.4 or 2.1 MPa. And, as with other systems of units, a rounded or even interval may be more convenient—for example, in this case, 1.5 and 2.0 MPa.

Similar examples could be given for engineering stresses. Either kilopascals or megapascals, kPa or MPa, or kilo- or meganewtons per square metre, kN/m^2 or MN/m^2, will become commonly used for foundation stresses, lateral earth pressures, allowable bearing values, etc. In the laboratory, force is measured by a proving ring or load cell and then converted to stress (for example, in the unconfined compression or direct shear tests), so the computational process will be no more complicated than it is now. Similarly, with electrical pressure transducers, a calibration factor must be used to convert millivolts (mV) output to pressure in whatever units are used.

A convenient approximation, part of which is already in use in geotechnical engineering practice, is the following:

$$\begin{aligned}
&1\ \text{British (short) ton-force/ft}^2 \cong 1\ \text{kg-force/cm}^2 \cong 1\ \text{atmosphere}\\
&\cong 10\ \text{metric ton-force/m}^2 \cong 100\ \text{kPa} \cong 100\ \text{kN/m}^2
\end{aligned}$$

[3]Standard temperature and pressure, not a motor oil additive or Soil Test Probe.

The error involved is between 2% and 4%, which is certainly less than ordinary engineering accuracy requirements.

Example A.4

Given:

The pressure or stress is 100 kPa.

Required:

Convert this pressure or stress to (a) psi (lb-force/in.^{2}), (b) ksi (kips/in.^{2}), (c) tsf (British ton-force/ft.^{2}), (d) kg-force/cm^2, (e) bar, (f) metric ton-force/m^2, (g) mm of mercury, (h) ft of water, and (i) m of water.

Solution: A simple way to convert from one set of units to another is to set up an equation with the equivalents in either the numerator or denominator of the equation so that the appropriate cancellations occur.

a. $$p = 100\,\text{kPa} = 100\frac{\text{kN}}{\text{m}^2}\left(\frac{1\,\text{lbf}}{4.448\,\text{N}}\right)\left(\frac{1000\,\text{N}}{\text{kN}}\right)\left(\frac{0.0254\,\text{m}}{1\,\text{in.}}\right)^2$$

$$= 14.5\,\text{psi}$$

Note: The exact conversion value is 14.503 773 77 kN/m^2, which comes about if you use the exact value for 1 lbf = 4.448 221 615 260 5 N. 1 in. is exactly equal to 0.0254 m.

b. $$p = 100\,\text{kPa}$$

$$= 100\frac{\text{kN}}{\text{m}^2}\left(\frac{1\,\text{lbf}}{4.448\,\text{N}}\right)\left(\frac{1000\,\text{N}}{\text{kN}}\right)\left(\frac{1\,\text{kip}}{1000\,\text{lbf}}\right)\left(\frac{0.0254\,\text{m}}{1\,\text{in.}}\right)^2$$

$$= 0.0145\,\text{ksi}$$

Again, as in part **a**, the exact conversion value is slightly different.

c. $$p = 100\,\text{kPa}$$

$$= 100\frac{\text{kN}}{\text{m}^2}\left(\frac{1\,\text{lbf}}{4.448\,\text{N}}\right)\left(\frac{1000\,\text{N}}{\text{kN}}\right)\left(\frac{1\,\text{tonf}}{2000\,\text{lbf}}\right)\left(\frac{0.3048\,\text{m}}{1\,\text{ft}}\right)^2$$

$$= 1.04\,\text{tonf/ft}^2$$

d. $$p = 100\,\text{kPa} = 100\frac{\text{kN}}{\text{m}^2}\left(\frac{1\,\text{lbf}}{9.807\,\text{N}}\right)\left(\frac{1000\,\text{N}}{\text{kN}}\right)\left(\frac{\text{m}}{100\,\text{cm}}\right)^2$$

$$= 1.02\,\text{kgf/cm}^2$$

Note: The exact conversion for kgf to N is 9.806 65.

e. $$p = 100\,\text{kPa} = 100\,\text{kPa}\left(\frac{1\,\text{bar}}{10^5\,\text{Pa}}\right)\left(\frac{10^3\,\text{Pa}}{1\,\text{kPa}}\right) = 1\,\text{bar}$$

f. $$p = 100\,\text{kPa} = 100\frac{\text{kN}}{\text{m}^2}\left(\frac{1\,\text{kgf}}{9.807\,\text{N}}\right)\left(\frac{1000\,\text{N}}{\text{kN}}\right)\left(\frac{1\,\text{tonf}}{1000\,\text{kgf}}\right)$$

$$= 10.2\,\text{metric tonf/m}^2$$

g. For p in mm of mercury, we need to remember or look up the density of Hg. It is 13.6 g/cm^3. Also recall from hydrostatics that $p = \gamma z = \rho g z$, where z is the depth of the fluid. Thus for pressure in cm of mercury, $z = p/\rho g$. So

$$z = 100\frac{\text{kN}}{\text{m}^2}\left(\frac{1000\text{ N}}{\text{kN}}\right)\left(\frac{\text{cm}^3}{13.6\text{ g}}\right)\left(\frac{1000\text{ g}}{\text{kg}}\right)\left(\frac{\text{m}}{100\text{ cm}}\right)^3\left(\frac{\text{s}^2}{9.807\text{ m}}\right)\left(\frac{1000\text{ mm}}{\text{m}}\right)$$

$$= 750\text{ mm Hg}$$

h. Again, use $z = p/\rho g$

$$z = 100\frac{\text{kN}}{\text{m}^2}\left(\frac{1000\text{ N}}{\text{kN}}\right)\left(\frac{\text{m}^3}{1000\text{ kg}}\right)\left(\frac{\text{s}^2}{9.807\text{ m}}\right)\left(\frac{1\text{ ft}}{0.3048\text{ m}}\right)$$

$$= 33.5\text{ ft of water}$$

i. $$z = 100\frac{\text{kN}}{\text{m}^2}\left(\frac{1000\text{ N}}{\text{kN}}\right)\left(\frac{\text{m}^3}{1000\text{ kg}}\right)\left(\frac{\text{s}^2}{9.807\text{ m}}\right)$$

$$= 10.2\text{ m of water}$$

Density and Unit Weight Density is defined as mass per unit volume. Its units in the SI metric system are kilograms per cubic metre, kg/m^3. In many cases, it may be more convenient to express density in megagrams per cubic metre, Mg/m^3. Conversions from the common laboratory and field densities are:

$$1\text{ lb-mass/ft}^3 = 16.018\text{ kg/m}^3$$

$$1\text{ g/cm}^3 = 10^3\text{ kg/m}^3 = 1\text{ Mg/m}^3 = 1\text{ t/m}^3$$

You will recall that the density of water, ρ_w, is exactly 1.000 g/cm^3 at 4°C, and the variation is relatively small over the range of temperatures encountered in ordinary engineering practice. Therefore it is usually sufficiently accurate to take $\rho_w = 10^3$ kg/m^3 = 1 Mg/m^3, which simplifies phase computations considerably. It is also useful to know that 1000 kg/m^3 is equal to 62.4 lb-mass/ft^3.

Typical densities that might be encountered in geotechnical practice are 1.2 Mg/m^3(74.8 lb/ft^3), 1.6 Mg/m^3(100 lb/ft^3), and 2.0 Mg/m^3(125 lb/ft^3). Ranges of different densities are also listed in Table 2.1. The commonly used density for concrete, 150 lb/ft^3, is almost exactly 2.4 Mg/m^3.

You should note that not all mass and volume ratios common in geotechnical engineering practice are affected by the use of SI units. For example, void ratio or water content of any given soil still has the same numerical value.

Unit weight or weight per unit volume is still the common measurement in geotechnical engineering practice. However, since weight should be avoided in technical work for all the reasons discussed earlier, then unit weight also should be avoided. ASTM recommends that density be used in place of unit weight. If you must convert from density to unit weight, then simply use $\gamma = \rho g$, which means you will have to consider the appropriate value for the acceleration due to gravity. The "standard" value of g is 9.807 m/s^2 (32.17 ft/s^2), which, as mentioned previously, can be used with sufficient accuracy for ordinary engineering work for most places on this earth. If you ever have a job on the moon or some other planet, then you must use the local value for g. Keep in mind, also, to be very careful which "pounds" you are working with, lbf or lbm, in these conversions.

Example A.5

Given:

The density of water is 1000 kg/m^3.

Required:

The density of water in (a) g/cm^3 and (b) lb/ft^3.

Solution: Set up an equation as follows:

a. $$1000\frac{\text{kg}}{\text{m}^3} = 1000\frac{\text{kg}}{\text{m}^3}\left(\frac{1000\text{ g}}{1\text{ kg}}\right)\left(\frac{1\text{ m}}{100\text{ cm}}\right)^3 = 1\frac{\text{g}}{\text{cm}^3}$$

b. $$1000\frac{\text{kg}}{\text{m}^3} = 1000\frac{\text{kg}}{\text{m}^3}\left(\frac{1\text{ lbm}}{0.4536\text{ kg}}\right)\left(\frac{0.3048\text{ m}}{1\text{ ft}}\right) = 62.43\frac{\text{lbm}}{\text{ft}^3}$$

Another way to do part **b** is to recall that 1 lbm/ft^3 = 16.018 kg/m^3, so

$$1000\frac{\text{kg}}{\text{m}^3} = 1000\frac{\text{kg}}{\text{m}^3}\left(\frac{1\text{ lbm/ft}^3}{16.018\text{ kg/m}^3}\right) = 62.43\frac{\text{lbm}}{\text{ft}^3}$$

Example A.6

Given:

Density of water, ρ_w = 1000 kg/m^3.

Required:

Convert this density to unit weight in (a) SI and (b) British engineering units.

Solution:

a. SI units: We know that $\gamma = \rho g$, so

$$\gamma = 1000\frac{\text{kg}}{\text{m}^3}\left(9.807\frac{\text{m}}{\text{s}^2}\right) = 9807\frac{\text{kg}\cdot\text{m}}{\text{m}^3\cdot\text{s}^2}$$

Recall that $1\text{ N} = 1\dfrac{\text{kg}\cdot\text{m}}{\text{s}^2}$

$$\therefore\quad \gamma = 9807\frac{\text{N}}{\text{m}^3} = 9.807\frac{\text{kN}}{\text{m}^3}$$

b. British engineering units: From Example A.5, we know that

$$1000\frac{\text{kg}}{\text{m}^3} = 62.43\frac{\text{lbm}}{\text{ft}^3}$$

$$\gamma = 62.43\frac{\text{lbm}}{\text{ft}^3}\left(32.17\frac{\text{ft}}{\text{s}^2}\right) = 2008\frac{\text{lbm}\cdot\text{ft}}{\text{s}^2\cdot\text{ft}^3}$$

If lbf are used, from part **a**,

$$\gamma = 9.8\frac{\text{kN}}{\text{m}^3}\left(\frac{1000\text{ N}}{1\text{ kN}}\right)\left(\frac{1\text{ lbf}}{4.448\text{ N}}\right)\left(\frac{0.3048\text{ m}}{1\text{ ft}}\right)^3$$
$$= 62.4\frac{\text{lbf}}{\text{ft}^3}$$

This is the commonly used value for the unit weight of fresh water.

Example A.7

Given:

A soil has a dry density of 1.7 Mg/m^3.

Required:

Convert this density into unit weights, in terms of both (a) SI and (b) British engineering units.

Solution:

a. SI units:

$$\rho_d = 1.7\text{ Mg/m}^3 = 1700\text{ kg/m}^3$$
$$\gamma = \rho g$$
$$\gamma = 1700\frac{\text{kg}}{\text{m}^3}\left(9.81\frac{\text{m}}{\text{s}^2}\right) = 16677\frac{\text{N}}{\text{m}^3} = 16.7\frac{\text{kN}}{\text{m}^3}$$

b. British engineering units, in terms of lbm:

$$\rho = 1700\frac{\text{kg}}{\text{m}^3}\left(\frac{1\text{ lbm/ft}^3}{16.018\text{ kg/m}^3}\right) = 106.13\frac{\text{lbm}}{\text{ft}^3}$$
$$\gamma = \rho g$$
$$\gamma = 106.13\frac{\text{lbm}}{\text{ft}^3}\left(32.17\frac{\text{ft}}{\text{s}^2}\right) = 3414\frac{\text{lbm}\cdot\text{ft}}{\text{s}^2\cdot\text{ft}^3}$$

In terms of lbf: From part **a**,

$$\gamma = 16.7\frac{\text{kN}}{\text{m}^3}\left(\frac{1000\text{ N}}{1\text{ kN}}\right)\left(\frac{1\text{ lbf}}{4.448\text{ N}}\right)\left(\frac{0.3048\text{ m}}{1\text{ ft}}\right)^3$$
$$= 106.3\text{ lbf/ft}^3$$

The latter value in terms of lbf is, of course, the more familiar figure.

Geostatic Stress For computations of geostatic stresses, the unit weights of the various soil layers can be easily replaced by the ρg of the layers. The usual formula

$$\sigma_v = \sum_{i=1}^{n}\gamma_i z_i$$

then becomes

$$\sigma_v = \sum_{i=1}^{n} \rho_i g z_i \tag{6.14c}$$

where σ_v = total vertical stress at some depth,
ρ_i = density of each layer,
z_i = thickness of each layer, and
g = acceleration of gravity.

If ρg is a constant throughout the depth h, then

$$\sigma_v = \rho g h \tag{6.14b}$$

By analogy, computation of the static pore water pressure u_o at some depth h_w below the groundwater table is

$$u_o = \rho_w g h_w \tag{6.15}$$

where ρ_w = the density of water (1 Mg/m^3).

Similarly, to obtain the effective vertical overburden stress, the effective or buoyant density ρ' for each layer below the groundwater table can be used or, perhaps more simply, $\sigma'_{vo} = \sigma_{vo} - u_o$.

Dimensional analysis of these equations for stress shows that if the densities are expressed in Mg/m^3, then stresses automatically result in kPa, or

$$\left(\frac{\text{Mg}}{\text{m}^3}\right)\left(\frac{\text{m}}{\text{s}^2}\right)\text{m} = 1000\frac{\text{kg}\cdot\text{m}}{\text{s}^2\cdot\text{m}^2} = 1000\frac{\text{N}}{\text{m}^2} = 1\ \text{kPa}$$

Several examples of geostatic stress computations using SI units can be found in Chapter 6.

Systems of units are constantly evolving. For example, Snedegar (1983) proposed a new system where length = 1 far, mass = 1 lump, and force = 1 shove. Because linear acceleration = 1 far/s^2, 1 shove = 1 lump far/s^2. Pressure or stress is called 1 gasp defined as 1 shove/far^2. Modulus of elasticity for most engineering materials would thus be expressed in gigagasps.

APPENDIX B.1

Derivation of Laplace's Equation

As mentioned in Sec. 7.7, a flow net is actually a graphical solution of Laplace's equation, Eq. (7.18). The assumptions necessary for the derivation of this equation are:

$S = 100\%$,
e = constant [i.e., no consolidation (Chapter 8) or compression of the medium occurs],
k is isotropic,
Darcy's law [Eq. (7.5)] is valid.

Consider the flow of water into an element with dimensions dx and dy (Fig. B.1.1). Two-dimensional flow is assumed here for simplicity; you could do the exact same thing in three dimensions, but it would just be more complicated. The term $(\partial v_x/\partial x)\,dx$ indicates the *rate of change* in velocity v_x in the x-direction; similarly, $(\partial v_y/\partial y)\,dy$ is the rate of change in v_y in the y-direction. From continuity, we know that q = constant = $VA_{in} = VA_{out}$. So

$$VA_{in} = v_x dy + v_y dx$$

$$VA_{out} = \left(v_x + \frac{\partial v_x}{\partial x}dx\right)dy + \left(v_y + \frac{\partial v_y}{\partial y}dy\right)dx$$

If we set these two equations equal, we get

$$\frac{\partial v_x}{\partial x}dx\,dy + \frac{\partial v_y}{\partial y}dx\,dy = 0$$

or

$$\frac{\partial v_x}{\partial x} + \frac{\partial v_y}{\partial y} = 0 \tag{B.1.1}$$

since dx and dy cannot be zero.

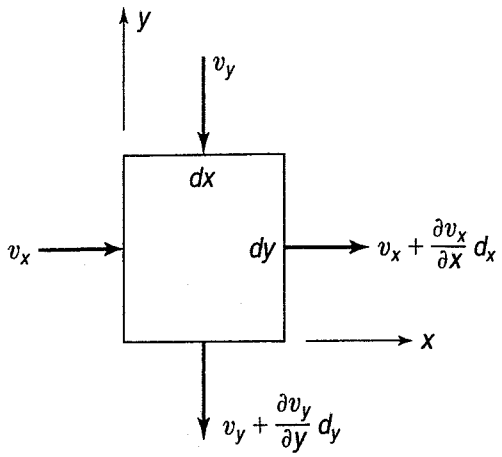

FIGURE B.1.1 Flow into and out of an element *dx* by *dy*.

From Darcy's law [Eqs. (7.2) and (7.5)], $v = ki = k\,\Delta h/L$. Thus we can write for our element:

$$v_x = k_x \frac{\partial h}{\partial x}, \qquad v_y = k_y \frac{\partial h}{\partial y}$$

Substituting these terms into Eq. (B.1.1) we obtain

$$k_x \frac{\partial^2 h}{\partial x^2} + k_y \frac{\partial^2 h}{\partial y^2} = 0$$

Since k was assumed to be isotropic, $k_x = k_y$. So we have

$$\frac{\partial^2 h}{\partial x^2} + \frac{\partial^2 h}{\partial y^2} = 0 \tag{7.18}$$

which is *Laplace's equation in two dimensions.* For the equation in three dimensions, simply add the term $\partial^2 h/\partial z^2$ to Eq. (7.18).

APPENDIX B.2

Derivation and Solution of Terzaghi's One-Dimensional Consolidation Theory

B.2.1 ASSUMPTIONS

To develop the Terzaghi one-dimensional consolidation theory, we need to assume the following:

1. The clay is homogeneous and 100% saturated.
2. Drainage is provided at both the top and bottom of the compressible layer.
3. Darcy's law [Eq. (7.5)] is valid.
4. The soil grains and water are incompressible.
5. Compression and flow are one-dimensional.
6. The small load increment applied produces essentially no change in thickness (that is, small strains), and k and a_v remain constant.
7. There is a *unique* linear relationship between the volume change Δe and the effective stress $\Delta\sigma'$. In other words, $de = -a_v\, d\sigma'$ and a_v is assumed constant over the increment of applied stress. This important assumption also implies that there is *no secondary compression.*

B.2.2 DERIVATION

Now let us borrow a little element from Fig. 9.1(f) and enlarge it in Fig. B.2.1. Our element exists at a depth z below the top of the compressible layer, has thickness dz, and has an area dx times dy. The volume change of the element is the difference between the amount of flow in and out of the element. Since consolidation under these conditions is directly dependent on the escape of pore water from the soil voids, we may develop the consolidation equation by considering the continuity of flow in our element. The hydraulic gradient i_z at the top of our element is given by

$$i_z = \frac{\text{head loss}}{\text{distance}} = \frac{\partial}{\partial z}\left(\frac{u}{\rho_w g}\right) = \frac{1}{\rho_w g}\frac{\partial u}{\partial z} \tag{B.2.1}$$

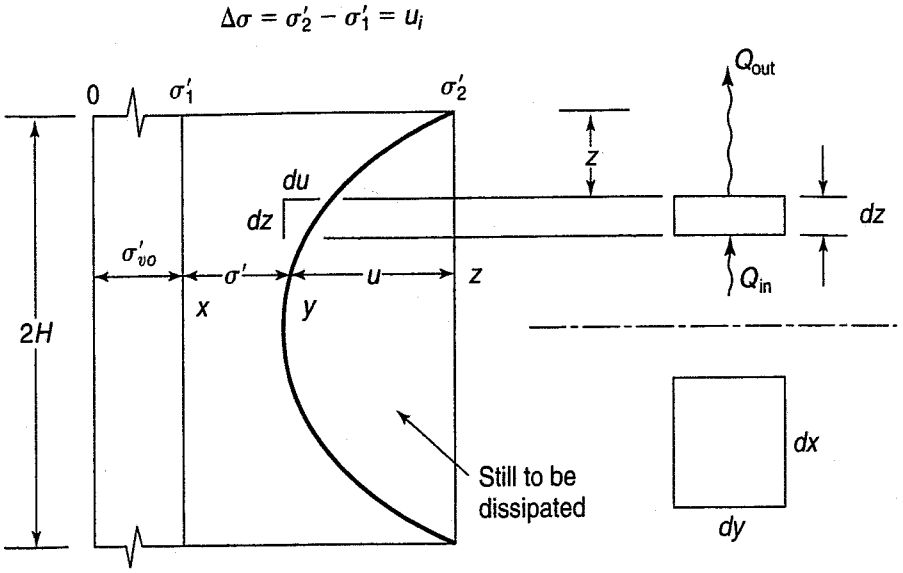

FIGURE B.2.1 Soil layer undergoing compression, similar to Fig. 9.1(f).

The corresponding hydraulic gradient at the bottom of our element dz is given by

$$i_{z+dz} = \frac{1}{\rho_w g}\frac{\partial u}{\partial z} + \frac{1}{\rho_w g}\frac{\partial^2 u}{\partial z^2}dz \tag{B.2.2}$$

From Darcy's law, $dQ = kia\,dt$, we may compute the quantity of flow dQ in time dt out of the top of our element by

$$dQ_{out} = k\frac{1}{\rho_w g}\frac{\partial u}{\partial z}dz\,dx\,dy\,dt \tag{B.2.3}$$

Likewise we may compute the quantity of flow in time dt at the bottom into the element by

$$dQ_{in} = k\frac{1}{\rho_w g}\left(\frac{\partial u}{\partial z} + \frac{\partial^2 u}{\partial z^2}\right)dz\,dx\,dy\,dt \tag{B.2.4}$$

We can now compute the volume change from the difference in rates of flow, $Q_{out} - Q_{in}$. Also we assume the area $dx\,dy$ to be a unit area. Therefore

$$\text{volume change} = dQ_{out} - dQ_{in} = -\frac{k}{\rho_w g}\frac{\partial^2 u}{\partial z^2}1\,dz\,dt \tag{B.2.5}$$

The volume change may also be determined from the laboratory consolidation test. Remember, from Chapter 8, that we would obtain a laboratory curve similar to Fig. 8.4, which we again show as Fig. B.2.2. From Eqs. (8.5a) and (b), the coefficient of compressibility a_v is

$$a_v = -\frac{de}{d\sigma'} = \frac{e_1 - e_2}{\sigma_2' - \sigma_1'} \tag{B.2.6}$$

To be correct, we should write these equations in terms of effective stresses. From Fig. B.2.2, you can see that the slope of the e–σ' curve is negative, and you know that e_1 is numerically larger than e_2.

From Eq. (8.4), $s = \Delta e H_o/(1 + e_o)$, or in terms of our element in Fig. B.2.1 and the e–σ' relationship in Fig. B.2.2, we obtain

$$s = \Delta dz = \frac{-de}{1 + e_1}dz \tag{B.2.7}$$

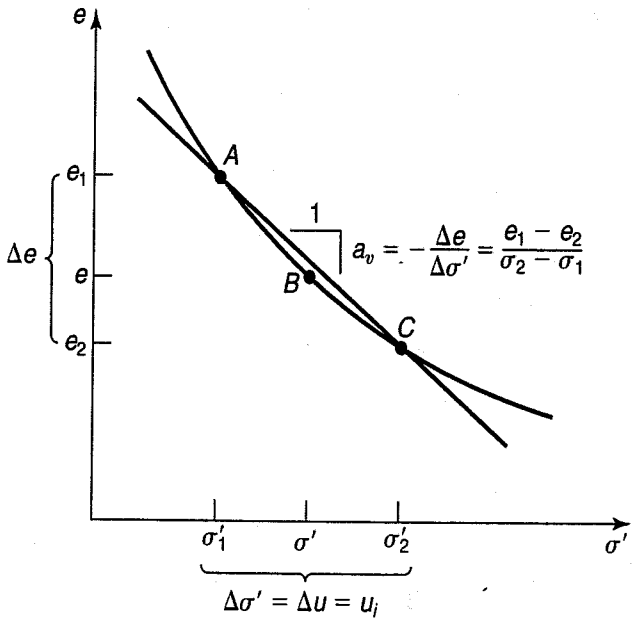

FIGURE B.2.2 Laboratory compression curve (same as Fig. 9.2).

where e_1 corresponds to the initial void ratio e_o. From Eq. (B.2.6), $-de = a_v\, d\sigma'$. Therefore

$$\Delta dz = \frac{a_v\, d\sigma'}{1 + e_1} dz \tag{B.2.8}$$

Now, from our discussion in Chapter 9, we know that as the excess pore water pressure dissipates, the effective stress in the soil skeleton increases. This is shown schematically in Figs. 9.1(c) and (f). Thus we can write that $\Delta\sigma' = -\Delta u$, because any *change* in effective stress is numerically equal to the negative of the change in excess pore water pressure. This relationship is true, of course, as long as the total stress does not change. Now, Eq. (B.2.8) can be written as

$$\Delta dz = -\frac{a_v\, du}{1 + e_1} dz \tag{B.2.9}$$

and since $du = (\partial u/\partial t)\, dt$, Eq. (B.2.9) becomes

$$\Delta dz = \frac{-a_v}{1 + e_1} \frac{\partial u}{\partial t} dt\, dz \tag{B.2.10}$$

By equating the volume change obtained in Eq. (B.2.5) and the volume change in Eq. (B.2.10), we have

$$-\frac{k}{\rho_w g} \frac{\partial^2 u}{\partial z^2} dz\, dt = -\frac{a_v}{1 + e_1} \frac{\partial u}{\partial t} dt\, dz \tag{B.2.11}$$

We can collect the soil properties terms as in Eq. (9.3),

$$c_v = \frac{k}{\rho_w g} \frac{1 + e_1}{a_v} \tag{9.3}$$

where c_v is called the *coefficient of consolidation*, since it governs the consolidation process. Note that it has units of L^2T^{-1}. We thus obtain

$$c_v \frac{\partial^2 u}{\partial z^2} = \frac{\partial u}{\partial t} \tag{9.2}$$

Equation (9.2) is the Terzaghi *one-dimensional consolidation equation.* If we assume c_v is a constant with respect to time and position, then Eq. (9.2) is a second-order partial differential equation with constant coefficients. There are a variety of ways to solve such equations; some are mathematically exact, others are only approximate. For example, Harr (1966) presents an approximate solution using the method of finite differences. Taylor (1948), following Terzaghi (1925a), provides a mathematically rigorous solution in terms of a Fourier series expansion. The development that follows is adapted from Taylor (1948) and Leonards (1962).

B.2.3 MATHEMATICAL SOLUTION

The boundary and initial conditions for the case of one-dimensional consolidation are as follows:

1. There is complete drainage at the top and bottom of the compressible layer.
2. The initial *excess* hydrostatic pressure $\Delta u = u_i$ is equal to the applied increment of stress at the boundary, $\Delta\sigma$. These boundary and initial conditions can be written

   when $z = 0$ and when $z = 2H$, $\quad u = 0$

   when $t = 0$, $\quad u = u_i = \Delta\sigma = (\sigma_2' - \sigma_1')$

The general solution of Eq. (9.2), when the initial excess pore pressure u_i is a function of the depth z, is

$$u = \sum_{n=1}^{n=\infty}\left(\frac{1}{H}\int_{z=0}^{z=2H} u_i \sin\frac{n\pi z}{2H}\,dz\right)\sin\frac{n\pi z}{2H}\exp\left(\frac{-c_v t n^2\pi^2}{4H^2}\right) \tag{B.2.12}$$

When u_i is a constant or varies linearly with depth, the solution becomes

$$u = (\sigma_2' - \sigma_1')\sum_{n=0}^{\infty}\frac{4}{(2n+1)\pi}\sin\left(\frac{2n+1}{2}\pi\underbrace{\frac{z}{H}}_{Z}\right) \times \exp -\left[\frac{(2n+1)^2}{4}\pi^2\underbrace{\frac{k(1+e_1)}{a_v\rho_w g}}_{c_v}\frac{t}{H^2}\right] \tag{B.2.13}$$

where σ_1' = initial effective stress, $\sigma_2' = \sigma_1' + \Delta\sigma$, and $n = 0, 1, 2, 3, \ldots$. The solution provides the instantaneous value of the pore water pressure u at any specified time and point in the soil mass. The only part of Eq. (B.2.13) that is a function of the soil properties is c_v.

You can see that the solution is in terms of two dimensionless quantities, Z and T—or, as we wrote in Eq. (9.4),

$$u = (\sigma_2' - \sigma_1')\sum_{n=0}^{\infty} f_1(Z) f_2(T) \tag{9.4}$$

You will recall that the dimensionless quantity T is called the *time factor*, and it is related to c_v [Eqs. (9.5) and (9.6)] by

$$T = c_v\frac{t}{H_{\text{dr}}^2} = \frac{k(1+e_o)}{a_v\rho_w g}\frac{t}{H_{\text{dr}}^2} \tag{B.2.14}$$

In this equation H_{dr} is the longest drainage path a drop of water has to follow in a compressible soil deposit to get to a free draining boundary. In Fig. B.2.1 you can see that the height of a doubly drained layer is $2H$. Therefore the drainage path H_{dr} is equal to H. If we had only a singly drained layer, we would consider only the top half of Fig. B.2.1, and again the drainage path would be the height of H.

The *consolidation ratio* U_z relates the change in volume at depth z and time t to the ultimate volume change at depth z, or

$$U_z = \frac{\text{volume change at depth } z \text{ and time } t}{\text{ultimate volume change at depth } z} \tag{B.2.15}$$

The change in volume, of course, means a change in void ratio, or, as we wrote in Eq. (9.7),

$$U_z = \frac{e_1 - e}{e_1 - e_2} \tag{9.7}$$

The changes in void ratio can be related to the stress increment through the coefficient of consolidation a_v. These relationships are shown in Fig. B.2.2. Because, in one-dimensional consolidation, the initial excess hydrostatic (pore) pressure is equal to the increment of applied stress, Eq. (9.7) becomes

$$U_z = \frac{\sigma' - \sigma_1'}{\sigma_2' - \sigma_1'} = \frac{\sigma' - \sigma_1'}{\Delta\sigma'} = \frac{u_i - u}{u_i} = 1 - \frac{u}{u_i} \tag{9.8}$$

Now we can write our solution to the consolidation equation [Eq. (9.4)] as in Eq. (9.9), or

$$U_z = 1 - \sum_{n=0}^{\infty} f_1(Z) f_2(T) \tag{9.9}$$

This equation is shown graphically in Fig. 9.3, and we explain in Chapter 9 how to use this figure to obtain the amount of consolidation at any depth and time in the consolidating layer (see Examples 9.1 and 9.2).

Generally in engineering practice we are interested in the volume change of the entire soil layer. So we want the *average degree or percent consolidation U*, which is defined as

$$U(\%) = \frac{\text{total volume change at time } t}{\text{ultimate total volume change}} \times 100\,(\%) \tag{B.2.16}$$

For one-dimensional compression, the change in volume is, of course, equal to the change in height of the layer. To obtain the average degree of consolidation over the entire layer we have to find the area under the curve corresponding to a given time factor in Fig. 9.3; this is shown in Fig. 9.5. Mathematically, $U(\%)$ = average value of U_z, or

$$U(\%) = \frac{\Sigma U_z\, dz}{2H} = \frac{1}{2H}\int_0^{2H} U_z\, dz \tag{B.2.17}$$

or from Fig. B.2.1,

$$U(\%) = \frac{\displaystyle\int_0^{2H} xy}{\displaystyle\int_0^{2H} xz} = \frac{\displaystyle\int_0^{2H} [(\sigma_2' - \sigma_1') - u]\, dz}{(\sigma_2' - \sigma_1')2H} \times 100 \tag{B.2.18}$$

Rewriting,

$$U(\%) = \frac{100}{2H(\sigma_2' - \sigma_1')}\int_0^{2H} [(\sigma_2' - \sigma_1') - u]\, dz \tag{B.2.19}$$

or

$$U(\%) = \frac{100}{2H(\sigma_2' - \sigma_1')}\left[\int_0^{2H} (\sigma_2' - \sigma_1')\, dz \int_0^{2H} u\, dz\right] \tag{B.2.20}$$

Substituting the value of u from Eq. (B.2.13) into Eq. (B.2.20) and integrating, we obtain:

$$U(\%) = \frac{100}{2H(\sigma_2' - \sigma_1')}\left[(\sigma_2' - \sigma_1')2H - (\sigma_2' - \sigma_1')\sum_{n=0}^{\infty}\frac{4}{(2n+1)\pi}\right.$$
$$\times (-1)\cos\frac{(2n+1)\pi}{2H}z\left(\frac{2H}{(2n+1)\pi}\right)$$
$$\left.\times \exp -\left(\frac{(2n+1)^2\pi^2}{4}T\right)\right|_0^{2H}\Bigg] \qquad \text{(B.2.21)}$$

Putting in the limits, we obtain

$$U(\%) = 100\left\{1 - \sum_{n=0}^{\infty}\frac{4}{(2n+1)^2\pi^2}(-1)(-1-1) \times \exp -\left[\frac{(2n+1)^2\pi^2}{4}T\right]\right\} \qquad \text{(B.2.22)}$$

or

$$U\,(\%) = 100\left\{1 - \sum_{n=0}^{\infty}\frac{8}{(2n+1)^2\pi^2} \times \exp -\left[\frac{(2n+1)^2\pi^2}{4}T\right]\right\} \qquad \text{(B.2.23)}$$

This solution is for the special case of constant or linear initial hydrostatic excess pressure and is valid for all values of U. Solutions for other initial pore pressure distributions are provided by Taylor (1948) and Leonards (1962), but the differences are negligible for practical purposes. The summation indicated by Eq. (B.2.23) can be carried out once and for all and tabulated (Table 9.1) or shown graphically (Fig. 9.5). Casagrande (1938) and Taylor (1948) give the following approximations for Eq. (B.2.23), which are useful to know:

For $U < 60\%$,

$$T = \frac{\pi}{4}U^2 \qquad (9.10)$$

For $U < 60\%$,

$$T = 1.781 - 0.933 \log (100 - U\%) \qquad (9.11)$$

For values of $U > 60\%$, the series in Eq. (B.2.23) converges extremely rapidly, so that only the first term is significant. Therefore, letting $n = 0$, Eq. (B.2.23) becomes

$$U(\%) = 100\left[1 - \frac{8}{\pi^2}\exp\left(-\frac{\pi^2}{4}T\right)\right] \qquad \text{(B.2.24)}$$

Rearranging, Eq. (B.2.24) gives Eq. (9.11).

APPENDIX B.3

Pore Pressure Parameters

B.3.1 DERIVATION OF SKEMPTON'S PORE PRESSURE EQUATION

The pore pressure parameters (Secs. 12.17 and 13.3), first defined by Skempton (1954), relate the change in pore water pressure to the change in *total* stress during undrained loading.

First, let's derive Eq. (12.15). This can be done in several ways. One simple way is to assume for a start that we have a triaxial specimen in equilibrium with the cell pressure σ_c acting on it. Assume for the moment that the soil skeleton is elastic and isotropic, and that there are both air and water in the voids (that is, $S < 100\%$). Now, when we apply a small change in the cell pressure $\Delta\sigma_c$ to the sample, by Terzaghi's principle of effective stress [Eq. (6.8)], the *change* in effective stress is

$$\Delta\sigma'_c = \Delta\sigma_c - \Delta u$$

The volume change ΔV caused by this change in stress is

$$\Delta V - C_{sk}V_o(\Delta\sigma'_c) = C_{sk}V_o(\Delta\sigma_c - \Delta u)$$

where C_{sk} is the compressibility of the soil skeleton and V_o is the original volume of the sample.

As mentioned in Chapter 8, the mineral grains themselves are relatively incompressible, so any decrease in the volume of the soil skeleton results in a decrease in volume of the voids, or

$$\Delta V = -V_v C_v \Delta u = -nV_o C_v \Delta u \tag{B.3.1}$$

where n is the porosity, and C_v is the compressibility of the pore fluid (air + water). If $S = 100\%$, then $C_v = C_w$, the compressibility of water. If we allow no drainage to occur, then these two changes in volume must be equal, or

$$-nV_o C_v \Delta u = -C_{sk}V_o(\Delta\sigma_c - \Delta u)$$

Solving for the ratio $\Delta u/\Delta\sigma_c$, we obtain Eq. (12.15):

$$\frac{\Delta u}{\Delta\sigma_c} = \frac{1}{1 + \dfrac{nC_v}{C_{sk}}} = B \tag{12.15}$$

where $\Delta\sigma_c = \Delta\sigma_3$. We discussed in Sec. 12.17 the values of B for different soils and test conditions (see Table 12.8). A more general way to obtain Eq. (12.15) is shown later in this appendix.

We can follow a similar development for the change in pore pressure due to the change in the principal stress difference or shear stress in our triaxial test specimen in order to derive Eqs. (12.17 through 12.19). Assume that the soil skeleton still behaves elastically; then the volume change caused by the change in effective stresses is

$$\Delta V = -C_{sk} V_o \frac{1}{3}(\Delta\sigma_1' + \Delta\sigma_2' + \Delta\sigma_3')$$

The symbols were previously defined. For the common triaxial compression test, $\Delta\sigma_2 = \Delta\sigma_3$, so

$$\Delta V = -C_{sk} V_o \frac{1}{3}(\Delta\sigma_1' + 2\Delta\sigma_3')$$

The coefficient $1/3$ comes about because for elastic isotropic materials the volume change is due to the *average* of the changes in the three principal stresses. Now add and subtract $3\Delta\sigma_3$ to the right-hand side of the equation, and invoke Terzaghi's principle of effective stress. We then obtain

$$\Delta V = -C_{sk} V_o \frac{1}{3}(\Delta\sigma_1 - \Delta\sigma_3 + 3\Delta\sigma_3 - 3\Delta u)$$

As before, the decrease in voids is

$$\Delta V = -nV_o C_v \Delta u \tag{B.3.1}$$

For undrained conditions, the two volumes must be equal. Solving for Δu and noting that

$$B = \frac{1}{1 + \dfrac{nC_v}{C_{sk}}} \tag{12.15}$$

we obtain

$$\Delta u = B\left[\Delta\sigma_3 + \frac{1}{3}(\Delta\sigma_1 - \Delta\sigma_3)\right] \tag{B.3.2}$$

Note that the coefficient $1/3$ for the stress difference term is for elastic materials and triaxial compression conditions. If we make a similar derivation for *triaxial extension* conditions ($\Delta\sigma_2 = \Delta\sigma_1$), we get

$$\Delta u = B\left[\Delta\sigma_3 + \frac{2}{3}(\Delta\sigma_1 - \Delta\sigma)\right] \tag{B.3.3}$$

(Note that you have to add and subtract $2\Delta\sigma_3$ in this case.) Thus for elastic soil skeletons, the pore pressure parameter in extension is twice that in compression.

Since soils in general are inelastic materials, Skempton (1954) replaced the two constants in Eqs. (B.3.2) and (B.3.3) by the coefficient A, so that

$$\Delta u = B\left[\Delta\sigma_3 + A(\Delta\sigma_1 - \Delta\sigma_3)\right] \tag{12.17}$$

Often it is convenient to write Eq. (12.17) as

$$\Delta u = B\Delta\sigma_3 + \overline{A}(\Delta\sigma_1 - \Delta\sigma_3) \tag{12.19}$$

where $\overline{A} = BA$. For saturated soils, we usually write Eq. (12.17) as

$$\Delta u = \Delta\sigma_3 + A(\Delta\sigma_1 - \Delta\sigma_3) \tag{12.18}$$

Other convenient ways to write the pore pressure equation (12.17) are given by Skempton (1954). For triaxial compression conditions,

$$\Delta u = B\left[\frac{1}{3}(\Delta\sigma_1 + 2\Delta\sigma_3) + \frac{3A-1}{3}(\Delta\sigma_1 - \Delta\sigma_3)\right] \tag{B.3.4}$$

and for triaxial extension conditions,

$$\Delta u = B\left[\frac{1}{3}(2\Delta\sigma_1 + \Delta\sigma_3) + \frac{3A-2}{3}(\Delta\sigma_1 - \Delta\sigma_3)\right] \tag{B.3.5}$$

These equations show that if soils behaved as perfectly elastic materials (that is, $A = 1/3$ in compression and $A = 2/3$ in extension), then the pore pressure would depend only on the average change in principal stress, which is the first part of Eqs. (B.3.4) and (B.3.5).

B.3.2 DEFINITION OF $\Delta\sigma_1$ AND $\Delta\sigma_3$ FOR ROTATION OF PRINCIPAL STRESSES

Law and Holtz (1978) showed that contradictory definitions of the pore pressure parameter A exist in the literature because of the lack of a consistent definition of principal stress increment for cases where the principal stresses rotate. They proposed the following system, to take care of any possible ambiguities when the principal stresses rotate 90°.

In this system, $\Delta\sigma_1$ and $\Delta\sigma_3$ are called the *major and minor principal stress increments*, respectively. A principal stress increment is defined as the maximum or minimum normal stress increment imposed on a given stress system. The sign convention is positive for compression and negative for tension. $\Delta\sigma_1$ is the *algebraically largest* normal component of a given system of stress increments, and $\Delta\sigma_3$ is the *algebraically smallest* normal component of that system.

The advantage of this system is that the stress increment is not connected to the original stress. Thus the direction of $\Delta\sigma_1$ is *independent* of the direction of the original or final σ_1, and so is $\Delta\sigma_3$. This point is illustrated in Table B.3.1, which shows some combinations of $\Delta\sigma_1$ and $\Delta\sigma_3$ being applied to typical existing stress systems represented by σ_1 and σ_3.

B.3.3 FORMULAS FOR PORE PRESSURE PARAMETERS FOR DIFFERENT STRESS PATH TESTS

To aid in calculating the correct value of the parameter A, Law and Holtz (1978) derived the appropriate expressions for A for the four types of triaxial stress path tests, AC, AE, LC, and LE (Secs. 13.2 and 13.4). These are shown in Table B.3.2. The derivation of these expressions is shown in the following example.

TABLE B.3.1 Examples Using the Proposed New Definition of Principal Stress Increments (units of stress are arbitrary, and axisymmetry in stress system is assumed)

Initial Stress System	Stress Increment	Final Stress State	$\Delta\sigma_1$		$\Delta\sigma_3$	
			Magnitude	Direction	Magnitude	Direction
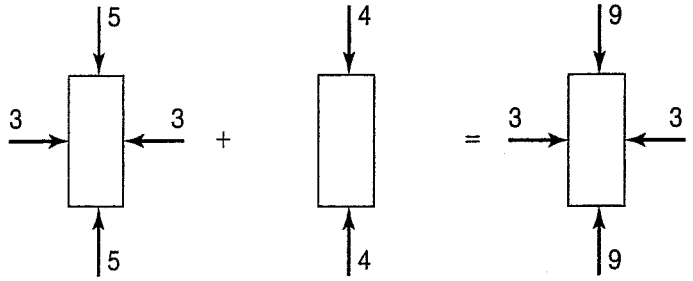			4	V[a]	0	H[a]
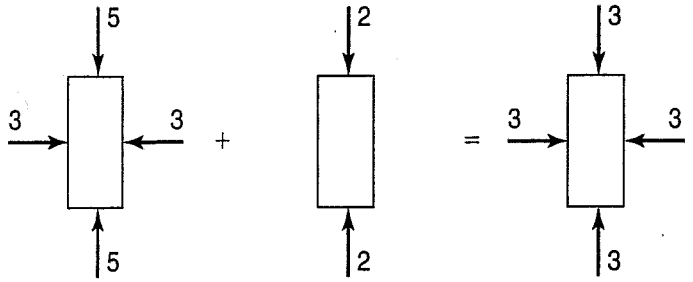			0	H	−2	V
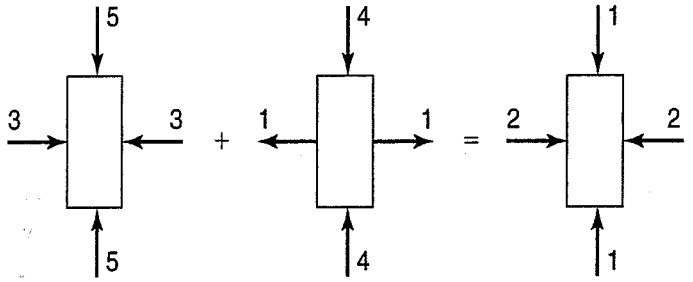			−1	H	−4	V

[a]V = Vertical: H = Horizontal.

After Law and Holtz (1978).

TABLE B.3.2 Definition of Principal Stress Increments and Formulas for Pore Pressure Parameters for Various Types of Triaxial Tests

Test Type	$\Delta\sigma_1$	$\Delta\sigma_2$	$\Delta\sigma_3$	Formula for A	Equation
Compression test:					
Axial compression, AC	$\Delta\sigma_v$	0	0	$A_{ac} = \Delta u/\Delta\sigma_v$	13.9
Lateral extension, LE	0	$\Delta\sigma_h$	$\Delta\sigma_h$	$A_{le} = 1 - \Delta u/\Delta\sigma_h$	13.10
Extension test:					
Axial extension, AE	0	0	$\Delta\sigma_v$	$A_{ae} = 1 - \Delta u/\Delta\sigma_v$	13.11
Lateral compression, LC	$\Delta\sigma_h$	$\Delta\sigma_h$	0	$A_{lc} = \Delta u/\Delta\sigma_h$	13.12

After Law and Holtz (1978).

Example B.3.1

Given:

An axial extension (AE) triaxial test is conducted on a saturated clay.

Required:

Determine the correct formula for the pore pressure parameter A.

Solution: In the AE test, the lateral (cell) pressure remains constant while the axial stress is decreased. Therefore

$$\Delta\sigma_1 = \sigma_2 = 0, \qquad \Delta\sigma_3 = \Delta\sigma_v$$

According to the definition of principal stress increments proposed by Law and Holtz (1978), $\Delta\sigma_v$ is negative, since it decreases. Thus it is algebraically the smallest component of the stress increment. Substituting these definitions for $\Delta\sigma_1$ and $\Delta\sigma_3$ into Eq. (12.17) (assume $B = 1$), we obtain

$$A_{ae} = 1 - \frac{\Delta u}{\Delta\sigma_v} \tag{13.11}$$

This formula is the same as shown for the AE test in Table B.3.2.

B.3.4 PROOF THAT $A_{ac} = A_{le}$ AND $A_{ae} = A_{lc}$

It was shown by example in Sec. 13.4 that the pore pressure parameter A was the same in axial compression (AC) as in lateral extension (LE). It was inferred that A in axial extension (AE) was identical to A in lateral compression (LC). The statements are true even though these sets of tests have different total stress paths. The proof of this contention was given by Law and Holtz (1978).

We first define $p' = (\sigma_1' + \sigma_3')/2$ as the average of the major and minor effective stresses, and $q = (\sigma_1 - \sigma_3)/2$ as half the principal stress difference (Sec. 13.2). We can express the slope at any point on the effective stress path in a p'–q diagram as

$$\left(\frac{dq}{dp'}\right) = \frac{d(\sigma_1 - \sigma_3)}{d(\sigma_1 + \sigma_3 - 2u)}$$

For the axial compression case $d\sigma_1 = d\sigma_v$ and $d\sigma_3 = 0$. Hence

$$\left(\frac{dq}{dp'}\right)_{ac} = \frac{1}{1 - 2A_{ac}}$$

For the lateral extension case $d\sigma_1 = 0$ and $d\sigma_3 = d\sigma_1$. Hence

$$\left(\frac{dq}{dp'}\right)_{le} = \frac{-1}{1 - 2(1 - A_{le})} = \frac{1}{1 - 2A_{le}}$$

Since both tests have the same effective stress paths (see, for example, Example 13.6) then

$$\left(\frac{dq}{dp'}\right)_{ac} = \left(\frac{dq}{dp'}\right)_{le}$$

Hence

$$A_{ac} = A_{le} \tag{13.13}$$

Similarly, we can show that

$$A_{ae} = A_{lc} \tag{13.14}$$

B.3.5 DERIVATION OF THE HENKEL PORE PRESSURE EQUATION AND COEFFICIENTS[1]

Assume an element of soil in equilibrium with stresses σ_1, σ_2, and σ_3 on it. When we apply stress increments $\Delta\sigma_1$, $\Delta\sigma_2$, and $\Delta\sigma_3$ to the element, an excess pore pressure Δu and a resulting change in effective stresses occur. So,

$$\Delta\sigma_1' = \Delta\sigma_1 - \Delta u, \quad \Delta\sigma_2' = \Delta\sigma_2 - \Delta u, \quad \Delta\sigma_3' = \Delta\sigma_3 - \Delta u$$

Assume for now that the soil skeleton is elastic and isotropic. Thus it has a bulk modulus $K_{sk} = E/3(1 - 2\nu)$. Since the definition of bulk modulus is the volumetric effective stress $\frac{1}{3}(\sigma_1' + \sigma_2' + \sigma_3')$ divided by the volumetric strain $\Delta V/V_o$,

$$K_{sk} = \frac{\frac{1}{3}(\sigma_1' + \sigma_2' + \sigma_3')}{\Delta V/V_o} = \frac{E}{3(1 - 2\nu)}$$

Rearranging, the volumetric strain of the soil skeleton is

$$\frac{\Delta V}{V_o} = \varepsilon_1 + \varepsilon_2 + \varepsilon_3 = C_{sk}\left(\frac{\sigma_1' + \sigma_2' + \sigma_3'}{3}\right)$$

where $C_{sk} = 1/K_{sk}$ is called the *compressibility of soil skeleton*, and ε_1, ε_2, and ε_3 are principal strains. Since E and ν are difficult to determine for a real soil, the general coefficient C_{sk} is more practical (Scott, 1963). Now, if we state this equation in terms of total stress changes and pore pressure, we have

$$\frac{\Delta V}{V_o} = C_{sk}\left(\frac{\Delta\sigma_1 + \Delta\sigma_2 + \Delta\sigma_3}{3} - \Delta u\right)$$

This equation states that the volumetric strain is a function only of the change in mean effective stress for a *linearly elastic* material (or, in fact, for any nondilative, no-volume-change-during-shear material). However, soils do change volume due to the change in shear stress, and this is accounted for by an empirical correction factor, $D|\Delta\tau_{oct}|$, where $|\Delta\tau_{oct}|$ is the absolute value of the *increment* in τ_{oct}. Thus we have

$$\frac{\Delta V}{V_o} = C_{sk}[\Delta\sigma_{oct} - u] + D|\Delta\tau_{oct}| \tag{B.3.6}$$

[1]After Scott (1963) and Perloff and Baron (1976).

because, by definition from continuum mechanics,

$$\sigma_{oct} = \frac{\sigma_1 + \sigma_2 + \sigma_3}{3} \tag{13.16}$$

and

$$\tau_{oct} = \frac{1}{3}\sqrt{(\sigma_1 - \sigma_2)^2 + (\sigma_2 - \sigma_3)^2 + (\sigma_3 - \sigma_1)^2} \tag{13.17}$$

As Perloff and Baron (1976) point out, since τ_{oct} is a nonlinear function of the principal stress differences, we cannot in general calculate it directly from the stress increments. Instead, we must determine $\Delta\tau_{oct}$ from the difference $(\tau_{oct})_2 - (\tau_{oct})_1$.

Now, as we did in Sec. B.3.1, let us look at what happens to the voids. The volumetric strain in the voids is

$$\frac{\Delta V_v}{V_v} = -C_v \Delta u \tag{B.3.1}$$

where C_v is the compressibility of the voids, and V_v, the volume of voids, is nV_o. If $S = 100\%$, then $C_v = C_w$, the compressibility of water. And if no change in volume is permitted (that is, undrained conditions prevail), then setting Eq. (B.3.1) equal to Eq. (B.3.6) and solving for Δu, we have

$$\Delta u = \frac{1}{1 + n\left(\frac{C_v}{C_{sk}}\right)}\left[(\Delta\sigma_{oct}) + \frac{D}{C_{sk}}|\Delta\tau_{oct}|\right] \tag{B.3.7}$$

Since soils are not linearly elastic materials, as before we use empirical coefficients which are to be determined by experiment,

$$B = \frac{1}{1 + \frac{nC_v}{C_{sk}}} \tag{12.15}$$

and

$$a = \frac{D}{C_{sk}} \tag{B.3.8}$$

So, Eq. (B.3.5) becomes

$$\Delta u = B(\Delta\sigma_{oct} + \Delta\tau_{oct}) \tag{13.15}$$

The coefficient a is the *Henkel pore pressure* parameter.

Although this derivation for Eq. (13.15) is rather elegant mathematically, it may be easier to simply write the equation as

$$\Delta u = B\frac{\Delta\sigma_1 + \Delta\sigma_2 + \Delta\sigma_3}{3} + \frac{a}{3}\sqrt{(\Delta\sigma_1 - \Delta\sigma_2)^2 + (\Delta\sigma_2 - \Delta\sigma_3)^2 + (\Delta\sigma_3 - \Delta\sigma_1)^2} \tag{B.3.9}$$

This latter formulation is more consistent with the definition of principal stress increments presented in Sec. B.3.2. With this definition, a systematic separation of the stress increments from the initial and final stress states is possible.

Equations (12.17) and (B.3.9) are useful, since they allow the separation of pore pressure effects observed in soils into two components—those due to (1) the change in mean or average stress, and (2) the change in shear stress.

The Henkel parameter a is, like the Skempton parameter A, nonlinear and must be determined for each stress path. It is also very dependent on strain, on the magnitude of σ_2, on the overconsolidation ratio, and on material properties such as anisotropy. The parameters a and B are for *general* changes in total stress. They enable the engineer to predict the pore pressure if the changes in the total stresses are known or can be estimated; therefore, they can be very useful in engineering practice.

Sometimes in the geotechnical literature the Henkel parameters are denoted by the symbol α, where $\alpha = a/3$. In this case, Eq. (B.3.9) would be

$$\Delta u = B\frac{\Delta\sigma_1 + \Delta\sigma_2 + \Delta\sigma_3}{3} + \alpha\sqrt{(\Delta\sigma_1 - \Delta\sigma_2)^2 + (\Delta\sigma_2 - \Delta\sigma_3)^2 + (\Delta\sigma_3 - \Delta\sigma_1)^2} \quad \text{(B.3.10)}$$

This is the way Henkel (1960) originally wrote his equation, but with the symbol a for α. Thus Henkel's original a or α was one-third our a. Later Henkel and Wade (1966) suggested the notation used herein, along with Eq. (13.15).

It is often useful to be able to convert between the Henkel parameter a and the Skempton parameter A. For the special case of triaxial compression (AC), $\sigma_2 = \sigma_3$ and $S = 100\%(B = 1)$, we have

$$\Delta\sigma_{oct} = \frac{1}{3}(\Delta\sigma_1 + 2\Delta\sigma_3)$$

and

$$\Delta\tau_{oct} = \frac{\sqrt{2}}{3}(\Delta\sigma_1 - \Delta\sigma_3)$$

so [Eq. (13.15)]

$$\Delta u = \frac{1}{3}(\Delta\sigma_1 + 2\Delta\sigma_3) + a\frac{\sqrt{2}}{3}(\Delta\sigma_1 - \Delta\sigma_3)$$

but since $\Delta\sigma_2 = \Delta\sigma_3 = 0$ (constant cell pressure) and $\Delta\sigma_1 = \Delta\sigma_v$,

$$\Delta u = \left(\frac{1}{3} + a\frac{\sqrt{2}}{3}\right)\Delta\sigma_v$$

From Eq. (12.17) and for triaxial compression conditions in Table B.3.2, we know that $A_{ac} = \Delta u/\Delta\sigma_v$. Therefore,

$$A_{ac} = \frac{1}{3} + a\frac{\sqrt{2}}{3} \quad \text{(13.18a)}$$

For the lateral extension (LE) test, $\sigma_2 = \sigma_3$, and Eq. (13.15) becomes

$$\Delta u = \frac{1}{3}(\Delta\sigma_1 + 2\Delta\sigma_3) + a\frac{\sqrt{2}}{3}(\Delta\sigma_1 - \Delta\sigma_3)$$

But since $\Delta\sigma_1 = 0$ and $\Delta\sigma_2 = \Delta\sigma_3 = \Delta\sigma_h$,

$$\Delta u = \frac{2}{3}\Delta\sigma_h - a\frac{\sqrt{2}}{3}\Delta\sigma_h = \left(\frac{2}{3} - a\frac{\sqrt{2}}{3}\right)\Delta\sigma_h$$

From Eq. (12.17) and Table B.3.2, we know that $A_{le} = 1 - \Delta u/\Delta\sigma_h$. Therefore,

$$A_{le} = 1 - \frac{2}{3} + a\frac{\sqrt{2}}{3} = \frac{1}{3} + a\frac{\sqrt{2}}{3} \tag{13.18b}$$

which is the same as Eq. (13.18a). This result should not be unexpected, since we have already shown that $A_{ac} = A_{le}$ [Eq. (13.13)].

For the case of axial extension (AE), $\sigma_2 = \sigma_1$, and Eq. (13.15) becomes

$$\Delta u = \frac{1}{3}(2\Delta\sigma_1 + \Delta\sigma_3) + a\frac{\sqrt{2}}{3}(\Delta\sigma_1 - \Delta\sigma_3)$$

But since $\Delta\sigma_1 = \Delta\sigma_2 = 0$ and $\Delta\sigma_3 = \Delta\sigma_v$,

$$\Delta u = \frac{1}{3}\Delta\sigma_v - a\frac{\sqrt{2}}{3}\Delta\sigma_v = \left(\frac{1}{3} - a\frac{\sqrt{2}}{3}\right)\Delta\sigma_v$$

From Eq. (12.17) and Table B.3.2, we know that $A_{ae} = 1 - \Delta u/\Delta\sigma_v$. Therefore,

$$A_{ae} = 1 - \frac{1}{3} + a\frac{\sqrt{2}}{3} = \frac{2}{3} + a\frac{\sqrt{2}}{3} \tag{13.19a}$$

For the lateral compression (LC) test, $\sigma_2 = \sigma_1$, so Eq. (13.15) becomes

$$\Delta u = \frac{1}{3}(2\Delta\sigma_1 + \Delta\sigma_3) + a\frac{\sqrt{2}}{3}(\Delta\sigma_1 - \Delta\sigma_3)$$

Since $\Delta\sigma_1 = \Delta\sigma_2 = \Delta\sigma_h$ and $\Delta\sigma_3 = 0$, we have

$$\Delta u = \left(\frac{2}{3} + a\frac{\sqrt{2}}{3}\right)\Delta\sigma_h$$

From Eq. (12.17) and Table B.3.2, we know that $A_{lc} = \Delta u/\Delta\sigma_h$. Therefore

$$A_{lc} = \frac{2}{3} + a\frac{\sqrt{2}}{3} \tag{13.19b}$$

As expected [Eq. (13.14)], $A_{ae} = A_{lc}$.

Note that for elastic materials, $A_{ac} = A_{le} = 1/3$ and $A_{ae} = A_{lc} = 2/3$, and $a = 0$. In general, since $A_{ac} \neq A_{lc}$, then the a parameters are not necessarily the same for the two cases, primarily because the compressibility of the soil skeleton C_{sk} is not the same in compression as in extension.

APPENDIX C

The Method of Fragments

The *method of fragments* (Sec. 7.7.3) presents a useful and rapid, although approximate, analytical design method for the solution of confined flow problems. After you learn the procedure, many cases may be investigated in little more than the time it usually takes to assemble paper, pencils, and erasers for drawing flow nets. The method originated with Pavlovsky (1956) and was brought to the attention of the western world by Harr (1962). Its basic assumption is that the equipotential lines at selected critical points in a flow net are *vertical* and that they divide the flow net into *fragments*. Table C.1 summarizes fragment types and form factors.

Perhaps the best way to illustrate the procedure is by an example. If you are interested in the theory behind the method, consult Harr (1962 and 1977).

Example C.1

Given:

The dam with the same data as in Example 7.15 (shown in Fig. Ex. C.1a).

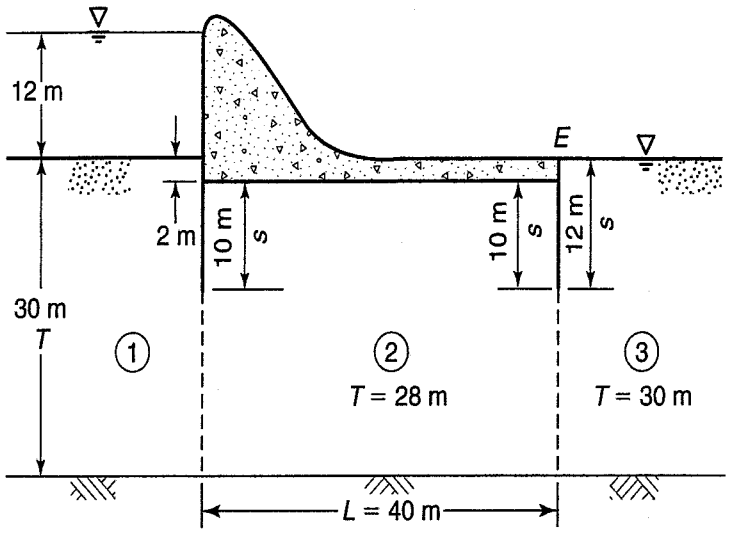

FIGURE Ex. C.1a

TABLE C.1 Summary of Fragment Types and Form Factors

Fragment Type	Illustration	Form Factor, Φ (h is head loss through fragment)
I	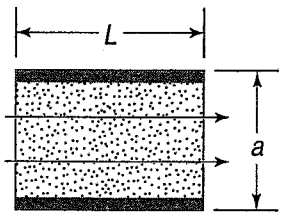	$\Phi = \frac{L}{a}$
II	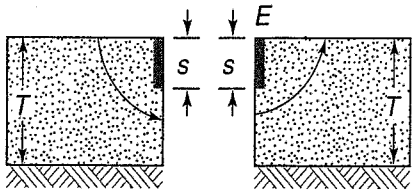	$\Phi = \frac{1}{2}\left(\frac{kh}{Q}\right)$ $i_E = \frac{h_m \pi}{2KTm}$ See also Fig. C.1 and Table C.2
III	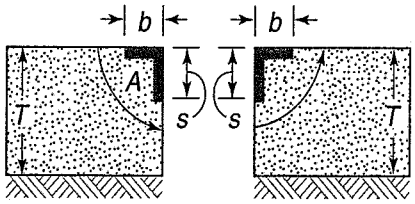	$\Phi = \frac{1}{2}\left(\frac{kh}{Q}\right)$ See also Fig. C.2 and Table C.2
IV	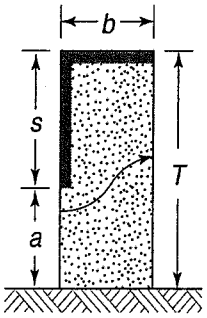 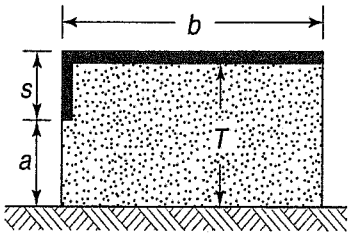	$s \geq b$: $\Phi = \ln\left(1 + \frac{b}{a}\right)$ $b \geq s$: $\Phi = \ln\left(1 + \frac{s}{a}\right) + \frac{b - s}{T}$
V	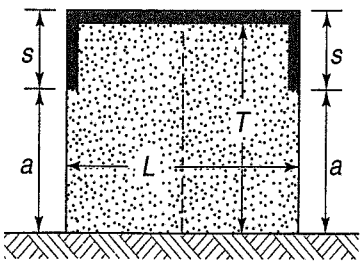	$L \leq 2s$: $\Phi = 2 \ln\left(1 + \frac{L}{2a}\right)$ $L \geq 2s$: $\Phi = 2 \ln\left(1 + \frac{s}{a}\right) + \left(\frac{L - 2s}{T}\right)$

Fragment Type	Illustration	Form Factor, Φ (h is head loss through fragment)
VI	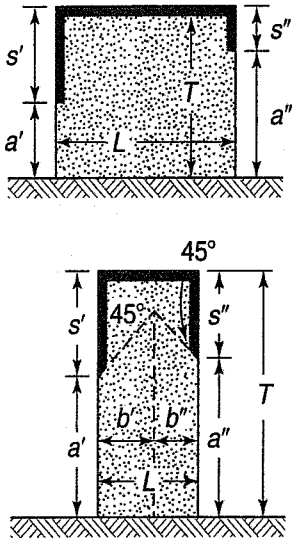	$L > s' + s''$: $\Phi = \ln\left[\left(1+\frac{s'}{a'}\right)\left(1+\frac{s''}{a''}\right)\right] + \frac{L-(s'+s'')}{T}$ $L = s' + s''$: $\Phi = \ln\left[\left(1+\frac{s'}{a'}\right)\left(1+\frac{s''}{a''}\right)\right]$ $L < s' + s''$ $\Phi = \ln\left[\left(1+\frac{b'}{a'}\right)\left(1+\frac{b''}{a''}\right)\right]$ where $b' = \frac{L+(s'-s'')}{2}$ $b'' = \frac{L-(s'-s'')}{2}$
VII	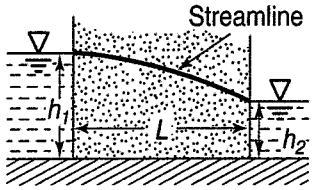	$\Phi = \frac{2L}{h_1 + h_2}$ $Q = k\frac{h_1^2 - h_2^2}{2L}$
VIII	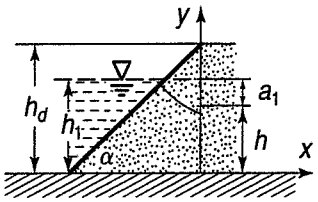	$Q = k\frac{h_1 - h}{\cot\alpha}\ \ln\frac{h_d}{h_d - h}$
IX	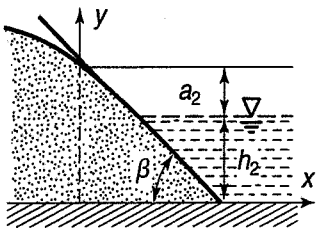	$Q = k\frac{a_2}{\cot\beta}\left(1 + \ln\frac{a_2 + h_2}{a_2}\right)$

*After Harr (1962, 1977).

Required:

By means of the method of fragments, compute:

a. The quantity of seepage loss under the dam when $k = 20 \times 10^{-4}$ cm/s, per metre of dam.

b. The exit gradient (at point E).

c. The pressure distribution on the base of the dam.

d. Compare these values with those obtained from the flow net in Example 7.15.

Solution:

a. Divide the flow system into fragments. The critical points chosen are the bottoms of the sheet piles. Refer to Table C.1 and review the fragments. The heavy lines represent impervious boundaries, which can be in vertical or horizontal directions. You choose the fragments to match the particular boundary conditions of your problem. Notice how the definitions of s and T are used. Their values are shown in Fig. Ex. C.1a. The vertical, dashed (equipotential) lines separate the flow regime into three fragments, as shown circled in the figure. Clearly, the flow q through each fragment must be the same and is stated by Eq. (7.19e). However, in the method of fragments this equation is changed slightly to

$$q = kh_L \frac{N_f}{N_d} = \frac{kh_m}{\Phi_m} \tag{C.1}$$

where h_m is the head loss in the mth fragment, where $m = 1, 2, 3, \ldots, n$, and Φ_m is the dimensionless *form factor* for the mth fragment. The form factor is equal to N_d/N_f.

In this example $h_L = 12\text{ m} = \sum h_m$, that is, the sum of the head loss in each fragment. Also, since the flow is equal in each fragment and is equal to the total flow, we have

$$\frac{q}{k} = h_1 \frac{N_f}{N_d} = h_2 \frac{N_f}{N_d} = h_3 \frac{N_f}{N_d} \tag{C.2}$$

or

$$\frac{q}{k} = \frac{h_1}{\Phi_1} = \frac{h_2}{\Phi_2} = \frac{h_3}{\Phi_3} = \frac{h}{\sum \Phi} \tag{C.3}$$

and, finally, the flow is

$$q = \frac{kh}{\sum_{m=1}^{n} \Phi} \tag{C.4}$$

The next step is to define the types of fragments for our problem and to determine the value of the form factors Φ for each fragment. Nine general types of fragments are shown in Table C.1, where the heavy lines represent impervious boundaries. Other fragments are also available in the literature. Also given are the values of Φ in terms of the geometry of each problem. If you study Fig. Ex. C.1a, you can see that fragments 1 and 3 are type II but fragment 2 is a type V fragment. Had the sheet piles been of different lengths, then fragment 2 would be a type VI instead of a type V fragment.

Next, we have to determine the form factors for our two types of fragments. For type II fragments, we see from Table C.1 that $\Phi = K/K'$. Both K and K' are functions of m, which is defined as

$$m = \sin \frac{\pi \cdot s}{2T} \tag{C.5}$$

where s = depth of the sheet pile, and
T = thickness of the soil layer.

Substituting the values for s and T of our example into Eq. (C.5), we find that

$$m = \sin\frac{\pi \cdot s}{2T} = \sin\frac{\pi}{2}\frac{12}{30} = 0.588$$

The value of K/K' can be found from Table C.2. For $m = 0.588$, $m^2 = 0.345$, so K/K' is equal to about 0.865 (by interpolation), which equals Φ_1. By inspection, Φ_1 is also equal to Φ_3. These values are tabulated in Table Ex. C.1.

TABLE Ex. C.1

Fragment	Type	Φ
1	II	$K/K' = 0.865$
2	V	1.598
3	II	$K/K' = 0.865$

For fragment 2, which is a type V, we need to compare L and $2s$ to obtain Φ. For our example, $L = 40$ m and $2s = 20$ m. Since $L > 2s$, Φ is given by

$$\Phi_2 = 2\ln\left(1 + \frac{s}{a}\right) + \frac{L - 2s}{T}$$

$$= 2\ln\left(1 + \frac{10}{18}\right) + \frac{40 - 2 \times 10}{28}$$

$$= 0.884 + 0.714 = 1.598$$

Note that the distance $a = 18$ m is the distance from the bottom impervious boundary to the bottom end of the sheet pile.

The quantity of flow is found from Eq. (C.4),

$$q = \frac{kh}{\sum_{m=1}^{n}\Phi} = \frac{20 \times 10^{-4}\dfrac{\text{cm}}{\text{s}}\left(\dfrac{\text{m}}{100\text{ cm}}\right)(12\text{ m})}{0.865 + 1.598 + 0.865}\text{ per metre}$$

$$= 7.21 \times 10^{-5}\text{ m}^2/\text{s per metre of dam}$$

$$= 8.65 \times 10^{-3}\text{ m}^3/\text{s for a dam 120 m long}$$

This compares satisfactorily with the value of 8.31×10^{-3} m^3/s obtained in Example 7.15.

An alternative way to determine the form factor is to use Fig. C.1. Since $s/T = 12/28 = 0.4$, find $1/(2\Phi)$ equal to 0.575 for $b/T = 0$. Solving for Φ, we obtain 0.87, which is close to our previously determined value of 0.865.

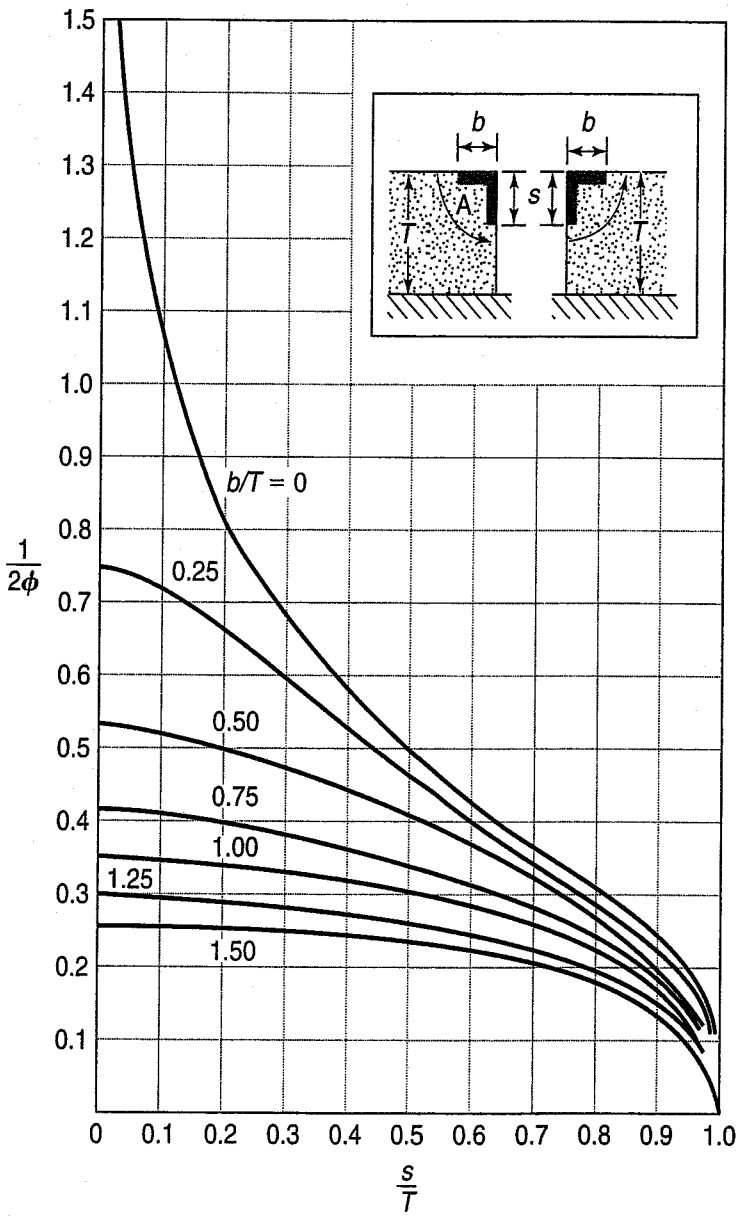

FIGURE C.1 Relationship between form factor Φ and *s*/*T* ratio for type II and type III fragments (after Harr, 1977).

b. Computation of the exit gradient i_E at point E is easy. From Table C.1, fragment type II, we find the formula for the exit gradient is

$$i_E = \frac{h\pi}{2KTm} \tag{C.6}$$

where the value of m is from Eq. (C.5) and equals 0.588; the value of h is the head loss in the third (exit) fragment. The value of K is found in Table C.2 for $m^2 = 0.345$; interpolating, $K = 1.741$. The value of h to use in Eq. (C.6) is the head loss in the *third fragment*, where the water exits, and it is from Eq. (C.3).

$$h_3 = \frac{\Phi_3 h}{\sum_{m=1}^{n} \Phi} = \frac{0.865 \times 12\text{ m}}{3.328} = 3.12\text{ m} \tag{C.7}$$

TABLE C.2 Values of Parameters Used for Types II and III Fragments Described in Table C.1

m^2	K	K'	K/K'	K'/K	m'^2	m^2	K	K'	K/K'	K'/K	m'^2
0.000	1.571	∞	0.000	∞	1.000	0.21	1.665	2.235	0.745	1.34	0.79
0.001	1.571	4.841	0.325	3.08	0.999	0.22	1.670	2.214	0.754	1.33	0.78
0.002	1.572	4.495	0.349	2.86	0.998	0.23	1.675	2.194	0.763	1.31	0.77
0.003	1.572	4.293	0.366	2.73	0.997	0.24	1.680	2.175	0.773	1.29	0.76
0.004	1.572	4.150	0.379	2.64	0.996	0.25	1.686	2.157	0.782	1.28	0.75
0.005	1.573	4.039	0.389	2.57	0.995	0.26	1.691	2.139	0.791	1.26	0.74
0.006	1.573	3.949	0.398	2.51	0.994	0.27	1.697	2.122	0.800	1.25	0.73
0.007	1.574	3.872	0.406	2.46	0.993	0.28	1.702	2.106	0.808	1.24	0.72
0.008	1.574	3.806	0.413	2.42	0.992	0.29	1.708	2.090	0.817	1.22	0.71
0.009	1.574	3.748	0.420	2.38	0.991	0.30	1.714	2.075	0.826	1.21	0.70
0.01	1.575	3.696	0.426	2.35	0.99	0.31	1.720	2.061	0.834	1.20	0.69
0.02	1.579	3.354	0.471	2.12	0.98	0.32	1.726	2.047	0.843	1.19	0.68
0.03	1.583	3.156	0.502	1.99	0.97	0.33	1.732	2.033	0.852	1.17	0.67
0.04	1.587	3.016	0.526	1.90	0.96	0.34	1.738	2.020	0.860	1.16	0.66
0.05	1.591	2.908	0.547	1.83	0.95	0.35	1.744	2.088	0.869	1.15	0.65
0.06	1.595	2.821	0.565	1.77	0.94	0.36	1.751	1.995	0.877	1.14	0.64
0.07	1.599	2.747	0.582	1.72	0.93	0.37	1.757	1.983	0.886	1.13	0.63
0.08	1.604	2.684	0.598	1.67	0.92	0.38	1.764	1.972	0.895	1.12	0.62
0.09	1.608	2.628	0.612	1.63	0.91	0.39	1.771	1.961	0.903	1.11	0.61
0.10	1.612	2.578	0.625	1.60	0.90	0.40	1.778	1.950	0.911	1.10	0.60
0.11	1.617	2.533	0.638	1.57	0.89	0.41	1.785	1.939	0.920	1.09	0.59
0.12	1.621	2.493	0.650	1.54	0.88	0.42	1.792	1.929	0.929	1.08	0.58
0.13	1.626	2.455	0.662	1.51	0.87	0.43	1.799	1.918	0.938	1.07	0.57
0.14	1.631	2.421	0.674	1.48	0.86	0.44	1.806	1.909	0.946	1.06	0.56
0.15	1.635	2.389	0.684	1.46	0.85	0.45	1.814	1.899	0.955	1.05	0.55
0.16	1.640	2.359	0.695	1.44	0.84	0.46	1.822	1.890	0.964	1.04	0.54
0.17	1.645	2.331	0.706	1.42	0.83	0.47	1.829	1.880	0.973	1.03	0.53
0.18	1.650	2.305	0.716	1.40	0.82	0.48	1.837	1.871	0.982	1.02	0.52
0.19	1.655	2.281	0.726	1.38	0.81	0.49	1.846	1.863	0.991	1.01	0.51
0.20	1.660	2.257	0.735	1.36	0.80	0.50	1.854	1.854	1.000	1.00	0.50
m'^2	K'	K	K'/K	K/K'	m^2	m'^2	K'	K	K'/K	K/K'	m^2

After Aravin and Numerov (1955).

Substituting these values and $m_3 = 0.588$ into Eq. (C.6), we obtain

$$i_E = \frac{3.12\ \text{m}(\pi)}{2 \times 1.741 \times 30\ \text{m} \times 0.588} = 0.16$$

This result compares well with the value of 0.14 found in Example 7.15.

An alternative procedure to find the exit gradient at point E is to use Fig. C.2. For this example, $s/T = 12/30 = 0.40$; enter the graph and find $(i_E \cdot s)/h_m = 0.6$. Solving for i_E, we find that

$$i_E = \frac{0.6h_m}{s} = \frac{0.6 \times 3.12\ \text{m}}{12\ \text{m}} = 0.16$$

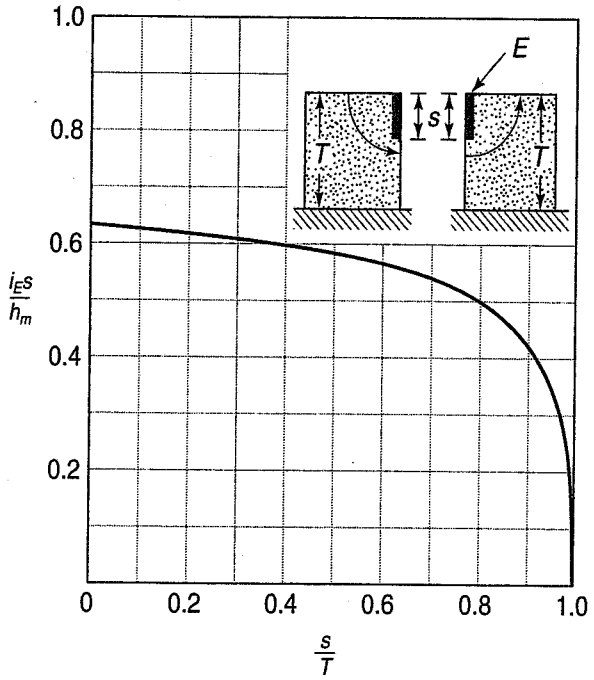

FIGURE C.2 Graph to evaluate the exit gradient i_E at point E for a type II fragment for a given s/T ratio (after Harr, 1977).

c. To compute the pressure distribution under the dam, we assume that the head loss varies *linearly* from fragment 1 to fragment 3.

Compute the head loss per fragment:

$$\sum \Phi = \Phi_1 + \Phi_2 + \Phi_3$$
$$= 0.865 + 1.598 + 0.865 = 3.328$$

The head loss per fragment is given by Eq. (C.7),

$$h_1 = \frac{\Phi_1 h}{\sum \Phi} = \frac{0.865 \times 12\text{ m}}{3.328} = 3.12\text{ m}$$

$$h_2 = \frac{\Phi_2 h}{\sum \Phi} = \frac{1.598 \times 12\text{ m}}{3.328} = 5.76\text{ m}$$

$$h_3 = h_1 \text{ due to symmetry}$$

Redraw the dam to scale and place the values of head at selected points (Fig. Ex. C.1b). At equipotential line A′, the head loss is $h_1 = 3.12$ m; the head loss is therefore

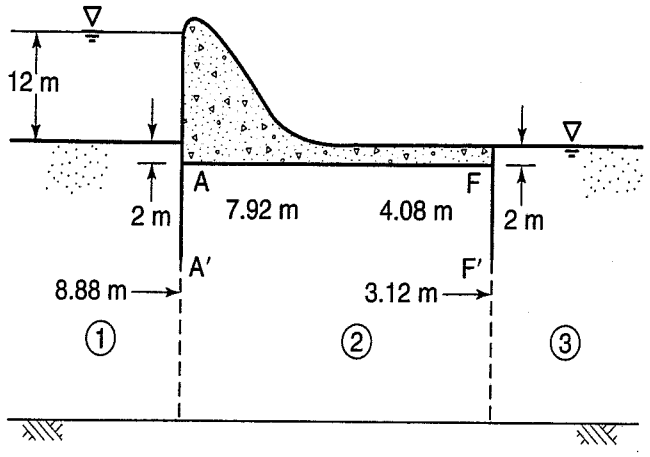

FIGURE Ex. C.1b

$h - h_1 = 12\text{ m} - 3.12\text{ m} = 8.88\text{ m}$. Similarly, at equipotential line F′, $h_2 = 5.76$ m. Therefore the head at F′ is

$$h - h_1 - h_2 = 12 - 3.12 - 5.76 = 3.12\text{ m}$$

Assuming that the head loss varies linearly from points A′ − A − F − F′, which is equal to the total distance of 10 m + 40 m + 10 m = 60 m, then the head loss per metre is h_2/60 m, or 5.76 m/60 m = 0.096 m/m. Thus the head at point A = the head at A′ − 10 m × 0.096 m per metre, or 8.88 − 10 × 0.096 = 7.92 m. Likewise, the head at F is 4.08 m.

To this head we add the tailwater head of 2 m. The vertical uplift pressures may now be computed, as shown in Fig. Ex. C.1c. These values compare almost exactly with those shown in Fig. Ex. 7.15.

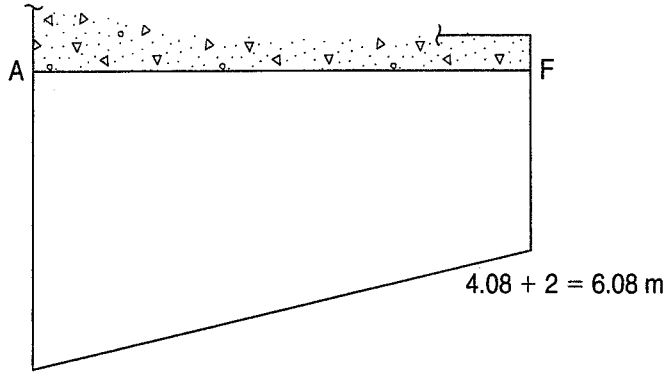

FIGURE Ex. C.1c

d. Comparison of values of flow, exit gradient, and uplift pressures as determined by the two different procedures are summarized in Table Ex. C.1b. If you look closely and round off, you will see that the two methods give about the same results. Analyzing with the MOF takes much less time than drawing a flow net or setting up and running a computational software solution!

TABLE Ex. C.1b

Parameter	From Flow Net	From Method of Fragments
q	8.31×10^{-3} m³/s	8.65×10^{-3} m³/s
i_E	0.14	0.16
Uplift pressures at A[a]	9.96 m	9.92 m
Uplift pressures at F[a]	6.04 m	6.08 m

[a]In metres of water.

Example C.2

Given:

Several cases of confined flow.

Required:

Identify the fragment types shown in Fig. Ex. C.2.

Solution:

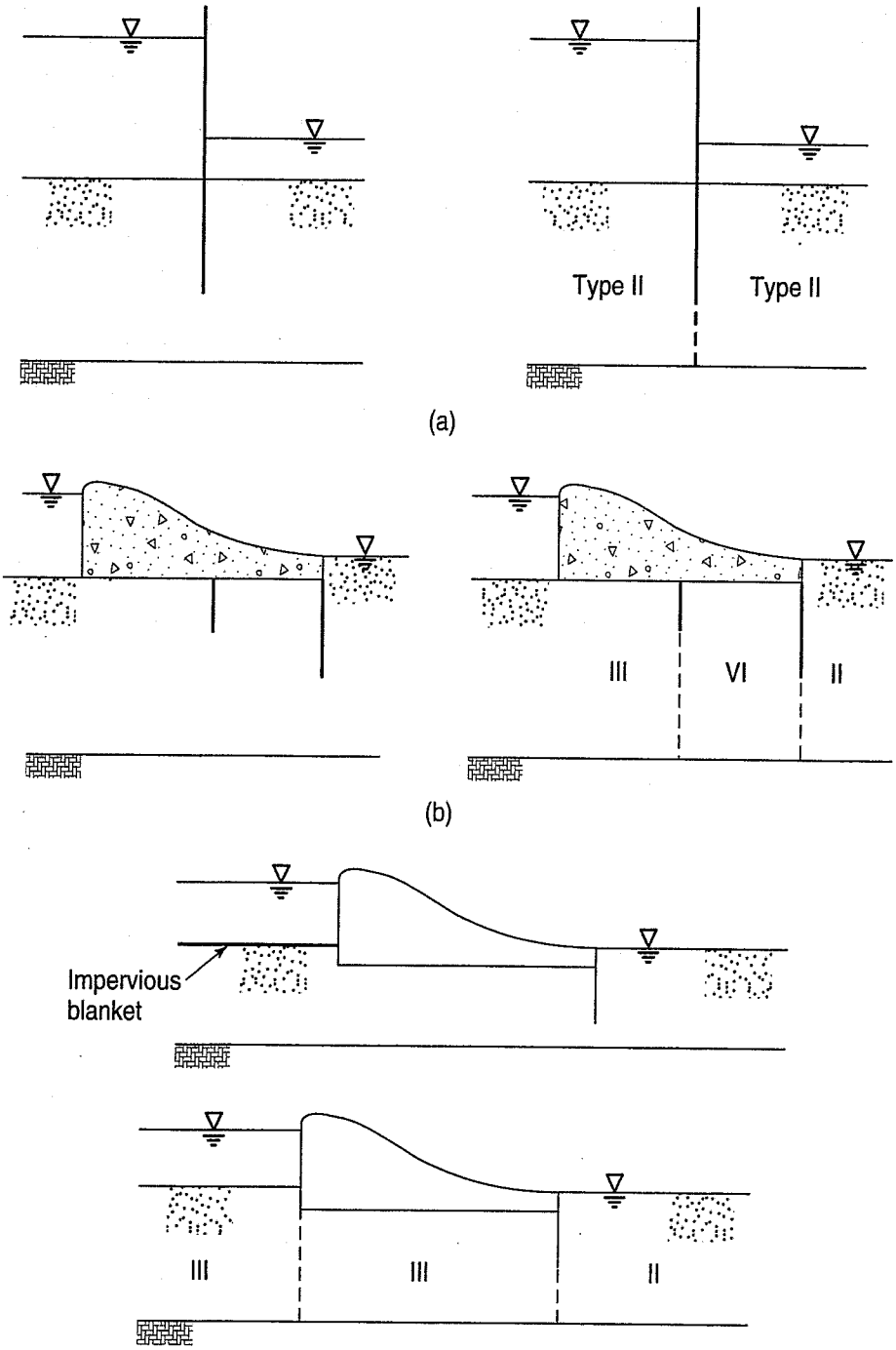

FIGURE Ex. C.2a, b, c

Example C.3

Given:

An impervious (relative to the foundation) earth dam with the dimensions shown in Fig Ex. C.3. The dam is underlain by a sand and gravel foundation soil with a permeability of 25,000 ft/yr.

Required:

Compute the length of an upstream impervious blanket to reduce the amount of seepage below the dam by one-half.

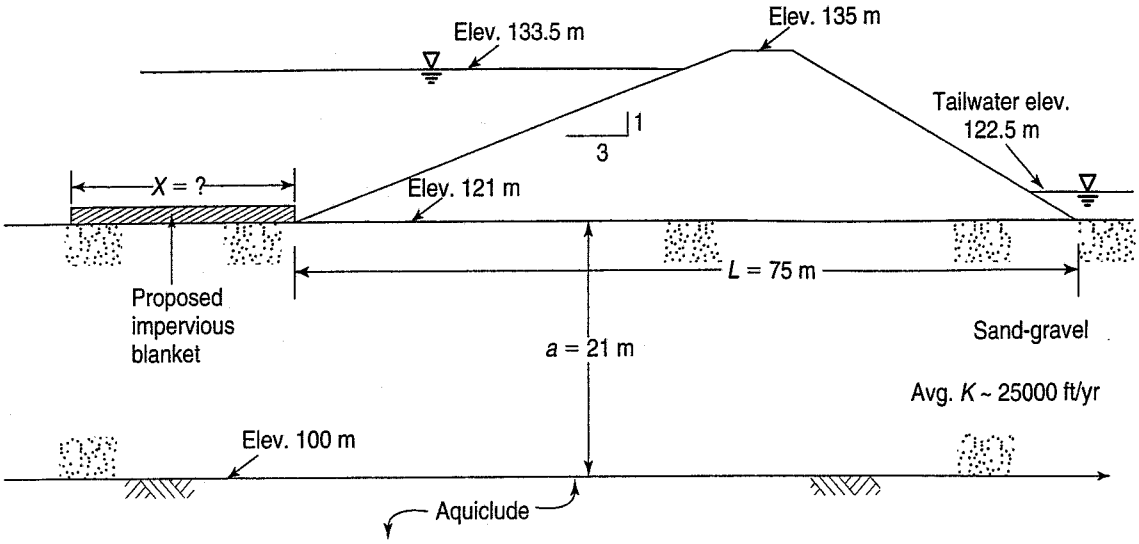

FIGURE Ex. C.3 (Modified after U.S. Dept. of Interior, 1987.)

Solution: First, change the k from ft/yr to m/sec

$$k = 25{,}000\frac{\text{ft}}{\text{yr}} \times (0.3048)\frac{\text{ft}}{\text{m}} \times 3.17098 \times 10^{-8}\frac{\text{yr}}{\text{sec}} = 2.42 \times 10^{-4}\frac{\text{m}}{\text{sec}}$$

Consulting Table C.1, we find that the problem is a Type I fragment, with

$$\Phi = \frac{L}{a} = \frac{75\text{ m}}{21\text{ m}} = 3.57$$

From Eq. (C.4),

$$q = \frac{kh}{\Phi} = \frac{2.42 \times 10^{-4}\dfrac{\text{m}}{\text{sec}} \times (133.5\text{ m} - 122.5\text{ m})}{3.57} = 7.46 \times 10^{-4}\frac{\text{m}}{\text{sec}}$$

To reduce the flow by one-half, Φ would have to be doubled. Because the distance a (the thickness of the pervious layer) remains the same, the length L would have to double. Obviously we don't want to make the dam larger, so the easiest way is to install an upstream impervious blanket with a length equal to 75 m, making the total length the water has to pass under the dam 150 m. Now, can you imagine how long it would have taken you to do this problem using flow nets?

It should be obvious now that the method of fragments is a powerful analytical and design technique. Solutions to many complex problems can be found quickly, whereas to solve a series of complex problems by means of flow nets would require a large amount of time. Take, for example, the problem illustrated by Example C.2c. A practical design question is: How long should the drainage blanket be to reduce the quantity of flow by one-third or to reduce the uplift pressures by one-half? Many trial and error flow net solutions would be required to solve the problem, whereas with the method of fragments the solution could be obtained directly!

References

Abbreviations

AASHTO – American Association of State Highway and Transportation Officials
AEG – Association of Engineering Geologists
ASCE – American Society of Civil Engineers
ASTM – American Society for Testing and Materials
BS – British Standard
BSCE – Boston Society of Civil Engineers
CFEM – Canadian Foundation Engineering Manual
CGS – Canadian Geotechnical Society
ESOPT – European Symposium on Penetration Testing
FHWA – Federal Highway Administration
IEEE – Institute of Electrical and Electronics Engineers
ISRM – International Society for Rock Mechanics
NCHRP – National Cooperative Highway Research Program
NGI – Norwegian Geotechnical Institute
TRB – Transportation Research Board
USA WES – U.S. Army Waterways Experiment Station

A

AASHTO (2010). *Standard Specifications for Transportation Materials and Methods of Sampling and Testing*, 30th ed., American Association for State Highway and Transportation Officials, Washington, D.C. Part I, Specifications, 828 p.; Part II, Tests, 998 p.

ABDELHAMID, M.S. AND KRIZEK, R.J. (1976). "At Rest Lateral Earth Pressure of a Consolidating Clay," *Journal of the Geotechnical Engineering Division*, ASCE, Vol. 102, No. GT7, pp. 721–738.

ABELEV, Y.M. (1957). "The Stabilization of Foundations of Structures on Loess Soils," *Proceedings of the Fourth International Conference on Soil Mechanics and Foundation Engineering*, London, Vol. I, pp. 259–263.

ADAMS, J. (1965). "The Engineering Behaviour of a Canadian Muskeg," *Proceedings of the Sixth International Conference on Soil Soil Mechanics and Foundation Engineering*, Montreal, Canada, Vol. 1, pp. 3–7.

AL-HUSSAINI, M.M. (1977). "Contribution to the Engineering Soil Classifications of Cohesionless Soils," *Final Report*, Miscellaneous Paper S-77–21, U.S. Army Engineer Waterways Experiment Station, Vicksburg, MS, 61 p.

AL-HUSSAINI, M.M. AND TOWNSEND, F.C. (1975). "Investigation of K_o Testing in Cohesionless Soils," *Technical Report S-75–11*, U.S. Army Engineer Waterways Experiment Station, Vicksburg, MS, 70 p.

ALPAN, I. (1967). "The Empirical Evaluation of the Coefficient K_o and K_{OR}," *Soils and Foundations*, Vol. VII, No. 1, pp. 31–40.

AMERICAN SOCIETY FOR TESTING AND MATERIALS [ASTM] (2010). *Annual Book of Standards*, Section 4, Construction, Vol. 4.08, Soil and Rock (I): D 420–D 4914; Vol. 4.09, Soil and Rock (II): D 4943–latest; Geosynthetics, West Conshohocken, PA.

AMERICAN SOCIETY OF PHOTOGRAMMETRY (1960). *Manual of Photographic Interpretation*, George Banta Co., Inc., Menahsa, WI, 868 p.

ANAGNOSTOPOLOUS, A., SCHLOSSER, F., KALTEZOITIS, N., AND FRANK, R. (Eds.) (1993). "Geotechnical Engineering of Hard Soils—Soft Rocks," *Proceedings of an International Symposium, Athens, Balkema*, 2 Vols., 1697 p.

ANDERSLAND, O.B. AND LADANYI, B. (1994). *An Introduction to Frozen Ground Engineering*, Chapman & Hall, New York, 352 p.

ANDERSLAND, O.B. AND LADANYI, B. (2004). *Frozen Ground Engineering*, 2nd ed., Wiley, New York, 363 p.

ARAVIN, V.I. AND NUMEROV, S. (1955). "Seepage Computations for Hydraulic Structures," *Stpoitel' stvu i Arkhitekture*, Moscow (referenced in Harr, 1962).

ARTHUR, J.R.F., BEKENSTEIN, S., GERMAINE, J.T., AND LADD, C.C. (1980). "Stress Path Tests with Controlled Rotation of Principal Stress Directions," *Laboratory Shear Strength of Soil*, ASTM Special Technical Publication 740, R.N. Yong and F.C. Townsend (Eds.), American Society for Testing and Materials, pp. 516–540.

ATKINSON, J.H. (2007). *The Mechanics of Soils and Foundations*, 2nd ed., E & FN Spon, London, 480 p.

ATKINSON, J.H. AND BRANSBY, P.L. (1978). *The Mechanics of Soils (An Introduction to Critical State Soil Mechanics)*, McGraw-Hill, 375 p.

ATTERBERG, A. (1905). "Die Rationelle Klassifikation der Sande und Kiese," *Chemiker-Zeitung*, Vol. 29, pp. 195–198.

ATTERBERG, A. (1911). "Lerornas Förhållande till Vatten, deras Plasticitetsgränser och Plasticitetsgrader," ("The Behavior of Clays with Water, their Limits of Plasticity and their Degrees of Plasticity"), *Kungliga Lantbruksakademiens Handlingar och Tidskrift*, Vol. 50, No. 2, pp. 132–158; also in *Internationale Mitteilungen für Bodenkunde*, Vol. 1, pp. 10–43 ("Über die Physikalische Bodenuntersuchung und über die Plastizität der Tone").

ATTERBERG, A. (1916). "Konsistensläran—En Ny Fysikalisk Lära" ("Consistency Science—A New Physical Science"), *The Swedish Journal of Chemistry*, Vol. 28, pp. 29–37.

AZIZ, F. (2000). *Applied Analysis in Geotechnics*, E & FN Spon, London, 753 p.

AZZOUZ, A.S., KRIZEK, R.J., AND COROTIS, R.B. (1976). "Regression Analysis of Soil Compressibility," *Soils and Foundations*, Vol. 16, No. 2, pp. 19–29.

B

BAGUELIN, F., JÉZÉQUEL, J.F., AND SHIELDS, D.H. (1978). *The Pressuremeter and Foundation Engineering*, Trans Tech Publications, Clausthal, Germany and Aedermannsdorf, Switzerland, 617 p.

BAILEY, T.D., HARNEY, M.D., AND HOLTZ, R.D. (2005). "Rapid Assessment of Geotextile Clogging Potential Using the Flexible Wall Gradient Ratio Test," *Proceedings of the GRI-18 Conference*, ASCE, Austin, TX (CD-ROM).

BALDI, G., BELLOTTI, R., GHIONNA, V.N., JAMIOLKOWSKI, M., LO PRESTI, D.C. (1989). "Modulus of Sands from CPT's and CMT's," *Proceedings of the Twelfth International Conference on Soil Mechanics and Foundation Engineering*, Rio de Janeiro, Vol. 1, pp. 165–170.

BALDI, G., BELLOTTI, R., GHIONNA, V., JAMIOLKOWSKI, M., MARCHETTI, S., AND PASQUELINI, E. (1986). "Flat Dilatometer Tests in Calibration Chambers," *Proceedings of the In Situ '86*, Geotechnical Special Publication 6, ASCE, New York, pp. 431–446.

BALIGH, M.M. (1976). "Cavity Expansion in Sands with Curved Envelopes," *Journal of Geotechnical Engineering Division*, Vol. 111, No. GT9, pp. 1108–1136.

BARA, J.P. (1978). "Collapsible Soils and Their Stabilization," in *Soil Improvement, History, Capabilities, and Outlook, Report by Committee on Placement and Improvement of Soils*, Geotechnical Engineering Division, ASCE, pp. 141–152.

BARDEN, L. AND MCGOWN, A. (1973). "Microstructural Disturbance in Soft Clays Resulting from Site Investigation Sampling," *Proceedings of the International Symposium on Soil Structure*, Gothenburg, Sweden, 213 p.

BARDET, J.P. (1986). "Bounding Surface Plasticity Model for Sands," *Journal of Engineering Mechanics*, ASCE, Vol. 112, No. 11, pp. 1198–1217.

BARDET, J.P. (1997). *Experimental Soil Mechanics*, Prentice-Hall, 583 p.

BARTON, N., LIEN, R., AND LUNDE, J. (1974). "Engineering Classification of Rock Masses for the Design of Tunnel Support," *Rock Mechanics*, Vol. 6, No. 4, pp. 189–236.

BECKER, D.E. (2001). "Site Characterization," Chapter 4 in *Geotechnical and Geoenvironmental Handbook*, R.K. Rowe (Ed.), Kluwer Academic Publishers, pp. 69–105.

BECKER, D.E., CROOKS, J.H., BEEN, K., AND JEFFERIES, M.G. (1987). "Work as a Criterion for Determining In Situ and Yield Stresses in Clays," *Canadian Geotechnical Journal*, Vol. 24, No. 4, pp. 549–564.

BEGEMANN, H.K.S.PH. (1953). "Improved Methods of Determining Resistance to Adhesion by Sounding through a Loose Sleeve Placed Behind the Cone," *Proceedings of the Third International Conference on Soil Mechanics and Foundation Engineering*, Zurich, Vol. I, pp. 213–217.

BELLOTTI, R., GHIONNA, V., JAMIOLKOWSKI, M., LANCELLOTTA, R., AND MANFREDINI, G. (1986). "Deformation Characteristics of Cohesionless Soil in In Situ Tests," *Proceedings of the In Situ* '86, Geotechnical Special Publication No. 6, ASCE, New York, pp. 47–73.

BENSON, C.H. AND BOSSCHER, P.J. (1999). "Time-Domain Reflectometry (TDR) in Geotechnics: A Review," in W.A. Marr and C.E. Fairhurst (Eds.), *Nondestructive and Automated Testing for Soil and Rock Properties*, ASTM Special Technical Publication 1350, ASTM, West Conshohocken, PA.

BERRE, T. (1972). "Sammenheng Mellon Tid, Deformasjoner og Spenninger før Normalkonsolidarde Marine Leirer," *Foredrager av den Sjätte Nordiska Geoteknikermøtet*, Trondheim, Norway; Norwegian Geotechnical Institute.

BESKOW, G. (1935). "Soil Freezing and Frost Heaving with Special Application to Roads and Railroads," *The Swedish Geological Society*, Series C, No. 375, 26th Yearbook No. 3; translated by J.O. Osterberg, Northwestern University, 1947, 145 p.

BIENIAWSKI, Z.T. (1974). "Geomechanics Classification of Rock Masses and its Application in Tunneling," *Proceedings of the Third International Congress on Rock Mechanics*, International Society of Rock Mechanics, Denver, 11A, pp. 27–32.

BIENIAWSKI, Z.T. (1976). "Rock Mass Classifications in Rock Engineering," *Proceedings of the Symposium on Exploration for Rock Engineering*, Cape Town, Balkema, pp. 76–106.

BIENIAWSKI, Z.T. (1988). "The Rock Mass Rating (RMR) System (Geomechanics Classification) in Engineering Practice," *Rock Classification Systems for Engineering Purposes*, ASTM Special Technical Publication 984, L. Kirkaldale (Ed.), ASTM, Philadelphia, pp. 17–34.

BISHOP, A.W. (1954). "Correspondence," *Géotechnique*, Vol. IV, No. 1, pp. 43–45.

BISHOP, A.W. (1958). "Test Requirements of Measuring the Coefficient of Earth Pressure at Rest," *Proceedings of the Conference on Earth Pressure Problems*, Brussels, Vol. I, pp. 2–14.

BISHOP, A.W., ALPAN, I., BLIGHT, G.E., AND DONALD, I.B. (1960). "Factors Controlling the Shear Strength of Partly Saturated Cohesive Soils," *Proceedings of the ASCE Research Conference on Shear Strength of Cohesive Soils*, Boulder, pp. 503–532.

BISHOP, A.W. AND HENKEL, D.J. (1962). *The Measurement of Soil Properties in the Triaxial Test*, 2nd ed., Edward Arnold Ltd., London, 228 p.

BISHOP, A.W. AND WESLEY, L.D. (1975). "Triaxial Apparatus for Controlled Stress Path Testing," *Géotechnique*, Vol. XXV, No. 4, pp. 657–670.

BJERRUM, L. (1954a). *"Theoretical and Experimental Investigations on the Shear Strength of Soils,"* Norwegian Geotechnical Institute, No. 5, 118 p.

BJERRUM, L. (1954b). "Geotechnical Properties of Norwegian Marine Clays," *Géotechnique*, Vol. IV, No. 2, pp. 49–69.

BJERRUM, L. (1967). "Engineering Geology of Norwegian Normally Consolidated Marine Clays as Related to Settlements of Buildings," *Géotechnique*, Vol. XVII, No. 2, pp. 81–118.

BJERRUM, L. (1972). "Embankments on Soft Ground," *Proceedings of the ASCE Specialty Conference on Performance of Earth and Earth-Supported Structures*, Purdue University, Vol. II, pp. 1–54.

BJERRUM, L. (1973). "Problems of Soil Mechanics and Construction on Soft Clays," *Proceedings of the Eighth International Conference on Soil Mechanics and Foundation Engineering*, Moscow, Vol. 3, pp. 111–159.

BJERRUM, L. AND SIMONS, N.E. (1960). "Comparison of Shear Strength Characteristics of Normally Consolidated Clays," *Proceedings of the ASCE Research Conference on the Shear Strength of Cohesive Soils*, Boulder, pp. 711–726.

BLACK, D.K. AND LEE, K.L. (1973). "Saturating Laboratory Samples by Back Pressure," *Journal of the Soil Mechanics and Foundations Division*, ASCE, Vol. 99, No. SM1, pp. 75–93.

BLACK, P.B. AND HARDENBERG, M.J. (Eds.) (1991). "Historical Perspectives in Frost Heave Research," *Special Report 91–23*, U.S. Army Cold Regions Research & Engineering Laboratory, Hanover, 174 p.

BLIGHT, G.E. (1980). "The Mechanics of Unsaturated Soils," Notes prepared for a series of lectures delivered as part of Course 270C at the University of California, Berkeley.

BLIGHT, G.E. (Ed.) (1997). *Mechanics of Residual Soils*, Rotterdam, Balkema, 237 p.

BOLTON, M. D. (1979). *A Guide to Soil Mechanics*, Macmillan, London, 456 p.

BOLTON, M.D. (1986). "The Strength and Dilatancy of Sands," *Géotechnique*, Vol. XXXVI, No. 1, pp. 65–78.

BONILLA, M.G. (1991). "Faulting and Seismic Activity," in G.A. Kiersch (Ed.), *The Heritage of Engineering Geology: The First Hundred Years*, Boulder, CO, Geological Society of America, Centennial Special Vol. 3, pp. 251–264.

BORCHERS, J.W. (Ed.) (1998). "Land Subsidence: Case Histories and Current Research," *Proceedings of the Dr. Joseph F. Poland Symposium on Land Subsidence*, Association of Engineering Geologists, Special Publication No. 8, 576 p.

BORDEN, R.H., SHAO, L., AND GUPTA, A. (1996). "Dynamic Properties of Piedmont Residual Soils," *Journal of Geotechnical Engineering*, Vol. 122. No. 10, pp. 813–821.

BOUSSINESQ, J. (1885). *Application des Potentiels à l'Étude de l'Équilibre et due Mouvement des Solides Élastiques*, Gauthier-Villars, Paris.

BOWDEN, F.P. AND TABOR, D. (1950). *The Friction and Lubrication of Solids*, Part I, Oxford University Press, London, 337 p.

BOWDEN, F.P. AND TABOR, D. (1964). *The Friction and Lubrication of Solids*, Part II, Oxford University Press, London, 544 p.

BOYLE, S.R. (1995). "Deformation Prediction of Geosynthetic Reinforced Soil Retaining Walls," Ph.D. dissertation, University of Washington, 391 p.

BOZOZUK, M. (1962). "Soil Shrinkage Damages Shallow Foundations at Ottawa, Canada," *The Engineering Journal*, Vol. 45, No. 7, pp. 33–37; also in *Research Paper No. 163*, Division of Building Research, National Research Council, Ottawa, Ontario, 7 p.

BOZOZUK, M. (1963). "The Modulus of Elasticity of Leda Clay from Field Measurements," *Canadian Geotechnical Journal*, Vol. I, No. 1, pp. 43–51.

BOZOZUK, M. AND LEONARDS, G.A. (1972). "The Gloucester Test Fill," *Proceedings of the ASCE Specialty Conference on Performance of Earth and Earth-Supported Structures*," Purdue University, Vol. I, Part 1, pp. 299–317.

BREITENBACH, A.J. (1993). "Rockfill Placement and Compaction Guidelines," *Geotechnical Testing Journal*, ASTM, Vol. 16, No. 1, pp. 76–84.

BREITENBACH, A.J. (2006). "Summary of Rockfill Placement and Compaction Guidelines for Mine Structures," on www.geoengineer.org/rockfill1.htm, accessed Sept. 2006.

BREWER, R. (1976). *Fabric and Mineral Analysis of Soils*, Krieger, 482 p.

BRIAUD, J.L. (1992). *The Pressuremeter*, Balkema, Rotterdam, 322 p.

BRIAUD, J.L. (2001). "Introduction to Soil Moduli," *Geotechnical News*, June 2001, BiTech Publishers Ltd., Richmond, British Columbia (geotechnicalnews@bitech.ca).

BRIAUD, J.L. AND MIRAN, J. (1992). "The Flat Dilatometer Test," U.S. Federal Highway Administration, Report No. FHWA-SA-91–044, 102 p.

BRINK, R. (1967). "Effective Angle of Friction for a Normally Consolidated Clay," *Proceedings of the Geotechnical Conference Oslo on the Shear Strength Properties of Natural Soils and Rocks*, Vol. I, Published by the Norwegian Geotechnical Institute, Olso, pp. 13–17.

BROMS, B.B. AND FORSSBLAD, L. (1969). "Vibratory Compaction of Cohesionless Soils," *Proceedings of the Specialty Session No. 2 on Soil Dynamics, Seventh International Conference on Soil Mechanics and Foundation Engineering*, Mexico City, pp. 101–118.

BROOKER, E.W. AND IRELAND, H.O. (1965). "Earth Pressures at Rest Related to Stress History," *Canadian Geotechnical Journal*, Vol. II, No. 1, pp. 1–15.

BROUSSEAU, P. (1983). "Généralisation des États Limites et de la Déstructuration des Argile Naturelles," M.S. thesis, Laval University, Quebec City, Quebec, Canada.

BRUMUND, W.F., JONAS, E., AND LADD, C.C. (1976). "Estimating In Situ Maximum Past Preconsolidation Pressure of Saturated Clays from Results of Laboratory Consolidometer Tests," *Special Report 163*, Transportation Research Board, pp. 4–12.

BS1377 (1990). "Methods of Testing Soils for Civil Engineering Purposes," Parts 1, 2, 3, 4, British Standards Institution.

BUDHU, M. (2007). *Soil Mechanics and Foundations*, 2nd ed., Wiley, New York, 634 p.

BURLAND, J.B. (1989). "Small is Beautiful–The Stiffness of Soils at Small Strains" (9th Laurits Bjerrum Memorial Lecture), *Canadian Geotechnical Journal*, Vol. 26, pp. 499–516.

BURLAND, J.B. (1990). "On the Compressibility and Shear Strength of Natural Clays," *Géotechnique*, Vol. XL, No. 3, pp. 329–378.

BURMISTER, D.M. (1948). Discussion of "Classification and Identification of Soils" by A. Casagrande, *Transactions*, ASCE, Vol. 113, pp. 971–977.

BURN, K.N. (1976). *Frost Action and Foundations*, Canadian Building Digest CBD-182, National Research Council, Ottawa, 4 p.

BURNS, S.E., SANTAMARINA, J.C., AND MAYNE, P.W. (Eds.) (2008). *Deformational Characteristics of Geomaterials*, Rotterdam, Millpress–IOS Press, 1111 p.

BUTTERFIELD, R. (1979). "A Natural Compression Law for Soils (An Advance on e-logp')," *Géotechnique*, Vol. XXIX, No. 4, pp. 469–480.

BYRNE, P.M., SALGADO, F., AND HOWIE, J.A. (1991). "G_{max} from Pressuremeter Test: Theory, Chamber Tests, and Field Measurements," *Proceedings of the Second International Conference on Recent Advances in Geotechnical Earthquake Engineering and Soil Dynamics*, St. Louis, MO, Vol. 1, pp. 57–63.

C

CADLING, L. AND ODENSTAD, S. (1950). "The Vane Borer," *Proceedings No. 2*, Royal Swedish Geotechnical Institute, pp. 1–88.

CALIFORNIA DWR (1962). "Review of the Visual Method of Classification and Description of Soils in Foundations and Borrow Areas Based on the USBR Earth Manual Designation E-3, DWR

Designation S-4," *Manual of Testing Procedures for Soils*, California Department of Water Resources, Sacramento, 7 p.

CAMPANELLA, R.G. AND ROBERTSON, P.K. (1991). "Use and Interpretation of a Research Dilatometer," *Canadian Geotechnical Journal*, Vol. 28, No. 1, pp. 113–126.

CAMPANELLA, R.G. AND VAID, Y.P. (1972). "A Simple K_o-Triaxial Cell," *Canadian Geotechnical Journal*, Vol. 9, No. 3, pp. 249–260.

CANADIAN GEOTECHNICAL SOCIETY (2006). *Canadian Foundation Engineering Manual*, 4th ed., Canadian Geotechnical Society, BiTech Publishers, Richmond, British Columbia, 488 p.

CARRIER, W.D., III (2003). "Goodbye, Hazen; Hello, Kozeny-Carman," *Journal of Geotechnical and Geoenvironmental Engineering*, ASCE, Vol. 129, No. 11, pp. 1054–1056.

CARRIGAN, R.A. (1978). "Decimal Time," *American Scientist*, Vol. 66, No. 3, pp. 305–313.

CARROLL, R.G. (1983). "Geotextile Filter Criteria," *Engineering Fabrics in Transportation Construction*, Transportation Research Record No. 916, pp. 46–53.

CARTER, D.L., MORTLAND, M.M., AND KEMPER, W.D. (1986). "Specific Surface," Chapter 16 in *Methods of Soil Analysis, Part 1, Physical and Mineralogical Methods*, Agronomy Monograph No. 9, 2nd ed., American Society of Agronomy—Soil Science Society of America, Madison, WI, pp. 413–423.

CASAGRANDE, A. (1932a). Discussion of "A New Theory of Frost Heaving," by A.C. Benkelman and F.R. Ohlmstead, *Proceedings of the Highway Research Board*, Vol. 11, pp. 168–172.

CASAGRANDE, A. (1932b). "Research on the Atterberg Limits of Soils," *Public Roads*, Vol. 13, No. 8, pp. 121–136.

CASAGRANDE, A. (1932c). "The Structure of Clay and Its Importance in Foundation Engineering," *Journal of the Boston Society of Civil Engineers*, April; reprinted in *Contributions to Soil Mechanics 1925–1940*, BSCE, pp. 72–113.

CASAGRANDE, A. (1936a). "Characteristics of Cohesionless Soils Affecting the Stability of Slopes and Earth Fills," *Journal of the Boston Society of Civil Engineers*, January; reprinted in *Contributions to Soil Mechanics 1925–1940*, BSCE, pp. 257–276.

CASAGRANDE, A. (1936b). "The Determination of the Pre-Consolidation Load and Its Practical Significance," Discussion D-34, *Proceedings of the First International Conference on Soil Mechanics and Foundation Engineering*, Cambridge, Vol. III, pp. 60–64.

CASAGRANDE, A. (1937). "Seepage Through Dams," *Journal of the New England Water Works Association*, Vol. 51, No. 2; Reprinted in *Contributions to Soil Mechanics 1925–1940*, BSCE, pp. 295–336.

CASAGRANDE, A. (1938). "Notes on Soil Mechanics—First Semester," Harvard University (unpublished), 129 p.

CASAGRANDE, A. (1948). "Classification and Identification of Soils," *Transactions*, ASCE, Vol. 113, pp. 901–930.

CASAGRANDE, A. (1950). "Notes on the Design of Earth Dams," *Journal of the Boston Society of Civil Engineers*, October; reprinted in *Contributions to Soil Mechanics 1941–1953*, BSCE, pp. 231–255.

CASAGRANDE, A. (1958). "Notes on the Design of the Liquid Limit Device," *Géotechnique*, Vol. VIII, No. 2, pp. 84–91.

CASAGRANDE, A. (1975). "Liquefaction and Cyclic Deformation of Sands, a Critical Review," *Proceedings of the Fifth Panamerican Conference on Soil Mechanics and Foundation Engineering*, Buenos Aires; reprinted as *Harvard Soil Mechanics Series*, No. 88, 27 p.

CASAGRANDE, A. AND FADUM, R.E. (1944). Closure to "Application of Soil Mechanics in Designing Building Foundations," *Transactions*, ASCE, Vol. 109, 467 p.

CATERPILLAR TRACTOR CO. (1977). *Caterpillar Performance Handbook*, Form AEKQ 3313, 8th ed., Chapter 14, Peoria, IL, 6 p.

CEDERGREN, H.R. (1989). *Seepage, Drainage, and Flow Nets*, 3rd ed., Wiley, New York, 465 p.

CHAMBERLAIN, E.J., GASKIN, P.N., ESCH, D., AND BERG, R.L. (1982). "Identification and Classification of Frost Susceptible Soils," *Preprint*, ASCE Spring Convention, Las Vegas, NV, April, 38 p.

CHANDLER, R.J. (1967). "The Strength of a Stiff Silty Clay," *Proceedings of the Geotechnical Conference Oslo on the Shear Strength Properties of Natural Soils and Rocks*, Vol. I, Published by the Norwegian Geotechnical Institute, Olso, pp. 103–108.

CHANDLER, R.J. (1987). "The In Situ Measurement of the Undrained Shear Strength of Clays Using the Field Vane," *Vane Shear Strength Testing in Soils: Field and Laboratory Studies*, A.F. Richards (Ed.), ASTM Special Technical Publication 1014, Philadelphia, pp. 13–44.

CHEN, F.H. (1988). *Foundations on Expansive Soils*, 2nd ed., Elsevier, Amsterdam, 298 p.

CHEN, W.F. (1994). *Constitutive Equations for Engineering Materials, Vol. 2—Plasticity and Modeling*, Elsevier, Amsterdam, 1096 p.

CHEN, W.F. AND BALADI, G.Y. (1985). *Soil Plasticity: Theory and Implementation*, Elsevier, Amsterdam, 231 p.

CHEN, W.F. AND SALEEB, A.F. (1982). *Constitutive Equations for Engineering Materials*, Vol. 1, Elasticity and Modeling, Wiley, New York, 580 p.

CHERNICOFF, S. AND VENKATAKRISHNAN, R. (1995). *Geology*, Worth Publishers, New York, 593 p.

CHRISTIAN, J.T. AND CARRIER, W.D. (1978). "Janbu, Bjerrum, and Kjaernsli's Chart Reinterpreted," *Canadian Geotechnical Journal*, Vol. 15, No. 1, pp. 123–128.

CHRISTIAN, J.T. AND URZUA, A. (1996). *Productivity Tools for Geotechnical Engineers*, Magellan Press, Newton, MA, 181 p. (with disk).

CHRISTOPHER, B.R. AND HOLTZ, R.D. (1985). *Geotextile Engineering Manual*, U.S. Federal Highway Administration, Washington, D.C., FHWA-TS-86/203, 1044 p.

CLARKE, B.G. (1995). *Pressuremeters in Geotechnical Design*, Blackie, London, 364 p.

CLAYTON, C.R.I. AND KHATRUSH, S.A. (1986). "A New Device for Measuring Local Strains on Triaxial Specimens," *Géotechnique*, Vol. XXXIV, No. 4, pp. 593–597.

CLEMENCE, S.P. AND FINBARR, A.O. (1981). "Design Considerations for Collapsible Soils," *Journal of the Geotechnical Engineering Division*, ASCE, Vol. 107, No. GT3, pp. 305–317.

CLEVENGER, W.A. (1958). "Experiences With Loess as a Foundation Material," *Transactions*, ASCE, Vol. 123, pp. 151–169.

COATS, D.R. (1991). "Glacial Deposits," Chapter 15 in *The Heritage of Engineering Geology; The First Hundred Years*, G.A. Kiersch (Ed.), Centennial Special Vol. 3, Geological Society of America, 308 p.

CODUTO, D.P. (2001). *Foundation Design: Principles and Practices*, 2nd ed., Prentice-Hall, Upper Saddle River, NJ, 883 p.

COLLIN, A. (1846). *Recherches Expérimentales sur les Glissements Spontanés des Terrains Argileux, Accompagnées de Considerations sur Quelques Principes de la Méchanicque Terrestre*, Carilian-Goeury and Dalmont, Paris. Translated by W.R. Schriever under the title "*Landslides in Clays by Alexandre Collin 1846*," University of Toronto Press, Canada, 1956, 161 p. (21 plates).

COLLINS, K. AND MCGOWN, A. (1974). "The Form and Function of Microfabric Features in a Variety of Natural Soils," *Géotechnique*, Vol. XXIV, No. 2, pp. 223–254.

CORNFORTH, D.H. (1964). "Some Experiments on the Influence of Strain Conditions on the Strength of Sand," *Géotechnique*, Vol. XIV, No. 2, pp. 143–167.

COULOMB, C.A. (1776). "Essai sur une application des règles de Maximus et Minimis à Quelques Problèmes de Statique, Relatifs à l'Architecture," *Mémoires de Mathématique et de Physique, Présentés a l' Académie Royale des Sciences, par Divers Savans, et lûs dans ses Assemblées*, Paris, Vol. 7 (Vol. for 1773 published in 1776), pp. 343–382.

CRAWFORD, C.B. (1965). "Resistance of Soil Structure to Consolidation," *Canadian Geotechnical Journal*, Vol. 11, No. 2, pp. 97–99.

CROOKS, J.H.A. AND BECKER, D.E. (1988). Discussion of "Slide in Upstream Slope of Lake Shelbyville Dam" by D.N. Humphrey and G.A. Leonards, *Journal of Geotechnical Engineering*, ASCE, Vol. 114, No. 4, pp. 506–508.

CRUDEN, D.M. AND VARNES, D.J. (1996). "Landslide Types and Processes," Chapter 3 in *Landslides: Investigation and Mitigation*, Special Report 247, Transportation Research Board, National Academy Press, Washington, pp. 36–75.

D

DAFALIAS, Y.F. (1986). "Bounding Surface Plasticity I: Mathematical Foundations and Hypo-Elasticity," *Journal of Engineering Mechanics*, ASCE, Vol. 112, No. 9, pp. 966–987.

DAFALIAS, Y.F. AND L.R. HERRMANN (1982). "Bounding Surface Formulations of Soil Plasticity," in *Soil Mechanics: Transient and Cyclic Loads—Constitutive Relations and Numerical Treatment*, G.N. Pande and O.C. Zienkiewicz (Eds.), Wiley, New York, pp. 253–282.

DAFALIAS, Y.F. AND POPOV, E.P. (1975). "A Model for Nonlinearly Hardening Materials for Complex Loading," *Acta Mechanica*, Vol. 21, pp. 173–192.

D'APPOLONIA, D.J., LAMBE, T.W., AND POULOS, H.G. (1971a). "Evaluation of Pore Pressures Beneath an Embankment," *Journal of the Soil Mechanics and Foundations Division*, ASCE, Vol. 97, No. SM6, pp. 881–897.

D'APPOLONIA, D.J., POULOS, H.G., AND LADD, C.C. (1971b). "Initial Settlement of Structures on Clay," *Journal of the Soil Mechanics and Foundations Division*, ASCE, Vol. 97, No. SM10, pp. 1359–1377.

D'APPOLONIA, D.J., WHITMAN, R.V., AND D'APPOLONIA, E.D. (1969). "Sand Compaction with Vibratory Rollers," *Journal of the Soil Mechanics and Foundations Division*, ASCE, Vol. 95, No. SM1, pp. 263–284.

DARCY, H. (1856). *Les Fontaines Publiques de la Ville de Dijon*, Dalmont, Paris.

DAVIS, T.N. (2001). *Permafrost: A Guide to Frozen Ground in Transition*, University of Alaska Press, Fairbanks, 368 p.

DAWSON, R.F. (1944). Discussion of "Relation of Undisturbed Sampling to Laboratory Testing," by P.C. Rutledge, *Transactions*, ASCE, Vol. 109, pp. 1190–1193.

DEERE, D.U. (1963). "Technical Description of Rock Cores for Engineering Purposes," *Rock Mechanics and Engineering Geology*, Vol. 1, pp. 18–22.

DEERE, D.U. AND DEERE, D.W. (1988). "The Rock Quality Designation (RQD) Index in Practice," in *Rock Classification Systems for Engineering Purposes*, ASTM Special Technical Publication 984, L. Kirkaldie (Ed.), American Society for Testing and Materials, Philadelphia, pp. 91–101.

DE MELLO, V.F.B. (1971). "The Standard Penetration Test," State of the Art Paper, *Proceedings of the Fourth Panamerican Conference on Soil Mechanics and Foundation Engineering*, Vol. I, pp. 1–86.

DEJONG, J.T. AND BOULANGER, R.W. (2000). "Introduction to Drilling and Sampling in Geotechnical Practice," *Educational Video*, 2nd ed., Department of Civil and Environmental Engineering, University of California, Davis, 35 min. See also http://cee.engr.ucdavis.edu/faculty/boulanger/video/DrillingAndSampling.mpg.

DELAGE, P., AUDIGUIER, M., CUI, Y.-J., AND HOWAT, M.D. (1996). "Microstructure of a Compacted Silt," *Canadian Geotechnical Journal*, Vol. 33, No. 1, pp. 150–158.

DIAZ-RODRÍQUEZ, J.A., LEROUEIL, S., AND ALEMÁN, J.D. (1992). "Yielding of Mexico City Clay and Other Natural Clays," *Journal of Geotechnical Engineering*, ASCE, Vol. 118, No. 7, pp. 981–995.

DIBIAGIO, E. AND STENHAMAR, P. (1975). "Prøvefylling til Brudd på Bløt Leire," *Proceedings of the Seventh Scandinavian Geotechnical Meeting*, Copenhagen, Polyteknisk Forlag, pp. 173–185.

DONOVAN, N.C. (1969). "Research Brief–Soil Dynamics Specialty Session," *Seventh International Conference on Soil Mechanics and Foundation Engineering*, Mexico City, 154 p.

DOWDING, C.H. (1985). *Blast Vibration Monitoring and Control*, Prentice-Hall, Upper Saddle River, NJ, 297 p.

DOWDING, C.H. (1996). *Construction Vibrations*, Prentice-Hall, Upper Saddle River, NJ, 610 p.

DRISCOLL, F.G. (Ed.) (1986). *Groundwater and Wells*, 2nd ed., Johnson Well Screen Co., St. Paul, MN, 1089 p.

DRNEVICH, V.P., HALL, J.R., Jr., AND RICHART, F.E., Jr. (1966). "Large Amplitude Vibration Effects on the Shear Modulus of Sand," *University of Michigan Report to Waterways Experiment Station, U.S. Army Corps of Engineers, Contract DA-22-079-Eng-340*, Oct. 1966.

DRUCKER, D.C., GIBSON, R.E., AND HENKEL, D.J. (1957). "Soil Mechanics and Work-Hardening Theories of Plasticity," *Transactions*, ASCE, Vol. 112, pp. 338–346.

DUDLEY, J.G. (1970). "Review of Collapsing Soil," *Journal of the Soil Mechanics and Foundation Engineering Division*, ASCE, Vol. 96, No. SM3, pp. 925–947.

DUNCAN, J.M. (1980). "Hyperbolic Stress-Strain Relationships," *Limit Equilibrium, Plasticity and Generalized Stress-Strain in Geotechnical Engineering*, Proceedings of the workshop sponsored by NSF and NSERC, McGill University, Montreal, R.N. Yong and H.Y. Ko (Eds.), ASCE, pp. 443–460.

DUNCAN, J.M. AND BUCHIGNANI, A.L. (1976). "An Engineering Manual for Settlement Studies," *Geotechnical Engineering Report*, University of California, Berkeley, 94 p.

DUNCAN, J.M., BYRNE, P., WONG, K.S., AND MABRY, P. (1980). "Strength, Stress-Strain and Bulk Modulus Parameters for Finite Element Analyses of Stresses and Movements in Soil Masses," *Geotechnical Engineering Report No. UCB/GT/80-01*, University of California, Berkeley, 70 p.

DUNCAN, J.M. AND CHANG, C.Y. (1970). "Nonlinear Analysis of Stress and Strain in Soil," *Journal of Soil Mechanics and Foundations Division*, ASCE, Vol. 96, No. SM5, pp. 1629–1653.

DUNCAN, J.M. AND WRIGHT, S.G. (2005). *Soil Strength and Slope Stability*, Wiley, New York, 297 p.

DUNNICLIFF, J. (1993). *Geotechnical Instrumentation for Monitoring Field Performance*, Wiley, New York, 608 p.

DYVIK, R. AND MADSHUS, C. (1985). "Lab Measurements of G_{max} Using Bender Elements," in V. Khosla (Ed.), *Advances in the Art of Testing Soils under Cyclic Conditions*, ASCE, pp. 186–196.

E

EDELEN, B. (Ed.) (1999). *Proceedings of the Behavioral Characteristics of Residual Soils (GeoCongress 1999)*, ASCE, Charlotte, NC, 178 p.

EDEN, W.J. (1971). "Sampler Trials in Overconsolidated Sensitive Clay," *Sampling of Soil and Rock*, ASTM Special Technical Publication No. 483, pp. 132–142.

EDEN, W.J. AND KUBOTA, J.K. (1962). "Some Observations on the Measurement of Sensitivity of Clays," *Proceedings of the American Society for Testing and Materials*, Vol. 61, pp. 1239–1249.

EDIL, T.B. AND SAWANGSURIYA, A. (2006). "Use of Stiffness and Strength for Earthwork Quality Evaluation," *Proceedings of the ASCE GeoShanghai Conference*, Shanghai, China, H. Zui, F. Zhang, E. Drumm, and C.T. Chin (Eds.), pp. 80–87.

EIDE, O. AND HOLMBERG, S. (1972). "Test Fills to Failure on the Soft Bangkok Clay," *Proceedings of the ASCE Specialty Conference on Performance of Earth and Earth-Supported Structures*, Purdue University, Vol. I, Part 1, 163 p.

EL-EHWANY, M. AND HOUSTON, S.L. (1990). "Settlement and Moisture Movement in Collapsible Soils," *Journal of Geotechnical Engineering*, ASCE, Vol. 116, No. 10, pp. 1521–1535.

EMMONS, W.H., THIEL, G.A., STAUFFER, C.R., AND ALLISON, I.S. (1955). *Geology: Principles and Processes*, McGraw-Hill, New York, 638 p.

ESCARIO, V. (1980). "Suction Controlled Penetration and Shear Tests," *Proceedings of the Fourth International Conference on Expansive Soils*, Denver, CO, Vol. 2, pp. 781–797.

ESOPT (1974). *Proceedings of the European Symposium on Penetration Testing*, Stockholm, Swedish Council for Building Research, Vols. 1, 2.1, 2.2, and 3.

F

FADUM, R.E. (1948). "Influence Values for Estimating Stresses in Elastic Foundations," *Proceedings Second International Conference on Soil Mechanics and Foundation Engineering*, Rotterdam, Vol. 3, pp. 77–84.

FAGAN, B.M. (2000). *The Little Ice Age: How Climate Made History, 1300–1850*, Basic Books, New York, 272 p.

FANG, H.Y. (1997). *Introduction to Environmental Geotechnology*, CRC Press, Boca Raton, FL, 652 p.

FANNIN, R.J., ELIADORANI, A., AND WILKINSON, M.T. (2005). "Shear Strength of Cohesionless Soils at Low Stress," *Géotechnique*, Vol. LV, No. 6, pp. 467–478.

FEDERAL HIGHWAY ADMINISTRATION (1991). *Rock and Mineral Identification for Engineers*, U.S. Department of Transportation, Washington, 50 p. (useful color pamphlet).

FELLENIUS, B.H. (2011). *Basics of Foundation Design*. www.fellnius.net, 362 pp., accessed Sept. 22, 2011. Referenced on p. 378, Table 8.2 [should say Fellenius (2011)]

FERNAU, E.A. (1977). "Application of Soil Taxonomy in Engineering," *Transportation Research Record 642*, Transportation Research Board, pp. 24–27.

FLAATE, K. AND PREBER, T. (1974). "Stability of Road Embankments," *Canadian Geotechnical Journal*, Vol. 11, No. 1, pp. 72–88.

FLEMING, R.W. AND VARNES, D.J. (1991). "Slope Movements," Chapter 9 in *The Heritage of Engineering Geology; The First Hundred Years*, G.A. Kiersch (Ed.), Centennial Special Vol. 3, Geological Society of America, pp. 201–218.

FLOYD, R.P. (1979). *Geodetic Bench Marks*, NOAA Manual NOS NGS 1, National Oceanic and Atmospheric Administration, 58 p.

FOSTER, C.R. AND AHLVIN, R.G. (1954). "Stresses and Deflections Induced by a Uniform Circular Load," *Proceedings of the Highway Research Board*, Vol. 33, pp. 467–470.

FOX, R.F. AND HILL, T.P. (2007). "An Exact Value for Avogadro's Number," *American Scientist*, Vol. 95, No. 2, pp. 104–107.

FREDLUND, D.G. (1973). "Volume Change Behavior of Unsaturated Soils," Ph.D. thesis, University of Alberta, Edmonton, Canada.

FREDLUND, D.G. (1997). "An Introduction to Unsaturated Soil Mechanics," in *Unsaturated Soil Engineering Practice*, S.L. Houston and D.G. Fredlund (Eds.), Geotechnical Special Publication No. 68, ASCE, New York, pp. 1–37.

FREDLUND, D.G. AND MORGENSTERN, N.R. (1977). "Stress State Variables for Unsaturated Soils," *Journal of the Geotechnical Engineering Division*, ASCE, Vol. 103, No. 5, pp. 447–466.

FREDLUND, D.G. AND RAHARDJO, H. (1993). *Soil Mechanics for Unsaturated Soils*, Wiley, New York, 517 p.

FREEZE, R.A. AND CHERRY, J.A. (1979). *Groundwater*, Prentice-Hall, Upper Saddle River, NJ, 604 p.

FUNG, Y.C. (1965). *Solid Mechanics*, Prentice-Hall, Upper Saddle River, NJ, 525 p.

G

GALSTER, R.W. (1992). Notes on Engineering Geology, CESM 599B, University of Washington, EG 2: "*Origin and Classification of Geologic Materials*," EG3/4, 11 p.; *Geologic Processes and their Importance in Civil Engineering*, 18 p.

GAN, J.K.M., FREDLUND, D.G., AND RAHARDJO, H. (1988). "Determination of the Shear Strength Parameters of an Unsaturated Soil Using the Direct Shear Test," *Canadian Geotechnical Journal*, Vol. 25, No. 3, pp. 500–510.

GARCIA-BENGOCHEA, I., LOVELL, C.W., AND ALTSCHAEFFL, A.G. (1979). "Pore Distribution and Permeability of Silty Clays," *Journal of the Geotechnical Engineering Division*, ASCE, Vol. 105, No. GT7, pp. 839–856.

GIBBS, H.J. (1969). Discussion, *Proceedings of the Specialty Session No. 3 on Expansive Soils and Moisture Movement in Partly Saturated Soils*, Seventh International Conference on Soil Mechanics and Foundation Engineering, Mexico City.

GOODMAN, R.E. (1989). *Introduction to Rock Mechanics*, 2nd ed., Wiley, New York, 562 p.

GOODMAN, R.E. (1993). *Engineering Geology*, Wiley, New York, 412 p.

GOODMAN, R.E. (1999). *Karl Terzaghi: The Engineer as Artist*, ASCE Press, 340 p.

GORMAN, C.T., HOPKINS, T.C., DEEN, R.C., AND DRNEVICH, V.P. (1978). "Constant-Rate-of-Strain and Controlled-Gradient Consolidation Testing," *Geotechnical Testing Journal*, ASTM, Vol. 1, No. 1, pp. 3–15.

GRAHAM, J., CROOKS, J.H.A., AND LAU, S.L.K. (1983). "Yield States and Stress-strain Relationships in a Natural Plastic Clay," *Canadian Geotechnical Journal*, Vol. 20, No. 3, pp. 502–516.

GRAY, H. (1945). "Simultaneous Consolidation of Contiguous Layers of Unlike Compressibility," *Transactions*, ASCE, Vol. 110, 1327 p.

GREENFIELD, S.J. AND SHEN, C.K. (1992). *Foundations in Problem Soils*, Prentice-Hall, Englewood Cliffs, NJ.

GREGORY, C.H. (1844). "On Railway Cuttings and Embankments with an Account of Some Slips in London Clay, on the Line of the London and Croydon Railway," *Minutes and Proceedings of the Institution of Civil Engineers*, Vol. 3, pp. 135–145. Reprinted in *A Century of Soil Mechanics*, Institution of Civil Engineers, London, 1969, 482 p.

GRIFFITH, A.A. (1924). "Theory of Rupture," *Proceedings of the First International Congress on Applied Mechanics*, Delft, pp. 55–63.

GRIM, R.E. (1959). "Physico-Chemical Properties of Soils: Clay Minerals," *Journal of the Soil Mechanics and Foundations Division*, ASCE, Vol. 85, No. SM2, pp. 1–17.

GROMKO, G.J. (1974). "Review of Expansive Soils," *Journal of the Geotechnical Engineering Division*, ASCE, Vol. 100, No. GT6, pp. 667–687.

H

HANDBOOK OF CHEMISTRY AND PHYSICS (2008). (89th ed.) D.R. Lide (Ed.), CRC Press, Boca Raton, FL.

HANDY, R.L. (1986). "Borehole Shear Tests and Slope Stability," *Use of In Situ Tests in Geotechnical Engineering*, Proceedings of the In Situ '86 Specialty Conference, Blacksburg, VA, S.P. Clemence (Ed.), Geotechnical Special Publication No. 6, ASCE, pp. 161–175.

HANDY, R.L. (1995). *The Day the House Fell: Homeowner Soil Problems—From Landslides to Expansive Clays and Wet Basements*, ASCE Press, Reston, VA, 230 p.

HANSBO, S. (1957). "A New Approach to the Determination of the Shear Strength of Clay by the Fall-Cone Test," *Proceedings No. 14*, Swedish Geotechnical Institute, 47 p.

HANSBO, S. (1960). "Consolidation of Clay with Special Reference to Influence of Vertical Sand Drains," *Proceedings No. 18*, Swedish Geotechnical Institute, pp. 45–50.

HANSBO, S. (1975). *Jordmateriallära*, Almqvist & Wiksell Förlag AB, Stockholm, 218 p.

HANSBO, S. (1994). *Foundation Engineering*, Elsevier Science B.V., Amsterdam, 519 p.

HARDER, L.F. AND SEED, H.B. (1986). "Determination of the Penetration Resistance for Coarse-Grained Soils Using the Becker Penetration Resistance," *Report No. UCB/EERC-86/06*, University of California, Berkeley, 119 p.

HARDIN, B.O. (1965). "The Nature of Damping in Sands," *Journal of the Soils Mechanics and Foundations Division*, ASCE, Vol. 91, No. SM1, Jan. 1965, pp. 63–67.

HARDIN, B.O. (1978). "The Nature of Stress-strain Behavior for Soils." *Proceedings of the Conference on Earthquake Engineering and Soil Dynamics*, ASCE, pp. 3–90.

HARDIN, B.O. AND DRNEVICH, V.P. (1970a). "Shear Modulus and Damping in Soils; I. Measurement and Parameter Effects," *University of Kentucky, College of Engineering, Technical Report UKY 26–70-CE2*, Soil Mechanics Series No. 1, July, 45 p.

HARDIN, B.O. AND DRNEVICH, V.P. (1970b). "Shear Modulus and Damping in Soils; II. Design Equations and Curves," *Technical Report UKY 26–70-CE3*, Soil Mechanics Series No. 2, University of Kentucky, College of Engineering, July, 49 p.

HARDIN, B.O. AND DRNEVICH, V.P. (1970c). "Shear Modulus and Damping in Soils; Design Equations and Curves," *Journal of the Soil Mechanics and Foundations Division*, ASCE, Vol. 98, No. SM7, Proceedings Paper 9006, July, pp. 667–692.

HARNEY, M.D. AND HOLTZ, R.D. (2001). "Flexible Wall Gradient Ratio Test," *Proceedings of the Geosynthetics Conference 2001*, Portland, OR, pp. 409–422.

HARR, M.E. (1962). *Groundwater and Seepage*, McGraw-Hill, New York, 315 p.

HARR, M.E. (1966). *Foundations of Theoretical Soil Mechanics*, McGraw-Hill, New York, 381 p.

HARR, M.E. (1977). *Mechanics of Particulate Media*, McGraw-Hill, New York, 543 p.

HATHEWAY, A.W. (2000). "'Clays'; Never Use the Term by Itself," *AEG News*, Vol. 43, No. 2, pp. 13–26.

HAUSMANN, M.R. (1990). *Engineering Principles of Ground Modification*, McGraw-Hill, New York, 632 p.

HAZEN, A. (1911). Discussion of "Dams on Sand Foundations," by A.C. Koenig, *Transactions*, ASCE, Vol. 73, pp. 199–203.

HEAD, K.H. (1996). *Manual of Soil Laboratory Testing, Vol. 2: Permeability, Shear Strength and Compressibility Tests*, 2nd ed., Wiley, 454 p.

HEAD, K.H. (1998). *Manual of Soil Laboratory Testing, Vol. 3: Effective Stress Tests*, 2nd ed., Wiley, 428 p.

HEAD, K.H. (2006). *Manual of Soil Laboratory Testing*, 3rd ed., Whittles Publishing, 416 p.

HEIM, G.E. (1990). "Knowledge of the Origin of Soil Deposits is of Primary Importance to Understanding the Nature of the Deposit," *Bulletin of the Association of Engineering Geologists*, Vol. XXVII, No. 1, pp. 109–112.

HENKEL, D.W. (1956). "The Effect of Overconsolidation on the Behaviour of Clays During Shear," *Géotechnique*, Vol. XI, No. 4, pp. 139–150.

HENKEL D.J. (1958). "Correlation Between Deformation, Pore Water Pressure, and Strength Characteristics of Saturated Clays," Ph.D. thesis in Engineering, Imperial College of Science and Technology, London.

HENKEL, D.J. (1960). "The Shear Strength of Saturated Remoulded Clays," *Proceedings of the ASCE Research Conference on Shear Strength of Cohesive Soils*, Boulder, pp. 533–554.

HENKEL, D.J. AND WADE, N.H. (1966). "Plane Strain Tests on a Saturated Remolded Clay," *Journal of the Soil Mechanics and Foundations Division*, ASCE, Vol. 92, No. SM6, pp. 67–80.

HENRY, V.J., DEAN, R.G., AND OLSEN, E.J. (1987). *Coastal Engineering: Processes, Practices and Impacts*, Symposium Series, No. 3, Association of Engineering Geologists, pp. 1–58.

HILF, J.W. (1961). "A Rapid Method of Construction Control for Embankments of Cohesive Soils," *Engineering Monograph No. 26*, revised, U.S. Bureau of Reclamation, Denver, 29 p.

HILF, J.W. (1991). "Compacted Fill," Chapter 8 in *Foundation Engineering Handbook*, 2nd ed., H.Y. Fang (Ed.), pp. 249–316.

HIRSCHFELD, R.C. (1963). "Stress-Deformation and Strength Characteristics of Soils," Harvard University (unpublished), 87 p.

HJULSTRÖM, J. (1935). "Studies of the Morphological Activity of Rivers as Illustrated by the River Fyris," *Bulletin of the Geological Institution of the University of Uppsala*, Vol. XXV, 325 p.

HO, D.Y.F. AND FREDLUND, D.G. (1982). "Increase in Shear Strength due to Soil Suction for Two Hong Kong Soils," *Proceedings of the ASCE Geotechnical Conference on Engineering and Construction in Tropical and Residual Soils*, pp. 263–295.

HO, D.Y.F. AND FREDLUND, D.G. (1989). "Laboratory Measurements of the Volumetric Deformation Moduli for Two Unsaturated Soils," *Proceedings of the Forty-Second Canadian Geotechnical Conference*, Winnipeg, pp. 50–60.

HOBBS, P. AND JONES, L. (2006). "Shrink Rethink," *Ground Engineering*, Vol. 39, No. 1, pp. 24–5.

HÖEG, K., ANDERSLAND, O.B., AND ROLFSEN, E.N. (1969). "Undrained Behaviour of Quick Clay Under Load Tests at Åsrum," *Géotechnique*, Vol. XIX, No. 1, pp. 101–115.

HOEK, E. (1983). "Strength of Jointed Rock Masses," 23rd Rankine Lecture, *Géotechnique*, Vol. XXXIII, No. 3, pp. 187–223.

HOEK, E. (2007). *Practical Rock Engineering*, updated shortcourse notes available as a pdf file from www.rockscience.com, 342 p.

HOEK, E. AND BROWN, E.T. (1980). "Empirical Strength Criteria for Rock Masses," *Journal of the Geotechnical Engineering Division*, ASCE, Vol. 106, No. GT9, pp. 1013–1035.

HOEK, E. AND BROWN, E.T. (1988). "The Hoek–Brown Failure Criterion—A 1988 Update," *Rock Engineering for Underground Excavations*, Proceedings of the Fifteenth Canadian Rock Mechanics Symposium, J.C. Curran (Ed.), Toronto, pp. 31–38.

HOEK, E. AND BROWN, E.T. (1997). Practical Estimates of Rock Mass Strength. *International Journal of Rock Mechanics & Mining Science and Geomechanics Abstracts*, Vol. 34, No. 8, pp. 1165–1186.

HOEK, E., KAISER, P.K., AND BAWDEN, W.F. (1995). *Support for Underground Excavations in Hard Rock*, Balkema, Rotterdam, 300 p.

HOGENTOGLER, C.A. AND TERZAGHI, C. (1929). "Interrelationship of Load, Road, and Subgrade," *Public Roads*, Vol. 10, No. 3, pp. 37–64.

HOLDEN, J.C. (1974). "Penetration Testing in Australia," *Proceedings of the European Symposium on Penetration Testing* (ESOPT), Vol. 1, pp. 155–162.

HOLL, D.L. (1940). "Stress Transmission in Earths," *Proceedings of the Highway Research Board*, Vol. 20, pp. 709–729; as cited by H.G. Poulos and E.H. Davis, (1974).

HOLM, G. AND HOLTZ, R.D. (1977). "A Study of Large Diameter Piston Samplers," *Proceedings of the Specialty Session No. 2, Ninth International Conference on Soil Mechanics and Foundation Engineering*, Tokyo, 77 p.; also in *Proceedings of the International Symposium on Soft Clay*, Bangkok, 381 p.

HOLTZ, R.D. (1989). "Treatment of Problem Foundations for Highway Embankments," *Synthesis of Highway Practice 147*, National Cooperative Highway Research Program, Transportation Research Board, 72 p.

HOLTZ, R.D. (1991). "Pressure Distribution and Settlement," Chapter 5, *Foundation Engineering Handbook*, 2nd ed., H.Y. Fang (Ed.), Van Nostrand Reinhold, New York, pp. 166–222.

HOLTZ, R.D. AND SCHUSTER, R.L. (1995). "Stabilization of Soil Slopes," Chapter 17 in *Landslides: Investigation and Mitigation*, Special Report 247, Transportation Research Board, pp. 439–473.

HOLTZ, R.D. (1980). "SI Units in Geotechnical Engineering," *Geotechnical Testing Journal*, ASTM, Vol. 3, No. 2, pp. 75–88.

HOLTZ, R.D., CHRISTOPHER, B.R., AND BERG, R.R. (1997). *Geosynthetic Engineering*, BiTech Publishers, Vancouver, British Columbia, 451 p.

HOLTZ, R.D., CHRISTOPHER, B.R., AND BERG, R.R. (2008). *Geosynthetic Design and Construction Guidelines*, U.S. Federal Highway Administration, National Highway Institute, Washington, D.C., Publication No. FHWA-NHI-07-092, 553 p.

HOLTZ, R.D. AND BROMS, B.B. (1972). "Long-Term Loading Tests at Skå-Edeby, Sweden," *Proceedings of the ASCE Specially Conference on Performance of Earth and Earth-Supported Structures*, Purdue University, Vol. I, Part 1, pp. 435–464.

HOLTZ, R.D. AND HOLM, G. (1979). "Test Embankment on an Organic Silty Clay," *Proceedings of the Seventh European Conference on Soil Mechanics and Foundation Engineering*, Brighton, England, Vol. 3, pp. 79–86.

HOLTZ, R.D., JAMIOLKOWSKI, M.B., AND LANCELLOTTA, R. (1986). "Lessons from Oedometer Tests on High-Quality Samples," *Journal of Geotechnical Engineering*, ASCE, Vol. 112, No. 8, pp. 768–776.

HOLTZ, R.D., SHANG, J.Q., AND BERGADO, D.T. (2001). "Foundation Soil Improvement," Chapter 15 in *Geotechnical and Geoenvironmental Engineering Handbook*, R.K. Rowe (Ed.), Springer, New York, pp. 429–462.

HOLTZ, W.G. (1959). "Expansive Clays—Properties and Problems," *Quarterly of the Colorado School of Mines*, Vol. 54, No. 4, pp. 89–125.

HOLTZ, W.G. AND GIBBS, H.J. (1956). "Engineering Properties of Expansive Clays," *Transactions*, ASCE, Vol. 121, pp. 641–677.

HOLZER, T.L. (1991). "Nontectonic Subsidence," Chapter 10 in *The Heritage of Engineering Geology: The First Hundred Years*, G.A. Kiersch (Ed.), Centennial Special Vol. 3, Geological Society of America, pp. 219–232.

HORN, H.M. AND LAMBE, T.W. (1964). "Settlement of Buildings on the MIT Campus," *Journal of the Soil Mechanics and Foundations Division*, ASCE, Vol. 90, No. SM5, pp. 181–196.

HOUGH, B.K. (1969). *Basic Soils Engineering*, 2nd ed., The Ronald Press Company, New York, 634 p.

HOUSTON, S.L., HOUSTON, W.N., AND SPADOLA, D.J. (1988). "Prediction of Field Collapse of Soils Due to Wetting," *Journal of Geotechnical Engineering*, ASCE, Vol. 114, No. 1, pp. 40–58.

HOUSTON, W.N. AND HOUSTON, S.L. (1989). "State-of-the-Art-Practice Mitigation Measures for Collapsible Soil Sites," *Proceedings of the Foundation Engineering Congress*, ASCE, Evanston, pp. 161–175.

HOWARD, A.K. (1984). "The Revised ASTM Standard on the Unified Soil Classification System," *Geotechnical Testing Journal*, ASTM, Vol. 7, No. 4, pp. 216–222.

HRYCIW, R.D. (1990). "Small-strain-shear Modulus of Soil by Dilatometer," *Journal of Geotechnical Engineering*, ASCE, Vol. 116, No. 11, pp. 1700–1716.

HUANG, A.B. (2008). Personal communication.

HUANG, A.B., HSU, S.P., AND KUHN, H.R. (1994). "A Multiple Purpose Soil Testing Apparatus," *Geotechnical Testing Journal*, ASTM, Vol. 17, No. 2, pp. 227–232.

HUANG, Y.T, HUANG, A.B., KUO, Y.C., AND TSAI, M.D. (2004). "A Laboratory Study on the Undrained Strength of a Silty Sand from Central Western Taiwan," *Soil Dynamics and Earthquake Engineering*, Vol. 24, No. 9/10, pp. 733–743.

HUMPHREY, D.N. AND LEONARDS, G.A. (1986). "Slide in Upstream Slope of Lake Shelbyville Dam," *Journal of Geotechnical Engineering*, ASCE, Vol. 112, No. 5, pp. 564–577; with discussion and closure, Vol. 114, No. 4, pp. 506–513.

HUNT, R.E. (2005). *Geotechnical Engineering Investigation Manual*, 2nd ed., McGraw-Hill, New York.

HVORSLEV, M.J. (1937). "Über die Festigkeitseigenshaften Gestörter Bindiger Böden" ("On the Strength Properties of Remolded Cohesive Soils"), thesis, published by Danmarks Naturvidenskablige Samfund, *Ingeniørvidenskabelige Skrifter*, Series A, No. 35, København, 159 p.

HVORSLEV, M.J. (1949). *Subsurface Exploration and Sampling of Soils for Civil Engineering Purposes*, U.S. Army Engineer Waterways Experiment Station, Vicksburg, MS, 521 p.; reprinted by the Engineering Foundation, 1962.

HVORSLEV, M.J. (1960). "Physical Components of the Shear Strength of Saturated Clays," *Proceedings of the ASCE Research Conference on the Shear Strength of Cohesive Soils*, Boulder, pp. 169–173.

I

IDRISS, I.M. (1966). "The Response of Earth Banks During Earthquakes," Ph.D. dissertation, University of California, Berkeley, 208 p.

IDRISS, I.M. AND BOULANGER, R.W. (2008). "Soil Liquefaction During Earthquakes," Earthquake Engineering Research Institute, Report No. MNO-12, 243 p.

IMAI, T. AND TONOUCHI, K. (1982). "Correlation of N-value with S-wave Velocity and Shear Modulus," *Proceedings of the Second European Symposium on Penetration Testing*, Amsterdam, pp. 57–72.

IEEE/ASTM (2002). *SI 10: American National Standard for Use of the Modern System of Units (SI): The Modern Metric System*, Designation SI 10–02, ASTM, 62 p.

INTERNATIONAL SOCIETY FOR ROCK MECHANICS (1978). "Suggested Methods for the Qualitative Description of Discontintuities in Rock Masses," *International Journal of Rock Mechanics, Mineral Science & Geomechanics, Abstracts*, Vol. 15, No. 6, pp. 319–368.

INTERNATIONAL SOCIETY FOR ROCK MECHANICS (1981). "Suggested Methods for the Quantitative Description of Discontinuities in Rock Masses," in *Rock Characterisation and Testing and Monitoring—ISRM Suggested Methods*, E.T. Brown (Ed.), Pergamon Press, 215 p.

INTERNATIONAL SOCIETY FOR SOIL MECHANICS AND FOUNDATION ENGINEERING (1977). "List of Symbols, Units, and Definitions," Subcommittee on Symbols, Units, and Definitions, *Proceedings of the Ninth International Conference on Soil Mechanics and Foundation Engineering*, Tokyo, Vol. 3, pp. 156–170.

ISENHOWER, W.M. (1979). "Torsional Simple Shear/Resonant Column Properties of San Francisco Bay Mud," M.S. thesis, Department of Civil Engineering University of Texas at Austin, 306 p.

ISHIBASHI, I. (1992). Discussion of "Effect of Soil Plasticity on Cyclic Response" by M. Vucetic and R. Dobry, *Journal of Geotechnical Engineering*, ASCE, Vol. 118, No. 5, pp. 830–832.

ISHIBASHI, I. AND ZHANG, X. (1993). "Dynamic Shear Moduli and Damping Ratios of Sand and Clay," *Soils and Foundations*, Vol. 33, No. 1, pp. 182–191.

IWAN, W.D. (1967). "On a Class of Models for the Yielding Behavior of Continuous and Composite Systems," *Journal of Applied Mechanics*, ASME, Vol. 34, pp. 612–617.

J

JAEGER, J.C., Cook, N.G.W., AND ZIMMERMAN, R.W. (2007). *Fundamentals of Rock Mechanics*, 4th ed., Blackwell, Malden, MA, 488 p.

JÁKY, J. (1944). "The Coefficient of Earth Pressure at Rest," *Magyar Mérnök és Ëpitész Egylet Közdönye* (*Journal of the Society of Hungarian Architects and Engineers*), Vol. 78, No. 22, pp. 355–358 (in Hungarian).

JÁKY, J. (1948). "Earth Pressure in Silos," *Proceedings of the Second International Conference on Soil Mechanics and Foundation Engineering*, Rotterdam, Vol. I, pp. 103–107.

JAMES, A.N. (1992). *Soluble Materials in Civil Engineering*, Ellis Horwood, 434 p.

JAMIOLKOWSKI, M., LADD, C.C., GERMAINE, J.T., AND LANCELLOTA, R. (1985). "New Developments in Field and Laboratory Testing of Soils," *Proceedings of the Eleventh International Conference on Soil Mechanics and Foundation Engineering*, San Francisco, Vol. 1, pp. 57–154.

JANBU, N. (1998). "Sediment Deformations," Bulletin 35, Norwegian University of Science and Technology, Department of Geotechnical Engineering, Trondheim, 86 p., 383 p.

JANBU, N., BJERRUM. L., AND KJAERNSLI, B. (1956). "*Veiledning ved Løsning av Fundamenteringsoppgaver*," Publication No. 16, Norwegian Geotechnical Institute, Oslo, 92 p.

JANBU, N. AND SENNESET, K. (1973). "Field Compressometer—Principles and Applications," *Proceedings of the Eighth International Conference on Soil Mechanics and Foundation Engineering*, Moscow, Vol. 1.1, pp. 191–198.

JANSEN, R.B. (Ed.) (1988). *Advanced Dam Engineering for Design, Construction, and Rehabilitation*, Van Nostrand Reinhold, New York, 811 p.

JARDINE, R.J., FOURIE, A., MASWOSWE, J., AND BURLAND, J.B. (1985). "Field and Laboratory Measurements of Soil Stiffness," *Proceedings of the Eleventh International Conference on Soil Mechanics and Foundation Engineering*, San Francisco, Vol. 2, pp. 511–514.

JENNINGS, J.E. AND BRINK, A.B.A. (1978). "Application of Geotechnics to the Solution of Engineering Problems—Essential Preliminary Steps to Relate the Structure to the Soil Which Provides Its Support," *Proceedings of the Institution of Civil Engineers*, Part 1, Vol. 64, pp. 571–589.

JOHNSON, A.W. AND SALLBERG, J.R. (1960). "Factors that Influence Field Compaction of Soils," *Bulletin 272*, Highway Research Board, 206 p.

JOHNSON, T.C., BERG, R.L., CHAMBERLAIN, E.J., AND COLE, D.M. (1986). *Frost Action Techniques for Roads and Airfields: A Comprehensive Survey of Research Findings*, U.S. Army Cold Regions Research and Engineering Laboratory Report No. 86–18.

JONAS, E. (1964). "Subsurface Stabilization of Organic Silt-Clay by Precompression," *Journal of the Soil Mechanics and Foundations Division*, ASCE, Vol. 90, No. SM5, pp. 363–376.

JÜRGENSON, L. (1934). "The Shearing Resistance of Soils," *Journal of the Boston Society of Civil Engineers*, July, reprinted in *Contributions to Soil Mechanics, 1925–1940*, BSCE, pp. 184–217.

K

KALIAKIN, V.N. AND DAFALIAS, Y.F. (1990a). "Theoretical Aspects of the Elastoplastic-Viscoplastic Bounding Surface Model for Cohesive Soils," *Soils and Foundations*, Japanese Society of Soil Mechanics and Foundation Engineering, Vol. 30, No. 3, pp. 11–24.

KALIAKIN, V.N. AND DAFALIAS, Y.F. (1990b). "Verification of the Elastoplastic-Viscoplastic Bounding Surface Model for Cohesive Soils," *Soils and Foundations*, Japanese Society of Soil Mechanics and Foundation Engineering, Vol. 30, No. 3, pp. 25–36.

KANE, W.F. AND AMADEI, B. (Eds.) (1991). "Detection of and Construction at the Soil/Rock Interface," *Proceedings of the Symposium*, Geotechnical Special Publication No. 28, ASCE, 156 p.

KARLSSON, R. (1977). "Consistency Limits," in cooperation with the Laboratory Committee of the Swedish Geotechnical Society, Swedish Council for Building Research, Document D6, 40 p.

KARLSSON, R. AND PUSCH, R. (1967). "Shear Strength Parameters and Microstructure Characteristics of a Quick Clay of Extremely High Water Content," *Proceedings of the Geotechnical Conference Oslo on the Shear Strength Properties of Natural Soils and Rocks*, Vol. I, Published by the Norwegian Geotechnical Institute, Olso, pp. 35–42.

KAUFMAN, R.I. AND SHERMAN, W.C., Jr. (1964). "Engineering Measurements for Port Allen Lock," *Journal of the Soil Mechanics and Foundations Division*, ASCE, Vol. 90, No. SM5, pp. 221–247; also in *Design of Foundations for Control of Settlement*, ASCE, pp. 281–307.

KAWAGUCHI, T., MITACHI, T., AND SHIBUYA, S. (2001). "Evaluation of Shear Wave Travel Time in Laboratory Bender Element Test," *Proceedings of the Fifteenth International Conference on Soil Mechanics and Geotechnical Engineering*, Istanbul, Vol. 1, pp. 155–158.

KAY, J.N. (1990). "Use of the Liquid Limit for Characterisation of Expansive Soil Sites," *Civil Engineering Transactions*, Institution of Engineers, Australia, Vol. 32, No. 3, pp. 151–156.

KEENE, P. (1964). Discussion of "Design of Foundations for Control of Settlement," *Proceedings of the ASCE*, Evanston, IL.

KENNEY, T.C. (1959). Discussion of "Geotechnical Properties of Glacial Lake Clays," by T.H. Wu, *Journal of the Soil Mechanics and Foundations Division*, ASCE, Vol. 85, No. SM3, pp. 67–79.

KENNEY, T.C. (1964). "Sea-Level Movements and the Geologic Histories of the Post-Glacial Marine Soils at Boston, Nicolet, Ottawa, and Oslo," *Géotechnique*, Vol. XIV, No. 3, pp. 203–230.

KENNEY, T.C. (1976). "Formation and Geotechnical Characteristics of Glacial-Lake Varved Soils," *Laurits Bjerrum Memorial Volume—Contributions to Soil Mechanics*, Norwegian Geotechnical Institute, Oslo, pp. 15–39.

KENNEY, T.C. AND LAU, D. (1985). "Internal Stability of Granular Filters," *Canadian Geotechnical Journal*, Vol. 22, No. 2, pp. 215–225.

KENNEY, T.C. AND LAU, D. (1986). "Internal Stability of Granular Filters," Reply to discussions, *Canadian Geotechnical Journal*, Vol. 23, No. 3, pp. 420–423.

KIERSCH, G.A. AND JAMES, L.B. (1991). *The Heritage of Engineering Geology; The First Hundred Years*, G.A. Kiersch (Ed.) (1991), Centennial Special Vol. 3, Geological Society of America, 605 p.

KIRKALDIE, L. (Ed.) (1988). *Rock Classification Systems for Engineering Purposes*, ASTM Special Technical Publication No. 984, 167 p.

KISHIDA, H. AND TAKANO A. (1970). "The Damping in the Dry Sand," *Proceedings of the Third Japan Earthquake Engineering Symposium, Tokyo*, pp. 159–166.

KOERNER, R.M. (2006). *Designing with Geosynthetics*, 5th ed., Prentice-Hall, Upper Saddle River, NJ, 816 p.

KONDNER, R.L. (1963). "Hyperbolic Stress-Strain Response: Cohesive Soils," *Journal of the Soil Mechanics and Foundation Division*, ASCE, Vol. 89, No. SM1, pp. 115–143.

KOOREVAAR, P., MENELIK, G., AND DIRKSEN, C. (1983). *Elements of Soil Physics*, Elsevier, Amsterdam, 228 p.

KORHONEN, K.H. AND LOJANDER, M. (1987). "Yielding of Perno Clay," *Constitutive Laws for Engineering Materials: Theory and Applications*, Elsevier, Vol. 2, pp. 1249–1255.

KOVACS, W.D. (1968). "An Experimental Study of the Response of Clay Embankments to Base Excitation," Ph.D. dissertation, University of California, Berkeley, 126 p.

KOVACS, W.D., EVANS, J.C., AND GRIFFITH, A.H. (1977). "Towards a More Standardized SPT," *Proceedings of the Ninth International Conference on Soil Mechanics and Foundation Engineering*, Tokyo, Vol. 2, pp. 269–276.

KOVACS, W.D., SEED, H.B., AND CHAN, C.K. (1971). "Dynamic Moduli and Damping Ratios for a Soft Clay," *Journal of the Soil Mechanics and Foundations Division*, ASCE, Vol. 97, No. SM1, pp. 59–75.

KRAHN, J., FREDLUND, D.G., AND KLASSEN, M.J. (1989). "Effect of Soil Suction on Slope Stability at Notch Hill," *Canadian Geotechnical Journal*, Vol. 26, No. 2, pp. 269–278.

KRAMER, S.L. (1996). *Geotechnical Earthquake Engineering*, Prentice Hall, Upper Saddle River, NJ, 653 p.

KRIZEK, R.J. AND FRANKLIN, A.G. (1967). "Energy Dissipation in a Soft Clay," *Proceedings of the Symposium on Wave Propagation and Dynamic Properties of Earth Materials*, University of New Mexico, Albuquerque.

KROPP, A.L., MCMAHON, D.J., AND HOUSTON, S.L. (1994). "Case History of a Collapsible Soil Fill," *Vertical and Horizontal Deformations of Foundations and Embankments*, A.T. Yeung and G.Y. Felio (Eds.), Geotechnical Special Publication No. 40, ASCE, Vol. 2, pp. 1531–1542.

KRYNINE, D.P. AND JUDD, W.R. (1957). *Principles of Engineering Geology and Geotechnics*, McGraw-Hill Book Co., New York, 730 p.

KULHAWY, F.H. (2005). "Estimation of Soil Properties for Foundation Design," Notes for a short course sponsored by the ASCE Seattle Section Geotechncial Group.

KULHAWY, F.H. AND MAYNE, P.W. (1990). *Manual on Estimating Soil Properties for Foundation Design, Final Report*, Report No. EL-6800, Research Project 1493–6, Electric Power Research Institute, Palo Alto, 308 p.

KULHAWY, F.H., TRAUTMAN, C.H., AND O'ROURKE, T.D. (1991). "The Soil-Rock Boundary: What is it and Where is it?" *Proceedings of the Symposium Detection of and Construction at the Soil/Rock Interface*, W.F. Kane and B. Amadei (Eds.), Geotechnical Special Publication No. 28, ASCE, pp. 1–15.

L

LACY, S.J. AND PREVOST, J.H. (1987). "Constitutive Model for Geomaterials," in *Proceedings of the Second International Conference on Constitutive Laws for Engineering Materials*, C.S. Desai, E. Krempl, P.D. Kiousis, and T. Kundu (Eds.), Elsevier, New York, pp. 149–160.

LADD, C.C. (1964). "Stress-Strain Behavior of Saturated Clay and Basic Strength Principles," *Research Report R64–17*, Department of Civil Engineering, Massachusetts Institute of Technology, 67 p.

LADD, C.C. (1971a). "Settlement Analyses for Cohesive Soils," *Research Report R71–2*, Soils Publication 272, Department of Civil Engineering, Massachusetts Institute of Technology, 107 p.

LADD, C.C. (1971b). "Strength Parameters and Stress-Strain Behavior of Saturated Clays," *Research Report R71–23*, Soils Publication 278, Department of Civil Engineering, Massachusetts Institute of Technology, 280 p.

LADD, C.C. (1972). "Test Embankment on Sensitive Clay," *Proceedings of the ASCE Specialty Conference on Performance of Earth and Earth-Supported Structures*, ASCE, Purdue University, Vol. I, Part 1, pp. 103 and 107.

LADD, C.C. (1975). "Foundation Design of Embankments Constructed on Connecticut Valley Varved Clays," *Research Report R75–7*, Geotechnical Publication 343, Department of Civil Engineering, Massachusetts Institute of Technology, 438 p.

LADD, C.C. AND DEGROOT, D.J. (2003). "Recommended Practice for Soft Ground Site Characterization: The Arthur Casagrande Lecture," *Proceedings of the Twelfth Panamerican Conference on Soil Mechanics and Foundation Engineering*, Cambridge, MA, Vol. 1, pp. 3–57.

LADD, C.C. AND EDGERS, L. (1972). "Consolidated-Undrained Direct-Simple Shear Tests on Saturated Clays," *Research Report R72–92*, Soils Publication 284, Department of Civil Engineering, Massachusetts Institute of Technology, 245 p.

LADD, C.C. AND FOOTT, R. (1974). "A New Design Procedure for Stability of Soft Clays," *Journal of the Geotechnical Engineering Division*, ASCE, Vol. 100, No. GT7, pp. 763–786.

LADD, C.C., FOOTE, R., ISHIHARA, K., SCHLOSSER, F., AND POULOS, H.G. (1977). "Stress-Deformation and Strength Characteristics," State-of-the-Art Report, *Proceedings of the Ninth International Conference on Soil Mechanics and Foundation Engineering*, Tokyo, Vol. 2, pp. 421–494.

LADD, C.C. AND LAMBE, T.W. (1963). "The Strength of Undisturbed Clay Determined from Undrained Tests," *Laboratory Shear Testing of Soils*, Special Technical Publication No. 361, ASTM, pp. 342–371.

LADD, C.C. AND LUSCHER, U. (1965). "Engineering Properties of the Soils Underlying the M.I.T. Campus," *Research Report R65–68*, Soils Publication 185, Department of Civil Engineering, Massachusetts Institute of Technology.

LADD, R.S. (1965). "Use of Electrical Pressure Transducers to Measure Soil Pressure," *Research Report R65–48*, Soils Publication 180, Department of Civil Engineering, Massachusetts Institute of Technology, 79 p.

LADE, P.V. (1977). "Elasto-Plastic Stress-Strain Theory for Cohesionless Soil with Curved Yield Surfaces," *International Journal of Solids and Structures*, ASCE, Vol. 13, pp. 1019–1035.

LADE, P.V. AND DUNCAN, J.M. (1975). "Elastoplastic Stress-Strain Theory for Cohesionless Soil," *Journal of the Geotechnical Engineering Division*, ASCE, Vol. 101, No. 10, pp. 1037–1053.

LADE, P.V. AND LEE, K.L. (1976). "Engineering Properties of Soils," University of California, Los Angeles, Report No. UCLA-ENG-7652, 145 p.

LAFLEUR, J., MLYNAREK, J., AND ROLLIN, A.L. (1989). "Filtration of Broadly Graded Cohesionless Soils," *Journal of Geotechnical Engineering*, ASCE, Vol. 115, No. 12, pp. 1747–1768.

LAMBE, T.W. (1950). "Capillary Phenomena in Cohesionless Soil," ASCE, Separate No. 4, January.

LAMBE, T.W. (1951). *Soil Testing for Engineers*, Wiley, New York, 165 p.

LAMBE, T.W. (1953). "The Structure of Inorganic Soil," *Proceedings of the ASCE*, Vol. 79, Separate No. 315, 49 p.

LAMBE, T.W. (1958a). "The Structure of Compacted Clay," *Journal of the Soil Mechanics and Foundations Division*, ASCE, Vol. 84, No. SM2, pp. 1654–1 to 1654–34.

LAMBE, T.W. (1958b). "The Engineering Behavior of Compacted Clay," *Journal of the Soil Mechanics and Foundations Division*, ASCE, Vol. 84, No. SM2, pp. 1655–1 to 1655–35.

LAMBE, T.W. (1964). "Methods of Estimating Settlement," *Journal of the Soil Mechanics and Foundations Division*, ASCE, Vol. 90, No. SM5, pp. 43–67; also in *Design of Foundations for Control of Settlement*, ASCE, pp. 47–72.

LAMBE, T.W. (1967). "Stress Path Method," *Journal of the Soil Mechanics and Foundations Division*, ASCE, Vol. 93, No. SM6, pp. 309–331.

LAMBE, T.W. AND MARR, W.A. (1979). "Stress Path Method: Second Edition," *Journal of the Geotechnical Engineering Division*, ASCE, Vol. 105, No. GT6, pp. 727–738.

LAMBE, T.W. AND WHITMAN, R.V. (1969). *Soil Mechanics*, Wiley, New York, 553 p.

LAMBERT, D. AND THE DIAGRAM GROUP (1988). *The Field Guide to Geology*, Facts On File, Inc., New York, 256 p.

LAMBRECHTS, J.R. AND LEONARDS, G.A. (1978). "Effects of Stress History on Deformation of Sand," *Journal of the Geotechnical Engineering Division*, ASCE, Vol. 104, No. GT11, pp. 1371–1387.

LANE, K.S. AND WASHBURN, S.E. (1946). "Capillarity Tests by Capillarimeters and by Soil Filled Tubes," *Proceedings of the Highway Research Board*, Vol. 26, pp. 460–473.

LAROCHELLE, P. AND LEFEBVRE, G. (1971). "Sampling Disturbance in Champlain Clays," *Sampling of Soil and Rock*, Special Technical Publication No. 483, ASTM, pp. 143–163.

LAROCHELLE, P., TRAK, B., TAVENAS, F., AND ROY, M. (1974). "Failure of a Test Embankment on a Sensitive Champlain Clay Deposit," *Canadian Geotechnical Journal*, Vol. 11, No. 1, pp. 142–164.

LAROCHELLE, P., SARRAILH, J., TAVENAS, F., ROY, M., AND LEROUEIL, S. (1981). "Causes of Sampling Disturbance and Design of a New Sampler for Sensitive Soils," *Canadian Geotechnical Journal*, Vol. 18, No. 1, pp. 52–66.

LARSSON, R. (1977). "Basic Behavior of Scandinavian Soft Clays," *Report No. 4*, Swedish Geotechnical Institute, 138 p.

LAW, K.T. AND HOLTZ, R.D. (1978). "A Note on Skempton's *A* Parameter with Rotation of Principal Stresses," *Géotechnique*, Vol. XXVIII, No. 1, pp. 57–64.

LEA, N.D. AND BRAWNER, C.O. (1963). "Highway Design and Construction Over Peat Deposits in Lower British Columbia," *Highway Research Record*, No. 7. pp. 1–32.

LEE, K.L. (1965). "Triaxial Compressive Strength of Saturated Sands Under Seismic Loading Conditions," Ph.D. dissertation, University of California, Berkeley, 520 p.

LEE, K.L. AND FOCHT, J.A. (1976). "Strength of Clay Subjected to Cyclic Loading," *Marine Geotechnology*, Vol. 1, No. 3, pp. 165–185.

LEE, K.L. AND SEED, H.B. (1967). "Drained Strength Characteristics of Sands," *Journal of the Soil Mechanics and Foundations Division*, ASCE, Vol. 93, No. SM6, pp. 117–141.

LEE, K.L. AND SINGH, A. (1971). "Compaction of Granular Soils," *Proceedings of the Ninth Annual Symposium on Engineering Geology and Soils Engineering*, Boise, Idaho, pp. 161–174.

LEE, W.F. (2000). "Internal Stability Analyses of Geosynthetic Reinforced Retaining Walls," Ph.D. thesis/dissertation, Doctor of Philosophy, University of Washington, 380 p.

LEONARDS, G.A. (Ed.) (1962). *Foundation Engineering*, McGraw-Hill, New York, 1136 p.

LEONARDS, G.A. (1973). Discussion of "The Empress Hotel, Victoria, British Columbia: Sixty-five Years of Foundation Settlements," *Canadian Geotechnical Journal*, Vol. 10, No. 1, pp. 120–122.

LEONARDS, G.A. (1976). "Estimating Consolidation Settlements of Shallow Foundations on Overconsolidated Clays," *Special Report 163*, Transportation Research Board, pp. 13–16.

LEONARDS, G.A. (1977). Discussion to Main Session 2, *Proceedings of the Ninth International Conference on Soil Mechanics and Foundation Engineering*, Tokyo, Vol. 3, pp. 384–386.

LEONARDS, G.A., ALARCON, A., FROST, J.D., MOHAMEDZEIN, Y.E., SANTAMARINA, J.C., THEVANAYAGAM, S., TOMAZ, J.E., AND TYREE, J.L. (1986). Discussion of "Dynamic Penetration Resistance and the Prediction of the Compressibility of a Fine-Grained Sand—A Laboratory Study," by C.R.I. Clayton, M.B. Hababa, and N.E. Simons, *Géotechnique*, Vol. XXXVI, No. 2, pp. 275–279.

LEONARDS, G.A. AND ALTSCHAEFFL, A.G. (1964). "Compressibility of Clay," *Journal of the Soil Mechanics and Foundations Division*, ASCE, Vol. 90, No. SM5, pp. 133–156; also in *Design of Foundations for Control of Settlement*, ASCE, pp. 163–185.

LEONARDS, G.A., CUTTER, W.A., AND HOLTZ, R.D. (1980). "Dynamic Compaction of Granular Soils," *Journal of the Geotechnical Engineering Division*, ASCE, Vol. 106, No. 1, pp. 35–44.

LEONARDS, G.A. AND GIRAULT, P. (1961). "A Study of the One-Dimensional Consolidation Test," *Proceedings of the Fifth International Conference on Soil Mechanics and Foundation Engineering*, Paris, Vol. I, pp. 116–130.

LEONARDS, G.A. AND RAMIAH, B.K. (1959). "Time Effects in the Consolidation of Clay," *Papers on Soils—1959 Meeting*, American Society for Testing and Materials, Special Technical Publication No. 254, pp. 116–130.

LEROUEIL, S., MAGNAN, J.P., AND TAVENAS, F. (1990). *Embankments on Soft Clays*, a translation by D. Muir Wood of *Remblais sur Argiles Molles*, 1985, Ellis Horwood, 360 p.

LEROUEIL, S., TAVENAS, F., MIEUSSENS, C., AND PEIGNAUD, M. (1978b). "Construction Pore Pressures in Clay Foundations Under Embankments. Part II: Generalized Behaviour," *Canadian Geotechnical Journal*, Vol. 15, No. 1, pp. 66–82.

LEROUEIL, S., TAVENAS, F., TRAK, B., LAROCHELLE, P., AND ROY, M. (1978a). "Construction Pore Pressure in Clay Foundations Under Embankments. Part I: The Saint-Alban Test Fills," *Canadian Geotechnical Journal*, Vol. 15, No. 1, pp. 54–65.

LITTLE, A.L. (1969). "The Engineering Classification of Residual Tropical Soils," *Proceedings of the Specialty Session on the Engineering Properties of Lateritic Soils*, Vol. 1, Seventh International Conference on Soil Mechanics and Foundation Engineering, Mexico City, pp. 1–10.

LIU, T.K. (1970). "A Review of Engineering Soil Classification Systems," *Special Procedures for Testing Soil and Rock for Engineering Purposes*, 5th ed., ASTM Special Technical Publication 479, pp. 361–382.

LO, K.Y. AND HEFNY, A.M. (2001). "Basic Rock Mechanics and Testing," Chapter 6 in *Geotechnical and Geoenvironmental Handbook*, R.K. Rowe (Ed.), Kluwer Academic Publishers, pp. 147–172.

LOBECK, A.K. (1939). *Geomorphology*, An Introduction to the Study of Landscapes, Mc-Graw-Hill Book Company, New York, 731 p.

LOJANDER, M. (1988). "The Parameters of the Mechanical Model of Anisotropic Clay," *Proceedings of the Nordiska Geoteknikermote*, Oslo, Norway.

LOOS, W. (1936). "Comparative Studies of the Effectiveness of Different Methods for Compacting Cohesionless Soils," *Proceedings of the First International Conference on Soil Mechanics and Foundation Engineering*, Cambridge, Vol. III, pp. 174–179.

LOWE, J., III. (1974). "New Concepts in Consolidation and Settlement Analysis," *Journal of the Geotechnical Engineering Division*, ASCE, Vol. 100, No. GT6, pp. 574–612.

LOWE, J., III. AND ZACCHEO, P.F. (1991). "Subsurface Explorations and Sampling," Chapter 1 in *Foundation Engineering Handbook*, 2nd ed., H.Y. Fang (Ed.), Van Nostrand Reinhold, New York, pp. 1–71.

LOWE, J., III., ZACCHEO, P.F., AND FELDMAN, H.S. (1964). "Consolidation Testing with Back Pressure," *Journal of the Soil Mechanics and Foundations Division*. ASCE, Vol. 90, No. SM5, pp. 69–86; also in *Design of Foundations for Control of Settlement*, ASCE, pp. 73–90.

LU, N. AND LIKOS, W.J. (2004). *Unsaturated Soil Mechanics*, Wiley, Hoboken, 556 p.

LUKAS, R.G. (1980). "Densification of Loose Deposits by Pounding," *Journal of the Geotechnical Engineering Division*, ASCE, Vol. 106, No. GT4, pp. 435–446.

LUKAS, R.G. (1995). "Dynamic Compaction," *Geotechnical Engineering Circular No. 1*, FHWA Publication No. 1, Report No. FHWA-SA-95-037, Office of Technology Applications, Washington, 105 p.

LUNNE, T., ROBERTSON, P.K., AND POWELL, J.J.M. (1997). *Cone Penetration Testing in Geotechnical Practice*, Chapman & Hall, London.

LUPINI, J.F., SKINNER, A.E., AND VAUGHN, P.R. (1981). "The Drained Residual Strength of Cohesive Soils," *Géotechnique*, Vol. XXXI, No. 2, pp. 181–213.

LYONS ASSOCIATES (1971). *Laterite and Lateritic Soils and other Problem Soils of Africa*, An Engineering Study for the Agency for International Development, Lyon Associates Inc., Baltimore, MD, and Building and Road Research Institute, Kumasi, Ghana, 290 p.

M

MACDONALD, A.B. AND SAUER, E.K. (1970). "The Engineering Significance of Pleistocene Stratigraphy in the Saskatoon Area, Saskatchewan, Canada," *Canadian Geotechnical Journal*, Vol. 7, No. 2, pp. 116–126.

MAGNAN, J.P., SHAHANGUIAN, S., AND JOSSEAUME, H. (1982). "Étude en Laboratoire des États Limites d'une Argile Molle Organique," *Revue Française de Géotechnique*, Vol. XX, No. 1, pp. 13–19.

MAIR, R.J. AND WOOD, D.M. (1987). *Pressuremeter Testing: Methods and Interpretation*, CIRIA-Butterworths, London, 160 p.

MANNHEIM, B.R.S. (1979). "A New Conception of the Formation of the Kola Peninsula Apatite Deposit: The Coprogenic Impact Theory-CIT," *The Journal of Irreproducible Results, Society for Basic Irreproducible Research*, Society for Basic Irreproducible Research, Vol. 25, No. 1, pp. 6–7.

MANSUR, C.I. AND KAUFMAN, R.I. (1962). "Dewatering," Chapter 3 in *Foundation Engineering*, G.A. Leonards (Ed.), McGraw-Hill, pp. 241–350.

MARACHI, N.D., DUNCAN, J.M., CHAN, C.K., AND SEED, H.B. (1981). "Plane-strain Testing of Sand," *Laboratory Shear Strength of Soil*, R.N. Yong and F.C. Townsend (Eds.), ASTM Special Technical Publication 740, pp. 294–302.

MARCHETTI, S. (1980). "In-Situ Tests by Flat Dilatometer," *Journal of the Geotechnical Engineering Division*, ASCE, Vol. 106, No. GT3, pp. 299–321.

MARCHETTI, S. (1997). "The Flat Dilatometer: Design Applications," *Proceedings of the Third International Geotechnical Engineering Conference*, Cairo, Egypt, pp. 421–448 (as referenced in Sabatini, et al., 2002).

MARCUSON, W.F., HYNES M.E., AND FRANKLIN, A.G. (1990). "Evaluation and Use of Residual Strength in Seismic Safety Analysis of Embankments," *Earthquake Spectra*, Vol. 6, No. 3, pp. 529–572.

MARIN-NIETO, L. (1997). "Some Experiences with Clay Soil in Southwestern of Ecuador," *Proceedings of the Fourteenth International Conference on Soil Mechanics and Geotechnical Engineering*, Hamburg, Germany, Vol. 1, pp. 157–160.

MARIN-NIETO, L. (2007). "Correlación Entre los Parámetros Climáticos y los Movimientos de una Zapata Cimetada en Rocas Expansivas, al Suroeste del Ecuador" ("Correlation Between Climatic Parameters and the Movements of a Footing on Expansive Rock, Southwest Ecuador"), *Proceedings of the Thirteenth Panamerican Conference on Soil Mechanics and Geotechnical Engineering*, Isla de Margarita, Venezuela, pp. 54–58 (CD-ROM).

MARINOS, P. AND HOEK, E. (2000). "GSI—A Geologically Friendly Tool for Rock Mass Strength Estimation," *Proceedings of the GeoEngineering 2000 Conference*, Melbourne, Australia, pp. 1422–1442.

MARINOS, P. AND HOEK, E. (2001). "Estimating the Geotechnical Properties of Heterogeneous Rock Masses Such as Flysch," *Bulletin of the Engineering Geology and the Environment (IAEG)*, Vol. 60, pp. 85–92.

MARINOS, P. AND HOEK, E. (2004). "Discussion of Rock Mass Characterization," presented at the *Forty-Seventh Annual Meeting*, Association of Engineering Geologists, Dearborn, MI (abstract).

MASSARSCH, K.R. (1979). "Lateral Earth Pressure in Normally Consolidated Clay," *Proceedings of the Seventh European Conference on Soil Mechanics and Foundation Engineering*, Brighton, England, Vol. 2, pp. 245–250.

MASSARSCH, K.R., HOLTZ, R.D., HOLM, B.G., AND FREDRICKSSON, A. (1975). "Measurement of Horizontal In Situ Stresses," *Proceedings of the ASCE Specialty Conference on In Situ Measurement of Soil Properties*, Raleigh, NC, Vol. I, pp. 266–286.

MATSUOKA, H. AND NAKAI, T. (1977). "Stress-strain Relationship of Soil Based on the 'SMP'," *Proceedings of Specialty Session 9, Ninth International Conference Soil Mechanics and Foundation Engineering*, Tokyo, pp. 153–162.

MATSUSHITA, K., KISHIDA, H., AND KYO, K. (1967). "Experiments on Damping of Sands," Transactions of the Architectural Institute of Japan, Summaries of Technical Papers (Annual Meeting of AIJ, 1967), 166 p.

MAYA, J. AND RODRIGUEZ, J. (1987). "El Subsuelo de Bogotá y los Problemas de Cimentaciones," *Proceedings of the Eighth Panamerican Conference on Soil Mechanics and Foundation Engineering*, Colombia, pp. 197–264.

MAYNE, P.W. (2006). "Critical State Soil Mechanics for Dummies," http://geosystems.ce.gatech.edu/Faculty/Mayne/papers/index.html, last accessed August, 2006.

MAYNE, P.W. (2007). "Cone Penetration Testing," *Synthesis of Highway Practice 368*, National Cooperative Highway Research Program, Transportation Research Board, 162 p.

MAYNE, P.W., CHRISTOPHER, B.R., AND DEJONG, D.J. (2001). "Manual on Subsurface Investigations, National Highway Institute, Federal Highway Administration, Publ. No. FHWA NHI-01-031, 394 p.

MAYNE, P.W. AND KULHAWY, F.H. (1982). "K_o-OCR Relationships in Soil," *Journal of the Geotechnical Engineering Division*, ASCE, Vol. 108, No. GT6, pp. 851–872.

MAYNE, P.W. AND POULOS, H.G. (1999). "Approximate Displacement Influence Factors for Elastic Shallow Foundations," *Journal of Geotechnical and Geoenvironmental Engineering*, ASCE, Vol. 125, No. 6, pp. 453–460; and closure to discussion by Fowler et al. (2001), Vol. 127, No. 1, pp. 99–102.

MAYNE, P.W. AND RIX, G.J. (1993). "G_{max}–q_c Relationship for Clays," *Geotechnical Testing Journal*, ASTM, Vol. 16, No. 1, pp. 54–60.

MCCARRON, W.O. AND CHEN, W.F. (1994). "Soil Plasticity and Implementation," Chapter 8 in *Constitutive Equations for Engineering Materials, Vol. 2: Plasticity and Modeling*, W.F. Chen and A.F. Saleeb (Eds.), pp. 991–1059.

MCGOWN, A. (1973). "The Nature of the Matrix in Glacial Ablation Tills," *Proceedings of the International Symposium on Soil Structure*, Gothenburg, Sweden, 95 p.

MCKEEN, R.G. (1992). "Investigating Field Behavior of Expansive Clay Soils," *Expansive Clay Soils and Vegetative Influence on Shallow Foundations*, C. Vipulanandan, M.B. Addison, and M. Hasan (Eds.), Geotechnical Special Publication No. 115, ASCE, pp. 82–94.

MCNEILL, R.L. (1969). "Machine Foundations—The State-of-the-Art,"*Proceedings of the Specialty Session 2, Seventh International Conference of Soil Mechanics and Foundation Engineering*, Mexico City, Mexico, pp. 67–100.

MEANS, R.E. AND PARCHER, J.V. (1963). *Physical Properties of Soils*, Charles E. Merrill Books, Inc., Columbus, OH, 464 p.

MEEHAN, R.L. (1967). "The Uselessness of Elephants in Compacting Fill," *Canadian Geotechnical Journal*, Vol. IV, No. 3, pp. 358–360.

MEIGH, A.C. (1987). *Cone Penetration Testing: Methods and Interpretation*, CIRIA-Butterworths, London, 141 p.

MÉNARD, L.F. (1956). "An Apparatus for Measuring the Strength of Soils in Place," MSCE thesis, University of Illinois.

MÉNARD, L.F. (1975). "The Ménard Pressuremeter," *Les Éditions Sols-Soils*, No. 26, pp. 7–43.

MÉNARD, L.F. AND BROISE, Y. (1975). "Theoretical and Practical Aspects of Dynamic Consolidation," *Géotechnique*, Vol. XXV, No. 1, pp. 3–18.

MESRI, G. (1973). "Coefficient of Secondary Compression," *Journal of the Soil Mechanics and Foundations Division*, ASCE, Vol. 99, No. SM1, pp. 123–137.

MESRI, G. (1975). Discussion of "New Design Procedures for Stability of Soft Clays," *Journal of the Geotechnical Engineering Division*, ASCE, Vol. 101, No. GT4, pp. 409–412.

MESRI, G. (1989). "A Reevaluation of $s_{u(mob)} = 0.22\sigma'_p$ Using Laboratory Shear Tests," *Canadian Geotechnical Journal*, Vol. 26, No, 1, pp. 162–164.

MESRI, G. AND CASTRO, A. (1987). "C_α/C_c Concept and K_o During Secondary Compression," *Journal of Geotechnical Engineering*, ASCE, Vol. 113, No. 3, pp. 230–247.

MESRI, G., FENG, T.W., ALI, S., AND HAYAT, T.M. (1994). "Permeability Characteristics of Soft Clays," *Proceedings of the Thirteenth International Conference on Soil Mechanics and Foundation Engineering*, New Dehli, Vol. 1, pp. 187–192.

MESRI, G. AND GODLEWSKI, P.M. (1977). "Time- and Stress-Compressibility Interrelationship," *Journal of the Geotechnical Engineering Division*, ASCE, Vol. 103, No. GT5, pp. 417–430.

MEYERHOF, G.G. (1956). "Penetration Tests and Bearing Capacity of Cohesionless Soils," *Journal of the Soil Mechanics and Foundations Division*, ASCE, Vol. 82, No. SM1, pp. 1–19.

MILLIGAN, V. (1972). Discussion of "Embankments on Soft Ground," *Proceedings of the ASCE Specialty Conference on Performance of Earth and Earth-Supported Structures*, Purdue University, Vol. III, pp. 41–48.

MILLS, W.T. AND DE SALVO, J.M. (1978). "Soil Compaction and Proofrolling," *Soils*, Newsletter of Converse, Ward, Davis, and Dixon, Inc., Pasadena, CA, and Caldwell, NJ, Autumn, pp. 6–7.

MILOVIĆ, D.M. (1970). "Contraintes et Déplacemens dan une Couche Élastique d'Épaisseur Limitée, Produits par une Foundation Circulaire, *Le Génie Civil*, T. 147, No. 5, pp. 281–285.

MITCHELL, J.K. AND SITAR, N. (1982). "Engineering Properties of Tropical Soils," *Proceedings of the ASCE Geotechnical Engineering Division Specialty Conference on Engineering and Construction in Tropical and Residual Soils*, ASCE, Honolulu, HI, pp. 30–57.

MITCHELL, J.K. AND GARDNER, W.S. (1975). "In Situ Measurement of Volume Change Characteristics," State-of-the-Art Report, *Proceedings of the ASCE Specialty Conference on In Situ Measurement of Soil Properties*, Raleigh, NC, Vol. II, 333 p.

MITCHELL, J.K. AND SOGA, K. (2005). *Fundamentals of Soil Behavior*, 3rd ed., Wiley, 577 p.

MOH, Z.C., BRAND, E.W., AND NELSON, J.D. (1972). "Pore Pressures Under a Bund on Soft Fissured Clay," *Proceedings of the ASCE Specialty Conference on Performance of Earth and Earth-Supported Structures*, Purdue University, Vol. I, Part 1, pp. 243–272.

MOHR, O. (1887). "Über die Bestimmung und die Graphische Darstellung von Trägheitsmomenten ebener Flächen," *Civilingenieur*, columns 43–68; also in *Abhandlungen aus dem Gebiete der Technischen Mechanik*, 2nd ed., W. Ernst u. Sohn, Berlin, pp. 90 and 109 (1914).

MOHR, O. (1900). "Welche Umstände Bedingen die Elastizitätsgrenze und den Bruch eines Materiales?" *Zeitschrift des Vereines Deutscher Ingenieure*, Vol. 44, pp. 1524–1530; 1572–1577.

MORAN, D.E. et al. (1958). "Study of Deep Soil Stabilization by Vertical Sand Drains," OTS *Report, PB 151 692*, Bureau of Yards & Docks, Department of the Navy, Washington.

MORGENSTERN, N.R. AND EISENSTEIN, Z. (1970). "Methods of Estimating Lateral Loads and Deformation," *Proceedings of the ASCE Specialty Conference on Lateral Stresses in the Ground and Design of Earth-Retaining Structures*, Cornell University, pp. 51–102.

MORRIS, D.A. AND JOHNSON, A.I. (1967). "Summary of Hydrologic and Physical Properties of Rock and Soil Materials," as analyzed by the Hydrologic Laboratory of the U.S. Geological Survey, U.S. Geology Survey of Water-Supply Paper 1839-D, 42 p.

MOULIN, G. (1988). "Etat limite d'une Argile Naturelle—L'argile de Pornic," Ph.D. thesis, Ecole National Superieure de Mecanique, Nantes, France.

MOULIN, G. (1989). "Caractérisation de l'État Limite de l'Argile de Pornic," *Canadian Geotechnical Journal*, Vol. 26, No. 4, pp. 705–717.

MROZ, Z. (1967). "On the Description of Anisotropic Hardening," *Journal of Mechanics and Physics of Solids*, Vol. 15, pp. 163–175.

MUIR WOOD, D. (1990). *Soil Behaviour and Critical State Soil Mechanics*, Cambridge University Press, 462 p.

MUIR WOOD, D. (2004). *Geotechnical Modelling*, E & FN Spon, London, 488 p.

MURFF, J.D. (1987). "Pile Capacity in Calcareous Sands: State of the Art," *Journal of the Geotechnical Engineering Division*, ASCE, Vol. 113, No. 5, pp. 490–507.

N

NATIONAL COOPERATIVE HIGHWAY RESEARCH PROGRAM (2006). Rock-socketed Shafts for Highway Structure Foundations, *NCHRP Synthesis 360*, Transportation Research Board, Washington, D.C., 109 p.

NELSON, J.D. AND MILLER, D.J. (1992). *Expansive Soils: Problems and Practice in Foundation and Pavement Engineering*, Wiley, New York, 259 p.

NEWLAND, P.L. AND ALLELY, B.H. (1960). "A Study of the Consolidation Characteristics of a Clay," *Géotechnique*, Vol. X, pp. 62–74.

NEWMARK, N.M. (1935). "Simplified Computation of Vertical Pressures in Elastic Foundations," *University of Illinois Engineering Experiment Station Circular 24*, Urbana, IL, 19 p.

NEWMARK, N.M. (1942). "Influence Charts for Computation of Stresses in Elastic Foundations," *University of Illinois Engineering Experiment Station Bulletin*, Series No. 338, Vol. 61, No. 92, Urbana, IL, Reprinted 1964, 28 p.

NICHOLS, T.C. AND COLLINS, D.S. (1991). "Rebound, Relaxation, and Uplift," Chapter 13 in *The Heritage of Engineering Geology; The First Hundred Years*, G.A. Kiersch (Ed.), Centennial Special Vol. 3, Geological Society of America, pp. 265–276.

NOE, D.C., JOACHIM, C.L., AND RODGERS, W.P. (2007). *A Guide to Swelling Soils for Colorado Homebuyers and Homeowners*, 2nd ed., Special Publication 43, Colorado Geological Survey, Denver, 76 p.

NOORANY, I. (1989). "Classification of Marine Sediments," *Journal of Geotechnical Engineering*, ASCE, Vol. 115, No. 1, pp. 23–37.

NOORANY, I. AND GIZIENSKI, S.F. (1970). "Engineering Properties of Submarine Soils: State-of-the-Art Review," *Journal of the Soil Mechanics and Foundation Division*, ASCE, Vol. 96, No. 5, pp. 1735–1762.

NOORANY, I. AND SEED, H.B. (1965). "In-Situ Strength Characteristics of Soft Clays," *Journal of Soil Mechanics and Foundations Division*, ASCE, Vol. 91, No. SM2, pp. 49–80.

NOORANY, I. AND STANLEY, J.V. (1994). "Settlement of Compacted Fills Caused by Wetting," *Vertical and Horizontal Deformations of Foundations and Embankments*, Geotechnical Special Publication No. 40, ASCE, Vol. 2, pp. 1516–1530.

O

OHTA, Y. AND GOTO, N. (1976). "Estimation of S-wave Velocity in Terms of Characteristic Indices of Soil," *Butsuri-Tanko*, Vol. 29, No. 4, pp. 34–41.

O'KELLY, B.C. AND NAUGHTON, P.J. (2008)."Use of Proximity Transducers for Local Radial Strain Measurements in a Hollow Cylinder Apparatus," *Proceedings of the Fourth International Symposium on Deformation Characteristics of Geomaterials*, Atlanta, GA, Vol. 2, pp. 793–800.

OKA, F., ADACHI, T., AND MIMURA, M. (1988). "Elasto-visco Plastic Constitutive Models for Clays," *International Conference on Rheology and Soil Mechanics*, Coventry, UK, Vol. 1, pp. 12–28.

OSTERBERG, J.O. (1957). "Influence Values for Vertical Stresses in a Semi-infinite Mass Due to an Embankment Loading," *Proceedings of the Fourth International Conference on Soil Mechanics and Foundation Engineering*, London, Vol. I, pp. 393–394.

OSTERBERG, J.O. (1963). "Current Practice in Foundation Design-II," *Chicago Soil Mechanics Lecture Series*, ASCE and Illinois Institute of Technology, pp. 6–22.

OSTERBERG, J.O. (1967). Lecture Notes, CE D-50, Soil Mechanics, Northwestern University (recorded by R.D. Holtz, February 7).

OSTERMAN, J. (1960). "Notes on the Shearing Resistance of Soft Clays," *Acta Polytechnica Scandinavica*, Series CI-2 (AP 263 1959), pp. 1–22.

P

PAPAGIANNAKIS, A.T. AND MASAD, E.A. (2008). *Pavement Design and Materials*, Wiley, Hoboken, NJ, 542 p.

PARSONS, A.W., KRAWCZYK, J., AND CROSS, J.E. (1962). "An Investigation of the Performance on an 8 ½ Ton Vibrating Roller for the Compaction of Soil," Road Research Laboratory, Laboratory Note No. LN/64/AWP. JK. JEC.

PAVLOVSKY, N.N. (1956). *Collected Works*, Akad. Nauk USSR, Leningrad.

PCA. (1992). *PCA Soil Primer*, Portland Cement Association, Skokie, IL, 40 p.

PECK, R.B. (1974). "The Selection of Soil Parameters for the Design of Foundations," *Second Nabor Carrillo Lecture, Seventh National Meeting of the Mexican Society for Soil Mechanics*, Guadalajara, Mexico, pp. 9–49.

PECK, R.B., HANSON, W.E., AND THORNBURN, T.H. (1974). *Foundation Engineering*, 2nd ed., Wiley, New York, 514 p.

PENNER, E. (1963). "Sensitivity in Leda Clay," *Nature*, Vol. 197, No. 4865, pp. 347–348.

PERLOFF, W.H. (1975). "Pressure Distribution and Settlement," Chapter 4 in *Foundation Engineering Handbook*, 1st ed., H.F. Winterkorn and H.Y. Fang (Eds.), Van Nostrand Reinhold, New York, pp. 148–196.

PERLOFF, W.H. AND BARON, W. (1976). *Soil Mechanics—Principles and Applications*, The Ronald Press Company, New York, pp. 359–361.

PERZYNA, P. (1963). "The Constitutive Equations for Rate Sensitive Plastic Materials," *The Quarterly of Applied Mathematics*, Vol. 20, No. 4, pp. 321–332.

PESTANA, J.M. (1994). "A Unified Constitutive Model for Clays and Sands" MIT Sc.D. thesis, 473 p.

PÉWÉ, T.L. (1991). "Permafrost," Chapter 14 in *The Heritage of Engineering Geology; The First Hundred Years*, G.A. Kiersch (Ed.), Centennial Special Vol. 3, Geological Society of America, pp. 277–298.

PHILIP, J.R. (1995). "Desperately Seeking Darcy in Dijon," *Soil Science Society of America Journal*, Vol. 59, No. 2, pp. 319–324.

PIHLAINEN, J.A. (1963). "A Review of Muskeg and Its Associated Engineering Problems," Technical Report 97, Cold Regions Research and Engineering Laboratory, U.S. Army, Hanover, NH, 67 p.

POULOS, H.G. (1988a). "The Mechanics of Calcareous Sediments" Jaeger Memorial Lecture, *Proceedings of the Fifth Australia-New Zealand Geomechanics Conference*, Sydney, pp. 8–41.

POULOS, H.G. (1988b). *Marine Geotechnics*, Unwin Hyman, London, 512 p.

POULOS, H.G. AND DAVIS, E.H. (1974). *Elastic Solutions for Soil and Rock Mechanics*, Wiley, New York, 411 p.

POULOS, S.J. (1981). "The Steady State of Deformation," *Journal of the Geotechnical Engineering Division*, ASCE, Vol. 107, No. 5, pp. 553–562.

POWRIE, W. (2004). *Soil Mechanics: Concepts and Applications*, 2nd ed., E & FN Spon, London, 704 p.

PREVOST, J.H. (1977). "Mathematical Modeling of Monotonic and Cyclic Undrained Clay Behavior," *International Journal for Numerical and Analytical Methods in Geomechanics*, Vol. 1, No. 2, pp. 195–216.

PREVOST, J.H. AND POPESCU, R. (1996). "Constitutive Relations for Soil Materials," *Electronic Journal of Geotechnical Engineering*, 43 p.

PROCTOR, R.R. (1933). "Fundamental Principles of Soil Compaction," *Engineering News-Record*, Vol. 111, Nos. 9, 10, 12, and 13.

PUPPALA, A.J., INTHARASOMBAT, N., AND VEMPATI, R.K. (2005). "Experimental Studies on Ettringite-Induced Heaving in Soils," *Journal of Geotechnical and Geoenvironmental Engineering*, ASCE, Vol. 131, No. 3, pp. 325–337.

PUSCH, R. (1973). General Report on "Physico-Chemical Processes which Affect Soil Structure and Vice Versa," *Proceedings of the International Symposium on Soil Structure*, Gothenburg, Sweden, Appendix p. 33.

Q

QUIGLEY, R.M. AND THOMPSON, C.D. (1966). "The Fabric of Anisotropically Consolidated Sensitive Marine Clay," *Canadian Geotechnical Journal*, Vol. III, No. 2, pp. 61–73.

R

RAJU, A.A. (1956). "The Preconsolidation Pressure in Clay Soils," MSCE thesis, Purdue University, 41 p.

RANKINE, W.J.M. (1857). "On the Stability of Loose Earth," Abstracts of the Papers Communicated to the Royal Society of London, *Proceedings of the Royal Society*, London, Vol. VIII, pp. 185–187.

RAYMOND, G.P. AND WAHLS, H.E. (1976). "Estimating One-Dimensional Consolidation, Including Secondary Compression of Clay Loaded from Overconsolidated to Normally Consolidated State," *Special Report 163*, Transportation Research Board, pp. 17–23.

RAYMOND, G.P., TOWNSEND, D.L., AND LOJKACEK, M.J. (1971). "The Effects of Sampling on the Undrained Soil Properties of the Leda Soil," *Canadian Geotechnical Journal*, Vol. 8, No. 4, pp. 546–557.

RECHENMACHER, A.L. AND FINNO, R.J. (2004). "Digital Image Correlation to Evaluate Shear Banding in Dilative Sands," *Geotechnical Testing Journal*, ASTM, Vol. 27, No. 1, pp. 13–22.

REDDI, L.N. (2003). *Seepage in Soils: Principles and Applications*, Wiley, 448 p.

REED, M.A., LOVELL, C.W., ALTSCHAEFFL, A.G., AND WOOD, L.E. (1979). "Frost Heaving Rate Predicted from Pore Size Distribution," *Canadian Geotechnical Journal*, Vol. 16, No. 3, pp. 463–472.

RENDULIC, L. (1936). "The Relation Between Void Ratio and Effective Stresses for a Remoulded Silty Clay," Discussion D-27, *Proceedings of the First International Conference on Soil Mechanics and Foundation Engineering*, Cambridge, MA, Vol. III, pp. 48–51.

RENDULIC, L. (1937). "Ein Grundesetz der Tonmechanik und Sein Experimenteller Beweiss" ("A Fundamental Principal of Soil Mechanics and Its Experimental Verification"), *Der Bauingenieur*, Vol. 18, pp. 459–467.

REYNOLDS, O. (1885). "On the Dilatancy of Media Composed of Rigid Particles in Contact, with Experimental Illustrations," *Philophical Magazine, Series 5*, Vol. 20, 469 p. (as referenced/quoted in Scott, 1963).

RICHARDS, A.F. (Ed.) (1988). *Vane Shear Strength Testing in Soils: Field and Laboratory Studies*, ASTM Special Technical Publication No. 1014, 378 p.

RICHART, F.E., Jr., HALL, J.R., AND WOODS, R.D. (1970). *Vibrations of Soils and Foundations*, Prentice-Hall, Englewood Cliffs, NJ, 414 p.

RIX, G.J. AND STOKE, K.H. (1991). "Correlation of Initial Tangent Modulus and Cone Penetration Resistance," *Calibration Chamber Testing*, International Symposium on Calibration Chamber Testing, A.B. Huang (Ed.), Elsevier Publishing, New York, pp. 351–362.

ROBERTSON, P.K. AND CAMPANELLA, R.G. (1983). "Interpertation of Cone Penetration Tests. Part I: Sand," *Canadian Geotechnical Journal*, Vol. 20, No. 4, pp. 718–733.

ROBERTSON, P.K., CAMPANELLA, R.G., GILLESPIE, D., AND BY, T. (1988). "Excess Pore Pressures and the Flat Dilatometer Test," *Proceedings of the First International Symposium on Penetration Testing (ISOPT-1)*, Orlando, Vol. 1, pp. 567–576.

ROGERS, C.D.F. (1994). "Types and Distribution of Collapsible Soils," in *Proceedings of the NATO Advanced Research Workshop on Genesis and Properties of Collapsible Soils*, E. Derbyshire, T. Dijkstra, and I.J. Smalley (Eds.), pp. 1–17.

ROSCOE, K.H. AND BURLAND, J.B. (1968). "On the Generalized Stress-Strain Behaviour of Wet Clays," in J. Heyman and F.A. Leckie (Eds.), *Engineering Plasticity*, Cambridge University Press, pp. 535–609.

ROWE, P.W. (1962). "The Stress-Dilatancy Relation for Static Equilibrium of an Assembly of Particles in Contact," *Proceedings of the Royal Society A*, Vol. 269, pp. 500–527.

ROWE, P.W. (1972). "The Relevance of Soil Fabric to Site Investigation Practice," Twelfth Rankine Lecture, *Géotechnique*, Vol. XXII, No. 2, pp. 195–300.

ROWE, P.W., BARDEN. L., AND LEE, I.K. (1964). Energy Components During the Triaxial Cell and Direct Shear Tests," *Géotechnique*, Vol. XIV, No. 3, pp. 247–261.

RUTLEDGE, P.C. (1944). "Relation of Undisturbed Sampling to Laboratory Testing," *Transactions*, ASCE, Vol. 109, pp. 1162–1163.

RUTLEDGE, P.C. (1947). Review of "Cooperative Triaxial Shear Research Program of the Corps of Engineers," USAE Waterways Experiment Station, Vicksburg, MS, 178 p.

S

SAADA, A.S. AND BIANCHINI, G.F. (1975). "Strength of One Dimensionally Consolidated Clays," *Journal of the Geotechnical Engineering Division*, ASCE, Vol. 101, No. GT11, pp. 1151–1164.

SABATINI, P.J., BACHUS, R.C., MAYNE, P.W., SCHNEIDER, J.A., AND ZETTLER, T.E. (2002). Evaluation of Soil and Rock Properties, Geotechnical Engineering Circular No. 5, Federal Highway Administration, Report No. FHWA-IF-02–034, 385 p.

SÄLLFORS, G. (1975). "Preconsolidation Pressure of Soft, High-plastic Clays," Ph.D. thesis, Chalmers University of Technology, Gothenburg, Sweden, 231 p.

SAMTANI, N.C. AND NOWATSKI, E.A. (2006). Soils and Foundations Workshop Reference Manual, NHI Course No. 132012, Federal Highway Administration, Publication No. FHWA-NHI-06–088, 944 p.

SANGLERAT, G. (1972). *The Penetrometer and Soil Exploration*, Elsevier, Amsterdam, 464 p.

SANTAGATA, M.C., GERMAINE, J.T., AND LADD, C.C. (2005). "Factors Affecting the Initial Stiffness of Cohesive Soils," *Journal of Geotechnical and Geoenvironmental Engineering*, ASCE, Vol. 131, No. 4 pp. 430–441.

SANTI, P.M. AND SHAKOOR, A. (Eds.) (1997). *Characterization of Weak and Weathered Rock Masses*, Association of Engineering Geologists Special Publication No. 9, 233 p.

SATIJA, B.S. (1978). "Shear Behaviour of Partly Saturated Soils," Ph.D. thesis, Indian Institute of Technology, Delhi, 327 p.

SAWANGSURIYA, A., EDIL, T.B., AND BOSSCHER, P.J. (2003). "Relationship Between Soil Stiffness Gauge Modulus and Other Test Moduli for Granular Soils," *Transportation Research Record No. 1849*, Transportation Research Board, Washington, DC, pp. 3–10.

SCHMERTMANN, J.H. (1955). "The Undisturbed Consolidation Behavior of Clay," *Transactions*, ASCE, Vol. 120, pp. 1201–1233.

SCHMERTMANN, J.H. (1970). "Suggested Method for Screw-Plate Load Test," *Special Procedures for Testing Soil and Rock for Engineering Purposes*, 5th ed., ASTM Special Technical Publication 479, pp. 81–85.

SCHMERTMANN, J.H. (1975). "Measurement of In Situ Shear Strength," State-of-the-Art Report, *Proceedings of the ASCE Specialty Conference on In Situ Measurement of Soil Properties*, Raleigh, NC, Vol. II, pp. 57–138.

SCHMERTMANN, J.H. (1978). *Guidelines for Cone Penetration Test, Performance and Design*, Federal Highway Administration, Report FHWA-TS-78–209, 145 p.

SCHMERTMANN, J.H. (1986). "Suggested Method for Performing the Flat Dilatometer Test," *Geotechnical Testing Journal*, ASTM, Vol. 9, No. 2, pp. 93–101.

SCHMERTMANN, J.H. (1993). "Conical Test Load to Measure Soil Compressibility," Technical Note, *Journal of Geotechnical Engineering*, ASCE, Vol. 119, No. 5, pp. 965–971.

SCHMERTMANN, J.H. (1994). Closure to discussion of 1993 paper, *Journal of Geotechnical Engineering*, ASCE, Vol. 120, No. 11, 2075 p.

SCHMIDT, B. (1966). Discussion of "Earth Pressures at Rest Related to Stress History," *Canadian Geotechnical Journal*, Vol. III, No. 4, pp. 239–242.

SCHMIDT, B. (1967). "Lateral Stresses in Uniaxial Strain," *Bulletin No. 23*, Danish Geotechnical Institute, pp. 5–12.

SCHOFIELD, A. AND WROTH, P. (1968). *Critical State Soil Mechanics*, McGraw-Hill, London.

SCHOLEY, G.K., FROST, J.D., LOPRESTI, D.C.F., AND JAMIOLKOWSKI, M. (1995). "A Review of Instrumentation for Measuring Small Strains during Triaxial Testing of Soil Specimens," *Geotechnical Testing Journal*, ASTM, Vol. 18, No. 2, pp. 137–156.

SCHUSTER, R.L. AND MULLINEAUX, D.R. (1991). "Volcanic Activity," Chapter 11 in *The Heritage of Engineering Geology; The First Hundred Years*, G.A. Kiersch (Ed.), Geological Society of America, Boulder, CO, Vol. 3, pp. 233–250.

SCHWAB, E.F. (1976). "Bearing Capacity, Strength, and Deformation Behaviour of Soft Organic Sulphide Soils," Ph.D. thesis, Institutionen för Jord- och Bergmekanik, Kungliga Tekniska Högskolan, Stockholm, 368 p.

SCOTT, R.F. (1963). *Principles of Soil Mechanics*, Addison-Wesley, Reading, MA, pp. 267–275.

SEED, H.B. (1964). Lecture Notes, CE 271, "Seepage and Earth Dam Design," University of California, Berkeley (recorded by W.D. Kovacs, April 13).

SEED, H.B. (1979). "Soil Liquefaction and Cyclic Mobility Evaluation for Level Ground During Earthquakes," *Journal of the Geotechnical Engineering Division*, ASCE, Vol. 105, No. GT2, pp. 201–255.

SEED, H.B. (1987). "Design Problems in Soil Liquefaction," *Journal of Geotechnical Engineering*, ASCE, Vol. 113, No. 8, pp. 827–845.

SEED, H.B. AND CHAN, C.K. (1959). "Structure and Strength Characteristics of Compacted Clays," *Journal of the Soil Mechanics and Foundations Division*, ASCE, Vol. 85, No. SM5, pp. 87–128.

SEED, H.B. AND IDRISS, I.M. (1970). "Soil Moduli and Damping Factors for Dynamic Response Analyses, *Report No. EERC 70–10*, Earthquake Engineering Research Center, Berkeley, CA, 40 p.

SEED, H.B. AND LEE, K.L. (1967). "Undrained Strength Characteristics of Cohesionless Soils," *Journal of the Soil Mechanics and Foundations Division*, ASCE, Vol. 93, No. SM6, pp. 333–360.

SEED, H.B., WONG, R.T., IDRISS, I.M., AND TOKIMATSU, K. (1984). "Moduli and Damping Factors for Dynamic Analysis of Cohesionless Soils," Report No. UBC/EERC 84/14, University of California, Berkeley, 40 p.

SEED, H.B., WONG, R.T., IDRISS, I.M., AND TOKIMATSU, K. (1986). "Moduli and Damping Factors for Dynamic Analysis of Cohesionless Soils," *Journal of Geotechnical Engineering*, ASCE, Vol. 112. No. 11, pp. 1016–1032.

SEED, H.B., WOODWARD, R.J., AND LUNDGREN, R. (1962). "Prediction of Swelling Potential for Compacted Clays," *Journal of the Soil Mechanics and Foundations Division*, ASCE, Vol. 88, No. SM4, pp. 107–131.

SELIG, E.T. AND LADD, R.S. (Eds.) (1973). "Evaluation of Relative Density and Its Role in Geotechnical Projects Involving Cohesionless Soils", *Proceedings of a Symposium*, ASTM Special Technical Publication No. 523, 510 p.

SELIG, E.T. AND YOO, T.S. (1977). "Fundamentals of Vibratory Roller Behavior," *Proceedings of the Ninth International Conference on Soil Mechanics and Foundation Engineering*, Tokyo, Vol. 2, pp. 375–380.

SHARP, R.P. (1960). *Glaciers*, Condon Lectures, Oregon State System of Higher Education, Eugene, 78 p.

SHEAHAN, T.C. AND KALIAKIN, V.N. (Eds.) (1996). *Measuring and Modeling Time Dependent Soil Behavior*, Geotechnical Special Publication No. 61, ASCE, New York, 273 p.

SHEAHAN, T.C., LADD, C.C., AND GERMAINE, J.T. (1996). "Rate-dependent Undrained Shear Behavior of Saturated Clay," *Journal of Geotechnical Engineering*, ASCE, Vol. 122, No. 2, pp. 99–108.

SHERARD, J.L., WOODWARD, R.J., GIZIENSKI, S.F., AND CLEVENGER, W.A. (1963). *Earth and Earth-Rock Dams; Engineering Problems of Design and Construction*, Wiley, New York, 725 p.

SILVER, M.L. AND SEED, H.B. (1971). "Volume Changes in Sands Due to Cyclic Loading," *Journal of the Soil Mechanics and Foundations Division*, ASCE, Vol. 97, No. 9, pp. 1171–1182.

SIMONS, N.E. (1958). Discussion of "Test Requirements for Measuring the Coefficient of Earth Pressure at Rest," *Proceedings of the Conference on Earth Pressure Problems*, Brussels, Vol. III, pp. 50–53.

SIMONS, N.E. (1974). "Normally Consolidated and Lightly Overconsolidated Cohessive Materials," General Report, *Proceedings of the Conference on Settlement of Structures*, Cambridge University, British Geotechnical Society, pp. 500–530.

SITAR, N. (Ed.) (1988). *Geotechnical Aspects of Karst Terrains: Explaoration, Foundation Design and Performance, and Remidial Measures*, Geotechnical Special Publication No. 14, ASCE, 165 p.

SKEMPTON, A.W. (1953). "The Colloidal Activity of Clays," *Proceedings of the Third International Conference on Soil Mechanics and Foundation Engineering*, Vol. I, pp. 57–61

SKEMPTON, A.W. (1954). "The Pore-Pressure Coefficients *A* and *B*," *Géotechnique*, Vol. IV, pp. 143–147.

SKEMPTON, A.W. (1960). "Effective Stress in Soils, Concrete and Rocks," in *Proceedings of the Conference on Pore Pressure and Suction in Soils*, Butterworths, London, pp. 4–16.

SKEMPTON, A.W. AND HENKEL, D.J. (1953). "The Post-Glacial Clays of the Thames Estuary at Tillbury and Shellhaven," *Proceedings of the Third International Conference on Soil Mechanics and Foundation Engineering*, Zurich, Vol. I, pp. 302–308.

SKEMPTON, A.W. AND NORTHEY, R.D. (1952). "The Sensitivity of Clays," *Géotechnique*, Vol. III, No. 1, pp. 30–53.

SKEMPTON, A.W. AND SOWA, V.A. (1963). "The Behaviour of Saturated Clays During Sampling and Testing," *Géotechnique*, Vol. XIV, No. 4, pp. 269–290.

SLADEN, J.A., KRAHN, J., AND HOLLANDER, R.D. (1986). Discussion of "A State Parameter for Sands," by K. Been and M.G. Jefferies, Vol. XXXV, No. 2, pp. 99–112; *Géotechnique*, Vol. XXXIV, No. 1, pp. 123–124.

SMSS (1990). *Keys to Soil Taxonomy*, Soil Management Support Services Survey Staff, SMSS Technical Monograph No. 6, 4th ed., Blacksburg, VA, 422 p.

SMITH, R.E., GABR, M.A., AND KULA, J.R. (1991). "Soil-Rock Transition Zone: Uncertainties for Design and Construction," in W.F. Kane and B. Amadei (Eds.), *Detection of and Construction at the Soil/Rock Interface, Proceedings of the Symposium*, Geotechnical Special Publication No. 28, ASCE, pp. 91–106.

SMITH, R.E. AND WAHLS, H.E. (1969). "Consolidation Under Constant Rates of Strain," *Journal of the Soil Mechanics and Foundations Division*, ASCE, Vol. 95, No. 2, pp. 519–539.

SNEDEGAR, W.H. (1983). Letter to the Editor, *American Journal of Physics*, Vol. 51, No. 8, 684 p.

SODERMAN, L.G. AND KIM, Y.D. (1970). "Effect of Groundwater Levels on Stress History of the St. Clair Clay Till Deposit," *Canadian Geotechnical Journal*, Vol. 7, No. 2, pp. 173–187.

SOIL CLASSIFICATION WORKING GROUP (1998). *The Canadian System of Soil Classification*, 3rd ed., Agriculture and Agri-Food Canada, Publication 1646 (Revised), 187 p.

SOWERS, G.F. (1979). *Introductory Soil Mechanics and Foundations: Geotechnical Engineering*, 4th ed., Macmillian, New York, 621 p.

SOWERS, G.F. (1992). "Natural Landslides," in *Stability and Performance of Slopes and Embankments-II, Proceedings of a Specialty Conference*, R.B. Seed and R.W. Boulanger (Eds.), Geotechnical Special Publication No. 31, ASCE, pp. 804–833.

SOWERS, G.F. (1996). *Building on Sinkholes: Design and Construction of Foundations in Karst Terrain*, ASCE Press, 202 p.

SOWERS, G.F. AND RICHARDSON, T.L. (1983). "Residual Soils of the Piedmont and Blue Ridge," *TRR 919*, National Academy Press, Washington, D.C., pp. 10–16.

SRIDHARAN, A. AND PRAKASH, K. (2000). "Classification Procedures for Expansive Soils," *Geotechnical Engineering*, Proceedings of the Institution of Civil Engineers, Vol. 143, pp. 235–240.

STATENS JÄRNVÄGERS GEOTEKNISKA KOMMISSION (1922). *1914–1922 Slutbetänkande, (1914–1922 Final Report)*, Presented to the Board of the Royal Swedish Railroads, Stockholm, 180 p. (42 plates).

STOKOE, K.H., II AND LODDE, P.F. (1978). "Dynamic Response of San Francisco Bay Mud," *Proceedings of the Earthquake Engineering and Soil Dynamics Conference*, Los Angeles, ASCE, Vol. II, pp. 940–959.

STOKOE, K.H., II, DARENDELI, M.B., ANDRUS, R.D., AND BROWN, L.T. (1999). "Dynamic Soil Properties: Laboratory, Field and Correlation Studies," *Proceedings of the Second International Conference on Earthquake Geotechnical Engineering*, Lisbon, Portugal, June, pp. 811–845.

SULTAN, H.A. AND SEED, H.B. (1967). "Stability of Sloping Core Earth Dams," *Journal of the Soil Mechanics and Foundation Division*, ASCE, Vol. 93, No. SM4, pp. 45–67.

T

TAN, T.K. (1957). "Structure Mechanics of Clays," *Academia Sinica*, Soil Mechanics Laboratory, Institute of Civil Engineering and Architecture, Harbin, China, pp. 1–17.

TATSUOKA, F. AND SHIBUYA, S. (1992). "Deformation Characteristics of Soils and Rocks from Field and Laboratory Tests," *Report of the Institute of Industrial Science, The University of Tokyo*, Vol. 37, No. 1 (Serial No. 235), 136 p.

TAVENAS, F.A., BLANCHETTE, G., LEROUEIL, S., ROY, M., AND LAROCHELLE, P. (1975). "Difficulties in the In Situ Determination of K_o in Soft Sensitive Clays," *Proceedings of the ASCE Specialty Conference on In Situ Measurement of Soil Properties*, Raleigh, NC, Vol. I, pp. 450–476.

TAVENAS, F.A., CHAPEAU, C., LAROCHELLE, P., AND ROY, M. (1974). "Immediate Settlements of Three Test Embankments on Champlain Clay," *Canadian Geotechnical Journal*, Vol. 11, No. 1, pp. 109–141.

TAVENAS, F. AND LEROUEIL, S. (1977). "Effects of Stresses and Time on Yielding of Clays," *Proceedings of the Ninth International Conference on Soil Mechanics and Foundation Engineering*, Tokyo, Vol. 1, pp. 319–326.

TAVENAS, F. AND LEROUEIL, S. (1979). "Les Concepts d'Étude Limite et l'État Critique et Leurs Application Pratiques à l'Étude des Argiles," *Revue Française de Géotechnique*, Vol. VI, pp. 27–49.

TAVENAS, F. AND LEROUEIL, S. (1985). "Structural Effects on the Behaviour of Natural Clays," Discussion on Session 2B on Laboratory Testing, *Proceedings of the Eleventh International Conference Soil Mechanics and Foundation Engineering*, Vol. 5, pp. 2693–2694.

TAYLOR, D.W. (1948). *Fundamentals of Soil Mechanics*, Wiley, New York, 712 p.

TAYLOR, P.W. AND BACCHUS, D.R. (1969). "Dynamic Cyclic Strain Test on a Clay," *Proceedings of the Seventh International Conference on Soil Mechanics and Foundation Engineering*, Mexico City, Vol 1, pp. 401–409.

TAYLOR, P.W. AND HUGHES, J.M. (1965). "Dynamic Properties of Foundation Subsoil as Determined from Laboratory Tests," *Proceedings of the Third World Conference on Earthquake Engineering*, New Zealand, Vol. 1, pp. 196–209.

TAYLOR, P.W. AND MENZIES, B.K. (1963). "Damping Characteristics of Dynamically Loaded Clay," *Proceedings of the Fourth Australian–New Zealand Conference on Earthquake Engineering*, New Zealand, Vol. 1, pp. 196–211.

TERZAGHI, CH. (1920). "New Facts about Surface Friction," *The Physical Review, N.S.*, Vol. XVI, No. 1, pp. 54–61.

TERZAGHI, K. (1922). "Der Grundbruch an Stauwerken and seine Verhütung," *Die Wasserkraft*, Vol. 17, No. 24, pp. 445–449; reprinted in *From Theory to Practice in Soil Mechanics*, Wiley, New York, pp. 114–118.

TERZAGHI, K. (1925a). *Erdbaumechanik auf Bodenphysikalischer Grundlage*, Franz Deuticke, Leipzig und Wein, 399 p.; "*Structure and Volume of Voids of Soils*," pp. 10–13 (translated by A. Casagrande) in Terzaghi (1960).

TERZAGHI, K. (1925b). "Modern Conceptions Concerning Foundation Engineering," *Journal of the Boston Society of Civil Engineers*, Vol. 12, No. 10; also published in *Contributions to Soil Mechanics 1925–1940*, BSCE, pp. 1–43.

TERZAGHI, K. (1927). "Concrete Roads—A Problem in Foundation Engineering," *Journal of the Boston Society of Civil Engineers*, May; reprinted in *Contributions to Soil Mechanics 1925–1940*, BSCE, pp. 57–58.

TERZAGHI, K. (1929). "Effect of Minor Geologic Details on the Safety of Dams," American Institute of Mining and Metallurgical Engineers, *Technical Publication No. 215*, pp. 31–44.

TERZAGHI, K. (1938). "Die Coulombsche Gleichung für den Scherwiderstand bindiger Boden" ("The Coulomb Equation for the Shearing Resistance of Cohesive Soils"), *Die Bautechnik*, Vol. 16, No. 26, pp. 343–346.

TERZAGHI, K. (1943). *Theoretical Soil Mechanics*, Wiley, New York, 510 p.
TERZAGHI, K. (1960). *From Theory to Practice in Soil Mechanics*, Wiley, New York, 425 p.
TERZAGHI, K. AND FRÖHLICH, O.K. (1936). *Theorie der Setzung von Tonschichten* ("*Theory of the Consolidation of Clay Layers*,") F. Deuticke, Vienna.
TERZAGHI, K. AND PECK, R.B. (1967). *Soil Mechanics in Engineering Practice*, 2nd ed., Wiley, New York, 729 p.
TERZAGHI, K., PECK, R.B., AND MESRI, G. (1996). *Soil Mechanics in Engineering Practice*, 3rd ed., Wiley, New York, 549 p.
THIERS, G.R. AND SEED, H.B. (1968). "Cyclic Stress-Strain Characteristics of Clay," *Journal of the Soil Mechanics and Foundation Division*, ASCE, Vol. 94, No. SM2, pp. 555–569.
THOMPSON, J.C., LELIEVRE, B., BECKIE, R.D., NEGUS, K.J. (1987). "A Simple Procedure for Computation of Vertical Soil Stresses for Surface Regions of Arbitrary Shape and Loading," *Canadian Geotechnical Journal*, Vol. 24, No. 1, pp. 143–145.
THORNBURY, W.D. (1954). *Principles of Geomorphology*, Wiley, New York, 618 p.
THORNBURY, W.D. (1969). *Principles of Geomorphology*, 2nd ed., Wiley, New York, 594 p.
TODD, D.K. (1980). *Groundwater Hydrology*, 2nd ed., Wiley, New York, 535 p.
TODD, D.K. AND MAYS, L.W. (2004). *Groundwater Hydrology*, 3rd ed., Wiley, New York, 656 p.
TORREY, V.H. AND DONAGHE, R.T. (1994). "Compaction Control of Earth-Rock Mixtures: A New Approach," *Geotechnical Testing Journal*, ASTM, Vol. 17, No. 3, pp. 371–386.
TRANSPORTATION RESEARCH BOARD (TRB) (1977). *Soil Taxonomy and Soil Properties, TRR 642*, Transportation Research Board, 81 p.
TURNBULL, W.J. (1950). "Compaction and Strength Tests on Soil," presented at Annual Meeting, ASCE, January, as cited by Lambe, T.W. and Whitman, R.V. (1969), *Soil Mechanics*, Wiley, New York, 517 p.
TURNBULL, W.J. AND FOSTER, C.R. (1956). "Stabilization of Materials by Compaction," *Journal of the Soil Mechanics and Foundations Division*, ASCE, Vol. 82, No. SM2, pp. 934–1 to 934–23; also in *Transactions*, ASCE, Vol. 123, (1958), pp. 1–26.
TURNER, H.K. AND SCHUSTER, R.L. (Eds.) (1996). *Landslides: Investigation and Mitigation*, Special Report 247, Transportation Research Board, National Academy Press, Washington, 673 p.

U

ULUSAY, R. AND HUDSON, J. (Eds.) (2007). *The Complete ISRM Suggsted Methods for Rock Characterization, Testing, and Monitoring: 1974–2006*, International Society for Rock Mechanics, Laboratório Nacional de Engenharia Civil, Lisboa, Portugal.
U.S. ARMY CORPS OF ENGINEERS (1986). "Laboratory Soils Testing," *Engineer Manual EM 1110–2–1906*, 282 p.
U.S. ARMY CORPS OF ENGINEERS (1994). "Engineering and Design-Rock Foundations," *Engineer Manual EM 1110–1–2908*, 119 p.
U.S. ARMY CORPS OF ENGINEERS (1999). *Construction Control for Earth and Rockfill Dams*, Technical Engineering and Design Guides as adapted from the U.S. Army Corps of Engineers, No. 27, ASCE Press, 100 p.; also published as U.S. Army Corps of Engineers Engineering Manual. EM-1110–2–1911.
U.S. ARMY CORPS OF ENGINEERS (1994). *Settlement Analysis*, Technical Engineers and Design Guide No. 9, Reprinted by ASCE, 136 p.
U.S. ARMY ENGINEER WATERWAYS EXPERIMENT STATION (1949). "Compaction Studies on Silty Clay," *Report No. 2 of Technical Memorandum 3–271*.
U.S. ARMY ENGINEER WATERWAYS EXPERIMENT STATION (1949). "Simplification of the Liquid Limit Test Procedure," *Technical Memorandum No. 3–286*, Correlations of Soil Properties with Geologic Information, Report No. 1, Corps of Engineers, U.S. Army, 48 p.

U.S. Army Engineer Waterways Experiment Station (1960). "The Unified Soil Classification System," *Technical Memorandum No. 3-357*; Appendix A, Characteristics of Soil Groups Pertaining to Embankments and Foundations, 1953; Appendix B, Characteristics of Soil Groups Pertaining to Roads and Airfields, 1957.

U.S. Bureau of Reclamation (1974). *Earth Manual*, 2nd ed., Denver, 810 p.

U.S. Department of the Army (1983). *Foundations in Expansive Soils*, Technical Manual No. TM 5-818-7, Office of the Chief of Engineers, Washington, D.C., 98 p.

U.S. Department of the Army (1984). *Engineering and Design - Pavement Criteria for Seasonal Frost Conditions - Mobilization Construction*, Engineer Manual EM 1110-3-138, 98 p.

U.S. Department of the Army (1987). *Arctic and Subartic Construction—General Provisions*, Vol. 1, Technical Manual TM 5-852-1, 55 p.

U.S. Department of the Army, Navy, and Air Force (1971). "Dewatering and Groundwater Control for Deep Excavations," Chapter 6 in *Army Tecchnical Manual No. 5-818-5/NAVFAC Manual P-418/Air Force Manual 88-5*, 187 p.

U.S. Department of Defense 13 Soil Dynamics and Special Design Aspects Publ. MIL-HDBK-1007/3, U.S. Navy Naval Facilities Engineering Command, Norfolk, VA, 145 p.

U.S. Department of the Interior (1987). *Design of Small Dams*, 3rd ed., Bureau of Reclamation, U.S. Government Printing Office, Denver, 860 p.

U.S. Department of the Interior (1990). *Earth Manual*, Part 1, 3rd ed., Materials Engineering Branch, 311 p.

U.S. Department of the Interior (1998). *Earth Manual*, Part 2, 3rd ed., Materials Engineering Branch, 1270 p.

U.S. Department of the Interior (1995). *Ground Water Manual*, 2nd ed., Bureau of Reclamation, U.S. Government Printing Office, Washington, 661 p.

U.S. Department of the Interior (1998). *Engineering Geology Field Manual*, U.S. Government Printing Office, Washington, D.C. 478 p.

U.S. Navy (1971). "Soil Mechanics, Foundations, and Earth Structures," *NAVFAC Design Manual DM-7*, Washington, D.C.

U.S. Navy (1986). "Soil Mechanics, Foundations, and Earth Structures," *NAVFAC Design Manual DM-7.2*, Washington, D.C.

V

Vaid, Y.P. and Campanella, R.G. (1974). "Triaxial and Plane Strain Behavior of Natural Clay," *Journal of the Geotechnical Engineering Division*, ASCE, Vol. 100, No. 3, pp. 207-224.

Van Der Merwe, D.H. (1964). "The Prediction of Heave from the Plasticity Index and the Percentage Clay Fraction of Soils," *Civil Engineering in South Africa*, Vol. 6, No. 6, pp. 103-107; as referenced in Nelson and Miller (1992) and Canadian Geotechnical Society (2006).

Van Olphen, H. (1991). *An Introduction to Clay Colloid Chemistry: For Clay Technologists, Geologists, and Soil Scientists*, 2nd ed., Krieger Publ. Co., Malabar, FL, 318 p.

Vipulanandan, C., Addison, M.B., and Hasen, M. (Eds.) (2001). "Expansive Clay Soils and Vegetative Influence on Shallow Foundations," *Proceedings of the Geo-Institute Shallow Foundations and Soil Properties Committee Sessions and the ASCE 2001 Civil Engineering Conference*, Geotechnical Special Publication 115, ASCE, 265 p.

Von Bandat, H.F. (1962). *Aerogeology*, Gulf Publishing Company, Houston, TX, 350 p.

Von Rosenvinge, T. (2006). Personal communication.

Vucetic, M. and Dobry, R. (1991). "Effect of Soil Plasticity on Cyclic Response," *Journal of Geotechnical Engineering*, Vol. 117, No. 1, pp. 89-107.

W

WAHLS, H.E. (1962). "An Analysis of Primary and Secondary Consolidation," *Journal of the Soil Mechanics and Foundations Division*, ASCE, Vol. 88, No. SM6, pp. 207–231.

WALLACE, G.B. AND OTTO, W.C. (1964). "Differential Settlement at Selfridge Air Force Base," *Journal of the Soil Mechanics and Foundations Division*, ASCE, Vol. 90, No. SM5, pp. 197–220; also in *Design of Foundations for Control of Settlement*, ASCE, pp. 249–272.

WARSHAW, C.M. AND ROY, R. (1961). "Classification and a Scheme for the Identification of Layer Silicates," *Geological Society of America Bulletin*, Vol. 72, pp. 1455–1492.

WEISSMAN, G.F. AND HART, R.R. (1961). "The Damping Capacity of Some Granular Soils," Symposium on Soil Dynamics, *ASTM Special Technical Publication No. 305*, June 1961, pp. 45–54.

WELSH, R.A., VALLEJO, L.E., LOVELL, C.W., AND ROBINSON, M.K. (1991). "The U.S. Office of Surface Mining (OSM) Proposed Strength-Durability Classification System," in W.F. Kane and B. Amadei (Eds.), *Detection of and Construction at the Soil/Rock Interface*, Geotechnical Special Publication No. 28, ASCE, pp. 1–15.

WESLEY, L.D. AND IRFAN, T.Y. (1997). "Classification of Residual Soils," Chapter 2 in *Mechanics of Residual Soils*, G.E. Blight (Ed.), Balkema, 237 p.

WEST, T.R. (1995). *Geology Applied to Engineering*, Prentice-Hall, Englewood Cliffs, NJ, 560 p.

WESTERGAARD, H.M. (1938). "A Problem of Elasticity Suggested by a Problem in Soil Mechanics: A Soft Material Reinforced by Numerous Strong Horizontal Sheets," in *Contributions to the Mechanics of Solids, Stephen Timoshenko 60th Anniversary Volume*, Macmillan, New York, pp. 268–277.

WHITMAN, R.V. AND K.A. HEALY (1962). "Shear Strength Testing of Sands During Rapid Loading," *Journal of the Soil Mechanics and Foundations Division*, ASCE, Vol. 88, No. 2, pp. 99–132.

WHITTLE, A.J. (1987). "A Constitutive Model for Overconsolidated Clays with Application to the Cyclic Loading of Friction Piles," MIT Sc.D. thesis, 641 p.

WILLIAMSON, D.A. AND KUHN, D.R. "The Unified Rock Classification System," *Rock Classification Systems for Engineering Purposes*, ASTM Special Technical Publication 984, L. Kirkaldale (Ed.), American Society for Testing and Materials, Philadelphia, pp. 7–16.

WILSON, S.D. (1970). "Suggested Method of Test for Moisture-Density Relations of Soils Using Harvard Compaction Apparatus," *Special Procedures for Testing Soil and Rock for Engineering Purposes*, 5th ed., ASTM Special Technical Publication 479, pp. 101–103.

WINELAND, J.D. (1975). "Borehole Shear Device," *Proceedings of the ASCE Specialty Conference on In Situ Measurement of Soil Properties*, Raleigh, NC, Vol. I, pp. 511–522.

WISSA, A.E.Z. (1969). "Pore Pressure Measurement in Saturated Stiff Soils," *Journal of the Soil Mechanics and Foundations Division*, ASCE, Vol. 95, No. SM4, pp. 1063–1073.

WISSA, A.E.Z., CHRISTIAN, J.T., DAVIS, E.H., AND HEIBERG, S. (1971). "Consolidation Testing at Constant Rates of Strain," *Journal of the Soil Mechanics and Foundations Division*, ASCE, Vol. 97, No. 10, pp. 1393–1413.

WOLFF, T.F. (1995). *Spreadsheet Applications in Geotechnical Engineering*, PWS Publishing, Boston, 305 p., with disk.

WONG, P.K.K. AND MITCHELL, R.J. (1975). "Yielding and Plastic Flow of Sensitive Cemented Clay," *Géotechnique*, Vol. XXV, No. 4, pp. 763–782.

WOODS, R.D. (Ed.) (1994). *Geophysical Characterization of Sites*, ISSMFE Technical Committee No. 10, Oxford & IBS Publishing, 141 p.

WOODS, K.B., MILES, R.D., AND LOVELL, C.W. (1962). "Origin, Formation, and Distribution of Soils in North America," Chapter 1 in *Foundation Engineering*, G.A. Leonards (Ed.), pp. 1–65.

WROTH, C.P. (1972). "General Theories of Earth Pressures and Deformations," General Report, *Proceedings of the Fifth European Conference on Soil Mechanics and Foundation Engineering*, Madrid, Vol. II, pp. 33–52.

WROTH, C.P. (1975). "In Situ Measurement of Initial Stresses and Deformation Characteristics," *Proceedings of the ASCE Specialty Conference on In Situ Measurement of Soil Properties*, Raleigh, NC, Vol. II, pp. 181–230.

WYLLIE, D.C. (1999). *Foundations on Rock*, 2nd ed., E & FN Spon, London, 432 p.

WYLLIE, D.C. (1996). "Stabilization of Rock Slopes," Chapter 18 in *Landslides: Investigation and Mitigation*, Special Report 247, Transportation Research Board, National Academy Press, Washington, pp. 474–504.

XYZ

YAMAMURO, J.A. AND ABRANTES, A.E. (2005). "Behavior of Medium Sand Under Very High Strain Rates," in J.A. Yamamuro and J. Koseki (Eds.), *Geomechanics: Testing, Modeling, and Simulation*, Geotechnical Special Publication 143, ASCE, pp. 61–70.

YODER, E.J. AND WITCZAK, M.W. (1975). *Principles of Pavement Design*, Wiley, New York, 711 p.

YONG, R.N. AND KO, H.Y. (Eds.) (1980). Limit Equilibrium, Plasticity and Generalized Stress-Strain in Geotechnical Engineering, *Proceedings of the Workshop Sponsored by NSF and NSERC*, McGill University, Montreal, ASCE, 871 p.

YONG, R.N. AND SHEERAN, D.E. (1973). "Fabric Unit Interaction and Soil Behaviour," *Proceedings of the International Symposium on Soil Structure*, Gothenburg, Sweden, pp. 176–183.

YONG, R.N. AND WARKENTIN, B.P. (1975). *Soil Properties and Behaviour*, Elsevier, New York, 449 p.

YU, X. AND DRNEVICH, V.P. (2004). "Soil Water Content and Dry Density by Time Domain Reflectometry," *Journal of Geotechnical and Geoenvironmental Engineering*, ASCE, Vol. 130, No. 9, pp. 922–934.

ZIMMIE, T.F. (1973). "Soil Tests on a Clay from Skå-Edeby, Sweden," Norwegian Geotechnical Institute, Internal Report No. 50306–3, 21 p.

ZIPCZECK, Z.Z. (1956). "Soknak cask szemét, ami nekünk Kenyér meg vaj," ("Some People Call It Dirt, We Call it Bread & Butter"), *Proceedings of the Hungarian Academy of Sciences*, Vol. 104, pp. 47–65 (in Hungarian).

Index

(n following page number indicates note, t indicates table)

D

Q

R

S

T

U